

Materials

2018 Annual Progress Report

Vehicle Technologies Office

(This page intentionally left blank)

Disclaimer

This report was prepared as an account of work sponsored by an agency of the United States government. Neither the United States government nor any agency thereof, nor any of their employees, makes any warranty, express or implied, or assumes any legal liability or responsibility for the accuracy, completeness, or usefulness of any information, apparatus, product, or process disclosed or represents that its use would not infringe privately owned rights. Reference herein to any specific commercial product, process, or service by trade name, trademark, manufacturer, or otherwise does not necessarily constitute or imply its endorsement, recommendation, or favoring by the United States government or any agency thereof. The views and opinions of authors expressed herein do not necessarily state or reflect those of the United States government or any agency thereof.

Acknowledgements

First and foremost, the Principal Investigators from industry, academia, and the national laboratories who supplied the content of these reports are to be acknowledged and commended. It is their work that moves our nation forward to improved and more affordable transportation, as well as increased energy security.

Thank you to the project managers at the National Energy Technology Laboratory for continued support administering these projects.

We would also like to acknowledge Energetics for their help in preparing and publishing this report.

H. Felix Wu, Ph. D

Technology Manager, Composite Materials
Vehicle Technology Office

Jerry L. Gibbs

Technology Manager, Propulsion Materials
Vehicle Technology Office

Sarah Kleinbaum

Technology Manager, Lightweight Materials
Vehicle Technology Office

Acronyms and Abbreviations

symbols

α	yarn angle (when referring to fabrics)
α	a fitting constant used in a power law relationship for solidification modeling
$\alpha(T)$	the temperature-dependent coefficient of thermal expansion
β	a fitting constant used in a power law relationship for solidification modeling
β phase	In Mg-Al alloy, $Mg_{17}Al_{12}$, the main precipitate and reinforced phase
ε	strain
γ'	major strengthening phase
η	thermoelectric module efficiency
μ	friction coefficient
μ_f	friction coefficient for the faying (sheet/sheet) interface
μ_{hs}	friction coefficient for the hone/sheet interface
μm	micrometer
μs	microsecond
$\mu V/K$	microvolts per Kelvin
θ	inter-yarn angle or fiber misalignment angle (when used for modeling of fabric materials)
θ	total energy of the deleterious phase (when used in modeling of metal precipitates)
θ'	total energy of the strengthening precipitate (when used in modeling of metal precipitates)
σ	stress (or strength)
σ_{UTS}	ultimate tensile strength
σ_{ys}	yield strength
$\tau 10$	a bimetallic automotive component consisting of an Al-Si light alloy ($Al_{12}Fe_5Si_3$) reinforced with a cast-iron insert
1D	one-dimensional
2D	two-dimensional
2T	two thickness
3D	three-dimensional
3T	three thickness
5xxx	series designation of Al alloyed with Mg
6xxx	series designation for Al alloyed with Mg and Si
6-311G**	designation for a basis set with polarization functions on heavy atoms and hydrogen

A

a	the fraction solid at which the eutectic begins to form used in a modified-Scheil equation
A2Mac1	A2Mac1 Automotive Benchmarking is a company with comprehensive manufacturing market coverage, exhaustive teardowns and data capture, combined with state-of-the-art software and global data delivery platform, who provides information to easily compare large quantities of data
A319-T7	aluminum (Al) alloy with silicon (Si) plus copper (Cu) and/or magnesium (Mg) that is solution heat-treated and stabilized (overaged) having excellent casting and machining characteristics as well as corrosion resistance and weldability that is used in engine parts and gas and oil pans
A356	Al alloy with greater elongation, higher strength and considerably higher ductility than Alloy 356 because of lower iron (Fe) content that is typically used for airframe castings, machine parts, truck chassis parts, aircraft and missile components, and structural parts requiring high-strength
A365	a primary die-casting alloy (AlSi ₉ MgMn) widely used to manufacture automotive parts
AA	Aluminum Association
AA3003	Al alloy with moderate strength, which can be increased by cold working, and good corrosion resistance
AA5182	wrought alloy with good corrosion resistance and weldability containing 4.5% Mg, 0.35% Mn, and the balance Al
AA5754	wrought Al alloy containing 94.2 to 97.4% Al, 0.3% max Cr, 0.1% max Cu, 0.4% max Fe, 2.6 to 3.6% Mg, 0.5% max Mn, 0.4% max Si, 0.15% max Ti, 0.2% max Zn and 0.15% max residuals formed by rolling, extrusion, and forging, but not casting that can be cold worked to produce tempers with a higher strength but a lower ductility
AA6022	heat treatable low Cu precipitation hardenable Al sheet alloy containing 0.8 to 1.5% Si and 0.45 to 0.70% Mg
AA6061	precipitation hardening Al alloy containing 0.8 to 1.2% Mg and 0.4 to 0.8% Si as its major alloying elements
AA6063	the most common alloy used for Al extrusion of complex shapes to be formed with very smooth surfaces fit for anodizing with a composition of 0.2 to 0.6% Si, 0.35% Fe, 0.10% Cu, 0.10% Mn, 0.45 to 0.9% Mg, 0.10% Cr, 0.10% Zn, 10% Ti, and the remainder Al
AA6082	a medium strength alloy with excellent corrosion resistance with the highest strength of the 6,000 series alloys
AA6111	wrought Al alloy that is a heat treatable and possesses high-strength and excellent stretch-forming characteristics containing 0.6 to 1.1% Si, 0.5 to 1.0% Mg, 0.1 to 0.45% Mn, 0.5 to 0.9% Cu, and 0.15% Zn
AA7055	Al alloy used in the aerospace sector and other high-strength requirement areas
AA7075	Al alloy with strength comparable to many steels, good fatigue strength, and average machinability

ABAQUS	software suite for finite element analysis and computer-aided engineering
ACMZ	designation for Al alloys containing Al, Cu, manganese (Mg), and zirconium (Zr)
ACN	acrylonitrile
ACP	Advanced Carbon Products
acum	the unit of measurement for sound sharpness derived from Latin meaning “sharp”
ADC12Z	A die-cast Al alloy used for intricate components requiring improved die filling characteristics such as automobile engine blocks
AIREBO	adaptive intermolecular reactive empirical bond order
AET	Applied Engineering & Technology Integration, Inc.
AFA	Al ₂ O ₃ -forming austenitic alloys
AFS	American Foundry Society
A-hr/l	ampere-hour per liter
AHSS	advanced high-strength steel
Al	aluminum
Al ₂ O ₃	Al oxide
AM	additive manufactured - Mg-alloy designation with Al and Mn as principal alloying metals
AM50	Mg-alloy 5.0% Al and less than 0.5% Mn
AM60	Mg-alloy 5.6 to 6.5% Al and less than 0.25% Mn
AMIPC	additively manufactured interpenetrating phase composite
ANSYS	specialists in finite element analysis, computational fluid dynamics, electronics, semiconductors, embedded software and design optimization
APB	anti-phase boundary
APT	atom probe tomography
Arconic	company specializing in lightweight metals engineering and manufacturing
AS4	a continuous, high-strength, high strain, polyacrylonitrile (PAN)-based carbon fiber (CF) available in 3,000 (3K), 6,000 (6K), and 12,000 (12K) filament count tows and surface treated and sized to improve its interlaminar shear properties, handling characteristics, and structural properties
AS7GU-T64	A cast Al alloy derived from the A356 alloy with an addition of 0.5% Cu to increase strength at elevated temperature and is usually used in high-performance engine cylinder head
ASPEN Plus	simulation software by AspenTech that combines accuracy and engineering collaboration with time-saving workflows
ASTM	American Society for Testing and Materials International
at. %	atomic percent
AT31	Mg-alloy comprised of 3% Al and 1% Sn

ATR	attenuated total reflection
Aural 2	Al alloy used for thin wall structural components
AZ	Mg-alloy designation with Al and zinc as the principal alloying metals
AZ21	Mg-alloy with 2% Al and 1% zinc
AZ31B	most widely available Mg grade alloy, high-strength-to-weight ratio with a composition of 2.5 to 3.5% Al and 0.7 to 1.3% Zn
AZ91	Mg-alloy with composition of 9% Al and 1% Zn
B	
B	boron
B10, B50, B90	defect size in microns at 10%, 50%, and 90% of the total number of defect sizes in a sample
B3LYP	B3 is Becke's three parameter exchange correlation functional and LYP is the Lee Yang and Parr correlation functional
B319	Al alloy with 6% Si, 3.5% Cu, and 1.0% Fe maximum with excellent casting and machining characteristics, corrosion resistance and weldability are very good used for engine parts, engine crankcases, gas and oil pans, and general commercial applications
bar	measurement of pressure equal to one atmosphere
BASF	largest chemical company in the world
BCC	body centered cubic
BIW	body-in-white
BMW	Bayerische Motoren Werke AG; a German luxury automobile, motorcycle, and engine manufacturing company
Bonderite®	an electro ceramic coating that can be applied from 3 to 50 µm thicknesses and provides excellent corrosion protection, high resistance to chemicals and temperatures up to 1,100°C while facilitating weight reduction for individual parts by using light metals instead of steel
BP	budget period
BSE	back-scattered electron
BX	designation for a multiaxial fabric having a multi-axis and multi-layered reinforcement produced using multiple axes (0°, 90°, +45°, -45°) or combined with chopped mat and multiple layers of veil and/or non-woven materials with typical applications for vacuum infusion, pultrusion, filament winding, hand lay-up molding
C	
°C	degrees Centigrade
C	carbon
C	concentration when used in an equation for a modified-Scheil model
<i>c</i>	the curing state (when used in modeling a cure process)

C ₀	concentration as a function of the alloy composition in a modified-Scheil equation
C677F	Al alloy optimized for castability and good thermal conductivity designed for high-pressure die-cast components that require high tensile strength and fatigue resistance at elevated temperatures
Ca	calcium
CAD	computer-aided design
CAE	computer-aided engineering
CALPHAD	CALculation of PHase Diagrams
CATIA	computer-aided three-dimensional interactive application
cc/sec	cubic centimeter per second
CCS	Collaborative Composite Solutions Corporation
CCT	cyclic corrosion testing
CDME	Center for Design and Manufacturing Excellence
Ce	cerium
CEM	computational electromagnetics model
CETP	corrosion evaluation test procedure
CF	carbon fiber
CF8C-Plus	cast stainless steel developed to provide higher temperature capability and reliability for advanced diesel engine
CFD	computational fluid dynamics
CFR	Code of Federal Regulations
CFRC	carbon fiber reinforced composite
CFRE	carbon fiber reinforced epoxy
CFRP	carbon fiber reinforced polymer
CFTF	Carbon Fiber Technology Facility
CGI	compacted graphite iron
Chomarat	international, privately owned, textile group producing textile and plastic coatings, textile finishing, and special reinforcement materials
CHT	conjugate heat transfer
cm	centimeter
cm ²	square centimeter
CN-12	type of stainless steel with improved high-temperature strength and ductility
CNT	carbon nanotube
Co	cobalt
CO	carbon monoxide
CO ₂	carbon dioxide

COMSOL	a cross-platform finite element analysis, solver and multiphysics simulation software that allows conventional physics-based user interfaces and coupled systems of partial differential equations
CONVERGE	computational fluid dynamic software by Convergent Science Inc. with autonomous meshing capabilities that eliminates the grid generation problems from the simulation process
cP	centipoise
CPEC	close proximity electromagnetic carbonization
Cr	chromium
Cr ₂ O ₃	chromium oxide
CRADA	Cooperative Research and Development Agreement
CSC	cracking susceptibility coefficient
CSP	Continental Structural Plastics
CTE	coefficient of thermal expansion
CTP	coal tar pitch
CTP-NMP	N-methyl-2-pyrrolidone coal tar pitch
CTS	cross-tension strength
Cu	copper
Cu-C	copper-carbon
CuO	cupric oxide
D	
D	deuterium
DAF	Doorne's Aanhangwagen Fabriek
DataHUB	data-centric architecture for data storage
dB	decibels
DB	deformable barrier
DFT	density functional theory
DI	de-ionized
DIC	digital image correlation
DICTRA	Diffusion-Controlled TRAnsfOrmations in multicomponent systems, a software diffusion module within Thermo-Calc for accurate simulation of diffusion-controlled reactions in multicomponent alloy systems
Digmat®	nonlinear multiscale material and structure modeling platform by MSC Software
DIW	door-in-white
DMSO	dimethyl sulfoxide
DOE	U.S. Department of Energy

DoE	design of experiments (when referring to experimental procedures)
DOS	density-of-state
DP	dual-phase
DP590	advanced high-strength formable steel for inner body side, inner quarter panel, rear rails, and rear shock reinforcements
DP600	dual-phase steel consisting of a ferrite matrix containing a hard second phase and usually islands of martensite that is used in automobile safety cage components (β -pillar, floor panel tunnel, engine cradle, front sub-frame package tray, seat)
DP980	dual-phase steel consisting of a ferrite matrix containing a hard second phase
DP1180	high-ductility, dual-phase, ultra-high-strength steel with an ultimate tensile strength greater than or equal 1180 MPa
DSC	differential scanning calorimeter (or calorimetry)
E	
e.g.	abbreviation meaning “for example”
EBM	electron beam melting
EBM	Eagle Bend Manufacturing
EBSD	electron backscatter diffraction
EC	electrodeposition coating or electro ceramic coating
E-coat	electrophoretic coating
EDAG	EDAG, Inc. a company that provides integrated development and optimization of vehicles, production facilities, derivatives and modules
EDS	energy dispersive spectroscopy
EDXS	energy dispersive x-ray spectroscopy
EERE	Office of Energy Efficiency and Renewable Energy
EFP	E-Form Plus
EGR	exhaust gas recirculation
EL	electrode life (when referring to welding electrodes)
EL	elongation (when referring to a material property)
EN-AW-4xxx	Al alloy consisting primarily of Al, Fe, and Si with Si being the major alloying element to lower the melting point of Al, without producing brittleness which produces excellent welding wire and brazing alloys and is one of the most widely used filler alloys for welding for structural and automotive applications
EPIKOTE™	EPIKOTE™ Resin 05475 with EPIKURE Curing Agent 05443: a system with low viscosity, a relatively long injection window, excellent wetting and adhesion to CFs, and superior thermal and mechanical performance
EPMA	electron probe microanalysis or electron probe micro analyzer
ER125	designation for the heptane-soluble fraction of gilsonite

ESC	externally solidified crystal
ESI	Engineered Solutions, Inc. Group
et al.	abbreviation meaning “and others”

F

F	fluorine
f_i	distribution function for fluid density
f_s	fraction solid
FAST	friction stir assisted scribe technique
FBJ	friction bit joining
FCA US LLC	Fiat Chrysler Automobiles U.S. LLC
FCC	face centered cubic
FDS	flow-drill screw
Fe	iron
FE	finite element
FEA	finite element analysis
FEM	finite element method (or model)
FE-safe	fatigue analysis software for finite element models used to determine fatigue life and optimize designs for industries involved with transport and mobility, aerospace and defense, general manufacturing, power generation, marine and offshore applications
FIB	focused ion beam
FLOW-3D®	a computational fluid dynamics simulation platform for investigating the dynamic behavior of liquids and gas in a wide range of industrial applications including microfluidics, bio-medical devices, water civil infrastructure, aerospace, additive manufacturing, inkjet printing, laser welding, automotive, offshore, energy and automotive
FMVSS	Federal Motor Vehicle Safety Standards
FSI	friction stir interlocking
F-SPR	friction self-piercing riveting
FSSW	friction stir spot welding
FSW	friction stir welding
ft	foot or feet
FTIR	Fourier Transform Infrared
ft-lb	foot-pound
FY	fiscal year

G

g	gram(s)
g/sec	grams per second
g_i	distribution function for energy
GCMS	gas chromatography - mass spectrometry
GD-OES	Glow Discharge - Optical Emission Spectrometry
GEN	generation
GG-MIT	Grossman Group at Massachusetts Institute of Technology
GHG	Gorilla hybrid glass
GITE	gross indicated thermal efficiency
GM	General Motors LLC
G-NAC	GTEKT North American Corporation
GPa	gigapascals
g/s	grams per second
gsm	grams per square meter
GREET®	Greenhouse Gas Regulated Emissions and Energy in Transportation
GTDI	gasoline turbocharged direct injection
GT-POWER	simulation software by Gamma Technologies Inc. used to predict engine performance quantities such as power, torque, airflow, volumetric efficiency, fuel consumption, turbocharger performance and matching, and pumping losses
GT-SUITE	simulation software by Gamma Technologies Inc. used for concept design to detail system or subsystem/component analyses, design optimization, and root cause investigation

H

h or hr	hour(s)
H	hydrogen (when referring to the element)
H	total heat generation over the complete curing process
H	atomic hydrogen
H ₂	molecular hydrogen
H ₂ O	water
HAZ	heat-affected zone
HBM	company providing sensors, transducers, strain gauges, amplifiers, data acquisition systems, and software for structural durability investigations, tests, and analysis
HC	heavy chain
HCF	high-cycle fatigue
HCP	hexagonal close packed

HD	heavy-duty
HDG	hot-dip galvanized
HDPE	high-density polyethylene
HE	hydrogen embrittlement
HER	hole-expansion (extrusion) ratio
HEXRD	high-energy x-ray diffraction
HP	Henkel pretreatment
HPC	high-performance computing
HPC4Mfg	high-performance computing for manufacturing
HPDC	high-pressure die-casting
HPEC	Henkel pretreatment + E-coated
HPOL	high-pressure oil line
HP-RTM	high-pressure resin transfer molding
HR-STEM	high-resolution scanning transmission electron microscope (or microscopy)
HAS	high-strength Al
HSLA	high-strength low-alloy
HSLA 350	steel consisting of a ferrite matrix containing a hard second phase, usually islands of martensite, with a yield strength of 350 MPa, ultimate tensile strength of 450 MPa and total elongation of 23-27%
HSS	high-strength steel
HyperMesh	multidisciplinary finite element pre-processor with advanced model assembly tools
Hz	hertz

I

i3	five-door urban electric vehicle
i8	coupe with an advanced plugin hybrid drivetrain
IA	intercritical annealing
IACMI	Institute for Advanced Composites Manufacturing Innovation
iCMD [®]	Integrated Computational Materials Design – a modeling software system developed by QuesTek Innovations LLC that integrates proprietary and commercial mechanistic modeling tools to facilitate rapid design and the development of new materials
ICME	integrated computational materials engineering
iCPT	isotropic coal tar pitch
ICT	Institute of Chemical Technology
i.e.	abbreviation for “id est,” a Latin phrase meaning “that is”
IEA-AMT	International Energy Agency-Advanced Materials for Transportation
IMC	intermetallic compound

iSIGHT	software used to combine multiple cross-disciplinary models and applications together in a simulation process flow, automate their execution across distributed computer resources, explore the resulting design space, and identify the optimal design parameters
<i>in-situ</i>	onsite or in place
IP	integration point (when referring to analysis)
IP	inner panel (when referring to door assembly)
iPP	isotropic petroleum pitch
IR	infrared
IR200	designation for the heptane-insoluble fraction of gilsonite
ITMS	International Manufacturing Technology Show
IX	internal expulsion
J	
J ₂	von-Mises yield criterium
JAVA script	high-level, interpreted programming language which is characterized as dynamic, weakly typed, prototype-based and multi-paradigm
JMatPro [®]	simulation software which calculates a wide range of materials properties for alloys and is particularly aimed at multicomponent alloys used in industrial practice
Jython	an alternate implementation of Python
K	
K	degree Kelvin
K	potassium
K _{TH}	threshold stress intensity
k _f	the constant value that represents the constant force required to extrude Mg
kg	kilogram
kHz	kilohertz
kJ	kilojoules
kJ/mol	kilojoules per mole
kN	kilonewton
Ksi, ksi, and kpsi	kilopound per square inch
kv	velocity-dependent partition coefficient
kWh/kg	kilowatt-hour per kilogram
KWN	Kampmann and Wagner Numerical (method)

L

L	liter
L_c	characteristic size of crystallites
L&L Products	technology driven business-to-business company with unique expertise in static sealing, acoustics, vibration reduction, structural reinforcements, and composite components
LAMMPS	Large-scale Atomic/Molecular Massively Parallel Simulator
lb	pound(s)
lb	pound(s)
LC	light chain
LCCF	low-cost CF
LCF	low-cycle fatigue (when referring to allow tests)
LCMS	low-cost Mg sheet
LCS	low carbon steel
LD	light-duty
LEAP	local electrode atom probe
LightMAT	Lightweight Materials Consortium
LIMS	Laboratory Information Management System
LLC	Limited Liability Company
LPSI	low speed pre-ignition
LS-DYNA	advanced, general-purpose, multiphysics simulation software package
LS-PREPOST	an advanced interactive program for preparing input data for LS-DYNA and processing results from LS-DYNA analyses in an optimization sequence
LSTC	Livermore Software Technology Corporation
M	
m^2	square meter
$m\Omega$	megaohm
M	molar
m_o	oxidation mass
M_xC_y	carbide where M designates randomly dispersed Fe, Cr, Ni and C is carbon
ma/cm ²	milliamp per square centimeter
MACOR [®]	trademark for a machineable glass-ceramic developed and sold by Corning Inc. that is a white material with good thermal insulation characteristics and is stable up to temperatures of 1,000°C, with very little thermal expansion or outgassing
MAE S.p.A	Machinery and Engineering Società per Azioni - a machinery manufacturer company with engineering capabilities specializing in manufacturing of units and complete lines for monomer and polymer processing in the form of fibers or foams

MAGMASOFT®	modular simulation software for casting process simulation
Magna	Magna International Inc.
Mag-tec	company offering full service die-casting in Mg, Al, and Zn
MAT	material
MAT_COMPRF or MAT_293	software in LS-DYNA for woven pattern prepreg composite preforming simulation
MATLAB	<u>MA</u> TriX <u>LAB</u> oratory, a multi-paradigm numerical computing environment and programming language
MaSp	major ampullate spidroins
MCrAlY	bond coats where M = Fe, Co or Ni that exhibit a two-phase microstructure $\beta+\gamma$ which increases the ductility of the coating thereby improving thermal fatigue resistance
MD	molecular dynamic
MDA	molecular dynamic analysis
MDB	moving deformable barrier
MDF	Manufacturing Demonstration Facility
MDO	multidisciplinary design optimization
MDS	multiscale design system
MEAM	modified embedded-atom method
Mg	magnesium
MgH ₂	magnesium hydride
Mg(OH) ₂	magnesium hydroxide
MgO	magnesium oxide
MIC	maximal information coefficient
MICRESS ®	MICRostructure Evolution Simulation Software – software enabling the calculation of microstructure formation in time and space during phase transformations, especially in metallurgical systems
microCT	micro-computed tomography
mil or mils	unit of length equal to one thousandth (10^{-3}) of an inch
min	minute(s)
MiSp	minor ampullate spidroins
ML	machine-learning
mm	millimeters
mm/min	millimeters per minute
mm/sec	millimeters per second
MMC	metal matrix composites

mN	milli-Newtons
Mn	manganese
Mo	molybdenum
MOBAI3	a kinetic database containing mobility data for Al-based alloys present in a format suitable for simulation of diffusion-controlled phenomena using DICTRA and TC-PRISMA
modeFRONTIER®	software for streamlining the design process with workflows, innovative algorithms, and sophisticated post-processing tools
Moldex3D	computer-aided engineering software for simulating plastics injection molding processes to optimize product design and manufacturability, shorten time-to-market, and maximize product return on investment
MPa	megapascals
mpg or MPG	miles per gallon (when referring to fuel usage)
MPG	Michigan Proving Ground (when referring to Ford's corrosion testing)
mph	miles per hour
MPP	mesophase petroleum pitch
m/s	meters per second
ms	milliseconds
MSC-Simufact	software to simulate complex welding processes that may involve multiple welding sequences and to predict distortions of the components, while considering phase transformations occurring during the process
MSI or Msi	million pounds per square inch
MSU	Michigan State University
MT	metric tons
MT/yr.	metric tons per year
MTS	MTS Systems Corporation
MUD	multiples of uniform density
N	
N	newtons
Na	sodium
NaCl	sodium chloride
Nano-Al	nanostructured Al
NARC	neural apoptosis-regulated convertase
NASTRAN	multidisciplinary structural analysis application for performing static, dynamic, and thermal analysis across the linear and nonlinear domains
Nb	niobium

NbFeSb	niobium-iron-antimony, an alloy identified as promising high-temperature thermoelectric materials with a figure of merit $zT > 1$, and relatively high thermal conductivity
NCAP	New Car Assessment Program
NCF	non-crimped fabric
nCode	engineering data analysis tool with special concentration in fatigue and durability
Nd	neodymium
NDE	non-destructive evaluation
NFE	non-federal entity
NH ₃	ammonia
NH ₄ NO ₃	ammonia nitrate
NHTSA	National Highway Traffic Safety Administration
Ni	nickel
NirC	designation for a bacterial membrane protein that facilitates the transport of nitrite anions across lipid bilayers for cytoplasmic detoxification
NIST	National Institute of Standards and Technology
nm	nanometers
nm ³	cubic nanometer
Nm	Newton-meter
NMP	N-methyl-2-pyrrolidone
N/nm	newtons per nanometer
NO _x	nitrogen oxides (NO and NO ₂)
NPT	Number of particles-Pressure-Temperature used in a statistical mechanical ensemble
ns	nanoseconds
NSC	NO _x storage converter
NSGA-II	Non-dominated Sorting Genetic Algorithm II
NLSL	National Synchrotron Light Source
NTRC	National Transportation Research Center
NU	Northwestern University
NVH	noise, vibration, and harshness
O	
OBD	on-board diagnosis
OCP	open-circuit potential – the potential of a metal or conductive sample when immersed in an electrolyte
OD	outer diameter
OEM	original equipment manufacturer

ORNL	Oak Ridge National Laboratory
OSU	The Ohio State University
P	
P	pressure
Pa	pascal
Pa s	pascal-second (unit of viscosity)
PA-66	polyamide 66 (or Nylon 66)
PAM-COMPOSITES	composites manufacturing software that defines and optimizes process parameters for composites manufacture
PAM-FORM	software program enabling realistic and predictive simulation of dry textiles or prepregs forming processes
PAM-RTM	pluggable authentication module-resin transfer molding
PAN	polyacrylonitrile
PanAl	a thermodynamic database developed to understand/predict the effects of major and minor alloying elements on the selected properties of an Al alloy
Pandat™	an integrated computational tool based of the CALPHAD (CALculation of PHase Diagram) approach for multicomponent phase diagram calculation and materials property simulation
PanMg	database used for a wider spectrum of Mg-alloy design and related processing parameters and the usefulness of the CALPHAD modeling tool in Mg technology
PanPrecipitation	module in the Pandat™ software simulating precipitation kinetics during heat-treatment process
PBO	poly(p-phenylene-2,6-benzobisoxazole
PCC	Pearson's correlation coefficient
PCP	peak cylinder pressure
Pd	palladium
PEEQ	the ABAQUS parameter name for the equivalent plastic strain
pH	quantitative measure of the acidity or basicity of aqueous or other liquid solutions
PI	principal investigator
pkp	probability-kinetics of oxidation: cyclic oxidation model for determining of alloy consumption
PLC	Portevin-Le Châtelier
PM	particulate matter
PM10	particulate matter smaller than ten micrometers
PNNL	Pacific Northwest National Laboratory
PP	polypropylene (when referring to polymers)
PPG	Pittsburgh Plate Glass

ppm	parts per million
PRISMS	PRedictive Integrated Structural Materials Science
PRISMS-CPFE	PRedictive Integrated Structural Materials Science -Crystal Plasticity Finite Element
ps	picoseconds
psi	pounds per square inch
PSU	Pennsylvania State University
Pt	platinum
Q	
Q	heat generation during curing
QT	QuesTek Innovations, LLC
R	
R	value for local cooling rate in an equation defining grain size
R&D	research and development
R ²	coefficient of determination
R _β	the initial radius of the β phase
R _{tot}	the radius of the grain
R41	a super alloy with nickel as its base metal with cobalt, chromium, Al, and molybdenum added that is hardened by precipitation to give high-temperature mechanical properties and corrosion resistance
Ra	average length between the peaks and valleys of measured surface roughness
RA	retained austenite
RADIOSS	a multidisciplinary finite element solver developed by Altair Engineering to solve both linear and nonlinear problems using implicit and explicit integration schemes for engineering solutions from linear statics and linear dynamics to nonlinear transient dynamics and mechanical systems
RAMCO	Ramaco Carbon LLC
RAV4 EV	a “zero emission”, plugin, all-electric vehicle produced by Toyota from 1997 to 2003 powered by an advanced nickel-metal hydride (NiMH) battery pack with 27 kWh capacity
RE	rare-earth
Re	Reynolds number
ReaxFF	reactive force field
Redox	reduction-oxidation
Rene 41 (R41)	a precipitation hardening, nickel-based high-temperature alloy possessing high-strength in the 1,200/1,800°F (649/982°C) temperature range designed for use in severely stressed high-temperature applications
RF	radio frequency

Rh	rhodium
RIVTAC®	a high-speed process supplied by Bollhoff for joining Al, steel, plastics, and non-ferrous metals as well as for mixed joints, multilayer joints and hybrid joints of these materials
RMX	RMX Technologies, an advanced materials technology company with ceramics and various commercialized products (company name changed to 4X Technologies)
RP	rigid pole
RPM or rpm	revolution(s) per minute
RSR	resistance spot rivet
RSW	resistance spot weld
RT	room-temperature
RTM	resin transfer molding
RVE	Representative Volume Element
Rz	average vertical distance from the highest peak to the lowest valley of measured surface roughness
S	
s	seconds
S	yarn spacing (when referring to fabric weave)
S3 and S4R	general-purpose shell elements in ABAQUS software
SAE	Society of Automotive Engineers
SAEJ2334	SAE lab test procedure used when determining corrosion performance for a particular coating system, substrate, process, or design and can be used as a validation tool as well as a development tool
SAR-AD™	saturates, aromatics, and resins Asphaltene Determinator™
SAXS	small-angle x-ray scattering
SC	South Carolina
SCA	self-consistent clustering analysis
SCC	stress corrosion cracking
Scheil Model	model for describing the microsegregation present in primary phase dendritic growth and directional solidification
SCR	selective catalytic reduction
SDAS	secondary dendrite arm spacing
SDR	software defined radios
SEA	statistical energy analysis
SEAM®	statistical energy analysis model by Cambridge Collaborative Inc.
SECAT	a metallurgical research laboratory specializing in Al product and process technologies with ISO 17025:2005 certification

SEL347	designation for whole gilsonite
SEM	scanning electron microscope (or microscopy)
SFE	process automation software with predefined variables and their value ranges
ShAPE™	shear-assisted processing and extrusion
Si	silicon
SiC	silicon carbide
SIMS	secondary ion mass spectrometry
SLDC	solid-liquid diffusion couples
SLG	soda lime glass
SMART	partnership between Swatch and Mercedes (s+m) and their design of an “artful” little car
SMC	sheet molding compound
Sn	tin
SolidWorks®	a three-dimensional CAD system used to analyze detailed designs and make quick modifications as needed through the product development process
Solvay	Solvay Composites
sones	a unit of loudness for how loud a sound is perceived
SPL	sound pressure level
SPR	self-pierce rivet
Sr	strontium
SRI	Southwest Research Institute
SSDC	solid-solid diffusion couples
STEM	scanning transmission electron microscope (or microscopy)
STL	sound transmission loss
SVDC	super vacuum die-casting
T	
t	time
T	temperature
\dot{T}_c	cooling rate
T_g	glass transition temperature
T4	temper designation for a solution heat-treated material used for castings which require high-strength and maximum toughness
T5	temper designation for material cooled from hot working and artificially aged (at elevated
T64	temper designation for solution heat-treated and then artificially aged alloy in under-aging conditions (between T6 and T61) to improve formability

T7	temper designation for solution heat-treated and then artificially overaged
TCAL5	a thermodynamic database for Al-based alloys for use with Thermo-Calc and the add-on Diffusion Module (DICTRA) and/or Precipitation Module (TC-PRISMA) that is based on the critical evaluation of binary, ternary and important higher order systems which enables predictions to be made for multicomponent systems and alloys of industrial importance
TCF	textile CF
TCMG4	a thermodynamic database for Mg-based alloys used with the Thermo-Calc software package for a wide range of compositions from pure Mg to very complex Mg-based commercial alloys
Tcl	script file in Hypermesh utilized to provide support for more advanced tasks
TC-PRISMA	software based on Langer-Schwartz theory that adopts the Kampmann-Wagner numerical (KWN) method to compute the concurrent nucleation, growth, and coarsening of dispersed phase(s)
TEA	techno-economic analysis
Techmer PM	a major supplier of color and additives to the automotive plastics and fiber industries, with a strong emphasis on the automotive interior trim industry
TEM	transmission electron microscope (or microscopy)
TEMRT-LBM	thermal entropic multi-relaxation time lattice Boltzmann method
Thermo-Calc	software package for thermodynamic
Ti	titanium
Ti-Al	titanium aluminide
Ti:2B	a mixture of one part Ti and two parts B
TiB ₂	titanium boride
TiC	titanium carbide
TiO ₂	titania
TM	transition metal
TMAZ	thermo-mechanically affected zone
TOF	time-of-flight
TOF-SIMS	time-of-flight secondary ion mass spectrometry
TP	thermoplastic
TPI	TPI Composites, Inc.
TRIP	transformation-induced plasticity
TRL	technology readiness level
TS	Toray G83C_7-11
TSS	tensile shear strength
TWB	tailor-welded blanks

U

U520	nickel-chromium-cobalt alloy with tungsten and molybdenum added resulting in age-hardening and strengthening of this alloy manufactured by UDIMET®
U720	a nickel base alloy, solid-solution strengthened with tungsten and molybdenum and precipitation-hardened with Ti and Al manufactured by UDIMET®
UD	unidirectional
UD-CCM	University of Delaware Center for Composite Materials
UDIMET® 720	a nickel base alloy, solid-solution strengthened with tungsten and molybdenum and precipitation-hardened with Ti and Al
UF	University of Florida
UFEN	unit-free error numbers
UGNX	UNigraphics NeXt generatin – a drafting application used to create drawings with views of the part, dimensions, and necessary drafting annotations
UHMWPE	ultra-high-molecular-weight polyethylene
UHS	ultra-high-strength
UHSS	Ultra-High-Strength Steel
UIUC	University of Illinois at Urbana-Champaign
UM	University of Michigan-Dearborn
UP	University of Pennsylvania
USAF	United States Air Force
USAXS	ultra-small-angle x-ray scattering
USCAR	U.S. Council for Automotive Research
U.S.	United States
USW	ultrasonic welding
UT	University of Tennessee
UTK	University of Tennessee Knoxville
UTS	ultimate tensile strength
UV	ultraviolet
UVA	University of Virginia
UW	ultrasonic welding (when referring to metal joining)
UW	University of Wyoming (when referring to academia)

V

V	vanadium
V_{β}	the volume of the β phase
V_{β}^f	the volume fraction of the β phase
V_{tot}	the volume of the grain

Materials

v	solidification front velocity
v	fiber volume fraction (when referring to fabrics)
VARTM	vacuum assisted resin transfer molding
VASP	Vienna Ab-Initio Simulation Package – software for performing ab-initio quantum-mechanical molecular dynamics based on density functional theory using pseudopotentials and a plane wave basis set
VCCD	Virtual Cast Component Development
VFAW	vaporizing foil actuator welding
vis	visible spectroscopy
viz	synonym for “namely,” “that is to say,” and “as follows”
VMT	vehicle mile(s) of travel
vs	versus
V _{SCE}	voltage of the saturated calomel electrode
VTO	Vehicle Technologies Office
VULCAN	the official title for the Spallation Neutron Source engineering diffractometer at ORNL
W	
w	with
w/o	without
W	watts
W	tungsten
W _b	surface structure value for appearance from 0.3-1 mm
W/cmK	watts per centimeter degree Kelvin
Ws	watt-seconds
WE43	high-strength casting alloy used in temperatures of up to 300°C (572°F)
WF	warm-forming
W/mK	watts per meter-Kelvin
WRI	Western Research Institute
wt%	percent by weight
WV	water vapor
X	
x	x is the fraction solid used in a modified-Scheil equation
XCT	x-ray computed tomography
XRD	x-ray diffraction

Y

Y	yttrium
YS	yield strength

Z

ZE10A	a novel Mg-alloy with reduced content of rare-earth metals with a composition of Mg-1.2Zn-0.25Zr-0.5Nd
ZE20	Mg-alloy with a composition of Mg-2%Zn-0.2%Ce) that exhibits outstanding ductility and strength
ZEK100	Mg-alloy composed of zinc, RE elements, and Zr
ZK60	Mg wrought alloy consisting of primary matrix α (Mg) and the eutectic
Zn	zinc
Zr	zirconium
ZrH ₂	zirconium(II) hydride
zT	a figure of merit related to the ability of a given material to efficiently produce thermoelectric power

Executive Summary

The Materials Technology Program supports the Vehicles Technologies Office's mission to help consumers and businesses reduce their transportation energy costs while meeting or exceeding vehicle performance expectations. The propulsion materials research portfolio seeks to develop higher performance materials that can withstand increasingly extreme environments and address the future properties needs of a variety of high-efficiency powertrain types, sizes, fueling concepts, and combustion modes. Advanced lightweight materials enable improvements in fuel economy by providing properties that are equal to or better than traditional materials at a lower weight. Because it takes less energy to accelerate a lighter object, replacing cast-iron and traditional steel components with lightweight materials such as high-strength steel, magnesium (Mg), aluminum (Al), and polymer composites can directly reduce a vehicle's fuel consumption. Materials technology activities focus on the following cost and performance targets: (1) enable a 25% weight reduction for light-duty (LD) vehicles including body, chassis, and interior as compared to a model year 2012 baseline at no more than a \$5/lb-saved increase in cost; and (2) validate a 25% improvement in high-temperature (300°C) development of engine exhaust catalyst materials strength relative to components made with 2010 baseline cast Al alloys (A319 or A356) for improved efficiency LD engines.

Propulsion Materials

In fiscal year (FY) 2018, the Propulsion Materials Subprogram portfolio included research in three main areas: (1) use of Integrated Computational Materials Engineering (ICME) to predict materials properties needed to achieve increases in brake thermal efficiency for heavy-duty (HD) vehicles; (2) development of advanced cast Al alloys for high-temperature engine components; and (3) development of catalyst materials for high-temperature exhaust gases, composite brakes to reduce weight and anti-fouling materials that allow for energy recovery and aftertreatment.

Heavy-duty internal combustion engines for the transportation sector are operating at increasingly high peak cylinder pressure (PCP) to achieve required increases in brake thermal efficiency. One project in the propulsion materials portfolio is using ICME to estimate combustion intensity and heat transfer and to evaluate the thermomechanical effects on materials. In this way, it is possible to identify properties requirements of materials suitable to withstand a lifetime of operation at the elevated temperatures and pressures in future higher-efficiency HD engines.

To increase engine efficiency in LD vehicles, the maximum operating temperature of engine components has increased from approximately 170°C in earlier generation engines to peak temperatures well above 200°C in current engines. This increase in operational temperatures requires materials with optimized properties in terms of tensile, creep, and fatigue strength. Several projects focus on developing advanced cast Al alloys for automotive engine applications to meet these challenging requirements. Another potential approach to achieving improved combustion engine efficiency and specific power is by retaining more heat in the exhaust gas to recover using a turbocharger. However, higher exhaust gas temperatures increase the operational temperature requirements of structural and dynamic components in the exhaust gas path, particularly the exhaust valves. Identifying engine materials with adequate high-temperature mechanical properties and oxidation resistance to enable achieving the projected engine operating parameters without exceeding the cost constraints is the focus of another propulsion material project in this report.

Finally, the goal of several projects in the propulsion materials portfolio is to develop and test new catalysts for gasoline and diesel engines at lower operating temperatures that may occur with future, more efficient vehicles. Specifically, the goal is to achieve conversion efficiencies of 90% at temperatures as low as 150°C. This will enable the deployment of lean combustion powertrains with significantly increased fuel efficiencies, but lower exhaust temperatures. In addition, current aftertreatment technologies such as exhaust gas

recirculation (EGR) are being studied in order to provide information to industry about the properties of deposit build-up so as to enable improved models and potential design improvements to reduce fouling and its impact on the performance of EGR coolers.

Lightweight Materials

In FY 2018, the Lightweight Materials Subprogram portfolio included research in the following three areas: (1) improving the manufacturability of lightweight automotive metals such as advanced high-strength steel (AHSS), Al, and Mg; (2) reducing the cost of carbon fibers (CFs), investigating biomass materials as alternatives to other polymer composites, and creating ICME models for manufacturing of CF composites; and (3) developing novel methods to enable multi-material joining systems. A few projects were cross-cutting and involved using lightweight metals, carbon fiber composites, and novel multi-material joining techniques to reduce the weight of door assemblies.

Substitution of lightweight metals for mild steel can result in weight savings of 25-60% per component, which increases fuel efficiency. However, there are several challenges with the increased use of lightweight metals including material cost, room-temperature formability, and limitations within the existing manufacturing infrastructure. During cold stamping of AHSS parts, the most commonly observed failure mode is edge-splitting, and the sheared-edge stretchability appears to depend on a complex combination of factors. One lightweight metals project is working to enhance the sheared-edge stretchability of AHSS by developing quantitative and predictive understanding of the microstructure effects on sheared-edge fracture and stretchability, hence enabling implementation of AHSS in vehicle structures. Projects on Al are pursuing unique pathways to develop a high-strength 7xxx series Al alloy and demonstrate its ability to replace an ultra-high-strength automotive component at a cost of less than \$2 per pound saved while another is investigating methods for stamping high-strength Al at room-temperature. Similarly, the use of high-performance Mg alloys in the automotive industry is currently limited due to the addition of costly rare-earth elements, need for high-temperature forming, and difficulties in applying pretreatments and paints. Two projects in this report aim to eliminate the need for rare-earth additives, while simultaneously improving the processing methods and additional steps necessary to create and assemble Mg components.

Carbon fiber reinforced polymer (CFRP) composites also have the potential to reduce component weight by more than 60%. One of the main barriers to widespread implementation is the high cost of CF, which is due in large part to the cost of input material (precursor) and the carbonization process. One project is addressing this challenge by developing higher throughput, low-temperature carbonization of CF, thus lowering manufacturing costs and increasing production rates. Three projects are investigating potential low-cost CF precursors and using ICME models to guide their research. Another challenge that the Lightweight Materials Subprogram is addressing is the lack of predictive modeling available, which is necessary to accelerate development-to-deployment of CFRP automotive components. Two projects are creating ICME models in order to predict the manufacturing and structural performance of CF composites. Material design and manufacturing process information, such as geometric dimension, fiber layout, and fiber orientation, are inputs for multiscale models to generate local material constitutive relations used in following noise, vibration, and harshness, crash safety, and durability analyses. The integrated tools are being applied to component design and optimization, demonstrating that the ICME approach generates powerful tools for the most efficient usage of CFRP, leading to optimized weight savings with minimum cost increase.

The most effective way to reduce the overall weight of a vehicle is to tailor the material selection to each component's needs. However, joining dissimilar materials to create a multi-material structure is a significant challenge. In FY 2018, the Joining Core Program was launched as a research collaboration between three national laboratories to address specific challenging material pairs including Mg-CFRP, CFRP-Steel, and Mg-Steel. The methods being developed in the Joining Core Program include ultrasonic welding, novel methods

for mechanical fastening, over molding, adhesives, and friction stir welding. Several other projects investigate the use of friction-based solid-state welding processes to join Al to steel and Al to CFRP composites, as well as dissimilar Al alloy combinations. Solid-state welding allows for joining materials with vastly different melting temperatures, which is not possible with fusion welding. Two projects incorporate fasteners into welding processes, both solid-state and fusion, in order to provide a strong spot joint comparable to resistance spot welds in steel to steel joints. Research in this portfolio also includes adhesives that address concerns with the coefficient of thermal expansion mismatch seen in dissimilar material joints, a novel joining process being developed based on impact welding, and various modeling efforts to investigate residual stress in welds, identification of poor quality welds, and ideal interface properties for strong joints.

Table of Contents

Vehicle Technologies Office Overview	1
Organization Chart	1
Materials Technology Program Overview.....	2
Introduction	2
Goals.....	2
State-of-the-Art	3
Program Organization Matrix.....	4
I Propulsion Materials.....	5
I.1 Integrated Computational Materials Engineering.....	5
I.1.A Applied Computational Methods for Advanced Propulsion Materials (Oak Ridge National Laboratory).....	5
I.1.A.1 Task 1E: Future Engine Requirements – Modeling Advanced Engine Materials	6
I.1.A.2 Task 2E: Materials Properties for Modeling and Screening.....	11
I.1.A.3 Task 4E: CFD Analysis of Cooler Materials, Deposits, and Geometries.....	15
I.1.A.4 Task 5E: Computational Development of Thermoelectric Materials.....	20
I.1.B ICME Guide Development of Advanced Cast Aluminum Alloys for Automotive Engine Application (Ford Motor Company).....	23
I.1.C Computational Design and Development of a New, Lightweight Cast Alloy for Advanced Cylinder Heads in High-Efficiency, LD Engines (General Motors).....	40
I.2 High-Temperature Engine Materials	56
I.2.A Lightweight High-Temperature Alloys Based on the Al-Fe-Si System (University of Florida).....	56
I.2.B Advanced Fe-Ni-Cr-base Alloys for Higher Temperature Engine Components (Oak Ridge National Laboratory)	63
I.2.B.1 Task 1B: Computation-Guided Development of Lower Cost Alumina-Forming Alloys.....	64
I.2.B.2 Task 2B: Oxidation-Resistant Coated Exhaust Valves for High-Temperature Applications	68
I.2.B.3 Task 3B: High-Temperature Components: Alumina-Forming Cast Turbo Housing Alloys Capable of 950°C	71
I.2.C High-Temperature Lightweight Engine Materials (Oak Ridge National Laboratory).....	74
I.2.C.1 Task 1C: High-Temperature Lightweight Components: Fundamental Properties and Processing to Develop Higher Temperature Al Alloys	75
I.2.C.2 Task 2C: Additive Manufactured (AM) Bimetallic Material Bonding for Increased Knock Survival in Lightweight Pistons	79
I.2.C.3 Task 3C: Development of New Turbocharger Compressor Wheels for HD Engines (CRADA with Cummins Inc.)	85
I.2.C.4 Task 4C: High-Temperature Lightweight Components: Alloy Development for Higher Performance Powertrains	91
I.2.D Fundamentals of High-Temperature Environmental Resistance (Oak Ridge National Laboratory).....	95
I.2.D.1 Task 1A: High-Temperature Components: High-Temperature Oxidation Mapping of Advanced Exhaust Path Materials	96
I.2.D.2 Task 2A: High-Temperature Components: Application of Machine-Learning Methods to Predict High-Temperature Oxidation of Exhaust Path Materials.....	101

I.3	Materials for Energy Recovery and Aftertreatment	104
I.3.A	Innovative SCR Materials and Systems for Low-Temperature Aftertreatment (Pacific Northwest National Laboratory)	104
I.3.B	Metal Matrix Composite Brakes Using Titanium Diboride (Pacific Northwest National Laboratory).....	109
I.3.C	Direct Extruded High-Conductivity Copper for Electric Machines (Pacific Northwest National Laboratory and General Motors Research and Development)	117
I.3.D	Waste Heat Recovery and Aftertreatment (Oak Ridge National Laboratory).....	125
I.3.D.1	Task 1D: Materials Issues Associated with EGR Coolers	126
I.3.D.2	Task 2D: Materials for Waste Heat Recovery/International Energy Agency - Advanced Materials for Transportation	130
II	Lightweight Materials.....	133
II.1	Automotive Metals	133
II.1.A	Advancing Properties, Processes, and Enabling Tools for Lightweight Metals (Pacific Northwest National Laboratory).....	133
II.1.A.1	Enhancing Sheared-Edge Stretchability of Advanced High-Strength Steel/Ultra High-Strength Steel through Integrated Manufacturing Process Simulations.....	134
II.1.A.2	Cost-Effective Mg Extrusions.....	141
II.1.A.3	Optimizing Heat-Treatment Parameters for Third-Generation AHSS with High-Throughput <i>in-situ</i> Experiments and Integrated Modeling Frameworks	149
II.1.A.4	RT Stamping of High-Strength Al Alloys.....	160
II.1.B	Development of Low-Cost High-Strength Automotive Al Sheet (Arconic).....	164
II.1.C	Phase Transformation Kinetics and Alloy Microsegregation in High-Pressure Die-Cast Mg Alloys (The University of Michigan)	172
II.1.D	Low-Cost Mg Sheet Component Development and Demonstration Project (Fiat Chrysler Automobile, U.S., LLC).....	180
II.1.E	Understanding Protective Film Formation by Mg Alloys in Automotive Applications (Oak Ridge National Laboratory)	208
II.1.F	Thin AHSS with CFRP Coating (Oak Ridge National Laboratory and Idaho National Laboratory).....	214
II.2	Carbon Fiber & Polymer Composites.....	223
II.2.A	Close Proximity Electromagnetic Carbonization (Oak Ridge National Laboratory).....	223
II.2.B	Carbon Fiber Technology Facility (Oak Ridge National Laboratory)	229
II.2.C	Integrated Computational Materials Engineering Development of CF Composites for Lightweight Vehicles (Ford Motor Company).....	237
II.2.D	Development and Integration of Predictive Models for Manufacturing and Structural Performance of CF Composites in Automotive Applications (General Motors)	260
II.2.E	ICME Predictive Tools for LCCF for Lightweight Vehicles (University of Virginia)	286
II.2.F	Consortium for the Production of Affordable CFs in the U.S. (Western Research Institute)	304
II.2.G	Spider Silk MaSp1 and MaSp2 Proteins as CF Precursors (Oak Ridge National Laboratory).....	334
II.3	Multi-Material Joining.....	340
II.3.A	Solid-State Body-in-White Spot Joining of Al to AHSS at a Prototype-Scale (Oak Ridge National Laboratory)	340
II.3.B	Solid-State Joining of Mg Sheet to High-Strength Steel (Pacific Northwest National Laboratory).....	346

II.3.C	Corrosion Protection of Dissimilar Material and Joining for Next-Generation Lightweight Vehicles (Arconic, Inc.).....	355
II.3.D	HPC Tools to Advance Materials Joining Technology (General Motors).....	367
II.3.E	Corrosion Control in CFRP Composite-Al Closure Panel Hem Joints (PPG Industries, Inc.).....	378
II.3.F	High-Strength Steel-Al Components by Vaporizing Foil Actuator Welding (The Ohio State University).....	389
II.3.G	HPC and High-throughput Characterizations towards Interfaces-by-Design for Dissimilar Materials Joining (Oak Ridge National Laboratory).....	401
II.3.H	Adhesive Bonding of Thermoplastic CFRP to AHSS (Oak Ridge National Laboratory) .	411
II.3.I	Mechanical Joining of Mg Alloys to CFRPs (Pacific Northwest National Laboratory)	419
II.3.J	Mitigating Corrosion in Mg Sheet in Conjunction with a Sheet-Joining Method that Satisfies Structural Requirements within Sub-assemblies (Pacific Northwest National Laboratory).....	429
II.3.K	Non-Destructive Inspection of Al-Steel Weld Bond (Oak Ridge National Laboratory)....	437
II.4	Crosscutting.....	446
II.4.A	Materials Goal Setting Analysis (Argonne National Laboratory).....	446
II.4.B	Ultralight Door Design, Manufacturing and Demonstration Project (Magna).....	455
II.4.C	Ultralight Hybrid Composite Door Design and Rapid Manufacture (TPI Composites, Inc.).....	461
II.4.D	Functionally Designed Ultra-Lightweight CF Reinforced Thermoplastic Composites Door Assembly (Clemson University).....	482

List of Figures

Figure I.1.A.1.1. Materials effects on (a) engine GITE and (b) maximum temperature in the head with increased specific output, resulting in higher PCP. Results from GT-Power.	9
Figure I.1.A.1.2. Maximum head temperatures at the baseline (190 bar) and intensified (225 bar) combustion conditions. Results from CFD.	10
Figure I.1.A.2.1. Thermal conductivity of CGI between room-temperature and 650°C.....	13
Figure I.1.A.2.2. Effect of temperature on the yield strength of CGI. Also superposed are the current and anticipated future temperature ranges for cylinder heads [5].....	13
Figure I.1.A.3.1. Average deposit thickness along one period near the inlet for three flow rates obtained from numerical model along with the average of all 20 experimentally fouled coolers.....	18
Figure I.1.A.4.1. The calculated temperature and doping dependence of the Seebeck coefficient, S , in NbFeSb. Note the thermopower magnitudes greater than 200 $\mu\text{V}/\text{K}$ for n-type doping, indicating that, as with p-type doping, n-type doping can also attain high ZT.	21
Figure I.1.A.4.2. (a) The anti-phase boundary (APB) believed responsible for n-type doping in NbFeSb. Note the two Fe sites: “APB Fe” (near the APB) and “non-APB Fe”. (b) The regular bulk NbFeSb structure without an APB. (c) Convergence check on the APB formation energy. (d) Calculations of the density-of-states (DOS) of bulk NbFeSb (black) and two APB-containing supercells (blue and green curves). (e) The DOS of a 4x1x1 APB-containing supercell of NbFeSb....	21
Figure I.1.B.1. Graphical representation of (a) a 1.5L GTDI cylinder head prototyped with Ford-SPMC-w/oSr at Qin’an, China plant; (b) the locations from the deck face (red rectangular) and the bolt boss (green circle) for mechanical tests; and (c) the computed tomography scan results for the 1.5L GTDI cylinder heads showing the distribution of pores. Source: Ford.	26
Figure I.1.B.2. Graphical representation of (a) tensile testing results at room and elevated, and 150°C endurance limit testing results for (b) sub-size and (c) regular samples sectioned from the torpedo samples showing geometrics has little effect on mechanical properties. Source: Ford Motor Company.	28
Figure I.1.B.3. Graphical representation of (a) UTS, (b) YS, and (c) elongation at different temperatures of the AS7GU-T64, Ford-SPMC-w/oSr-3stage, and Ford-SPMC-w/Sr-3Stage sectioned from the torpedo samples, and deck face and bolt boss 1.5L GTDI cylinder heads, showing the proposed alloys and heat-treatment combinations have superior tensile properties at elevated temperatures. Source: Ford Motor Company.	30
Figure I.1.B.4. Graphical representation of (a) a I4-Bearing - Beams castings prototyped with Ford-HPDC alloys at Mag-tec, MI, and X-ray results showing the distribution of the pores; and (b) a Journal-Piece casting prototyped with the C677F alloys at Ryobi, Japan, and the cross-section showing no pores is observed. Source: (a) Ford and (b) Alcoa.	31
Figure I.1.B.5. Graphical representation of (a) UTS and (b) YS at different temperatures of the ADC12Z-T5, C677F-T5, and Ford-HPDC-T5 sectioned from the torpedo samples, I4-Bearing-Beam, and Journal-Piece, showing the mechanical properties of torpedo samples cannot be achieved by the HPDC processes. Source: Ford Motor Company.	32
Figure I.1.B.6. Graphical representation of the flow chart of the cost model showing the key factors. Source: Ford Motor Company.	33

Figure I.1.B.7. Graphical representation of the cost of components calculated by the cost model of a 1.5L GTDI head made from (a) AS7GU-T65 and (b) Ford-SPMC-3stage; (c) the premium of GTDI heads made from Ford-SPMC-3stage over AS7GU-T64 showing the new alloys do not exceed 110% of the cost using incumbent alloys. Source: Ford Motor Company..... 34

Figure I.1.B.8. Graphical representation of the comparison between experiments and ICME simulations: (a) solidification; (b) first stage aging; (c) solution treatment; and (d) second-stage aging, showing the capability and gap for ICME tools. Source: Ford Motor Company. 37

Figure I.1.C.1. Tensile properties of a baseline A356 0.5%Cu alloy (Alloy 1 Trial 2) and the developed alloy (Alloy 2 Trial 2) with comparison to DOE targets identified by colored stars. Tensile specimens were extracted from the deckface and combustion chambers. Samples tested above 150 °C were conditioned for 100 hours at test temperature before testing. Source: GM. 43

Figure I.1.C.2. The relationship between tensile ductility (total elongation) and area fraction of porosity on the tensile fracture surfaces of two alloys at RT. Source: GM..... 45

Figure I.1.C.3. A comparison of defect sizes observed in the tensile fracture surfaces of samples taken from HPOL locations of engine heads made of both Alloy 1 Trial 2 and Alloy 2 Trial 2 and tested at RT. Source: GM..... 45

Figure I.1.C.4. SEM image showing a shrinkage-dominated pore that initiated fatigue crack and significantly reduce the fatigue life in an Alloy 1 deckface sample (740971 cycles at 74MPa, Equivalent Circular Diameter (ECD) of pore: 687µm). Source: GM. 47

Figure I.1.C.5. A comparison of size distributions of defects that initiated fatigue cracks in the deckface and combustion chamber areas of engine heads made of both Alloy 1 and Alloy 2. Source: GM. 48

Figure I.1.C.6. SEM image showing a large slip plane that initiated fatigue crack in a deckface sample of Alloy 1. Source: GM. 48

Figure I.1.C.7. A comparison of size distributions of defects that initiated fatigue cracks in the bolt boss areas of engine heads made of both Alloy 1 and Alloy 2. Source: GM. 49

Figure I.1.C.8. A comparison of size distributions of defects that initiated fatigue cracks in the HPOL locations of engine heads made of both Alloy 1 and Alloy 2. Source: GM..... 50

Figure I.1.C.9. SEM image showing a large slip plane together with porosity that initiated fatigue crack in the HPOL samples of Alloy 1. Source: GM..... 50

Figure I.1.C.10. A comparison of size distributions of defects and shear planes that initiated fatigue cracks in the HPOL locations of engine heads made of both Alloy 1 and Alloy 2. Source: GM. 51

Figure I.1.C.11. Measured thermal expansion of cylinder head specimens with 200 hour preconditioning. Source: GM..... 53

Figure I.2.A.1.(a) A SEM BSE image taken from the τ_{10}/Co SSDC annealed at 800 °C for 500 h, showing the phase formation by interdiffusion and the EPMA line scan location; and (b) EPMA composition profiles collected by performing an EPMA line scan across all the phase interfaces in (a). The vertical dashed lines in (b) show the locations of phase interfaces (University of Florida unpublished results). 58

Figure I.2.A.2. A SEM BSE image taken from the τ_{10} /Cu SSDC annealed at 800 °C for 350 h, showing the phase formation by interdiffusion: (a) Low-magnification image showing the entire diffusion region; (b) High-magnification image showing the phase interface between $\text{Al}_{13}\text{Fe}_4$ and τ_{10} ; and (c) EPMA composition profiles collected by performing an EPMA line scan across the phase interface in (b). The vertical dashed lines in (c) show the location of $\text{Al}_{13}\text{Fe}_4/\tau_{10}$ phase interface (University of Florida unpublished results).....	58
Figure I.2.A.3. A SEM BSE image taken from the τ_{10} /Zn SLDC annealed at 800 °C for 8 h, showing the phase formation by interdiffusion: (a) Low-magnification image showing the entire diffusion region; (b) High-magnification image of the red box location in (a); and (c) EPMA composition profiles collected by performing an EPMA line scan across the phase interface in (b). The vertical dashed lines in (c) show the location of $\text{Al}_{13}\text{Fe}_4/\tau_{10}$ phase interface (University of Florida unpublished results).....	59
Figure I.2.A.4. SEM BSE images taken from the τ_{10} alloys with Co additions that were annealed at 800 °C for 400 h: (a) Al-23.5Fe-10.2Si-1.0Co and (b) Al-22.5Fe-10.2Si-2.0Co. The compositions are all in at.% (University of Florida unpublished results).	60
Figure I.2.A.5. SEM BSE images of τ_{10} alloys with Cu additions that were annealed at 800 °C for 400 h: (a) Al-24.0Fe-11.0Si-1.0Cu and (b) Al-23.0Fe-11.0Si-2.0Cu. The compositions are all in at.% (University of Florida unpublished results).....	60
Figure I.2.A.6. SEM BSE images taken from the τ_{10} alloys with Mn additions that were annealed at 800 °C for 400 h: (a) Al-23.0Fe-11.0Si-1.5Mn and (b) Al-20.0Fe-11.0Si-4.5Mn. The compositions are all in at.% (University of Florida unpublished results).....	61
Figure I.2.A.7. SEM BSE images of τ_{10} alloys with Ni additions that were annealed at 800 °C for 400 h: (a) Al-25.0Fe-10.0Si-1.0Ni and (b) Al-25.0Fe-9.0Si-2.0Ni. The compositions are all in at.% (University of Florida unpublished results).....	61
Figure I.2.B.1.1. Effect of alloy composition on mass change during oxidation at 950 °C in Air + 10% water vapor environment. Source: ORNL.....	66
Figure I.2.B.1.2. New ORNL alloys have improved YSs at 950 °C. Source: ORNL.....	66
Figure I.2.B.1.3. Effect of temperature and time on the USAXS/SAXS data. (a) ~ 835 °C, and (b) 900 °C. Source: ORNL.....	67
Figure I.2.B.2.1. Aluminide coatings at the surface of 31V coupons fabricated at temperatures varying from 750 to 1,000 °C. Source: ORNL.	69
Figure I.2.B.2.2. Comparison of the HCF properties at 816 °C of bare and NiCoCrAlY-coated 31V valve alloy. Source: ORNL.....	69
Figure I.2.B.3.1. Cyclic oxidation at 950 °C in air with 10% H ₂ O. Source: ORNL.	73
Figure I.2.B.3.2. Tensile properties for second generation cast AFA vs. 1.4826. Source: ORNL.....	73
Figure I.2.C.1.1. X-ray non-destructive evaluation of welded AA6061 (top) and Al6.6wt%Cu specimen (bottom). Source: ORNL.....	76
Figure I.2.C.1.2. Experimental setup for pulsed-laser welding study. Source: ORNL.	77
Figure I.2.C.1.3. Design of experiments to determine the effect of pulsed-laser parameters on microstructure of an ACMZ alloy with 6.6 wt% Cu. Source: ORNL.....	77

Figure I.2.C.1.4. Representative secondary electron micrographs of laser tracks demonstrating the main effects of point distance, exposure time, and heat input on microstructure—see Figure I.2.C.1.3 for labels with conditions. The double-headed arrow in (c) highlights the weld depth. All scale bars are 20 μm . Source: ORNL..... 78

Figure I.2.C.2.1. Project feature on the cover of the October 2017 issue of *Advanced Materials and Processes* [2]. Source: ASM International. 80

Figure I.2.C.2.2.(a) Low-magnification microCT reconstruction of A356/316L composite with the 316L shown in dark contrast and the A356 in bright contrast; and (b) Higher magnification microCT reconstructions showing a single unit cell with interfacial porosity, microporosity in the A356, and microporosity in the 316L highlighted in red, blue, and yellow, respectively [3]. Source: Additive Manufacturing..... 81

Figure I.2.C.2.3. Ternary diagram with contours of constant \tilde{K} for body centered cubic composites with either microporosity or interfacial porosity. Source: Additive Manufacturing 82

Figure I.2.C.2.4. Macroscopic loading of different volume fractions (VF) (i.e., 20VF, 30VF, 40VF, and 50VF, for 20, 30, 40, and 50% reinforcement by volume, respectively) and Al356 (no reinforcement). Results highlight that below a 50% volume fraction, the stress is a function of the Al356, where the maximum strain (displacement) is a function of the reinforcement, where a critical volume fraction (~40% volume fraction) displays a significant increase in the strain. Source: ORNL. 83

Figure I.2.C.2.5. Microscopic stress and lattice strain as measured by neutron diffraction for Al and stainless steel (Fe) in the 311 crystallographic plane for the 40% volume fraction stainless steel sample in tensile loading. Source: Rice/ORNL. 83

Figure I.2.C.3.1. A summary figure showing (a) the as-built preforms, (b) the x-ray diffraction (XRD) pattern from the as-built samples, porosity detection with (c) and (d) x-ray computed tomograms showing how HIP eliminates porosity, and (e) the equiaxed microstructures resulting in (f) good tensile properties. Source: ORNL. 86

Figure I.2.C.3.2.(a) The calculated phase diagram for the Ti-48Al composition from the CALPHAD simulations; (b) the Scheil simulation showing the solidification sequence for Ti-48Al and Ti-48Al-2Cr-2Nb compositions; and (c) the Scheil simulation showing the formation range of the γ (Ti-Al) and α phases for Ti-48Al and Ti-48Al-2Cr-2Nb compositions. The α phase circled with red in (a) corresponds to the α phase in (b) and (c). 88

Figure I.2.C.3.3. The powder particle size distribution of the sieved powder. 89

Figure I.2.C.4.1. Analytical stability map for the θ' to θ transformation at 200°C. Source: ORNL..... 92

Figure I.2.C.4.2. Snapshots of phase-field simulations in conditions where (a) θ' phase is stable compared to (b) the θ phase and vice versa. Source: ORNL. 93

Figure I.2.C.4.3. The true stress-strain behavior of Al5CuMg (A206) alloy with different heat-treatments. Source: ORNL..... 93

Figure I.2.C.4.4. Anisotropy in strain hardening under various conditions suggests a change in the mechanism of deformation under the reported four conditions. Source: ORNL..... 94

Figure I.2.D.1.1. Mass change curves of candidate exhaust valve alloys during laboratory cyclic oxidation testing in air + 10% water vapor (WV) at: (a) 800°C, (b) 850°C, (c) 900°C, and (d) 950°C. Source: ORNL. 98

Figure I.2.D.1.2. Cross-sectional SEM backscatter electron images of three alloys after 500 one hour cycles of furnace oxidation testing at 900 °C in 10% WV: (a, d) F31VST, (b, e) FN80ST, and (c, f) R41ST. Source: ORNL.	100
Figure I.2.D.2.1. Automatically fitted k_p , p , and m_0 parameters of ORNL cyclic oxidation dataset using autopkp code: (a) good fitting with high R^2 and low root mean square error (RMSE) and (b) bad fitting with low R^2 and high RMSE. The bad fitting is attributed to the intrinsic limitation of pkp model that is designed to describe smooth parabolic high-temperature oxidation behavior of alloys. Source: ORNL.....	102
Figure I.2.D.2.2.(a) Correlation analysis between elemental compositions of 78 Ni-Cr alloys and their respective rate constant k_p using Pearson method and (b) trained neural network machine-learning model with top 5 features from Pearson analysis (right). Source: ORNL.	102
Figure I.2.D.2.3. Accuracy (represented with Pearson coefficients) of five machine-learning models (RF: random forest, LR: linear regression, NN: neural network, KR: kernel ridge regression, and BR: Bayesian regression) to predict k_p of Ni-Cr alloys at 950 °C cyclic oxidation as a function of number features (n) used within the individual training. Source: ORNL.....	103
Figure I.3.A.1. Standard SCR performance of three SCR catalysts (A, B, and C) prepared using zeolite substrates synthesized in different batches. Source: PNNL.....	105
Figure I.3.A.2. DFT simulated Cu(II) and Na ⁺ structures in SSZ-13. (A) Cu ²⁺ in 6MR and Na ⁺ in 8MR; (B) Na ⁺ in 6MR and [Cu ^{II} (OH)] ⁺ in 8MR. Structure (B) is ~43 kJ/mol less stable than (A). Color codes: Cu: green; Na: blue; O: red; H: white. Source: PNNL.....	106
Figure I.3.A.3. DFT simulated [Cu ^{II} (OH)] ⁺ hydrolysis to Cu(OH) ₂ with and without the presence of Na ⁺ . (A) Initial structure, [Cu ^{II} (OH)] ⁺ + H ₂ O in cage next to 8MR; (B) Final structure, Cu(OH) ₂ + H ⁺ in cage next to 8MR; (A') Initial structure, [Cu ^{II} (OH)] ⁺ + Na ⁺ + H ₂ O in cage next to 8MR; (B') Final structure, Cu(OH) ₂ + Na ⁺ H ⁺ in cage next to 8MR Structure. The latter hydrolysis is energetically much more facile than the former. Color codes: Cu: green; Na: blue; O: red; H: white. Source: PNNL.	107
Figure I.3.A.4. Standard SCR performance of the second and third SCR catalysts after hydrothermal aging at 700 °C. Source: PNNL.....	108
Figure I.3.B.1. Conventional brake design utilizing an Al caliper and a cast-iron brake disc. Source: PNNL.	110
Figure I.3.B.2. Project tasks. Source: PNNL.....	111
Figure I.3.B.3. Tilt-pour stir-casting equipment at PNNL used for the casting trials. Flat-bladed impeller installed in mixer head. Source: PNNL.....	112
Figure I.3.B.4. Impeller designs for mixing trials. Source: PNNL.	112
Figure I.3.B.5. Brake-friction pair test-stand at PNNL. Source: PNNL.	113
Figure I.3.B.6. (a) Brake pad holder and (b) tested subscale brake rotor. Source: PNNL.	113
Figure I.3.B.7. (a) Wear-track profilometry and (b) transfer layer chemistry characterization. Source: PNNL.	114
Figure I.3.B.8. (a) Stir-casting trials and (b) cast plates of 5 vol % TiB ₂ reinforced A356 alloy. Source: PNNL.	114
Figure I.3.B.9. As-cast 5 vol % TiB ₂ -reinforced A356. Source: PNNL.....	115

Figure I.3.B.10. 5 vol % TiB₂-reinforced A356 hot-rolled 30% reduction. Source: PNNL. 115

Figure I.3.B.11. 5 vol % TiB₂-reinforced A356 hot-rolled, solutionized, and artificially aged to T7. Source: PNNL. 116

Figure I.3.C.1. Induction motor rotor and an example of a shorting bar. Source: PNNL..... 118

Figure I.3.C.2. Shear-Assisted Extrusion machine. Source: PNNL..... 119

Figure I.3.C.3. Schematic diagram of ShAPE. Source: PNNL. 120

Figure I.3.C.4. Cu cylinder drilled and filled with C powder Source: PNNL..... 120

Figure I.3.C.5. Carbon additions used for high-conductivity Cu-C composite: (a) graphite, (b) graphene and (c) C nanotubes. Source: PNNL. 121

Figure I.3.C.6. Cu wire made from (a) pure Cu powder and (b) pure Cu solid billet. Source: PNNL. . 121

Figure I.3.C.7. Cross-sections of wire made from pure Cu powder and solid cylinder, as compared with conventional extruded Cu wire in transvers and longitudinal directions. Source: PNNL. 122

Figure I.3.C.8. Microstructure of Cu-C ShAPE wire (a) transverse cross-section, (b) longitudinal cross-section, (c) vertical cross-section of remnant disc, (d) grain structure with phase mapping and (e) scanning electron microscope image with higher magnification (black is C and grey is Cu). Source: PNNL. 123

Figure I.3.C.9. Overview of the conductivity of Cu-C ShAPE wire. Source: PNNL. 124

Figure I.3.D.1.1. Average deposit thickness near the inlet, middle, and outlet of cooler. Flow direction left to right. Source: ORNL. 127

Figure I.3.D.2.1.(a) Calculated and measured module efficiency from the international round-robin; (b) Typical test setup for efficiency measurements; and (c) Effect of applied load on heat flux. Source: ORNL. 131

Figure II.1.A.1.1. Computational modeling method to predict the edge stretchability of sheared/trimmed samples. Source: PNNL. 135

Figure II.1.A.1.2. Comparison of experimental data (i.e., fracture mode and load-displacement curve) of two DP980 steels. Source: Oakland University & PNNL. 136

Figure II.1.A.1.3. Validation of computational modeling method against the experimental data of the two DP980 steels. Source: PNNL. 137

Figure II.1.A.1.4.(a) Microstructure of tempered DP2 steel; (b) phase stress-strain curves from HEXRD test; (c) comparison of HER between DP2 and tempered DP2; and (d) simulations showing the increase of edge stretchability after tempering. Source: AK Steel & PNNL..... 138

Figure II.1.A.1.5. Schematics of (a) “dull punch with a support” [2] and (b) “shear” [3] trimming processes with (c) a comparison of trimming-induced edge damage level between the three different trimming processes and (d) simulations showing some increase of edge stretchability based on these two trimming processes as compared to the conventional trimming process. Source: PNNL. 139

Figure II.1.A.2.1. Cross-section of tooling showing a direct tubular extrusion of the ShAPE™ process. Source: PNNL. 142

Figure II.1.A.2.2. ShAPE™ machine with new torque module capable of 2987 Nm @ 25 to 160 rpm. Source: PNNL.....	142
Figure II.1.A.2.3. Portal bridge die design for extruding a square tube using ShAPE™ for (a) assembly, (b) eight-scroll pattern, (c) the square mandrel and (d) weld chamber with cooling channel and square port. Source: PNNL.....	143
Figure II.1.A.2.4. Process parameters (a) and extruded tubing (b) made directly from as-cast ZK60 using ShAPE™. Source: PNNL.....	144
Figure II.1.A.2.5. Microstructural comparison of as-cast and wrought ZK60 billets (a) before and (b) after ShAPE™ extrusion. Source: PNNL.....	146
Figure II.1.A.2.6. Microstructural comparison of as-cast and wrought ZK60 billets before and after ShAPE™ extrusion. Source: PNNL.....	147
Figure II.1.A.2.7. Orientation of tensile specimens relative to extrudate. Source: PNNL.....	148
Figure II.1.A.3.1.(a) Example of tensile stress-strain curve and austenite volume fraction evolution of a 7Mn steel, and examples of simulation showing (b) Lüders banding behavior, and (c) resulting yield point elongation. Source: PNNL.....	151
Figure II.1.A.3.2. <i>Ex-situ</i> heat-treatment and characterization of 5Mn steel. (a) Heat-treatment profile; (b) austenite volume fractions; and (c) microstructures for four different conditions. Source: PNNL & Colorado School of Mines.....	153
Figure II.1.A.3.3.(a) <i>In-situ</i> measurement of austenite volume fraction versus the time for different holding temperatures with as-quenched 5Mn steel using HEXRD and (b) Mn mobility determined for the DICTRA simulation by fitting with the experimental results. Source: PNNL.....	154
Figure II.1.A.3.4. ShAPE™ machine with new torque module capable of 2987 Nm @ 25-160 rpm. Source: PNNL.....	155
Figure II.1.A.3.5. Austenite growth prediction during IA from MICRESS® Simulation 1.....	156
Figure II.1.A.3.6. MICRESS® simulation results for IA of a 0.19C-4.39Mn steel: (a) Microstructural evolution and solute partitioning for initial microstructure consisting of equiaxed ferrite. (b) Initial microstructure consisting of elongated ferrite, and predictions for microstructural evolution after 200 seconds for conditions (c) 2i, (d) 2ii, and (e) 2iii. Source: Colorado School of Mines.....	158
Figure II.1.A.4.1. Images of the steel side-impact beam: (a) Top view; (b) Bottom view. Source: PNNL.....	161
Figure II.1.A.4.2. A simulated image of the steel impact beam reconstructed after scanning the actual beam and corresponding to the view shown in Figure II.1.A.4.1(b). Source: Magna Intl.....	162
Figure II.1.A.4.3. Schematic of the stamping simulations performed showing the process sequence: (a) crash form, where the sheet is free to move; and (b) draw form, where the sheet is clamped, and its movement is controlled. Source: PNNL.....	162
Figure II.1.A.4.4. Image of an Al side-impact beam produced by stamping simulations. Locations 1–7 refer to places where the post-formed sheet thickness is measured, and the corresponding strain is listed in Table II.1.A.4.1. Source: Magna Intl.....	163
Figure II.1.B.1. Demonstration part geometry. Source: Honda.....	165
Figure II.1.B.2. Forming cell. Source: Cosma.....	166

Figure II.1.B.3. Selected results from forming trial. Source: Cosma.	166
Figure II.1.B.4. Section of demonstration part used for three-point bend tests. Source: Cosma.....	167
Figure II.1.B.5. Schematic views of the Al7055T6 hat section setup under three-point bending load. Source: Cosma.....	167
Figure II.1.B.6. Typical performance of samples in a three-point bend test. Source: Cosma.....	168
Figure II.1.B.7. Comparison of load deflection curve from three-point bend testing. Source: Arconic.	168
Figure II.1.B.8. UTs measured from formed parts. Source: Arconic.....	169
Figure II.1.B.9. Elongations measured from warm-formed and paint-baked parts. Source: Arconic.	169
Figure II.1.B.10. Three-point bend test results. Source: Cosma.....	170
Figure II.1.B.11. Part formed using a tailor-welded blank. Source: TWB Company.....	171
Figure II.1.C.1. SDAS/grain size as a function of cooling rate in AZ and AM series alloys with the empirical fit.....	174
Figure II.1.C.2.(a) Illustration of the setups and assumptions used in the Forward Model simulation; (b) Comparison between using Forward Model simulation and EPMA measurements of Al concentration in as-cast AM70 alloys as a function of fraction at different locations; (c) the velocity-dependent partition coefficient, k_v , is inferred based on the average Al concentration equation and EMPA macro-segregation results. These values are in good agreement with the Forward Model prediction; (d) Comparison between k_v value using the two different methods; data points represent micro-model calculations and lines represent the experimental measurements.	175
Figure II.1.C.3.(a) β phase dissolution model [UM]; and (b) The comparisons between SEM measurements and the DICTRA simulation of β phase volume fraction of Mg-11Al 2.5 mm plate at various time at 420 °C.	177
Figure II.1.D.1. Illustration of the 2013 Ford Fusion door showing the progression from baseline steel to Multi-Material Lightweight Vehicle Al to Al-intensive door with Mg inner and outer panels selected for demonstration in warm-forming. Source: Ford Motor Company.....	181
Figure II.1.D.2. Iso-concentration projection of solutes (a) Al, (b) Ca, (c) Zn, and (d) Mn in a Mg matrix at 430°C. Source: OSU.....	184
Figure II.1.D.3.(a) Scheil calculation and (b) equilibrium calculation of Alloy 2 using Pandat software. Source: OSU.....	185
Figure II.1.D.4.(a) Single-phase homogenization model; (b) homogenization profile; and solute distribution of (c) Zn; (d) Ca; (e) Ce; and (f) Mn in Alloy 2. Source: OSU.....	186
Figure II.1.D.5. Microstructures of Alloy 2 under (a) as-cast; (b) homogenized at 350°C (H350); (c) homogenized at 375°C (H375C); (d) as-rolled at 350°C (H350); (e) H350-R350-A350 for ten minutes; (f) H350-R350-A350 for 1 hr; and (g) grain size evolution. Source: OSU.....	188
Figure II.1.D.6. (a) Maximum amount of Ca in solid-solution as a function of temperature in Mg and (b) the phase diagram of Mg-0.35 wt.% Ca as a function of Zn composition. Source: UF.	190

Figure II.1.D.7. (a) XRD pattern obtained from the as-cast and homogenized Mg-0.1 wt.% Ca alloy and (b) a spot EDS spectrum of a Mg ₂ Ca particle from the homogenized alloy with the inset showing the particle and location from which the spectrum was obtained. Source: UF.....	190
Figure II.1.D.8. Effect of solutes on the change in yield stress required to move basal [3] and 1012 twinning dislocations at RT showing (a) the change in yield stress versus solute concentration for both deformation modes; and (b) the ratio of the total twinning yield stress to the total basal yield stress versus solute concentration. Source: University of Illinois.....	192
Figure II.1.D.9. Electron backscatter diffraction pole figures and RT Erichsen domes (where available) for the four Mg-alloy sheets (RD = radial direction; TD = transverse direction). Source: UM.....	193
Figure II.1.D.10. Deep draw cups of ZEK100 and EFP performed at (a) 100°C and (b) 250°C. Source: UM.....	193
Figure II.1.D.11. The basic concepts of the Anton Parr Rheometer and the two test conditions: (a) dry and (b) wet. Source: Fuchs.....	195
Figure II.1.D.12. Representative results of comparative testing of five candidate Fuchs lubricants at (a) 200°C; (b) 100°C; and (c) ambient temperature. Source: Fuchs.....	197
Figure II.1.D.13. Results of lubricant tests on EFP sheets are similar, without or with Henkel pretreatment. Source: Fuchs.....	198
Figure II.1.D.14. A typical automotive pretreatment (PT) sequence, prior to electrocoat. Source: PPG.....	200
Figure II.1.D.15. Baseline door inner and outer dies to be used to produce Mg parts. Source: Vehma International.....	205
Figure II.1.E.1. Cross-section images by SEM (a, b) and STEM (c, d) showing the as-coated structure formed on wrought AZ31B-H24 and WE43 alloys with an initial, inner EC layer and a subsequent E-Coat top coat. Source: ORNL.....	210
Figure II.1.E.2. Corrosion rates calculated from hydrogen evolution measurements for seven day exposures in 0.1M NaCl solution for AZ31B-H24, AZ91D, ZE10A, and WE43 uncoated, with an initial EC layer, and dual-layer EC + E-Coat (triplicate samples exposed). Data courtesy E.A. McNally and J.R. Kish, McMaster University.....	211
Figure II.1.E.3. Cross-section SEM images showing corrosion attack at the scribe-coating interface for (a) AZ31B-H24, (b) AZ91D, (c) ZE10A, and (d) WE43 EC + E-Coated after an initial seven day immersion in 0.1M NaCl solution as-coated, and then an additional eight day immersion after scribing. Source: ORNL.....	212
Figure II.1.F.1. Fiber orientation in CFRE in both directions when applied to the steel substrate. Images (a) and (b) are the longest fibers, while (c) and (d) are the shortest fibers. Source: ORNL..	216
Figure II.1.F.2. Cross-section of CFRE coating on a DP500 steel substrate: (a) internal voids; (b) surface voids; (c) fiber failure at surface; and (d) adherence to the steel substrate. Source: ORNL.....	217
Figure II.1.F.3. Application of the CFRE for (a) total coverage and (b) isolated coverage. Source: ORNL.....	218

Figure II.1.F.4. (a) Dent test result for various thickness DP500 steel panels with and without CFRE patches applied. (b) Test sample showing the three test locations and the dent testing indenter. Source: ORNL. 219

Figure II.1.F.5. Typical thermal expansion behavior exhibited by composite samples. After the transient observed during the heating segment of the first cycle, the curves have an increasing slope with temperature, indicating the thermal expansion behavior of the material is nonlinear. Source: ORNL. 220

Figure II.1.F.6. Plot of the derivative of thermal strain with temperature as a function of temperature between 70 °C and 160 °C. Source: ORNL. 221

Figure II.2.A.1. Example of a CEM of a wide-tow (partial top view) traveling from left to right through a section of CPEC-4. Source: 4X Technologies. 226

Figure II.2.B.1. (a) and (b) Highlights from joint projects [4-6]. Source: ORNL. 233

Figure II.2.B.2. Tensile properties for Montefibre textile CF: (a) tensile strength and (b) tensile modulus. Source: ORNL..... 234

Figure II.2.B.3. *In-situ* concepts for CF manufacturing. Source: ORNL..... 235

Figure II.2.C.1. Ultrasonic probe setup. Pulse is the applied ultrasonic signal. Front-wall and back-wall echoes are the measured responses of the sample. Sampling “gates” are time-distributed subsamples of the output that are correlated to “slices” within the thickness of the sample. Source: NU..... 241

Figure II.2.C.2. Representative impact-surface image from UD [0/90/90/0/0/0]_s hat section. Source: NU..... 241

Figure II.2.C.3. Representative image from dynamic 3-point bending tested woven [0/90]₄ hat section. Source: NU..... 241

Figure II.2.C.4. Set of five successive ultrasonic scans showing internal damage at different locations through the material thickness. In each figure (a) through (e), the bright features show strong acoustic echoes, indicative of damage at a given location (or depth). Red marks highlight the “bright” leading edge of the damage zone in each scan image. Source: NU..... 242

Figure II.2.C.5. Punch force comparison for different material models. Source: NU. 243

Figure II.2.C.6. Final part shapes and yarn angle distributions (values for locations A – E given in Table II.2.C.2). Source: NU. 244

Figure II.2.C.7. Double-dome preforming punch force comparison. Source: NU..... 244

Figure II.2.C.8. (a) The Moldflow model of SMC sub-frame upper molding; and (b) fiber orientation prediction. Source: Ford Motor Company..... 245

Figure II.2.C.9. (a) Stress contour in matrix phase of the circular RVE; (b) stress contour in matrix phase of the bean RVE; (c) plastic strain contour of circular fiber; and (d) plastic strain contour of bean fiber. Source: NU..... 246

Figure II.2.C.10. Normal stress vs. displacement plot from SCA simulation with (a) gauge for the fiber direction, (b) the resultant stress-strain curve and (c) displacement of the sample in the y-direction. Source: NU. 247

Figure II.2.C.11. Comparison between experiments and simulation of delamination in UD dynamic 3-point bending test for (a) the top and (b) the side wall. Source: Ford Motor Company...	248
Figure II.2.C.12. Constant fatigue life diagrams of woven composites in (a) weft, (b) warp, and (c) 45 degree orientations. Source: Ford Motor Company.....	249
Figure II.2.C.13. (a) The undeformed structure: bottom end is clamped, top end is pulled by 1 mm. (b) through (d): spatial variations in yarn angle (in degrees); fiber volume fraction (percentage); and fiber misalignment angle (in degrees), respectively, across the integration points for case 10 in Table II.2.C.3.(e) through (g): those of case 8 in Table II.2.C.3. Source: NU. ...	250
Figure II.2.C.14. Effect of spatial variations on force-displacement curves and stress in the mid-section: (a) average and (b) standard deviation of force-displacement curves. (c) Mean and (d) standard deviation of von-Mises stress at the mid-section. In cases 3 through 10, the mean and standard deviation are calculated for 30 simulations. Source: NU.	252
Figure II.2.C.15. Integrated process for SMC-intensive sub-frame. Source: Ford Motor Company...	253
Figure II.2.C.16. Status of parametric models for three “seed” designs. Source: Ford Motor Company.....	255
Figure II.2.C.17. MDO process steps for sub-frame design. Source: Ford Motor Company.....	256
Figure II.2.C.18. Interesting initial design regions being further investigated and refined. Source: Ford Motor Company.....	257
Figure II.2.D.1. Draping results of BX240 V114CHA without using the frame. Folds are highlighted in red circles. (a) Image of the fabric from the experiment. (b) Simulation results. Source: GM.	264
Figure II.2.D.2. The preforming rig in the (a) open and (b) closed positions. Source: ESI.	265
Figure II.2.D.3.(a) Test vs (b) simulation for NCF (+/-45) fabric with fibers in 45° along length. Source: ESI.	266
Figure II.2.D.4.(a) Test vs (b) simulation for a central blank holding mechanism. Source: ESI.....	266
Figure II.2.D.5.(a) Test vs (b) simulation for NCF fabric draping 0° along the length of reinforcement. Source: ESI.....	267
Figure II.2.D.6.(a)Test vs (b) simulation showing no wrinkles with slits. Source: ESI.....	267
Figure II.2.D.7. Slit patterns used in the draping of reinforcement. Source: CSP.	268
Figure II.2.D.8.(a) Deformed shape after gravity test; (b) Deformed shape after punch test; (c) Deformed shape after gravity simulation; and (d) Deformed shape after punch simulation. Source: ESI.	268
Figure II.2.D.9. Pressure evolution for peripheral injection - test vs simulation. Source: ESI.....	269
Figure II.2.D.10. Void formation comparison for (a) test and (b) simulation. Source: ESI.	270
Figure II.2.D.11. Molded RTM plaque with overlap location indicated. Source: CSP.	270
Figure II.2.D.12. Different overlap configurations. Source: CSP.....	271
Figure II.2.D.13. Force-displacement plots of R5 simulation for a three-point bend model overlaid with experimental data. Source: Altair.....	272

Figure II.2.D.14.(a) Images of a double-hat beam during the experiment with (b) the approximate correlating frame of the simulation. Source: Altair.....	273
Figure II.2.D.15. Description of geometric attributes of twill weave unit. Source: GM.....	274
Figure II.2.D.16. Non-orthogonal models sheared at different angles. Source: GM.	275
Figure II.2.D.17. MDS predictions compared to the experimental results for twill tensile specimen modulus vs average angle. Source: GM.	275
Figure II.2.D.18. Framework of multiphysics problem of the curing process, with arrows denoting the direction of coupling between various physical fields. Source: GM.	276
Figure II.2.D.19. Spatial distribution of permeability following draping process. Stochasticity in spatial distribution is induced by fiber properties and initial orientation of fibers. Source: USC.	279
Figure II.2.D.20. PDF of (a) fill time and of (b) maximum stress following distortion analysis. The two curves show results for two successive reduced models, indicating convergence of analysis. Results show a 12% coefficient of variation. Source: USC.	279
Figure II.2.D.21. Probability distribution function of (a) axial modulus and (b) strength obtained for tensile test simulation. Source: GM.	280
Figure II.2.D.22. PDF of (a) flex modulus and (b) strength obtained from three-point bend test simulation. Source: GM.	281
Figure II.2.E.1. Process for spinning of filament fibers: (a) fibers are wet-spun through a series of chemical baths from a spinneret, (b) bundle of fiber cross-sections viewed using SEM and (c) individual precursor PAN fiber images with SEM. Source: UVA.	289
Figure II.2.E.2. Wet-spun PAN fibers and their properties. Laboratory-scale processed PAN fibers in: (a) a polymer filament state; and progressing through (b) stabilization; and (c) carbonization. (d) XRD peaks at each processing step; and (e) mechanical properties of the carbonized CF. Source: UVA.	290
Figure II.2.E.3. PAN/graphene blend CFs and mechanical properties: (a-f) Cross-sections of carbonized PAN fibers with increasing concentrations of graphene (0.00 wt.% - 0.01 wt.%). (g-h) Mechanical properties of PAN/graphene blend fibers. Source: UVA.....	291
Figure II.2.E.4. Considered polymers and comparison between DFT and ReaxFF for PAN-related chemistry. Molecular structure of the considered polymers: (a) idealized ladder PAN; (b) proposed oxidized PAN; (c) PBO; and (d) reaction energy for $\text{CH}_3 + \text{N}_2 \rightarrow \text{CH}_3\text{N}_2$ reaction. ReaxFF2018 predicts this reaction to be endothermic, the same as DFT, while ReaxFF2012 makes it very exothermic. (e) Removal of N_2 molecule from ladder PAN structure and formation of two neighboring 5-membered C rings. (f) Formation of ladder PAN from linear PAN. The DFT numbers are calculated using B3LYP hybrid functional and 6-311G** basis set. The cyan, blue, and white spheres represent C, N, and H atoms, respectively. Source: PSU.....	293
Figure II.2.E.5. MD with ReaxFF, and stress-strain simulations. A comparison between data obtained with ReaxFF2012 and ReaxFF2018: time evolution of 6-membered rings during the carbonization process and small molecule production for (a, d) idealized ladder PAN; (b, e) proposed oxidized PAN; and (c, f) PBO, respectively. Different initial configurations (g) random vs align, and idea for simulations (h) without and with hot-stretching. (i) Stress-strain data for ladder PAN obtained for strain rate 10^{10}s^{-1} . Source: PSU.	295

Figure II.2.E.6. Schematic of the atomistic procedure for obtaining the 3D microstructure of CFs. The C contents and hydrogen atoms are shown with green and white colors, respectively. Source: UVA.....	296
Figure II.2.E.7. Pore distribution and simulated XRD of PAN. Atomic configuration of one of the fibers generated in atomistic simulations and several structural parameters used in the characterization of the fiber microstructure. Source: UVA.....	297
Figure II.2.E.8. Exploratory work converting Nylon to CFs: (a) Potential process for conversion of Nylon to carbon; and (b) Parametric study results of conversion of Nylon 6 fibers to CFs indicating that it is possible to convert Nylon to carbon. Source: ORNL.....	300
Figure II.2.E.9. Illustration of CF production. Schematic of the oxidation/carbonization process and the corresponding XRD and Raman results. Source: Solvay.....	301
Figure II.2.F.1. Organization for the Consortium for Production of Affordable CF in the United States. Source: WRI.....	307
Figure II.2.F.2. Scanning electron microscope images showing (a) fibers spun using CTP-containing insolubles that caused surface defects and (b) fibers from the same CTP source after removing NMP-insolubles showing no surface defects. Source: ORNL.....	310
Figure II.2.F.3. Cross-polarized light optical microscopy micrographs showing the progress of mesophase during pyrolysis of iCTP6-MMP at different stages of the thermal reaction. (a) Micrograph of mostly isotropic pitch with large mesophase spheres and several much smaller mesophase spheres, (b) very large mesophase spheres starting to coalesce into a continuous phase and (c) the complete conversion to coalesced mesophase. Source: WRI.....	312
Figure II.2.F.4. A photograph of the ACP 10 continuous pitch processing equipment. Source: ACP.	313
Figure II.2.F.5. Cross-polarized light optical microscopy micrograph showing 95+% mPP produced from M50 iPP by ACP. Source: WRI.....	314
Figure II.2.F.6. Micrographs of CFs from SEL347 (a) as-spun, (b) after stabilization and (c) after carbonization. Source: ORNL.....	315
Figure II.2.F.7. Cross-polarized light optical microscopy of attempted mesophase conversion of (a) gilsonite IR200 and (b) gilsonite ER125 in sealed reactors. Source: WRI.....	315
Figure II.2.F.8.(a) Optical micrograph of the final CF with an average diameter of 7.55 μm and (b) stress vs strain plot for 10 CF samples derived from textile-grade PAN. Source: ORNL.....	316
Figure II.2.F.9. Chemical and physical characterization schema use by WRI to characterize CTP, PP, and gilsonite materials. Source: WRI.....	319
Figure II.2.F.10. Example SAR-AD™ chromatogram using an evaporative light scattering detector (approximate wt.%) and a variable optical absorbance wavelength detector set at 500 nm (concentration of brown colored material). Details to the right of the chromatogram explains some of the compositional details for what reports to the various fractions. Source: WRI.....	319
Figure II.2.F.11. Parallel plots of SAR-AD™ data showing the fingerprints of some of the materials evaluated under this work. Source: WRI.....	320
Figure II.2.F.12. (a) MD approaches adopted for simultaneously capturing reactions at the atomistic level and bulk properties at the continuum-level, (b) MD and traditional non-reactive	

and reactive force field techniques and (c) course-grained model development for PAN precursors, where each monomer is lumped into one bead. Source: GG-MIT.	322
Figure II.2.F.13. Computational workflow to simulate the full CF synthesis process. Source: GG-MIT.	323
Figure II.2.F.14. Representative molecular models studied up to date for (a) benchmarking models for mesophase preparation, (b) testing systems for oxidation and pyrolysis, and (c) CF precursors selected from literature [26–29].	324
Figure II.2.F.15. Key results for anisotropic alignment of molecules for (a) mixture of coronene and tetracene and (b) 100% coronene, (c) product distribution, and (d) reaction pathways observed and (e) CF snapshot. The corresponding molecular models are shown for each panel. Source: GG-MIT.	326
Figure II.2.F.16. Hexagonal fiber packing model images for (a) longitudinal normal stresses under longitudinal loading and (b) longitudinal shear stresses under longitudinal shear loading. Source: UW.	327
Figure II.2.F.17. Four separate stochastic realizations of a microstructure ensemble with morphology-based meshing strategy along with images of failure of synthetic microstructures initiating between fibers under transverse loading. Source: UW.	328
Figure II.2.F.18. Tow-level composite plate with tabs attached. Source: UW.	328
Figure II.2.F.19.(a) Cost distribution pie chart for biomass to ACN production and ACN production cost sensitivity with respect to (b) sugar; (c) NH ₃ ; and (d) H ₂ price. Source: SR.	329
Figure II.2.G.1. Thermogravimetric analysis of MaSp1 using four different pretreatments. The ramp was set at 10 °C/min after stabilization. This plot shows that MaSp1 produces between 19% and 27% char yield, according to selected procedure. This makes this material theoretically suitable for carbonization. Source: ORNL.	337
Figure II.2.G.2. Optical microscopy images of two examples of isolated MaSp1 filament highlighting the irregularity of the cross-section of these filaments. Source: ORNL.	337
Figure II.2.G.3. Observation of the cross-section of fused filaments of a MaSp1 non-degummed after conversion. Source: ORNL.	338
Figure II.3.A.1. A schematic of the component for in-situ DIC measurement. Source: ORNL.	343
Figure II.3.A.2. Comparison of gap measured by DIC and predicted numerical model at peak paint-bake temperature. Source: ORNL.	344
Figure II.3.A.3. Concept of FBJ work cell. Source: ORNL.	345
Figure II.3.B.1. Data for (a) mean interface temperature trends at various FSW runs and (b) spindle torque and power required for length of welds. Source: PNNL.	348
Figure II.3.B.2. Relative interfacial motion during the welding of the Mg-Mg stack showing that interfacial heat generation is associated with the occurrence of sliding (e.g., high amplitudes on the relative velocity curves) during USW. Source: ORNL.	349
Figure II.3.B.3. Ultrasonic C-Scan non-destructive analysis of the Mg-Mg weld samples (14 mm × 14 mm image area). Source: ORNL.	349

Figure II.3.B.4. Load vs. extension plot of for joints made between AZ31 and DP590 steel made using (a) friction stir scribe technique and (b) ultrasonic welds. Source: (a) PNNL and (b) ORNL.	350
Figure II.3.B.5. Fracture surface and representative joint cross-section of DP 590/Mg joints made with (a) Zn-coating and (b) without Zn-coating with the USW joint cross-sections and micrographs shown below the fracture image. Source: ORNL.	352
Figure II.3.B.6. Friction stir scribe joint fracture surface. Back-scattered and secondary images of Mg and Steel side show elemental and topography of the fracture. Source: PNNL.	352
Figure II.3.B.7. Interfacial structures for (a) friction stir scribe setup showing material stackup and (b) schematic representation of welded joints showing hook features. The highlighted yellow square indicates the locations with a higher magnification of SEM images that are shown for joints made with (c) hot dipped galvanized (HDG) coating; (d) partially removed Zn coating; (e) 10 μ m electro-galvanized (EG) coating; and (f) no coating. (g) Close-up SEM image of a continuous interlayer observed in the joint made with 20 μ m Zn coating. (h) SEM image of interface outside the weld region showing Mg/Zn eutectic IMC. Source: PNNL.....	353
Figure II.3.B.8. Mg/Zn-coated steel joint cross-section that was exposed to 72 hours inside a salt-fog chamber per ASTM B117 showing areas with different extents of corrosion. Source: PNNL.....	354
Figure II.3.C.1. EL Trial: 1.2 mm 980MPa to 1.2 mm 980MPa to 3.0 mm Aural 2-T7 (9 mm Pilot in Steel Sheets) through Dow 5055-C with F7-5 Rivet.	358
Figure II.3.C.2. Weld Sections of (a) 1.2 mm 980MPa to 1.2 mm 980MPa to 3.0 mm Aural 2-T7 and (b) using the F7-5 and 9 mm Pilot Holes in the Steel Sheets – left no adhesive, right Dow 5055-C adhesive. Source: Arconic.....	358
Figure II.3.C.3. EL Trial: 4.0mm CFRP to 3.0mm 6013-T4 with Dow 5055-C Adhesive, F7-7 Rivet, 9mm Pilot.	359
Figure II.3.C.4. EL Trial: 1.2 mm 980MPa to 3.0 mm Aural 2 (6 mm pilot) through Dow 5055-C with R4-6GA-V: (a) Weld #7 Section, (b) Weld #107 Section, and (c) Weld #194 Section. Source: Arconic.	359
Figure II.3.C.5. Macro-photographs of RSR samples after 32.4 days of ASTM B117 exposure. Source: OSU.....	361
Figure II.3.C.6. Macro-photographs of RSR samples after 21 days of ASTM G85 exposure. Source: OSU.....	361
Figure II.3.C.7. Macro-photographs of RSR and SPR joints of the same metallurgy after ASTM B117 exposure. Source: OSU.....	362
Figure II.3.C.8. Macro-photographs of RSR and FDS joints of the same metallurgy after ASTM B117 exposure. Source: OSU.....	362
Figure II.3.C.9. Mechanical testing results of steel RSR coupons made with 980MPa steel and various Al alloys after (a) ASTM B117 and (b) G85 exposure.....	363
Figure II.3.C.10. Mechanical testing result of steel RSR and FDS coupons made with AA7055-T76 and 980MPa steel after (a) ASTM B117 and (b) G85 exposure.	364
Figure II.3.C.11. Mechanical testing results of steel RSR and SPR coupons made with AA6013-T4 and 590MPa steel after (a) ASTM B117 and (b) G85 (right) exposure.....	364

Figure II.3.C.12. Cross-section and corrosion depth attack of a steel RSR joint between AA7055-T76 sheet (top) and 980MPa sheet (bottom) exposed to ASTM G85 for 21 days. Red circles highlight areas of accelerated corrosion. Source: OSU.	365
Figure II.3.C.13. Syringe cell polarization curve overlays of in 5 wt% NaCl solution acidified to pH 3. The black box shows the galvanic corrosion rates in a ASTM B117 like solution (5 wt% NaCl at neutral pH).....	366
Figure II.3.D.1. Illustrative real-world examples taken from the: (a) automotive; and (b) nuclear power industry, for which HPC welding simulation would make a major impact. Source: (a) GM; (b) Electric Power Research Institute.....	368
Figure II.3.D.2. Laser beam welding of panel structure: (a) laser beam configuration; and (b) fixture setup. Source: GM.	371
Figure II.3.D.3. Welding pass layout for the EPRI round-robin model. Source: ORNL.	372
Figure II.3.D.4. Comparison of simulation results between ABAQUS and the in-house codes: (a) Von-Mises stress; and (b) equivalent plastic strain. Source: ORNL.	373
Figure II.3.D.5. Computed hoop stress in full view and cut view. Source: ORNL.....	374
Figure II.3.D.6. Thermal analysis results: (a) transient temperature at three seconds; and (b) weld penetration shape. Source: ORNL, GM for photomicrograph.	375
Figure II.3.D.7. Simulated distorted shape of the auto-body panel: (a) left panel by in-house code; (b) right panel by in-house code; (c) left panel by ABAQUS code; and (d) right panel by ABAQUS code. Source: ORNL.	377
Figure II.3.E.1. Potentiodynamic polarization plot showing overlap of primed and unprimed CFRP and AA6xxx.	381
Figure II.3.E.2. Stress intensity curve for freely corroding and Held OCP conditions in 3.5 wt% NaCl under slow strain rate rising displacement testing on AA6111-T8-like showing threshold stress intensity at $12.7 \text{ MPa}\sqrt{\text{m}}$ and $8.5 \text{ MPa}\sqrt{\text{m}}$, respectively. Inset plot shows the fluctuation of corrosion potential over a range of approximately 70 mV _{SCE} during SCC testing under the freely corroding condition.	382
Figure II.3.E.3. Twelve week chamber exposed coupons of uncoated and e-coated AA6111-Random. Source: OSU.	383
Figure II.3.E.4. Images of prototype and control electrocoats on an AA 6011 substrate upon ASTM A2 G-85 corrosion test for (a) three weeks and (b) six weeks. Source: PPG.	384
Figure II.3.E.5. Storage modulus and the glass transition temperature (T _g) as a function of temperature for developmental adhesive. Source: PPG.	385
Figure II.3.E.6. Images (first row: 3D false color images from a Macroscope; and second row: $5700 \mu\text{m} \times 7500 \mu\text{m}$ optical images) of the CFRP surface with and without two primers. Source: PPG.....	386
Figure II.3.E.7. Geometry of surrogate hem coupon. Adhesive in the root of the hem joint is not shown for clarity. Inner panel (blue) is CFRP and outer panel (gold) is Al. Source: Ford.	387
Figure II.3.E.8. Maximum stress in CFRP/Al hem joint with different hem adhesives. Source: Ford.	387

Figure II.3.E.9. Maximum deflection of adhesively bonded CFRP/Al surrogate hem joints with different adhesives. Source: Ford.....	388
Figure II.3.F.1. Illustrations of (a) the lap joint showing the dimple length (L) and width (W) which varied and (b) the VFAW lay-up with the interlayer. Source: OSU.....	391
Figure II.3.F.2. Different configurations considered for modeling the impact welding process with the interlayer. The target was kept at the same angle of 20° and the initial velocity of flyer was 770 m/s. Three configurations differ in the angle of the interlayer: (a) 0° (b) 5° and (c) 10°. Source: OSU.....	392
Figure II.3.F.3. Model for the lap shear test configuration of the joint showing (a) the assembled lap shear configuration and (b) the exploded view of the weld assembly showing the Al flyer, the interlayer, and the steel target. Source: OSU.....	393
Figure II.3.F.4. Results of lap shear testing of welds made with 3.3 mm thick AA5754-O flyers and 2.2 mm thick HSLA 340 targets where (a) samples have a cross head motion perpendicular to the longer dimension of the weld and (b) samples have welds loaded along their parallel length dimension. Source: OSU.....	393
Figure II.3.F.5. Results of lap shear testing of welds made with 4 mm thick AA5754-O flyers and 2.2 mm thick HSLA 340 targets where (a) samples were created with 6 kJ of input energy from the Magneform capacitor bank and (b) samples were created with 4.2 kJ of input energy from the CDME bank.	394
Figure II.3.F.6. Results of lap shear and fatigue testing of welds made with 4 mm thick AA5754-O flyers and 2.2 mm thick HSLA 340 targets with 3.8kJ on the CDME bank where (a) the sample was pulled parallel to the weld, (b) the sample was pulled perpendicular to the weld and (c) the sample was subjected to tension-tension cyclic loading with 40% maximum load and experienced base metal failure after 1.1M cycles. Source: OSU.....	396
Figure II.3.F.7. Current sub-frame stiffness performance. Source: OSU.....	397
Figure II.3.F.8. Redesigned sub-frame: (a) original design for 20% weight reduction and (b) redesign for a 5-12% weight reduction showing more locations for vapor foil welds. Source: OSU.....	398
Figure II.3.F.9. Design of the weld head: (a) weld head in open position; (b) part clamped with long anvil; (c) part clamped with short anvil; and (d) part clamped with adjusted-angle anvil. Source: OSU.....	399
Figure II.3.F.10. Weld interface predicted from the simulation for the case when the interlayer is kept at an angle of 10°	399
Figure II.3.G.1. Ultrasonic welding system setup (a) and measured sonotrode vibration (b).....	402
Figure II.3.G.2. Comparison of temperature history at faying interface among (a) cases A~D and (b) cases E-F with experimental measurements (open squares and circles).	402
Figure II.3.G.3. Temperature distribution by IR measurement and ABAQUS 2D plane strain FE simulation: (a) t = 0.5 s, (b) t = 1.0 s.....	403
Figure II.3.G.4. Temperature by IR measurement and simulation: (a) Profile at center, and (b) Numerical results from ABAQUS 2D plane strain FE simulations.	404

Figure II.3.G.5. Stress-strain for the (a) Mg-Mg and (b) Mg-Fe static bonding tensile test from MD simulation results using LAMMPS.	406
Figure II.3.G.6.(a) The stress-strain curves for different cooling rates after impact loading and Mg-Fe interface failure at (b) 30% strain after rapid cooling and (c) 10% strain after relatively slow cooling from MD simulation results using LAMMPS.....	407
Figure II.3.G.7.(a) Model representation showing the welded Mg (blue) and steel (red) plates and the tool. (b) Temperature history prediction at the interface between Mg and Steel plates at three different locations (in mm) along the length of the weld from ABAQUS coupled Eulerian-LaGrangian FE models.....	408
Figure II.3.G.8.(a) Schematic compact tension test setup of FSW joints; (b) Quarter FEM for the test; and (c) Load-displacement predictions of the model for three different values of fracture energies.	409
Figure II.3.H.1. Overall research plan. Source: ORNL.....	412
Figure II.3.H.2. Laser profilometry of (a) 40% CF-PA66 plaque ‘smooth region’ and (b) ‘rough region’ with 18 μm and 28 μm maximum profile heights, respectively. Source: PNNL.....	413
Figure II.3.H.3.(a) Cross-section SEM image of as-received DP980 and (b) and (c) TOF SIMS images showing a Zn coat on DP980. Source: ORNL.....	414
Figure II.3.H.4. Summary of lap shear tensile testing with different material combinations and adhesives. Source: ORNL.	415
Figure II.3.H.5. Strain map by DIC capturing localized deformation for double lap shear coupon during shear tensile testing. Source: ORNL.	416
Figure II.3.H.6. Water contact angles of DP980 steel with (a) zinc-coating, (b) zinc removed through abrasion and (c) laser textured on a steel surface. Source: PNNL.....	416
Figure II.3.H.7. Scanning acoustic microscope images in time-of-flight for back surface response (Left) and amplitude of back surface response (Right) reveal unbonded regions in thermoset CFRP/thermoset CFRP joint. Source: PNNL.....	417
Figure II.3.I.1. The five Mg-CFRC joining methods investigated in FY 2018. Source: PNNL and ORNL.....	420
Figure II.3.I.2.(a) FSI and (b) proof-of-concept joints before and after interlocking. Source: PNNL. .	420
Figure II.3.I.3.(a) Defect free stir zone (b) and tool design with associated process parameters. Source: PNNL.	421
Figure II.3.I.4. FSI joint showing (a) incomplete mixing between the Mg sheet and the Mg pin and (b) with better mixing. Source: PNNL.....	421
Figure II.3.I.5. Corrosion test with thermal bonding film incorporated. Source: PNNL.....	422
Figure II.3.I.6. Failed bolted Mg to TS-CFRC lapshear samples: (A) unmodified and un-corroded; and (B) modified and after 100 hours of corrosion conditions. Source: ORNL.	423
Figure II.3.I.7. Cross-section samples using scanning electron microscopy and energy dispersive spectroscopy evaluation showing (a) unmodified sample after corrosion exposure in the joint and (b) modified sample with no corrosion in the joint but corrosion at the Mg-Steel interface. Source: ORNL.	423

Figure II.3.I.8. (a) Edge-view of a CFRP coupon (black color) after being dipped in molten Al, showing solidified Al (i.e., shiny, silvery color) adhering to the CFRP. (b) CF bundle embedded inside an Mg casting. (c) Close-up of (b) showing good adhesion of Mg to CFs via Mg neck formation between individual CFs [scale bar – 1 μ m]. Source: PNNL.....	424
Figure II.3.I.9. (a)Cross-tension and lap shear configurations for F-SPR of Mg to thermoplastic CFRC. (b) Joint strength after corrosion testing. (c) Tensile testing after 200 hour exposure to ASTM B117. Source: ORNL.	426
Figure II.3.I.10.(a) Initial welding process window that produces effective bond but with excessive indentation and (b) the lap shear weld coupon with optimized process parameters. Source: ORNL.	427
Figure II.3.I.11. Weld joint produced with pre-textured surface on AZ31B. (a) Surface texture on AZ31B before welding. (b) AZ31B and TP-CFRP joint. (c) Expanded view of TP-CFRP melted into AZ31B alloy. Source: ORNL.	428
Figure II.3.J.1. (a) Salt-fog test setup at PNNL; (b) Bare and coated (HP and HPEC) AZ31 coupons ready for testing. Source: PNNL.	431
Figure II.3.J.2. External appearance of the corrosion coupons after the ASTM B117 test; bare untested AZ31 – (a) t = 0 hours, (b) t = 1,200 hours; HP – (c) t = 0 hours, (d) t = 1,200 hours; HPEC – (e) t = 0 hours, and (f) t = 1,200 hours. Arrows indicate localized corrosion product build-up. Source: PNNL.	432
Figure II.3.J.3. Change in coupon weight vs. test duration following ASTM B117 testing: (a) bare AZ31; (b) HP; and (c) HPEC. Source: PNNL.	433
Figure II.3.J.4. Back-scattered SEM image of (a) the transverse cross-section of a bare AZ31 coupon after corrosion testing for t = 500 hours. (b) Mg(OH) ₂ , the corrosion product, is noted to form on the surface, and contains multiple cracks that might be responsible for continuation of the corrosion process. Source: PNNL.	434
Figure II.3.J.5. SEM images of the transverse cross-section of HP coupons: (a) after 500 hours; (b) after 850 hours; (c) after 850 hours, some areas showed build-up of Mg(OH) ₂ corrosion product; and (d) after 1,500 hours. Source: PNNL.....	434
Figure II.3.J.6. SEM images of the transverse cross-section of HPEC coupons: (a) after 500 hours; (b) after 850 hours; and (c) after 1,500 hours. Arrows show cracks at the HP/AZ31 interface. Source: PNNL.	435
Figure II.3.J.7. SEM image of the indents in HP coupons; (a) indent along HP/AZ31 interface, (b) indent inside the HP layer, (c) some cracking noted around the indent. Source: PNNL.	435
Figure II.3.J.8. SEM image of the indents in HPEC coupon: (a) indent along HP/EC interface; and (b) indent inside EC layer. Source: PNNL.....	436
Figure II.3.K.1. Weld setup with thermal camera. Source: ORNL.....	438
Figure II.3.K.2. Schematic of experimental setup. A pulsed light acted as the heat source, while an IR camera was positioned on the opposite side of the sample for data collection. Source: GM.	439
Figure II.3.K.3. Examples of steel, Al, and Al-steel weld cross-sections with nugget diameters highlighted by red arrows. Three nugget diameters for each stackup and weld size have been	

measured. This data is used as a comparison to the nugget diameters predicted by each of the NDE methods. Source: GM..... 442

Figure II.3.K.4. GM predicted diameters versus real measured diameters for the entire sample set. The expected trend is represented by the dashed grey line. Source: ORNL and GM. 443

Figure II.3.K.5. Processed post-weld IR images by ORNL’s existing induction heating method and algorithms (1.2 mm 6022 - 2.0 mm HDG LCS). Source: ORNL. 444

Figure II.3.K.6. Post-weld thermal signatures for (a) nugget size and (b) surface indentation related that were obtained by ORNL’s induction heating method and algorithms as a function of nominal nugget size (1.2 mm 6022 - 2.0 mm HDG LCS). Source: ORNL. 445

Figure II.4.A.1. EPA (dark blue) and A2Mac1 (colors denote vehicle) reported vehicle weights. 448

Figure II.4.A.2. Mass of vehicle glider and body subsystems showing trends (2011–2016)..... 448

Figure II.4.A.3. Vehicle door mass and composition analysis and comparison for three North American vehicles..... 449

Figure II.4.A.4. (a) OEM cost and (b) OEM cost per pound saved for different weight reduction options cited within the literature. The majority of opportunities investigated were in the body and chassis..... 450

Figure II.4.A.5. Parametric analyses of cost per part considering part volume (a), cycle time (b), and direct worker wage (c). 452

Figure II.4.A.6. OEM cost per pound saved by replacing a 10-kg body part mild 140–270 steel with Al (blue), HSS (black), and AHSS (green) variants using material substitution ratios (complement of mass reduction)..... 453

Figure II.4.B.1. Door-in-white subsystem to achieve an 8.11 kg mass reduction. Source: Magna International Inc..... 456

Figure II.4.B.2. Side glass construction to achieve a 1.9 kg mass reduction. Source: Magna International Inc..... 457

Figure II.4.B.3. Stress crack near the hinge mounting surface induced by the loss of bolt torque. Source: Magna International, Inc..... 460

Figure II.4.C.1. Systems approach for reducing weight in complex automotive structures including the use of FE tools for detailed design. Source: University of Delaware..... 462

Figure II.4.C.2. Integrated predictive engineering environment. Source: University of Delaware. 463

Figure II.4.C.3. Composites allow part consolidation, which further reduces cost and weight. Source: Composites World (<http://www.compositesworld.com/articles/auto-composites-quest-one-minute-cycle-time>). 464

Figure II.4.C.4. Ply clamping showing (a) right side of mold; and (b) left side of mold. Source: Alpex..... 467

Figure II.4.C.5. Ply pressing trial showing (a) ply stack pre-pressing; and (b) ply stack post-pressing. Source: Alpex..... 467

Figure II.4.C.6. Inner door preform tool with (a) placing pre-consolidated ply stacks in a mold; and (b) cured finished part. Source: TPI Composites..... 468

Figure II.4.C.7. Nesting ply shapes for optimum material usage. Source: TPI Composites.	468
Figure II.4.C.8. Krauss Maffei fabric gripper. Source: TPI Composites.....	469
Figure II.4.C.9. Resin application to the ply stack. Source: TPI Composites.....	470
Figure II.4.C.10. Loading the preform into (a) the empty tool; and (b) with the loading tool and form in place. Source: TPI Composites.....	471
Figure II.4.C.11. Part removal from tool starting with (a) the top of the empty tool with (b) the cured molded part; and (c) the part being manually removed. Source: TPI Composites.....	471
Figure II.4.C.12. Finished molded outer door. Source: TPI Composites.....	472
Figure II.4.C.13. Images of (a) the Al preform tool with (b) the silicone vacuum bag. Source: TPI Composites.....	473
Figure II.4.C.14. Preform fabrication showing (a) preform on the mold; and (b) preform after consolidation and trimming. Source: TPI Composites.	473
Figure II.4.C.15. Preform breakup on the inner door at (a) five locations for (b) preformed door. Source: TPI Composites.....	474
Figure II.4.C.16. Finished preforms ready to ship to Germany. Source: TPI Composites.....	474
Figure II.4.C.17. Completed inner door tool (a) mounted in the press with (b) lower surface and (c) upper surface. Source: TPI Composites.	475
Figure II.4.C.18. Partial tool filling for (a) 50% fill; and (b) 90% fill. Source: TPI Composites.	476
Figure II.4.C.19. Inner door in tool with (a) dry preforms; and (b) molded part. Source: TPI Composites.....	477
Figure II.4.C.20. Sliding preform at the mirror mount for (a) the area of interest; and (b) at the displaced location. Source: TPI Composites.	477
Figure II.4.C.21. Preforms separating during injection at (a) three separate locations and enhanced images at (b) first location, (c) second location, and (d) third location. Source: TPI Composites.....	478
Figure II.4.C.22. Part wrinkling. Source: TPI Composites.	479
Figure II.4.C.23. Door mass breakdown.....	479
Figure II.4.C.24. Baseline door cost and mass.	480
Figure II.4.D.1. Anti-intrusion beam design update. Source: Clemson University.	484
Figure II.4.D.2. Inner panel design update. Source: Clemson University.	484
Figure II.4.D.3. Outer panel stiffener of the door. Source: Clemson University.	485
Figure II.4.D.4. Forming setup and components. Source: Clemson University.....	486
Figure II.4.D.5. Forming setup and components. Source: Clemson University.....	486
Figure II.4.D.6. Thickness distribution for BS and IP for two designs of composite door (a) with composite anti-intrusion beam and (b) with steel anti-intrusion beam. Source: Clemson University.....	488

Figure II.4.D.7. (a) Quasi-static pole performance targets; (b) metal door response; and (c) metal door model. Source: Clemson University..... 489

Figure II.4.D.8. Force-displacement response with baseline metal and composite impact beam for Trim 16. Trim 16 design uses a composite IP with a metal insert near the window regulator location. Trim 20 is another design, which provided lower force in the OEM Stage 3 zone. Source: Clemson University..... 490

Figure II.4.D.9. RP full car simulation results for two locations (a) and (b) of the composite door with composite intrusion beam and (c) the metal intrusion beam. Source: Clemson University..... 490

Figure II.4.D.10. Deformation and damage under DB impact conditions. Source: Clemson University..... 491

Figure II.4.D.11. Deformation and damage under DB impact conditions. Source: Clemson University..... 492

Figure II.4.D.12. SPL at driver ear at low frequencies for (a) Baseline vs Composite door; and (b) Conventional window vs Gorilla hybrid window. Source: Clemson University. 493

Figure II.4.D.13. Plot of STL vs frequency (a) Baseline vs Composite door; (b) effect of leakage area on baseline door; and (c) effect of Gorilla hybrid window on composite door. Source: Clemson University..... 494

Figure II.4.D.14. Thermoforming process layout. Source: Clemson University..... 495

List of Tables

Table I.1.B.1. Elevated Temperature HCF Strength of the Torpedo Samples, Deck Face and Bolt Boss from 1.5L GTDI Cylinder Heads for the AS7GU-T64, Ford-SPMC-w/Sr-3stage, and Ford-SPMC-w/oSr-3Stage. 30

Table I.1.C.1. A Comparison of Measured Alloy Properties to DOE Targets for a Common Production Alloy (Alloy 1) and for the Strengthened Q-Phase Alloys (Alloy 2 Trial 1 and Alloy 2 Trial 2)..... 42

Table I.1.C.2. RT Tensile Properties in Bolt Boss Regions in Engine Cylinder Heads of a Baseline Alloy (Alloy 1 Trial 2) and the Developed Alloy (Alloy 2 Trial 2) in Comparison to DOE Targets. 43

Table I.1.C.3. RT Tensile Properties in HPOL Regions in Engine Cylinder Heads of a Baseline Alloy (Alloy 1 Trial 2) and the Developed Alloy (Alloy 2 Trial 2) in Comparison to DOE Targets..... 43

Table I.1.C.4. Measured Elastic Modulus of Alloy 2 Specimens Tested Above 150 °C and Conditioned for 100 Hours at Temperature..... 44

Table I.1.C.5. HCF Strength (10^7 Cycles) of Cylinder Head Casting Samples from Two Casting Trials. 46

Table I.1.C.6. LCF Strength (10^4 Cycles) in Engine Cylinder Heads..... 51

Table I.1.C.7. X-ray Analysis of Trial 2 Cylinder Head Castings. 52

Table I.1.C.8. Continuation of X-ray Analysis of Trial 2 Cylinder Head Castings. 53

Table I.2.B.3.1. Calculated Volume Fraction in Percentage (As-Cast at 25 °C Predicted by JMatPro v9). 72

Table I.2.C.3.1 Elemental Composition of the Ti-48Al-2Cr-2Nb Powder, as Obtained from Wet Chemical Analysis.	89
Table I.2.D.1.1. Measured Compositions in Weight Percentages for Commercial Exhaust Valve Alloys Tested at 800, 850, 900, and 950 °C as Discussed Herein.....	97
Table I.3.C.1. Overview of the Extrudability of Cu-C Composite Wire by ShAPE as of September 2018.....	122
Table I.3.D.1.1. Coefficients Corresponding to the Best Fit Models from Multiple Regression Analysis for the Average Deposit Layer Thickness. Asterisks Indicate the Absence of the Factor in the Best Fit Model.....	128
Table II.1.A.2.1. Hardness in HV of ShAPE™ Tubing in the As-Extruded and Heat-Treated Conditions.....	147
Table II.1.A.2.2. Tensile Properties for ZK60-T5 Bar Extruded by ShAPE™.	148
Table II.1.A.3.1. Parameters for MICRESS® Simulations.	156
Table II.1.A.4.1. Thickness Strains in the Stamped Al Impact Beam.	163
Table II.1.C.1. Target Alloy Compositions in Weight Percentages Used in This Study.....	173
Table II.1.D.1. Status of Project Tasks and Milestones at the End of FY 2018.....	182
Table II.1.F.1. Flexural Strength in Newtons of Dual-Phase (DP500) Steel with the CFRE Coating Applied (CFRE Thickness is 0.5 mm for All Samples).....	217
Table II.1.F.2. Flexural Strength (Newtons) of DP500 with the CFRE Coating Applied (CFRE and Steel Thickness Were Both Varied).....	218
Table II.1.F.3. Coefficients α_0 and α_1 as a Function of Direction for X and Y Percentage CF-Containing CFRE.....	221
Table II.2.A.1. Phased Approach for the CPEC Project.	224
Table II.2.A.2. Mechanical Properties of Fully Carbonized Samples at High-Temperature Carbonization and Constant Parameters.	225
Table II.2.B.1. Industry/ORNL joint projects.....	231
Table II.2.C.1. Tensile and compression tests of woven coupons with different tow sizes.	240
Table II.2.C.2. Draw-in distance and yarn angle comparison between the simulation and the experiment.....	244
Table II.2.C.3. Cases considered to quantify the macro-scale uncertainties. The variations are changed in a controlled manner from case to case. Gaussian processes (GP) are employed to generate random realizations in all cases.	251
Table II.2.D.1. Permeability Values of the Non-Crimp CF Fabric.....	269
Table II.2.D.2. Geometric Attributes Values Used in This Study.	274
Table II.2.D.3. Parameters Included for the Uncertainty Analysis (β Distribution).	278
Table II.2.D.4. Elastic and Inelastic Properties for Multiscale Designer.....	279
Table II.2.E.1. Project Parameters and Requirements.	287

Table II.2.E.2. Microstructure Parameters of Different Fibers Generated in Atomistic Simulations. 297

Table II.2.E.3. Mechanical Properties of Different Fibers Generated from Atomistic Simulations.... 298

Table II.2.E.4. Results of Graphene Additions on the Polyethylene-based Fibers..... 299

Table II.2.E.5. Success Metric of the Initial ICME Framework with PAN-based CF..... 302

Table II.2.F.1. Project Parameters and Requirements. 306

Table II.2.F.2. General Description of Each Consortium Member’s Primary Responsibility. 308

Table II.2.F.3. Milestones for BP 1..... 309

Table II.2.F.4. Summary of iCTP, mPP, and Gilsonite Tensile Properties after Carbonization at 1,000°C. 315

Table II.2.F.5. Summary of Inorganic Impurity Testing. 318

Table II.2.F.6. Summary of Organic Impurity Testing..... 318

Table II.2.F.7. Physical Properties for Napthalene and Methylnapthalene Calibrations and Literature Values Used for Validation. 323

Table II.2.F.8. Young’s Modulus for Three Pitches. 326

Table II.2.G.1. Detail of the Major Phases of the Spider Silk Conversion Project..... 335

Table II.2.G.2. Range of Mechanical Properties for MiSp and MaSP1 Samples. 337

Table II.2.G.3. Mechanical Data of Carbonized Bundles..... 338

Table II.3.A.1. Distortion Gap Summary for Different Conditions at Peak Paint-Bake Temperature (197°C). 343

Table II.3.C.1. Test Plan Matrix for Preliminary EL, Mechanical, and Corrosion Tests. 356

Table II.3.C.2. EL Target Criteria versus Actual Results. 360

Table II.3.D.1. Definition of Welding Cases under Different Clamping Methods..... 371

Table II.3.D.2. Comparison of Time Cost by the Two Codes..... 373

Table II.3.D.3. Key Properties of Selected Primers..... 374

Table II.3.E.1. Formulation Details and Key Properties of Prototype and Control Electrocoats. 384

Table II.3.E.2. Lap Shear Strengths of the Control and Prototype Adhesive..... 385

Table II.3.E.3. Key Properties of Selected Primers. 386

Table II.3.I.1. Summary of Surface Profiles for Thermoplastic CFRP and DP980. 414

Table II.3.J.1. Materials used in the Mg-CFRC Task..... 420

Table II.3.J.2. Summary of F-SPR Lap Shear Test Results. 425

Table II.3.L.1. Experimental Test Matrix with Weld Sizes..... 440

Table II.3.L.2. Example Chart Showing Weld Nugget Size Comparisons..... 442

Table II.4.B.1. NCAP Impact Testing Results..... 458

Table II.4.B.2. NVH Test Results. 459

Table II.4.C.1. Status to Target.....	480
Table II.4.D.1. Project participants.	482
Table II.4.D.2. Optimization results for composite door designs.....	488

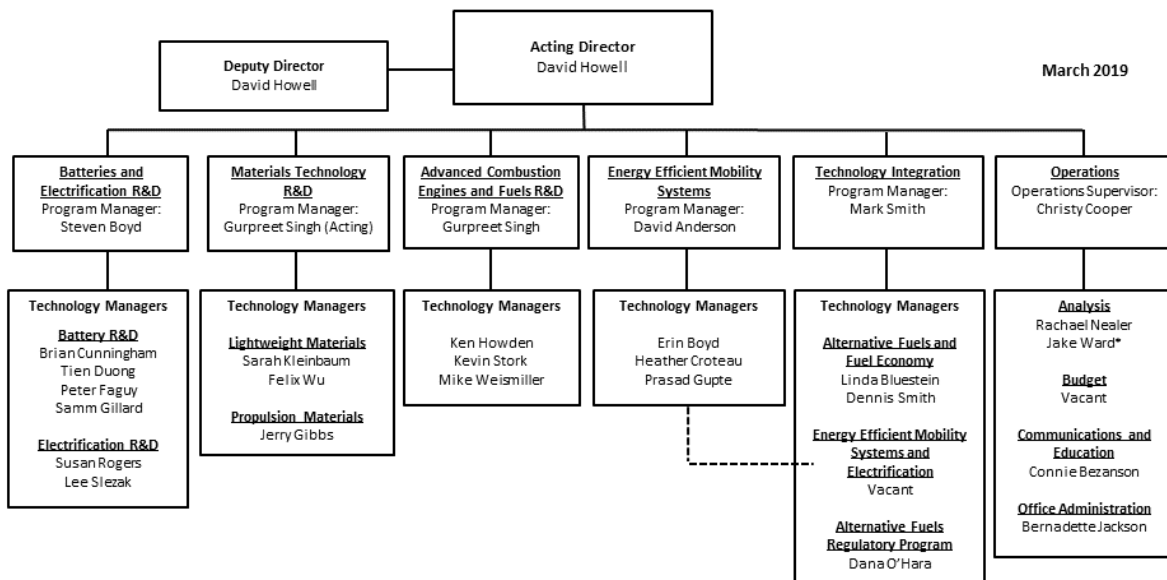
Vehicle Technologies Office Overview

Vehicles move our national economy. Annually, vehicles transport 11 billion tons of freight¹ – more than \$32 billion worth of goods each day² – and move people more than 3 trillion vehicle-miles.³ Growing our national economy requires transportation and transportation requires energy. The transportation sector accounts for 70% of U.S. petroleum use. The United States imports 20% of the petroleum consumed – sending more than \$15 billion per month⁴ overseas for crude oil. The average U.S. household spends nearly one-sixth of its total family expenditures on transportation⁵, making transportation the most expensive spending category after housing.

To strengthen national security, enable future economic growth, improve energy efficiency, and increase transportation energy affordability for Americans, the Vehicle Technologies Office (VTO) funds early-stage, high-risk research on innovative vehicle and transportation technologies. VTO leverages the unique capabilities of the national laboratory system and engages private sector partners to develop innovations in electrification, including advanced battery technologies; advanced combustion engines and fuels, including co-optimized systems; advanced materials for lighter-weight vehicle structures; more efficient powertrains; and energy efficient mobility systems.

VTO is uniquely positioned to address early-stage challenges due to strategic public-private research partnerships with industry (e.g., U.S. DRIVE, 21st Century Truck Partnership) that leverage relevant expertise. These partnerships prevent duplication of effort, focus DOE research on critical R&D barriers, and accelerate progress. VTO focuses on research that industry does not have the technical capability to undertake on its own, usually due to a high degree of scientific or technical uncertainty or is too far from market realization to merit industry resources.

Organization Chart



¹ Bureau of Transportation Statistics, DOT, 2016. Table 3-1 Weight and Value of Shipments by Transportation Mode https://www.bts.gov/archive/publications/transportation_statistics_annual_report/2016/tables/ch3/table3_1

² Ibid.

³ Transportation Energy Data Book 37th Edition, ORNL, 2018. Table 3.8 Shares of Highway Vehicle-Miles Traveled by Vehicle Type, 1970-2016.

⁴ EIA Monthly Energy Review <https://www.eia.gov/totalenergy/data/monthly/pdf/mer.pdf>

⁵ Bureau of Labor Statistics, Consumer Expenditure Survey, 2017. Average annual expenditures and characteristics of all consumer units, 2013-2017. <https://www.bls.gov/cex/2017/standard/multiyr.pdf>

Materials Technology Program Overview

Introduction

The Materials Technology Program supports vehicle lightweighting and improved propulsion (powertrain) efficiency through early-stage research and development (R&D) to increase understanding of novel materials and to enable industry to develop and deploy more fuel-efficient LD and HD vehicles. The research focus is on activities that have a high-degree of scientific or technical uncertainty, or that are too far from market realization to merit sufficient industry focus and critical mass. The Materials Technology Program accomplishes its technical objectives through research programs with academia, national laboratories, and industry.

The Propulsion Materials Subprogram portfolio is closely aligned with other Vehicle Technologies Office (VTO) subprograms to identify critical materials needs for next-generation high-efficiency powertrains for both HD and LD vehicles. Strategies for achieving high-efficiency powertrains include improved powertrain thermal efficiency, increased power density resulting from lightweighting, and petroleum displacement through fuel substitution strategies. In FY 2018, the Propulsion Materials portfolio included research in three main areas: (1) use of ICME to predict materials properties needed to achieve increases in brake thermal efficiency for HD vehicles; (2) development of new advanced cast Al alloys for high-temperature engine components; and (3) development of new catalyst materials, improved composite brake and electric machine materials, and anti-fouling materials that will facilitate energy recovery and aftertreatment.

The Lightweight Materials team works closely with industry through the USDRIVE (Driving Research and Innovation for Vehicle efficiency and Energy sustainability) Partnership to understand HD and LD vehicle structural weight reduction goals and to identify technical challenges that prevent the deployment of lightweight materials. The most promising and likely approach for lightweighting is a multi-material approach, which focuses on the use of the right material for the application. The Lightweight Materials Subprogram research portfolio addresses significant technology gaps for each family of structural materials: Mg, AHSS, Al, and CF composites. In addition, there is a growing focus on dissimilar material joining in order to enable the reliable assembly of these multi-material systems.

Goals

The Materials Technology Program supports the VTO's mission to help consumers and businesses reduce their transportation energy costs while meeting or exceeding vehicle performance expectations. Lighter vehicles with more efficient engines reduce fuel use and save consumers money. The structural and powertrain systems that the program targets to improve are limited by materials performance. By improving the properties of powertrain and structural materials, the program can enable a significant improvement in fuel economy for future vehicles. Increasing the strength and oxidation resistance of high-temperature materials will enable new combustion strategies while improving properties in structural materials such as stiffness, strength, joinability, and crash energy absorption—all with lower cost—will accelerate the deployment of lightweight materials in the automotive market.

The specific performance and cost targets for the Materials Technology Program are:

1. Validate a 25% improvement in high-temperature (300°C) component strength relative to components made with model year 2010 baseline cast Al alloys (A319 or A356) for improved efficiency LD engines.
2. Enable a 25% weight reduction for LD vehicles including body, chassis, and interior as compared to a model year 2012 baseline at no more than a \$5/lb-saved increase in cost.

State-of-the-Art

Automakers are seeking to improve fuel economy while maintaining or improving vehicle performance and safety. Reducing the weight of the structure of the vehicle improves fuel economy and reduces strain on the powertrain of the vehicle, allowing for further fuel savings. For structural components, the market is shifting from traditional steel components to lighter weight materials such as AHSSs, Al alloys, Mg alloys, and CF composites. Lighter structures allow for downsized engines. These engines are typically turbocharged to achieve increased power density, which requires lightweight materials with low-density, high-strength, and high-stiffness at elevated temperatures.

In order to meet material property requirements of increasingly severe combustion environments, new cast Al alloys are needed. This is due, in part, to inadequate thermal performance, as well as very high PCPs in advanced engine applications. As engine thermal efficiency improves, the temperature experienced by downstream exhaust components is decreased. This leads to a need for low-temperature catalyst development in order to maintain effective reduction of tailpipe emissions. Moreover, inadequate databases, modeling, and design tools are significant barriers for further development of new materials. By evaluating existing computational tools, identifying gaps that must be overcome to achieve seamless integration across multiple-length scales, and increasing understanding of the basic behavior of the material (i.e., effects of solute at the atomistic level, microstructural development, microstructure/property relationships, fracture and failure mechanisms, durability, temperature-dependent behavior, etc.), more accurate design tools and predictive models can be established. High-quality, consistent, and accessible databases are needed to support this development.

AHSS is the most mature lightweight material in terms of widespread use in industry due to its compatibility with existing manufacturing infrastructure and vehicle materials. The application of third-generation high-strength steel has the potential to reduce component weight by up to 25%, particularly in strength-limited designs. However, technical challenges remain to achieve room-temperature formability, improved weldability, and reliable and accurate predictive performance models. Al continues to see steady growth in market share in the automotive industry despite issues of material cost, room-temperature formability, and limitations within the existing manufacturing infrastructure. This is due to the 40% weight savings that can be achieved with Al along with the well-established domestic supply chain. Mg has the potential to significantly reduce vehicle component weight by 55% or greater; however, there are several significant technical barriers preventing increased use of this material in vehicle designs. Mg has high raw material costs and price volatility, relatively low-specific stiffness, difficulty in forming sheet at low temperatures, low ductility of finished components, and a limited alloy set, among other challenges. CF composites have the potential to reduce component weight by more than 60%. The main barriers to widespread CF use are the high cost to manufacture the CF, lack of high-volume composite manufacturing methods, and a need for reliable predictive tools for both part design and performance prediction.

When combinations of the above lightweight materials are used, the resulting multi-material structures have challenges of their own. Traditional joining methods used in automotive assembly, such as resistance spot welding and riveting, are inefficient for joining of dissimilar metals and for some combinations, infeasible. In the near-term, friction stir scribe welding and resistance spot riveting are showing promising advances for joining of AHSS and Al (the more mature lightweight metals). An additional challenge posed by multi-material structures is the increased risk of corrosion due to galvanic coupling. As the barriers to introduction of Mg and CF are overcome, breakthroughs in joining technology will also be necessary.

Program Organization Matrix

The Materials Technology subprogram is led by Acting Program Manager, Gurpreet Singh.

1. Lightweight Materials Subprogram consists of three research portfolios:
 - Automotive Metals (open position) – which includes research on property improvement and processing advances for AHSS, Al, and Mg.
 - CF and Polymer Composites (Felix Wu) – which includes research on low-cost production of CF and predictive performance models of CF composites.
 - Multi-Material Joining (Sarah Kleinbaum) – which includes research on solid-state and mechanical joining methods for dissimilar materials, as well as galvanic corrosion mitigation.
2. Propulsion Materials Subprogram consists of two research portfolios:
 - High-Temperature Materials (Jerry L. Gibbs) – which includes research on the material characteristics that influence temperature-dependent behavior, as well as alloy development.
 - Materials for Aftertreatment and Emissions Control (Jerry L. Gibbs) – which includes development of new catalyst materials, improved composite brake and electric machine materials, and anti-fouling materials that will facilitate energy recovery and aftertreatment.

All of the activities within the Materials Technology Program utilize computational methods for material discovery, prediction of structure, understanding failure mechanisms including corrosion and the effects of processing on properties.

I Propulsion Materials

I.1 Integrated Computational Materials Engineering

I.1.A Applied Computational Methods for Advanced Propulsion Materials (Oak Ridge National Laboratory)

J. Allen Haynes, Principal Investigator

Propulsion Materials
Oak Ridge National Laboratory
1 Bethel Valley Rd.
Knoxville, TN 37831
E-mail: haynesa@ornl.gov

Jerry L. Gibbs, DOE Technology Manager

U.S. Department of Energy
E-mail: jerry.gibbs@ee.doe.gov

Start Date: October 1, 2016	End Date: September 30, 2019	
Project Funding (FY18): \$370,000	DOE share: \$370,000	Non-DOE share: \$0

Project Introduction

The Applied Computational Methods for Advanced Propulsion Materials Project consists of four tasks that are focused on early-stage research in pursuit of advancing the basic mechanical properties, manufacturability, and addressing the affordability of propulsion materials. These tasks have the common goal to use ICME to predict materials properties needed to achieve increases in brake thermal efficiency for HD vehicles. The specific tasks include the following:

1. Future Engine Requirements—Modeling Advanced Engine Materials.
2. Materials Properties for Modeling and Screening.
3. Computational Fluid Dynamics Analysis of Cooler Materials, Deposits, and Geometries.
4. Computational Development of Thermoelectric Materials.

The following sections of this report outline the specific task work conducted at Oak Ridge National Laboratory (ORNL) in the areas of predictive engineering, process development, and enabling technologies for propulsion materials. Each task supports one or more goals within the VTO mission of developing higher performance materials that can withstand increasingly extreme environments and address the future properties needs of a variety of high-efficiency powertrain types, sizes, fueling concepts, and combustion modes.

I.1.A.1 Task 1E: Future Engine Requirements – Modeling Advanced Engine Materials

Charles E.A. Finney, Principal Investigator

Oak Ridge National Laboratory
National Transportation Research Center
2360 Cherahala Blvd
Knoxville, TN 37932
E-mail: finneyc@ornl.gov

Jerry L. Gibbs, DOE Technology Manager

U.S. Department of Energy
E-mail: jerry.gibbs@ee.doe.gov

Start Date: October 1, 2016

Project Introduction

HD internal combustion engines for the transportation sector operate at high PCP to achieve required performance and brake thermal efficiency. Current PCP operation peaks at about 190 bar [1 bar = 10^5 Pa], where it has been maintained for almost two decades following nearly four decades of steady increase. This hiatus in PCP operation increase has a variety of causes, with a prominent reason being materials limitations. The current generation of materials, such as the family of grey cast-irons, is widely considered inadequate for the projected elevated-pressure environment of future higher-efficiency engines. Although candidate replacement materials, such as compacted graphite iron (CGI), are being developed and evaluated for use in intermediate-term applications, a robust understanding of engine cylinder materials stresses and the materials properties necessary to enable desired engine efficiency and power densities of future HD engines is lacking. Internal combustion engines, in both LD and HD applications, have been trending towards higher specific output (for instance, output torque relative to engine displacement) to enable downsizing for fuel economy benefits.

Numerical simulations offer insight into the cylinder environment at such elevated operating cylinder pressures and temperatures and can help identify design needs and changes more comprehensively than can be identified experimentally, particularly with materials temperatures and heat fluxes. The current practice of simulation can achieve low- or high-dimensional modeling of the combustion environment or the cylinder/engine structure, but a fully coupled, high-dimensional computational fluid dynamics (CFD) - finite element analysis (FEA) simulation of combustion, heat transfer, and consequential material temperatures and stresses is a fundamental development need.

Part of this limitation is the time and level of detail required to setup simulations. For FEA particularly, a proper meshing of complex geometries for high-fidelity calculation of materials stresses with conjugate heat transfer can be very labor-intensive. However, with simplifications, a sufficient first-order estimate of future required materials properties can be gauged with simulations. This project is employing an incremental process for this problem, starting with the use of CFD results, guided by low-dimensional modeling, as inputs to FEA simulations and fatigue analysis. A concurrent experimental project to measure the properties of a relevant grade of CGI is providing the needed data for the combustion, materials modeling, and analysis.

Objectives

An important objective of this project is to study the effects of operating HD internal combustion engines at increased levels of specific output, which will require higher PCPs and temperatures, with a goal to increase engine and system efficiency. This objective will require evaluation of the performance of currently available materials at current and projected future specific-output and PCP conditions. The principal objective of this project is to identify properties requirements of materials suitable to withstand a lifetime of operation at the elevated temperatures and pressures in future higher-efficiency HD engines. This objective will account for fatigue and creep properties of candidate materials.

Approach

The project approach utilizes several computational tools informed by selective experimental materials measurements. The first stage is estimation of the thermal environment in the cylinder materials boundaries as a function of varying degrees of combustion intensification. The second stage is to use the thermomechanical boundary conditions (e.g., heat fluxes and pressures) to evaluate stresses and strains in the cylinder materials boundaries using FEA. The third stage is to utilize a constitutive model of the materials to estimate fatigue life, or the inverse problem of defining the materials properties based on a fatigue life required by a lifetime of commercial operation.

Combustion modeling is performed using two approaches: a high-level (0–1 dimensional) modeling suite, and a high-dimensional (3-D with fine spatial resolution) CFD package. The low-dimensional modeling is implemented using GT-Suite and GT-Power (Gamma Technologies, Inc.) [1], which is an industry-standard simulation package. A unique feature of GT-Suite is the ability to integrate a 3D thermal solution with the low-dimensional engine model. The solution speed allows for rapid evaluation of large parameter spaces and makes it suitable for defining boundary conditions for and verifying trends in the higher-fidelity CFD simulations. The high-dimensional modeling is implemented using CONVERGE CFD (Convergent Science, Inc.) [2], an industry-standard software package. This code employs state-of-the-art models and numerical techniques to achieve a high-degree of fidelity, but with higher computational expense.

Both combustion models utilize design data for a 2013 model year 15-liter engine provided by a HD engine company. Both models implement schemes for the co-solution of combustion with materials heat transfer in a technique called conjugate heat transfer (CHT). The use of CHT provides more accurate simulations, especially in defining wall heat fluxes, than using a fixed estimate of wall temperatures, which was standard practice until recently. The CHT solutions span the entire engine block and head and utilize materials data from standard references for conventional materials and from an ongoing experimental program at ORNL for an engine-grade cast-iron, CGI-450.

The overall approach is to model combustion at the baseline condition (190 bar) and at various levels of intensified combustion to achieve high specific output using the same engine geometry, which results in higher pressures (exceeding 250 bar) and temperatures. The heat fluxes across the cylinder boundaries—the head, valves, liner, and piston—are then used in the FEA simulations, which employ ANSYS (ANSYS, Inc.) [3], and utilize materials properties from standard references or from ORNL measurement data for CGI-450. At each combustion condition, stresses and strains in the cylinder components of interest are evaluated using a nonlinear stress model. The principal area of interest is in the cylinder head, specifically in the bridge between the exhaust valves, where the highest materials temperatures are anticipated, and which could be an area of concern in actual operation.

The results of the FEA simulations are used in a fatigue and creep model to estimate the service life at each combustion condition. The required service life is estimated from the established HD Federal certification cycle where the highest or most stressed load conditions are identified.

Results

Work in FY 2018 focused on the following activities:

- Change in combustion targeting strategy to focus on increased specific output.
- Evaluation of high-level modeling to define trends and provide boundary conditions for CFD analysis.
- Change in CFD workflow for iterative solution of coolant and combustion simulations to reflect best practices.
- Refinement of the FEA model to focus on areas of greatest concern in the head.

An important aspect of the combustion modeling is the effect of materials properties on combustion, as reflected in thermal diffusivity, as well as the heat flux from the cylinder through the engine material to the environment. As engine-specific output is increased from the baseline condition of the engine design, the peak pressures and temperatures rise because of the intensified combustion. The effects of increasing the engine-specific output are seen in Figure I.1.A.1.1, which shows engine Gross Indicated Thermal Efficiency (GITE), as well as the maximum head temperature as a function of increased specific output, reflected in the PCP, as a function of head material; the broken lines represent uncertainty from a range of parametric perturbations used to gauge model error. The grey cast-iron properties were chosen as a representative material and may not reflect variants used by engine manufacturers. From the simulations, the material type does not significantly affect the GITE, but it does strongly affect the maximum head temperature. While these simulations are still undergoing refinement as additional input data and boundary conditions are identified, they do illustrate that with intensified combustion, certain areas in the head could approach or exceed the materials yield strength at those temperatures, based on measured materials properties. These excursions would make the material susceptible to fatigue and creep failure and reduce the useful lifetime of the engine.

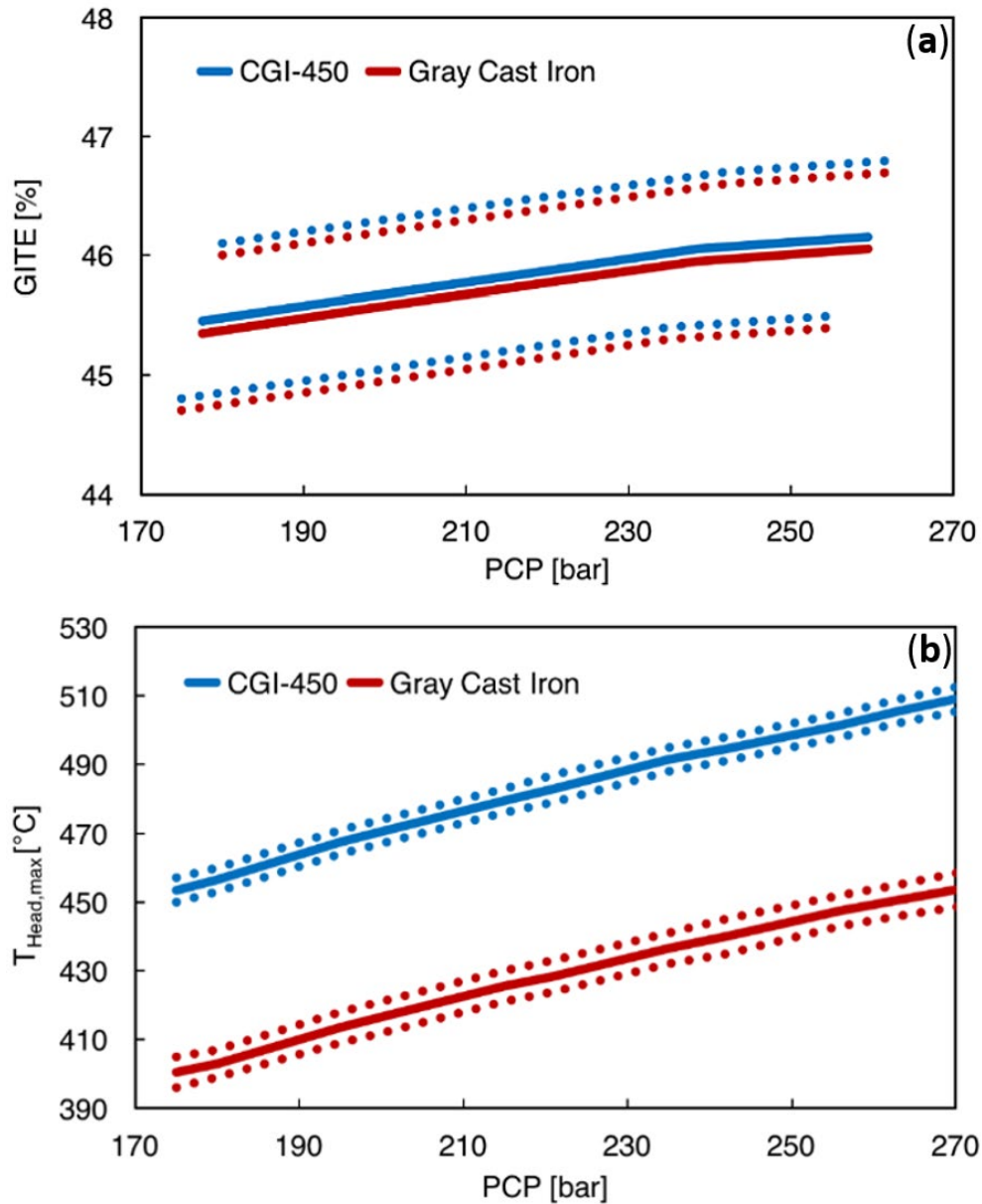


Figure I.1.A.1.1. Materials effects on (a) engine GITE and (b) maximum temperature in the head with increased specific output, resulting in higher PCP. Results from GT-Power.

These trends are also seen in the CFD analysis, as shown in Figure I.1.A.1.2, which depict maximum head temperature along with a range of uncertainty, for two combustion conditions. As the iterative simulations become more refined, their predictions help improve the finite element modeling.

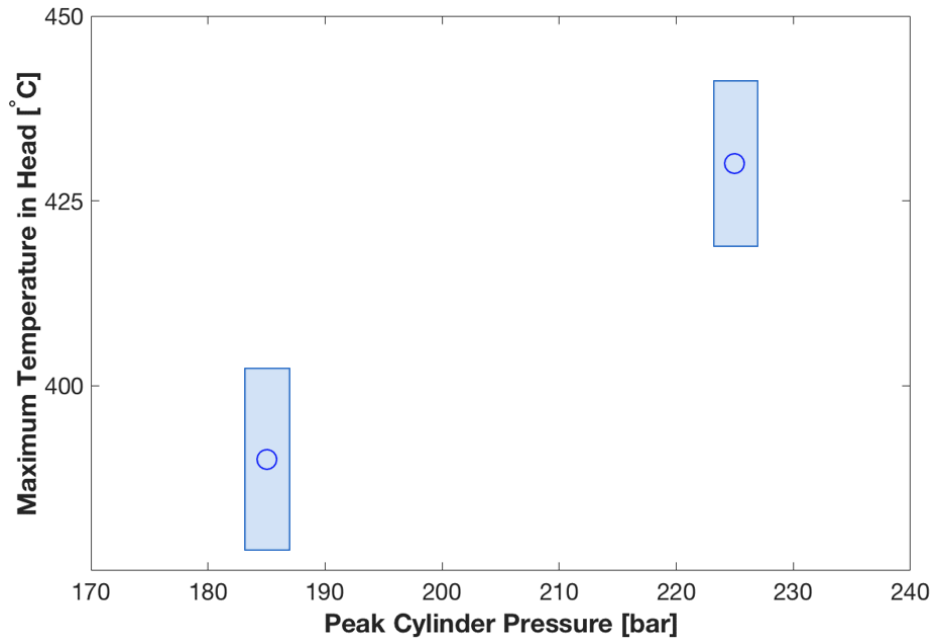


Figure I.1.A.1.2. Maximum head temperatures at the baseline (190 bar) and intensified (225 bar) combustion conditions. Results from CFD.

Conclusions

An integrated experimental and computational approach shows promise for virtual evaluation of materials properties in the absence of an extensive experimental program; this approach can also provide guidance for future materials research. The computational strategies employed in this project are evolving to reflect best practices to provide the most confidence in simulated results. From the simulations and experimental mechanical properties measurement data, it is apparent that current materials will be highly stressed with increased combustion intensification.

Ongoing activities should include the following:

- Evaluate thermal and mechanical stresses and strain in selected engine components at increased specific-output conditions using FEA and estimate fatigue life.
- Identify properties needed for candidate materials to be suitable for future production environments.
- Continue integration of a constitutive model for CGI-450 to assist in engine analysis and design.

Key Publications

1. Finney, C. E. A., G. Muralidharan, Z. G. Mills, and J. A. Haynes, 2018, "Future engine requirements," 2018 U.S. DOE Vehicle Technologies Office Annual Merit Review, MAT057.

References

1. Gamma Technologies, LLC. GT-Suite software. <https://www.gtisoft.com>.
2. Convergent Science, Inc. CONVERGE CFD software. <https://convergecf.com>.
3. ANSYS, Inc. ANSYS Mechanical Enterprise software. <https://www.ansys.com/products/structures>.

Acknowledgements

Co-investigators in this project include Govindarajan Muralidharan and Zachary Mills of ORNL and Andrew Miles of the SimuTech Group of Atlanta, Georgia.

I.1.A.2 Task 2E: Materials Properties for Modeling and Screening

Govindarajan Muralidharan, Co-Principal Investigator

Oak Ridge National Laboratory
Materials Science and Technology Division
1 Bethel Valley Road
Knoxville, TN 37831
E-mail: muralidhargn@ornl.gov

Hsin Wang, Co-Principal Investigator

Oak Ridge National Laboratory
Materials Science and Technology Division
1 Bethel Valley Road
Knoxville, TN 37831
E-mail: wangh2@ornl.gov

Jerry L. Gibbs, DOE Technology Manager

U.S. Department of Energy
E-mail: jerry.gibbs@ee.doe.gov

Start Date: October 1, 2016

Project Introduction

There is a significant need to evaluate and characterize emerging materials for applications in advanced high-efficiency HD truck engines. A roadmap for HD engine operation projects higher PCP and temperatures into the foreseeable future. For example, the SuperTruck I program showed that > 50% Brake Thermal Efficiency can be achieved with ~ 225 bar PCP, which is higher than current PCP values. As outlined in a companion report on Task 1e, preliminary CFD, structural finite element models, and engine models (GT-power) suggest that such an increase in PCP may result in increased **stresses** AND increased **temperatures** in critical regions in the grey cast-iron heads used in HD diesel engines. However, the effect of using advanced alternate materials on stresses and temperatures is not known.

An example of an alternate material is CGI. The graphite particles in this material are “worm-shaped,” shorter, and more rounded than those in grey iron, and are connected to their neighbors within the 3D volume. This graphite morphology is known to inhibit crack initiation and growth and hence result in improved mechanical properties when compared to grey iron [1-3]. Material properties, particularly thermal-physical and mechanical properties, are required as a function of temperature to assess the effect of materials substitution on temperatures and stresses using available computational models. In addition, materials property evaluation combined with validated computational models can be used for rapid screening of other advanced materials.

Objectives

The objective of this project is to provide critical materials thermal, physical, and mechanical properties data to enable predictions on the effect of varying PCP on temperatures and stresses using computational models and to assess the effect of new engines operating conditions on materials lifetime in HD engine applications. CGI was down-selected as the material.

Approach

Based upon the requirements for computational modeling, the following temperature-dependent properties were identified as being critical for initial thermal-mechanical modeling of temperatures and stresses in a HD

engine block. A temperature range of room-temperature up to 650°C was identified as being relevant to measurements conducted on the thermal-physical properties. Properties that were obtained include:

1. Thermal conductivity
2. Specific heat
3. Coefficient of thermal expansion
4. Elastic modulus.

In addition, the following isothermal, high-temperature mechanical properties were identified as being important to predict material stresses and lifetimes in the engine application:

1. Uniaxial tensile properties – yield strength, tensile strength, and ductility (up to 800°C)
2. Creep properties
3. Fatigue properties.

CGI-450 cast plates were obtained from an original equipment manufacturer and was used to obtain properties #1 through #7 above. Uniaxial tensile testing was conducted at several temperatures up to 800°C. Creep properties were measured through step-loading tests, and constant load tests at temperatures up to 500°C. High-cycle fatigue life was measured at 450°C and 500°C at a range of stress levels.

Results

Figure I.1.A.2.1 shows the results from thermal conductivity measurements from CGI obtained using laser flash diffusivity measurements over the temperature range of room-temperature to 650°C from specimens prepared in two different directions in the casting: longitudinal and transverse. Thermal conductivity measurements were considered critical in determining the temperatures within the cylinder heads. Over this temperature range, the thermal conductivity was observed to vary from about 33 W/mK to about 38 W/mK. Previous experiments show that the thermal conductivity of CGI is approximately 25% less than that of pearlitic grey iron at room-temperature, and about 15-20% less at 400°C [2]. Comparison with thermal conductivities in the literature suggests that the measured thermal conductivities are about 15-20% less than that of pearlitic grey cast-iron at higher temperatures [2-4]. The impact of this reduced thermal conductivities in critical regions in the cylinder heads on stresses and lifetimes must be evaluated through computational modeling techniques.

Figure I.1.A.2.2 shows the effect of temperature on the yield strengths of CGI measured in the present study superposed on the current peak temperature range estimated in cylinder heads and the temperatures anticipated in future high-efficiency engines. It can be observed from the figure that the strength of CGI decreases significantly over the anticipated future temperature ranges. The effect of this decrease in strength combined with contributions from creep at these temperatures on anticipated lifetime and reliability must be evaluated using experimental work and computational modeling techniques. Creep and fatigue properties are currently being measured to help understand the effect of temperature on these properties.

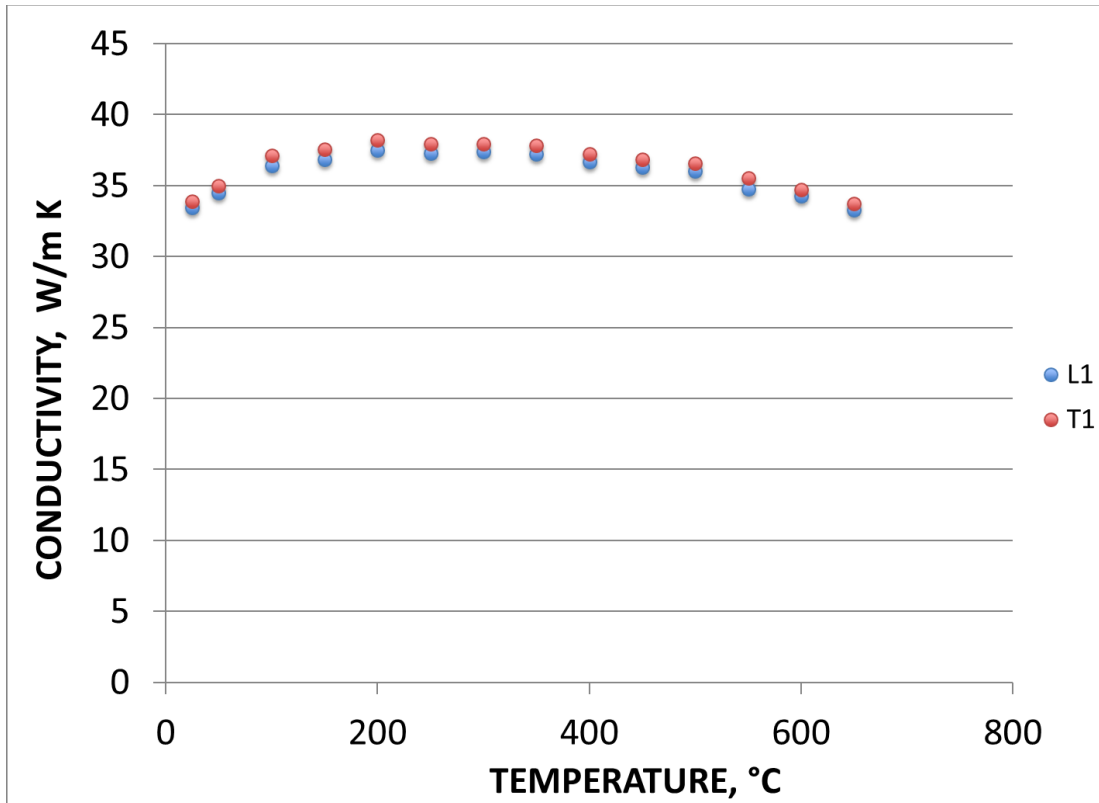


Figure I.1.A.2.1. Thermal conductivity of CGI between room-temperature and 650°C.

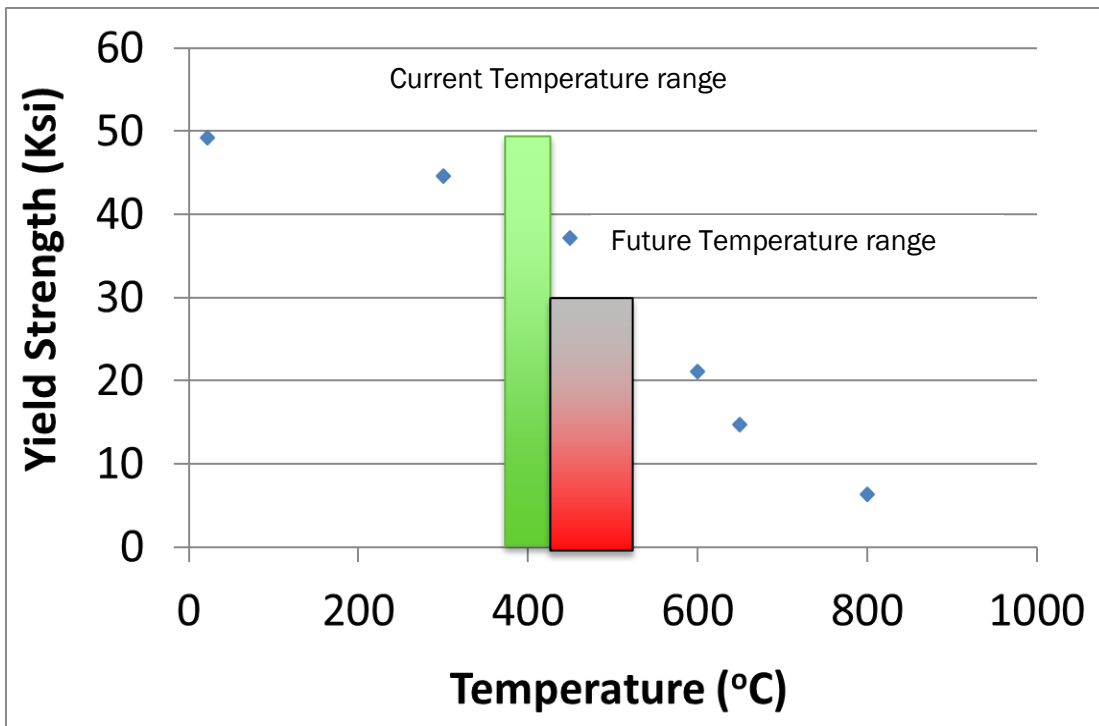


Figure I.1.A.2.2. Effect of temperature on the yield strength of CGI. Also superposed are the current and anticipated future temperature ranges for cylinder heads [5].

Conclusions

Thermal conductivity, specific heat, coefficient of thermal expansion, and elastic moduli have been measured for CGI to enable incorporation of these parameters into finite element models. These models will be used to evaluate the effect of the new thermal-physical properties on stresses developed in various regions within the cylinder head. Tensile, creep, and fatigue data are also being measured to assess the effects of temperature and stresses on materials lifetime and reliability when used in cylinder head applications.

References

1. Compacted Graphite Iron, Materials Data Sheet, www.sintercast.com.
2. Compacted Graphite Iron, Mechanical and Physical Properties for Engine Design, www.sintercast.com.
3. Dawson, S., "Compacted Graphite Iron: A New Material for Highly Stressed Cylinder Blocks and Cylinder Heads," www.sintercast.com.
4. Holmgren, D., A. Diószegi, and I. L. Svensson, 2008, "Effects of C content and solidification rate on the thermal conductivity of grey cast-iron," *Tsinghua Sci. Technol.*, Vol. 13, No. 2.
5. Finney, C. E. A., G. Muralidharan, Z. G. Mills, and J. A. Haynes, 2018, "Future engine requirements," 2018 U.S. DOE Vehicle Technologies Office Annual Merit Review Presentation, June 20, 2018, ORNL.

I.1.A.3 Task 4E: CFD Analysis of Cooler Materials, Deposits, and Geometries

Michael J. Lance, Principal Investigator

Oak Ridge National Laboratory
1 Bethel Valley Road
Knoxville, TN 37831
E-mail: lancem@ornl.gov

Hsin Wang, Co-Principal Investigator

Oak Ridge National Laboratory
Materials Science and Technology Division
1 Bethel Valley Road
Knoxville, TN 37831
E-mail: wangh2@ornl.gov

Jerry L. Gibbs, DOE Technology Manager

U.S. Department of Energy
E-mail: jerry.gibbs@ee.doe.gov

Start Date: October 1, 2009

Project Introduction

In order to meet the strict regulations on nitrogen oxide (NO_x) emissions, diesel engine manufacturers commonly utilize a process known as exhaust gas recirculation (EGR). In this process, a certain amount of exhaust gas is diverted into a cooler where its temperature is reduced before being re-introduced into the engine cylinders along with fresh air. The mostly inert gases that the exhaust is composed of act to increase the heat capacity of the cylinder contents. This greater heat capacity acts to lower the temperature within the cylinder during combustion, leading to a reduction in NO_x generation, which is highly temperature-dependent. As the exhaust is cooled in the heat exchanger, the particulate matter and unburned hydrocarbons contained in the gas deposit on the cooler surface through thermophoresis and condensation, respectively. Due to the high levels of particulate matter and hydrocarbon contained in diesel exhaust, the fouling layer in EGR coolers forms rapidly, causing a significant decrease in the cooler effectiveness. This results in higher cylinder temperatures and, in turn, an increase in the NO_x generated by the engine.

To address the problem of fouling in EGR heat exchangers, manufacturers have begun utilizing complex geometries in their cooler designs. A geometry commonly employed in EGR coolers is one which contains sinusoidal fins, as empirical evidence has shown it is less prone to the effects of fouling. Previous experimental studies performed at ORNL in conjunction with nine diesel engine manufacturers (i.e., Caterpillar, Cummins, Detroit Diesel, Ford, GM, John Deere, Navistar, DAF Trucks, and Volvo/Mack) and one heat exchanger supplier (i.e., Modine) found that geometry induces a non-uniform thickness across the length of each sinusoidal period. Furthermore, the thinnest region of the deposit coincides with the area of greatest heat transfer, reducing the drop in effectiveness caused by fouling. The thinner layer in this region is thought to be a result of the increased shear stress associated with the sinusoidal geometry; however, a computational investigation is necessary to verify this theory. The goal of this project is to develop a computational model capable of simulating fouling in sinusoidal finned coolers. This model will be used to better understand the physics driving the formation of the fouling layer. Furthermore, the model will allow for the examination of the performance of various sinusoidal configurations (i.e., varied amplitude and period) to determine the geometry that is most capable of mitigating the effects of fouling.

Objectives

To use CFD methods to provide a better understanding how the internal cooler geometry affects fouling and deposit removal in order to recommend better cooler designs.

To investigate the fouling layer growth resulting from soot deposition, multiple coupled numerical models were utilized to simulate the physics driving the system. These included a hybrid thermal entropic lattice Boltzmann model for the fluid flow and heat transfer, a Lagrangian particle tracking model for the transport of soot particles, and a custom fouling layer model for the growth of the fouling layer and its effects on the system. These models were implemented using the OpenCL framework, allowing for the use of graphics processing units to accelerate the calculations.

Because the flow of exhaust through EGR coolers is turbulent, the thermal entropic multi-relaxation time lattice Boltzmann method (TEMRT-LBM) was chosen to simulate the fluid flow and heat transfer within the cooler. The TEMRT-LBM simulates thermal flows using two distribution functions: one representing the fluid density, f_i , and the other representing the energy, g_i . Relevant macroscopic variables can be obtained from the moments of these distribution functions with $\rho = \sum_i f_i$, $\rho U_\alpha = \sum_i c_{\alpha,i} f_i$, and $T = (\rho^{-1} \sum_i g_i - U^2)/3$. The evolution of these distribution functions proceeds as sequential collision and propagation steps, which are defined as [1-2]:

$$f_i(\mathbf{r} + \mathbf{c}_i \Delta t, t + \Delta t) = f_i'(\mathbf{r}, t) = (1 - \beta) f_i + \beta f_i^{mirr} \quad (1)$$

$$g_i(\mathbf{r} + \mathbf{c}_i \Delta t, t + \Delta t) - g_i(\mathbf{r}, t) = 2\beta(g_i^{eq} - g_i) + (2\beta - \omega_{1,f})(g_i^* - g_i^{eq}) \quad (2)$$

Here, $f_i'(\mathbf{r}, t)$ and $g_i'(\mathbf{r}, t)$ represent the post-collision distributions, $f_i(\mathbf{r} + \mathbf{c}_i \Delta t, t + \Delta t)$ and $g_i(\mathbf{r} + \mathbf{c}_i \Delta t, t + \Delta t)$ represent the distributions after propagation, f_i^{mirr} is the mirror state of f , g_i^{eq} and g_i^* are the equilibrium and quasi-equilibrium populations of g_i , and β and $\omega_{1,f}$ are relaxation parameters, which define the fluid viscosity and thermal diffusivity, respectively.

The equilibrium and quasi-equilibrium populations are computed from moments of the distributions, while the mirror state defined as $f_i^{mirr} = k_i + (2s_i^{eq} - s_i) + [(1 - \gamma)h_i + \gamma h_i^{eq}]$ where k_i is the kinematic part of f_i composed of only locally conserved fields, s_i is the shear part of f_i composed of the stress tensor moments, h_i is composed of the remaining higher order moments of f_i , such that $f_i = k_i + s_i + h_i$, and the superscript eq represents the equilibrium form of the respective part [1]. The entropic stabilizer, γ , is calculated at every time step for each lattice site to ensure entropy is maximized. By maximizing entropy, the entropic stabilizer allows this method to retain numerical stability and accurately reproduce the hydrodynamics of under-resolved turbulent flows [3].

The transport of particles within the cooler channel was modeled using a Lagrangian particle tracking method. The main transport mechanisms for these particles are advection, thermophoresis, eddy diffusion, and gravitational drift [4]. Because the effects of eddy diffusion and gravitational drift are negligible compared to those of advection and thermophoresis, they have been neglected in the model [5]. Furthermore, due to the small sizes of the particle (e.g., tens to hundreds of nanometers) and their small volume fraction within the fluid, the particles are assumed to not experience inertial effects or particle-particle interactions. With these assumptions, the explicit equation of motion for the particles is given by [6-7]:

$$\mathbf{r}(t + \Delta t) = \mathbf{r}(t) + \mathbf{u}[\mathbf{r}(t)]\Delta t - K_{th} \frac{\mu_g \nabla T[\mathbf{r}(t)]}{\rho_g T_p} \quad (3)$$

Here, $\mathbf{r}(t)$ is the position of the particle at time t , $\mathbf{u}[\mathbf{r}(t)]$ fluid velocity at the particle location, K_{th} is the thermophoretic coefficient calculated from the Brock-Talbot correlation, $\nabla T[\mathbf{r}(t)]$ is the thermal gradient at the particle location, T_p is the particle temperature, and ρ_g and μ_g are the density and viscosity of the fluid.

Due to the small size of the particles, the particle temperature is assumed to be equal to the temperature of the fluid at that location.

In order to capture the effect of the flowrate and wall shear on the deposition and removal of particles as they contact the surface, sticking probability and the shear removal model have been implemented. The sticking probability model uses the material properties of the surface and the impinging object, as well as the kinetic energy of the object to calculate a probability that it will adhere to the surface [8]. If the particle has sufficient kinetic energy, it will be specularly reflected and re-entrained in the flow, otherwise it will deposit. Initially, the deposition of particles is treated as temporary. It is during this temporary deposition period that the particles can be sheared from the surface if the shear is greater than a critical value, which is calculated from a moment balance on the particle, and re-entrained in the flow [9]. After a set amount of time the particle is considered permanently deposited and will be re-released at the inlet, allowing for the number of particles used in the simulation to remain constant.

The formation of a deposit layer along the walls of the heat exchanger has a significant impact on all aspects of the system. As the thickness of the layer grows, the effective height of the channel decreases. This affects the flow by inducing higher fluid velocities leading to higher shear stresses at the surface. The high porosity of the layer (~98%) [10] allows for it to act as a highly effective thermal insulator, reducing the thermal gradients in the fluid and, in turn, the effectiveness of the cooler. These are a few examples of the many, interconnected effects resulting from the development of the fouling layer. Therefore, it is necessary for a method to capture the growth of the layer to be implemented. The fouling layer model consists of two steps: a shift step and an update step. In the shift step, the location of the surface elements defining fluid-solid interface are shifted to simulate the growth of the layer. With the location of the fluid-solid interface moved, the update step corrects the variables describing fouling layer to reflect the change in the fouling layer thickness. This update step ensures the fluid flow, heat transfer, and particle motion are coupled to the growth of the fouling layer.

Results

In a separate project funded by the VTO, 20 sinusoidal finned coolers were fouled under varying operating conditions. These coolers were machined-open, and the thickness of the deposit layer was measured with an optical microscope. These measurements will be used to verify the numerical model upon completion. Currently, the numerical model is in the last stages of completion. Due to unknown limitations of the lattice Boltzmann method originally implemented in the model, it did not accurately capture the hydrodynamics of turbulent flow in two dimensions. Specifically, the fluid retained the characteristics of laminar flow and, as a result, contained a thicker boundary layer and produced lower wall shear stresses.

The limitation of the model in two dimensions was not realized until after the several simulations were performed. Results from these simulations are provided in Figure I.1.A.3.1, which contains a plot of the average deposit thickness along a single period near the inlet of the cooler. Here, it can be seen that, as the flow rate increases, the location of the thickest deposit shifts from the upstream side of the fin peak to the downstream side. This indicates that the shear stress along the upstream side plays an important role in the formation of the fouling layer. Furthermore, the fouling layer for the higher Reynolds number (Re) flows exhibit a similar shape to those obtained from experiments in which the flows range from $Re \sim 3,000$ to $5,000$.

Although these results show the original model captures the basic characteristics of the fouling layer, it fails to produce sufficiently accurate results to justify using the model to examine the effect of varying the amplitude and period of the sinusoidal walls. Upon completion of the updated model, new simulations will be performed, and additional tuning of parameters used in the sticking probability and shear removal models will be made to ensure that the model accurately reproduces the formation of the fouling layer pending additional funding. Once the model is validated, it will be used to investigate the effect of amplitude and period of the walls on the fouling layer in order to determine the optimum geometry for mitigation fouling layer development.

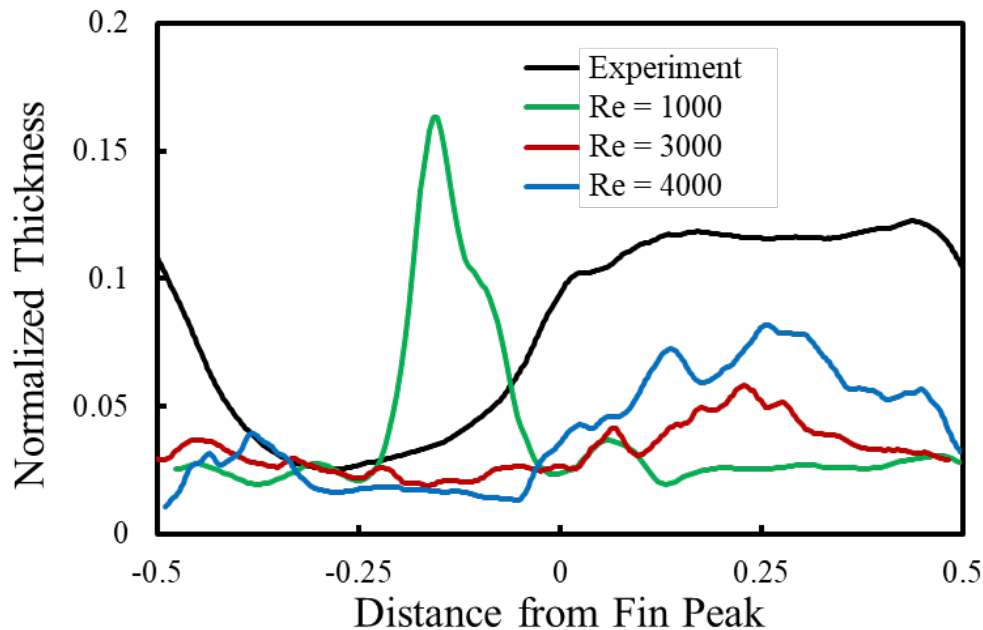


Figure 1.1.A.3.1. Average deposit thickness along one period near the inlet for three flow rates obtained from numerical model along with the average of all 20 experimentally fouled coolers.

Conclusions

A numerical model is being developed that is capable of simulating the formation of the fouling layer in sinusoidal finned EGR coolers. The model utilized the TEMRT-LBM to simulate the fluid flow and heat transfer in the cooler, a Lagrangian particle tracking method for the particle motion and a custom fouling layer model to capture the effects of the growing fouling layer. Preliminary results from the model show that as the flow rate is increased from $Re \sim 1,000$ to $Re \sim 4,000$, the thickest region of the deposit layer shifts from upstream of the fin peak to downstream, indicating that shear has a large influence on the formation of the deposit layer. Furthermore, the general shape of the high Re numerical results is similar to those obtained from experiments with the thinnest and thickest deposits upstream and downstream, respectively. The completed and validated model will allow for a range of geometric parameters to be investigated to determine the optimum geometry for mitigating fouling, a task that is prohibitively expensive to do experimentally.

References

1. Karlin, I. V., F. Bösch, and S. S. Chikatamarla, 2014, "Gibbs' principle for the Lattice-Kinetic Theory of fluid dynamics," *Phys. Rev. E*, Vol. 90, No. 3, Art. 031302(R).
2. Karlin, I. V., D. Sichau, and S. S. Chikatamarla, 2013, "Consistent two-population lattice Boltzmann model for thermal flows," *Phys. Rev. E*, Vol. 88, No. 6, Art. 063310.
3. Bösch, F., S. S. Chikatamarla, and I. Karlin, 2015, "Entropic multi-relaxation models for simulation of fluid turbulence," *ESAIM Proc.*, Vol. 52, pp. 1-24. doi:10.1051/proc/201552001.
4. Abarham, M., J. Hoard, J., D. N. Assanis, D. Styles, E. W. Curtis, and N. Ramesh, 2010, "Review of soot deposition and removal mechanisms in EGR coolers," *SAE Int. J. Fuels Lubr.*, Vol. 3, No. 1, Art. 2010-01-1211, pp. 690–704.
5. Warey, A., S. Balestrino, P. Szymkowicz, and M. R. Malayeri, 2012, "A one-dimensional model for particulate deposition and hydrocarbon condensation in exhaust gas recirculation coolers," *Aerosol Sci. Technol.*, Vol. 46, No. 2, pp. 198–213.

6. Verberg, R., A. Alexeev, and A. C. Balazs, 2006, "Modeling the release of nanoparticles from mobile microcapsules," *J. Chem. Phys.*, Vol. 125, Art. 224712. doi:10.1063/1.2404955.
7. Housiadas, C., and Y. Drossinos, 2005, "Thermophoretic deposition in tube flow," *Aerosol Sci. Technol.*, Vol. 39, No. 4, pp. 304–318.
8. Somorjai, G. A., and Y. Li, 2010, *Introduction to Surface Chemistry and Catalysis*, Wiley.
9. Soltani, M., and G. Ahmadi, 1994, "On particle adhesion and removal mechanisms in turbulent flows," *J. Adhes. Sci. Technol.*, Vol. 8, No. 7, pp. 763–785.
10. Lance, M. J., C. S. Sluder, H. Wang, and J. M. E. Storey, 2009, "Direct measurement of EGR cooler deposit thermal properties for improved understanding of cooler fouling," *SAE Int.*, Art. 2009-01-1461.

I.1.A.4 Task 5E: Computational Development of Thermoelectric Materials

David S. Parker, Principal Investigator

Oak Ridge National Laboratory
1 Bethel Valley Road
Knoxville, TN 37831
E-mail: parkerds@ornl.gov

Jerry L. Gibbs, DOE Technology Manager

U.S. Department of Energy
E-mail: jerry.gibbs@ee.doe.gov

Start Date: October 1, 2017

Project Introduction

Thermoelectric materials offer the promise of converting a significant fraction of waste heat—heat rejected from combustion processes—into directly usable energy. These materials do this by converting this energy into an electrical current by means of the Seebeck effect. This current can then be used to power electrical devices in a waste heat recovery environment, such as the exhaust stream of a motor vehicle. Despite their promise, however, thermoelectric devices have not yet been widely implemented, due principally to the lack of sufficiently efficient materials. Computational techniques have proven highly useful in discovering and optimizing high thermoelectric performance (measured as the dimensionless figure of merit ZT) [1-4] and this project continues and expands upon this effort.

Objectives

The objective of this project is to design and discover high-performance thermoelectric materials by employing an ICME approach, as described below.

Approach

This project achieves its objective by a combination of first-principles (e.g., density functional theory) calculations, along with Boltzmann transport calculations of the Seebeck coefficient and electrical conductivity – key parameters entering the expression for ZT that require a careful and simultaneous optimization. The project also devotes significant attention to *doping* strategies—techniques for converting a semiconductor, of little initial utility for thermoelectric applications, into a high ZT material with high electrical conductivity, large Seebeck coefficient, and low thermal conductivity—the desired properties for high thermoelectric performance.

Results

This project comprises two main results. First, we have calculated the Seebeck coefficient of NbFeSb, which has already shown a *p*-type ZT value of 1.5 [5]. However, far less attention has been devoted to *n*-type doping, which poses a difficulty as any thermoelectric device must use *both n*-type and *p*-type thermoelectric “legs” in order to function. There is a substantial advantage, given difficulties associated with thermal expansion, to using the same semiconductor (one leg *n*-type, one *p*-type) in a thermoelectric device. Hence, obtaining high ZT in *n*-type NbFeSb is of great technological importance.

As shown in Figure I.1.A.4.1, *n*-type NbFeSb can be expected to obtain substantial Seebeck coefficients (e.g., higher in magnitude than 200 $\mu\text{V/K}$) even at temperatures as high as 1,000 K. There is, therefore, a substantial opportunity for high thermoelectric performance in *n*-type NbFeSb, if carrier concentrations in the vicinity of 10^{20} cm^{-3} can be achieved. To our knowledge, these have not previously been studied, and accordingly we have conducted a theoretical analysis of possible doping strategies in this material. The second main result

regarding doping strategies is depicted in Figure I.1.A.4.2, which presents a detailed analysis of the doping properties of *n*-type NbFeSb.

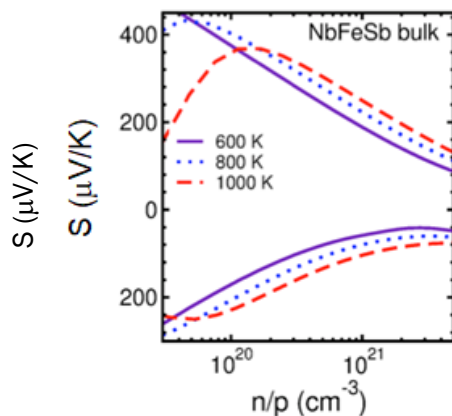


Figure I.1.A.4.1. The calculated temperature and doping dependence of the Seebeck coefficient, *S*, in NbFeSb. Note the thermopower magnitudes greater than 200 $\mu\text{V}/\text{K}$ for *n*-type doping, indicating that, as with *p*-type doping, *n*-type doping can also attain high ZT.

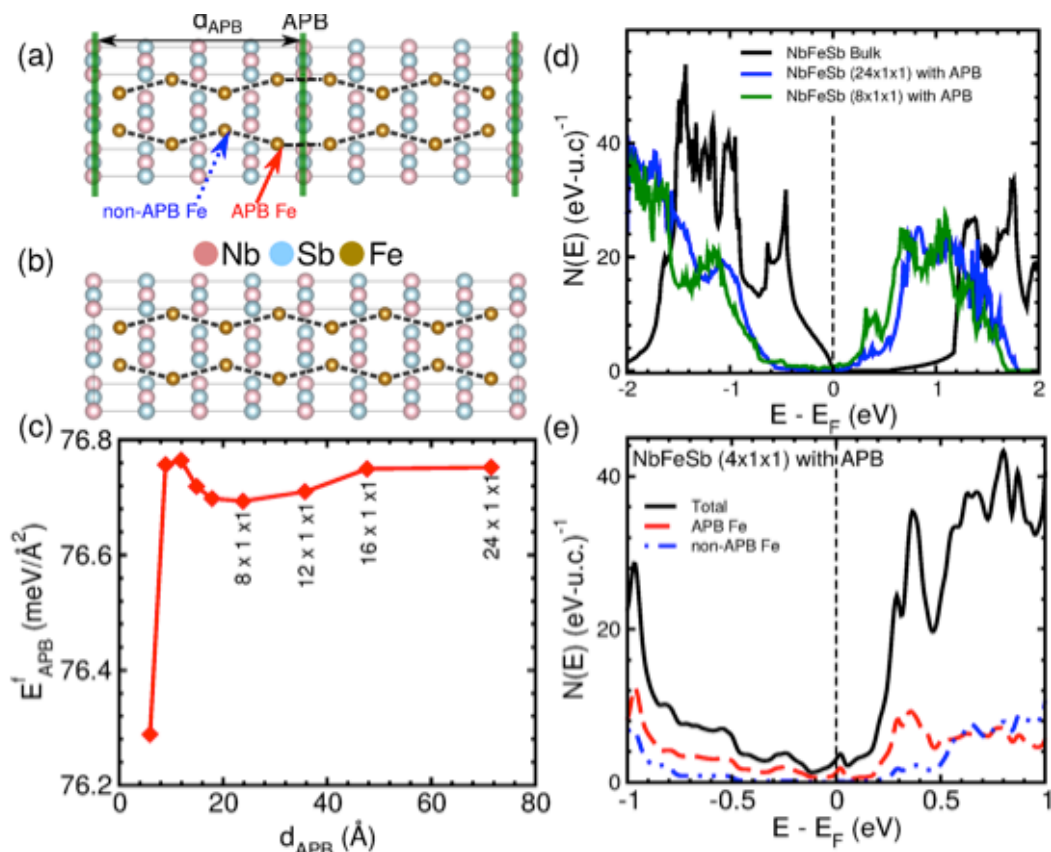


Figure I.1.A.4.2. (a) The anti-phase boundary (APB) believed responsible for *n*-type doping in NbFeSb. Note the two Fe sites: “APB Fe” (near the APB) and “non-APB Fe”. (b) The regular bulk NbFeSb structure without an APB. (c) Convergence check on the APB formation energy. (d) Calculations of the density-of-states (DOS) of bulk NbFeSb (black) and two APB-containing supercells (blue and green curves). (e) The DOS of a 4x1x1 APB-containing supercell of NbFeSb.

Our analysis shows that APBs, the breaking of crystalline symmetry by a reflection plane as shown in Figure I.1.A.4.2.(a), are a useful means of generating the desired n -type behavior. As shown in Figure I.1.A.4.2.(d), these APBs have the effect of moving the valence and conduction bands lower in energy (blue and green curves), thereby moving the Fermi level into the conduction band, yielding the n -type doping. Our analysis also indicates that the iron atoms nearest the APB (“APB Fe”) play an important role in this, yielding an impurity band seen as the red curve in Figure I.1.A.4.2.(e), unlike the iron atoms away from the APB (“non-APB Fe”), which still retain their semiconducting (insulating) character. Hence, we have identified from our calculations an important new doping strategy for obtaining n -type behavior in NbFeSb, and this strategy can likely be applied to other such materials in the “Half-Heusler” family (the name is a technical reference to a particular crystal structure).

Conclusions

From our theoretical calculations, we have determined optimal carrier concentrations for high ZT in n -type NbFeSb. We have also found APBs to be a useful means of obtaining technologically important n -type doping in this high-performance p -type thermoelectric, and most likely numerous other compounds as well.

Key Publications

1. Hobbis, D., R. P. Hermann, H. Wang, D. S. Parker, T. Pandey, J. Marti, K. Page, and G. S. Nolas, 2018, “Structural, chemical, electrical, and thermal properties of n -type NbFeSb,” under editorial review, *Inorg. Chem.*

References

1. Parker, D. S., and D. J. Singh. 2010, “High-temperature thermoelectric performance of heavily doped PbSe.” *Phys. Rev. B*, Vol. 82, Art. 035204.
2. Parker, D. S., A. F. May, and D. J. Singh, 2015, “Benefits of carrier-pocket anisotropy to thermoelectric performance: The case of p -type AgBiSe₂.” *Phys. Rev. Appl.*, Vol. 3, Art. 064003.
3. Parker, D. S., X. Chen, and D. J. Singh, 2013, “High three-dimensional thermoelectric performance from low-dimensional bands,” *Phys. Rev. Lett.*, Vol. 110, Art. 146601.
4. Parker, D. S., and D. J. Singh, 2011, “Potential thermoelectric performance from optimization of hole-doped Bi₂Se₃,” *Phys. Rev. X*, Vol. 1, Art. 021005.
5. Fu, C., S. Bai, Y. Liu, Y. Tang, L. Chen, X. Zhao, and T. Zhu, 2015, “Realizing high figure of merit in heavy-band p -type half-Heusler thermoelectric materials,” *Nat. Commun.*, Vol. 6, Art. 8144.

Acknowledgements

The author gratefully acknowledges Hsin Wang of ORNL for helpful collaboration.

I.1.B ICME Guide Development of Advanced Cast Aluminum Alloys for Automotive Engine Application (Ford Motor Company)

Dr. Mei Li, Principal Investigator

Ford Motor Company
2101 Village Rd. RM 2014
Dearborn, MI 18124
E-mail: mli9@ford.com

Jerry L. Gibbs, DOE Technology Manager

U.S. Department of Energy
E-mail: jerry.gibbs@ee.doe.gov

Start Date: February 1, 2013

End Date: August 31, 2018

Project Funding: \$4,630,000

DOE share: \$3,240,000

Non-DOE share: \$1,390,000

Project Introduction

Recently legislated fuel economy standards require new U.S. passenger vehicles to achieve at least 34.1 miles per gallon (MPG) on average by model year 2016 and 58 MPG by 2030, up from 28.8 MPG in 2013. Two major methods of achieving improved fuel economy in passenger vehicles are reducing the weight of the vehicle and developing high-performance engines. To increase engine efficiency, however, the maximum operation temperature of these components has increased from approximately 170°C in earlier engines to peak temperatures well above 200°C in recent engines [1-2]. The increase in the operational temperatures requires a material with optimized properties in terms of tensile, creep and fatigue strength. This program focuses on developing advanced cast Al alloys for automotive engine applications to meet these challenging requirements.

Two combinations of alloys and heat-treatments—Ford Semi-Permeant Mold Cast with novel three-stage heat-treatment (Ford-SPMC-3Stage) and Ford High-Pressure Die-Cast with conventional T5 heat-treatment (Ford-HPDC-T5)—have been developed in the past five years at the Ford research laboratory. The microstructures benefitting elevated temperature performance have been well navigated in these two combinations through ICME tools such as Thermo-Calc, Diffusion-Controlled TRAnsformations (DICTRA) within Thermo-Calc, and PanPrecipitation by CompuTherm and advanced characterization technologies, including SEM, TEM, EPMA, and APT. The mechanical properties of these two combinations, including tensile and endurance limits at both room and elevated temperatures, have been proved on torpedo shape samples that are cast using permanent molds. First of all, the 300°C yield strength of Ford-SPMC-3Stage and Ford-HPDC-T5 after 100 hours of pre-exposure at testing temperatures exceed DOE's requirement, while the baseline alloy, AA319-T7, cannot meet the DOE target. It is worth mentioning that the 300°C yield strength of Ford-HPDC-T5 exhibits a 30% increase over other alloys. On the other hand, the endurance limits of Ford-SPMC-3Stage and Ford-HPDC-T5 show significant improvement once the testing temperatures are above 150°C, as compared to both the current AA319-T7 and AS7GU-T64 alloys for high-performance engines. To the knowledge of the authors, Ford-SPMC-3Stage and Ford-HPDC-T5 have the best high-cycle fatigue (HCF) performance at elevated temperatures (>150°C) in all of the Al alloys intended for engine applications. Based on the experimental results of torpedo samples, Ford-SPMC-3Stage and Ford-HPDC-T5 show promising applications for cylinder heads and engine blocks. To demonstrate the performance of these two alloys and heat-treatment combinations on component levels, several prototyping projects have been conducted in the past year. The results will be presented in detail in this final report. In addition, a comprehensive cost model and a summary of ICME tool development and gap identification will be discussed.

Objectives

- To develop a new class of advanced, cost-competitive Al casting alloys providing a 25% improvement in component strength relative to components made with A319 or A356 alloys using sand and semi-permanent casting processes for high-performance engine applications.
- To demonstrate the power of ICME tools for accelerating the development of new materials and processing techniques, as well as to identify the gaps in ICME capabilities.
- To develop comprehensive cost models to ensure that components manufactured with these new alloys do not exceed 110% of the cost using incumbent alloys A319 or A356.
- To develop a technology transfer and commercialization plan for development of these new alloys in automotive engine applications.

Approach

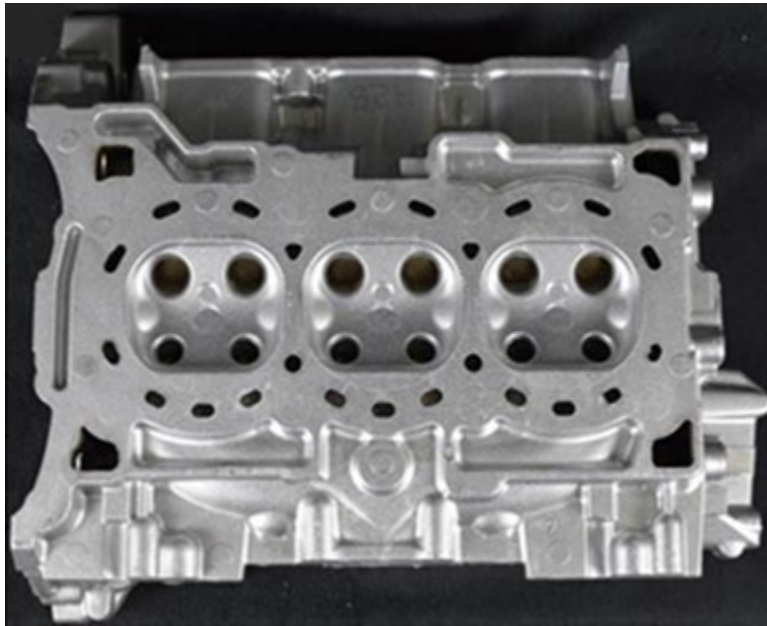
- Start the alloy design process with a baseline alloy in line with 356/319 alloys with well quantified properties.
- Evaluate the heat-treatment response and strengthening effect of some heat resistance elements of interests in simple model alloys, particularly at high-temperature (i.e., 300°C).
- With the aid of ICME tools, design and optimize the chemical composition and heat-treatment process of the baseline alloys with novel alloying additions.
- Demonstrate the performance of these new alloys at both room and elevated temperature by a series of mechanical tests, including yield strength, ultimate tensile strength, and endurance limits.
- With the aid of ICME tools, develop a commercialization prototyping plan and investigate the performance of new alloys as automotive engine components with this prototyping plan.

Results

In the past five years, it has been demonstrated that these two alloys and heat-treatment combinations perform extremely well at elevated temperatures as torpedo samples that are prepared by permanent mold cast. Although the permanent molds used in the Ford research laboratory are modified with heat transfer coating to approach the solidification rates in industrial production, the production processes of torpedo samples are still quite simpler than those used in industrial productions for both cylinder heads and engine blocks. For instance, cylinder heads have a much more complicated geometry and engine blocks are cast at much higher pressure conditions. Aiming to implement these two combinations in industrial production, the performance of these two alloys and heat-treatment combinations need to be demonstrated at the component level. As a result, three prototyping projects were conducted in the past year: (1) the 1.5L Gasoline Turbocharged Direct Injection (GTDI) cylinder heads program at Qin'an, China, to test the performance of the Ford-SPMC-3Stage; (2) the 2.0L GTDI Duratec Bearing-Beam program in Jackson, MI; and (3) the Ryobi single-cap castings program in Japan to test the performance of Ford-HPDC-T5.

First of all, 50 GTDI cylinder head castings were made using three compositions—the Ford-SPMC-with strontium (w/Sr), the Ford-SPMC-without strontium (w/oSr), and the AS7GU—at Qin'an, China plant, as shown in Figure I.1.B.1.(a). High-quality castings were obtained, as indicated by the computed tomography scan shown in Figure I.1.B.1.(c). Samples used for tensile and endurance limit testing were sectioned from two locations with different cooling rates in each GTDI cylinder head—the bolt boss (see Figure I.1.B.1.(b) right) with a slow cooling rate and the deck face (see Figure I.1.B.1.(b) left) with a fast cooling rate. After the sectioning, testing samples were heat-treated with corresponding conditions—novel three-stage heat-treatment was used for the Ford-SPMC-w/Sr and the Ford-SPMC-w/oSr, while traditional T64 was used for the AS7GU. In addition, 100 hours of pre-exposure at testing temperatures was performed after heat-treatment. The samples, however, sectioned from GTDI heads were too small to be machined into the same geometry used by the torpedo samples. As a result, the sub-size samples were used for both tensile and endurance limit tests. The

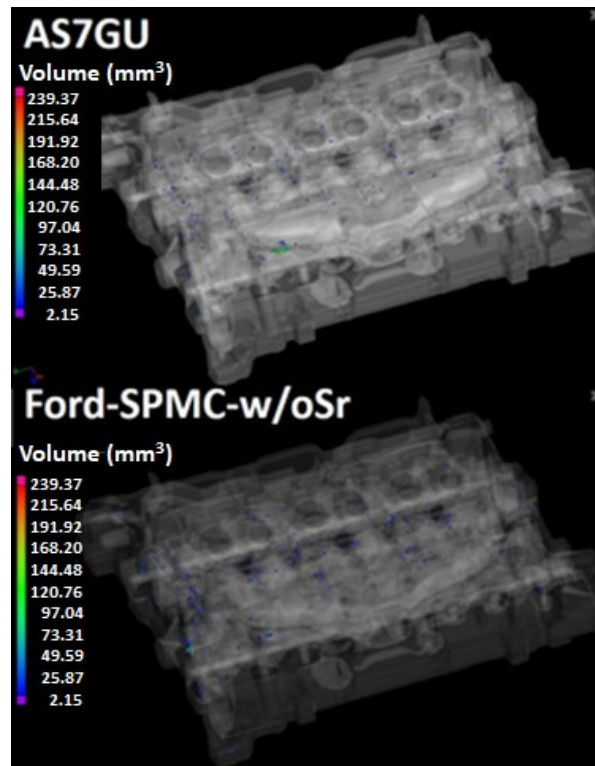
correlation between the sub-size and regular-size samples in mechanical properties was studied. As shown in Figure I.1.B.2, both tensile properties and endurance limits for regular-size and sub-size samples machined from torpedo samples are comparable. Thus, geometries of testing samples have little impact on both tensile properties and endurance limits.



(a)



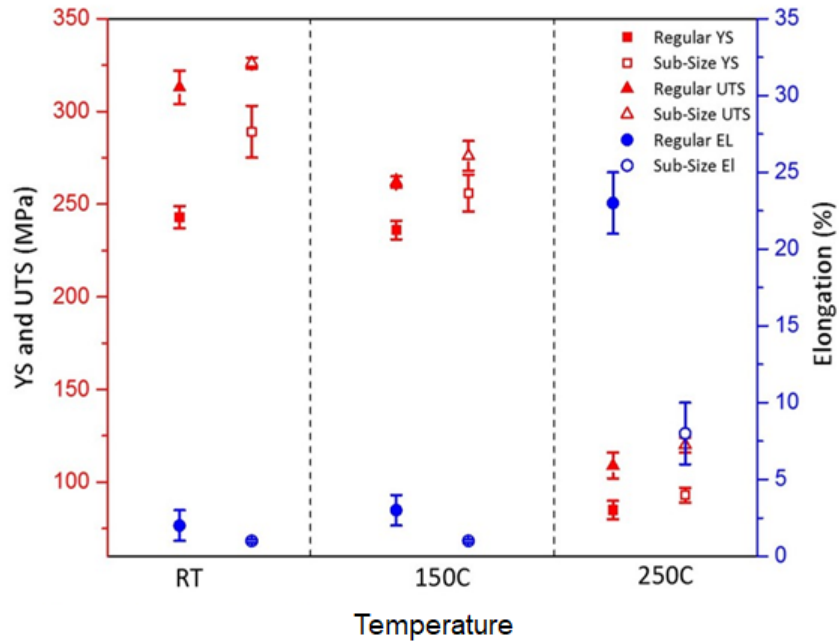
(b)



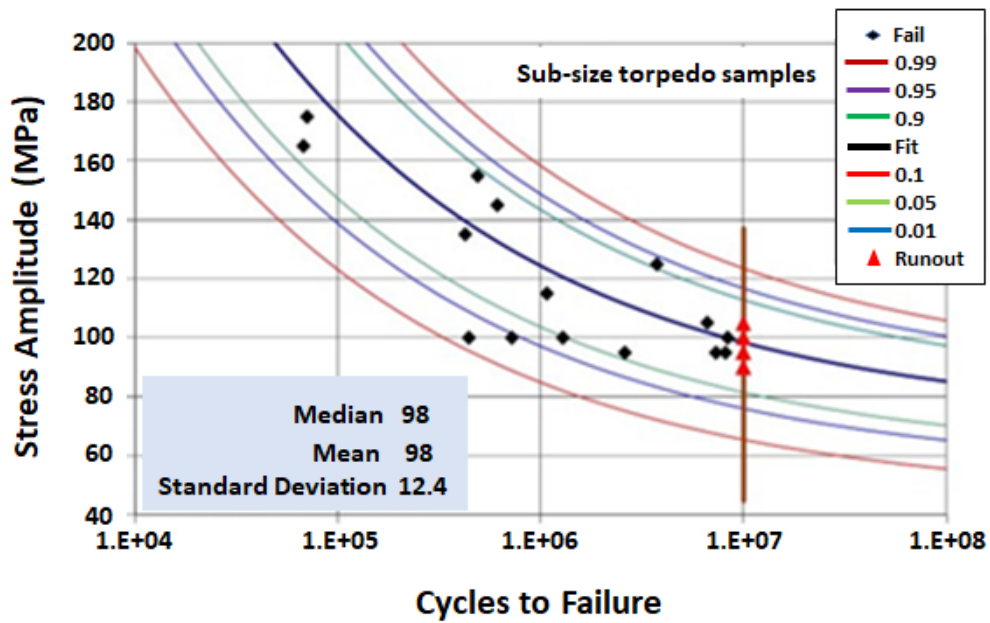
(c)

Figure I.1.B.1. Graphical representation of (a) a 1.5L GTDI cylinder head prototyped with Ford-SPMC-w/oSr at Qin'an, China plant; (b) the locations from the deck face (red rectangular) and the bolt boss (green circle) for mechanical tests; and (c) the computed tomography scan results for the 1.5L GTDI cylinder heads showing the distribution of pores. Source: Ford.

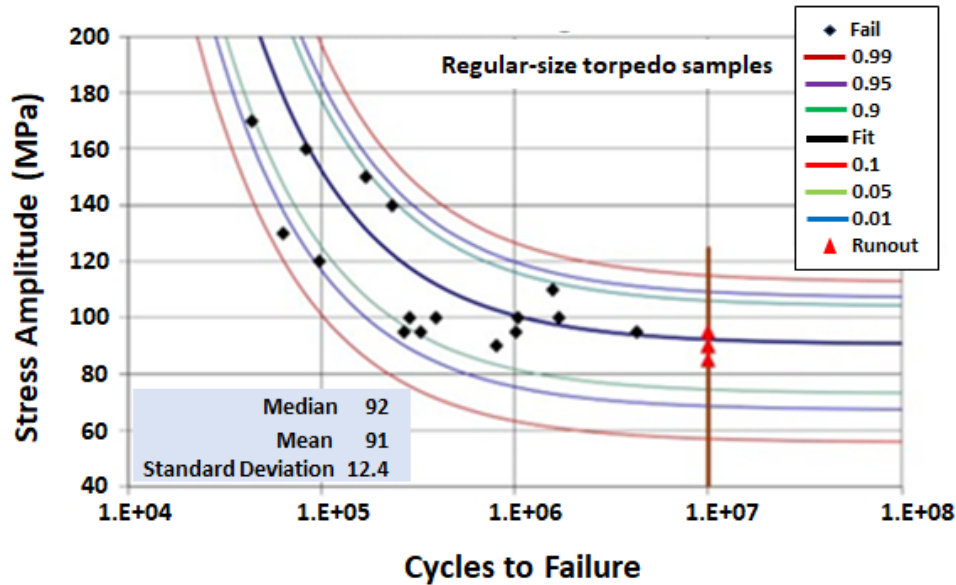
The tensile properties, including the yield strength (YS), ultimate tensile strength (UTS), and elongation (EL), of the AS7GU-T64, Ford-SPMC-w/Sr-3Stage, and Ford-SPMC-w/oSr-3Stage are summarized in Figure I.1.B.3. Several conclusions can be drawn from the tensile testing results: (1) the YS and UTS show the same behavior (i.e., those with high YS always have high UTS as well); (2) the YS and UTS decrease with corresponding increases in testing temperatures, while the EL increases with corresponding increases in testing temperatures; (3) the YS and UTS of the deck face are higher than the bolt boss, and the YS and UTS of the bolt boss are higher than the torpedo samples; (4) the YS and UTS of the bolt boss for the three combinations are comparable to each other; (5) the YS and UTS of the deck face from Ford-SPMC-w/Sr-3Stage and Ford-SPMC-w/oSr-3Stage are higher than that from the AS7GU-T64; (6) the EL of the torpedo samples is higher than the deck face and the bolt boss; (7) the AS7GU-T64 has a much higher EL at low temperatures; and (8) the Ford-SPMC-w/Sr-3Stage has a higher EL than the Ford-SPMC-w/oSr-3Stage.



(a)



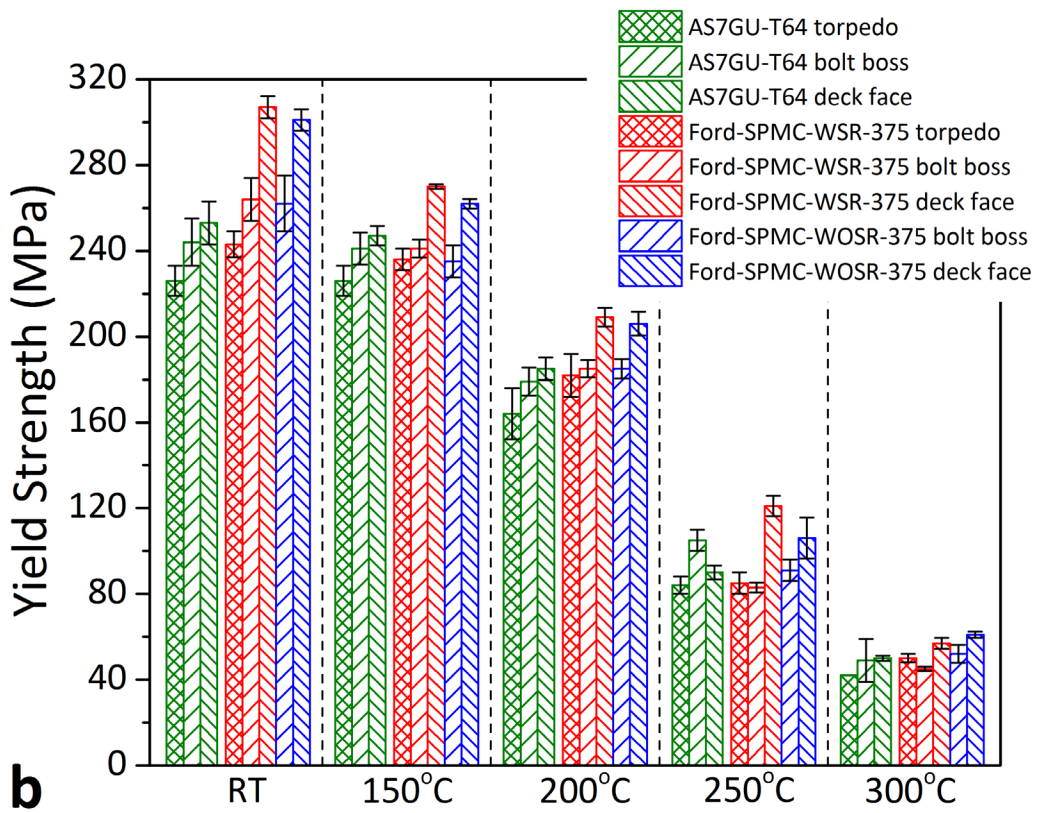
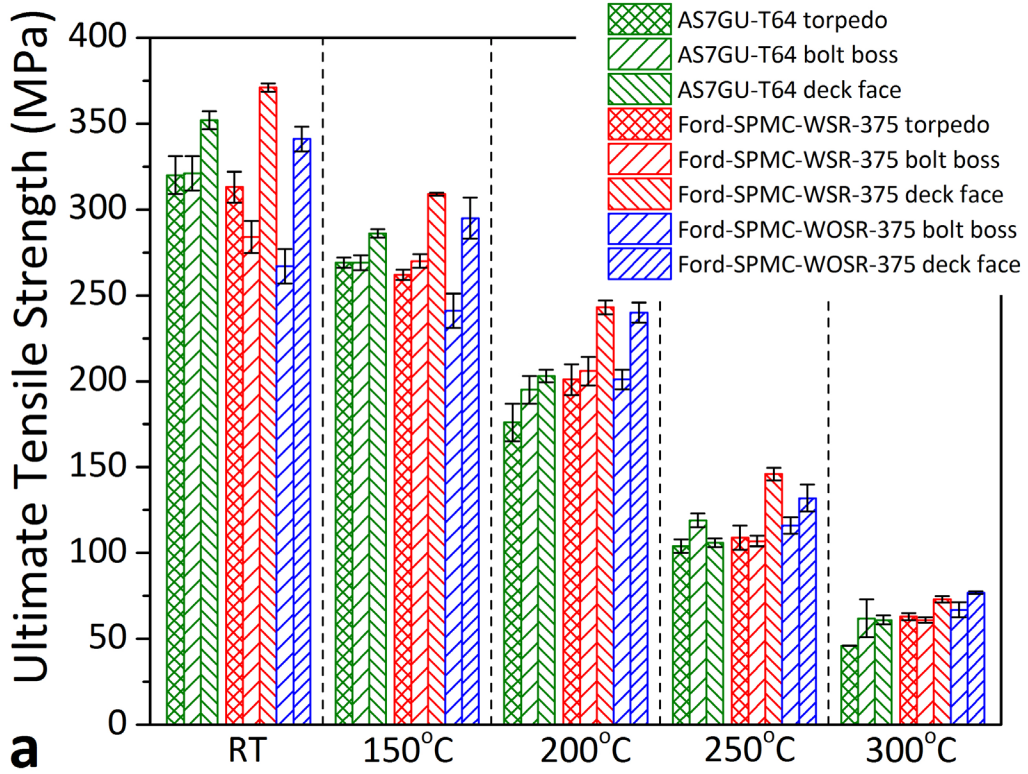
(b)



(c)

Figure I.1.B.2. Graphical representation of (a) tensile testing results at room and elevated, and 150°C endurance limit testing results for (b) sub-size and (c) regular samples sectioned from the torpedo samples showing geometrics has little effect on mechanical properties. Source: Ford Motor Company.

The results of endurance limit tests at elevated temperatures are shown in Table I.1.B.1. First, 150°C HCF strength of the deck face from the Ford-SPMC-w/Sr and Ford-SPMC-w/oSr are close to that from the torpedo samples after novel three-stage heat-treatment, while 150°C HCF strength of the deck face from the AS7GU is higher than that from the torpedo samples after traditional T64 heat-treatment. The deck face from the AS7GU-T64 and Ford-SPMC-w/oSr-3Stage have comparable 150°C HCF strength. Once the testing temperature increases to 180°C, the HCF strength of the deck face from the Ford-SPMC-w/oSr-3Stage is still above 90 MPa, while the HCF strength of the deck face from the AS7GU-T64 drops to 70 MPa. At last, the 150°C HCF strength of bolt boss from the AS7GU-T64 is above 70 MPa, while the Ford-SPMC-w/Sr-3Stage and Ford-SPMC-w/oSr-3Stage are below 60 MPa. It is well-known that the pressures and temperatures at the deck face are much higher than that at the bolt boss, resulting in more severe working conditions at the deck face. Thus, most fatigue failures happen at the deck face rather than the bolt boss in cylinder heads. The improved elevated temperature endurance limit observed in the deck face from the Ford-SPMC-w/oSr-3Stage cylinder heads shows promise for replacing the current used alloys in industrial productions.



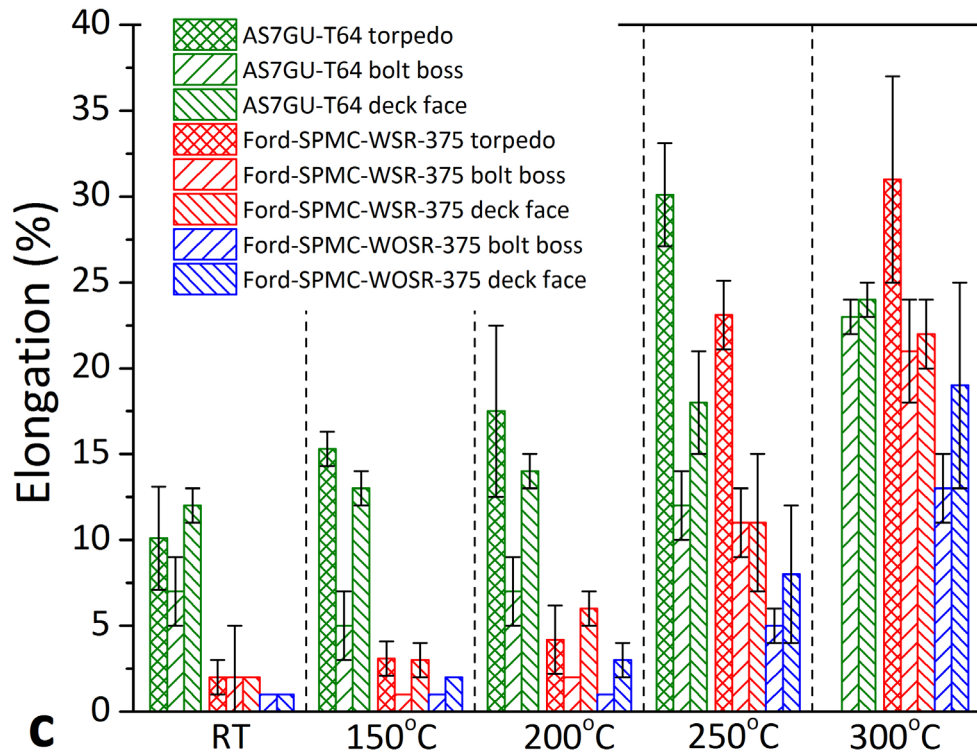


Figure I.1.B.3. Graphical representation of (a) UTS, (b) YS, and (c) elongation at different temperatures of the AS7GU-T64, Ford-SPMC-w/oSr-3stage, and Ford-SPMC-w/Sr-3Stage sectioned from the torpedo samples, and deck face and bolt boss 1.5L GTDI cylinder heads, showing the proposed alloys and heat-treatment combinations have superior tensile properties at elevated temperatures. Source: Ford Motor Company.

Table I.1.B.1. Elevated Temperature HCF Strength of the Torpedo Samples, Deck Face and Bolt Boss from 1.5L GTDI Cylinder Heads for the AS7GU-T64, Ford-SPMC-w/Sr-3stage, and Ford-SPMC-w/oSr-3Stage.

	Locations	HCF Strength @ 150 °C (MPa)	HFC Strength @180 °C (MPa)
AS7GU-T64	Torpedo	62±6	
	Deck face	93±11	70±6
	Bolt boss	72±11	
Ford-SPMC-w/Sr-3Stage	Torpedo	72±7	
	Deck face	67±7	
	Bolt boss	59±6	
Ford-SPMC-w/oSr-3Stage	Torpedo	91±12	92±12
	Deck face	92±10	92±9
	Bolt boss	51±6	

Second, two prototyping projects were conducted to evaluate the performance of Ford-HPDC alloys under the HPDC process. An I4-Bearing-Beam die with five caps was used at Mag-tec, MI, and a Journal-Piece die with only one cap was used at Ryobi, Japan. The samples made by these two projects are shown in Figure I.1.B.3. In addition, another two alloys were used as benchmark alloys—ADC12Z, currently used alloy for the engine block, and C677F, a commercial alloy from Alcoa. All the samples were heat-treated with the conventional T5 condition, and a 100-hours pre-exposure at testing temperatures was performed for elevated temperature tests.

The porosity of five caps from the I4-Bearing-Beam was examined by x-ray and are depicted by Figure I.1.B.4.(a). Due to the relatively low porosity level compared to the other caps, cap four was used for tensile and endurance limit tests. In addition, no pores can be observed by optical microscope in the cross-section of the Journal-Piece, as shown in Figure I.1.B.4.(b). The UTS and YS at three temperatures of the torpedo samples, I4-Bearing-Beam, and Journal-Piece are summarized in Figure I.1.B.5.(a) and (b), respectively. In general, the UTS and YS of the samples made by HPDC processes, the I4-Bearing-Beam and Journal-Piece, are not as high as the torpedo samples for the ADC12Z-T5, Ford-HPDC-T5, and C677F-T5. The only exception is the ADC12Z-T5 at room-temperature, whose tensile properties as the torpedo samples is lower than the I4-Bearing-Beam and Journal-Piece. The 150°C HCF strength for ADC12Z-T5 as the I4-Bearing-Beam is only 36 ± 4 MPa, which is significantly lower than the torpedo samples (~ 90 MPa). Many pores that are beyond the resolution of x-ray analysis can be observed in the fracture surface from the I4-Bearing-Beam by SEM. The HPDC processes have limitations on casting samples with complicated geometries, like a bearing-beam or an engine block. As such, in addition to the optimization of an alloy's composition and heat-treatment, the HPDC processes, such as gating, feeding, etc., need to be modified further.

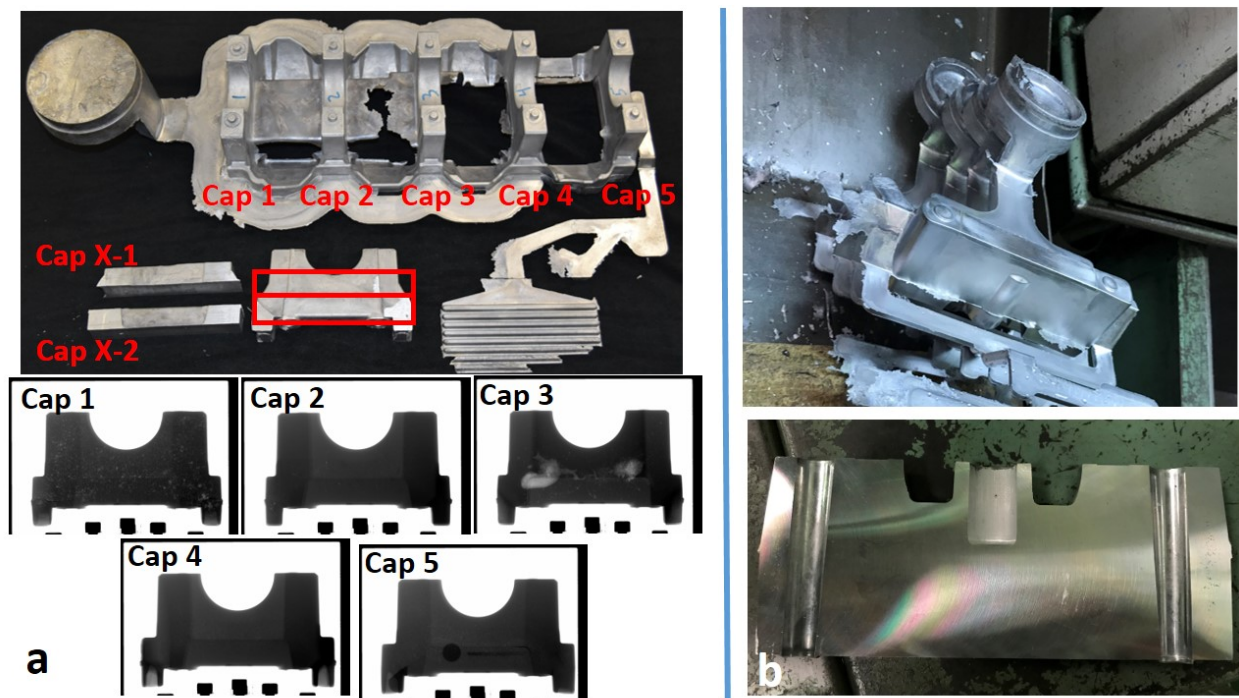
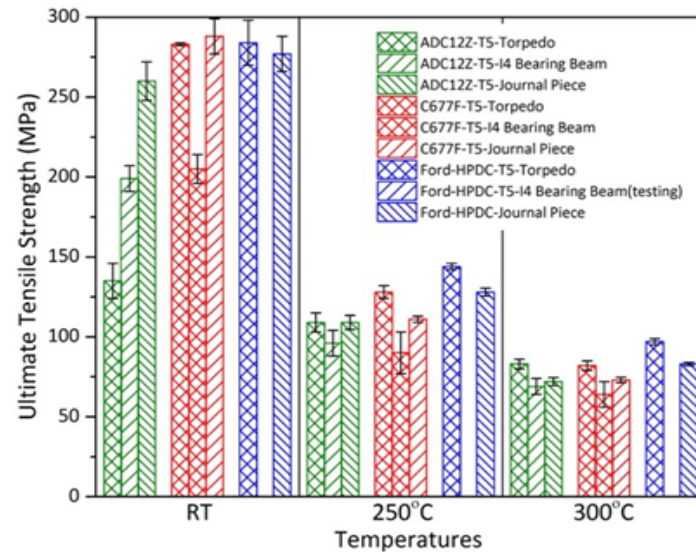
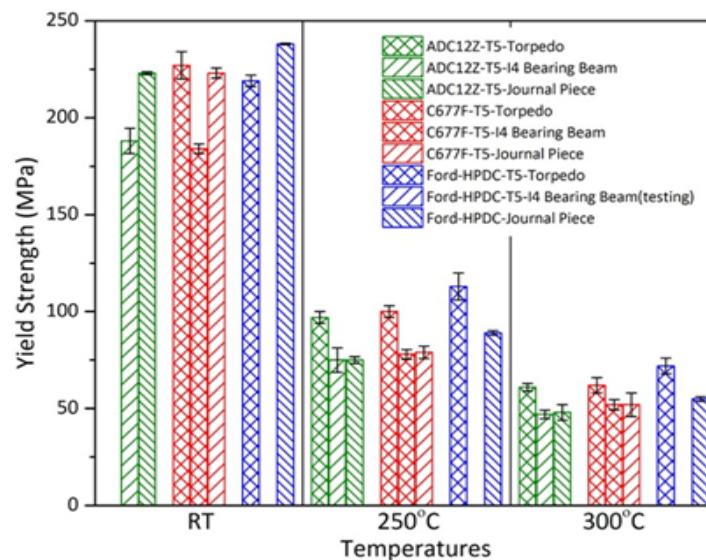


Figure I.1.B.4. Graphical representation of (a) I4-Bearing - Beams castings prototyped with Ford-HPDC alloys at Mag-tec, MI, and X-ray results showing the distribution of the pores; and (b) a Journal-Piece casting prototyped with the C677F alloys at Ryobi, Japan, and the cross-section showing no pores is observed. Source: (a) Ford and (b) Alcoa.



(a)



(b)

Figure I.1.B.5. Graphical representation of (a) UTS and (b) YS at different temperatures of the ADC12Z-T5, C677F-T5, and Ford-HPDC-T5 sectioned from the torpedo samples, I4-Bearing-Beam, and Journal-Piece, showing the mechanical properties of torpedo samples cannot be achieved by the HPDC processes.

Source: Ford Motor Company.

Third, a comprehensive cost model, as shown by the flow chart in Figure I.1.B.6 was developed at Ford. This model takes all the semi-permanent mold casting processes into account, such as molding, melting, casting, materials and heat-treatment. The premium of making new GTDI cylinder heads using the Ford-SPMC-3Stage over the AS7GU-T64 were evaluated by this model. The parameters for GTDI cylinder head mold was set in the “Global Inputs” module, including total weight, maximum and average wall thickness, project area and surface area, etc. Second, the prices for a baseline alloy (i.e., AS7GU) and new alloys with transition metal additions were obtained from Tier 1 suppliers and put into the “Virgin Ingot” module. The power input was adjusted in the “Melt” module because the melting temperatures of the new alloys are higher than the baseline

alloys. Finally, the cost from the heat-treatment was considered in “Heat-treat” module. This three-stage heat-treatment needs more labor cost because there are three steps rather than two steps in T64 tempering. But the power input of this heat-treatment is lower since the high-temperature solution treatment is shorter than T64. It’s shown that the cost of “melting and casting” and “heat-treatment” mainly contribute to the total premium, as shown in Figure I.1.B.7. The total premium of producing GTDI cylinder heads using the Ford-SPMC-3stage is 10.5% over the AS7GU-T64. This is within the DOE target that components manufactured with these new alloys do not exceed 110% of the cost using incumbent alloys.

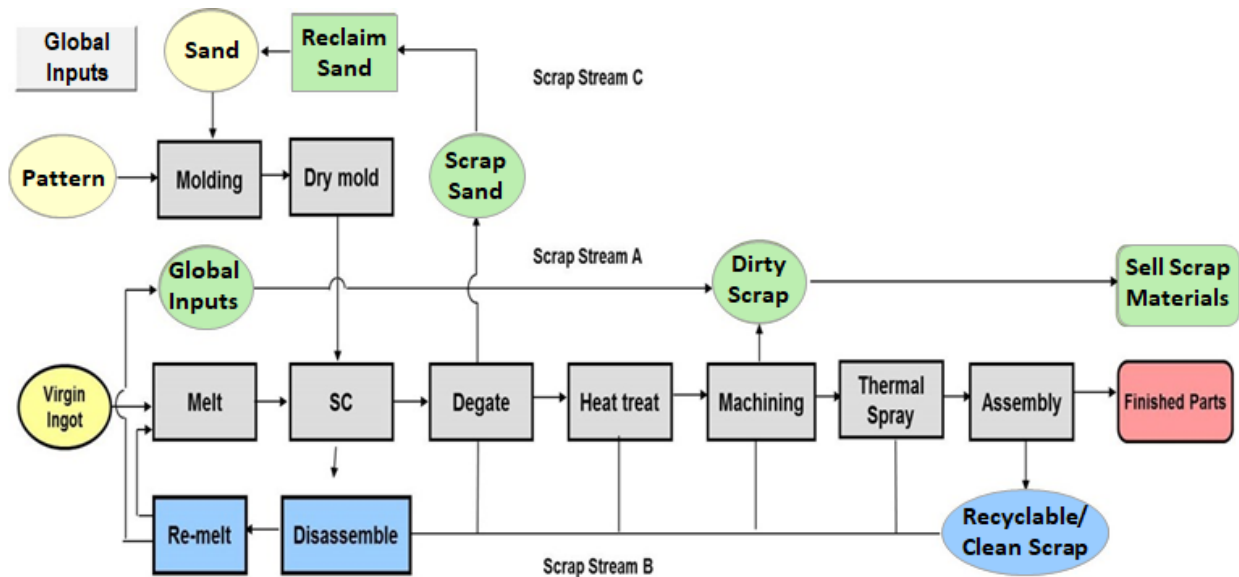
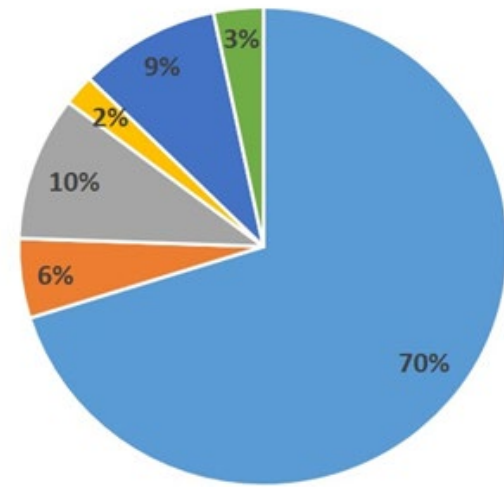
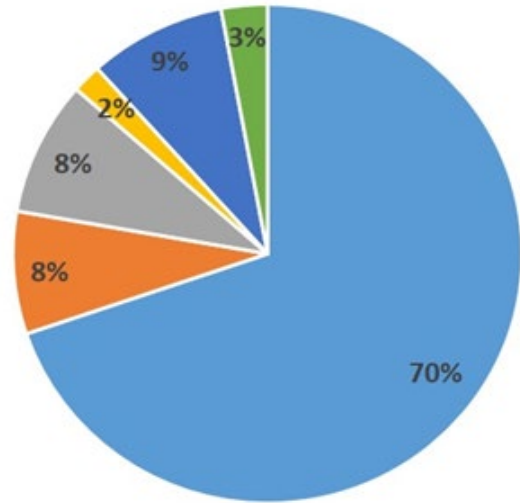


Figure I.1.B.6. Graphical representation of the flow chart of the cost model showing the key factors.
Source: Ford Motor Company.

Cost components of 1.5L GTDI heads made from AS7GU-T64

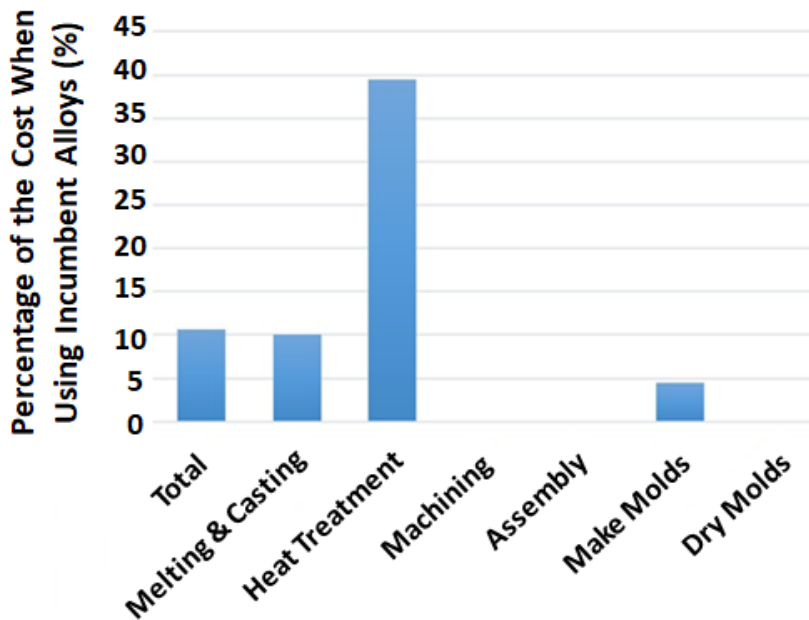


Cost components of 1.5L GTDI heads made from Ford-SPMC-w/oSr-3Stage



(a)

(b)



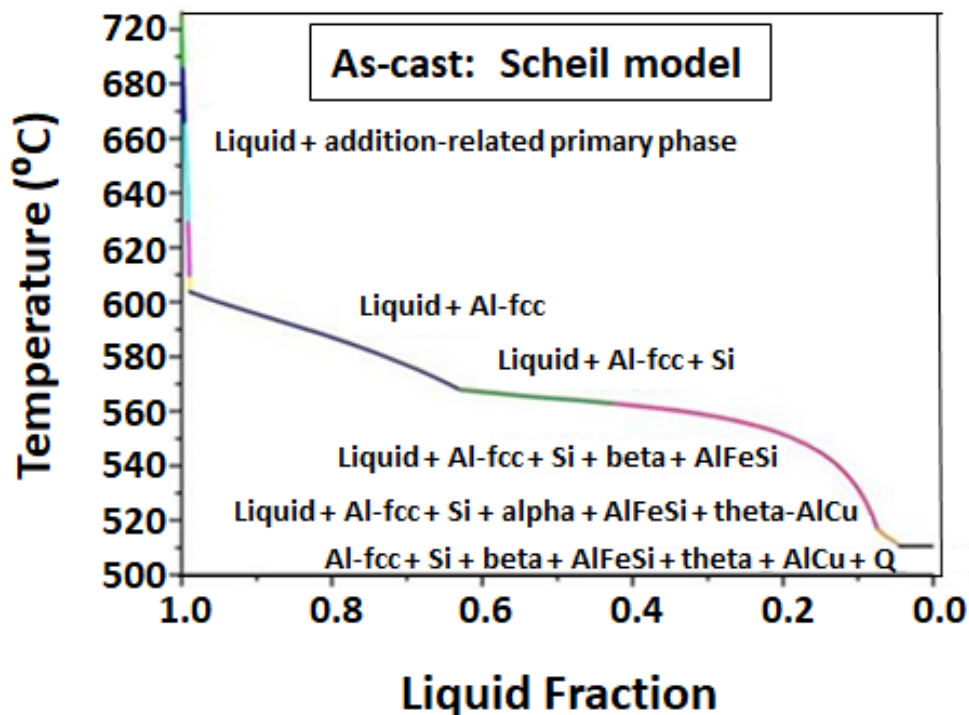
(c)

Figure I.1.B.7. Graphical representation of the cost of components calculated by the cost model of a 1.5L GTDI head made from (a) AS7GU-T65 and (b) Ford-SPMC-3stage; (c) the premium of GTDI heads made from Ford-SPMC-3stage over AS7GU-T64 showing the new alloys do not exceed 110% of the cost using incumbent alloys. Source: Ford Motor Company.

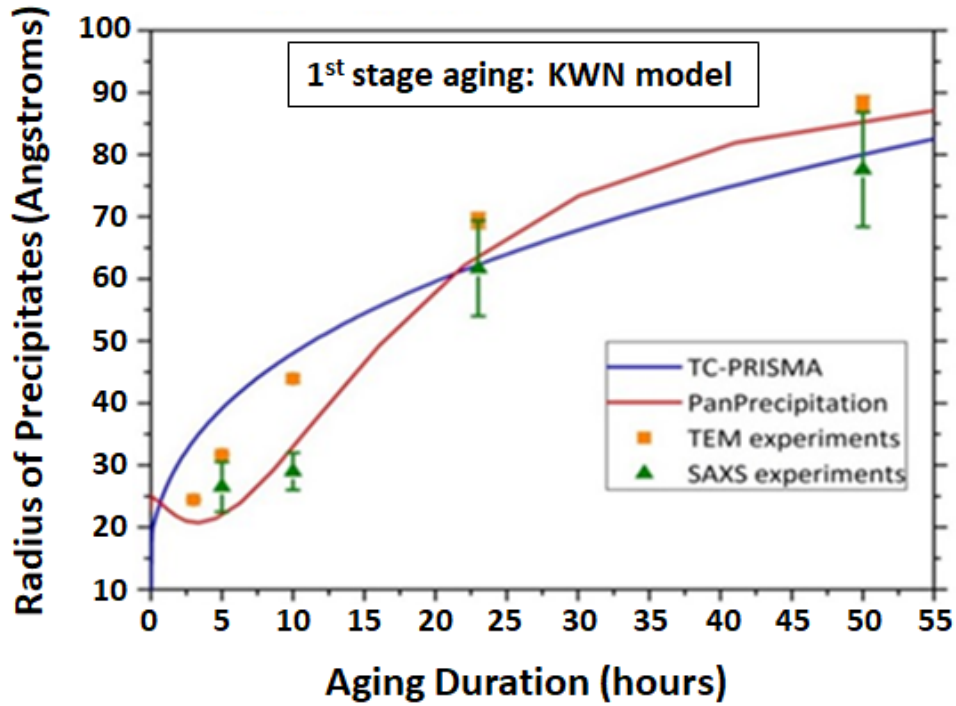
The basic design philosophy of Ford-SPMC-3stage and Ford-HPDC-T5 is to add transition metal (TM) elements, which can improve high-temperature performance for Al alloys [3-6], into conventional Al-Si-Cu-Mg alloys that have excellent low-temperature strength contributed from Cu/Mg-containing precipitates [7]. The performance of these designed alloys highly depends on the microstructures related to the addition of TMs and Cu/Mg. Several ICME tools utilized to provide insights of microstructural evolution during heat-treatments are summarized below and the gaps between simulation and experiments are also identified.

The Scheil solidification model was used to simulate the solidification pathway of Ford-SPMC, which is available in both Thermo-Calc and Pandat™. The Scheil simulation, shown in Figure I.1.B.8.(a) indicates that the solidification pathway is via TM-containing primary precipitates → face centered cubic-Al matrix → Al-Si eutectic → beta-Al₁₉Fe₂Si₂ → theta-Al₂Cu → Q-AlMgSiCu. This result shows good agreement with SEM observation. The quantitative results from the Scheil model, however, show inconsistencies with the differential scanning calorimetry (DSC) results. First, the transformation temperatures in the Scheil model do not agree with the DSC measurements. Then, the fractions of phases predicted by the Scheil model are not related to solidification rates. However, DSC measurements show that the fractions of phases, especially the theta-Al₂Cu phase, change with solidification. A robust model, which takes solidification rates into account, is in demand.

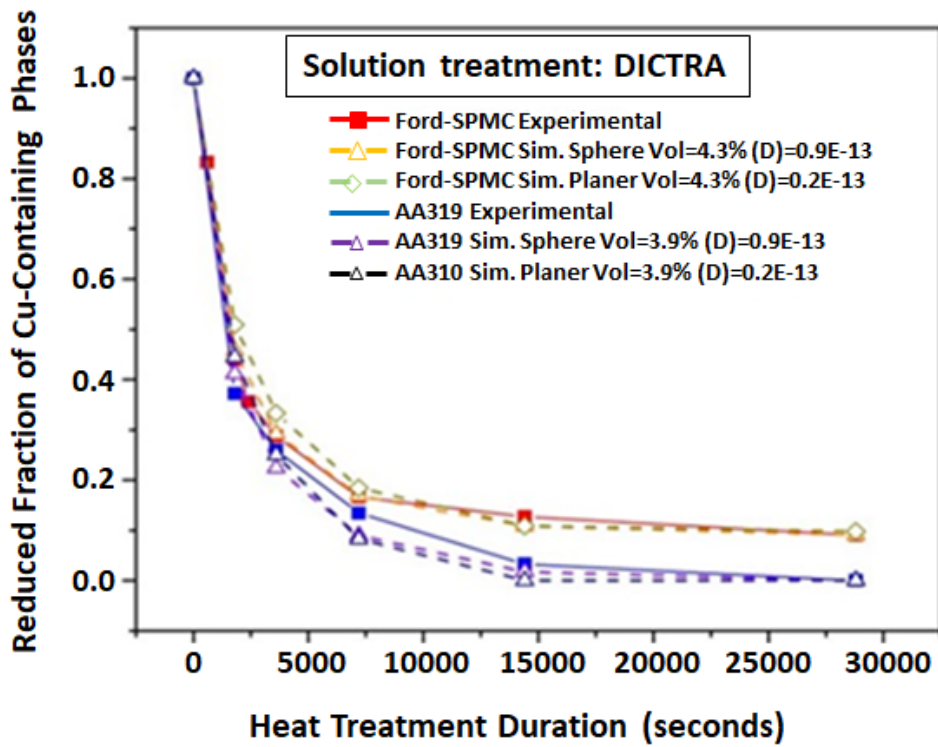
First stage aging to form spherical-shaped TMs containing precipitates was simulated by two different ICME tools, using the KWN method [8]: TC-PRISMA with the TCAL5 and MOBA13 databases and PanPrecipitation with the PanAl-TH+MO-2017 database. Experimental data, such as precipitate size and number density of Zr-containing precipitates, were obtained from TEM and small-angle x-ray scatter. Through optimization of the kinetic database, the simulation results show good agreement with the experimental results, as shown in Figure I.1.B.8.(b).



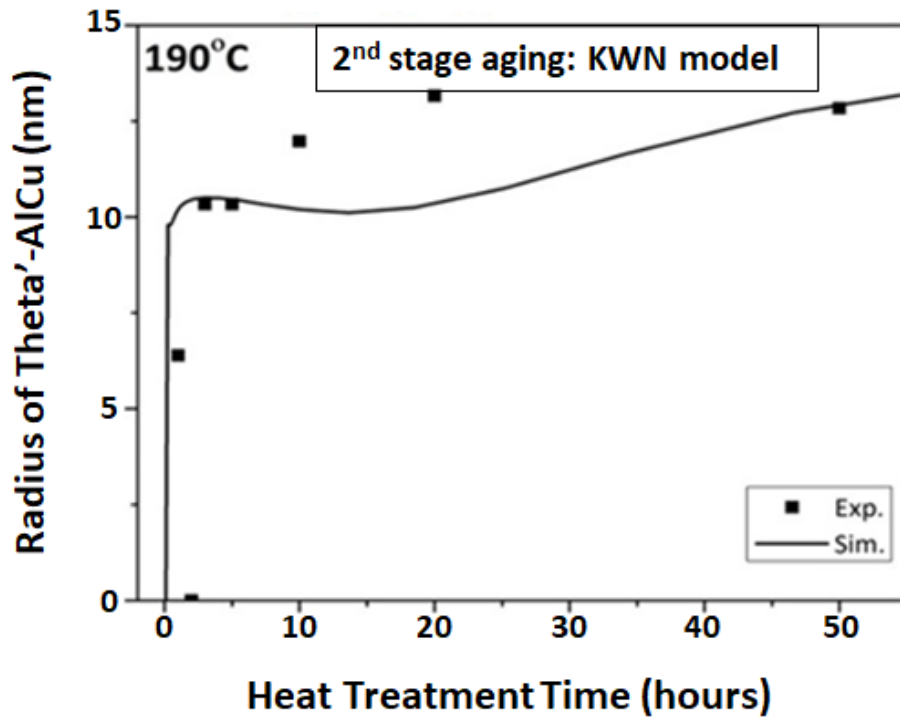
(a)



(b)



(c)



(d)

Figure I.1.B.8. Graphical representation of the comparison between experiments and ICME simulations: (a) solidification; (b) first stage aging; (c) solution treatment; and (d) second-stage aging, showing the capability and gap for ICME tools. Source: Ford Motor Company.

Solution treatment at 495°C to dissolve Cu-containing phases for Ford-SPMC and AA319 was studied. DSC were used to collect experimental data. Both the Ford-SPMC and AA319 were solutionized at 495°C for different durations and followed by quenching, and then measured by DSC. The fractions of Cu/Mg-containing phases decrease with a corresponding increase in solution treatment time. Due to the lack of some important information, such as latent heat and formula of phase transformation, the fraction of Cu/Mg-containing phases cannot be obtained directly from DSC results. A reduced fraction is proposed here, which is the ratio of Cu/Mg-containing phases in samples after solution treatment to that in an as-cast sample, based on two assumptions: (1) solution treatment only dissolves Cu-containing phases, but does not affect other phases and (2) formula of melting of Cu/Mg-containing phases are fixed. The reduced fraction can be expressed as:

$$\frac{f_{n=0.5,1,2,4,8}}{f_{n=0}} = \frac{1 - Area_{n=0.5,1,2,4,8}^{theta/Q}}{1 - Area_{n=0}^{theta/Q}} \times \frac{Area_{n=0}^{theta/Q}}{Area_{n=0.5,1,2,4,8}^{theta/Q}} \quad (1)$$

Simulation of the solution treatment was performed in DICTRA using the TCAL5 thermodynamic database and the MOBAl3 mobility database. Four geometries were considered: planer, cylinder, sphere-1, and sphere-2. The initial conditions of the fraction of Cu/Mg-containing phases were obtained from Scheil prediction and density measurement by the Archimedes method. With the modification of diffusivity, the simulated results from planer and sphere-2 show good agreement with the DSC results, as shown in Figure I.1.B.8.(c). However, gaps still exist: (1) Zr and vanadium cannot be included; and (2) a more reasonable geometry is needed.

The second-stage aging to form plate-like Al₂Cu precipitates were also simulated by the KWN model, which is a one-dimension model that can only simulate spherical shape precipitates. As such, an equivalent sphere radius (r_{eq}) was assumed for plate-shape precipitates using Equation (2):

$$r_{eq} = \sqrt[3]{\frac{3}{4} dia^2 * thickness} \quad (2)$$

The precipitation kinetics of Al₂Cu precipitates in AA319 alloys at several temperatures were characterized and published by Ford [9]. The PanPrecipitation simulated results, compared with experimental data, are shown in Figure I.1.B.8.(d). It's shown that the KWN model does not work well for plate-shape precipitates. The phase-field model is a better choice for plate-shape precipitates simulation.

Conclusions

The following five conclusions can be drawn:

1. Two Al alloys and heat-treatment combinations—Ford Semi-Permanent Mold Cast with novel three-stage heat-treatment and Ford High-Pressure Die-Cast with T5 heat-treatment—were developed, which are applicable for cylinder head and engine block application, respectively.
2. The torpedo samples prepared at Ford laboratory for the Ford-SPMC-3stage and Ford-HPDC-T5 met all of the requirements proposed by DOE and showed superior properties over baseline alloys. The 150°C HCF strength of the Ford-SPMC-3stage and Ford-HPDC-T5 is above 90 MPa, which is much higher than the strength of the AS7GU-T64. To the knowledge of the authors, these two alloys have the best HCF performance at elevated temperatures (>150°C) than any of the Al alloys intended for engine applications.
3. The performance of Ford-SPMC-3stage and Ford-HPDC-T5 were demonstrated on the component level through three prototyping plans: (1) the 1.5L GTDI cylinder head project at Qin'an, China, demonstrated that the deck face from the Ford-SPMC-w/oSr-3stage has great high-temperature performance, and both tensile and endurance testing showed that the deck face from Ford-SPMC-w/oSr-3stage have superior properties over torpedo samples; on the other hand, the performance of Ford-HPDC-T5 was limited by the processes of high-pressure die-cast and the properties cannot achieve that of the torpedo samples, demonstrated by (2) 2.0L GTDI Duratec Bearing-Beam program at Jackson, MI; and (3) the Ryobi single-cap castings program in Japan. The component level demonstration provides us opportunities to collaborate internally to redesign engines with higher performance by less weight.
4. Several existing ICME tools, mainly including Thermo-Calc, Pandat, and MagmaSoft, were evaluated and used in this project to provide guidance in alloys and heat-treatments design, and casting process optimization. Although some gaps between simulation and experiment still exist, the whole processes, from initial alloys design to component level demonstration, is significantly shorten to 5 years, and lots of cost saving opportunities is realized.
5. According to the comprehensive cost model develop internally, the total premium for a 1.5L GTDI heads from Ford-SPMC-3stage is 10.5% over the AS7GU-T64. This is within the DOE target that the components manufactured with these new alloys do not exceed 110% of the cost using incumbent alloys.

Key Publications

1. Shi, Q., Huo, Y., Berman, T., Ghaffari, B., Li, M., and Allison, J., "Distribution of TM elements (Zr, V, Ti) in a 319-type Al alloy," submitted to *Scripta Materialia*.
2. Patent application, "Advanced Cast Al Alloys for Automotive Engine Application with Superior High-Temperature Properties," filed on July 28, 2017.

References

1. Shaha, S. K., Czerwinski, F., Kasprzak, W., Friedman, J., and Chen, D. L., "Effect of Zr, V, and Ti on hot compression behavior of the Al-Si cast alloy for powertrain applications," *Journal of Alloys and Compounds*, Vol. 615, pp. 1019–1031, 2014.
2. Garat, M., "Casting made from Al alloy, having high hot creep and fatigue resistance," U.S. Patent No. 9982328, May 29, 2018.
3. Knipling, K. E., Dunand, D. C., and Seidman, D. N., "Criteria for developing castable, creep-resistant Al-based alloy: A review," *Z. Metallkd*, Vol. 97, pp. 246–266, 2006.
4. Seidman, D. N., Marquis, E. A., and Dunand, D. C., "Precipitation strengthening at ambient and elevated temperature of heat treatable Al(Sc) alloys," *Acta Mater.*, Vol. 50, pp. 4021–4035, 2002.
5. Zedalis, M. S., and Fine, M. E., "Precipitation and ostwald ripening in dilute Al base-Zr-V alloys," *Metall. Mater. Trans. A*, Vol. 17A, pp. 2187–2198, 1986.
6. Chen, Y. C., Fine, M. E., and Weertman, J. R., "Microstructural evolution and mechanical properties of Rapid solidified Al-Zr-V alloys at high temperatures," *Acta Metall. Mater.*, Vol. 38, pp. 771–780, 1990.
7. Javidani, M., and Larouche, D., "Application of cast Al-Si alloys in internal combustion engine components," *Int. Mater. Rev.*, Vol. 59, pp. 132–158, 2014.
8. Wagner, R. and Kampmann, R. "Homogeneous Second Phase Precipitation," In: Haasen, P, editor. *Materials Science and Technology: A Comprehensive Treatment*. Weinheim: Wiley-VCH, 1991. p. 213.
9. Weakly-Bollin, S. C., Donlon, W., Wolverson, C., Jones, J. W., and Allison, J. E., "Modeling the age-hardening behavior of Al-Si-Cu alloys," *Metall. Mater. Trans. A*, Vol. 35A, pp. 2407–2418, 2004.

I.1.C Computational Design and Development of a New, Lightweight Cast Alloy for Advanced Cylinder Heads in High-Efficiency, LD Engines (General Motors)

Mike J. Walker, Principal Investigator

General Motors Research and Development Center
30470 Harley Earl Blvd.
Warren, MI 48090-9055
E-mail: mike.j.walker@gm.com

Qigui Wang, Principal Investigator

General Motors Global Propulsion Systems
800 North Glenwood Ave.
Pontiac, MI 48340-2925
E-mail: qigui.wang@gm.com

Jerry L. Gibbs, DOE Technology Manager

U.S. Department of Energy
E-mail: jerry.gibbs@ee.doe.gov

Start Date: February 1, 2013
Project Funding: \$4,033,567

End Date: June 30, 2018
DOE share: \$2,742,826

Non-DOE share: \$1,290,741

Project Introduction

The U.S. Department of Energy–Energy Efficiency and Renewable Energy (DOE-EERE) program is targeting a 25% lighter powertrain by 2025 and a 40% lighter powertrain by 2050. As a result, the engine power density will be increased significantly. This will result in higher exhaust temperatures and a doubling of cylinder peak pressures by 2050. To meet these requirements and achieve the stated goals, the properties of the state-of-the-art materials, like cast Al alloys, must increase substantially. Today, methods such as ICME and advanced experimental analytical tools such as the Focused Ion Beam Microscope (FIB), High-Resolution Scanning Transmission Electron Microscope (HR-STEM), and Local Electrode Atom Probe (LEAP) are now available to accelerate the timeframe usually required to develop new alloys. Combining ICME tools with expert knowledge from the field and judicious experiments for verification and validation is the quickest and most effective way to achieve the goals of developing a new high-temperature capable Al alloy for cylinder head production.

Objectives

The primary objective of this project is to develop an alloy capable of handling the higher temperatures and pressures utilized in the smaller, more efficient engines with a material and production cost penalty of no more than 10% above current production alloys and production methods. Room-temperature (RT) tensile strength is to exceed current baseline Al alloys by 25%, while 300°C tensile strength is to exceed 250°C strength by 25%. The project will utilize state-of-the-art computational methods for development, and by experimental validation, will assess the true capabilities of these methods and establish gaps that should be filled in the future to accelerate alloy development.

Approach

This collaborative project between General Motors, LLC (GM), QuesTek Innovations, LLC (QT), Northwestern University (NU), Camano Associates, the American Foundry Society (AFS), and Dr. Fred Major (an expert in casting processing and Al alloys) is to use ICME tools, expert knowledge, and experimental validation to identify coarsening resistant precipitate structures in the alloy to meet the high-temperature requirements. QT's proprietary Integrated Computational Materials Design (iCMD®) platform is a core modeling software system that integrates proprietary and commercial mechanistic modeling tools to facilitate rapid design and the development of new materials. NU has advanced microstructure characterization equipment and facilities such as transmission electron microscope, atom probe, and DSC, in addition to software for phase property calculations, phase-field modeling, and ICME methodologies and tools.

As a world manufacturer of automobiles, GM has vast knowledge in the design and manufacture of engines and cylinder heads. In addition to its casting experience, GM utilizes many computational methods for engine design and manufacture. GM's Virtual Cast Component Development (VCCD) system interfaces with commercial software such as MagmaSoft®, FLOW-3D®, ABAQUS, FE-safe, Pandat, iSIGHT, and UGNX to integrate manufacturing processes with component design to produce reliable and high-quality cast structural components with minimum lead time and cost.

AFS and Dr. Fred Major are long-time experts in casting processing and Al alloys. Thus, the strong collaboration will utilize state-of-the-art ICME tools, such as first-principles calculations, computational thermodynamic and kinetic models, virtual casting modules, and commercially available casting process simulation and structural and durability analysis software to design a new, lightweight cast alloy with ideal multiscale microstructures and minimum tendency for casting defects to achieve the desired high-temperature strength and fatigue performance requirements in complex castings.

Results

Comparison of Developed Cast Alloy Properties to DOE Targets

A comparison of DOE targets for the Cast Lightweight Alloy Project is made to a common production alloy (Alloy 1), as well as the newly developed strengthened Q-phase alloys. This program carried out two cylinder head casting trials and the alloys' chemistries and designations are identified in Table I.1.C.1. Alloy 1 is basically an A356.1 alloy with 0.5 wt% Cu added. Alloy 2 Trial 1 increases the amount of Q-phase by adding additional Cu and Mg. It also adds Si and Ni, which has been shown to increase higher temperature properties, as well as Zr and V, which have been shown to segregate to and stabilize the Q-phase. Alloy 1 is used again in Trial 2 as the baseline comparison. Alloy 2 Trial 2 again increases the Cu and Mg contents to increase the amount of Q-phase, but adds the Q-phase stabilizing elements Zr and V. Because of the low ductility seen in Alloy 2 Trial 1, however, Si was not increased, and Ni was not added.

The material property comparisons to the DOE targets were based on combustion chamber and deckface samples of cylinder head castings. These regions were chosen for this comparison because these are the most critical areas of the head for ductility and high-temperature properties. These regions are cast next to the water-cooled steel tooling for the lowest secondary dendrite arm spacing (SDAS) and the highest ductility. Tensile property measurements made above 200°C were only performed in the combustion chambers and deckface regions because it is only in these locations that such temperatures exist in an engine. Samples were also extracted from other regions, such as high-pressure oil galleries and head bolt bosses. These regions are isolated from the chilled surfaces and are surrounded by sand cores. In these regions, SDAS is larger, porosity is typically greater, and ductility is typically lower. Material property comparisons to targets in these slower cooled regions will also be highlighted. Material tensile strength and fatigue properties measured above 150°C were first preconditioned at the test temperature for 100 hours. Preconditioning coarsens precipitate structures and lowers material properties.

Table I.1.C.1. A Comparison of Measured Alloy Properties to DOE Targets for a Common Production Alloy (Alloy 1) and for the Strengthened Q-Phase Alloys (Alloy 2 Trial 1 and Alloy 2 Trial 2).

Property	DOE Cast Lightweight Alloy Target	Alloy 1 Trial 1/2		Alloy 2 Trial 1	Alloy 2 Trial 2
Tensile Strength @ RT (MPa)	276	313	311	323	321
YS @ RT (MPa)	207	251	260	275	265
Density (g/cc)	<6.4	2.7		2.7	2.7
Elongation (%)	3.5	6.2	6.1	2.3	4.5
Fatigue Strength @ 10 ⁷ Cycles (MPa)	75	65	80	90	69
Fatigue Strength @ 10 ⁴ Cycles (MPa)	No Target	N/A	218	N/A	228
Castability (Fluidity and Hot Tearing Resistance)	Excellent	Excellent		Excellent	Excellent
Tensile Strength@300°C, 100 hours (MPa)	65	42	42	56	52
YS @ 300°C, 100 hours (MPa)	45	40	40	49	45
Elongation @ 300°C, 100 hours	<20%	28	44	9	37

Tensile Properties

A plot of Alloy 2 Trial 2 tensile properties in the combustion chamber and deckface regions with a comparison to the targets are shown in Figure I.1.C.1. At RT, both alloys were able to achieve the DOE targets. Q-phase-based alloys (Alloys 1 and 2) provide RT strengths well above those of an A356 alloy. The ductility of Q-phase-based alloys is better than the Theta-Q alloys, such as B319 achieving the RT DOE ductility target. The increase in intermetallics by the addition of additional Cu and the minor elements in Alloy 2 resulted in slightly lower ductility compared to Alloy 1.

At 300°C, the strengthened Q-phase alloy achieved the YS target while the production alloy did not. Neither alloy was able to achieve the UTS targets or a total elongation target of less than 20%. With regards to both the total elongation and UTS targets at 300°C, any significant yielding of the material will result in engine distortion and would be unacceptable. As the greatest stresses and temperatures are in the bridge areas between valves, head distortion could cause valve seat distortion resulting in poor valve seating/sealing, loss of compression, lower power, and higher emissions.

Of greater concern is the lack of improvement of strength properties in the mid-temperature range of 200°C and 250°C. Although the minor elements Zr and V have stabilized the Q-phase and produced an increase in tensile strength at 300°C, property improvement at these midrange temperatures is insignificant.

Tensile properties for the bolt boss and high-pressure oil line (HPOL) regions at RT are shown in Table I.1.C.2 and Table I.1.C.3. HPOLs are surrounded by sand and have poor directional solidification from the deckface to the risers. This results in increased porosity and larger intermetallic structures that are detrimental to the ductility. Fracture analysis was carried out on the HPOL samples to determine the main cause of failure.

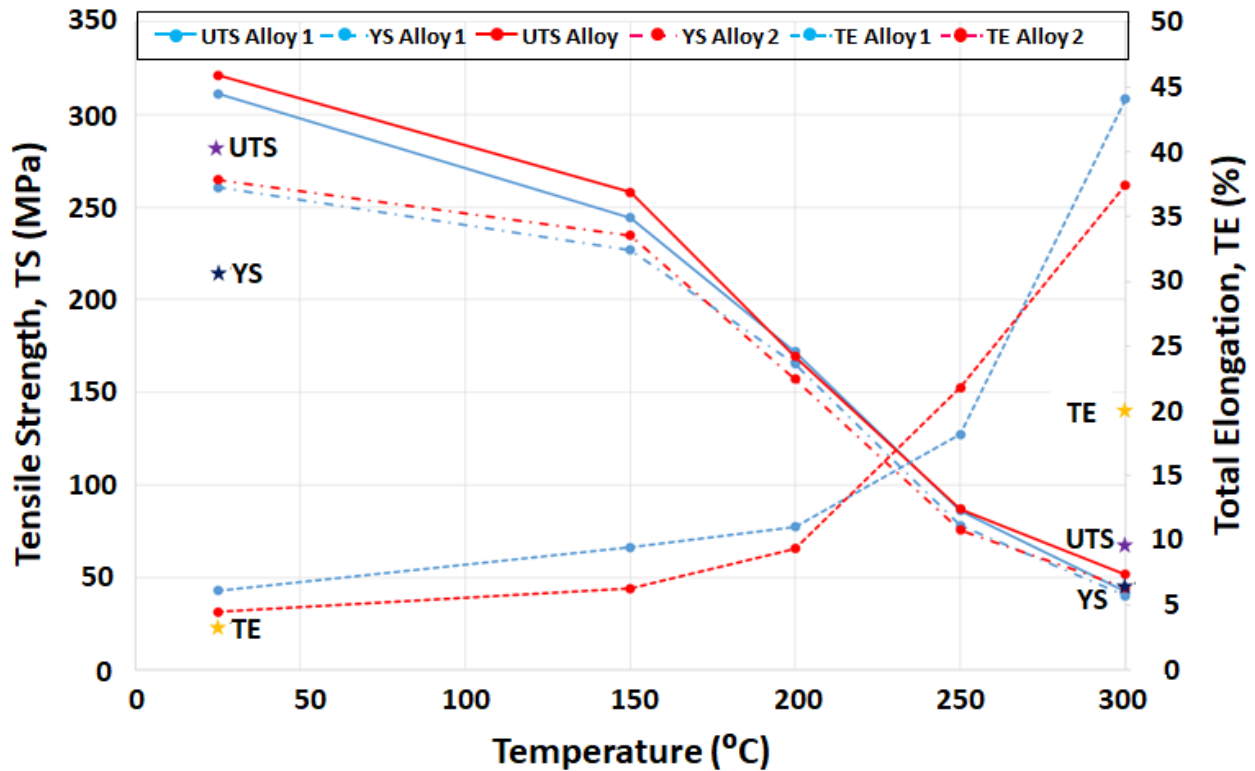


Figure I.1.C.1. Tensile properties of a baseline A356 0.5%Cu alloy (Alloy 1 Trial 2) and the developed alloy (Alloy 2 Trial 2) with comparison to DOE targets identified by colored stars. Tensile specimens were extracted from the deckface and combustion chambers. Samples tested above 150 °C were conditioned for 100 hours at test temperature before testing. Source: GM.

Table I.1.C.2. RT Tensile Properties in Bolt Boss Regions in Engine Cylinder Heads of a Baseline Alloy (Alloy 1 Trial 2) and the Developed Alloy (Alloy 2 Trial 2) in Comparison to DOE Targets.

	DOE Targets	Alloy 1 Trial 2	Alloy 2 Trial 2
Tensile Strength (MPa)	276	302	303
YS (MPa)	207	253	261
Total Elongation (%)	3.5	4.6	2.2

Table I.1.C.3. RT Tensile Properties in HPOL Regions in Engine Cylinder Heads of a Baseline Alloy (Alloy 1 Trial 2) and the Developed Alloy (Alloy 2 Trial 2) in Comparison to DOE Targets.

	DOE Targets	Alloy 1 Trial 2	Alloy 2 Trial 2
Tensile Strength (MPa)	276	276	267
YS (MPa)	207	253	252
Total Elongation (%)	3.5	1.2	0.8

Elastic Modulus

The elastic modulus was measured for each of the tensile specimens. All samples at each temperature were averaged together. The results are shown in Table I.1.C.4. Samples tested above 150°C were all conditioned for 100 hours at temperature. Results are similar to A356 and A356+0.5Cu.

Table I.1.C.4. Measured Elastic Modulus of Alloy 2 Specimens Tested Above 150 °C and Conditioned for 100 Hours at Temperature.

Temperature °C	Average Elastic Modulus (GPa)	Number of Samples
25	72	26
150	62	26
200	55	26
250	37	9
300	27	9

Fracture Analysis of HPOL Tensile Specimens

The HPOLs were selected for fracture analysis because both the baseline alloy (Alloy 1 Trial 2) and the newly developed alloy (Alloy 2 Trial 2) showed very poor ductility at RT. Furthermore, UTSs dropped significantly compared to both the bolt boss and the deckface specimens. The YSs were comparable, which suggests that the UTSs were limited by the significant number of defects that led to premature failure.

The reduced ductility can be attributed to two aspects in the material for a given heat-treatment condition. One is the increased volume fraction of intermetallic phases as observed in the first casting trial study. The other reason is the porosity. Porosity is commonly known as the most important factor affecting the tensile ductility of cast Al alloys. Pores are stress risers and act as crack initiators. Along with other cracked Si intermetallic particles, porosity provides weak paths for crack propagation. In general, the area fraction of porosity observed on the fracture surfaces can be more than ten times higher than the volumetric fraction of porosity in the bulk material, indicating that the porosity is the weak link for crack initiation and propagation. Figure I.1.C.2 shows the relationships between ductility and the area fraction of porosity observed on the fracture surfaces of the tensile samples of three alloys. In general, ductility decreases with the increase of porosity observed on the fracture surfaces, particularly for the baseline alloy (Alloy 1). For Alloy 2, it appears that the increased volume fraction of intermetallic phases has notably reduced the sensitivity of ductility with porosity.

The size and volume fraction of porosity in Al castings is strongly related to alloy composition, melt treatment, and particularly, the casting process. For a given casting process and melting practice, a small variation of alloying elements can play a role in porosity as they affect castability of the material including freezing range, fluidity, feeding capability, hot tearing, etc. In our trial #2 casting study, however, the overall porosity observed in the HPOL tensile samples between Alloy 1 and Alloy 2 is comparable partly due to the very small alloy composition change and partly due to the limitation of the current head casting process and sampling location. The alloy composition is contributing to the higher tensile strength. In the HPOL tensile samples tested and characterized, the average area fraction and one standard deviation of porosity observed on the fracture surfaces is 3.43%±1.83% and 3.75%±1.3% for Alloy 1 and Alloy 2, respectively. Similar observations are also made in pore sizes in the HPOL tensile samples for both alloys, as shown in Figure I.1.C.3.

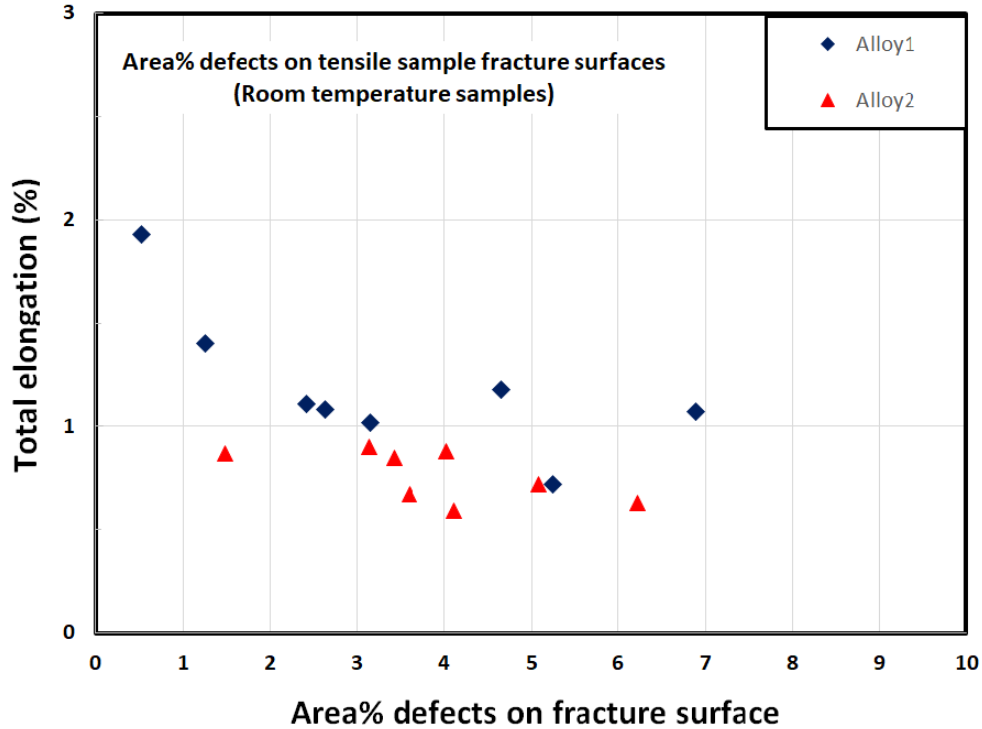


Figure I.1.C.2. The relationship between tensile ductility (total elongation) and area fraction of porosity on the tensile fracture surfaces of two alloys at RT. Source: GM.

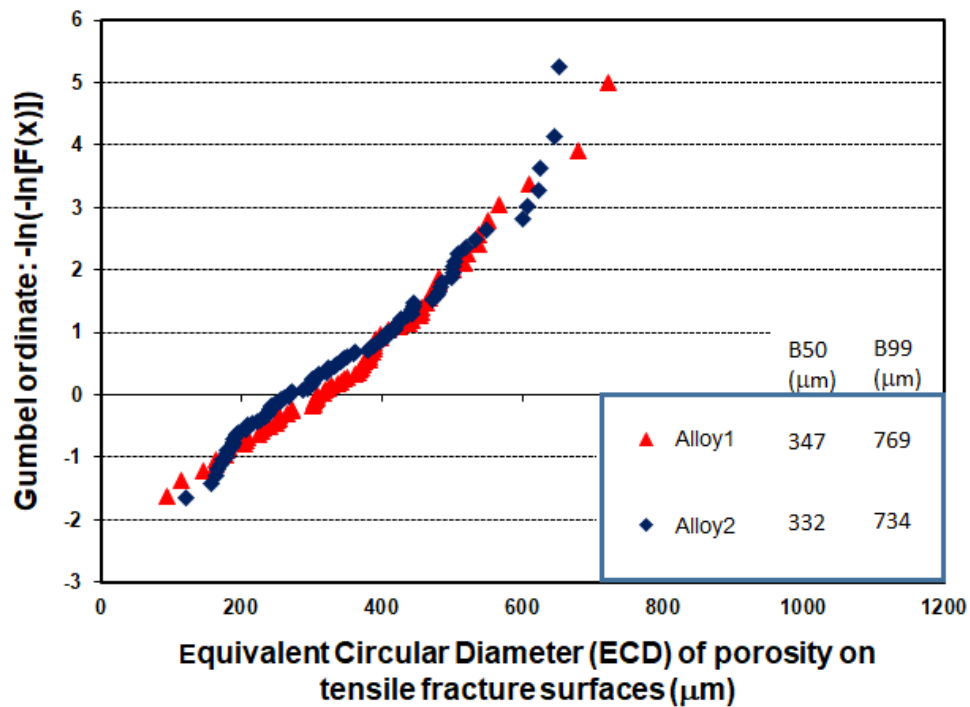


Figure I.1.C.3. A comparison of defect sizes observed in the tensile fracture surfaces of samples taken from HPOL locations of engine heads made of both Alloy 1 Trial 2 and Alloy 2 Trial 2 and tested at RT. Source: GM.

HCF Strength

In Table I.1.C.1, it was shown that the HCF strength of the newly developed Alloy 2 Trial 1 exceeded the DOE target of 75 MPa; however, Alloy 2 Trial 2 did not achieve the target. It must be recognized that fatigue results are subject to considerable variability from one test to another. Furthermore, because HCF is controlled by defects such as porosity or oxides in Al alloys, the HCF strength is determined more by the casting process, hydrogen degassing, and metal cleanliness than the alloy composition. Table I.1.C.5 shows the measured HCF strength measured in two alloys in two casting trials. Beginning with Trial 1, Alloy 2 Trial 1 showed very promising HCF results in the deckface, combustion chamber, and bolt boss regions as compared to the baseline alloy. However, the addition of the alloying components will increase eutectic Si, Q-phase precipitates, and other intermetallics. The tensile strengths of Alloy 2 Trial 1 are not significantly improved over the baseline alloy and the ductility of these alloys are worse than the baseline. Therefore, the HCF strength should not be improved based on the alloying additions and is more likely based on improved degassing or a change in the oxide distribution. For the second head casting trial in the combustion region, the Alloy 2 Trial 2 properties were worse than those for Alloy 1 Trial 2 in general. However, in the bolt boss and HPOL regions, the Alloy 2 Trial 2 properties were better than those for Alloy 1 Trial 2, and for the bolt boss regions nearly met the DOE target. In summary, what can be concluded is that the HCF strength of the developed alloys are not significantly different from the baseline alloy. HCF and low-cycle fatigue (LCF) (10^4 cycles) strengths are the most critical material properties for cylinder head design. Unless a significant improvement in these properties can be shown in a new alloy or process, changes to the current bill of process or bill of materials will not be made. Further research is needed to improve the casting processes to produce engine cylinder heads before the improved high-temperature properties of the alloys can be utilized.

Table I.1.C.5. HCF Strength (10^7 Cycles) of Cylinder Head Casting Samples from Two Casting Trials.

Region	Test Temperature (°C)	HCF Strength (MPa)			
		Trial 1		Trial 2	
		Alloy 1	Alloy 2	Alloy 1	Alloy 2
Deckface and Combustion Chamber	25	65.5	90.3	80.4	69.4
	150	63.6	76.2	78.5	56.5
	200	62.3	N/A	57.0	75.6
	250	48.7	52.7	48.9	47.1
Bolt Boss	25	N/A	N/A	73.7	73.7
	150	64.2	85.0	65.0	70.0
	200	N/A	N/A	62.5	63.7
	250	45.8	52.5	N/A	N/A
HPOL	25	71.2	70.5	43.5	60.2
	150	64.5	68.0	47.2	51.8
	200	N/A	N/A	46.7	40.7
	250	44.5	47.2	N/A	N/A

Fracture Analysis of HCF Samples for Trial 2

Fracture analysis of the fatigue samples for the second casting trial has been carried out. In general, fatigue failure was caused by defects (porosity) in the samples. Figure I.1.C.4 shows an example of a shrinkage-dominated pore that initiated the fatigue crack.

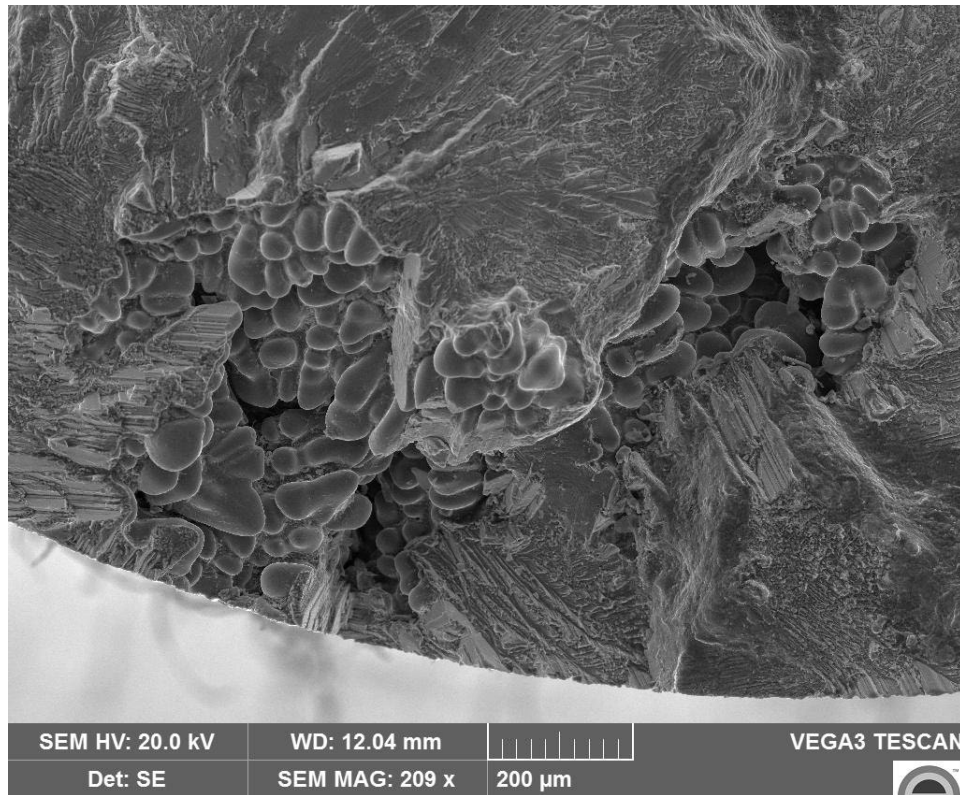


Figure I.1.C.4. SEM image showing a shrinkage-dominated pore that initiated fatigue crack and significantly reduce the fatigue life in an Alloy 1 deckface sample (740971 cycles at 74MPa, Equivalent Circular Diameter (ECD) of pore: 687μm).
Source: GM.

In the deckface and combustion chamber areas, the HCF strengths of Alloy 1 are slightly better than those of Alloy 2 except for the 200°C samples. This can be explained from the measured sizes of defects (porosity and oxides) that initiate cracks in the fatigue failure samples. As shown in Figure I.1.C.5, the average (B50) defect size is 137μm in Alloy 1 and 152μm in Alloy 2. For the 200°C samples, more samples were failed by large slip planes in Alloy 1, although the average defect size in Alloy 1 is slightly smaller than that for Alloy 2. Figure I.1.C.6 shows the large slip plane initiating the fatigue crack in one of the Alloy 1 samples.

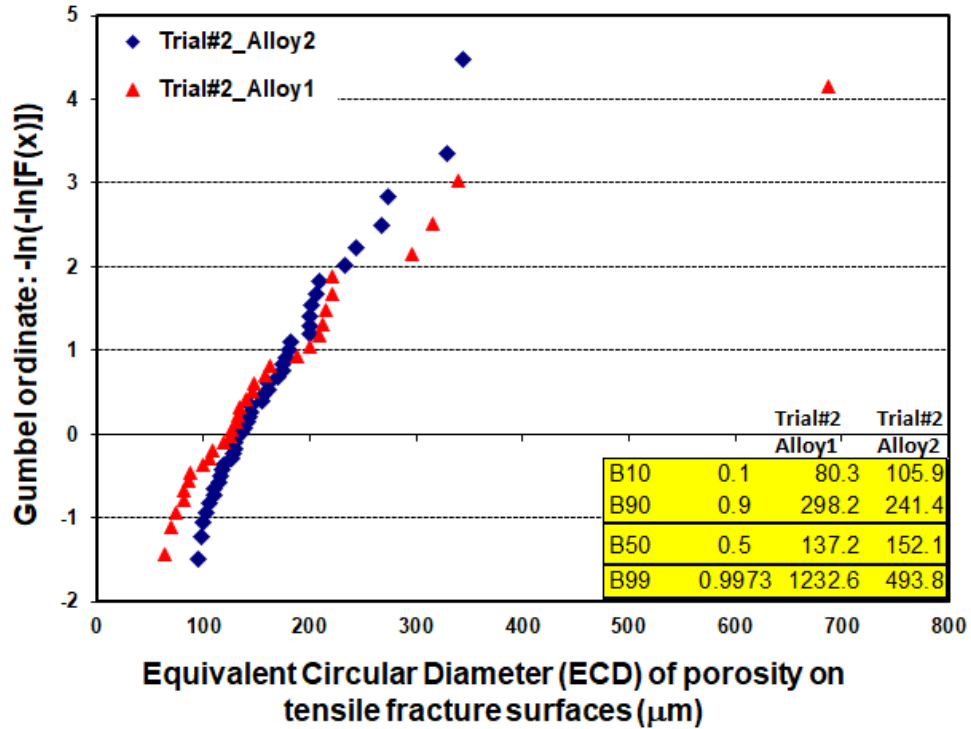


Figure I.1.C.5. A comparison of size distributions of defects that initiated fatigue cracks in the deckface and combustion chamber areas of engine heads made of both Alloy 1 and Alloy 2. Source: GM.

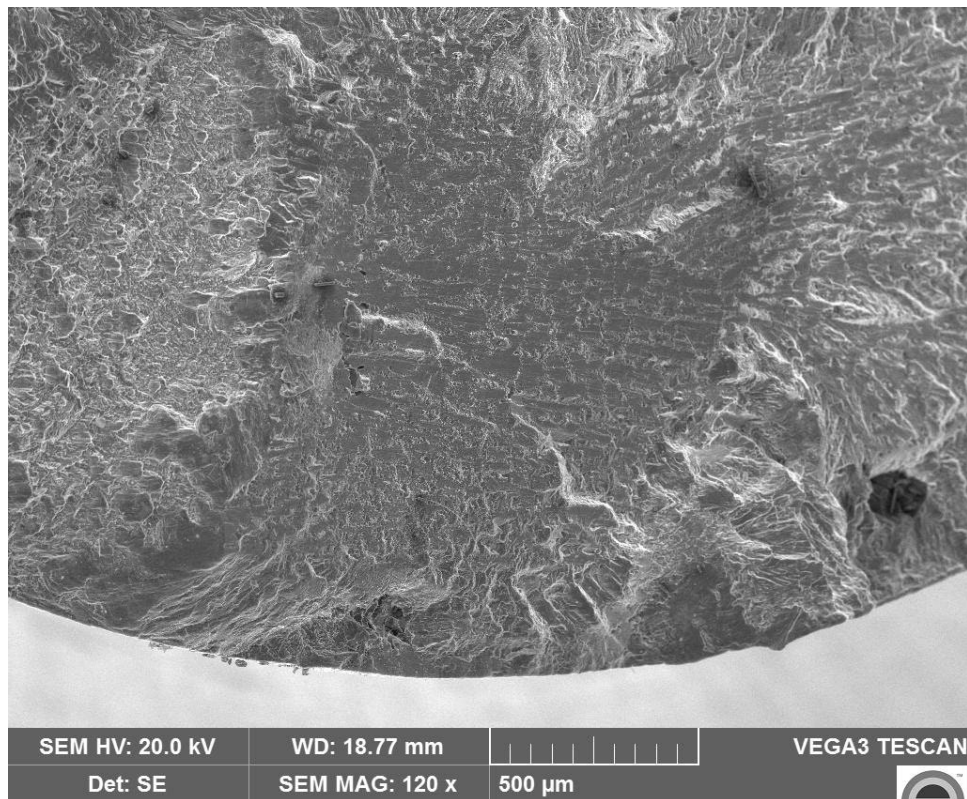


Figure I.1.C.6. SEM image showing a large slip plane that initiated fatigue crack in a deckface sample of Alloy 1. Source: GM.

In the bolt boss locations, the fatigue strengths are quite comparable between two alloys at all three temperatures tested. As expected, the average (B50) sizes of defects that initiated fatigue cracks are also very comparable (216 μm for Alloy 1 and 220 μm for Alloy 2) as shown in Figure I.1.C.7. Interestingly, it is noted that the scatter of defect sizes in Alloy 1 is larger than that for Alloy 2, which is similar to the results seen in the deckface and combustion chamber locations.

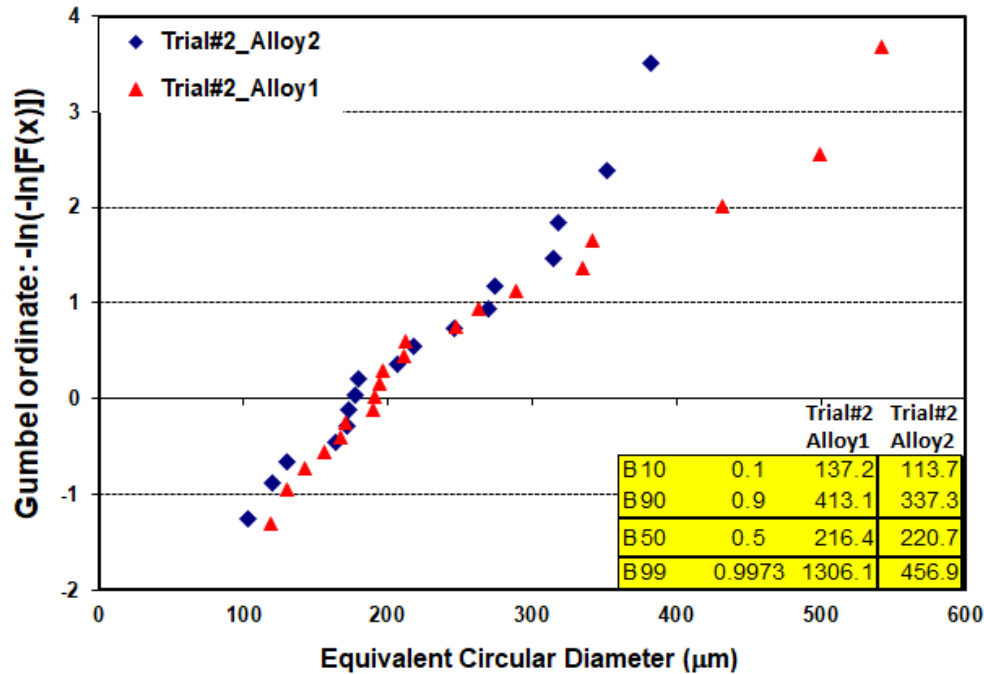


Figure I.1.C.7. A comparison of size distributions of defects that initiated fatigue cracks in the bolt boss areas of engine heads made of both Alloy 1 and Alloy 2. Source: GM.

In the HPOL areas, the fatigue strengths of Alloy 1 are generally lower than those of Alloy 2 at both RT and 150°C. At 200°C; however, the fatigue strength of Alloy 1 is higher than that for Alloy 2. Figure I.1.C.8 compares the defect sizes in all HPOL samples between both alloys. It is interesting to note that the defect sizes in Alloy 1 are generally smaller than those in Alloy 2 (B50: 355 μm for Alloy 1 and 424 μm for Alloy 2), which does not fully explain the lower fatigue strengths tested in Alloy 1 at both RT and 150°C. Based on the fractographic observations, it was found that many HPOL samples in Alloy 1 failed by large shear planes in addition to some small pores, as shown in Figure I.1.C.9. After including the shear planes in the crack initiators, shown in Figure I.1.C.10, the new “defect” sizes in Alloy 1 are larger than those in Alloy 2 (B50: 559 μm for Alloy 1 and 424 μm for Alloy 2). This indicates that large shear planes, probably due to columnar grain structure, can significantly reduce fatigue properties even though the defect sizes are small.

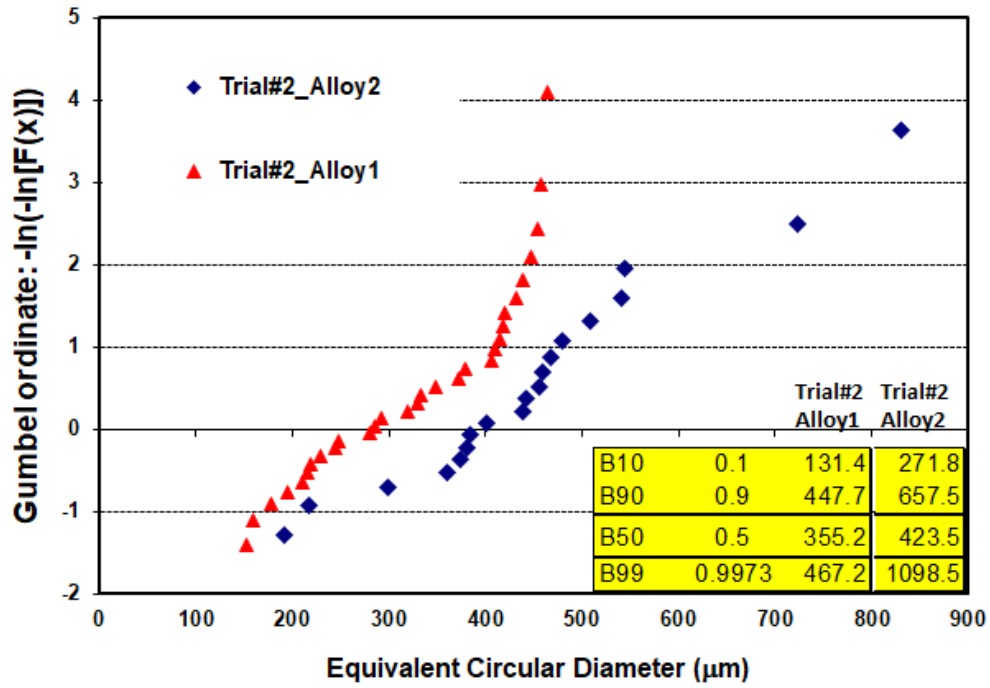


Figure I.1.C.8. A comparison of size distributions of defects that initiated fatigue cracks in the HPOL locations of engine heads made of both Alloy 1 and Alloy 2. Source: GM.

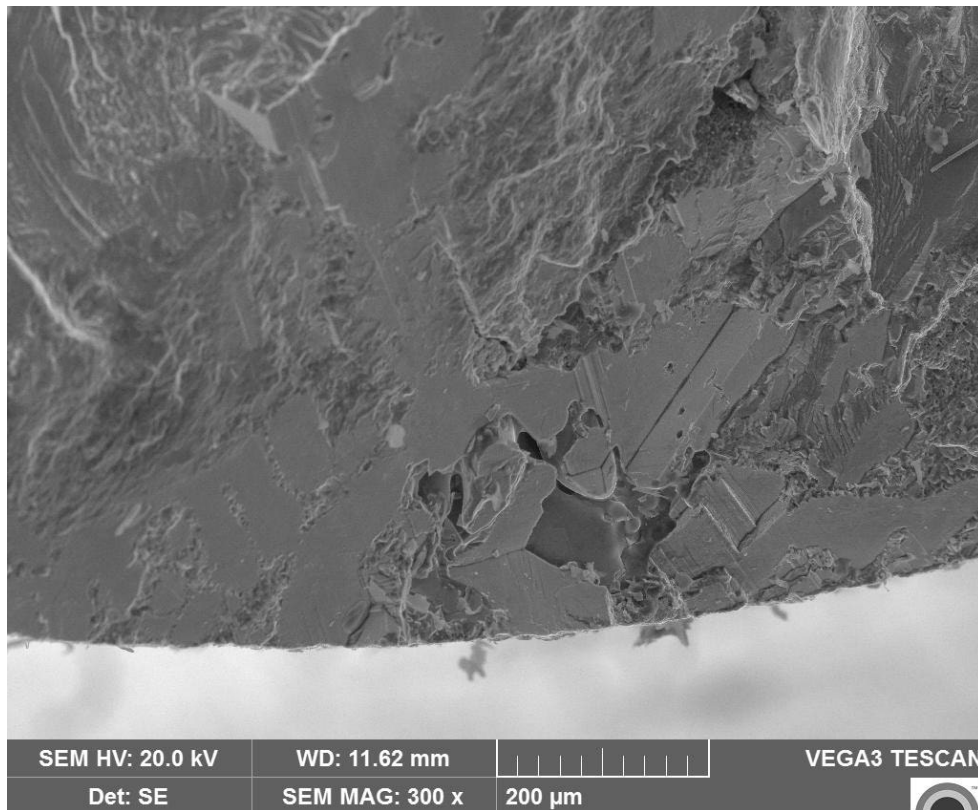


Figure I.1.C.9. SEM image showing a large slip plane together with porosity that initiated fatigue crack in the HPOL samples of Alloy 1. Source: GM.

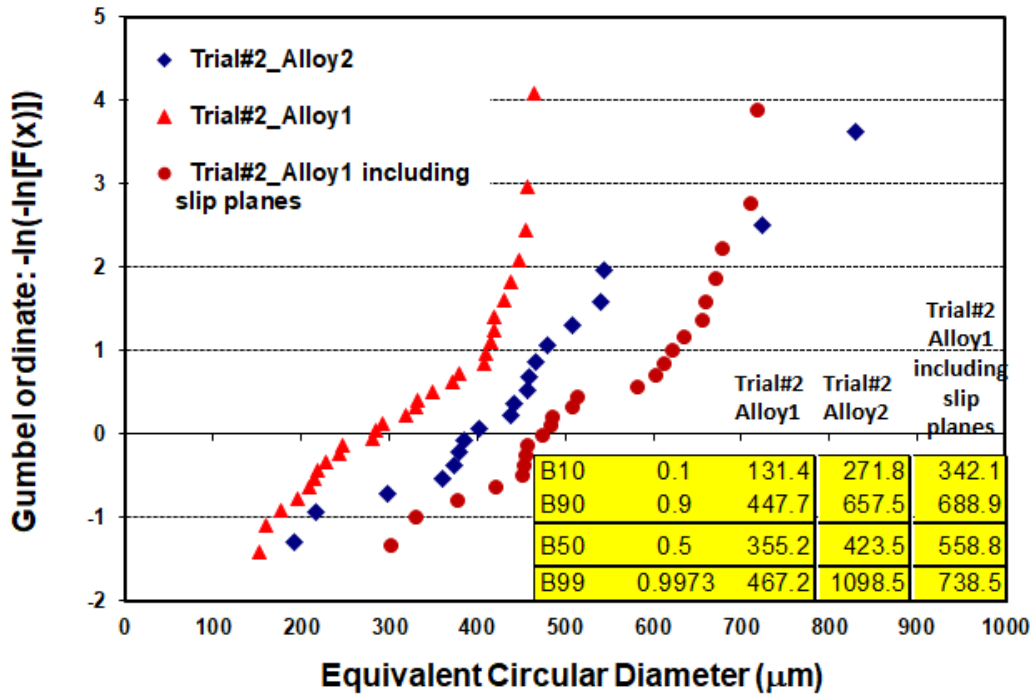


Figure I.1.C.10. A comparison of size distributions of defects and shear planes that initiated fatigue cracks in the HPOL locations of engine heads made of both Alloy 1 and Alloy 2. Source: GM.

LCF Strength

A summary of the LCF strength (10^4 cycles) is shown in Table I.1.C.6. The newly developed alloy (Alloy 2 Trial 1 and Alloy 2 Trial 2) has comparable LCF with the baseline alloy (Alloy 1). This again indicates that the fatigue properties of cast Al alloys are strongly dependent upon defect sizes in the materials and to a much less degree upon on alloy matrix tensile strength.

Table I.1.C.6. LCF Strength (10^4 Cycles) in Engine Cylinder Heads.

Region	Test Temperature (°C)	LCF Strength (MPa)			
		Trial 1		Trial 2	
		Alloy 1	Alloy 2	Alloy 1	Alloy 2
Deckface and Combustion Chamber	25	N/A		218	220
	150	200	200	200	195
	200	N/A		137	132
	250	70	79	73	73
Bolt Boss	150	200	200	159	159
	200	N/A		129	126
	250	78	73	N/A	
HPOL	150	167	166	165	159
	200	N/A		113	117
	250	70	71	N/A	

Hot-Tear Resistance and Castability

The hot tearing tendencies are indicated by cracking susceptibility coefficients. The cracking susceptibility coefficient (CSC) is defined as:

$$CSC = \frac{t_v}{t_R} \quad (1)$$

where t_v is the time during solidification in which the casting is “vulnerable” to cracking, and t_R is the time available for the stress relief process. Following Clyne et al. [1] and Yan et al. [2], t_R is defined as the time spent during solidification when the liquid volume fraction is between about 0.6 and 0.1 and t_v is the time spent when the liquid volume fraction is between 0.1 and 0.01. Both alloys have low hot tearing tendencies and Alloy 2 is comparable with the production alloy, Alloy 1. Therefore, with regards to hot-tear resistance, the new alloy is considered excellent.

Hot-tear resistance and fluidity can be lumped together into the term “castability” (i.e., the ability to fill and produce a good casting). Castability also includes shrinkage and is often defined by criteria related to the fraction solid curve and solidification range. Shrinkage may also be affected by minor elements that precipitate during solidification and impede fluid flow during solidification. Since heads were produced in this project, the best way to assess castability of the alloy is by x-ray of those heads. As shown in Table I.1.C.7, the castability of the newly developed alloy appears better than the baseline A356 +0.5%Cu. Because the base for Alloy 2 was Alloy 1, however, these improved results are more likely a result of process variations such as improved cleanliness or reduced oxides. Nevertheless, what can be concluded is that the newly developed alloy has excellent castability and is comparable to standard production alloys such as A356.

Table I.1.C.7. X-ray Analysis of Trial 2 Cylinder Head Castings.

	Alloy 1	Alloy 2
Number of Castings	35	49
Number of defects per 100 castings	43	6
Number of defect casting per 100 castings	31	6

Thermophysical Properties

Thermal-physical property measurements including thermal diffusivity, specific heat, and linear thermal expansion were made on 12 specimens of Alloy 2 Trial 2. From these measurements, and bulk density calculated on the sample volume and mass, thermal conductivity and coefficient of thermal expansion were also calculated. The specimens were extracted from the chain-guard region of twelve different heads after typical production heat-treatment. The specimens were divided into three groups. The first group was tested at RT, the second group was heated to 250°C for 200 hours, and the third group was heated to 300°C for 200 hours prior to testing. Thermal conductivity is an important physical property for engine cylinder heads because the heat of combustion needs to be extracted from the combustion chamber area to reduce the maximum temperature of the material in that area. An alloy with improved high-temperature capability may allow higher temperatures in the combustion chamber; however, if the thermal conductivity is significantly reduced compared to current alloys, such as A356, the rise in combustion chamber temperature may overwhelm the benefits of improved high-temperature tensile properties. Furthermore, increases in combustion chamber temperatures may also increase creep rates, which lead to distortion and potential reductions in engine efficiency and increased emissions. The measured specific heat and thermal conductivity of Alloy 2 Trial 2 is shown in Table I.1.C.8. Insignificant differences in specific heat with or without conditioning were seen, so only one table of values is shown. However, the thermal conductivity improves with preconditioning at 250°C or 300°C. The thermal conductivity is between the thermal conductivity of A356 and B319.

Table I.1.C.8. Continuation of X-ray Analysis of Trial 2 Cylinder Head Castings.

Temperature (°C)	Specific Heat (Ws/gK) 300 °C preconditioned	Thermal Conductivity (W/cmK) No preconditioning	Thermal Conductivity (W/cmK) 250 °C preconditioned	Thermal Conductivity (W/cmK) 300 °C preconditioned
23	0.8614	1.421975	1.588165	1.565083
50	0.877875	1.45356	1.616073	1.588333
75	0.892125	1.482165	1.638948	1.607433
100	0.90585	1.509313	1.659583	1.624825
125	0.9179	1.532235	1.676305	1.639305
150	0.9297	1.55568	1.6927	1.65357
175	0.940375	1.576333	1.70652	1.665785
200	0.9508	1.596615	1.717943	1.676948
225	0.960975	1.615608	1.72914	1.68802
250	0.971125	1.648868	1.737508	1.699038
300	0.9838	1.696538	1.74936	1.720568

The measured thermal expansion of Alloy 2 Trial 2 is shown in Figure I.1.C.11. Unconditioned samples experience added thermal expansion above about 250°C. This is a result of increased precipitation. Samples preconditioned at either 250°C or 300°C do not experience this change because all of the precipitates would have come out of solution at elevated temperatures during the preconditioning.

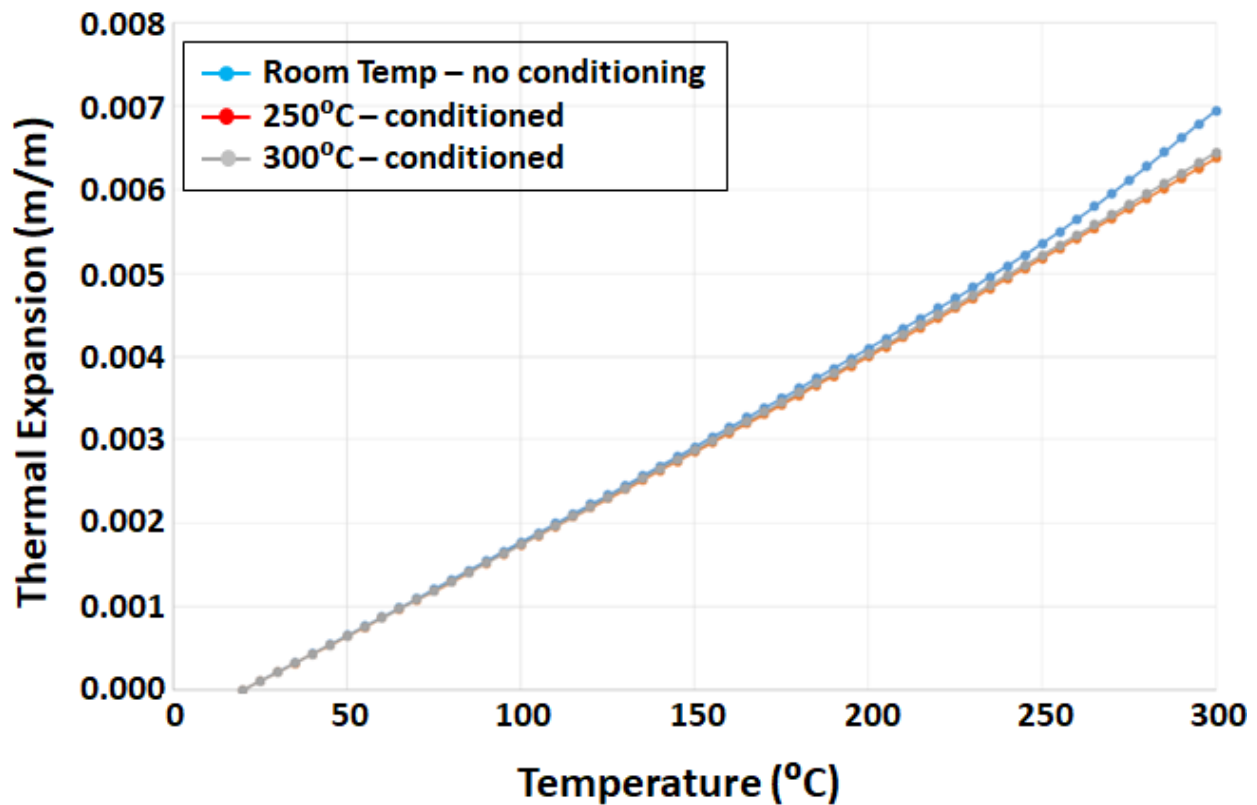


Figure I.1.C.11. Measured thermal expansion of cylinder head specimens with 200 hour preconditioning. Source: GM.

Recyclability Analysis

GM collaborated with AFS and SECAT (a metallurgical research laboratory specializing in Al product and process technologies) to evaluate the recyclability of the alloy developed for high-temperature lightweight cast alloy for advanced cylinder heads in high-efficiency, LD engines. Because the chemistry of the final alloy is confidential, a set of five alloys were developed for analysis and compared to a baseline A356.1 material. These five alloys encompass the selection of element combinations that would be used in the final alloy. Each of the elements is evaluated on the potential impact on the recyclability of the material. Furthermore, the list of five alloys progresses from the baseline A356.1 alloy to A356.1+0.5 Cu to A356.1+0.5 Cu with each of the added minor elements. In this manner, an evaluation of the added cost of each can be obtained, as well as the increased cost of the total alloy. The alloy costs are then used in the cost models developed for the semi-permanent mold casting process used for cylinder head production. The impact of Cu and the minor elements on the recyclability stream was proven to be negligible. Due to the large cycling stream for Al, these minor elements will be essentially diluted to negligible amounts. Also, as these elements are contained in other wrought or cast Al alloys, these elements are not seen as detrimental to the Al recyclability market.

Cost Analysis

GM subcontracted Camanoe Associates to develop a comprehensive cost model covering alloy production, capital costs, processing methods, and component finishing costs for annual production runs up to 500,000 units, in increments of 100,000 units. The cost models made a direct comparison of capital alloy production, processing, and component finishing costs with baseline component costs sufficient to complete evaluation of the cost-effectiveness of the new material. The set of five alloys use in the recyclability analysis were also used in this cost analysis. Only for the fifth alloy composition did the overall costs exceed 110% of the baseline alloy process costs.

Conclusions

ICME and extensive experimental techniques were used to develop a high-temperature stabilized Q-phase alloy for engine cylinder heads. This alloy met or exceeded most of the DOE targets defined in the program. In the final year of the program, material properties from two engine cylinder head casting trials were evaluated and compared. The Q-phase alloy demonstrated improved high-temperature properties at the target temperature of 300°C but did not show improvement in the mid-200°C to 250°C range. Castability was shown to be excellent, and the thermal conductivity was well within the range of current cylinder head casting alloys. However, the new alloys did not show any discernable difference in fatigue properties. As highlighted in this report, fatigue properties are determined by defect population and sizes in the castings caused by the casting process rather than the alloying elements. This highlights the necessity to improve on the casting process to benefit from improved high-temperature properties of an alloy.

Key Publications

1. Kim, K., Roy, A., Gururajan, M. P., Wolverton, C., and Voorhees, P. W., "First-principles/Phase-field modeling of θ' precipitation in Al-Cu alloys," *Acta Mater.*, Vol. 140, pp. 344–354, 2017.
2. Bobel, A., Kim, K., Wolverton, C., Walker, M., and Olson, G. B., "Equilibrium composition variation of Q-phase precipitates in Al alloys," *Acta Mater.*, Vol. 138, pp. 150–160, 2017.
3. Kim, K., Zhou, B. C., and Wolverton, C., "First-principles study of crystal structure and stability of T1 precipitates in Al-Li-Cu alloys," *Acta Mater.*, Vol. 145, pp. 337–346, 2018.
4. Kim, K., and Voorhees, P. W., "Ostwald ripening of spheroidal particles in multicomponent alloys," *Acta Mater.*, Vol. 152, pp. 327–337, 2018.
5. Kim, K., Bobel, A., Brajuskovic, V., Zhou, B. C., Walker, M., Olson, G. B., and Wolverton, C., "Energetics of native defects, solute partitioning, and interfacial energy of Q precipitate in Al-Cu-Mg-Si alloys," *Acta Mater.*, Vol. 154, pp. 207–219, 2018.

6. Kim, K., Bobel, A., Baik, S. I., Walker, M., Voorhees, P. W., and Olson, G. B., “Enhanced coarsening resistance of Q-phase in Al alloys by the addition of slow diffusing solutes,” *Mater. Sci. Eng. A*, Vol. 735, pp. 318–323, 2018.
7. Kim, K., Zhou, B. C., and Wolverton, C., “Interfacial stability of θ' /Al in Al-Cu alloys,” *Scr. Mater.*, Vol. 159, pp. 99–103, 2019.
8. Bobel, A., M. Walker, and G. B. Olson, “High-temperature aging of Al-Si-Mg alloys: A CALPHAD precipitation growth model,” manuscript in process.
9. Bobel, A., M. Walker, and G. B. Olson, “High-temperature aging of Al-Si-Mg alloys: A CALPHAD precipitation strengthening model,” manuscript in process.

References

1. Clyne, T. W., and Davies, G. J., “Influence of composition on solidification cracking susceptibility in binary alloy systems,” *Br. Foundryman*, Vol. 74, pp. 965–973, 1981.
2. Yan, X., and Lin, J. C., “Prediction of hot tearing tendency for multicomponent Al alloys,” *Metall. Mater. Trans.*, Vol. 37B, No. 6, pp. 913–918, 2006.

I.2 High-Temperature Engine Materials

I.2.A Lightweight High-Temperature Alloys Based on the Al-Fe-Si System (University of Florida)

Michele V. Manuel, Principal Investigator

University of Florida
549 Gale Lemerand Dr.
Gainesville, FL 32611
E-mail: mmanuel@mse.ufl.edu

Donovan N. Leonard, Co-Principal Investigator

University of Florida
549 Gale Lemerand Dr.
Gainesville, FL 32611
E-mail: rhennig@mse.ufl.edu

Jerry L. Gibbs, DOE Technology Manager

U.S. Department of Energy
E-mail: jerry.gibbs@ee.doe.gov

Start Date: October 1, 2016	End Date: September 30, 2019	
Project Funding : \$1,102,082	DOE share: \$991,873	Non-DOE share: \$110,209

Project Introduction

Automotive applications need low-cost lightweight, high-temperature alloys to enhance efficiencies in systems such as internal combustion engines. The Al-Fe-Si system provides an opportunity to develop such a material, as it comprises three of the lowest cost elements abundant in nature. Specifically, the τ_{10} -Al-Fe-Si ($\text{Al}_4\text{Fe}_{1.7}\text{Si}$) ternary intermetallic phase is a lightweight and low-cost phase that exhibits excellent mechanical properties at high temperatures. However, the τ_{10} - $\text{Al}_4\text{Fe}_{1.7}\text{Si}$ phase has an extremely small compositional range, which should be expanded in order to use this alloy at commercial scale. To increase this compositional range, the equilibrium phase boundaries can be manipulated and expanded via alloy design and non-equilibrium processing and the parts can potentially be fabricated by additive manufacturing.

Objectives

The objective of this project is to design alloy chemistries to create phases with an excellent combination of mechanical properties and to 3D laser print them to exploit the nearly non-equilibrium nature of the total melting and solidification process. Additions of a quaternary solute X to an Al-Fe-Si system will be examined. It is expected that the alloys produced will have three times the tensile strength of competing intermetallics and have a density comparable to Ti-Al alloys.

Approach

An integrated computational approach was used that spans electronic structure calculations to thermodynamic models that are paired with strategic experiments for alloy characterization and thereby validation to produce revolutionary automotive components that will supersede current commercial and research-grade high-temperature alloys.

The project will be conducted in three budget periods:

Budget Period 1: Candidate solute elements were identified that have the potential to increase the compositional range over which the τ_{10} -Al₄Fe_{1.7}Si phase is stable. Ternary and quaternary alloys were cast via arc melting. The Go/No-Go milestone decision was to deliver alloys that have the potential to display a stable τ_{10} Al-Fe-Si-X phase. This deliverable was achieved through the experimental demonstration of the desired τ_{10} phase in the Al-Fe-Si-X alloy system (where X = nickel (Ni)).

Budget Period 2: For the candidate solute elements, the compositional range of the τ_{10} phase was expanded by computationally evaluating its energetic and thermodynamic stability. The Go/No-Go milestone decision was to create a list of chemistries suitable for powder processing via 3D printing. This deliverable was achieved through computational prediction and experimental demonstration of the desired τ_{10} phase in the Al-Fe-Si-X alloy system (where X = Cu, Mn, Ni and Zn).

Budget Period 3: Specimens for mechanical and microstructural characterization will be produced using 3D powder bed processing for component manufacturing. The Go/No-Go milestone decision will be based on the production of mechanical test samples using additive manufacturing.

Results

To stabilize the τ_{10} -Al₄Fe_{1.7}Si phase and expand its phase boundaries, there are a large number of possible alloying additions. Potential quaternary elements were selected based on cost, aiming for elements with a bulk price of <\$100/kg and element solubility in the competing Al₁₃Fe₄ phase, based on the hypothesis that the element having a low solubility in the Al₁₃Fe₄ phase has the potential to destabilize it. Thermodynamic calculations via Thermo-Calc software and density functional theory (DFT) calculations via VASP code were used to search for such quaternary elements, X. Utilizing the two computational approaches, the candidate elements were narrowed to nine common metals with relatively low price (i.e., Co, Cu, Mn, Mo, Nb, Ni, Sn, Ti and Zn). Then, a diffusion couple approach was utilized to quickly evaluate the solubility of these nine elements in the τ_{10} phase at 800°C. Seven solid-solid diffusion couples (SSDCs) were fabricated by mechanically bonding τ_{10} and a pure element of Co, Cu, Mo, Nb, Ni, Ti, or the Fe-30 at.% Mn master alloy, as well as two solid-liquid diffusion couples (SLDCs) of τ_{10} /Sn and τ_{10} /Zn were also fabricated by taking advantage of the liquid phase formation at 800°C (above the melting points of Sn and Zn). Concentration profiles obtained by performing electron probe microanalysis (EPMA) line scan across the phase interfaces in the diffusion region were used to define the maximum solubility of these nine candidate elements in τ_{10} . Among them, Cu, Mn, Mo, Nb, Ti, and Sn were confirmed to have very limited solubility in τ_{10} , while Co, Ni, and Zn show a solubility of 3.5, 2.0, and 7.2 at.% in τ_{10} at 800°C, respectively. Owing to space constraints, the present report only shows the experimental results obtained from τ_{10} /Co, τ_{10} /Ni and τ_{10} /Zn diffusion couples.

Figure I.2.A.1.(a) is a SEM back-scattered electron (BSE) image taken from the τ_{10} /Co SSDC, showing the phase formation in the diffusion region. Three layers between pure Co and τ_{10} phase were observed, which were identified to be β -CoAl, Co₄Al_{7+x}Si_{2-x}, and Al₁₃Fe₄ phases based on the EPMA/ energy dispersive spectroscopy composition analysis and the corresponding binary and ternary phase diagrams. Across these phase interfaces, a quantitative EPMA line scan with a step size of 1 μ m was performed. The line scan location, as a red line with a right arrow showing the direction, is superimposed on the diffusion region in Figure I.2.A.1.(a). The measured composition profiles are plotted in Figure I.2.A.1.(b), from which the solubility of Co in τ_{10} was defined to be 3.5 at.% at 800°C. In addition, the Co predominately replaces Fe, while the Al and Si contents in the τ_{10} phase exhibit little change.

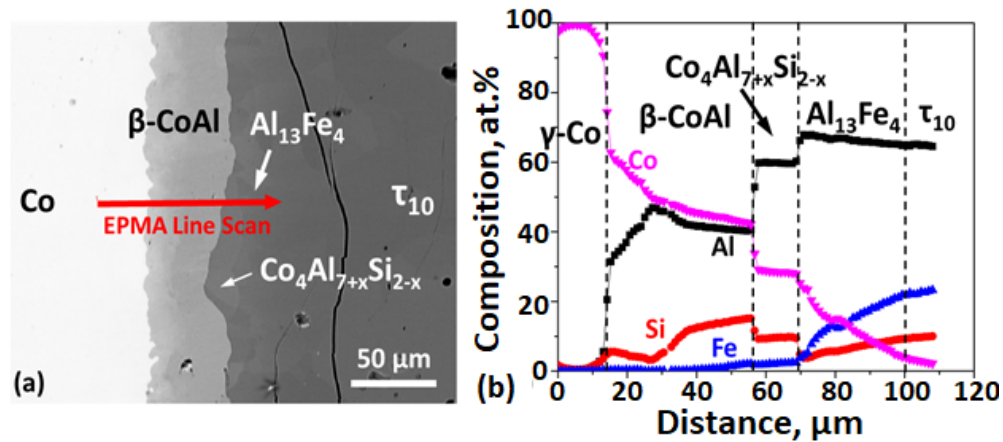


Figure I.2.A.1.(a) A SEM BSE image taken from the τ_{10}/Co SSDC annealed at 800°C for 500 h, showing the phase formation by interdiffusion and the EPMA line scan location; and (b) EPMA composition profiles collected by performing an EPMA line scan across all the phase interfaces in (a). The vertical dashed lines in (b) show the locations of phase interfaces (University of Florida unpublished results).

Figure I.2.A.2.(a) shows the entire diffusion region formed in the τ_{10}/Cu SSDC after the heat-treatment at 800°C for 350 h. Figure I.2.A.2.(b) is a high-magnification image showing the interface between $\text{Al}_{13}\text{Fe}_4$ and τ_{10} phases. The composition profiles obtained by performing EPMA line scan across this phase interface is plotted in Figure I.2.A.2.(c). From the composition profiles, the solubility of Cu in τ_{10} is extremely low, only ~ 0.2 at.% at 800°C .

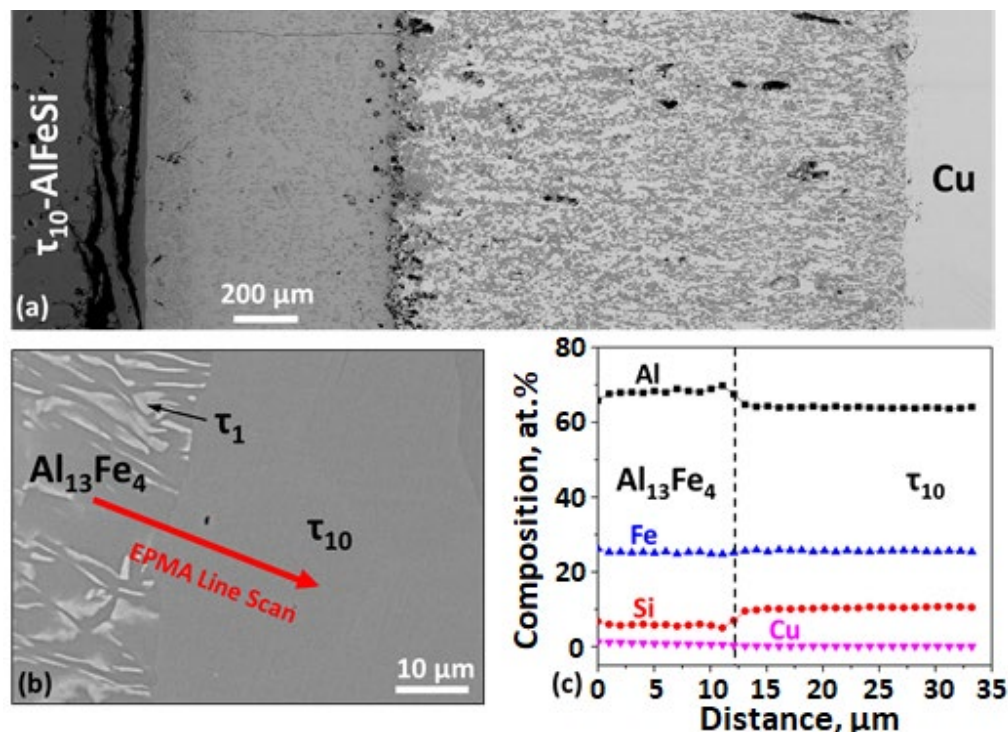


Figure I.2.A.2. A SEM BSE image taken from the τ_{10}/Cu SSDC annealed at 800°C for 350 h, showing the phase formation by interdiffusion: (a) Low-magnification image showing the entire diffusion region; (b) High-magnification image showing the phase interface between $\text{Al}_{13}\text{Fe}_4$ and τ_{10} ; and (c) EPMA composition profiles collected by performing an EPMA line scan across the phase interface in (b). The vertical dashed lines in (c) show the location of $\text{Al}_{13}\text{Fe}_4/\tau_{10}$ phase interface (University of Florida unpublished results).

A SEM BSE image taken from the τ_{10} /Zn SLDC is shown in Figure I.2.A.3.(a), wherein the solidified Zn and intermetallic phases formed by interdiffusion can be clearly identified. Figure I.2.A.3.(b) is a high-magnification SEM BSE image showing the phase interface between the $\text{Al}_{13}\text{Fe}_4$ and τ_{10} phases. A quantitative EPMA line scan was performed across this interface, shown in Figure I.2.A.3.(b), and the obtained concentration profiles are plotted in Figure I.2.A.3.(c). The results indicate Zn has a relatively high solubility of 7.2 at.% in the τ_{10} phase at 800°C.

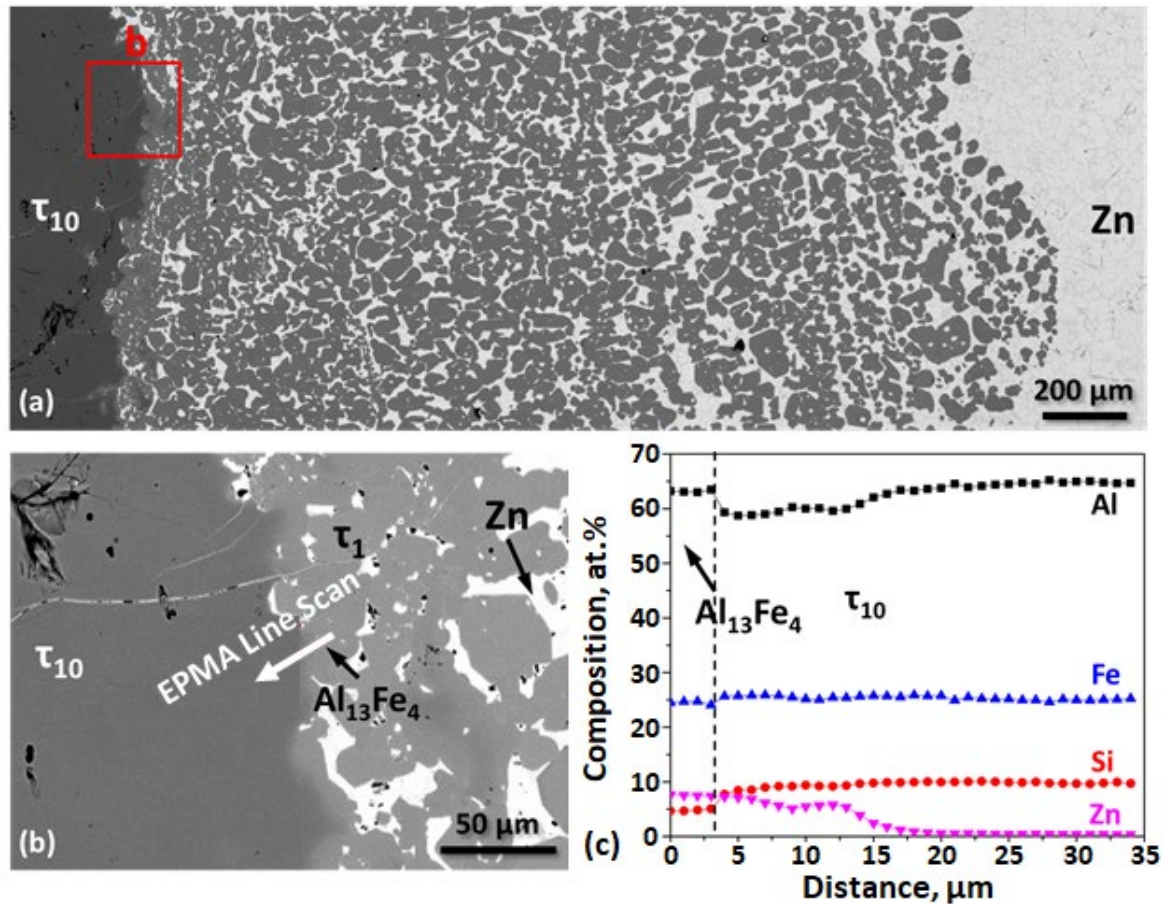


Figure I.2.A.3. A SEM BSE image taken from the τ_{10} /Zn SLDC annealed at 800°C for 8 h, showing the phase formation by interdiffusion: (a) Low-magnification image showing the entire diffusion region; (b) High-magnification image of the red box location in (a); and (c) EPMA composition profiles collected by performing an EPMA line scan across the phase interface in (b). The vertical dashed lines in (c) show the location of $\text{Al}_{13}\text{Fe}_4/\tau_{10}$ phase interface (University of Florida unpublished results).

Two Al-Fe-Si-Co alloys with 1.0 at.% and 2.0 at.% Co were fabricated and annealed at 800°C for 400 h. The microstructures of the two alloys are shown in Figure I.2.A.4. It can be observed that the competing $\text{Al}_{13}\text{Fe}_4$ phase coexists with the τ_{10} phase in both alloys. This can be due to the high solubility of Co in the binary $\text{Al}_{13}\text{Fe}_4$ intermetallic. In the Al-Fe-Si-Co quaternary system, Co has a solubility of ~20 at.% in the $\text{Al}_{13}\text{Fe}_4$ phase. Such a high solubility of Co in $\text{Al}_{13}\text{Fe}_4$ makes Co a poor candidate for the destabilization of this intermetallic.

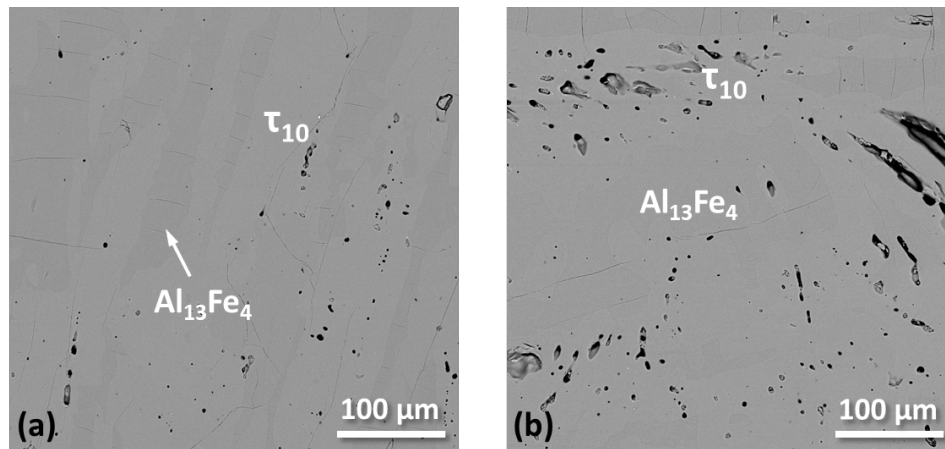


Figure I.2.A.4. SEM BSE images taken from the τ_{10} alloys with Co additions that were annealed at 800°C for 400 h: (a) Al-23.5Fe-10.2Si-1.0Co and (b) Al-22.5Fe-10.2Si-2.0Co. The compositions are all in at.% (University of Florida unpublished results).

Figure I.2.A.5 shows the microstructures of Al-24.0Fe-11.0Si-1.0Cu and Al-23.0Fe-11.0Si-2.0Cu (all in at.%) alloys after the heat-treatment at 800°C for 400 h. As can be seen, no $\text{Al}_{13}\text{Fe}_4$ phase was observed in these two τ_{10} alloys, suggesting Cu addition can destabilize the $\text{Al}_{13}\text{Fe}_4$ phase. However, a large amount of B2-AlFe phase formed in these alloys. In order to obtain a complete τ_{10} single-phase, new alloy compositions by decreasing Fe and Si concentrations are still being explored to avoid the formation of B2 phase.

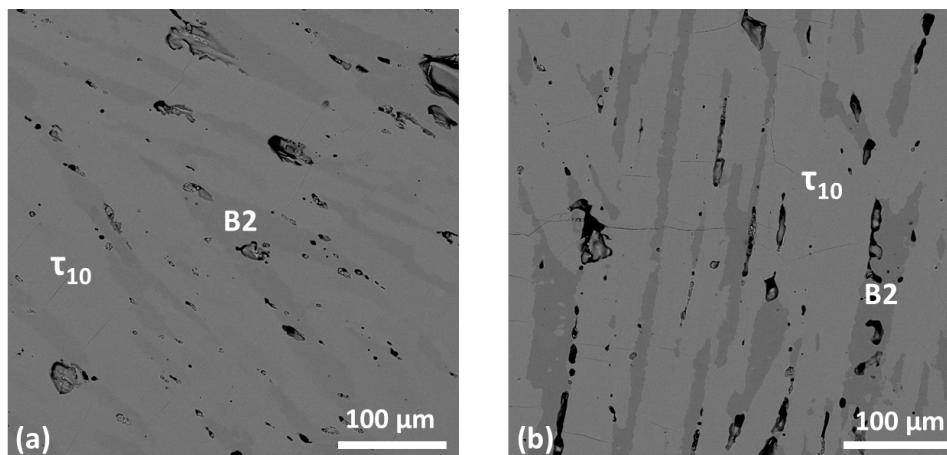


Figure I.2.A.5. SEM BSE images of τ_{10} alloys with Cu additions that were annealed at 800°C for 400 h: (a) Al-24.0Fe-11.0Si-1.0Cu and (b) Al-23.0Fe-11.0Si-2.0Cu. The compositions are all in at.% (University of Florida unpublished results).

Two τ_{10} alloys with nominal compositions of Al-23.0Fe-10.2Si-1.5Mn and Al-20.0Fe-10.2Si-4.5Mn (all in at.%) were fabricated. The microstructures of both alloys are shown in Figure I.2.A.6. As can be observed, the alloy with 1.5 at.% Mn addition is a mixture of τ_{10} phase and a very small amount of τ_2 and $\text{Al}_{13}\text{Fe}_4$ phases, while the alloy with 4.5 at.% Mn is a complete τ_{10} single-phase. The results suggest that Mn is a promising quaternary alloying addition that can be used to destabilize the competing $\text{Al}_{13}\text{Fe}_4$ phase. According to the results from the two Al-Fe-Si-Mn alloy samples, we believe that the Mn has a relatively high solubility in τ_{10} and Mn is substituting for Fe in the τ_{10} phase.

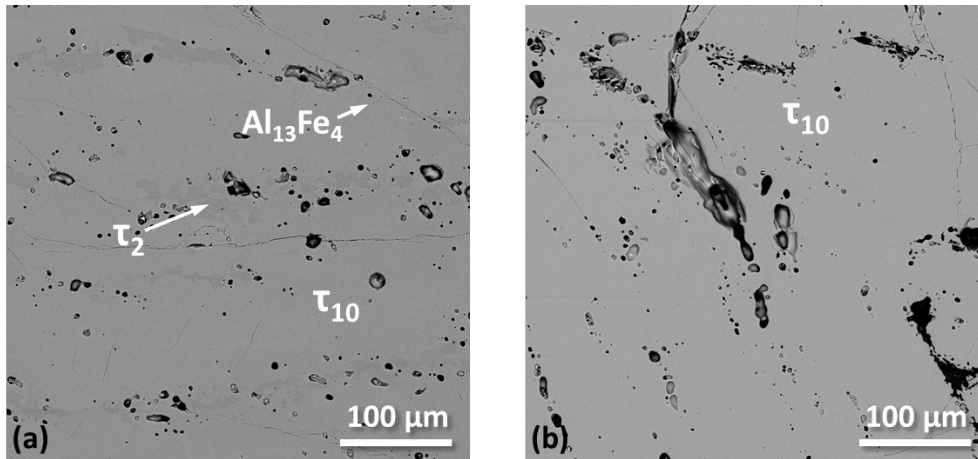


Figure I.2.A.6. SEM BSE images taken from the τ_{10} alloys with Mn additions that were annealed at 800 °C for 400 h: (a) Al-23.0Fe-11.0Si-1.5Mn and (b) Al-20.0Fe-11.0Si-4.5Mn. The compositions are all in at.% (University of Florida unpublished results).

Al-25.0Fe-10.0Si-1.0Ni and Al-25.0Fe-9.0Si-2.0Ni (all in at.%) were cast and heat-treated at 800 °C for 400 h. These two compositions were optimized from an alloy with a nominal composition of Al-24.5Fe-8.2Si-2.0Ni, which was confirmed to be τ_{10} single-phase at 950 °C. The Si concentration in these two new alloys was increased to avoid the formation of the $\text{Al}_{13}\text{Fe}_4$ phase at a lower temperature of 800 °C. Figure I.2.A.7 shows the microstructures of these two alloys. It can be observed that the two alloys are three-phase mixtures of τ_{10} and a very small amount of τ_1 and $\text{Al}_{13}\text{Fe}_4$ phases, demonstrating that Ni addition is effective for destabilizing the $\text{Al}_{13}\text{Fe}_4$ phase. In order to avoid the formation of undesirable τ_1 phase, new τ_{10} compositions by decreasing Fe concentration (below 24.5 at.%) are being explored.

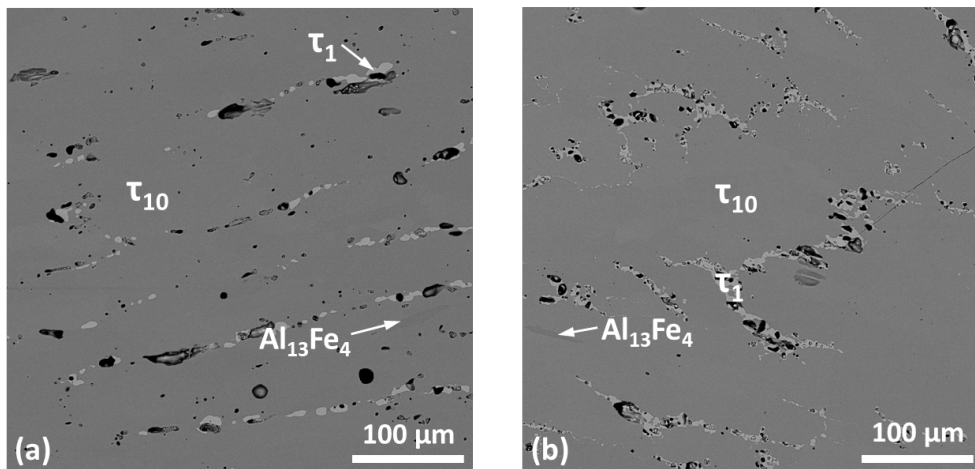


Figure I.2.A.7. SEM BSE images of τ_{10} alloys with Ni additions that were annealed at 800 °C for 400 h: (a) Al-25.0Fe-10.0Si-1.0Ni and (b) Al-25.0Fe-9.0Si-2.0Ni. The compositions are all in at.% (University of Florida unpublished results).

In BP 2, we focused on expanding the compositional range of the τ_{10} phase by quaternary additions. Among the nine candidate elements (i.e., Co, Cu, Mn, Mo, Nb, Ni, Sn, Ti, and Zn) explored, Cu, Mn, and Ni were demonstrated to be effective additions for τ_{10} stabilization and/or $\text{Al}_{13}\text{Fe}_4$ destabilization. Next, we will continue optimizing the compositions of τ_{10} alloys with Cu, Mn, and Ni additions, as well as explore the phase stability of τ_{10} alloys with Zn addition. The optimized compositions will be manufactured in powders and then used in a laser 3D printing machine to produce the desired parts.

Conclusions

Both computational and experimental techniques were utilized in the present period to stabilize the τ_{10} phase while destabilizing the competing $\text{Al}_{13}\text{Fe}_4$ phase using quaternary alloy additions. Computational approaches, including thermodynamic calculations using Thermo-Calc software, and DFT calculations were used to predict the elements that could potentially stabilize the τ_{10} phase. Experimental techniques were also utilized through fabricating diffusion couples to determine the solubility of quaternary elements in the τ_{10} phase, as well as alloy samples to study the phase stability of τ_{10} alloys with quaternary additions. These samples were then characterized using SEM, especially BSE imaging, energy dispersive spectroscopy and EPMA. The main conclusions drawn from this period are as follows:

- Nine elements of Co, Cu, Mn, Mo, Nb, Ni, Sn, Ti, and Zn were firstly identified as quaternary candidate elements using computational approaches of thermodynamic and DFT calculations.
- Both SSDCs and SLDCs were made to extract the exact solubility of these nine quaternary alloying elements in the τ_{10} phase at 800°C. Cu, Mn, Mo, Nb, Ti, and Sn were confirmed to have very limited solubility in τ_{10} , while Co, Ni, and Zn show a solubility of 3.5, 2.0, and 7.2 at.%, respectively.
- Cu, Mn, and Ni were found to be promising to destabilize the competing $\text{Al}_{13}\text{Fe}_4$ phase. The alloy with nominal composition of Al-20.0Fe-11.0Si-4.5Mn (in at.%) was confirmed to be τ_{10} single-phase at 800°C. Meanwhile, new τ_{10} compositions with Cu, Ni, and Zn additions are being explored to obtain complete τ_{10} single-phase at 800°C.

Key Publications

1. Soto, S., B. Rijal, L. L. Zhu, R. Hennig, and M. V. Manuel, 2018, "Microstructure evolution of the high-temperature intermetallic phase $\tau_{10}\text{-Al}_4\text{Fe}_{1.7}\text{Si}$," Oral presentation in The Minerals, Metals, & Materials Society (Ed.), *TMS 2018 147th Annual Meeting & Exhibition Supplemental Proceedings*, March 13, 2018.
2. Rijal, B., R. Hennig, M. V. Manuel, and S. Soto, 2018, "Extension of the stability range of τ_{10} phase in Al-Fe-Si Alloy: Cluster expansion approach," Oral presentation in The Minerals, Metals, & Materials Society (Ed.), *TMS 2018 147th Annual Meeting & Exhibition Supplemental Proceedings*, March 13, 2018.
3. Cohen, M., C. Hernandez, C. Orozco, S. Medina, B. Rijal, L.L. Zhu, R. Hennig, and M. V. Manuel, 2018, "Al-Fe-Si-based intermetallic compounds for high-temperature applications," 2nd Place Award at the 2018 Undergraduate Design Competition, August 2018.
4. Soto, S., L. L. Zhu, B. Rijal, R. Hennig, and M. V. Manuel, 2019, "Experimental measurement of the phase boundary of the $\tau_{10}\text{-Al}_4\text{Fe}_{1.7}\text{Si}$ intermetallic phase," to be submitted in February 2019.
5. Zhu, L. L., S. Soto, R. Hennig, and M. V. Manuel, 2019, "Experimental investigation of the Al-Co-Fe phase diagram over the whole composition range," to be submitted in February 2019.

I.2.B Advanced Fe-Ni-Cr-base Alloys for Higher Temperature Engine Components (Oak Ridge National Laboratory)

J. Allen Haynes, Principal Investigator

Propulsion Materials
Oak Ridge National Laboratory
1 Bethel Valley Rd.
Knoxville, TN 37831
E-mail: haynesa@ornl.gov

Jerry L. Gibbs, DOE Technology Manager

U.S. Department of Energy
E-mail: jerry.gibbs@ee.doe.gov

Start Date: October 1, 2016	End Date: September 30, 2018	
Project Funding (FY18): \$580,000	DOE share: \$580,000	Non-DOE share: \$0

Project Introduction

The Advanced Fe-Ni-Cr-base Alloys for Higher Temperature Engine Components Project consists of three tasks focused on early-stage research in pursuit of advancing the basic mechanical properties, manufacturability, and addressing the affordability of propulsion materials. These tasks have the common goal to develop advanced cast Al alloys for high-temperature engine components. The specific tasks include the following:

1. Computation-Guided Development of Lower Cost Alumina-Forming Alloys.
2. Oxidation-Resistant Coated Exhaust Valves for High-Temperature Applications.
3. HT Components: Alumina-Forming Cast Turbo Housing Alloys Capable of 950°C.

The following sections of this report outline the specific task work conducted at ORNL in the areas of predictive engineering, process development, and enabling technologies for propulsion materials. To increase engine efficiency in LD vehicles, the maximum operating temperature of engine components has increased from approximately 170°C in earlier engines to peak temperatures well above 200°C in current engines. Each task supports one or more goals within the Vehicle Technologies Office (VTO) mission of developing advanced cast Al alloys for automotive engine applications to meet these challenging requirements.

I.2.B.1 Task 1B: Computation-Guided Development of Lower Cost Alumina-Forming Alloys

Govindarajan Muralidharan, Principal Investigator

Oak Ridge National Laboratory
Materials Science and Technology Division
1 Bethel Valley Road
Oak Ridge, TN 37831
E-mail: muralidhargn@ornl.gov

Jerry L. Gibbs, DOE Technology Manager

U.S. Department of Energy
E-mail: jerry.gibbs@ee.doe.gov

Start Date: October 1, 2016

End Date: September 30, 2018

Project Funding (FY18): \$240,000

DOE share: \$240,000

Non-DOE share: \$0

Project Introduction

Improving the engine efficiencies of passenger and commercial vehicles is a major goal of the Vehicle Technologies Program and materials play a significant role in achieving this objective. One potential approach to achieving improved engine efficiency while reducing emissions is through retaining more heat in the exhaust gas. Retaining more heat in the exhaust gas results in higher exhaust gas temperatures, thus increasing the operational temperature requirements of components in the exhaust gas path including exhaust valves. It has been projected that exhaust gas temperatures would increase from a current value of 760°C to values of at least 870°C and very likely reach as high as 1,000°C in the long-term [1-2]. Availability of materials with adequate high-temperature mechanical properties and oxidation resistance to enable the projected engine operating parameters without exceeding the cost constraints is a barrier to adoption of new high-efficiency technologies. In particular, at higher temperatures, oxidation resistance in a water vapor-containing environment becomes more critical for materials exposed to exhaust gases.

High-performance exhaust valves currently used at temperatures up to ~760°C are fabricated using nickel (Ni)-based alloys such as Alloy 751. Other high-performance Ni-based alloys primarily developed for aerospace applications have the potential to operate at temperatures of 1,000°C with desired strength but may be expensive for automotive applications and may be very difficult to fabricate into desirable shapes. Additionally, at temperatures greater than 850°C, achieving good oxidation resistance in exhaust gases containing water vapor may be challenging for existing high-strength alloys, such as Alloy 751, which depend on chromia-scale formation for oxidation resistance. Hence, new alloys with appropriate strength, oxidation resistance, and formability may have to be specifically developed for the operating characteristics and lifetime expectations for automotive valves. This project focuses on alumina-forming alloys with the potential for improved oxidation resistance in water vapor-containing environments when compared to chromia-forming alloys.

Objectives

The primary objective of this project is the identification/development of materials for alumina-forming exhaust valves that could operate at temperatures up to 1,000°C. These alloys should have the appropriate combination of oxidation resistance and high-temperature mechanical strength required for valve applications.

Approach

The overall approach used in this project focused on identifying alloys with an appropriate combination of two key properties—oxidation resistance and mechanical properties. As part of this project, properties of commercial alloys were evaluated, and the development of new materials were targeted to achieve required properties at low-cost.

A recently concluded project successfully addressed the development of new lower cost alloys for use in exhaust valves at temperatures up to 870°C through a synergistic approach that included computational modeling and selected experimental evaluation of properties [3-4]. The technical basis of this approach was that mechanical properties can be directly correlated with microstructure, particularly the strengthening phases. Different phase fractions of strengthening phases and their compositions can be achieved through alloying element additions, thermomechanical processing, and heat-treatment. Microstructural characteristics of existing alloys can be correlated with their mechanical properties to identify desirable microstructures. Once such correlations are established, computational modeling of untested compositions can be used to identify compositions that have the potential for improved properties. Small heats of targeted materials can then be processed to confirm the modeled properties and to broaden the correlation database.

In an earlier study on automotive valves for performance at 870°C and 950°C, a synergistic computational and experimental aspects was used to develop cost-effective chromia-forming Ni-based alloys for use at this temperature [3-4]. A range of Ni-based alloys with potentially varying weight fractions (or volume fractions) of the major strengthening phase, γ' , were identified in efforts to correlate the fatigue properties with the microstructure of the alloys. The selection of nine commercial Ni-based alloys included Alloy 751, Waspaloy, Udimet 520, and Udimet 720. The Ni+Co contents ranged from 66 wt.% to 76 wt.%. To obtain initial information on the microstructures of these alloys at equilibrium, thermodynamic calculations were carried out. Comparison of the results of the calculations showed that all alloys have a matrix of γ with the major strengthening phase as γ' . One or more carbide phases, such as $M_{23}C_6$, MC, and M_7C_3 , may also be present in different alloys. The primary difference between the microstructures of the various alloys was the weight percent of the γ' phase at a given temperature and the highest temperature at which the γ' phase is stable in the different alloys. Since the size of the strengthening precipitates is also critical, it was anticipated that the kinetics of the coarsening of this phase would also be influential in the long-term performance of the alloys in this application. Using the microstructures of these alloys as a guide, computational thermodynamics was used to design new alloys with microstructure similar to the commercial alloys in an effort to obtain materials with desirable properties. In contrast to the commercially available alloys with Ni+Co contents greater than 66 wt.%, the Ni+Co content in these newly identified candidate alloys was lower than 50 wt.% (Ni being replaced with other elements such as iron(Fe)) with the potential to achieve comparable properties. While it has been shown that strength targets are achievable, the oxidation resistances at 950°C of the newly developed alloys have scope for improvement. This stems from the fact that this study focused on alloys that achieve oxidation resistance through the formation of chromia scales. Alloys that rely on the formation of an alumina scale have the potential for improved oxidation resistance and the focus of the current work is alumina-forming alloys. The focus of the current work is to use a similar approach to develop new alloys that form an alumina scale, but also possess the required tensile and fatigue strengths.

Results

Figure I.2.B.1.1 shows a comparison between the oxidation behavior in an air + 10% water vapor environment of a commercial alumina-forming alloy Haynes HR-214[®] (Ni-16Cr-3Fe-4.5Al-0.01Y—0.04C) compared with that of Udimet[®]520 and ORNL developmental alloys—ORNL Alloy A—and those of alloys developed this year—Alloy 2D, 2E, and 2F. Note that ORNL alloys A, 2D, and 2E show low-mass changes for over 2,500 cycles at 950°C. Alloy 2F starts with low-mass change but after about 500 one-hour cycles at 950°C, gradual but significant mass losses are observed suggesting the loss of a protective Al oxide scale.

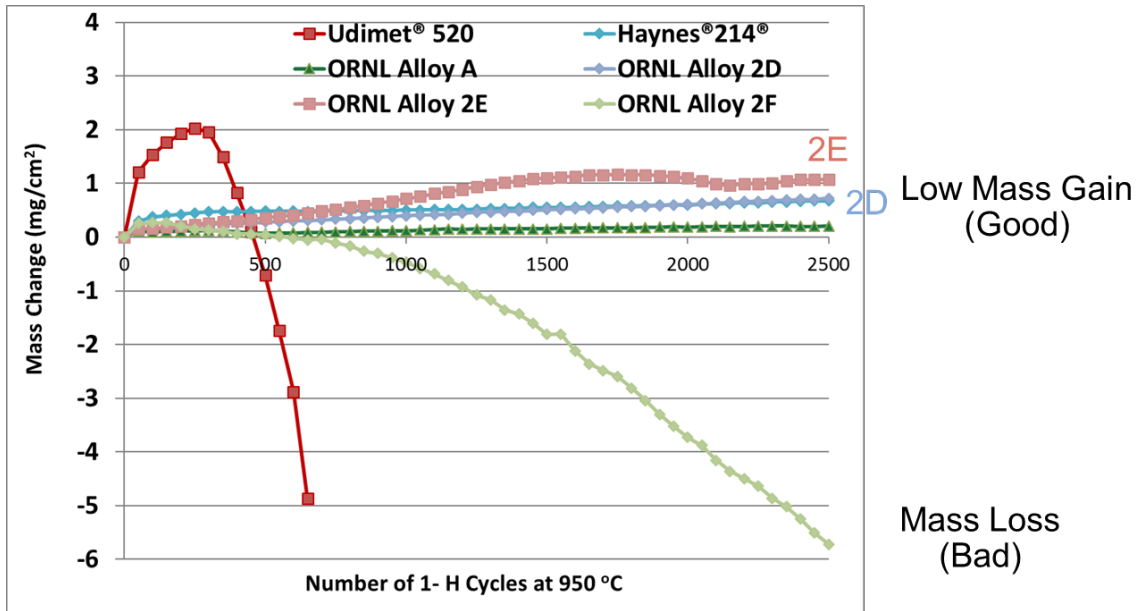


Figure I.2.B.1.1. Effect of alloy composition on mass change during oxidation at 950°C in Air + 10% water vapor environment. Source: ORNL.

Figure I.2.B.1.2 compares the YSs at 950°C of commercial alumina-formers (e.g., Haynes®214® and Haynes®224®) with those of ORNL alloys A-C, 2D-2F. Note that all ORNL alloys have significantly greater YSs at 950°C and **have met the milestone target for this project**. Furthermore, alloys 2D-2F have lower-Ni+Co contents and thus would result in materials cost savings over ORNL alloy A-C and commercial alloy Haynes®214®. However, it should be noted that the design stresses for exhaust valves are anticipated to result in targeted YSs of ≥ 35 Ksi for the next-generation of alloys, but without compromising the good oxidation resistance achieved so far in these alloys.

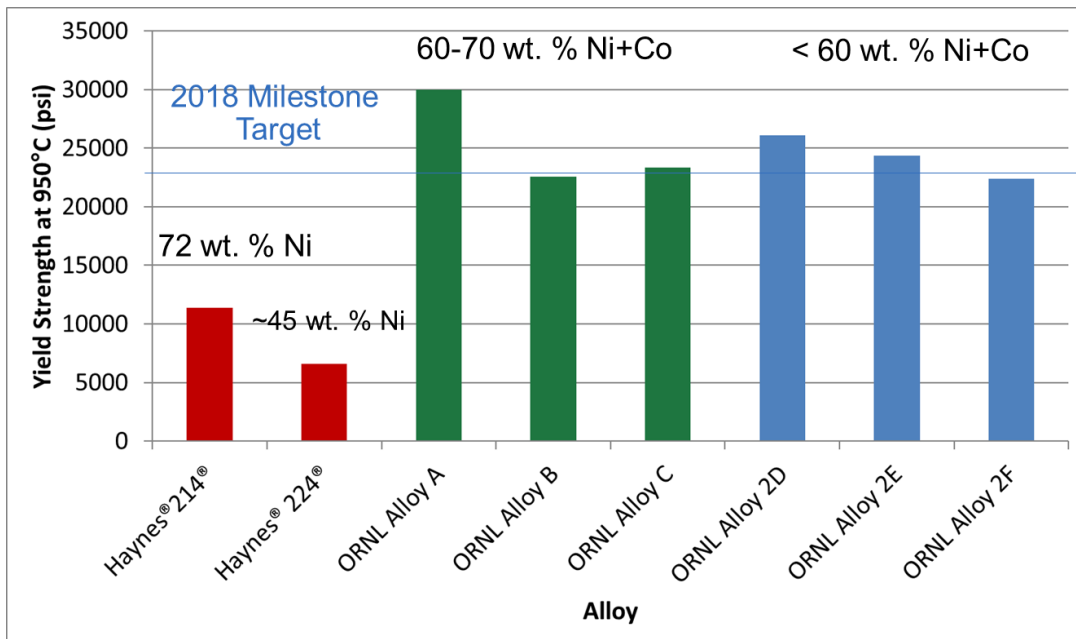


Figure I.2.B.1.2. New ORNL alloys have improved YSs at 950°C. Source: ORNL.

To enable the design of improved alloys, *in-situ* ultra-small-angle x-ray scattering (USAXS)/small-angle x-ray scattering (SAXS)/wide-angle x-ray scattering experiments are being performed at different temperatures at the Advanced Photon Source in collaboration with Dr. Matt Frith and Dr. Jan Ilavsky to better understand precipitation in the newly designed alloys. Figure I.2.B.1.3 shows the time dependence of the USAXS/SAXS at two different temperatures—835°C and 900°C. Note that microstructural evolution is faster at 900°C with the likely precipitation of additional phases, which may lead to lower strength. Further analyses of this data are in progress.

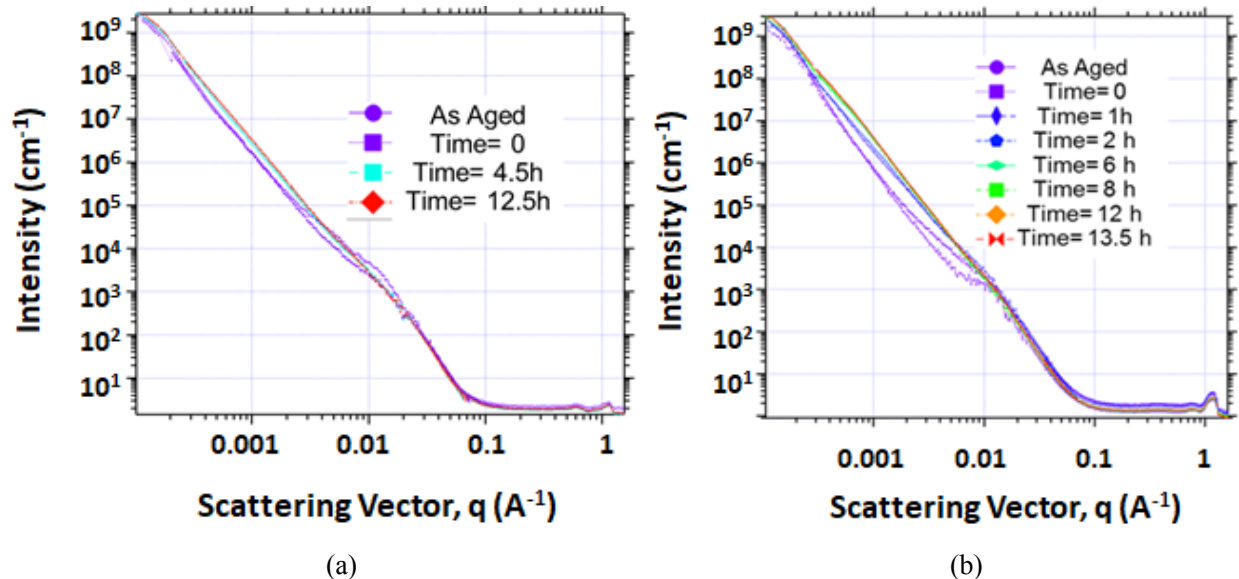


Figure I.2.B.1.3. Effect of temperature and time on the USAXS/SAXS data. (a) ~ 835°C, and (b) 900°C. Source: ORNL.

Conclusions

New alumina-forming alloys with significantly improved strengths over commercially available alloys have been developed for operation at temperatures up to 950°C. Further improvements in strength are needed to compete with high-strength, commercially available chromia-forming alloys. USAXS/SAXS experiments that are being performed in collaboration with researchers at the Advanced Photon Source help us to understand precipitation in the novel alloys at the higher temperatures and to define paths for further improvements in strength.

References

1. DOE Vehicle Technologies Office, 2013, “LD Vehicles Technical Requirements and Gaps for Lightweight and Propulsion Materials,” DOE VTO Workshop Report No. DOE/EE-0868, February 2013.
2. DOE Vehicle Technologies Office, 2013, “Trucks and HD Vehicles Technical Requirements and Gaps for Lightweight and Propulsion Materials,” DOE VTO Workshop Report No. DOE/EE-0867, February 2013.
3. Muralidharan, G., “Low-cost Fe-Ni-Cr alloys for high-temperature valve applications,” U. S. Patent No. 9,605,565, March 28, 2017.
4. Muralidharan, G., “Low-cost, high-strength Fe-Ni-Cr alloys for high-temperature exhaust valve applications,” U. S. Patent No. 9,752,468 B2, September 5, 2017.

I.2.B.2 Task 2B: Oxidation-Resistant Coated Exhaust Valves for High-Temperature Applications

Sebastien Dryepontdt, Principal Investigator

Oak Ridge National Laboratory
1 Bethel Valley Road
Oak Ridge, TN 37932
E-mail: dryeponttsn@ornl.gov

Jerry L. Gibbs, DOE Technology Manager

U.S. Department of Energy
E-mail: jerry.gibbs@ee.doe.gov

Start Date: October 1, 2016	End Date: September 30, 2018	
Project Funding (FY18): \$160,000	DOE share: \$160,000	Non-DOE share: \$0

Project Introduction

The expected temperature increase in LD and HD internal combustion engines to improve engine efficiency will require new material solutions. New high-temperature high-strength alloys may suffer from corrosion, and corrosion-resistant coatings might be required to reach the expected component lifetime. One main concern is the coating impact on the alloy mechanical properties, and in particular its fatigue resistance. ORNL is, therefore, developing coatings for valve application and is conducting fatigue testing on valve Alloy 31V (57Ni-23Cr-13Fe-2Mo-2.3Ti-1.3Al-0.9Nb) with and without a protective aluminide or MCrAlY coating at the specimen surface.

Objectives

The overall goal of this project is to develop and characterize oxidation-resistant coatings that improve the mechanical performance of valve alloys in aggressive environments. In FY 2018, the project focused on developing new procedures to fabricate slurry coatings at various temperatures to match the 31V alloy heat-treatment. Another objective was to assess the impact of NiCoCrAlY coatings on the HCF performance of Alloy 31V at 816°C.

Approach

Several 31V coupons were dipped in ORNL's slurry mixture and then annealed in vacuum at 750 to 1,000°C for duration ranging from 3 to 10h. The specimens were then cross-sectioned using standard metallography techniques to assess the coating thickness and alloy grain size. 31V fatigue specimens were machined and then sent to Stony Brook University for NiCoCrAlY-coating deposition. The specimens were then annealed along with bare specimens according to the standard 31V heat-treatments: solution anneal for 1h at 1,100°C, first aging treatment at 850°C for 4h and second aging treatment at 730°C for 4h. The bare and coated specimens were finally fatigue tested at 816°C with applied stresses varying from 345 MPa to 483 MPa.

Results

The slurry aluminide coatings fabricated at the surface of Alloy 31V after annealing for 3 to 10 h at 750 to 1,000°C are shown in Figure I.2.B.2.1. All of the coatings were quite uniform with a coating thickness lying between 40 μm and 60 μm, except for the coating annealed at 750°C for 6h. The coating thickness for the coupon annealed at 850°C for 6h was superior to the coating thicknesses of the coupons annealed for 6h at 950°C or 10h at 850°C. This is a very surprising result since the coating thickness is expected to increase with increasing temperature and annealing duration. Further work is required to precisely control the coating thickness at a given temperature, but these results clearly highlight the possibility to fabricate good coatings at

850 to 1,100°C. In particular, an attractive option is to fabricate the slurry coating during the 31V first aging treatment at 850°C.

The HCF performance of bare and NiCoCrAlY-coated 31V specimens at 816°C is compared in Figure I.2.B.2.2. Clearly, the coating does not degrade the fatigue properties of the 31V Alloy. These tests were conducted in air and one could assume that if similar tests were conducted in more aggressive environments containing H₂O or sulfur dioxide, the HCF properties of the bare alloy would degrade significantly while the HCF properties of the coated alloy would remain the same.

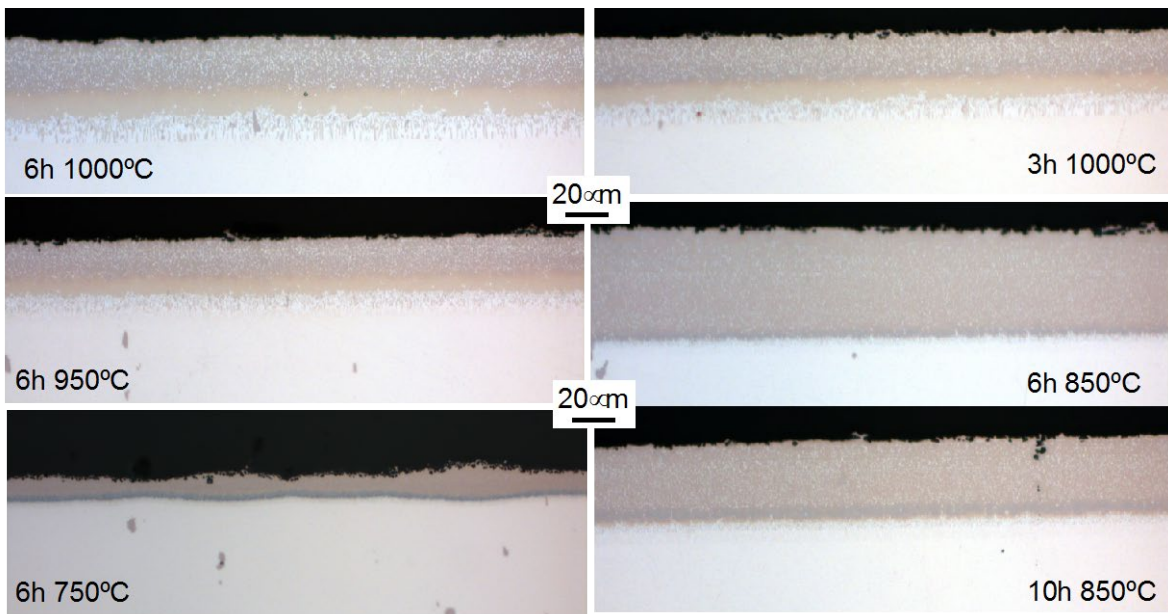


Figure I.2.B.2.1. Aluminide coatings at the surface of 31V coupons fabricated at temperatures varying from 750 to 1,000 °C. Source: ORNL.

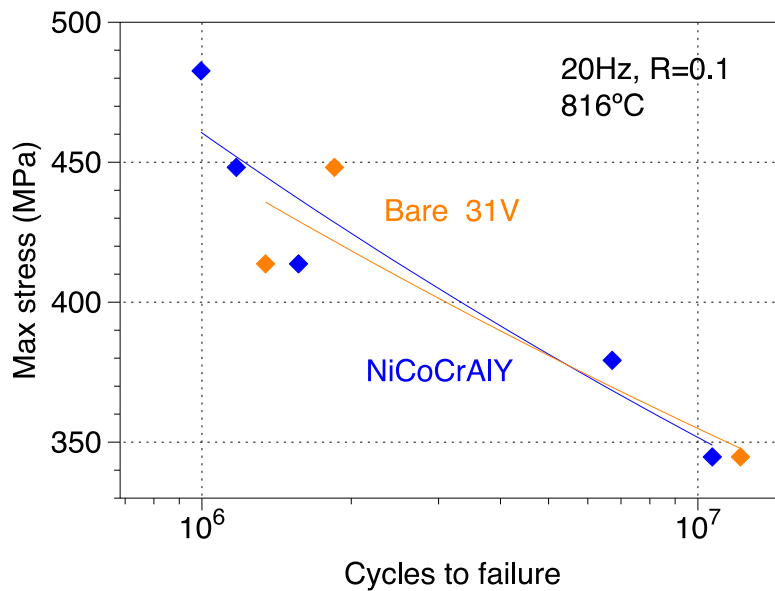


Figure I.2.B.2.2. Comparison of the HCF properties at 816°C of bare and NiCoCrAlY-coated 31V valve alloy. Source: ORNL.

Conclusions

Successful fabrication of slurry aluminide coatings at the surface of 31V coupons were achieved at temperatures ranging from 850 to 1,000°C. This result highlights the possibility to match Alloy 31V heat-treatment during the coating fabrication process. The HCF performance of the NiCoCrAlY-coated 31V alloy was similar to the HCF performance of bare 31V at 816°C, which confirmed that corrosion-resistant coatings are a viable solution for exhaust valve applications at very high-temperature.

Key Publications

1. Dryepontd, S., B. Armstrong, J. A. Haynes, and Y. Zhang, 2018, “HCF performance of bare and coated 31V alloy,” *International Conference on Metallurgical Coatings and Thin Films 2018*, April 23–27, 2018, San Diego, CA, USA.

Acknowledgements

The author would like to thank C. S. Hawkins, T. Lowe, T. Jordan, M. Howell, N. Schaflein, and A. E. Marquez Rossy for helping with the experimental work.

I.2.B.3 Task 3B: High-Temperature Components: Alumina-Forming Cast Turbo Housing Alloys Capable of 950 °C

Michael P. Brady, Principal Investigator

Oak Ridge National Laboratory
Materials Science and Technology Division
1 Bethel Valley Road
Oak Ridge, TN 37831
E-mail: bradymp@ornl.gov

Jerry L. Gibbs, DOE Technology Manager

U.S. Department of Energy
E-mail: jerry.gibbs@ee.doe.gov

Start Date: October 1, 2016

End Date: September 30, 2018

Project Funding (FY18): \$180,000

DOE share: \$180,000

Non-DOE share: \$0

Project Introduction

Automotive exhaust components will see temperatures of ≥ 900 to 950°C in the near-future in order to reach efficiency targets. The cast alloys currently used for turbocharger housings and exhaust manifolds are at their upper-temperature limit for creep and/or oxidation. Therefore, new, cost-effective alloys will be required to meet these increasing operating temperature requirements.

Objectives

The goal of this subtask is to increase the upper-temperature oxidation limit to ≥ 900 to 950°C for next-generation cast austenitic stainless steel exhaust gas components. Candidate alloys will utilize an Fe(Ni) base with ≤ 25 -30 wt.% Ni to remain cost-competitive, as well as minimize use of other costly alloying additions such as Mo, Nb, W, etc.

Approach

The approach of this effort is to increase the upper-temperature oxidation limit of cast alloys to ≥ 900 to 950°C for next-generation exhaust gas components by formation of aluminum oxide (Al_2O_3) as the protective oxide scale, as opposed to conventional cast stainless steels, which use chromium(III) oxide (Cr_2O_3) for oxidation protection. Although Al_2O_3 is far more protective (order of magnitude slower-growing) in exhaust environments containing high levels of corrosive water vapor, it is challenging to balance the ability to form Al_2O_3 with needed mechanical properties and cost targets. To accomplish this, an alloy design strategy leveraging past successful development of Cr_2O_3 -forming cast CF8C-Plus and CN12-Plus alloys for exhaust components, in light of recent successes at ORNL for development of wrought and cast forms of Al_2O_3 -forming austenitic (AFA) alloys, was pursued.

Results

In FY 2016 and FY 2017, exploratory alloy development efforts were directed towards design and initial evaluation of an Al-modified cast form of CF8C-Plus. Screening of oxidation and mechanical properties of first generation cast AFA stainless steels in laboratory arc-cast (< 1 kg) and small industrial cast heats with collaborator MetalTek International (< 500 kg) showed potential to achieve both oxidation resistance and mechanical property targets at ≤ 25 weight percent (wt.%) Ni. Although cyclic oxidation specific mass change data showed initially promising behavior, cross-section analysis in FY 2018 showed that these alloys did not form continuous Al_2O_3 scales, but rather exhibited a moderate degree of internal oxidation above 800°C in the aggressive screening conditions used (1-h cycles in air + 10% H_2O to simulate exhaust gas). A second iteration of cast alloys refined from this feedback were manufactured in laboratory-scale vacuum arc-castings in the

latter half of FY 2018. Design modification strategies were further informed by computational thermodynamics and leveraged recent findings from ORNL development efforts devoted to 35Fe/35Ni-base cast AFA alloys for use up to 1,100°C in industrial process environments (these higher Ni alloys are too costly for exhaust applications).

Computational thermodynamic calculations of volume fraction percentages for the candidate cast AFA alloys are shown in Table I.2.B.3.1. The alloys were designed to utilize a range of key carbide and intermetallic strengthening phases, with Ni levels of 22–25 wt.% and Al, Cr, and microalloying additions potentially capable to achieve protective Al₂O₃ scale formation at 950°C. For reference comparative purposes, a laboratory arc-casting of the conventional Cr₂O₃-forming alloy 1.4826 was also manufactured.

Table I.2.B.3.1. Calculated Volume Fraction in Percentage (As-Cast at 25 °C Predicted by JMatPro v9).

Alloy ID	FCC-Fe	MC	M7C3	M23C6	M2(C,N)	M6C	NiAl	MB2	M3B2	BCC-Fe	Melting point, °C
Gen. 2 AFA1	90.74	1.48	1.40	2.18			4.19	0.01			1215
Gen. 2 AFA2	88.55	1.48	0.30	3.51		0.87	5.21		0.08		1215
Gen. 2 AFA3	90.68	2.98	0.00	1.24			5.10	0.01			1190
Gen. 2 AFA4	83.57	1.59		5.25			8.30		0.06	1.22	1095
Gen. 2 AFA5	88.89	0.69	2.19	4.48			3.72		0.03		1250
1.4826 [1]	84.61		0.59	8.56	0.16					6.08	1275

Initial in progress cyclic oxidation data are shown in Figure I.2.B.3.1 for the five candidate second generation cast AFA alloys relative to two of the best performing first generation cast AFA alloys and several commercial cast Cr₂O₃-forming alloys under an aggressive screening condition of 1.0 h cycles at 950°C in air with 10% H₂O. All of the second generation cast AFA alloys showed low, positive specific mass changes consistent with protective Al₂O₃-scale formation; whereas the first generation cast AFA and commercial Cr₂O₃-forming alloys exhibited scale spallation and mass loss. Figure I.2.B.3.2 shows initial tensile data obtained at room temperature, 700°C, and 900°C. The candidate second generation cast AFA alloys showed superior strength to the 1.4826 reference control. Although elongations of the second generation cast AFA alloys were lower than that observed for 1.4826, all but one candidate AFA alloy exhibited total plastic elongations in excess of ~10%.

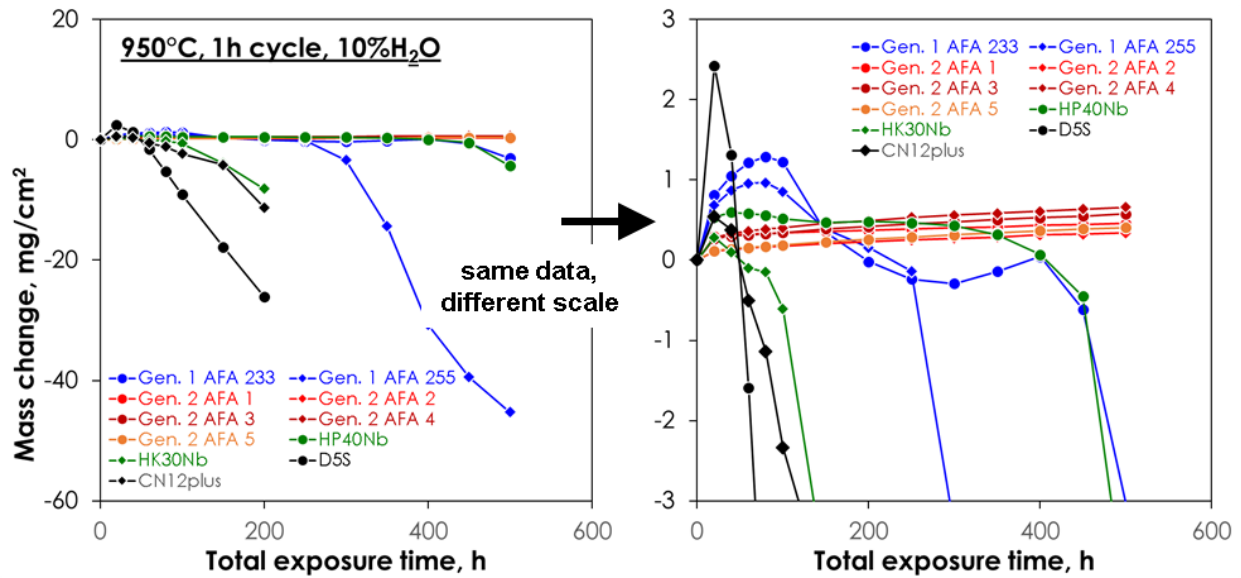


Figure I.2.B.3.1. Cyclic oxidation at 950°C in air with 10% H₂O. Source: ORNL.

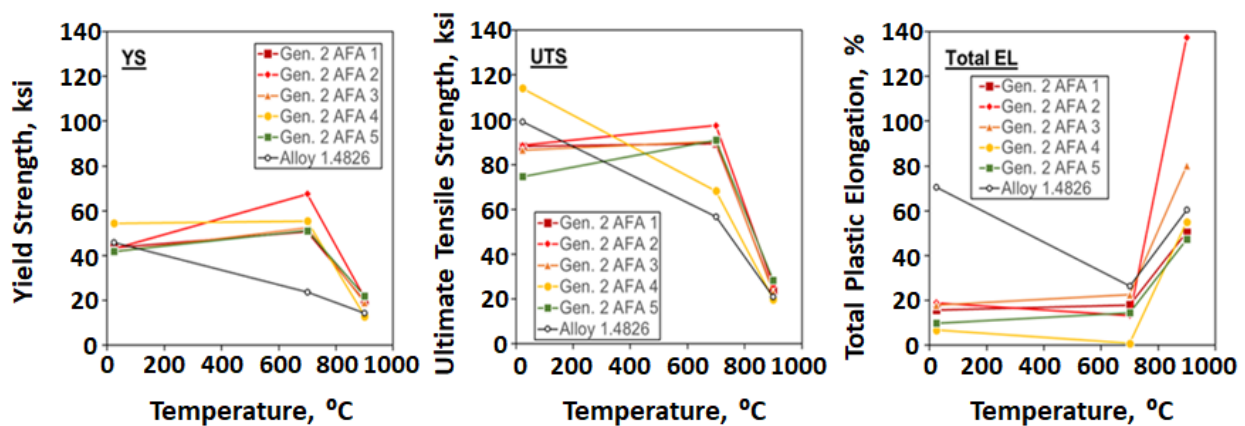


Figure I.2.B.3.2. Tensile properties for second generation cast AFA vs. 1.4826. Source: ORNL.

Conclusions

The second generation cast AFA candidate alloys show good promise for oxidation resistance via protective Al₂O₃ scale formation at 950°C, as well as promising tensile properties. Longer-term oxidation exposures, creep studies, and thermophysical properties will be pursued in FY 2019, with a down-select of two compositions for trial small-scale industrial heats. Alloy optimization will be guided by advanced characterization of the oxide scale structure and strengthening precipitates, as well as computational activities including CALPHAD and machine-learning.

Key Publications

1. Maziasz, P. J., 2018, "Development of creep-resistant and oxidation-resistant austenitic stainless steels for high-temperature applications," *JOM*, Vol. 70, No. 1, pp. 66–75.

Acknowledgements

The authors thank P. J. Maziasz, who was the original principal investigator for this project and retired in 2018.

I.2.C High-Temperature Lightweight Engine Materials (Oak Ridge National Laboratory)

J. Allen Haynes, Principal Investigator

Propulsion Materials
Oak Ridge National Laboratory
1 Bethel Valley Rd.
Knoxville, TN 37831
E-mail: haynesa@ornl.gov

Jerry L. Gibbs, DOE Technology Manager

U.S. Department of Energy
E-mail: jerry.gibbs@ee.doe.gov

Start Date: October 1, 2016	End Date: September 30, 2018	
Project Funding (FY18): \$660,000	DOE share: \$660,000	Non-DOE share: \$0

Project Introduction

The High-Temperature Lightweight Engine Materials Project consists of four tasks that are focused on early-stage research in pursuit of advancing the basic mechanical properties, manufacturability, and addressing the affordability of propulsion materials. These tasks have the common goal to develop advanced cast Al alloys for high-temperature engine components. The specific tasks include the following:

1. High-Temperature Lightweight Components: Fundamental Properties & Processing to Develop Higher Temperature Al Alloys.
2. Additive Manufactured (AM) Bimetallic Material Bonding for Increased Knock Survival in Lightweight Pistons.
3. Development of New Turbocharger Compressor Wheels for HD Engines (CRADA with Cummins Inc.).
4. High-Temperature Lightweight Components: Alloy Development for Higher Performance Powertrains.

The following sections of this report outline the specific task work conducted at ORNL in the areas of predictive engineering, process development, and enabling technologies for propulsion materials. Each task supports one or more goals within the VTO mission of developing higher performance materials that can withstand increasingly extreme environments and address the future properties needs of a variety of high-efficiency powertrain types, sizes, fueling concepts, and combustion modes.

I.2.C.1 Task 1C: High-Temperature Lightweight Components: Fundamental Properties and Processing to Develop Higher Temperature Al Alloys

Amit Shyam, Co-Principal Investigator

Oak Ridge National Laboratory
1 Bethel Valley Rd.
Oak Ridge, TN 37831
E-mail: shyama@ornl.gov

J. Allen Haynes, Co-Principal Investigator

Oak Ridge National Laboratory
1 Bethel Valley Rd.
Oak Ridge, TN 37831
E-mail: haynesa@ornl.gov

Jerry L. Gibbs, DOE Technology Manager

U.S. Department of Energy
E-mail: jerry.gibbs@ee.doe.gov

Start Date: October 1, 2016	End Date: September 30, 2018	
Project Funding (FY18): \$180,000	DOE share: \$180,000	Non-DOE share: \$0

Project Introduction

A family of cast Al alloys, called AlCuMnZr (ACMZ) alloys, were developed at ORNL with two industry partners over a four-year period. This family of alloys displays unique properties, such as good castability, hot-tear resistance, and excellent elevated temperature mechanical properties at a modest price increase compared to A356 or A319 type of commercial alloys. In this project, the feasibility of applying unique processing conditions, such as additive or wrought processing, was explored. Since the hot-cracking resistance of some ACMZ alloys is outstanding, weld processing was also explored. This report summarizes the results of those feasibility trials on lightweight high-temperature Al alloys.

Objectives

The overall project had the following two objectives:

- To perform wrought processing and weldability trials on at least one ACMZ alloy composition.
- To perform rapid solidification processing on at least one ACMZ alloy composition to determine the feasibility of additive manufacturing in ACMZ alloys.

Approach

The work consisted of two parts. The first part consisted of wrought processing and gas tungsten arc welding of one composition of ACMZ alloy with 6.6 wt% Cu. This composition was compared with the welding behavior of AA6061 alloy plates. The microstructure in the weld zone was compared with and without the addition of filler metal for AA6061 and the ACMZ alloy with 6.6 wt% Cu. The second part of the work consisted of understanding the rapid solidification behavior of ACMZ type alloys through performing laser track experiments. A design of experiments study was performed to vary a range of parameters while the laser tracks were made on five compositions of ACMZ alloys (with 6.0, 6.6, 7.3, 8.0, and 9.0 wt% Cu). The microstructural features associated with the laser weld cross-sections along with the heat-affected zones were characterized by optical and SEM techniques. Select compositions were also analyzed by melt spinning techniques. Together, the experiments that were performed determined the feasibility of wrought, weld, and additive processing of select ACMZ alloys.

Results

Characterization of the weld processed specimens through x-ray non-destructive evaluation is shown in Figure I.2.C.1.1. The plates were wrought processed prior to welding. The top image (marked #1) corresponds to an AA6061-type alloy, while the bottom image (marked #3) corresponds to an ACMZ alloy with 6.6 wt% Cu. Within the images, the top weld was made with a filler metal and the bottom weld was made without filler metal.

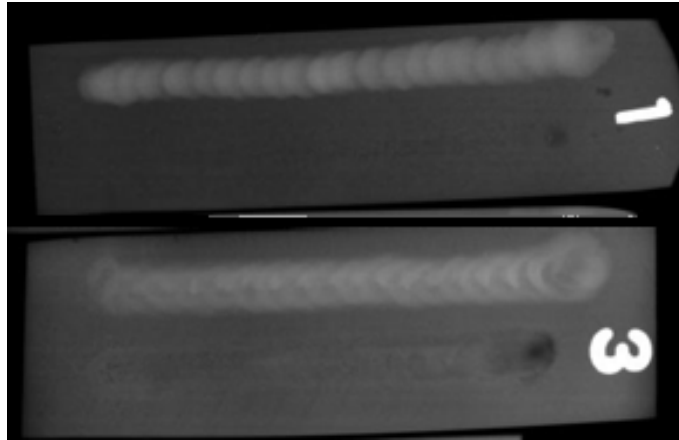


Figure I.2.C.1.1. X-ray non-destructive evaluation of welded AA6061 (top) and Al6.6wt%Cu specimen (bottom).
Source: ORNL.

The porosity around the welds are displayed as dark spots in Figure I.2.C.1.1. The porosity was observed mainly in the weld without the filler metal. Porosity was observed in both AA6061 and the ACMZ alloy with 6.6 wt% Cu. Better cleaning procedures prior to welding may help reduce or eliminate residual porosity. There is no center crack in all welds, with and without filler metal. The unconstrained coupon benefited the welding quality; constrained welds may not produce better quality welds. Overall, it was demonstrated with the limited testing and microstructural evaluation that the welding behavior of the 6.6 wt% Cu variant of the ACMZ alloy was comparable to an AA6061 alloy.

The experimental procedure for pulsed-laser welding study on ACMZ alloys is shown in Figure I.2.C.1.2. The experiments were carried out using the Renishaw AM250 laser additive manufacturing system at the Manufacturing Demonstration Facility (MDF) at ORNL.

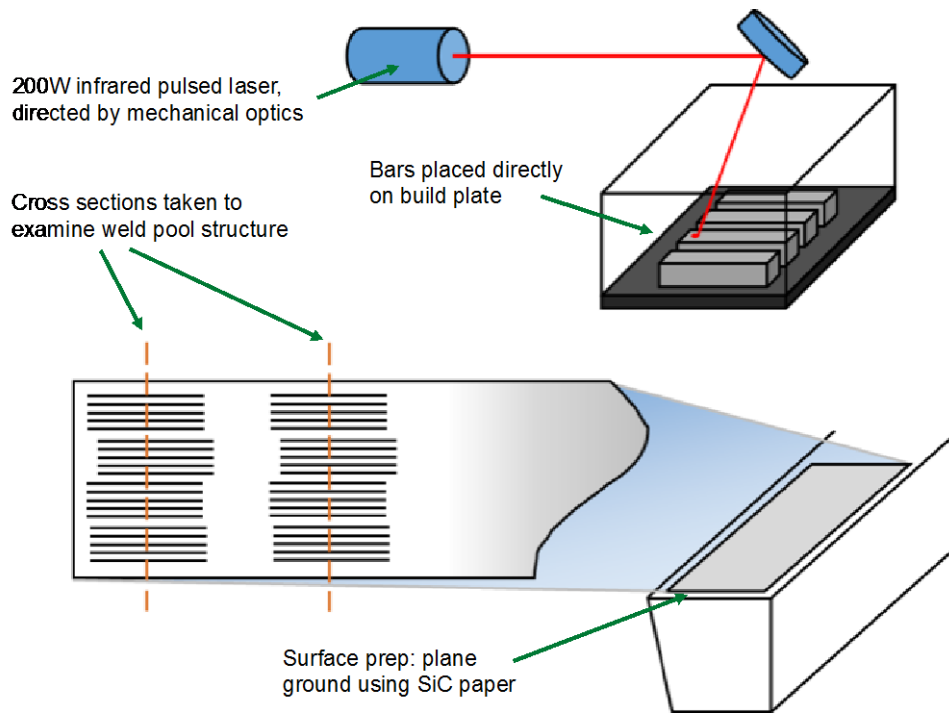


Figure I.2.C.1.2. Experimental setup for pulsed-laser welding study. Source: ORNL.

Design of experiments was performed to examine the effect of point distance and exposure time on weld pool size, cracking, and microstructure. Five laser welds are made with parameters specified by each cyan point in Figure I.2.C.1.3. Points are selected to distinguish the main effects of point distance and exposure time (blue arrows), and the effects of heat input and effective velocity (red arrows). Here, point distance is a machine parameter setting the spacing of laser spots along the length of the weld. That is, the weld line is made up of a series of laser points at certain distance apart. The effects of the laser pulsing parameters on the cross-section of welds are shown in Figure I.2.C.1.4. All scale bars in this image are 20 μm .

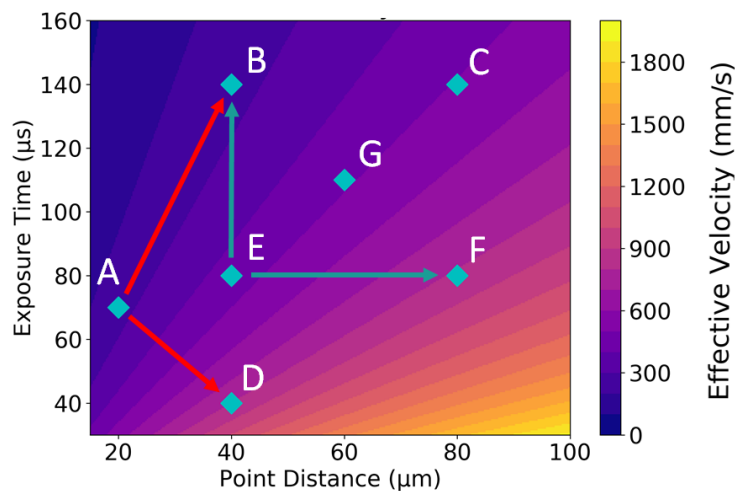


Figure I.2.C.1.3. Design of experiments to determine the effect of pulsed-laser parameters on microstructure of an ACMZ alloy with 6.6 wt% Cu. Source: ORNL.

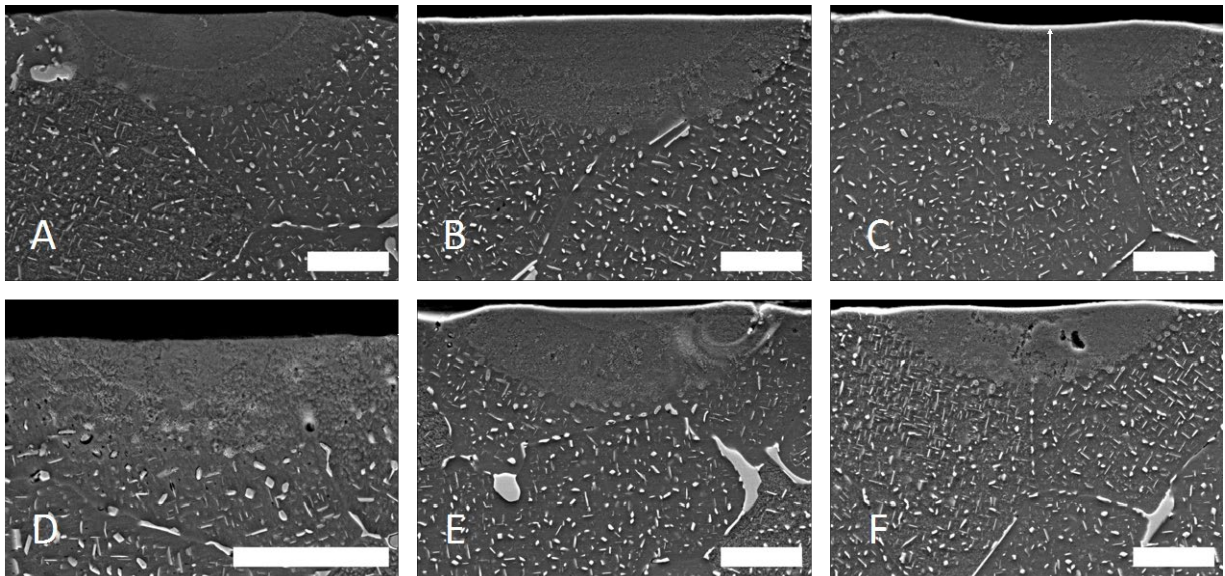


Figure I.2.C.1.4. Representative secondary electron micrographs of laser tracks demonstrating the main effects of point distance, exposure time, and heat input on microstructure—see Figure I.2.C.1.3 for labels with conditions. The double-headed arrow in (c) highlights the weld depth. All scale bars are 20 μm . Source: ORNL.

Common defects that were observed included porosity in the heat-affected zone near the edge of the weld pool. Quantitative analysis of the laser weld pool dimensions was performed under various conditions. It was concluded that increasing duty cycle and linear heat input by increasing exposure time in pulsed-laser welding of ACMZ alloys increases the size of the weld pool and decreases the number of solidification defects. Based on the results, optimum conditions for selected laser melting-based additive manufacturing of these alloys was identified. Melt spinning was also performed for selected conditions of ACMZ alloys at a Michigan Technological University facility, where it was revealed that the melt-spun microstructures were comparable to the microstructures revealed by weld-tracking of the same alloys.

Conclusions

A focused study on a selected composition of ACMZ alloys revealed that wrought, weld, and rapid solidification processing of these cast Al alloys is feasible. More studies are needed to define the optimum processing range of these alloys—especially the Cu content-specific processing schemes. These will be the subject of future investigations.

Acknowledgements

Tom Muth and Wei Tang of ORNL are acknowledged for their assistance with the wrought and weld processing. Phil Staublin of Michigan Technological University was employed a summer intern at ORNL during this work. He and Keith Carver of ORNL are also acknowledged for their contributions to the rapid solidification processing portion of the work.

I.2.C.2 Task 2C: Additive Manufactured (AM) Bimetallic Material Bonding for Increased Knock Survival in Lightweight Pistons

Derek Splitter, Co-Principal Investigator

Oak Ridge National Laboratory
1 Bethel Valley Rd.
Oak Ridge, TN 37831
E-mail: splitterda@ornl.gov

Amit Shyam, Co-Principal Investigator

Oak Ridge National Laboratory
1 Bethel Valley Rd.
Oak Ridge, TN 37831
E-mail: shyama@ornl.gov

Jerry L. Gibbs, DOE Technology Manager

U.S. Department of Energy
E-mail: jerry.gibbs@ee.doe.gov

Start Date: October 1, 2016	End Date: September 30, 2018	
Project Funding (FY18): \$130,000	DOE share: \$130,000	Non-DOE share: \$0

Project Introduction

Low Speed Pre-Ignition (LSPI) has been the focus of ongoing areas of study in boosted, downsized spark-ignited engines that often result in terminated engine operation. While the root causes of LSPI are still being explored, little has been done regarding mitigating piston failure due to LSPI. In FY 2016, ORNL developed an initial project to explore a potential toughening mechanism that could localize strengthening while maintaining global properties. By combining additive manufacturing with casting, a metal-metal additively manufactured interpenetrating phase composite (AMIPC) was developed with the expectation that the harder reinforcing phase would increase the strength of the composite over the monolithic material with an increase in ductility as well. In FY 2017, the produced AMIPCs were characterized across mechanical and thermal properties. This work was highlighted in an article that was published in *Materials and Design* [1], as well as on the cover of the October 2017 issue of ASM International's *Advanced Materials and Processes* magazine [2], as shown in Figure I.2.C.2.1. In FY 2016 and FY 2017, it was determined that the AMIPC system has unique thermomechanical properties that were observed in initial traditional materials testing processes, tensile, compression testing, and thermal conductivity determination. Based on the evaluated performance of the project in FY 2017, the project was selected to continue into FY 2018, where furthering the understanding of the thermomechanical behavior of the AMIPC material system was undertaken. In FY 2018, the work has centered on understanding how mechanical load is shared in the two material phases of the AMIPC system, and how porosity and material constituent bonding can affect thermal conductivity.



Figure I.2.C.2.1. Project feature on the cover of the October 2017 issue of *Advanced Materials and Processes* [2].
Source: ASM International.

Objectives

This task aims to increase piston survivability of extreme knock and super-knock by employing the overcasting of an Al alloy onto optimally placed higher strength alloys, such as steel and Ti. The approach aims to improve the local knock survival in high-stress areas while retaining global material properties for knock-free operation. For FY 2018, the objective was to determine the constituent contributions to the macro-scale tensile performance using neutron diagnostics and porosity and material bonding effects on thermal conductivity using a simulation-based approach.

Approach

A paper was published in *Additive Manufacturing* that described results from activities conducted in FY 2018 in thermal conductivity modeling. [3] The results highlighted two factors. One was that lattice geometry, specifically body centered cubic and octet truss lattices, had varying effects on thermal conductivity of the AMIPC system. The results were simulation-based on theoretical limits, which were supported by theoretical effects of porosity and porosity locations using micro-computed tomography (microCT) measurements of as-produced porosity. A secondary effort was also undertaken to investigate load-sharing behavior of the constituents in the AMIPC system, using neutron diffraction measurements. This approach was used to study if and how load-sharing in tensile loading of various volume fractions of reinforcements in the AMIPC system behaved. For both the thermal conductivity and tensile testing work, materials of Al A356 for the infiltrate and 316L stainless steel for the reinforcement in the CALPHAD (CALculation of PHase Diagram) system were used.

Results

Figure I.2.C.2.2 shows microCT reconstructions of an as-fabricated AMIPC, with the 316L shown in dark contrast and the A356 in bright contrast. The low-magnification reconstruction shown in Figure I.2.C.2.2.(a) displays several unit cells, illustrating the periodic three-dimensional structure of the interpenetrating phase composite. The higher magnification reconstructions shown in Figure I.2.C.2.2.(b) are of the same unit cell

and are colored to highlight interfacial porosity, porosity in the A356, and porosity in the 316L. Both the A356 and 316L contain closed spheroidal pores, but the pores in the A356 have a mean spherical diameter of $120\ \mu\text{m}$ and are significantly larger than the pores in the 316L, which have a mean spherical diameter of $30\ \mu\text{m}$. The irregular three-dimensional pores found in the A356 are commonly observed in Al alloy castings and have been ascribed to solidification shrinkage.

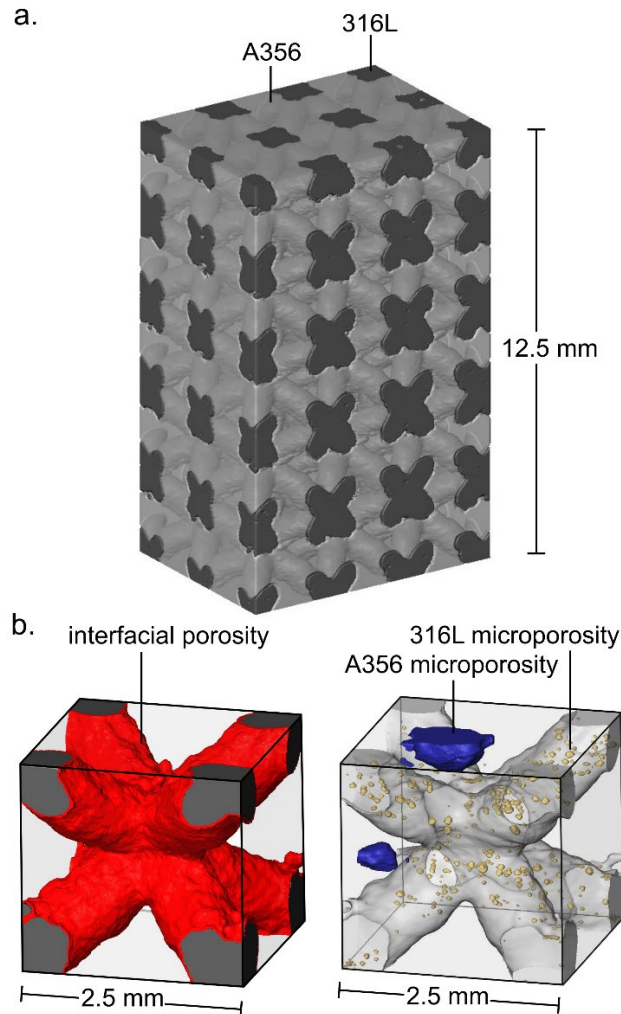


Figure I.2.C.2.2.(a) Low-magnification microCT reconstruction of A356/316L composite with the 316L shown in dark contrast and the A356 in bright contrast; and (b) Higher magnification microCT reconstructions showing a single unit cell with interfacial porosity, microporosity in the A356, and microporosity in the 316L highlighted in red, blue, and yellow, respectively [3]. Source: Additive Manufacturing.

Finite element simulations were performed in the COMSOL multiphysics software package using an unstructured mesh with tetrahedral elements. Results using a normalized thermal conductivity, \tilde{K} , defined as:

$$\tilde{K} = \frac{K_{\text{eff}} - \min(K_1, K_2, \dots)}{\max(K_1, K_2, \dots) - \min(K_1, K_2, \dots)} \quad (1)$$

are shown in Figure I.2.C.2.3. The arguments of the *min* and *max* functions are the thermal conductivities in the constituents. For the fully dense composites, there are only two constituents – phases 1 and 2 with volume

fractions of $V_{f,1}$ and $V_{f,2}$ respectively. For the porous composites, the porosity is treated as a third constituent with concentration, p .

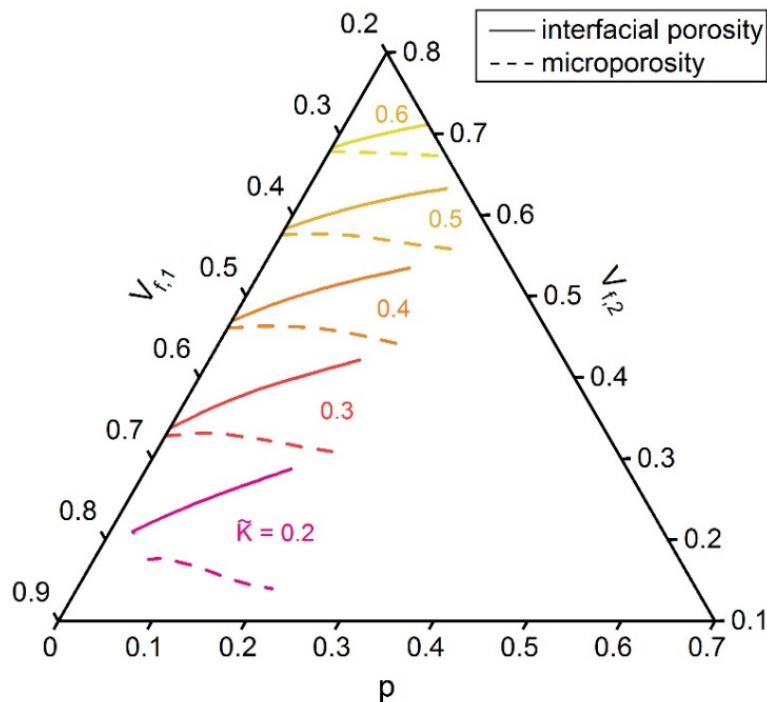


Figure I.2.C.2.3. Ternary diagram with contours of constant \tilde{K} for body centered cubic composites with either microporosity or interfacial porosity. Source: Additive Manufacturing.

A key difference between fully dense composites and composites with interfacial porosity is that fully dense composites possess rescaling invariance (meaning their effective thermal conductivity does not depend on the unit cell size), while composites with interfacial porosity do not. The results indicate that the interfacial porosity reduces the thermal conductivity more than the inter-material porosity or microporosity in the AMIPC system.

The second aspect analyzed on the AMIPC system in FY 2018 was tensile loading. The project analyzed the tension tests performed on AMIPCs using neutron diffraction for microscopic and conventional load frame macroscopic analysis techniques. The tests were conducted on AMIPCs with different volume fractions of 316L stainless steel, with 20%, 30%, 40%, and 50% by volume 316L stainless steel composite in comparison to a bare A356 sample. Tests with 30% stainless steel reinforcement without Al, as well as just the Al (i.e., no stainless steel reinforcement), were conducted. The results of the macroscopic tests are presented in Figure I.2.C.2.4, which highlight several aspects. First, the specimens appear to load like the A356 up until the failure point of the A356. Thereafter, specimens with volume fractions less than 40% nominal stainless steel show behavior where the displacement (i.e., strain) cannot be furthered much more than the A356 sample, but the stress is limited to that of the Al. However, the volume fractions of 40% and 50% stainless steel exhibited a significant increase in the strain, with no loss in load-carrying capability. This behavior is under current analysis and understanding this change in behavior as a function of volume fraction is planned. Interestingly, the stress carried in the plastic deformation phase appears to be qualitatively proportional the volume fraction of the reinforcement.

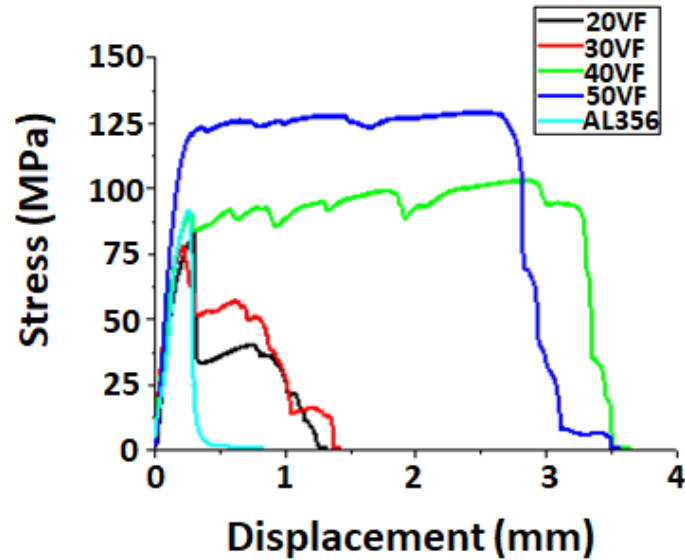


Figure I.2.C.2.4. Macroscopic loading of different volume fractions (VF) (i.e., 20VF, 30VF, 40VF, and 50VF, for 20, 30, 40, and 50% reinforcement by volume, respectively) and Al356 (no reinforcement). Results highlight that below a 50% volume fraction, the stress is a function of the Al356, where the maximum strain (displacement) is a function of the reinforcement, where a critical volume fraction (~40% volume fraction) displays a significant increase in the strain. Source: ORNL.

These macro-level aspects are currently being investigated at the microscopic level in the phase-specific loading of the different specimens. For example, the 40% volume fraction sample has been initially analyzed, where the results indicated there were non-uniform strains in the lattice of the two constituents. Specifically, results in Figure I.2.C.2.5 show that the lattice strain in the Al constituent are higher than those in the stainless steel phase (e.g., Fe311 in Figure I.2.C.2.4). Note that Figure I.2.C.2.5 only illustrates the 311 crystallographic orientations, but the preliminary analysis indicated that similar results are present in other crystallographic orientations.

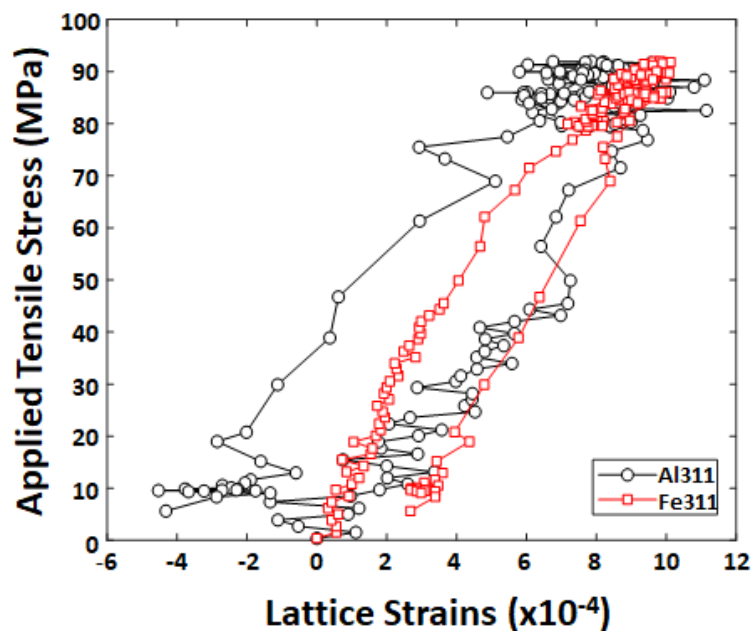


Figure I.2.C.2.5. Microscopic stress and lattice strain as measured by neutron diffraction for Al and stainless steel (Fe) in the 311 crystallographic plane for the 40% volume fraction stainless steel sample in tensile loading. Source: Rice/ORNL.

Conclusions

This work demonstrated through finite element simulations that the structure of the A356/316L interface influences the effective thermal conductivity of AMIPCs. In perfectly bonded composites, the thermal conductivity is independent of the lattice parameter. Moreover, in composites with interfacial porosity, the size and structure of the porosity influence thermal conductivity. Specific relations of these findings are under further investigation on how to influence the mechanical behaviors of the composites. The second significant finding of this year's progress was the load-sharing of the AMIPC system. Macroscopic findings highlighted that the strain carrying capability of the AMIPC system is a function of the reinforcement, where there is a nonlinear behavior and where volume fractions of 40% nominal reinforcement performed significantly better than volume fractions less than 40%. Microscopic behavior indicated that the strain sharing of the AMIPC constituents was non-uniform. This preliminary finding is under further investigation but indicates the fundamental mechanics that need to be further understood to optimize the AMIPC system.

Key Publications

1. Pawlowski, A. E., Z. C. Cordero, M. R. French, T. R. Muth, J. K. Carver, R. B. Dinwiddie, A. M. Elliott, A. Shyam, and D. A. Splitter, 2017, "Producing hybrid metal composites by combining additive manufacturing and casting," *ASM Advanced Materials and Process*, October 2017, pp. 16–21.
2. Moustafa, A. R., R. B. Dinwiddie, A. E. Pawlowski, D. A. Splitter, A. Shyam, and Z. C. Cordero, 2018, "Mesostructure and porosity effects on the thermal conductivity of AMIPCs," *Additive Manufacturing*, Vol. 22, pp. 223–229. doi: 10.1016/j.addma.2018.05.018.

References

1. Pawlowski, A. E.; Z. C. Cordero; M. R. French; T. R. Muth; and D. A. Splitter, 2017, "Damage-tolerant metallic composites via melt infiltration of additively manufactured preforms," *Materials & Design*, Vol. 127, 5 August 2017, pp. 346-351.
2. Pawlowski, A. E., Z. C. Cordero, M. R. French, T. R. Muth, J. K. Carver, R. B. Dinwiddie, A. M. Elliott, A. Shyam, and D. A. Splitter, 2017, "Producing hybrid metal composites by combining additive manufacturing and casting," *ASM Advanced Materials and Process*, October 2017, pp. 16–21.
3. Moustafa, A. R., R. B. Dinwiddie, A. E. Pawlowski, D. A. Splitter, A. Shyam, and Z. C. Cordero, 2018, "Mesostructure and porosity effects on the thermal conductivity of AMIPCs," *Additive Manufacturing*, Vol. 22, pp. 223–229. doi: 10.1016/j.addma.2018.05.018.

I.2.C.3 Task 3C: Development of New Turbocharger Compressor Wheels for HD Engines (CRADA with Cummins Inc.)

Thomas R. Watkins, Co-Principal Investigator

Oak Ridge National Laboratory
1 Bethel Valley Rd.
Oak Ridge, TN 37831
E-mail: watkinstr@ornl.gov

Corey Trobaugh, Co-Principal Investigator

Cummins Inc.
1900 McKinley Ave.
Columbus, IN 47201
E-mail: corey.trobaugh@cummins.com

Jerry L. Gibbs, DOE Technology Manager

U.S. Department of Energy
E-mail: jerry.gibbs@ee.doe.gov

Start Date: October 1, 2016	End Date: September 30, 2018	
Project Funding (FY18): \$140,000	DOE share: \$140,000	Non-DOE share: \$0

Project Introduction

Ti-Al is an intermetallic alloy with high specific strength, good corrosion/oxidation resistance at relatively high temperatures and excellent strength retention until the brittle ductile transformation temperature (~800°C) is reached. Recently, there has been increased interest in using Ti-Al for the manufacture of high-temperature engineering components, such as gas turbine blades and turbocharger components. However, its brittle nature at low temperatures makes it difficult to machine into complex shapes. Additive manufacturing holds the potential to revolutionize the manufacturing of such intricate components from this brittle alloy.

From previous work, Ti-48Al-2Cr-2Nb preforms have been successfully manufactured using the Arcam Electron Beam Melting (EBM) technique using standard build parameters. Hot Isostatic Pressing (HIP) was employed to eliminate pores and homogenize the microstructures, post-manufacture.

X-ray diffraction residual stress measurements revealed negligible residual stresses in the as-built parts as expected from the high-temperature of the powder bed during the build. The x-ray diffraction phase identification measurements revealed two phases with the matrix γ -Ti-Al and the precipitate Ti_3Al (α_2) phases. The presence of these phases was confirmed with electron backscatter diffraction measurements and microstructures were found to be consisting of equiaxed grains.

SEM-BSE images revealed these phases to be present in a duplex microstructure. Tensile tests were performed both at RT and at 500°C. Good tensile properties (YS=546±25 MPa, UTS=641±25 MPa, strain to failure=2.66±0.65%), on-par with or better than traditionally manufactured counterparts, were achieved with excellent strength retention at high-temperature in the HIPed condition. The excellent tensile properties at RT were related to the equiaxed duplex microstructures. A summary of these results is presented in Figure I.2.C.3.1.

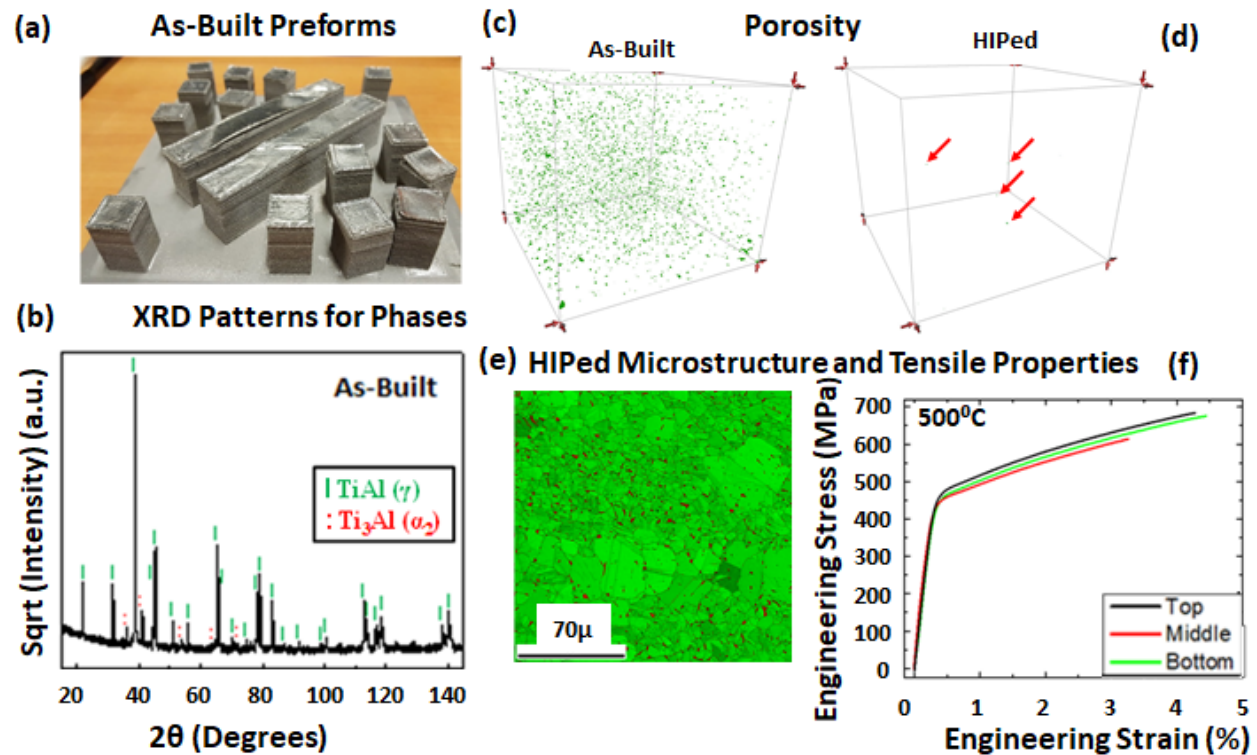


Figure I.2.C.3.1. A summary figure showing (a) the as-built preforms, (b) the x-ray diffraction (XRD) pattern from the as-built samples, porosity detection with (c) and (d) x-ray computed tomograms showing how HIP eliminates porosity, and (e) the equiaxed microstructures resulting in (f) good tensile properties. Source: ORNL.

A new batch of Ti-48Al-2Cr-2Nb powder was obtained and characterized for morphology and phase identification. Trial runs to print a prototype turbocharger compressor wheel were initiated and continued for two weeks. However, these builds failed due to a phenomenon known as ‘smoking,’ which is related to the incomplete sintering of the freshly raked powder. When enough un-sintered powder particles are present, an electrical charge builds up. The charged powder particles repel each other, blowing out the excess powder, and hence, the name ‘smoking.’ When the smoking is severe enough, it leads to inconsistent raking and sintering followed by a ‘chain-smoking’ event, thereby ending the build process.

Objectives

To develop an improved high-temperature, low-mass, cost-neutral turbocharger compressor wheel for HD engine applications using additive manufacturing, utilizing its unique ability to fabricate high-strength, low-weight structures.

Approach

The major tasks for FY 2018 were as follows:

1. Perform detailed CALculation of PHase Diagrams (CALPHAD) analyses to understand the solidification mechanisms.
2. Adjust the powder size distribution to the required spec.
3. Perform elemental analysis of the Ti-48Al-2Cr-2Nb powder.
4. Print the prototype compressor wheel.

Results

The calculated phase diagram and Scheil [1] simulations for the Ti-48Al-2Cr-2Nb (at%) alloy are presented in Figure I.2.C.3.2. Based on the composition indicated with the right dotted line (labeled 1 wt% Al loss) on the phase diagram in Figure I.2.C.3.2(a), the solidification path is expected to start in the body centered cubic B2 phase (L+B2) field. As experimentally observed and verified with the calculated phase diagram, the as-solidified structure consists of the ordered face centered tetragonal, γ -Ti-Al, and the ordered hexagonal close packed (HCP) α_2 -Ti₃Al phases. As Figure I.2.C.3.2.(a) shows, γ and α_2 phases govern the phase stability of Ti-Al binary at the composition range between the dotted lines labeled Ti-48Al (at%) and 1wt% Al loss due to evaporation (Ti-47.3Al) upon equilibrium cooling. Further, the precipitation of α_2 -Ti₃Al is promoted as the relative amount of Ti increases by losing Al during the EBM process (a total of 1 wt.% Al loss was documented with wet chemical analysis).

The Scheil simulations, as shown in Figure I.2.C.3.2.(b) and (c), are used to predict the solidification sequence under non-equilibrium solidification conditions (i.e., closer to additive manufacturing conditions). Both binary (Ti-48Al) and quaternary (Ti-48Al+Nb/Cr) systems, with the composition to replicate experimentally observed 1 wt.% loss of Al, are used (i.e., Ti-47.3Al and Ti-47.2Al-2Nb-2Cr, respectively). Here Figure I.2.C.3.2.(b) shows the solidification sequence from the liquid phase, whereas Figure I.2.C.3.2.(c) shows the formation range of the γ and α phases. The Scheil simulations are performed down to around 1350°C, which remains in the γ + α regime. For example, as to how Figure I.2.C.3.2.(b) and (c) correspond, the TiAlNbCr (Scheil) curve in Figure I.2.C.3.2.(b) indicates that α phase solidification starts at ~1505°C. Points WW and UU in Figure I.2.C.3.2.(b) and (c), respectively, correspond indicating that only α phase is precipitating out of the liquid. This continues to points XX, YY, and TT, respectively, wherein the γ phase starts to precipitate out of the liquid as well. Thus, both γ and α phases precipitate out of the liquid following curve segments XX-ZZ, YY-SS, and TT-VV. Note that the α phase is circled with red in Figure I.2.C.3.2.(a) in the equilibrium phase diagram. The α_2 phase forms from the α through a solid-state phase transformation. A similar approach can be used to interpret the Ti-Al (Scheil) binary curves.

Overall, the Scheil simulations predict that the solidification starts with the α phase, which is then joined by γ . Intriguingly, the addition of Nb and Cr affects the profile of binary Ti-48Al cooling particularly at the later stage as shown in Figure I.2.C.3.2.(b). While the binary Ti-48Al has a plateau in the ternary eutectic (L+ α + γ), that of modified quaternary extends over a much wider temperature range. The difference is attributed to the formation of γ over a wide temperature as shown in Figure I.2.C.3.2.(c) in the case of the quaternary.

These results support our hypothesis that the complex solidification path that starts in the L+B2 phase-field and ends in the γ + α_2 phases and effectively breaks the epitaxial growth during the deposition due to having different crystal structures. The numerous phase transformations during solidification and subsequent heating further refine the microstructure. Additionally, since these microstructures are phase transformation-driven, they are expected to be relatively part geometry-independent.

Following discussions with colleagues at the MDF, the existing powder size distribution was concluded to be the main cause behind the build failure and that a coarser cut of powder was needed. Powder was transported to the main campus from MDF and sieved to a -100/+200 mesh size (74-149 μ m) distribution, which was quantified using a laser diffraction powder size distribution analyzer. The sieved powder size distribution is presented in Figure I.2.C.3.3 with a mean powder size of 104 μ m.

Next, the major alloying elements, Ti, Al, Nb, and Cr, were quantified using wet chemical analysis. The results are presented in Table I.2.C.3.1. The analysis showed that our powder feedstock is within the theoretical compositional specification of Ti-48Al-2Cr-2Nb in at.%. While a computer-aided design model was obtained earlier from Cummins Inc. for prototype printing, the EBM machines at the MDF were/are currently booked until September 30, 2019. Outsourcing the printing of a prototype turbocharger compressor wheel will not occur.

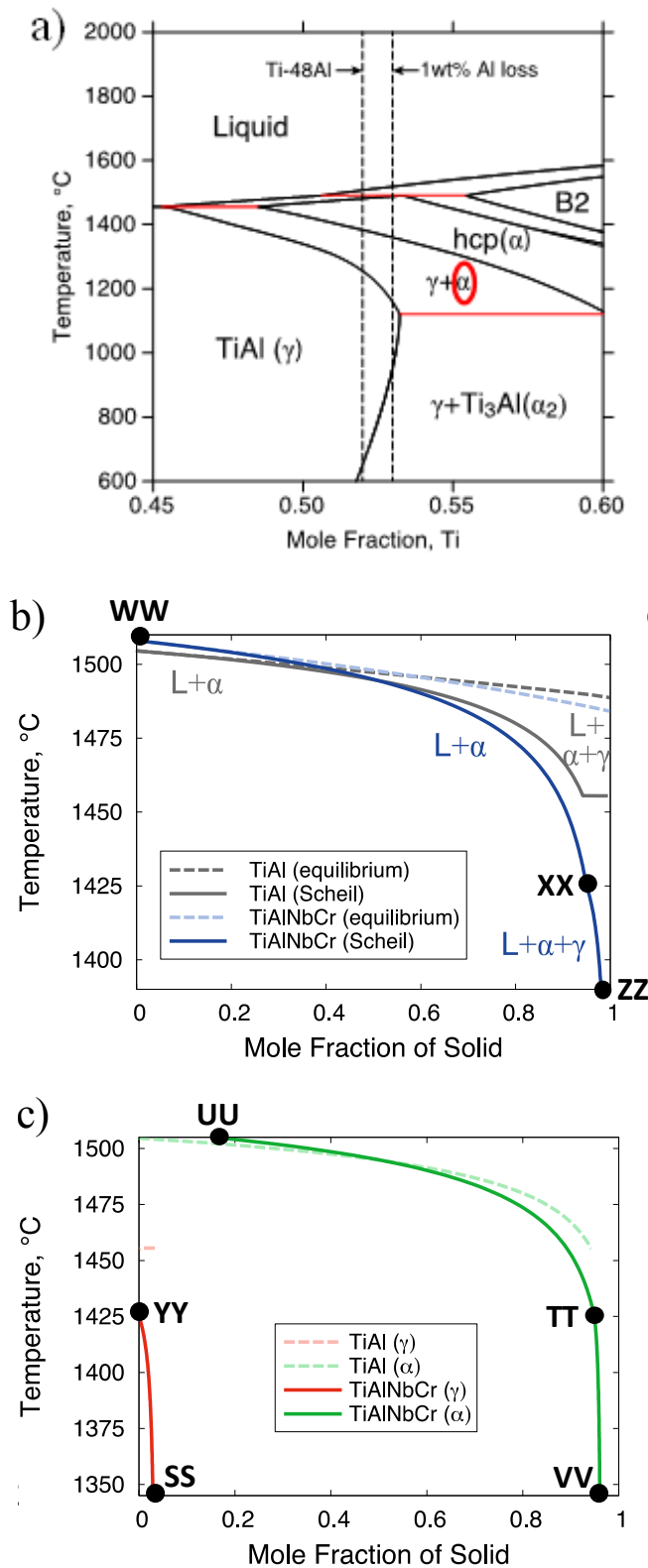


Figure I.2.C.3.2.(a) The calculated phase diagram for the Ti-48Al composition from the CALPHAD simulations; (b) the Scheil simulation showing the solidification sequence for Ti-48Al and Ti-48Al-2Cr-2Nb compositions; and (c) the Scheil simulation showing the formation range of the γ (Ti-Al) and α phases for Ti-48Al and Ti-48Al-2Cr-2Nb compositions. The α phase circled with red in (a) corresponds to the α phase in (b) and (c).

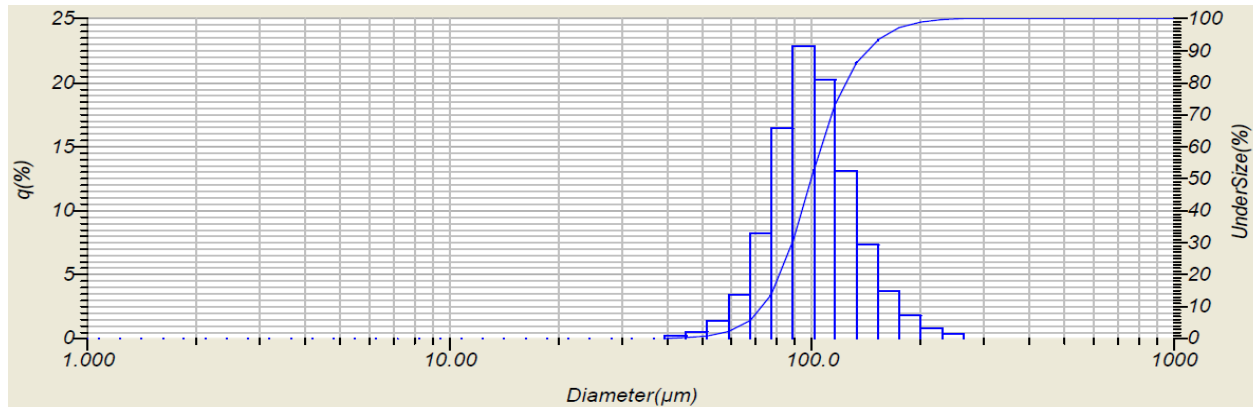


Figure 1.2.C.3.3. The powder particle size distribution of the sieved powder.

Table 1.2.C.3.1 Elemental Composition of the Ti-48Al-2Cr-2Nb Powder, as Obtained from Wet Chemical Analysis.

Element	Wt.%	At.%
Ti	59.8	48.43
Al	33.2	47.80
Cr	2.54	1.90
Nb	4.45	1.86

Overall, this work has shown that the phase transforming nature of the Ti-Al alloys enable obtaining equiaxed microstructures in an as-built state without the need for tedious beam parameter manipulations. The HIPed structures have good RT tensile properties that will enable them to be surface-machined to the required tolerance that can then be heat-treated to obtain the desired microstructures. Additionally, the negligible residual stresses stemming from the high build chamber temperatures ensure the parts are formed without cracks (one of the major issues in traditional manufacturing of these intermetallics).

The project will be concluded with a heat-treatment study to optimize the microstructures for high-temperature working environments (e.g., improved creep resistance). With the heat-treatments performed, we will have achieved a complete roadmap from manufacturing to processing for the successful manufacture of components out of the Ti-48Al-2Cr-2Nb alloy with good mechanical properties and microstructures.

Conclusions

This project investigates the feasibility of manufacturing a turbocharger compressor wheel from a Ti-48Al-2Cr-2Nb alloy using EBM. Preforms were successfully manufactured, HIPed, and extensively characterized using XRD, x-ray computed tomography, SEM with energy dispersive x-ray spectroscopy and electron backscatter diffraction and mechanical testing (i.e., RT and 500°C). Equiaxed microstructures were observed in the as-built condition and were retained post-HIP to yield excellent tensile properties on-par with, or better than, conventionally manufactured counterparts. Negligible residual stresses were observed in the as-built state as expected from the high build chamber temperatures. This established the proof-of-principle for using EBM to manufacture components out of Ti-Al alloys.

After the proof-of-principle work was successfully established, a computer-aided design model for the turbocharger compressor wheel was obtained from Cummins Inc. The required Ti-Al powder stock was acquired and characterized for morphology and phase identification. Trial runs for printing the prototype were started and continued for two weeks. The initial trials resulted in failure due to a phenomenon called ‘smoking’ that results in the explosion of electrically charged powder particles during the build.

Further research indicated that a coarser cut of the feedstock powder could help mitigate the smoking problem. Accordingly, the powders were sieved to a -100/+200 mesh size (74–149 μm) distribution and quantified to have a mean powder size of 104 μm . Wet chemical analyses revealed the powder feedstock to be within the expected compositional range. However, the printing of the prototype turbocharger compressor wheel has been put on hold indefinitely given: (1) unavailability of machine-time at the MDF; and (2) a diminished collaborator interest in the project.

In the final quarters, it is proposed to perform a set of heat-treatment studies to obtain microstructures that can maximize the creep life of Ti-48Al-2Cr-2Nb components under service conditions. With these results, a roadmap for successful manufacture of microstructure and mechanical performance optimized Ti-48Al-2Cr-2Nb alloys will have been established.

Key Publications

1. Cakmak, E., P. Nandwana, D. Shin, Y. Yamamoto, T. R. Watkins, I. Sen, R. R. Dehoff, J. A. Haynes, and R. D. England, “Manufacturing Ti-Al parts with EBM: Processing - microstructure - mechanical property relationships,” *Science and Technology Meeting and Exhibition (MS&T17)*, October 8–12, 2017, Pittsburgh, PA, USA.
2. Cakmak, E., P. Nandwana, D. Shin, Y. Yamamoto, M. N. Gussev, T. R. Watkins, J. A. Haynes, and R. D. England, “Manufacturing Ti-48Al-2Cr-2Nb preforms with EBM: A comprehensive study,” *67th Annual Denver X-ray Conference*, August 6–10, 2018, Westminster, CO, USA.
3. Cakmak, E., P. Nandwana, D. Shin, Y. Yamamoto, M. N. Gussev, I. Sen, T. R. Watkins, and J. A. Haynes, “A comprehensive study on the fabrication and characterization of Ti-48Al-2Cr-2Nb preforms manufactured using EBM,” projected to be submitted to *Acta Materialia*.

References

1. Kaufman, L., and H. Bernstein, 1970, *Computer Calculation of Phase Diagram*, Academic Press: New York.
2. Scheil, E., 1942, “Bemerkungen zur Schichtkristallbildung,” *Z. Metallkd.*, Vol. 34, pp. 70–72.

Acknowledgements

We would like to acknowledge Dr. Dongwon Shin for his valuable contributions to the CALPHAD simulations. We would also like to acknowledge Mr. Rick Lowden and Ms. Makayla Edwards for their help sieving the powders. Dr. Fred Montgomery is acknowledged for his assistance with the powder size distribution analysis, and Dr. Yukinori Yamamoto is acknowledged for valuable discussions regarding the phase transformation observed in this alloy system.

I.2.C.4 Task 4C: High-Temperature Lightweight Components: Alloy Development for Higher Performance Powertrains

Amit Shyam, Co-Principal Investigator

Oak Ridge National Laboratory
1 Bethel Valley Rd.
Oak Ridge, TN 37831
E-mail: shyama@ornl.gov

J. Allen Haynes, Co-Principal Investigator

Oak Ridge National Laboratory
1 Bethel Valley Rd.
Oak Ridge, TN 37831
E-mail: haynesa@ornl.gov

Jerry L. Gibbs, DOE Technology Manager

U.S. Department of Energy
E-mail: jerry.gibbs@ee.doe.gov

Start Date: October 1, 2016	End Date: September 30, 2018	
Project Funding (FY18): \$210,000	DOE share: \$210,000	Non-DOE share: \$0

Project Introduction

A family of cast Al alloys called AlCuMnZr (ACMZ) were developed at ORNL with two industry partners over a four-year period. This family of alloys displays unique properties such as good castability and hot-tear resistance, excellent elevated temperature mechanical properties at a modest price increase compared to A356 or A319 type commercial alloys. In this project, experimental and simulation approaches to developing cast Al alloys with favorable properties for engine applications was explored. Since the hot-cracking resistance of some ACMZ alloys is outstanding, weld processing was also explored. This report summarizes the results of those feasibility trials on lightweight high-temperature Al alloys.

Objectives

The overall project had the following two objectives:

- To design cast Al alloys with improved selected properties compared to ACMZ alloys.
- To understand the behavior of thermally stable cast Al alloys with simulation and neutron diffraction techniques.

Approach

The work consisted of two parts. The first consisted of the synthesis of alloys with improvements in specific properties of ACMZ alloys. The work performed in that portion of the project cannot yet be reported publicly due to intellectual property requirements. The second part involved phase-field simulations of the thermal stability of microstructures and a neutron diffraction-based study of the deformation behavior of a variety of cast Al alloys. Results from the second part are reported here. The neutron diffraction experiments and simulations will help in the design of the next-generation of cast Al alloys for engine applications.

Results

An analytical model was constructed to measure the total energy of θ' (strengthening precipitate) and θ (deleterious phase) precipitates. The contributions to the total energy included the contributions of volumetric free energy, interfacial energy of various interfaces, and strain energy around the precipitate. Results of this

analytical model can be applied to make an analytical stability map, such as the one shown in Figure I.2.C.4.1. This map was constructed for 200°C and the orange line is the analytical prediction of the critical aspect ratio (for a given volume) above which the θ' phase is stable and vice versa. Experimental data points from a number of sources represent the calculated volume and aspect ratio of the θ' phase observed experimentally at 200°C. It is concluded based on this figure that the analytical model does a reasonably good job of predicting the stability of the strengthening phase for this class of Al alloys. Similar conclusions were drawn for the calculations and corresponding experimental results at 25, 300, and 350°C. Taken together, the conclusion of this investigation was that the tendency of θ' to transform to θ is primarily governed by its size, aspect ratio, and temperature. In addition, it was determined that to prevent this detrimental phase transformation, particle coarsening, and particularly particle thickening, should be impeded.

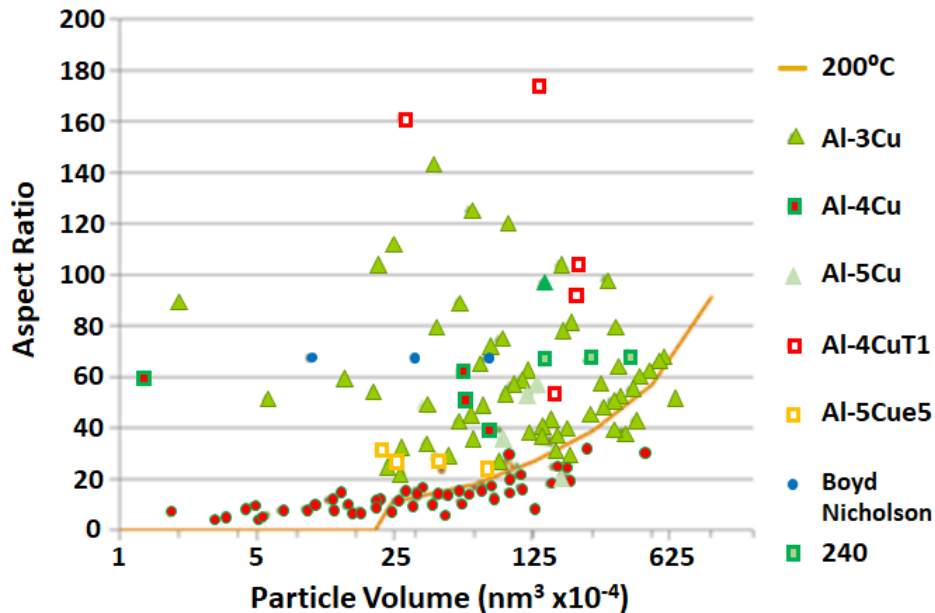


Figure I.2.C.4.1. Analytical stability map for the θ' to θ transformation at 200 °C. Source: ORNL.

Phase-field simulations of composite precipitates (with θ' and θ precipitates present together) were performed under the conditions where one of the phases was stable compared to the other phase. Figure I.2.C.4.2 presents the results at 350°C. It is observed that under the conditions where the θ' phase is stable (left), the θ phase is quickly consumed by the θ' phase due to the high aspect ratio of the θ' phase reducing the total energy of the composite precipitate. Conversely, it is also observed that under the conditions where the θ phase is stable (right), the θ' phase is consumed by the θ phase due to the low aspect ratio of the θ' phase leading to the total energy of the composite precipitate getting reduced through this phase transformation. Since this phase transformation is vital to the retention of high-temperature mechanical properties of Al-Cu alloy, development of the analytical stability map along with the corresponding phase simulations will provide a useful tool for the design of high-temperature Al-Cu alloys with desirable precipitate morphologies.

The true stress-strain behavior at RT of a commercial A206 alloy with different heat-treatments is shown in Figure I.2.C.4.3. The alloy has the highest strength in the peak-aged heat-treatment (190°C for 5 hours) and the overage treatments that consist of 200-hour treatments at 200 and 300°C lead to a reduction in strength.

It is observed in the macroscopic stress-strain curves that the 300°C overage or preconditioning treatment leads to the lowest strength. Even so, the overall strain hardening behavior (i.e., the slope of the curve after yielding) under all conditions is relatively similar. This is, however, not the case when grain orientation-specific measurements were performed at the VULCAN beamline at the Spallation Neutron Source at ORNL. Results for the conditions shown in Figure I.2.C.4.3 are reported in Figure I.2.C.4.4 for four specific grain orientations.

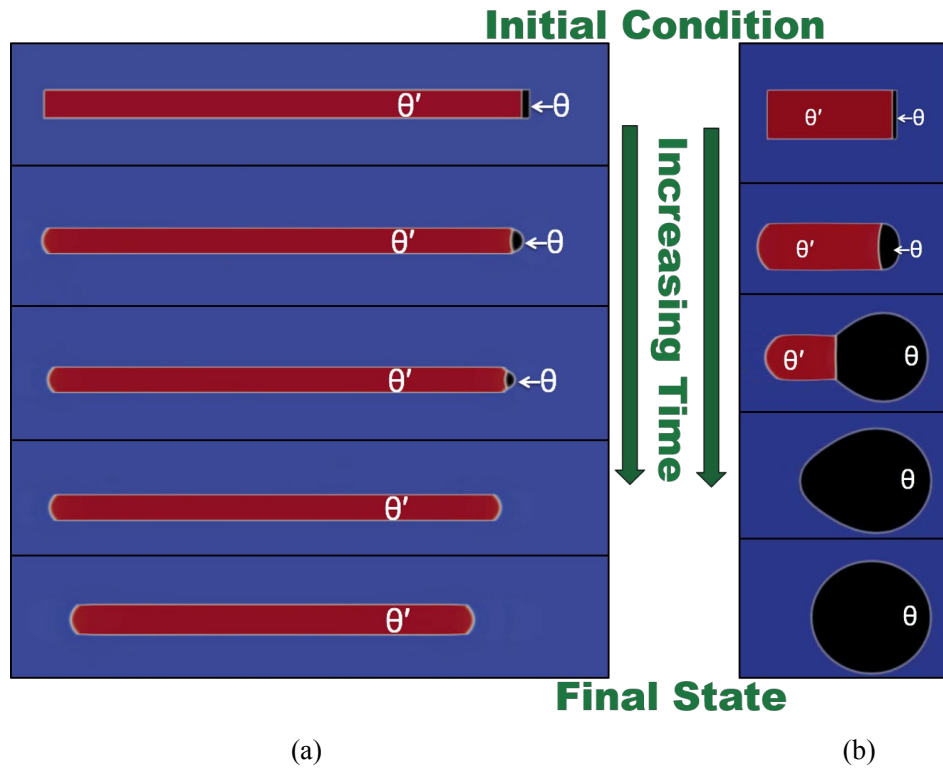


Figure I.2.C.4.2. Snapshots of phase-field simulations in conditions where (a) θ' phase is stable compared to (b) the θ phase and vice versa. Source: ORNL.

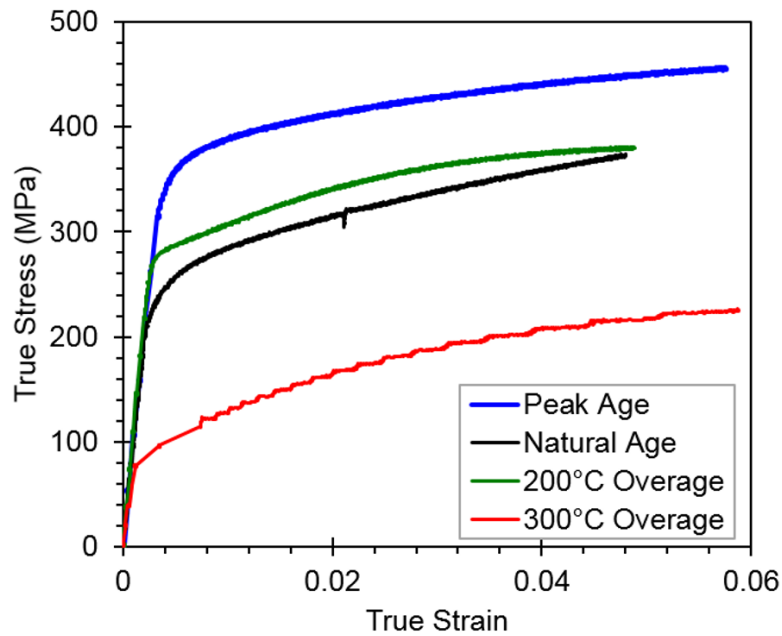


Figure I.2.C.4.3. The true stress-strain behavior of Al5CuMg (A206) alloy with different heat-treatments. Source: ORNL.

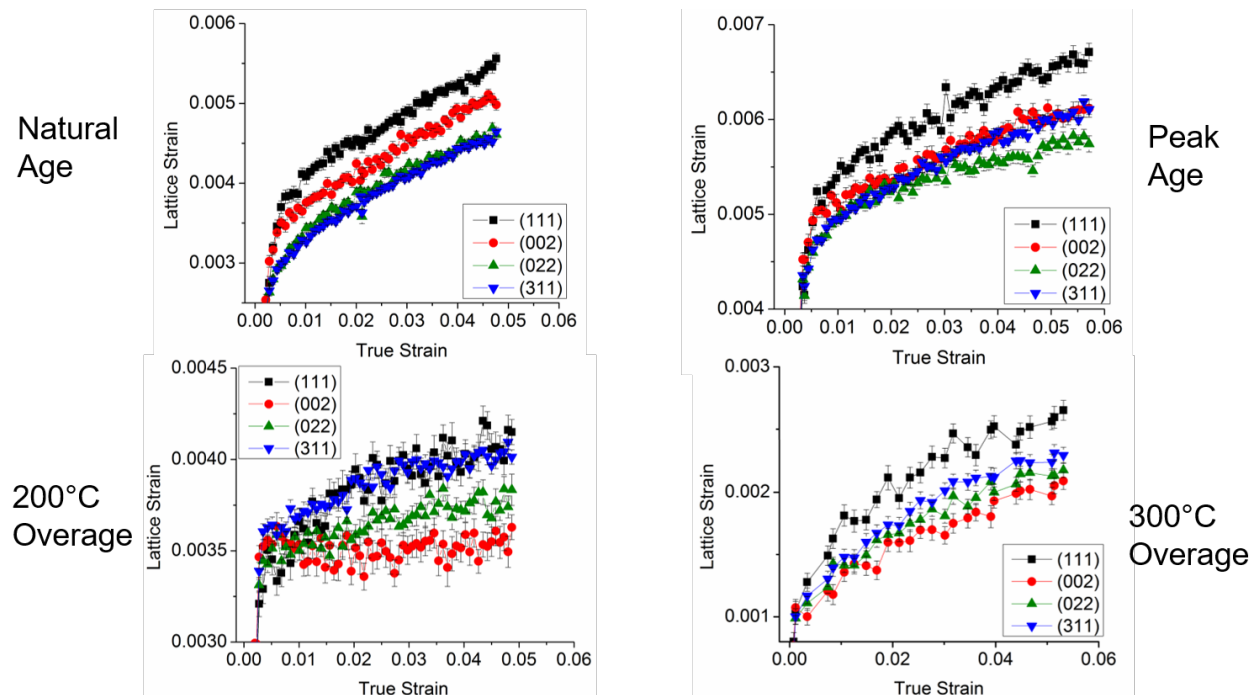


Figure I.2.C.4.4. Anisotropy in strain hardening under various conditions suggests a change in the mechanism of deformation under the reported four conditions. Source: ORNL.

It is noted that strain hardening is relatively isotropic for the natural age and the peak age conditions. It is our hypothesis that this is due to the relative ease with which precipitates or solute clusters can be sheared by dislocations under these conditions. At 200°C overage conditions, the strain hardening response becomes anisotropic and this is due to the delayed shearing of θ' precipitates. The shearing in this case becomes a strong function of the orientation of the grains. At 300°C overage conditions, the strain hardening response becomes relatively isotropic again since the θ' (and θ) precipitates are too thick to be sheared under these conditions and are overcome by dislocations through Orowan looping mechanisms. A quantitative model for this phenomenon is being developed.

Conclusions

A variety of advanced simulation and experimental techniques were applied to advance the development of high-temperature capable Al alloys. New Al alloys were synthesized based on this understanding and will be reported on in the future. Phase-field simulations are particularly useful both to verify and define the microstructural stability of strengthening precipitates under various conditions of interest for automotive engine applications. *In-situ* neutron diffraction with tensile loading was assessed to be a powerful tool for understanding the strain hardening of commercially available and experimental cast Al alloys.

Acknowledgements

The authors gratefully acknowledge Patrick Shower (University of Tennessee - Knoxville/ORNL) for the phase-field simulations. Brian Milligan (Colorado School of Mines) and Dong Ma (ORNL) are also acknowledged for the neutron diffraction-based measurements.

I.2.D Fundamentals of High-Temperature Environmental Resistance (Oak Ridge National Laboratory)

J. Allen Haynes, Principal Investigator

Propulsion Materials
Oak Ridge National Laboratory
1 Bethel Valley Rd.
Knoxville, TN 37831
E-mail: haynesa@ornl.gov

Jerry L. Gibbs, DOE Technology Manager

U.S. Department of Energy
E-mail: jerry.gibbs@ee.doe.gov

Start Date: October 1, 2016	End Date: September 30, 2018	
Project Funding (FY18): \$410,000	DOE share: \$410,000	Non-DOE share: \$0

Project Introduction

The Fundamentals of High-Temperature Environmental Resistance Project consists of two tasks that are focused on early-stage research in pursuit of advancing the basic mechanical properties, manufacturability, and addressing the affordability of propulsion materials. These tasks have the common goal to develop advanced cast Al alloys for high-temperature engine components. The specific tasks include the following:

1. High-Temperature Oxidation Mapping of Advanced Exhaust Path Materials.
2. Application of Machine-Learning Methods to Predict High-Temperature Oxidation of Exhaust Path Materials.

The following sections of this report outline the specific task work conducted at ORNL in the areas of predictive engineering, process development, and enabling technologies for propulsion materials. Each task supports one or more goals within the VTO mission of developing higher performance materials that can withstand increasingly extreme environments and address the future properties needs of a variety of high-efficiency powertrain types, sizes, fueling concepts, and combustion modes.

I.2.D.1 Task 1A: High-Temperature Components: High-Temperature Oxidation Mapping of Advanced Exhaust Path Materials

J. Allen Haynes, Co-Principal Investigator

Oak Ridge National Laboratory
1 Bethel Valley Rd.
Oak Ridge, TN 37831
E-mail: haynesa@ornl.gov

Jerry L. Gibbs, DOE Technology Manager

U.S. Department of Energy
E-mail: jerry.gibbs@ee.doe.gov

Start Date: October 1, 2016 End Date: September 30, 2019
Project Funding (FY18): \$245,000 DOE share: \$245,000 Non-DOE share: \$0

Project Introduction

Peak exhaust temperatures for exhaust valves and turbocharger systems within LD and HD internal combustion engines are steadily increasing, moving towards the realm of gas turbine engine temperatures in response to regulatory demands for higher efficiencies. Moreover, the auto industry is technically constrained by extreme cost sensitivity due to high-volume production and global competition. Approaching global standards require unprecedented leaps in fuel economy over the next decade, demanding historic rates of further improvement in the efficiency of internal combustion engines. Near-term strategies for higher-efficiency powertrains, therefore, are projected to require significant additional increases in PCPs and exhaust temperatures. For example, exhaust valve peak temperatures of downsized, heavily boosted LD engines are projected to rise from 870°C today to ~950°C by 2025 and to 1,000°C by 2050 [1]. Thus, affordable, stronger, higher temperature alloys with very good high-temperature oxidation resistance in exhaust gas streams are required for next-generation valves and turbo systems. However, the industry currently has limited understanding of materials oxidation behavior at temperatures beyond ~850°C, since traditional engines have operated at or below that peak temperature range.

Objectives

This project aims to characterize and compare laboratory high-temperature cyclic oxidation behavior in simulated exhaust gas at relevant current and future temperatures of a range of commercial alloys that have been, or are being considered as candidates for, turbocharger and exhaust valve systems. The study is providing scientific knowledge for improved understanding of correlations between alloy composition and structure and the resultant oxidation behavior at increasing temperatures. A second objective is to support the development of a potential solutions map of candidate materials systems for specific future design temperatures, strength levels, fatigue behavior, cost boundaries, and engine service lives. This experimental dataset will also support the development of data analytics models that contribute to development of new advanced alloys for future higher-efficiency engines with more extreme operating conditions. This project also provided program management to the overall ORNL program.

Approach

Selected commercial and prototype alloys for exhaust valve and turbocharger applications are being exposed to laboratory cyclic oxidation furnace testing at simulated engine component peak temperature environments of 800, 850, 900, 950, and 1,000°C. Not all alloys in the study are being tested at all temperatures, as some are not relevant across the entire temperature range. An exhaust gas environment was simulated during furnace testing by using 10 vol% water vapor in air, and cyclic oxidation was conducted using coupons in automated vertical furnaces programmed for 60-minute exposure at peak temperature, with 10-minute cooling cycles back

to ~30°C. Specimens were introduced into furnaces at target temperature and controlled atmospheres but were removed to cool in ambient air. Specimens were removed from testing and mass changes measured and recorded at either 20- or 50-cycle intervals. It should be noted that 1 hr peak temperature cycles in 10% water vapor is an aggressive test, as most peak temperature events within an engine are on the order of seconds (e.g., accelerating to merge) or minutes (e.g., pulling a freight load up a hill or mountain). Multiple specimens of each alloy type are scheduled to be tested. Alloy compositions in Table I.2.D.1.1 were measured by inductively coupled plasma spectroscopy, optical emission spectroscopy, and combustion techniques. Selected specimens and their oxidation products were characterized by optical microscopy, SEM, and with energy dispersive spectroscopy or XRD.

Table I.2.D.1.1. Measured Compositions in Weight Percentages for Commercial Exhaust Valve Alloys Tested at 800, 850, 900, and 950 °C as Discussed Herein.

Alloy	Fe	Ni	Cr	Co	Mn	Mo	Nb	Si	Al	Ti	W	Zr	C	Ni+Co
FN80A	0.4	76.6	18.5	0.0	0.23	0.0	0.01	0.03	1.6	2.4	<0.01	0.07	0.056	76.7
F751	7.1	72.5	15.3	0.0	0.29	<0.01	0.92	0.06	1.3	2.4	<0.01	0.04	0.041	72.5
F31V	14.1	56.8	22.3	0.0	0.08	2.0	0.85	0.07	1.3	2.2	0.01	<0.01	0.043	56.9
Waspaloy	1.6	57.6	19.3	12.6	0.02	4.2	0.12	0.02	1.3	2.9	0.02	0.05	0.037	70.3
CN90	0.7	59.6	19.4	15.9	0.05	0.1	0.03	0.13	1.4	2.4	0.01	0.07	0.085	75.5
FN90	0.5	59.2	19.6	16.2	0.04	0.2	0.03	0.12	1.5	2.4	0.01	0.06	0.086	75.4
R41	0.1	56.4	18.4	10.4	0.01	9.8	<0.01	0.02	1.6	3.3	0.01	<0.01	0.067	66.8

Note: Alloys shown in this table are a subset of the total group of valve and turbocharger alloys being tested.

Results

Since previous year's reports focused on higher temperatures for valve and turbo alloys, for brevity, this year's report focuses only on exhaust valve materials, which are being tested from 800 to 950°C in 10% water vapor. Table I.2.D.1.1 shows the measured compositions of the commercial alloys referenced in this report (but does not represent the full matrix of alloys being tested, as that also includes prototype alloys and turbocharger component alloys). Testing is progressing on schedule, as FY 2018 was Year 2 within a three-year experimental test matrix launched in FY 2017. As can be seen from Table I.2.D.1.1, most alloys in the study are Ni-based, with Ni+Co totals ranging from a low of 66.8 wt.% in alloy R41 to 76.7% in alloy FN80A. Co contents range from 0% in several alloys to 16% in alloy FN90. The Co content is particularly significant since Co cost has rapidly risen over the past two years due to ever increasing demands for battery manufacturing.

Figure I.2.D.1.1 compares representative oxidation mass change curves for selected alloys at 800, 850, 900, and 950°C, using a similar vertical axis scale for each to illustrate impact of temperature on oxidation rates. Figure I.2.D.1.1.(a) compares oxidation behavior of selected alloys at 800°C to 1,000 cycles (1,000 hrs), which is within the peak temperature range of current automotive engines. Ideally, a very slow-growing, adherent, protective oxide scale forms on the surface of the alloy. Mass loss is an indication of either spallation of some portion of the protective oxide scale on the surface of the alloy, or of volatilization of the oxide scale, or both. As anticipated, most alloys performed very well at 800°C, even in this aggressive laboratory test. Two alloys showed differing behavior than the others. Alloy Rene 41 (R41ST) began to show evidence of mass loss/spallation at 350 cycles, with a modest rate of continuing mass loss thereafter. The edge of temperature capacity for this alloy in a water vapor-containing environment appears to be 800°C, and the present results do not indicate it is an ideal candidate for extended use at this temperature or beyond in a combustion environment. As will be seen in subsequent figures, this alloy also shows rapidly deteriorating oxidation behavior as temperatures increase. The R41 alloy is low-Ni, lower-Cr, higher-Ti, high-Mo, and Zr-free, all of which likely contribute to its inferior oxidation resistance compared to the other alloys. The F31V alloy seemed to show similar behavior, but on closer examination it actually exhibited an extremely low rate of mass gain, rather than spallation. This was an indication of very good oxidation resistance for F31VST (perhaps the

best in this set) as was affirmed by testing at 900°C and beyond. Figure I.2.D.1.1 (b) shows mass change curves at 850°C, and again the R41ST alloy shows signs of the earliest (i.e., 850 cycles) and most significant rate of spallation, albeit still modest. Also, at this temperature, the Waspalloy alloy, which performed very well at 800°C, begins to show signs of spallation initiation at 900 cycles. From an oxidation perspective, neither of these alloys appear to be ideal for long-term, high-stress applications with peak temperatures in the range of 850°C.

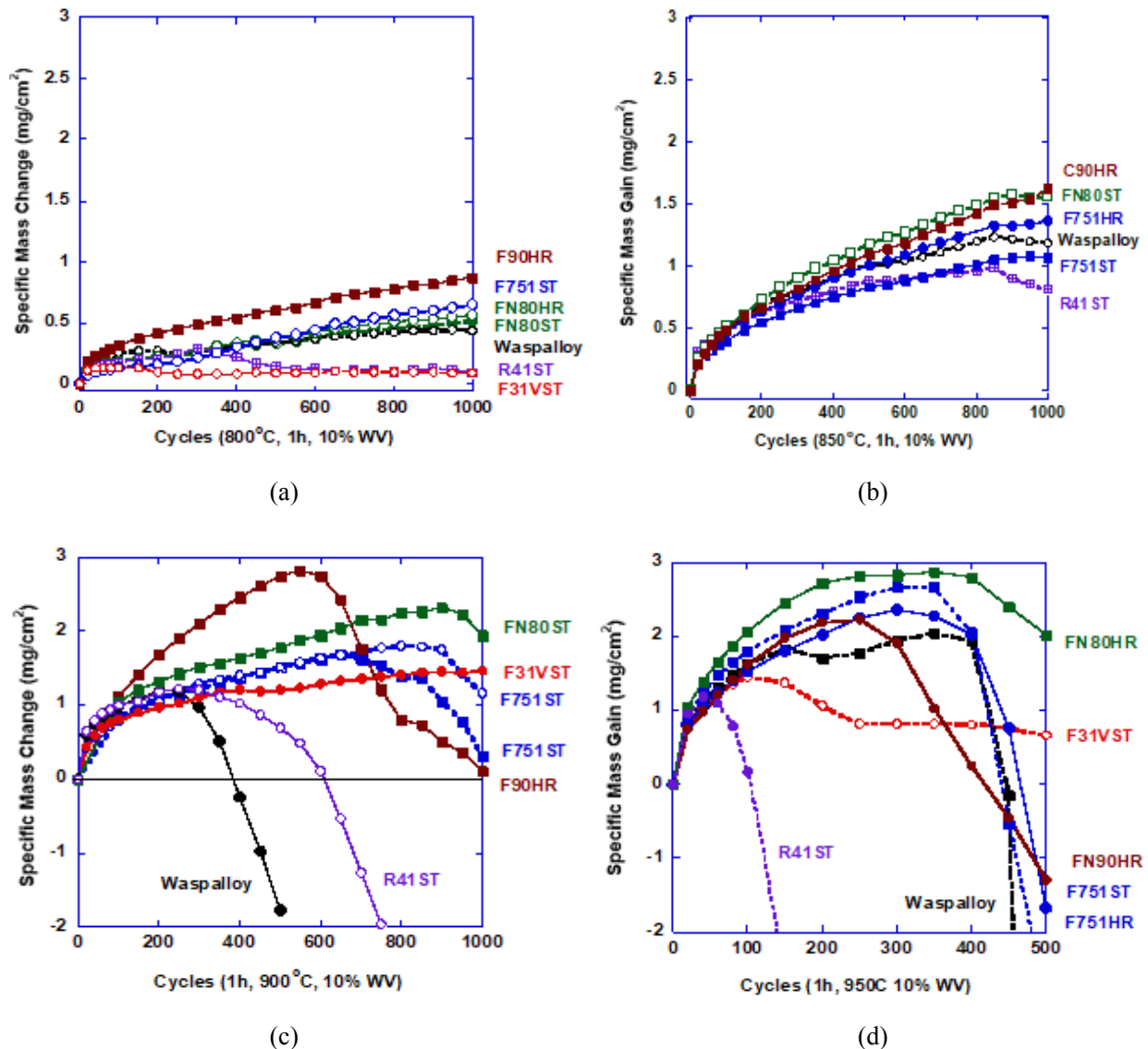


Figure I.2.D.1.1. Mass change curves of candidate exhaust valve alloys during laboratory cyclic oxidation testing in air + 10% water vapor (WV) at: (a) 800°C, (b) 850°C, (c) 900°C, and (d) 950°C. Source: ORNL.

Figure I.2.D.1.1.(c) compares mass change curves at 900°C. This is a threshold temperature for most alloys that depend on Cr for oxidation resistance, and thus, behavior changes significantly for most of these alloys, since they are all classified as chromia-formers. The Waspalloy alloy shows the earliest and most rapid spallation, with R41ST showing similar behavior. The F90HR alloy shows the highest rate of mass gain and begins to show significant rates of mass loss at 600 cycles, indicating inadequate oxidation resistance at this temperature and environment. These three are all lower-Ni alloys, with less than 20% Cr content, both of which would be expected to reduce oxidation resistance. The Waspalloy and R41ST alloys also have the highest Ti content, which can be detrimental to higher temperature oxidation, as well as the highest Mo

content, although the effects of Mo on alloy oxidation are not as clearly understood. Alloy F751ST, with much higher Ni content, is interesting as it is considered the state-of-the-art in-production exhaust valve alloys. Slight variabilities in oxidation behavior are common, as illustrated by the two F751ST curves, although both specimens began spalling prior to 1,000 cycles, with one initiating mass loss as early as 600 cycles. The F751ST alloy is designed for operation at a peak temperature of $\sim 870^{\circ}\text{C}$, as the gamma prime strengthening phase begins to rapidly dissolve beyond that temperature. Thus, it would not be a realistic valve alloy candidate for engines with 900°C peaks due to inadequate strength at that temperature. The FN80ST alloy shows better oxidation resistance, with very modest spallation initiating at 900 cycles. Finally, the alloy that shows the best oxidation resistance, with no signs of spallation after 1,000 cycles, is alloy F31VST. The microstructures for F31VST, FN80ST and R41ST after 500 1 hr cycles of furnace oxidation testing at 900°C in 10% WV are shown in Figure I.2.D.1.2. There were similar surface oxide thicknesses and depths of internal oxidation in each alloy, and all formed Cr- and Ti-rich oxides. The driving force(s) for the significant reduction in spallation resistance on Rene 41 at 600 cycles and beyond was not clearly apparent at 500 cycles. It should be noted that F31VST is a lower-Ni alloy also, but it has the highest Cr (22.3 wt.%) and lowest Ti (2.2 wt.%) contents of any of the alloys evaluated here (see Table I.2.D.1.1, which undoubtedly contributes to its superior oxidation resistance. However, our previous studies have shown that at 870°C , the strength of F31VST drops below the targeted minimum YS of 50 ksi due to accelerated dissolution of the gamma prime strengthening phase. Inadequate strength at higher temperatures removes this alloy from consideration as a valve alloy candidate at 900 and 950°C , but its superior oxidation behavior (compared to the other alloys) is nonetheless important to study and understand to better inform new, higher strength, affordable alloys that are being designed by ORNL for more severe environments.

Figure I.2.D.1.1.(d) compares cyclic oxidation behavior of selected alloys at 950°C to 500 cycles. This temperature is beyond the oxidation performance limit for all of the alloys shown in the figure, although both FN80HR and F31VST perform notably better than the other alloys. However, it is anticipated that a chromia-forming alloy will not have adequate oxidation resistance at 950°C for extended engine operation. Although it is possible that some alloys with adequate strength, such as commercial alloys U520 and U720 or some of the prototype alloys also being tested and characterized in this study as discussed later, might offer a solution if the highest temperature surfaces are protected with an oxidation-resistant coating. Higher strength commercial alloys are also being evaluated in this study but are not shown in the present report due to space limits and their prohibitive materials and manufacturing costs for high-volume transportation applications.

XRD data are being collected for each specimen after oxidation testing. Results thus far indicate the formation of a variety of mixed oxides on various alloys at various temperatures, with those oxide phases including TiO_2 (rutile), Cr_2MnO_4 (manganochromite), Cr_2NiO_4 , $\text{Cr}_{1.3}\text{Fe}_{0.7}\text{O}_3$, Cr_2O_3 , FeCr_2O_4 , NiO, Co-Ni-O, and Ti-Cr-O oxides. Analyses are not yet complete, but early results do not indicate any clear correlations between oxide phases formed in the early stages of oxidation and scale durability. Extensive microstructural and chemical (x-ray mapping) characterization has been performed on multiple alloys sets, evaluating and comparing the oxidation products formed on the various alloys and temperatures and will be presented in a future report. Data from this effort is also being provided to the machine-learning activities in another task and will also be applied to better inform alloy design efforts for exhaust valve-type alloys that are both stronger and more oxidation-resistant at 900°C and beyond.

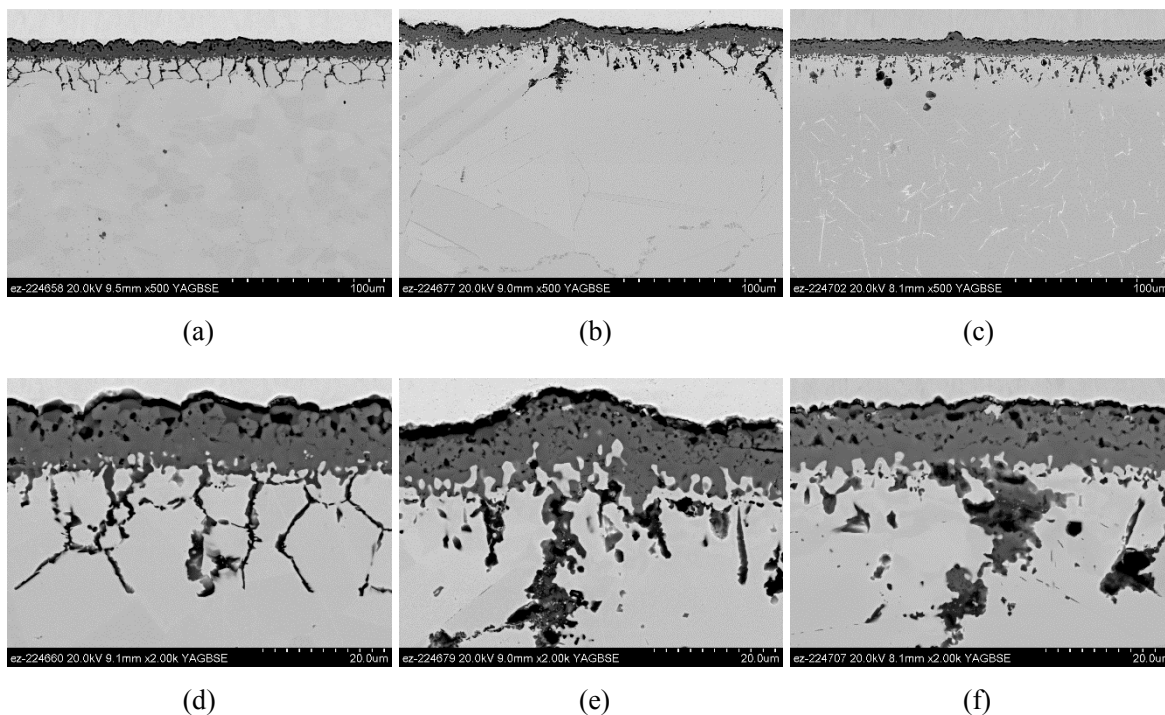


Figure I.2.D.1.2. Cross-sectional SEM backscatter electron images of three alloys after 500 one hour cycles of furnace oxidation testing at 900 °C in 10% WV: (a, d) F31VST, (b, e) FN8OST, and (c, f) R41ST. Source: ORNL.

Conclusions

Oxidation behavior of relevant commercial and prototype exhaust valve alloys are reported at peak temperatures ranging from 800 – 950°C. Only one of the commercial alloys (alloy FM31VST) showed adequate oxidation behavior to survive long-term in a simulated, aggressive (1h peak cycles) exhaust gas environment with extended temperature peaks of 900°C or beyond. However, the strength of the higher-Cr alloy FM31VST is not anticipated to be adequate for exhaust valve applications beyond 870°C. Design of next-generation alloys will have to first provide adequate strength and stability at 900°C and beyond, but also a strategy for enabling adequate oxidation behavior—either intrinsically or through affordable and durable coatings/surface treatments in peak temperature regions.

References

1. Workshop Report: Trucks and HD Vehicles Technical Requirements and Gaps for Lightweight and Propulsion Materials, DOE/EE-0867, February 2018
https://www.energy.gov/sites/prod/files/2014/03/f13/wr_trucks_hdvehicles.pdf

Acknowledgements

George Garner and Tracie Lowe in the Corrosion Science and Technology group at ORNL are acknowledged for conducting oxidation testing and for SEM characterization, respectively. Ercan Cakmak of ORNL provided the XRD analyses.

I.2.D.2 Task 2A: High-Temperature Components: Application of Machine-Learning Methods to Predict High-Temperature Oxidation of Exhaust Path Materials

Dongwon Shin, Principal Investigator

Oak Ridge National Laboratory
1 Bethel Valley Road
Oak Ridge, TN 37831
E-mail: shind@ornl.gov

Jerry L. Gibbs, DOE Technology Manager

U.S. Department of Energy
E-mail: jerry.gibbs@ee.doe.gov

Start Date: October 1, 2016

End Date: September 30, 2018

Project Funding (FY18): \$165,000

DOE share: \$165,000

Non-DOE share: \$0

Project Introduction

High-temperature oxidation, specifically the formation, growth, and adherence of thermally grown oxide scales on the surface of dynamic, multicomponent alloys, is not yet adequately understood. This explicit knowledge gap hampers effective prediction of oxidation performance of structural components, even though numerous prior studies. Consequently, the design of new oxidation-resistant alloys and coatings, as well as the selection of existing materials for new applications, remains a slow, expensive, and high-risk empirical process.

Objectives

This project aims to demonstrate the feasibility of developing machine-learning models that can predict oxidation behavior of high-temperature materials for automotive applications by leveraging ORNL's high-quality experimental data collected over decades.

Approach

An emerging materials data analytics approach was used, consisting of correlation analysis and machine-learning, to predict parameters in the pkp model (cyclic oxidation model) of various high temperatures Ni-Cr alloys. ORNL's consistent, well-documented experimental datasets from high-temperature oxidation testing have been used to derive p and k_p parameters to be used in the training of machine-learning models where p and k_p represent a probability of oxide scale to spall off and parabolic growth of oxide scale, respectively. In addition, we have used m_0 as a term in the pkp model to capture alloys exhibit abrupt mass change in the early-stage of cyclic oxidation. We performed a series of Pearson's correlation coefficient (PCC) and advanced maximal information coefficient (MIC) analyses prior to training machine-learning models to identify features that affect p , k_p , and m_0 parameters. Then, we trained machine-learning algorithms to develop surrogate models that can predict oxidation behavior of alloys represented from given alloy compositions. The current dataset is limited to cyclic oxidation of Ni-Cr alloys at 950°C with 10% WV, using 78 data points.

Results

We developed a code to automatically evaluate parameters of the pkp model (i.e., p , k_p , and m_0) from experimentally measured mass change data to represent cyclic oxidation behavior of alloys. Among the 78 entries of Ni-Cr alloys cyclic oxidation data, 67 datasets could be successfully represented with the evaluated three model parameters with small fitting errors. The coefficient of determination (R^2) for these data was higher than 0.7. Certain datasets could not be well-represented with a pkp model that is intended to describe smooth parabolic oxidation behavior of alloys, and R^2 values of such datasets were lower than 0.5. Figure I.2.D.2.1 shows two representative examples of good and bad fittings to describe cyclic oxidation dataset with pkp model.

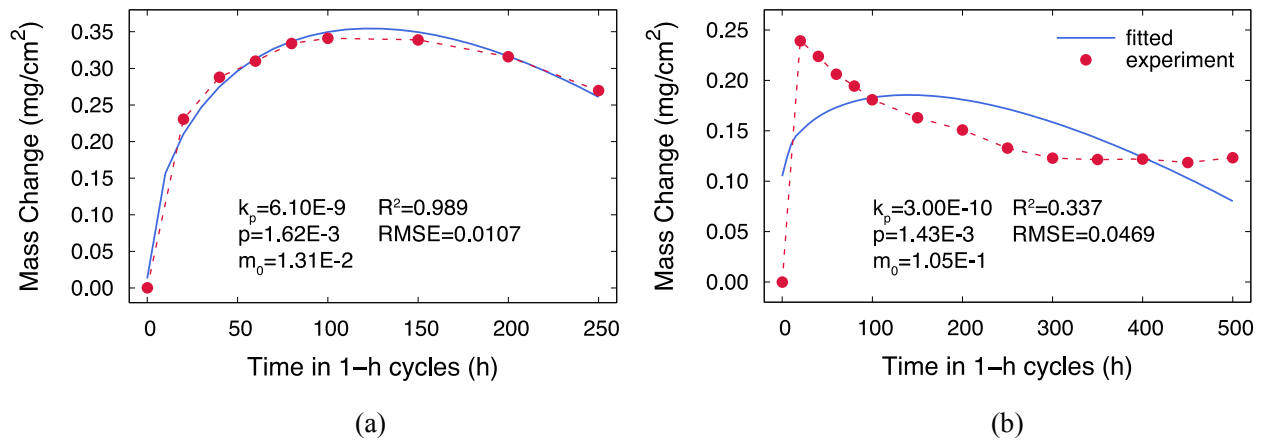


Figure I.2.D.2.1. Automatically fitted k_p , p , and m_0 parameters of ORNL cyclic oxidation dataset using autopkp code: (a) good fitting with high R^2 and low root mean square error (RMSE) and (b) bad fitting with low R^2 and high RMSE. The bad fitting is attributed to the intrinsic limitation of pkp model that is designed to describe smooth parabolic high-temperature oxidation behavior of alloys. Source: ORNL.

From the evaluated p , k_p , and m_0 parameters for each alloy data, we performed correlation analysis to identify key features that affect each parameter. We used two different correlation analysis techniques: conventional Pearson's PCC and MIC [1]. Once rankings of features are obtained, we trained machine-learning models with selected features. Figure I.2.D.2.2 shows the correlation between elemental compositions and k_p of Ni-Cr alloys in the dataset (left) and the comparison between actual and predicted k_p from neural network machine-learning models (right).

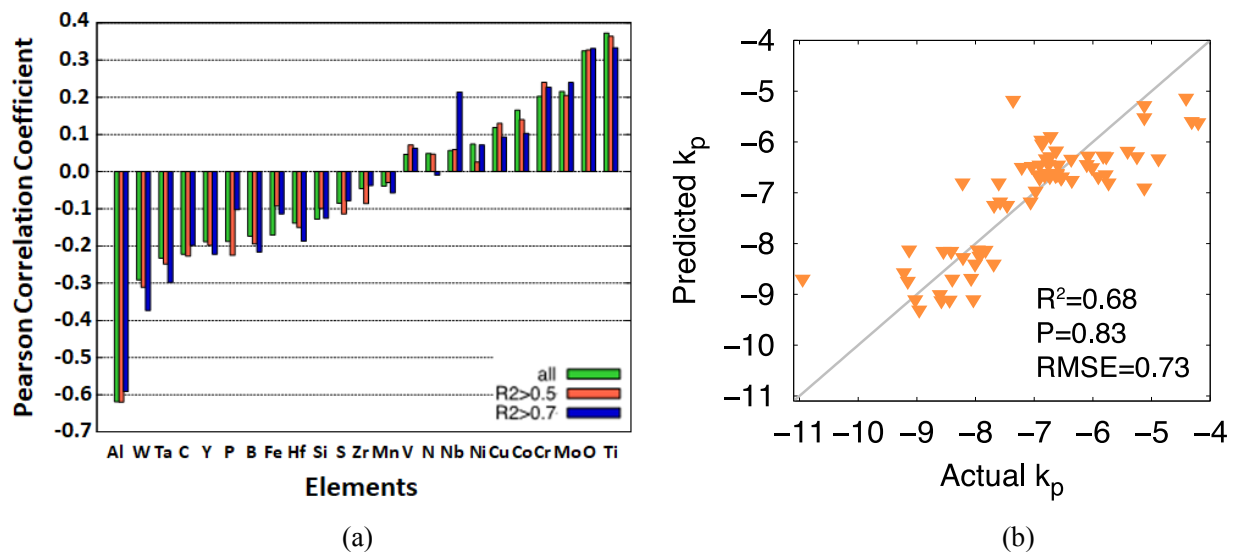


Figure I.2.D.2.2.(a) Correlation analysis between elemental compositions of 78 Ni-Cr alloys and their respective rate constant k_p using Pearson method and (b) trained neural network machine-learning model with top 5 features from Pearson analysis (right). Source: ORNL.

As selecting features for individual machine-learning models is an optimization problem, we tested the performance of five different machine-learning models with respect to the features selected from two different correlation analyses. Figure I.2.D.2.3 shows the accuracy of five trained machine-learning models with a varying number of features ranked from Pearson and MIC analyses. The results shown here are trained with all

78 data even though fitted p , k_p , and m_0 parameters of certain alloys do not represent experimentally observed cyclic oxidation behavior. Intriguingly, using fewer data decreased the accuracy of trained machine-learning models, although their fitted pkp model parameter is better. This observation strongly indicates that more experimental data is highly desirable to increase the fidelity of machine-learning models to predict the high-temperature cyclic oxidation behavior of alloys. Top n features determined from both MIC and Pearson analyses are provided. A perfect machine-learning model would have a Pearson coefficient of one between predicted and actual k_p values. Ten different trainings for each machine-learning model at given number of features have been performed, and averaged accuracy and associated error bars from standard deviation are shown.

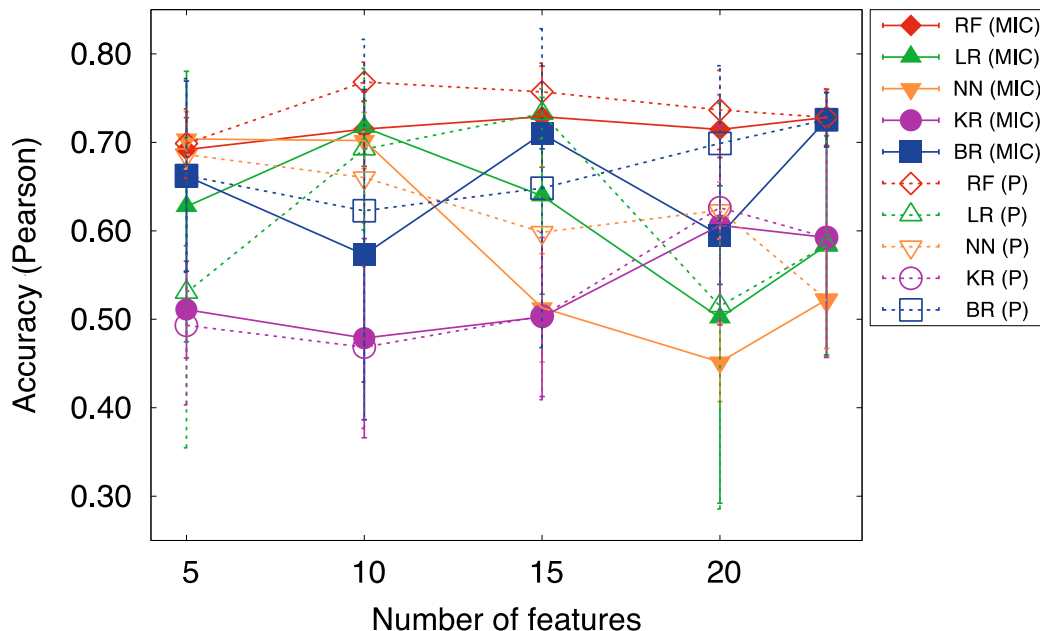


Figure I.2.D.2.3. Accuracy (represented with Pearson coefficients) of five machine-learning models (RF: random forest, LR: linear regression, NN: neural network, KR: kernel ridge regression, and BR: Bayesian regression) to predict k_p of Ni-Cr alloys at 950 °C cyclic oxidation as a function of number features (n) used within the individual training. Source: ORNL.

Conclusions

We have demonstrated the feasibility of applying modern data analytics approach to predict oxidation behavior of high-temperature alloys represented with the pkp model. Reasonable accuracy (~80% with Pearson) was obtained with relatively small amount of 78 dataset and simple elemental composition as input features. To further improve the proposed approach, we need to increase the number of the experimental datasets, as well as scientific alloy features to be included in the correlation analysis.

References

1. Reshef, D. N., Y. A. Reshef, H. K. Finucane, S. R. Grossman, G. McVean, P. J. Turnbaugh, E. S. Lander, M. Mitzenmacher, and P. C. Sabeti, 2011, "Detecting novel associations in large data sets," *Science*, Vol. 334, No. 6062, pp. 1518–1524. doi: 10.1126/science.1205438.

Acknowledgements

Jiheon Jun, Sebastien Dryepondt, and Bruce Pint in the Corrosion Science and Technology group at ORNL are acknowledged for providing oxidation dataset and guidance on evaluating pkp model parameters to represent alloy oxidation behavior. Linqing Peng at Grinnell College and Adam Payzant at Carleton University are acknowledged for developing autopkp code.

I.3 Materials for Energy Recovery and Aftertreatment

I.3.A Innovative SCR Materials and Systems for Low-Temperature Aftertreatment (Pacific Northwest National Laboratory)

Yong Wang, Co-Principal Investigator

Pacific Northwest National Laboratory
902 Battelle Blvd.
Richland, WA 99354
E-mail: yong.wang@pnnl.gov

Craig DiMaggio, Co-Principal Investigator

Fiat Chrysler Automobile, U.S., LLC
1000 Chrysler Dr.
Auburn Hills, MI 48326-2766
E-mail: cld62@chrysler.com

Jerry L. Gibbs, DOE Technology Manager

U.S. Department of Energy
E-mail: jerry.gibbs@ee.doe.gov

Start Date: July 1, 2015

End Date: June 30, 2018

Project Funding: \$2,000,000

DOE share: \$1,500,000

Non-DOE share: \$500,000

Project Introduction

The key focus of this program is to further develop newly invented materials for the selective catalytic reduction (SCR) of nitrogen oxides (NO_x) by ammonia (NH₃) that show promise for significantly reducing ‘light-off’ temperatures compared to current commercial catalysts. Specifically, the goal of the proposed work is to achieve ‘light-off’ of NH₃ SCR at 150°C in order to realize conversion efficiencies of 90% at these low temperatures. This will enable the deployment of lean combustion powertrains with significantly increased fuel efficiencies, but lower exhaust temperatures. To accomplish these overall goals, it will be essential to also identify an appropriate NH₃ supply strategy for the SCR aftertreatment device that can controllably deliver NH₃ at these low temperatures.

Objectives

- Develop an enabling SCR catalyst system that will function at very high-efficiency to attain the most demanding emissions regulations and thereby facilitate the market introduction of advanced powertrains that will support domestic energy independence and security.
- Further develop newly invented materials for the SCR of NO_x by NH₃ that show promise for significantly reducing ‘light-off’ temperatures compared to current commercial catalysts. Specifically, the goal of the proposed work is to address the challenge of ‘light-off’ of NH₃ SCR at 150°C in order to realize conversion efficiencies of 90% at these low temperatures.

Approach

This project adapts a newly developed SCR material to function with high-efficiency under conditions consistent with low-temperature portions of drive cycles. We will demonstrate the SCR catalyst, aged under realistic conditions (lean or stoichiometric), will provide 90% conversion efficiency at/near 150°C. For the aftertreatment system, we will demonstrate that a SCR catalyst system will attain Tier III and Super Ultra-Low Emission Vehicle 30mg/mi emissions using an engine or simulated engine federal test procedure cycle. We will evaluate SCR catalyst system activity using alternate upstream NO_x control and NH₃ generation strategies

to achieve Tier 3 criteria emissions control and greenhouse gas emissions minimization, and to estimate the fuel penalty, control/OBD (on-board diagnosis) complexity, and component/system cost.

Results

This research involves preparation of large quantities of SCR catalysts (> 500 g) at Pacific Northwest National Laboratory (PNNL) that were delivered to Fiat Chrysler Automobiles U.S. LLC (FCA) for washcoating on monolith substrates. The zeolite synthesis vessels at PNNL only have low capacities (10-20 g per batch). Therefore, reproducibility in zeolite synthesis and solution ion exchange is of high importance. Figure I.3.A.1 shows that SCR catalysts prepared using three different batches of zeolites displaying almost identical catalytic performance, thus demonstrating high reproducibility for our catalyst preparation.

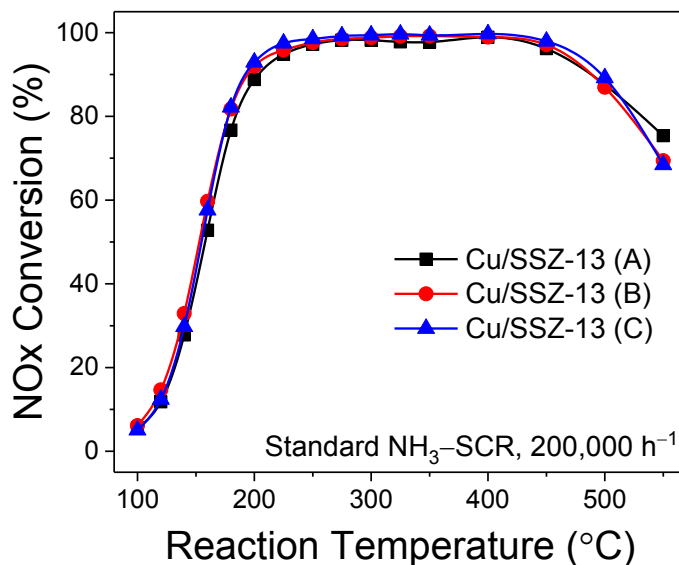


Figure I.3.A.1. Standard SCR performance of three SCR catalysts (A, B, and C) prepared using zeolite substrates synthesized in different batches. Source: PNNL.

In FY 2017, a second generation catalyst was synthesized to further improve the low-temperature NO_x reduction. This catalyst provided additional active sites and continues to maintain high Cu dispersion, allowing ~80% NO_x conversion at 150°C at an application relevant space velocity of 200,000 h^{-1} . This catalyst, however, could not maintain its excellent performance of the freshly prepared form after harsh hydrothermal aging at 700°C. To further improve long-term stability of the catalyst without sacrificing low-temperature performance, a third-generation catalyst was designed that contains less Cu than in the second generation, and a certain amount of alkali co-cations for structural stabilization. Our research indicated that the nature and the quantity of the co-cation are critical for the preparation of optimized catalysts. Using Na^+ co-cation as an example, DFT simulations were used to demonstrate the varying roles a co-cation can play. Figure I.3.A.2 displays a simple calculation to simulate energy difference of the catalyst under two scenarios: (1) Cu^{2+} is positioned in the window of 6-membered ring (6MR) and Na^+ co-cation is placed in the window of 8MR; and (2) Cu^{2+} is positioned in the window of 8MR (stays as $[\text{Cu}^{\text{II}}(\text{OH})]^+$ as a charge-balancing requirement), and Na^+ is located in the window of 6MR. The simulation demonstrates that the latter scenario is ~43 kJ/mol less stable than the former, suggesting that at optimized Cu^{2+} and Na^+ loadings, Na^+ will not destabilize Cu^{2+} (i.e., displacing it from its energetically most favorable position, windows of 6MR). Rather, it neutralizes residual Brønsted acid sites of the zeolite substrate, thus preventing dealumination in hydrothermal aging.

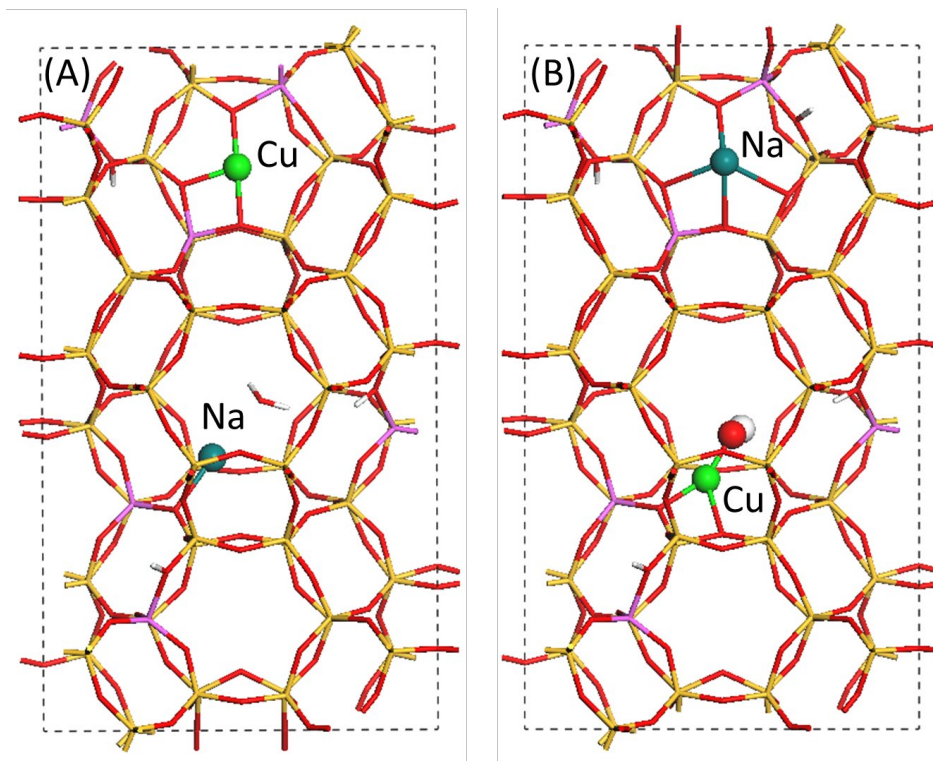


Figure I.3.A.2. DFT simulated Cu(II) and Na⁺ structures in SSZ-13. (A) Cu²⁺ in 6MR and Na⁺ in 8MR; (B) Na⁺ in 6MR and [Cu^{II}(OH)]⁺ in 8MR. Structure (B) is ~43 kJ/mol less stable than (A). Color codes: Cu: green; Na: blue; O: red; H: white. Source: PNNL.

DFT simulations were conducted to investigate whether co-cations destabilize [Cu^{II}(OH)]⁺ active sites. In this case, a [Cu^{II}(OH)]⁺ active site was placed in the zeolite cage next to 8MR with and without the presence of a Na⁺ in the proximity (in the same cage, next to the same 8MR), as shown in Figure I.3.A.3. Activation energy barriers for hydrolyzing this active site to a free Cu(OH)₂ that can be readily removed from the cage were calculated. It was found that in the absence of Na⁺, the activation energy barrier was 120.6 kJ/mol; however, in the presence of Na⁺ to stabilize the reaction intermediate, the activation energy barrier decreased to 61.2 kJ/mol. This demonstrates that Na⁺ can indeed destabilize [Cu^{II}(OH)]⁺ during hydrothermal aging, thus promoting the formation of unwanted CuO_x clusters, which form via condensation of Cu(OH)₂ molecules.

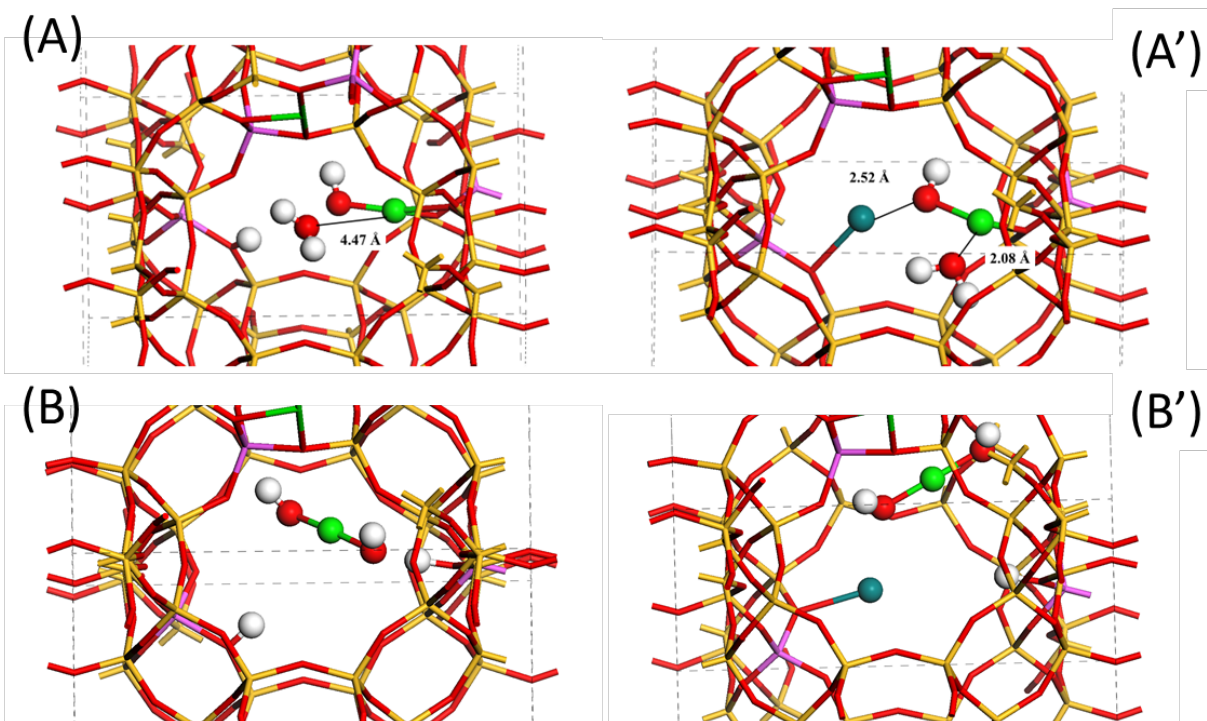


Figure I.3.A.3. DFT simulated $[\text{Cu}^{\text{II}}(\text{OH})]^+$ hydrolysis to $\text{Cu}(\text{OH})_2$ with and without the presence of Na^+ . (A) Initial structure, $[\text{Cu}^{\text{II}}(\text{OH})]^+ + \text{H}_2\text{O}$ in cage next to 8MR; (B) Final structure, $\text{Cu}(\text{OH})_2 + \text{H}^+$ in cage next to 8MR; (A') Initial structure, $[\text{Cu}^{\text{II}}(\text{OH})]^+ + \text{Na}^+ + \text{H}_2\text{O}$ in cage next to 8MR; (B') Final structure, $\text{Cu}(\text{OH})_2 + \text{Na}^+ \text{H}^+$ in cage next to 8MR Structure. The latter hydrolysis is energetically much more facile than the former. Color codes: Cu: green; Na: blue; O: red; H: white. Source: PNNL.

On the basis of combined experimental and theoretical work, a third-generation catalyst was formulated. Figure I.3.A.4 presents SCR performance comparison between the second and the third-generation catalysts. Note that both catalysts have been hydrothermally aged at 700°C . At 160°C , NO_x conversion efficiency reaches $\sim 80\%$ for the second generation catalyst; however, performance above 400°C becomes unsatisfactory due to the presence of large quantities of unwanted CuO_x clusters in this catalyst, which selectively catalyze ammonia oxidation at such temperatures. On the other hand, even though the third-generation catalyst sacrifices $\sim 6\%$ NO_x conversion efficiency loss at 160°C , it greatly gains high-temperature SCR selectivity. More importantly, the long-term stability of the third catalyst is expected to be much-improved than the second generation.

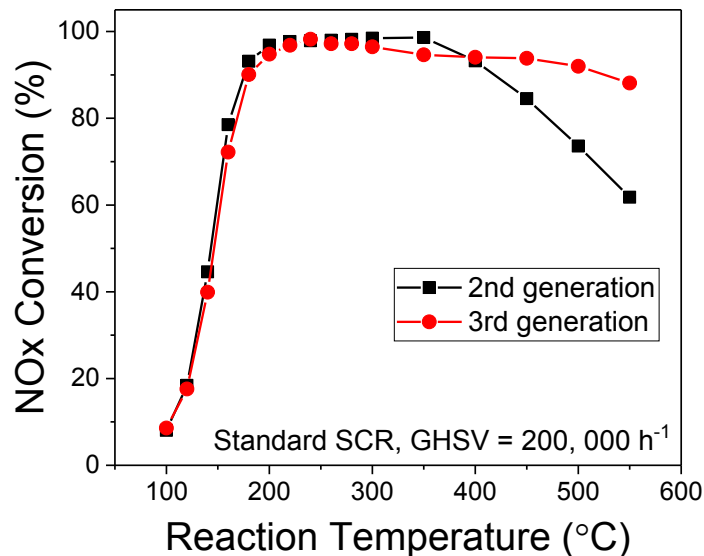


Figure I.3.A.4. Standard SCR performance of the second and third SCR catalysts after hydrothermal aging at 700 °C.

Source: PNNL.

Conclusions

In summary, the following efforts were accomplished:

- Determined an optimized composition of the third-generation low-temperature SCR catalyst containing alkali co-cations based on both experimental and theoretical approaches.
- Verified sufficient hydrothermal stability of the third-generation catalyst formulation which excels in both low and high-temperature SCR conditions.
- Demonstrated varying roles of co-cations via theoretical simulations with DFT.
- Demonstrated light-off of the second and third-generation SCR catalysts is improved over industry-standard (>75% NO_x @ 175°C).
- Successfully synthesized large quantities of the third-generation catalyst for washcoating needs and transferred the material to a monolith for pre-vehicle evaluation.
- Down-selected alternatives to urea NH₃ generation.
- Derived a kinetic model to predictively control the function of a three-way catalyst (TWC) + NO_x storage converter catalyst technology for NO_x control & NH₃ generation.

I.3.B Metal Matrix Composite Brakes Using Titanium Diboride (Pacific Northwest National Laboratory)

Glenn Grant, Principal Investigator

Pacific Northwest National Laboratory
902 Battelle Blvd.
Richland, WA 99354
E-mail: glenn.grant@pnnl.gov

James McMillen, Co-Principal Investigator

Arconic Technical Center
100 Technical Dr.
New Kensington, PA, 15069
E-mail: james.mcmillen@arconic.com

Jerry L. Gibbs, DOE Technology Manager

U.S. Department of Energy
E-mail: jerry.gibbs@ee.doe.gov

Start Date: October 1, 2017
Project Funding: \$350,000

End Date: September 30, 2019
DOE share: \$100,000

Non-DOE share: \$250,000

Project Introduction

There is currently no viable, cost-competitive alternative to cast-iron brake rotors for the automotive market. While in past years, many weight savings materials and designs have come to other parts of the vehicle, the brake assembly remains tied to nearly fifty-year-old technology, as shown in Figure I.3.B.1. Metal matrix composites (MMCs) present an opportunity to replace cast-iron brakes in certain vehicles. By replacing cast-iron rotors with lighter weight MMCs there is an opportunity to reduce the unsprung weight of the brake assembly and adjacent components, such as the suspension arms and springs. A 50% savings in mass in a rotating and unsprung location can lead to a 0.25 to 0.35 mpg fuel savings in a mid-sized car. In addition, Al MMC brakes can provide combinations of high-friction coefficient, particular heat transfer characteristics, and increased wear life that can favorably affect system life cycle cost. A 50% increase in wear life can double the interval between rotor change-outs and can affect the economics for those vehicles sensitive to down time. Lower wear also means fewer wear particles are generated during braking. These wear particles are the second largest source of particulate emissions from a vehicle. “In urban areas, around 55% of total non-exhaust PM10 (particulate matter smaller than ten micrometers) emissions is from brake wear” [1].

Al MMC brake rotors have been investigated in the past in DOE-funded programs during the early 2000s. A commercial application of Al MMC silicon carbide (SiC) rotors was implemented in a limited number of Plymouth Prowler vehicles in 1998, and numerous manufacturers have implemented Al MMC rotors and drums in limited production vehicles (i.e., Toyota RAV4-EV, General Motors EV1, Lotus Elise, and Volkswagen Lupo). But in all cases, cost avoidance could not be fully demonstrated from replacing the cast-iron equivalent part.



Figure I.3.B.1. Conventional brake design utilizing an Al caliper and a cast-iron brake disc. Source: PNNL.

The current automotive landscape, however, has changed in the past 10 years and the changes may be opportunities to look again at Al MMC brakes. One of the significant changes comes from electric/hybrid vehicles. Energy harvesting in electric/hybrid vehicle operation decreases the amount of energy that must be dissipated by the mechanical brakes by as much as 40%. This can allow for much lower front brake temperatures, enabling the use of lighter weight, lower melting temperature alloys as rotors. Also, cast-iron rusts and the friction coefficient of rusty surfaces is not consistent, making it difficult to manage in brake-by-wire systems tasked with balancing mechanical brake force with energy harvesting. Consumers demand a smooth stop (i.e., driver feel and noise, vibration, and harshness issues) and corrosion-resistant and low-wear alloys (i.e., Al MMCs) may provide better control. Another factor is the coming change in duty cycle for a vehicle. The next-generation of personal transportation vehicles may need drastically improved durability and longer maintenance intervals if they are to be used in new mobility strategies like 24/7 ride-sharing or fleet-ownership scenarios.

Barriers to more widespread use of MMCs for vehicle lightweighting are: (1) the costs of the feedstock, especially the insoluble reinforcement (e.g., particle, whisker, or fiber), usually SiC; (2) the cost of combining the reinforcement with the matrix in-production, which requires cost and effort to ensure the SiC particles are “sized” or coated correctly to promote wetting in molten Al; and (3) the cost of shaping/machining MMC components. One of the concepts to address the barriers above is to develop an alternative reinforcing particle. TiB₂-reinforcement offers an opportunity to improve wear resistance at a lower particle loading because of improved ceramic-Al bonding. SiC reinforcement is costly when prepared for inclusion in an Al composite (i.e., particle size fraction constraints, SiO₂ coating, etc.). TiB₂ has much-improved wetting with Al allowing for finer particle size, better homogeneity, and may prove to be at a lower cost overall due to lower particle loading required and reduced compositing time for the same friction and wear performance.

Recent Arconic improvements to the TiB₂ production process may make it a more viable technical ceramic for MMCs than in the past. This LightMAT funded project will utilize TiB₂ as a substitute for more traditional MMC efforts using SiC in an effort to improve performance, wear life, and cost in brake rotors.

Objectives

The objective of this project is to reduce the weight of brake rotors by >50% over current cast-iron materials, and at the same time, improve brake performance, wear life, and life cycle cost over cast-iron systems. The project will develop an Al MMC material that shows appropriate wear resistance, friction coefficient, and tribologic properties, and shows a potential for a cost/benefit ratio appropriate for commercial development.

Approach

The overall approach to the work will be to cast TiB₂-reinforced Al brake rotors in several different reinforcement loadings and test for friction and wear performance. The data will be compared to a large DOE-generated database of properties developed on Al-SiC (and other) MMC brake materials in the early 2000s.

The project will proceed through six tasks, as shown in Figure I.3.B.2. The first task involves the production of a 50 volume percent reinforced master alloy produced at the Arconic Technology Center. This master alloy is produced by liquid Al infiltration of a TiB₂ preform. Eventually, if wear testing is favorable, it is envisioned that the final composite will be made by direct powder addition and rapid mixing in the melt state, and not by preform infiltration, but this route gets the project to the initial wear test trials.

Task Number & Brief Description	FY17				FY18				FY19			
	Q1	Q2	Q3	Q4	Q1	Q2	Q3	Q4	Q1	Q2	Q3	Q4
Task 1: Raw Material Production (Arconic Task)												
Task 2: Casting of MMC Billet												
Task 3: Machining of MMC Test Rotors												
Task 4: Material Characterization (Arconic Task)												
Task 5: Brake Wear Testing												
Task 6: Final Report												

Figure I.3.B.2. Project tasks. Source: PNNL

In a second task, PNNL will use the Al-TiB₂ master alloy along with an Al A356 ingot to cast four MMC billets of MMC composition (i.e., 5, 10, 15, 20 vol% TiB₂) utilizing PNNL MMC stir-casting technology and equipment, as shown in Figure I.3.B.3 and Figure I.3.B.4.

These billets are then machined to subscale rotors for wear testing, which is comprised of mounting the subscale rotors on an instrumented brake testing rig (see Figure I.3.B.5) capable of rotating the rotor or pad holder and applying clamping loads appropriate for automotive braking conditions. Several energy profiles were investigated including low-temperature, low-load continuous torque tests, and high-load, high-temperature transients.

After testing, the data on loads, torque, power, and temperature are compiled, and friction coefficients are calculated and correlated to test conditions. During the tests, the rotors are paired with several different pad compositions, as shown in Figure I.3.B.6, to measure the effect and to optimize the friction pair.



Figure I.3.B.3. Tilt-pour stir-casting equipment at PNNL used for the casting trials. Flat-bladed impeller installed in mixer head. Source: PNNL.



Figure I.3.B.4. Impeller designs for mixing trials. Source: PNNL.



Figure I.3.B.5. Brake-friction pair test-stand at PNNL. Source: PNNL.

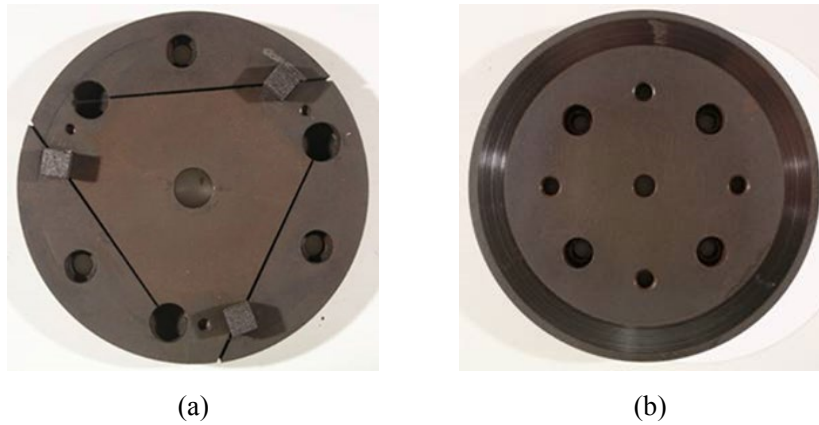


Figure I.3.B.6. (a) Brake pad holder and (b) tested subscale brake rotor. Source: PNNL.

After testing, rotors and pads are measured and weighed to establish mass gain or loss and the rotor wear tracks are analyzed for geometry, as shown in Figure I.1.B.7. The transfer layer usually formed on the rotor is also analyzed for chemistry and pad reactions. The testing data will be utilized to evaluate the feasibility and advantages of using TiB₂ as a reinforcement for an Al MMC brake rotor.

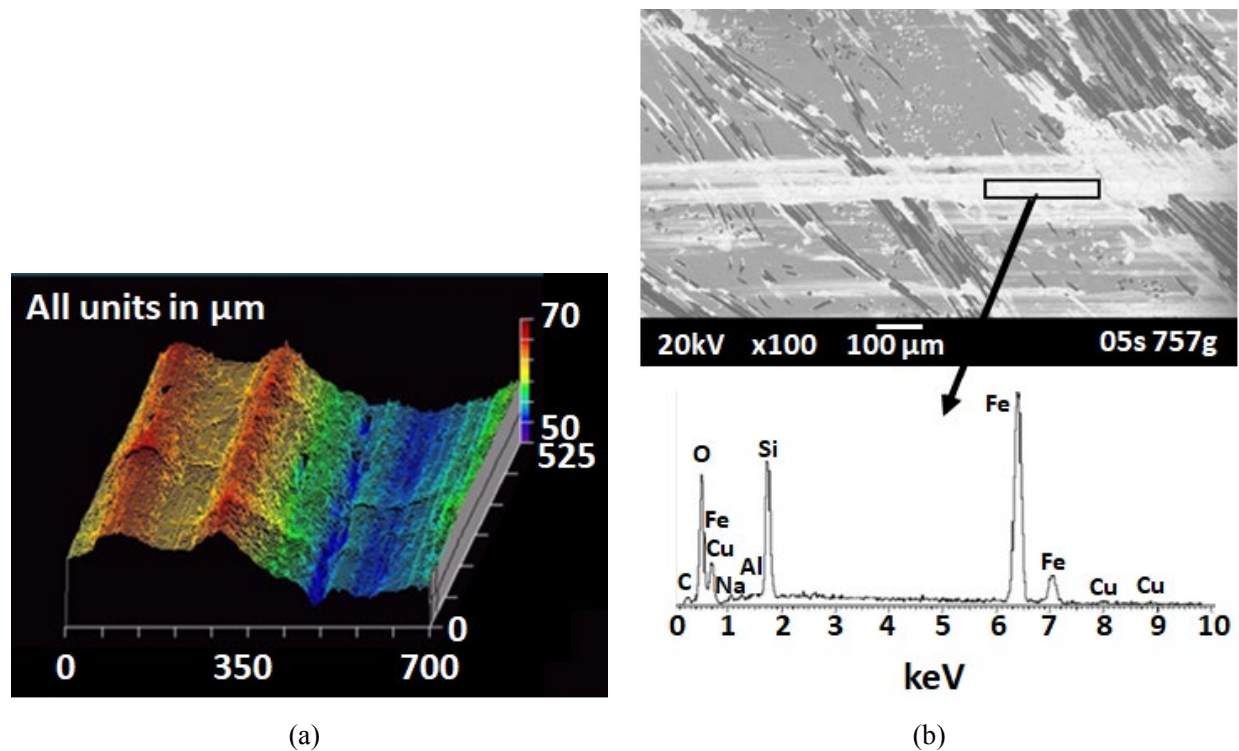


Figure I.3.B.7. (a) Wear-track profilometry and (b) transfer layer chemistry characterization. Source: PNNL.

Results

During FY 2018, a master alloy was fabricated at Arconic by infiltrating a TiB₂ preform with Al A356 in a book mold. The master alloy castings are approximately 50% Al and 50% TiB₂ based on microstructure and density measurements. The master alloy and A356 ingot were then sectioned and combined in a crucible at appropriate ratios to produce 5 vol% reinforced melts. A series of stir-casting trials were also initiated to establish mixing times, melt temperatures, mixing paddle geometry, and mixing paddle speeds, as shown in Figure I.3.B.8.

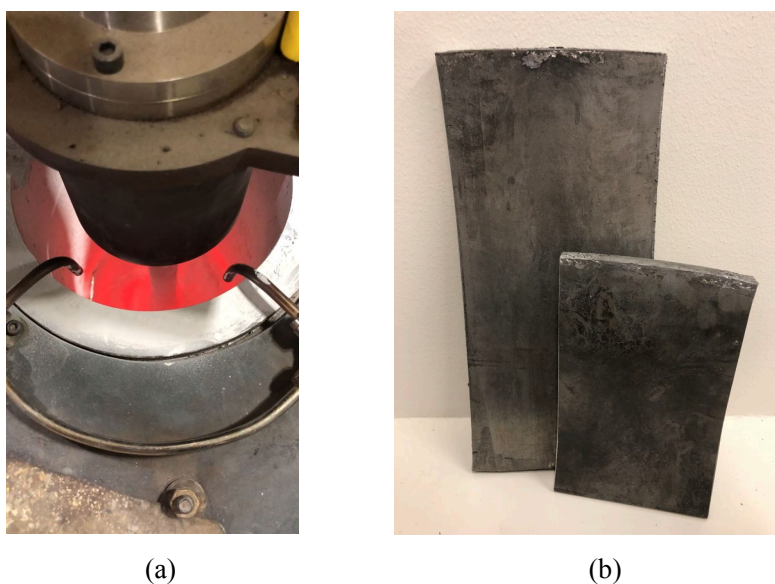


Figure I.3.B.8. (a) Stir-casting trials and (b) cast plates of 5 vol % TiB₂ reinforced A356 alloy. Source: PNNL.

After a sufficient mixing time, the melts were poured into open steel-book molds to produce rectangular castings approximately 10 in x 7 in x 1 in. Initial microscopy on these castings revealed minor porosity <5%. Production Al MMC rotors would likely be fabricated by squeeze-casting or high-pressure die-casting where porosity would be minimized, so we decided to hot-roll the plates to better mimic a final product configuration.

The as-cast plates were hot-rolled at 450°C for two passes with approximately 30% total reduction. Figure I.3.B.9, Figure I.3.B.10, and Figure I.3.B.11 show the evolution of the microstructures from the as-cast, hot-rolled, and rolled-plus solutionized and heat-treated plates (T7), respectively. Observed porosity in the as-cast plates was partially closed and healed during hot rolling, as anticipated, and subsequent overaged T7 heat-treating caused rounding of eutectic constituent morphology as expected.

In FY 2019, we will continue casting trials to produce Al MMCs at higher particle loadings of 10 and 15 vol%. Plates will be machined to subscale rotor configurations and wear and tribologic testing should begin in the second quarter of FY 2019.

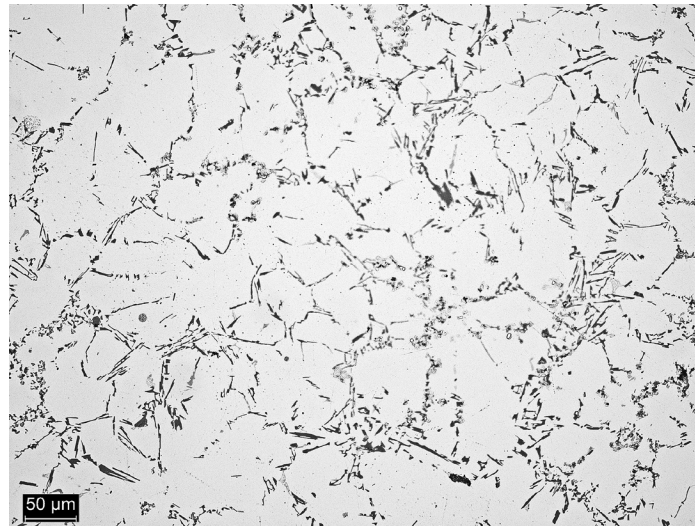


Figure I.3.B.9. As-cast 5 vol % TiB₂-reinforced A356. Source: PNNL.

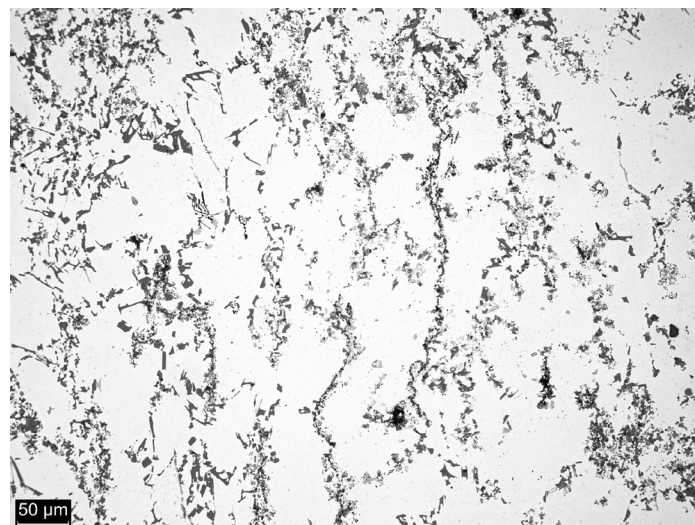


Figure I.3.B.10. 5 vol % TiB₂-reinforced A356 hot-rolled 30% reduction. Source: PNNL.

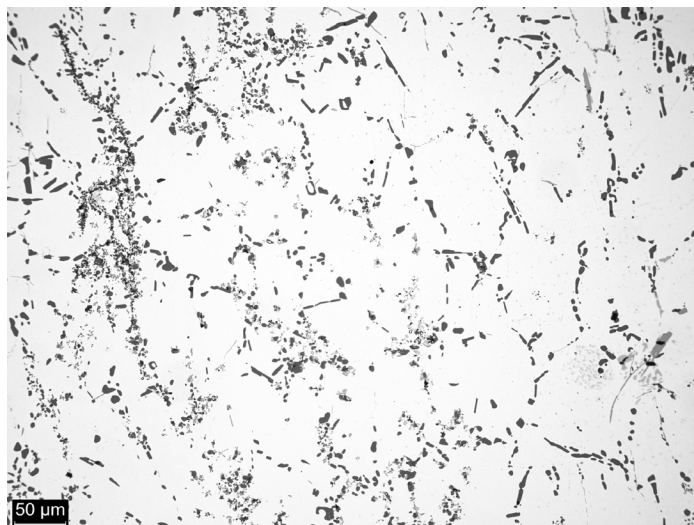


Figure I.3.B.11. 5 vol % TiB₂-reinforced A356 hot-rolled, solutionized, and artificially aged to T7. Source: PNNL.

Conclusions

PNNL and Arconic have completed the first stage of casting master Al composite alloys of A356 and TiB₂, and subsequently cast into plates in which wear and tensile test coupons will be fabricated from. Future, stage-2, task will include mechanical testing this material for wear and strength properties.

Vehicle platforms have created opportunities to re-evaluate Al MMC brakes. Lightweight brake rotors have an opportunity to contribute to vehicle lightweighting efforts and offer the possibility of a 50% weight savings in rotating and unsprung mass in some vehicle applications. This project investigates a potentially lower cost reinforcement than the more traditional SiC. The project will assess this concept by fabricating TiB₂-reinforced subscale brake rotor components, test them for wear and tribologic performance and compare this performance to a large dataset of performance characteristics generated by DOE projects on Al/SiC MMCs in the early to mid-2000s. The results of this work will inform an opportunity for lightweighting this important contributor to vehicle mass.

References

1. Halonen, A. "Is Now the Time for Lightweight Brakes?" The BRAKE Report, January 14, 2016. <https://thebrakereport.com/is-now-the-time-for-lightweight-brakes/>.

I.3.C Direct Extruded High-Conductivity Copper for Electric Machines (Pacific Northwest National Laboratory and General Motors Research and Development)

Glenn Grant, Principal Investigator

Pacific Northwest National Laboratory
902 Battelle Blvd.
Richland, WA 99354
E-mail: glenn.grant@pnnl.gov

James Schroth, Principal Investigator

General Motors Research and Development Laboratory
30470 Harley Earl Blvd.
Warren, MI 48090
E-mail: james.g.schroth@gm.com

Jerry L. Gibbs, DOE Technology Manager

U.S. Department of Energy
E-mail: jerry.gibbs@ee.doe.gov

Start Date: October 1, 2017	End Date: September 30, 2019	
Project Funding (FY18): \$350,000	DOE share: \$100,000	Non-DOE share: \$250,000

Project Introduction

The efficiency, weight, power density, and cost of an electric machine could be improved if the primary conductors could be made with much higher conductivity than standard electric Cu. This project is developing a high power induction motor that utilizes a rotor “squirrel cage” (shorting bars and wire) composed of a new high-conductivity, Cu-C composite material fabricated by shear-assisted extrusion, a new manufacturing process being developed at PNNL.

The Cu composites are fabricated using our ShAPE™ (Shear-Assisted Processing and Extrusion) process, which allows us to create non-equilibrium alloys and composites that cannot be made by conventional processing. The process is used to mix, shear, and extrude Cu composite wire and bar that are combinations of Cu and various forms of carbon, including nanotubes, graphene, and graphite. The solid-state ShAPE process allows us to mix and densify the composite without the restrictions imposed by conventional melt-solidification processes. Cu-C composites are well-known in the research world for their enhanced conductivity and ampacity, but scalable methods to fabricate products (to densify and evenly mix these composites) have been elusive. We envision developing commercially relevant wire products, like square bar for windings and shaped rod extrusions (that are used to fabricate induction motor rotor shorting bars), by using the shear-assisted extrusion process.

Objectives

The objective of the project is to improve the performance of an induction motor rotor of commercial interest to hybrid/electric vehicle propulsion. The project is developing solid-phase methods to create higher conductivity Cu-C composites to increase the efficiency of the electric drive. Our focus is on using Cu-C composite materials for wire and shorting bar applications in the motor rotor, and potentially the stator as well. The target application is the induction rotor shorting bar. An induction rotor is shown in Figure I.3.C.1. The shorting bars are the linear blade-like parts that run the height of the rotor from end cap to end cap. These bars can be seen in Figure I.3.C.1 just protruding out of the grey electric steel laminates, forming thin Cu-colored vertical lines. The bars allow for current to flow between the end caps during motor operation. Higher conductivity in this bar will allow for greater torque to be generated, which can lead to potential improvements in performance or downsizing and lightweighting opportunities, depending on product drivers.



Figure I.3.C.1. Induction motor rotor and an example of a shorting bar. Source: PNNL.

The ShAPE process, which is like a conventional extrusion process with a simultaneous high-shear component added at the die throat, is being developed for the three forms of Cu-C composite: (1) Cu/graphite, (2) Cu/graphene, and (3) Cu/carbon-nanotubes. The objective is to extrude wire and bar forms and measure electrical and other properties. This work is accomplished on a new first of its kind shear-assisted extrusion machine. This device, as shown in Figure I.3.C.2, is capable of extruding billet or powder feedstocks with a 100-ton force and 1,000 ft/lbs of rotational torque at the billet face.

The rod and wire product forms will be sent to GM where they will be roll-formed to the cross-section appropriate for the test rotor shorting bars. The bars will then be sectioned and assembled into actual rotors. The rotors will be returned to PNNL to be friction stir welded into a complete assembly, and then sent back to GM for testing. If successful, it is anticipated that this could lead to a step change in motor efficiency, weight, packaging, and potentially even affect some current motor challenges related to moving to a higher voltage or higher rpm.

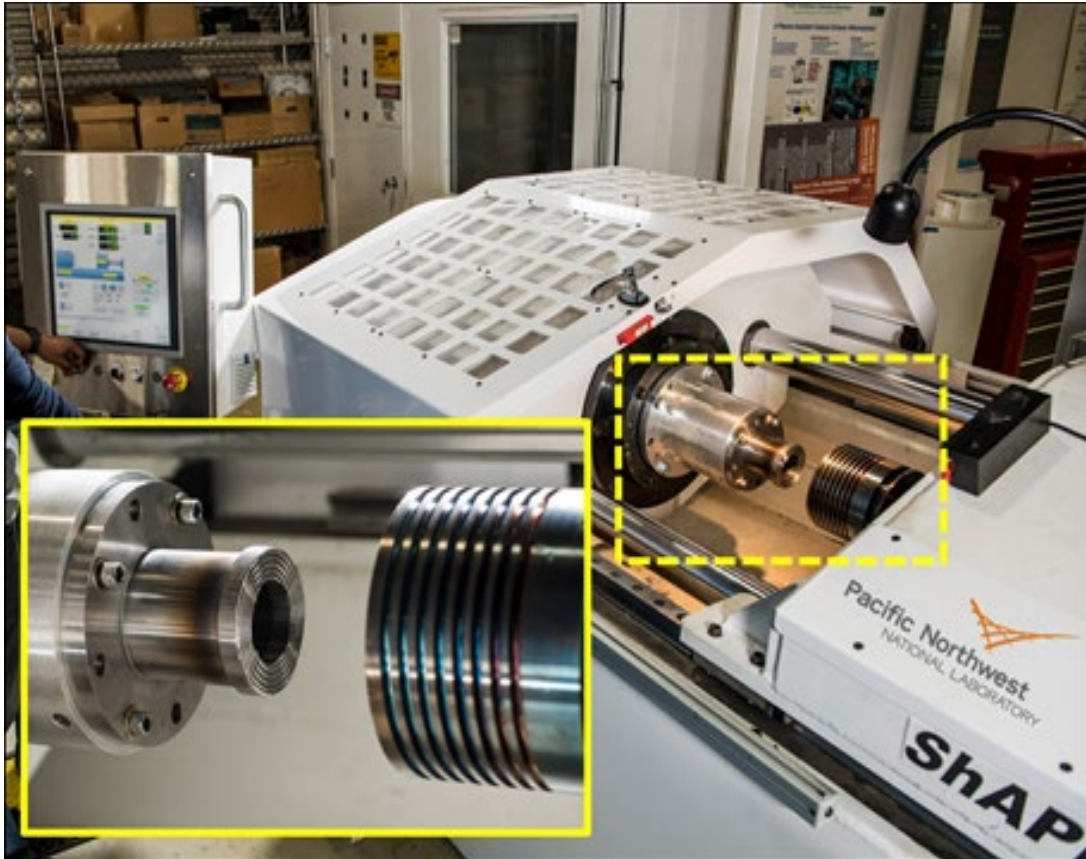


Figure I.3.C.2. Shear-Assisted Extrusion machine. Source: PNNL.

The project is a 50%/50% cost share Cooperative Research and Development Agreement with GM and will develop a motor application relevant to their commercial transportation market. GM researchers play active roles in the effort in the areas of electrical performance measurement and fabrication testing.

Approach

This project will develop a unique, high-shear process (ShAPE), as shown in Figure I.3.C.3, for the fabrication of high-conductivity Cu materials. The main difference between ShAPE and conventional extrusion is that ShAPE uses intense rotational shear to deform material simultaneously with material flow through the die opening. The intense shear heats and deforms the billet, or heats and densifies a powder charge as it is extruded. The high-shear also acts to homogenize and mix discontinuous second phase particles, powders, or composite phases into a single dense extrudate with unique texture and grain refinement.

The project uses this process to create composites between Cu and three forms of carbon: (1) graphite, powder; (2) graphene, powder or foil; and (3) carbon nanotubes (CNT), powder. Three different processing schemes have been implemented: (1) powder blending and direct extrusion, where Cu powder and C powder are pre-mixed as precursor materials, and then loaded into a can and extruded directly; (2) powder blending, consolidation, and then extrusion, where Cu powder and C powder are also pre-mixed, but prior to extrusion, precursors are consolidated by a shear-assisted densification process prior to extrusion (the pre-extrusion step ensures that the extrudate is solid, especially when a high-carbon loading is adopted); and (3) drilling holes in a solid Cu billet and filling the holes with C powder or C foil, and then the composite billet is extruded by ShAPE. Figure I.3.C.4 provides an example of the latter processing scheme.

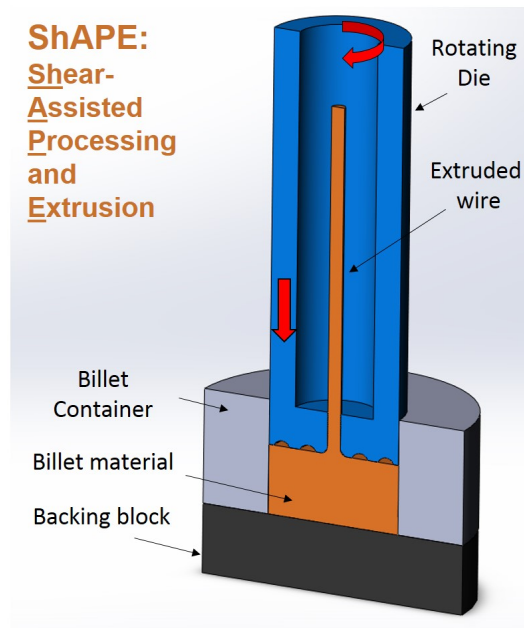


Figure I.3.C.3. Schematic diagram of ShAPE. Source: PNNL.



Figure I.3.C.4. Cu cylinder drilled and filled with C powder Source: PNNL.

The project will deliver quantitative experimental results of mechanical and electrical testing. After the development stage, a rod or wire product form will be produced by shear-assisted extrusion. This product form will be a shaped extrusion similar to the wire shape used as a preform for the shorting bar stock used in the induction rotor. The preform will be rolled into shorting bar shape by GM and assembled into rotors. Final end cap welding will be accomplished at both PNNL and GM using friction stir welding and other joining methods. Fabricated rotors will be tested in GM facilities for electrical, thermal, and mechanical performance. In addition, the project will transfer to GM data on aspects of the process of interest to economic modeling, including extrusion speed, die cost, tool life, and practical aspects of fixturing, power, and process control.

This comprehensive path from material, through product form development and finally to rotor assembly, should allow for rapid commercialization of the concept. Figure I.3.C.5 provides examples of the three forms of carbon additions this project plans to study, while Figure I.3.C.6 shows examples of the wire we intend to employ.

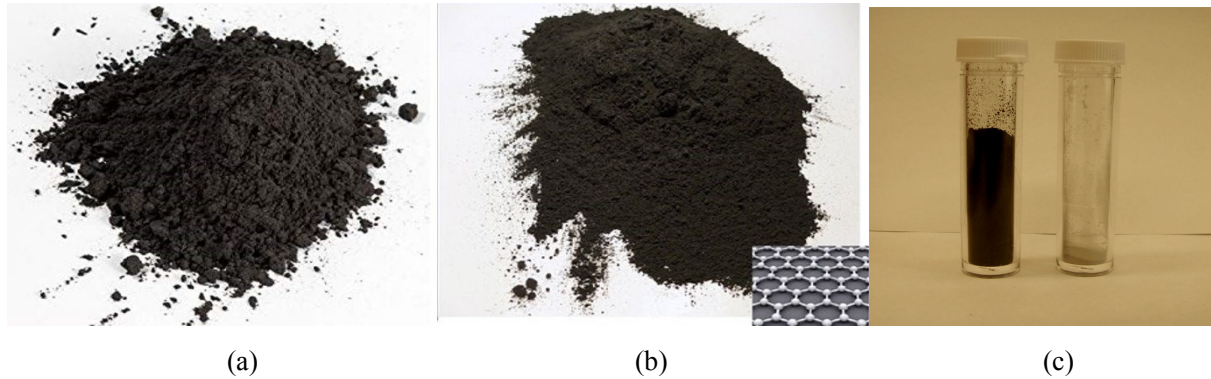


Figure I.3.C.5. Carbon additions used for high-conductivity Cu-C composite: (a) graphite, (b) graphene and (c) C nanotubes. Source: PNNL.

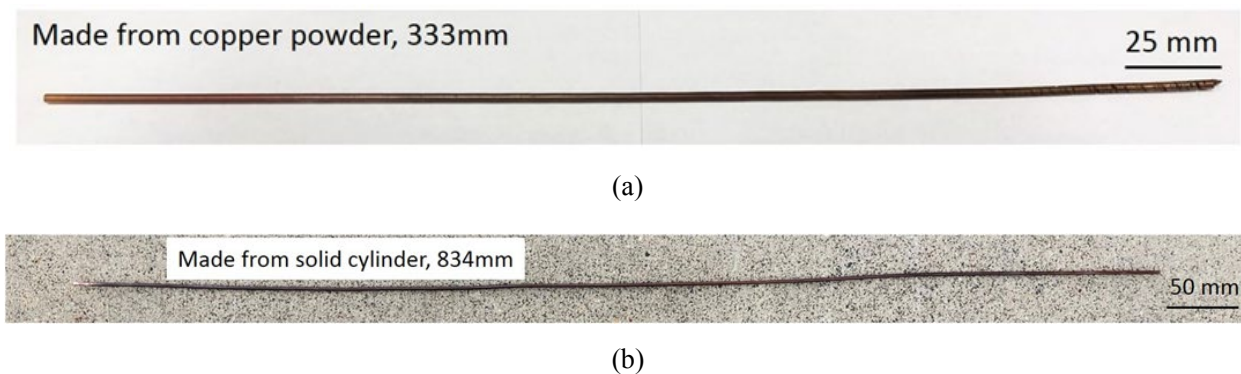


Figure I.3.C.6. Cu wire made from (a) pure Cu powder and (b) pure Cu solid billet. Source: PNNL.

Results

During FY 2018, the efforts to establish the methods and processes to produce ShAPE extruded wire were developed initially on pure Cu. Process variables such as die rotation rate, extrusion, or ram speed, die geometry and extrusion ratio were systematically varied to discover the process window for making fully dense wire and rod. Pure Cu powder and pure Cu solid cylinders were used as precursor materials. Solid wires with good surface finish have been made from both powder and solid billet precursors. Both transverse and longitudinal cross-sections, as shown in Figure I.3.C.7, show that the wires have fully dense microstructures.

Three different Cu-C composites were investigated utilizing the three different processing schemes. In addition, different tool features and processing parameters (i.e., die rotational speed and feed rate) were investigated to optimize the performance of the extrudate for each different C content and form of precursors. A brief overview of the extrudability of Cu-C ShAPE wire is given in Table I.3.C.1.

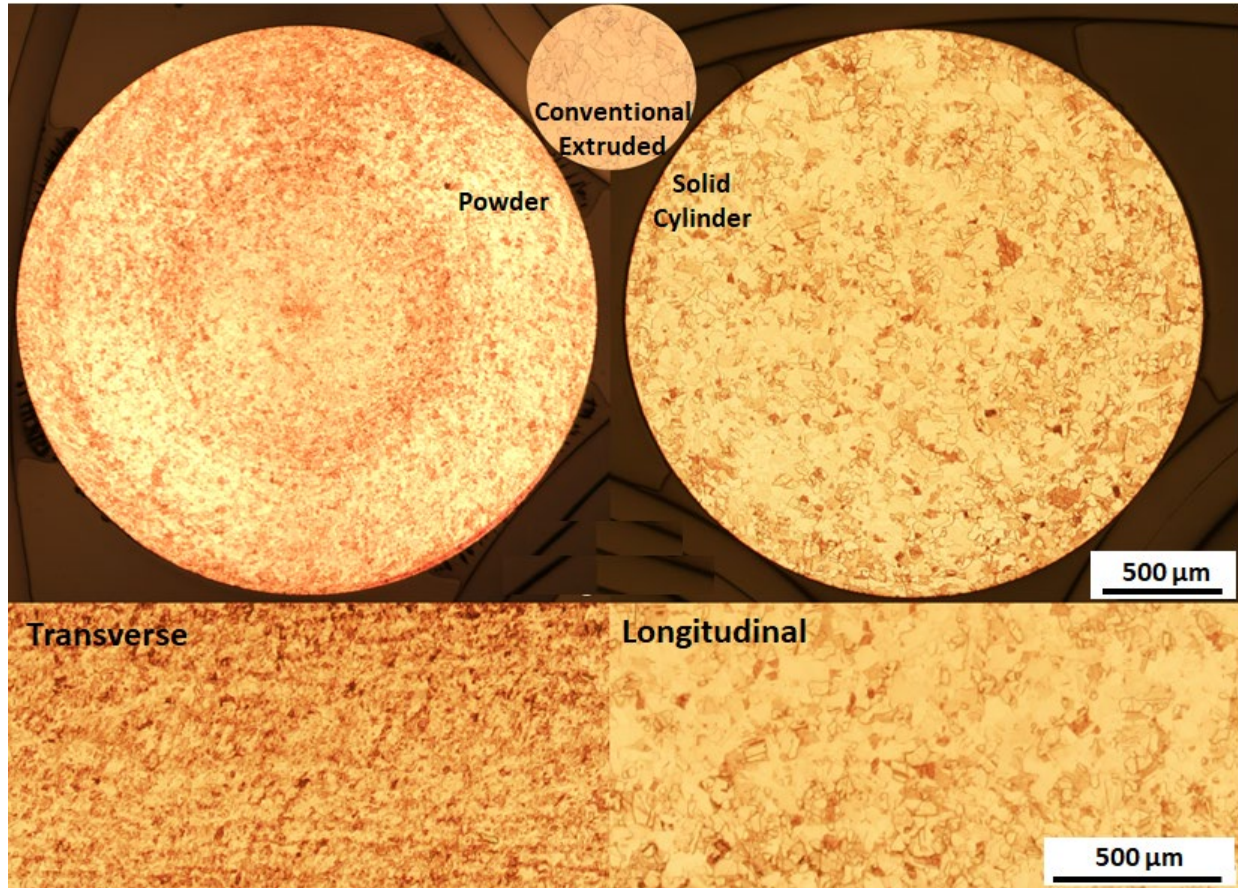


Figure I.3.C.7. Cross-sections of wire made from pure Cu powder and solid cylinder, as compared with conventional extruded Cu wire in transvers and longitudinal directions. Source: PNNL.

Table I.3.C.1. Overview of the Extrudability of Cu-C Composite Wire by ShAPE as of September 2018.

Cu-C-ShAPE Material	Processing Schemes	Powder Blending, then Extrusion	Power Blending, Consolidation, and then Extrusion	Drill and Fill on Solid Cu Cylinder
Pure Cu	0 wt. %	Good	-	Good
Graphite	0.5 wt. %	Good	-	Good
	1 wt. %	Good	-	Good
	2 wt. %	Good	-	-
	4 wt. %	No wire	Good	-
	8 wt. %	-	Good	-
Graphene	1 wt. %	Good	-	Broken wire
	2 wt. %	Good	-	-
	Pure Foil	-	-	Good
CNT	<1% CNT	-	-	Good
	1% 1-4nm CNT	Broken wire	-	-
	1% 8nm CNT	Broken wire	-	-

The microstructure of the Cu-C ShAPE wire is presented in Figure I.3.C.8. ShAPE processed wire shows full density and displays a very homogenized dispersion of the C particles throughout the entire cross-section. In the example of Figure I.3.C.8, the particle size of the C powder started at about 40 μm , but after ShAPE processing it was broken down to below 1 μm . Significant grain refinement is also observed in the scanning electron microscope and transmission electron microscope images (Figure I.3.C.8).

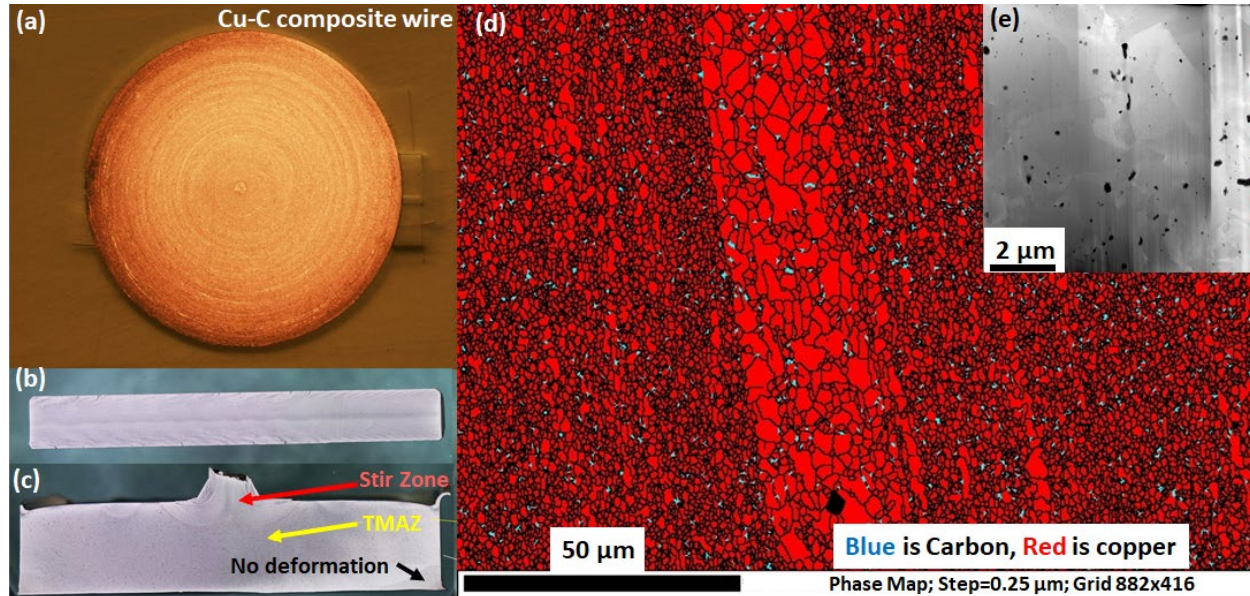


Figure I.3.C.8. Microstructure of Cu-C ShAPE wire (a) transverse cross-section, (b) longitudinal cross-section, (c) vertical cross-section of remnant disc, (d) grain structure with phase mapping and (e) scanning electron microscope image with higher magnification (black is C and grey is Cu). Source: PNNL.

The measured conductivity of the Cu-C ShAPE wire has been summarized and shown in Figure I.3.C.9. The results show that under some conditions of composition and processing, the ShAPE wire has increased electrical conductivity. In one case of a Cu/graphene composite, conductivity was significantly improved above 25% over the International Annealed Copper Standard. This occurred at near RT conditions. However, the increased conductivity is not maintained at high-temperature. This may be due to increased scattering on the interface of the Cu and graphene particles or another as yet undiscovered mechanism. Our focus going forward will be to understand these effects and explore methodologies to raise the elevated temperature conductivity further. Our future focus will be on Cu-graphene powder and Cu-CNT compositions and on methodologies to increase C continuity in the long direction of the extrudate.

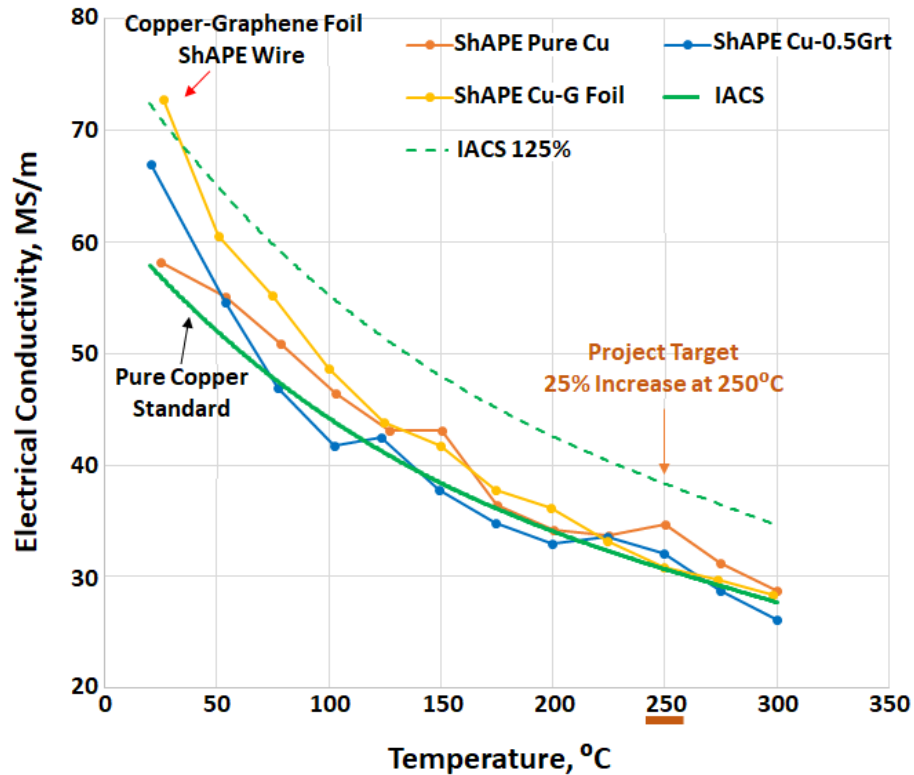


Figure I.3.C.9. Overview of the conductivity of Cu-C ShAPE wire. Source: PNNL.

Conclusions

The first year of the project focused heavily on the development of the shear-assisted extrusion process for making Cu-C composite wires with full density and uniform C distribution. The electrical conductivity results have shown that we have achieved the targeted value of a 25% increase in conductivity at RT, but we have not yet seen a dramatic improvement in conductivity at elevated temperature.

Key Publications

1. Li, X., and G. J. Grant, 2018, "Characterization of pure Cu wire produced by shear-assisted processing and extrusion," *Abs. Materials Science and Technology 2018 (MS&T 18)*, October 18, 2018, Columbus, OH, USA.
2. Li, X., G. J. Grant, C. Zhou, H. Wang, T.A. Perry, and J.G. Schroth, 2019, "Cu-graphite composite wire made by shear-assisted processing and extrusion," presentation to be made at the upcoming *TMS 2019 Friction Stir Welding and Processing X*, March 10-14, 2019, San Antonio, TX, USA.

I.3.D Waste Heat Recovery and Aftertreatment (Oak Ridge National Laboratory)

J. Allen Haynes, Principal Investigator

Propulsion Materials
Oak Ridge National Laboratory
1 Bethel Valley Rd.
Knoxville, TN 37831
E-mail: haynesa@ornl.gov

Jerry L. Gibbs, DOE Technology Manager

U.S. Department of Energy
E-mail: jerry.gibbs@ee.doe.gov

Start Date: October 1, 2016	End Date: September 30, 2019	
Project Funding (FY18): \$75,000	DOE share: \$75,000	Non-DOE share: \$0

Project Introduction

The Waste Heat Recovery and Aftertreatment Project consists of two tasks that are focused on early-stage research in pursuit of advancing the basic mechanical properties, manufacturability, and addressing the affordability of propulsion materials. These tasks have the common goal to develop catalyst materials for energy recovery and aftertreatment for gasoline and diesel engines at lower operating temperatures that may occur with future, more efficient vehicles. The specific tasks include the following:

1. Materials Issues Associated with Exhaust Gas Recirculation (EGR) Coolers.
2. Materials for Waste Heat Recovery/International Energy Agency-Advanced Materials for Transportation (IEA-AMT).

The following sections of this report outline the specific tasks and work conducted at ORNL in the areas of predictive engineering, process development, and enabling technologies for propulsion materials. Each task supports one or more goals within the mission of the Vehicle Technologies Office to develop higher performance materials that can withstand increasingly extreme environments and address the future properties needs of a variety of high-efficiency powertrain types, sizes, fueling concepts, and combustion modes.

I.3.D.1 Task 1D: Materials Issues Associated with EGR Coolers

Michael J. Lance, Principal Investigator

Oak Ridge National Laboratory
1 Bethel Valley Road
Oak Ridge, TN 37831-6068
E-mail: lancem@ornl.gov

Jerry L. Gibbs, DOE Technology Manager

U.S. Department of Energy
E-mail: jerry.gibbs@ee.doe.gov

Start Date: October 1, 2009

End Date: September 30, 2018

Project Funding (FY18): \$25,000

DOE share: \$25,000

Non-DOE share: \$0

Project Introduction

Vehicle manufacturers often utilize exhaust gas recirculation (EGR) as a method of reducing nitrogen oxide (NO_x) emissions to meet strict environmental regulations. In this process, a certain amount of exhaust gas is diverted into a cooler, where its temperature is reduced, before it is re-introduced into engine cylinders along with fresh air. Fouling of EGR coolers is a significant issue as large concentrations of particulate matter and unburned hydrocarbons in the exhaust can cause rapid formation of a fouling layer along the cooler walls. Due to its high porosity [1], this fouling layer can act as an excellent insulator between the cool wall and hot gases, reducing the effectiveness of the heat exchanger. As the effectiveness of the cooler drops, the temperature of the exhaust gas re-introduced into the cooler increases. This results in higher combustion temperatures and, in turn, greater NO_x generation during combustion. One common method employed to reduce the rate of fouling in EGR coolers is the use of sinusoidal shaped fins within the cooler. Although these coolers have been shown to be more resistant to the effects of fouling than those utilizing simple rectangular or circular channel cross-sections, the physical mechanisms driving these differences in performance are not well understood. In this report, we describe our investigations of the effect of varying engine operating conditions on the deposit thickness along the length of the cooler channels.

At the start of this project, an advisory team consisting of engineers responsible for EGR systems was assembled from nine diesel engine manufacturers—Caterpillar, Cummins, Detroit Diesel, Ford, GM, John Deere, Navistar, DAF Trucks, and Volvo/Mack—and one heat exchanger supplier, Modine. They were asked what the biggest problem facing EGR cooling systems is and the clear winner was fouling. Over the course of this project, the EGR team has been notified of results generated and have contributed coolers for forensic analysis of fouling deposits.

Objectives

To provide information to industry about fouling deposit properties so as to enable improved models and potential design improvements to reduce fouling and its impact on the performance of EGR coolers.

Approach

One of the EGR team members, John Deere, was gracious enough to provide 20 coolers that were fouled using different operating conditions at a cost that exceeded \$1,000,000. Each cooler had 12 oblong tubes bundled in a 6 by 2 pattern inside a shell that contained the coolant. Each tube was 48 cm long, 4.4 cm tall, and 0.76 cm wide. There were 20 fins inside each tube spaced ~0.2 cm apart from each other.

Along the flow direction, the fins formed a sinusoidal wave with a wavelength of 1 cm and an amplitude of ~0.065 cm. The coolers were fouled using a 9-liter HD engine and ultra-low sulfur diesel fuel while varying five factors [ranges provided in brackets]: (A) EGR flow rate [83.3-154 g/s], (B) EGR inlet gas temperature

[350-550°C], (C) coolant temperature [85-100°C], (D) smoke level Filter Smoke Number [0.50-2.0], and (E) hydrocarbon (HC) concentration [25-75 ppm]. A five-factor, two-level design of experiments required 16 coolers to test all combinations, with an additional four coolers operated at midpoints for some factors. Coolers were run until the effectiveness stabilized (typically 40-70 h), were cooled down to RT and then run for an additional few hours to measure the change in effectiveness due to shut down.

To measure the true deposit thickness and how it varies across a sinusoidal fin, measurements were performed using a Keyence VR-3100 optical profilometer. Measurements were made on sections near the inlet, center, and outlet of a single channel in each of the 20 coolers. The deposit thickness was calculated from the difference of the surface heights before and after removal of the deposit. The thickness data was analyzed using multiple regression analysis to examine the influence of individual engine operating parameters on the fouling layer thickness at each of the three channel locations.

Results

In all 20 fouled coolers, the deposit maintains the same general shape across each period over the entire length of the channel, as shown in Figure I.3.D.1.1. The deposit was thinnest and thickest on the upstream and downstream sides of the fin peak, respectively. This is due to the fin geometry, which coupled with the high flow rates, is sufficient to produce the shear necessary to inhibit deposit growth along the upstream side of fin for all flow rates investigated. Although the same general deposit shape was found for all conditions, the overall average thickness across each period varies. Furthermore, the engine operating conditions that influence the average thickness varied with position along the length of the channel.

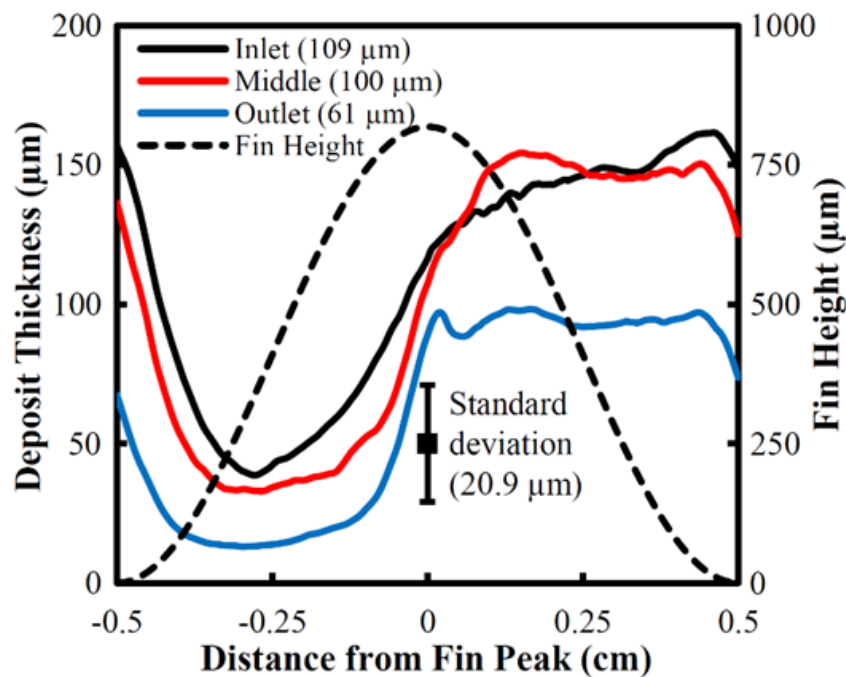


Figure I.3.D.1.1. Average deposit thickness near the inlet, middle, and outlet of cooler. Flow direction left to right.

Source: ORNL.

Using multiple linear regression analysis, the influence of the engine operating conditions on the thickness of the deposit near the inlet, middle, and outlet of the channel was examined. Coefficients corresponding to the resulting best fit model of the average deposit thickness data at each location are provided in Table I.3.D.1.1. In this table, the letters A, B, D, and E represent the EGR flow rate, EGR inlet gas temperature, smoke level (soot concentration), and HC concentration. The first five columns of coefficients, which contain only single

letters, represent the contribution of the corresponding operating condition to best fit models. These can be interpreted as the influence of the operating condition on the deposit thickness, with positive coefficients indicating a positive correlation with the thickness and vice versa. Furthermore, the larger the magnitude of these coefficients, the larger the operating conditions influence on the deposit thickness. The remaining coefficient columns, each of which contain a pair of letters, represent the interaction between the two corresponding operating conditions. These coefficients quantify how one operating condition's influence on the deposit thickness is modified by another.

As seen in Table I.3.D.1.1, the engine operating conditions with the greatest influence on the deposit thickness varies along the length of the channel. Near the channel inlet, the exhaust gas temperature entering the cooler has the largest influence with the deposit thickness decreasing with increasing temperature. This is because higher temperatures enhance the effect of mud-cracking which aids in the removal of large regions through spallation [2-3]. Halfway down the length of the channel, the temperatures are insufficient to induce mud-cracking, but still generate significant thermophoretic deposition, which has the greatest effect on the thickness at this location. Here, the thermal gradients, and therefore the magnitude of thermophoresis, depend heavily on gas residence time. As a result, the flow rate of the exhaust gas has a greatest influence on the deposit thickness in the center of the channel length. Near the outlet of the cooler, the exhaust has been sufficiently cooled for condensation of the HC species to occur. This condensation acts to create a denser deposit, which increases its thermal conductivity. This higher thermal conductivity allows for continued thermophoretic deposition, resulting in formation of a thicker deposit [4]. As a result, of the five operating conditions, the HC concentration has the greatest effect on the deposit thickness near the cooler outlet.

Table I.3.D.1.1. Coefficients Corresponding to the Best Fit Models from Multiple Regression Analysis for the Average Deposit Layer Thickness. Asterisks Indicate the Absence of the Factor in the Best Fit Model.

Location	Factor Coefficients										
	A	B	C	D	E	AB	AD	AE	BC	CE	DE
Inlet	*	-47	*	*	*	-31	*	*	-31	*	*
Middle	27.0	*	*	*	-8.9	*	-14	-15	*	12	-20
Outlet	*	25	*	-16	-40	*	NA	*	*	*	-54

Conclusions

EGR coolers were fouled by varying five engine operating conditions using a 9-liter HD engine. An optical profilometer was used to measure the thickness of the deposit along a single channel near the inlet, middle, and outlet of each of the 20 fouled EGR coolers. Using statistical methods, the engine operating conditions influencing the deposit thickness near the inlet middle and outlet sections of the cooler were investigated.

The greatest influences on deposit thickness in engine operating conditions varies along the length of the channel. Near the inlet of the channel, the exhaust gas temperature entering the cooler has the largest influence, with the deposit thickness decreasing with increasing temperature. Halfway down the length of the channel, the flow rate governs the thermal gradient as it defines the residence time of the fluid in the channel. Because the rate of thermophoretic deposition strongly depends on the thermal gradient, the flow rate has the greatest influence on deposit thickness at this location. Lastly, near the outlet of the cooler, the hydrocarbon concentration begins to have an influence on deposit thickness because temperatures are sufficiently low for significant condensation of HC species that act to form a denser deposit. The higher thermal conductivity of the dense HC-rich deposit allows for continued thermophoretic deposition, increasing deposit thickness. The results of these studies will enable industry to improve models resulting in potential design improvements that will reduce fouling and its impact on the performance of EGR coolers.

Key Publications

1. Lance, M. J., Z. G. Mills, J. C. Seylar, J. M. E. Storey, and C. S. Sluder, 2018, “The effect of engine operating conditions on exhaust gas recirculation cooler fouling,” *Int. J. Heat Mass. Tran.*, Vol. 126, pp. 509–520.

References

1. Lance, M. J., C. S. Sluder, H. Wang, and J. M. E. Storey, 2009, “Direct measurement of EGR cooler deposit thermal properties for improved understanding of cooler fouling,” SAE Technical Paper No. 2009-01-1461.
2. Lance, M. J., J. Storey, C. S. Sluder, H. Meyer III, B. Watkins, M. Kaiser, and P. Ayyappan, 2013, “Microstructural analysis of deposits on HD EGR coolers,” SAE Technical Paper No. 2013-01-1288.
3. Abarham, M., J. Hoard, D. N. Assanis, D. Styles, E. W. Curtis, and N. Ramesh, 2010, “Review of soot deposition and removal mechanisms in EGR coolers,” *SAE International Journal of Fuels and Lubricants*, 3(2010-01-1211) 690-704.
4. Sluder, C. S., J. M. E. Storey, and M. J. Lance, 2014, “Effectiveness Stabilization and Plugging in EGR Cooler Fouling,” in SAE International.

I.3.D.2 Task 2D: Materials for Waste Heat Recovery/International Energy Agency - Advanced Materials for Transportation

Hsin Wang, Principal Investigator

Oak Ridge National Laboratory
1 Bethel Valley Road
Oak Ridge, TN 37831
E-mail: wangh2@ornl.gov

Jerry L. Gibbs, DOE Technology Manager

U.S. Department of Energy
E-mail: jerry.gibbs@ee.doe.gov

Start Date: October 1, 2016

End Date: September 30, 2019

Project Funding (FY18): \$50,000

DOE share: \$50,000

Non-DOE share: \$0

Project Introduction

Thermoelectric material is a class of materials that captures waste heat from engine operations and can contribute significantly to the energy efficiency of cars and trucks. Recent development in materials research presented promising candidates for vehicle waste heat power generation with energy conversion efficiency of 8-10% or higher. However, there is a lack of reproducibility in the performance of laboratory-developed materials and inconsistency on properties of materials ready for scale-up. The creation of a standard test procedure coupled with standard reference materials issued under international collaboration will pave the way for rapid commercialization thermoelectric waste heat recovery materials.

Objectives

The main objectives of this project are to lead the thermoelectric materials annex for the International Energy Agency-Advanced Materials for Transportation (IEA-AMT) organization with the focus on evaluating transport properties measurement methods and develop standard testing procedures to evaluate the figure of merit, zT . Developing measurement standards of bulk thermoelectric materials and devices for vehicle waste heat recovery applications in the temperature range of 300-800K.

Approach

IEA-AMT Annex VIII is to develop standard test methods and precision statements to enable the accurate measurement of thermoelectric materials properties and device performance. Five rounds of international round-robin testing on thermoelectric materials and devices have been carried out. Results have been reported to IEA and the international thermoelectric community.

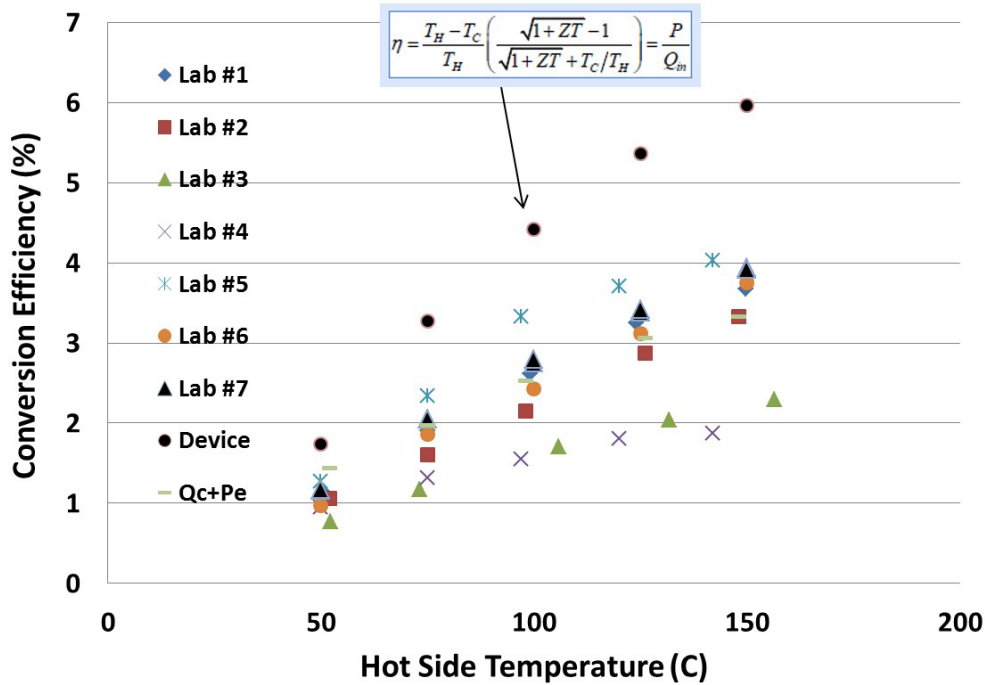
The Annex VIII participants and affiliations are as follows:

- Canada: Led by Dr. Yu-Chih Tseng, Canmet, MATERIALS, Canada
- China: Led by Prof. Lidong Chen, Shanghai Institute of Ceramics, CAS, China
- Germany: Led by Dr. Jan Konig, Fraunhofer Institute for Phys. Meas, Germany
- Korea: Led by Dr. H.W. Lee, Korea Electro Technology Institute, Korea
- UK: Led by Dr. Alexandre Cuenat, National Physical Laboratory, UK
- US: Led by Dr. Hsin Wang, ORNL, USA (Annex VIII leader)

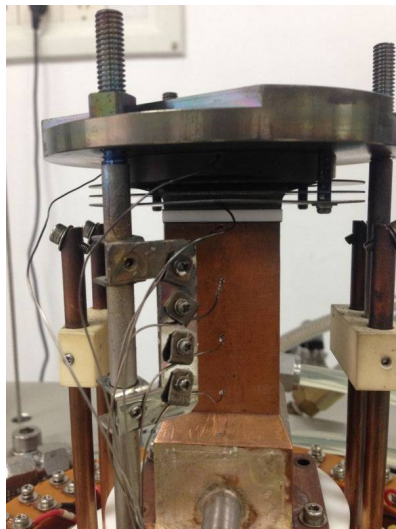
Results

In FY 2018, the main task was to complete the low-temperature (300-450K) thermoelectric module efficiency test round-robin and initial the final international round-robin of thermoelectric modules to include vehicle exhaust temperature up to 800K.

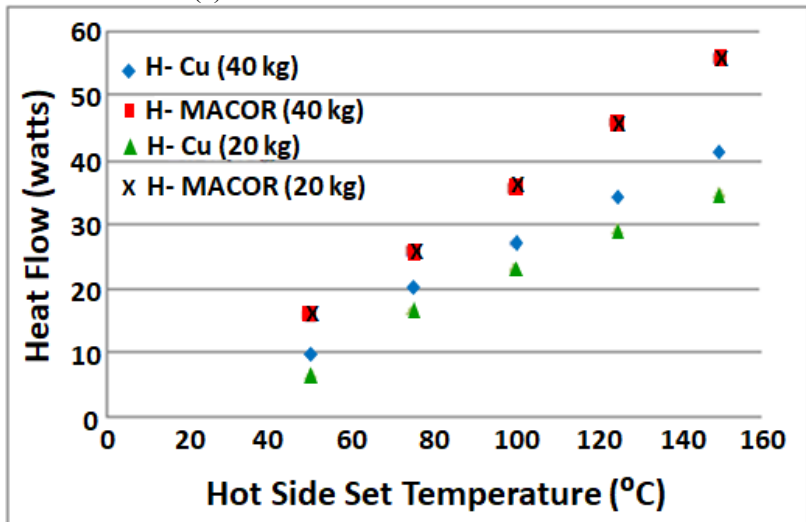
Figure I.3.D.2.1.(a) shows the latest results of the international round-robin of seven laboratories. Calculated efficiency, η , based on Carnot efficiency and thermoelectric figure of merit, zT , is also shown as the upper limit. The results showed very large scatter of device efficiency on the same module. It was identified that heat flux measurement is the key factor. A typical efficiency test setup is shown in Figure I.3.D.2.1.(b), in which heat flux is determined by four thermocouples on the cold-side Cu block. Figure I.3.D.2.1.(c) shows how the applied load to the system affects heat flux. Using a MACOR[®] block to replace the thermoelectric module, heat flux through the MACOR[®] and Cu is calculated using the known thermal conductivity of the two materials. It is shown at a 20 kg load, the heat flux values determined from the MACOR[®] and Cu show a large difference. However, when the load increased to 40 kg, the two heat flux values become identical.



(a)



(b)



(c)

Figure I.3.D.2.1.(a) Calculated and measured module efficiency from the international round-robin; (b) Typical test setup for efficiency measurements; and (c) Effect of applied load on heat flux. Source: ORNL.

Conclusions

The international round-robin on low-temperature thermoelectric module efficiency testing has been completed. Improvement has been focused on heat flux determination. The final round-robin testing on high-temperature modules was initiated. Testing procedures/protocols for thermoelectric materials and devices will be used to achieve the project goals. Calculated efficiencies showed a very large scatter of the device efficiencies for the same module because of heat flux. Heat flux values for MACOR® and Cu modules showed a large difference for a 20 kg load but were identical for a 40 kg load.

References

1. Cramer, C. L., H. Wang, and K. Ma, 2018, “Performance of functionally graded thermoelectric materials and devices: A review,” *J. Electron. Mater.*, Vol. 47, No. 9, pp. 5122–5132.
2. Wei, K., D. Hobbis, H. Wang, J. Martin, and G. S. Nolas, 2018, “Wittichenite Cu_3BiS_3 : Synthesis and transport properties,” *J. Electron. Mater.*, Vol. 47, No. 4, pp. 2374–2377.
3. Zhao, Y., H. Wang, B. Qian, H. Li, and F. Ren, 2018, “Cu-polydopamine composite derived from bioinspired polymer coating,” *J. Alloys Compd.*, Vol. 742, pp. 191–198.

Acknowledgements

This project is under the direction of the IEA-AMT and the executive committee. We would like to acknowledge financial support of each Annex VIII member country.

II Lightweight Materials

II.1 Automotive Metals

II.1.A Advancing Properties, Processes, and Enabling Tools for Lightweight Metals (Pacific Northwest National Laboratory)

Darrell Herling, Principal Investigator

Pacific Northwest National Laboratory
902 Battelle Blvd.
Richland, WA 99352
E-mail: darrell.herling@pnnl.gov

Jerry L. Gibbs, DOE Technology Manager

U.S. Department of Energy
E-mail: jerry.gibbs@ee.doe.gov

Start Date: October 1, 2015	End Date: September 30, 2019	
Project Funding (FY18): \$675,000	DOE share: \$500,000	Non-DOE share: \$175,000

Project Introduction

The Advancing Properties, Processes, and Enabling Tools for Lightweight Metals Project consists of four tasks that are focused on early-stage research in pursuit of advancing the basic mechanical properties, manufacturability, and addressing the affordability of lightweight materials. These tasks have the common goal to reduce the technical risk of implementing lightweight material systems and accelerating the adoption into the automotive market. The specific tasks include the following:

1. Enhancing Sheared-Edge Stretchability of Advanced High-Strength Steel/Ultra High-Strength Steel (AHSS/UHSS) through Integrated Manufacturing Process Simulations.
2. Cost-Effective Mg Extrusion.
3. Optimizing Heat-Treatment Parameters for Third-Generation AHSS with High-Throughput *in-situ* Experiments and Integrated Modeling Frameworks.
4. RT Stamping of High-Strength Al Alloys.

The following sections of this report outline the specific task work conducted at PNNL in the areas of predictive engineering, process development, and enabling technologies for lightweight metals and associated manufacturing processes. Each task supports one or more goals within the VTO mission of achieving better fuel efficiency through lighter weight vehicle structures.

II.1.A.1 Enhancing Sheared-Edge Stretchability of Advanced High-Strength Steel/Ultra High-Strength Steel through Integrated Manufacturing Process Simulations

Kyoo Sil Choi, Principal Investigator

Pacific Northwest National Laboratory
902 Battelle Blvd.
Richland, WA 99352
E-mail: kyoosil.choi@pnnl.gov

Jerry L. Gibbs, DOE Technology Manager

U.S. Department of Energy
E-mail: jerry.gibbs@ee.doe.gov

Start Date: November 1, 2015 End Date: May 31, 2018
Project Funding (FY18): \$460,000 DOE share: \$260,000 Non-DOE share: \$200,000

Project Introduction

During cold stamping of AHSS/UHSS parts, the most commonly observed failure mode is edge-splitting, and the sheared-edge stretchability appears to depend on a combination of factors including edge-stretching mode, edge-shearing/trimming conditions, as well as the initial sheet properties defined by the microstructural characteristics and damage occurrence in the steel sheets. The contributions of these various factors to the material edge stretchability are not well understood due to the complex interactions of these factors during the edge preparation and the subsequent forming operations.

The edge damage caused by a piercing operation depends upon the microstructure of the material, and the difference in the edge-stretching limit between different dual-phase (DP) steels of the same UTS level could be due to different levels of edge damage produced by the hole-piercing operation. But quantitative and predictive capabilities linking the microstructure characteristics to the sheared-edge stretchability under different loading modes (i.e., tensile stretching or hole-expansion) are not available. Moreover, the experimental data available from the open literature are typically only valid for the specific material under the specific combination of edge preparation and stretching conditions due to the lack of fundamental understanding of microstructure effects on sheared-edge stretchability. There is a keen interest from the steel producers for more fundamental understandings on the key microstructure features influencing the macroscopic properties (i.e., tensile properties, hole-expansion ratio [HER] and localized formability of AHSS/UHSS) in the steel development process. On the other hand, there is an urgent need from automotive original equipment manufacturers in obtaining a quantitative and predictive understanding on whether a specific type of macroscopic test result can be used to infer these steels' in die behaviors in their efforts to establish robust manufacturing processes for the new generations of AHSS/UHSS.

Objectives

The purpose of this project is to enhance the sheared-edge stretchability of AHSS/UHSS by developing quantitative and predictive understandings of the microstructure effects on sheared-edge fracture and stretchability, hence accelerating the development of next-generation AHSSs and enabling a rapid and cost-effective implementation of AHSS/UHSS in vehicle structures for substantial mass savings.

Approach

In this project, a combined experimental and modeling approach has been adopted to develop a quantitative understanding and predictive capability on the effects of microstructure features on sheared-edge fracture and stretchability for AHSS/UHSS sheet steels with UTS of 980 MPa. We proposed to focus on two or three

UHSS sheets with minimum UTS of 980 MPa (referred as DP980 hereafter) as our example material systems, but the overall approach should be extendable to other AHSS/UHSS grades.

For the experimental approach in FY 2016 and FY 2017, two different DP980 steels (i.e., DP1 and DP2) were obtained from different suppliers. Various experiments (e.g., the tensile test, high-energy XRD [HEXRD] test, etc.) were subsequently performed with these materials for material characterization. Tensile stretchability tests and hole-extrusion tests were also performed with these steels to assess the effects of microstructure features and cutting clearance on the edge stretchability of their sheared samples. For the modeling approach, a computational modeling method was developed for predicting tensile stretchability with consideration of the shearing (or trimming)-induced edge damage.

In FY 2018, the developed modeling method was validated against the experimental data obtained on the DP1 and DP2 steels. The modeling method was then applied to different microstructural features and trimming processes to improve the edge stretchability of the DP980 steels. Our FY 2018 accomplishments are reported below.

Results

Figure II.1.A.1.1 shows the computational modeling method developed to predict the tensile edge stretchability of straight-die trimmed samples. Trimming-induced edge damage (i.e., edge shape, plastic strain, voids) obtained from two-dimensional (2D) trimming simulations are first mapped into three-dimensional (3D) stretchability models. Then, the porosity-based Gurson model is adopted in the 3D model where damage accumulation is calculated based on the combination of strain and porosity. Since the 3D model is generated with large-sized elements, the fracture strain curves and critical void growth curves were appropriately adjusted considering the mesh size effects. As shown in Figure II.1.A.1.1, the ductility can be significantly different depending on the level of edge damage.

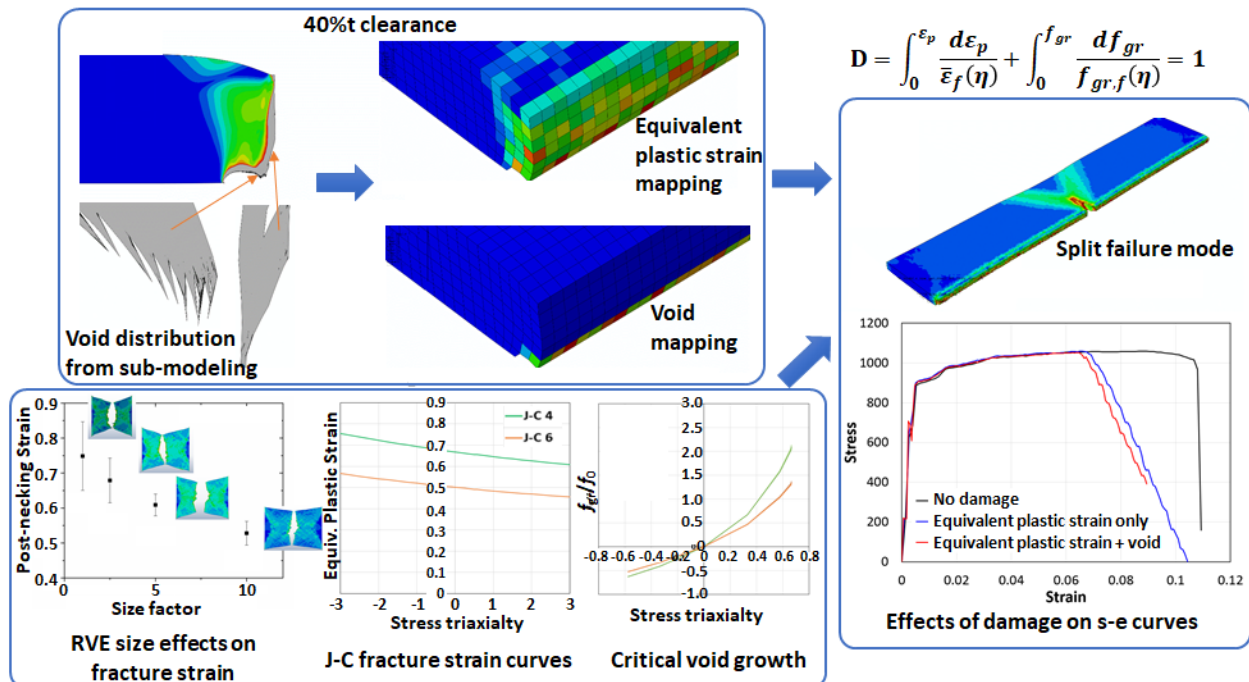


Figure II.1.A.1.1. Computational modeling method to predict the edge stretchability of sheared/trimmed samples.

Source: PNNL.

Figure II.1.A.1.2 compares the fracture modes and load-displacement curves obtained from tensile edge stretchability tests of DP1 and DP2 steels. As shown in Figure II.1.A.1.2, DP1 steel fails in diffuse and localized necking mode even under high cutting clearance (i.e., ~40%) and shows high and consistent ductility for all the cutting clearance adopted in this study. However, DP2 steel fails prior to the necking limit under high cutting clearance and shows the split failure mode. Therefore, the ductility of DP2 steel is quite low for relatively higher cutting clearance (i.e., 20~40%) as shown in Figure II.1.A.1.2. More experimental data of interest for the two DP980 steels can be found in the FY 2017 annual report [1].

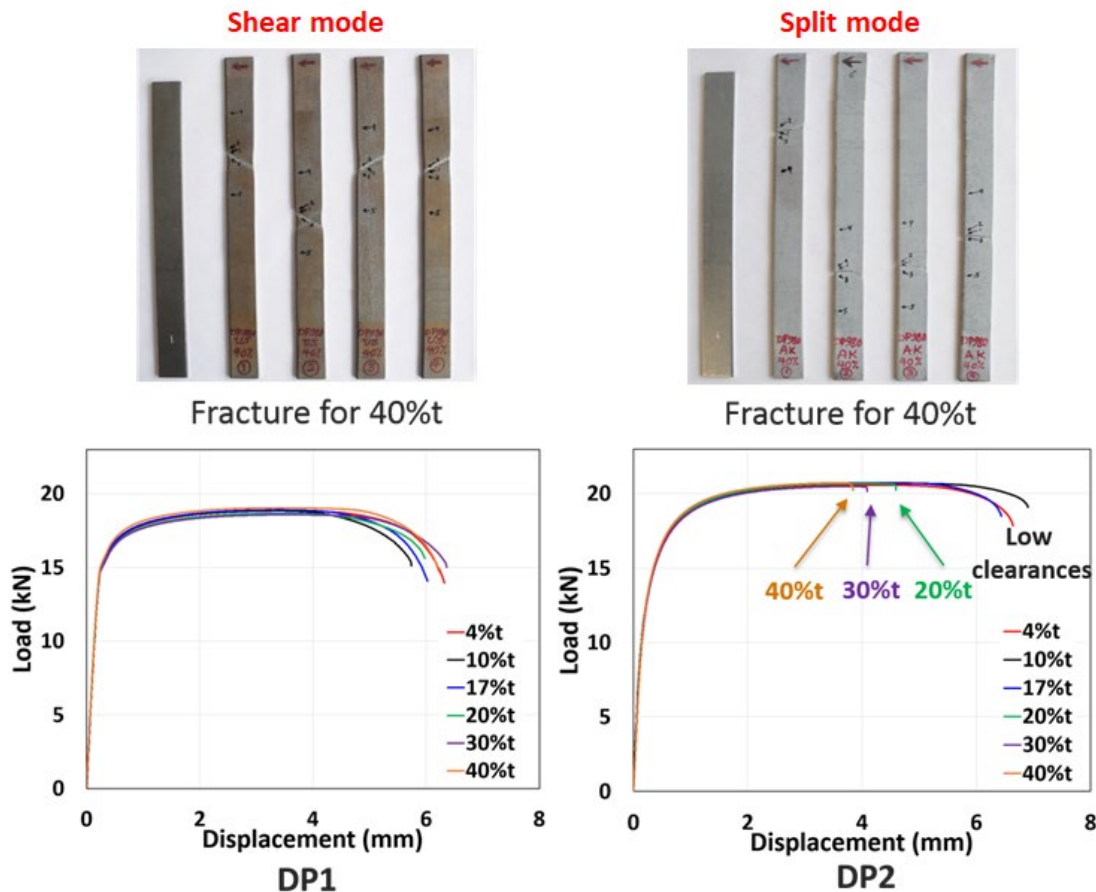


Figure II.1.A.1.2. Comparison of experimental data (i.e., fracture mode and load-displacement curve) of two DP980 steels. Source: Oakland University & PNNL.

Figure II.1.A.1.3 shows the validation of the computational modeling method against the experimental data of the two DP980 steels. For the validation, various material parameters of the two DP980 steels [1] were employed into the developed computational modeling method. It is noted that some material parameters were determined by fitting due to their unavailability from experimental approach. As shown in Figure II.1.A.1.3, the predicted fracture mode and ductility of the two DP980 steels are in agreement with the experimental observation and data presented in Figure II.1.A.1.2.

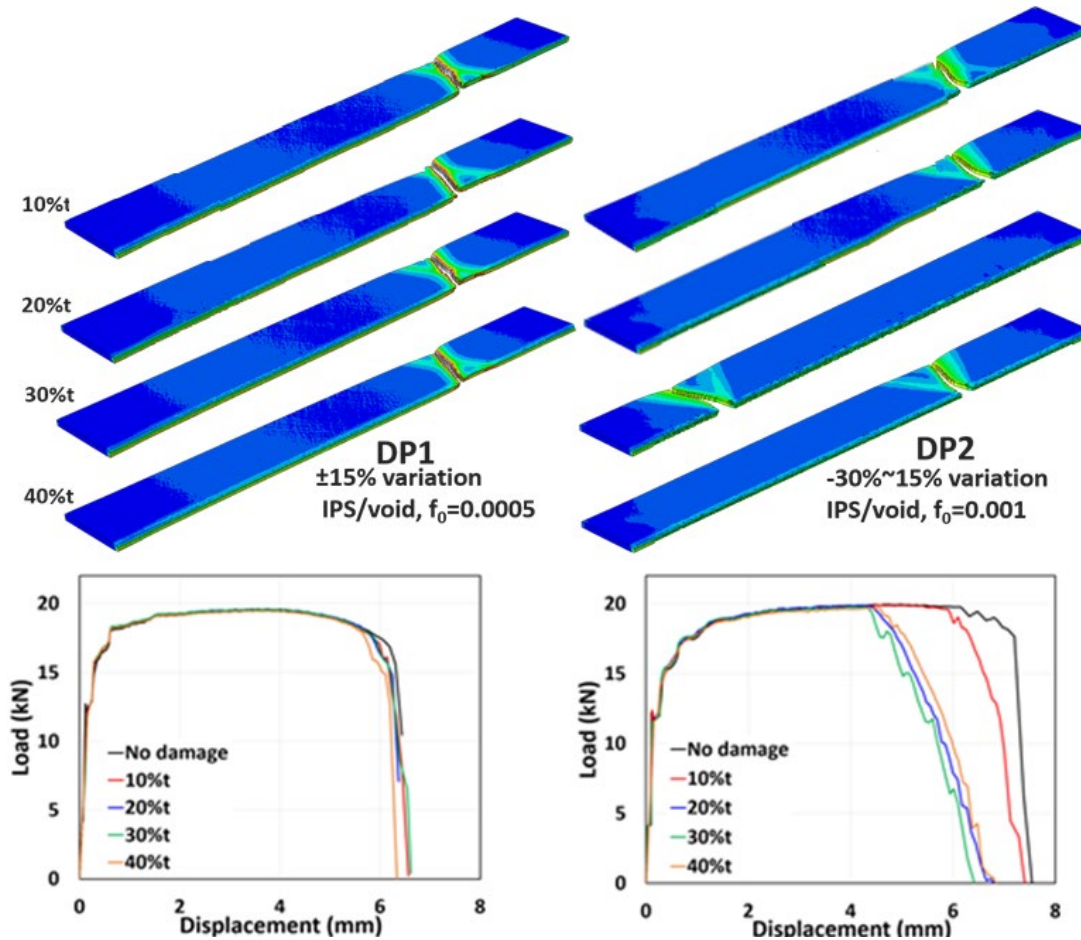


Figure II.1.A.1.3. Validation of computational modeling method against the experimental data of the two DP980 steels.
Source: PNNL.

It was reported that the DP2 steels have higher strength disparity and show more trimming-induced voids near the edge, as compared to the DP1 steel [1]. In FY 2018, it was found that the higher phase strength disparity of DP2 steel leads to its lower true fracture strain; as such, its lower edge stretchability is the result of the combined effects of its lower fracture strain and larger trimming-induced voids near the edge. In summary, a key finding in this study is that the phase strength disparity between the ferrite and martensite phases is a primary factor influencing the material's true fracture strain and, subsequently, trimmed edge stretchability. Note that the material's true fracture strain can be measured by the sample's area reduction during tensile test, not by the uniform or total elongation.

Based on the obtained results above, DP2 steel was tempered with an intention to improve its edge stretchability. From the tempering, it is expected that its phase strength disparity can be reduced with the microstructure remaining the same. Figure II.1.A.1.4.(a) and (b) show that, as expected, the tempered DP2 (DP2T) steel has the reduced phase strength disparity, but still with the same microstructures as that of the base material. Experimental results in Figure II.1.A.1.4.(c) show that the percentage of HER of DP2T steel significantly increases compared to the base material. Figure II.1.A.1.4.(d) also shows some simulation results that the edge stretchability and fracture mode of DP2T improves compared to the base material. The experimental and computational results presented in Figure II.1.A.1.4 show that the phase strength disparity between the phases can have a significant influence on the edge stretchability of DP980 steels, as mentioned above, and lower strength disparity is preferred for higher edge stretchability. The tempering process can help to reduce the phase strength disparity, hence, to increase the true fracture strain for DP980 steels.

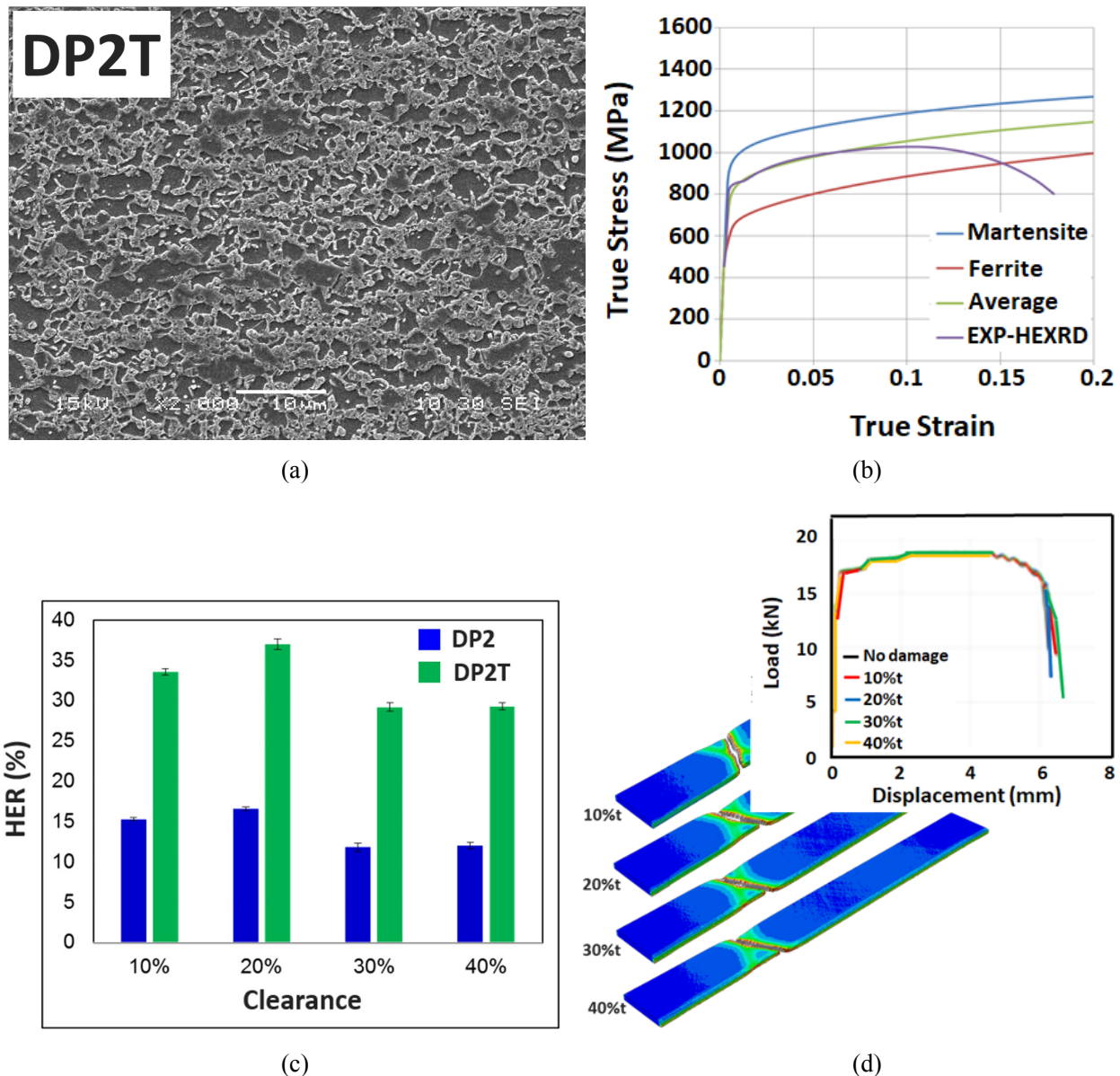


Figure II.1.A.1.4. (a) Microstructure of tempered DP2 steel; (b) phase stress-strain curves from HEXRD test; (c) comparison of HER between DP2 and tempered DP2; and (d) simulations showing the increase of edge stretchability after tempering.

Source: AK Steel & PNNL.

Different trimming processes were also tested in order to improve the edge stretchability of DP2 steel. Figure II.1.A.1.5.(a) and (b) show the two trimming processes that were tested in this study. In the “dull punch with a support” trimming [2] shown schematically in Figure II.1.A.1.5.(a), the punch radius is quite large compared to the conventional punch, and a support is also placed under the punch. In the “shear” trimming process [3] shown schematically in Figure II.1.A.1.5.(b), the punch (i.e., upper blade) and die (i.e., lower blade) have quite sharp corners, and the upper blade also has a shear rake angle in front view, basically leading to 3D trimming processes. The computational modeling method shown previously in Figure II.1.A.1.1 was employed to these trimming processes and the edge stretchability was predicted for the two trimming processes. Note that, due to the complexity of the 3D trimming simulation, only a 2D side view was considered for the “shear” trimming process. Figure II.1.A.1.5.(c) compares the trimmed edge shapes and the amount of damage level/depth (in terms of equivalent plastic strain) between the different trimming processes.

It can be seen in Figure II.1.A.1.5 that, for the two trimming processes, the trimmed edge shape and/or the damage amount are different and lower as compared to those for the conventional trimming process. The simulation results in Figure II.1.A.1.5.(d) show that the edge stretchability from these two trimming processes improve compared to that of the conventional trimming process. This improvement is due to the less amount of damage level/depth of the two trimming processes.

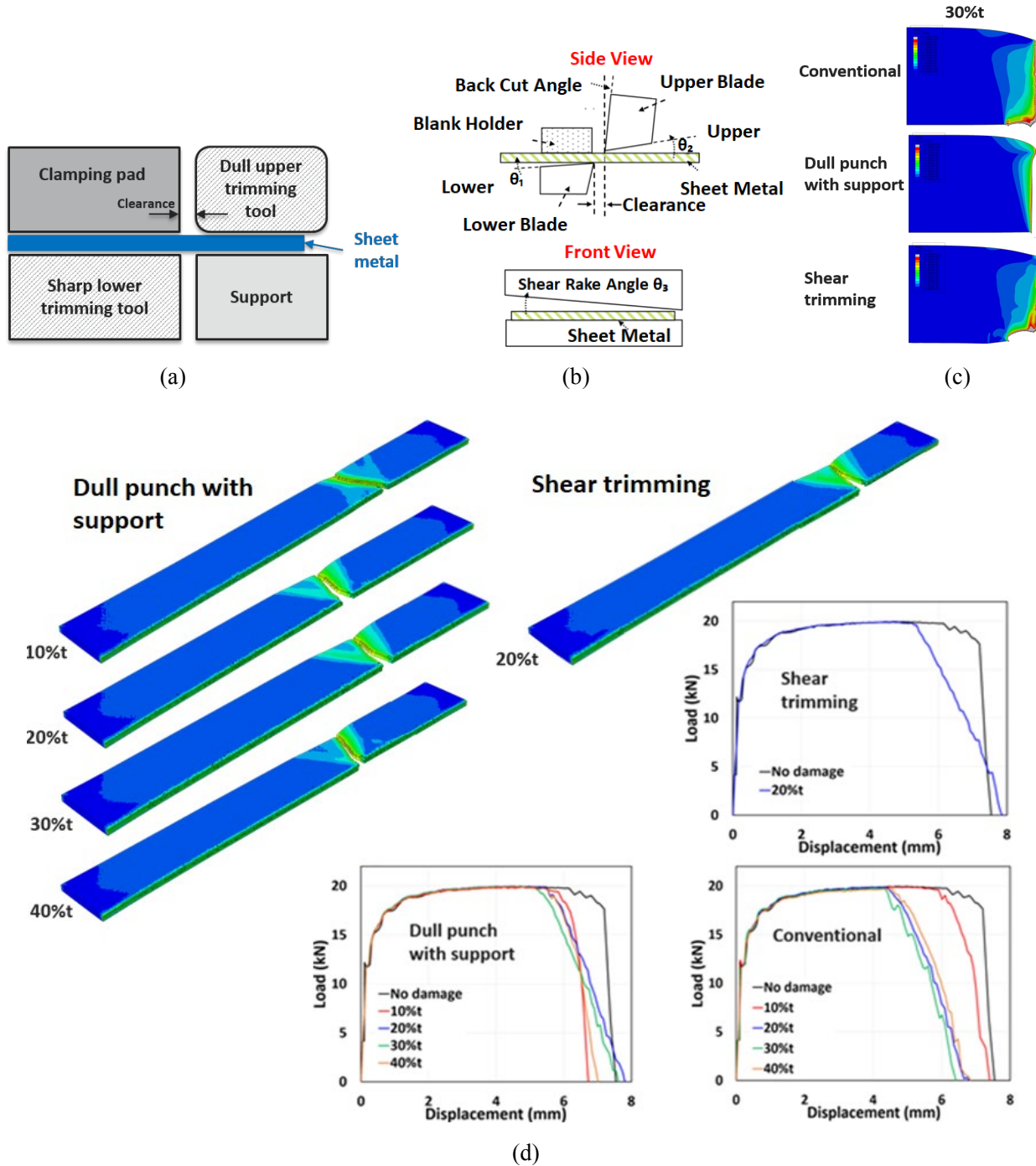


Figure II.1.A.1.5. Schematics of (a) “dull punch with a support” [2] and (b) “shear” [3] trimming processes with (c) a comparison of trimming-induced edge damage level between the three different trimming processes and (d) simulations showing some increase of edge stretchability based on these two trimming processes as compared to the conventional trimming process. Source: PNNL.

Conclusions

The computational modeling method for predicting edge stretchability was validated against the experimental data with two different DP980 steels. The fundamental understandings from these studies are that the phase strength disparity can be a primary factor influencing on the material's true fracture strain and, subsequently, the trimmed edge stretchability, and that the lower phase strength disparity is preferred for better edge stretchability. Based on these understandings, different microstructural features and trimming processes were examined for improving the edge stretchability of DP980 steels. For material development perspective, a new chemistry and/or a new heat-treatment process, which will lead to less phase strength disparity can be helpful for higher fracture strain and edge stretchability. For the trimming process perspective, the cutting parameters were difficult to optimize in this study. Instead, two additional trimming processes were examined to understand the key differences among those trimming processes. The results suggest that the trimming process can be devised such that the trimming-induced edge damage level/depth (i.e., magnitude of plastic strain, damaged area) becomes less.

References

1. U.S. Department of Energy, 2018, "Materials 2017 Annual Progress Report," VTO, DOE-EERE, DOE/EE-1711, pp. 76–97.
2. Hu, X. H., K. S. Choi, X. Sun, and S. F. Golovashchenko, 2014, "Edge fracture prediction of traditional and advanced trimming processes for AA6111-T4 sheets," *J. Manuf. Sci. Eng.*, Vol. 136, No. 2, pp. 021016-1–021016-11. doi: 10.1115/1.4026273.
3. Shih, H., C. Hsiung, and B. Wendt, B., 2014, "Optimal Production Trimming Process for AHSS Sheared-Edge Stretchability Improvement," SAE Technical Paper 2014-01-0994. doi: 10.4271/2014-01-0994.

Acknowledgements

This project was performed based on collaboration with various industrial and academic partners. The principal investigator would like to acknowledge the assistance of Drs. Xin Sun and Xiaohua Hu from ORNL; Drs. Constantin Chiriac and Raj Sohmshtetty from Ford Motor Corporation; Drs. Ming Shi and Brandon Hance from U.S. Steel; Drs. Kavesary Raghaven and Yu-wei Wang from AK Steel; and Dr. Sergey Golovashchenko from Oakland University for the material preparations, the experiments for material characterization, and for helpful discussions, which were crucial to the success of this project.

II.1.A.2 Cost-Effective Mg Extrusions

Curt Lavender, Co-Principal Investigator

Pacific Northwest National Laboratory
902 Battelle Blvd.
Richland, WA 99354
E-mail: curt.lavender@pnnl.gov

Tim Skszek, Co-Principal Investigator

Magna Cosma International
1807 East Maple Rd.
Troy, MI 48083
E-mail: curt.lavender@pnnl.gov

Jerry L. Gibbs, DOE Technology Manager

U.S. Department of Energy
E-mail: jerry.gibbs@ee.doe.gov

Start Date: November 1, 2015	End Date: September 30, 2018	
Project Funding (FY18): \$400,000	DOE share: \$300,000	Non-DOE share: \$100,000

Project Introduction

PNNL and Magna Cosma International (Magna) have been collaborating on technologies relevant to the automotive industry that support DOE's mission of improving process and product efficiencies while reducing the weight of automobiles. The use of high-performance Mg alloys in the automotive industry is presently limited due to the addition of costly rare-earth (RE) elements and the slow rate of the processing (i.e., conventional extrusion techniques). This project aims to eliminate the need for RE additives while simultaneously improving the processing rate and energy efficiency.

Objectives

This project is designed to develop low-cost extruded Mg alloys that do not rely on RE alloying elements for their strength, ductility, and energy absorption properties. A novel low-cost, high-speed, processing method, in conjunction with Mg alloys containing RE substitutes, will be developed to produce the microstructure and properties needed for the automotive applications in a cost-effective manner. The primary objectives in FY 2018 were to continue process development for non-RE Mg alloys, and to develop technology for extruding non-circular cross-sections in anticipation of future industrial pull for rectangular and multi-zone extrusions.

Approach

In this project, ShAPE™ is being developed to fabricate extruded parts with improved material properties and process efficiency. In ShAPE™, the extrusion die, and Mg billet are rotated counter to each other, while significant heating occurs due to friction at the billet/die interface, as shown in Figure II.1.A.2.1. In this schematic, the extrusion die rotates, but does not traverse. Instead, the non-rotating Mg billet traverses from right to left and presses against the rotating extrusion die. In this configuration, the tube is extruded in the direction of billet translation, thus being classified as a direct extrusion. The amount of heat generation is proportional to the applied torque and rotational speed of the die. As temperature increases, the billet face softens and plastically flows through the spiral scroll features inward towards the extrusion orifice. Material flowing out of the individual scrolls is consolidated between the mandrel and die bearing surface prior to exiting through the die relief.

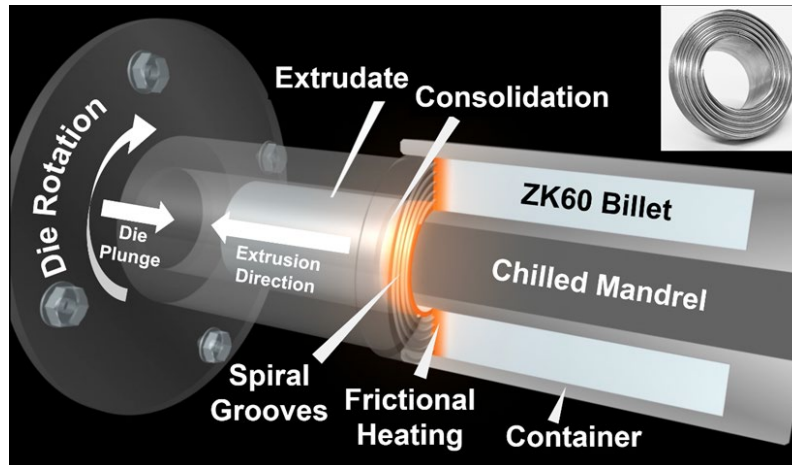


Figure II.1.A.2.1. Cross-section of tooling showing a direct tubular extrusion of the ShAPE™ process. Source: PNNL.

Recrystallization occurs within the deforming material and when shear and temperature are suddenly reduced, a refined microstructure can be obtained in the extrudate. Due to the complex shear and thermal conditions present during ShAPE™, crystallographic texture is thought to develop as a combination of recrystallization mechanisms due to the interplay between rotational speed, extrusion rate, and thermal conditions. Advantages of ShAPE™ may include enhanced grain refinement leading to better material properties, the ability to align crystallographic texture, lower extrusion forces leading to smaller tonnage equipment, and lower process energy consumption. From experience gained during FY 2015 through FY 2017, it was learned that a novel die design would be required to form non-circular cross-sections and current machine torque would be inadequate.

Results

Although capable of extruding ZK60 Mg tubing with a 50 mm outer diameter (OD) and a 1.5–3.0 mm wall thickness, these dimensions were at the limit of the ShAPE™ machine torque capability. Based on conversations with potential industry partners, it was clear that larger tubes and especially large, closed section, non-circular shapes, were of particular interest. In anticipation of future work for VTO in this area, PNNL contracted with Bond Technologies, Inc., to upgrade the torque capability of the ShAPE™ machine. The torque was increased from 995 Newton-meter (Nm) @ 50 to 480 rpm to 2987 Nm @ 25 to 160 rpm. The upgrade was completed on September 26, 2018, and Figure II.1.A.2.2 shows the location of the new torque module containing a new jackshaft and pulley system. The upgraded ShAPE™ machine will be exercised in early FY 2019 to make long circular tubes with the small amount of carryover remaining on this project.

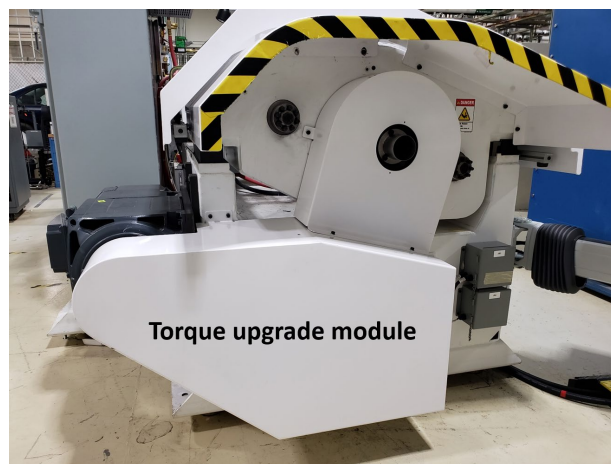


Figure II.1.A.2.2. ShAPE™ machine with new torque module capable of 2987 Nm @ 25 to 160 rpm. Source: PNNL.

In FY 2018, new tooling and die concepts were considered for the purpose of producing non-circular cross-sections using ShAPE™. It was determined that a portal bridge die approach offered the best opportunity for creating non-circular cross-sections in the ShAPE™ process. A patent was filed on the novel die features required to adapt the portal bridge die approach from conventional extrusion to the ShAPE™ process. Figure II.1.A.2.3.(a) shows the assembled two-piece portal bridge die ready for integration into the ShAPE™ machine. Figure II.1.A.2.3.(b) shows an eight-scroll pattern feeding into four distinct portals. Figure II.1.A.2.3.(c) shows a square mandrel, which defines the inner dimension of the tube. Figure II.1.A.2.3.(d) shows the weld chamber and square port defining the OD of the tube. A cooling channel is also visible, which extracts heat from the die face. Extrusion of a non-circular cross-section using ShAPE™ will be attempted in the second quarter of FY 2019 with the carryover remaining on this project.

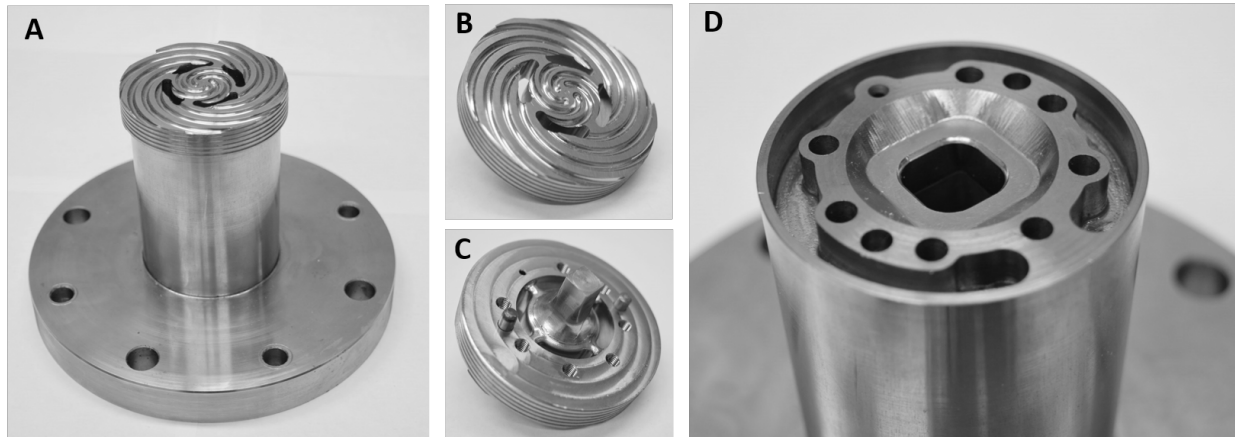


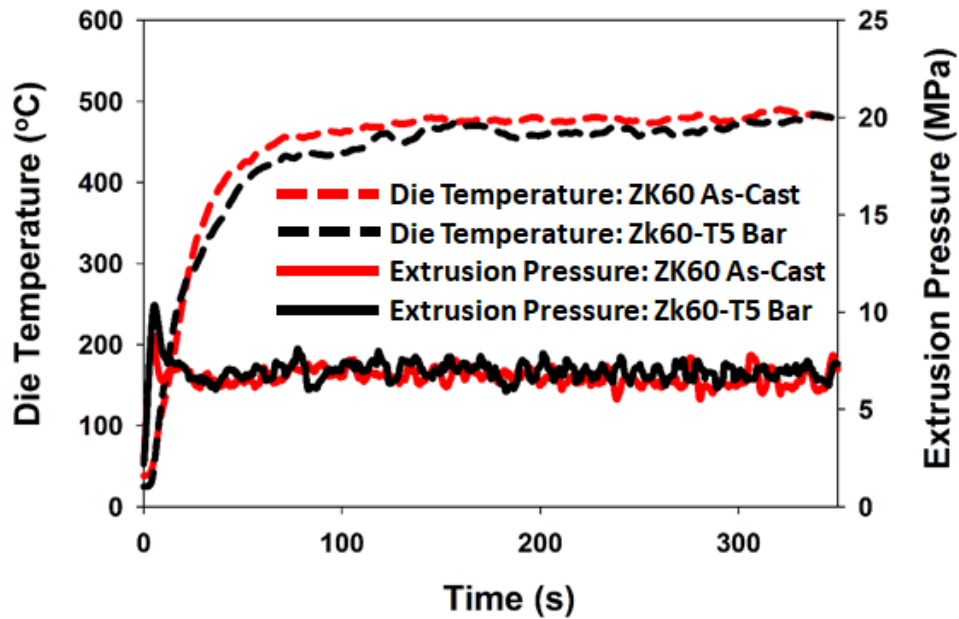
Figure II.1.A.2.3. Portal bridge die design for extruding a square tube using ShAPE™ for (a) assembly, (b) eight-scroll pattern, (c) the square mandrel and (d) weld chamber with cooling channel and square port. Source: PNNL.

During FY 2018, additional progress was made on extruding circular Mg ZK60 tubes on the ShAPE™ machine prior to the torque upgrade. Process parameters and die designs were refined until tubes measuring two feet in length with a decent surface finish were achieved. The remainder of this report discusses research that was performed to characterize the effect of the ShAPE™ process on microstructure, texture, and hardness for cast and wrought ZK60 starting billets.

ZK60-T5 bar and ZK60 as-cast billets were extruded into round tubes using the ShAPE™ process. During extrusion, the rotating die was rammed into the billet container at a constant speed of 3.81 mm/min while rotating at 300 rpm. Pressure and temperature build rapidly, as shown in Figure II.1.A.2.4.(a); with pressure rising to a peak (e.g., breakthrough) of 9.5 MPa for billets made from ZK60-T5 bar and ZK60 as-cast. After breakthrough, pressure falls off sharply indicating that the material has softened enough to flow through the spiral grooves and extrude through the die. The extrusion pressure stabilized roughly 30 seconds after breakthrough to an average level of 6.8 MPa. In order to build temperature slowly, the die rotation was gradually reduced from 300 to 150 rpm during the first 150 seconds, after which the temperature stabilized in the 470–480°C range for each run. An example tube extruded from ZK60 as-cast is shown in Figure II.1.A.2.4.(b), which measured 50.64 mm ±0.01 mm for the OD with an average wall thickness of 1.95 mm ±0.19 mm. For the tube made from ZK60-T5 bar, the OD measured 50.68 mm ±0.21 mm with an average wall thickness of 1.93 mm ±0.38 mm.

Using the steady state force of 31.1 kN and 29.7 kN, which is the underlying force data used to report pressure in Figure II.1.A.2.4, k_f is calculated to be 2.55 MPa and 2.43 MPa for the extrusions made from ZK60-T5 bar and ZK60 as-cast, respectively. The ram force and k_f are remarkably low compared to conventionally extruded Mg where k_f ranges from 68.9–137.9 MPa. As such, the ShAPE™ process achieved a 20–50 times reduction in ram force and k_f as compared to conventional extrusion. This dramatic reduction with ShAPE™ is due to three

primary differences. First, only a thin layer of material at the die/billet interface is deformed in contrast to the large volume of deformation in conventional extrusion. Second, the thin layer of plasticized material flows through the spiral grooves, which facilitates material flow towards the extrusion orifice. Third, friction between the billet and container is entirely eliminated because the billet does not slide through the container as is the case in conventional extrusion. These effects combine to lower k_f , and thus force, and could lead to extrusion equipment with a much smaller footprint, lower energy consumption, and reduced capital cost as compared to conventional extrusion.



(a)

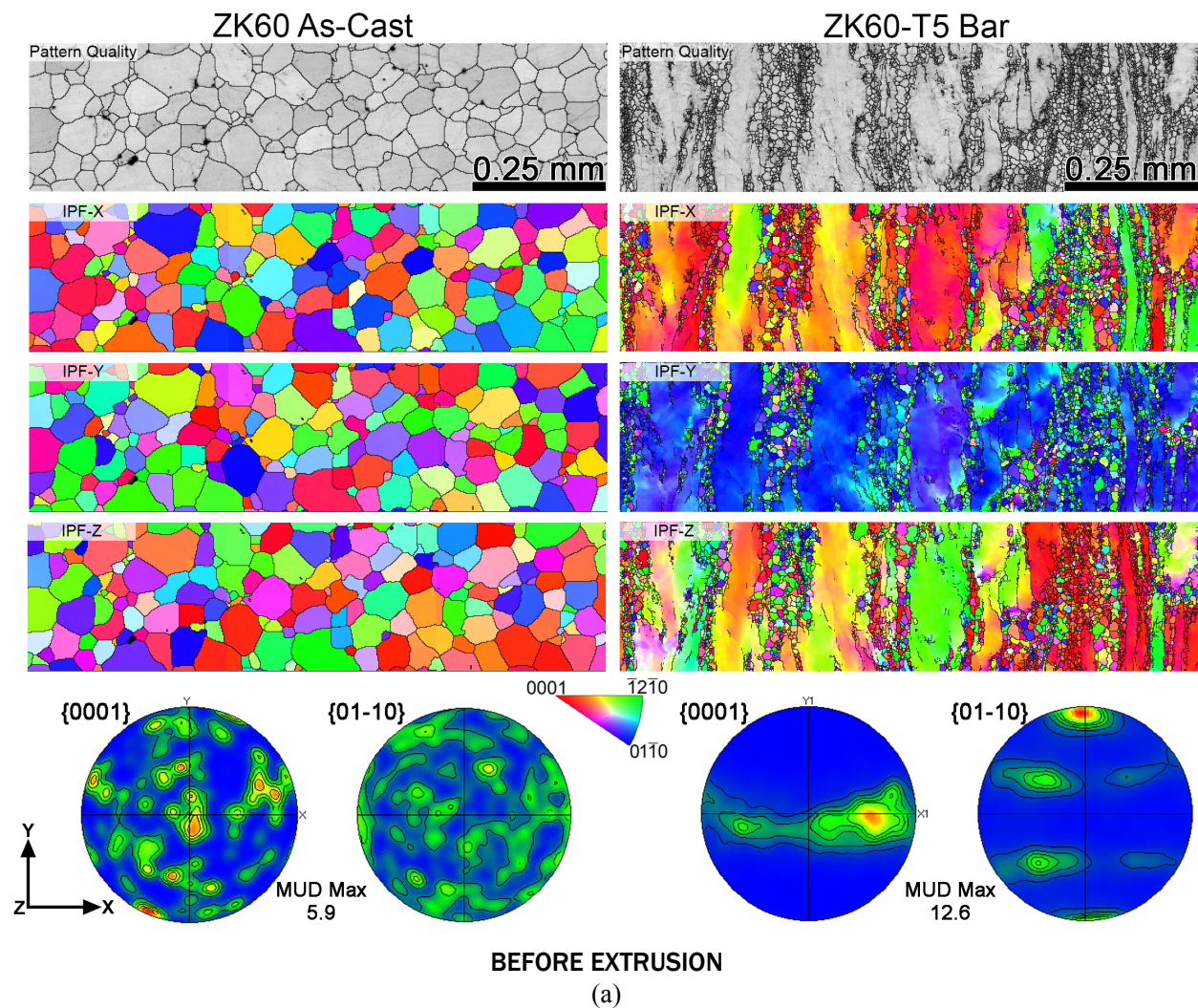


(b)

Figure II.1.A.2.4. Process parameters (a) and extruded tubing (b) made directly from as-cast ZK60 using ShAPE™. Source: PNNL.

Prior to ShAPE™ extrusion, microstructural characterization was performed on both the ZK60 as-cast and ZK60-T5 bar feedstock materials. Electron backscatter diffraction analysis of the as-cast and T5 bar feedstock material was performed as shown in Figure II.1.A.2.5.(a). The as-cast material exhibited a relatively homogeneous microstructure, free of any significant texture development. The average grain diameter of the as-cast material was $41 \pm 24 \mu\text{m}$. The T5 bar material exhibited a typical extruded microstructure with significant grain elongation in the extrusion direction with some grains exceeding 1 mm in length. Significant texture development was also observed in the T5 bar, which doubled the multiples of uniform density (MUD) value when compared to the as-cast material.

Electron backscatter diffraction analysis was performed on the extrudate cross-sections to better visualize deformation texture and grain morphology. Results of this study are shown in Figure II.1.A.2.5.(b) where the extrusion direction is downward, and the left side of the image was in contact with the mandrel. For the cast and wrought starting billets, considerable grain refinement, second phase refinement, and texture development was achieved. After extrusion, the average grain size of both specimens was approximately $4\text{-}5 \mu\text{m}$ and texture became highly oriented and tilted roughly 20 degrees away from the extrusion direction.



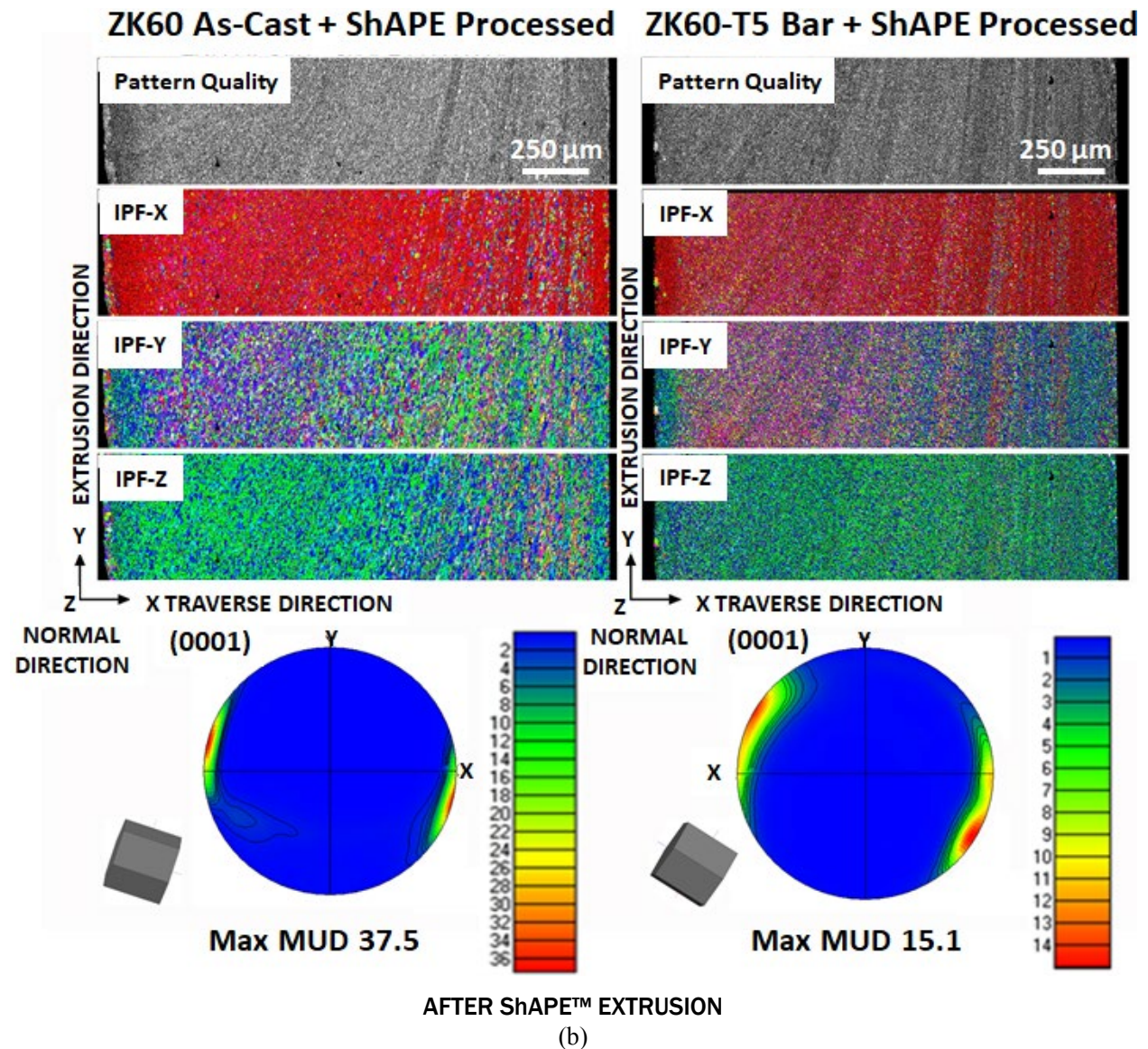


Figure II.1.A.2.5. Microstructural comparison of as-cast and wrought ZK60 billets (a) before and (b) after ShAPE™ extrusion. Source: PNNL.

Hardness measurements were performed on as-extruded and heat-treated specimens on the planar (A), transverse (B), and longitudinal (C) surfaces, according to the sketch in Figure II.1.A.2.6. An artificial aging condition of 175°C for 24 hours was chosen, which is consistent with the literature for ZK60. A total of 25 indents were made per test plane and each indent was approximately 25–30 μm across and hence covered at least 300 μm² of region, which roughly corresponds to an indent that crossed across five grains and the precipitates that formed near them. Hardness was measured along a 3-mm length in all three of the aforementioned directions, covering over 200 grains and their precipitates. The hardness measurements for all three planes of the ShAPE processed tubing are shown in Table II.1.A.2.1.

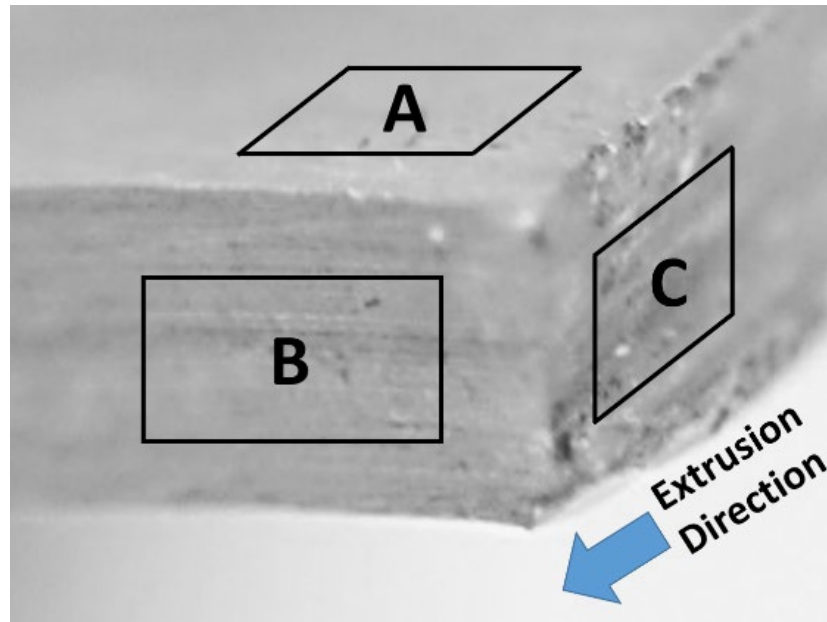


Figure II.1.A.2.6. Microstructural comparison of as-cast and wrought ZK60 billets before and after ShAPE™ extrusion. Source: PNNL.

Table II.1.A.2.1. Hardness in HV of ShAPE™ Tubing in the As-Extruded and Heat-Treated Conditions.

Test Plane	ZK60 As-Cast After ShAPE™	ZK60 As-Cast After ShAPE™ + HT	ZK60 Wrought T5 Bar After ShAPE™	ZK60 Wrought T5 Bar After ShAPE™ + HT
A-Planar	67.5 ± 1.9	68.4 ± 2.1	64.9 ± 2.9	76.1 ± 3.5
B-Transverse	67.5 ± 2.3	70.0 ± 2.1	64.6 ± 4.7	77.3 ± 4.2
C-Longitudinal	63.2 ± 2.1	77.0 ± 3.0	65.3 ± 3.4	81.1 ± 3.7
Average	66.1 ± 3.0	72.3 ± 4.1	64.9 ± 3.8	78.2 ± 4.4

After ShAPE, no statistical difference was observed in the hardness of tubes made from as-cast and T5 bar starting materials. After ShAPE + heat-treatment, there was also no statistical difference observed in the hardness of tubes made from as-cast and T5 bar starting materials. This is not surprising given that the grain size, basal texture alignment, and degree of second phase refinement and distribution was similar in tubes made from both starting materials as shown in Figure II.1.A.2.5. An additional observation is that, for all starting material and heat-treatment combinations, hardness in the planar and transverse directions were nearly identical. The longitudinal direction was statistically different from the planar and transverse directions, but only slightly. Upon aging at 175°C for 24 hours, the average hardness for all test planes increased to 72.3 and 78.2 HV for tubes extruded from as-cast and T5 bar respectively. Unlike conventional extrusion, which exhibits high anisotropy in Mg alloys, the hardness of ZK60 extruded by ShAPE is fairly uniform for the directions indicated in Figure II.1.A.2.6. This uniformity of hardness is manifest in the tensile data that the authors previously reported for ZK60-T5 bar extruded by ShAPE. For the directions indicated in Figure II.1.A.2.7, UTS and elongation were shown to be fairly consistent, as summarized in Table II.1.A.2.2. These results suggest that ShAPE may be effective at reducing anisotropy in extruded Mg alloys.

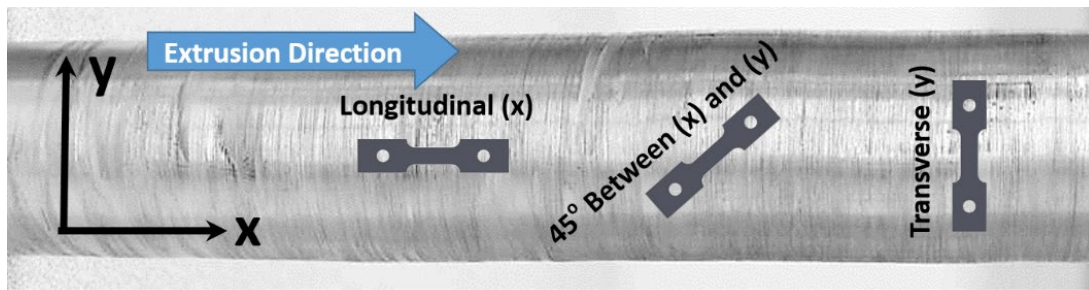


Figure II.1.A.2.7. Orientation of tensile specimens relative to extrudate. Source: PNNL.

Table II.1.A.2.2. Tensile Properties for ZK60-T5 Bar Extruded by ShAPE™.

Test Direction	UTS (MPa)	Elongation (%)	Sample Size (n)
Longitudinal (x)	254 ± 2.1	20 ± 1.9	10
45° between (x) and (y)	280 ± 1.0	21 ± 6.4	6
Transverse (y)	297 ± 1.5	25 ± 2.8	11

Conclusions

In FY 2018, progress was made towards designing and fabricating dies for ShAPE™ extrusion of non-circular cross-sections. In anticipation of work on larger tubular and non-circular cross-sections, the ShAPE™ machine was upgraded to 3x the torque capacity. Additional development was performed on Mg where billets made from wrought bar and casting were extruded and compared. Very similar microstructures were achieved in the extrudates, even though the starting microstructures were very different.

Key Publications

1. Whalen, S., N. Overman, V. Joshi, D. Graff, and C. Lavender, 2018, “Friction extrusion of cast and wrought ZK60 magnesium alloy using ShAPE,” Submitted to *Mater. Sci. Eng. A*.
2. Joshi, V., S. Whalen, J. Darsell, A. Rohatgi, G. Grant, C. Lavender, S. Whalen, S. Jana, and D. Catalini, 2018, “Functionally graded coatings and claddings and through-wall texture control,” U.S. Patent Application 15/898,515, filed on February 17, 2018.
3. Whalen, S., V. Joshi, Md. Reza-E-Rabby, G. Grant, and C. Lavender, 2018, “Method for forming hollow profile non-circular extrusions using ShAPE,” U.S. Patent Application 16/028,173, filed on July 5, 2018.
4. R&D 100 Finalist for ShAPE™ Process – Winners not yet announced at the time of writing this report.

II.1.A.3 Optimizing Heat-Treatment Parameters for Third-Generation AHSS with High-Throughput *in-situ* Experiments and Integrated Modeling Frameworks

Kyoo Sil Choi, Co-Principal Investigator

Pacific Northwest National Laboratory
902 Battelle Blvd.
Richland, WA 99354
E-mail: kyoosil.choi@pnnl.gov

Emmanuel De Moor, Co-Principal Investigator

Advanced Steel Processing and Products Research Center
Colorado School of Mines
1500 Illinois St.
Golden, CO 80401
E-mail: edemoor@mines.edu

Jerry L. Gibbs, DOE Technology Manager

U.S. Department of Energy
E-mail: jerry.gibbs@ee.doe.gov

Start Date: October 1, 2015	End Date: September 30, 2019	
Project Funding (FY18): \$600,000	DOE share: \$500,000	Non-DOE share: \$100,000

Project Introduction

Medium manganese (Mn) transformation-induced plasticity (TRIP) steels represent potential important products to achieve the performance requirements of third-generation AHSS in efforts to improve the fuel efficiency of lightweight vehicles while meeting or exceeding safety regulations. Mn steels typically contain 5-10 wt.% Mn and other alloying elements similar to those used in selected current AHSS grades. It is well-known that the mechanical properties of these steels are extremely sensitive to certain chemical compositions (C and Mn content) and intercritical annealing (IA) temperatures, which in turn determine the volume fraction and thermodynamic stability of the retained austenite (RA) in the corresponding microstructures. Given a certain microstructure of the multiphase steel (i.e., volume fraction, morphology, and stability of the RA), our team's prior work has established an integrated experimental and computational approach linking the microstructures to the corresponding mechanical properties [1–2]. However, traditional experimental heat-treatment and characterization techniques applied in optimizing the heat-treatment parameters for strength and ductility combinations are often laborious and time-consuming. Complete descriptions, efficient experimental characterization techniques and predictive capabilities, as well as the applications of these to describe relationships between chemical compositions, initial microstructures, heat-treatment parameters and subsequent RA volume fraction, RA stability, and mechanical properties have not been established.

Objectives

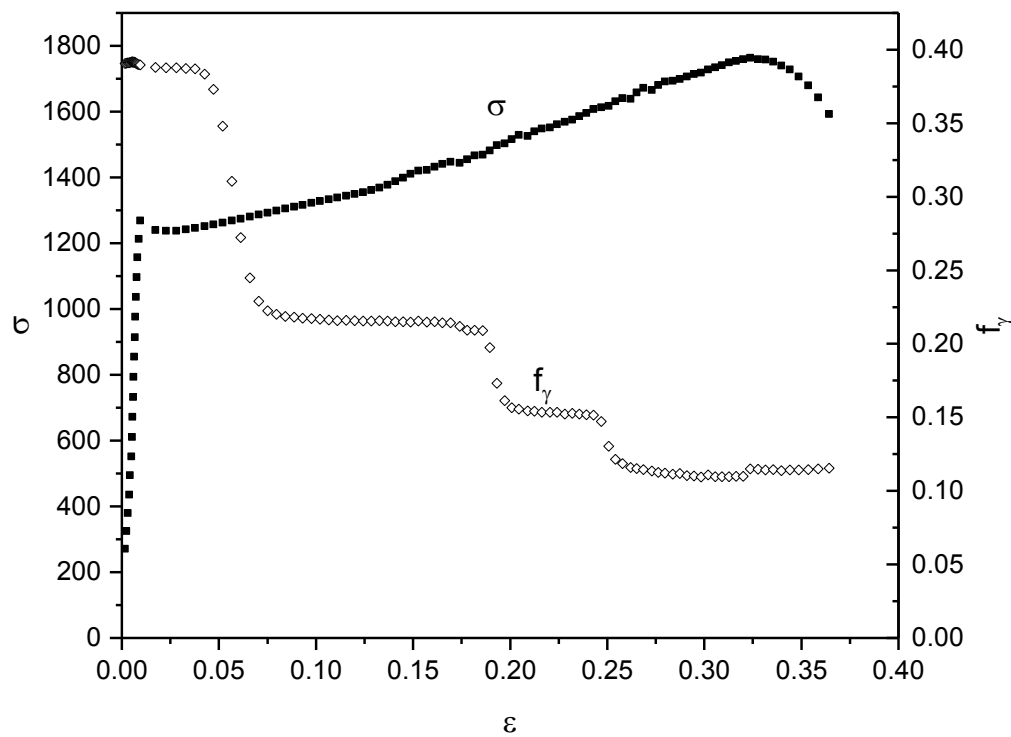
The purpose of this project is to determine accurate thermodynamic parameters and obtain optimized IA parameters, microstructure, and superior combined mechanical properties of ductility and strength for medium Mn steels by developing an integrated *in-situ* and *ex-situ* experimental and computational modeling framework. This will help to accelerate the development of next-generation AHSS and enable a rapid and cost-effective implementation of AHSS in vehicle structures for substantial mass savings.

Approach

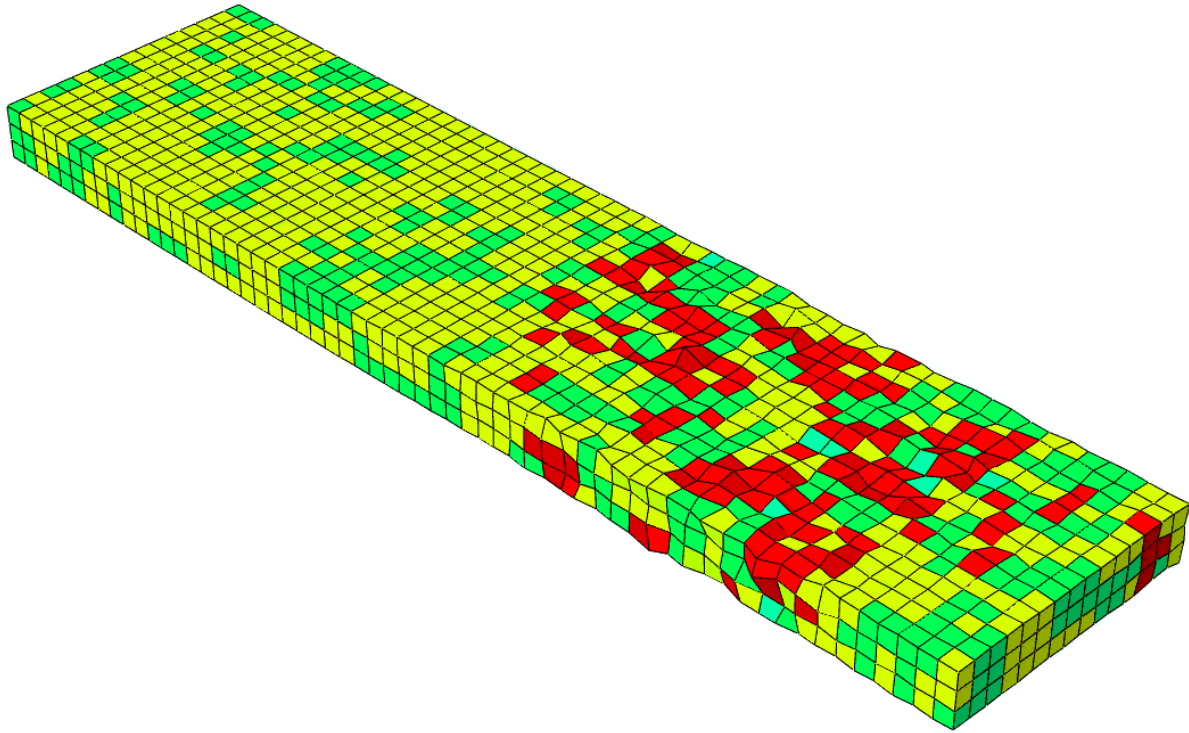
In this project, the following approaches are proposed: (1) Perform conventional experimental mechanical and microstructural characterization and heat-treatment experiments to study the RA volume fraction and alloy elements partitioning for as-received and heat-treated medium Mn steels; (2) Develop an *in-situ* HEXRD characterization technique to determine the austenite formation kinetics of medium Mn TRIP steels on heating and during IA to enable the accelerated development of future third-generation AHSS; (3) Develop a Thermo-Calc[®]/DICTRA and phase-field based modeling capability to predict the volume fraction, morphology (including grain size), and stability (C and Mn concentration) of the austenite formed during the IA process; (4) Link the predicted microstructures, including the austenite volume fraction retained after cooling, stability, and morphology to the mechanical properties; and (5) Optimize the strength and ductility of medium Mn TRIP steels by judicious IA temperature selection.

Results

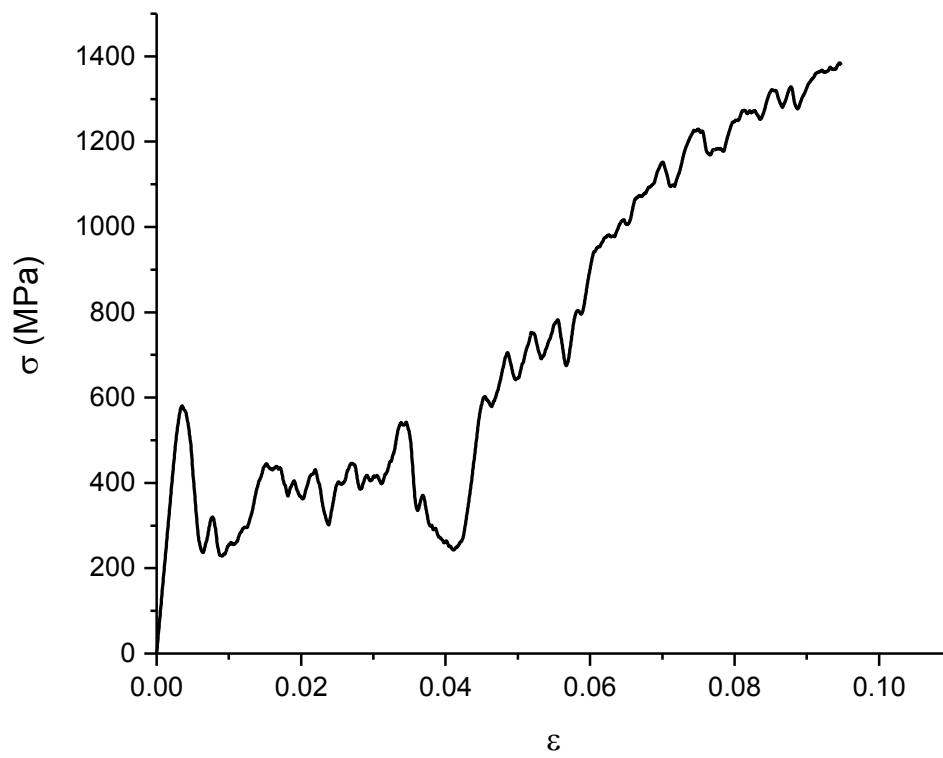
Medium Mn steels (e.g., 7Mn and 10Mn steels) show large yield point elongation and Lüders band, followed by Portevin-Le Châtelier (PLC)-type propagating banding behavior. For example, Figure II.1.A.3.1.(a) shows the Lüders banding behavior and the associated long plateaus in an austenite volume fraction evolution curve for a 7Mn steel [3]. These phenomena have been supported by digital image correlation techniques [4]. Mechanisms of the Lüders banding behaviors of medium Mn steels are not clearly known. However, these behaviors need to be considered for accurately predicting the mechanical behaviors of medium Mn steels. Material user-subroutine codes were developed with consideration of volume expansion associated with phase transformation for the purpose of simulating the Lüders banding behavior. Figure II.1.A.3.1.(b) and (c) show the Lüders banding behaviors and resulting yield point elongation from an example of a microstructure-based modeling/simulation approach. As shown in Figure II.1.A.3.1, these phenomena were successively captured from simulation. The codes are to be further upgraded to more accurately predict the mechanical behaviors.



(a)



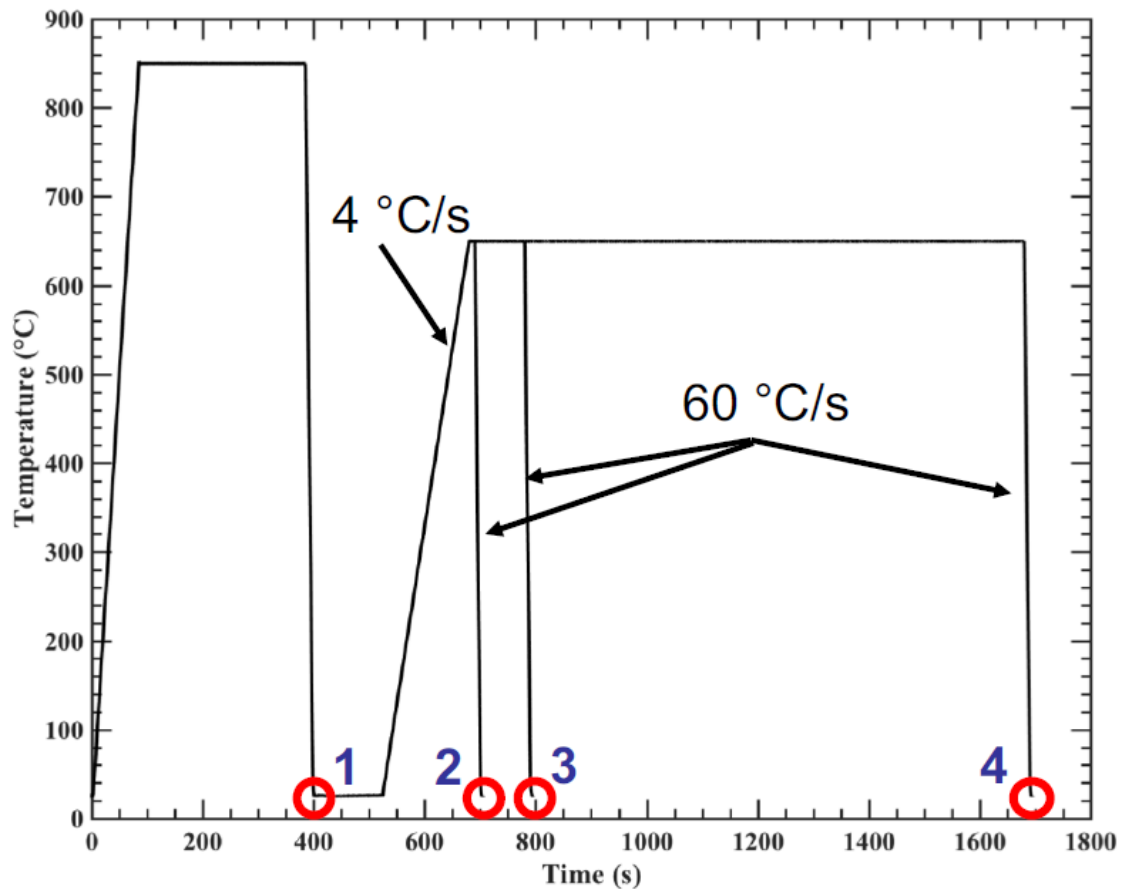
(b)



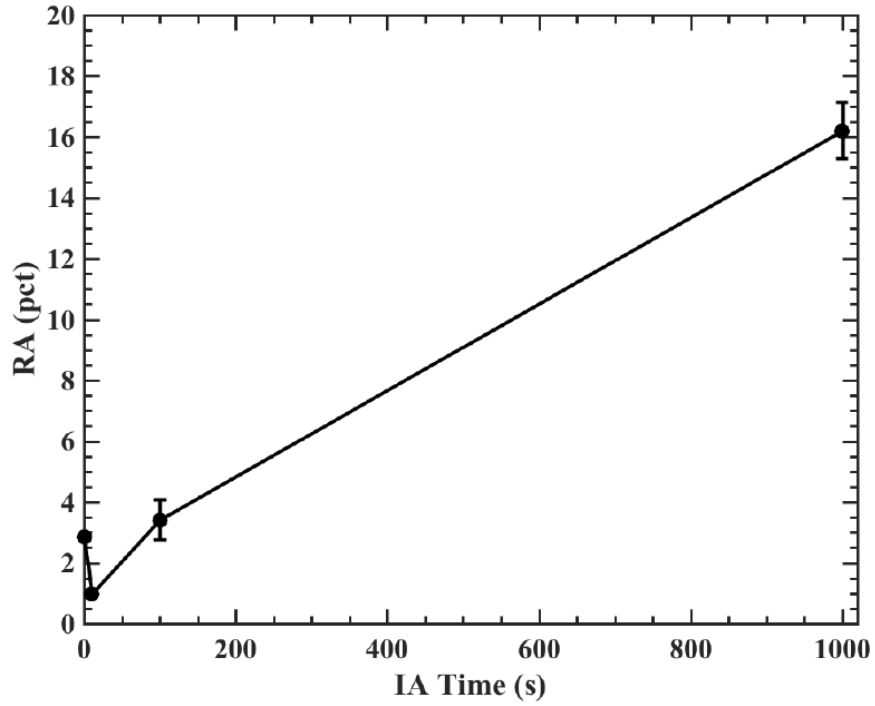
(c)

Figure II.1.A.3.1.(a) Example of tensile stress-strain curve and austenite volume fraction evolution of a 7Mn steel, and examples of simulation showing (b) Lüders banding behavior, and (c) resulting yield point elongation. Source: PNNL.

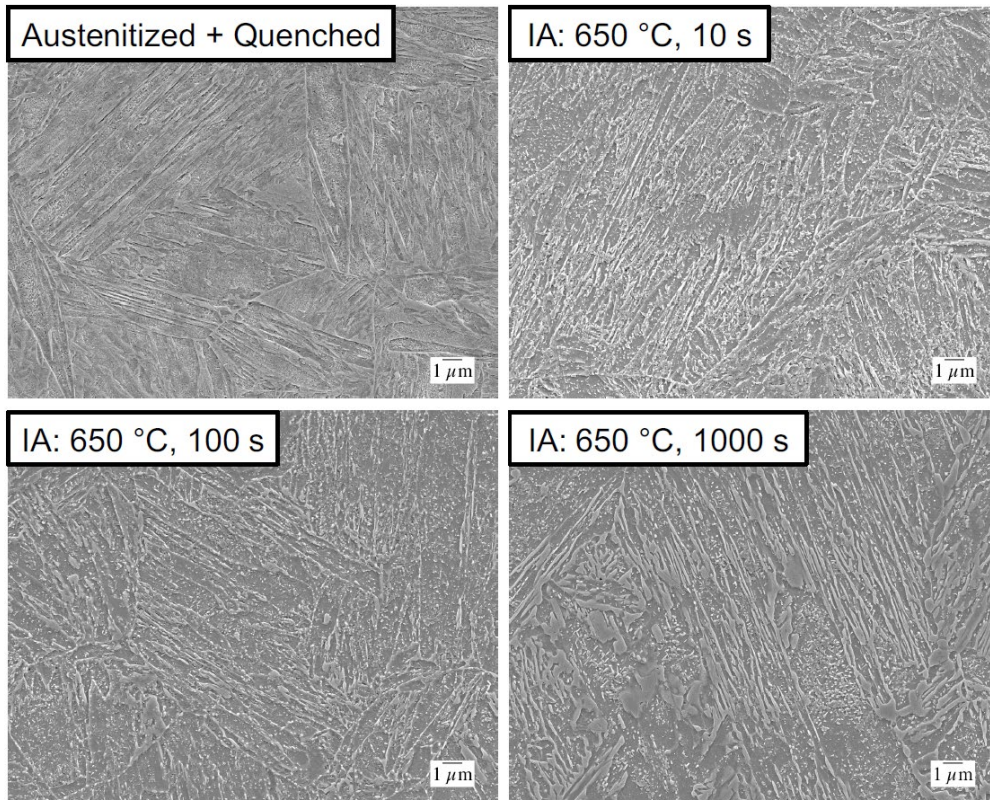
In FY 2018, 5Mn steel was also selected as a model steel to validate the modeling approaches adopted in this study and to determine some thermodynamic parameters (e.g., C or Mn diffusivity in different phases). Figure II.1.A.3.2.(a) shows the heat-treatment profile adopted for the 5Mn steel in this study. As shown in the figure, four different conditions (labeled 1 - 4) were considered. Condition 1 represents the as-quenched condition and conditions 2 to 4 represent the different IA time. Due to the different IA times of 10, 100 and 1,000 seconds, the microstructures of the generated four samples are different as shown in Figure II.1.A.3.2.(c). *Ex-situ* HEXRD measurement of austenite volume fraction for different IA time is also plotted in Figure II.1.A.3.2.(b). As can be seen from Figure II.1.A.3.2, more thin-lath type austenite can be observed with the increase of IA time.



(a)



(b)



(c)

Figure II.1.A.3.2. *Ex-situ* heat-treatment and characterization of 5Mn steel. (a) Heat-treatment profile; (b) austenite volume fractions; and (c) microstructures for four different conditions. Source: PNNL & Colorado School of Mines.

In-situ measurement of austenite volume fraction evolution was performed with the as-quenched 5Mn steel (i.e., Condition 1) for two holding different temperatures using HEXRD heat-treatment. Figure II.1.A.3.3.(a) shows the austenite volume fraction versus time for the two holding temperatures. As shown in Figure II.1.A.3.3, the austenite, which initially existed, is decomposed during the heating process, appears/increases again during the temperature holding process, and then decreases again during the last cooling process. A substantial increase of austenite volume fraction can be seen for the holding temperature of 650°C. One-dimensional (1D) DICTRA simulations were performed to model austenite growth within the 5Mn steel during temperature holding. The half-widths for martensite and austenite in the initial microstructure were 208.5 nm and 0.05 nm, respectively. The initial compositions for martensite and austenite are 0.001C-4.39Mn and 0.2C-4.39Mn, respectively. The mobility of Mn in martensite can be significantly greater than in ferrite due to the high defect density present in martensite [5]. DICTRA allows the user to apply a mobility enhancement factor to a species in a phase (e.g., Mn in martensite phase). For the 5Mn steel, the mobility enhancement factor has been calibrated to be ~ 5 by comparing the austenite volume fraction obtained from the 1D DICTRA simulation with *in-situ* and *ex-situ* HEXRD measurement of austenite volume fractions, as shown in Figure II.1.A.3.3.(b). It needs to be noted that the time scale of the HEXRD experiment has been shifted, so that the time when the holding starts is set to be zero seconds, in order to be compared to DICTRA simulation results where heating is not considered. Phase lattice parameter variations were also measured for the 5Mn steel from *in-situ* HEXRD heat-treatment tests.

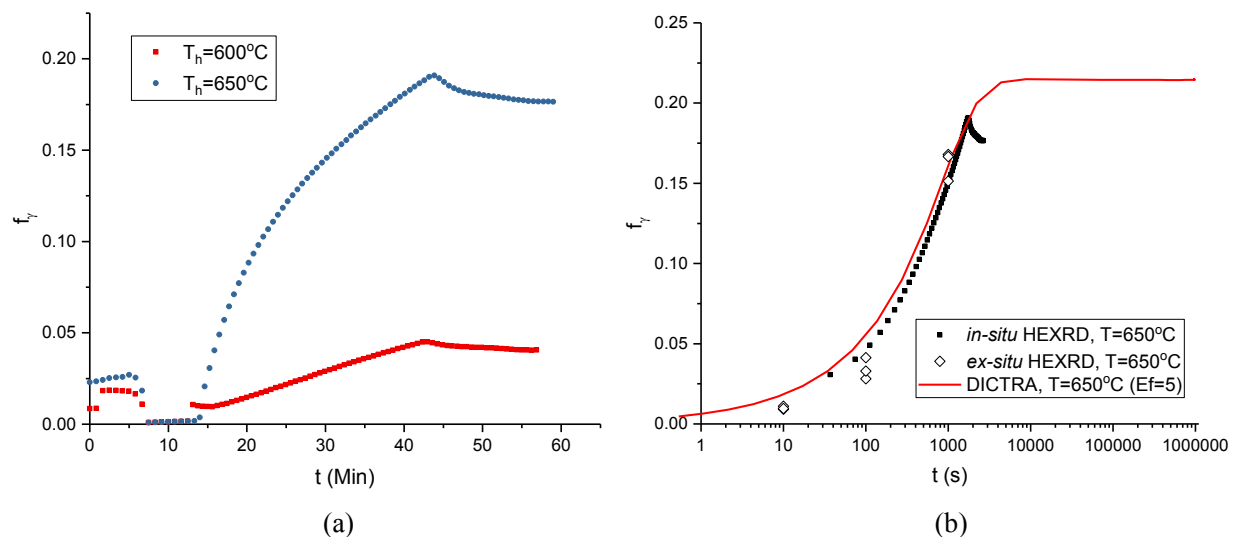
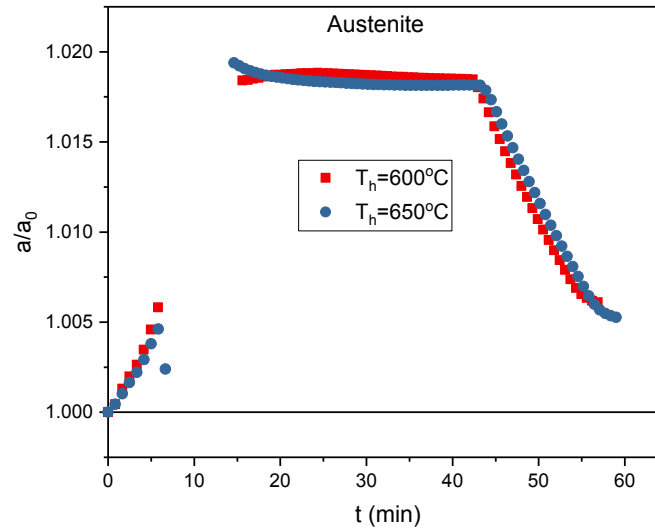
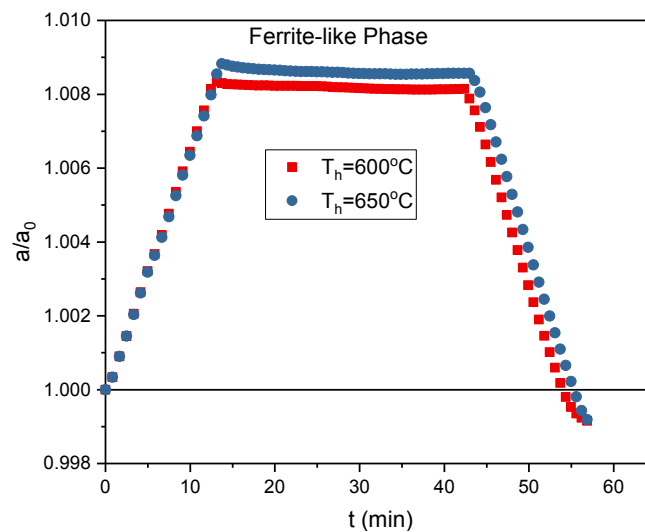


Figure II.1.A.3.3.(a) *In-situ* measurement of austenite volume fraction versus the time for different holding temperatures with as-quenched 5Mn steel using HEXRD and (b) Mn mobility determined for the DICTRA simulation by fitting with the experimental results. Source: PNNL.

Figure II.1.A.3.4.(a) shows the lattice parameter variations for the austenite phase and Figure II.1.A.3.4.(b) shows the variations for the ferrite-line phase during the heating cycle. The rapid increase and decrease at initial and final stages are due to the thermal expansion and contraction during the heating and cooling processes. During the holding temperature, the lattice parameters slightly change due to the partitioning of alloy elements (i.e., C or Mn). The results in Figure II.1.A.3.4 indicate that the austenite have slightly higher C or Mn content after the heating cycle. These phase lattice parameters may be related to the chemical compositions within the phases. Finding the correlations between this data is currently underway.



(a)



(b)

Figure II.1.A.3.4. ShAPE™ machine with new torque module capable of 2987 Nm @ 25-160 rpm. Source: PNNL.

In FY 2018, phase-field simulations using MICRESS® software for various conditions have also been pursued. Simulations employing two different initial microstructures will be discussed here. Simulation 1 has an initial microstructure consisting of equiaxed ferrite, while Simulation 2 has an initial microstructure consisting of elongated ferrite. Three simulations with varying amounts of nucleation seeds were conducted with Simulation 2, the elongated initial microstructure. Parameters for the simulations are listed in Table II.1.A.3.1. Austenite fraction plotted against IA time for Simulation 1 is shown in Figure II.1.A.3.5; predictions for the microstructural evolution and solute partitioning for Simulation 1 are shown in Figure II.1.A.3.6.(a). The initial microstructure for Simulation 2 and predictions for the microstructural evolution at 200 seconds for Simulations 2i, 2ii, and 2iii are shown in Figure II.1.A.3.6.(b) through (e). As shown in Figure II.1.A.3.6.(a), MICRESS® simulations predict partitioning of C and Mn to austenite during austenite growth. Simulation 1 predicts that the austenite growth rate diminishes as the austenite fraction approaches approximately 25%, as shown in Figure II.1.A.3.5. Additionally, the predicted austenite fraction after 200 seconds for Simulations 2i, 2ii, and 2iii are 27.3, 36.6, and 37.2%, respectively. The equilibrium austenite fraction for this composition

calculated from the TCFE9 database of Thermo-Calc[®] is 40.3%. It appears that limiting the number of austenite nucleation seeds has a substantial effect on the predicted austenite growth rate. Increasing the amount of nucleation seeds also causes the austenite grains to impinge on one another, leading to a finer microstructure with elongated ferrite and austenite. For Simulations 2ii and 2iii, as shown in Figure II.1.A.3.6.(d) and (e), the austenite grains saturate the ferrite grain boundaries, inhibiting the ferrite from coarsening; in Simulation 2i, as shown in Figure II.1.A.3.6.(c), the austenite grains grow uniformly and the ferrite is allowed to coarsen.

Table II.1.A.3.1. Parameters for MICRESS[®] Simulations.

Simulation	1	2		
		i	ii	iii
Phases	1:Ferrite (isotropic), 2: Austenite (isotropic)			
Concentration	Ferrite: 0.19C-4.39Mn, Austenite: NA			
Microstructure	Equiaxed	Equiaxed		
Interface Mobility (cm ⁴ /J s)	α - α : 1.0×10^{-7} (isotropic) γ - γ : 1.0×10^{-5} (isotropic)			
Interfacial Energy (J/cm ²)	α - α : 2.0×10^{-5} (isotropic), γ - γ : 2.0×10^{-5} (isotropic), α - γ : 2.0×10^{-5} (isotropic)			
Interface Width (nm)	75			
Thermal Profile	Isothermal: 650 °C			
Driving Force	Thermo-Calc (T-C) Coupled			
Diffusion	T-C Coupled, Mn in ferrite specified: $D_0=7560$ cm ² /s, $Q=2.245 \times 10^5$ J/mol			
Nucleation: Site	Ferrite Triple Points	Ferrite-Ferrite interfaces		
Nucleation: Max Seeds	20	100	500	unlimited
Nucleation: Shield Time (s)	1	0.01		
Nucleation: Shield Dist. (μ m)	0.5	0.05		

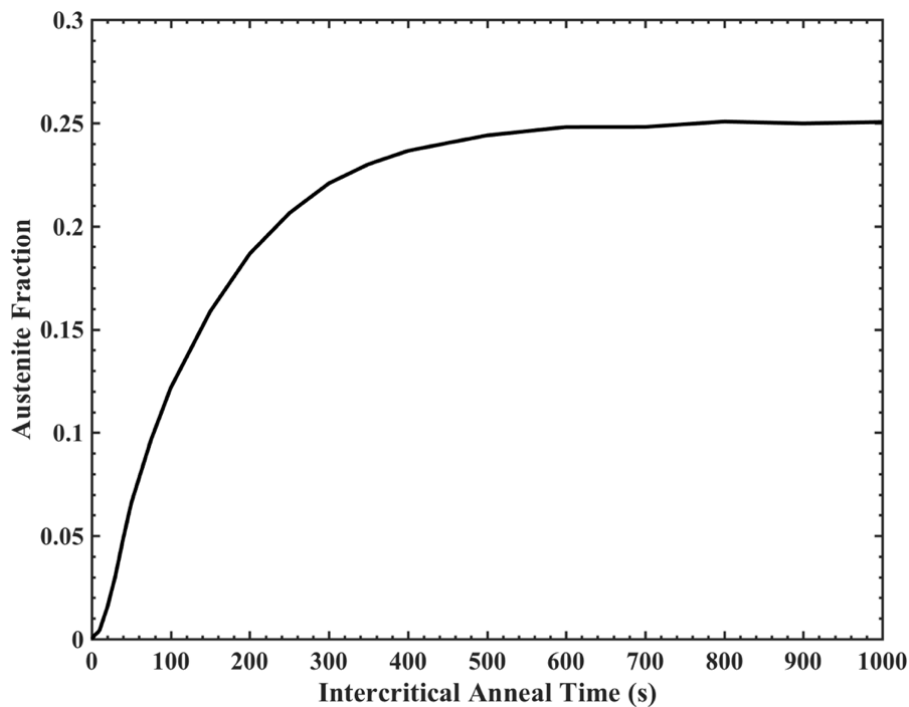
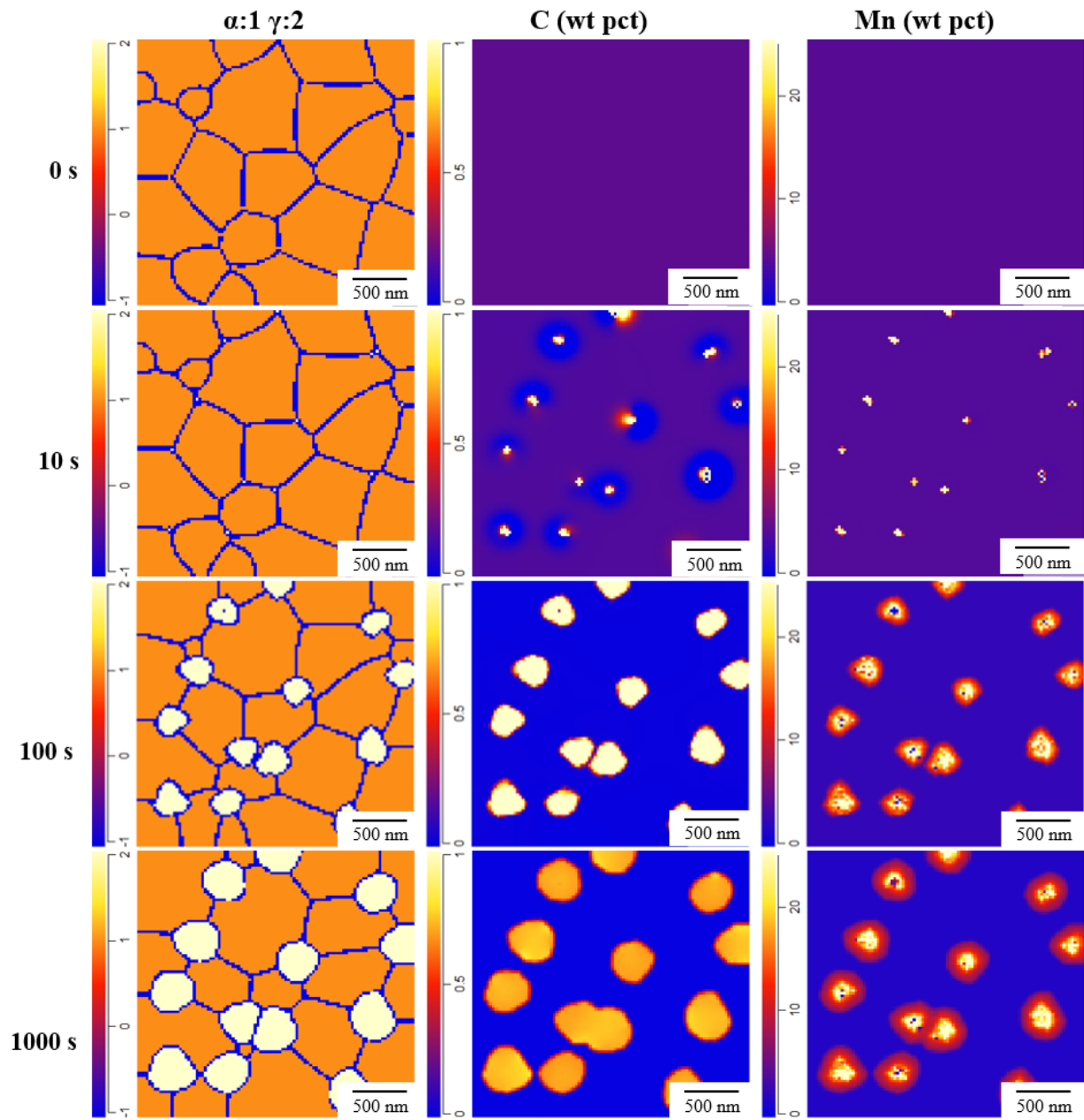


Figure II.1.A.3.5. Austenite growth prediction during IA from MICRESS[®] Simulation 1.



(a)

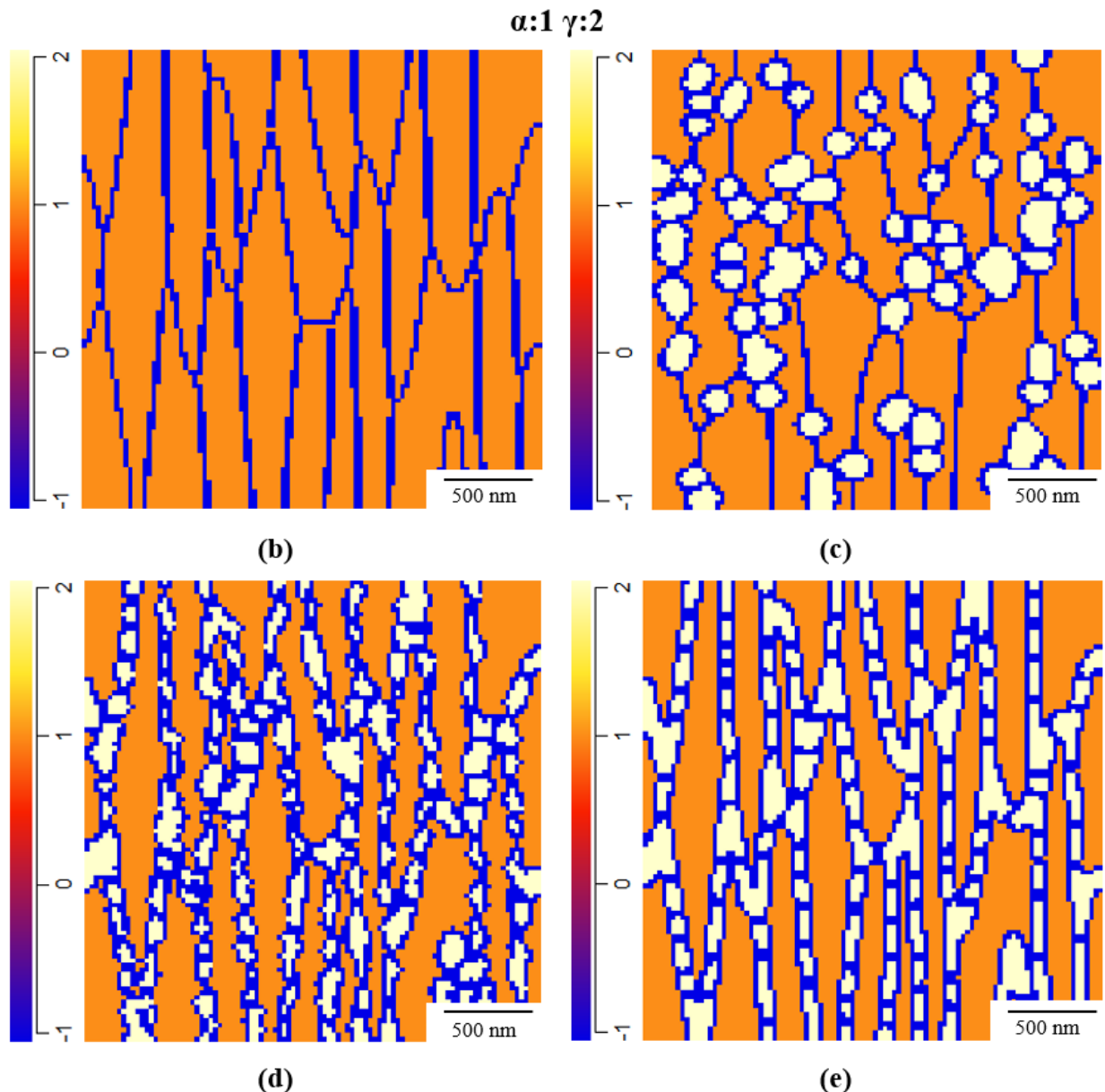


Figure II.1.A.3.6. MICRESS[®] simulation results for IA of a 0.19C-4.39Mn steel: (a) Microstructural evolution and solute partitioning for initial microstructure consisting of equiaxed ferrite. (b) Initial microstructure consisting of elongated ferrite, and predictions for microstructural evolution after 200 seconds for conditions (c) 2i, (d) 2ii, and (e) 2iii.

Source: Colorado School of Mines.

The microstructural evolution during IA is likely influenced by the nucleation behavior of austenite. It has been reported that ferrite recrystallization and austenite nucleation can occur simultaneously during IA of low C DP steels [6–8]. Yang et al. [6] intercritically annealed a cold-rolled 0.08C-1.45Mn-0.21Si steel with an initial microstructure consisting of deformed ferrite and pearlite. After IA, austenite was observed at the grain boundaries of deformed and recrystallized ferrite. It was also reported that spheroidized cementite particles were observed to be enveloped within recrystallized ferrite and only stimulated austenite nucleation after ferrite recrystallization was complete. Furthermore, it was found that larger cementite particles would stimulate austenite nucleation while many smaller cementite particles would not. While these reports pertain to steels with ferrite-pearlite initial microstructures, it is suspected that austenite nucleation in intercritically annealed

medium Mn steels exhibits similar behavior. To accurately simulate austenite nucleation occurring simultaneously with the recrystallization of ferrite, it will be required to incorporate the recrystallization of ferrite into the MICRESS[®] simulations, which is a focus area of continuing simulations.

Conclusions

Microstructure/mechanism-based phenomenological and crystal plasticity finite element modeling methods were developed with consideration of martensitic phase transformation. These modeling methods successively captured the Lüders banding behavior and yield point elongation for medium Mn steels. A new 5Mn steel was selected as a model steel to validate the modeling approaches and to determine thermodynamic parameters of medium Mn steels. The Mn mobility in ferrite/martensite phase of the 5Mn steel was then determined by integrated experimental (i.e., *ex-situ* and *in-situ*) and numerical modeling framework. A phase-field modeling framework has also been established. Initial simulation results have been obtained and linkage with prior and further experimental data is ongoing. Furthermore, additional changes to input parameters to the simulation are further explored and will be guided by experimental validation of simulation results.

References

1. Choi, K. S., W. N. Liu, X. Sun, M. A. Khaleel, Y. Ren, and Y. D. Wang, 2008, “Advanced micromechanical model for TRIP steels with application of *in-situ* HEXRD method,” *Metall. Mater. Trans. A*, Vol. 39, pp. 3089–3096.
2. Choi, K. S., A. Soulam, W. N. Liu, X. Sun, and M. A. Khaleel, 2010, “Influence of various material design parameters on deformation behaviors of TRIP steels,” *Comput. Mater. Sci.*, Vol. 50, pp. 720–730.
3. U.S. Department of Energy, 2018, “Materials 2017 Annual Progress Report,” VTO, DOE-EERE, DOE/EE-1711, pp. 76–97.
4. Abu-Farha, F., X. Hu, X. Sun, Y. Ren, L. G. Hector, G. Thomas, and T. W. Brown, 2018, “*In-situ* local measurement of austenite mechanical stability and transformation behavior in third-generation AHSSs,” *Metall. Mater. Trans. A*, Vol. 49, pp. 2583–2596.
5. Dmitrieva, O., D. Ponge, G. Inden, J. Millán, P. Choi, J. Sietsma, and D. Raabe, 2011, “Chemical gradients across phase boundaries between martensite and austenite in steel studied by atom probe tomography and simulation,” *Acta Mater.*, Vol. 59, pp. 364–374.
6. Yang, D. Z., E. L. Brown, D. K. Matlock, and G. Krauss, 1985, “Ferrite recrystallization and austenite formation in cold-rolled intercritically annealed steel,” *Metall. Trans. A*, vol. 16, pp. 1385–1392.
7. Huang, J., W. J. Poole, and M. Militzer, 2004, “Austenite formation during IA,” *Metall. Mater. Trans. A*, Vol. 35, pp. 3363–3375.
8. Chbihi, A., D. Barbier, L. Germain, A. Hazotte, and M. Gouné, 2014, “Interactions between ferrite recrystallization and austenite formation in high-strength steels,” *J. Mater. Sci.*, Vol. 49, pp. 3608–3621.

Acknowledgements

This research used resources from the Advanced Photon Source, a U.S. Department of Energy–Office of Science User Facility, operated by Argonne National Laboratory under Contract No. DE-AC02-06CH11357. The Principal Investigators would like to acknowledge the assistance of Drs. Xiaohua Hu and Xin Sun from ORNL, and Josh Mueller, PhD student at the Colorado School of Mines, for the material characterization experiments, modeling works and helpful discussions that are crucial for the success of this project.

II.1.A.4 RT Stamping of High-Strength Al Alloys

Aashish Rohatgi, Principal Investigator

Pacific Northwest National Laboratory
902 Battelle Blvd.
Richland, WA 99352
E-mail: aashish.rohatgi@pnnl.gov

Jerry L. Gibbs, DOE Technology Manager

U.S. Department of Energy
E-mail: jerry.gibbs@ee.doe.gov

Start Date: November 1, 2016	End Date: September 30, 2019	
Project Funding (FY18): \$600,000	DOE share: \$400,000	Non-DOE share: \$200,000

Project Introduction

This project is addressing the challenge that Al sheet alloys possess limited formability at RT and under high-strength conditions; in other words, it is difficult to stamp a high-strength Al sheet at RT into a structural component with complicated geometry because the sheet is unable to deform uniformly and instead, cracks during forming/stamping. Warm/hot-forming can increase the formability of Al but is expensive due to added costs of heated dies, forming lubricants, lubricant clean-up, etc. Unlike hot-stamped steels that undergo austenite to martensite phase transformation during quenching and achieve the high-strength at the end of the stamping process itself, Al alloy matrix does not undergo such phase transformation upon quenching. Hence, warm/hot-forming results in lower post-formed strength such that heat-treatment, in addition to paint-bake, is needed (adding cost) to regain the strength. Thus, the use of an Al sheet is limited to lower strength Al alloys and/or simple shapes (e.g., hood, deck lids, door inner, etc.) and many sheet components are still stamped in steel in the high-volume automotive industry. As such, the ability to form high-strength Al alloys cost-effectively, such as at RT, will expand Al use for structural components (i.e., crash beams, B-pillars, etc.) as well, and has the potential to result in significant lightweighting.

Objectives

This project aims to develop processing techniques that will overcome the formability limitations of high-strength Al alloys and enable their forming at RT. Eventually, this knowledge needs to be leveraged to fabricate an automotive component. Thus, the project objectives are to:

- Identify automotive components that, if formed out of high-strength Al, can provide lightweighting, relative to if they were made of high-strength steels.
- Develop constitutive relations and perform stamping simulations to determine the feasibility of stamping a selected component out of a high-strength Al alloy.
- Integrate microstructure and mechanical property models for the selected Al alloy.
- Fabricate and characterize a prototype component stamped out of the selected Al alloy.

Approach

The focus in this project is on understanding the microstructure-formability-strength interplay in high-strength Al alloys with the expectation that microstructural control during processing could enable sufficient formability and strength in a prototypical automotive component. The project is structured to be performed in three phases over a duration of three years.

During the first phase of the project in FY 2017, we performed a qualitative assessment of the commercial potential of stamped high-strength 7xxx series Al alloys. We surveyed the published literature and held

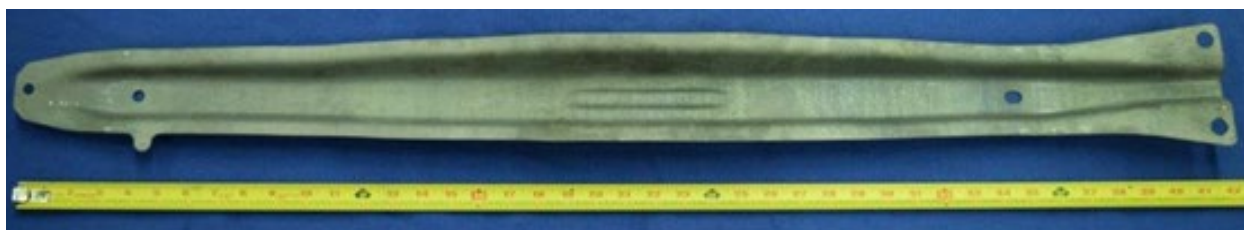
discussions with industry partners. Consequently, multiple potential automotive components were identified that, if made out of high-strength Al, could provide a 30–50% weight savings relative to high-strength steel. Based on feedback from industry partners, a door-side-impact beam was selected as the prototypical component for this project, while AA7075 was selected as the high-strength Al alloy.

In the second phase of the project from FY 2017 to FY 2018, our goal was to determine the feasibility of achieving both high-strength and RT formability suitable for a side-impact beam made out of AA7075. An in-production side-impact beam made of a hot-stamped steel, as shown in Figure II.1.A.4.1, was provided by GM as a prototypical component that could serve as an initial design for an Al side-impact beam. The mechanical property data of Al for these simulations was determined through mechanical testing at PNNL. The steel beam design was used as a basis by Magna to perform forming simulations using AA7075 as the sheet material. A summary of this work is presented in this report.

During the third phase of the project in FY 2019, we will develop microstructure and mechanical property models of AA7075. Microstructural evolution (e.g., precipitation kinetics) during aging will be determined. Analytical models from the literature will be used to correlate microstructural evolution (i.e., precipitation nucleation and growth) and mechanical properties (i.e., strength and fracture) to understand the resulting strength and formability of this alloy. The models, in turn, will guide the stamping approach. We will work with our industry partners to design a die and stamp a prototypical side-impact beam in AA7075 at RT. The stamped component will be characterized for formability and strength to evaluate our stamping approach towards meeting the target properties.



(a)



(b)

Figure II.1.A.4.1. Images of the steel side-impact beam: (a) Top view; (b) Bottom view. Source: PNNL.

Results

Figure II.1.A.4.1.(a) and (b) show the top and bottom views, respectively, of the steel impact beam that was used as an initial target design for the stamping simulations using high-strength Al. The steel beam was scanned into a digital format (3D CAD model) and Figure II.1.A.4.2 shows a reconstructed simulated view of the beam from the digital file, corresponding to the view shown in Figure II.1.A.4.1.(b) of the actual beam. Two types of stamping simulations were performed – (1) crash form and (2) draw form. In the crash form simulation approach, as shown schematically in Figure II.1.A.4.3.(a), the male punch and female die are “crashed” together with the blank in between (illustrated as steps A, B and C) while allowing the blank to move freely [1]. In the draw form approach, shown schematically in Figure II.1.A.4.3.(b), the blank is clamped

(illustrated by the green line) to control its stretch and prevent wrinkling during stamping (illustrated as steps A, B and C) [1]. Although the crash form approach may be simpler and cheaper, it is difficult to know if the stamped component will be free from wrinkles and splits.

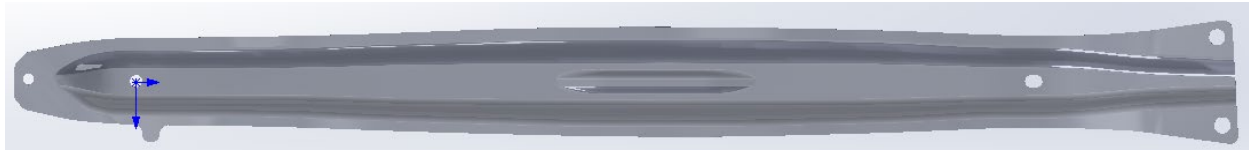


Figure II.1.A.4.2. A simulated image of the steel impact beam reconstructed after scanning the actual beam and corresponding to the view shown in Figure II.1.A.4.1(b). Source: Magna Intl.

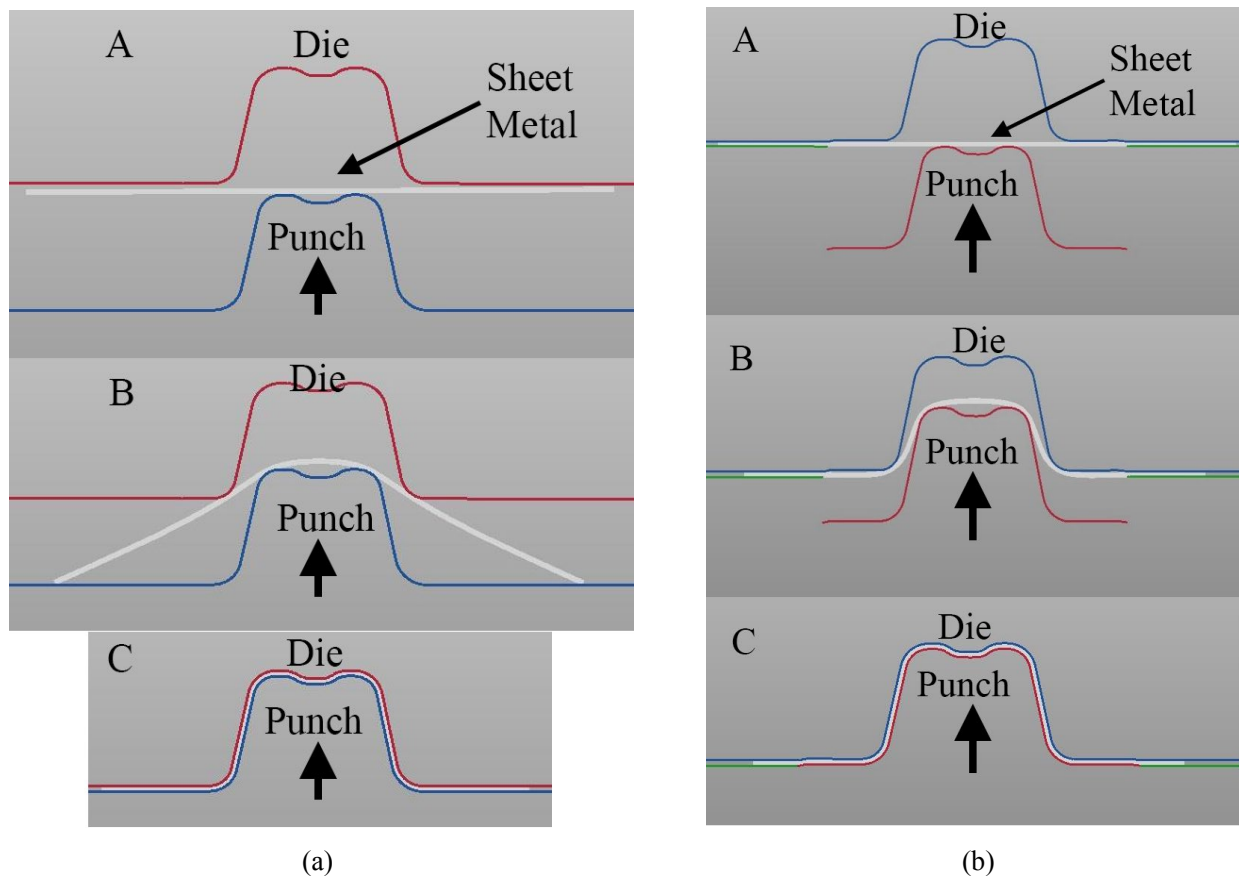


Figure II.1.A.4.3. Schematic of the stamping simulations performed showing the process sequence: (a) crash form, where the sheet is free to move; and (b) draw form, where the sheet is clamped, and its movement is controlled. Source: PNNL.

Figure II.1.A.4.4 shows an example of the simulated stamped beam, produced by the sheet stamping simulations using an AA7075 sheet. The thickness of the simulated stamped component was determined at multiple locations along the beam, as indicated by locations 1 through 7 in Figure II.1.A.4.4. The resulting thickness strains calculated by the simulation at these locations are listed in Table II.1.A.4.1, which shows that while locations 1 and 2 experienced some thickening compression (indicated by positive strain values), the remainder of the locations underwent thinning (indicated by negative strain values). Further, the maximum thinning strain was $\sim 11\%$ and 10% , respectively, for the crash form and draw form simulations and is considered a reasonable value for stamping Al. Additional analyses with respect to springback is ongoing. Further work also includes comparison of the energy absorption behavior (e.g., during a simulated crash) of an Al versus steel beam.

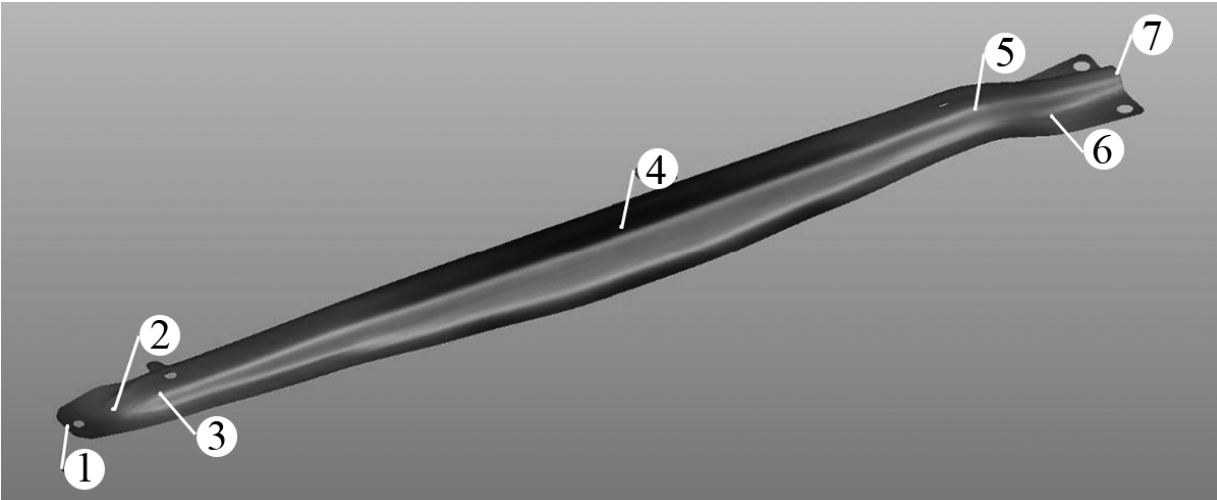


Figure II.1.A.4.4. Image of an Al side-impact beam produced by stamping simulations. Locations 1–7 refer to places where the post-formed sheet thickness is measured, and the corresponding strain is listed in Table II.1.A.4.1. Source: Magna Intl.

Table II.1.A.4.1. Thickness Strains in the Stamped Al Impact Beam.

Simulation Type/Location	Point 1	Point 2	Point 3	Point 4	Point 5	Point 6	Point 7	Max.
Crash Form	1.2%	3.6%	-3.6%	-0.13%	-4.4%	-4.5%	-6.2%	-11%
Draw Form	0.4%	2.6%	-3.8%	-0.08%	-5.2%	-4.4%	-5.9%	-10.1%

Conclusions

The overall aim of this project is to enable RT stamping of high-strength Al alloys to replace automotive structural components that are typically made of steel. In the current work, an in-production side-impact beam made of hot-stamped steel was used as the component to base a potential Al side-impact beam. AA7075 was selected as the representative high-strength Al alloy and its stamping behavior in different tempers was simulated (using the steel beam as the target design). Initial results from the stamping simulations suggest that AA7075 may be stampable in the selected design. Further analyses with respect to springback and energy absorption (e.g., during a simulated crash) is in progress to provide a more complete picture of this stamping approach.

References

1. Stamping Simulation website, “What’s the difference between a crash and a draw form?,” <https://stampingsimulation.com/whats-the-difference-between-a-crash-and-a-draw-form/>

Acknowledgements

The technical contributions of PNNL staff supporting this research is gratefully acknowledged; in particular, Ms. E. Stephens for her support in performing the limiting dome height tests and data analysis, Dr. A. Soulami for performing the numerical simulations, and Mr. K. Mattlin and Mr. M. Dahl for their help in conducting heat-treatments and mechanical tests. We would like to acknowledge the technical support provided by Mr. B. Kokosza and his team at Magna-Stronach Centre for Innovation for technical discussions and support and performing stamping simulations. Finally, we are grateful to the technical staff at GM R&D, in particular, Mr. J.T. Carter and Dr. A.K. Sachdev, for their insightful comments and discussions and providing the steel impact beam for this research, as well as providing information on lightweighting analyses for automotive components.

II.1.B Development of Low-Cost High-Strength Automotive Al Sheet (Arconic)

Russell Long, Co-Principal Investigator

Arconic
100 Technical Drive
New Kensington, PA 15069
E-mail: russell.long@arconic.com

John Newman, Co-Principal Investigator

Arconic
100 Technical Drive
New Kensington, PA 15069
E-mail: john.newman@arconic.com

Jerry L. Gibbs, DOE Technology Manager

U.S. Department of Energy
E-mail: jerry.gibbs@ee.doe.gov

Start Date: October 1, 2014 End Date: January 31, 2019
Project Funding (FY18): \$465,258 DOE share: \$152,491 Non-DOE share: \$312,767

Project Introduction

The goal of the project is to develop an automotive high-strength 7xxx Al alloy and demonstrate its ability to replace an ultra-high-strength steel component with significant weight savings at a cost of less than \$2 per pound saved.

Objectives

The initial phase of this project was based on alloy development to reach the DOE targets stated in this report. Corrosion and forming requirements are being developed by Honda and Cosma, respectively. The alloy development trials targeted an ultimate strength of 600 MPa with 8% minimum elongation while meeting corrosion and formability requirements.

A demonstration part has been defined, which includes the critical features in the current production hot-stamped steel component. The geometry of this demonstration part was evaluated in forming simulations using the material properties developed during the alloy development phase. The demonstration part tooling was also built, as well as the oven to heat the blanks. The tooling and oven are installed in a press line. Several forming trials of the new alloys have been completed.

ORNL evaluated the properties in tailor-welded blanks produced using friction stir welding in these experimental alloys. ORNL procedures were used to produce a large number of full-size tailor-welded blanks of these alloys. Some of the tailor-welded blanks were successfully stamped in recent forming trials.

Approach

The first year of the contract provided a definition of the detailed requirements. Specifications were developed during the alloy development phase based on the requirements. Multiple new alloys were produced at a laboratory-scale. These alloy development trials were used to define several alloys that were produced at full-scale in existing Arconic facilities. A demonstration part, developed by Honda and Cosma, which includes all the critical features needed for the current ultra-high-strength steel production part, is shown in Figure II.1.B.1.

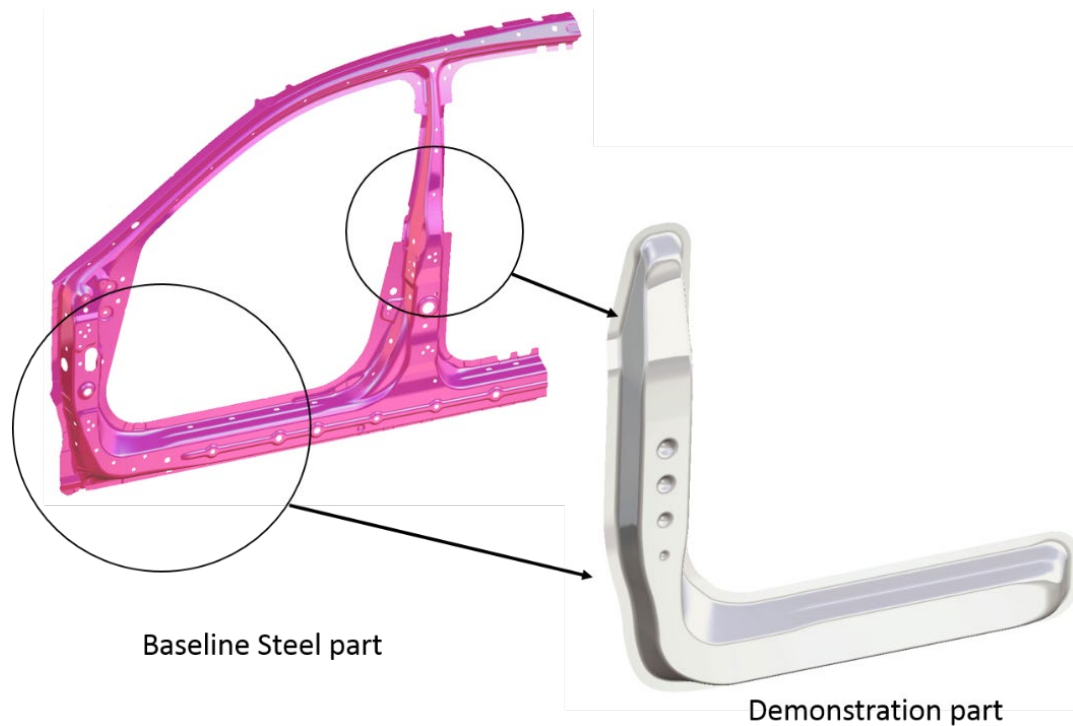


Figure II.1.B.1. Demonstration part geometry. Source: Honda.

The forming tooling was designed and built to form this part at elevated temperatures. A warm-forming oven that can heat a single blank with rapid heat-up times was built as a part of the project.

Results

There are several paths that can be used to form 7xxx materials. For roll-formed or simple shapes, a RT forming path can be used on tempered materials. The complex stamped shape of the baseline steel parts cannot be formed at RT in these alloys. This shape could be hot-formed using procedures similar to those used for hot-forming steel, but at much lower temperatures. The other alternative is to warm-form, which means that the material forming temperature is significantly lower than the solution heat-treating temperature of the alloy. Contract requirements stipulated that the forming be done at a maximum temperature of 225°C, which falls more into the warm-forming range.

A forming cell press, an oven for blank heating, a robotic transfer system, and all tooling has been setup in an existing press line at Eagle Bend Manufacturing. This forming setup is shown in Figure II.1.B.2.

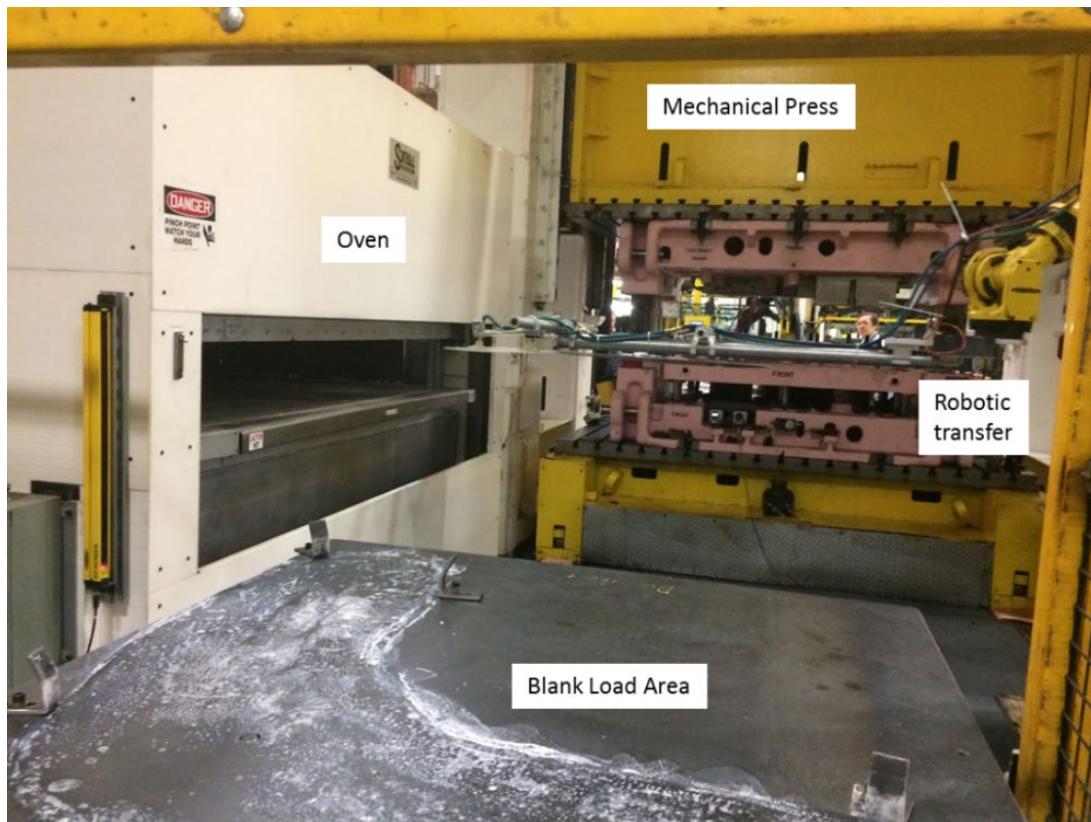


Figure II.1.B.2. Forming cell. Source: Cosma.

This cell was used to explore the impact of blank shape, blank temperature, lubricant, and tooling temperature on each alloy. The forming result for one of the experimental alloys is shown in Figure II.1.B.3 for four different temperatures. The part was successfully formed in three of four experimental alloys. The forming improved by increasing blank temperature with successful parts being formed at 220–230°C.

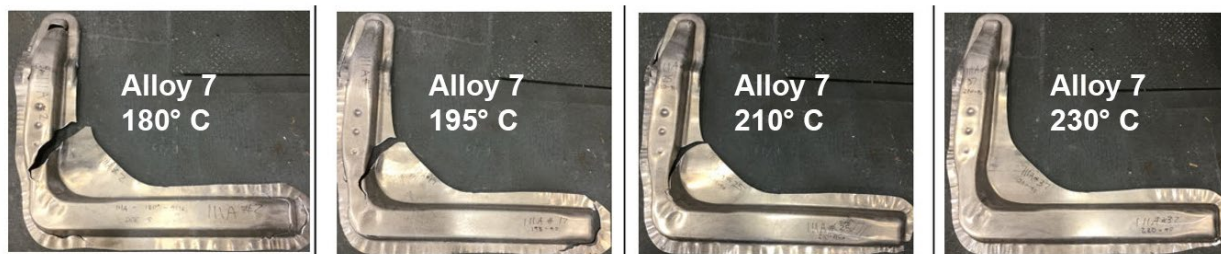


Figure II.1.B.3. Selected results from forming trial. Source: Cosma.

The demonstration part includes a straight section representing the rocker, which can be tested in a three-point bend test to simulate the side-impact test in the full vehicle. Simple hat-shaped samples formed from the two best performing experimental alloys were given a paint-bake cycle of 185°C for 20 minutes. A close-out plate made of the same material (with the same paint-bake cycle) was riveted to the hat-shaped sample as shown in Figure II.1.B.4. These samples were then tested using a three-point bend test, as shown in Figure II.1.B.5. A 7055 baseline sample undergoing this test is shown in Figure II.1.B.6.

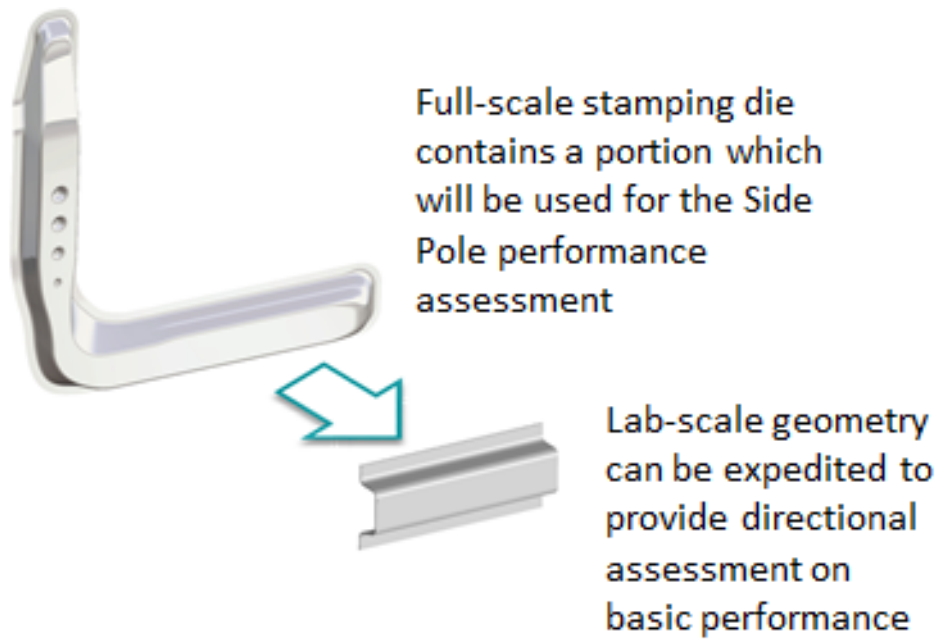


Figure II.1.B.4. Section of demonstration part used for three-point bend tests. Source: Cosma.

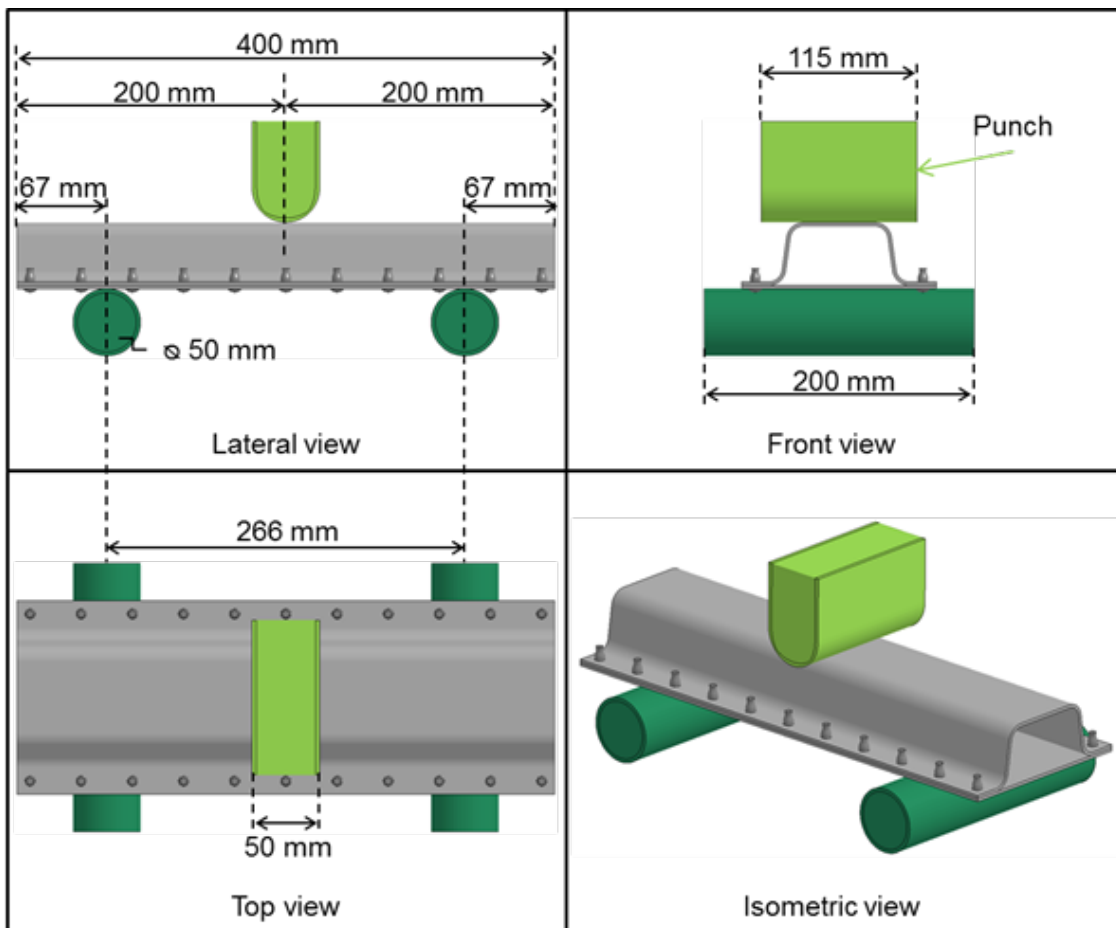


Figure II.1.B.5. Schematic views of the Al7055T6 hat section setup under three-point bending load. Source: Cosma.



Figure II.1.B.6. Typical performance of samples in a three-point bend test. Source: Cosma.

The load deflection curves corresponding to hot-stamped ultra-high-strength steel (e.g., UTS = 1,500 MPa) and the 7055-T76 samples are shown in Figure II.1.B.7. The three-point bend test results in an initial peak load until local deformation of the side walls begins. As the loading continues, any load drops are associated with cracking. The goal is to minimize cracking and have a load recovery after initial cracking. The 1.5 mm thick ultra-high-strength steel incumbent material and the 2.5 mm 7055-T76 material compare quite well and likely a 2.3 mm or 2.4 mm 7055-T76 sample would match the steel performance closely.

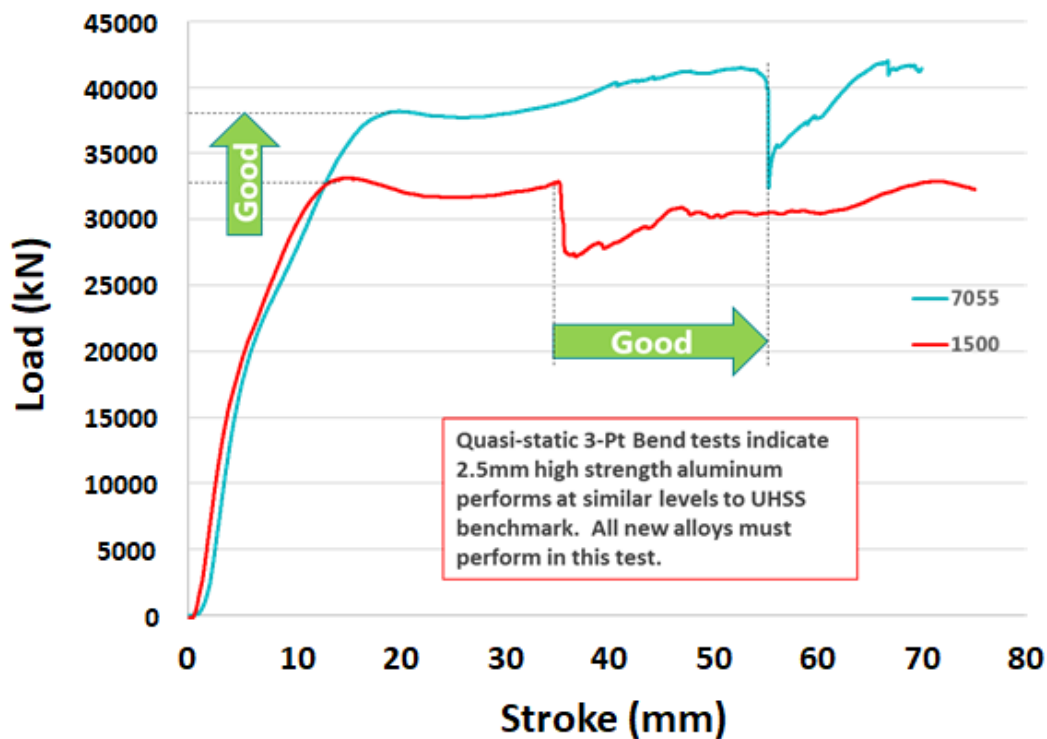


Figure II.1.B.7. Comparison of load deflection curve from three-point bend testing. Source: Arconic.

Samples were cut from the formed parts to measure their mechanical properties. The strengths of the formed parts were then measured with and without this paint-bake cycle. Those results are shown in Figure II.1.B.8.

The strengths of each alloy increase with the addition of the paint-bake cycle, so the warm-forming step is not resulting in over-aging at the 230°C blank temperature for a 90-second cycle. The ultimate strengths after the paint-bake cycle ranged from 560–580 MPa. This is 20–40 MPa below the project target. Based upon these results of alloys 180-101 and 180-111, an additional rolling trial was conducted using new compositions and

processing paths to produce new alloy blanks that can reach the DOE ultimate strength target of 600 MPa and a second new alloy to enhance performance in the three-point bend test. Material tests on these new alloys show that the alloy designated WF (for warm-forming) New 1 can reach the DOE goal of 600 MPa ultimate strength with compromises in elongation and toughness. The second new alloy falls short of the ultimate strength target, but improves elongation, toughness, and in vehicle performance.

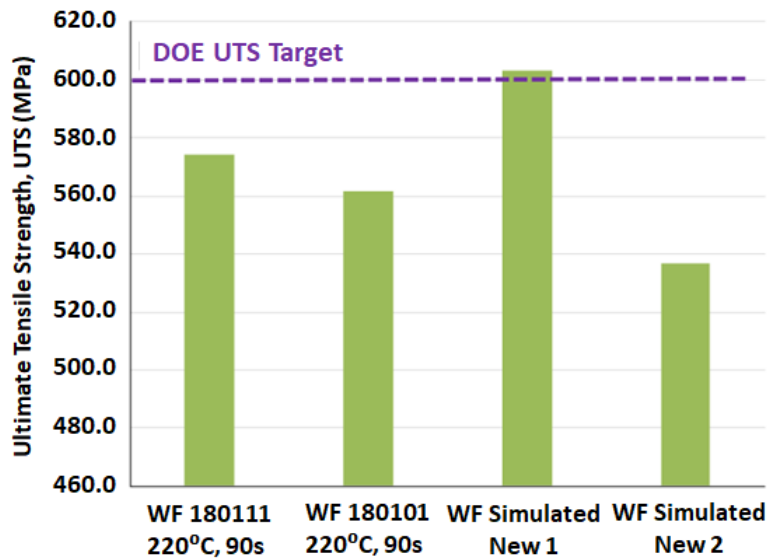


Figure II.1.B.8. UTSs measured from formed parts. Source: Arconic.

One target of this project is to maintain at least 8% elongation at ultimate strength levels at or approaching 600 MPa. The elongations measured from samples cut from warm-formed parts produced with alloys 180-111 and 180-101 with and without the paint-bake cycle are shown in Figure II.1.B.9. The results shown for new alloys 1 and 2 were cut from flat panels and applied a simulated warm-form and paint-bake cycle. These results will be repeated using samples cut from warm-formed parts, once the forming trial has been completed.

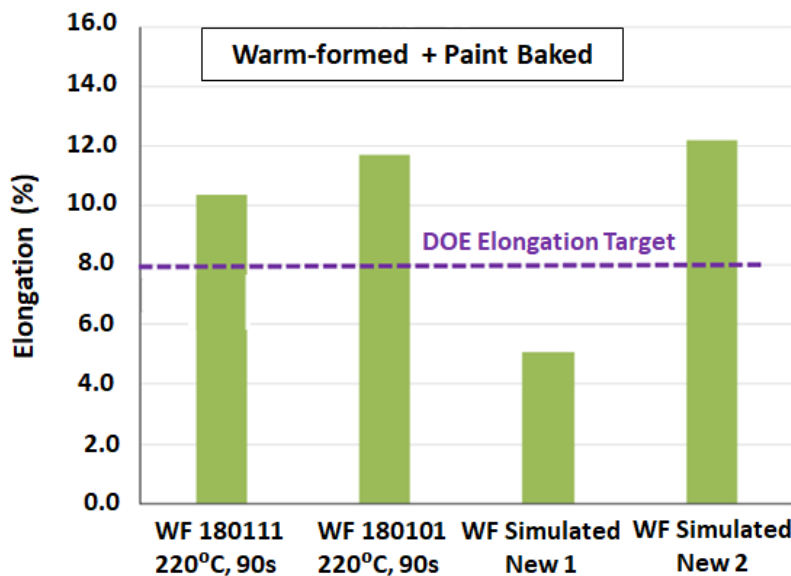


Figure II.1.B.9. Elongations measured from warm-formed and paint-baked parts. Source: Arconic.

Three-point bend tests were conducted on 180-101, new Alloy 1 and new Alloy 2 and results are shown in Figure II.1.B.10.(a), (b), and (c), respectively. The three-point bend performance of new Alloy 1, which reached the ultimate strength goal, was poor. The performance of new Alloy 2 showed little cracking in the three-point bend testing. The performance of alloy 180-101 was between them.

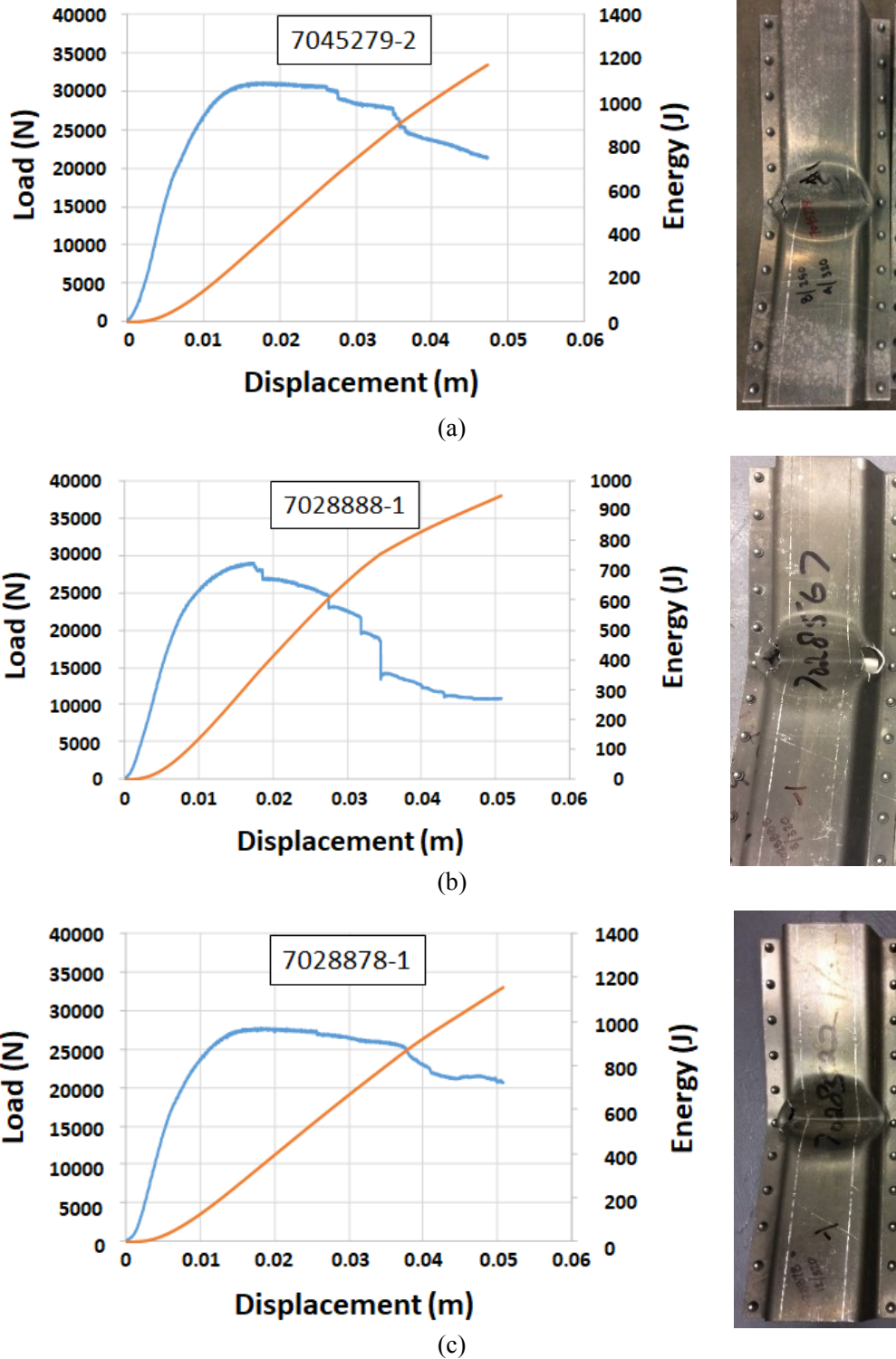


Figure II.1.B.10. Three-point bend test results. Source: Cosma.

The TWB Company in Monroe, MI, was contracted to produce the remaining blanks because they have participated in other DOE programs producing tailored-welded blanks. As part of a previous DOE contract, TWB was equipped with a gantry friction stir welding system including vacuum-clamping, which allows for faster full-scale blank welding. Initial forming trials were unsuccessful because of weld quality issues. The weld line was located very close to a blank shape change. A second series of blanks were produced with the weld line relocated 50 mm to move it away from the blank shape change and improvements in weld quality. The addition of root bend testing at TWB improved the weld quality. One of the TWB formed parts is shown in Figure II.1.B.11 and a close-up image of the weld.

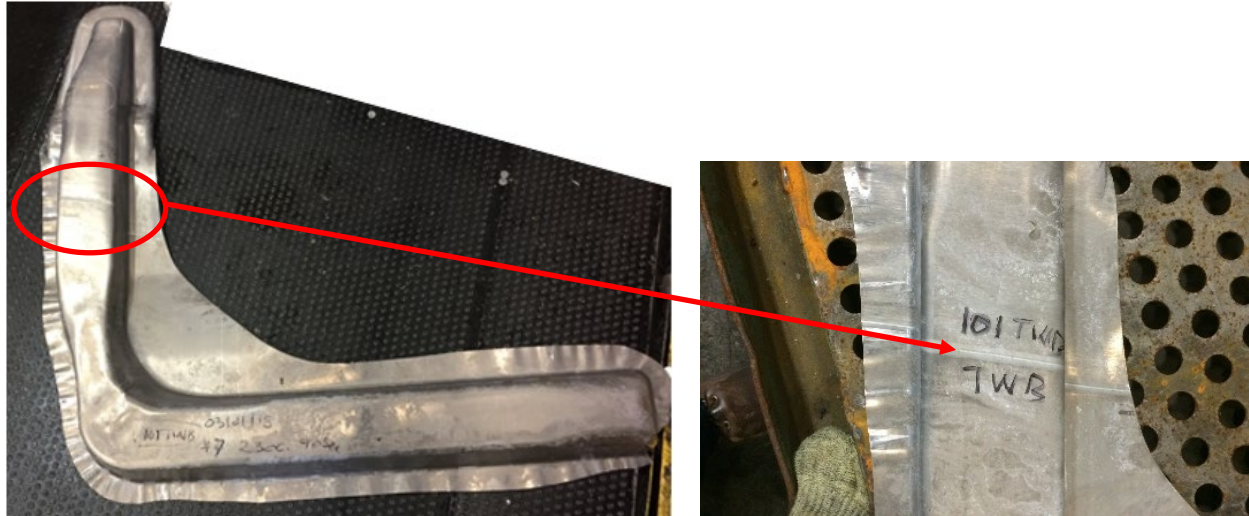


Figure II.1.B.11. Part formed using a tailor-welded blank. Source: TWB Company.

A cost study was conducted to compare the cost of the baseline hot-stamped steel part to the warm-formed tailor-welded 7xxx part. The study included material costs from Arconic, as well as estimates from Cosma and TWB for future production at three volume levels of 50,000 vehicles/year, 100,000 vehicles/year, and 400,000 vehicles/year. At 400,000 vehicles per year, the cost per pound of weight savings was less than \$2.50/lb-saved. This is very close to the original cost target of \$2/lb-saved.

Conclusions

In the fourth year of this contract, a demonstration part was successfully formed using multiple experimental alloys. Properties from many locations within the part were measured. Three-point bend tests were added to simulate in vehicle performance of all alloys. Samples from these parts are undergoing corrosion testing. An additional forming trial will be conducted on the newest alloys. Two sets of full-scale tailor-welded blanks were produced and formed. The initial set of blanks were not successfully formed because of weld quality issues and a weld location that was close to the shape transition on the final blank shape. The second set of blanks was successfully formed.

The tailor-welded blanks improved the material utilization. The cost study resulted in a high-strength Al part at a cost less than \$2.50/lb-saved over the baseline hot-stamped steel part.

II.1.C Phase Transformation Kinetics and Alloy Microsegregation in High-Pressure Die-Cast Mg Alloys (The University of Michigan)

John Allison, Principal Investigator

Materials Science & Engineering
The University of Michigan
2200 Bonisteel Boulevard
Ann Arbor, MI 48104
E-mail: johnea@umich.edu

Sarah Kleinbaum, DOE Technology Manager

U.S. Department of Energy
E-mail: sarah.kleinbaum@ee.doe.gov

Start Date: October 1, 2013	End Date: September 30, 2018	
Project Funding (FY18): \$600,000	DOE share: \$600,000	Non-DOE share: \$0

Project Introduction

High-pressure die-casting (HPDC) is used to manufacture over 90% of commercial Mg products [1]. This process is fast, economical, and produces complex thin wall Mg components that cannot be fabricated by other means. The cooling rate involved in HPDC and super vacuum die-casting (SVDC) are extremely high and range from 10 to 1,000°C/s [2–3]. The solidification processes experienced in this region are far from equilibrium conditions. Under such extreme conditions, the solidification kinetics, phase transformations, and redistribution of alloying elements cannot be predicted using equilibrium thermodynamics or the typical modifications to predict alloy partitioning, such as those represented by a Scheil model [4]. There is essentially no systematic, quantitative information on eutectic phase formation or microsegregation in this region. This represents a significant and distinct gap in our scientific understanding of this important manufacturing process.

The redistribution of alloying elements during non-equilibrium solidification leads to microscale segregation across the dendrite/cell and this microscale segregation is strongly dependent on the cooling rate. Although microsegregation has been the subject of a limited number of investigations in Mg alloys [5–11], there is no known microsegregation study for Mg alloys under HPDC conditions in the open literature. Previous studies of microsegregation in Mg alloys have been obtained in directionally solidified castings or in samples cast under moderate cooling rate conditions.

Research on heat-treatment of die-cast Mg alloys has been limited due to the blistering that occurs when entrapped air expands during solution treatment. A new processing technology, SVDC for Al and Mg-alloy components [12–13], significantly reduces or eliminates air entrapment thus enabling heat-treatment of die-casting alloys and components. This advanced processing route offers new approaches for alloy development and improved Mg component properties. To date, studies of the dissolution of eutectic phases and precipitate evolution during heat-treatment of die-cast alloys have been very limited [14–16], and there has been no systematic investigation of alloying and processing effects.

Precipitation hardening has the potential to be a major strengthening mechanism in heat treatable SVDC Mg alloys; however, SVDC Mg alloys have not yet been the subject of extensive studies. Gradients in alloy microsegregation and eutectic phase transformation that will be exhibited during SVDC will likely have a key influence on the development of new alloy systems. In addition, quantitative characterization of precipitation microstructure under different heat-treatment conditions is crucial to optimize the effects of precipitation strengthening and building physics-based strengthening models.

Objectives

The primary objective of this project is to conduct a systematic, quantitative study of phase transformation kinetics and microsegregation in HPDC Mg alloys in both as-cast and heat-treated conditions. These results will be used to develop and validate physics-based phase transformation kinetics micro-models that quantitatively capture microstructural evolution and microsegregation during HPDC and heat-treatment of Mg alloys. Finally, this knowledge will be transferred to industry and the wider research community through these micro-models and the experimental data that will be stored in the National Institute of Standards and Technology (NIST)-DOE Energy Efficiency and Renewable Energy Advanced Automotive Cast Mg Alloys Repository, as well as a new repository, the University of Michigan Department of Energy Predictive Integrated Structural Materials Science (UM-DOE-PRISMS) Materials Commons. To accomplish these goals, a systematic and comprehensive experimental study is being combined with computational modeling and simulation.

Approach

The target alloy compositions used in this study are shown in Table II.1.C.1. The alloy matrix was selected to include a wide range of compositions that will provide for optimization of current commercial alloys AM50/AM60 and AZ91. The Ford Research and Innovation Center at Mag-Tec Corporation provided the castings. These castings were processed using SVDC casting procedures.

Die-casting process controls linked with precision MAGMASOFT® HPDC simulation were used to provide an estimate of the cooling rate as a function of location in casting and casting geometry. The simulations used a fine finite difference mesh (i.e., at least 5 to 10 elements through the cross-section; however, some have been completed with 30 to 45 elements) and high-fidelity HPDC interfacial heat transfer coefficients for HPDC developed by Zhi-peng et al. and Li et al. [17–18] to estimate cooling rate as a function of location.

Table II.1.C.1. Target Alloy Compositions in Weight Percentages Used in This Study.

Alloy	Mg	Al	Zn	Mn
Mg-Al Binaries	balance	3, 4, 5, 9, 11		
AM Series	balance	5, 6, 7		0.5
AZ Series	balance	9	0.5, 1, 2	

Both solidification and solution treatment phase transformation kinetics were quantified using comprehensive microstructural characterization, including optical metallography and SEM coupled with advanced image analysis. The primary characteristics that were quantified are eutectic volume fraction and grain size as a function of alloy, location, sample thickness, and process condition. Microsegregation profiles of alloying elements (i.e., Al, Mn, Zn) versus solidification fraction were quantitatively characterized using the electron probe microanalysis (EPMA) scan method [5–7]. These microsegregation results were compared with Calphad-based Scheil solidification estimates of alloy partitioning.

The quantitative and systematic results described above were used to develop state-of-the-art phase transformation kinetics micro-models for HPDC alloys. A comprehensive solidification kinetics micro-model was developed that considers solute trapping, dendrite arm coarsening, and dendrite tip undercooling. It also couples these calculations directly with multicomponent phase diagram computations. Given solidification conditions and alloy compositions, this micro-model was capable of predicting SDAS, types, and fractions of various non-equilibrium phases, liquid concentrations, and solute concentration profiles in the primary Mg phase under the extreme high heat extraction conditions that exist in HPDC and SVDC. A dissolution kinetics micro-model was developed to account for eutectic phase dissolution and compositional homogenization.

The information produced in this study will be uploaded to the NIST-DOE-EERE Advanced Automotive Cast Mg Alloys Repository, as well as a new repository, the UM-DOE-PRISMS Materials Commons, a knowledge

repository that is under development within the UM-DOE-PRISMS Center within six months of the completion of the project.

Results

The local grain size in the HPDC Mg alloys can be predicted from MAGMASOFT® solidification modeling by a power law relationship in the form of Equation (1):

$$d_{\text{grain}} = \alpha R^{-\beta} \quad (1)$$

where α and β are fitting constants and R represents the local cooling rate. The R is calculated as the derivative of the cooling curve just below the liquidus temperature. For a Mg-7Al alloy, a liquidus temperature of $\sim 613^\circ\text{C}$ was calculated using Thermo-Calc. The resolution of the MAGMASOFT® simulations was not sufficient to capture the gradient near the surface of the plates, and therefore an exponential fit was used to extrapolate the cooling rate in the regions of interest.

Data from several pieces of literature [9, 11, 19–21], along with data from the HPDC Mg-Al alloys, were used to relate the cooling rate to SDAS/grain radius using Equation (1). The relationship between data in the literature and results obtained during the current effort are shown in Figure II.1.C.1. The best fit parameters were found to be 46 for α and 0.32 for β .

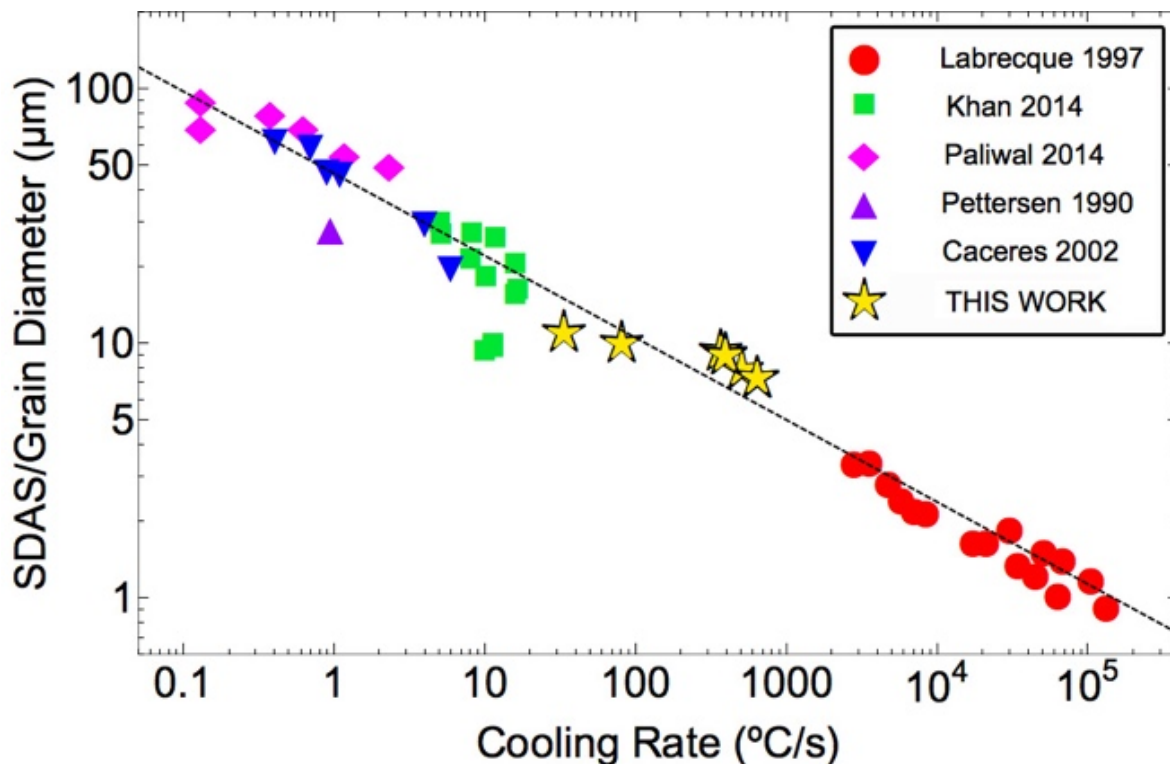


Figure II.1.C.1. SDAS/grain size as a function of cooling rate in AZ and AM series alloys with the empirical fit.

The microstructure and microsegregation have been completely characterized in the HPDC AM series and Mg-Al binaries plates. The composition measurements were conducted using EPMA and the results were filtered and assigned to a fraction solid using the Weighted Interval Rank and Sort method [5]. It has been found that for all the alloys studied so far, microsegregation does not depend on casting thickness. All alloys show macrosegregation that results in an Al-rich skin on the casting surface.

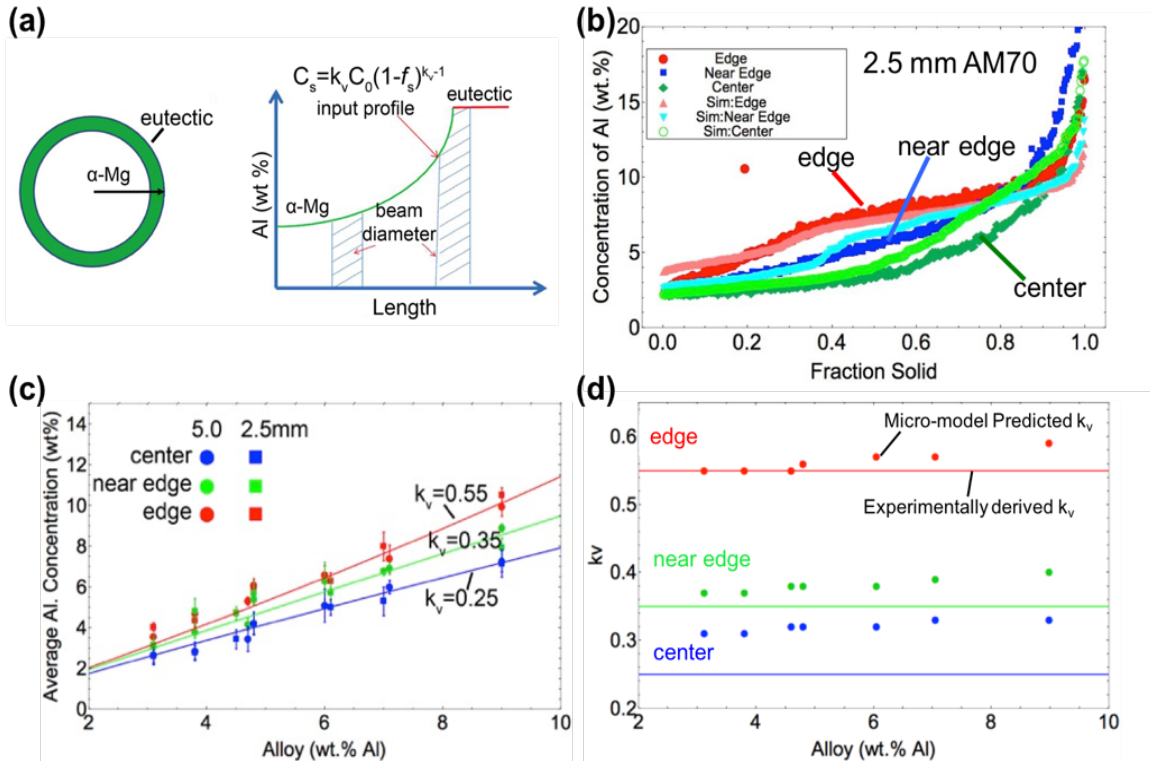


Figure II.1.C.2.(a) Illustration of the setups and assumptions used in the Forward Model simulation; (b) Comparison between using Forward Model simulation and EPMA measurements of Al concentration in as-cast AM70 alloys as a function of fraction at different locations; (c) the velocity-dependent partition coefficient, k_v , is inferred based on the average Al concentration equation and EMPA macro-segregation results. These values are in good agreement with the Forward Model prediction; (d) Comparison between k_v value using the two different methods; data points represent micro-model calculations and lines represent the experimental measurements.

A “Forward Model” has been developed to quantitatively evaluate the effect of microstructure parameters and experimental conditions on the measured microsegregation behavior. Figure II.1.C.2.(a) provides a schematic representation to illustrate the Forward Model. The microsegregation profile can be modeled by an input function (shown as modified-Scheil equation in Equation (2)) from the center to the edge of the grain until it reaches a constant value at the eutectic. The variables of the model are the assumed solidification profile, the grain size distribution, the fraction of eutectic, and the average solute content. The electron interaction volume is $4.5 \mu\text{m}$ in diameter, which is used to represent the integration length. Notice that the average grain diameter in the HPDC plates is approximately two times the interaction volume, indicating the EPMA microsegregation profiles are distorted. This Forward Model simulation is an important tool to aid interpretation of the EPMA results. Furthermore, this Forward Model simulation is used to determine the velocity-dependent partition coefficients (k_v) assuming the concentration of Al (C) as a function of fraction solid (f_s) follows a modified-Scheil model:

$$C = k_v C_0 (1 - f_s)^{(k_v - 1)} \quad (2)$$

Values for k_v were obtained for all HPDC alloys by using a least-squares difference approach to compare the Forward Model simulation results for a selected partition coefficient to the experimental EPMA profiles. Figure II.1.C.2.(b) shows the example Forward Model simulation results against the EPMA microsegregation profiles from the 2.5 mm thick AM70 sample.

Manipulation of the Scheil equation provides an understanding of how solute trapping impacts macro-segregation and the fraction of eutectic phases. The average Al concentration as a function of the alloy composition, C_0 , can be estimated by fixing k_v and calculating the following:

$$C_{ave} = \int_0^a C_0 k_v (1 - x)^{(k_v - 1)} dx + \int_a^1 33.3 dx \quad (3)$$

where x is the fraction solid and a is the fraction solid at which the eutectic begins to form. The composition at which the eutectic precipitates is approximated at 13 wt.%, the maximum solubility of Al in Mg at the eutectic temperature. The second expression in the equation represents the total amount of Al in the β -phase, which has a composition of approximately 33 wt.% Al. The partition coefficients that lead to the best agreement with the measured average Al concentration in solution treated samples are $k_v=0.25$ (center), 0.35 (near edge), and 0.55 (edge), as shown in Figure II.1.C.2.(c). These location-dependent partition coefficients are in good agreement with those determined by comparing the as-cast microsegregation profiles with the Forward Model simulation results.

The other primary objective is to develop a physics-based microsegregation micro-model. This micro-model is based on the work of Kraft, Rettenmayr, and Exner [22]. This numerical model allows for determination of non-equilibrium phase diagrams for high-cooling rates where the composition at the solid/liquid interface becomes a function of the solidification front velocity, v . The numerical model developed by Kraft builds upon modeling by Carrard et al. and Aziz and Kaplan [23–24]. The results are shown in Figure II.1.C.2.(d). The points at different alloy compositions are the value of k_v calculated using the micro-model. The lines represent the experimentally derived k_v , as determined in Figure II.1.C.2.(c). The micro-model is able to capture the trends of k_v at edge and near edge location; however, the experimental values is much lower than predicted at center of the plate. This can be attributed to the existence of large externally solidified crystals (ESCs) in the center. From the microscopic observation, the ESCs segregate to the center of the plates during solidification. Since they solidify in the shot sleeve at higher temperatures, the ESCs have a low solute concentration. The micro-model does not consider the effect of ESCs on the partition coefficients. As a result, the k_v values derived from the experimental measurements are lower than the micro-model prediction. Improvements to the model can be made by measuring the volume fraction and partition coefficient of ESCs incorporating these results into the micro-model to give a more accurate prediction.

In Mg-Al binaries, $Mg_{17}Al_{12}$ (β phase) exists as microstructural inhomogeneity and affects the Al content in the matrix for solid-solution strengthening during aging. The dissolution model is used to characterize the volume fraction of the β phase after different solution treatments. Experimental results from SEM imaging characterization are compared with the simulation results from DICTRA software. This investigation will help understand the dissolution kinetics and improving commercial software setup to optimize solution treatment conditions.

SEM microstructure characterization was conducted to determine the volume fraction of β phase in Mg-5Al, Mg-9Al, and Mg-11Al binaries. All these samples were heat-treated at 380°C, 400°C and 420°C for 2 min, 5 min, 10 min, 30 min, 1 hour, and 2 hours. The amount of β phase was measured from edge, near edge, and center of samples. The volume fraction of β phase was calculated from the SEM images by using the MATrix LABoratory (MATLAB)-based image processing algorithm. The commercial DICTRA software was applied to simulate the volume fraction evolution at different conditions. A schematic representation of the model setup for the simulation is shown in Figure II.1.C.3.(a). The β phase is located at the center of the cell model and surrounded by the α -Mg matrix/secondary Mg phase. The volume fraction of β phase is calculated based on the spherical model assumption, which provides Equation (4):

$$\frac{R_{\beta}^3}{R_{tot}^3} = \frac{V_{\beta}}{V_{tot}} = V_{\beta}^f \quad (4)$$

where R_β and R_{tot} are the initial radius of β phase and the radius of the grain, respectively; V_β and V_{tot} are the volume of the β phase and grain, respectively; and V_β^f is the volume fraction of the β phase. R_β can be determined by the initial volume fraction of β phase from the as-cast sample. An example simulation result and experimental measurements are shown in Figure II.1.C.3.(b). They are both from Mg-11Al sample after solution treatment at 420°C. The simulation results match well with the experimental measurements as time evolves. The initial volume fraction of the β phase calculated from DICTRA using fast cooling condition is consistent with the SEM measurements. Simulations of the evolution of the volume fraction as a function of time closely follows the experimental results. The simulation was shown to be appropriate for all three temperatures and alloys studied. When comparing among different temperatures and alloys, it has been found that a higher initial volume fraction will increase dissolution time needed; while a higher solution treatment temperature can decrease solution treatment time. The duration needed for complete dissolution can also be quantitatively calculated. These results demonstrate that the sphere-shaped model setup can be used to successfully model the initial microstructure produced during rapid cooling and the diffusion process. The newest version of kinetic database of Mg alloys now has the capability to accurately capture the β phase dissolution rate in the α -Mg matrix. This setup is feasible in predicting the dissolution kinetics in Mg alloys and DICTRA is a promising software to optimize the solution treatment procedure.

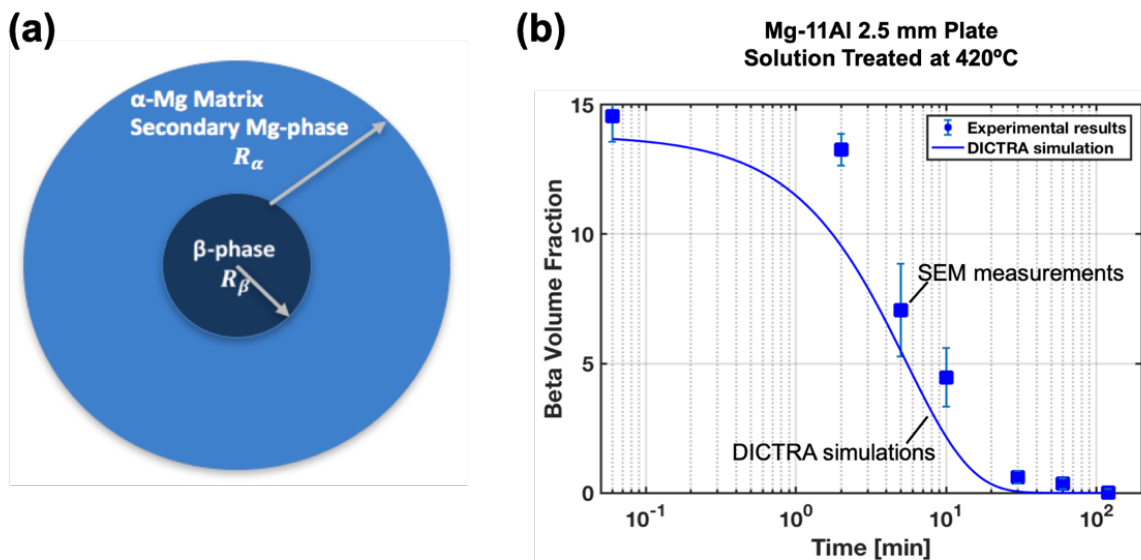


Figure II.1.C.3.(a) β phase dissolution model [UM]; and (b) The comparisons between SEM measurements and the DICTRA simulation of β phase volume fraction of Mg-11Al 2.5 mm plate at various time at 420°C.

Conclusions

Microsegregation and phase transformation kinetics in both as-cast and solution treated HPDC plates have been systematically studied. Experimental measurements and physics-based micro-models successfully characterized the microstructural and microsegregation behavior. The grain size analysis provided a quantitative guideline for predicting the grain size for a given cooling rate in the HPDC regime. Experimental solute microsegregation behavior was used to calculate the local velocity-dependent partition coefficients, which were used to calibrate a physics-based solidification model. The model results give a better quantitative understanding of how solidification velocity is related to the microsegregation in HPDC samples. The experimental data reveal that solution treatment temperature and duration strongly affect the dissolution of secondary phase process. The DICTRA simulation shows the capability of predicting the dissolution kinetics. These improved models can be combined to provide a better understanding of microsegregation and phase transformation kinetics and will allow for optimization of casting, solution treatment, and aging processes in super vacuum HPDC Mg alloys.

Key Publications

1. Allison, J., 2013, “Phase Transformation Kinetics and Alloy Microsegregation in High-Pressure Die-Cast Mg Alloys,” *Program Kick-Off Meeting*, November 8, 2013, Washington, D.C., USA.
2. Berman, T. D., and J. Allison, 2015, “Phase Transformation Kinetics and Alloy Microsegregation in High-Pressure Die-Cast Mg Alloys,” *USCAR Materials Tech Team*, February 11, 2015.
3. Allison, J., 2015, “Phase Transformation Kinetics and Alloy Microsegregation in High-Pressure Die-Cast Mg Alloys,” *Annual Performance Review Meeting*, April 10, 2015, Washington, D.C., USA.
4. Berman, T. D., M. Li, and J. Allison, 2017, “Microsegregation in High-Pressure Die-Cast Mg Alloys,” invited keynote presentation at *2017 TMS Annual Meeting & Exhibition*, February 28, 2017, San Diego, CA, USA.
5. Berman, T. D., M. Li, and J. Allison, 2017, “Microsegregation in high-pressure die-cast Mg alloys,” *Magnesium Technology 2017*, Part of The Minerals, Metals & Materials Series. Springer, pp. 73–78. https://link.springer.com/chapter/10.1007/978-3-319-52392-7_13.
6. Deda, E., T. D. Berman, and J. Allison, 2017, “The influence of Al content and thickness on the microstructure and tensile properties in high-pressure die-cast Mg alloys,” *Metall. Mater. Trans. A*, Vol. 48, No. 4, DOI: 10.1007/s11661-017-3958-4.
7. Berman, T. D., Z. Yao, M. Li, and J. Allison, “Measuring and modeling microsegregation in fine-grained Mg-Al alloys produced by SVDC,” (in preparation).
8. Yao, Z, T. D. Berman, and J. Allison, “Phase transformation kinetics during solution treatment of HPDC Mg-Al alloys,” (in preparation).

References

1. Slade, S., 2010, “Mg: Bridging diverse metal markets,” *Magnesium Technology 2010*, Wiley-TMS, pp. 91–95.
2. Gjestland, H., and H. Westengen, 2007, “Advancements in HPDC of Mg,” *Adv. Eng. Mater.*, Vol. 9, pp. 769–776. doi:10.1002/adem.200700168. doi:10.1002/adem.200700168.
3. Kim, J. S., M. Isac, and R. I. L. Guthrie, 2004, “Metal-mold heat transfer and solidification of Mg alloys in belt casting processes.” *Magnesium Technology 2004*, pp. 247–255.
4. Porter, D. A., K. E. Easterling, and M. Y. Sherif, 2014, *Phase Transformations in Metals and Alloys*, Third Edition, CRC Press, 138. doi:10.1146/annurev.ms.03.080173.001551.
5. Mirković, D., and R. Schmid-Fetzer, 2009, “Directional solidification of Mg-Al alloys and microsegregation study of Mg alloys AZ31 and AM50: Part I. Methodology,” *Metall. Mater. Trans. A*, Vol. 40A, pp. 958–973. doi:10.1007/s11661-009-9787-3.
6. Terbush, J. R., N. D. Saddock, J. W. Jones, and T. M. Pollock, 2010, “Partitioning of solute to the primary α -Mg phase in creep-resistant Mg-Al-Ca-based cast alloys,” *Metall. Mater. Trans. A*, Vol. 41, pp. 2435–2442. doi:10.1007/s11661-010-0271-x.
7. Zheng, X., A. A. Luo, C. Zhang, J. I. E. Dong, and R. A. Waldo, 2012, “Directional solidification and microsegregation in a Mg-Al-Ca alloy,” *Metall. Mater. Trans. A*, Vol. 43A, pp. 3239–3248. doi:10.1007/s11661-012-1159-8.
8. Zhang, C., D. Ma, K. Wu, H. Cao, G. Cao, and S. Kou, 2007, “Microstructure and microsegregation in directionally solidified Mg-4Al alloy,” *Intermetallics*, Vol. 15, pp. 1395–1400. doi:10.1016/j.intermet.2007.01.009.
9. Paliwal, M., D. H. Kang, E. Essadiqi, and I. H. Jung, 2014, “The evolution of as-cast microstructure of ternary Mg-Al-Zn alloys: An experimental and modeling study,” *Metall. Mater. Trans. A Phys. Metall. Mater. Sci.*, Vol. 45, No. 8, pp. 3596–3608. doi:10.1007/s11661-014-2288-z.

10. Liu, S., G. Yang, and W. Jie, 2014, "Microstructure, microsegregation, and mechanical properties of directional solidified Mg-3.0Nd-1.5Gd alloy," *Acta Metall. Sin. English Lett.*, Vol. 27, No. 6, pp. 1134–1143. doi:10.1007/s40195-014-0151-2.
11. Khan, I., A. O. Mostafa, M. Aljarrah, E. Essadiqi, and M. Medraj, 2014, "Influence of cooling rate on microsegregation behavior of Mg alloys," *J. Mater.*, Vol. 2014, Article ID 657647, 18 pages. <http://dx.doi.org/10.1155/2014/657647>.
12. Sadayappan, K., W. Kasprzak, Z. Brown, L. Quimet, and A. A. Luo, 2009, "Characterization of Mg automotive components produced by SVDC process," *Mater. Sci. Forum*, Vol. 618–619, pp. 381–386. doi:10.4028/www.scientific.net/MSF.618-619.381.
13. Luo, A. A., A. K. Sachdev, and B. R. Powell, 2010, "Advanced casting technologies for lightweight automotive applications," *China Foundry*, Vol. 7, No. 4, pp. 463–469.
14. Li, M., R. Zhang, and J. Allison, 2010, "Modeling casting and heat-treatment effects on microstructure in SVDC AZ91 Mg-alloy," *Magnesium Technology 2010*, Wiley-TMS, pp. 623–627.
15. Miao, J., M. Li, and J. E. Allison, 2012, "Microstructure evolution during heat-treatment in a SVDC AZ91 alloy," in *Mg2012: 9th International Conference on Magnesium Alloys and Their Applications*, 493–498.
16. Wang, J., et al., 2010, "A microstructural evolution model for Mg17Al12 precipitates in AZ91," *Magnesium Technology 2010*, Wiley-TMS, pp. 163–170.
17. Zhi-peng, G., X. Shou-mei, L. Bai-cheng, M. Li, and J. Allison, 2008, "Determination of the heat transfer coefficient at metal-die interface of HPDC process of AM50 alloy," *Int. J. Heat Mass Transf.*, Vol. 51, pp. 6032–6038.
18. Li, S., S. Xiong, B. Liu, M. Li, and J. E. Allison, 2010, "Numerical simulation of flow-induced air entrapment defects in the HPDC process." *Magnesium Technology 2010*, Wiley-TMS, pp. 613–616.
19. Labrecque, C., R. Angers, R. Tremblay, and D. Dubé, 1997, "Inverted disk centrifugal atomization of AZ91 Mg-alloy," *Can. Metall. Q.*, Vol. 36, pp. 169–175.
20. Pettersen, K., O. Lohne, and N. Ryum, 1990, "Dendritic solidification of Mg-alloy AZ91," *Metall. Trans. A*, Vol. 21, pp. 221–230.
21. Càceres, C. H., C. J. Davidson, J. R. Griffiths, and C. L. Newton, 2002, "Effects of solidification rate and aging on the microstructure and mechanical properties of AZ91 alloy," *Mater. Sci. Eng. A*, Vol. 325, pp. 344–355.
22. Kraft, T., M. Rettenmayr, and H. E. Exner, 1996, "An extended numerical procedure for predicting microstructure and microsegregation of multicomponent alloys," *Model. Simul. Mater. Sci. Eng.*, Vol. 4, No. 2, pp. 161–177. doi:10.1088/0965-0393/4/2/004.
23. Carrard, M., M. Gremaud, M. Zimmermann, and W. Kurz, 1992, "About the banded structure in rapidly solidified dendritic and eutectic alloys," *Acta Metall. Mater.*, Vol. 40, No. 5, pp. 983–996. doi:10.1016/0956-7151(92)90076-Q.
24. Aziz, M. J., and T. Kaplan. 1988. "Continuous Growth Model for Interface Motion During Alloy Solidification." *Acta Metall. Mater.*, Vol. 36, No. 8, pp. 2335–2247. doi:10.1016/0001-6160(88)90333-1.

Acknowledgements

The authors want to acknowledge Mei Li and co-workers from Ford Motor Company for providing the castings and solidification simulations as well as for their suggestions during this project.

II.1.D Low-Cost Mg Sheet Component Development and Demonstration Project (Fiat Chrysler Automobile, U.S., LLC)

Randy Gerken, Principal Investigator

Fiat Chrysler Automobile, U.S., LLC
800 Chrysler Drive, CIMS: 485-00-15
Auburn Hills, MI 48326
E-mail: randy.gerken@fcagroup.com

Sarah Kleinbaum, DOE Technology Manager

U.S. Department of Energy
E-mail: sarah.kleinbaum@ee.doe.gov

Start Date: October 1, 2016	End Date: March 31, 2020	
Project Funding (FY18): \$3,196,433	DOE share: \$2,081,496	Non-DOE share: \$1,114,937

Project Introduction

The value of the Low-Cost Magnesium Sheet (LCMS) Project to original equipment manufacturers lies in the potential availability of a lower cost, more formable Mg sheet alloy, and reduced cost of using a Mg sheet in automotive applications due to: (a) improved formability at reduced temperatures; and (b) improved corrosion protection and reduced coating costs as a result of improved forming lubricant and coating technologies.

Objectives

The objective of this project is to research, develop, and demonstrate at least one large, challenging Mg sheet component on a model year 2013 (MY13) or newer vehicle at a manufacturing cost of less than \$2.50 per pound of weight saved.

Approach

The U.S. Automotive Materials Partnership, LLC (USAMP), has employed a technical approach that integrates experimental, computational, and data tools that can accelerate the development and deployment cycle of low-cost Mg sheets. To accomplish the project objective, USAMP proposed to research, develop, test, and evaluate at least one Mg-alloy and commensurate processing suitable for rolling automotive appearance grade sheet, and forming inner and outer door panels based on the 2013 Ford Fusion (see Figure II.1.D.1) to validate the results.

The 42-month LCMS Project consists of the following major activities conducted over seven technical tasks: (1) technical cost guidance to identify key cost drivers associated with current Mg component production; (2) material characterization and modeling studies; (3) rolling trials on ingots; (4) pretreatment, coating application, and lubrication studies; (5) forming studies; (6) scaling to warm-forming of large components; and (7) joining studies. Public data and code developed as part of the project will be curated and hosted in the DataHUB repository developed and maintained by the LightMat Consortium.

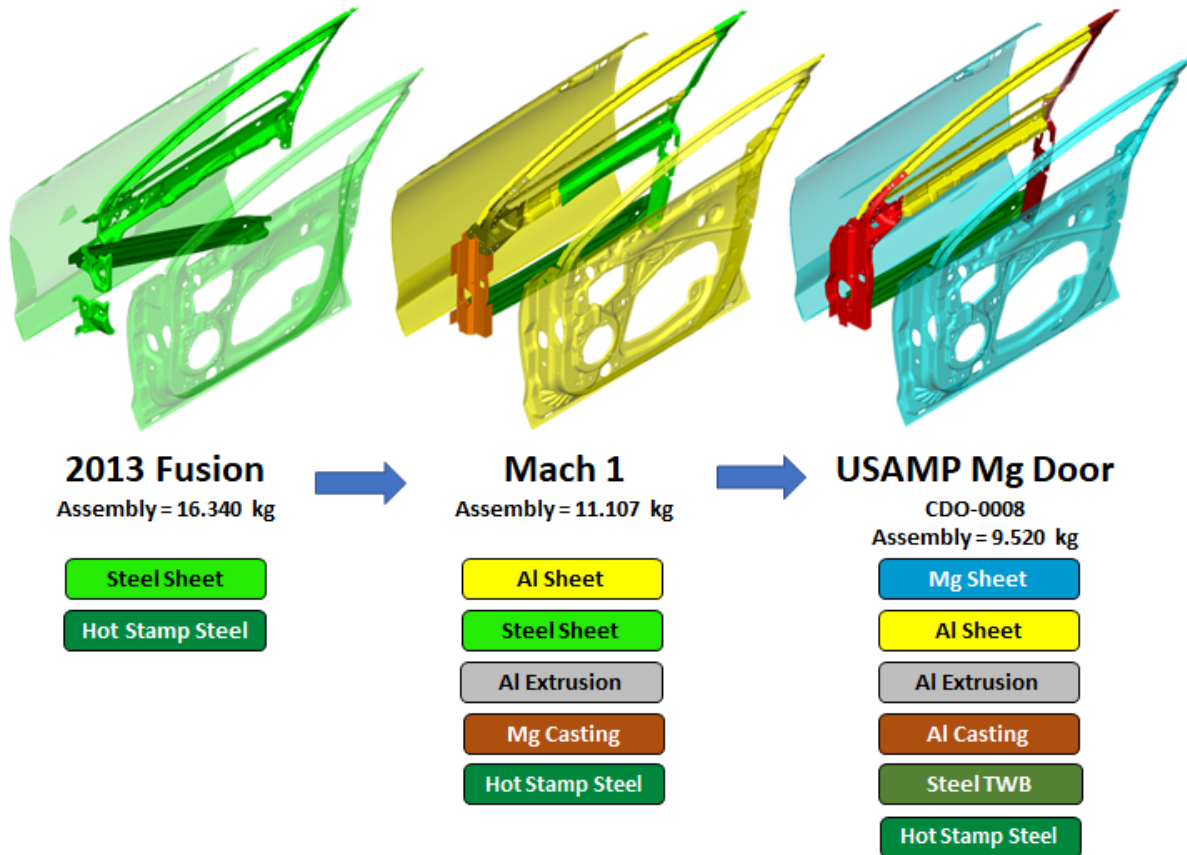


Figure II.1.D.1. Illustration of the 2013 Ford Fusion door showing the progression from baseline steel to Multi-Material Lightweight Vehicle Al to Al-intensive door with Mg inner and outer panels selected for demonstration in warm-forming. Source: Ford Motor Company.

The project encompasses two aspects as part of a comprehensive research approach to achieving the objective:

1. In the first aspect, the practical understanding of Mg alloys will be expanded with the intent of developing new alloys optimized for complex automotive manufacturing systems.
2. The second aspect focuses on improvement of processes, pretreatments, and coatings to enable greater use of using existing Mg-alloy sheet. Due to this dual path approach, many of the tasks and subtasks in this project will occur concurrently over three budget periods (BP) and throughout the duration of the program.

The LCMS Project participants are listed below:

Sub-awardees: Applied Engineering & Technology (AET) Integration, Inc.; Fuchs Lubricants Co.(Fuchs); Henkel Corporation; PPG) Industries, Inc.; Quaker Chemical Corporation; Vehma International of America, Inc.; Xtalic Corporation; The Ohio State University (OSU); University of Florida (UF); University of Illinois at Urbana-Champaign (UIUC); University of Michigan (UM); and University of Pennsylvania (UP).

Vendors: Bucciero & Associates, LLC; Camanoe Associates; M-Tech International, LLC; (POSCO); and the Korea Mg Industry.

DOE National Labs: PNNL; and ORNL.

The project is divided into 11 milestones to be achieved over the three BPs. Table II.1.D.1 lists the percentage completion status of each milestone (at the end of FY 2018).

Table II.1.D.1. Status of Project Tasks and Milestones at the End of FY 2018.

BP	Milestone Number	Milestone Type	Task	Description	Status
1	1	Go/No-Go	Task 0: Project Management/Contracting	100% of POs issued to subs.	Complete
	2	Technical	Task 1: Technical Cost Guidance	Baseline cost model for Mg sheet complete.	Complete
	3	Technical	Task 2: Alloy and Sheet Processing Development	New Mg-alloy sheet composition(s) identified.	Complete
2	4	Technical	Task 2: Alloy and Sheet Processing Development	Constitutive model for textured Mg-alloy completed and ideal texture suggested.	35%
	5	Technical	Task 2: Alloy and Sheet Processing Development	Forming analysis completed on medium sheet.	20%
	6	Technical	Task 3: Sheet Coatings and Lubricant Evaluation and Development	Forming lubricant composition identified.	60%
	7	Go/No-Go	Task 5: Mg-alloy Sheet Production	Manufacture and deliver experimental medium-width sheets.	20%
3	8	Technical	Task 3: Sheet Coatings and Lubricant Evaluation and Development	Evaluation of corrosion protection coating completed.	35%
	9	Technical	Task 5: Mg-alloy Sheet Production	Delivery of wide sheet.	0%
	10	Technical	Task 6: Mg-alloy Large Body Component Production	Mg-alloy panels formed to specifications.	10%
	11	Technical	Task 7: Component(s) Demonstration	Final delivery and performance evaluation completed.	5%

Note: There is no milestone associated with Task 4.

Results

USAMP has achieved all three BP1 Milestones on schedule as described below. Research progress is summarized under each task area and by subrecipient's contributions towards the milestones. Only those tasks that were pursued by the subrecipients in FY 2018 are reported herein, hence task numbers may not flow in sequence. References listed are specific to each subrecipient's task report and, for simplicity, have been included within the same section wherein they were cited.

Task 1: Technical Cost Guidance

Achieved Milestone 2: Baseline Cost Model for Mg Sheet Complete. The USAMP Task 1 team worked with vendor Camanoe Associates to complete a baseline cost model for Mg sheet application for demonstration component and identified cost drivers relative to benchmark steel door.

The objective for Subtask 1.1 is to provide a summary of existing cost drivers of current Mg sheet and automotive component production and assembly. The approach was to use information developed in a

previous DOE-USAMP AMD 603, “Mg Front-End Research and Development” project, from 2010 as the starting point (where Camanoe conducted the analyses). This was combined with publicly available literature, and preliminary cost modeling analyses performed for the LCMS Project. The approach for the other tasks is to use process-based cost modeling to quantify costs of parts production, coating, and assembly of the Mg and Steel doors.

Camanoe Associates has calculated the cost of a benchmark steel door to use as a comparison with the Mg door design. A process chart for low-volume production of the steel door baseline was developed by the USAMP original equipment manufacturer team to guide Camanoe’s analysis for establishing the baseline cost model. It will be adapted for the envisioned stamping process for Mg door inners towards the end of the project when alloy materials, coatings, and stamping processes are established and validated. Findings from this task indicate that the lightweighting cost is highly sensitive to the price of the Mg sheet. Camanoe concluded the \$2.50/lb-saved target can be achieved for the door inner below the Mg sheet price of \$7.50/kg.

Task 2: Alloy and Sheet Processing Development

Achieved Milestone 3: New Mg-Alloy Sheet Compositions Identified. The Task 2 team achieved Milestone #3 by specifying three experimental Mg alloys after engaging the university researcher team and vendor. In early 2018, USAMP sourced Experimental Alloy 1 ingots for detailed characterization, computational modeling, and sheet formability trials. Due to Alloy 1 not meeting key formability criteria, as discussed in detail below, USAMP sourced a second Experimental Alloy 2 material (ingots and sample sheets) that was delivered in the final quarter of FY 2018. The university research team is evaluating the formability of this alloy, and a decision will be made whether to proceed with sourcing intermediate width sheets for further testing and formability trials.

Under the USAMP’s ICME thrust, university researchers are applying analytical methods to help predict and validate improved alloy chemistry(ies) and thermomechanical processing to achieve the following outcomes:

- Establish a constitutive model for textured Mg-alloy and recommend ideal texture.
- Conduct sheet rolling and forming experiments on Alloy 2, establish material cards needed to perform computer-aided engineering (CAE), and thereby demonstrate improved formability with reduced rolling and forming temperatures.
- Characterize mechanical properties sufficiently to perform CAE and identify formability/processing window for components incorporating Mg sheet materials.

Progress summaries for these research efforts during the reporting period follow below.

Subtask 2.1 – 2.2: Alloy Design, Experimental Validation, and Alloy Evaluation – OSU

1. **Task Objectives and Approach:** OSU will design, develop, and validate computational models for Mg sheet alloys. This will include thermodynamic, kinetic, DFT, and continuum models. Forming limits will be established. OSU will further optimize ZE20, and additional alloying elements will be introduced based on atomic scale simulations. They will prepare, as needed, exploratory alloy compositions and carry out casting and characterization studies.

2. Progress and Accomplishments:

1. Thermodynamic Study

1.1 EFP Alloy

The optimization of concentration of solutes Zn and Ca into Mg-2.0Al-(0.6-1.4)Zn-(0.1-1)Ca-0.3Mn alloy has been carried out using Thermo-Calc software with TCMG4 database. The iso-concentration projection of solutes in Mg matrix at 430°C is shown in Figure II.1.D.2.(a)-(d). It shows: (1) the addition of Zn has very little influence on the solutes Al, Ca, and Mn, but significantly increases solute Zn; (2) the addition of Ca decreases solute Al and increases solutes Ca and Mn, but has very little influence on solute Zn; (3) the 0.8wt% addition of Ca is suggested if solute Al > 1wt%; and (4) the 1wt% of Zn is suggested by considering casting issue, if Zn > 1wt%. Thus, the optimized concentration is Mg-2.0Al-1.0Zn-0.8Ca-0.3Mn, which is close to the measured composition for EFP: Mg-1.7Al-0.9Zn-0.7Ca-0.3-Mn.

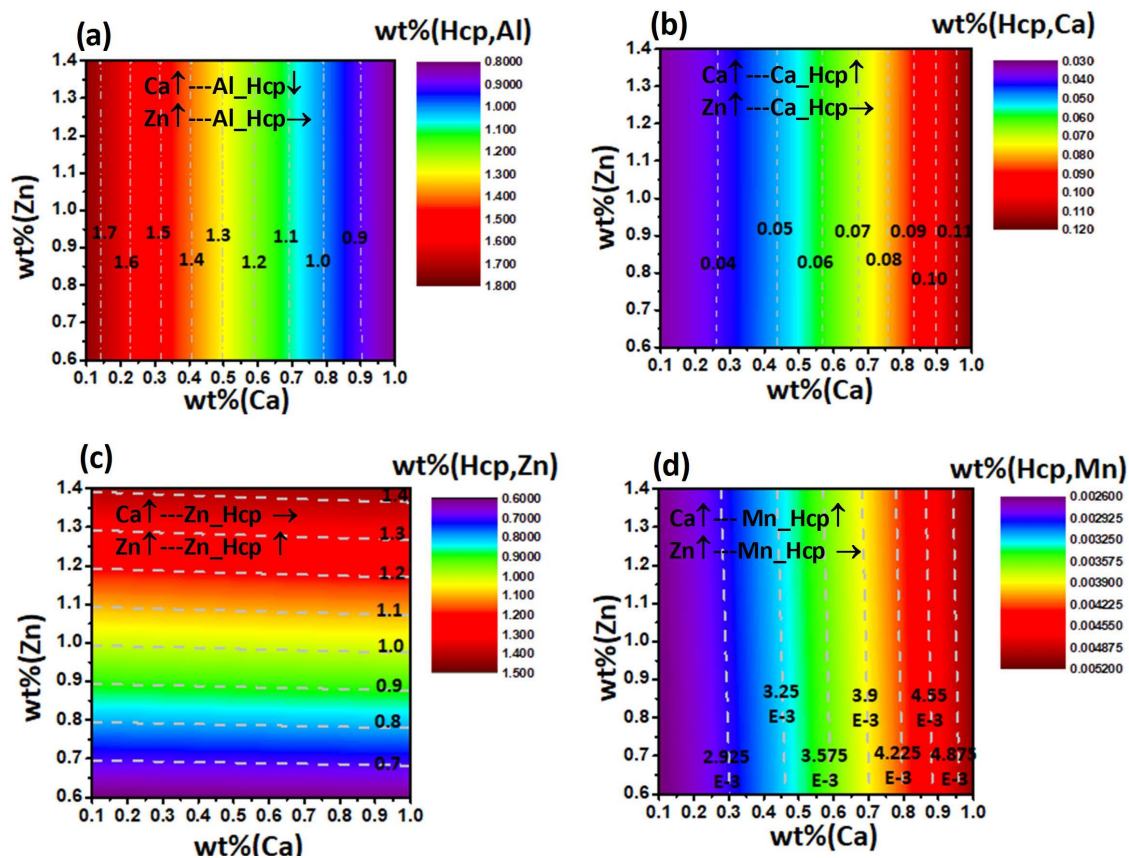
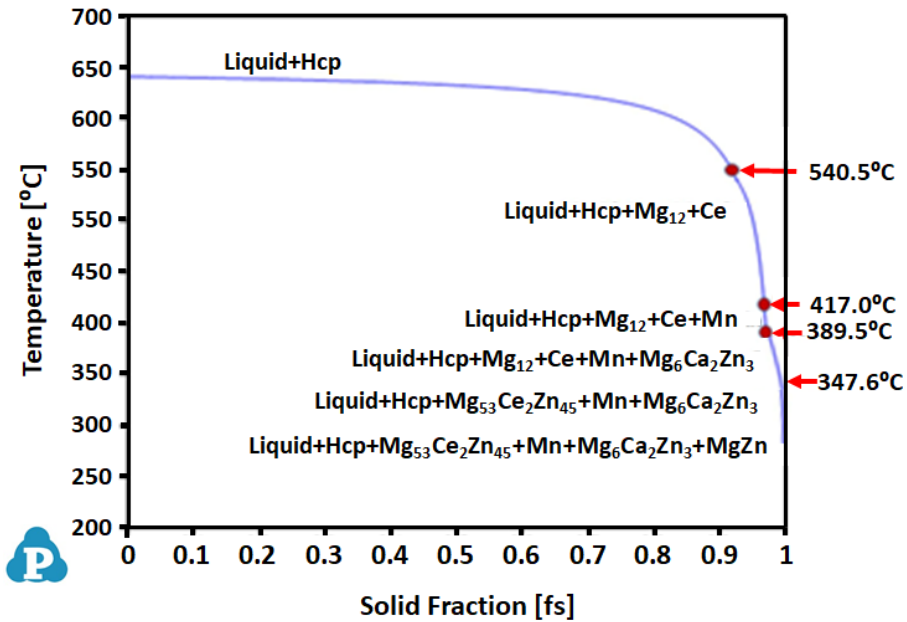


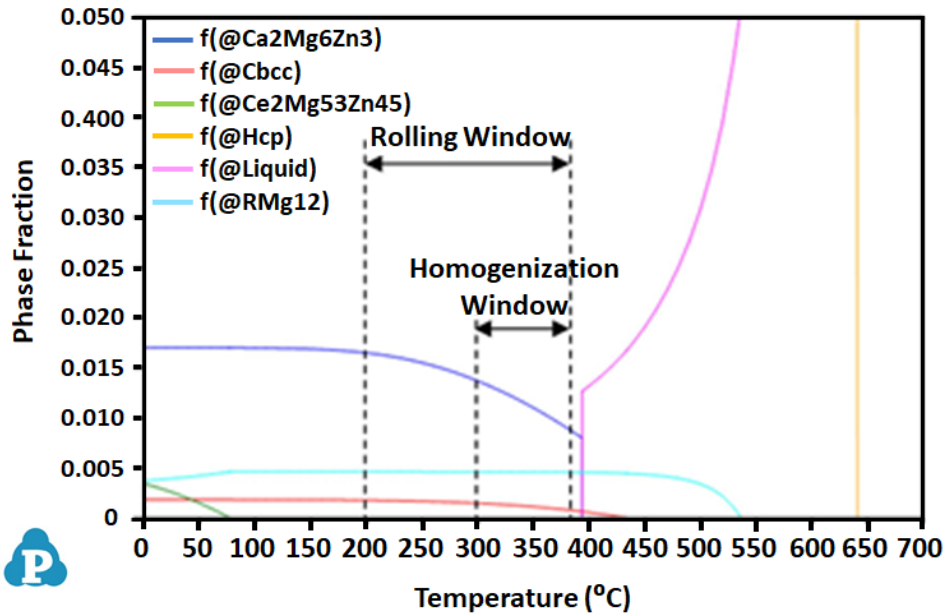
Figure II.1.D.2. Iso-concentration projection of solutes (a) Al, (b) Ca, (c) Zn, and (d) Mn in a Mg matrix at 430°C.
Source: OSU.

1.2 Experimental Alloy 2 (2Zn-0.5Ca-0.4Mn-0.2Ce, wt%)

Ca addition can be used to modify the texture and contribute to solid-solution strengthening. Thus, Ca is added to ZE20 to improve strength and ductility. After optimization, 0.5wt% of Ca is added to ZE20 as a new proposed USAMP Experimental Alloy 2 (Mg-2Zn-0.5Ca-0.4Mn-0.2Ce, wt%). The Scheil model solidification path in Figure II.1.D.3.(a) and phase equilibrium diagram in Figure II.1.D.3.(b) have been calculated by using Pandat software with PanMg database. Figure II.1.D.3.(a) shows that several phases formed during solidification ($Mg_{12}Ce$, Mn, $Mg_6Ca_2Zn_3$, $Mg_{53}Zn_{45}Ce_2$ and MgZn), while Figure II.1.D.3.(b) shows the thermal window for homogenization, rolling, annealing heat-treatments.



(a)



(b)

Figure II.1.D.3.(a) Scheil calculation and (b) equilibrium calculation of Alloy 2 using Pandat software. Source: OSU.

2. Kinetic Study

Homogenization of Alloy 2 has been carried out by using DICTRA with single-phase model shown in Figure II.1.D.4.(a). Two homogenization profiles at 350°C and 375°C are shown in Figure II.1.D.4.(b). The homogenization results in Figure II.1.D.4.(c)-(f) show that higher temperature improves the homogenization of solutes.

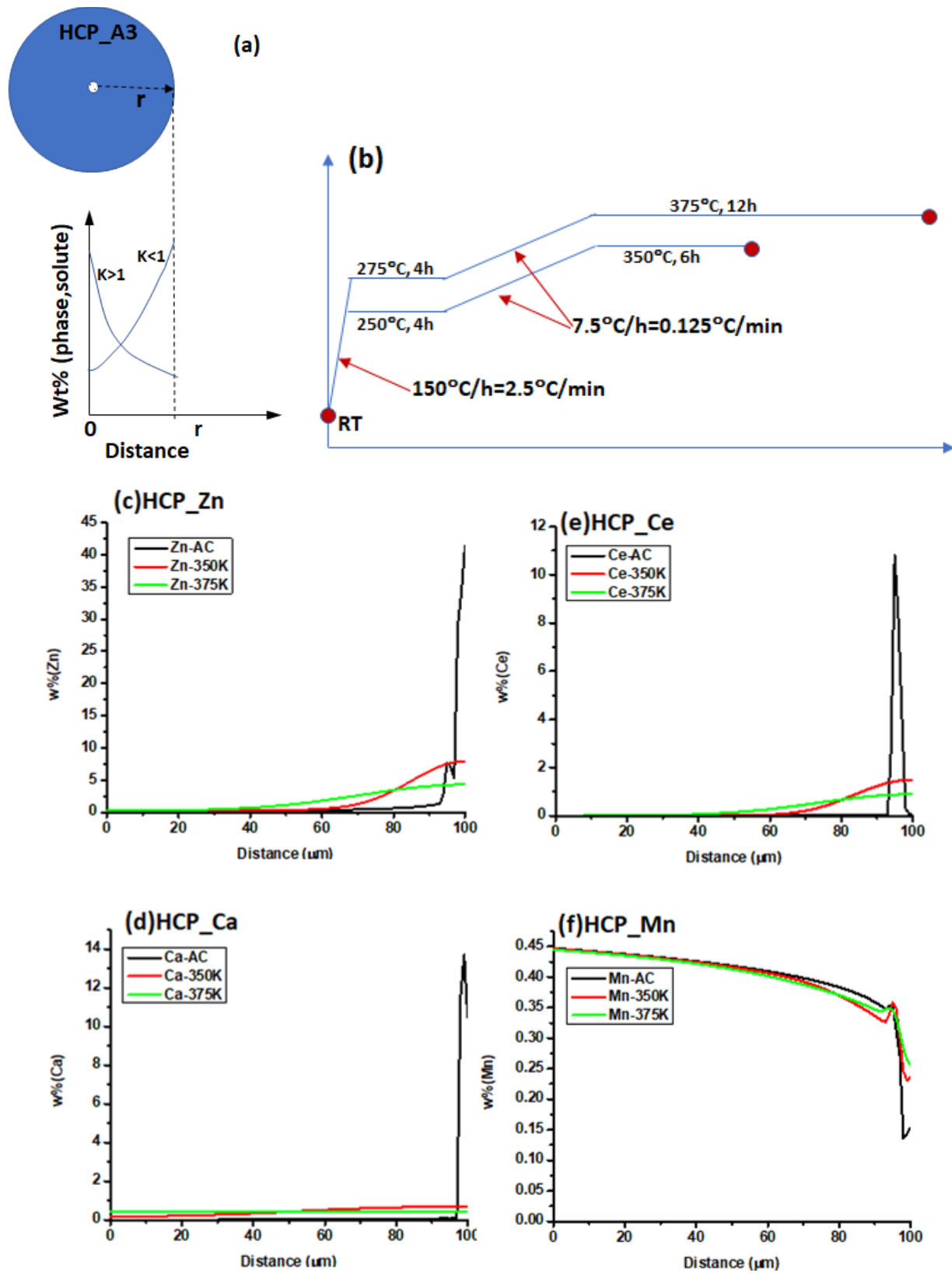


Figure II.1.D.4. (a) Single-phase homogenization model; (b) homogenization profile; and solute distribution of (c) Zn; (d) Ca; (e) Ce; and (f) Mn in Alloy 2. Source: OSU.

3. Microstructure evolution of Alloy 2

Based on Figure II.1.D.3.(b), 350°C (H350) and 375°C (H375) were selected as the homogenized temperatures which are both below the solidus line. The as-cast microstructures of H350 at 6-hour and H375 at 12-hour show that many coarse second phases inside the grains and along the grain boundaries formed during solidification, as shown in Figure II.1.D.5.(a)-(c). Following homogenization treatment, the coarse second phases become dissolved and refined precipitates are formed near grain boundaries. Large amounts of $Mg_6Zn_3Ca_2$ and $Mg_{12}Ce$ phases are still stable up to the solidus points. In order to improve the solubilization and homogenization, a new homogenized profile needs to be proposed. Figure II.1.D.5.(d)-(f) show microstructure evolution during rolling and annealing treatment at 350°C: Figure II.1.D.5.(d) shows both deformed and dynamic recrystallized regions; and Figure II.1.D.5.(e) and (f) show the complete formation of the static recrystallized grain at 10 min and further growth of the static recrystallized grain at 1hr. Figure II.1.D.5.(g) shows the evolution of grain size was significantly refined after rolling.

4. Microstructure evolution of Alloy 2

The lab-scale study of Alloy 2 will continue and will focus on the following activities:

- Optimizing heat-treatment conditions for RT mechanical property and formability of Alloy 2.
- Studying the influence of heat-treatments (e.g., homogenization, pre-heat temperature before each rolling pass, annealing temperature) on microstructure evolution: texture, recrystallization, grain growth of Alloy 2.

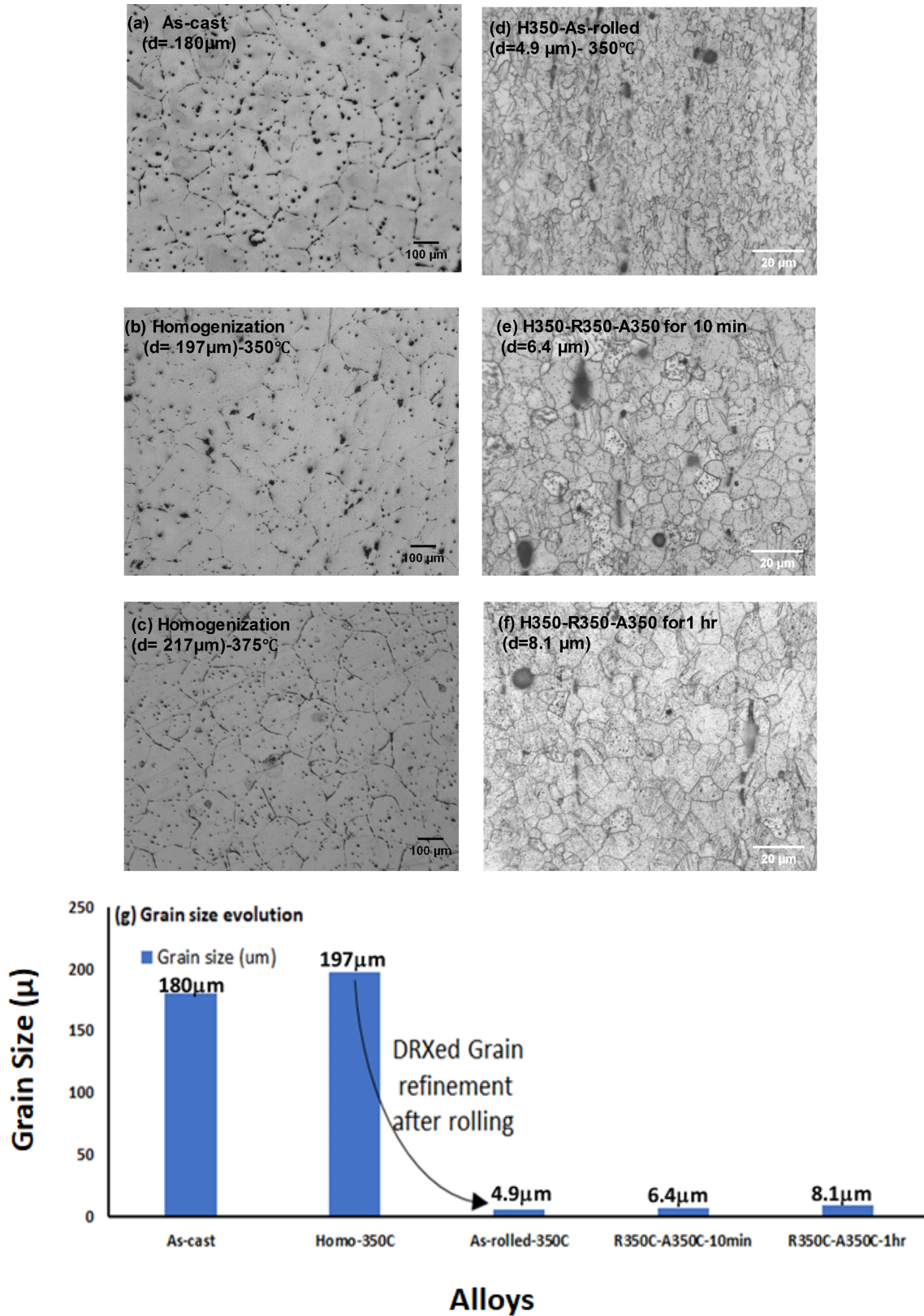


Figure II.1.D.5. Microstructures of Alloy 2 under (a) as-cast; (b) homogenized at 350°C (H350); (c) homogenized at 375°C (H375C); (d) as-rolled at 350°C (H350); (e) H350-R350-A350 for ten minutes; (f) H350-R350-A350 for 1 hr; and (g) grain size evolution. Source: OSU.

Subtask 2.3: Mg Thermodynamic and Kinetic Alloy Database – UF

- 1. Task Objectives and Approach:** UF will focus on the generation of missing data on binary alloys that is not already available in databases and the integration of binary and ternary interaction parameters in Mg and relevant phases. Any defined higher order interactions, for example, a four-component alloy, will also be performed.
- 2. Progress and Accomplishments:**

Experimental Alloy 1:

USAMP Experimental Alloy 1 (Mg–3Al–1Sn–0.3Zn–0.40Mn wt. %) was designed in FY 2018 based on the AT31 (Al-Tin) composition. This alloy was homogenized at 420°C for 14 hrs and preliminary microstructure characterization was performed. SEM revealed the presence of a uniform distribution of Al-Mn-based intermetallic particles in an Mg matrix in both the as-cast and homogenized alloy. The presence of this second phase was consistent with computational thermodynamics predictions. However, Alloy 1 also showed a strong basal texture (per tests performed by the UM). Consequently, it was decided to not study this composition any further. Instead, a simpler alloy chemistry with fewer elements has been identified for further study—USAMP Experimental Alloy 3—allowing UF to systematically study the effect of those solute elements on Mg and also elucidate the interaction between the solute elements. UF will optimize the alloy chemistry by studying the effect of Zn and Ca on dynamic strain aging in Mg alloys.

Experimental Alloy 3:

A literature review on hot-rolled alloys was performed to shortlist the elements for USAMP Experimental Alloy 3. Ca was selected because it has an atomic size similar to that of RE elements, such as Ce and Nd. The addition of REs, such as Ce and Nd, have been shown to enhance formability via texture modification when rolling is performed at certain temperatures and strain rates [1]. These conditions can be identified by performing compression tests as a function of temperature and strain rate. The texture modification in Mg-RE alloys is attributed to dynamic strain aging, which is a diffusion-controlled process [2]. Thus, Ca has the potential to cause dynamic strain aging, and thereby, texture modification in Mg-Ca alloys. A ternary element, Zn, will be added subsequently to enhance strength. Literature review indicates that Mg-Ca-Zn (ZX-based) alloys have good formability and strength, but there is a lack of systematic understanding linking the composition to microstructure to properties. UF's proposed study to investigate the effects of Ca in solid-solution on dynamic strain aging in dilute Mg-Ca binary and Mg-Zn-Ca ternary alloy compositions will bridge that knowledge gap.

The alloy composition was selected based on the following criteria: (1) No second phase formation in binary and ternary alloys to ensure that both Ca and Zn will be present as solutes in the matrix; and (2) The maximum amount of Zn was capped because Zn lowers the melting point of the alloy.

Figure II.1.D.6.(a) shows the calculated maximum amount of Ca in solid-solution as a function of temperature in Mg-Ca binary. These calculations were performed in Thermo-Calc 2018b using database TCMG4. The two binary compositions to be studied are Mg-0.1 wt. % Ca and Mg-0.35 wt. % Ca. To study the ternary alloy compositions, 0.50 wt. % Zn will be added to Mg-0.1 wt. % Ca and Mg-0.35 wt. % Ca, as shown in Figure II.1.D.6.(b).

Preliminary experiments on the binary composition Mg-0.1wt. % Ca have been completed. Mg₂Ca particles, as shown in Figure II.1.D.7, were detected in the as-cast and homogenized samples (475°C/24 hrs) in the temperature and composition region where the binary phase diagram predicts a single-phase. Therefore, longer homogenization treatments were performed to investigate the effect of homogenization time on the Mg₂Ca stability. Microstructural characterization on the samples homogenized for longer times will be performed in FY 2019.

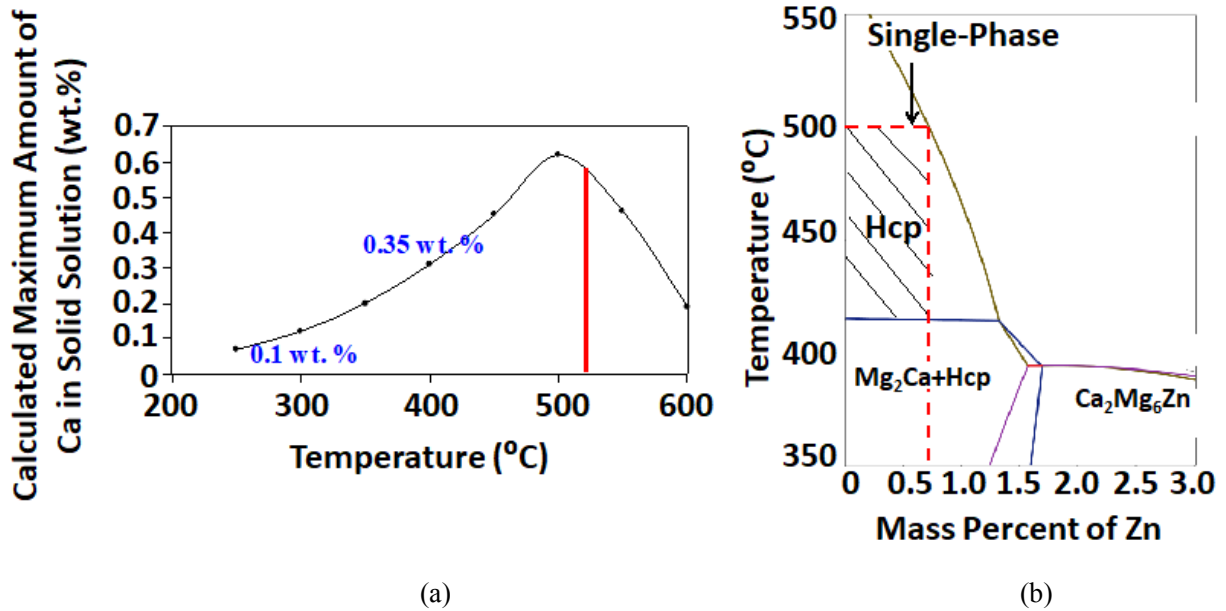


Figure II.1.D.6. (a) Maximum amount of Ca in solid-solution as a function of temperature in Mg and (b) the phase diagram of Mg-0.35 wt.% Ca as a function of Zn composition. Source: UF.

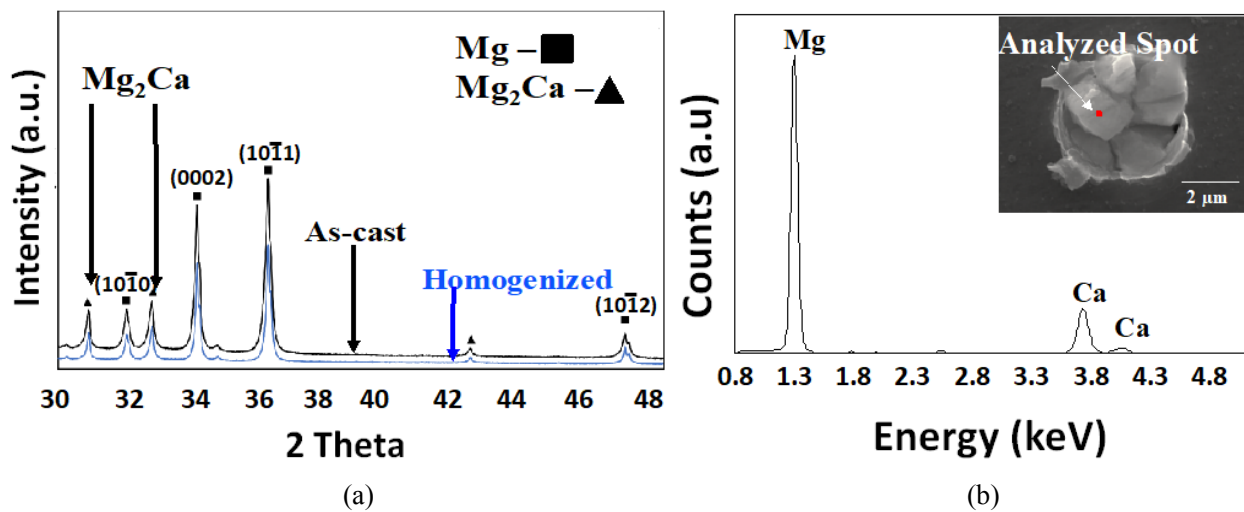


Figure II.1.D.7. (a) XRD pattern obtained from the as-cast and homogenized Mg-0.1 wt.% Ca alloy and (b) a spot EDS spectrum of a Mg_2Ca particle from the homogenized alloy with the inset showing the particle and location from which the spectrum was obtained. Source: UF.

Subtask 2.4: Compute the Energy Landscape for Solutes – UIUC

1. **Task Objective:** The UIUC will compute the energy landscape for solutes in $\langle c+a \rangle$ and twinning dislocations using DFT methods. This data will serve as the input for predictive models of critical resolved shear stress with chemistry, composition, temperature, and strain rate.

2. **ICME-Based Approach:** The low ductility of Mg alloys at RT is a direct consequence of the anisotropic response of the HCP crystal structure to loading, where the slip of basal dislocations occurs at a much lower critical stress compared to non-basal dislocations resulting in too few independent slip systems available for appreciable ductility. A promising approach for improving the ductility of Mg is adding solutes that interact with dislocations to potentially lower the difference in the stresses required to move basal and non-basal dislocations. The key inputs to solution strengthening models are [3–5]: (a) accurate dislocation core geometries for computing solute-dislocation interactions; (b) solute volumetric misfits, which determine the interaction strengths of solutes with the dislocation strain field; and (c) solute chemical misfits, which determine the interaction strengths of solutes with either stacking faults or twin boundaries.

3. **Progress and Accomplishments:** The UIUC has generated DFT data for input to solution strengthening models of the $\langle c + a \rangle$ edge and screw dislocations. The core structures of $\langle c + a \rangle$ edge and screw dislocations were optimized using DFT with lattice Green function-based flexible boundary conditions, which eliminates the need for dislocation multipole arrangements or fixed boundary conditions that can lead to errors in core structure geometries. The cores of both the edge and the screw dislocations dissociate into $1/2\langle c + a \rangle$ partial edge or partial screw dislocations separated by a pyramidal II stacking fault region. The UIUC also calculated chemical “misfits” for the pyramidal II stacking fault, as well as volumetric misfits of Al, Ca, Mn, Sn, and Zn solutes in Mg. Recent work on solution strengthening of $\langle c + a \rangle$ edge dislocations in Mg due to Y solutes has shown that Y causes large changes in the dislocation core geometry [3], and the local strain and slip distributions must account for these changes to produce accurate interaction energies. The UIUC have performed initial calculations for Al, Ca, Mn, Sn, and Zn solutes at sites in the partial core and stacking fault regions of the edge dislocation that show that Ca, Mn, and Zn also cause large changes in the core structure. Further calculations are in progress to determine the strain and slip energy contributions for Ca, Mn, and Zn at all sites in the edge and screw dislocation cores. This data will be input into solution strengthening models [3] to predict changes in yield stress as a function of solute concentration, temperature, and strain rate.

Data required to predict solution strengthening of $(10\bar{1}2)$ and $(10\bar{1}1)$ twinning dislocations in Mg was generated. A previous study on strengthening of $(10\bar{1}2)$ twinning dislocations due to Al and Zn solutes showed that the volumetric strain contributions to the solute-dislocation energies for Zn can be accurately determined by scaling directly computed Al interaction energies by the Zn volumetric misfit, and the chemical interaction can be computed from solute- $(10\bar{1}2)$ twin boundary interaction energies. They have obtained the $(10\bar{1}2)$ twinning dislocation geometry and the direct Al interactions from the authors of Ref. [4] and have scaled these energies by the volumetric misfits of Ca, Mn, Sn, and Zn. The interaction energies of Al, Ca, Mn, Sn, and Zn solutes with the $(10\bar{1}2)$ and $(10\bar{1}1)$ twin boundaries were computed, which determine the chemical interactions of these solutes with the $(10\bar{1}2)$ and $(10\bar{1}1)$ twinning dislocations. UIUC used this information to compute the solute-interaction energy landscapes for all the solutes in the $(10\bar{1}2)$ twinning dislocation geometry and have input this information into the solution strengthening model in Ref. [4]. Figure II.1.D.8 shows the changes in yield stress for basal and twinning dislocations due to Al, Ca, Mn, Sn, and Zn solutes, as well as the ratio of the total twinning yield stress to the total basal yield stress. Low solute concentrations are more effective at strengthening basal slip, whereas strengthening of the twinning dislocation dominates at higher concentrations.

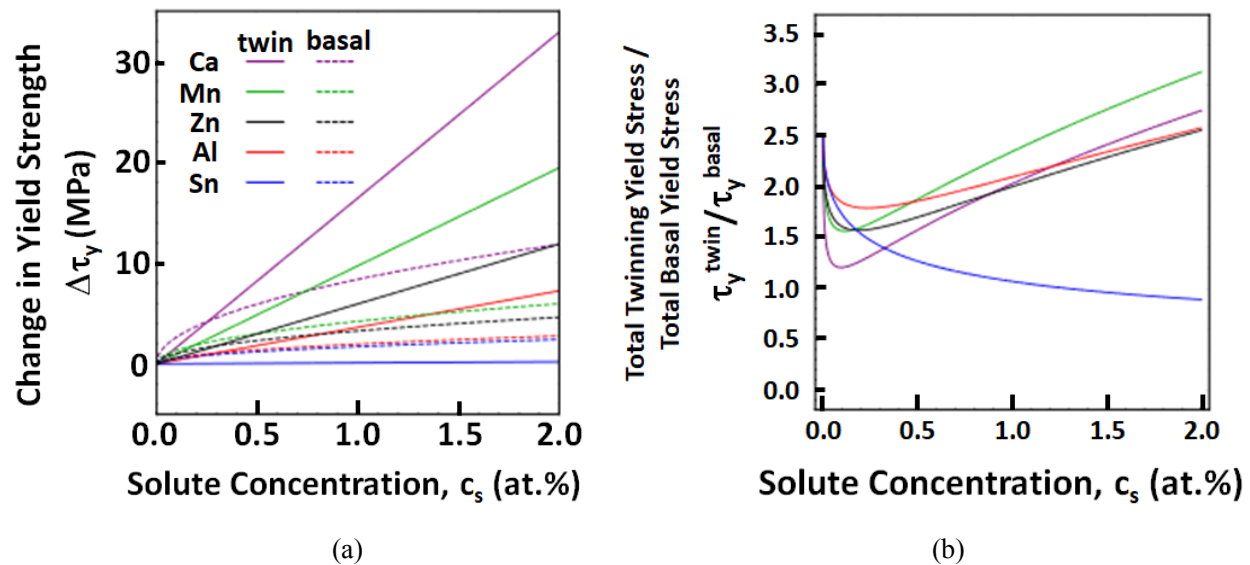


Figure II.1.D.8. Effect of solutes on the change in yield stress required to move basal [3] and $(10\bar{1}2)$ twinning dislocations at RT showing (a) the change in yield stress versus solute concentration for both deformation modes; and (b) the ratio of the total twinning yield stress to the total basal yield stress versus solute concentration. Source: University of Illinois.

Subtask 2.5: Dynamic Recrystallization, Texture, and Grain Growth — UM

Subtask 2.6: Precipitate Evolution and Alloy Development — UM

Subtask 2.7: Recrystallization Model Development — UM

- Task Objectives and Approach:** Characterize the dynamic recrystallization and texture development that occurs during sheet rolling and sheet forming operations, as well as any subsequent heat-treatment. Also characterize precipitation during the simulated paint-bake cycle of the automotive production process in Mg-alloy sheets chosen for the panel fabrication to take advantage of age-hardening for acceptable dent resistance properties in outer panels.

The UM work will calibrate and validate the PRISMS-CPFE code to include dynamic recrystallization and its effect on stress-strain response during rolling and forming, as well as subsequent heat-treatment of Mg-alloy. This code will be used in ICME infrastructures.

- Progress and Accomplishments:** Electron backscatter diffraction and Erichsen cupping tests were conducted for the purposes of benchmarking and for rapid assessment of sheet formability, as shown in Figure II.1.D.9.

It is well-known that a weak texture is a necessary, though not sufficient, requirement for formable Mg-alloy sheet. ZEK100 and EFP, the commercially available sheets, both exhibit a desirable texture. This “rare-earth-like” texture is characterized by a weak maximum texture intensity and a splitting of the basal poles along the transverse direction of the sheet. Correspondingly, both alloys demonstrate a similar maximum dome height, of approximately 6.5 mm, in RT Erichsen cupping tests. In contrast, Alloy 1 exhibited the undesirable strong basal texture commonly observed in conventional AZ31 sheets and also performed poorly in Erichsen cupping tests. The crystallographic texture of the Alloy 2 sheets provided by POSCO is very similar to that observed in the ZEK100 and EFP. All four sheets have a similar grain size of $\sim 10\ \mu\text{m}$ in diameter.

Deep draw tests were also conducted on ZEK100 (1.6 mm thick) and EFP (1.2 mm thick) sheets at 250°C and 100°C. EFP performed significantly better than ZEK100 at 250°C; the full draw (30 mm) was nearly achieved (see Figure II.1.D.10). However, at the lower temperature, both alloys achieved approximately the same draw before failure. The RT Erichsen cupping tests and crystallographic texture are comparable, this suggests a microstructural characteristic that is not fully captured by texture becomes important at temperatures above 100°C. Future work will include an assessment of the formability of the Alloy 2 sheets.

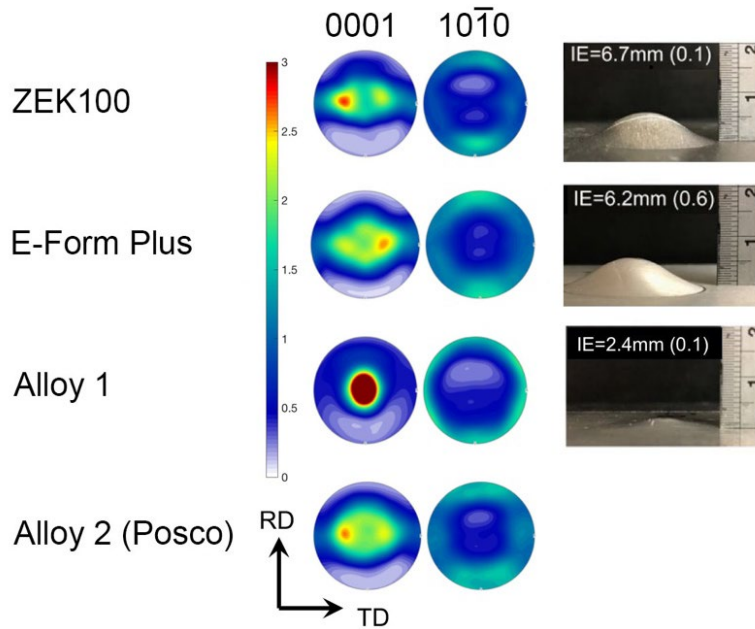


Figure II.1.D.9. Electron backscatter diffraction pole figures and RT Erichsen domes (where available) for the four Mg-alloy sheets (RD = radial direction; TD = transverse direction). Source: UM.

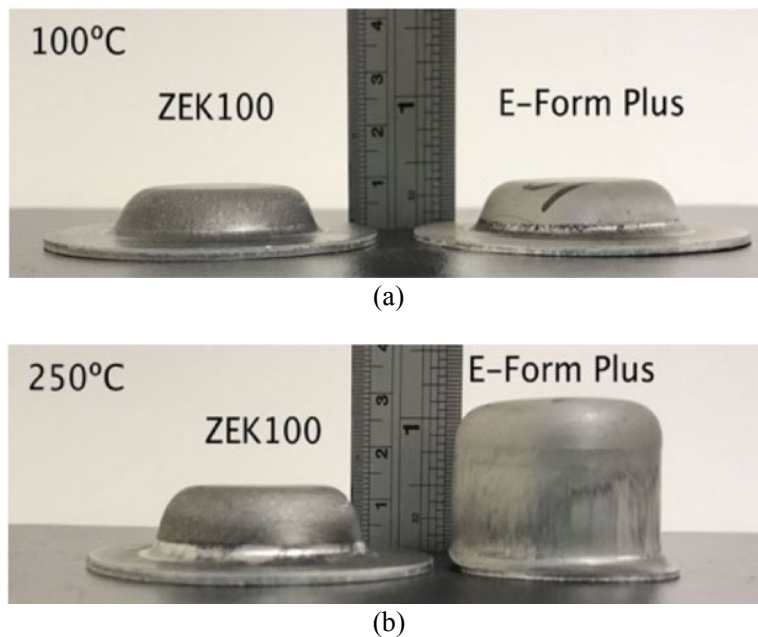


Figure II.1.D.10. Deep draw cups of ZEK100 and EFP performed at (a) 100°C and (b) 250°C. Source: UM.

Subtask 2.8: Develop Continuum-Level Constitutive Model for Textured Mg-Alloy Sheets and a Finite Element Material User-Subroutine – UP

1. **Task Objectives:** Develop a continuum-level constitutive model for textured Mg-alloy sheets undergoing plastic deformation by both slip and twinning mechanisms and a finite element material user-subroutine for implementation in the finite element program. The modeling methods will be with experimental studies.
2. **Progress and Accomplishments:** Primary features of the anisotropic elastic-plastic model account for a continuous evolution of (i) the anisotropy differential, (ii) material symmetry, and (iii) the strength differential. For non-uniform deformation, such as in forming a car door panel, those properties will vary continuously throughout a component. Previous studies have shown that anisotropy and microstructure evolution have a strong influence on micro- and macroscopic behaviors associated with forming limits.

Preliminary experiments carried out at PNNL on the ZEK100 sheet material provided data on the as-received anisotropy, as well as on hardening and R-value evolution in off-axis loading. The Bassani-Pan model [6] for calculating evolution of the material symmetry includes materials governed by yield criteria with tension/compression asymmetry. Studies are progressing to investigate the effects of anisotropy and strength differentials on shear localization via a bifurcation calculation that was previously employed in studies of other metals. Both effects can significantly affect the onset of strain localization, which is a characteristic of limits to formability.

Task 3: Sheet Coatings and Lubricant Evaluation and Development

Subtask 3.1: Sheet Lubricant Evaluation and Development – Fuchs

1. **Task Objectives:** This subtask is addressed by two suppliers, Fuchs and Quaker, each pursuing a different approach. It is concerned with developing effective, low-cost stamping lubricants, which are compatible with downstream body shop and paint shop processes. It comprises two key elements:
 - Develop a forming lubricant that can facilitate stamping of low-cost Mg sheet metal at up to 100°C.
 - Test same lubricant candidates, or, if necessary, design a separate lubricant that can facilitate forming of low-cost Mg at temperatures as high as 250°C without adverse effects to lubricity or residue.
2. **Technical Approach:** Fuchs utilized its previous experience in lubricant development work conducted for Mg, steel, and Al in warm and hot-forming processes. Through experiments, the Fuchs team determined appropriate tribology equipment, compared results to established benchmark lubricants, assessed results in ambient wet conditions, and assessed results in heated (dry film) condition to 100°C. The learnings were used to establish a theoretical formula strategy and were the starting point to produce newer experimental formulas based on basic product criteria (e.g., fluid stability, wetting characteristics, etc.). Candidate lubricants are to be tested under an established tribology regime to evaluate performance and modify where necessary to recommend the final forming lubricant(s).

3. Progress and Accomplishments:

3.1 Selected Forge Ease Al278 as an Initial Benchmark Lubricant – Based upon previous work in forming high-strength (AA 5xxx and AA 6xxx) Al, Fuchs R&D group had determined that Fuchs' Forge Ease Al278, a water-based emulsion with dispersed additives, was an appropriate benchmark (baseline) lubricant for work with soft metal with very low ductility.

3.2 Developed Two Initial Test Formulas for Use in LCMS Program – These are Renoform 10 ALWF and Renoform 25 ALWF. The formulary work for both products involved substantial screening of

additives, discussions with raw material suppliers, and testing to determine ingredient compatibility, solubility, and/or emulsifying characteristics. Formulas were reviewed for stability, safety, color, and odor. Fuchs' standard new product release quality control methods were followed.

3.3 Selected Anton Parr RheoCompass for Initial Testing – This instrument is capable of testing wet and dry applications, as shown in Figure II.1.D.11, and also capable of heating tools from ambient to 200°C. Fuchs reviewed several sets of tribology equipment for use in determining performance on low ductility soft metals in a stamping environment. The following pieces were tested using both new candidate lubricants on AA 6082. The following equipment was used: Strip Draw (SLT), Twist Compression (starvation testing), Falex Pin and V-Block, Cup Draw, and Anton Parr ReoCompass (tribometer). Ultimately, the tribometer was determined to provide best initial tribology results.

3.4 Performed Initial Testing on Al AA6082 – The Fuchs R&D group performed comparative testing on the Anton Parr RheoCompass to determine performance as samples of (initial) baseline ZEK100 Mg were not yet available from USAMP until late 2017, so testing was performed using available Al AA 6082, which is a warm-forming alloy. The lubricants were comparatively tested neat (undiluted) and diluted 4:1 (20%).

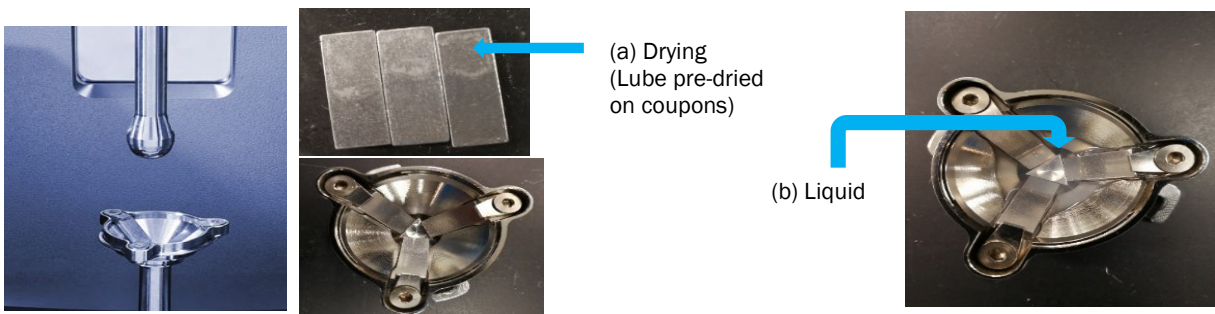


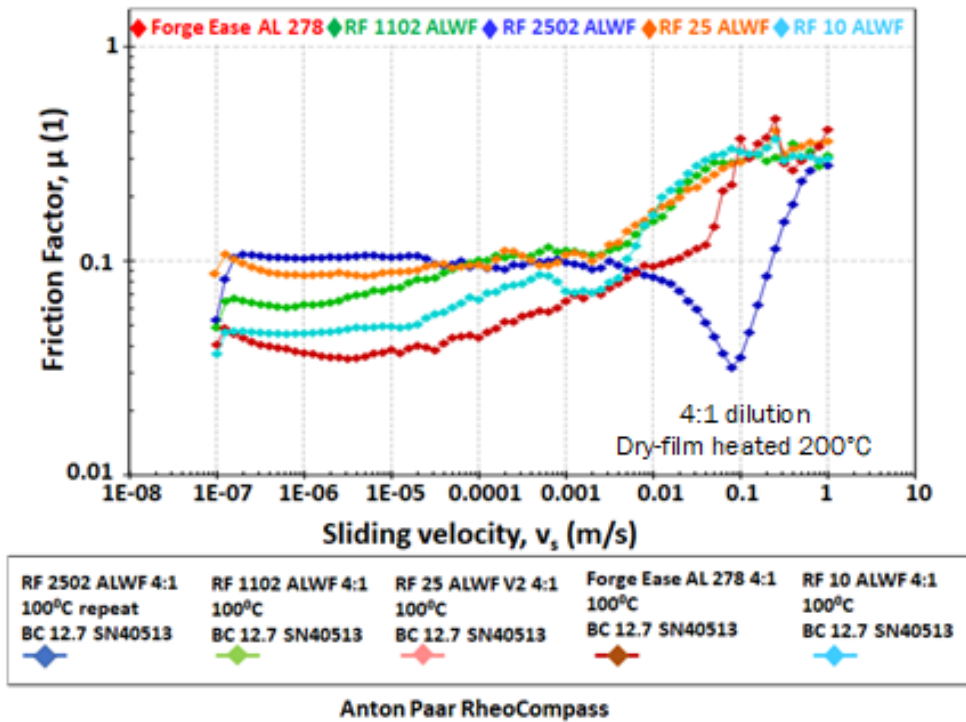
Figure II.1.D.11. The basic concepts of the Anton Parr Rheometer and the two test conditions: (a) dry and (b) wet.
Source: Fuchs.

Test results: Tribology testing indicates Coefficient of Friction rating as follows:

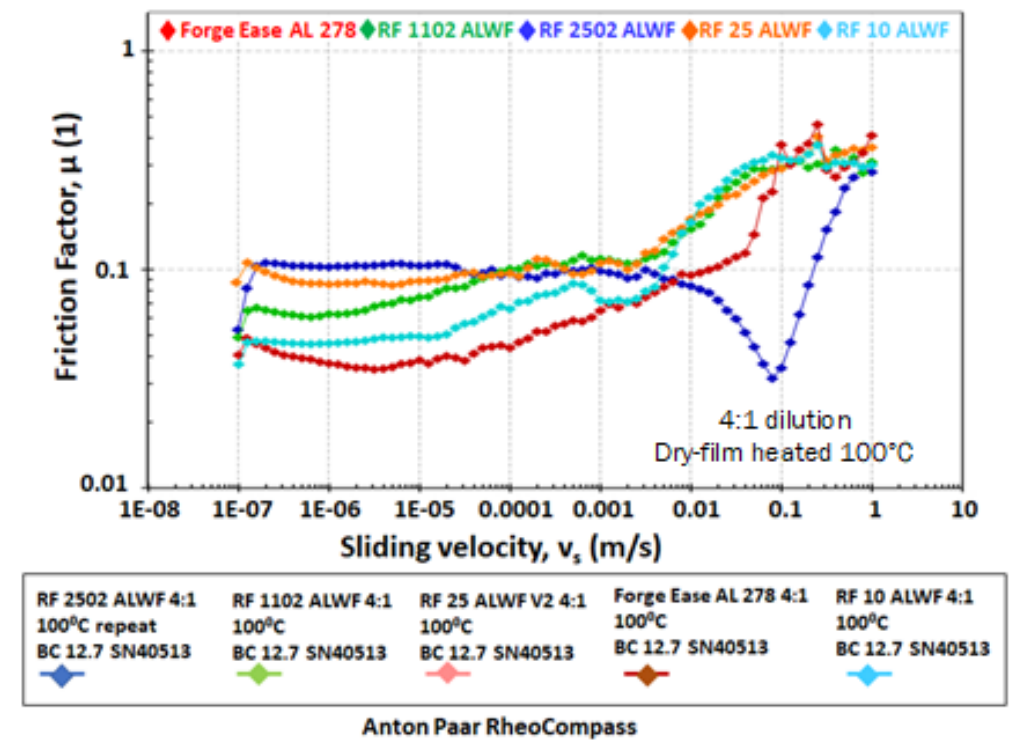
- When products were run neat and as a dry film heated to 200°C, lubricants performed in the following order best to worst: *Reniform 10 ALWF* > *Reniform 25 ALWF* > *Forge Ease AL278*.
- When products were run 4:1 as a dry film and heated to 200°C, products performed in the following order best to worst: *Reniform 10 ALWF* > *Forge Ease AL278* > *Reniform 25 ALWF*.
- When comparing the neat lubricant to 4:1 diluted lubricants in a dry condition and heated to 200°C, all three lubricants performed better diluted with water than run neat.
- When products were run neat, wet and at ambient temperature they performed in the following manner best to worst: *Reniform 10 ALWF* > *Reniform 25 ALWF* / *Forge Ease AL278*:
(Increased Coefficient of Friction for all lubricants compared to respective dry film runs).

During the latter part of FY 2018, USAMP also supplied cut samples of EFP Mg sheets, which were subjected to the same types and conditions of comparative tribology testing of Fuchs lubricants using the Anton Parr RheoCompass for ZEK100 and EFP. Based on the test results, Fuchs improved the formulas for candidate lubricants by eliminating BN as an ingredient, better wetting characteristics, and reduced carbonization at high temperatures. Resulting modified products were *Reniform 1102 ALWF* and *Reniform 2502 ALWF*.

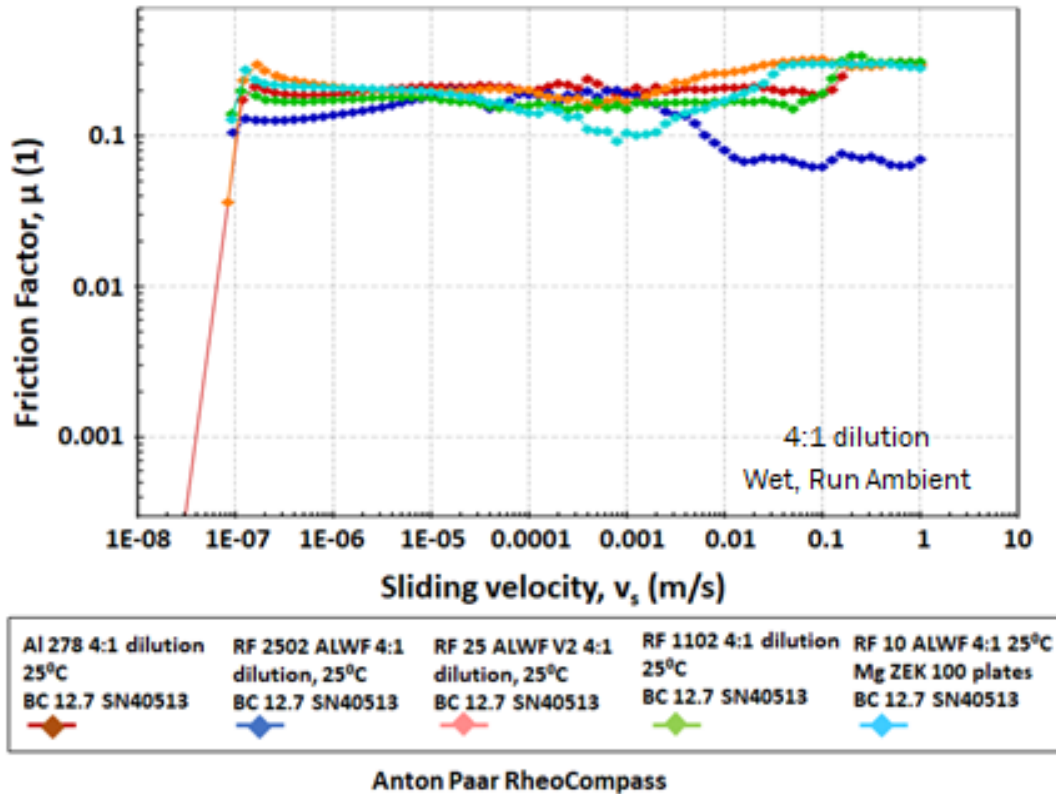
3.5 Performed Comparative Tribology Testing against Initial Candidates and Control Benchmark Using Modified Lubricants – Figure II.1.D.12 (a), (b), and (c) show the test conditions and results.



(a)



(b)



(c)

Figure II.1.D.12. Representative results of comparative testing of five candidate Fuchs lubricants at (a) 200 °C; (b) 100 °C; and (c) ambient temperature. Source: Fuchs.

3.6 Compared tool wear characteristics of each lubricant – It was determined that ZEK100 Mg and EFP performed very similar with the lubricant candidates. Based on coefficient of friction and tool wear studies, Renoform 2502 ALWF was found to be the best performing lubricant with the lowest plate wear on ZEK100.

3.7 Compared EFP with and without Henkel Pretreatment – Using three down-selected lubricant candidates, Fuchs compared and found similar tribology results, with or without pretreatment, as shown in Figure II.1.D.13.

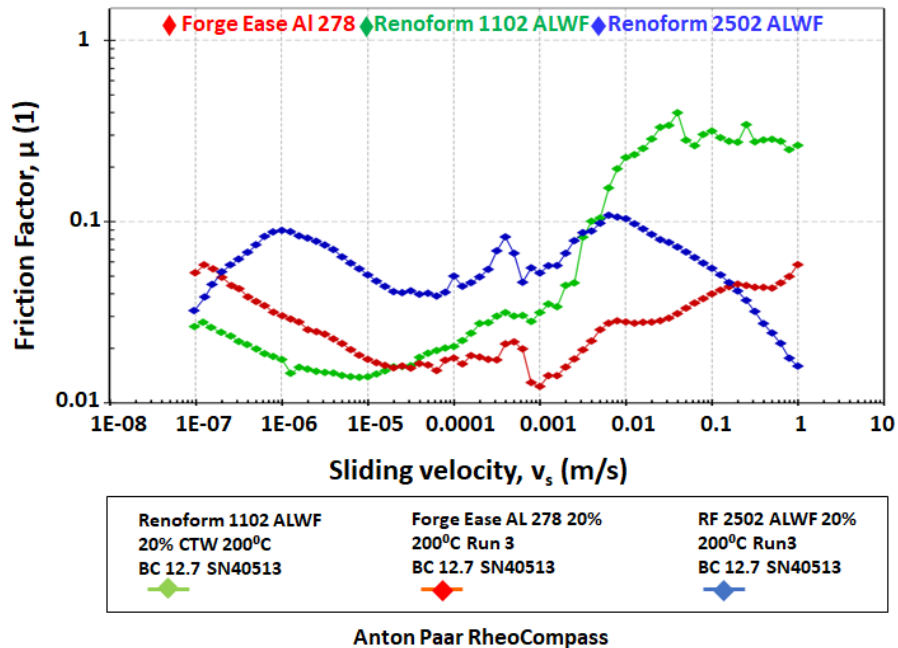


Figure II.1.D.13. Results of lubricant tests on EFP sheets are similar, without or with Henkel pretreatment.
Source: Fuchs.

- Summary of Results:** In summary, the Renoform 2502 ALWF appears to provide the lowest friction coefficient at temperatures of 200°C, 100°C, and ambient. It provides the most consistent results on the various alloys: ZEK100, EFP, and EFP with pretreatment. In the next phase, Fuchs will use a batch of EFP panels with and without Henkel pretreatment, and coat with Renoform 2502 ALWF, and submit them to PPG for cleanability studies and AET Integration for joinability studies.

Subtask 3.2: Sheet Lubricant Evaluation and Development – Quaker

Quaker pursued a similar work plan and technical objective in lubricant development as described in Task 3.1:

- Technical Approach:** The initial lubricant development focused on screening existing product formulae for performance under the intended conditions. Candidate formulae were selected from Quaker’s existing product portfolio based on historical commercial performance or known inherent properties. Candidate formulae were subjected to a series of tests designed to stress the lubricant in the anticipated conditions of the Mg warm-forming process. The testing conducted in Project Year 1 included lubricant thermal stability at 100°C and up to 315°C, metal reactivity of the selected formulae at 100°C, metal corrosion resistance performance in humid environments, lubrication performance at 100°C and up to 250°C, and removability/cleanability of the formulated lubricants. Lubricant evaluation was conducted on ZEK100 alloy, EFP alloy, and Henkel pretreated alloy.

Lubrication performance was evaluated by the Reciprocating Wear Test and Twist Compression Testing. Thermal stability testing was conducted to verify the stability of the selected lubricants at the planned process temperatures. Metal reactivity testing was conducted to evaluate each lubricants compatibility with the Mg-alloy and used as an indicator for subsequent corrosion resistance and removability performance. Metal corrosion resistance was conducted to evaluate a lubricant formula’s corrosion protection for the selected alloy. Cleanability testing was performed to evaluate each product formula’s removability after going through a simulated heating and stamping cycle. These tests were conducted to approximate conditions expected from a Mg warm-forming process and subsequent end-user needs.

At USAMP's request, the first material tested was ZEK100 alloy during Project Quarters 1-3 for lubricant evaluation. Next, EFP alloy was provided by USAMP and used for lubricant evaluation in Project Quarters 4-5 as this material was noted to be, ideally, closer to the final project Mg-alloy that will be developed and formed for demonstration parts during this project.

Progress and Accomplishments: Lubricant formulations were evaluated for thermal stability at 100°C and up to 315°C (changed to 250°C after Project Quarter 1). Most of the evaluated lubricants were not thermally stable at the high-end of the temperature range. The most thermally stable products were further evaluated for metal reactivity, cleanability, corrosion resistance, and lubrication of ZEK100 Mg-alloy sheet by Reciprocating Wear Test and Twist Compression Testing. Additional formula modifications were generated of the best performing lubricant on ZEK100 alloy under the conditions noted above. Of these formula modifications, Formula 1 Modification 3 was selected as the best performing lubricant formulation for ZEK100 alloy at 100°C and up to 250°C.

Once EFP Mg-alloy sheets samples became available, Formula 1 Modification 3 was evaluated for use on this alloy. Formula 1 Modification 3 performance on EFP alloy was significantly lower than on ZEK100 alloy. This is likely attributed to both chemical and physical differences between the ZEK100 and EFP sheet samples supplied for testing. ZEK100 alloy sheet samples were noted to be several years old and have accumulated a thick corrosion layer on the surface. The EFP samples were noted to be polished with a minimal corrosion layer. Several lubricants were, therefore, re-evaluated on EFP alloy at 100°C and up to 250°C. Two lubricant formulations were successful in this testing and were selected for use on EFP at 100°C.

Additional lubricant formulations were evaluated for use on EFP at 250°C. The product selection was expanded for this testing and two lubricant formulations were identified as “successful” lubricants at 250°C – i.e., Formulas 2B and 4A, which were subsequently tested on EFP with Henkel pretreatment “C.” Formula 4A was found to be successful on both, the bare and pretreated metal. Formula 2B was found not to offer adequate lubrication on the pretreated surface, but raw data analysis suggests there is good metal separation in the Twist Compression Testing test. Formula 4A will be optimized for use on EFP at 250°C.

Subtask 3.3: Test Coil-applied Anti-Corrosion Mg Treatments – Henkel

1. **Objective and Approach:** Henkel's responsibility for Task 3 is to apply surface treatment to the Mg alloys investigated in this project meeting technical requirements for adhesion and corrosion performance. Henkel has agreed to cut, pretreat, and distribute pretreated Mg panels to project subrecipients. Initial pretreatment evaluations were done on ZEK100 baseline sheet samples provided by USAMP, but these were soon replaced by new EFP sheets received from POSCO.
2. **Progress and Accomplishments:**

2.1 Results of Tests on ZEK100 – 70 ZEK100 Mg-alloy sheets (1216 x 1019 mm) were received by Henkel in August 2017. Panels were cut in preparation for cleaning and pretreatment. Glow Discharge - Optical Emission Spectrometry (GD-OES) analysis revealed a Mg oxide/hydroxide layer of 200–300 nm. SEM analysis showed multiple irregularities along a “ridged” surface profile.

Henkel pretreatment systems were screened and optimization work started on ZEK100 during January and February of 2018. Marginal progress was made based on successful deoxidation of the metal surface and deposition passivating/barrier pretreatment components, as determined in the GD-OES depth profile analysis.

2.2 Results of Tests on EFP – 240 EFP Mg-alloy sheets (500 x 550mm) were received by Henkel in March 2018. With the arrival of the EFP Mg sheet, development work on the ZEK100 Mg sheet was suspended, per agreement among task members during the Task 3 meeting in late February 2018.

The surface of the EFP Mg-alloy was analysed using GD-OES and SEM revealing a very clean surface with minimal oxidation, minimal surface pitting or other irregularities.

2.3 Pre-treating and Distributing EFP – Henkel “pretreatment C” was developed and evaluated for corrosion resistance and for adhesive lap shear strength and was found to meet technical requirements. This pretreatment process was applied to 200 EFP panels (60 cm x 30 cm) and were distributed to the Task 3 team members: Fuchs, Quaker, PPG, and AET.

Pretreated panels were randomly selected and analysed using GD-OES depth profiling where overall film thickness and coating weights of passivating/barrier components were evaluated. The average coating weight of Component A was 28 Mg/m², while Component B was 0.4 Mg/m².

2.4 Process Improvement – Fingerprints and other smudge marks were visible on some of the pretreated panels. By separating the cleaning/etching bath to an alkaline cleaning bath following by an acid etchant, Henkel achieved improved cleaning outcomes and increased the coating weight of the passivating/barrier material desirable for corrosion resistance. Corrosion resistance was found to be equivalent to “Pretreatment Process C.”

Subtask 3.4: Understanding Alloys and Interactions – PPG

- Task Objective:** As part of Task 3 on the LCMS Project, PPG focused on two sub-subtasks:

Subtask 1.3.4 and 2.3.4: Understanding Alloys and Interactions. To test currently available coil-applied and secondarily finished part-applied corrosion protection coatings. Work in BP1 focused on ZEK100, whereas work in BPs 1.5–2 has focused primarily on EFP.

Subtask 1.3.5 and 2.3.5: Formula Development. To formulate prototype products for pretreatment and corrosion coatings. Work in BP1 focused on ZEK100, whereas work in BPs 1.5–2 has focused primarily on EFP.

- Technical Approach:** PPG approached the problem of metal pretreatment holistically, considering the entire process from cleaning and surface preparation, to pretreatment formulation, to sealers and other post-rinses for maximum corrosion protection. A typical pretreatment line sequence is shown in Figure II.1.D.14.

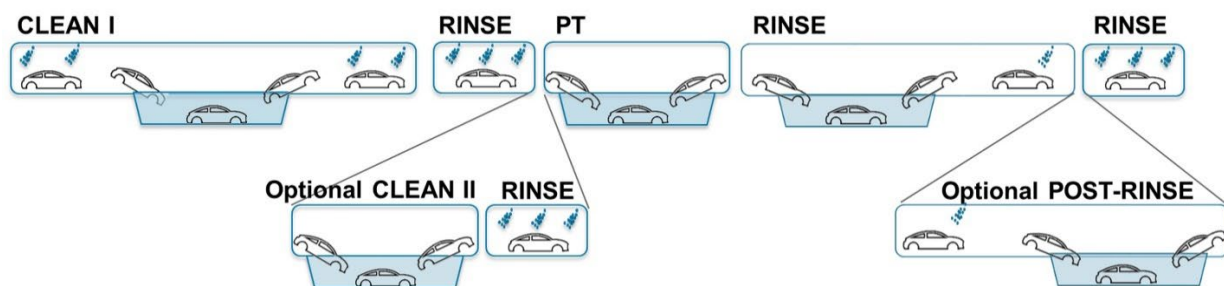


Figure II.1.D.14. A typical automotive pretreatment (PT) sequence, prior to electrocoat. Source: PPG.

3. **Progress and Accomplishments:** The following sections describe how PPG applied their expertise in metal treatment to study the cleaning and pretreatment of ZEK100 and EFP Mg samples during the reporting period.

3.1 Evaluation of Cleaner Compatibility with Mg Alloys – A comprehensive study was performed to evaluate the relationship between cleaner pH, dissolved Mg, and panel surface morphology. Only trace amounts of Mg were dissolved in cleaners with a pH > 10, as expected. For cleaners with a pH < 6, the amount of dissolved Mg (measured by inductively coupled plasma optical emission spectrometry of the cleaner bath) varied widely.

Panel samples were also submitted for SEM analysis to correlate the amount of dissolved metal with surface texture. A rough texture or surface possessing a large amount of surface area was beneficial for adhesion of the top layers of paint to the surface of the substrate. No correlation was observed between bath pH and panel surface morphology.

3.2 Benchmarking of Pretreatments on Mg Alloys with Different Cleaner Systems – A variety of commercially available Group IV, RE, and organic pretreatments were benchmarked for corrosion performance on both ZEK100 and EFP alloys. These pretreatment solutions were run in line with an alkaline cleaner only (“Cleaner 1”), or an alkaline cleaner in combination with a subsequent cleaner. For both alloys, the combination of an alkaline cleaner, followed by a proprietary “Cleaner 2,” drastically improved the corrosion performance in American Society for Testing and Materials B117 Salt-Spray Test and cyclic corrosion tests for the Group IV and RE pretreatments. Other cleaners (following the alkaline cleaning step) did not show this benefit. Organic pretreatments performed best on alkaline only-cleaned panels.

3.3 Optimization of Cleaners for Corrosion Performance – Several studies were performed to identify and improve upon the active components of Cleaner 2. Component 2A alone offered substantially less corrosion protection than Cleaner 2 with both components (e.g., 2A and 2B). Cleaner 2B with certain other additives offered significant corrosion performance improvements over the original formulation.

Testing of these Cleaner 2 prototypes on both alloys revealed that: (1) EFP did better in corrosion than ZEK100 overall; and (2) both alloys showed similar trends for the best and worst cleaners when it comes to corrosion performance.

3.4 Novel Pretreatment Formula Development for Mg Alloys – In addition to cleaners, new formulations of RE and organic pretreatments were explored to improve corrosion performance of ZEK100. Pretreatment formulations with a higher concentration of RE substantially improved corrosion performance over low-concentration RE pretreatments, which corresponded with an increase in deposited RE observed by x-ray fluorescence. Nanomaterial additives to the organic pretreatments have shown an adhesion benefit.

3.5 Evaluation of Pretreatment Compatibility with Other Task 3 Coatings – ZEK100 panels coated with a forming lubricant were received from Quaker. Three cleaners were tested for lubricant removal efficacy at three immersion times (e.g., 30, 60, and 120 s). Cleaner 1, a strong alkaline cleaner, consistently removed enough lubricant to pass a water drop test where the drop wets the surface instead of beading. It is noted, however, that worse corrosion and adhesion properties were observed even after cleaning and pretreatment of the Quaker-coated panels (relative to uncoated panels). This result indicates incomplete removal of the lubricant, despite good wettability. Further work is needed to optimize the lubricant removal process.

EFP panels coated with a coil pretreatment were received from Henkel at the end of FY 2018 for evaluation of the compatibility of this coil coating with subsequent cleaner and pretreatments in the next year.

Subtask 3.7: Al Plating of Mg Sheet for Corrosion Resistance – Xtalic

1. **Task Objective and Approach:** The work plan and objective for this task was comprised of the following main activities:
 - Finalizing the desired performance specification for a nanostructured Al corrosion coating.
 - Developing prototype plated parts which show good adhesion and meet initial performance standards in screening tests.
 - Evaluating options to further reduce cost of plating using ionic liquids – in particular exploring options to control or reduce water contamination susceptibility.
 - Manufacturing a set of prototype parts to prove feasibility of the manufacturing system and the performance of the coated Mg sheet.

2. **Progress and Accomplishments:** Xtalic made significant advances on all four of the primary objectives of the project during FY 2018.

2.1 Plating of Nanostructured Al onto Mg – Nanostructured Al is applied by electrodeposition in an ionic liquid electrolyte devoid of water and oxygen and allows for the direct application of Al onto oxidized Al substrates when cleaning is performed *in-situ*. Xtalic attempted to extend this approach to Mg-alloy substrates using ZEK100. Various etching and reverse pulse activation processes were tested but found to provide inadequate activation and cleaning of the substrate, such that adhesion was poor. A zincation process was developed for ZEK100, which displaced the oxide layers and provided a basis for Al plating.

The direct zincation was followed by an *in-situ* zinc electroplating process on ZEK100. Parts could then be coated by Al-Mn or Al-Zr alloys for ASTM B117 salt-spray testing. Parts survived 96 hours of salt-spray but failed catastrophically by 120 hours. It is clear that once the coating is breached, the corrosion proceeds rapidly. The thick oxide layer of the ZEK100 samples made the activation and coating of this material more difficult. Xtalic briefly tested Mg-alloy WE43 for activation and coating and found that the cast alloy was difficult to activate, and that the coating performance was worse than for ZEK100.

USAMP later instructed Xtalic to focus on the new EFP alloy, which had a clean surface with an oxide that was easier to activate. The zincation, zinc plating, and Al processes could be used on this alloy. Parts coated with 20 μm of Al-Zr survived more than 360 hours of salt-spray without corrosion. Xtalic provided samples of this coating to the task partners at PPG who applied a commercial e-coat process onto the Al surface. These samples were tested for salt-spray performance and lasted about 2,200 hours. The failure mode is difficult to diagnose but may have been related to a failure in the masking used to cover the unplated sections. This higher life of salt-spray performance indicates a strong potential for this coating method to provide adequate protection in automotive applications.

The part plating process was scaled-up to a larger reactor (20 liter) to produce larger test pieces. Xtalic developed tooling and plating parameters needed to make high-quality coatings on 5 x 10 cm test coupons.

2.2 Ionic Liquid Cost – A significant concern for the cost of the plating solution is the fundamental cost of the ionic liquid electrolyte as some losses occur either through drag-out after plating or bath loss due

to manufacturing error or bath breakdown. An alternate source for the 1-ethyl-3-methylimidazolium chloride ionic liquid has been identified, which can manufacture in significantly larger batch quantities. This provides two potential benefits: (1) scale-up potential for larger quantity manufacturing; and (2) cost reductions due to economy of scale for making the ionic liquid. Xtallic also evaluated the stability of the ionic liquid in an oxygen bearing environment that is dry. There were some visible changes to both the plating performance and color of the electrolyte after exposure. This may be due to a small excursion in moisture that occurred during the experiment.

Since the cost of the ionic liquid is high, it is important to extend the life of the electrolyte for as long as possible. To do this, Xtallic devised a test method to accelerate aging of the electrolyte. The performance of the bath age is measured in units of amp-hours/liter, with a target of 5,000 A-hr/l. The bath was aged, taking samples at various increments, and it was found that the bath survived well to 5,000 A-hr/l with some discoloration of the bath, but good quality in the deposits made from the bath throughout the aging process. Fourier Transform Infrared analysis of the bath showed good stability, but some change in certain peaks with time. This technique may allow quantification of bath age.

2.3 Test Method Development – The qualification test method used to evaluate performance has been finalized. The nanostructured Al coating is proposed as a sheet-applied pretreatment prior to forming. Corrosion performance is needed to survive from the application at the sheet rolling mill until the coil is formed. After forming, the parts will be assembled and then go through a body-in-white style coating and protection process. As such, 24 hours of salt-spray after coating is sufficient. After forming and e-coat is applied, the performance should extend to 3,000 hours of salt-spray.

Xtallic have also addressed the concern about formability of the coating when applied to the sheet stock. Many oxide style coatings will crack at low strains. Ideally, the Al coating provides crack-free protection through forming until the part gets to final coating. Xtallic built a simple formability tester which uses a 12 mm sphere to press a hemispherical shape into the sheet. Cracking can be observed, and the limiting dome height can be measured to quantify the formability. It was found that the zincation and zinc-coating processes retain all formability of the EFP Mg sheet. Initial testing on the Al-Mn alloy showed that the Mn content was too high in the deposit, which led to early cracking. Future tests will be performed on lower Mn content alloys, which have increased ductility.

2.4 Manufacture of Prototype Parts – Xtallic has built about 50 high-quality 5 x 10 cm parts to date and can scale the process to larger sizes (i.e., 15 x 20 cm) within the bounds of its existing infrastructure. Samples have been provided to upstream partners in the project to conduct further evaluations of the surface treatment.

Task 4: Joining Process Evaluation and Development

1. **Task Objectives:** AET Integration, Inc., initially proposed evaluating the following joining methods and developing welding process parameters to join Mg-based alloys:
 - Resistance Spot Welding (RSW)
 - Arplas Welding
 - Friction Stir Welding (FSW)
 - Laser Welding
 - Self-Pierce Riveting.

From USAMP's feedback in the context of the Mg door inner demonstration part, AET focused on RSW, Arplas, and laser welding studies.

2. **Technical Approach:** AET will perform mechanical testing on ZEK100 and AZ21 to determine a baseline for the development of joining methods for the new low-cost Mg sheet when available. Additionally, they are developing and optimizing process parameters for each of the joining methods listed above.
3. **Progress and Accomplishments:** The effort in FY 2018 focused on understanding the effect of the ZEK100 as-received surface conditions on weldability. It is recognized that due to the high contact resistance of the as-received ZEK100 samples (i.e., highly oxidized surface due to long-term storage), rapid heat generation results in expulsion and poor quality RSW joints. However, AZ21 as-received condition appears to produce consistent welds with no occurrence of surface melting. AET's testing of electrical contact resistance exhibited variations, with an average contact resistance of 0.84 mΩ for AZ21 and of 5.31 mΩ for ZEK100. This confirms that ZEK100 in as-received condition has unacceptable surface condition for RSW. Sandblasting and "deoxidizing" the sheet surfaces improved the ability to weld the ZEK100 using RSW, which was confirmed in an earlier quarter of FY 2018.

Further trials were performed at the end of FY 2018, focused on developing parameters for FSW for both AZ21 and ZEK100. Optimal parameters were identified, and sample panels were successfully produced for mechanical testing. The mechanical tests were conducted under quasi-static loading conditions using tensile shear to assess performance of FSW versus resistance welding processes. The results from the mechanical tests indicate that the average joint peak load values are relatively at the same level. However, FSW joints of ZEK100 resulted in a higher peak load due to the larger specific weld area.

4. **Next Steps:** AET's research plans for FY 2019 will focus on the following activities:
 - Evaluate contact resistance of clean ZEK100 (either sandblasted or cleaned and deoxidized by Henkel) to determine how much of the contact resistance differential between ZEK100 and AZ21 is related to the chemistry vs. how much is due to the oxidation of the ZEK100 over the past six years.
 - Evaluate effect of electrode cleaning on the RSW process window and electrode life.
 - Explore laser welding of as-received 1.5 mm ZEK100 and 1.2 mm AZ21 materials.
 - Investigate resistance welding process on pretreated AZ21 and AZ21 with the forming lubricant, if that material is available.

Task 6: Production of Large Automotive Body Components – Vehma

1. **Objective and Approach:** While this task is not scheduled to begin until FY 2019, significant preliminary work was done by Vehma to guide the CAE activities on material model development, model calibration, and validation on intermediate parts and establishing a warm-forming process window. Vehma's three subtasks include: (1) conduct Mg-alloy panel forming simulations comparing existing and new alloys; (2) modify existing dies, if necessary; and (3) form Mg-alloy panels to USAMP specifications.
2. **Progress and Accomplishments:** Vehma worked with USAMP, LSTC, and Autoform to finalize the material characterization and simulation plan for Task 6 in the spring and summer of 2018. This provided the Voice of the Customer from the standpoint of a commercial CAE end-user. A material test matrix was developed in FY 2018 to ensure the Task 2 deliverables represent realistic Mg warm-forming process scenarios and boundary conditions, when incorporated into the commercial CAE packages. They will use material characterization data provided by the USAMP project team to conduct warm-forming simulation of door inner and outer components. Vehma already received the baseline dies from USAMP and will modify the dies, if necessary. Vehma will then manufacture one-stage, warm-formed, and laser-trimmed prototypes of the Mg door inner and outer panels.

Task 7: Demonstration of Components – Vehma

1. **Objective and Approach:** Vehma is to develop a manufacturable 3D CAD data design for the side door while utilizing Mg sheet inner and outer panels. They will analyze the door design for performance such as dent resistance, A- and B-Pillar Stiffness, Inner and Outer Belt Stiffness, Sag, Set and Overcheck, and Modal Analysis. Vehma will develop and analyze the side door design performance by utilizing material characterization data provided by the USAMP project team.
2. **Progress and Accomplishments:** During FY 2018, Vehma tried out the baseline door inner and outer dies in September 2017 using Al sheets (5182-O), as shown in Figure II.1.D.15.
 - In fall 2017, USAMP proposed using a common gauge for both the inner and outer tools for cost reasons. Vehma conducted forming simulations and finalized with USAMP to use a 1.2 mm gauge for producing both inner and outer door components for Task 6. Modification of the outer die is required because the original die was built for 1 mm gauge. Since both the outer and inner panels will be stamped using 1.2 mm thick sheets of the new Mg-alloy, re-cutting of the outer die is required.



Door Inner Draw Die



Door Inner



Door Outer Draw Die



Door Outer

Figure II.1.D.15. Baseline door inner and outer dies to be used to produce Mg parts. Source: Vehma International.

3. **Plans for FY 2019 and FY 2020:** Vehma will conduct forming simulations and develop final door designs after receiving the necessary material cards, as well as help USAMP modify the baseline dies. During FY 2020, Vehma will conduct warm-forming trials with the final Mg-alloy, and ship door panels to USAMP for evaluation. They will also participate in Camanoe's completion of the cost modeling study outlined in Task 1.

Conclusions

USAMP overcame the initial slow start in BP1 and was able to achieve the three planned milestones in FY 2018, by establishing EFP as a baseline Mg sheet material for conducting the most detailed testing, characterization, formability analysis and coating studies.

In FY 2019 (BP2), USAMP expects to validate ICME predictions for formability and primary and secondary mechanical properties, using the constitutive model for textured Mg-alloy, which would be completed, and recommend an ideal texture (*Milestone 4*). Material testing and characterization of commercial EFP Mg will

continue in order to steer the development of a new material model that can be scaled and applied for simulation modeling of the demonstration inner and outer door parts.

Based on formability evaluations of USAMP-developed experimental alloy strips, a decision would be made early in FY 2019 to source medium-width sheet of the top candidate alloy for further forming analysis (**Milestone 5**) with intermediate size and complexity parts. The new Mg sheet material will be optimized in rolling trials, forming properties characterized and performance compared with baseline ZEK100 and EFP sheet (**Milestone 7**).

The university team will continue to produce and evaluate new RE-free alloys containing <0.2wt% Zr to accomplish grain refinement and texture randomization without using strip-casting technology.

The coatings research team will continue development of low-cost coil-applied pretreatments, down-select warm-forming lubricants, and coatings compatible with EFP (**Milestone 6**). The project team will also evaluate suitable joining processes for Mg-Mg sheets.

In summary, while alloy development is a complicated and involved activity, the USAMP's approach is to accelerate the program by collaboratively conducting important assessments of the state-of-the-art, and thereby to spur advances in Mg warm-forming process simulation, as well as in protective coatings and lubricant technology for high-volume warm-forming of low-cost Mg sheet.

Key Publications

1. Carter, J. T., 2018, "Challenges and opportunities for implementing Mg in automotive applications," Keynote presentation at the 11th International Conference on Mg Alloys and Their Applications, July 24–27, 2018, Beaumont Estate, Old Windsor, UK.
2. Bong, H. J., X. Hu, X. Sun, and Y. Ren, 2018, "Mechanism-based constitutive modeling of ZEK100 Mg-alloy with crystal plasticity and *in-situ* HEXRD experiment," *Int. J. Plasticity*, in press, corrected proof. <https://doi.org/10.1016/j.ijplas.2018.09.005>.
3. Bong, H. J., X. Hu, X. Sun, Y. Ren, and R. K. Mishra, 2018, "Crystal plasticity based constitutive modeling of ZEK100 Mg-alloy combined with *in-situ* HEXRD experiments," *J. Phys. Conf. Ser.*, Vol. 1063, No. 1, Art. 012031. doi:10.1088/1742-6596/1063/1/012031.

References

1. Jiang, L., J. J. Jonas, and R. Mishra, 2011, "Effect of dynamic strain aging on the appearance of the RE texture component in Mg alloys," *Mater. Sci. Eng. A*, Vol. 528, No. 21, pp. 6596–6605.
2. Lee, J. Y., Y. S. Yun, B. C. Suh, N. J. Kim, W. T. Kim, and D. H. Kim, 2014, "Comparison of static recrystallization behavior in hot-rolled Mg–3Al–1Zn and Mg–3Zn–0.5Ca sheets," *J. Alloy Compd.*, Vol. 589, pp. 240–246.
3. Yasi, J. A., L. G. Hector Jr., and D. R. Trinkle, 2010, "First-principles data for solid-solution strengthening of Mg: From geometry and chemistry to properties," *Acta Mat.*, Vol. 58, No. 17, pp. 5704–5713.
4. Ghazisaeidi, M., L. G. Hector Jr., and W. A. Curtin, 2014, "Solute strengthening of twinning dislocations in Mg alloys," *Acta Mat.*, Vol. 80, pp. 278–287.
5. Buey, D., L. G. Hector Jr., and M. Ghazisaeidi, 2018, "Core structure and solute strengthening of second-order pyramidal <c+a> dislocations in Mg–Y alloys," *Acta Mat.*, Vol. 147, pp. 1–9.
6. Bassani, J., and H. Pan, 2012, "A phenomenological model for microstructural evolution during plastic flow," *CR Mec.*, Vol. 340, pp. 369–377.

Acknowledgements

This project is a continuing collaboration with many researchers from Ford Motor Company, Fiat Chrysler Automobiles US LLC, General Motors, and sponsor/support/subrecipient/vendor organizations. The contributions of the following past or retired (shown with *) and present task leaders are gratefully acknowledged: Leland Decker, Aslam Adam, and Steve Logan* (FCA); Bitu Ghaffari and Mei Li (Ford Motor); Jon Carter*, Lou Hector, Raj Mishra*, and Anil Sachdev (GM); Aaron Yocum (DOE-NETL); Eric McCarty (Materials Technologies Consulting); Manish Mehta (M-Tech International); and Gloria Bucciero and Jenna Wiland (Bucciero and Associates).

II.1.E Understanding Protective Film Formation by Mg Alloys in Automotive Applications (Oak Ridge National Laboratory)

Michael P. Brady, Principal Investigator

Materials Science and Technology Division
Oak Ridge National Laboratory
1 Bethel Valley Road
Oak Ridge, TN 37831-6156
E-mail: bradymp@ornl.gov

Donovan N. Leonard, Co-Principal Investigator

Materials Science and Technology Division
Oak Ridge National Laboratory
1 Bethel Valley Road
Oak Ridge, TN 37831-6156
E-mail: leonarddn@ornl.gov

Sarah Kleinbaum, DOE Technology Manager

U.S. Department of Energy
E-mail: sarah.kleinbaum@ee.doe.gov

Start Date: October 1, 2015	End Date: June 30, 2019	
Project Funding (FY18): \$400,000	DOE share: \$400,000	Non-DOE share: \$0

Project Introduction

Mg alloys are of great interest to automotive manufacturers because of their attractive combination of low-density, good strength, amenability to casting, and ease of recycling. A major obstacle to widespread adoption of Mg alloys is their susceptibility to corrosion [1–3]. Surface treatments and/or coatings are needed for many applications [3]; these result in increased cost and can lead to component durability issues. The inability of Mg alloys to establish a continuous and fully protective surface film under many exposure conditions is a key factor underlying their susceptibility to corrosive attack. Alloying has been shown to modify surface film performance and impact the nature and protectiveness of reactive-based coating processes typically used for Mg alloys; however, a detailed understanding of how and why this is the case is currently lacking [1–2,4]. This understanding is needed to provide a basis for developing improved alloys and coatings to permit more widespread adoption of Mg alloys in automotive applications.

Objectives

The objective of this project is to enhance fundamental understanding of Mg corrosion to provide the basis for designing improved Mg alloys and coatings to permit more widespread automotive adoption of Mg. Two classes of Mg alloys are under study: (1) conventional Mg-Al base alloys; and (2) state-of-the-art Zr and RE element modified Mg alloys of interest for their improved formability characteristics [5], particularly in sheet form. The project is devoted to understanding the impact of alloying additions on film formation and potentially detrimental hydrogen migration into the underlying Mg-alloy during aqueous exposures of uncoated (bare) alloys [6], as well as the impact of substrate alloying segregation tendencies on the formation of surface coatings by electro ceramic (EC) and electrocoating (E-Coat) techniques. New insights are achieved through the use of advanced electron microscopy and neutron and isotopic tracer characterization tools not previously widely applied to Mg corrosion.

Approach

This project is using advanced electron microscopy, neutron scattering and spectrometry, and isotopic tracer characterization tools not previously widely applied to Mg corrosion to provide the improved fundamental

insights needed to successfully design Mg alloys and coatings with improved corrosion resistance. The work is focusing on select state-of-the-art commercial Mg alloys and coatings relevant to automotive applications and chosen in consultation with project collaboration partners Magnesium Elektron North America (a Mg-alloy producer), Henkel Corporation (a coating producer), Magna International (a Tier 1 automotive supplier), McMaster University (for electron microscopy and electrochemistry), McGill University (for Zr-free developmental Mg sheet alloys), and the University of Manitoba (for secondary ion mass spectrometry [SIMS] sputter depth profile analysis of isotopic tracers). Commercial alloys under study include in weight percent (wt.%): wrought AZ31B-H24 (AZ31B for short) (Mg-3Al-1 zinc (Zn)) base; cast AZ91D (Mg-9Al-1Zn) base; wrought ZE10A (Mg-1.5Zn-0.25Zr<0.5 neodymium (Nd)) base; and WE43 (Mg-(3.7–4.3) yttrium (Y)-(2.3–3.5)RE-0.2Zr) base.

The effort will specifically focus on two key corrosion aspects:

1. Understanding effects of Al, Zr, Ca, and RE alloy additions on corrosion film structure and potentially detrimental enhanced hydrogen migration phenomena into Mg alloys during aqueous and/or WV exposures. This phenomenon is potentially relevant to stress corrosion cracking/hydrogen embrittlement susceptibility and dissimilar metal interface corrosion. An understanding of hydrogen uptake is also needed to more fully describe and successfully model aqueous corrosion processes for Mg alloys.
2. Establishment of substrate alloy impacts on the chemistry, morphology, and performance of state-of-the-art EC and E-Coat coatings to provide a basis for the optimal design of alloys/coating processing systems. The focus will be on better understanding of why coating protectiveness varies with the substrate alloy in these composition ranges.

Results

Corrosion protection schemes for Mg alloys involve multi-layered coatings, typically a surface pretreatment inner layer (EC, conversion coatings, anodization, etc.); an intermediate layer (E-coats, platings, powder coatings, organic coatings, etc.); and a final, outer layer(s) of sealant and/or paint [3,7]. Efforts in FY 2018 focused on the study of the impact of the Mg-alloy substrate on the resultant morphology, chemistry, and protectiveness of a state-of-the-art EC coating, with and without an E-coat top coat. In collaboration with Henkel Corporation, Bonderite® EC coatings were applied to AZ31B, AZ91D, ZE10A, and WE43 Mg-alloy substrates using the same process parameters, with additional samples further coated with an Axalta ES27 E-coat top coat. Key behaviors of interest included: (1) how the substrate Mg-alloy impacted the initial EC layer (studied in FY 2017 [8]); (2) how the inner EC layer is impacted when the E-coat topcoat layer is applied; and (3) how the bare, EC coated, and EC + E-Coated alloys behave in corrosion. Corrosion behavior was studied in collaboration with McMaster University by immersion in 0.1M NaCl solution, with corrosion rates calculated from hydrogen evolution measurements. Corrosion of the EC + E-Coated samples was studied both as-coated, and after intentional mechanical damage through the coating (scribing).

Cross-section SEM and scanning transmission electron microscopy (STEM) analysis found that the substrate Mg-alloy had an unexpectedly strong impact on EC coating thickness and morphology [8]. The Mg substrate alloys with higher levels of Al or RE additions resulted in much rougher and thicker EC coatings and, in the case of high RE additions in WE43, an unexpected striated local layered structure at the alloy-coating interface [8]. EC coating thicknesses ranged from a few microns for AZ31B to several tens of microns on WE43, with considerable variability across the sample surface [8]. Segregation of Al from the alloy to the EC was observed for AZ31B and AZ91D, whereas Zr and RE additions were not observed to migrate to the EC coatings formed on ZE10A and WE43 [8].

Cross-section analysis by SEM and STEM indicated that the inner EC layers were fully preserved after E-Coating, as shown in Figure II.1.E.1. This finding is in contrast to a recent study under this program of conversion coatings, which were degraded by subsequent E-Coat processing [9]. The E-Coat top coats were also found to thoroughly percolate to the inner regions of the porous EC structures for all Mg alloys studied,

even the striated local EC structure formed on WE43 (shown in Figure II.1.E.1 for AZ31B and WE43), which is anticipated to be beneficial for adherence and protectiveness.

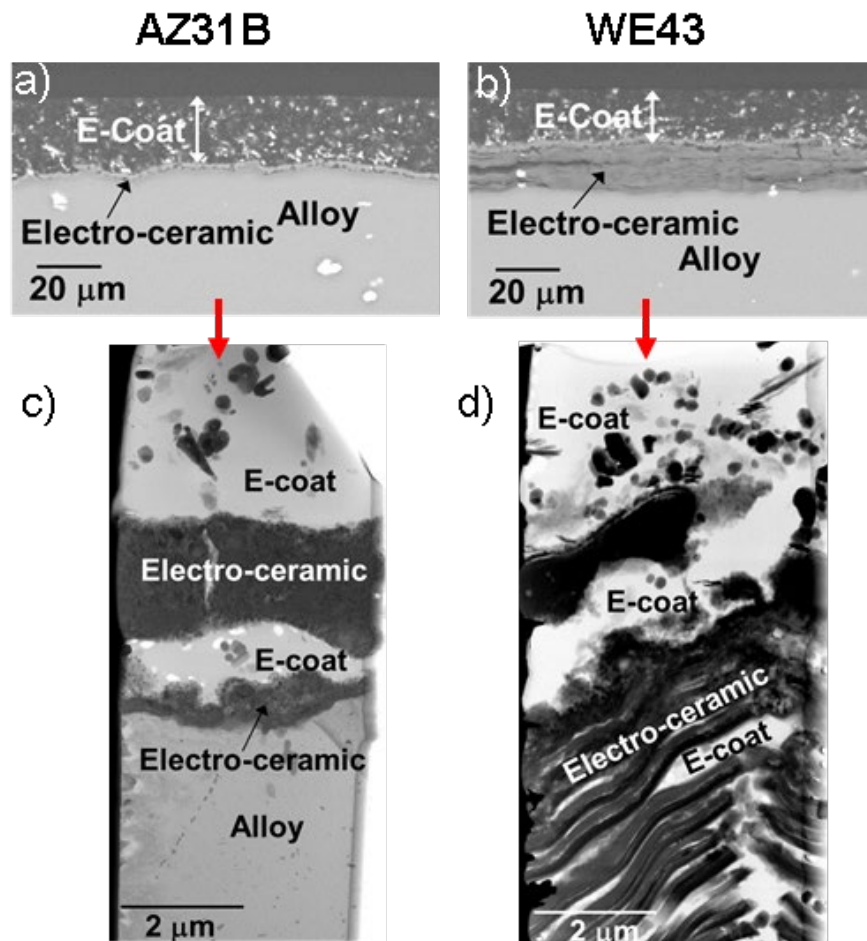


Figure II.1.E.1. Cross-section images by SEM (a, b) and STEM (c, d) showing the as-coated structure formed on wrought AZ31B-H24 and WE43 alloys with an initial, inner EC layer and a subsequent E-Coat top coat. Source: ORNL.

The corrosion resistance of the EC coated alloys after seven days in 0.1M NaCl followed trends observed for the bare (uncoated) alloys qualitatively in the order from most to least corrosion-resistant of AZ91D > WE43 > ZE10A > AZ31B, as shown in Figure II.1.E.2. The EC corrosion data showed considerable scatter, which is not unexpected as the EC layer is not designed to be prime reliant, but rather intended to enhance top coat bonding, as well as contribute to the overall corrosion resistance of multilayer coating systems. The addition of the E-Coat top coat resulted in comparable, excellent corrosion resistance for all four alloys, as shown in Figure II.1.E.2. However, corrosion exposures for scribed (intentionally damaged) EC + E-Coat samples resulted in a significant degradation of corrosion resistance for one each of the triplicate scribed coated WE43 and ZE10A alloy samples studied. In contrast, the corrosion resistance of the EC + E-Coating on the AZ31B and AZ91D after scribing showed far less scatter than the ZE10A and WE43, and a far greater degree of protectiveness. The corrosion rates for the worst-performing EC + E-Coated samples after scribing are shown in Figure II.1.E.2. Corrosion rates for EC + E-Coated AZ31B and AZ91D were on the order of only ~ 0.001 Mg/cm²/day, too low to be visible on the scale of the plot. Select EC + E-Coated samples were scribed after the initial seven day immersion, and subsequently immersed for an additional eight day exposure. The scribed data shown (chart on right) was for the poorest performing samples of the triplicate samples studied.

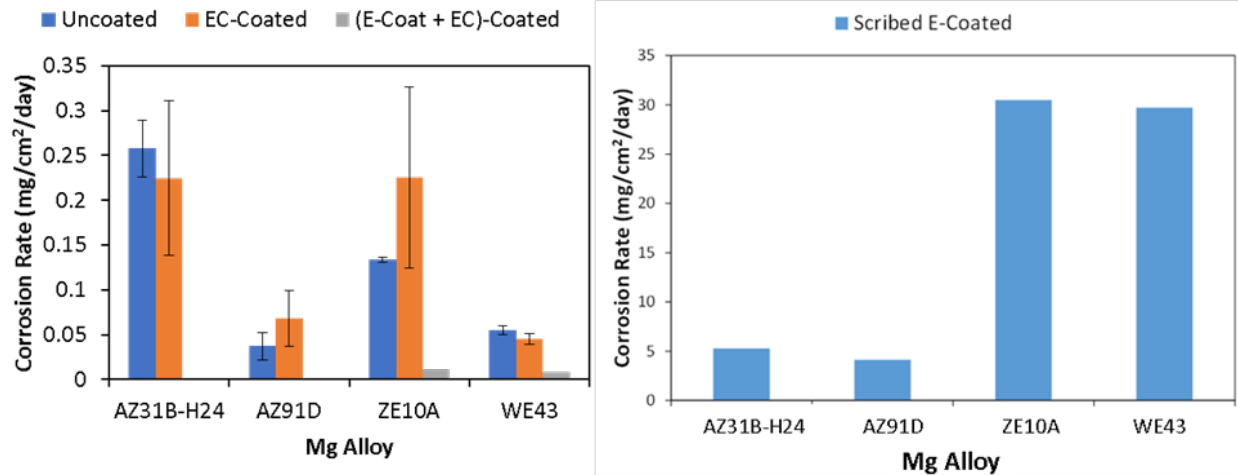


Figure II.1.E.2. Corrosion rates calculated from hydrogen evolution measurements for seven day exposures in 0.1M NaCl solution for AZ31B-H24, AZ91D, ZE10A, and WE43 uncoated, with an initial EC layer, and dual-layer EC + E-Coat (triplicate samples exposed). Data courtesy E.A. McNally and J.R. Kish, McMaster University.

Preliminary SEM analysis of the corrosion attack at the scribed-coating interface indicated that WE43 and ZE10A may be more susceptible to corrosion undercutting the coating at a scribed region of damage than are AZ91D and AZ31B, as shown in Figure II.1.E.3. The WE43, in particular, showed extensive corrosion and cracking in the scribed region, with further lateral attack undercutting the inner EC layer extending nearly 1 mm from the scribe-coating interface. It is hypothesized that the WE43 is susceptible to this attack due to the striated local layered EC structure formed at the alloy-coating interface. Further characterization of corrosion attack in the scribed-coating interface regions for all four alloys by electron probe microanalysis and STEM are in progress.

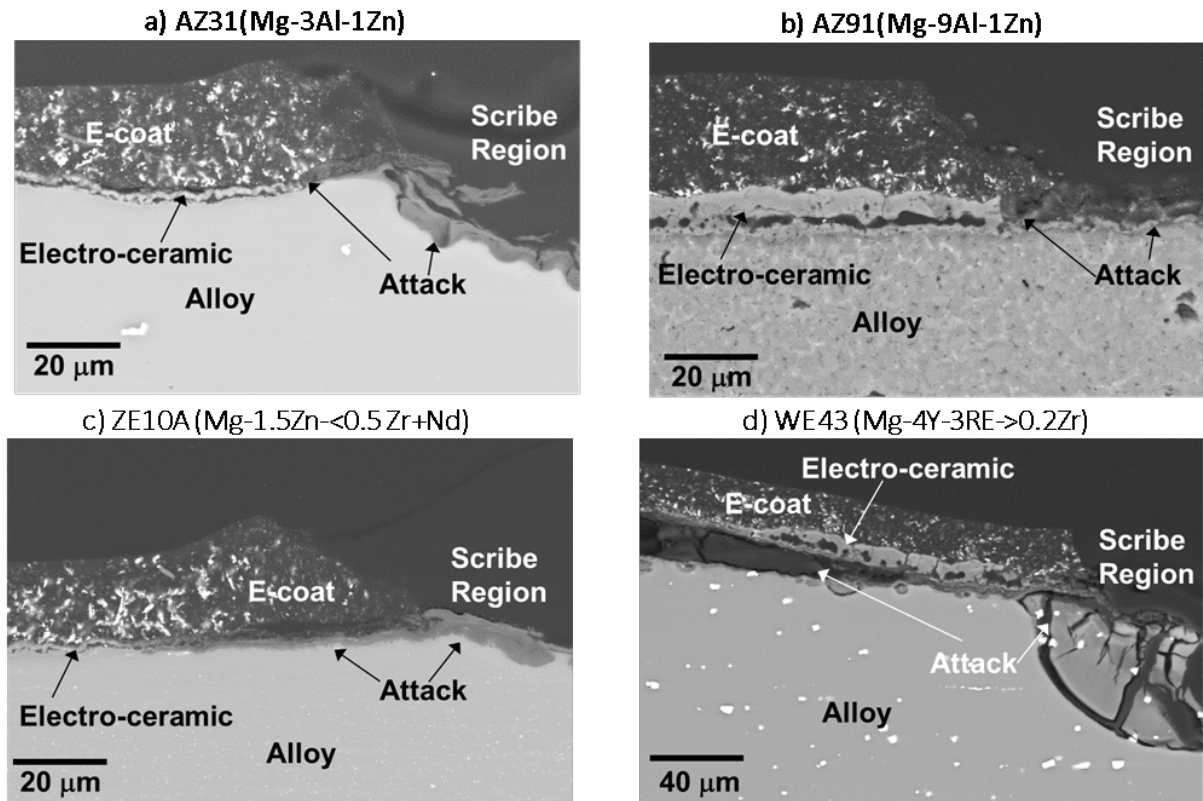


Figure II.1.E.3. Cross-section SEM images showing corrosion attack at the scribe-coating interface for (a) AZ31B-H24, (b) AZ91D, (c) ZE10A, and (d) WE43 EC + E-Coated after an initial seven day immersion in 0.1M NaCl solution as-coated, and then an additional eight day immersion after scribing. Source: ORNL.

Conclusions

Efforts in FY18 focused on study of the impact of the Mg-alloy substrate on the resultant morphology, chemistry, and protectiveness of a state-of-the-art EC coating, with and without an E-Coat top coat. Key findings were:

1. EC coating chemistry, morphology, and structure were well preserved during subsequent E-Coat top coat processing (i.e., the EC layer was not degraded by the E-coat processing). The E-coat was also able to thoroughly percolate into the porous inner EC layers, which can be of benefit to coating adherence.
2. The corrosion resistance of the EC coating alone followed the trends of the bare (uncoated) alloy corrosion resistance. From most to least corrosion-resistant: AZ91D > WE43 > ZE10A > AZ31B. Subsequent E-coat top coating resulted in equivalent, good corrosion resistance for all four substrate alloys: AZ91D ~ WE43 ~ ZE10A ~ AZ31B.
3. The Al-modified substrate alloys AZ31B and AZ91D showed greater resistance to corrosion after scribing of the EC + E-Coat dual-layer coating than the Zr- and RE-modified ZE10A and WE43 alloys: AZ91D ~ AZ31B > WE43 ~ ZE10A. The susceptibility of the coated WE43 was hypothesized to be related to enhanced, lateral undercutting corrosion attack of the inner, striated EC structure formed on this alloy.
4. These findings indicate that the Mg-alloy substrate significantly impacts EC coatings, and protectiveness of EC + E-Coat dual-layer coating systems. Understanding of this behavior can provide a basis to optimize coating processing for a given substrate alloy and/or select or design Mg alloys to be more amenable to coating.

Key Publications

1. Brady, M. P., M. Fayek, D. N. Leonard, H. M. Meyer III, J. K. Thomson, L. M. Anovitz, G. Rother, G.-L. Song, and B. Davis, 2017, "Tracer film growth study of the corrosion of Mg alloys AZ31B and ZE10A in 0.01% NaCl solution," *J. Electrochem. Soc.*, Vol. 164, No. 7, pp. C367–C375.
2. Brady, M. P., W. J. Joost, and C. D. Warren, 2017, "Insights from a recent meeting: Current status and future directions in Mg corrosion research," *Corrosion*, Vol. 73, No. 5, pp. 452–462.
3. Brady, M. P., A. V. Ievlev, M. Fayek, D. N. Leonard, M. G. Frith, H. M. Meyer III, A. J. Ramirez-Cuesta, L. L. Daemen, Y. Cheng, W. Guo, J. D. Poplawsky, O. S. Ovchinnikova, J. Thomson, L. M. Anovitz, G. Rother, D. Shin, G.-L. Song, and B. Davis, 2017, "Rapid diffusion and nanosegregation of hydrogen in Mg alloys from exposure to water," *ACS Appl. Mater. Interfaces*, Vol. 9, No. 43, pp. 38125–38134.
4. Rossouw, D., D. Fu, D. N. Leonard, M. P. Brady, G. A. Botton, and J. R. Kish, 2017, "Characterization of localized filament corrosion products at the anodic head on a model Mg Zn Zr alloy surface," *Corrosion*, Vol. 73, No. 5, pp. 518–525.

References

1. Song, G. L., and A. Atrens, 2007, "Corrosion mechanisms of Mg alloys," *Advan. Eng. Mater.*, Vol. 9, No. 3, pp. 177–183.
2. Song, G. L., 2005, "Recent progress in corrosion and protection of Mg alloys," *Advan. Eng. Mater.*, Vol. 7, No. 7, pp. 563–586.
3. Gray, J. E., and B. Luan, 2002, "Protective coatings on Mg and its alloys—A critical review," *J. Alloy Compd.*, Vol. 336, Nos. 1–2, pp. 88–113.
4. Gusieva, K., C. H. J. Davies, J. R. Scully, and N. Birbilis, 2015, "Corrosion of Mg alloys: The role of alloying," *Int. Mater. Rev.*, Vol. 60, No. 3, pp. 169–194.
5. Bohlen, J., M. R. Nürnberg, J. W. Senn, D. Letzig, and S. R. Agnew, 2007, "The texture and anisotropy of Mg zinc RE alloy sheets," *Acta Mater.*, Vol. 55, No. 6, pp. 2101–2112.
6. Brady, M. P., A. V. Ievlev, M. Fayek, D. N. Leonard, M. G. Frith, H. M. Meyer III, A. J. Ramirez-Cuesta, L. L. Daemen, Y. Cheng, W. Guo, J. D. Poplawsky, O. S. Ovchinnikova, J. Thomson, L. M. Anovitz, G. Rother, D. Shin, G.-L. Song, and B. Davis, 2017, "Rapid diffusion and nanosegregation of hydrogen in Mg alloys from exposure to water," *ACS Appl. Mater. Interfaces*, Vol. 9, No. 43, pp. 38125–38134.
7. Brady, M. P., W. J. Joost, and C. D. Warren, 2017, "Insights from a recent meeting: Current status and future directions in Mg corrosion research," *Corrosion*, Vol. 73, No. 5, pp. 452–462.
8. Brady, M. P., and D. N. Leonard, 2017, "II.3. An Understanding protective film formation by Mg alloys in automotive applications," VTO 2017 Annual Progress Report, pp. 252–268.
9. Brady, M. P., D. N. Leonard, H. M. Meyer, J. K. Thomson, K. A. Unocic, H. H. Elsentriecy, G.-L. Song, K. Kitchen, and B. Davis, 2016. "Advanced characterization study of commercial conversion and electrocoating structures on Mg alloys AZ31B and ZE10A," *Surf. Coat. Tech.*, Vol. 294, pp. 164–176.

Acknowledgements

The contributions of Bruce Davis, John Kukalis, Bruce Goodreau, Omar Abu Shanab, Kirk Kramer, Beth McNally, Joey Kish, and Harry Meyer III to the design, execution, and interpretation of the experimental findings related to the coating work under this project are gratefully acknowledged.

II.1.F Thin AHSS with CFRP Coating (Oak Ridge National Laboratory and Idaho National Laboratory)

C. David Warren, Co-Principal Investigator

Oak Ridge National Laboratory
1 Bethel Valley Rd.
Oak Ridge, TN 37831
E-mail: warrencd@ornl.gov

Gabriel O. Ilevbare, Co-Principal Investigator

Idaho National Laboratory
P.O. Box 1625, MS 2211
Idaho Falls, ID 83415
E-mail: gabriel.ilevbare@inl.gov

Sarah Kleinbaum, DOE Technology Manager

U.S. Department of Energy
E-mail: sarah.kleinbaum@ee.doe.gov

Start Date: April 3, 2018	End Date: March 30, 2020	
Project Funding: \$639,000	DOE share: \$300,000	Non-DOE share: \$339,000

Project Introduction

Diversitak, a company based in Detroit, MI, has developed a proprietary, low-specific gravity, carbon fiber reinforced epoxy (CFRE). Preliminary testing on this new material conducted in collaboration with ArcelorMittal Steel Company proved out the concept. A thin layer of a CFRE was applied to a stamped sheet of steel with residual stamping oils from a mill, in a time corresponding to automotive processing (~15 secs) and processed following automotive e-coat procedures (phosphating + 175-200°C heating), to complete the curing. No problems with adherence or performance were noted. While the CFRE does add weight to a thin gauge steel panel, it weighs much less than what is displaced by using thicker conventional mild steel gauges. The application of the coating showed a significant increased dent resistance, oil canning resistance, and part stiffness.

This project is designed to mature this new technology to near manufacturing readiness to reduce the weight of a vehicle and lower the cost of weight reduction. The process involves the use of thinner gauge steels than are currently used, stiffened by CFRE application on one side. The development (collaborative) team includes two industrial manufacturers, Diversitak and ArcelorMittal Steel Company; LightMAT; and two national laboratories, ORNL and Idaho National Laboratory (INL). The team is developing a new manufacturing process with an understanding of how to apply the coating, along with how it will perform in-service. Evaluating the long-term durability of materials manufactured using this technology is also a goal.

Objectives

Recent steel industry advances have led to the development of AHSS, which can be of a thinner gauge and thus lighter than conventional sheet steels, while supporting vehicle structural functions. Thinner gauge steel panels are subject to inherent sheet forming defects that limit their applicability. Those defects can result in an increased potential for denting, vibration at high vehicle speeds, and “oil canning” (waviness in the steel sheet). Those defects are caused by residual stresses, which are induced during coil production and tend to become more exaggerated as the strength level of the rolled sheet is increased to meet the need for a thinner, and thus lighter, sheet. Conventional auto-body sheet steel averages 1.1 mm thick, ranging from 0.65 mm to 2.5 mm depending on the location, but typical exterior panels are often 0.75 mm thick. Reducing total body panel thickness from 0.75 to 0.55 mm could reduce body mass from 130 to 95 kg (i.e., a 27% reduction) [1].

The goal of this work is to develop CFRE technology so that AHSS body panels may be reduced in thickness from 0.75 to 0.55 mm to reduce component mass. To accomplish this goal, the optimal reinforcement fiber length and fiber concentration must first be determined. Following that phase, the coefficient of thermal expansion in all three directions must be determined to feed into manufacturing models and methods for rapidly and inexpensively applying the coating must be determined. This is being followed by panel level evaluations of the coating and steel combination and then followed by a full-part demonstration of the technology on door panels. The final step will conclude with corrosion testing of the parts.

Approach

This is a two-year effort. ORNL's tasks include optimization and selection of the best CFRE material. This included a determination of the optimal fiber length, optimal fiber concentration, and a determination of the optimal coating thickness for best vehicle structural function and performance at the least cost. ORNL, along with the suppliers, developed a durable CFRE application process (e.g., gun material, design, robotic dispensing process) and identified the adhesion stability of the CFRE during process holding. An approach to ensure that application/curing timing conforms to conventional assembly line speed and plant cycle times is being determined. ORNL also determined the coefficient of thermal expansion of the material in all three directions and performed all material SEM analysis.

INL will perform characterization of corrosion properties of steel panels coated with CFRE during the next year. The panels are being investigated for suitability as replacement materials used in automotive body panels to reduce mass. After an optimized CFRE formulation is achieved, test coupons will be supplied to INL for testing in the already coated form. The testing will include corrosion testing of test coupons and body panels.

Diversitak produced different epoxy formulations and determined the physical and chemical properties that are critical to mixing with CFs and producing a stable coating that can be cured in the time range to support automotive assembly processing (~10-15 secs). They also mixed different amounts and types of CF with a range of epoxy formulations and measured the cured coating properties. ArcelorMittal characterized several AHSS characteristics (i.e., metallurgy heat-treatment for required AHSS properties versus sheet thickness, state of internal stress, and adhesion of the CFRE to the steel as a function of sheet rolling and stamping preparation).

Results

The first step in the development process was to determine the optimal fiber length and fiber concentration in the epoxy resin system. For this program, recycled CF was used. Three fiber lengths (i.e., 100, 200, and 400 μm) were chosen. Three fiber lengths (100, 200, and 400 μm) were also chosen. Flat steel samples were then coated with CFRE and cross-sectioned for SEM analysis at ORNL. Figure II.1.F.1 shows the (a) longitudinal and (b) transverse views of the 400- μm fibers and (c) longitudinal and (d) transverse views of the 100-micron (c) and (d) fibers. As can be seen from the micrographs in the figure, there is a definite tendency for the fibers to be aligned along the direction of application.

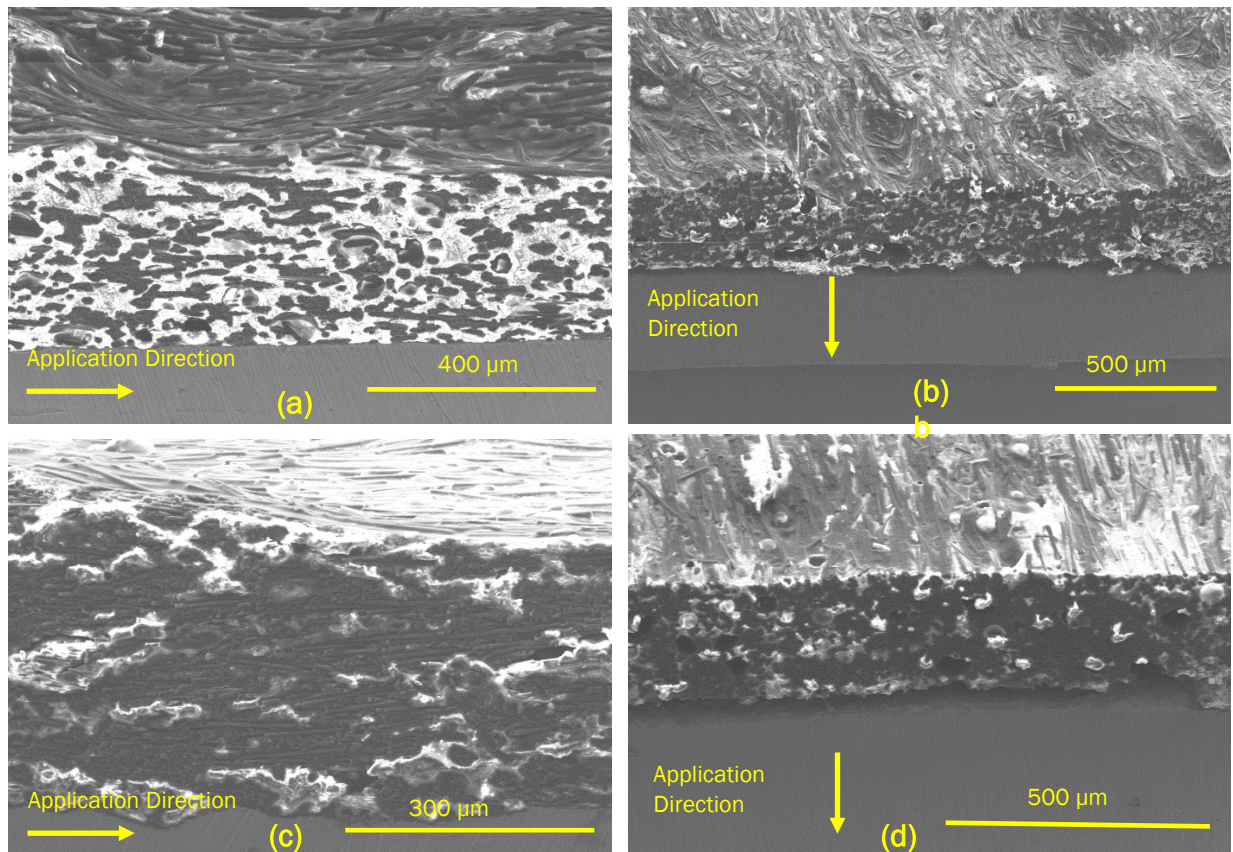


Figure II.1.F.1. Fiber orientation in CFRE in both directions when applied to the steel substrate. Images (a) and (b) are the longest fibers, while (c) and (d) are the shortest fibers. Source: ORNL

It was noted that the fibers were dispersed throughout the thickness of the composite layer; however, there was a greater concentration of fibers on the surface than in the bulk of the composite formed from the longer fiber samples. The shorter fibers seemed to be much more homogeneous in distribution throughout the thickness of the coating. Further investigation revealed that the longer fibers act more as a web or nest. Due to spray pressure and gravity, the resin would flow downward but not the fibers. Smaller fibers are freer to flow, while larger fibers bridge one another and stay in place as the resin flows downward resulting in great inhomogeneity. For this reason, any advantages gained from longer fiber lengths were negated by the lack of homogeneity that accompanied the longer fiber lengths. When samples were tested with varying fiber lengths and concentrations, it was found that the shorter fibers in lower concentration showed just as much improvement in properties as the longer fibers or higher fiber concentrations, as is shown in Table II.1.F.1.

Noted in the SEM evaluation was the presence of internal and external voids in the CFRE coating as shown in Figure II.1.F.2.(a) through (c), which increased with frequency as the fiber length and concentration increased. These may have contributed to a partial lack of increase in material properties as the fiber length and density increased. Also noted was a very uniform interface between the CFRE and the steel with very few voids being found. There was also a strong adherence of the epoxy resin to the fibers since fracture surfaces did not reveal bare fibers but rather fractures through the epoxy with residual epoxy still on the fiber surface as can be seen in Figure II.1.F.2.(d). As a result, the final coating selected was with the 100- μm fiber at the lowest concentration evaluated.

Table II.1.F.1. Flexural Strength in Newtons of Dual-Phase (DP500) Steel with the CFRE Coating Applied (CFRE Thickness is 0.5 mm for All Samples).

CF Parameters		Flexural Strength (Newtons)		
CF Content (wt.%)	Fiber Length (μm)	Steel Thickness (mm)		
		0.5	0.55	0.6
No Coating	-	22	29	32
Epoxy, No Fiber	-	25.22	32.37	36.18
15	100	35.78	43.88	54.58
20	100	38.31	44.81	55.26
25	100	37.36	45.38	54.72
15	200	36.69	38.56	54.14
20	200	38.04	44.01	56.62
25	200	38.46	48.64	56.88
15	400	37.07	38.67	53.14
20	400	39.98	45.95	55.16
25	400	39.12	45.12	56.47

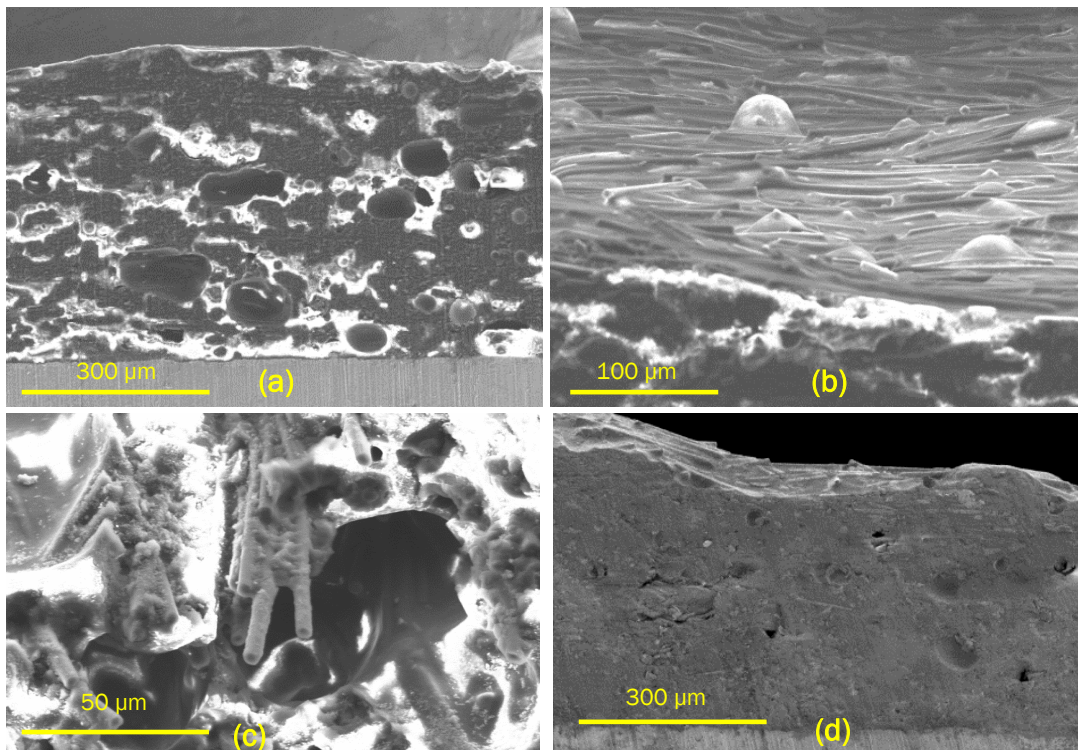


Figure II.1.F.2. Cross-section of CFRE coating on a DP500 steel substrate: (a) internal voids; (b) surface voids; (c) fiber failure at surface; and (d) adherence to the steel substrate. Source: ORNL.

Stiffening of door panels with the CFRE occurs by applying the coating to the interior section of the panel, thereby leaving the external side of the panel available for painting. Two methods for applying the CFRE coating were evaluated. The first was a complete door coverage, as depicted in Figure II.1.F.3.(a). The second was through a selective patch application, shown in Figure II.1.F.3.(b). The total coverage added 450 g of mass to the door while the coverage with isolated patches added 115 g for a 0.5 mm thick patch and 230 g for a 1.0 mm thick patch.



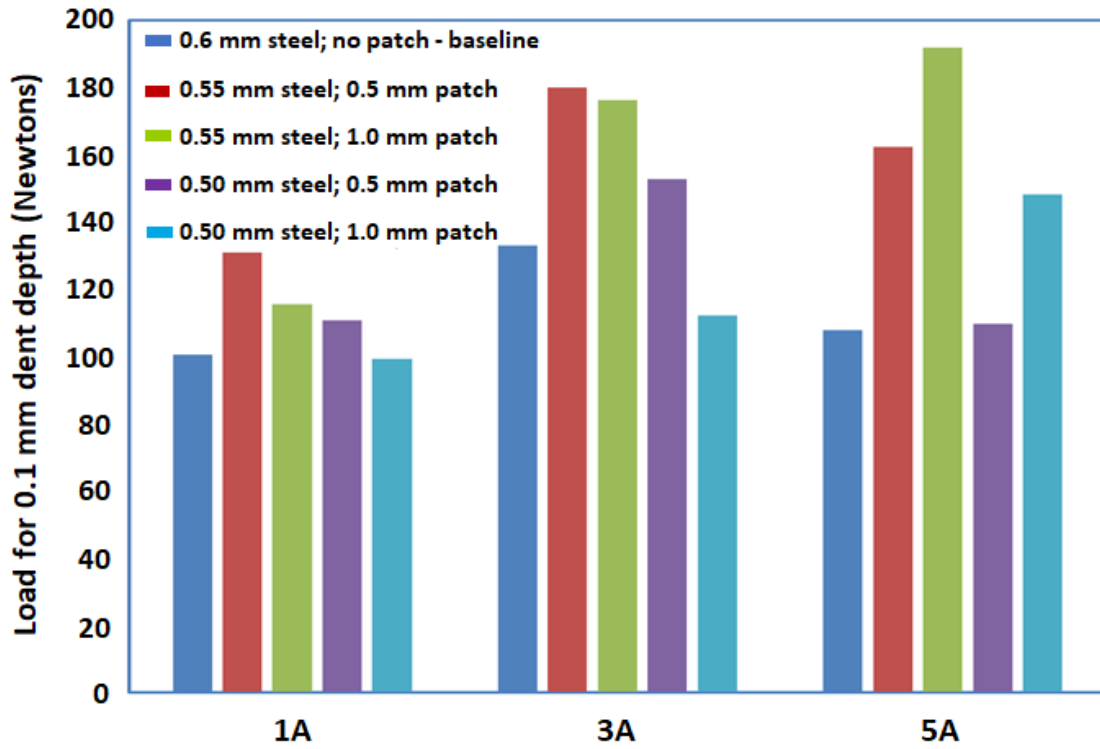
Figure II.1.F.3. Application of the CFRE for (a) total coverage and (b) isolated coverage. Source: ORNL.

The next issue to be addressed was the thickness of the CFRE coating that was to be applied. Bend tests were conducted on coated and uncoated steel samples varying both the coating thickness and the thickness of the steel substrate. As can be seen from Table II.1.F.2, a steel thickness of 0.80 mm could be replaced by a steel door thickness of 0.60 mm with a 0.5 mm CFRE coating.

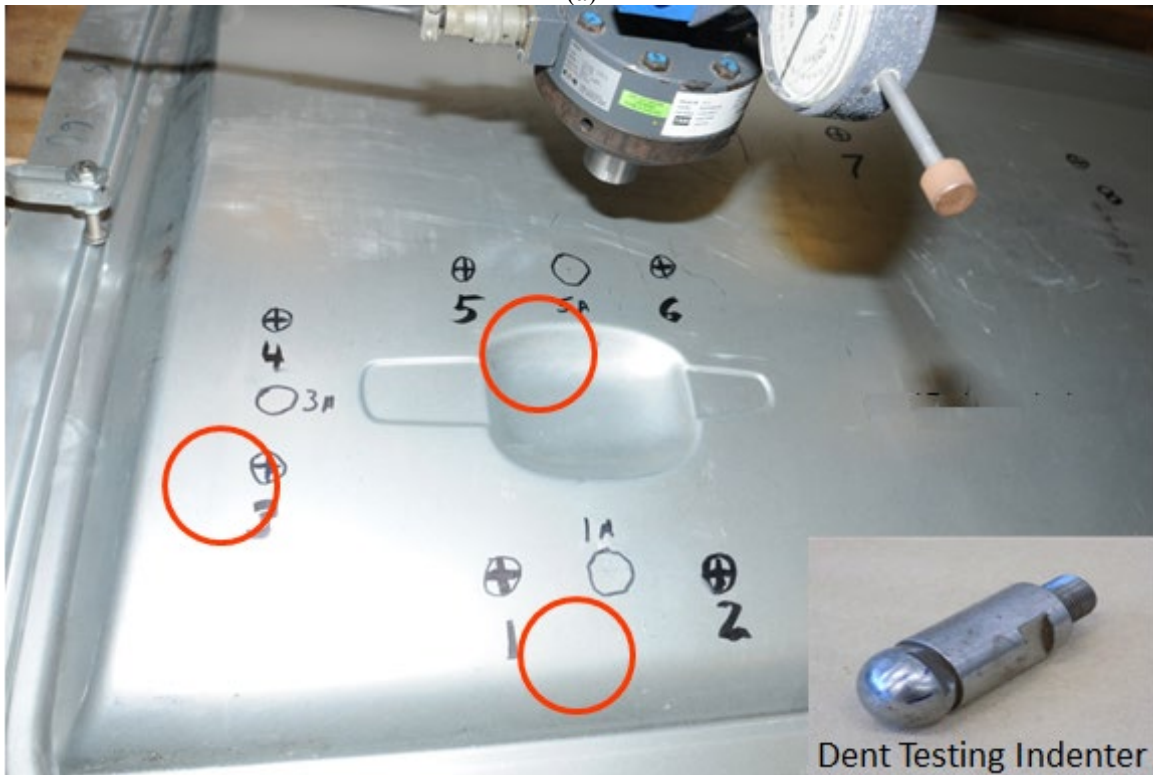
Table II.1.F.2. Flexural Strength (Newtons) of DP500 with the CFRE Coating Applied (CFRE and Steel Thickness Were Both Varied).

		Flexural Strength (Newtons)				
Steel Thickness (mm)		0.60	0.66	0.70	0.80	0.93
CFRE Thickness (mm)	0	25	30	35	42	52
	0.5	40	45	50	55	70
	1.0	60	65	70	80	95
	2.0	100	115	120	130	135

Dent testing of the coated and uncoated steel samples were conducted next. As seen in Figure II.1.F.4.(a), steel samples that varied from 0.5 – 0.6 mm thick were manufactured with the CFRE coating applied to the back side of the door panels. The patch was either 0.5 or 1.0 mm thick. A 25.4 mm diameter hemispherical indenter was used to apply a vertical load at the three locations shown. The amount of force necessary to create an indentation of 0.1 mm was then recorded. As can be seen from Figure II.1.F.4.(b), a 0.5 mm door panel with the patch applied provided the same or better dent resistance than a 0.6 mm door panel without the patch applied.



(a)



(b)

Figure II.1.F.4. (a) Dent test result for various thickness DP500 steel panels with and without CFRE patches applied. (b) Test sample showing the three test locations and the dent testing indenter. Source: ORNL.

Coefficient of thermal expansion measurements were necessary to model the interaction between the CFRE and the steel substrate during the paint-bake and usage cycles. Due to the anisotropic nature of the CFRE, it was necessary to make those measurements in each of the three primary directions. Thermal expansion measurements were performed using a Thermomechanical Analyzer Model TMA Q400 supplied by TA Instruments. Each test consisted of three cycles between ambient conditions up to 170°C at a constant heating/cooling rate of 3°C/min. Quartz disks were used between the test specimens and the platform and probe of the testing equipment to isolate the sample and prevent any reaction with the system.

All of the test specimens exhibited the same thermal expansion behavior. During the first cycle, they expanded, but experienced contraction between 90°C and 110°C, as illustrated by the plot in Figure II.1.F.5. After 110°C, the test specimens started to expand again until the maximum temperature of the cycle. The cooling segment of the first cycle followed the trend observed during the second and third heating/cooling cycles. It was found that the heating/cooling segments during cycles 2 and 3 were similar for all test specimens as also illustrated by the plot in Figure II.1.F.5. The experimental results were analyzed by taking the first derivative of the strain versus temperature data, which corresponds to the coefficient of thermal expansion. Then, the coefficient of thermal expansion was plotted as a function of temperature to determine its dependence on temperature. The analysis was performed over the temperature interval between 60°C and 160°C, as illustrated in Figure II.1.F.6. In some cases, it became necessary to break down the analysis into two temperature segments between 60°C and 100°C, and between 100°C and 160°C.

According to this analysis, the thermal strain experienced by these materials would be calculated as follows:

$$\varepsilon_{thermal} = \int_{T_1}^{T_2} \alpha(T) dT \quad (1)$$

where $\alpha(T)$ is the temperature-dependent coefficient of thermal expansion. Since the coefficient of thermal expansion has a linear dependence on temperature, as illustrated by Figure II.1.F.6, it can be expressed as follows where α_0 is the coefficient at initial conditions and α_1 is at final conditions:

$$\alpha(T) = \alpha_0 + \alpha_1 T \quad (2)$$

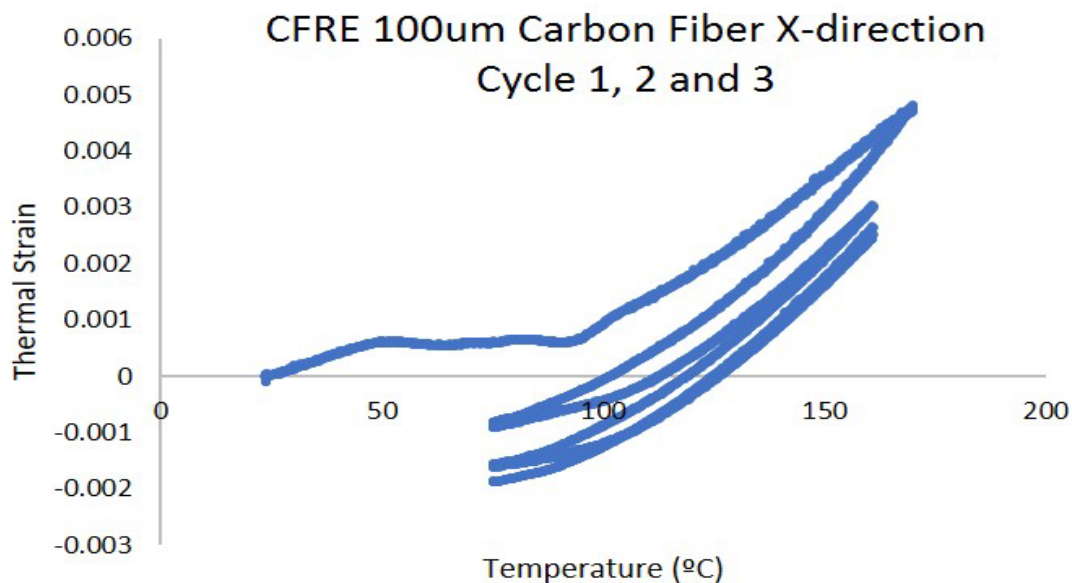


Figure II.1.F.5. Typical thermal expansion behavior exhibited by composite samples. After the transient observed during the heating segment of the first cycle, the curves have an increasing slope with temperature, indicating the thermal expansion behavior of the material is nonlinear. Source: ORNL.

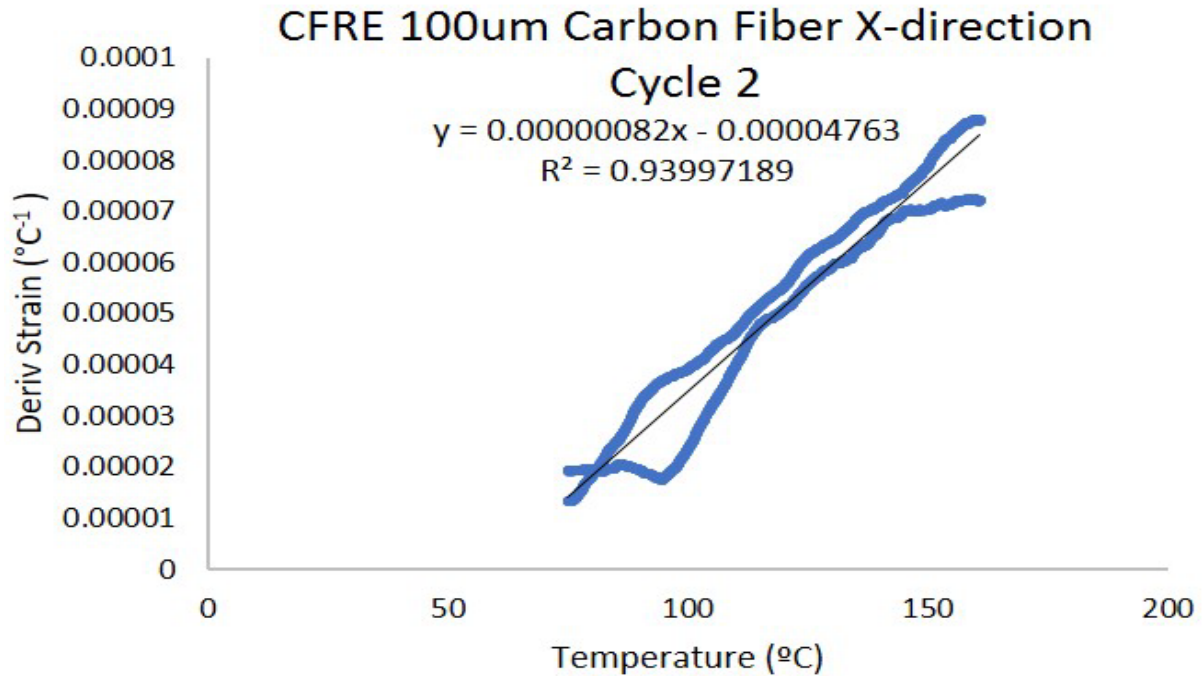


Figure II.1.F.6. Plot of the derivative of thermal strain with temperature as a function of temperature between 70 °C and 160 °C. Source: ORNL.

Table II.1.F.3 summarizes values of α_0 and α_1 for the two aforementioned temperature segments. The “X” direction is the application direction of the CFRE and the direction that most of the fibers are oriented. The “Y” direction is perpendicular to the “X” and the “Z” direction is through the thickness of the CFRE coating.

Table II.1.F.3. Coefficients α_0 and α_1 as a Function of Direction for X and Y Percentage CF-Containing CFRE.

Percentage of CFRE	Cycle 2 (100–160 °C)		Cycle 3 (100–160 °C)		Averages	
	α_1	α_0	α_1	α_0	Average α_1	Average α_0
Epoxy (no CFRE)	1.00E-07	1.63E-04	2.00E-07	1.45E-04	1.50E-07	1.54E-04
CFRE X% 100 μ m X-direction	4.20E-07	-1.61E-05	4.13E-07	-1.60E-05	4.17E-07	1.60E-04
CFRE X% 100 μ m Y-direction	4.51E-07	1.85E-05	5.02E-07	1.03E-05	4.77E-07	1.44E-05
CFRE X% 100 μ m Z-direction	3.71E-07	2.86E-04	3.16E-07	2.92E-04	3.44E-07	2.89E-04
CFRE Y% 100 μ m X-direction	7.92E-07	-4.33E-05	7.81E-07	-3.99E-05	7.86E-07	-4.16E-05
CFRE Y% 100 μ m Y-direction	4.17E-07	-3.69E-05	4.15E-07	-3.63E-05	4.16E-07	-3.66E-05
CFRE Y% 100 μ m Z-direction	5.68E-07	1.61E-04	4.93E-07	1.70E-04	5.31E-07	1.66E-04

The majority, if not all, of the INL work on this project will be carried out in FY 2019. Tests will begin immediately after the CFRE coated panels are received from Diversitak. The following tests are planned:

1. **SAE J2334 Corrosion Coupon Testing.** This will include:
 - A. Corrosion cycling of up to 100 CFRE bonded lap shear strength coupons of 1 in. x 4 in. dimensions.
 - B. Corrosion cycling of up to 100 CFRE coated flexural strength coupons of 1 in. x 6 in. dimensions.
 - C. Corrosion cycling of up to 50 CFRE coated evaluation coupons of 4 in. x 12 in. dimensions.

2. **SAE J2334 Corrosion Testing Body Panels.** This will include:
 - A. Corrosion cycling of up to four outer door panels.
3. **Environmental Corrosion Coupon Testing.** This will include:
 - A. Corrosion cycling of up to 100 CFRE coated flexural strength coupons of 1 in. x 6 in. dimensions.
 - B. Environmental cycling of up to 50 CFRE coated evaluation coupons of 4 in. x 12 in. dimensions.
4. **Environmental Corrosion Testing Body Panels.** This will include:
 - A. Environmental cycling of up to four CFRE coated outer door panels.
5. **Humidity Corrosion Coupon Testing.** This will include:
 - A. Humidity testing of up to 100 CFRE coated flexural strength coupons of 1 in. x 6 in. dimensions.
 - B. Humidity testing of up to 50 CFRE coated evaluation coupons of 4 in. x 12 in. dimensions.
6. **Humidity Corrosion Testing Body Panels.** This will include:
 - A. Humidity testing of up to four CFRE coated outer door panels.

Conclusions

- The fibers will preferentially align in the direction of the application.
- A more homogeneous CFRE is developed when shorter fibers in lower concentrations are used.
- Without CF in the epoxy, there is no improvement in the flexural strength of the panel.
- The strength enhancement differences are minimal between different ratios of fiber in the epoxy.
- The CF length did not result in a significant difference in the overall flexural strength. This may be due to the distribution efficiency of fiber in the epoxy as shown in the ORNL SEM data.
- Based on the viscosity and flexural strength, 15% loading by weight and 100 μm fiber is optimum in the formulation.
- The average strength improvement between a blank panel and the 0.5 mm CFRE coated panels range from 50 – 70% higher.
- The increase in flexural strength is linear with the increase in applied thickness.

Key Publications

1. Sadagopan, S., M. Kuo, M. Lizak, R. Robison, R. Eadara, T. Brewer, J. M. Joseff, C. D. Warren, and G. Ilevbare, 2018, “Door Lightweighting Using Ultra-Thin AHSS Reinforced with Low-Density CFRE Materials,” *Proceedings of the 17th Annual Great Design in Steels Conference*, May 16, 2018, Detroit, MI, USA.

References

1. Singh, H., and G. Coates, 2014, “Lightweighting with AHSS: Minimum Thickness Study & Application Guidelines, Version 5.0,” *Proceedings of the 13th Annual Great Design in Steels Conference*, May 14, 2014, Livonia, MI, USA.

II.2 Carbon Fiber & Polymer Composites

II.2.A Close Proximity Electromagnetic Carbonization (Oak Ridge National Laboratory)

Felix L. Paulauskas, Principal Investigator

Materials Science and Technology Division
Oak Ridge National Laboratory
1 Bethel Valley Road
Oak Ridge, TN 37831-6053
E-mail: paulauskasfl@ornl.gov

H. Felix Wu, Ph. D, DOE Technology Manager

U.S. Department of Energy
E-mail: mailto:felix.wu@ee.doe.gov

Start Date: October 1, 2015	End Date: September 30, 2018	
Project Funding (FY18): \$1,570,000	DOE share: \$1,500,000	Non-DOE share: \$70,000

Project Introduction

The close proximity electromagnetic carbonization (CPEC) project is a joint development project funded by DOE between 4XTechnologies (formerly RMX Technologies) and ORNL. Preliminary work on electromagnetic carbonization was jointly conducted by both institutions dating back to 2013. This former work is the impetus of the CPEC project. This report outlines the progress of the work on the CPEC project over FY 2018 building upon significant progress from FY 2017. By the end of FY 2018, the CPEC-4 building was still in progress because the construction experienced significant delays from some suppliers.

At the beginning of FY 2018, CPEC-3 was capable of producing low-temperature CF, on a continuous basis, with direct electromagnetic radiation. The output fiber was measured to have a density of 1.5g/cc or greater and, by November 2017, the final CF (after full carbonization) reached the milestone requirements. Additionally, the damages previously observed on the tow were eliminated by the isolation and mitigation of the root cause.

The modeling of the next iteration of the CPEC system, CPEC-4, began near the end of the previous FY 2017 and was completed in April 2018. To fulfill this task, the same computational electromagnetics model (CEM) as the one for CPEC-3 was used to model CPEC-4 interactions. For scalability and cost reasons, the design of CPEC-4 has been entirely revisited. The new design can process from 4 to 8 tows and work at a lower power per unit mass of material than the previous version. Running under optimal condition requires the use of an appropriate radio frequency (RF) generator (power supply). Eventually, CPEC-4 is expected to be more tunable than CPEC-3.

Two important events interrupted the continuity of the projects: (1) funding was stopped between October 1, 2017, and April 6, 2018; (2) the procurement of some components experienced significant delays up to several months:

- The funding status of this project remained uncertain until a conference call with DOE on April 5, 2018. The uncertainty of the budget had a strong impact on the organization of the project and its progress over this period. One of the major consequences was the postponement of the construction phase by approximately four months. Instead, the design phase, which was cheaper to operate, was extended with the aim to reduce the cost of fabrication of CPEC-4. Furthermore, despite the funding situation at the time

(i.e., February 2018), the remaining funds were dedicated to the order of the power supply, which was the component with the longest lead time. This action was undertaken in order to limit the delay of the foreseen construction phase.

- The second issue that the program encountered in FY 2018 is related to the procurement. Some suppliers experienced significant delays, up to almost six months in the case of the power supply.

These two events generated months of delay on the original schedule. First, the hold on the funding necessitated a modification of the DOE Annual Operating Plan for FY 2018, as well as an extension at no cost of six months into FY 2019 in order to secure enough time to complete the project. Thereafter, the six-month delay on the procurement of the power supply prevents on-time attainment of at least the last milestone of FY 2018 and the first of FY 2019. Nevertheless, several options are being investigated to mitigate the impact of this delay on the program.

Objectives

The objective of the project is to develop a faster and more efficient carbonization process than the conventional process. The concept is to elevate the temperature of the material only and to increase the throughput by approximately 30%, while producing the same or better quality CF. Also, it is expected to reduce unit energy consumption of the low-temperature carbonization stage in kWh/kg by approximately 50% (which represents about 5% of the cost-reduction on the CF overall manufacturing process). Physically, the CPEC technology will be scaled to a nameplate capacity of one annual metric ton and will demonstrate this capability by the end of the project.

Approach

The CPEC project is split into four major design and construction phases with each phase related to a separate experimental setup. These phases are reported in Table II.2.A.1. This chart shows the four phases of the project, from its preliminary work (FY 2013) to its end (FY 2019). All of the tasks accomplished in FY 2018 are encompassed in Phase 4. The two main tasks over the past year are the design and the construction of CPEC-4. CPEC-4 is the fourth iteration of electromagnetic low-temperature carbonization furnace, co-developed by ORNL and 4XTechnologies.

Table II.2.A.1. Phased Approach for the CPEC Project.

Phase	Name	Date	Status (Sept. 2016)	Description
1	CPEC-1	FY 2013	Completed	Demonstration of feasibility (static mode).
2	CPEC-2	FY 2016	Aborted	Upgrade of CPEC-1 (with automatic impedance matching); abandoned in favor of CPEC-2V.
	CPEC-2V	FY 2016	Completed	Optimization of the CPEC concept using a computational model.
3	CPEC-3	FY 2016	Completed	Physical construction of CPEC-2V (continuous process at lab-scale).
4	CPEC-4	FY 2017 FY 2018	In progress	Scale-up of CPEC-3 to a 1 ton/year furnace.

Results

CPEC-3 Validation

By the end of November 2017, four tests with similar run conditions were conducted with CPEC-3. These four tests produced fully carbonized batches with a relatively good homogeneity in their mechanical properties for tensile strength of about 300 Ksi and a modulus in the range of 22-25 Msi. These results are reported in Table II.2.A.2. They demonstrate that CPEC-3 can provide reproducible results. Furthermore, two of those batches exhibited simultaneously mechanical properties above 250 Ksi for the tensile strength and 25 Msi for

the modulus with a minimum of 1% strain (see the bold green text in Table II.2.A.2), which was the condition to satisfy the project milestone. Furthermore, the residence times were lower than required, maintaining the cost benefits of energy saving.

In the low-temperature carbonization stage using CPEC-3, temperature and residence time were the only parameters that were changed. The residence time is indicated in the last column as “Long” or “Short.” Both residence times in CPEC-3 are shorter than 90 seconds. The values highlighted in green bold text surpassed the dual programmatic requirements of 250 Ksi tensile and 25 Msi modulus simultaneously. No parameter optimization was undertaken.

Table II.2.A.2. Mechanical Properties of Fully Carbonized Samples at High-Temperature Carbonization and Constant Parameters.

Test #	Density (g/cc)	Diameter (Avg) μm	Std. Deviation	Tensile Strength (Avg) Ksi	Std. Deviation	Modulus (Avg) Msi	Std. Deviation	Strain (Avg) %	Std. Deviation	Residence Time
1	1.8032	8.05	0.35	348.70	77.50	23.42	1.84	1.49	0.28	Long
2	N/A	8.20	0.41	303.00	87.50	22.73	2.76	1.40	0.32	Short
2	1.7924	8.44	0.74	356.60	135.30	24.88	3.83	1.42	0.47	Long
2	N/A	8.00	0.80	254.20	88.90	21.42	2.59	1.22	0.43	Long
3	N/A	8.40	0.53	333.00	149.80	25.44	3.45	1.29	0.51	Short
3	N/A	8.22	0.63	292.00	91.70	22.79	3.31	1.27	0.27	Short
3	N/A	8.42	0.46	331.30	125.00	23.44	1.84	1.48	0.55	Long
4	N/A	8.09	0.62	354.60	97.60	23.64	2.42	1.48	0.32	Short
4	N/A	8.06	0.72	263.60	132.80	22.31	3.61	1.13	0.44	Short
4	1.8138	8.91	0.63	340.20	101.70	25.14	1.73	1.39	0.43	Long
4	1.8135	8.73	0.56	285.50	98.50	23.07	2.03	1.23	0.37	Long

CPEC-4 Process Design Using A CEM

The objective of the last reactor is different from its previous version. CPEC-3 was a lab-scale reactor designed for validation of a concept while being cost-effective, whereas CPEC-4 is a simulation of a part of a production line with a nameplate capacity of one metric ton per year.

The design phase of CPEC-4 began at the end of FY 2017, prior to the completion of the testing phase of CPEC-3. At that time, CPEC-3 had not yet produced the fiber samples whose properties are reported in Table II.2.A.2. However, the likelihood of success was sufficiently high to be confident in the concept and initiate the design of CPEC-4. While the concept of CPEC-3 was successful, its design showed some limitations, such as the difficulty of scalability and the lack of an ability to be tuned, among others. The design of CPEC-4 presented the opportunity to address most of the limitations experienced with CPEC-3. As a result, the concept of CPEC-3 was preserved, but the design and layout are different in many aspects, such as:

- the type of generator that has to be used
- the transmission line design
- the antenna system design
- the vessel design and size (enlarged)
- the integrated fiber handling system.

The design of CPEC-4 is larger and more complex than CPEC-3, with the theoretical capacity of being installed in line with the other pieces of equipment of a production line. Its design is proprietary and cannot be disclosed in this report.

CEM was used to model process interactions. On the process side, as shown on Figure II.2.A.1, the map of field density (pattern of radiation) of CPEC-4 is not homogeneous. However, the temperature elevation is efficient, and the radiation becomes homogeneous across the width of the tow at the end of the process, once the tow has completed its entire travel through the cavity. The pattern of radiation is static and unique to each tuning combination. Areas in red constitute the spots where the highest temperature is expected by the material. These red areas match with the pattern of radiation. Locally, the radiation pattern across the width of the tow is heterogeneous, but once integrated along the entire path through the setup, the amount of radiation across the width of the tow is homogeneous.

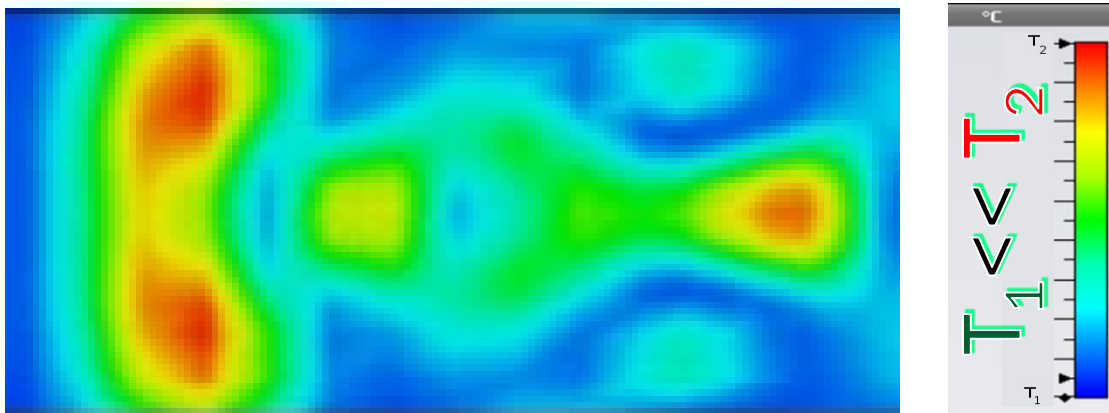


Figure II.2.A.1. Example of a CEM of a wide-tow (partial top view) traveling from left to right through a section of CPEC-4.
Source: 4X Technologies.

CPEC-4 CAD Hardware Design

The design of the setup was completed by June 30, 2018, using SolidWorks® three-dimensional (3D) computer-aided design (CAD) software. Whereas the CEM was required to model the electromagnetic field distribution inside of the cavity and provide a first 3D vision of the future entire setup, this 3D model does not match with the technical drawing standards. Indeed, the CEM is focused on electromagnetic performance rather than dimension and tolerances for manufacturability. Hence, the creation of a CAD was required to build each custom part of the vessel of CPEC-4.

The 3D CAD has been highly valuable for the specification of the peripheral functions of the setup, such as the purge, the exhaust system, and the management of physical constraints associated with the weight of the equipment or the available lab space. The high-level of details of this CAD document has been equally helpful for the assembly of this complex setup (i.e., management of the parts, method of assembly, etc.).

CPEC-4 Construction

Construction began at 4XTechnologies in June 2018 with the modification of existing structures and the installation of the frame designed to receive all the components of the vessel, as well as the fiber handling system. However, the procurement started sooner with the purchase of the power supply (RF generator) and its cooling system.

As of September 30, 2018, the vessel itself is totally assembled and adjusted. Nevertheless, some components are still missing due to supplier-side delay in the procurement. Additionally, the electrical power available in the facility was insufficient for the power supply (RF generator). For administrative and legal reasons, the solution that was originally planned was blocked in late July. As of September 30, 2018, a backup solution has been implemented. As a result, at the end of FY 2018, the construction of CPEC-4 is not completed, and the setup is not operational and cannot be entirely commissioned. Therefore, milestone to have CPEC-4 commissioned on September 30, 2018 is not completed.

Delays on CPEC-4

Whereas most of the delays related to hardware install or suppliers will be cleared in the first few days of FY 2019 (e.g., power in the facility, transmission line, and fiber handling system), the power supply (RF generator) is still not planned to be delivered for several months.

The delay on supplying power in the facility was discussed previously. This task was scheduled to be completed by December 2018.

The fiber handling system is almost completed. Although this system experienced a delay of more than six weeks, it is now almost complete. As of September 30, 2018, only one minor issue remains to resolve with the system software. This could have been resolved during the installation at 4XTechnologies, but because of the delays by other suppliers, it has been agreed with the manufacturer not to ship the system before its completion. This equipment was shipped to 4XTechnologies in October 2018.

The transmission line experienced a four-week delay due to an issue of procurement by the manufacturer. As of September 28, 2018, this equipment had been shipped to 4XTechnologies.

The generator, however, deserves special attention because as of September 30, 2018, it is the limiting factor to the progress of the project. The generator of interest is a critical element to the success of this project, because the design of the applicators relies on some of its specific features. To mitigate the risks of delay on this, it was ordered by the earliest date possible, February 21, 2018, even though at that time the funding status of the project remained uncertain. Despite this precaution, the manufacturer experienced more technical issues than expected. The most recent one occurred in September 2018, while testing a sub-component after manufacturing. The system that will be used by this project requires several of these sub-components in series to operate at the expected level of performance. This failure in the testing phase after manufacturing created an additional delay of approximately three months.

Several options are being investigated for a backup solution. If one of them fits within the established budget and helps with the reduction of the commissioning time, it will be implemented. However, as of September 28, 2018, none of the considered options satisfy the technical and financial requirements simultaneously. Consequently, they can only be temporary.

Conclusions

During FY 2018, the concept of CPEC-3 was validated by reaching the project milestone on November 30, 2017. By that time, the design of the next iteration (CPEC-4) was initiated. The effort of the first quarter was mostly dedicated to development of the applicators and the inner cavity of the vessel using a CEM. The funding issue experienced by this project over the first two-quarters of the fiscal year imposed a delay on the construction phase of approximately four months. Meanwhile, the effort was maintained on the CEM with an approach of cost optimization for the future build. With funding restored to its initial level, the construction phase was initiated with the completion of a 3D CAD model, detailed mechanical drawings, and the specification of the sub-components with long lead time that had to be purchased (with the exception of the power supply that was already ordered). An extension of six months at no additional cost was successfully negotiated between 4XTechnologies, ORNL, and DOE.

The setup of the assembly began when the first parts were received at 4XTechnologies in June 2018. The last quarter of FY 2018 was dedicated to the specification and the order of the parts with the shortest lead time.

At the end of FY 2018, the setup is not complete and is unable to be commissioned, which is the completion criteria for another project milestone. Four items/tasks experienced some delay: (1) the appropriate power in the facility; (2) the fiber handling system; (3) the transmission line; and (4) the power supply (RF generator). While the resolution of the issues related to the three first items is imminent, the one involving the power supply (RF generator) will affect the next project milestone, and likely the entire milestone schedule might have to be revisited. To mitigate the consequences of the delay on the power supply (RF generator), backup solutions were investigated.

Acknowledgements

This research was sponsored by DOE-EERE, VTO, and performed at ORNL, managed by UT-Battelle, LLC, for DOE under contract DEAC05-00OR22725.

II.2.B Carbon Fiber Technology Facility (Oak Ridge National Laboratory)

Merlin Theodore, Principal Investigator

Energy and Environmental Sciences
Oak Ridge National Laboratory
1 Bethel Valley Rd.
Oak Ridge, TN 37831
E-mail: theodore@ornl.gov

Amit Naskar, Co-Principal Investigator

Oak Ridge National Laboratory
1 Bethel Valley Rd.
Oak Ridge, TN 37831
E-mail: naskarak@ornl.gov

Rich Davies, Co-Principal Investigator

Oak Ridge National Laboratory
1 Bethel Valley Rd.
Oak Ridge, TN 37831
E-mail: daviesrw@ornl.gov

H. Felix Wu, Ph. D, DOE Technology Manager

U.S. Department of Energy
E-mail: mailto:felix.wu@ee.doe.gov

Start Date: March 1, 2011	End Date: Project continuation evaluated annually
Project Funding (FY18): \$1,000,000	DOE share: \$1,000,000 Non-DOE share: \$0

Project Introduction

In March 2009, DOE-EERE issued a competitive call for proposals to construct and operate a highly flexible, highly instrumented, LCCF technology facility for demonstrating and evaluating new low-cost manufacturing technologies at a pilot-scale. ORNL responded to the call and was awarded the project. Construction of the CFTF began in March 2011, and the facility, a revolutionary pilot production plant pursued under DOE's Clean Energy Manufacturing Initiative, was commissioned for operations in March 2013.

The CFTF offers a unique, highly flexible, highly instrumented CF line for demonstrating advanced technology scale-up and for producing market development volumes of prototypical CFs. The CFTF's unique capabilities, including the flexibility to process a range of feed stocks and product forms, are unmatched anywhere in the world. Designed to bridge what has been called the "valley of death" between laboratory research and commercial scale deployment of LCCF technologies, the CFTF fills a critical need for support for industrial competitiveness in the manufacture of CF in this nation.

The semi-production-scale facility is capable of producing up to 25 tons of CF each year (this estimate is based on processing with 24k polyacrylonitrile (PAN) precursor in tow format). In addition to a conventional conversion line, the CFTF has a melt-spun precursor fiber production line with a rated capacity of 65 tons per year. The 42,000 square foot facility has the capacity for future expansion to include the addition of an advanced technology conversion line.

Objectives

The objective of this project is to develop LCCF from alternative precursors and accomplish the safe and reliable operation of the CFTF to further DOE's objectives for large-scale commercialization of LCCFs. The tasks covered under these agreements are co-funded by the VTO and the Advanced Manufacturing Office in support of DOE-EERE's efforts in transitioning technologies to industry, specifically with respect to LCCF composite materials in high-volume energy applications. The CFTF serves as a national resource to assist industry in overcoming the barriers of CF cost, technology scaling, and product and market development. The CFTF is intended to be the bridge from R&D to deployment and commercialization of LCCF.

Approach

The CFTF is open for tours so that industry and others can see the technology and process science being developed to produce LCCF with industry-appropriate mechanical properties from alternative precursor materials. Currently, no commercial manufacturer of this particular LCCF exists, so the CFTF plans to identify cost-effective alternative sources of precursors based on availability, C yield, cost, and spinnability. Once the chemistry of the precursor is developed and baseline properties of 250 Ksi tensile strength and 25 Msi modulus are met, a sufficient amount of material will be produced for scaling up to the next level at CFTF. Staff members working at CFTF then develop process conditions for converting the precursor material into LCCF exceeding baseline properties. Enough will be produced for deployment to industry to evaluate, thus showcasing the quality of the LCCF on a multitude of end-user platforms. This work is intended to produce industry demand for the technology. CFTF staff members continue to hold discussions with industrial partners that are interested in scaling the processes being developed at CFTF. The financial investment for industry to scale the technology is significant and thus not quickly decided upon. One CFTF mission is to transition this technology to industry for scaling, but numerous technical challenges remain that must be overcome to further reduce the risk for industry to implement the technology. These technical challenges are being addressed at the CFTF in collaboration with industry in order to reduce implementation risks. Some of these challenges are handling the large-tow, increasing throughput, splicing and splitting the large-tow, and developing appropriate sizing for the LCCF for specific composite applications. The CFTF continues to be a training ground for technical staff in the production of CF.

Key strategies to be implemented by the project in FY 2018 include:

- Establish and perform collaborative R&D projects to reduce technical uncertainties. This task will investigate process variables and determine quantitative relationship to oxidation time, process throughput, tensile properties, product quality, and variability.
- Investigate CF intermediate forms and technical challenges in composite applications. Under this task, an inventory of large-tow CF with documented and consistent properties will be produced and supplied to composites manufacturers to reveal and understand knowledge gaps in the application of wide-tow textile acrylic fiber based in vehicle and industrial composites. This task will also investigate new intermediate product forms to enable the improved downstream use of wide-tow CF.
- Investigate potential alternative CF precursors. This task will select a candidate precursor not previously studied and investigate effects of supplier-to-supplier variations in precursor chemistry and physical characteristics on product variability and performance.
- Establish artificial intelligence -based data analysis framework and correlate process data to product characteristics. This task will evaluate the current data management architecture recorded in the Wonderware Historian database and evaluate its fit with and usefulness in a machine-learning environment.
- Investigate and develop in process measurement, sensing, and control methods. This task will collect data on the three tested concepts to develop correlations between the generated data and physical CF.

Results

Visitors/Tours

In FY 2018, the CFTF hosted 579 visitors representing 171 organizations.

Awards





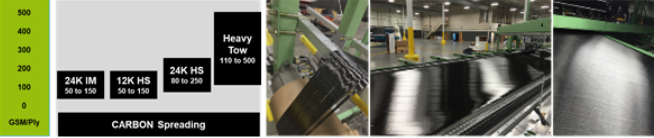
ORNL received a 2018 Excellence in Technology Transfer Award from the Federal Laboratory Consortium for Technology Transfer for strategic advancements in CF manufacturing and the development of the CFTF [1]. The award names ORNL's James Roberto, Ron Ott, Alan Liby, Tom Rogers, Michael Paulus, Amit Naskar, Nestor Franco, Jesse Smith, Marc Filigenzi, and Tammy Graham.

Joint Projects/CF Intermediate Forms



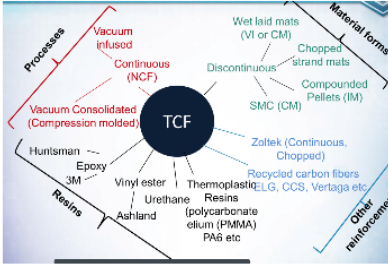


The CFTF has generated 26 industrial/ORNL joint projects in FY 2018. The partnerships are listed in Table II.2.B.1. Highlights from a few projects were presented in a panel discussion entitled "Working with Textile CF" at the Institute for Advanced Composites Manufacturing Innovation (IACMI) Summer Annual Meeting from July 24–27, 2018, in Knoxville, TN, USA. Other highlights are described in Figure II.2.B.1. The International Manufacturing Technology Show also featured the joint Fender project [2-3] with ORNL/IACMI/Techmer PM (a supplier of additives to plastics and fibers)/Michigan State University (MSU) at the IMTS Conference from September 10–15, 2018, in Chicago, IL, USA.

Table II.2.B.1. Industry/ORNL joint projects.

Joint Projects			
CCS/UT/IACMI Chomarat	CCS/IACMI University of Southern Mississippi	UTK College of Architecture & Design Research Studio	CCS/IACMI Composites Recycling Technology Facility
Sandia/Martin Pultrusion	CCS/IACMI Gates Corporation	National Spinning Co., Inc.	MDF/NTRC-2 (Vlastimil)/Berndorf Band Group
Mitsubishi Heavy Industries America, Inc.	CCS/IACMI Technical Fibre Products (TFP)	Polimotor LLC	ORNL/MAE S.p.A
Plastic Omnium Auto Exterior	ORNL Building Envelopes & Urban Systems Research/Chattanooga	CCS/IACMI MSU	CCS/IACMI/Neenah
CCS/IACMI Volkswagen Group of America	CCS/IACMI Dow/Ford	CCS/IACMI Magna	Ascend Manufacturing LLC
CCS/IACMI Cytec	USAF Research Laboratory	Sumitomo Bakelite North America (SBNA)	ORNL Building Envelopes & Urban Systems Research/MDF
CCS/IACMI McCoy	CCS/IACMI Techmer PM		

Project Team	Project Objective	Summary
ORNL/IACMI/ Techmer PM/MSU	<p>Demonstrate large scale parts using Textile Carbon Fiber</p>  	<p>ORNL, in collaboration with TechmerPM and IACMI, successfully injection molded >20 Saturn fenders at IACMI's Scale-Up Research Facility (SURF) using ORNL's textile PAN-based low-cost carbon fiber (TCF). This achievement marks the first time a full part has been molded with ORNL textile PAN LCCF and the first time IACMI successfully produced a functional part at SURF in Michigan.</p> 
ORNL/IACMI/ MSU	<p>Evaluate the feasibility of using textile carbon-fiber for large-scale, cost-effective manufacturing, in-specific: stitch-bonding technique. To identify applications, manufacturing efficiency, material characterization parameters, etc., and to provide recommendations for possible applications leading to rapid transition of lab-scale successes to industrial applications (with constant interactions with CFTF).</p>	 <p>Lay-stitch Method using TCF, Pre-infused Textile Preform Control Arm (Net-Shape), and Epoxy Infused VARTM Control Arm finished Part.</p>
ORNL/IACMI/ Chomarat	<p>Produce non-crimp fabric using textile carbon fiber TCF. The NCF will be used for composites fabrication trials by IACMI core partners and members. In addition, it will also be tested to grow the composite material properties database for TCF reinforced composites. Fabrication methods will include wet lamination, liquid compression molding and liquid infusion variations, including VARTM and High-Pressure RTM.</p>	 <p>⁴Non-crimp fabric improved handleability over UD with similar performance and an increase in performance over woven. It can provide a wide range of fabric areal weights & fiber orientations, 110 – 500 gsm/ply, using TCF with a single input. A 457 K TCF was assembled and fabricated into non-crimp stitched fabric provides continuous fiber format for Textile Carbon Fiber that can be processed with all standard manufacturing methods.</p>

(a)

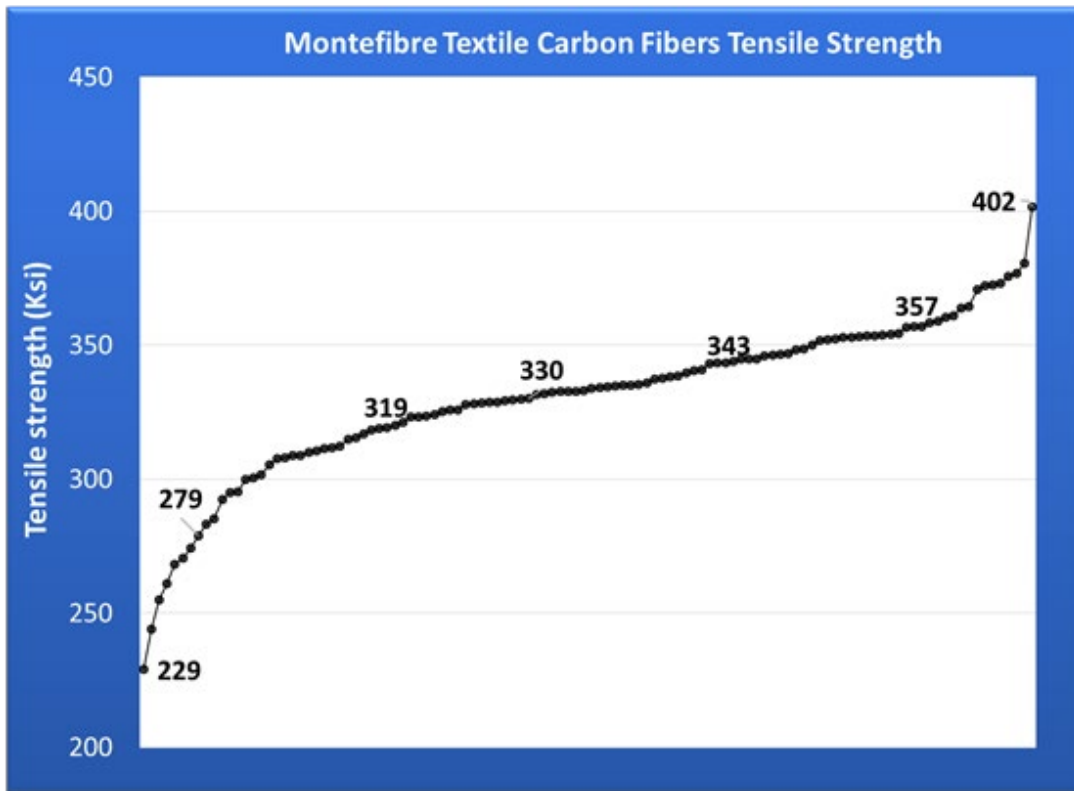
<p>ORNL/IACMI/McCoy Machinery</p>	<p>One of the remaining barriers to commercial deployment of textile carbon fibers is the current lack of capability to package these textile carbon fibers so that they can be efficiently and reliably used for producing composite intermediates or composite structures. This project develop commercially relevant packaging and payout technology for textile carbon fibers and demo its utility in non-crimp fabric production.</p>	 <p>⁵The team have designed and built a take-up winder to accommodate the trials for new packaging options. This packaging will be a cost-effective means of, not only winding the fiber, but also transporting and processing it downstream.</p>																																																
<p>ORNL/IACMI/CRTC</p>	<p>This project is to develop/evaluate chopping techniques for TCF sized with various sizing and chop length.</p>	<p>CRTC have designed and build a carbon fiber chopper that can chopped un-sized TCF and sized TCF with various sizing. Fibers were chopped at various length ranging from 25 mm - 0.025 mm.</p> 																																																
<p>ORNL/IACMI/UT</p>	<p>This project is undertaking a study to generate a basic TCF properties database and use in carbon fiber composites. The database generated will be used to aid IACMI focus areas such as design, modeling and application development.</p> 	<p>The TCF database is being generated evaluating TCF coated with a variety of sizings mixed in different resin systems for evaluation in several compositing methods. This database will be continuously updated.</p> <p>Studies includes: Shielding effectiveness, Flammability Studies, Resin infused composites, Vacuum infused composites, Battery Mold composites, Composite Tensile properties, Compression strength, SMC evaluation</p> <table border="1" data-bbox="769 701 992 919"> <thead> <tr> <th colspan="3">Resin infused-Vacuum Consolidated</th> </tr> <tr> <th>Property</th> <th>TCF (66% V_f) Epoxy</th> <th>Zoltek (68% V_f) Epoxy</th> </tr> </thead> <tbody> <tr> <td>Tensile strength (MPa)</td> <td>548 (79.46 ksi)</td> <td>1001 (145.18 ksi)</td> </tr> <tr> <td>Tensile modulus (GPa)</td> <td>84</td> <td>77</td> </tr> <tr> <td>Flexural strength (MPa)</td> <td>655 (95 ksi)</td> <td>758 (109.93 ksi)</td> </tr> <tr> <td>Flexural Modulus (GPa)</td> <td>73</td> <td>75.5</td> </tr> <tr> <td>Compression Strength (MPa)</td> <td>456 (66.13 ksi)</td> <td>470 (69.47 ksi)</td> </tr> <tr> <td>Compression Modulus (GPa)</td> <td>72</td> <td>69</td> </tr> <tr> <td>ILSS (MPa)</td> <td>45 (6.52 ksi)</td> <td>52 (7.54 ksi)</td> </tr> </tbody> </table> <table border="1" data-bbox="769 926 992 1129"> <thead> <tr> <th colspan="3">Vacuum Infused</th> </tr> <tr> <th>Property</th> <th>TCF (41% V_f) Epoxy</th> <th>Zoltek (48% V_f) Epoxy</th> </tr> </thead> <tbody> <tr> <td>Tensile strength (MPa)</td> <td>550 (79.77 ksi)</td> <td>700 (101.52 ksi)</td> </tr> <tr> <td>Tensile modulus (GPa)</td> <td>60 (8.7 Msi)</td> <td>58 (8.41 Msi)</td> </tr> <tr> <td>Flexural strength (MPa)</td> <td>600 (87.02 ksi)</td> <td>750 (108.77 ksi)</td> </tr> <tr> <td>Flexural Modulus (GPa)</td> <td>50 (7.25 Msi)</td> <td>48 (6.96 Msi)</td> </tr> <tr> <td>ILSS (MPa)</td> <td>NA</td> <td>48 (6.96 ksi)</td> </tr> </tbody> </table> 	Resin infused-Vacuum Consolidated			Property	TCF (66% V _f) Epoxy	Zoltek (68% V _f) Epoxy	Tensile strength (MPa)	548 (79.46 ksi)	1001 (145.18 ksi)	Tensile modulus (GPa)	84	77	Flexural strength (MPa)	655 (95 ksi)	758 (109.93 ksi)	Flexural Modulus (GPa)	73	75.5	Compression Strength (MPa)	456 (66.13 ksi)	470 (69.47 ksi)	Compression Modulus (GPa)	72	69	ILSS (MPa)	45 (6.52 ksi)	52 (7.54 ksi)	Vacuum Infused			Property	TCF (41% V _f) Epoxy	Zoltek (48% V _f) Epoxy	Tensile strength (MPa)	550 (79.77 ksi)	700 (101.52 ksi)	Tensile modulus (GPa)	60 (8.7 Msi)	58 (8.41 Msi)	Flexural strength (MPa)	600 (87.02 ksi)	750 (108.77 ksi)	Flexural Modulus (GPa)	50 (7.25 Msi)	48 (6.96 Msi)	ILSS (MPa)	NA	48 (6.96 ksi)
Resin infused-Vacuum Consolidated																																																		
Property	TCF (66% V _f) Epoxy	Zoltek (68% V _f) Epoxy																																																
Tensile strength (MPa)	548 (79.46 ksi)	1001 (145.18 ksi)																																																
Tensile modulus (GPa)	84	77																																																
Flexural strength (MPa)	655 (95 ksi)	758 (109.93 ksi)																																																
Flexural Modulus (GPa)	73	75.5																																																
Compression Strength (MPa)	456 (66.13 ksi)	470 (69.47 ksi)																																																
Compression Modulus (GPa)	72	69																																																
ILSS (MPa)	45 (6.52 ksi)	52 (7.54 ksi)																																																
Vacuum Infused																																																		
Property	TCF (41% V _f) Epoxy	Zoltek (48% V _f) Epoxy																																																
Tensile strength (MPa)	550 (79.77 ksi)	700 (101.52 ksi)																																																
Tensile modulus (GPa)	60 (8.7 Msi)	58 (8.41 Msi)																																																
Flexural strength (MPa)	600 (87.02 ksi)	750 (108.77 ksi)																																																
Flexural Modulus (GPa)	50 (7.25 Msi)	48 (6.96 Msi)																																																
ILSS (MPa)	NA	48 (6.96 ksi)																																																
<p>ORNL/IACMI/Prolink</p>	<p>Develop evaluation of concepts for pre-pegging with TCF. If evaluations are promising, we expect to follow up with an IACMI project to develop and demonstrate high-rate and high-quality prepreg production utilizing TCF.</p>	<p>The team successfully fabricated pre-peg material using TCF and PLR20 Thermoset Epoxy Resin with an areal weight ~110g/m².</p> 																																																

(b)

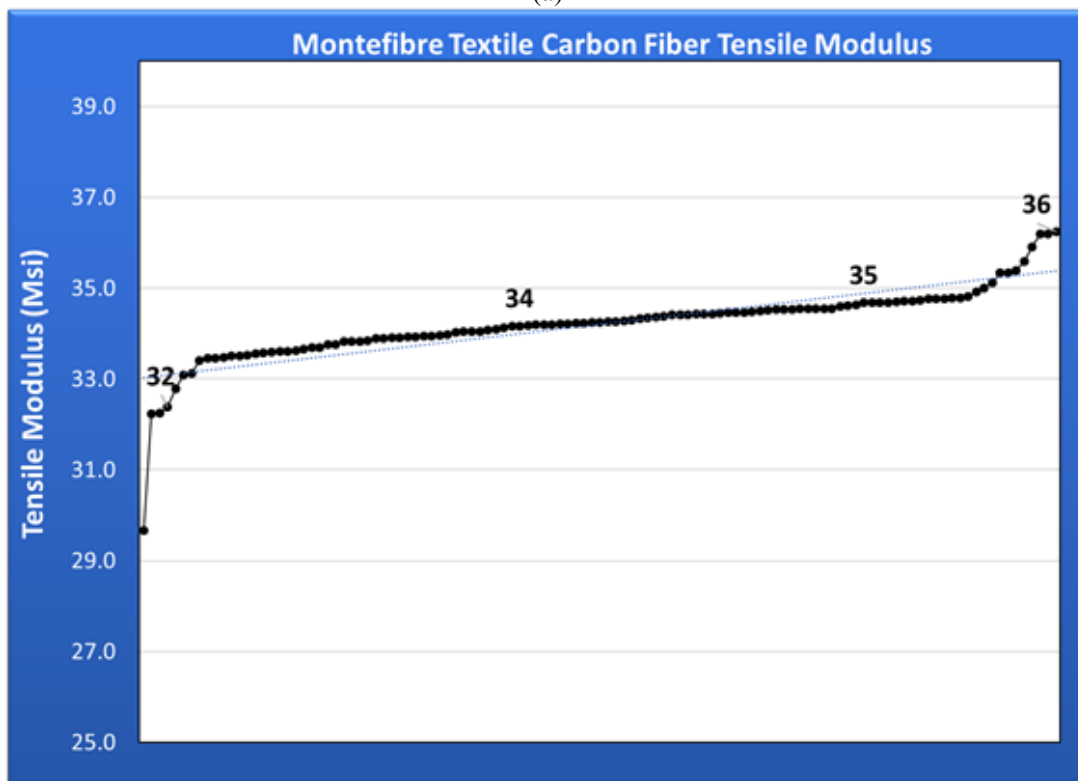
Figure II.2.B.1. (a) and (b) Highlights from joint projects [4-6]. Source: ORNL.

Identify Source of Alternative Precursor

CFTF recently joined forces with Montefibre Group, a European acrylic textile fiber producer that has the capacity to process 100,000 tons per year of cost-efficient textile polyacrylonitrile (T-PAN)-based precursor material. This precursor material was processed into CF with standard properties within 24 hours. The highest average properties achieved to date are 402 Ksi tensile strength, and 36 Msi tensile modulus as shown in Figure II.2.B.2. The team continuous R&D efforts is evident in the improvement of the tensile properties.



(a)



(b)

Figure II.2.B.2. Tensile properties for Montefibre textile CF: (a) tensile strength and (b) tensile modulus. Source: ORNL.

Data Analytic Framework for CF Manufacturing

The data analytics framework for CF manufacturing has been established and consists of five modules: Data Management & Tracking, Data Visualization, Computer Vision/Quality Control, Sensing, and Machine-Learning.

Python scripts were developed for capturing the data for the machine-learning module. These scripts allow the team to extract fractions of the CF manufacturing process database and partition it based on their provenance.

Concepts shown in Figure II.2.B.3 developed for the computer vision and sensing modules were tested and proven viable for information of the precursor as it is processed into CF. *In-situ* measurements of CF tow enable process variables to be tuned and optimized during the manufacturing process improving quality, efficiency, throughput, structure-property relationship and correlations, better process capability and control, thus reducing energy usage and scrap.

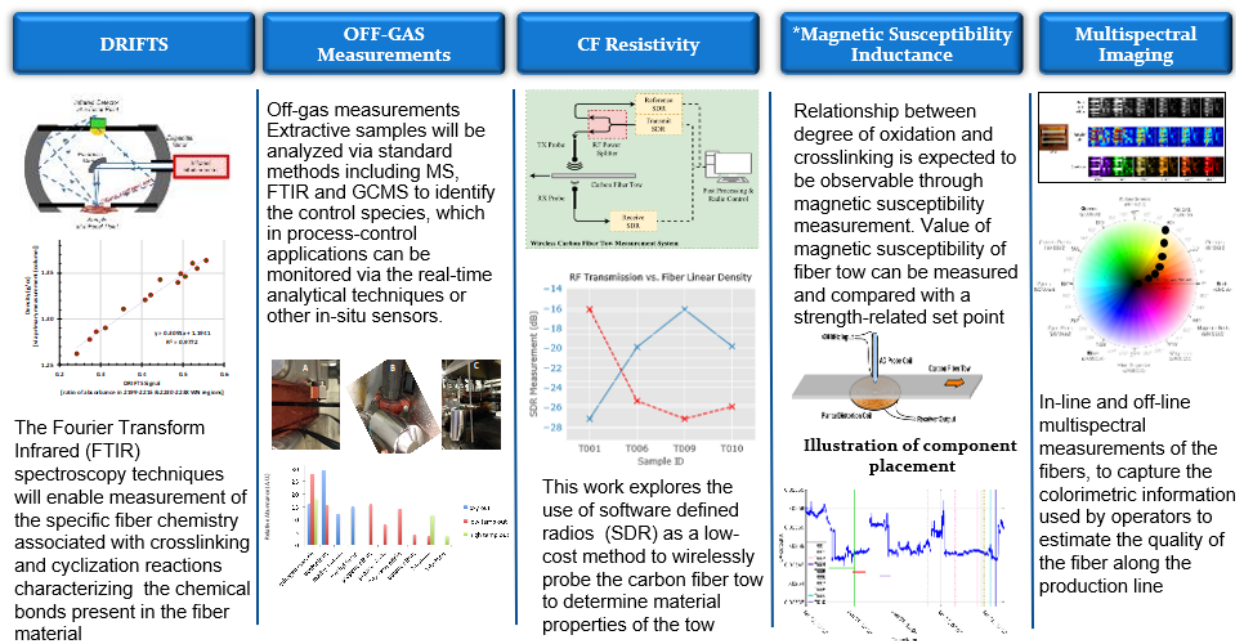


Figure II.2.B.3. *In-situ* concepts for CF manufacturing. Source: ORNL.

Conclusions

Significant progress was made in developing processes to convert textile acrylic fiber to CF with mechanical properties suitable for use in vehicle and other industrial products. The ORNL Partnerships Office solicited interest from industry to license intellectual property related to increased throughput of textile acrylic fiber.

Lemond Composites and three other companies (not yet publicly announced) have licensed provisional patents for production of CF from textile precursors. A total of three Cooperative Research and Development Agreements (CRADAs) were established to support reducing the technical uncertainties enabling domestic commercial sources of textile CF. Two new CRADAs, NFE-17-06665 and NFE-18-07246, were executed in FY 2018.

The data analytics framework established for CF manufacturing will aid in reducing costs; however, much process development work remains to enable commercial production of CF using textile precursors, a clear pathway to reduction of up to 50% of the cost of production relative to existing commercial operations has been established.

Key Publications

1. Humphries, J. R., R. A. Kisner, S. M. Killough, Y. Polsky, and M. Theodore, 2018, “CF tow inspection technique using software defined radios,” *IEEE Sens. Lett.*, Vol. 2, No. 4, Art. 6000904. doi: 10.1109/LESENS.2018.2877304.
2. Singh, D. K., A. Vaidya, U. Vaidya, and M. Theodore, 2018, “Finite element modeling of the fiber-matrix interface in polymer composites,” submitted for publication to *Polymer Composites*.
3. Uday, V., D. K. Singh, V. Thomas, A. Vaidya, and M. Theodore, 2018, “Surface and interface characterization of CFs,” submitted for publication to the *Journal of Composite Materials*.
4. Joint Laboratory-Directed Research and Development proposal, “Intelligent Streaming Data and Event Analysis for Sensors (IDEAS)” LOIS Project 9412, awarded funding.

References

1. The Federal Laboratory Consortium for Technology Transfer, 2018 FLC Award Winners, 2018. <https://www.federallabs.org/successes/awards/2018-flc-award-winners>.
2. The 2018 IndustryWeek Manufacturing and Technology Conference and Expo, Raleigh, NC, May 8, 2018. https://www.youtube.com/watch?v=NRk_v3fPyCI.
3. The Institute for Advanced Composites Manufacturing Innovation (IACMI), Knoxville, TN, September 9, 2018. <https://iacmi.org/2018/09/09/iacmi-and-oak-ridge-national-laboratory-showcase-breakthroughs-in-materials-speeds-and-technologies-at-imts/>.
4. IACMI Members Meeting, “ORNL Textile Carbon Fiber C-Ply™,” Oak Ridge National Laboratory, Knoxville, TN, July 24–26, 2018. https://iacmi.org/wp-content/uploads/2018/08/TextileCF_Chomorat_Summer2018MM1.pdf.
5. Theodore, M. “Working with Textile Carbon Fibers (TCM),” Presentation at the IACMI Members Meeting, Oak Ridge National Laboratory, Knoxville, TN, July 24–26, 2018. https://iacmi.org/wp-content/uploads/2018/08/TextileCF_McCoy_Summer2018MM.pdf.
6. “Montefibre Carbon,” Presentation at the IACMI Members Meeting, Oak Ridge National Laboratory, Knoxville, TN, July 24–26, 2018. <https://iacmi.org/wp-content/uploads/2018/09/MontefibreCarbon.pdf>.

Acknowledgements

The CFTF Team would like to acknowledge H. Felix Wu, Ph. D, DOE Technology Manager; Craig Blue and Mohammad Khaleel, IACMI Institute; and James Parks II, Raynella Connatser, Vincent Paquit, James Humphries, Yarom Polsky, Roger Kisner, Dr. Mongi Abidi, Dr. Vaidya Uday, Cliff Eberle, Michael Lance, Edward Western, William Peter, Edgar Lara-Curzio, James Klett, Nadya Ally, Jennifer Burke, Jennifer Palmer, Lori Frye, Karen Triplett, Samuel Lewis, Daljeet Singh, Vinoy Thomas, Amol Vaidya, Catherine Schuman, Angie Blankenship, Debra Garrett, Teddie Reagan, Alan Liby, Hiram Rogers, Randal Strong, Claus Daniel, Josh Crabtree, and Dayakar Penumadu for their sponsorship, contributions and/or support of the ORNL CFTF program.

II.2.C Integrated Computational Materials Engineering Development of CF Composites for Lightweight Vehicles (Ford Motor Company)

Dr. Xuming Su, Co-Principal Investigator

Ford Research and Advanced Engineering
 Ford Research and Innovation Center
 2101 Village Rd.
 Dearborn, MI 48124
 E-mail: xsul@ford.com

Dr. David Wagner, Co-Principal Investigator

Ford Research and Advanced Engineering
 Ford Research and Innovation Center
 2101 Village Rd.
 Dearborn, MI 48124
 E-mail: dwagner6@ford.com

H. Felix Wu, Ph. D, DOE Technology Manager

U.S. Department of Energy
 E-mail: mailto:felix.wu@ee.doe.gov

Start Date: October 1, 2014	End Date: December 31, 2018	
Project Funding (FY18): \$2,582,737	DOE share: \$1,807,916	Non-DOE share: \$774,821

Project Introduction

Vehicle lightweighting is a very important concept for automotive manufacturers to consider meeting the ever increasing demand of fuel efficiency and to reduce greenhouse gas emissions and dependency on foreign oil. CFRP composites, with a density of 1.55 g/cm³ and a tensile strength of about 2,000 MPa in the fiber direction, are among the most promising candidates to replace the metals currently used for structural components. The goal of this project is to design, develop, and optimize, using CAE only, a LD vehicle CF sub-frame capable of achieving greater than a 25% weight reduction with a cost increase of less than \$4.27 per pound of weight saved when compared to the baseline technology to be replaced.

Unlike many metals typically used in automotive vehicles, the mechanical properties of CFRP are highly direction-dependent. The strength of the material in fiber reinforced-direction could be an order of magnitude higher than in the direction perpendicular to it. It is important to note that the fiber orientation in a component is decided not only by the initial fabric layout, but also the preforming and molding processes. An optimized vehicle component design will thus need tools that are capable of predicting the performance of CFRP parts based on fiber architecture, molding process, and curing history, with considerations of uncertainties and probabilistic nature of materials, processes, and in-service conditions. The current project will develop these ICME tools to meet the design challenge.

ICME tools developed in the project will be robust, accurate, and reliable constitutive models for each constituent material, as well as the composite assembly under expected service conditions including high strain rates utilizing physics-based models. The manufacturing process (including variability from both process and material) is simulated to predict the fiber orientation and other microstructural features of manufactured products. This information is passed to performance analysis. Material design, manufacturing simulation, and performance analysis are integrated. Local material properties are related to the composite architecture and microstructure by multiscale models. Design and manufacturing process are optimized simultaneously to achieve the most efficient usage of the material.

Objectives

The project will simultaneously develop a structural CF composite sub-frame to support immediate weight reduction in LD vehicles while also developing ICME techniques to support a reduced development-to-deployment lead time in all lightweight materials systems. Additionally, the project includes dissemination of results through infrastructure and methods identified by NIST.

The project will design, develop, and optimize a LD vehicle CF composite sub-frame capable of achieving greater than a 25% weight reduction with a cost increase of less than \$4.27 per pound of weight saved when compared to the baseline technology to be replaced. The sub-frame will significantly contribute to the structural performance of the vehicle in driving and crash conditions. The developed CF composite sub-frame will achieve functional and packaging requirements of the baseline sub-frame to be replaced.

This project will utilize an ICME approach to develop, integrate, and implement predictive models for CFRP composites that link the materials design, molding process, and final performance, with considerations of uncertainties and probabilistic nature of materials, processes, and in-service conditions. The developed ICME techniques will then be applied to the design, development, and optimization of an integrated CFRP sub-frame chassis system with performance, weight, and cost compared to a baseline assembly.

The project will be conducted in four (4) BPs:

Budget Period 1: *CFRP Material Characterization and ICME Model Development* – Experimental characterization of each constituent of CFRP composite at the coupon level and the development of ICME models will be initiated.

Budget Period 2: *ICME Model Database and Validation* – Models with the consideration of variations and uncertainties will be validated at the constituent level

Budget Period 3: *ICME Model Integration and Validation* – ICME models will be integrated in commercial software.

Budget Period 4: *ICME-Based Design and Optimization* – ICME tools will be evaluated via a sub-frame design and optimization, connecting structure/process/property.

Approach

Using CAE only, the project will design, develop, and optimize a LD vehicle CF sub-frame capable of achieving greater than a 25% weight reduction with a cost increase of less than \$4.27 per pound of weight saved when compared to the baseline technology to be replaced. This objective will be achieved by developing ICME tools and numerical procedures to optimize both the design and the manufacturing process so that CFRP is most efficiently used.

The ICME tools relate performance requirements of a vehicle to material design and processes. While material performances are expressed at the continuum macro-scale, they are decided by material microstructures and microstructural features at the microscale and again by molecular bonds and crosslinking at the nanoscale. The material microstructures and microstructural features, bonding, and crosslinking are results of material design and manufacturing processes. ICME tools are thus multiscale models and approaches that bridge the different material scales. These models are based on physical principles, testing measurements, and observations. Test data are also needed in validating material models. Modeling and testing are always hand-in-hand in successful development of ICME tools. The project team consists of Ford Motor Company, an automotive manufacturer; Dow Chemical, a material manufacturer; NU, an institution of highly regarded academics; and the NIST, a world-renowned test lab. As such, the team has all of the elements needed to make a breakthrough in developing ICME tools. The research team also includes software developers from Livermore Software

Technology Corporation (LSTC) (LS-DYNA), Autodesk (Moldflow), ESTECO (modeFrontier®), and HBM (nCode). The ICME tools developed in the project can be numerically implemented and available through popular engineering software and disseminated.

The project will be conducted in four BPs: (1) CFRP material characterization and ICME model development; (2) ICME model database and validation; (3) ICME model integration and validation; and (4) ICME-based design and optimization. The first two BPs constitute Phase I: Model Development and Model-Level Validation. The remaining two BPs constitute Phase II: ICME Integration and System Design. FY 2018 represents the second year of Phase II.

Results

The project is organized in four main tasks: Task 1 consists of CFRP material characterization and development of the ICME model database; Task 2 focuses on ICME model development and validation; Task 3 deals with ICME model integration and validation; and Task 4 is centered on ICME-based design and optimization. FY 2018 represents the second year of Phase II. Only Tasks 3 and 4 are active. Still, Tasks 1 and 2 continue to produce interesting results and will be discussed in this report, as well as the results of Tasks 3 and 4.

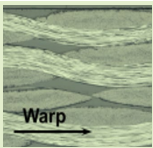
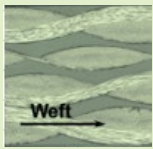
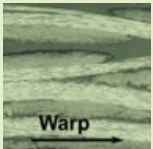
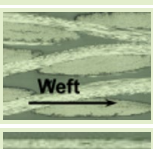
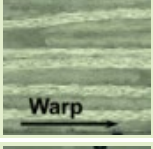
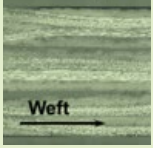
Task 1: Material Characterization and ICME Database Model Development

Task 1 characterizes CFRP material and its constituents at the coupon level. The results are bases of multiscale and other material models of ICME. All tests originally planned for the project were completed by end of FY 2017. Additional tests were performed, and a test method was developed to enhance the material database for ICME model validation.

Forty-two (42) plaques in unidirectional lay-up, 28 plaques in a 660 gsm (grams per square meter) 2x2 woven twill, and 40 plaques in a 400 gsm 2x2 woven twill were molded in early FY 2018 to study the impact of details of laminate lay-up and sizes of the fiber tow on the mechanical properties of the composites. Tensile coupons cut at various directions were tested to provide data for the validation of robustness of multiscale models. Table II.2.C.1 compares three woven composites studied in the project, which clearly demonstrates the impact of the size and geometry of the fiber tow on the properties of the material. The higher modulus and strength of 400 gsm twill when compared to those of 660 gsm twill are explained by the larger wavelength and smaller amplitude, or smaller waviness, of the 400 gsm twill, as can be observed by micrographs in the table. Additionally, differences in properties along warp and weft direction of the laminates are shown in Table II.2.C.1.

Six summer interns, all undergraduate students from the Materials Science and Engineering Department at the University of Maryland, were hired in the summer of FY 2018 to conduct a metallographic analysis of the fiber content and morphology in the composite plaques, along with a comprehensive assessment of the defects found in the materials. Weave yarn angles, amplitudes, and wavelengths are measured in random sections throughout the various materials, as well as fiber density at a range of magnifications.

Table II.2.C.1. Tensile and compression tests of woven coupons with different tow sizes.

		2.5 mm Tensile and Compression				5-mm Compression		
	Dir.	E (GPa) (Std dev/ cov%)	UTS (MPa) (Std dev/ cov%)	E (GPa) (Std dev/ cov%)	UCS (MPa) (Std dev/ cov%)	E (GPa) (Std dev/ cov%)	UCS (MPa) (Std dev/ cov%)	Micrograph
Plain 660	Warp	61.4 (1.6/2.5)	723.0 (10.8/1.5)	55.9 (1.4/2.5)	263.0 (13.5/5.1)	58.4 (1.2/2.0)	303.0 (12.9/4.3)	
	Weft	52.1 (1.3/2.5)	462.0 (13.9/3.0)	42.5 (0.2/0.5)	162.0 (5.5/3.4)	47.3 (0.4/0.8)	160.0 (5.3/3.3)	
Twill 660	Warp	62.8 (0.6/1.0)	805.0 (9.3/1.2)	62.6 (0.8/1.2)	376.0 (43.2/11.5)	60.5 (1.0/1.7)	357.0 (22.8/6.4)	
	Weft	59.5 (0.6/1.0)	559.0 (25.4/4.5)	55.2 (1.0/1.8)	303.0 (32.8/10.8)	58.1 (2.8/4.9)	275.0 (18.2/6.6)	
Twill 400	Warp	64.4 (0.4/0.6)	978.0 (49.7/5.1)	70.5 (3.5/5.0)	429.0 (104.9/24.5)			
	Weft	65.2 (1.1/1.7)	898.0 (13.9/3.0)	61.8 (4.1/6.6)	606.0 (45.8/7.6)			

E = Elastic Modulus; UTS = ultimate tensile strength; UCS = ultimate compressive strength; Std. dev. = standard deviation; cov% = coefficient of variation percentage

As a means of roughly assessing composite plaque quality, and large-scale (millimeter-size and larger) void content, efforts with water-immersion-based ultrasonic scanning were undertaken. An ultrasonic focused-probe setup (by Sonix) mated to a 3-axis translation system (by MetroTek) atop a water tank was used to perform C-scans (successive line-scans) of individual composite plaques. The ultrasonic probe was driven by a software package capable of selectively collecting ultrasonic echoes from the scanning process at different times-of-flight (i.e., “time-gating” of collected data). The setup, as depicted in Figure II.2.C.1, was used to generate a set of images at different depths through the thickness direction of the composite, loosely correlated to the locations of individual plies.

The technique was used to study the delamination of a hat section, after a dynamic 3-point bending test, in an effort to better correlate experimental results of FEA crash simulations. Tested samples of both unidirectional (UD) and woven laminates were imaged, with an emphasis on attempting to assess three-dimensional (3D) damage profiles.

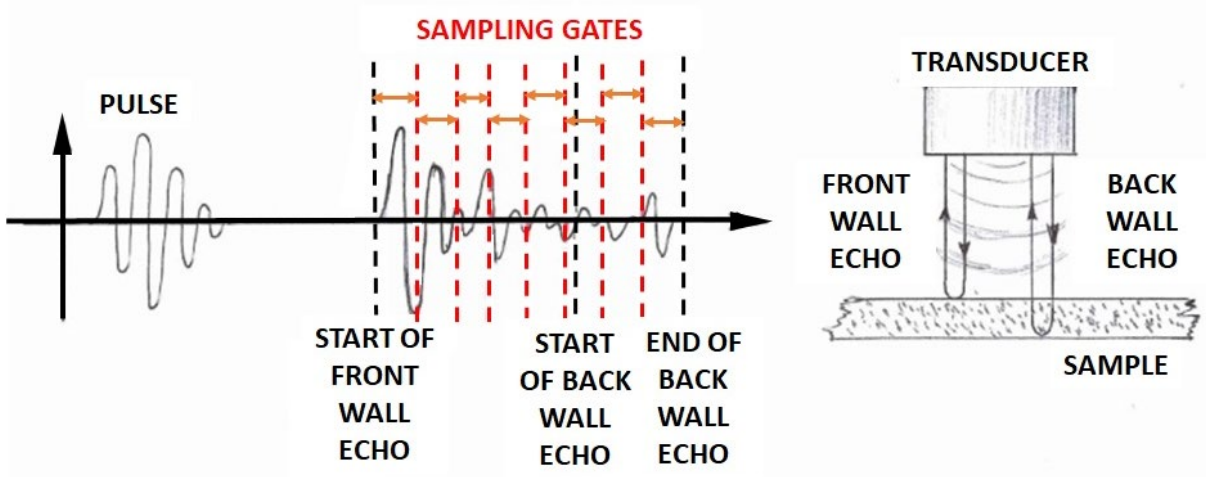


Figure II.2.C.1. Ultrasonic probe setup. Pulse is the applied ultrasonic signal. Front-wall and back-wall echoes are the measured responses of the sample. Sampling “gates” are time-distributed subsamples of the output that are correlated to “slices” within the thickness of the sample. Source: NU.

Scans generated sets of 16 images per sample face; thus, 64 images per hat section. The images showed markedly different damage patterns in the different types of composite laminates. Hat-sections comprised of UD laminates (see Figure II.2.C.2) showed relatively large delamination zones overall, as the UD laminates possess fairly low fracture toughness characteristics, making it easy to grow large cracks in interfaces between different ply orientations. Hat-sections comprised of woven laminates (see Figure II.2.C.3) showed smaller delamination zones, but most likely a greater amount of “total” damage, including undoubtedly more intra-tow cracking. In general, damage profiles were seen to “evolve” through the thickness of surfaces subject to impact loadings (see Figure II.2.C.4), which is expected given the more complex stress state that exists around the indenter.

These images and analyses further confirm the failure mode of dynamic 3-point bending test of hat-sections where large-scale degradation of structure stiffness was detected.



Figure II.2.C.2. Representative impact-surface image from UD [0/90/90/0/0/0]_s hat section. Source: NU.

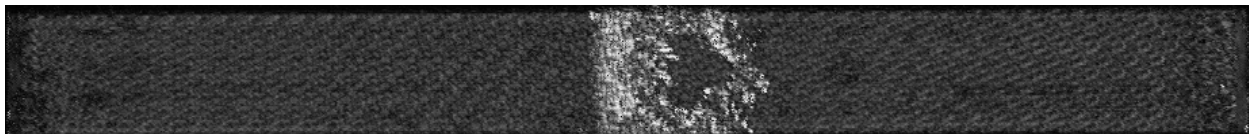


Figure II.2.C.3. Representative image from dynamic 3-point bending tested woven [0/90]₄ hat section. Source: NU.

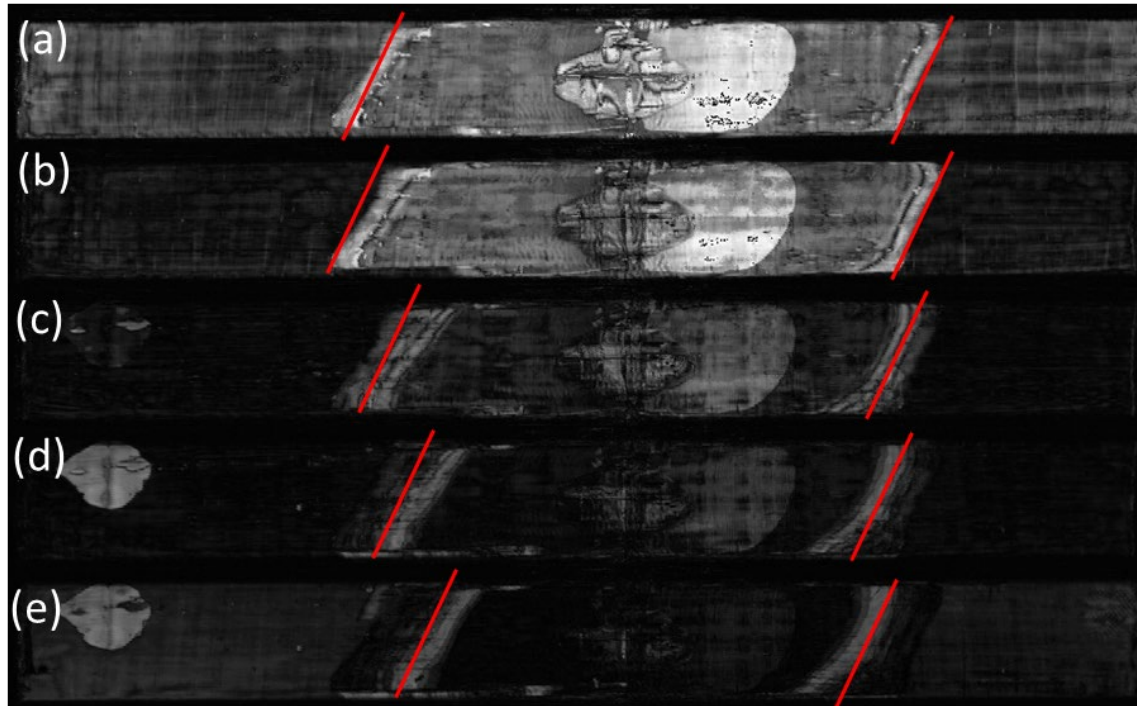


Figure II.2.C.4. Set of five successive ultrasonic scans showing internal damage at different locations through the material thickness. In each figure (a) through (e), the bright features show strong acoustic echoes, indicative of damage at a given location (or depth). Red marks highlight the “bright” leading edge of the damage zone in each scan image. Source: NU.

Task 2: ICME Model Development and Validation

ICME material models are developed in Task 2. All material models originally planned for the ICME project were completed and validated by the end of FY 2017. However, almost all subtasks of Task 2 are still active throughout FY 2018. Biweekly meetings continue to be packed with attendees and updates. Researchers are focused on further improvement and extension of the developed models.

Subtask 2.1 – Atomistically Informed Resin Infusion Models

No update in FY 2018.

Subtask 2.2 – Preform and Compression Molding Process Models

Subtask 2.2.1 – Preforming Modeling

In FY 2017, a non-orthogonal model was implemented in LS-DYNA as MAT_COMPRF (MAT_293). The model was validated by preforming and simulation of the preforming of double-dome structures. The model was shown to predict draw-ins and changed fiber angles of the preformed double-dome satisfactorily. The parameters of the model are reversely calibrated by using the uniaxial tension, bias-extension, and bending tests. In FY 2018, efforts focused on improving accuracy of the model by taking temperature into consideration and using a multiscale model to replace tests needed for MAT_293.

Temperature Dependency of Preforming Analysis

The coupled thermo-mechanics solver in ABAQUS Explicit was selected to take thermal behavior into consideration. The user-defined non-orthogonal material model was revised to take the temperature at each integration point into consideration. Incremental form of the material model was used in the analysis to avoid discontinuity of material behavior due to changes of temperature. The mechanical properties obtained via the prepreg uniaxial tension and bias-extension tests at 60°C and 23°C were utilized. The prepreg mechanical properties at the whole forming temperature region were calculated via linear interpolation.

Three analyses are compared. They are: (a) original temperature independent analysis (e.g., temperature kept constant at 60°C); (b) analysis using a total form of temperature-dependent stress-strain relation; and (c) analysis using incremental form of temperature-dependent stress-strain relation. The punch force curves from the three analyses are shown in Figure II.2.C.5. The differences in the punch force from the three analyses are large. When the previous material model is utilized, the punch force is nearly zero, which is incorrect. Predictions using temperature-dependent models provide punch force as high as 1,000 N, which is close to the measurements.

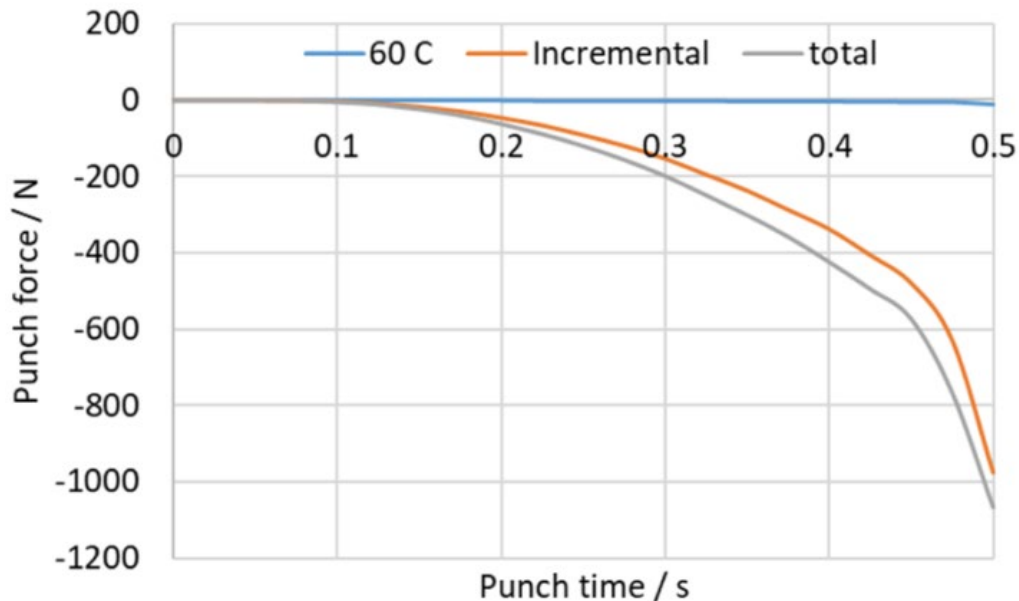


Figure II.2.C.5. Punch force comparison for different material models. Source: NU.

Representative Volume Element (RVE) for Preforming Analysis

Multiscale models are developed to provide material inputs for preforming analysis to replace physical tests that are currently required to obtain these inputs. The 2×2 twill woven prepreg RVE was developed and calibrated to generate an emulator that is capable of predicting the stress within 0-2% yarn stretch ratio and 0-1 radian shear angle based on the Bayesian Calibration algorithm. The mesoscopic stress emulator is implemented into ABAQUS Explicit as vectorized user material (VUMAT) for the macroscopic preforming process simulation.

The double-dome benchmark preforming experiment is simulated with the multiscale VUMAT for the prepreg at 23°C. One layer of prepreg in ±45 degree fiber orientation is formed in this process where the displacement of the punch is 90 mm, and the binder force increases linearly from 4,000 to 8,200 N-based on experimental measurements. The tools are set as rigid bodies and both the prepreg and the tools are discretized by the S4R and the S3 shell elements in ABAQUS. The friction coefficient between the tool and the prepreg is set to 0.3, according to the experimental measurement.

The simulation result is compared against the one obtained from the simulation with tension-shear decoupled non-orthogonal material model that was calibrated via the same experimental data. The final geometry of the prepreg sheet and the predicted yarn angle distribution are demonstrated in Figure II.2.C.6 together with the experimental part. The draw-in distance and the yarn angle at the sampling locations from the simulation and the experiment are listed in Table II.2.C.2. The comparison indicates that the multiscale method with the tension-shear coupling effect more accurately predicts the draw-in and yarn angle compared to the decoupled model.

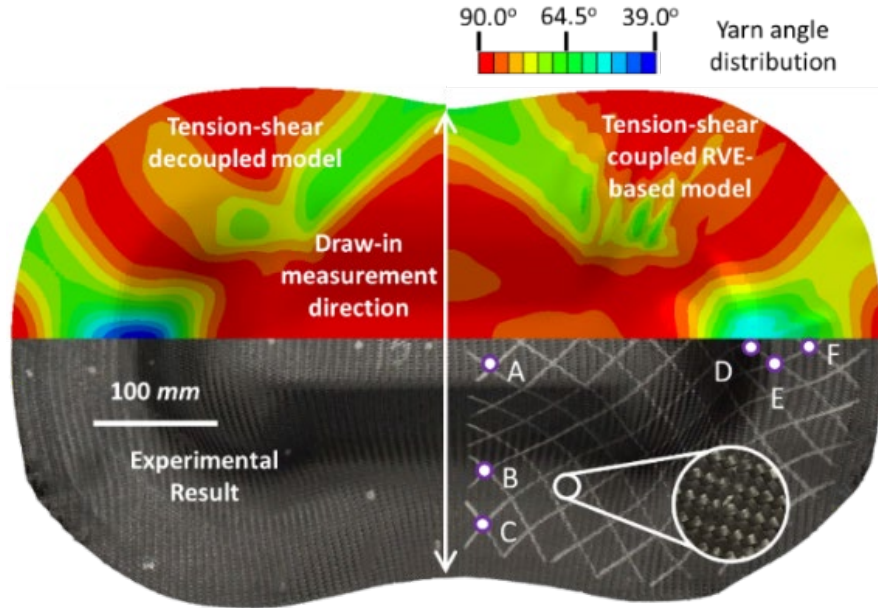


Figure II.2.C.6. Final part shapes and yarn angle distributions (values for locations A – E given in Table II.2.C.2). Source: NU.

Table II.2.C.2. Draw-in distance and yarn angle comparison between the simulation and the experiment.

Comparison	Draw-in	A	B	C	D	E	F
Multiscale Model	42.25 mm	86°	88°	73°	54°	57°	67°
Decoupled Model	40.22 mm	89°	89°	71°	40°	45°	65°
Experiment	49.02 mm	80°	88°	71°	49°	56°	66°

The punch force-displacement curves from the two simulation cases and the experiment are compared in Figure II.2.C.7. The plots demonstrate that the new multiscale preforming simulation method results in a significant improvement over the simulation using the decoupled material model and it has a great capability for the punch force prediction.

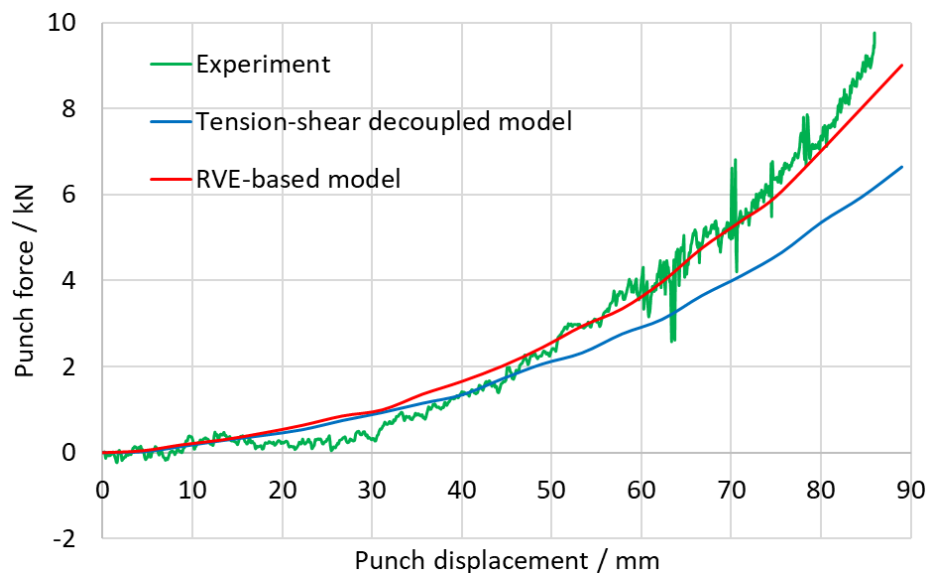


Figure II.2.C.7. Double-dome preforming punch force comparison. Source: NU.

Subtask 2.2.2 – Sheet Molding Compound (SMC) Compression Molding

The methodology of compression molding simulation using Moldflow has been applied to simulate the manufacturing process for a design of SMC sub-frame. Modeling this complex part geometry with many ribs and steep wall features is found to be challenging. To solve this problem, the meshing procedure is improved by integrating the Hypermesh and Moldflow to ensure the part is meshed correctly. The CAD file containing the two-dimensional (2D) surfaces enclosing the volume of the SMC sub-frame part is imported into Hypermesh. The 2D automeshing function in Hypermesh is then applied to generate the triangular elements with acceptable quality for these surfaces. Once the mesh is imported into Moldflow, its automesher is utilized to generate layered tetra elements that are refined enough for the SMC compression molding simulation. The creation of the initial charge elements is also achieved following a similar procedure. The part and initial charge elements are finally combined in Moldflow and other parameters of the model, including processing conditions, material properties, and fiber orientation model, can then be assigned. This modeling process combines the advantages of Hypermesh on 2D meshing and Moldflow on 3D layered tetra meshing and proves to be effective when dealing with such complex part geometry. The model and fiber orientation prediction of the compression molding simulation of the sub-frame upper half is shown in Figure II.2.C.8.(a) and (b), respectively. There are some small regions with slightly aligned fiber orientation, for example, the positions marked in Figure II.2.C.8.(b), where the preferential fiber orientation is along X-axis.

The local material properties are computed as a function of the fiber orientation tensor on each integration point and defined in a separate file to replace the homogenous material definition in performance analysis. A comparison is performed to check the difference in prediction results from the models using homogenous material properties and the ones using mapped local properties. Based on the Moldflow simulation results, the material properties in most regions of this demonstrated sub-frame design are close to an in-plane isotropic state since the initial charges cover most of the mold surface and limited flow is expected during molding. This is reflected in the comparison between results from reference and mapped CAE models, where part performance prediction shows mostly similar results. The averaged difference of displacement of loading points in NASTRAN analysis is 4.4%. The prediction of the force during crash simulation in LS-DYNA for the two material models is also close. However, it should be noted that once initial charge pattern is changed to allow stronger flow during molding, the results of reference and mapped models is expected to show a larger difference.

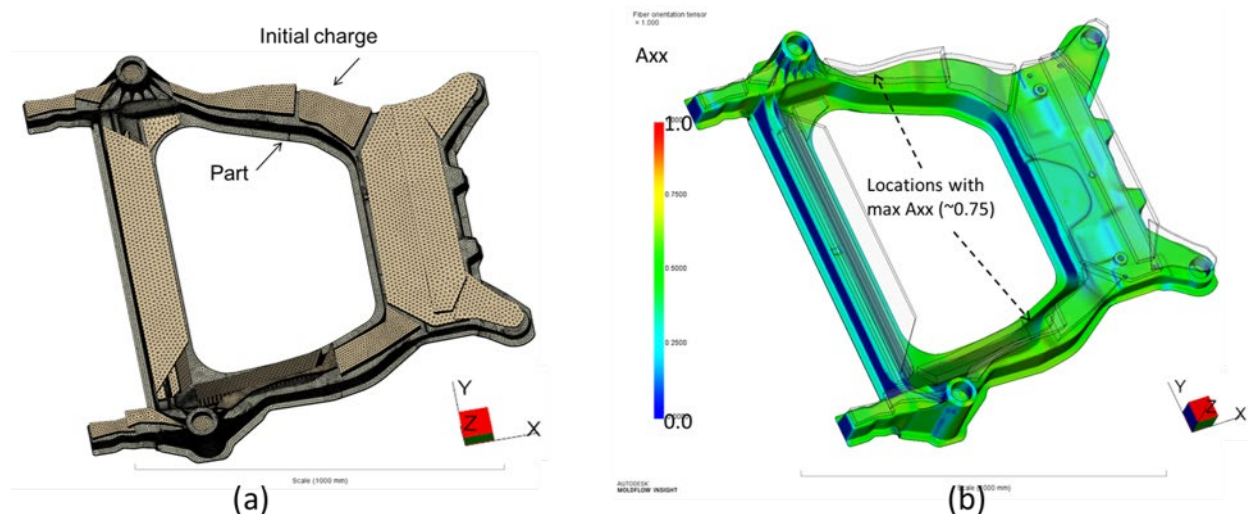


Figure II.2.C.8. (a) The Moldflow model of SMC sub-frame upper molding; and (b) fiber orientation prediction.

Source: Ford Motor Company.

Subtask 2.3 – Preform and Compression Molding Process Models

Multiscale models of UD, woven, and SMC composites have been developed and validated in previous years and have been used intensively to study various aspects of the material. In FY 2018, multiscale models have been further developed to study the impact of microstructure on material properties and material failure. Approaches to speed up multiscale analysis have also been explored.

The fiber provided by Dow Chemical in the project was found to be bean-shaped in diameter. The UD RVE, however, assumes the fiber to be circular. To study the impact of the section geometry of fiber on material properties, both bean-shaped and circular shaped RVEs were generated. The volume fraction of the circular one is 51.76% and is 51.39% for the bean fiber.

The material law assumes fiber as elastic material and epoxy as elastoplastic material with J_2 plasticity. The plastic strain and the stress contour of the matrix phase of both RVEs are shown in Figure II.2.C.9. As shown in Figure II.2.C.9.(d), there are regions with highly localized plastic strain in the bean shape compared to the identical circular one. It is expected that the damage initiated in these localized regions, which is one possible cause of the failure of the material.

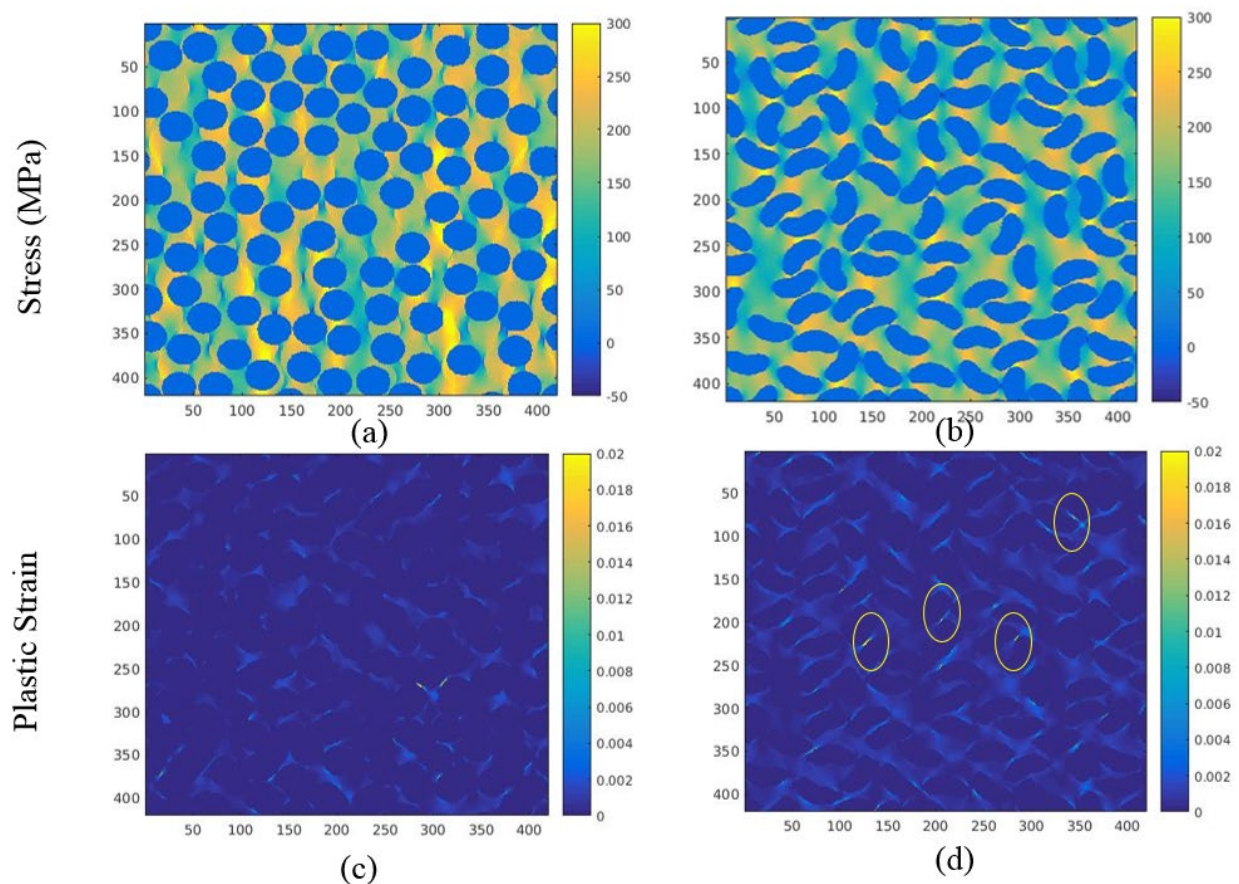


Figure II.2.C.9. (a) Stress contour in matrix phase of the circular RVE; (b) stress contour in matrix phase of the bean RVE; (c) plastic strain contour of circular fiber; and (d) plastic strain contour of bean fiber. Source: NU.

As discussed in the FY 2017 annual report, the self-consistent clustering analysis (SCA) method is a powerful analysis approach in reducing the size of high-fidelity micro- or meso-scale RVE modeling and greatly speed up analysis. SCA was studied further in FY 2018.

SCA is used to simulate a tensile test to confirm the accuracy of the method. The concurrent modeling of coupon model with geometry tested at NIST was established. A UD RVE with fiber volume fraction of 51% was assigned to all integration points in the model to compute UD material law on-the-fly. SCA was used to compute UD RVE responses.

The coupon model is shown in Figure II.2.C.10.(a), where the 10° off-axis to fiber direction is clearly marked by the red arrow at lower left. A reduced-order model of the UD RVE is assigned to each integration point and SCA homogenization scheme is called at each integration point to solve UD RVE responses at a given macroscopic deformation, such as macroscopic strain.

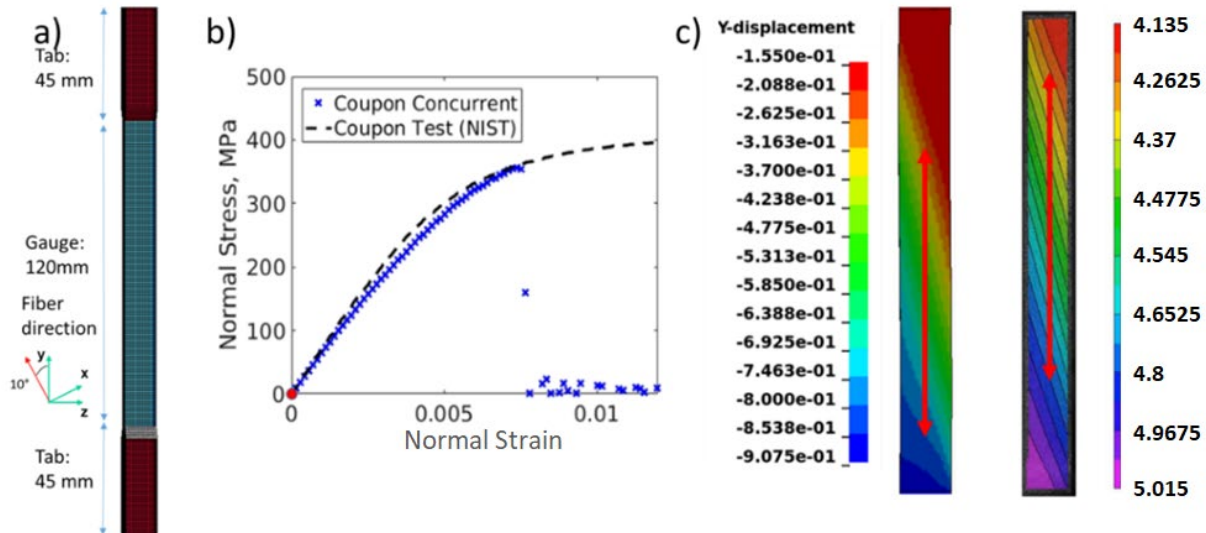


Figure II.2.C.10. Normal stress vs. displacement plot from SCA simulation with (a) gauge for the fiber direction, (b) the resultant stress-strain curve and (c) displacement of the sample in the y-direction. Source: NU.

To validate the coupon model result, normal stress and y-direction displacement are shown in Figure II.2.C.10.(b) and (c). The predicted final normal stress of 10° off-axis tensile coupon is 380 MPa, slightly under the measured value, which is 400 MPa. By improving material law of the epoxy matrix, a better prediction is expected. The y displacement contours of both experiments and coupon simulation are also available for comparison. For each case, vertical distance, as marked by the red double arrows in Figure II.2.C.10.(c) between -0.26 mm and -0.80 mm contour bands, is measured. The prediction, 71.65 mm, is very close to experimental measurement, which is 76.18 mm, with a relative difference of 6%. The coupon model shows that the concurrent scheme makes good prediction as validated by experimental data.

Subtask 2.4 – Fracture Models and Energy Absorption Models

An automated workflow to generate the LS-DYNA model of CFRP laminate parts with thick shells and cohesive elements was developed. With the input parameters, such as thickness and layer numbers, a Hypermesh Tcl script file is written in MATLAB to convert the previous model with thin shell elements to a model of multilayer thick shell elements.

The delamination in the dynamic 3-point bending test is simulated and compared with experimental measurement (from ultrasonic scan), as shown in Figure II.2.C.11. The delamination areas in both the top (see Figure II.2.C.11.(a)) and side wall (see Figure II.2.C.11.(b)) of the hat section sample match well with the experimental observation. The ultrasonic scan results further validate the accuracy of current method in CFRP crash simulation.

MAT_262 in LS-DYNA for UD material was investigated and the results show there was a significant limitation in axial crash simulation where the premature matrix failure results in a low loading force. Therefore, MAT_262 would not be further considered for crash simulation in this project.

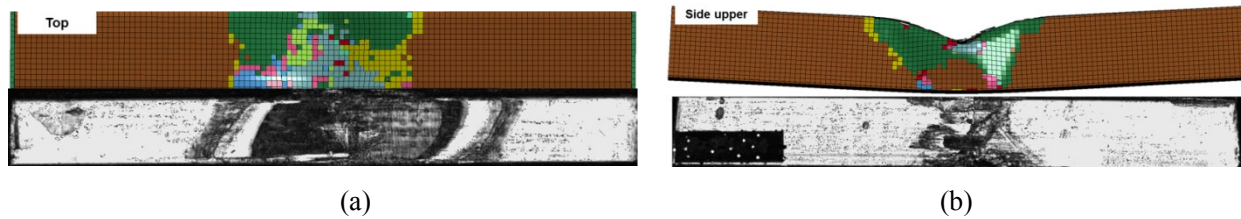


Figure II.2.C.11. Comparison between experiments and simulation of delamination in UD dynamic 3-point bending test for (a) the top and (b) the side wall. Source: Ford Motor Company.

Subtask 2.5 – Fatigue and Durability Models

A CFRP fatigue analysis module was implemented in HBM nCode and validated in previous years. Coupon level tests on UD, woven, and SMC were completed in FY 2018 to characterize the material and provide input for nCode durability analysis.

The important findings in FY 2018 can be summarized as follows:

1. To investigate the size effect on the fatigue lives of UD laminates, fatigue tests for samples with different gauge lengths have been carried out for 0° and 90° UD laminates. We found that the size effect cannot be ignored for tensile dominated fatigue failure for 90° UD laminates, and longer samples generated a shorter fatigue life. To include the size effect into our fatigue prediction, a fatigue model accounting for the size of the sample was proposed based on Weibull distribution.
2. Constant fatigue life diagrams for 0° , 10° , and 90° UD laminates were established based on the fatigue tests using four different methods: Piecewise model, Kawai's three-segment model and four-segment model [1-2], and Harris's Bell-shape model [3]. The comparison between prediction results and experimental data shows that Kawai's four-segment model is able to provide the most accurate prediction of fatigue life at various stress ratios for 0° and 90° UD laminates.
3. Using advanced digital image correlation measurements on both sides of the sample, we accurately pinpointed the elastic moduli of woven CF composites. In addition, the DIC technique guaranteed that the frame was properly aligned and that the sample did not buckle during compression tests.
4. Constant fatigue life diagrams for woven composites in both warp and weft directions were established, as shown in Figure II.2.C.12.(a-b). It is observed that the cycles to failure at a given R-ratio is much higher for warp direction compared to the weft direction. Especially at lower stress amplitudes, tension-tension fatigue tests at $R=0.1$ have higher fatigue lives compared to the critical R-ratios for weft directions.
5. Constant fatigue life diagrams for 45° woven composites were established, as shown in Figure II.2.C.12.(c). The aim of conducting 45° fatigue tests is to understand the shear properties of woven composites. The failure of 45° samples was predominantly by shearing on the 45° planes, thus the data generated were considered valid.

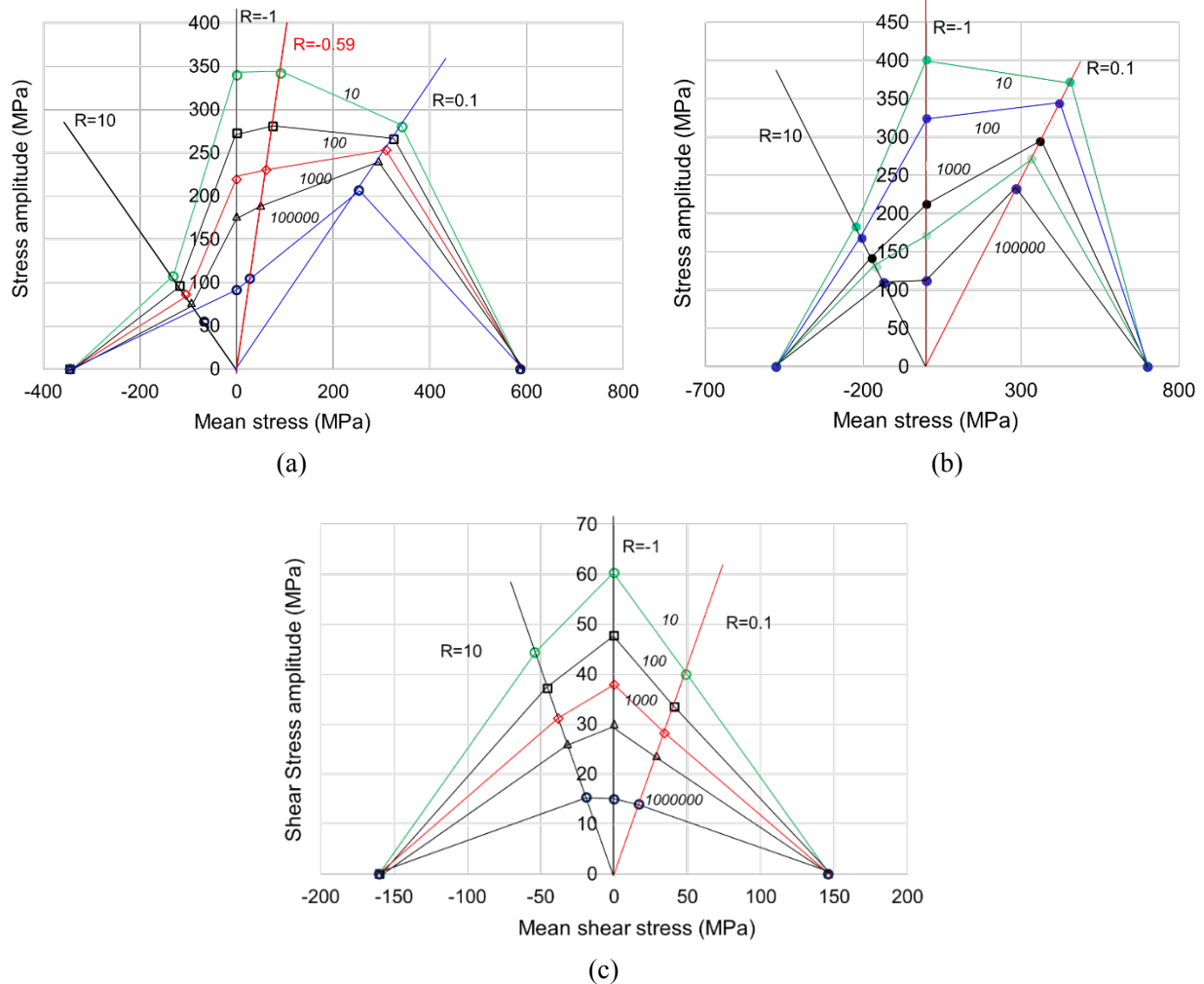


Figure II.2.C.12. Constant fatigue life diagrams of woven composites in (a) weft, (b) warp, and (c) 45 degree orientations. Source: Ford Motor Company.

Subtask 2.6 – Uncertainty Quantification and Propagation in Multiscale Materials

The effect of microstructural correlations and uncertainties at three scales: micro-, meso-, and macro-scale were investigated. Major sources of uncertainty at each length scale of the material system of interest were identified. At each particular scale, the spatial correlations among the quantities or parameters of interest are modeled as a function of the spatial coordinates at the next higher scale via a random field. Sensitivity analyses were carried out to make sure that dominant sources of uncertainty at the meso- and macro-scale are identified.

In FY 2018, Uncertainty Quantification and Uncertainty Propagation of both UD and woven composites were further studied. Especially, how uncertainty is propagating across scale was demonstrated by a number of examples. An example of Uncertainty Quantification and Uncertainty Propagation applicable to multiscale simulation of woven fiber composites is discussed below.

The goal of this example is to quantify the macro-scale uncertainty in the elastic response of a three-scale laminate structure as a function of spatial variations in the fiber volume fraction (i.e., present in the micro- and meso-scale) (v), yarn angle (α), and fiber misalignment angles (i.e., present in the meso-scale) (θ). Our laminate structure in Figure II.2.C.13.(a) is composed of four identical plies. The plies are stacked in the same orientation and constitute a total thickness of 2.4 mm. The bottom of the sample is clamped while the other end

is pulled by 1 mm to generate the bias tension deformation. The three scales are denoted with numbers: 1 → Macro, 2 → Meso, and 3 → Micro. Superscripts and subscripts denote scales and integration points, respectively. Variables with a bar represent averaged quantities over all the integration points at a scale. For instance, v_i^1 denotes the fiber volume fraction assigned to the i^{th} integration point at the macro-scale. $\bar{\theta}^2 = \frac{1}{N} \sum_{i=1}^N \theta_i^2$ represents the average misalignment (zenith) angle at the meso-scale for a woven RVE.

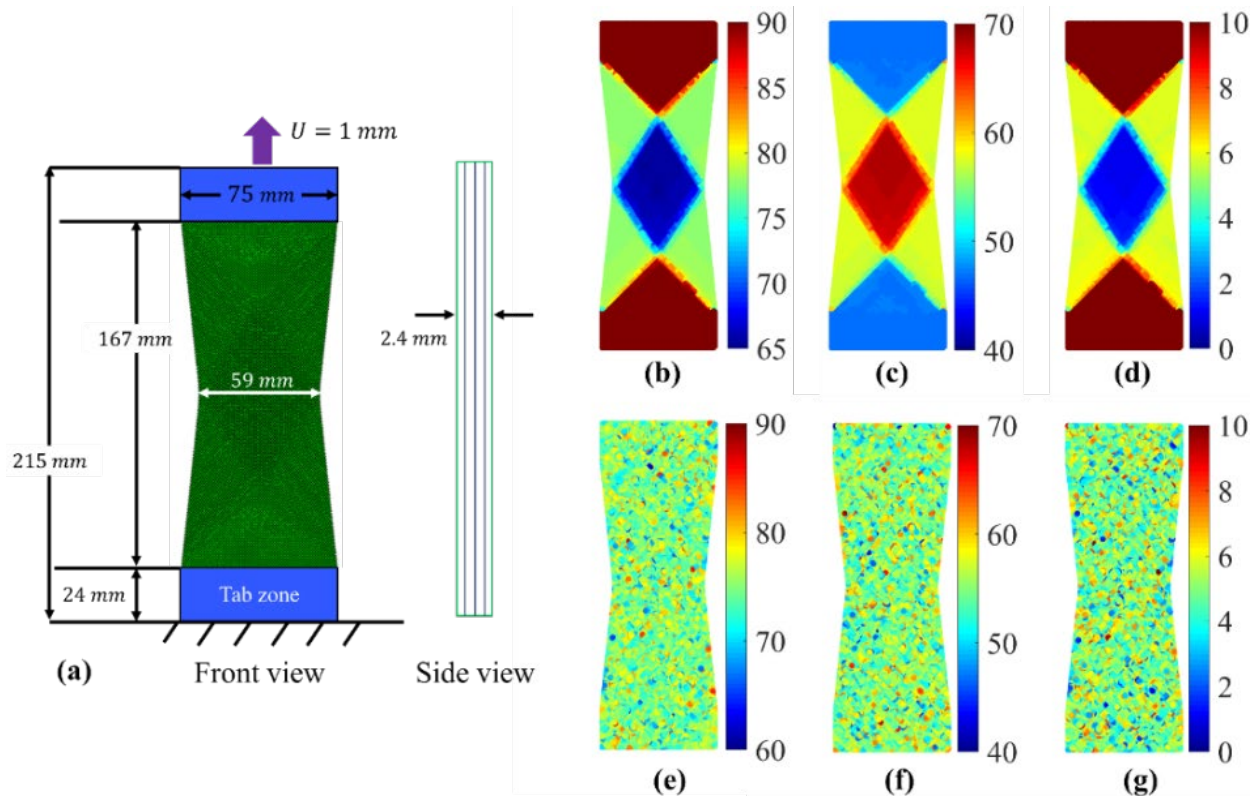


Figure II.2.C.13. (a) The undeformed structure: bottom end is clamped, top end is pulled by 1 mm. (b) through (d): spatial variations in yarn angle (in degrees); fiber volume fraction (percentage); and fiber misalignment angle (in degrees), respectively, across the integration points for case 10 in Table II.2.C.3. (e) through (g): those of case 8 in Table II.2.C.3.

Source: NU.

Multiple macro simulations were conducted where α_i^1 , v_i^1 , and θ_i^1 change spatially across the macro-scale IPs in each simulation and the fitted metamodel was used to predict the stiffness matrix of the woven RVEs associated with these integration points. Ten cases were considered, as detailed in Table II.2.C.3. Except for the first two cases, 30 independent macro-scale simulations were conducted for each case to account for randomness.

Figure II.2.C.14.(a) compares resultant applied tensile force for the ten cases where, for cases 3 through 10, the force-displacement curve was averaged over the 30 multiscale simulations. It is evident that with spatial variations, especially in α , a larger force is needed to achieve 1 mm displacement at the upper end of the sample. In particular, the three bottom lines in Figure II.2.C.14.(a) correspond to the cases where there are no spatial variations in the yarn angle (see cases 1, 4, and 6). Figure II.2.C.14.(b) demonstrates the standard deviation of the 30 simulations for cases 3 through 10. As it can be observed, the global response of the structure is not noticeably sensitive to the spatial variations.

To illustrate the effect of spatial variations on local behavior, the average and standard deviation of the von-Mises stress field over the entire structure can be compared. However, stress concentrations might occur at both ends of the sample since we have employed an explicit solver in our FEA simulations. For this reason, in Figure II.2.C.14.(c) and (d), the mean and standard deviation of the von-Mises stress along the mid-section of the part are plotted. It is observed that the stresses are quite significantly underestimated when the spatial variations in the yarn angle are not considered (see cases 1, 4, and 6 in Figure II.2.C.14.(c)). The largest variations come from case 9, followed by case 3 in Figure II.2.C.14.(d). Finally, we note that the zigzag pattern in the stresses in Figure II.2.C.14.(c) and (d) are due to the rough changes in the yarn angle in the adjacent macro-scale IPs (and not the distortion of the finite elements).

Table II.2.C.3. Cases considered to quantify the macro-scale uncertainties. The variations are changed in a controlled manner from case to case. Gaussian processes (GP) are employed to generate random realizations in all cases.

	Description
Case 1	1 simulation: No misalignment, no spatial variations in v^1 and α^1 , $\bar{v}^1 = 55\%$ and $\bar{\alpha}^1 = 90$
Case 2	1 simulation: No misalignment, no spatial variations in v^1 and $\bar{v}^1 = 55\%$, α^1 from processing simulations
Case 3	30 simulations: No misalignment, no spatial variations in v^1 and $\bar{v}^1 = 55\%$, α^1 changes spatially via GP
Case 4	30 simulations: No misalignment, spatial variations in v^1 via GP and $\bar{v}^1 = 55\%$, no spatial variations in α^1 and $\bar{\alpha}^1 = 90$
Case 5	30 simulations: No misalignment, spatial variations in v^1 via GP and $\bar{v}^1 = 55\%$, α^1 from processing simulations
Case 6	30 simulations: $\bar{\theta}^1 = 5$ and spatial variations with GP, no spatial variations in v^1 and α^1 , $\bar{v}^1 = 55\%$ and $\bar{\alpha}^1 = 90$
Case 7	30 simulations: $\bar{\theta}^1 = 5$ and spatial variations with GP, no spatial variations in v^1 and $\bar{v}^1 = 55\%$, α^1 from processing simulations
Case 8	30 simulations: α^1 , v^1 and θ^1 change spatially via an MRGP (Multi-Response Gaussian Process) (uncorrelated changes)
Case 9	30 simulations: α^1 , v^1 and θ^1 change spatially via an MRGP (correlated changes)
Case 10	30 simulations: v^1 and θ^1 change spatially via an MRGP (changes are correlated and conditioned on the spatial variations of α^1 from processing simulations)

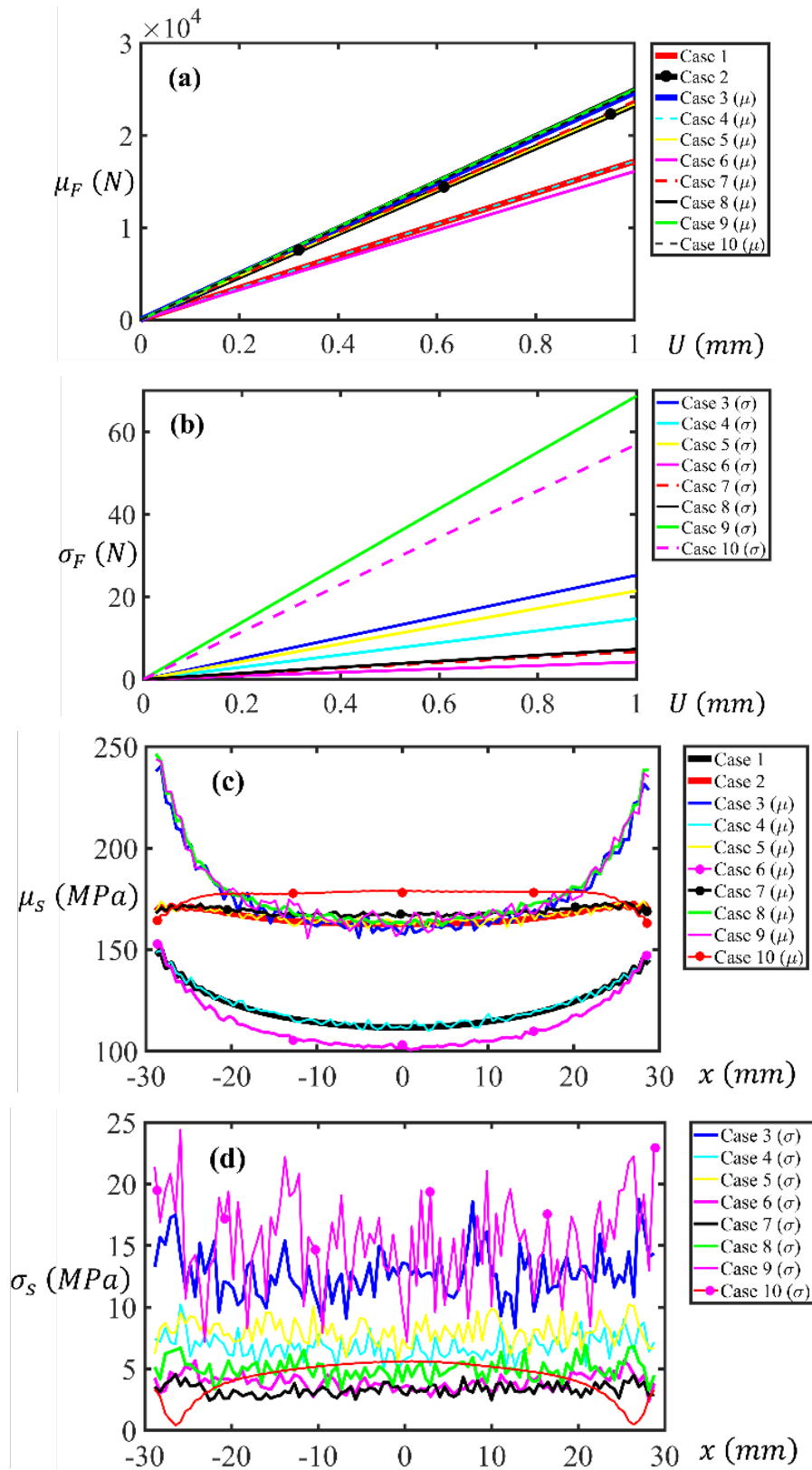


Figure II.2.C.14. Effect of spatial variations on force-displacement curves and stress in the mid-section: (a) average and (b) standard deviation of force-displacement curves. (c) Mean and (d) standard deviation of von-Mises stress at the mid-section. In cases 3 through 10, the mean and standard deviation are calculated for 30 simulations. Source: NU.

Task 3: ICME Model Integration and Structure Optimization

In FY 2018, structure optimization workflow is completed for the process integration and design of SMC-intensive sub-frame. The fully integrated optimization process was demonstrated on the hat section example first. This workflow was tested by Design of Experiment (DOE) runs to demonstrate that all simulation models and scripts can be automatically executed. The focus was then turned to the development of integrated process for the two sub-frame designs: (1) the SMC sub-frame design, and (2) the extruded Al sub-frame design, both with patches of continuous CF composites.

The integrated process for SMC sub-frame design is shown in Figure II.2.C.15. A parallel structure is proposed to minimize the turnaround time of structure performance simulations. At the beginning of the process, parametric structure models and the correspondent CAE input deck is generated based on the gauge and composite lay-up design variables. Then, the five performance analysis (e.g., stiffness, durability, strength, impact, and cost) are submitted to the High-Performance Computing (HPC) system simultaneously.

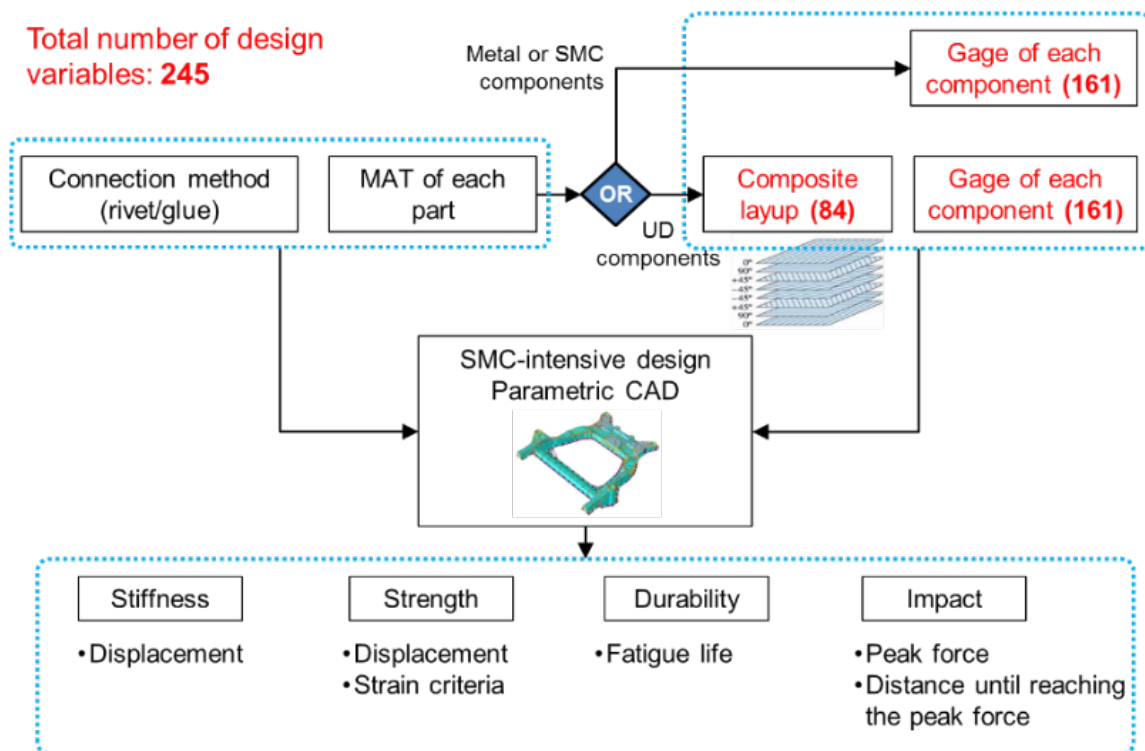


Figure II.2.C.15. Integrated process for SMC-intensive sub-frame. Source: Ford Motor Company.

The following models/commercial software tools are included in the workflow:

1. Material selection for each part (by JAVA script). A vector of design variables is defined using the built-in variable nodes of modeFrontier[®]. Each element in the vector corresponds to one part in the structure.
2. Part gauge or composite lay-up design (by Jython scripts). The composite lay-up design variables are defined by the built-in variable nodes of modeFrontier[®]. When metal or SMC is selected for one part, the gauge variable is activated to assign a thickness value to this part. When continuous fiber composites (UD or woven) are selected, the layouts variables are activated to assign values to the number of layers, and the orientation angle of each layer.
3. Connection method selection (by Jython script). A design variable is defined for selecting adhesive (0) or welding (1). This design variable is created by the built-in variable node of modeFrontier[®].

4. Jython script, which generates the composite lay-up information for NASTRAN, ABAQUS, and LS-DYNA input deck, if continuous composites (woven or UD) are selected for the current design.
5. Jython script, which checks the existing materials in the current design. The process control files will be generated accordingly (for the next step).
6. Linux shell scripts for controlling the start/end of all the commercial software, which include SFE, NASTRAN, ABAQUS, and LS-DYNA.
7. Jython script for controlling the fatigue simulation process.
8. SFE concept, which provides the parametric CAD model for geometry optimization and the mesh for CAE analysis.
9. NASTRAN, which is used for the stiffness analysis and durability analysis.
10. nCode, which predicts the fatigue life for each material that exists in the current design.
11. ABAQUS, which predict the strength of the design. The post-processing is done by a Jython script.
12. LS-DYNA and LS-PREPOST, which are used for the impact simulation and post-processing of the simulation results.

To further accelerate the optimization process, the number of design variables are reduced from 200 to less than 12. This is achieved through two major approaches. The first is to combine part IDs. For example, the multiple ribs in the local region are combined into a single part ID. All components of the same part ID share the same thickness design variable. The second is to identify the trivial design variables via sensitivity analysis and engineering judgement. We fix the trivial design variables as constants during optimization, while keeping the most impactful variables with respect to the design objectives and the design constraints.

Generation-based NSGA-II and FAST algorithms in modeFrontier[®] are employed for optimization. The runs are parallelized to evaluate the performances of 20 designs simultaneously. In the computation environment of Ford HPC, there are three challenges that prohibit evaluation of a large number of designs in parallel. First, the computational infrastructure needed to run all attribution simulations of a design in parallel requires 141 central processing units (CPUs). There is a restriction on central processing unit usage of a single user at Ford. The second challenge results when submission of a large number of simulations to HPC requires a lot of memory, which encounters another restriction. The third is the limitations in licenses where there are a limited number of licenses for all the simulations software used in this project. For example, we only have one license of SFE and one license of nCode.

By analyzing the optimization results for different combinations of materials, it is suggested that the design that meets both the cost and weight target would likely be an SMC-intensive sub-frame with some steel components. The work ongoing is to start on the most promising concepts and allow additional SMC sections to be replaced by steel and check if a design exists that meets the target of greater than 25% weight reduction and less than \$4.27 per pound of weight saved. In addition, the cost models are being refined to better reflect expected real scenarios in manufacturing.

Task 4: ICME Model Integration and Structure Optimization

This task applies the newly developed ICME tools to the design and optimization of a front sub-frame, connecting structural performance to the local material properties that depend on the manufacturing process.

Subtask 4.1 – Sub-frame Concept Development and Topology Optimization

Three concepts have been developed for the sub-frame based on the topology results. These three concepts are: (1) SMC-intensive design, (2) UD/non-crimp fabric (NCF) intensive design, and (3) AI-intensive design.

These three designs serve as the “seed” initial starting points for the multidisciplinary design optimization (MDO) ICME-based Design Optimization. The parameterized designs are in place for these three starting points. Additionally, the stiffness, strength, durability, and safety (energy absorption) are in place. These are incorporated into the full MDO workflow as described in the following sections.

Figure II.2.C.16 details the status of three parametric sub-frame models which were used in MDO process.

Three Variants

- V1: SMC intensive Design with
 - UD/NCF-Z local reinforcement
 - Steel compression limiters
 - **Complete Parametric Model**
- V2: UD/NCF-Z intensive Design with
 - SMC local ribbing reinforcement
 - Steel compression limiters
 - **In Progress (debugging)**
- V3: Aluminum Intensive Design with
 - UD/SMC local reinforcement
 - Steel compression limiters
 - **Complete Parametric Model**

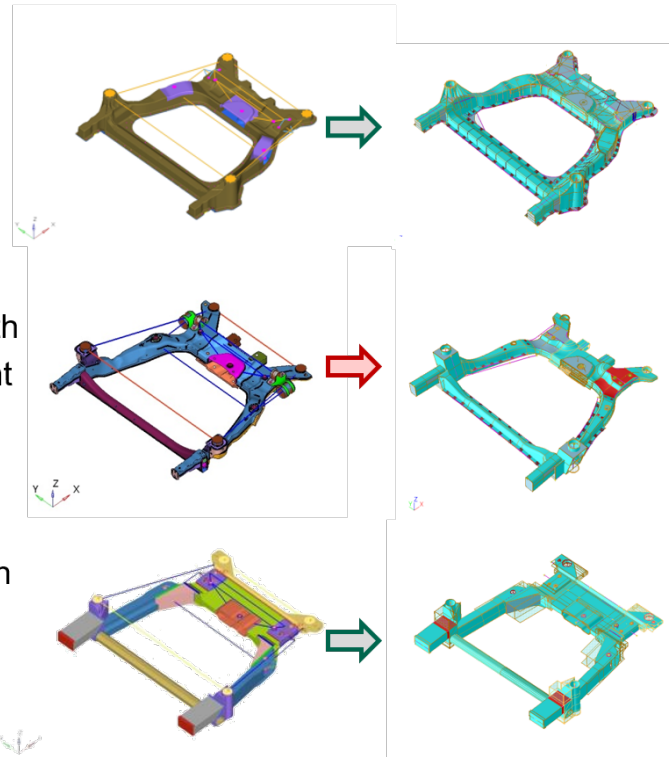


Figure II.2.C.16. Status of parametric models for three “seed” designs. Source: Ford Motor Company.

Subtask 4.2 – ICME-Based Design Optimization

The overall MDO process starts with global design variables and a DOE, and then: (1) using geometric design variables within parametric models for the subframes to generate the performance models; (2) creating header files for the FEA simulations generated from the concept model and cost estimation which use the ICME-based material models; (3) defining design variables; (4) extracting responses of interest for constructing the response surface models; and (5) optimizing and verifying the final design. Figure II.2.C.17 depicts the MDO process for the sub-frame designs without local manufacturing-based material properties.

The team has been exercising the sub-frame ICME-based MDO. These efforts have identified areas for improvements in the SFE modeling, the HCF analysis, and performance results post-processing. Currently, we generate approximately 80 DOE points per day to develop the response surface for the overall sub-frame optimization.

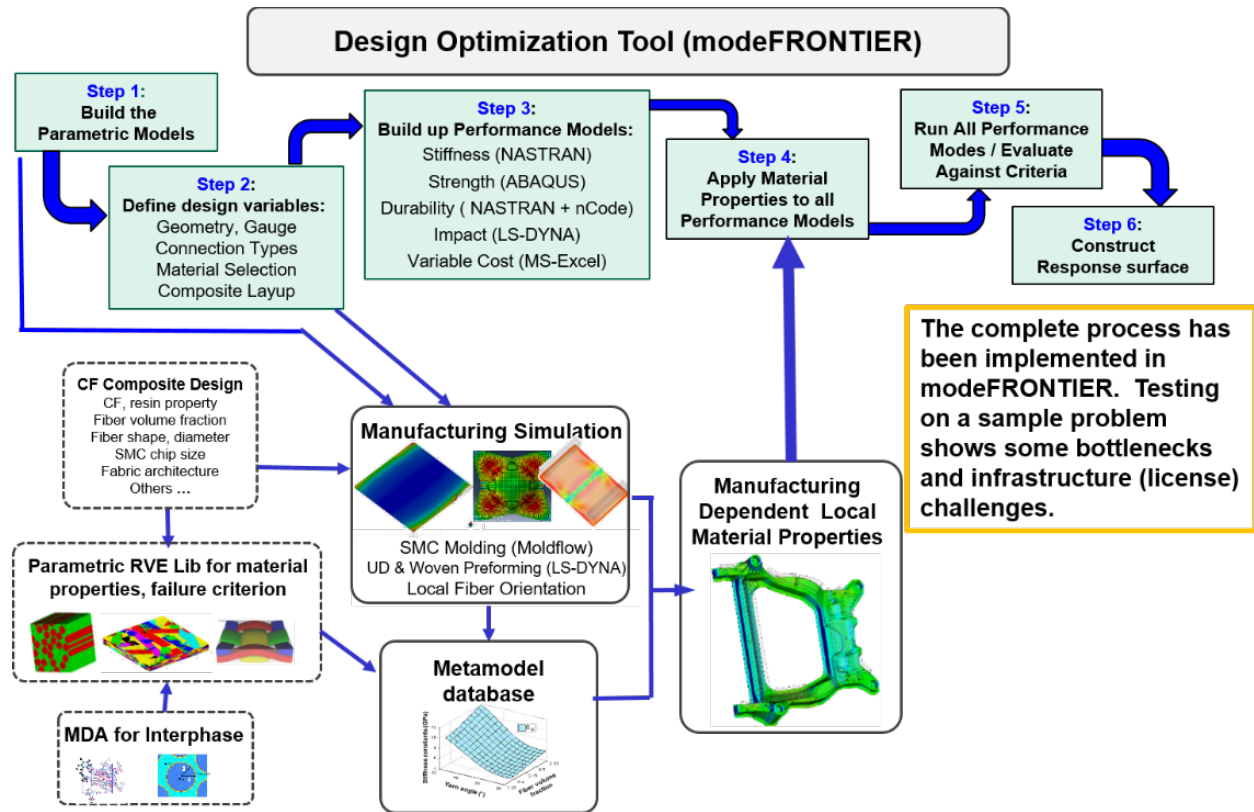


Figure II.2.C.17. MDO process steps for sub-frame design. Source: Ford Motor Company.

Subtask 4.3 – Performance Analysis and Model Demonstration

For the full sub-frame evaluation, the stiffness, strength, durability, and safety performance analyses have been identified and tested within the MDO workflow. Additionally, the performance metrics for all the performance analyses have been identified and the post-processing scripts to automatically obtain results from FEA simulations are in place. These results are crucial to generating the response surface for the optimization. The first sub-frame seed design has been evaluated through the complete flow.

Subtask 4.4 – Weight and Cost Analysis

The cost-estimating module in the MDO workflow was completed. The model estimates the variable cost based on the weight of the materials used in the sub-frame. The estimate uses weighted ratios of the materials coupled with our internal Ford material and manufacturing costs for stamped steel, Al, and CF composite subframes as the reference points. The cost-estimating model is working efficiently within the MDO flow. The weight for each candidate design follows directly from the design. The material density and design geometry determine the weight of each design iteration. Figure II.2.C.18 shows interesting designs on the percentage weight saved versus additional variable cost per pound saved plot. These initial designs include a primarily stamped steel design with less than 5% unidirectional CF composite at approximately 10% weight saved at \$4 per pound saved. Another initial design that will be further refined uses over 80% random chopped CF SMC plus steel and unidirectional CF composite reinforcements. This design exceeds the weight reduction target but costs more than the cost target at approximately 40% weight saved and \$8 per pound saved. These attractive initial designs are being further investigated, refined and verified for accuracy and completeness.

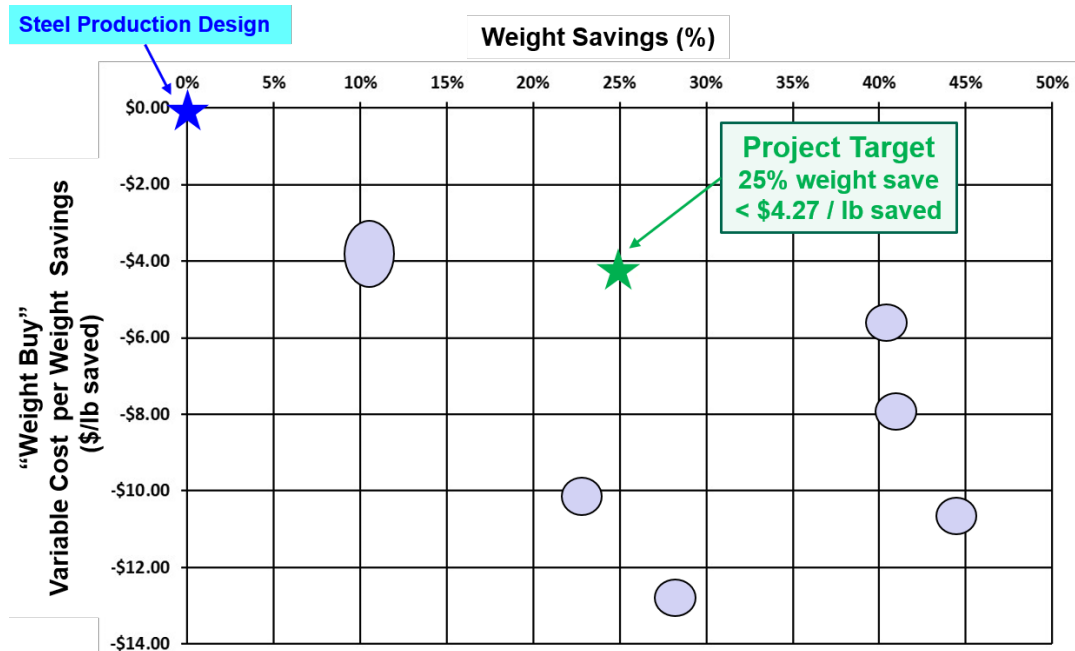


Figure II.2.C.18. Interesting initial design regions being further investigated and refined. Source: Ford Motor Company.

Conclusions

FY 2018 was the last year of the “ICME Development of CF Composites for Lightweight Vehicles” project, which develops ICME tools for CFRP composites and use ICME tools to design structural CF composite sub-frame to support immediate weight reduction in LD vehicles and reduce development-to-deployment lead time.

Active tasks in FY 2018 are Task 3 and 4 (i.e., the ICME Model Integration and Validation and the ICME-based Design and Optimization, respectively). However, efforts are continuously ongoing to further improve and extend ICME models, which were established and validated in previous years. Among new developments in testing and modeling, new ultrasonic imaging techniques were applied to dynamic 3-point bending hat section samples to study the laminate delamination failure. These images and analyses were collaborated and confirm the results of crash analysis, which clearly showed large-scale degradation of structure stiffness.

All fatigue tests are completed with a wealth of reliable data for nCode durability analysis for UD, woven, and SMC CFRP. Fatigue tests of CFRP are very challenging. Issues such as specimen size dependency, specimen and tabbing area overheating, and specimen bucking, etc., exist. No testing standard was available and publications in literature were limited and, in some cases, inconsistent. These and other testing issues were resolved by numerous tries and innovations throughout the duration of the project and consistent fatigue data are finally obtained.

Uncertainty qualification and propagation is another area where great progress has been made in FY 2018. A tool set consisting of a number of codes was developed, which characterizes variations in macro-scale primers such as elasticity parameters, or structure stiffness in terms of variations of yarn angles, shapes, volume fractions for woven composite and fiber waviness, and volume fractions of UD.

Great progress has been made by Task 3 and 4. In FY 2018, the structure optimization workflow is developed for the process integration and design of an SMC-intensive sub-frame. modeFrontier is chosen as the platform for ICME tool integration and design optimization. Existing capabilities and added scripts enabled a seamless integration of manufacturing simulation and vehicle performance analysis. The fully integrated optimization

process was demonstrated on the hat section example first, and then used for the sub-frame design. This workflow was tested by DOE runs to demonstrate that all simulation models and scripts can be automatically executed. In the integration workflow, a parallel structure is used to minimize the turnaround time of structure performance simulations. Parametric structure models and the correspondent CAE input deck is generated based on the gauge, composite lay-up, and other design variables. Then, the five performance analysis components (e.g., stiffness, durability, strength, impact, and cost) are submitted to the HPC system simultaneously.

Two concepts have been developed for the sub-frame based on the topology results. The two concepts are SMC-intensive design and AI-intensive design, respectively. These two designs serve as the “seed” initial starting points for the MDO ICME-based Design Optimization. The parameterized designs are in place for these two starting points. Additionally, the stiffness, strength, durability, and safety (peak load) are in place. These are incorporated into the full MDO workflow. The metrics for all the performance analyses have been identified and the results post-processing scripts efficiently obtain the results. The cost-estimating module in the MDO workflow was completed and integrated into the MDO flow. The estimate uses weighted ratios of the materials coupled with Ford internal material and manufacturing costs for stamped steel, AI and CF composite subframes as the reference points.

Current MDO suggested that the design that meets both the cost and weight target would likely be an SMC-intensive sub-frame with some steel components. The work to obtain the most promising concepts is still ongoing, which would be close to the target of greater than 25% weight reduction and less \$4.27 per pound of weight saved.

The ICME tools that have been developed have and will continuously be implemented in popular software packages, such as LS-DYNA for stress and crash analysis, nCode for durability, Moldflow for molding, and modeFrontier® for process integration and optimization.

Key Publications

1. Bostanabad, R., B. Liang, J. Gao, W. K. Liu, J. Cao, D. Zeng, X. Su, H. Xu, Y. Li, and W. Chen, 2018, “Uncertainty quantification in multiscale simulation of woven fiber composites,” *Comput. Methods Appl. Mech. Eng.*, Vol. 338, pp. 506–532.
2. Chen, Z., T. Huang, Y. Shao, Y. Li, H. Xu, K. Avery, D. Zeng, W. Chen, and X. Su, 2018, “Multiscale finite element modeling of SMC composite structure based on stochastic mesostructure reconstruction,” *Compos. Struct.*, Vol. 188, pp. 25–38.
3. Cheng, H., J. Gao, O. L. Kafka, K. Zhang, B. Luo, and W. K. Liu, 2017, “A microscale cutting model for UD CFRP composites with thermomechanical coupling,” *Compos. Sci. Technol.*, Vol. 153, pp. 18–31.
4. Fenner, J. S., and I. M. Daniel, 2018, “Testing the 2-3 Shear Strength of Unidirectional Composite,” Society for Experimental Mechanics Annual Conference, June 4–7, 2018, Greenville, SC, USA.
5. Gao, J., B. Liang, W. Zhang, Z. Liu, P. Cheng, R. Bostanabad, J. Cao, W. Chen, W. K. Liu, X. Su, D. Zeng, and J. Zhao, 2017, “Multiscale Modeling of CFRP for ICME Process,” 31st Annual Technical Conference, American Society for Composites, October 23–25, 2017, San Antonio, TX, USA.
6. Li, Y., Z. Chen, L. Su, W. Chen, X. Jin, and H. Xu, 2018, “Stochastic reconstruction and microstructure modeling of SMC chopped fiber composites,” *Compos. Struct.*, Vol. 200, pp. 153–164.
7. Sun, Q., D. Zeng, D. Li, and X. Su, 2018, “Experiment and Simulation Study on Unidirectional CF Composite Component under Dynamic 3-Point Bending Loading,” SAE Congress 2018, April 10–12, 2018, Detroit, MI, USA.

8. Tang, H., Z. Chen, G. Zhou, Y. Li, K. Avery, H. Guo, H. Kang, D. Zeng, and X. Su, 2018, “Correlation Between Failure and Local Material Property in Chopped CF Chip-reinforced SMC Composites under Tensile Load,” *Polym. Composite*, open access. doi:10.1002/pc.24767.
9. Zhang, W., J. L. Xuan Ma, Z. Zhang, Q. J. Wang, X. Su, D. Zeng, M. Mirdamadi, and J. Cao, 2018, “Experimental characterization and numerical modeling of the interaction between CF composite prepregs during a preforming process,” *J. Manuf. Sci. Eng.*, Vol. 140, No. 8, Art. 081003. doi:10.1115/1.4039979.
10. Zhang, W., R. Bostanabad, B. Liang, X. Su, D. Zeng, M. A. Bessa, Y. Wang, W. Chen, and J. Cao, 2018, “A numerical Bayesian-calibrated characterization method for multiscale prepreg preforming simulations with tension-shear coupling,” *Compos. Sci. Technol.*, in review.

References

1. Kawai, M., and M. Koizumi, 2007, “Nonlinear constant fatigue life diagrams for carbon/epoxy laminates at RT,” *Compos. Part A Appl. Sci. Manuf.*, Vol. 38, No. 11, pp. 2342–2353.
2. Kawai, M., and N. Itoh, 2014, “A failure mode based anisomorphic constant life diagram for a unidirectional carbon/epoxy laminate under off-axis fatigue loading at RT,” *J. Compos. Mater.*, Vol. 48, No. 5, pp. 571–592.
3. Harris, B., N. Gathercole, J. A. Lee, H. Reiter, and T. Adam, 1997, “Life-prediction for constant-stress fatigue in carbon-fibre composites,” *Philos. Trans. Royal Soc. A*, Vol. 355, No. 1727, pp. 1259–1294.

Acknowledgements

The authors thank and gratefully acknowledge our colleagues in Ford Research and Advanced Engineering, Dow Chemical Company, NU, NIST, and the University of Maryland for their efforts and support of this research project. Researchers and developers from Livermore Software Technology Corporation, HBM Prencia, Autodesk, and ESTECO have also contributed to this exciting project. Over 100 research scientists and engineers have contributed to this project. Additionally, the authors thank our technology manager and project manager at DOE-EERE’s VTO.

This material is based upon work supported by the DOE’s National Energy Technology Laboratory under Award “ICME Development of CF Composites for Lightweight Vehicles - DE-EE0006867”.

This report was prepared as an account of work sponsored by an agency of the U.S. Government. Neither the U.S. Government nor any agency thereof, nor any of their employees, makes any warranty, express or implied, or assumes any legal liability or responsibility for the accuracy, completeness, or usefulness of any information, apparatus, product, or process disclosed, or represents that its use would not infringe privately owned rights. Reference herein to any specific commercial product, process, or service by trade name, trademark, manufacturer, or otherwise does not necessarily constitute or imply its endorsement, recommendation, or favoring by the U.S. Government or any agency thereof. The views and opinions of authors expressed herein do not necessarily state or reflect those of the U.S. Government or any agency thereof. Such support does not constitute an endorsement by DOE of the work or the views expressed herein.

II.2.D Development and Integration of Predictive Models for Manufacturing and Structural Performance of CF Composites in Automotive Applications (General Motors)

Venkateshwar Aitharaju, Principal Investigator

Chemical Sciences and Material Systems Laboratory
 General Motors R&D Center
 30470 Harley Earl Blvd.
 Warren MI 48092-2031
 E-mail: venkat.aitharaju@gm.com

H. Felix Wu, Ph. D, DOE Technology Manager

U.S. Department of Energy
 E-mail: felix.wu@ee.doe.gov

Start Date: May 1, 2015	End Date: April 30, 2019	
Project Funding (FY18): \$1,948,630	DOE share: \$1,364,041	Non-DOE share: \$584,589

Project Introduction

GM was the first North American automotive original equipment manufacturer to develop and commercialize CF composites for Class A body panel (i.e., closure) applications. Going forward, our objective is to advance beyond closure components and implement CF composites in structural body panels that undergo the complex loading conditions represented in crash and durability. To enable these broader automotive structural applications of CF composites, three key issues must be addressed. First, significant variability in material properties incurred during the manufacturing process need to be understood and predicted. Second, prediction of the structural performance of composites undergoing complex loading (i.e., crash) under varied environmental conditions is required. Third, the effect of manufacturing on the performance of the final components needs to be understood and predicted. Without a good handle on these issues, automotive designs can be overly conservative, thereby increasing cost significantly and limiting the weight reduction potential of CF composites. The present project addresses all of these needs by developing a suite of ICME tools to predict manufacturing performance and structural performance of CF composites, including stochastic effects.

Objectives

The goal of this project is to develop an integrated suite of state-of-the-art computational modeling tools that are critically needed to enable structural CF applications in automobiles. These tools help to predict the manufacturing and structural performance of CF composites, including stochastic effects. The project team is comprised of researchers from GM, Engineered Solutions, Inc. (ESI), Group (i.e., software company, owner of composite manufacturing tool PAM-COMPOSITES for composites, which include PAM-RTM for resin transfer molding and PAM-FORM for forming of composites), Altair (i.e., software company, owner of the multiscale structural performance predictive tool for composites), Continental Structural Plastics (CSP) (i.e., molder/material supplier for composite materials and GM-Corvette composite parts supplier), and the University of Southern California (i.e., leader in uncertainty quantification of DOE's-funded Scientific Discovery through Advanced Computing Institute for Uncertainty Quantification). During the first phase of the project, both the manufacturing and structural performance tools, including a stochastic driver, were calibrated and validated against coupon and component level tests. The difference between predictions and experimental results was limited to less than 15%. During the second phase of the project, the manufacturing and performance tools will be integrated by mapping the manufacturing outcome (e.g., fiber angles, residual stresses, degree of cure, and defects [voids, dry patches, and wrinkles]) into structural models.

In FY 2018, major efforts were spent in designing a composite CF automotive assembly for a high-volume, medium-duty automobile currently made of steel using the integrated manufacturing and structural performance tools developed in this project. Various CF materials friendly to high-volume automotive manufacturing (e.g., non-crimp, woven, chopped systems) and manufacturing processes (e.g., such as RTM and compression molding) were used. Final designs of the assembly components were provided to the CSP for building the tools. The tools are expected to be delivered by the end of 2018.

In FY 2019, the optimized CF automotive assembly will be certified, and the developed numerical models will be validated by comparing the numerical and experimental results for the performance of the assembly. Also, the optimized CF assembly design, weight, cost, and performance will be compared with the existing design.

The availability of ICME tools to predict stochastic manufacturing and structural performance of structural composites to an original equipment manufacturer, like GM, can potentially eliminate significant bottlenecks that currently exist with large-scale implementation of CF composites in an automobile.

Approach

Four key components of probabilistic ICME will be at the core of our approach, namely model integration, optimization, validation, and design certification. The computational engine will be constructed by the integration of state-of-the-art tools and capabilities from specific domains, namely, composites manufacturing (from GM and CSP), process simulation software for composites (from ESI), integrated multiscale/multiphysics structural software (using the multiscale design system [MDS] of Altair), probabilistic methods and probabilistic software (from the University of Southern California), and, finally, the largest U.S. automaker with considerable expertise and a record of accomplishment in the design and manufacturing of composite cars (e.g., the Chevrolet Corvette [from GM]) leads the project and integrates these modules. By model validation, we refer to making a prediction of the variables of interest and comparing the specific variables under the same conditions. By certification of a component, we mean the assurance that once designed, manufactured, and loaded (i.e., crash-tested), these components will perform satisfactorily up to preset specifications. Enabling model validation and component certification requires retooling of the deterministic scientific process, specifically by requiring evidential attributes to be attached to model-based predictions. During this project, we will identify the limitations of existing software components comprising the computational engine and offer alternative technologies and solutions that facilitate integration for design optimization. Once the computational engine has been developed and validated, the chosen CF assembly will be designed, optimized, tested, and certified, and the resulting composite component will be compared to current steel design.

The present CF ICME project is organized into ten tasks executed over a 48-month period. An outline of the tasks carried out during FY 2018 is as follows:

- Task 1.0: Project planning, coordination, and reporting – ongoing.
- Task 2.0: Select the automotive assembly preliminary design – completed.
- Task 3.0: Identify preliminary CF material systems and manufacturing processes – completed.
- Task 4.0: Develop and validate the manufacturing and crash simulation engines – completed.
- Task 5.0: Integrate the manufacturing and structural models – completed.
- Task 6.0: Design and optimize automotive assembly for manufacturing and performance – completed.
- Task 7.0: Design and fabricate assembly and the test fixture – completed.
- Task 8.0: Manufacture the automotive assembly – not started.
- Task 9.0: Certify the automotive assembly – not started.
- Task 10.0: Assessment of the assembly: correlation of predictions with experimental results – not started.

Results

In FY 2018, most of the work focused on engineering the automotive assembly chosen for demonstration, but this item is protected from public disclosure. In addition to this activity, several tasks were accomplished solving some of the more challenging problems. This enabled us to accomplish the 100% virtual design of a large CF assembly for a challenging load case of crashworthiness. Those items are not protected and are therefore provided in this report.

The salient items covered in the area of manufacturing simulation are: (1) development and validation of draping models for automotive friendly NCFs; (2) validation of resin injection and curing models for a state-of-the-art fast curing resin from Hexion; (3) multiscale structural simulation; (4) validation of progressive damage model for bending of a double-hat section beam; and (5) stochastic manufacturing simulation of the complete molding process, including draping, injection, curing and demolding. Beside these items, a status on the tools built for manufacturing the components of the CF assembly is presented.

Manufacturing Model Development

In FY 2018, the team engineered four large components for high-pressure RTM using the PAM-COMPOSITES tool developed and validated in this project. Manufacturing steps such as draping, injection, and curing were simulated for all assembly components. Besides this activity, the ESI team continued validating material models on coupon and component levels for different resin and preform systems. The ESI team assisted the academic partner, USC, in building stochastic models to demonstrate the manufacturing integration – ICME – of different processes. The ESI team also assisted the industrial partner, CSP, in designing tools that can produce parts in accordance to GM targets.

The manufacturing models calibrated and validated for the selected resin and preform systems were used to simulate the assembly chosen for demonstration. Draping feasibility analysis for automotive friendly NCFs was performed, including establishing slit designs where regular flat blanks would not work. For resin injection simulations, different sizes and shapes of resin runners were considered for faster filling to enable the use of fast curing resins. Also, race-tracking effects were included to account for the uncertainty at ply-drops and edges. The size and shape of the injection channels were virtually designed/engineered by simulating the entire process, considering the equipment capabilities (i.e., GM and CSP), such as the maximum injection pressure, flow rate, molding tonnage, etc. Before that, a material model of the fast curing resin from Hexion was developed and validated by correlating with experiments conducted by the CSP team. Detailed simulations provided optimum locations for venting and channel systems and optimized process conditions, such as mold temperature and flow rates.

In FY 2019, the models required for the demolding phase, namely PAM-DISTORTION models, will be investigated to study the post curing residual stresses and distortions. The effect of the thermal cycle will be studied in order to minimize these residual stresses and distortions.

Draping Model Development

Two NCFs, provided by Chomarat North America (Anderson, SC, USA) with differing areal weights, 300 g/m² and 240 g/m², were used for these experiments. Additionally, the 240 g/m² fabric contained a 12 g/m² thermoplastic co-polyamide veil binder. Both fabrics used tricot stitching with a 3.3 mm stitch length and a 5 mm stitch gauge.

The PAM-FORM material model, MAT 140, was used to simulate the draping of NCF material with different fabric parameters. The nonlinear shear stiffness measured using the bias-extension test method was calibrated using a small simulation model, and these results were imposed on the model via a test curve function. For fabric bending, a methodology similar to the Pierce Cantilever Bending method was developed and modeling performed accordingly. Calibrations for both properties were performed for both NCF materials. The data from

the calibrated coupon models were then used in conjunction with the truncated pyramid model to predict the draping behavior of the NCF fabrics.

For characterizing the shear behavior, a coupon-scale finite element model was developed in PAM-FORM. The model is a simple tension model with fibers aligned $\pm 45^\circ$ to the loading direction. The modeling scheme is similar to the work previously done by Rodgers et al. [1] on woven fabrics.

It is evident that the shear response is different in the different stitch directions, making it directionally dependent. When the stitch is in the loading direction, resistance is added to the fabric shearing, whereas when the stitch is transverse to the loading direction, it adds little resistance to the shearing of fiber tows, since in this test direction the stitch is actually in compression. Therefore, it was established that positive shear is when the stitch is in the loading direction and the angle established between Fiber 1 ($+45^\circ$) and Fiber 2 (-45°) closes during the test. Negative shear is when the stitch is transverse to the loading direction and the angle between Fiber 1 and Fiber 2 opens during the test.

The combined shear stress vs shear strain curves for the two fabrics were used to describe the shear stiffness in the draping simulation of the truncated pyramid form. The shape of these curves closely reproduced the results from the original bias-extension evaluations. The BX240 V114CHA fabric displayed nearly double the shear stiffness when compared to the BX300 fabric.

Similar to the bias-extension tests, a coupon-scale finite element model representing a cantilever beam was developed in PAM-FORM to characterize the bending behavior. In this setup, the fibers were aligned in the 0° direction with the stitching running in the $\pm 45^\circ$ direction. In the model, the fabric was allowed to fall under its own weight until convergence of the assumed bending stiffness was reached. The final deformed shape of the model was then compared to the experiments for calibration. For the BX300 fabric, a bending stiffness of 300 MPa in the fiber direction was determined. A calibrated constant bending stiffness of 210 MPa was determined for the BX240 V114CHA fabric, which was used in the truncated pyramid simulation.

Draping Model Validation – Truncated Pyramid Tool

Following the successful coupon level calibrations for shear and bending behavior, the performance of selected NCF materials was further validated using the truncated pyramid tool and the calibrated input data.

For testing, the fabrics were cut into squares along the roll direction and draped to the truncated pyramid tool. Forming the BX240 V114CHA fabric without using a metal frame as a fabric holder resulted in the formation of several large folds and wrinkles on the sloped surfaces of the pyramid, as shown in Figure II.2.D.1. Repeated draping experiments using this fabric showed good consistency of the wrinkle locations. In a second set of experiments using the metal frame, the large folds did not form, and only minor waviness of the fabric was observed.

The BX300 fabric did not form any large folds whether the metal frame was used or not. This difference in behavior is due to the shear and bending stiffness differences between these two fabrics due to their respective areal weights and construction. The wrinkling phenomenon in the draped fabric is caused by compressive forces during forming. These forces are determined by the fabric bending and shear stiffness in combination. When the fabric could no longer accommodate the orthogonal compressive forces, it buckled and produced wrinkles that could not be removed. From these observations, it appears that increasing the shear stiffness and/or reducing the bending stiffness leads to an increased chance of forming folds during draping.

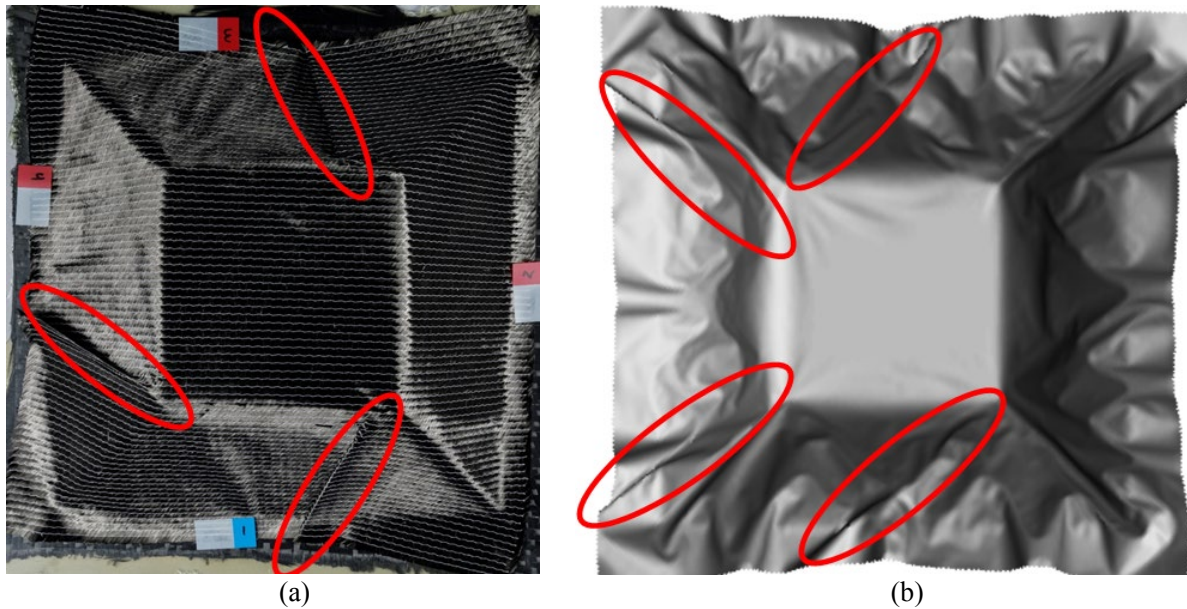


Figure II.2.D.1. Draping results of BX240 V114CHA without using the frame. Folds are highlighted in red circles.
 (a) Image of the fabric from the experiment. (b) Simulation results. Source: GM.

Since buckling is caused by nonlinear instabilities, it is difficult to quantify the size of the large folds or the exact extent of the buckling, but the location and shape of the wrinkles can be compared between the experiments and draping simulations.

For this validation study, a single-ply shell model for the BX300 and BX240 V114CHA fabrics was constructed. The die and punch tools were modeled as rigid bodies. A tool closing velocity of 200 mm/s was used in the simulations. A stop criterion for the moving tool was set to 2.4 mm from the two halves of the tool being in contact to be representative of the way the experiments were conducted. Two different configurations were simulated for each selected material, one without using a frame and one using a frame. For the BX240 V114CHA, an additional layer representing the veil was modeled using an isotropic material model. A sticky contact was used between the two layers to represent the way the veil contacted the CF fabric. For the BX240 V114CHA fabric, the draw-in shape, formation, and location of folds match well with the experimental results shown in Figure II.2.D.1 above. When the frame is used during the deformation of the BX240 V114CHA fabric, no folds were observed in the simulation or the experiment, and the draw-in of the fabric also matched the draw-in observed from the experiments well.

For the deformation of the BX300 material, either with or without the frame, the draw-in shapes matched well between the experiment and the simulation.

It is clear from both the experiments and the simulations that the fabric architecture had an impact on the formability of these materials. Although from these results alone, it is not possible to tell if the difference in behavior is due to the effect of the presence of the veil or due to an effect from the different areal mass. Even though large folds are now being predicted, more refinement of the modeling, perhaps involving additional experimental testing or perhaps evaluating different draping conditions, may be required.

Draping Model Validation – Reinforcement Tool

The PAM-FORM model calibrated for NCF fabrics on the truncated pyramid component was used to predict the draping behavior of NCFs on the reinforcement preforming tool for validation. The simulations were run using various blank designs for single- and multi-layers and compared with experiments.

The CSP team built a wooden preforming tool for a single reinforcement hat section that we selected to validate the simulation models. This reinforcement geometry is quite complex and provides an excellent test case. Using this preforming tool, different preforming strategies were considered, including virgin preforms and also preforms with slits. Pictures of the test rig are shown in Figure II.2.D.2. The test rig is operated using a hydraulic jack to simulate automatic closing of the tools during a preforming operation.

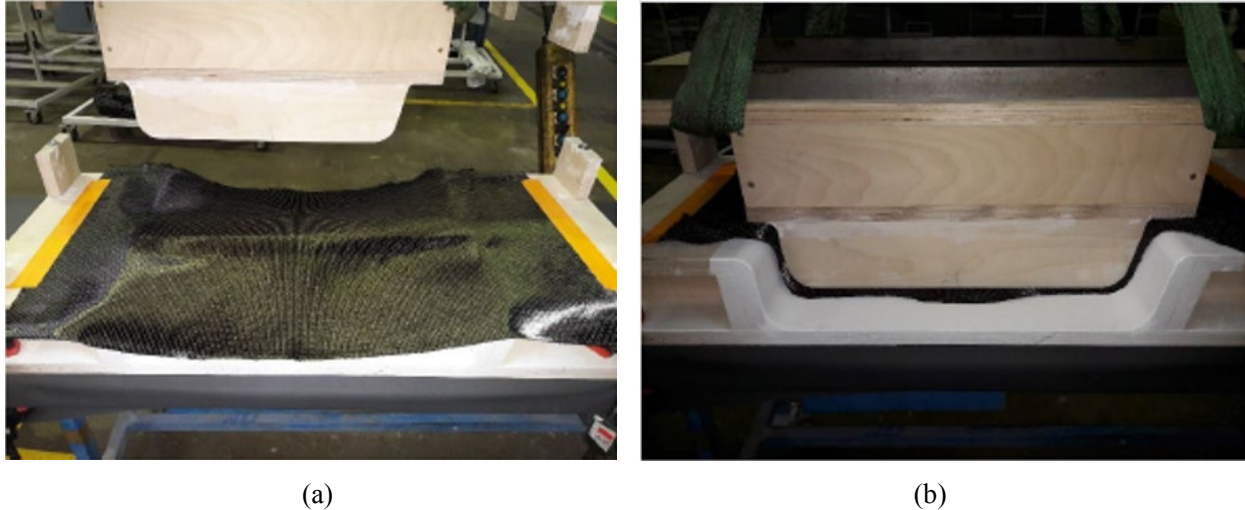


Figure II.2.D.2. The preforming rig in the (a) open and (b) closed positions. Source: ESI.

Figure II.2.D.2 also shows the setup for a full rectangular blank, using tape to simulate the effect of blank holders on both sides. Experiments were performed on a variety of NCFs with different fiber orientations to create experimental data points for validating the draping model.

During the investigation, the team learned that as much as 30% raw material cost can be saved by using heavier weight CF fabrics. Heavier weight fabrics have the disadvantage, however, of lower drapeability. The CF assembly intended for demonstration for the project has several components which are 5-mm thick, requiring 20 layers when lightweight fabrics, such as 240 g/m² are used. For this reason, we explored using heavier CF fabrics, such as 600 g/m² material. We also expect significant savings in preforming costs due to fewer layers being required for preforming. In FY 2019, several studies will be made with 600 g/m² material. Conducting experiments and simulations enabling the use of heavier areal weight fabrics for the chosen CF automotive assembly can make the business case stronger. Initial experimental results suggest that using the heavier NCFs may not significantly reduce the preforming capability.

Case Study #1

In the first prototype study, an NCF with +/-45° fiber orientation in a fabric with different stitch directions was used and simulations were carried out to match the experiments. Figure II.2.D.3 shows the experimental setup for a +/-45 NCF fabric with fibers oriented at 45° and stitching at 0° with respect to the reinforcement length axis. The wrinkles that formed between the blank-holder edge and the reinforcement edge were also predicted in the simulation shown in Figure II.2.D.3. The side wrinkles seen in the simulation were mainly of numerical origin due to dynamic effects caused by not having the tool closed completely.

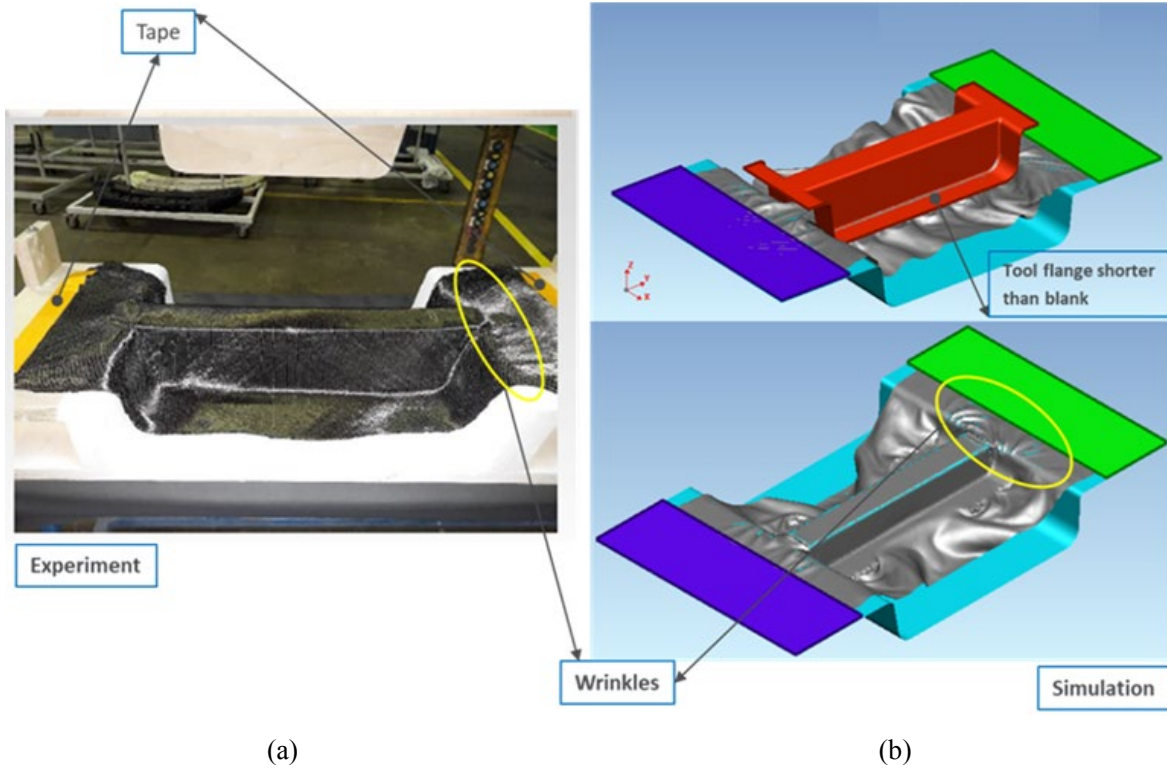


Figure II.2.D.3.(a) Test vs (b) simulation for NCF (+/-45) fabric with fibers in 45° along length. Source: ESI.

Case Study #2

In the second study, double-sided tape was used to represent a central blank-holder. Figure II.2.D.4 shows modeling and test setups for central blank-holder/tape mechanisms. NCF (+/-45) fabric with fibers in the 0° direction was used for this test. Figure II.2.D.5 shows the comparison where the predicted wrinkles match the experiment.

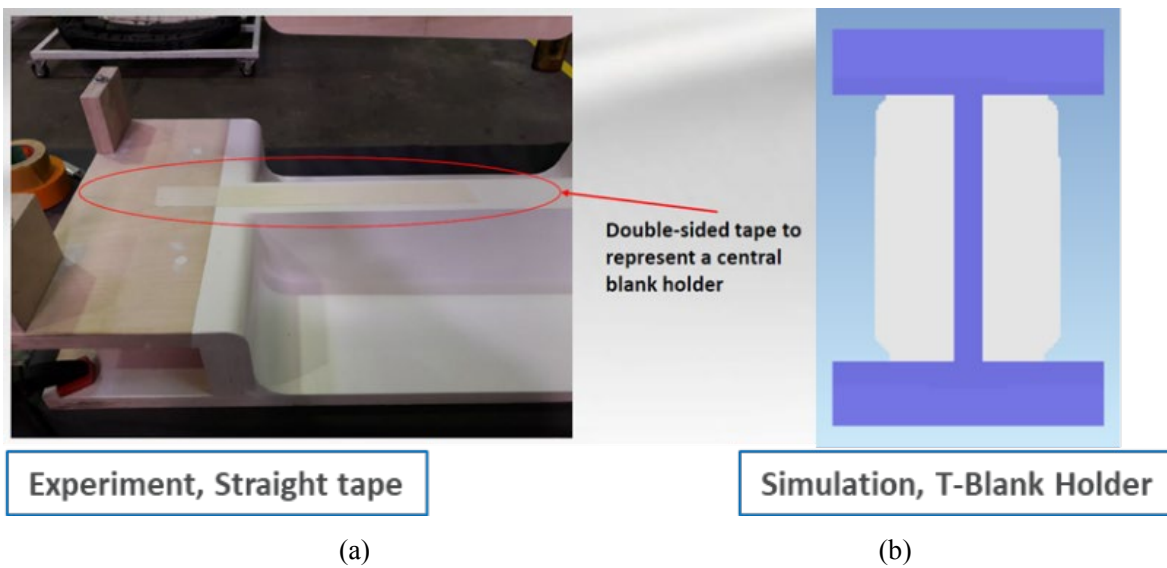


Figure II.2.D.4.(a) Test vs (b) simulation for a central blank holding mechanism. Source: ESI.

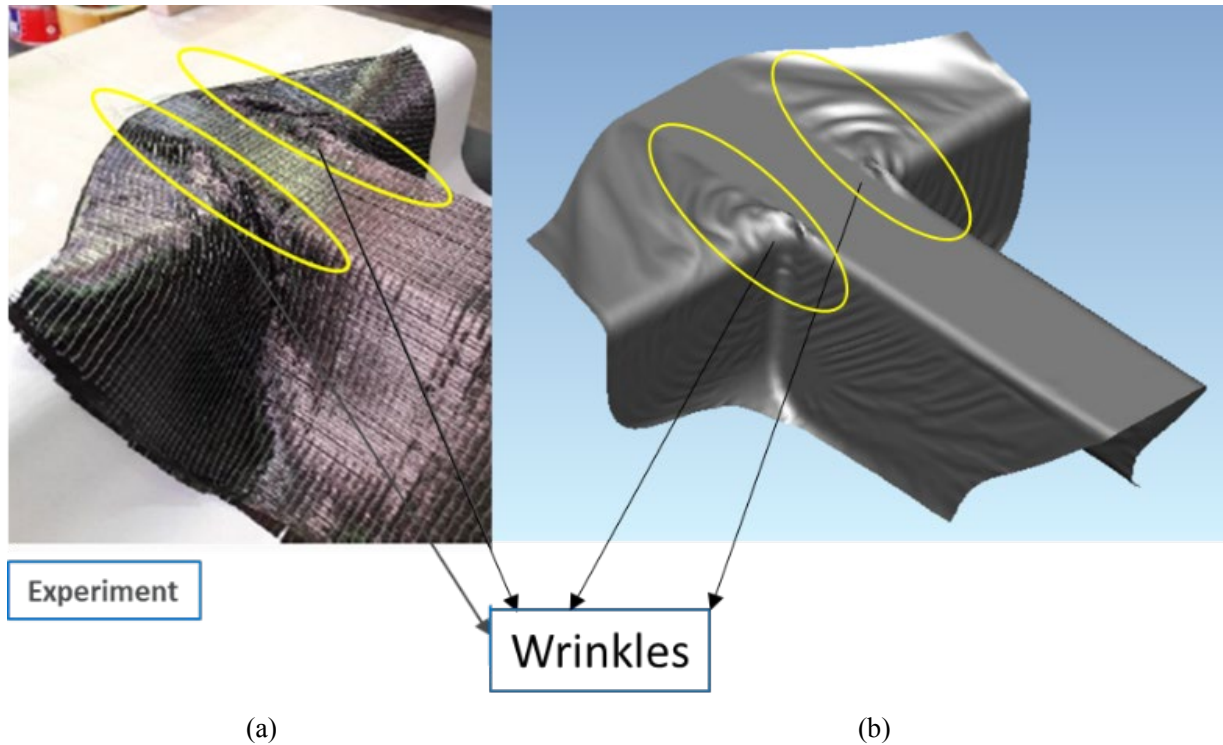


Figure II.2.D.5.(a) Test vs (b) simulation for NCF fabric draping 0° along the length of reinforcement. Source: ESI.

Case Study #3

In the third study, slits were added to the blank along the vertical edges (wrinkle prone zone from Study 3). Figure II.2.D.6 shows the modeling and experimental results. The comparison was in good agreement with the draped preform being wrinkle-free. Experiments confirm the prediction of the simulation model.

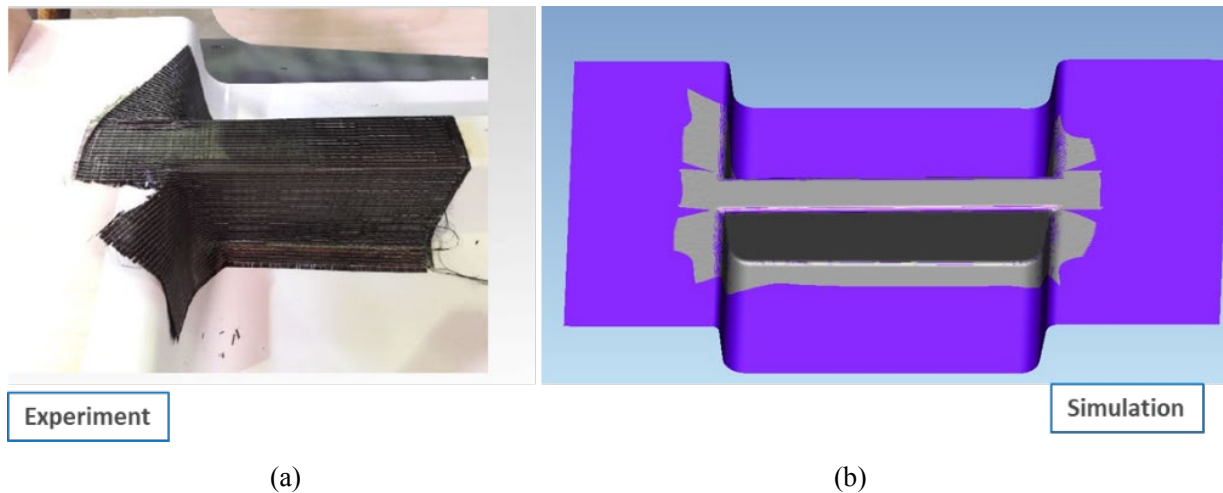


Figure II.2.D.6.(a) Test vs (b) simulation showing no wrinkles with slits. Source: ESI.

Case Study #4

Two different slit patterns, as shown in Figure II.2.D.7, were used in this test case. Figure II.2.D.8.(a) shows the initial deformed shape of the 2-ply stack due to gravity, while Figure II.2.D.8.(b) shows the punch operation. Correlations are in good agreement with overall good global behavior. There are a few noticeable differences, such as the one closing the tabs on the bottom flange area and waviness in simulation. Simulations

shows less closing of the tabs as compared to experiments. This could be attributed to variation in slit size, placement over the tool, or other numerical effects that need to be further investigated. The waviness in the simulation is due to the fact that the punch tool does not close completely in the final stage and this is mainly a numerical effect.



Pattern-1



Pattern-2

Figure II.2.D.7. Slit patterns used in the draping of reinforcement. Source: CSP.

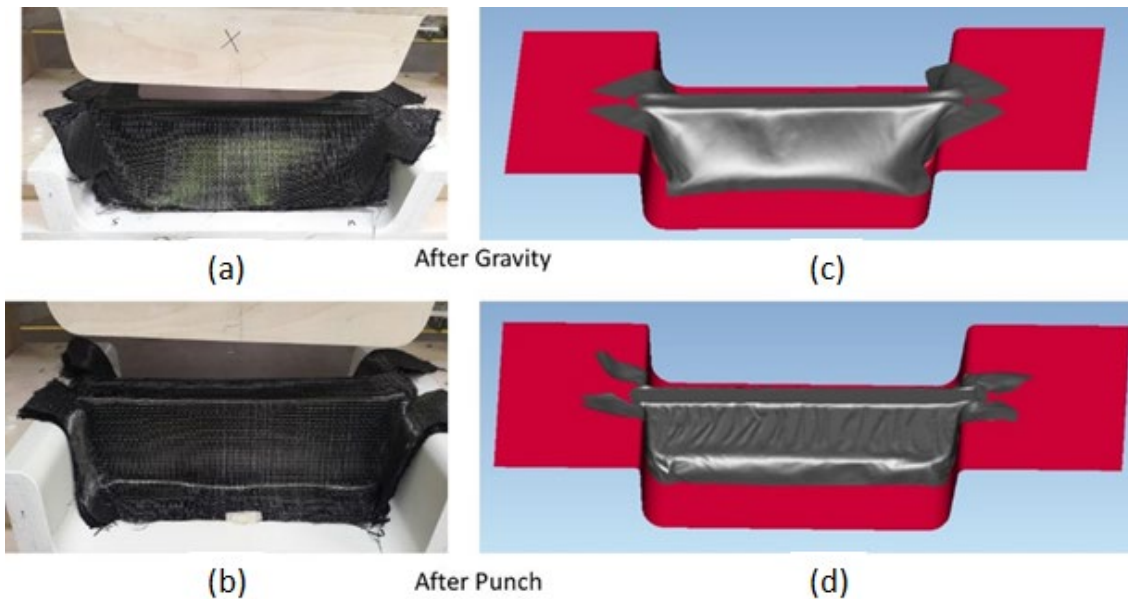


Figure II.2.D.8.(a) Deformed shape after gravity test; (b) Deformed shape after punch test; (c) Deformed shape after gravity simulation; and (d) Deformed shape after punch simulation. Source: ESI.

Model Validation for Hexion Fast Curing Resin System 06170

This experiment was designed to validate the injection and curing model developed for the selected Hexion resin, the state-of-the-art fast curing resin system we will be using to manufacture the components of the CF assembly that is the focus of this project. The Hexion 06170 resin system was used and injected at an initial resin temperature of 50°C. The fabric lay-up used Chomarat C-ply SP BT240 with an architecture of $[90/0]_{4s}$. The resin was injected into a 110°C mold using a flow rate of 41 cc/sec. The vacuum port was then closed after 15 seconds, while the injection continued for a total of 25 seconds. Upon de-molding, a dry region was observed in the center of the plaque. The simulation was conducted for this case using the following parameters for the predictions.

Material parameters:

- Hexion EPIKOTE™ 06170/06170 System
- The CSP team measured the permeability of these fabrics at the 56% fiber volume fraction provided in Table II.2.D.1
- Equivalent permeability calculated for the resin channel: $K_1=K_2=K_3=1.8E-07 \text{ m}^2$.

Boundary conditions:

- Injection was set as a constant flow rate with a maximum pressure:
 - 41 cc/s
 - 70 bars.

Table II.2.D.1. Permeability Values of the Non-Crimp CF Fabric.

Permeability - Direction	Value
K1 - along the fiber length	1.20E-11 m ²
K2 - perpendicular to the fiber length	7.01E-12 m ²
K3 - thickness of the lamina	5.90E-14 m ²

A peripheral channel was modeled as per the experimental setup. An equivalent permeability was calculated for the channel based on the channel dimensions. Because of the peripheral channel, the resin flows faster along the periphery and then closes in towards the center creating an area that is not wetted. Some discrepancy was noted between test and simulation in the location of air bubble either due to uncertainty of the actual permeability of the channel or due to some other reason, but the possibility of void formation was confirmed. Since the resin injection only starts at the 5-second mark, the numerical data has been offset to start at the same time. The pressure starts to build as the mold fills and the pressure evolution over time has been well-correlated with the experiment, as shown in Figure II.2.D.9. Figure II.2.D.10 shows the formation of a bubble in the model and in the tested plaque.

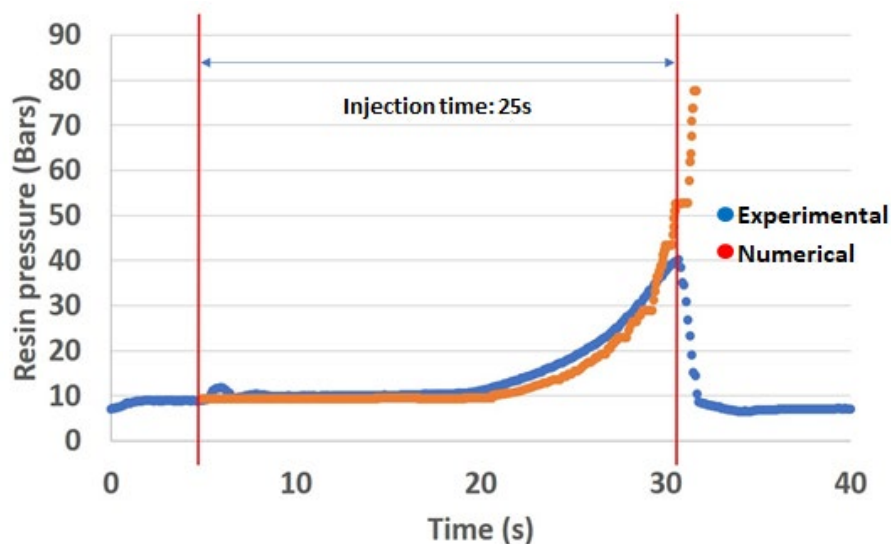


Figure II.2.D.9. Pressure evolution for peripheral injection - test vs simulation. Source: ESI.

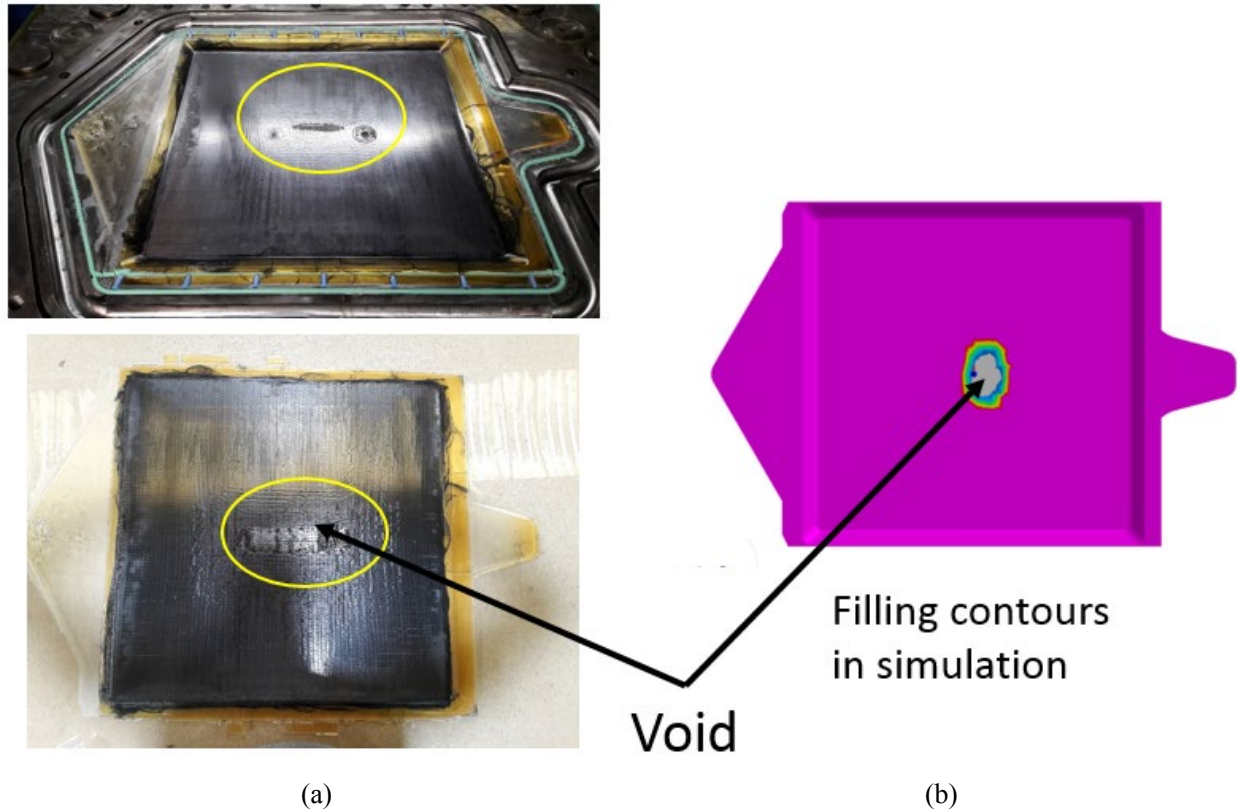


Figure II.2.D.10. Void formation comparison for (a) test and (b) simulation. Source: ESI.

Optimum Overlap

The CSP team performed molding experiments in order to determine the effect of different lengths of overlapping textile layers in a preform while keeping the overall thickness constant. A total of six plaques were molded, each with a different overlap length. An example is shown in Figure II.2.D.11.

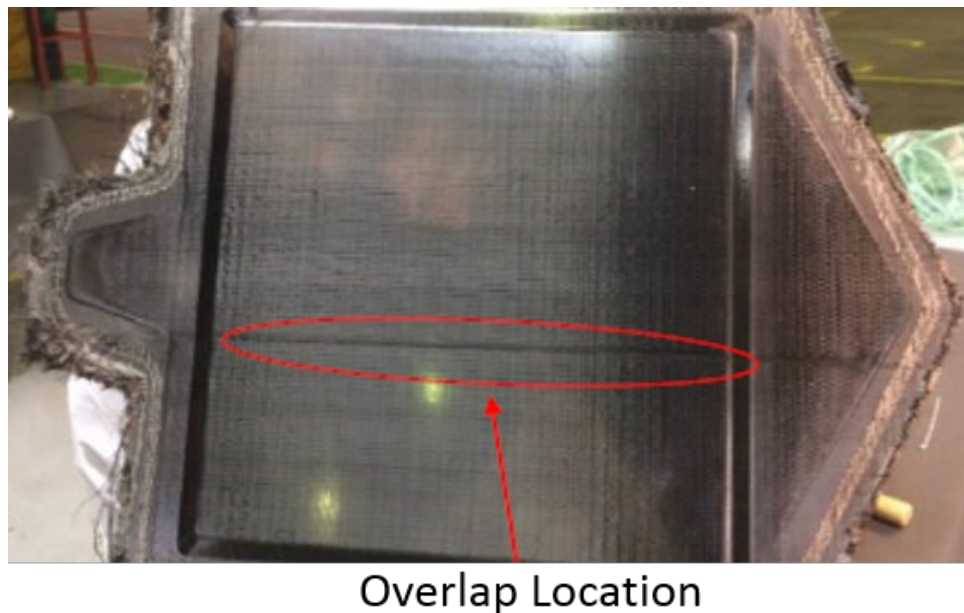


Figure II.2.D.11. Molded RTM plaque with overlap location indicated. Source: CSP.

Each plaque featured eight layers. A control plaque was molded that featured no overlap. Three plaques were molded with a single overlap (i.e., four plies on top, four plies on the bottom), with overlaps of 20, 50, and 100 mm. Two plaques were molded with multiple overlaps with an overlap length of 10 and 20 mm. These three different overlap configurations are shown in Figure II.2.D.12.

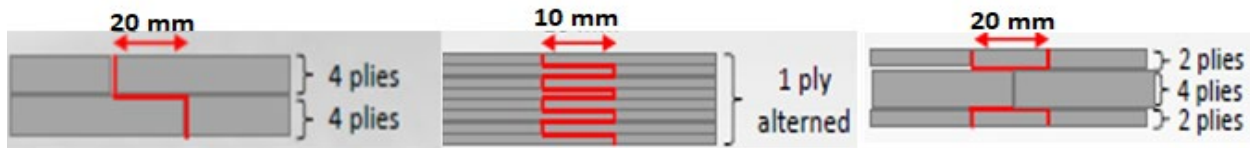


Figure II.2.D.12. Different overlap configurations. Source: CSP.

Regardless of the overlap length or configuration, the tensile strength was reduced by roughly 60% for specimens with overlaps compared to specimens without overlaps. Similarly, flexural strength dropped roughly 50% for all of the specimens with overlaps and the flexural modulus was significantly reduced in all cases, as well.

This work suggested that no overlap method can match the strength of non-overlapped layups and there is no preferred overlap length if the overall thickness in the overlap region is unchanged. From a design standpoint, this indicated that when overlaps are necessary, they must be positioned in non-critical areas where high tensile (or compressive) strength is not crucial. This study is very helpful in designing the ply drop-offs for the components of the CF assembly built-in this project.

Structural Performance Model Development

Besides the simulation work conducted on the CF assembly in FY 2018, the Altair team developed: (1) improved element deletion criteria; (2) a blind simulation and prediction of a three-point bending test of a double-hat section beam; (3) a single-precision multiscale designer/ls-dyna plugin; (4) customized user material shared libraries for LS-DYNA and scripts; (5) a revised residual thermal stress capability combined with damage; and (6) a preliminary multiscale modeling of cure process. The following sections describe these items in further detail.

Improved Element Deletion Criteria

In previous versions of the MDS, our element deletion criteria required complete failure of every material phase in every direction before the element was deleted. These criteria proved to be too conservative; we observed highly distorted elements that should be deleted, but remained intact, nonetheless. These “undeleted” elements led to the previously discussed numerical difficulties.

In the new version of the MDS, we provide users an extended element deletion framework that allows more flexible, less conservative, and more realistic element deletion criteria. Previously, the element deletion criteria were specified with a single scalar value. Once all of the damage scalars in every phase surpassed these criteria, the element was deleted. In the new version of the MDS, the element deletion criteria are specified with six scalar values. Having this wider failure criteria for element deletion, we have more flexibility to calibrate these criteria for multiple experiments before validation. Along with this failure criteria, additional criteria (including strain based criteria, plastic work criteria, damage scalar criteria, etc.) can be prescribed.

Three-Point Beam Bending of Double-Hat Section Beam

A blind simulation and prediction of a three-point bending test of a fabricated double-hat section beam was carried out by the Altair team to get more confidence in the design of the CF assembly chosen for demonstration. A finite element mesh of the experimental model was provided by the GM team to Altair. The three-point beam model was then run with RADIOSS and the MDS using the same NCF material studied earlier in the project. A plot of the experimental force-displacement curves with the fifth revision (R5) version

of code development, the simulation results is shown in Figure II.2.D.13, indicating good correlation between the simulation and the experiments. Figure II.2.D.14 show screen captures from a video of the experiment and the approximate correlating frame of the simulation.

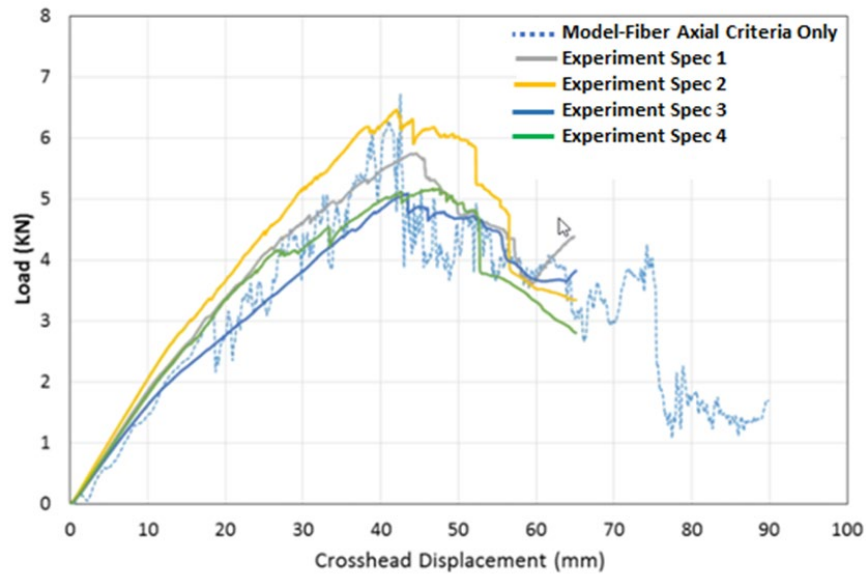


Figure II.2.D.13. Force-displacement plots of R5 simulation for a three-point bend model overlaid with experimental data.
Source: Altair.

The simulation shows a crack propagating across the flange and continuing downward into the bottom half of the model, which was not observed in the experimental testing. It is believed that this may be a result of the tied contact joining the two halves of the model at the flange. The experimental images provided in Figure II.2.D.14 show a downward inclination of the flange, likely caused by shear forces and a resulting slight displacement.

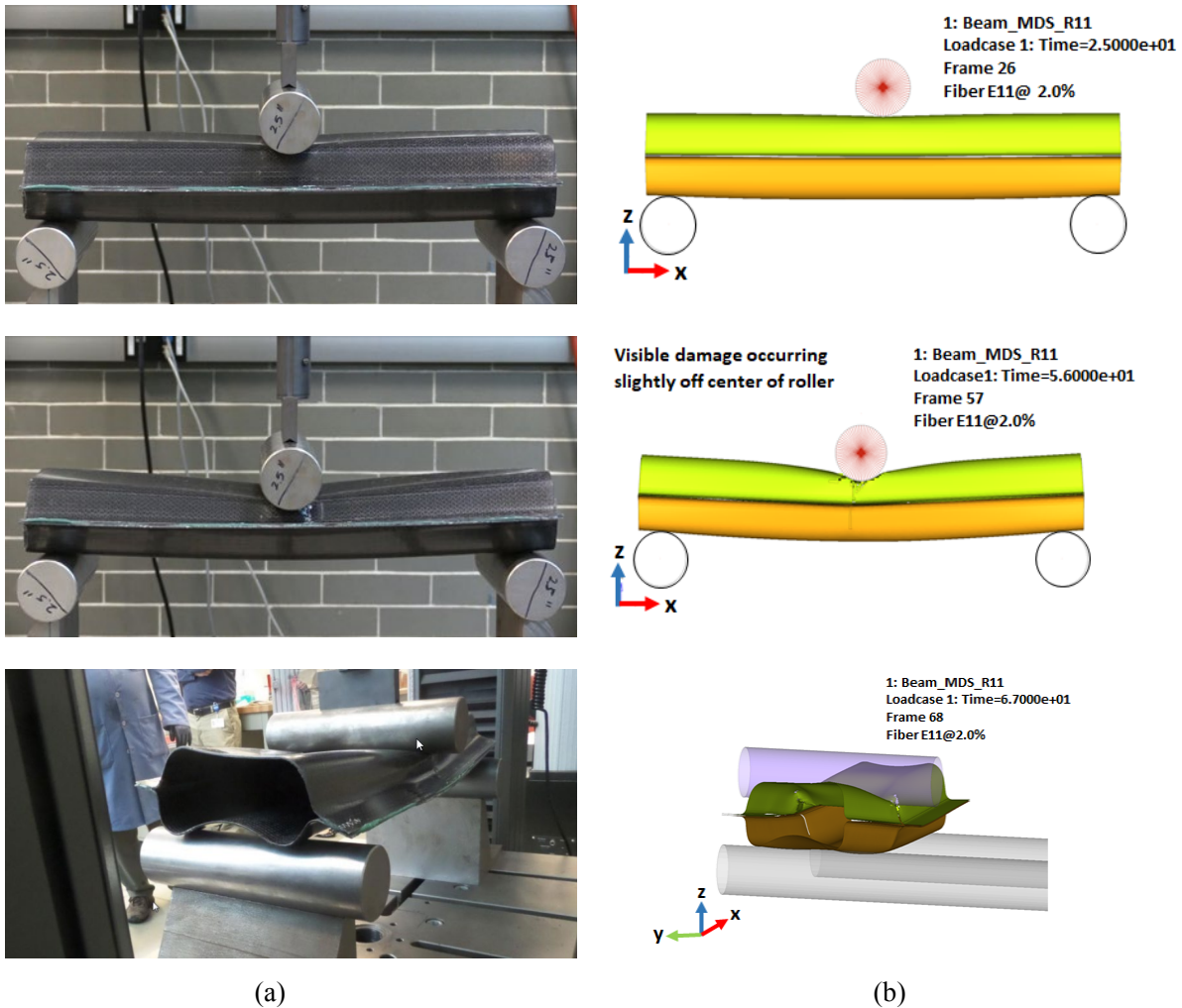


Figure II.2.D.14.(a) Images of a double-hat beam during the experiment with (b) the approximate correlating frame of the simulation. Source: Altair.

Single-Precision Multiscale Designer/LS-DYNA Plugin

Previously, the MDS was built on the distributed memory, Linux, IBM platform Message Passing Interface, double-precision build package. During FY 2018, we chose to switch to a single-precision build. This change in the build package required code modification, update of the build environment, update of the compiler flags used during the plugin build, and an update to the makefile that drives the build of the shared library containing the MDS/LS-DYNA material subroutines. Each of these tasks were completed during FY 2018. To avoid the problems with round-off errors, we used a hybrid precision approach where the crucial equilibrium calculations are carried out in double-precision and the results of this computation are converted back to single-precision before returning them to LS-DYNA. This approach allows the single-precision performance gains discussed above while dodging the problems associated with round-off error. After switching to this hybrid precision approach, we have experienced subsequent gains in simulation performance.

Modeling of Non-Orthogonal Weaves

The orthogonal twill weave unit cell model was developed using MDS. The description and specific values of geometric attributes of twill weave unit cell are given in Table II.2.D.2, and the unit cell is shown in Figure II.2.D.15 (fiber tows are shown).

Table II.2.D.2. Geometric Attributes Values Used in This Study.

Geometric Parameters of the Twill Weave	

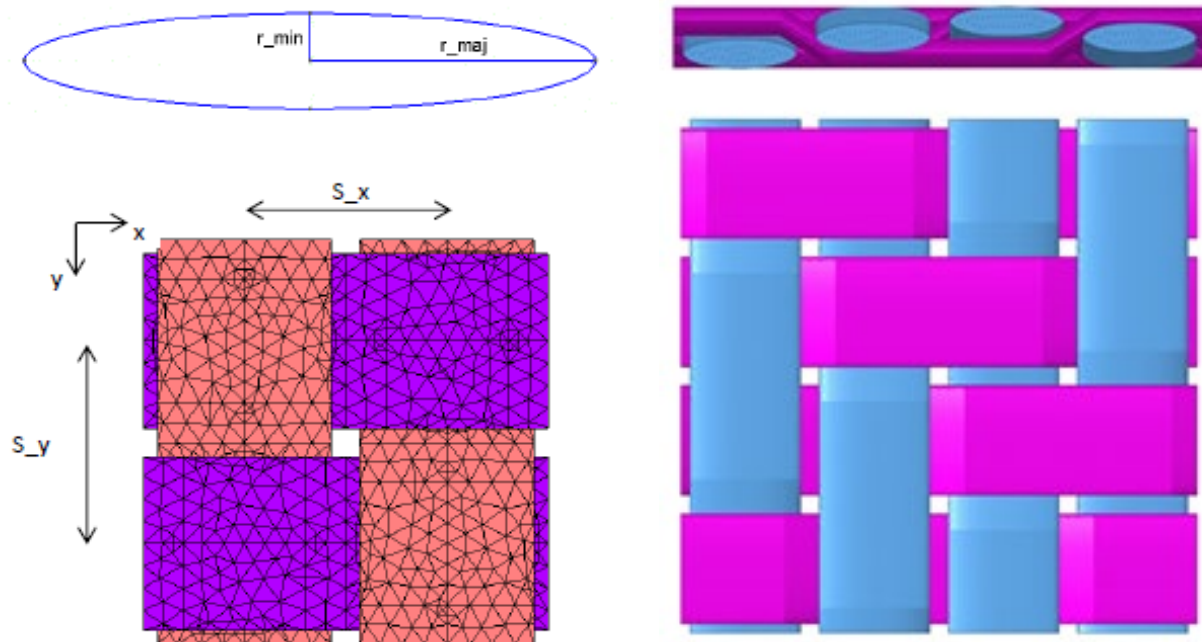


Figure II.2.D.15. Description of geometric attributes of twill weave unit. Source: GM.

In the linear material characterization step of the MDS, the matrix was modeled with the isotropic material model, whereas tows of the unit cell were modeled by considering the transversely isotropic material model. The forward-homogenization approach was adopted in this step to characterize macro-homogenized material properties. In the forward-homogenization approach, all of the micro-phase properties are prescribed *a priori* and the corresponding macro-unit cell homogenized properties are computed by solving a forward-homogenization problem. The non-orthogonal models were developed by using the previously validated orthogonal model through morphing in the Hypermesh computer program. The weft tow of orthogonal model was sheared at different angles using an in-built Tool Command Language script of MDS known as “UnitCellib::Main”. The geometric attributes were kept similar to the orthogonal model to develop the non-orthogonal models, except volume fraction (45%). The non-orthogonal unit cell models sheared at 10° , 15° , and 30° are shown in Figure II.2.D.16.

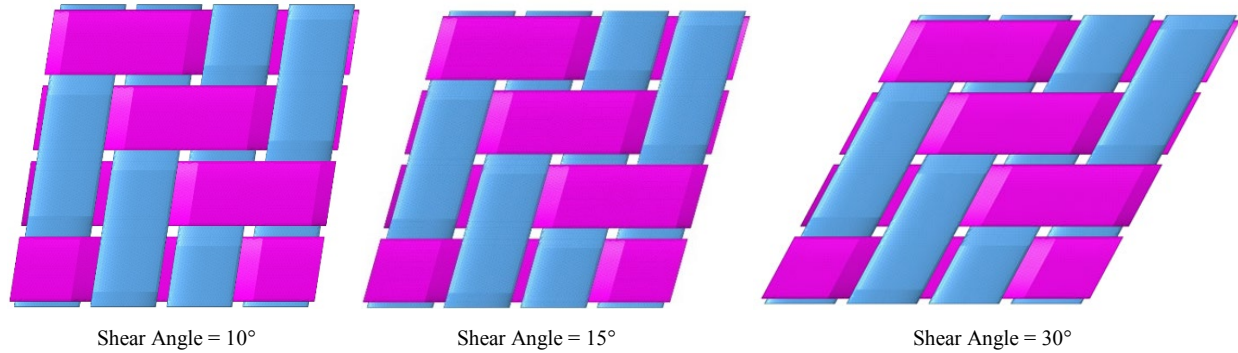


Figure II.2.D.16. Non-orthogonal models sheared at different angles. Source: GM.

After the development of the non-orthogonal models, the linear material characterization step was performed similarly to the orthogonal case utilizing the same micro-properties of the matrix and two phases. The MDS unit cell predictions were compared to the experimental results and are described by Figure II.2.D.17. The MDS unit cell analysis shows good agreement with the experimental results with minimal error.

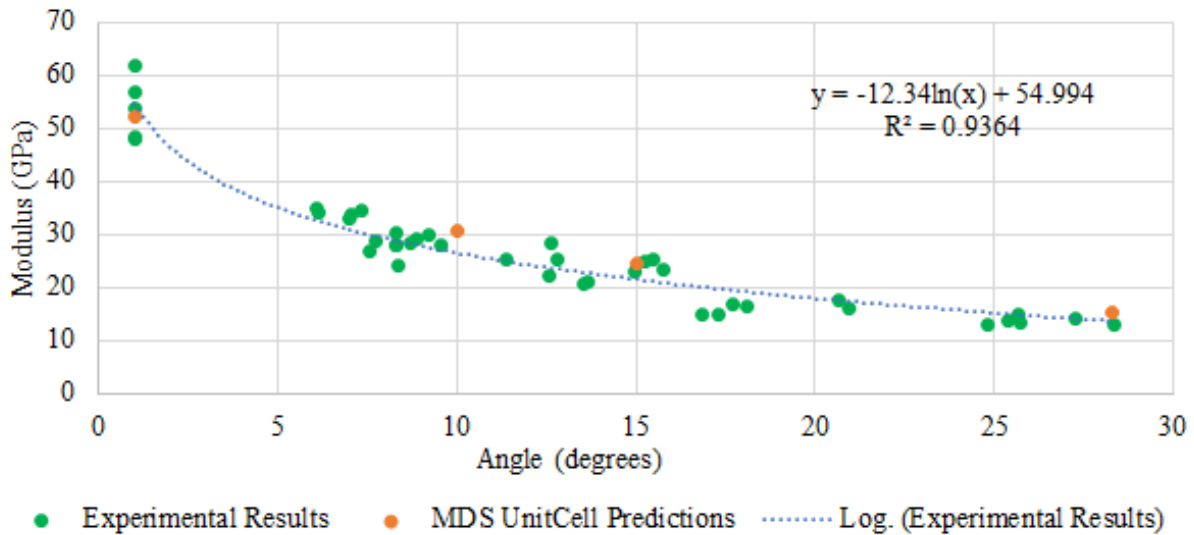


Figure II.2.D.17. MDS predictions compared to the experimental results for twill tensile specimen modulus vs average angle. Source: GM.

Preliminary Multiscale Modeling of Cure Process

We describe here the development of a theoretical framework of the multiscale/multiphysics process during the curing stage. The multiphysics problem, including two-way coupling of mechanical and thermal fields and a scalar quantity named curing state variable, \mathcal{C} , which represents the state of curing of resin material, are introduced. The evolution of the curing state, \mathcal{C} , is governed by the kinetics, which produces heat and introduces chemical shrinkage strain, and thus leads to coupling with thermal and mechanical fields, respectively. The schematic framework for multiphysics problem is demonstrated in Figure II.2.D.18.

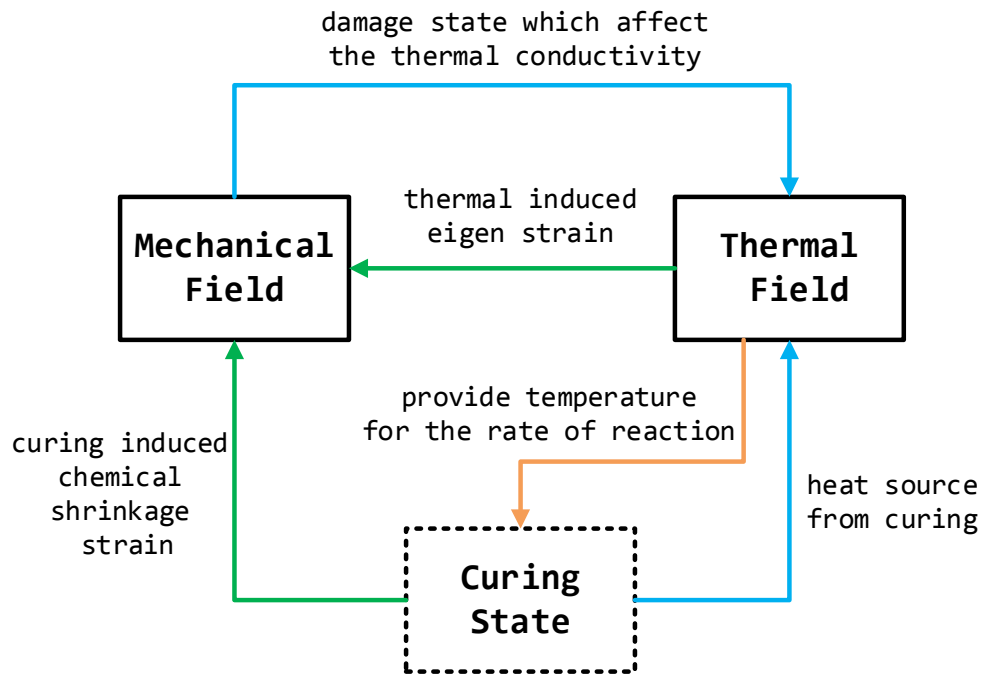


Figure II.2.D.18. Framework of multiphysics problem of the curing process, with arrows denoting the direction of coupling between various physical fields. Source: GM.

The curing state variable, $c \in [0, 1]$, represents the state of curing at a material point, where $c = 0$ represents the initial state and $c = 1$ represents the fully cured state.

The kinetics of curing is described by the rate form that:

$$\frac{dc}{dt} = \begin{cases} (K_1 + K_2 c)(1-c)(0.47-c) & c \leq 0.3 \\ K_3(1-c) & c > 0.3 \end{cases} \quad (1)$$

where $K_i, i = 1, 2, 3$ follows Arrhenius-like functions that:

$$K_i = A_i \exp\left\{-\frac{E_i}{RT}\right\} \quad (2)$$

where $A_i, E_i, i = 1, 2, 3$ are kinetic constants. Thus, the update of the curing state variable requires the magnitude of temperature. The coupling from the thermal field is depicted as the orange arrows in Figure II.2.D.18.

The heat generation, Q , during the curing is given as:

$$Q = H \frac{d\alpha}{dt} \quad (3)$$

where H is the total heat generation over the complete curing process.

The kinetics of curing is a local reaction equation that allows the updating of the curing state variable at each material point. The heat generated by cure affects thermal conduction problem:

$$\rho c_p \dot{T} = k(\omega) \nabla^2 T + Q \quad (4)$$

where ρ denotes the density of resin; c_p denotes the heat capacity; $k(\omega)$ denotes the thermal conductivity; Q denotes the heat source per unit mass from the curing process defined in Equation (4).

It can be seen that for $k(\omega = 0) = k_0$ which represents the thermal conductivity of damage-free material; while $k(\omega \rightarrow 1) = k_d \ll k_0$ represent the residual thermal conductivity when the material point is completely damaged. This capability will be implemented in the MDS in FY 2019.

Stochastic Model Development

Stochastic Modeling of Manufacturing Process

On the stochastic manufacturing side, we have completed the integration of fabric draping/resin injection/resin curing/part demolding simulations through the stochastic workflow developed in this project. Once the linear part of the analysis is computing, higher order approximations for any quantity of interest can be readily and efficiently computed. We have focused on three quantities of interest: fill time, cure time, and maximum residual stress. Table II.2.D.3 shows the stochastic input parameters for a comprehensive integrated analysis with 69 random input variables. Figure II.2.D.19 shows the spatial heterogeneity induced by the manufacturing process into the permeability field. The permeability was not modeled as a stochastic process with a specified covariance function. Instead, its stochastic properties were induced by processing, with uncertainty in the fiber properties modeled as random variables and the initial waviness of the fibers and modeled using a 5-term Karhunen-Loeve expansion in each direction. In this manner, there is no need to characterize a covariance function from limited data. We believe that whenever such a process model is available, it is more realistic and incurs fewer assumptions than proposing a covariance function model for permeability. Figure II.2.D.20 shows the probability density functions (PDF) of fill time and maximum von-Mises stress in the composite following demolding. These results are obtained for a significantly large coefficient of variation of 12%. Results for a 4% coefficient of variation were also obtained, but not shown here. These results indicate that even a one-dimensional reduction is sufficient to capture the uncertainty in these quantities of interest. It should be noted that the final model is non-Gaussian.

Table II.2.D.3. Parameters Included for the Uncertainty Analysis (β Distribution).

	Parameter	Probabilistic Model		Parameter	Probabilistic Model
Draping Simulation	$E_{f1,t}$ (GPa)	$\beta(59.904,80.096,6,6)$	Demolding Simulation	$E_{11,g,ply}$ (GPa)	$\beta(55.882,74.718,6,6)$
	$E_{f2,t}$ (GPa)	$\beta(59.904,80.096,6,6)$		$E_{22,g,ply}$ (GPa)	$\beta(55.882,74.718,6,6)$
	$E_{f1,b}$ (MPa)	$\beta(42.789,57.211,6,6)$		$E_{33,g,ply}$ (GPa)	$\beta(6.350,8.490,6,6)$
	$E_{f2,b}$ (MPa)	$\beta(42.789,57.211,6,6)$		$\nu_{12,g,ply}$	$\beta(0.022,0.030,6,6)$
	θ_{f1} (deg)	$\beta(41.755,48.245,6,6)$		$\nu_{13,g,ply}$	$\beta(0.236,0.316,6,6)$
	θ_{f2} (deg)	$\beta(131.106,138.894,6,6)$		$\nu_{23,g,ply}$	$\beta(0.236,0.316,6,6)$
Injection Simulation	V_f	$\beta(0.446,0.554,6,6)$		$G_{12,g,ply}$ (GPa)	$\beta(2.696,3.604,6,6)$
	$k_{f,1}$ (W/m.K)	$\beta(1.712,2.288,6,6)$		$G_{13,g,ply}$ (GPa)	$\beta(2.276,3.044,6,6)$
	$k_{f,2}$ (W/m.K)	$\beta(0.428,0.572,6,6)$		$G_{23,g,ply}$ (GPa)	$\beta(2.276,3.044,6,6)$
	$k_{f,3}$ (W/m.K)	$B(0.428,0.572,6,6)$		$\alpha_{11,g,ply}(K^{-1}) \times 10^{-6}$	$\beta(1.780,2.380,6,6)$
	$C_{p,f}$ (J/kg.K)	$\beta(607.602,812.398,6,6)$		$\alpha_{22,g,ply}(K^{-1}) \times 10^{-6}$	$\beta(1.780,2.380,6,6)$
	ρ_f (kg/m ³)	$\beta(1454.823,1945.177,6,6)$		$\alpha_{33,g,ply}(K^{-1}) \times 10^{-5}$	$\beta(3.420,4.580,6,6)$
	k_{r1} (W/m.K)	$\beta(0.094,0.126,6,6)$		$\phi_{11,g}$	$\beta(0.0010,0.0013,6,6)$
	k_{r2} (W/m.K)	$\beta(0.094,0.126,6,6)$		$\phi_{22,g}$	$\beta(0.0010,0.0013,6,6)$
	k_{r3} (W/m.K)	$\beta(0.094,0.126,6,6)$		$\phi_{33,g}$	$\beta(0.0133,0.0178,6,6)$
	$C_{p,r}$ (J/kg.K)	$\beta(1031.212,1378.788,6,6)$		$E_{11,r,ply}$ (GPa)	$\beta(53.058,70.942,6,6)$
	ρ_r (kg/m ³)	$\beta(941.356,1258.644,6,6)$		$E_{22,r,ply}$ (GPa)	$\beta(53.058,70.942,6,6)$
	T_r (C)	$\beta(285.102,381.198,6,6)$		$E_{33,r,ply}$ (GPa)	$\beta(1.968,2.632,6,6)$
	P_l (kPa)	$\beta(322.727,431.503,6,6)$		$\nu_{12,r,ply}$	$\beta(0.009,0.011,6,6)$
	P_V (Pa)	$\beta(86.712,115.938,6,6)$		$\nu_{13,r,ply}$	$\beta(0.424,0.500,6,6)$
	$K_{rt,1}$ (m ²) $\times 10^{-08}$	$\beta(1.583,2.117,6,6)$		$\nu_{23,r,ply}$	$\beta(0.424,0.500,6,6)$
	$K_{rt,2}$ (m ²) $\times 10^{-08}$	$\beta(1.583,2.117,6,6)$		$G_{12,r,ply}$ (MPa)	$\beta(33.589,44.911,6,6)$
	$\delta_{K_1^{(0)}}$ (m ²) $\times 10^{-11}$	$\beta(1.734,1.986,6,6)$		$G_{13,r,ply}$ (MPa)	$\beta(34.180,45.700,6,6)$
	$\delta_{K_2^{(0)}}$ (m ²) $\times 10^{-11}$	$\beta(1.734,1.986,6,6)$		$G_{23,r,ply}$ (MPa)	$\beta(34.180,45.700,6,6)$
	c_1 (m ² /s)	$\beta(0.337,0.451,6,6)$		$\alpha_{11,r,ply}(K^{-1}) \times 10^{-6}$	$\beta(1.095,1.465,6,6)$
	c_2	$\beta(0.0642,0.0858,6,6)$		$\alpha_{22,r,ply}(K^{-1}) \times 10^{-6}$	$\beta(1.095,1.465,6,6)$
Curing Simulation	A_1	$\beta(0.101,0.135,6,6)$		$\alpha_{33,r,ply}(K^{-1}) \times 10^{-4}$	$\beta(1.155,1.545,6,6)$
	$A_2 \times 10^6$	$\beta(2.901,3.879,6,6)$	$\phi_{11,r}$	$\beta(0.0003,0.0004,6,6)$	
	m	$\beta(0.391,0.523,6,6)$	$\phi_{22,r}$	$\beta(0.0003,0.0004,6,6)$	
	n	$\beta(1.027,1.373,6,6)$	$\phi_{33,r}$	$\beta(0.0201,0.0269,6,6)$	
	B	$\beta(0.992,1.000,5,2)$	α_g	$\beta(0.599,0.801,6,6)$	
	E_1	$\beta(3971.451,4268.549,6,6)$	T_{g0} (K)	$\beta(190.967,255.333,6,6)$	
	E_2	$\beta(7755.197,7924.803,6,6)$	T_{ginf} (K)	$\beta(331.588,443.352,6,6)$	
	$T_{top/bot}$ (K)	$\beta(400.2,406.0,6,6)$	λ	$\beta(0.757,1.012,6,6)$	
	h (J/kg)	$\beta(299.522,400.478,6,6)$			

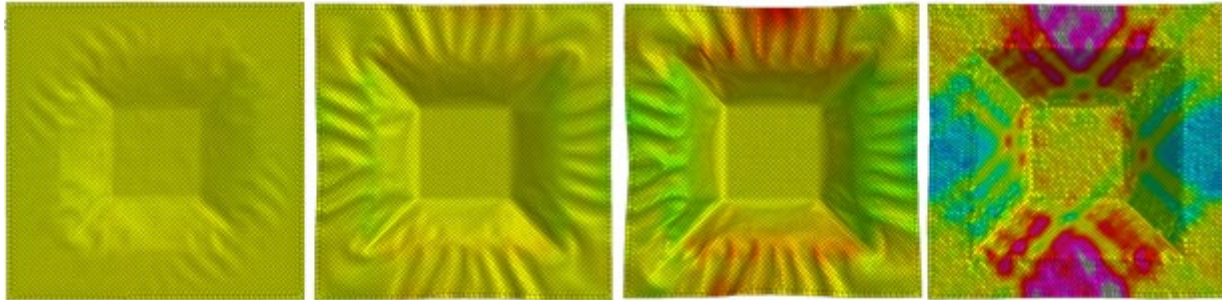


Figure II.2.D.19. Spatial distribution of permeability following draping process. Stochasticity in spatial distribution is induced by fiber properties and initial orientation of fibers. Source: USC.

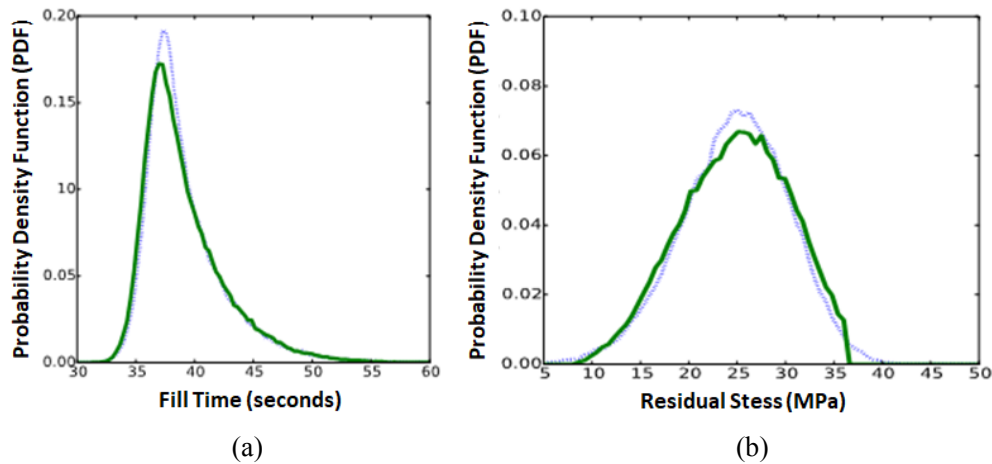


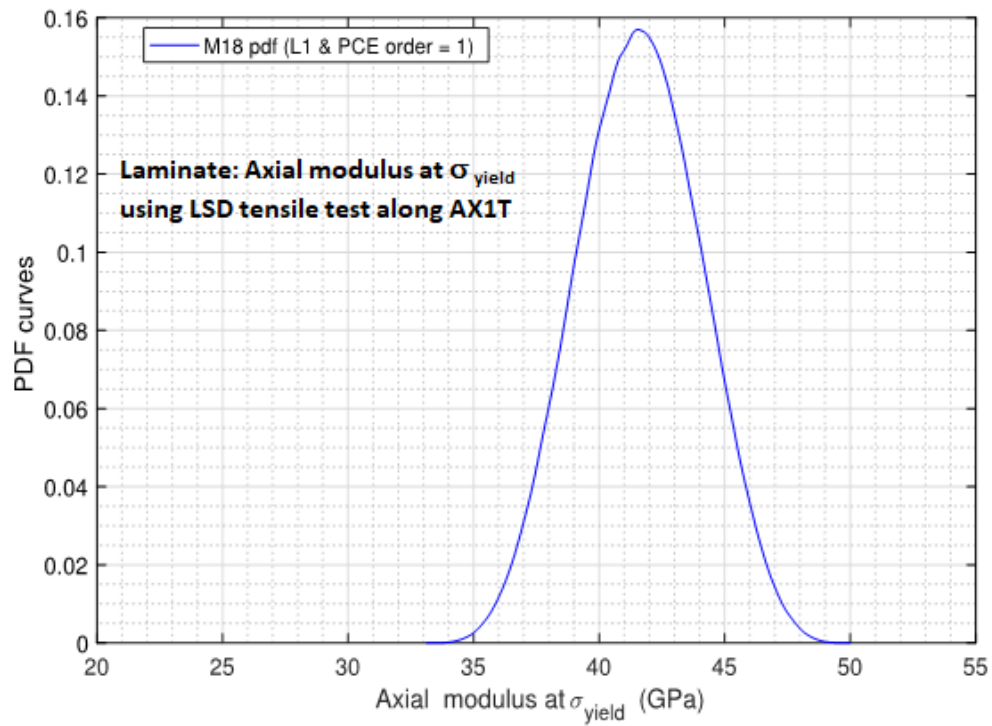
Figure II.2.D.20. PDF of (a) fill time and of (b) maximum stress following distortion analysis. The two curves show results for two successive reduced models, indicating convergence of analysis. Results show a 12% coefficient of variation. Source: USC.

Stochastic Modeling of Structural Performance

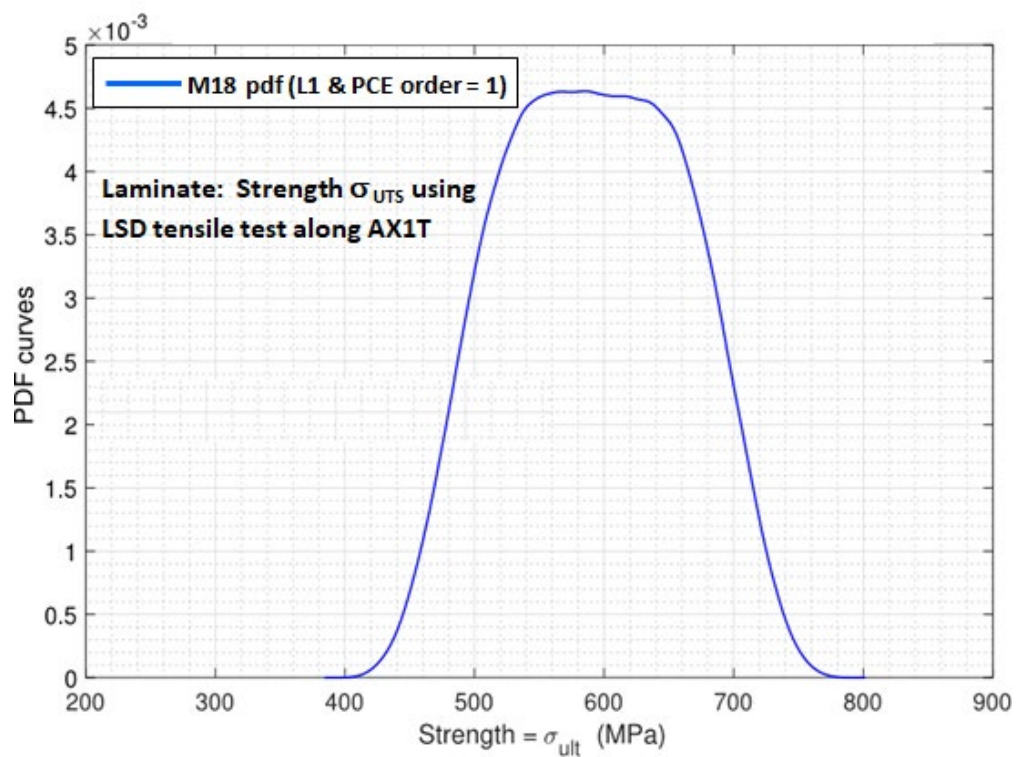
We have completed the validation of the three-point bend predictions, using a model calibrated against tensile test coupons. We found that having the correct mechanics in the fiber/resin interaction was key for achieving this validation, and that the model could not be validated without it. Table II.2.D.4 shows the values of the elastic and inelastic properties used in the simulations. Figure II.2.D.21 shows the PDF of the axial properties from the tensile test and Figure II.2.D.22 shows the flexural properties obtained from the three-point bend tests calculated at different displacement ranges (example 0 - 0.5 mm). These results correlate well with the experimental data.

Table II.2.D.4. Elastic and Inelastic Properties for Multiscale Designer

Group	Variable	Mean Value
Elastic	Resin Modulus E_m	3.4e9 GPa
	Poisson's Ratio ν_m	0.36
Inelastic	Resin Yield Strength S_{0m}	28e6 GPa
	Resin hardening modulus 1 K_{0m}	32.6E6 GPa
	Resin hardening modulus 2 K_{1m}	53E6 GPa
	Radius of Curvature of stress/strain curve δ_m	42 mm
	H_m	3.4e6 GPa

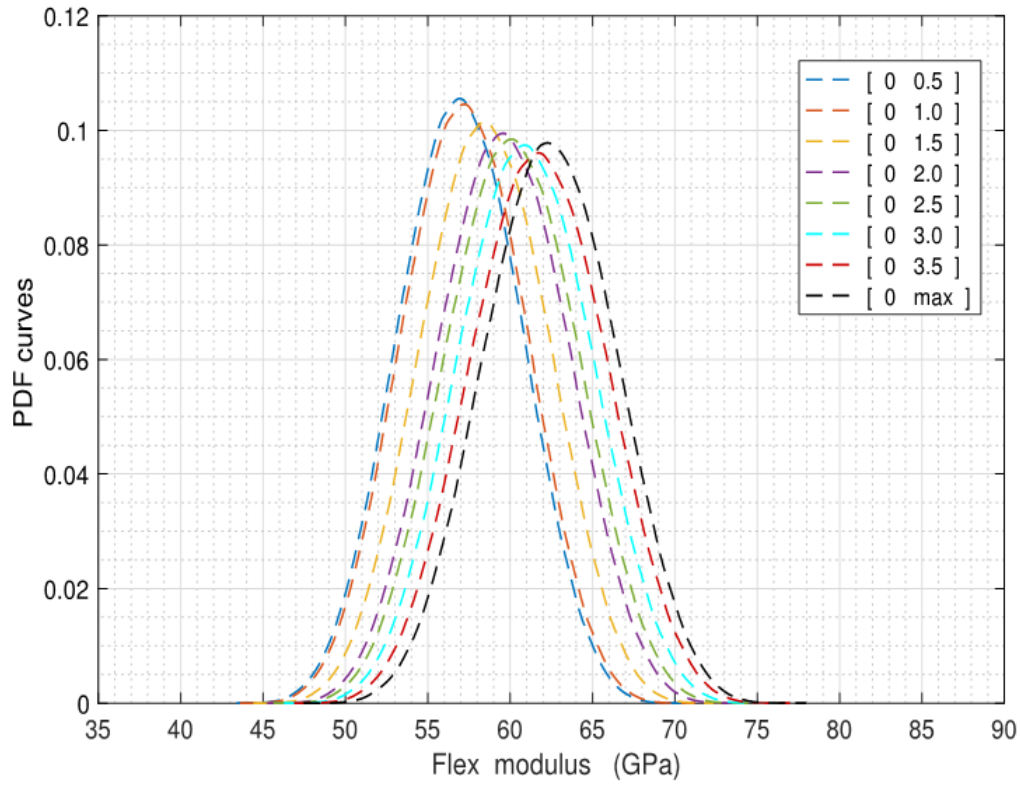


(a)

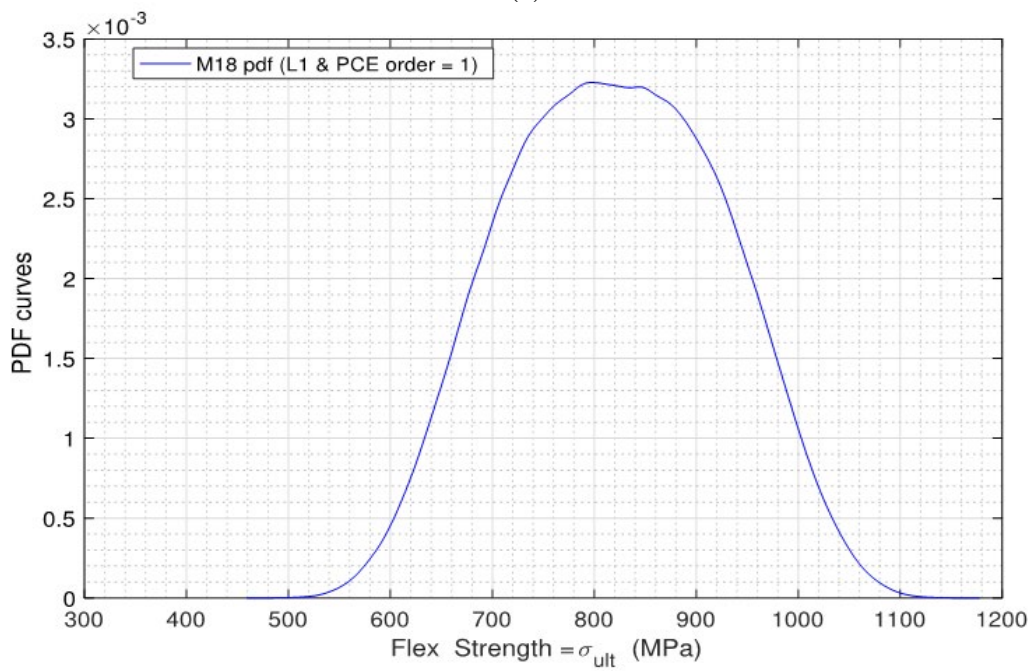


(b)

Figure II.2.D.21. Probability distribution function of (a) axial modulus and (b) strength obtained for tensile test simulation. Source: GM.



(a)



(b)

Figure II.2.D.22. PDF of (a) flex modulus and (b) strength obtained from three-point bend test simulation. Source: GM.

Prototype Build, Testing, Validation of the Design of the CF Assembly

In order to further validate the models and provide more confidence in the design approach, a prototype assembly replicating the automotive assembly that will be built for demonstration was identified. This assembly represented the functional crash area of the full-scale design. It consists of seven distinct components. Two components of the prototype assembly were molded by GM using an existing tool. Two more components were produced by a prototype shop, Deluxe Technologies, in conjunction with CSP. Additional parts needed for the assembly were made from flat plaques using a waterjet at CSP. The energy absorber tubes were produced by Teijin, the parent company of CSP. The components were manufactured with appropriate lay-up and thickness as per the design obtained after several simulations and optimization of the CF assembly. These components were made via resin infusion or squeeze molding, which are typical low-cost options for producing prototype versions of HP-RTM parts. The energy absorbers were made from a CF reinforced Nylon material and were produced via compression molding of consolidated blanks. The backing and alignment plates were also made from this material and were used to help integrate the individual energy absorbers into a functional array. GM produced the two of the prototype parts via squeeze molding. The components at the Deluxe prototype shop were manufactured using an infusion-grade epoxy resin system. Standard biaxial NCFs from Chomarat were used.

Components were molded to obtain six assemblies for sled testing. All components of the assembly were adhesively bonded together using a methacrylate adhesive. Glass spacer beads were lightly sprinkled onto the adhesive beads to set the bond gap. A RT cure of 24 hours was utilized for each curing step. Rivets were also included in strategic locations to reduce the likelihood of peel failures.

Three assemblies were crash-tested during the beginning of 2018. These crash tests demonstrated that the design was able to meet the performance requirements and the numerical predictions correlated well with the experimental results. The energy absorbers progressively crushed, as intended, and most of the damage was contained. A second round of prototype testing will be taking place in the next two months to try out a new energy absorber design, determine if one of the component accounting for major load and energy absorption can be thinned out, and try an alternative fiber orientation.

Tooling of the CF Assembly

During the prototype assembly, the team came to realize that assembly of the energy absorber inside the assembly involved significant manual work and could be a bottleneck for the high-volume manufacturing. The team quickly brainstormed and modified the energy absorber design. This new design requires a fewer number of components in the absorber array and consists of corrugated plaque components that can be assembled into a honeycomb structure. A new energy absorber tool was designed as a steel insert that fits into an existing compression mold tool base to lower some of the tooling costs. The insert tooling was completed and installed in the mold base.

The RTM tooling for the components of the assembly will be made with Al and they are currently in build. A great deal of design, simulation, and optimization work for the tool design was accomplished in 2018. The first challenge was to determine the best injection strategy for each component using newly available fast curing resins in the market by (a) a lower cycle time by minimizing the fill time and cure time and (b) keeping the resin cured to a limited value during the injection. Further, each molding tool was embedded with dielectric and pressure sensors in the tools to allow for the collection of real-time temperature, pressure, and cure data to compare with the predictions. These sensors can also be used to determine when the resin is arriving at each sensor location, which can inform the team about the nature of the flow front. The technical area, which is the area of the tool just beyond the part boundary, allows the tool to be sealed during injection and cure, as well as often containing injection ports and resin channels. The design of these technical areas, including the size and shape of the resin channels, were crucial in obtaining a low-cycle time and a high-quality manufactured component. During the study, the manufacturing process designs were modified iteratively, relying on results of injection simulations from the models ESI developed, as well as the prior experience of CSP. Key results

from the simulations included the time needed to fill the part, the pressure and temperature evolutions during the injection, and the viscosity and degree of cure of the resin over time. The data is protected by GM.

One of the tools built for this project features a peripheral injection channel that is connected to an injection port on each side. Three vacuum ports are included along the centerline of the mold to allow for flexibility for the air to escape. Four pressure sensors and three dielectric sensors are embedded in the tool surface in a symmetric pattern to allow for the collection of process data during molding. The patches, which locally increase the thickness of the part in strategic locations, are accommodated by deeper pockets in the tool. These pockets are designed to minimize race-tracking of the resin around their perimeter.

In order to optimize the tooling costs, a single tool has been designed to mold two more components for the assembly. Two separate cavities are included in one single tool. Since the two components have significant different thicknesses, and thus different resin volumes, the tool is not designed to mold both of the components simultaneously. Rather, only one cavity is used at a time. The injection and vacuum ports, which are located on the periphery between the two cavities, are designed as insert blocks. No sensors are included in this tool.

Conclusions

During FY 2018, the project team successfully designed a large CF assembly using the state-of-the-art ICME models developed in previous years. The assembly chosen for demonstration is currently made from high-strength steel for the 2016 GM Malibu. On the manufacturing side, the components of the assembly were designed to be manufactured using HP-RTM. We believe HP-RTM is a game-changing manufacturing technology that is evolving for high-volume automotive manufacturing of composite materials resulting in lower cycle times. The injection strategy, vent locations, and process conditions (such as mold temperature, resin type, etc.) were engineered to minimize the cycle time, and thus maximize the throughput. On the structural design side, the CF assembly was designed for crashworthiness, which is a challenging load case for composites. The designed CF assembly is 30% lighter compared to the current steel design. The data and the assembly design that supports this weight reduction is protected information. In addition to the mass savings, we have achieved significant part consolidation by designing the parts with variable thicknesses. Cost models developed in the previous year were used to evaluate the cost of the CF assembly and compared those with the steel assembly. Our initial estimates show that the cost increase per pound saved is more than DOE metric of \$5/pound. However, our estimates did not account for the welding costs for the steel assembly. Therefore, we are further refining the cost models to make them more accurate. We expect to have the final cost estimates available by the end of Q1 of 2019. Studying the current results at hand, we observe that the material costs are found to be significant factor and to minimize those costs, we are working with material suppliers in different research areas to improve the manufacturability and predictability (i.e., high areal weight fabrics, large tows with high fiber number, 3D stitched CF preforms, etc.). In parallel, prototypes of the CF assembly were built and crash-tested to validate the design. The prototype design successfully met the performance requirements providing confidence for proceeding with the design of the main CF assembly. The tools to manufacture the four large components of the CF assembly are being built, and we are expecting the tools to be available for molding by the middle of November 2018. In FY 2019, the components of the assembly will be manufactured, and the manufacturing data collected during the molding trials will be compared with model predictions to verify the accuracy of the ICME stochastic manufacturing models developed in this project. Similarly, the results collected during the crash-testing of the assembly will be compared with model predictions to verify the accuracy of ICME stochastic structural models developed in this project. Further, a certification procedure will be developed to virtually certify the CF structural panels. We believe this project outcome will be a significant benefit to the entire automotive industry and will accelerate the implementation of CF composites for next level of lightweighting of automobiles.

Key Publications

1. Rodgers, W., P. Pasupuleti, S. Zhao, T. Wathen, M. Doroudian, and V. Aitharaju, 2017, “Numerical simulation with experimental validation of the draping behavior of woven fabrics,” In: *Proceedings of the American Society for Composites Thirty-Second Technical Conference*, W. Yu, R. B. Pipes, and J. Goodsell (eds.), pp. 675–689, Purdue University, West Lafayette, IN, USA.
2. Dereims, A., S. Zhao, H. Yu, P. Pasupuleti, M. Doroudian, W. Rodgers, and V. Aitharaju, 2017, “Accurate C-RTM simulation through fluid-solid coupled approach,” *American Society of Composites 32nd Technical Conference*, October 23–25, 2017, West Lafayette, IN, USA.
3. Wollschlager, J., D. Plakomytis, J. Fish, and V. Aitharaju, 2017, “Including the effects of weave draping within multiscale simulations,” *American Society of Composites 32nd Technical Conference*, October 23–25, 2017, West Lafayette, IN, USA.
4. Ghauch, Z., V. Aitharaju, W. Rodgers, P. Pasupuleti, A. Dereims, and R. Ghanem, “Integrated stochastic analysis of fiber composites manufacturing using adapted polynomial chaos expansions,” submitted to *Journal of Composites, Part A*.
5. Mehrez, L., J. Fish, V. Aitharaju, W. Rodgers, and R. Ghanem, 2017, “A PCE-based multiscale framework for the characterization of uncertainties in complex systems,” *Computational Mechanics 2017*, pp. 219–236.
6. Rodgers, W., P. Pasupuleti, S. Zhao, A. Dereims, M. Doroudian, and V. Aitharaju, 2018, “Draping Behavior of Non-Crimp Fabrics,” In: *Proceedings of the American Society for Composites – Thirty-Third Technical Conference*, Seattle, Washington, September 24–26, 2018, DEStech Publications, Inc., Lancaster, PA, USA.
7. Ghauch, Z., V. Aitharaju, W. Rodgers, P. Pasupuleti, A. Dereims, and R. Ghanem, 2018, “Fabrication to performance: A comprehensive multiscale stochastic predictive model for composites,” *American Society of Composites 33rd Technical Conference*, September 23–25, 2018, Seattle, WA, USA.
8. Mehrez, L., Z. Ghauch, V. Aitharaju, W. Rodgers, P. Pasupuleti, A. Dereims, and R. Ghanem, 2018, “Statistical machine-learning and sampling for composite fabrication and performance,” *American Society of Composites 33rd Technical Conference*, September 23–25, 2018, Seattle, WA, USA.
9. Mehrez, L., R. Ghanem, W. Rodgers, and V. Aitharaju, 2017, “Polynomial chaos characterization of uncertainty in multiscale models and behavior of carbon reinforced composites,” *American Society of Composites 32nd Technical Conference*, October 23–25, 2017, West Lafayette, IN, USA.
10. Ghanem, R., L. Mehrez, Z. Ghauch, V. Aitharaju, W. Rodgers, P. Pasupuleti, A. Dereims, P. Pasupuleti, A. Dereims, C. McAuliffe, R. Crouch, and J. Fish, 2018, “Stochastic ICME of composites,” *World Congress on Computational Mechanics*, July 23, 2018, New York City, NY, USA.
11. Ghanem, R., L. Mehrez, Z. Ghauch, V. Aitharaju, W. Rodgers, P. Pasupuleti, and A. Dereims, 2018, “Probabilistic learning and sampling for integrated manufacturing and performance of composites,” *World Congress on Computational Mechanics*, July 23, 2018, New York City, NY, USA.
12. Ghanem, R., L. Mehrez, Z. Ghauch, V. Aitharaju, W. Rodgers, P. Pasupuleti, and A. Dereims, 2018, “Polynomial chaos for multiscale characterization of material response and failure under uncertainty,” *SIAM Conference on Mathematical Aspects of Material Science*, July 9–13, 2018, Portland, OR, USA.
13. Mehrez, L., and R. Ghanem, 2018, “Stochastic modeling of multiscale materials,” *2018 SIAM Conference on Uncertainty Quantification*, April 16–19, 2018, Anaheim, CA, USA.

References

1. Rodgers, W., P. Pasupuleti, S. Zhao, T. Wathen, M. Doroudian, and V. Aitharaju, 2017, “Numerical Simulation with Experimental Validation of the Draping Behavior of Woven Fabrics,” In: *Proceedings of the American Society for Composites Thirty-Second Technical Conference*, W. Yu, R. B. Pipes, and J. Goodsell (eds.), pp. 675–689, Purdue University, West Lafayette, IN, USA.

Acknowledgements

We acknowledge Mr. John Terneus, Project Manager, National Energy Technology Laboratory, for providing constant guidance and encouragement during the course of this project.

II.2.E ICME Predictive Tools for LCCF for Lightweight Vehicles (University of Virginia)

Xiaodong (Chris) Li, Principal Investigator

University of Virginia
122 Engineer's Way
Charlottesville, VA 22904
E-mail: xl3p@virginia.edu

Leonid V. Zhigilei, Co-Principal Investigator

University of Virginia
Wilsdorf Hall, Room 303D
Charlottesville, VA 22904
E-mail: lz2n@virginia.edu

Adri van Duin, Co-Principal Investigator

Pennsylvania State University
240 Research Building East
University Park, PA 16802
E-mail: acv13@psu.edu

James W. Klett, Co-Principal Investigator

Oak Ridge National Laboratory
One Bethel Valley Road, Bldg 4508
Oak Ridge, TN 37831
E-mail: klettjw@ornl.gov

H. Felix Wu, Ph. D, DOE Technology Manager

U.S. Department of Energy
E-mail: felix.wu@ee.doe.gov

Start Date: October 1, 2017 End Date: September 30, 2020
Project Funding (FY18): \$1,122,478 DOE share: \$985,134 Non-DOE share: \$137,344

Project Introduction

In response to consumer demand for fuel-efficient vehicles and stringent vehicle emission regulations, automotive manufacturers are searching for alternative lightweight, high-strength materials to replace conventional metal structures in vehicle designs. Even compared to high-strength metal alloys, CFRP composites are a promising alternative due to their superior strength-to-weight ratio. Recent estimates have predicted that automotive weight reductions of 50% or greater will be necessary, in addition to enhanced engine and drive train efficiencies, to meet national and international emission standards. However, there are significant technical barriers, which must be overcome to bring CFRP materials into widespread acceptance; CFRP materials are produced via a complex and expensive procedure and often limited to small-scale production. A large portion of this cost is born by the precursor material preparation; 51% of the total CF cost may be attributed to the precursor. Therefore, this project aims to develop low-cost, alternative precursors and processing techniques through the implementation of an ICME framework to evaluate precursor conversion kinetics. This framework will be used to down-select precursors for laboratory-scale and pilot-scale production to validate resulting CFRP material properties and process cost savings.

Currently, the highest quality CFs are produced from polyacrylonitrile (PAN) precursors, which have a high-carbon yield and ideal polymer structure for conversion into CFs with excellent mechanical properties. Typical yields are ~ 50% CF for all the PAN precursor at the start of conversion, and the highest quality commercially

available CFs achieve strengths of up to 7 GPa (1,000 ksi). However, PAN-derived CFs are expensive due to their high precursor cost and energy-intensive processing, with costs of ~\$25/kg subject to petroleum price fluctuations. Although advanced manufacturing techniques may further lower the price towards \$15/kg, PAN-derived fibers will likely remain too expensive for widespread adoption in the automotive industry. Therefore, the two most promising approaches to reduce the cost of CFs are: (i) *to utilize new, low-cost precursors*; and (ii) *to reduce the energy requirements of CF processing*.

Objectives

The first objective is to develop, integrate, and demonstrate a suite of ICME framework and evaluate alternative precursors for suitability to manufacture low-cost CF. This ICME framework will predict CF properties, such as load-to-failure, failure mode, stiffness/deflection, dynamic performance, and microstructures capable of minimum modeling element accuracies within $\leq 15\%$ of measured properties to enable design, development, and optimization of precursor chemistry and kinetics associated with conversion into CF. The ICME framework will also include methodologies to simulate the manufacturing process(es), including variability from both process and material.

The second objective of this project is to research, develop, manufacture, and demonstrate CF precursor technology and processing techniques, where CF is a material consisting of thin, strong multi-crystalline filaments of C used as a reinforcement material especially in resins, capable of achieving the requirements in Table II.2.E.1.

Table II.2.E.1. Project Parameters and Requirements.

Parameter	Requirement
Cost	\leq \$5/pound
Strength	\geq 250 Ksi
Modulus	\geq 25 Msi
Strain	\geq 1%

Project performance is planned to span three federal FY BPss and includes the following tasks:

1. Assemble an ICME framework to model the conversion of precursors into CF, accounting for initial polymer properties and the stabilization, carbonization, and graphitization processes.
2. Validate ICME accuracy on PAN precursors against literature results and lab-scale CF synthesis, using multiscale microstructural and mechanical property characterization techniques.
3. Extend the ICME to model and evaluate alternative precursors for low-cost CF, including rayon, lignin, polyethylene, Nylon, polyester, poly(*p*-phenylene-2,6-benzobisoxazole (PBO, also known as Zylon), pitch, biomass, and others.
4. Perform pilot-scale production through the CFTF at ORNL to down-select precursors for low-cost CF, based on cost, performance, and properties.
5. Evaluate the performance of low-cost CF via multiscale mechanical testing, characterization, and modeling.

Approach

A closed loop approach has been adopted to assemble the ICME framework over the course of the project period, in which a cyclic system of experimentation and computational modeling refines the framework to reduce error. The core of the framework development is computational modeling; these models input parameters such as precursor chemistry, microstructure, and process temperatures and duration to extrapolate the resultant chemistry via ReaxFF (reactive force field) simulations and mechanical properties via large-scale

molecular dynamics (MD) simulations. The necessary input parameters and validation points are provided by experimental testing, which generates a wealth of mechanical properties and chemical characterization data at distinct stages during fiber conversion. The cyclic nature of running and refining the models with experimental results has achieved significant results in the first FY of the project.

The present ICME predictive tools for low-cost CF for lightweight vehicles project is organized into 11 tasks executed over a 36-month period. An outline of the tasks carried out in the current FY is given as follows:

- Task 1.1: Statistical analysis of PAN-based precursor stabilization.
- Task 1.2: Understanding the carbonization and graphitization of PAN-based CF.
- Task 1.3: Investigating meso-scale and fiber-level properties through large-scale MD simulations.
- Task 1.4: Optimizing the spinning process via limited production-scale testing.

Results

In the first FY of this project, significant progress has been made towards the project objectives to develop the ICME framework and identify low-cost alternative CF precursors. A key milestone in this first year was the demonstration of the preliminary ICME framework to predict properties of PAN-based CF within an allowable 15% error. The steps and research tasks, which made achieving this milestone possible, are described in detail here. This critical milestone, however, demonstrates a baseline level of success and reliability in the assembled framework, which will be extended to analyze more alternative precursors in the second year.

Task 1.1: Statistical Analysis of PAN Precursor Stabilization

Laboratory-scale PAN precursor fibers have been synthesized via a wet-spinning process, as shown in Figure II.2.E.1, at the University of Virginia (UVA). This spinning line is composed of two coagulation baths (mixtures of deionized [DI] water and dimethyl sulfoxide [DMSO] in different concentrations) and one washing bath (DI-water). Various PAN concentrations in DMSO solution were used to prepare the precursor fibers. The PAN-based precursor filaments were stabilized and carbonized at various temperatures and for different lengths of time, as shown in Figure II.2.E.1. The morphology, structure, and mechanical properties of the fibers after each processing step were systematically characterized with SEM, TEM, XRD, Raman spectroscopy, and single-fiber nano-tensile tests. Micro/nano X-ray computed tomography (XCT) was also utilized to investigate the porous structure of PAN and PAN/graphene CFs.

The goal for the first year of the project with this task is to establish a laboratory-scale continuous polymer filament spinning technique to synthesize, process, and systematically characterize PAN and PAN-based CFs in order to inform the ICME framework with various parameters and boundary conditions to model and predict the resultant mechanical properties of CFs. The typical manufacture process of CFs from PAN-based precursors includes polymerization of acrylonitrile, spinning of fibers, thermal stabilization, carbonization, and graphitization [1]. Wet-spinning is a widely used manufacturing process for CF from PAN-based polymer precursors, especially at laboratory-scale.

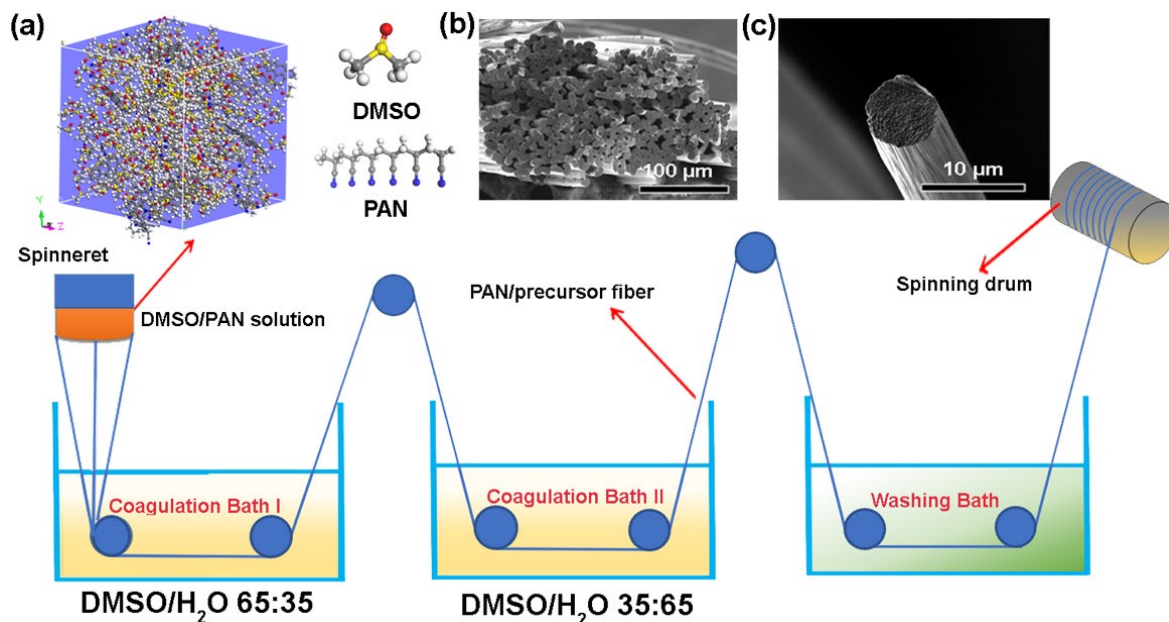


Figure II.2.E.1. Process for spinning of filament fibers: (a) fibers are wet-spun through a series of chemical baths from a spinneret, (b) bundle of fiber cross-sections viewed using SEM and (c) individual precursor PAN fiber images with SEM. Source: UVA.

As illustrated in Figure II.2.E.1, we have successfully built the wet-spinning line with continuous production capability. The spinneret has 50 holes, each with a diameter of 45 μm, to extrude fiber bundles. After a series of processing procedures, such as thermal oxidation under the tension and carbonization, the PAN-based CF demonstrated uniform and dense microstructure with a diameter under 10 μm, as shown from the SEM images in Figure II.2.E.1.(b) and (c).

In order to obtain a full understanding of the reaction mechanisms during CF synthesis, we conducted systematic characterization of the as-spun PAN-based fibers after each conversion step. The corresponding SEM images of the as-spun PAN-based fiber, oxidized PAN-based fiber, and carbonized PAN-based fiber are shown in Figure II.2.E.2.(a), (b), and (c), respectively, and revealed a carbonized fiber diameter of about 6 μm. Figure II.2.E.2.(d) shows the XRD patterns of the prepared fiber samples. The sharp and intense diffraction of the PAN fibers at ~ 16° corresponds to a lateral repeat distance that represents as a (100) diffraction in hexagonal lattice [2]. A weak and broad peak can be detected at around 24° for the carbonized fiber, which is ascribed to the (002) plane and is characteristic of the disordered C material [3]. Figure II.2.E.2.(e) presents the mechanical properties of the fiber; importantly, the carbonized fiber exhibited a tensile strength of 2.58 GPa, a Young's modulus of 300 GPa, and tensile strain of 1.1%, all of which exceed DOE target values.

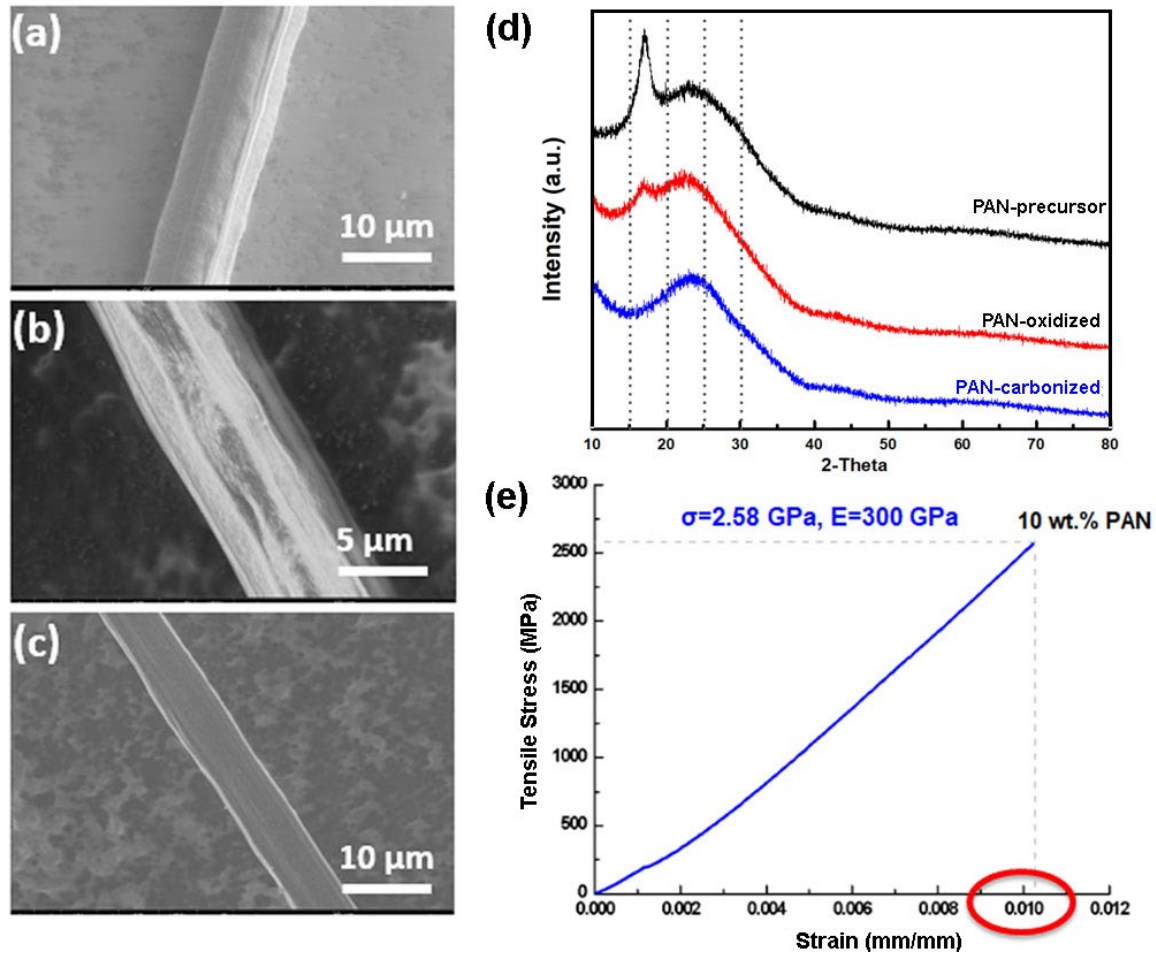


Figure II.2.E.2. Wet-spun PAN fibers and their properties. Laboratory-scale processed PAN fibers in: (a) a polymer filament state; and progressing through (b) stabilization; and (c) carbonization. (d) XRD peaks at each processing step; and (e) mechanical properties of the carbonized CF. Source: UVA.

Instead of directly replicating the commercial wet-spinning line to realize lab-scale synthesis of PAN-based CF, we have elected to use low-concentration PAN solution to meet cost and performance objectives by introducing graphene into the PAN precursor solution. Remarkably, we found that by “doping” the low-concentration PAN precursor with a small weight fraction of graphene, we can control the crystallization process and eliminate most defects in the CF to enhance the mechanical properties. Furthermore, high-quality graphene can be produced much more efficiently and at lower cost via shear-exfoliation. Other researchers have found similar results by using C nanotube nanofiller [4]. From our preliminary results, we have found that small quantities (*e.g.*, less than 0.100 wt.%) of graphene in low-concentration PAN solution can significantly increase the quality of fiber by tuning the microstructure and regulating defects during the fiber-spinning as shown in the electron micrographs of the cross-sections of PAN/graphene CF in Figure II.2.E.3. From these micrographs, it is clear that the pure PAN CF with no added graphene possesses a highly porous microstructure, as shown in Figure II.2.E.3.(a). In contrast, with the addition of graphene, even at very low concentrations (*e.g.*, lower than 0.100 wt.%), the PAN/graphene fiber shows significantly reduced porosity and a denser structure, as shown in Figure II.2.E.3.(b) through (f). Of critical importance, by reducing the defect content, the PAN/graphene (0.075 wt.%) CF achieved competitive mechanical properties with strength, modulus, and strain that meet our target goals as shown in Figure II.2.E.3.(g) and (h).

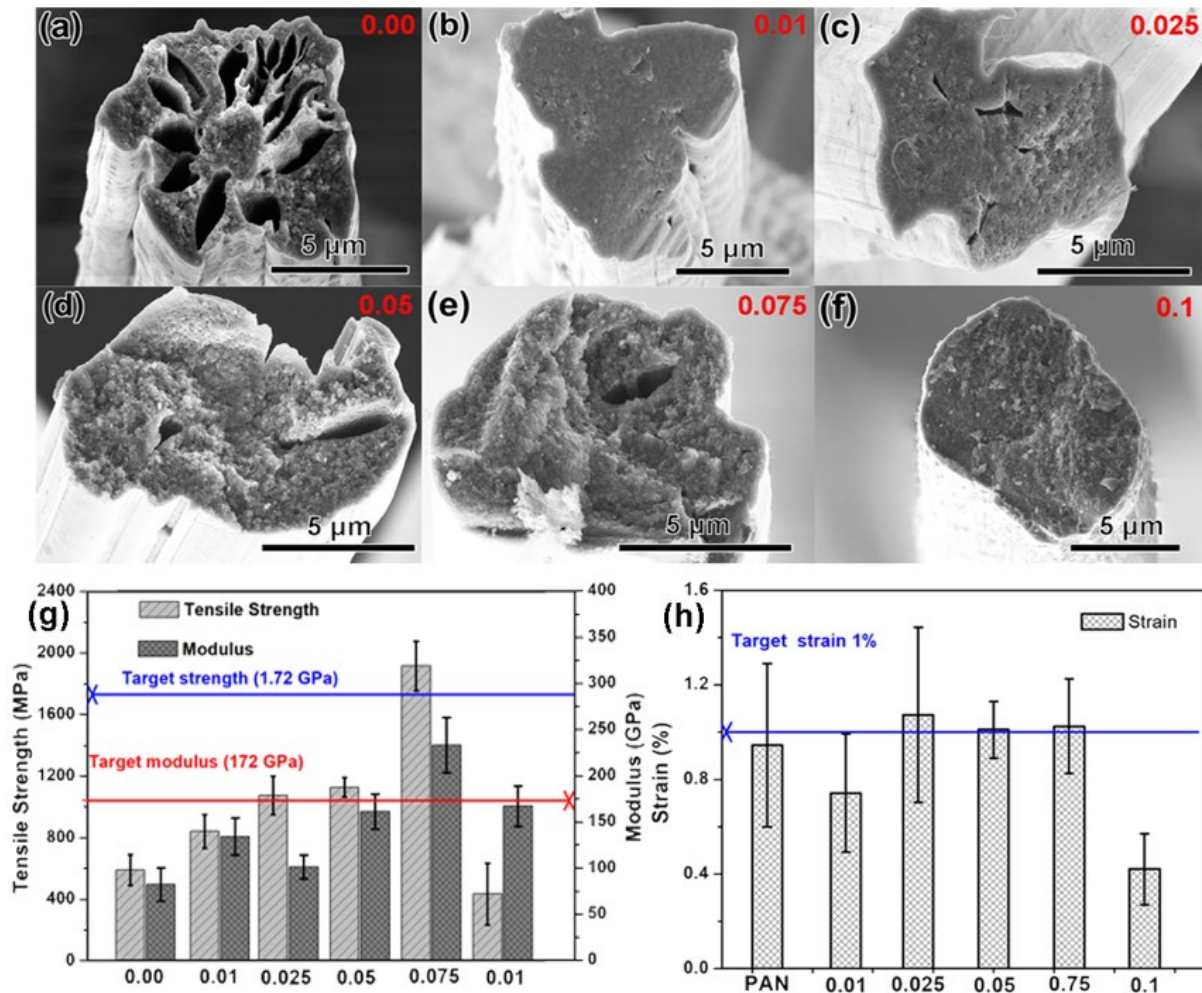
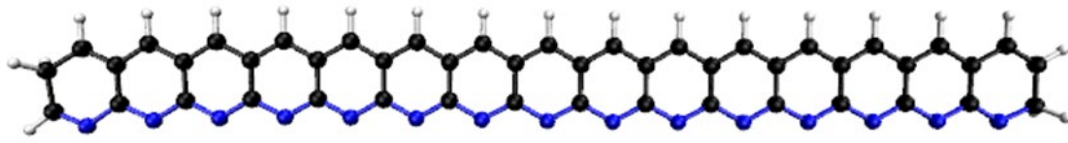


Figure II.2.E.3. PAN/graphene blend CFs and mechanical properties: (a-f) Cross-sections of carbonized PAN fibers with increasing concentrations of graphene (0.00 wt.% - 0.01 wt.%). (g-h) Mechanical properties of PAN/graphene blend fibers. Source: UVA.

Task 1.2: Understanding the Carbonization and Graphitization of PAN-based CF

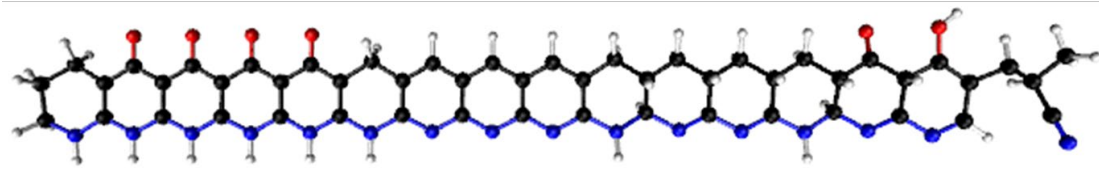
The objective of this task was to capture the chemical evolution from stabilized PAN filaments to CFs during carbonization and subsequent graphitization; this insight would then serve to guide large-scale mechanics simulations. This task was successfully completed with the application of the ReaxFF MD approach. Prior to this project, the only atomistic-scale simulation of the PAN carbonization process using a ReaxFF (where chemical reactions can be modeled via a set of potentials that direct molecular conformations), were reported by the Schatz group and their collaborators for idealized ladder PAN molecules, as shown in Figure II.2.E.4.(a) [5]. To investigate and compare the structural dependence of the carbonized samples at molecular detail, simulations of pure and oxidized PAN as well as for PBO, as shown in Figure II.2.E.4.(b) and (c) were performed.

ladder PAN



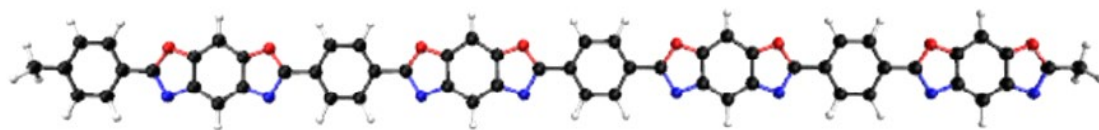
(a)

oxidized PAN

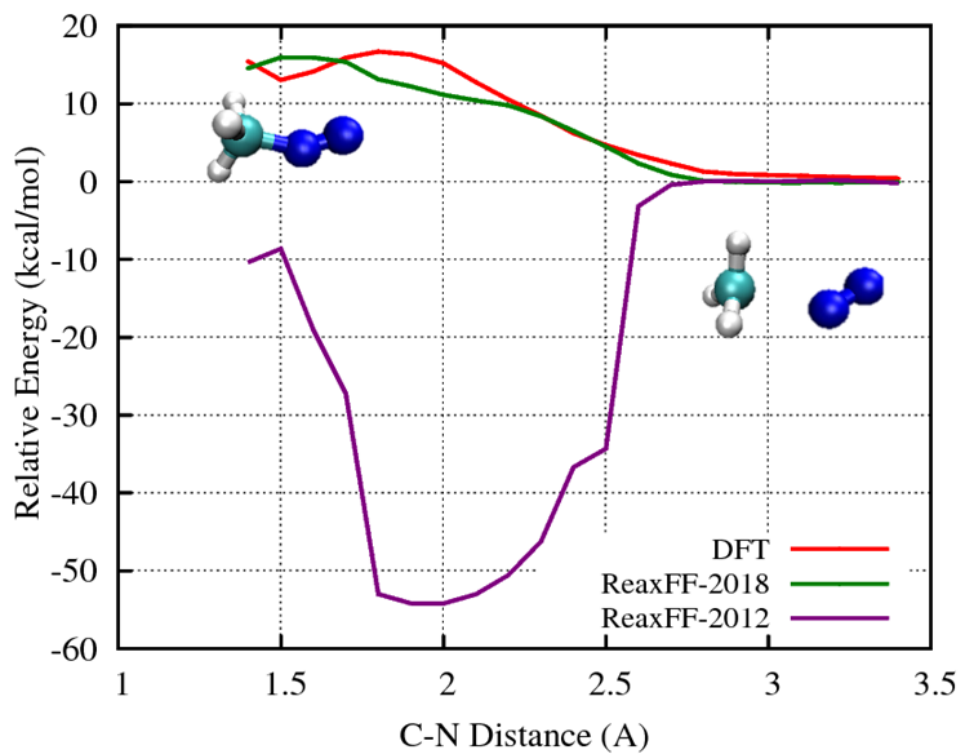


(b)

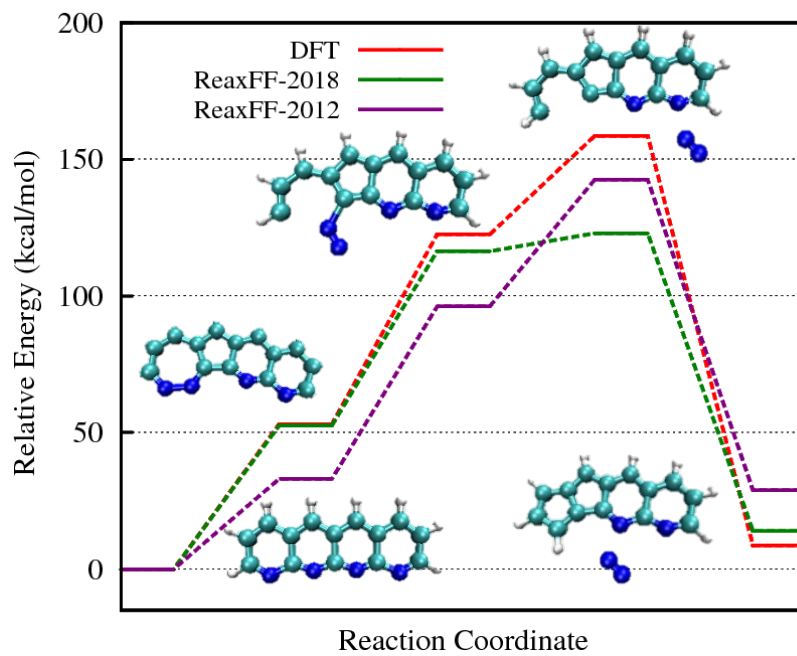
PBO



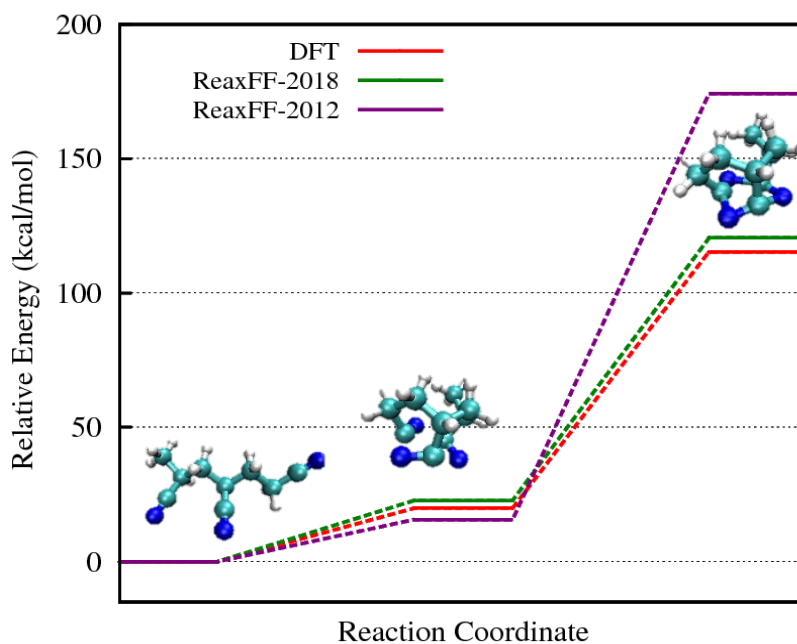
(c)



(d)



(e)



(f)

Figure II.2.E.4. Considered polymers and comparison between DFT and ReaxFF for PAN-related chemistry. Molecular structure of the considered polymers: (a) idealized ladder PAN; (b) proposed oxidized PAN; (c) PBO; and (d) reaction energy for $\text{CH}_3 + \text{N}_2 \rightarrow \text{CH}_3\text{N}_2$ reaction. ReaxFF2018 predicts this reaction to be endothermic, the same as DFT, while ReaxFF2012 makes it very exothermic. (e) Removal of N_2 molecule from ladder PAN structure and formation of two neighboring 5-membered C rings. (f) Formation of ladder PAN from linear PAN. The DFT numbers are calculated using B3LYP hybrid functional and 6-311G** basis set. The cyan, blue, and white spheres represent C, N, and H atoms, respectively. Source: PSU.

The quality of a molecular dynamic simulation depends on the accuracy of force field parameters, and these parameters need to be trained. Parameter training is typically done based on data from the theory of quantum mechanics, commonly using DFT methods, augmented with experimental data. The system of interest (*i.e.*, CF precursors) contains C, H, O, and N. For the C/H/O atoms, the recently developed CHO-2016 force field by Ashraf et al. [6] was used with an extension to incorporate N atoms into the force field. The CHO-2016 model is already trained for C/H/O chemistries, especially for chemistry of small molecules, so only the parameters involving N atoms needed to be trained as a part of this project. Moreover, the C parameters of the CHO-2016 force field are taken from Srinivasan et al. [7], which were developed to model the enhanced mechanical properties for graphene. Thus, these parameters are very much relevant to this project and our objective is to estimate the mechanical properties of the synthesized CFs.

Previously, the simulations of idealized ladder PAN, as shown in Figure II.2.E.4.(a), as a CF precursor were performed by Saha et al. [5] in 2012, where the reactive force field developed by Kamat et al. [8] was used (hereafter referred to as ReaxFF2012). Though the results obtained from Saha et al. [5] were encouraging, a new set of ReaxFF parameters for such systems were developed as motivated by the following factors:

1. The C parameters of ReaxFF2012 are not accurate for deriving the mechanical properties of graphene.
2. Preliminary simulations indicated that N₂ molecules in ReaxFF-2012 are not sufficiently stable and can react with C radical sites; therefore, very few stable N₂ molecules could be produced during the simulation, which is a paramount step in PAN initial chemistry.
3. In addition to ladder PAN, simulating oxidized PAN and PBO molecules in the first year of the project is also a priority, both of which contain oxygen atoms. Therefore, developing a new force field with C/H/O/N would support the long-term reliability of the ICME framework.

In the new reactive C/O/N/H force field (ReaxFF2018), all of the interaction potential parameters involving at least one nitrogen atom were trained, thus retaining the C/H/O 2016 parameters from Ashraf et al. [6]. In order to make N₂ molecule more stable (*i.e.*, less reactive in ReaxFF2018), a special triple bond stabilization term was implemented. A comparison between DFT and ReaxFF energies for three test configurations demonstrates that the new ReaxFF2018 model obtains better agreement than the previous ReaxFF2012 model, as shown in Figure II.2.E.4.(d) through (f).

Furthermore, ReaxFF2012 and ReaxFF2018 were directly compared by measuring 6-membered ring productions, which is a crucial metric for the evolution of the graphitic structure of PAN and alternative precursors as shown in Figure II.2.E.5.(a) through (c), as well as for the evolution of small molecules. This metric can be compared to experimental data to ensure that the correct initial precursor chemistry was being simulated as shown in Figure II.2.E.5.(d) through (f). ReaxFF2018, with its improved C-N chemistry, predicts faster ring productions, which is critical for further kinetic Monte Carlo parametrization for larger systems, and significant improvement for small molecular productions, with clear N₂ production without actively removing small molecules during the carbonization process. Significant H₂ production followed a slow evolution of N₂ molecules for ReaxFF2018, in close agreement with experimentally observed lower temperatures for dehydrogenation and higher temperatures for N₂ production [1].

All data presented so far modeled systems with initially randomly oriented polymers, effectively simulating an amorphous precursor. From experimental data, however, it is clear that precursor filaments possess a certain percentage of crystallinity; therefore, simulations with initially aligned polymers were conducted to investigate the alignment effects through simulated systems. Moreover, the possible influence of sample-stretching during the carbonization process, known experimentally as hot-stretching illustrated in Figure II.2.E.5.(i), was investigated numerically.

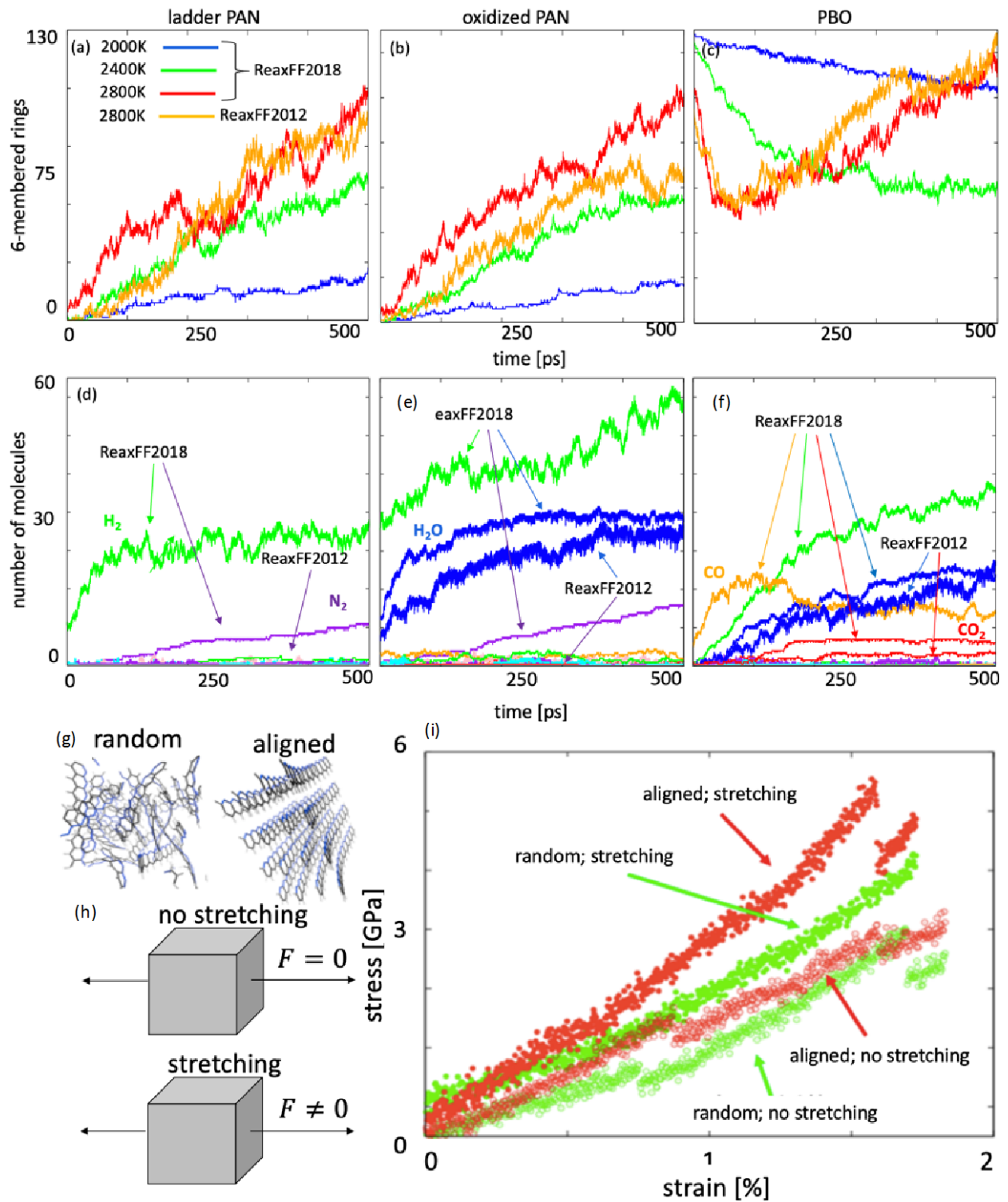


Figure II.2.E.5. MD with ReaxFF, and stress-strain simulations. A comparison between data obtained with ReaxFF2012 and ReaxFF2018: time evolution of 6-membered rings during the carbonization process and small molecule production for (a, d) idealized ladder PAN; (b, e) proposed oxidized PAN; and (c, f) PBO, respectively. Different initial configurations (g) random vs align, and idea for simulations (h) without and with hot-stretching. (i) Stress-strain data for ladder PAN obtained for strain rate 10^{10}s^{-1} . Source: PSU.

Ladder PAN in various initial configurations (random vs. aligned) and with/without applied stretching was investigated, as shown in Figure II.2.E.5.(h) through (j). The difference in slope, which is an indicator of Young's modulus, for initially aligned samples with and without applied stretching during the carbonization is greater than 10%. The resulting ring cluster analysis of 5-/6-/7-membered rings was then used as input parameters for large-scale MD simulations. Initial results suggested that: (i) there is a minimum system size required for the successful transfer of these coordinates from nanoscale to large-scale simulations; and (ii) initial simulated samples were carbonized to a low degree, so significant cluster alignment that might be crucial for further crystalline formation was not observed.

Task 1.3: Investigating Meso-scale and Fiber-Level Properties through Large-Scale MD Simulations

Building on the success of the nanoscale chemical simulations, large-scale MD simulations extended the structure of fibers produced by the chemical conversion to conduct structural characterization and simulate mechanical testing of PAN-based CF. This work was enabled by successfully developing a novel computational approach that can generate realistic 3D microstructures in atomistic simulations from combinations of stacked and unstacked PAN ladders. Previous studies on atomistic modeling of CF have investigated the chemistry of fiber processing, the effects of structural faults on mechanical properties, and the formation of 2D microstructures [9]. However, studies that discuss the generation and characterization of a realistic 3D microstructure using large-scale atomistic simulations are scant. As a result, there is still a lack of clear understanding of atomic scale structural features and mechanisms that control the structure-property relationship of CF. Hence, the overall goal of this task during the first year of the project was to develop a computational framework for generating and characterizing 3D CF microstructures. After creating computational samples with realistic microstructure, tensile test simulations were performed to calculate mechanical properties.

A novel computational approach, which allows for the generation of CF realistic microstructures in atomistic simulations, was successfully developed. The procedure is based on assembling different types of C ladders, such as idealized C sheets and cyclic C clusters obtained in PAN-ReaxFF MD simulations, as shown in Figure II.2.E.6. Atomistic simulations were performed using the LAMMPS [10] MD suite and the bond order dependent AIREBO potential [11]. To generate 3D microstructures with different characteristics, various combinations of PAN ladders and ladder orientations were used.

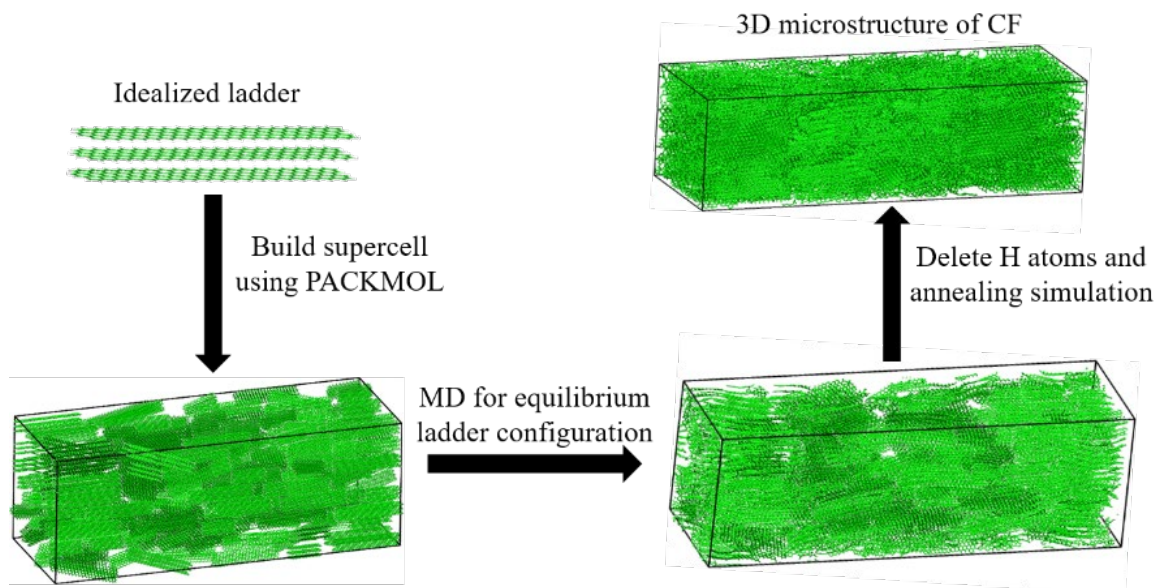


Figure II.2.E.6. Schematic of the atomistic procedure for obtaining the 3D microstructure of CFs. The C contents and hydrogen atoms are shown with green and white colors, respectively. Source: UVA.

The microstructures of the computational samples obtained in the atomistic simulations were then characterized by calculating key parameters, such as the hybridization state of C atoms, relative prevalence of different types of cyclic rings, fiber orientation, XRD profiles, crystallite size, pore size distribution, and degree of graphitization, as shown in Figure II.2.E.7, and presented in Table II.2.E.2.

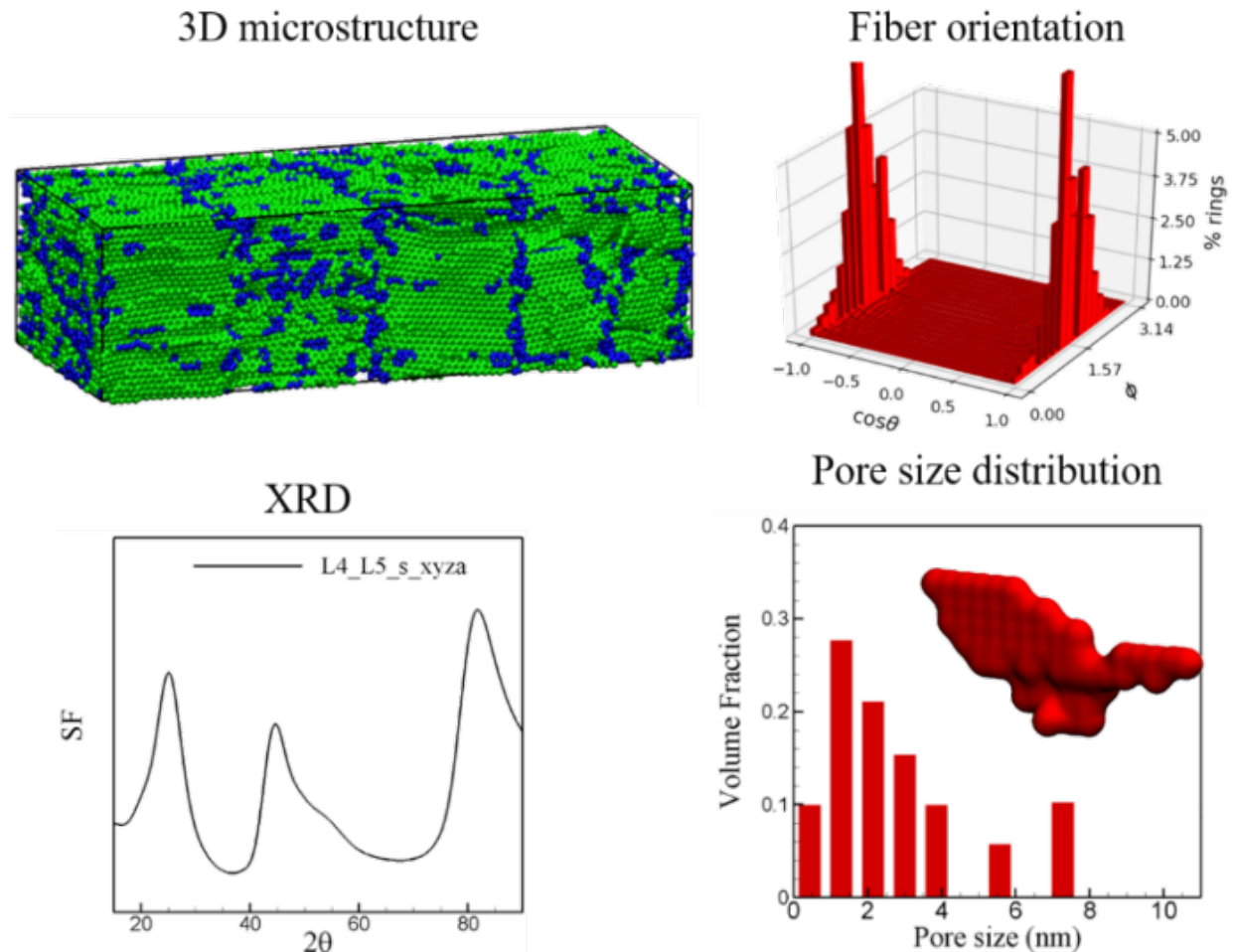


Figure II.2.E.7. Pore distribution and simulated XRD of PAN. Atomic configuration of one of the fibers generated in atomistic simulations and several structural parameters used in the characterization of the fiber microstructure. Source: UVA.

Table II.2.E.2. Microstructure Parameters of Different Fibers Generated in Atomistic Simulations.

Microstructure	Density (g/cm ³)	% graphitic carbon	% sp ² carbon	d ₀₀₂	L _c (Å)	Maximum pore size (nm)
Structure 1	1.82	14.7	92.7	3.64	12.96	5.5
Structure 2	1.80	18.5	92.5	3.57	14.34	8.1
Structure 3	1.93	31.2	95.0	3.55	19.78	7.6

To identify the hybridization states of C atoms (sp, sp², and sp³), the number of chemical bonds contributed by each C atom was calculated. The bond ring analysis was then performed using a Depth-First Search algorithm. To characterize the degree of orientational ordering in a CF, a statistical analysis of the orientations of individual C rings was performed. To derive the XRD patterns, a general approach as described in Lin and Zhigilei [12] was used. The XRD data was used to identify the d₀₀₂ spacing and to estimate the characteristic size of the crystallites (L_c). In existing literature, pore size and degree of graphitization were estimated using

indirect methods based on XRD patterns [13]. Instead, novel methods for calculating pore size and degree of graphitization in simulated microstructures was developed internally for this project. In order to identify the sizes and shapes of pores in the CF microstructure, regions that are either empty or have very few atoms were first isolated. Then, the pore size was defined as a line connecting the farthest surfaces of the pore without ever crossing the pore boundary. Such a line vector can be efficiently calculated using a modified version of Bresenham's line algorithm for each pore. The per-atom energies were used to identify the graphitic and turbostratic phases in simulated microstructures.

After validating the simulated microstructures against lab-synthesized fibers, the mechanical properties, including Young's modulus, tensile strength, and tensile strain, were calculated from the simulated system, as shown in Table II.2.E.3. The estimated values of Young's modulus and tensile strength are within the experimental range and satisfy DOE's target criteria. The tensile fracture strength and strain are higher than experimental values, which is expected for computational samples where the maximum void size is limited by the size of the computational cell. As a consequence, maximum pore sizes in the simulated samples varied between 4 to 8 nm, while the actual fiber had pores of about 30 nm or higher [14–15]. According to Griffith's Law [16–18], fracture stress is inversely related to the root of the pore diameter, $\sigma \propto \frac{1}{\sqrt{a}}$. Hence, a higher tensile stress and strain may be achieved with smaller pore sizes, as observed in the simulations. We can apply a correction factor based on Griffith's Law to adjust the immediate output of the simulations, which enabled direct comparison between simulation and experimental results, as addressed in the conclusion of this report.

Table II.2.E.3. Mechanical Properties of Different Fibers Generated from Atomistic Simulations.

Microstructure	Density (g/cm ³)	Tensile modulus (GPa)	Tensile strength (GPa)	Tensile strain (%)
Structure 1	1.82	230.4	18.2	7.9
Structure 2	1.80	262.5	16.8	6.4
Structure 3	1.93	280.8	14.6	5.2

Task 1.4: Optimizing the Melt Spinning Process via Limited Production-Scale Testing

The main objective of this task during the first year of the project was to kick-start the preliminary production-scale testing with fiber production using identified precursor materials and to optimize the melt spinning process, evaluate critical temperatures, and prepare detailed production recipes for evaluating the candidate precursors for the second year of the project. Through collaboration with the LightMat Consortium and ORNL, preliminary testing at ORNL was performed throughout the first year of the project to gather a wealth of experimental data to inform the multiscale simulations, to enable an evaluation of the scalability of CF production, and to optimize production-scale spinning of fibers. Critically, while the laboratory-scale experimentation and computational modeling has largely focused on PAN-based CF, the production-scale testing has maintained a broad focus to identify production parameters that may vary with material and begin to optimize these parameters for different precursors. In this manner, this regimen of tests will help the work in BP2 to focus on the identified critical parameters when exploring alternative precursors.

We have met this milestone with a preliminary regimen of production-scale testing of different fiber precursors and an evaluation of process effects. PAN, PBO, Nylon, pitch, and ultra-high-molecular-weight polyethylene (UHMWPE)-based fibers have been evaluated, in addition to some ongoing analysis of the effect of added nanoparticles, like graphene, and have provided a growing library of reference data.

The goal of the work with UHMWPE is to show that synthesis of a precursor to CF may not be necessary to meet DOE targets. These fibers are commercially available and already meet the required strength for the DOE program; however, their modulus is low. Hence, it was conceived that if graphene was added in small amounts (<1%), the modulus would increase enough to meet the DOE requirements. Importantly, graphene-enabled,

PE-based fibers may be capable of achieving target properties without stabilization, carbonization, and graphitization, which may reduce over 50% of the fiber costs (as estimated by Solvay). Furthermore, the costs associated with the added graphene are low (1 - 3 \$/lb); thus, the overall cost will be significantly reduced.

For ease of processing into a melt-spinnable fiber for the purpose of demonstrating the effect of the graphene addition on modulus, ORNL blended UHMWPE with high-density polyethylene (HDPE) in a 40/60 ratio. This was then extruded in a Randcastle-modified extruder into filaments. Fibers were initially made with and without graphene (0.1 wt.%) in the neat HDPE and then characterized for their strength and modulus. A blend of the HDPE/UHMWPE was also made, as was shown in Table II.2.E.4. Future work will focus on developing a higher draw ratio to reduce fiber size and work with the blends with the addition of graphene. As can be seen, the addition of just 0.1 wt.% did result in an increase in modulus in the limited samples tested. Full characterization will be conducted in the second year of the project. It is anticipated that the results will translate to the pure UHMWPE and demonstrate that a polymer fiber could indeed be used instead of the requirement for CFs.

Table II.2.E.4. Results of Graphene Additions on the Polyethylene-based Fibers.

Blend	Fiber Diameter (μm)	Peak Stress (MPa)	Modulus (GPa)
HDPE	57.2	59.3	0.83
HDPE + 0.1% graphene	74.3	51.0	0.97
HDPE/UHMWPE	66.3	45.5	0.90

Nylon 6 is a very cheap raw material with a market price of 1–5 \$/Kg (5 – 10 times lower than that of PAN precursor) and currently made into commercial fibers for use in products all over the world. If a method could be developed to convert this inexpensive fiber into a CF, then it may be possible to attain DOE's goals. An exhaustive literature survey found that a method has been explored in the past to convert Nylon fibers into CFs [19] as shown in Figure II.2.E.8. It is a similar process to converting rayon or PAN precursors but requires a pre-oxidation conditioning of the fibers with a Lewis acid, such as CuCl. This pretreatment is thought to create free radicals on the polymer chains, thus allowing the subsequent oxidation (stabilization) to cause crosslinking, preventing melting and leading to a successful conversion to C [19]. ORNL used Nylon 6 and spun fibers with their modified Rancastle extruder to produce fibers for this study. The purpose of spinning our own fibers is that we will eventually want to add graphene to the precursor and will need to have a baseline to compare the results. A parametric study on the soak time of the fiber in the CuCl pretreatment, as well as a time and temperature study of the stabilization process was conducted.

DSC of these studies for the oxidation temperature of 210°C indicates that oxidation time had a significant influence on stabilization (more than the CuCl variables) and fibers from the 40-hour stabilization were able to be successfully carbonized without melting. ORNL has spun, stabilized, carbonized, and delivered fibers to UVA for characterization. Plans to continue this research in further detail in the second year of the project involve optimizing fiber diameter and adding graphene to the precursor to increase strength.

Another goal of the ORNL LightMAT portion of this project was to develop a method to induce structure in the polymer precursor during the spinning process. The thought is that by developing physical structure in the axis of the fiber as it is spun, when it converts to carbon, this structure will be there to add strength. This would be similar to reducing grain size in metals and ceramics. Structure in the CF can be useful in preventing brittle failure of the fiber, thus increasing its ultimate strength. With this goal in mind, a proprietary spinnerette was developed to produce fibers in which structure is created as the fiber moves through the extrusion nozzle to become a fiber. A model polymer, which is very well characterized, that can be melt-spun is mesophase pitch. This model polymer will be used to characterize the effects of the novel spinnerette on the resulting CFs. With success, this technique can then be applied to other polymers being developed and modeled at Pennsylvania

State University (PSU) and UVA. Preliminary efforts show that the modified spinnerette is successful in developing this structure, and hence, further efforts will be conducted to fully characterize this concept.

It was found that adding graphene to polyethylene-based fibers could increase the modulus of the polymer fibers; further studies are warranted. Next, it was found that Nylon 6 could be spun into fibers and converted into CFs, warranting further study with graphene additions. It was also found that modification of the spinnerette could indeed affect the microstructure of the polymer precursor fibers and will be explored further with not only a model polymer (pitch), but suitable alternative polymers as the research progresses.

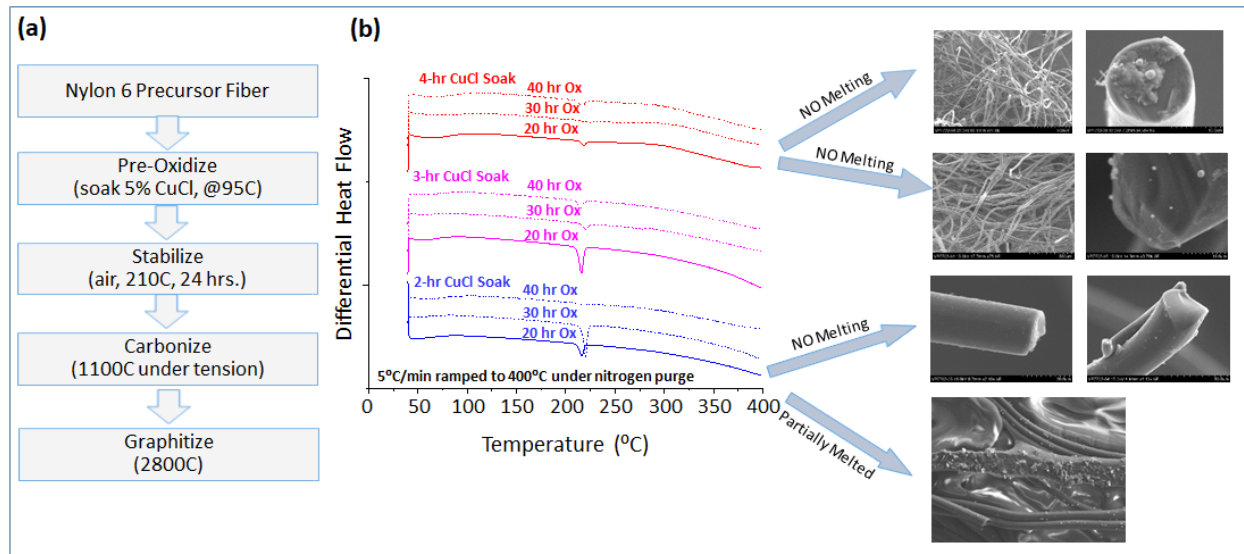


Figure II.2.E.8. Exploratory work converting Nylon to CFs: (a) Potential process for conversion of Nylon to carbon; and (b) Parametric study results of conversion of Nylon 6 fibers to CFs indicating that it is possible to convert Nylon to carbon.

Source: ORNL.

Contributions to Research by Industry Partner – Solvay Composites

Solvay possesses both the human expertise and experimental resources to translate laboratory results to industrial-scale production. Experimental resources include a 16-position, pilot-scale oxidation and carbonization line, which can treat fibers up to 2,800°C. Solvay is capable of developing various new types of CF precursors from lab-scale to pilot-scale to production-scale and then commercializing the new product. During FY1, Solvay provided close guidance and expertise on both the experimental and simulation aspects of PAN synthesis, spinning, and processing. Through monthly conference calls, Solvay engineers and scientists aided in down-selecting a list of potential alternative precursor polymers using decades of industry insight and knowledge. Furthermore, Solvay provided valuable insight regarding the impact of various processing parameters on the resultant CF, which enabled the fine-tuning of simulation parameters to accurately reflect mechanical properties.

During the first three-quarters of FY1, the UVA and PSU simulation teams developed computational models to simulate the chemical and physical changes of PAN precursor fiber structure in the oxidation and carbonization process. These simulation results are being verified against experimental data of an industrial CF production process to extend the model to alternative CF precursor materials. To support the project with reliable experimental data, two full oxidation/carbonization runs with various profiles with industry-grade PAN precursor fibers were run on the pilot line located in the Solvay CF Research and Innovation facility in Piedmont, SC. Each run took two weeks of pilot line time and shifted work for two engineers and seven technicians. The purpose of these runs was to provide accurate data in CF production environment for the simulation team to verify the model based on current PAN precursor fibers. A schematic chart of the oxidation/carbonization process and major findings are summarized in Figure II.2.E.9. The PAN precursor

fiber used in the pilot runs were acquired from the Development Spinning Line located in the same facility. The fibers went through a multiple stage oxidation process, a multiple zone pre-carbonization process, and a multiple zone carbonization process. The carbonization temperatures were varied to obtain multiple sets of data for the verification of the model. During each step, the properties of precursor fibers, oxidized fibers, and carbonized fibers, including chemical structure, crystallinity structure, graphitic structure, and tensile strength/modulus, were collected. This data will be compared with the results obtained from the computational model developed in the early phase of the project to support the optimization of simulation. Also, the laboratory-scale production line established in the UVA lab provided the possibility of easy and quick experimental data collection to support the project. The comparison between the data acquired from the pilot run at Solvay and the laboratory-scale line at UVA is expected to guide the improvement of the laboratory-scale line to get more accurate real-time results.

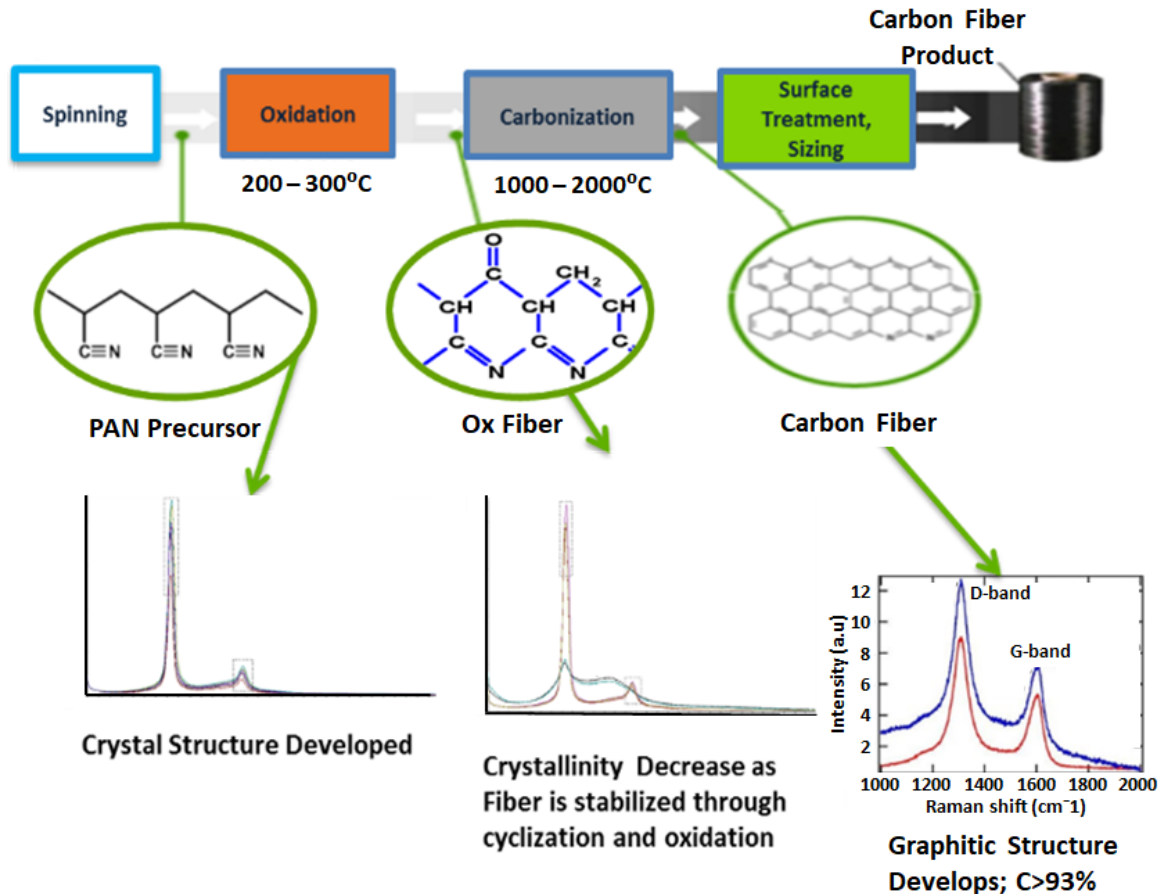


Figure II.2.E.9. Illustration of CF production. Schematic of the oxidation/carbonization process and the corresponding XRD and Raman results. Source: Solvay.

Contributions to Research by Industry Partner – Oshkosh Corporation

Oshkosh continues to be a leading designer, manufacturer, and marketer of specialty-access tactical and armored vehicles. These vehicles must strike a delicate balance between weight, cost, durability, and strength to meet mission-critical objectives; thus, Oshkosh is highly interested in potential low-cost, high-performance CFs. Oshkosh has provided and consulted with the research team regarding target mechanical properties and material costs to guide the proposed experimental modeling efforts. Practical concerns for CF applications in various industries have been an important guiding principle for the research team in down-selecting alternative candidate precursor polymers. The Oshkosh point of contact facilitated communication with Oshkosh engineers for targeted inquiries and provided use of its extensive network of suppliers and vendors in finding appropriate instrumentation and raw materials necessary for project success.

Conclusions

The project is on schedule and meets the first year milestones established at the start of the project. The success criterion for the first year of the project was to demonstrate the capability of the assembled ICME framework to predict properties of PAN-based CF within an allowable 15% error. The final assessment of this criterion will be made to contrast the properties of PAN-based CF produced in the laboratory with the framework-predicted properties of tensile strength, strain, and elastic modulus. An error within the ICME framework may be propagated across the multiscale computations, so it is critical to minimize error at each step.

Throughout FY1, the development of the ReaxFF2018 approach was conducted to minimize the inherent issues with the previous ReaxFF2012 approach. The total errors within the PAN-related chemistry in the ReaxFF training set reduced from 44195 unit-free error numbers (UFEN) for ReaxFF2012 to 1865 UFEN for ReaxFF2018, an improvement of **~95.7%**. This significant improvement empowered ReaxFF2018 simulations results to achieve a high-level of accuracy, within **5%** of DFT findings. These results then translated into more accurate chemical ring formations and structures for the meso-scale MD simulations and calculations of large-scale properties.

As was previously discussed, the large-scale MD simulations were corrected with a calibration factor derived from Griffith's Law [16-18] to account for differences between simulated fiber void size and actual void size due to current system size limitations of the computations. We see that Griffith's Law corrects for the disparity, achieving predictions of fiber tensile properties within our 15% allowable error success criteria, as demonstrated by the direct comparison between nano-tensile tests of a PAN-based CF and the ICME framework results of the PAN fiber. As shown in Table II.2.E.5, the ICME framework is still continuing to over-predict the mechanical properties of the resultant fiber; we will continue to optimize the framework throughout BP2 to address this issue. However, the difference between the predicted and experimentally obtained values fall **within the 15% target** to meet the designated go/no-go decision point and success criteria.

Table II.2.E.5. Success Metric of the Initial ICME Framework with PAN-based CF.

	Experimental Measurement	ICME Framework Prediction	Percent Difference
Tensile Strength	3827 ± 88 MPa	4203 MPa	9.8 %
Tensile Strain	1.54 ± 0.003 %	1.71 %	12.9 %
Modulus	276 ± 5 GPa	297 GPa	7.6 %

Key Publications

1. Zhu, J., Z. Gao, Y. Schwab, C. Bumgardner, K. Joshi, L. Zhang, L. V. Zhigilei, and X. Li, in preparation, "Polyacrylonitrile derived CFs: from atomistic simulations to microscale properties."
2. Joshi, K., M. Arefev, and L. V. Zhigilei, in preparation, "Atomistic modeling of CF microstructure."
3. Kowalik, M., C. M. Ashraf, and A. C. T. van Duin, in preparation, "Atomistic investigation of carbonization process for C/H/O/N-based polymers in CFs production."

References

1. Rahaman, M. S. A., A. F. Ismail, and A. Mustafa, 2007, "A review of heat-treatment on polyacrylonitrile fiber," *Polym. Degrad. Stab.*, Vol. 92, No. 8, pp. 1421–1432.
2. Wu, G., C. Lu, L. Ling, A. Hao, and F. He, 2005, "Influence of tension on the oxidative stabilization process of polyacrylonitrile fibers," *J. Appl. Polym. Sci.*, Vol. 96, No. 4, pp. 1029–1034.

3. Zhu, J., C. Chen, Y. Lu, Y. Ge, H. Jiang, K. Fu, and X. Zhang, 2015, "Nitrogen-doped C nanofibers derived from polyacrylonitrile for use as anode material in Na-ion batteries," *Carbon*, Vol. 94, pp. 189–195.
4. Li, Y., Y. Yu, Y. Liu, and C. Lu, 2018, "Interphase development in polyacrylonitrile/SWNT nanocomposite and its effect on cyclization and carbonization for tuning C structures," *ACS Appl. Nano Mater.*, Vol. 1, No. 7, pp. 3105–3113.
5. Saha, B., and G. C. Schatz, 2012, "Carbonization in polyacrylonitrile (PAN) based CFs studied by ReaxFF MD simulations," *J. Phys. Chem. B*, Vol. 116, No. 15, pp. 4684–4692.
6. Ashraf, C., and A. C. T. van Duin, 2017, "Extension of the ReaxFF combustion force field towards syngas combustion and initial oxidation kinetics," *J. Phys. Chem. A*, Vol. 121, No. 5, pp. 1051–1068.
7. Srinivasan, S.G., Ganesh, P. and van Duin, A.C.T., 2015, "Thermal decomposition of a large fullerene: A MD study using the ReaxFF reactive force field," *Journal of Physical Chemistry A*, Vol. 119, pp. 571–580.
8. Kamat, A. M., A. C. T. van Duin, and A. Yakovlev, 2010, "MD simulations of laser-induced incandescence of soot using an extended ReaxFF reactive force field," *J. Phys. Chem. A*, Vol. 114, No. 48, pp. 12561–12572.
9. Desai, S., C. Li, T. Shen, and A. Strachan, 2017, "Molecular modeling of the microstructure evolution during CF processing," *J. Chem. Phys.*, Vol. 147, No. 22, Art. 224705.
10. Plimpton, S., 1995, "Fast parallel algorithms for short-range MD," *J. Comput. Phys.*, Vol. 117, No. 1, pp. 1–19.
11. O'Connor, T. C., J. Andzelm, and M. O. Robbins, 2015, "AIREBO-M: A reactive model for hydrocarbons at extreme pressures," *J. Chem. Phys.*, Vol. 142, No. 2, Art. 024903.
12. Lin, Z., and L. V. Zhigilei, 2006, "Time-resolved diffraction profiles and atomic dynamics in short-pulse laser-induced structural transformations: MD study," *Phys. Rev. B*, Vol. 73, No. 18, Art. 184113.
13. Zou, L., B. Huang, Y. Huang, Q. Huang, and C. Wang, 2003, "An investigation of heterogeneity of the degree of graphitization in carbon-carbon composites," *Mater. Chem. Phys.*, Vol. 82, No. 3, pp. 654–662.
14. Johnson, D. J., and C. N. Tyson, 1969, "The fine structure of graphitized fibres," *J. Phys. D*, Vol. 2, No. 6, pp. 787–795.
15. S. Ozcan, F. Vautard, and A. K. Naskar, 2014, "Designing the structure of CFs for optimal mechanical properties," *Polymer Precursor-Derived Carbon*, American Chemical Society Division of Polymer Chemistry Symposium Series, Vol. 1173, pp 215-232.
16. Griffith, A. A., 1921, "The phenomena of rupture and flow in solids," *Phil. Trans. Roy. Soc. (London), ser. A*, Vol. 221, pp. 163-198.
17. Michler, G. H., and H.H. K.B. von Schmeling, 2013, "The physics and micro-mechanics of nano-voids and nanoparticles in polymer combinations." *Polymer*, Vol. 54, No. 13, pp. 3131–3144.
18. Yin, H., H. J. Qi, F. Fan, T. Zhu, B. Wang, and Y. Wei. 2015, "Griffith criterion for brittle fracture in graphene," *Nano Lett.*, Vol. 15, No. 3, pp. 1918–1924.
19. Karacan, I., and G. Baysal, 2012, "Investigation of the effect of cupric chloride on thermal stabilization of polyamide 6 as CF precursor," *Fiber. Polym.*, Vol. 13, No. 7, pp. 864–873.

II.2.F Consortium for the Production of Affordable CFs in the U.S. (Western Research Institute)

Dr. Jeramie Adams, Principal Investigator

Western Research Institute
3474 North 3rd Street
Laramie, WY 82072
E-mail: jeramie.adams@uwyo.edu

Don Collins, Co-Principal Investigator

Western Research Institute
3474 North 3rd Street
Laramie, WY 82072
E-mail: don.collins@uwyo.edu

Dr. Amit Naskar, Co-Principal Investigator

Oak Ridge National Laboratory
1 Bethel Valley Rd.
Oak Ridge, TN 37830
E-mail: naskarak@ornl.gov

Chris Boyer, Co-Principal Investigator

Advanced Carbon Products
3651 State Highway 773
Hitchins, KY 41146
E-mail: cboyer@advcarpro.com

Jeffrey Grossman, Co-Principal Investigator

Massachusetts Institute of Technology
77 Massachusetts Ave.
MIT 13-5134
Cambridge, MA 02139-4307
E-mail: jcg@mit.edu

Ray Fertig, Co-Principal Investigator

University of Wyoming
1000 E. University Ave.
Laramie, WY, 82071
E-mail: rfertig@uwyo.edu

Charlie Atkins, Co-Principal Investigator

Ramaco Carbon LLC
1101 Sugarview Drive, Suite 201
Sheridan, WY 82801-5383
E-mail: cca@wyoipark.com

Billy Harmon, Advisor Industrial

Solvay Composites
7139 Augusta Road
Piedmont, SC 29673-9692
E-mail: billy.harmon@solvay.com

Amit Goyal, Co-Principal Investigator

Southern Research Institute
 2000 Ninth Avenue South
 Birmingham, AL 35205-2708
 E-mail: agoyal@southernresearch.org

H. Felix Wu, Ph. D, DOE Technology Manager

U.S. Department of Energy
 E-mail: felix.wu@ee.doe.gov

Start Date: October 1, 2017 End Date: September 30, 2020
 Project Funding (FY18): \$4,192,820 DOE share: \$2,695,413 Non-DOE share: \$1,497,407

Project Introduction

Lightweight vehicles would produce several economic and environmental advantages; most notably, reduced fuel consumption and greenhouse gas emissions. Additional cascading benefits would include reductions in infrastructure costs and maintenance by virtue of less stress applied to roads and other transportation infrastructure, as well as far-reaching geopolitical impacts, such as higher national security by reducing the United States' (U.S.) dependency on foreign crude oil.

One such way to reduce the weight of vehicles, while not sacrificing strength, is to manufacture traditional stress-bearing metal components with lightweight advanced materials and composites, such as those from CF. These advanced materials can be engineered to have physical strength properties greater than steel at a fraction of the weight. Additionally, by properly selecting the correct materials and applying appropriate spinning processes, very strong and highly flexible materials can be produced. That is why CFs are used to produce materials as diverse as the spaceship nosecones to shafts of fly-fishing rods. This gives validity to pursuing CFs for future development of lightweight vehicles.

A difficulty in large-scale deployment of CF for the commercial vehicle industry is the availability of large quantities of CF with appropriate physical properties at a reasonable cost. To address these limitations, a consortium of academic, government, non-profit, and commercial entities has been assembled to study the feasibility of using large-volume, low-cost natural resources to produce CFs of the appropriate quality and cost for use in the vehicle industry. Some of the most abundant natural resources are those from current biomass, such as sugars derived from agricultural sources, or those from ancient biomass, such as coal and petroleum. The ability to study several different types of feedstocks, and blends of these feedstocks, provides for a robust roadmap for potential materials while also reducing economic risks that can arise by becoming too dependent on any one material that may be subject to climatic, environmental, geopolitical, and ultimately market, variations. Therefore, in this work, no particular preference is being given to any one feedstock and CFs are being produced from coal-, petroleum-, and biomass-based feedstocks.

Objectives

The objective of the research is to investigate the current landscape of appropriate raw starting materials from petroleum-, coal-, and biomass-based feedstocks as CF feedstocks and precursors to produce low-cost CF materials for lightweight vehicles in the U.S. This objective is divided into two complimentary parts:

1. Develop, integrate, and demonstrate a suite of ICME that predict CF properties such as load-to-failure, failure mode, stiffness/deflection, dynamic performance, and microstructures capable of minimum modeling element accuracies within $\leq 15\%$ of measured properties. This will enable the design, development, and optimization of precursor chemistry associated with conversion into CF and evaluate alternative precursors for suitability to manufacture low-cost CF. The ICME will also include

methodologies to simulate the manufacturing process(es) (including variability from both process and material). All non-proprietary and non-business sensitive public data and code, such as technical data used to support published journal articles or research code used for simulations, will be provided to the LightMat Consortium for curation and hosting.

2. Develop, manufacture, and demonstrate CF precursor technology and processing techniques, where CF is a material consisting of thin, strong multi-crystalline filaments of C used as a reinforcement material especially in resins, capable of achieving the requirements in Table II.2.F.1.

Table II.2.F.1. Project Parameters and Requirements.

Parameter	Requirement
Cost	≤ \$5/pound
Strength	≥ 250 Ksi
Modulus	≥ 25 Msi
Strain	≥ 1%

Approach

Our approach is to study readily available, large-volume feedstocks from biomass, coal, and petroleum to produce precursors of appropriate qualities that lend themselves to the production of CF with the appropriate physical properties and cost to be used in the commercial vehicle industry. Then, we will de-risk this process by developing predictive models that can be used to guide the development of CF materials from new or blended feedstocks. To achieve the objectives, a consortium was assembled from partners that have significant experience working with these different feedstocks, as well as experts in CF production, mechanical testing, and modeling from the molecular-, micro-, and macro-level. The team chosen for this project consists of:

- Western Research Institute (WRI): Prime-recipient
- ORNL: funded by a Field Work Proposal
- Grossman Group at Massachusetts Institute of Technology (GG-MIT): Subrecipient
- Southern Research Institute (SRI): Subrecipient
- University of Wyoming (UW): Subrecipient
- Advanced Carbon Products (ACP): Subrecipient
- Ramaco Carbon LLC (RAMACO): Subrecipient
- Solvay Composites (Solvay): Industrial Advisor.

Each member of the consortium brings a unique and complementary aspect to necessarily build-up fundamental scientific, and yet industrially relevant, understanding between the chemistry of different organic feedstocks and subsequent precursor formation, while following the production chain up through CF fabrication, mechanical characterization, and modeling. These individual aptitudes will be meshed together using a database with high-level data-mining through machine-learning (ML) and computational methods to deliver state-of-the-art holistic and robust models. The strengths of each consortium member are necessary for the wide scope set forth in the project while producing minimal overlap and duplication of efforts. Figure II.2.F.1 shows a high-level depiction of the consortium organization, while Table II.2.F.2 shows a simple summary of the primary strengths and responsibilities for each consortium member.

For the different feedstock materials, WRI is primarily responsible for coal and other petroleum-based and bituminous-based (gilsonite) materials; SRI is responsible for biomass sugars; and ACP is responsible for working with slurry oils from petroleum refining. Prior to forming CF, each feedstock needs to be processed

into intermediates, which under this program consist of the following: isotropic coal tar pitches derived from coal tar; isotropic petroleum pitch derived from slurry oils; and acrylonitrile (ACN), which is produced from biomass extracted sugars. Some of these intermediates, such as isotropic coal tar and petroleum pitch, can be directly spun to produce general-purpose CF, while other feedstocks, such as gilsonite, can also be used in their mined form to produce general-purpose CF. However, for most intermediates to produce CF of the appropriate mechanical properties, these intermediates need to be chemically converted into precursors. Anisotropic, or mesophase, precursors produced from coal tar and petroleum pitches are produced by thermal crosslinking of aromatic molecules, while monomeric ACN is polymerized to form polyacrylonitrile (PAN). The chemical characterization for coal, petroleum, and gilsonite materials was performed by WRI, while the chemical characterization dealing with ACN production was performed by SRI.

Appropriate feedstock materials, intermediates, and precursors are spun into CF at ORNL using a melt spinning procedure. In the case of ACN, the intermediate monomer from SRI is supplied to ORNL for polymerization of the material to the PAN-based precursor of the appropriate molecular weight range and polydispersity. Upon spinning CF, the as-spun, or “green,” fibers are stabilized through oxidation at elevated temperatures followed by carbonization > 1,000°C. Some materials need to be converted further at significantly higher temperatures to graphitize the material between 2,000 to 3,000°C. Materials produced after carbonization or graphitization are then tested to measure their mechanical properties. The physical crystalline properties are also evaluated using microscopy and XRD methods. In BP 2 and 3, CF tows produced at ORNL will be provided to UW, who will then manufacture CF tow resins to test the additional physical properties of the fibers that cannot be obtained directly from CF, but can be obtained from bulk resin composites.

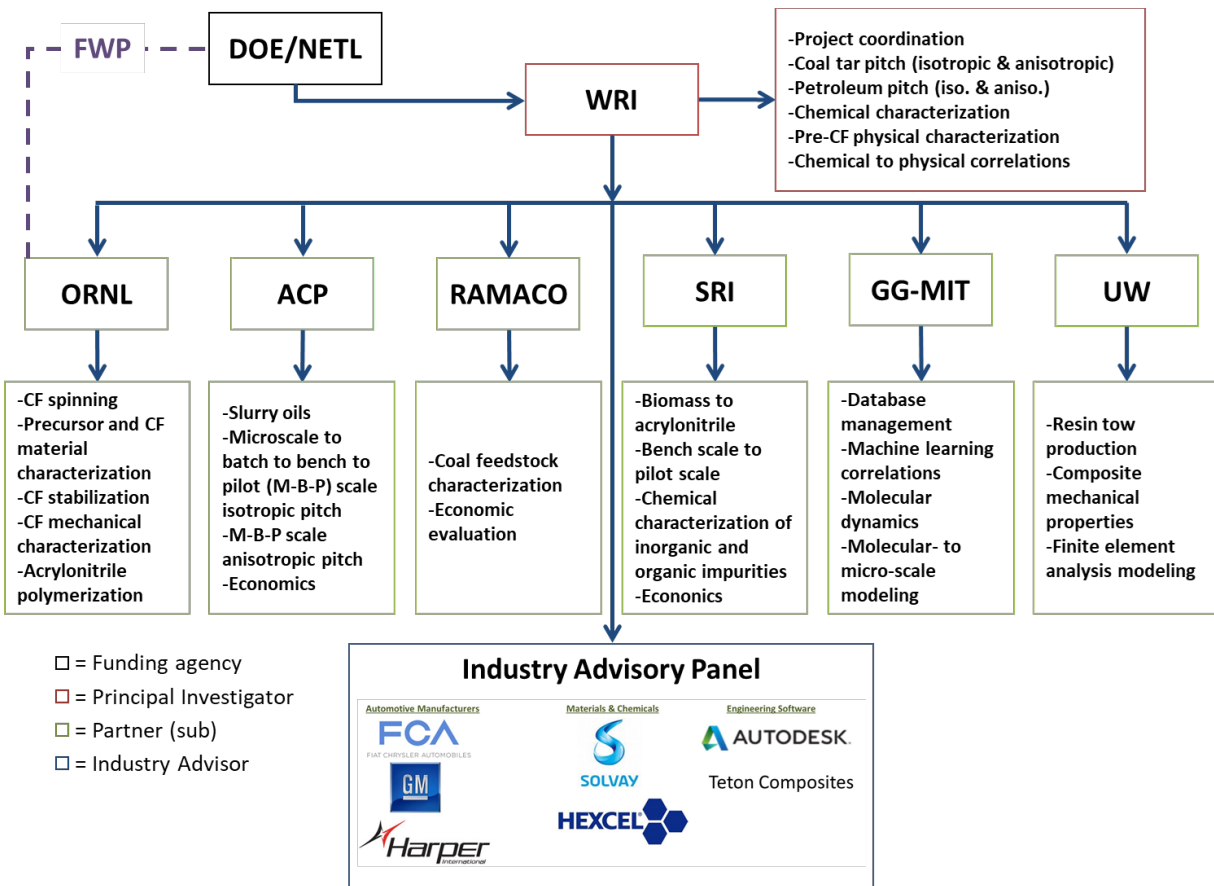


Figure II.2.F.1. Organization for the Consortium for Production of Affordable CF in the United States. Source: WRI.

Table II.2.F.2. General Description of Each Consortium Member's Primary Responsibility.

Primary Consortium Member Responsibility	WRI	GG-MIT	ORNL	SRI	ACP	UW	RAMACO	Solvay
Chemical Characterization of Petroleum and Coal Feedstocks and Precursors	X							
Physical Characterization of Petroleum and Coal Feedstocks	X							
Physical Characterization of Petroleum and Coal Precursors	X		X					
Production of Petroleum Precursors	X				X			
Production of Coal Precursors	X							
Production of Biomass Feedstock ACN (for PAN)				X				
Production of Biomass Precursor PAN			X					
Chemical Characterization of Biomass Feedstocks ACN				X				
Production of CF			X					
Characterization and Physical Testing of CF			X					
Production of Tow-level CF Resins						X		
Characterization and Physical Testing of Tow-level CF Resins						X		
Scale-up Evaluation and Economics for Petroleum and Coal (Pitch-Based)					X		X	
Scale-up Evaluation and Economics for Biomass (PAN-Based)					X			
Molecular Modeling		X						
Correlations between Feedstock and/or Precursors and CF Properties	X	X						
Database Management, Data-Mining, and ML		X						
Industry Requirements and Standards for CF and CF Resins								X

A techno-economic analysis (TEA) will be performed at the end of each BP to ensure that the team is on track to meet the \$5/lb. goal set by DOE. Members from ACP, RAMACO, SRI, WRI, and ORNL will be involved at various levels for producing TEA data based upon material costs, material processing, conversion of intermediates to precursors for CF spinning, and ultimately all of the steps applied during CF production (e.g., spinning, stabilization, carbonization, and graphitization). ACP is primarily focused on working out the TEA for slurry oil and anisotropic, or mesophase, conversion. WRI is focused on coal tar pitch and mesophase formation. RAMACO is assisting in understanding the economics of raw coal from U.S. mines to coal tar pitch, as well as assisting overall with TEA for coal and petroleum pitches. For biomass-based ACN, SRI is providing data based upon their current experience with their pilot-scale facilities. ORNL is responsible for providing input for the polymerization of ACN into PAN, as well as providing data for all of the stages of CF production.

Micro-level molecular structure and chemistry models of feedstocks, precursors, and CFs are being created with DFT-aided MD simulations, which are being validated with test data. These computational methods, as well as database management, are provided by GG-MIT. After down-selecting acceptable precursors, test specimens of CF composite material systems will be fabricated and subjected to physical testing at the extreme temperature conditions necessary for LD vehicles to refine and validate engineering macro-level and cost models. These macro-level models are being developed and will be operated by UW using advanced FEA. Upon growing a large set of models, ML algorithms will identify trends to aid identification of optimal parameter values. Structure-function relations of chemical and mechanical properties are being established and integrated into micro-level and macro-level models. ML will lead to identification, classification, and clustering of optimal precursor formulations and process conditions for producing both precursors and CFs,

thereby achieving the lowest CF production cost. ML correlations are being provided by GG-MIT, while additional chemometric linear regression correlations will be performed by WRI for quicker and simpler predictions. With these methods, the team is developing prediction capabilities for novel mechanisms of solid-state C synthesis from various organic precursors by computational tools via probable thermo-chemical paths and validating feasibility of those paths experimentally. Correlations between pitch composition and feedstock variability, and the resulting properties of manufactured CF materials, will be established and validated. Key to the modeling and data-mining efforts, as well as meeting the DOE requirement, a database is being developed to store all chemical, physical, mechanical, and experimental data. This database is being managed by GG-MIT.

Overall, this project is being conducted in three BPs:

BP 1: CF Precursor Screening and Down-Selection

CF feedstocks and precursors will be studied to down-select precursors capable of achieving the physical property goals at < \$5/lb. Micro-level models will be developed to optimize CF properties and production engineering cost trade-off studies. The milestones for this BP are shown in Table II.2.F.3.

Table II.2.F.3. Milestones for BP 1.

Title	Type	Milestone Description	Verification
Major Subcontracts Executed	Project Management	All major subcontracts have been negotiated and executed.	Executed Subcontracts.
Raw Material Feedstock Verified as Acceptable	Technical	Feedstock meets CF process requirements.	Yield > 15%.
Precursor Verified as Acceptable	Technical	Precursors make acceptable CFs.	Fibers successfully spun meeting requirements for further stabilization and carbonization.
CF Strength and Cost Goals Achieved	Go/No-Go	Checks to verify that precursors studied are acceptable to continue project.	Meets DOE strength goals at < \$5/lb.

BP 2: CF Tow-Level Material System Properties and Analyses

CF composite macro-level models will be created, and CF tow-level composites fabricated and tested at extreme temperature conditions for LD vehicle components to update micro-level and cost estimate models.

BP 3: Validation and Transfer of Models and Data to DOE ICME Program

The most promising CF materials will be further evaluated for producibility and to improve macro-level models while building a comprehensive performance database up to the tow-level. Macro- and micro-level models will be integrated and validated for industry use. Models and data will be transferred to the DOE ICME program and a final cost estimate produced.

Results

Coal Tar Pitch, Petroleum Pitch, Gilsonite and PAN Materials, and Preliminary CF Production

BP 1 of this project was heavily focused on investigating several different proven and potential feedstocks for the production of CF of the relevant mechanical properties at the DOE target of \$5/lb. Several different materials, including gilsonite, isotropic coal tar pitch (iCTP), and anisotropic or mesophase petroleum pitch (mPP) were successfully spun into CFs. Different iCTPs with various levels of quinoline-insolubles (unreacted coal or coke carry over), softening points, and compositions were also evaluated to produce CF. As expected, initial spinning trials with the as-received iCTPs lead to fibers with defects despite filtering using the materials

during melt spinning. These defects were caused by insoluble coal particles, traditionally referred to as quinoline-insolubles, in the iCTP materials. The insolubles were removed by dissolving the coal tar pitch (CTP) in N-methyl-2-pyrrolidone (NMP) and filtering to give NMP-soluble CTP (CTP-NMP), which was separated from the solvent by vacuum distillation. After removing the insolubles, defect free fibers were easily produced from the iCTP-NMP materials. Figure II.2.F.2 shows scanning electron microscopy images of iCTP fibers before and after the removal of NMP-insolubles. During the course of this study, it was found that NMP dissolves about the same amount of pitch as quinoline but has the advantages of being less toxic and noxious, while also having a lower boiling point by about 30°C. Additional efforts are needed for control of the filament freezing rate after exiting the spinning die that will allow for fabricating smaller diameter fibers which will improve the stabilization kinetics, strength performance and cost-effectiveness. Some difficulties were also identified when handling isotropic filaments after spinning that needs further resources to develop appropriate handling and processing methods at ORNL. A new protocol via solid-state spectroscopy needs to be established to characterize the networked structure of aromatic intermediates formed during oxidative stabilization. A significant quantity of fibers needs to be fabricated and tested to establish the distribution and standard deviation for use in ICME models for use by the automotive industry.

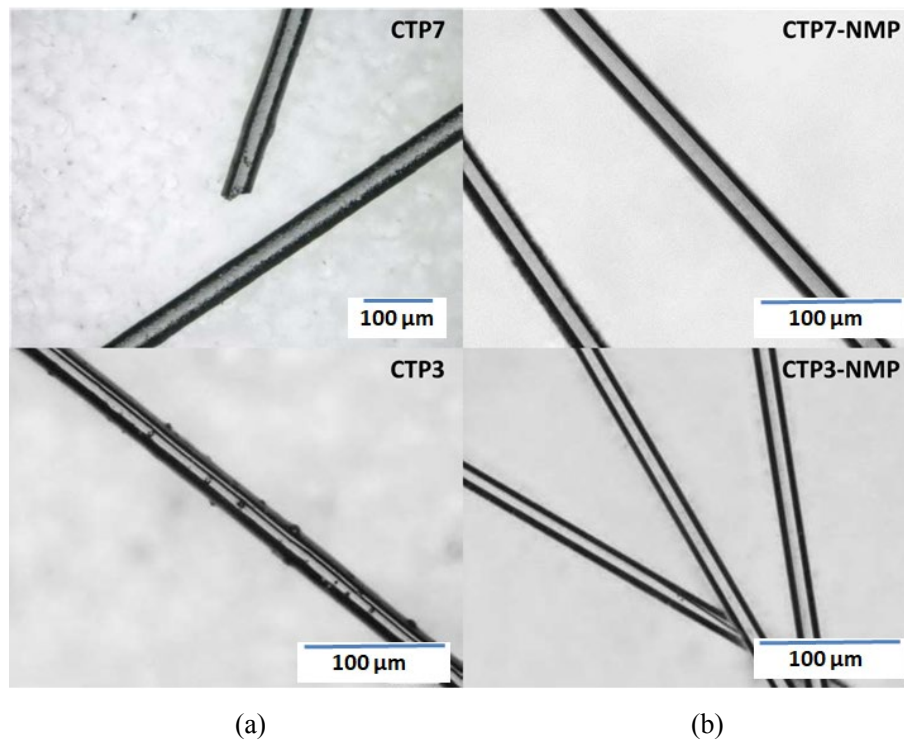
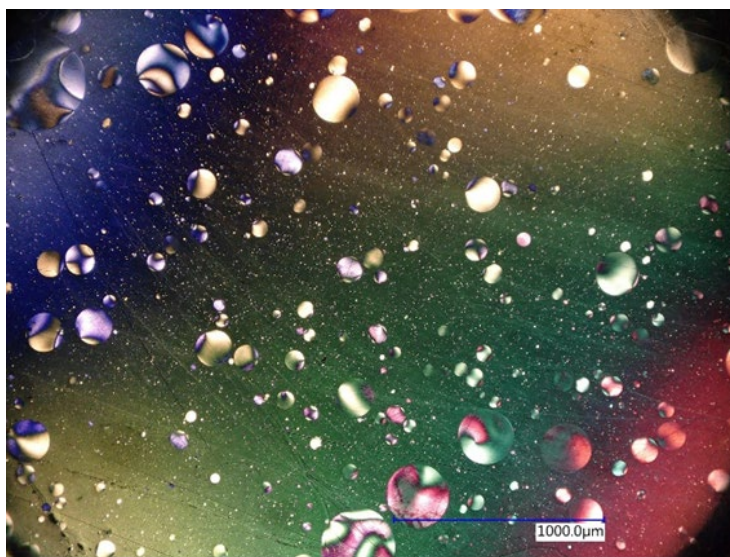


Figure II.2.F.2. Scanning electron microscope images showing (a) fibers spun using CTP-containing insolubles that caused surface defects and (b) fibers from the same CTP source after removing NMP-insolubles showing no surface defects.

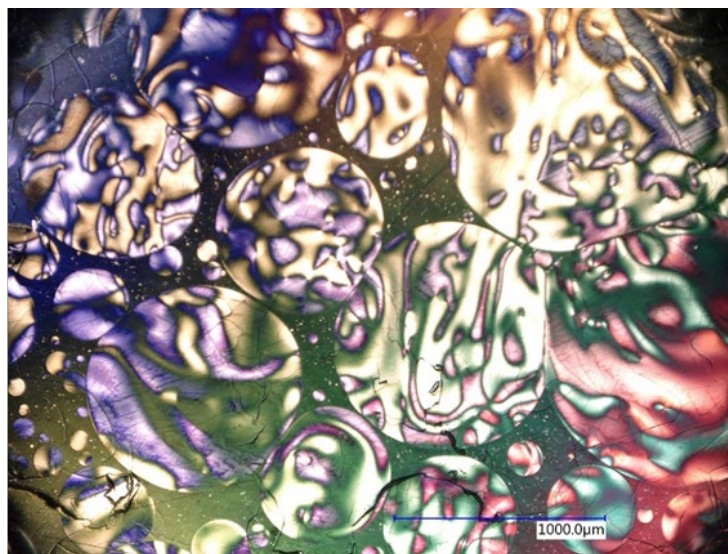
Source: ORNL.

A major finding during this study was that significantly stronger fibers could be produced when iCTP was spun into small diameter fibers (~6.7 μm). After stabilization and carbonization of these small diameter CFs, they had strength (205 Ksi) and modulus (17 Msi) values that were near the mechanical properties specified by DOE. This result is significant because it was achieved using isotropic pitch, which is generally assumed to produce low mechanical properties. To achieve higher strength, as required by DOE, it is generally accepted that isotropic pitch must be reacted to form anisotropic/mesophase liquid crystalline material that is highly ordered. These findings will continue to be researched to explore the range of CF properties achievable.

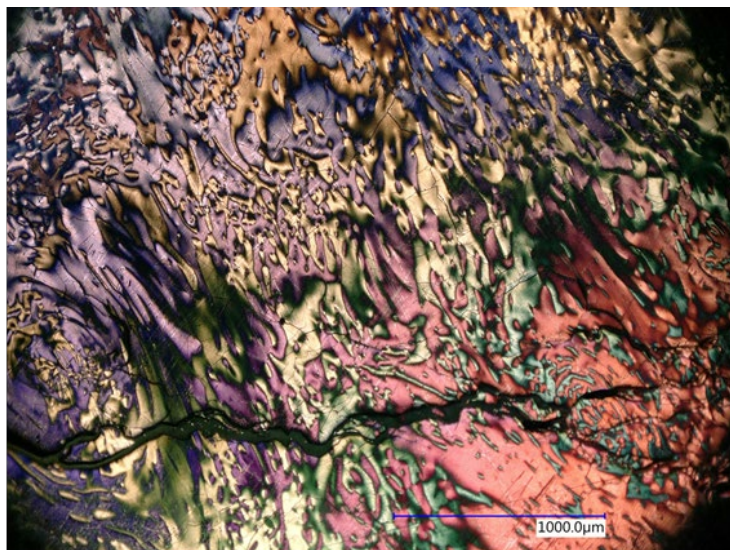
Several experiments have been underway to convert iCTP to anisotropic, or mesophase to CTP. Chemically crosslinking the highly aromatic molecules in the iCTP lead to large aromatic molecules, also known as mesogens, which have a critical number of fused aromatic rings that allows them to self-associate with other mesogens and phase separate from the isotropic material. As these mesogens form, they form small mCTP spheres in the iCTP that are clearly visible when observed using cross-polarized light with optical microscopy. As the number of these spheres increase, they coalesce to form larger spheres and eventually can form large flow domains as a liquid crystalline material. To create fibers with the highest possible degree of strength, it is desirable to create a mCTP that has a very high mesophase content. As mesophase is spun into CF, the large flat aromatic domains align themselves parallel to the direction of spinning. This causes the resulting CF to have several interlocking parallel layers of crystalline material similar to the concept of plywood. The most trivial way to produce mesophase, whether starting from iCTP or the isotropic petroleum pitch (iPP), is to thermally treat the materials at around 380–450°C. Figure II.2.F.3 shows the progression of mesophase formation for CTP6-NMP from the formation of small mesophase spheres to larger domains of mesophase and ultimately high continuous mCTP.



(a)



(b)



(c)

Figure II.2.F.3. Cross-polarized light optical microscopy micrographs showing the progress of mesophase during pyrolysis of iCTP6-MMP at different stages of the thermal reaction. (a) Micrograph of mostly isotropic pitch with large mesophase spheres and several much smaller mesophase spheres, (b) very large mesophase spheres starting to coalesce into a continuous phase and (c) the complete conversion to coalesced mesophase. Source: WRI.

To produce mesophase pitch suitable for melt spinning at ORNL, it is desirable to have a mesophase content of ~ 60 wt% or higher, have softening point of less than about 360°C, and have a high-carbon residue (~ 80+ wt.%). During 2018, 100 g batches of mCTP were produced at WRI to send to ORNL for CF spinning.

For mPP materials, ACP owns and operates a patented continuous isotropic and mesophase pitch production technology and process equipment designed to work with petroleum-based materials. This equipment was specifically designed to convert aromatic slurry oils, produced from fluidized catalytic cracking of petroleum during refining, into a higher aromatic content iPP. This iPP is then converted to high mPP in a heated flow loop. This equipment is suited to process several kilograms of material and may be used during BP 2 to scale-up mesophase production from select materials. In the meantime, a much smaller scale continuous mesophase apparatus, ACP 10, was built, which can process around 1–5 pounds of material per hour. Figure II.2.F.4 shows a photograph of the continuous ACP 10 pitch processing equipment.



Figure II.2.F.4. A photograph of the ACP 10 continuous pitch processing equipment. Source: ACP.

For BP 1, high mesophase mPP was produced from M50 iPP using a batch reactor instead of the large-scale continuous equipment. The iPP was converted into mPP by thermal treatment at around 400–450°C to form a high mesophase content (90+% by optical microscopy) with a softening point of 329°C. A micrograph showing the high mesophase content and highly ordered domains is shown in Figure II.2.F.5. The sample was taken from a softening point experiment, which heats the sample until it drops through an opening in the pan. It can be seen that the stress from the flowing pitch causes the mesophase domains to orient along the direction of the flow. The black circular inclusions are air voids in the sample. Maximum properties from mesophase pitch are generally obtained using smaller diameter fibers after graphitization at 2,000+°C to fuse the highly ordered material. The mPP from ACP has been successfully spun into fibers and stabilized and carbonized at ORNL; however, initial trials produced fibers with a larger diameter (~30 μm) than desired, which did not meet the desired strength and modulus requirements. Optimal fiber diameters should be obtained between 10–15 μm or less to maximize the tensile strength. Additional spinning of the mPP produced fibers with an average diameter of 14.2 μm. After carbonization, the fibers still produced mechanical properties below those specified for this project. These fibers will be graphitized to increase their physical properties.

In addition to large continuous pilot-scale equipment and smaller batch operations, ACP has also been studying the formation kinetics of mesophase for very small samples of iPP using hot-stage microscopy. This method allows mesophase formation to be observed in real-time, and when coupled to video imaging software, several hours of mesophase reactions can be condensed to a few minutes of video footage. The advantage to using this technique is that it can quickly give insight into relative reaction rates of different iPP materials relative to batch-scale operations.



Figure II.2.F.5. Cross-polarized light optical microscopy micrograph showing 95+% mPP produced from M50 iPP by ACP.
Source: WRI.

In addition to coal and petroleum, a naturally occurring bituminous material, which is commercially mined in Utah called gilsonite, was also investigated as a material for CF. It has the characteristics of a high melting solid that is soluble in C disulfide. Whole gilsonite (SEL347), heptane-soluble (ER125), and heptane-insoluble (IR200) fractions of gilsonite were studied. For these three materials, the softening point, aromaticity, C residue, and heteroatom content increase in the following order: ER125, SEL347, and IR200. Fibers were successfully spun for each material, but fibers from ER125 were too soft during the stabilization process causing inter-filament fusing of the fibers to occur. On the other hand, fibers from SEL347 and IR200 were amenable to oxidative stabilization without inter-filamentous fusing. Fibers produced from IR200 contained a scaly surface morphology, and as a result, no additional studies were performed with this material. However, fibers from SEL347 produced smooth homogenous fibers, yet after carbonization they did not produce acceptable mechanical properties. This was due to the fact that gilsonite does not have a high aromatic content and the large molecules in the material contain pyrrolic groups and smaller aromatic moieties substituted with several aliphatic side chains. These side chains become chemically cleaved around 400°C+ and are liberated as gas, which was confirmed by thermogravimetric analysis. As a significant amount of this gas escapes from the fibers, it damages the structure of the fibers causing them to become porous, thus resulting in poor mechanical properties. Figure II.2.F.6 shows micrographs of this phenomena with fibers spun from SEL347 as-spun, after stabilization, and after carbonization, respectively. Table II.2.E.4 gives a summary of CF strength and modulus for iCTP, mPP, and gilsonite materials spun during 2018.

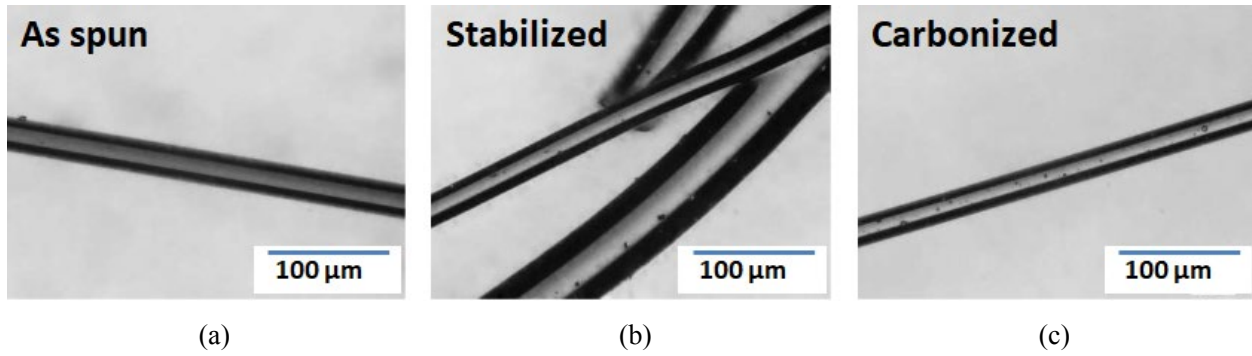


Figure II.2.F.6. Micrographs of CFs from SEL347 (a) as-spun, (b) after stabilization and (c) after carbonization. Source: ORNL.

Table II.2.F.4. Summary of iCTP, mPP, and Gilsonite Tensile Properties after Carbonization at 1,000 °C.

Sample	Peak Strength (MPa, ksi)	Modulus (GPa, Msi)	Average CF Diameter (μm)
SEL347	273, 39.6	17, 2.5	32.4
CTP3	171, 24.8	21, 3.0	16.8
CTP3-NMP	484, 70.2	30, 4.4	14.6
CTP4-NMP	212, 30.75	33, 4.8	10.7
CTP6-NMP	1416, 205.4	122, 17	6.7
ACP mPP	842, 122.1	73, 11	14.2

Attempted conversion of gilsonite materials into mesophase pitch was performed by WRI at 430°C for 4 hours in sealed reactors under slight agitation. The material rapidly formed 100% anisotropic material with a coarse texture as shown in Figure II.2.F.7 and as reported in the literature [1]. Gilsonite is highly reactive and rapidly forms anisotropic material; however, this material is infusible, meaning that it does not melt and is therefore not suitable as such to be melt-spun into CF. Additional thermal processing or blending with other materials may lead to a suitable gilsonite anisotropic pitch.

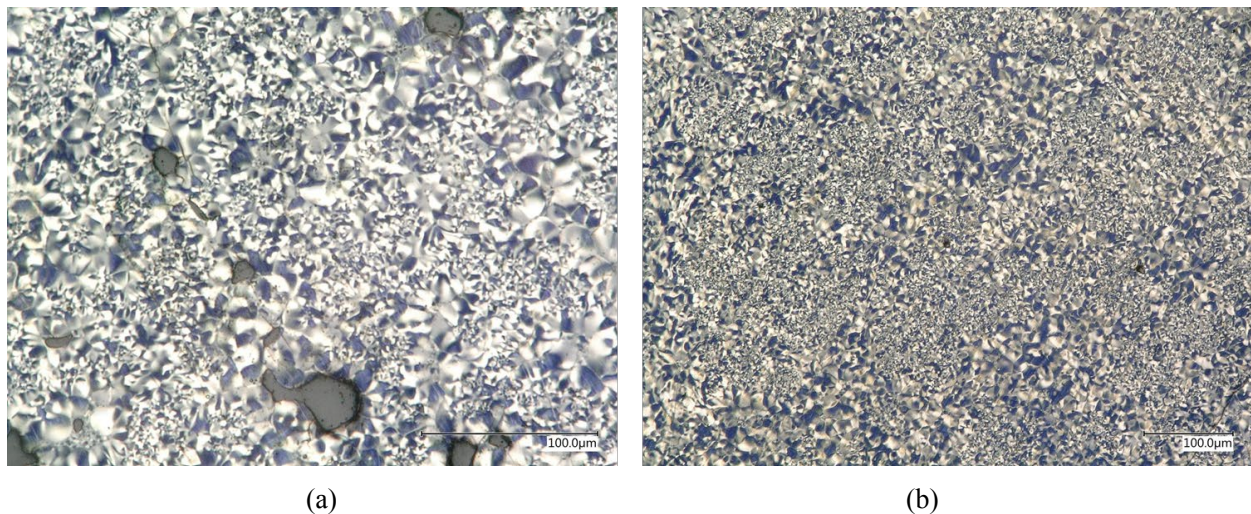


Figure II.2.F.7. Cross-polarized light optical microscopy of attempted mesophase conversion of (a) gilsonite IR200 and (b) gilsonite ER125 in sealed reactors. Source: WRI.

One alternative for producing cheaper PAN-based CF is to use lower cost textile-grade PAN as opposed to higher-cost higher-purity PAN than currently used to make many commercial PAN products. Textile-grade PAN is available at ORNL and a significant amount of work has been performed to spin this textile-grade PAN into quality fibers followed by carbonization with an average diameter of $7.55 \mu\text{m} \pm 0.6$. Figure II.2.F.8 shows a micrograph of textile-grade PAN CF produced at ORNL and a plot of the stress vs strain for this material. As expected, this material produced fibers that meet the strength and modulus requirements for this project. Measured values were 2575 MPa (373.6 Ksi) and 189 GPa (27.5 Msi), respectively. This performance was achieved while also preserving an average peak strain, ϵ , of 1.12%.

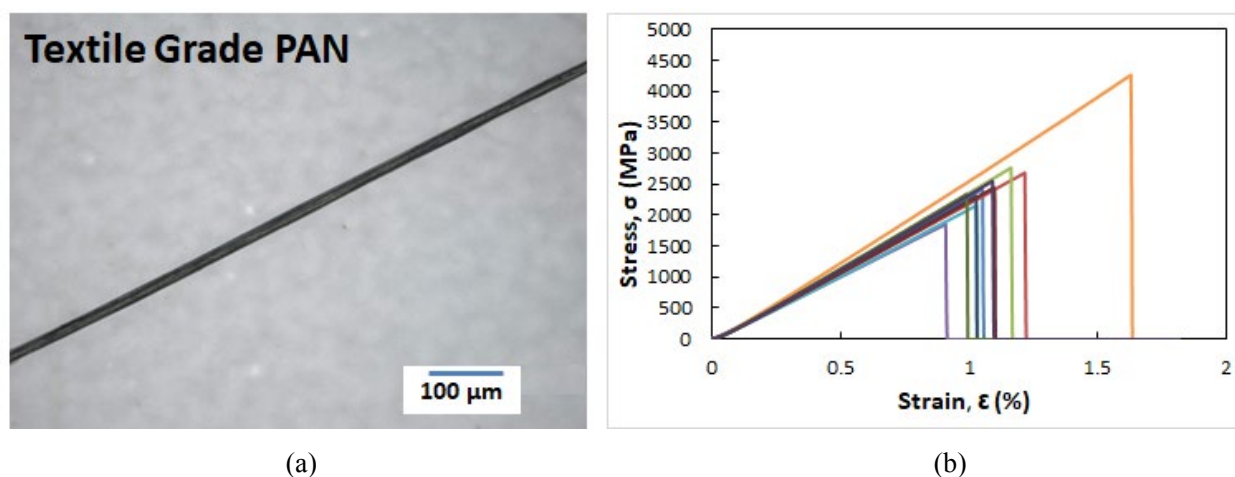


Figure II.2.F.8.(a) Optical micrograph of the final CF with an average diameter of $7.55 \mu\text{m}$ and (b) stress vs strain plot for 10 CF samples derived from textile-grade PAN. Source: ORNL.

Coal Tar Pitch, Petroleum Pitch, Gilsonite and PAN Materials, and Preliminary CF Production

Biomass-based feedstocks and intermediates are also being studied as a way to provide cheaper more consistent supply of ACN compared to petroleum-derived ACN. Currently, ACN is produced from propylene, which is produced in various methods during petrochemical refining. Propylene is a high-demand chemical as it is used to produce many major commodity chemicals for various industries. As a result, it is subject to significant market fluctuation of both petroleum and propylene prices, as well as other market demands that utilize ACN directly. An added potential long-term benefit for using biomass-based ACN is that it could potentially be developed as a resource in a sustainable and renewable fashion.

To produce CF from ACN, it must first be polymerized into PAN of the appropriate molecular weight and polydispersity for spinning into fibers. These fibers are then treated by oxidative stabilization and carbonization. As in the case of textile-grade PAN-based fibers, it is not likely that graphitization will be necessary for biomass-based PAN fibers to achieve the mechanical properties outlined by DOE. PAN-based fibers are just as strong, if not stronger in some cases, than pitch-based fibers and they are widely used in a variety of CF products, especially for applications that require greater flexibility than available from most types of pitch-based CFs. SRI has been developing laboratory- and pilot-scale facilities and equipment for the last several years to produce ACN in large quantities through a series of catalytic processes.

An initial literature survey was conducted by SRI to map out the maximum levels of inorganic and organic impurities present in various kinds of biomass-based sugars. The Bioenergy Feedstock Library, prepared and compiled by DOE and INL [2], was used to obtain information on feedstocks and impurity levels within various biomass sugars. This reference was used to shortlist nine different biomass feedstocks; three candidates—Sugarcane Bagasse, Hybrid Poplar, and Lodge Pole Pine—were identified as the most promising based on their percentages of convertible sugars, lignin, and inorganic impurities. The maximum amount of the most common inorganic and organic impurities was doped into a sugar, one at a time, and tested in the ACN

process to determine if there was any adverse effect on the process through primarily deactivation of catalysts or an effect on resulting ACN purity.

Inorganic impurities (Fe, K, Si, Mg, Ca, phosphorous, chloride, Ti, and Na) were tested. None of the materials were found to have an impact on the catalysts. Some of the inorganics did not show up in the end-product ACN, while at least a portion of most of the inorganics did show up. Mg, Ca, and Na showed up at higher levels in the product than in the feed. This was due to leaching from the catalyst. The organic impurities are not suspected of causing significant contamination problems of the ACN product since they can easily be removed by distillation. For the organic impurities, formic acid, acetic acid, levulinic acid, hydroxymethylfurfural, furfural, glycolic acid, vanillin, syringaldehyde, and benzoic acid were studied. For these compounds, none had any impact on catalyst performance, and several underwent some form of hydrolysis while others were not affected. ASPEN Plus modeling was performed to determine the distillation cutoffs where the various impurities could be separated from the ACN product. The fact that the catalytic activity was not affected by the highest levels of impurities highlights the robustness of the process in the presence of these impurities. Validation of this approach was confirmed using a commercial cellulose-based sugar that contained all of the tested impurities. From this test, there was no impact on the process or on the ACN quality.

A synthetic batch of the ACN, based upon the exact composition produced by SRI, was produced at ORNL and successfully polymerized to develop the polymerization method that would be used for the actual material produced by SRI. The synthetic blend was successfully polymerized to 120,000 Daltons with a reasonable polydispersity. Biomass-based ACN (99.2% pure on dry basis) was sent to ORNL for polymerization and subsequent CF spinning. The ACN from SRI has been polymerized by ORNL and will continue to be evaluated.

Chemical and Physical Characterization of Materials

Data needed for the atomistic and process modeling, as well as ML, is being primarily produced by SRI and WRI. For ACN produced by SRI, actual empirical data obtained for the ranges of nine inorganic (see Table II.2.F.5) and nine organic impurities (see Table II.2.F.6) of the various biomass sugars were provided to GG-MIT to check models and MD simulation techniques, and identify areas to improve prediction accuracy. The concentration of the impurities was determined after the production of ACN and compared to the spiked level of impurities. For inorganic impurities, the levels of these materials were quantified using inductively coupled plasma mass spectroscopy, while for organic impurities, they were quantified by high-pressure liquid chromatography, liquid chromatography, and gas chromatography-mass spectroscopy. A cellulose-based sugar feed was purchased from a commercial vendor that contained all of the tested impurities to verify that collectively they had no effect on the catalytic activity and product quality of the resulting ACN. When using this commercial sugar, there was no observable negative impact on catalyst performance for the time period tested. This feed and resulting intermediates allowed production of ACN with > 99.2% purity. It should be noted that the level of impurities found in the commercial sugar varied within the ranges of impurities determined by the literature survey.

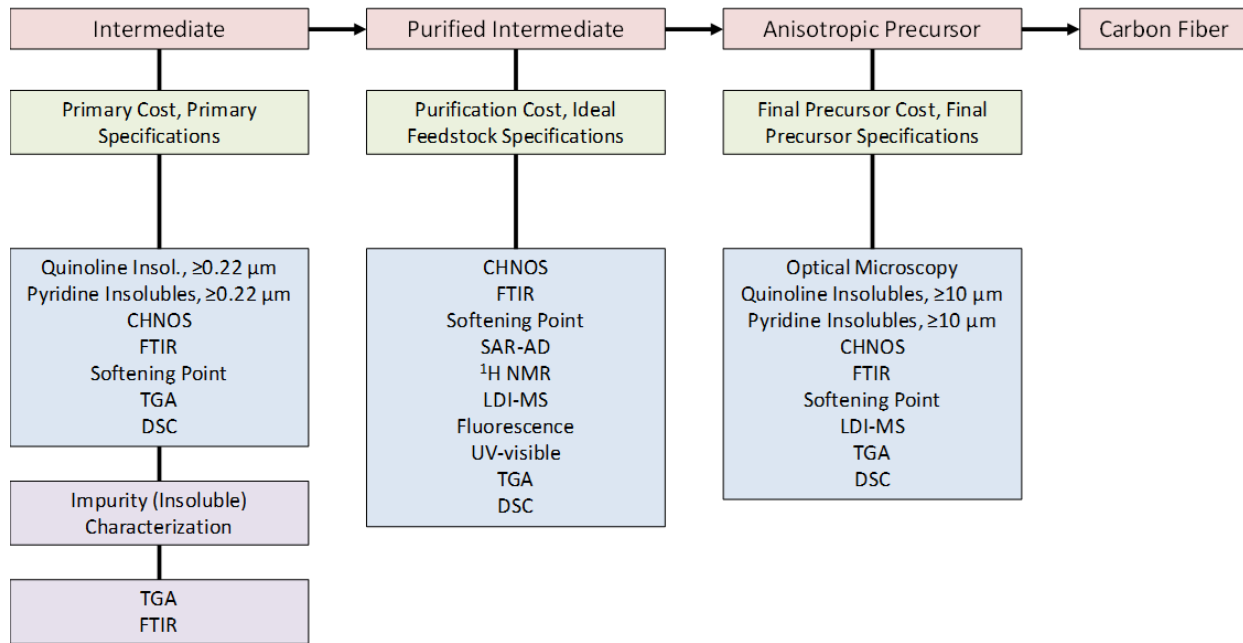
Table II.2.F.5. Summary of Inorganic Impurity Testing.

Impurity	Percentage of Feed Impurity in the Product	Remarks
Fe	100%	Catalyst activity not affected.
K	88%	Catalyst activity not affected.
Si	9%	Catalyst activity not affected.
Mg	379%	Catalyst activity not affected (Mg leaching from catalyst).
Ca	960%	Catalyst activity not affected (Ca leaching from catalyst).
P	0%	Catalyst activity not affected.
Cl	7%	Catalyst activity not affected.
Ti	0%	Catalyst activity not affected.
Na	1452%	Catalyst activity not affected (Na leaching from catalyst).

Table II.2.F.6. Summary of Organic Impurity Testing.

Impurity	Highest Value of Impurities in Pure Sugar (ppm)	Percentage of Feed Impurity in the Product	Remarks
Formic Acid	11080	18%	Catalyst activity not affected.
Acetic Acid	51340	100%	Catalyst activity not affected.
Levulinic Acid	7200	1%	Catalyst activity not affected.
HMF	5740	100%	Catalyst activity not affected.
Furfural	3000	100%	Catalyst activity not affected.
Glycolic Acid	6200	21%	Catalyst activity not affected.
Vanillin	60	56%	Catalyst activity not affected.
Syringaldehyde	30	100%	Catalyst activity not affected.
Benzoic Acid	60	70%	Catalyst activity not affected.

For CTP, polypropylene and gilsonite samples, WRI characterized these materials by various chemical and physical properties according to the methods commonly used to analyze petroleum- and coal-based materials as shown in Figure II.2.F.9. One of the unique characterization aspects is the use of WRI's saturates, aromatics, resins Asphaltene Determinator™ (SAR-AD™) separation (patent number US 20130067991), which is a combined chromatographic and solubility separation. The SAR-AD™ uses four different columns with four different solvents and is automated using high-pressure liquid chromatography instrumentation to separate material into eight different fractions. These fractions represent classes of compounds based on an increase in aromaticity, heteroatom content, and solubility/association tendencies. Figure II.2.F.10 shows an example chromatogram with an explanation of the various fractions. Quantification of the fractions provided by the SAR-AD™ provide a fingerprint of petroleum materials, which has been shown to correlate to various physical properties [3–5]. Figure II.2.F.11 shows an example fingerprint for some of the materials used in this study. CTP samples are in blue, gilsonite materials are in red, and polypropylene materials are in green. Most of them show clear and distinct composition patterns that will be exploited in the prediction models. Note that the data for the SAR-AD™ fractions are normalized to 100% for what was initially dissolved in chlorobenzene; they have not been scaled relative to the amount of material which dissolved in chlorobenzene.



Notation: CHNOS refers to combustion elemental composition; FTIR is Fourier transform infrared spectroscopy; TGA is thermogravimetric analysis; DSC is differential scanning calorimetry; SAR-AD™ is a proprietary separation patented by WRI for the separation of saturates, aromatics, and resins coupled to the Asphaltene Determinator™ separation; 1H NMR is proton nuclear magnetic resonance spectroscopy; LDI-MS is laser desorption ionization time-of-flight mass spectroscopy.

Figure II.2.F.9. Chemical and physical characterization schema use by WRI to characterize CTP, PP, and gilsonite materials. Source: WRI.

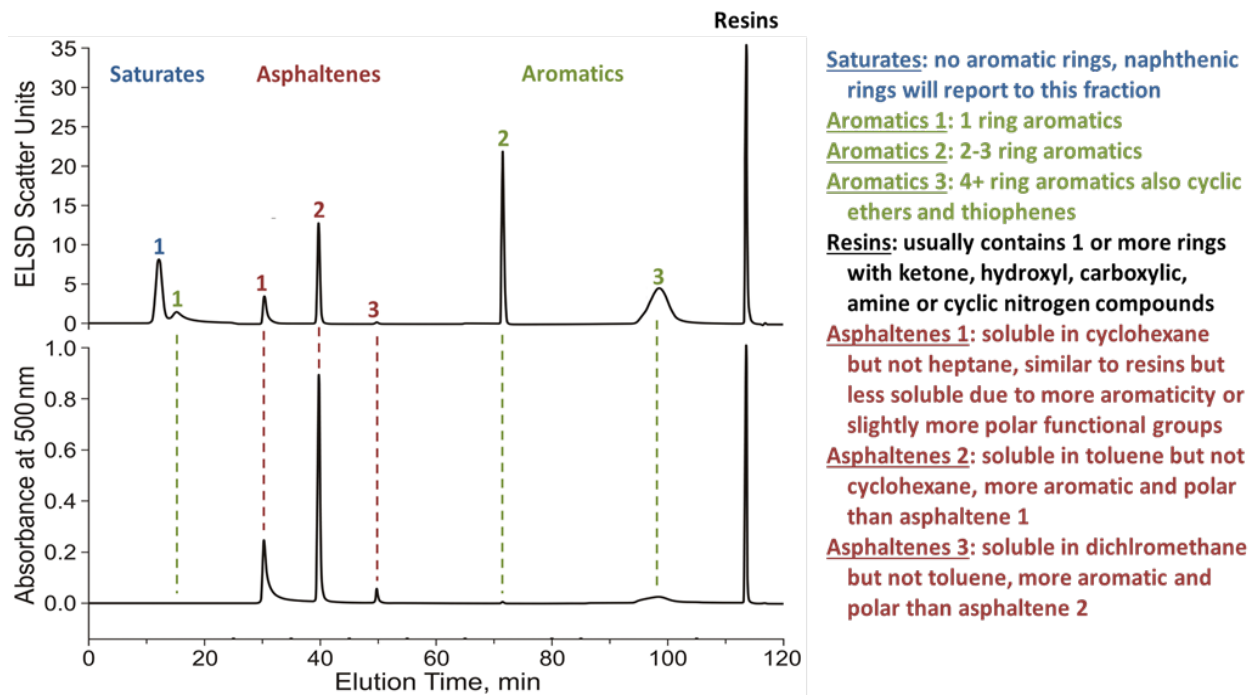


Figure II.2.F.10. Example SAR-AD™ chromatogram using an evaporative light scattering detector (approximate wt.%) and a variable optical absorbance wavelength detector set at 500 nm (concentration of brown colored material). Details to the right of the chromatogram explains some of the compositional details for what reports to the various fractions. Source: WRI.

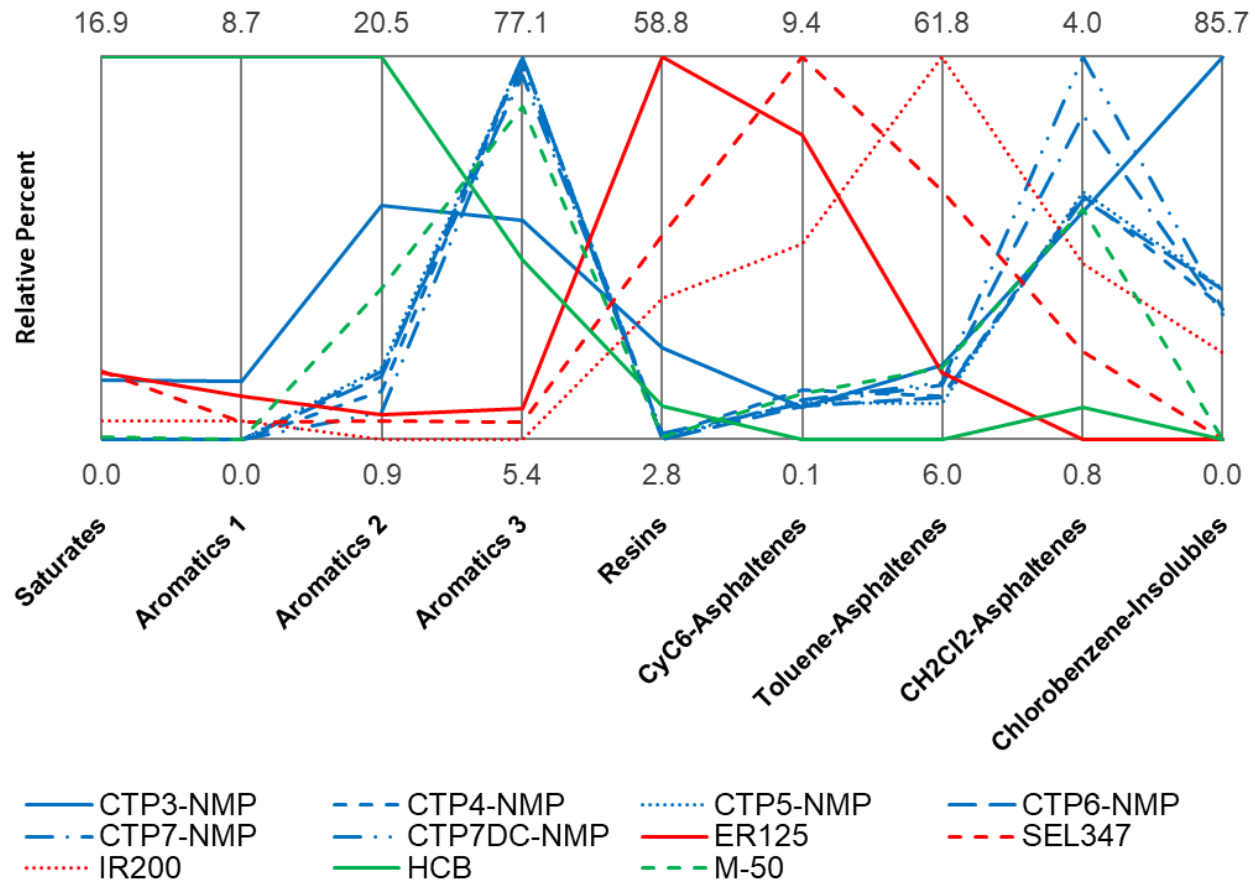


Figure II.2.F.11. Parallel plots of SAR-AD™ data showing the fingerprints of some of the materials evaluated under this work. Source: WRI.

Database, Modeling, and ML

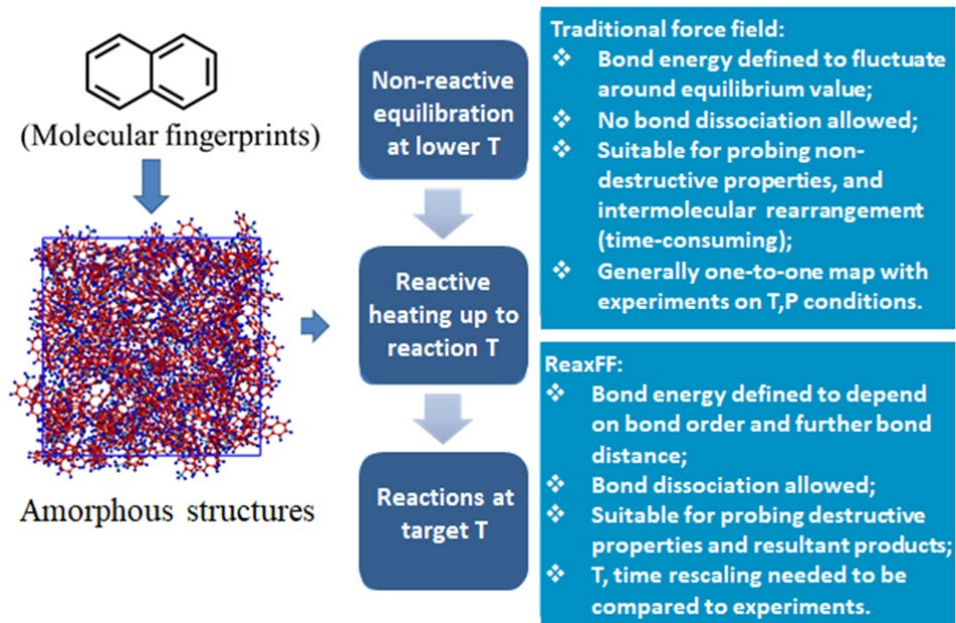
An overarching goal of this project is to relate the chemistry of the various feedstocks, intermediates, and precursors to CF mechanical properties so that predictive models can be developed to guide the future development of CF materials. A robust database of materials, chemical properties, physical properties, mechanical properties, and experimental data is being populated so that it can be mined using ML algorithms by GG-MIT. In addition to ML, GG-MIT is also responsible for maintaining the database of characterization and experimental data, as well as performing various modeling efforts. Modeling is being performed at the atomistic, microscopic, and macroscopic levels. These models will be used in the future to aid in designing new materials in understanding possible blending procedures of intermediates and precursors to tune physical properties, as well as providing a way to maximize economic benefits based upon the cost or processing requirements of various feedstocks, intermediates, and precursors.

Some of the data needed to build the macroscopic models are being developed by UW who is building CF tow-level resin composites for mechanical testing. UW has been developing methods and procedures to successfully embed CF tows in epoxy resins using various techniques for employing them when larger-scale CF tows become available during BP2 from ORNL. When the tows become available, they will be able to rapidly apply these methods and procedures with a high-degree of confidence. Mechanical testing of the preliminary resin composites is also taking place. A key aspect of the work that will be performed on the CF tow resin composites is advanced FEA that will also be used to complete the macroscopic modeling. The data and models produced will also be fed back to GG-MIT and additional ML will be applied to determine correlations from the chemistry up to CF tow resin composite level, as will be discussed later.

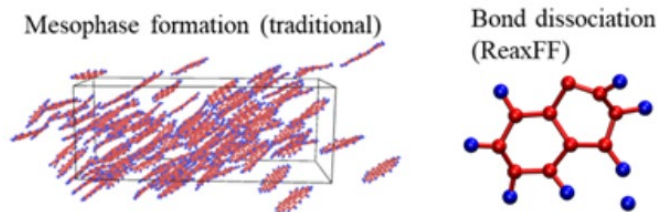
Modeling

Across CF production stages, one major and universal challenge for applying computational techniques is to accurately account for atomistic level reaction kinetics, while maintaining a comparable system size at the continuum-level for predicting bulk properties. Additionally, there remains the significant challenge in the applicability of this approach to highly heterogeneous chemical mixtures represented by CTP and petroleum pitch. During BP 1, a bottom-up approach was taken to generate molecular frameworks from any given set of molecular fingerprints that are subjected to the full manufacturing process leading to the resulting CF (see Figure II.2.F.12.(a). To do this, MD, DFT, and coarse-grained (CG) models were applied. Based on a literature survey [6–12], both MD and traditional non-reactive and reactive force field techniques as shown in Figure II.2.F.12.(b) (i.e., ReaxFF, parameters fitted by DFT [13–14]) were used to generate sample-specific atomistic models of molecular frameworks accounting for reaction kinetics at temperatures above 1,000 K. To demonstrate the robustness of the potentials and procedures for organic compounds, simplified proxy to CTP isotropic and mesophase systems were used as shown in Table II.2.F.7 (i.e., naphthalene and methylnaphthalene). The resulting molecular framework possesses physical and chemical properties—such as viscosity, density, and activation energy—that are predicted within +/- 30% accuracy of the experimental/literature data [15–19].

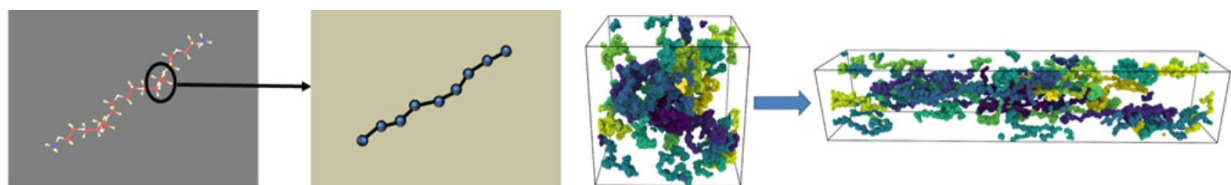
A different and separate approach was necessary to generate realistic PAN models. The ability to efficiently capture the polymeric nature of PAN requires modeling methods that can upscale beyond traditional atomistic modeling approaches. By definition, CG modeling considers a larger unit (a molecule, or a monomer in a polymer) in the models rather than the atomic constituents. In essence, CG modeling is an atomistic simulation where the "atom" is a larger unit. In polymer science, CG is usually employed by considering a single monomer as the grain or "atom", which needs to include all chemical and physical information that is representative of the monomer itself, as shown in Figure II.2.F.12.(c). In this regard, CG models are well-suited to complement MD modeling. This reduces system complexity and ensures an accurate conformational sampling on the continuum-level. To this end, existing CG models are being improved [12, 20] to simulate the polymerization and crosslinking of ACN to PAN while taking impurities into account. What is unique for this project is the inclusion of chemical information within the grain that allows for spatial and orientational interaction of a monomer with others under specific processing environments. In essence, in the presence of oxygen for example, we want to capture the formation of crosslinks across the polymers as observed in real PAN-based fibers. This is an extremely novel approach and it requires the use of DFT calculations to establish rotational dependence of chemical interactions of the single grain with other chemical species (oxygen, other grains, etc.). Compared with current uses of CG for studying unreactive processes, this will allow a more accurate investigation of the stabilization (and subsequent carbonization, etc.) of PAN into CF. This approach will provide an understanding of the combined effects of impurity and polymerization conditions on the quality of PAN and CF produced from PAN.



(a)



(b)



(c)

Figure II.2.F.12. (a) MD approaches adopted for simultaneously capturing reactions at the atomistic level and bulk properties at the continuum-level, (b) MD and traditional non-reactive and reactive force field techniques and (c) course-grained model development for PAN precursors, where each monomer is lumped into one bead. Source: GG-MIT.

Table II.2.F.7. Physical Properties for Naphthalene and Methyl-naphthalene Calibrations and Literature Values Used for Validation.

Chemicals	Viscosity (cp)	Density (g/cm ³)	Activation Energy (kJ/mol)
Naphthalene	0.987 @ 373K, 1 bar	0.958 @ 373K, 1 bar	357
Literature [15, 16]	0.761	0.963	199 - 446
Methyl-naphthalene	1.202 @ 353K, 1 bar	0.970 @ 353K, 1 bar	230
Literature [17, 18, 19]	1.10	0.972	121 - 198

The availability of atomistic models specific to the initial molecular precursors (i.e., “sample-specific”), allows for the application of GG-MIT utilized tools and methods to simulate the manufacturing of CF from corresponding intermediates or mesophase precursors. A schematic of the computational workflow proposed for this work is shown in Figure II.2.F.13. In brief, the molecular framework for isotropic conversion to mesophase pitch is then subjected to simulated oxidative stabilization, carbonization, and graphitization manufacturing steps. For these CF production steps, temperature and reaction times are calibrated through available experimental data by means of the molecular calculated activation energies. Intermediate chemical reactions and structural changes both at the molecular and meso-scale level—such as intermolecular interactions and alignment—are studied throughout each step, including the final resulting CF model. This can be achieved by using specifically designed analytical tools (i.e., product detection and categorization) and mapping between computations and experiments via the implementation of reaction theory [8–9, 21–25]. Mechanical properties such as Young’s modulus and complete stress-strain relationships are extracted from the final CF data and directly compared to the experimental data.

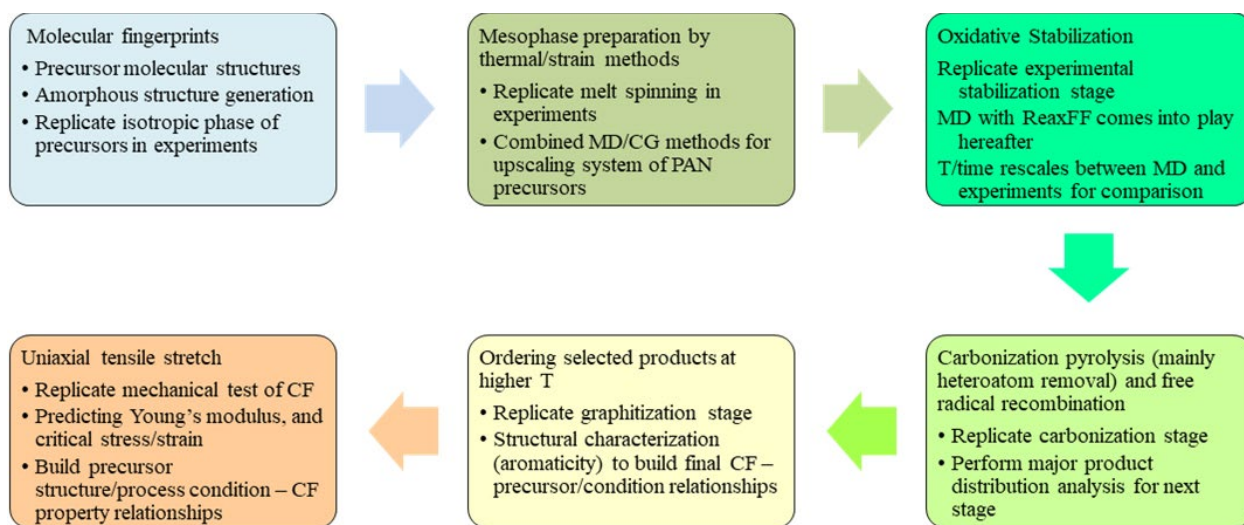


Figure II.2.F.13. Computational workflow to simulate the full CF synthesis process. Source: GG-MIT.

To test the various stages of the computational workflow shown in Figure II.2.F.13, different limited sets of model molecules were selected to verify their influence at different stages of CF production. To differentiate differences between isotropic and anisotropic CTP and petroleum pitch, aromatic molecules with distinctly different geometries are necessary. Initially, a small set of molecules with varying sizes and shapes as shown in Figure II.2.F.14.(a) were modeled at different mixing ratios, temperature, and pressure to evaluate the

importance of molecule geometry on the alignment of the extended molecular framework. This is important because isotropic pitch, by definition, has little to no molecular alignment, whereas mesophase pitch molecules exhibit significant alignment giving rise to liquid crystalline anisotropy. To evaluate reactivities due to pyrolysis during mesophase conversion, oxidative stabilization, carbonization, and graphitization, a proxy set of aromatic molecules for tar was constructed as shown in the middle panel of Figure II.2.F.14.(b).

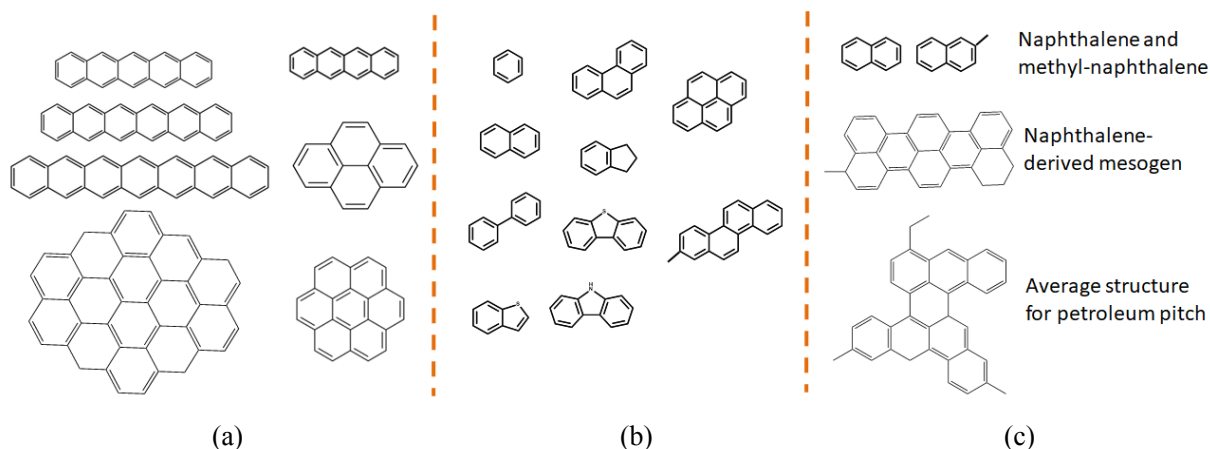


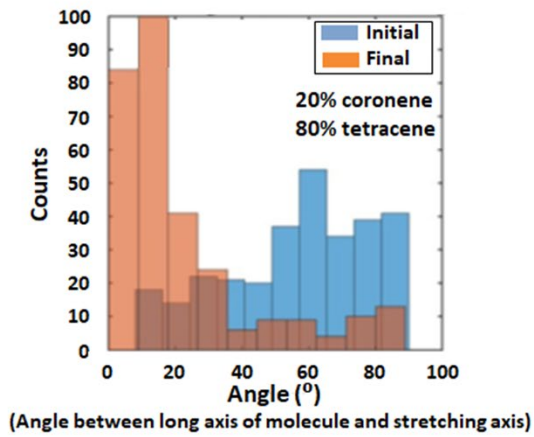
Figure II.2.F.14. Representative molecular models studied up to date for (a) benchmarking models for mesophase preparation, (b) testing systems for oxidation and pyrolysis, and (c) CF precursors selected from literature [26–29].

Through ongoing collaborations between WRI and GG-MIT, molecular systems were selected for three initial systems representing coal tar pitch—naphthalene-based for isotropic and mesogen [26–28] and isotropic petroleum pitch [29]—as shown in Figure II.2.F.14.(c). As described below, the mechanical properties of the CF resulting from the deployment of this modeling framework are found to be well within $\pm 30\%$ accuracy of the available experimental data from the literature.

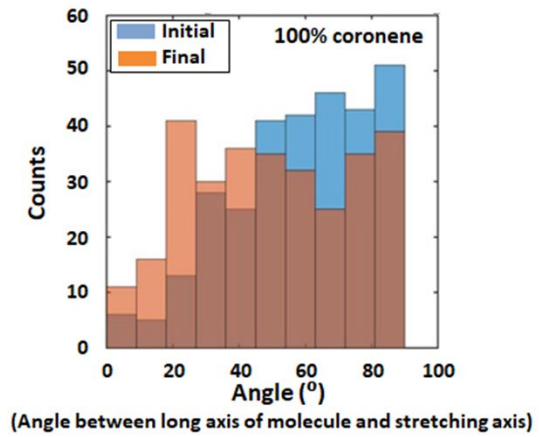
By using the molecule set present by Figure II.2.F.14.(a), initial insights about the intermolecular interaction between aromatic clusters with different shapes and alignments were determined. These results are shown in Figure II.2.F.15.(a) through (e). In essence, for an effective anisotropic alignment of molecules, there appears to be an optimal interplay between linear and round molecular systems (for example, 20% coronene and 80% tetracene) that guides the overall molecular alignment. Future studies planned for BP 2 of the program will consolidate these initial results for coal tar- and petroleum-based systems.

By using the molecule set presented in Figure II.2.F.14.(b), the chemical stability of these molecular frameworks was analyzed using well-defined experimental conditions (i.e., combustion, pyrolysis, and interaction with radicals). Select results from these simulations are shown in Figure II.2.F.15.(c) and (d). The simulations showed reactions that were validated experimentally and found to be accurately captured in the simulation. For example, for dibenzothiophene-based molecules, most reactions were initiated by ring opening, and pyrolysis was preceded with H abstraction [8–9, 21, 30–31]. Since these sets of preliminary tests were validated to some degree, these tools were then applied to simulate the synthesis of CF under different oxidative stabilization and carbonization conditions at various temperatures and pressures (T, P) as shown pictorially in Figure II.2.F.15.(e). These simulations were performed using a coal-based isotropic and mesophase molecular fingerprint based on naphthalene and petroleum mesophase pitch as shown in Figure II.2.F.14.(c). As can be seen from Table II.2.F.8, the predicted values for the CF Young's moduli are within $\pm 30\%$ accuracy of experimental values from the literature. Furthermore, Young's modulus of CF produced from isotropic pitch were typically lower than that from mesophase pitch by a factor of two to three,

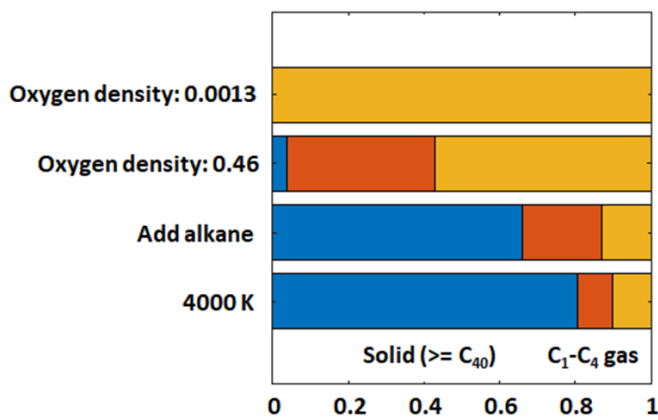
as expected [28, 32–34]. Among mesophase-derived CFs, the naphthalene mesogen produced CF with a larger modulus than isotropic petroleum pitch under the same T, P conditions, which is also in line with expectations.



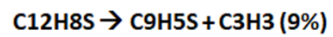
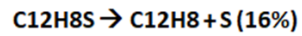
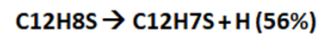
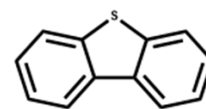
(a)



(b)

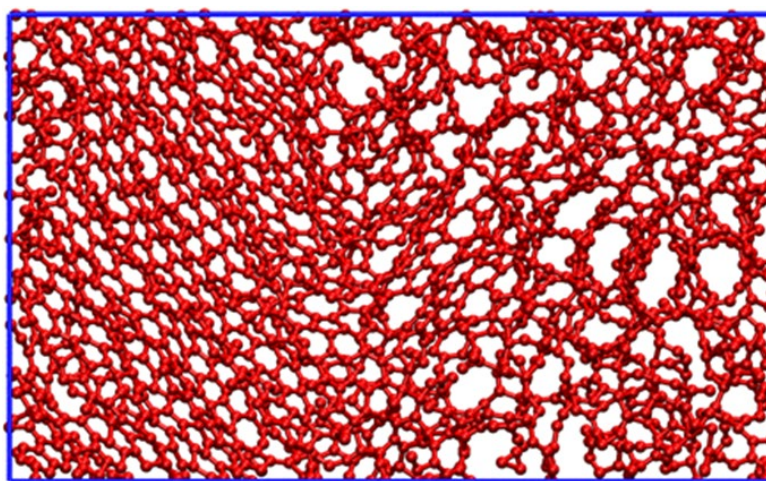


(c)



71% reactions initiated by ring opening

(d)



(e)

Figure II.2.F.15. Key results for anisotropic alignment of molecules for (a) mixture of coronene and tetracene and (b) 100% coronene, (c) product distribution, and (d) reaction pathways observed and (e) CF snapshot. The corresponding molecular models are shown for each panel. Source: GG-MIT.

Table II.2.F.8. Young's Modulus for Three Pitches.

Systems	Young's Modulus (GPa)	Young's Modulus (GPa) *
Mesophase Pitch (aromatic derived)	200 – 400	140 - 820
Mesophase (petroleum pitch derived)	140 – 200	
Isotropic Pitch	~ 20	30 - 40

* [25, 29 – 31]

ML

To determine correlations that will aid in the prediction of CF properties from various feedstocks, intermediates, and precursors, a highly flexible suite of data processing frameworks—using neural networks based on a Deep Multilayer Perceptron [35–36] capable of multi-label classification [37]—were utilized for ML. These methods were customized and tested using data from SRI to predict the impact of nine inorganic and nine organic impurities on the production of ACN from biomass. Using actual data on the variability of chemical components and the material balances throughout the multi-step ACN synthesis, training sets were developed to predict the concentration of impurities, such as water and acetonitrile, in the final ACN product. The efficient implementation of the neural network through Keras [38] and TensorFlow [39], allows the rapid generation of trained predictive models (~training is carried out in ~ 30 minutes) with accuracies > 98%. Such models can be readily applied for ultra-rapid (< 50 ms) inference and prediction. With the availability of data for the downstream can-based CF synthesis, the models should be able to predict the effects of various biomass-based impurities on the final CF performance.

Currently, a different approach is being applied to the characterization data of CTP and petroleum pitch. For these materials, chemical data are being used to correlate with measured physical parameters, such as the softening point and glass transition. Ultimately, these models will be extended to predict post-processing physical and chemical properties of mesophase pitches and the properties of the resulting CF.

Data Management

As part of the data management plan, the GG-MIT team has initiated the development of a web-based data repository for all consortium members with the goals of preserving data accumulated throughout the project to allow easy access of the consortium members and to provide a platform for data-mining and future development of ML models derived from such data. As a result of ongoing interactive collaboration, two main objectives were accomplished during the first year: (1) Two online workshops were organized by the GG-MIT team in the summer of 2018 that were used to design the data-structure or schema of chemical, physical, and processing parameters, and characterization data, to be tracked and preserved consistently and hierarchically for easy access; and (2) Development of a web-based platform based on this structure, which will be available in beta testing for consortium members to use by the end of October 2018 [40]. During BP 2, the data management platform is anticipated to be the “go-to” place for data-sharing, as well as a tool to establish progress and facilitate joint optimization workflow strategies across the consortium.

Tow-level Resin Composites and Mechanical Testing

The first objective of obtaining a complete elastic characterization of the CF requires a combination of simulation and experimental data. Tow-level composites are fabricated and tested in longitudinal tension, transverse tension, and longitudinal shear, with appropriate composite tow-level elastic moduli computed. In conjunction with this experimental effort, a hexagonal RVE will be modeled using FEA. By coupling knowledge of the elastic moduli of the matrix with the composite moduli properties obtained experimentally, the elastic properties of the CF will be computed using a gradient-based optimization algorithm.

The second objective to assess the performance of particular fiber types in tow-level composites from both static and durability perspectives requires evaluation of mechanical performance of composite tow structures fabricated from CFs provided by ORNL in BP 2. The performance metrics sought are static strengths and fatigue performance. Because multiaxial testing is extremely difficult and historically unreliable, simulations will be used to predict the full range of strength under arbitrary loadings after benchmarking with experimental solutions for uniaxial loadings. Accurately predicting strength in composites is significantly more challenging than predicting elastic modulus. This is because modulus is an average response of the system, while strength pertains to local failure initiation and propagation. To this end, an ensemble of stochastic finite element models using realistic microstructures with statistically similar microstructures is required. These microstructures are used in conjunction with failure modeling techniques such as the extended finite element method cohesive surfaces, and specialized user-defined materials to predict a *distribution* of strength and fatigue responses to arbitrary loadings. To this end, a model has been developed for a hexagonal fiber packing RVE, which will be used to infer fiber properties. A sample result from this model is shown in Figure II.2.F.16. Additionally, stochastic failure methodology has also been developed, which is shown in Figure II.2.F.17, along with close-up images of cracking between fibers.

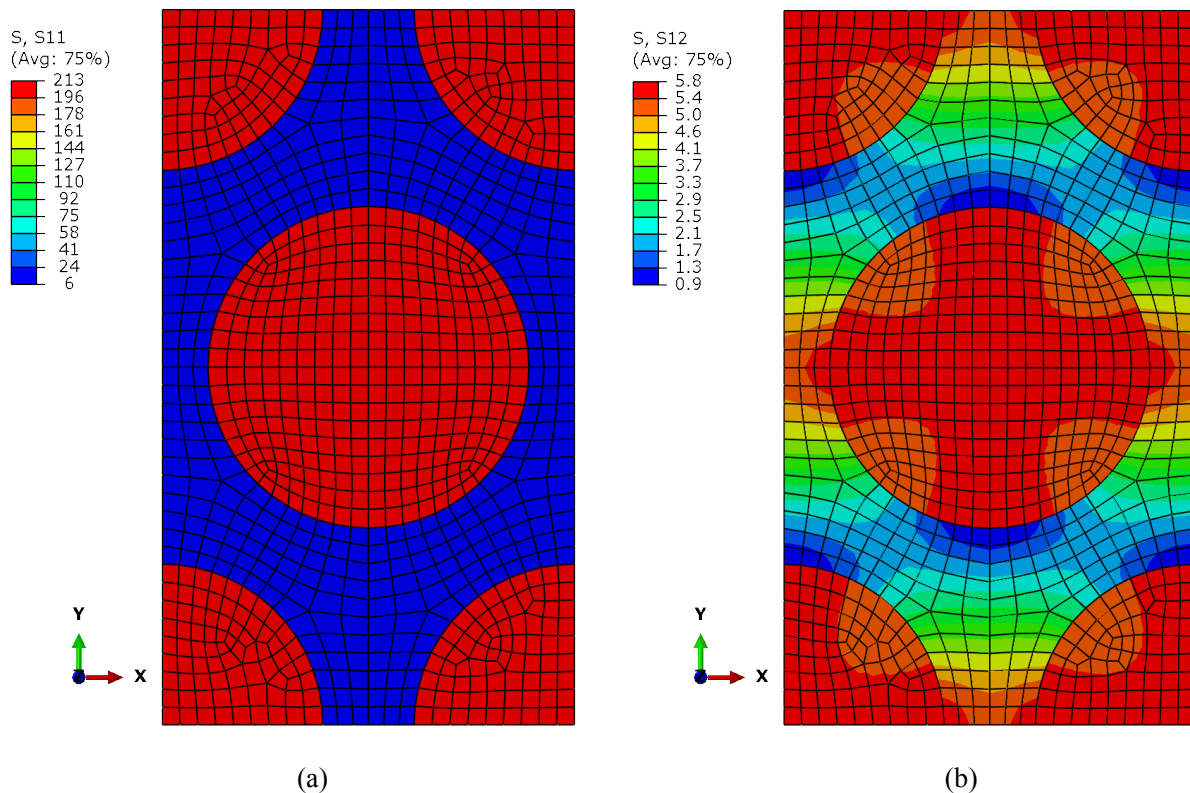


Figure II.2.F.16. Hexagonal fiber packing model images for (a) longitudinal normal stresses under longitudinal loading and (b) longitudinal shear stresses under longitudinal shear loading. Source: UW.

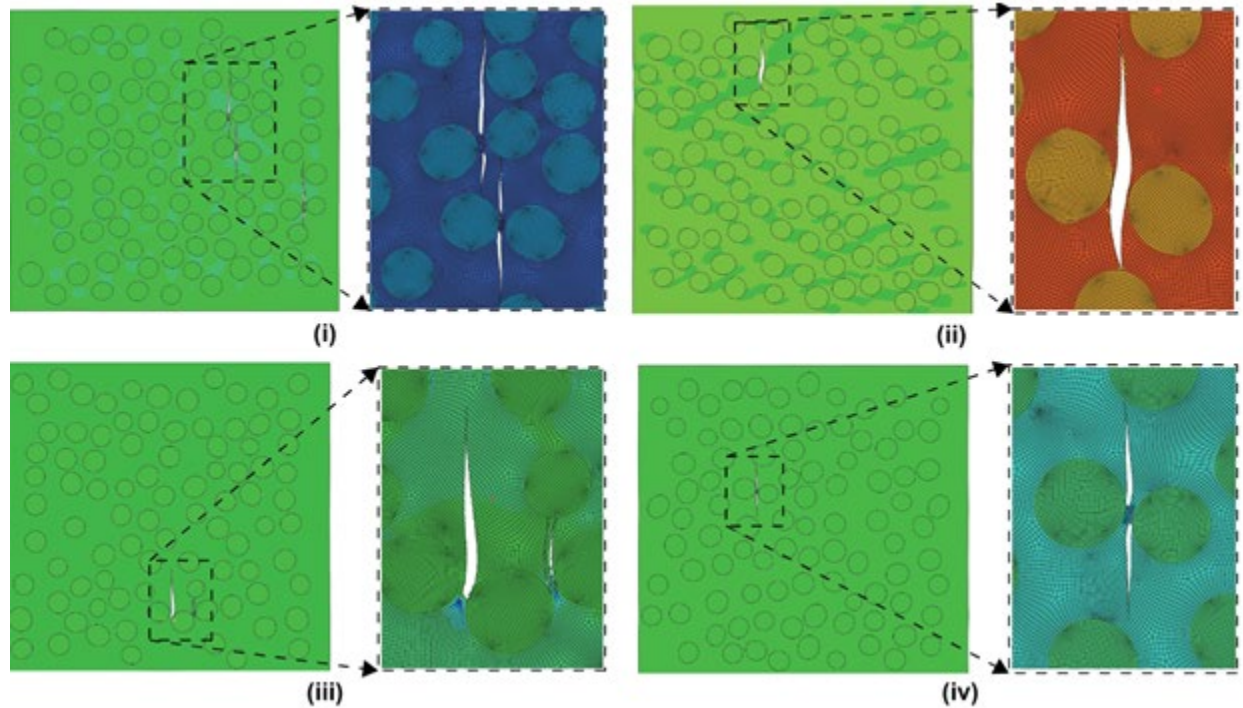


Figure II.2.F.17. Four separate stochastic realizations of a microstructure ensemble with morphology-based meshing strategy along with images of failure of synthetic microstructures initiating between fibers under transverse loading.
Source: UW.

In preparation of receiving CF in BP 2 from ORNL, methods were performed according to ASTM D3039 for tensile testing of unidirectional CF polymer matrix composites sizes. To achieve the most consistent properties for epoxy resin composites, commercial pre-impregnated (prepreg) CF tows were used for initial verification during BP 1. Sheets of prepreg measuring 12-in. x 12-in. were used to manufacture the tow-level CF plate using a press-clave and tabs were added to the sheets. Figure II.2.F.18 shows a picture of a tow-level CF plate with tabs attached. Additional methods were developed to work with receiving dry-fibers from ORNL during BP 2, which will need a modified method compared to working with prepreg.

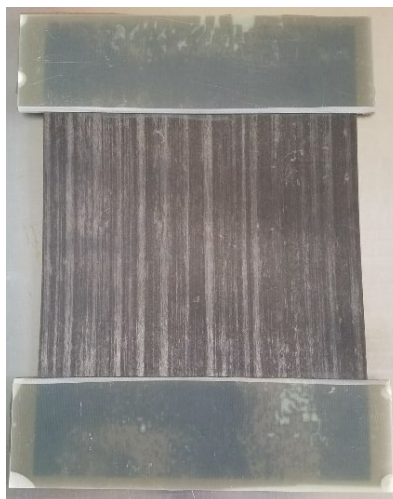


Figure II.2.F.18. Tow-level composite plate with tabs attached. Source: UW.

Techno-economic Analysis

A key DOE objective is to produce CF at \leq \$5/lb in order to make them economically viable for use in light weight vehicles. Therefore, a TEA of the different material CF production routes is necessary. The following describes a preliminary TEA of the various materials. Gilsonite is currently mined at a rate of 50,000 to 75,000 tons/yr. with a proven reserve of 187 years of mining at the current rate and the value for the whole gilsonite SEL347 is estimated to be around \$0.75/lb. The mPP from slurry oils, based on data from ACP, would have a selling price at \$1.50/lb. on a large-scale for around 30,000 to 50,000 tons per year and at lower volumes it could reach as high as \$2.50/lb. at around 5,000 to 10,000 tons per year. Similar figures are estimated for the production of mCTP, but they can be higher depending on filtration requirements and the technology needed to remove quinoline-insolubles from the pitch.

As for biomass-derived ACN, calculations were performed assuming a 5,000 MT/yr. biomass-derived non-food sugar delivered to the ACN production plant. A complete process was simulated on ASPEN Plus using the experimental results obtained by SRI. Capital costs were estimated and averaged (with standard deviation) from three different sources. Figure II.2.F.19.(a) shows a pie chart of the cost distribution for the biomass to ACN process. Raw materials, particularly sugar, were found to be the major cost driver (e.g., 68%). Hence, a sensitivity analysis with respect to type and/or price of raw materials was conducted and shown in Figure II.2.F.19.(b) through (d). Although the cost of ACN shows high sensitivity to sugar price, the economics remains favorable ($<$ \$1/lb) for a wide range of sugar price (\$300 to \$450/MT). On the other hand, the overall cost of ACN production would be less sensitive to the price volatility of other raw materials such as NH_3 and H_2 .

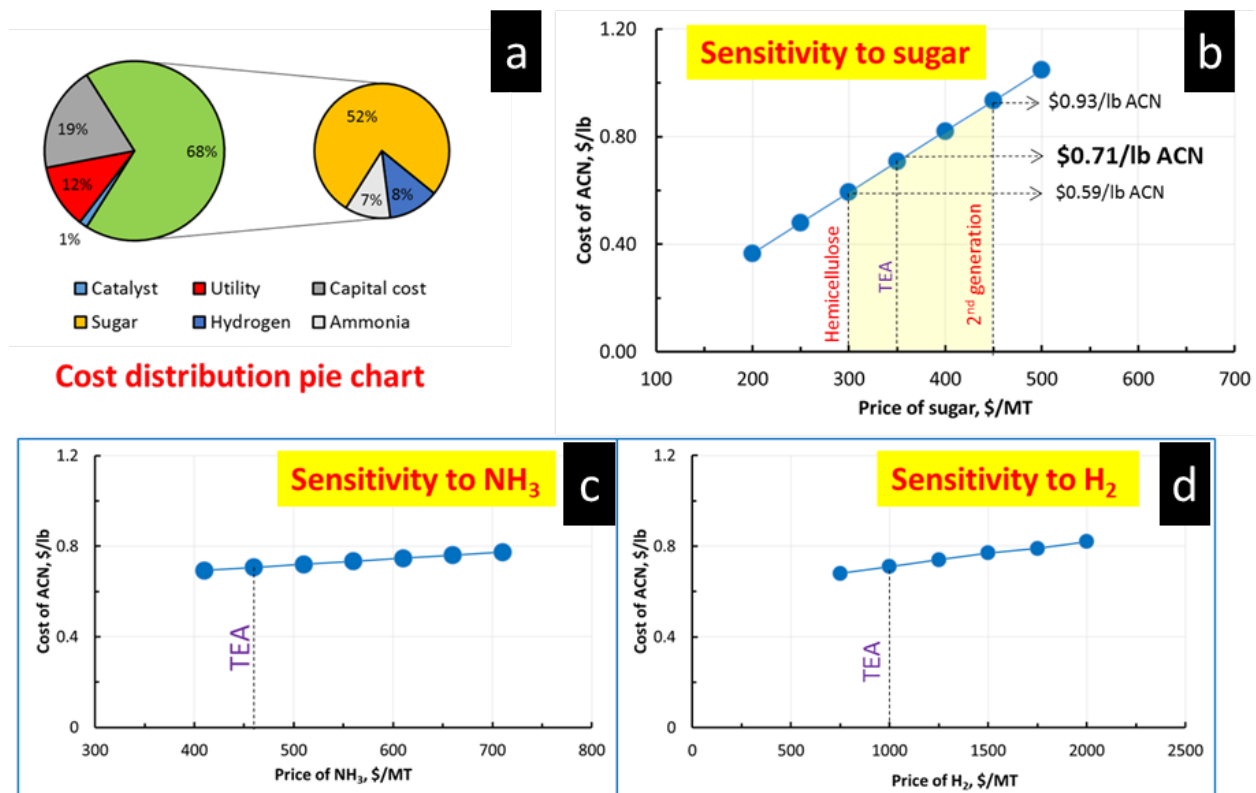


Figure II.2.F.19.(a) Cost distribution pie chart for biomass to ACN production and ACN production cost sensitivity with respect to (b) sugar; (c) NH_3 ; and (d) H_2 price. Source: SR.

Conclusions

A consortium of entities (WRI, SRI, ACP, and RAMACO) with expertise dealing in petroleum-, coal-, and biomass-based ACN has been assembled along with ORNL, UW, and GG-MIT to produce and predict CF properties that will achieve a tensile strength of ≥ 250 Ksi, a modulus of ≥ 25 Msi, and a strain of $\geq 1\%$ at $\leq \$5/\text{lb.}$ for use in lightweight vehicles. Several CFs were spun from low-cost high-volume materials, such as gilsonite, iCTP, mPP and low purity textile-grade PAN. Successfully spun CF from the textile-grade PAN easily exceeded the criteria set forth by DOE under this project. Textile-grade PAN provides another cheaper alternative to high-purity PAN currently used to produce CF. If the textile-grade PAN is taken into consideration, then all of the milestones for BP 1 were achieved. Besides the successful spinning of textile-grade PAN, it was surprising to discover that initial CF spun directly from iCTP came close to reaching the desired strength and modulus goals (iCTP values obtained were 205 Ksi and 17 Msi respectively). It is highly likely that by tuning the properties of the iCTP and by implementing additional spinning techniques, iCTP materials may produce CF of the desired quality. This is significant because it would bypass the added cost to convert these materials into a mesophase pitch. Gilsonite materials were easily spun into fibers; however, upon stabilization and carbonization, void defects were formed in the fibers due to volatile matter being released and resulting in poor mechanical properties. High mesophase content mPP, which is known to give very high-quality CF, was also successfully spun into CF. Ongoing graphitization of these fibers is expected to produce material that exceeds the desired mechanical properties. Fibers from biomass-based PAN have not yet been spun because the polymerization procedure of the biomass-based ACN is being refined to produce polymer with the appropriate properties. For evaluation of larger-scale CF mechanical properties, methods and procedures have been developed to fabricate tow-level CF resin composites.

For computational and data management, atomistic modeling through macro-level modeling tools have been put into place and validated to various degrees. ML has been applied to actual chemical characterization data sets and literature data sets to provide some level of confidence to predict both process outcomes as well as CF properties. A beta version of a database has been setup by GG-MIT as a repository for data, as well-experimental conditions, to serve as a digital notebook in addition to a framework for data-mining by ML.

Significant progress has been made with respect to characterizing with several different materials, conversion of intermediates to precursors, and successful CF spinning of various intermediates and precursors. It is expected in the next several months that CF produced from additional materials will meet and exceed the mechanical properties set forth, while easily maintaining $\leq \$5/\text{lb.}$

References

1. Whilte, J. L., and R. J. Price, 1974, "The formation of mesophase microstructures during the pyrolysis of selected coker feedstocks," *Carbon*, Vol. 12, No. 3, pp. 321–333.
2. INL, Biomass Feedstock National User Facility, Bioenergy Feedstock Library, <https://bioenergylibrary.inl.gov/>.
3. Delfosse, F., I. Drouadaine, S. Faucon-Dumont, S. Largeaud, B. Eckmann, J. P. Planche, and F. Turner, 2016, "In Impact of Bitumen Quality on Asphalt Mixes Performances," International Society of Asphalt Pavements (ISAP) 2016 Symposium, July 18–21, 2016, Jackson Hole, WY, USA.
4. Delfosse, F., I. Drouadaine, S. Faucon-Dumont, S. Largeaud, B. Eckmann, J. P. Planche, F. Turner, and R. Glaser, 2016, "In Impact of the Bitumen Quality on the Asphalt Mixes Performance," Sixth Eurasphalt and Eurobitume Congress, June 1–3, 2016, Prague, Czech Republic.
5. Glaser, R., J. P. Planche, F. Turner, R. Boysen, J. F. Schabron, F. Delfosse, I. Drouadaine, S. Faucon-Dumont, S. Largeaud, and B. Eckmann, 2016, "In Relationship between Solubility and Chromatographically Defined Bitumen Fractions and Physical Properties," Sixth Eurasphalt and Eurobitume Congress, June 1–3, 2016, Prague, Czech Republic.

6. de Tomas, C., I. Suarez-Martinez, and N. A. Marks, 2016, "Graphitization of amorphous carbons: A comparative study of interatomic potentials," *Carbon*, Vol. 109, pp. 681–693.
7. Saha, B., and G. C. Schatz, 2012, "Carbonization in polyacrylonitrile (PAN) based CFs studied by ReaxFF MD simulations," *J. Phys. Chem. B*, Vol. 116, No. 15, pp. 4684–4692.
8. Li, G.-Y., F. Wang, J.-P. Wang, Y.-Y. Li, A.-Q. Li, and Y.-H. Liang, 2016, "ReaxFF and DFT study on the sulfur transformation mechanism during the oxidation process of lignite," *Fuel*, Vol. 181, pp. 238–247.
9. Zhao, T., T. Li, Z. Xin, L. Zou, and L. Zhang, 2018, "ReaxFF-based MD simulation of the pyrolysis mechanism for polycarbonate," *Energy Fuels*, Vol. 32, No. 2, pp. 2156–2162.
10. Li, G.-Y., J.-X. Ding, H. Zhang, C.-X. Hou, F. Wang, Y.-Y. Li, and Y.-H. Liang, 2015, "ReaxFF simulations of hydrothermal treatment of lignite and its impact on chemical structures," *Fuel*, Vol. 154, pp. 243–251.
11. Feng, M., X. Z. Jiang, W. Zeng, K. H. Luo, and P. Hellier, 2019, "Ethanol oxidation with high water content: A reactive MD simulation study," *Fuel*, Vol. 235, pp. 515–521.
12. Desai, S., C. Li, T. Shen, and A. Strachan, 2017, "Molecular modeling of the microstructure evolution during CF processing," *J. Chem. Phys.*, Vol. 147, No. 22, Art. 224705. <https://doi.org/10.1063/1.5000911>.
13. van Duin, A. C. T., S. Dasgupta, F. Lorant, and W. A. Goddard, 2001, "ReaxFF: A reactive force field for hydrocarbons," *J. Phys. Chem. A*, Vol. 105, No. 41, pp. 9396–9409.
14. Castro-Marcano, F., A. M. Kamat, M. F. Russo, A. C. T. van Duin, and J. P. Mathews, 2012, "Combustion of an Illinois No. 6 coal char simulated using an atomistic char representation and the ReaxFF reactive force field," *Combust. Flame* Vol. 159, No. 3, pp. 1272–1285.
15. Evans, E. B., 1938, "The viscosities of hydrocarbons: Parts VII and VIII," *J. Inst. Petrol. Technol.*, Vol. 24, pp. 537–553.
16. Bruinsma, O. S. L., P. J. J. Tromp, H. J. J. de Sauvage Nolting, and J. A. Moulijn, 1988, "Gas phase pyrolysis of coal-related aromatic compounds in a coiled tube flow reactor: 2. Heterocyclic compounds, their benzo and dibenzo derivatives," *Fuel*, Vol. 67, No. 3, pp. 334–340.
17. Canet, X., P. Dauge, A. Baylaucq, C. Boned, C. K. Zéberg-Mikkelsen, S. E. Quiñones-Cisneros, and E. H. Stenby, 2001, "Density and viscosity of the 1-methylnaphthalene+2,2,4,4,6,8,8-heptamethylnonane system from 293.15 to 353.15 K at pressures up to 100 MPa," *Int. J. Thermophys.* Vol. 22, No. 6, pp. 1669–1689.
18. Mosio-Mosiewski, J., and I. Morawski, 2005, "Study on single-stage hydrocracking of vacuum residue in the suspension of Ni–Mo catalyst," *Appl. Catal. A Gen.*, Vol. 283, No. 1–2, pp. 147–155.
19. Leininger, J.-P., F. Lorant, C. Minot, and F. Behar, 2006, "Mechanisms of 1-methylnaphthalene pyrolysis in a batch reactor," *Energy Fuels*, Vol. 20, No. 6, pp. 2518–2530.
20. Kremer, K., and G. S. Grest, 1990, "Dynamics of entangled linear polymer melts: A molecular-dynamics simulation," *J. Chem. Phys.*, Vol. 92, No. 8, pp. 5057–5086. <https://doi.org/10.1063/1.458540>.
21. Liu, Y., J. Ding, and K.-L. Han, 2018, "MD simulation of the high-temperature pyrolysis of methylcyclohexane," *Fuel*, Vol. 217, pp. 185–192.
22. Zhan, J.-H., R. Wu, X. Liu, S. Gao, and G. Xu, 2014, "Preliminary understanding of initial reaction process for subbituminous coal pyrolysis with MD simulation," *Fuel*, Vol. 134, pp. 283–292.

23. Zhang, J., X. Weng, Y. Han, W. Li, J. Cheng, Z. Gan, and J. Gu, 2013, "The effect of supercritical water on coal pyrolysis and hydrogen production: A combined ReaxFF and DFT study," *Fuel*, Vol. 108, pp. 682–690.
24. Liu, G., Y. Han, L. Wang, X. Zhang, and Z. Mi, 2008, "Supercritical thermal cracking of *n*-dodecane in presence of several initiative additives: Products distribution and kinetics," *Energy Fuels*, Vol. 22, No. 6, pp. 3960–3969.
25. Zheng, M., Z. Wang, X. Li, X. Qiao, W. Song, and L. Guo, 2016, "Initial reaction mechanisms of cellulose pyrolysis revealed by ReaxFF MD," *Fuel*, Vol. 177, pp. 130–141.
26. Korai, Y., S.-H. Yoon, H. Oka, I. Mochida, T. Nakamura, I. Kato, and Y. Sakai, 1998, "The properties of Co-oligomerized mesophase pitch from methylnaphthalene and naphthalene catalyzed by HF/BF₃," *Carbon*, Vol. 36, No. 4, pp. 369–375.
27. Korai, Y., M. Nakamura, I. Mochida, Y. Sakai, and S. Fujiyama, 1991, "Mesophase pitches prepared from methylnaphthalene by the aid of HF/BF₃," *Carbon*, Vol. 29, No. 4–5, pp. 561–567.
28. Mochida, I., Y. Korai, C.-H. Ku, F. Watanabe, and Y. Sakai, 2000, "Chemistry of synthesis, structure, preparation, and application of aromatic-derived mesophase pitch," *Carbon*, Vol. 38, No. 2, pp. 305–328.
29. Kershaw, J. R., and K. J. T. Black, 1993, "Structural characterization of coal tar and petroleum pitches," *Energy Fuels*, Vol. 7, No. 3, pp. 420–425.
30. Wang, Q.-D., J.-B. Wang, J.-Q. Li, N.-X. Tan, and X.-Y. Li, 2011, "Reactive MD simulation and chemical kinetic modeling of pyrolysis and combustion of *n*-dodecane," *Combust. Flame*, Vol. 158, No. 2, pp. 217–226.
31. Ding, J., L. Zhang, Y. Zhang, and K.-L. Han, 2013, "A reactive MD study of *n*-heptane pyrolysis at high-temperature," *J. Phys. Chem. A*, Vol. 117, No. 6, pp. 3266–3278.
32. Kim, B.-J., T. Kotegawa, Y. Eom, J. An, I.-P. Hong, O. Kato, K. Nakabayashi, J. Miyawaki, B. C. Kim, I. Mochida, and S.-H. Yoon, 2016, "Enhancing the tensile strength of isotropic pitch-based CFs by improving the stabilization and carbonization properties of precursor pitch," *Carbon*, Vol. 99, pp. 649–657.
33. Hawthorne, H. M., C. Baker, R. H. Bentall, and K. R. Linger, 1970, "High-strength, high modulus graphite fibres from pitch," *Nature*, Vol. 227, No. 5261, pp. 946–947.
34. Matsumoto, T., 1985, "Mesophase pitch and its CFs," *Pure Appl. Chem.*, Vol. 57, No. 11, pp. 1553–1562.
35. Rosenblatt, F. X., 1961, *Principles of Neurodynamics: Perceptrons and the Theory of Brain Mechanisms*, Cornell Aeronautical Laboratory, Inc., Report No. VG-1196-G-8, Spartan Books, Washington DC, USA.
36. Rumelhart, D. E., G. E. Hinton, and R. J. Williams, 1986, "Learning Internal Representations by Error Propagation," In: D. E. Rumelhart, J. L. McClelland, and the PDP research group (eds.), *Parallel Distributed Processing: Explorations in the Microstructure of Cognition – Volume I. Foundations*. Ch. 8, pp. 318–362, MIT Press, Cambridge, MA, USA.
37. Ferralis, N., 2018. <https://github.mit.edu/feranick/DataML>.
38. Keras: The Python Deep Learning Library, 2018. <https://keras.io>.
39. TensorFlow, 2018. <https://tensorflow.org>.
40. Ugelstad, M., and N. Ferralis. n.d. *Data management system*. <https://carbonio.mit.edu>.

Acknowledgements

The Principal Investigators would like to acknowledge the DOE National Energy Technology Laboratory Project Manager, John Terneus, for administrative help and guidance during this project, as well as the DOE Technology Manager, H. Felix Wu, Ph. D, and Will James, for useful feedback. They would also like to acknowledge individuals who have contributed significantly to the technical success in several areas: Logan Kearney at ORNL for CF spinning, mechanical properties testing, and ACN polymerization; Nicola Ferralis at GG-MIT for spearheading the computation work, ML, and database; Don Malone at ACP for providing expert technical guidance on mesophase formation; and Khalid Baig at WRI for providing several pieces of analytical data, as well as conversion of isotropic CTP to mesophase; and Charlie Atkins at Ramaco for providing market and TEA analysis data and insights in addition to raw coal samples.

II.2.G Spider Silk MaSp1 and MaSp2 Proteins as CF Precursors (Oak Ridge National Laboratory)

Dr. Eng. Felix L. Paulauskas, Principal Investigator

Materials Science and Technology Division
Oak Ridge National Laboratory
1 Bethel Valley Rd.
Oak Ridge, TN 37831
E-mail: paulauskasfl@ornl.gov

Prof. Randy Lewis, Co-Principal Investigator

Utah State University
1600N 650E
North Logan, UT 84322
E-mail: randy.lewis@usu.edu

H. Felix Wu, Ph. D, DOE Technology Manager

U.S. Department of Energy
E-mail: felix.wu@ee.doe.gov

Start Date: January 1, 2018	End Date: December 31, 2018	
Project Funding (FY18): \$420,000	DOE share: \$420,000	Non-DOE share: \$0

Project Introduction

Spider silk fibers have a unique combination of tensile strength and elasticity that can be used directly to create composite materials with application to lightweight vehicles. For the past several years, the Utah State University group has developed methods to produce spider silk proteins, spin fibers from them, and conducted preliminary studies on the use of those fibers in epoxy-based composite materials. The fibers show very strong adherence to the composite matrix and the spider silk proteins themselves can serve as impressive adhesives. The aim of this project is to accelerate the development of genetically modified fiber/composite for use in the automotive industry.

Objectives

The objective of this project is to develop an unconventional non-petroleum-based CF precursor, which has the potential to be produced in high yield and quantities. Methods will be developed to produce pilot-scale quantities of fibers from spider silk proteins with mechanical properties at least 75% of that used in natural dragline silk fibers in terms of tensile strength and elongations of less than 5%. The precursor fibers will be converted to CFs, with a goal of >250 Ksi strength and 1-2% elongation. Cost analysis will then be performed, and the process optimized.

This project is a continuation of a funded project that already demonstrated the feasibility of converting “synthetic” spider silk fibers into CFs. This current project will determine the best fibers for conversion and develop an optimized conversion process. Utah State University will be developing the protein production and fiber-spinning methods while ONRL will develop the conversion processes.

Approach

In this project, six main tasks have been identified and distributed over four phases, as shown in Table II.2.G.1. Each of these steps involves some work on the development of the proteins, whereas the activity of conversion is mostly allocated over the two last phases. A description of each phase is provided after the table.

Table II.2.G.1. Detail of the Major Phases of the Spider Silk Conversion Project.

Phase	Name	Calendar	Status (Sept. 2018)	Description
1	Protein production	FY 2018 Q2	Completed	Production of 25 ft of 24 tow fiber from two spider silk proteins.
2	Filament extrusion	FY 2018 Q3	Completed	Production of five 1,000 ft samples with 24 filaments per tow from the best two proteins previously developed.
3	Protein production and conversion	FY 2018 Q4	In progress	Develop conversion parameters. Exceed best results of previous work (e.g., 100 ksi).
4	Protein production and optimization	FY 2019 Q1	To be done	Increase protein production by 2-fold, from 1g/l to 2g/l. Exceed best results of previous work (e.g., 100 ksi).

1. The testing of four different spider silk proteins will begin with the minor ampullate spidroin (MiSp) protein from the minor ampullate gland, which is similar to one of the dragline silk proteins but with much less elongation ability. The next two will be genetically made analogs of a combination of dragline and capture spiral (flagelliform) silk proteins known to have very interesting mechanical properties (i.e., FLAS and FLYS); one of which has a substantial percentage of amino acids that can be crosslinked via our new method. Finally, we will be testing aciniform silk protein, which has been tested very little in its natural form due to its very fine fiber diameter. It has a very different amino acid composition than most other silks, being low in glycine, which is the predominant amino acid in other silks and could aid in carbonization.
2. A proprietary crosslinking method will be used to determine if that will improve the carbonization process and generate improved CFs. This will involve developing a method of crosslinking *in-situ* (during the fiber-spinning process) or as a post treatment.
3. The effort will be focused on the fiber-spinning process, not on the fibers we produce as the starting material. The aim is to assess the effects of various spinning methods on the final CFs. In particular, a new 24-filament spinning head was specifically designed to prevent the fibers from fusing. New rollers with divided sections were implemented to prevent filament interaction. It is expected that several modifications to the current process will be required to create an unfused tow.
4. Improvement of the production levels of spider silk proteins by increasing both the protein produced in the fermentation, as well as the purification yield.
5. Extensive studies will be conducted to determine and develop an appropriate preliminary conversion protocol for a precursor without fused filaments. This will result in a fundamental understanding of what is required to convert the engineered polymer into CF. This step is somewhat independent of applied stretch and focuses on chemical changes in the precursor and on the use of single or small filament sample quantities.
6. Based on the accomplishments of the previous task, an optimization of the conversion process conditions will be conducted to increase the final fiber mechanical properties.

Results

At the beginning of this project, efforts were focused on the production of proteins spinning into filaments. Fibers have now been spun from bacterially produced spider silk protein. Furthermore, a new fermentation method has been constructed called “pCold.” In a preliminary study, this process doubled the protein production, as well as substantially increased the percentage of the full-length protein from initially 40–50% to now over 80%. This pCold system conducts both fermentation and protein production at much lower than typical temperatures for longer production times, which results in more protein at a lower cost.

Current Status of Protein Production

The following proteins have been produced:

- Minor silk protein (48 repeats, 180 kD) in the Light Chain (LC) locus
Minor silk protein (64 repeats, 230 kD) in the LC locus
- NIRC (minor silk protein, 230 kD) in the Heavy Chain (HC) locus
- NARC (major silk protein, 240 kD) in the HC locus
- NIRC/NARC hybrids
- MiSp 48 and 64 in LC/NARC hybrids.

Both major and minor ampullate silks have been tested because they are different spider silk proteins and are expected to produce different mechanical properties on the transgenic silkworm silk. Specifically, the minor ampullate has very little stretch, whereas the major ampullate has a noticeable stretch. On the other hand, the spider silk gene is in two different gene locations (e.g., HC and LC) in the silkworm, which may lead to different levels of the spider silk protein in the transgenic silk. In addition, it is possible to breed different transgenic strains and create hybrids to assess what impact multiple different spider silk proteins and gene locations may have. All of these parameters may affect the properties of the CF made from these silks.

Characterization of the Precursors

As of September 30, 2018, three available materials were tested for conversion: major ampullate spidroin (MaSp)-1, both degummed and non-degummed and MiSp degummed. Thermogravimetric analysis indicated a low char yield for these three materials. While slightly lower for both degummed materials, the char yield of the MaSp1 non-degummed was around and above 20%, which makes it the single eligible material suitable for conversion, as shown in Figure II.2.G.1. This analysis was confirmed by several experiments.

Each material was mechanically tested, but only MiSp degummed was equally tested after a thermal treatment at low-temperature (e.g., stabilization). Their mechanical properties were in the range of most polyacrylonitrile precursors (e.g., between 65 ksi and 75 ksi for the break stress), as shown in Table II.2.G.2, despite the irregularity and randomness of the cross-section of the filaments, as shown in Figure II.2.G.2. And, as expected, the mechanical properties of the MiSp depleted significantly after stabilization (see Table II.2.G.2). Since these materials are bio-polymers, a different approach for proper pretreatment may be needed to increase their mechanical strength. The material used in the current study was produced from transgenic silk worm silk and appears to be more difficult to convert than the pure synthetic spider silk previously investigated. By changing the material and its production process from that used in the previous study, significantly more material has been produced. Unfortunately, this material does not behave as well as the former material during the conversion process. Note that all tested precursors showed fused filaments. Despite the filaments being fused, the isolation of single specimens was possible on the raw materials, but not once any thermal treatment was applied.

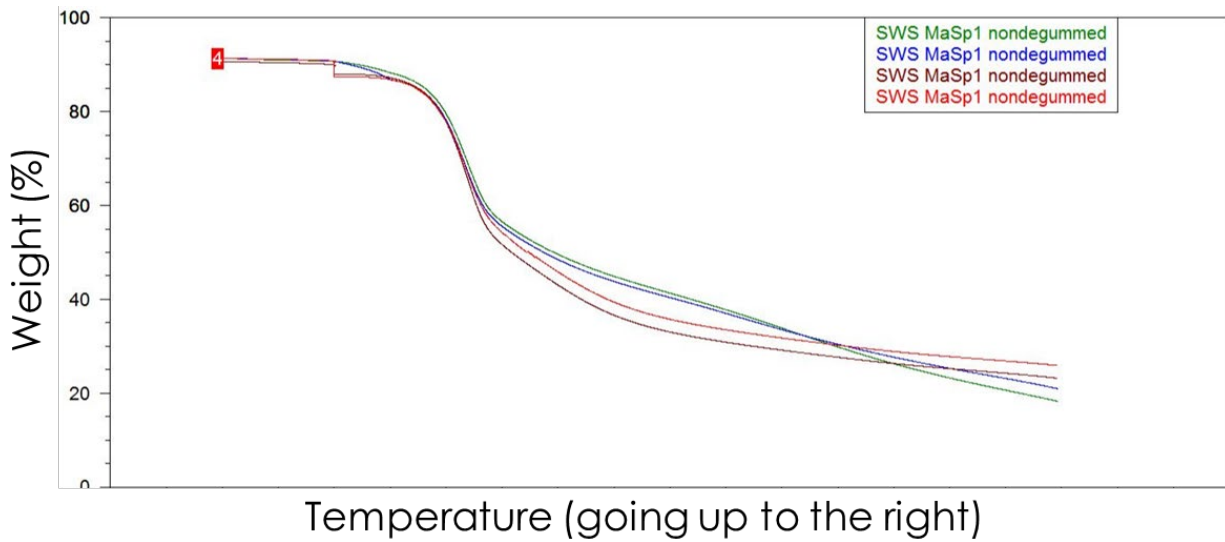


Figure II.2.G.1. Thermogravimetric analysis of MaSp1 using four different pretreatments. The ramp was set at 10°C/min after stabilization. This plot shows that MaSp1 produces between 19% and 27% char yield, according to selected procedure. This makes this material theoretically suitable for carbonization. Source: ORNL.

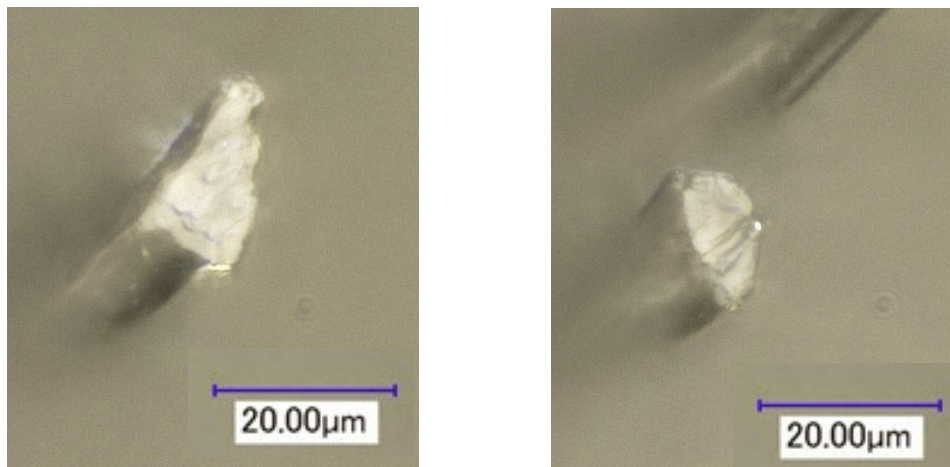


Figure II.2.G.2. Optical microscopy images of two examples of isolated MaSp1 filament highlighting the irregularity of the cross-section of these filaments. Source: ORNL.

Table II.2.G.2. Range of Mechanical Properties for MiSp and MaSP1 Samples.

Sample	Diameter (µm)	Break Stress (ksi)	Modulus (Msi)	Strain (%)
MiSp degummed	9.77 (0.95)	71.68 (10.61)	1.92 (0.21)	17.04 (4.20)
MaSp1 non-degummed	9.99 (1.05)	62.16 (7.77)	1.81 (1.05)	18.79 (4.99)
MaSp1 degummed	9.53	68.69	1.97	21.92
MiSp degummed <i>Stabilized</i> (BUNDLE)	<i>53.51 (5.91)</i>	<i>12.7 (5.8)</i>	<i>1.8 (0.4)</i>	<i>0.61 (0.19)</i>

Conversion

At the beginning of the task of conversion, three materials were available: MaSp1 non-degummed, MaSp1 degummed, and MiSp degummed. Characterization and preliminary conversion tests showed that the last two were not suitable for conversion. Only MaSp1 was able to survive through the entire conversion process. However, the survival of the sample highly correlated to the processing parameters, which means that this material is delicate to convert. Mechanical properties for seven sets of CFs are shown in Table II.2.G.3. Only bundles of fused filaments, as shown in Figure II.2.G.3, were tested (no single filaments). The mechanical properties are extremely weak, around 10 ksi for the best of them. All of the specimens were bundles of fused filaments. As a consequence, the cross-section of such bundles cannot be measured accurately on short samples like those that are produced. This introduces a large variation in the measurement of the mechanical properties, as shown in Table I.1.1.3. None of them received an appropriate tension through the entire process (because of both the material strength and the hardware configuration). The combination of welded filaments with inappropriate tension justify the poor properties of these batches.

Table II.2.G.3. Mechanical Data of Carbonized Bundles.

Sample	Diameter (μm)	Break Stress (ksi)	Modulus (Msi)	Strain (%)
1	43.36 (3.94)	2.2 (1.3)	N/A	N/A
2	53.52 (5.83)	8.8 (3.3)	2.5	0.42 (0.07)
3	56.59	2.4	N/A	0.32
4	53.51 (5.91)	12.7 (5.8)	1.8 (0.4)	0.61 (0.19)
5	59.67	8.6	0.1	0.93
6	49.01 (4.82)	6.1 (1.9)	1.2 (0.5)	0.56 (0.33)
7	57.13 (8.19)	9.2 (2.6)	2.4 (0.1)	0.41 (0.07)

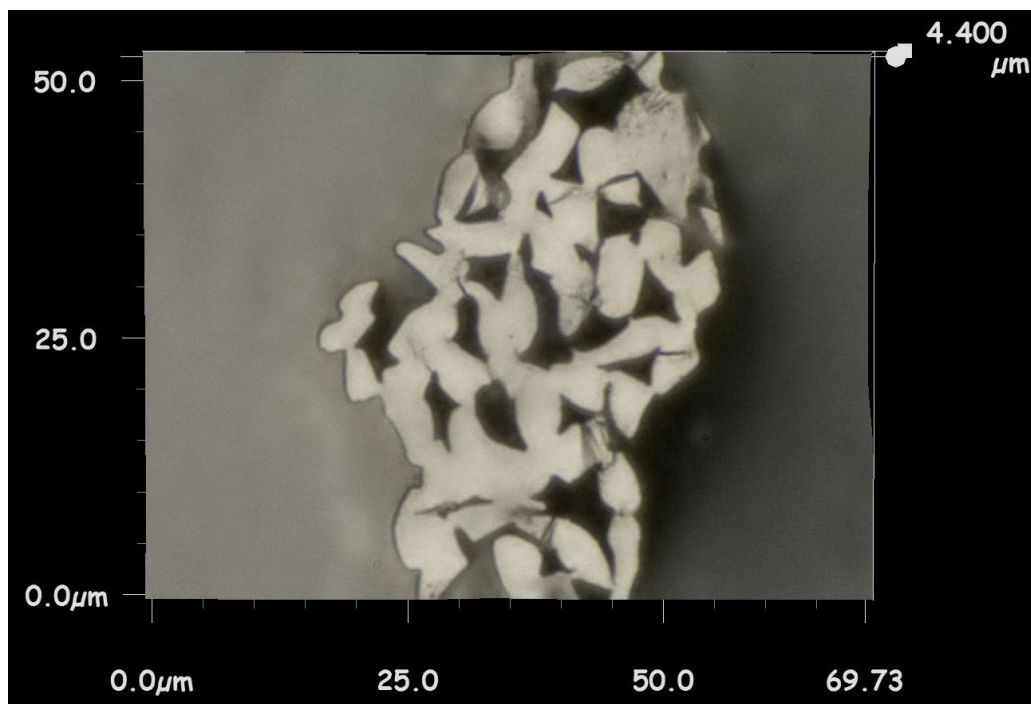


Figure II.2.G.3. Observation of the cross-section of fused filaments of a MaSp1 non-degummed after conversion. Source: ORNL.

The reason for the poor mechanical properties shown in Table II.2.G.3 is a combination of the following factors:

1. The pattern of the protein is inappropriate for carbonization.
2. The filaments are fused after the spinning phase, which worsens with the thermal treatment.
3. The cross-section of the filaments is irregular and random.
4. The procedure of conversion is not suitable; this includes the approach and hardware limitations.

In the past, comparable materials were already evaluated for conversion. Some of them proved similar, whereas others did significantly better. As a consequence, to estimate and handle issues related to factor (1) above, another variation based on hybrid silkworms with two spider silk proteins is currently in-production. In addition, a new type of fiber with another spider silk protein will be evaluated. Additionally, two solutions are currently in the design or implementation phase. These solutions will help to address limiting factors (2) and (3). Regarding the last limiting factor (4), two actions will be undertaken:

- On the procedure (immediately), a new conversion approach was recently envisioned that will be implemented on MaSp1 first, and then on other materials.
- On the hardware (within a few weeks), a new furnace will soon be operational; this future piece of equipment will allow for the maintaining of the tension on the samples over the entire process, which would address the current hardware limitation.

Conclusions

The implementation of the pCold process in FY 2018 has been a major achievement in the production of protein. This process doubles the amount of protein produced with a yield of over 80% full protein. This allowed for the production of five types of protein at a reduced cost. Among those, three proteins were spun into filaments and evaluated as precursors for CF.

Among the three precursors available for carbonization, only one was found to be suitable for this purpose. Lab tests provided C material with poor mechanical properties (around 10 ksi). These results are significantly lower than those obtained during preliminary work done back in 2016, where the threshold of 100 ksi was already reached.

Based on these results, certain actions have already been engaged. On the spinning side, a new hybrid combination of proteins will be used for future material production. Furthermore, some upgrades have already been implemented on the spinning line in order to improve the cross-section shape of the filaments and mitigate/eliminate the fused fibers. On the conversion side, a new procedure will be tested on the already available materials, as well as on the upcoming ones. Furthermore, a furnace was recently ordered. This new equipment will be more appropriate for this work than the existing one has proven to be. All of these actions should help to reach and exceed previously achieved performances.

Acknowledgements

This research was sponsored by DOE-EERE, VTO, and ORNL, which is managed by UT-Battelle, LLC, for DOE under contract DEAC05-00OR22725.

II.3 Multi-Material Joining

II.3.A Solid-State Body-in-White Spot Joining of Al to AHSS at a Prototype-Scale (Oak Ridge National Laboratory)

Zhilli Feng, Co-Principal Investigator

Oak Ridge National Laboratory
1 Bethel Valley Rd.
Oak Ridge, TN 37831
E-mail: fengz@ornl.gov

Eric Boettcher, Co-Principal Investigator

Honda R&D Americas, Inc.
21001 State Rte. 739
Raymond, OH 43067
E-mail: eboettvher@oh.hra.com

Sarah Kleinbaum, DOE Technology Manager

U.S. Department of Energy
E-mail: sarah.kleinbaum@ee.doe.gov

Start Date: November 1, 2014	End Date: May 31, 2019	
Project Funding (FY18): \$780,000	DOE share: \$380,000	Non-DOE share: \$400,000

Project Introduction

This project focuses on developing and demonstrating two emerging solid-state, friction-heating-based spot joining processes—friction bit joining (FBJ) and friction stir spot welding (FSSW)—to join AHSS to high-strength Al alloys (HSA alloys) from the coupon-scale to the prototype part level. Application of these joining processes to HSA and AHSS in the body-in-white (BIW) production environment requires further R&D to address a number of technical obstacles (i.e., joint performance, productivity, maintaining consistency of joint quality under expected dimensional variations of stamped and/or formed parts, and cost-effectiveness).

The project consists of two phases. During Phase 1, both FBJ and FSSW methods were developed and evaluated at a coupon-scale. Furthermore, because corrosion management is a primary concern for the joining of dissimilar materials, both FBJ and FSSW were combined with adhesive bonding as an isolation approach to protect the spot joint from galvanic corrosion. Finally, an integrated computational welding engineering modeling framework, developed by the project team over the years, is being adopted, refined, and applied. The purpose of the integrated computational welding engineering model is to (1) refine and optimize the solid-state joining process, (2) understand microstructure changes in the weld region and their effects on the strength/properties of an individual joint, and (3) optimize joinability and joint performance at the prototype assembly level. During Phase 2, FBJ was selected as the “winning” process for further development using prototype-scale BIW assembly level joining. Hardware of the winning joining process is being integrated with an assembly line welding robot. Prototype BIW subsystems, selected by the original equipment manufacturer (OEM), will be welded and assembled with the robotic joining system to evaluate and validate the production readiness of the joining technology for high-volume mass production BIW assembly. Al-steel joints, at both the coupon-scale and the prototype-scale, will be tested and characterized to determine performance of the joints in accordance with the requirements in the Funding Opportunity Announcement and a set of process and performance criteria from the OEM, Tier 1 supplier, and industry partners. The project assembled an excellent project team composed of automotive manufacturers and auto-part suppliers to carry out the proposed process R&D; engineering testing, joining system integration and eventual commercialization and implementation.

The project is led by ORNL, with participation from Honda R&D Americas, Alcoa, Dow Chemical, L&L Products, Cosma Engineering, G-NAC, MegaStir Technologies, Brigham Young University, and OSU.

Objectives

This project aims to develop, mature, and validate near-production readiness of a solid-state spot joining technology to join prototype-scale auto BIW subsystems made of AHSS and 7,000/6,000 series HSA alloys to meet the dissimilar metal joining challenges in high-volume mass production.

The project focuses on spot joints—the most common form of joints in BIW structures of high-volume production vehicles. Thus, it enables the broadest insertion of lightweight materials in BIW and has the highest potential as a joining technology to support the reduction of petroleum consumption, environmental impacts, and economic benefits in the transportation sector.

Approach

FBJ is a newly invented solid-state joining process particularly suitable for dissimilar materials. FBJ creates a metallurgical bonded spot joint in two or more sheets of dissimilar metals through a combination of frictional drilling and bonding action of a high-strength consumable joining bit. FSSW is a derivative of the FSW process. A rotating fixed-pin tool is plunged into the upper sheet with normal force to generate frictional heat. The heated and softened material adjacent to the tool deforms plastically and a solid-state bond is made between two dissimilar metals, such as Al and steel. After critical review of both processes by project teams, FBJ was down-selected for Phase 2.

The development of joining technology must be coupled with corrosion management, which is critical for automotive applications, especially for any joint between dissimilar materials. An adhesive was applied at all proposed contact locations between HSA and AHSS components to serve as an insulator. The solid-state joining techniques, adhesive bonding, and combination of the two were initially assessed using laboratory-scale coupons.

The *in-situ* distortion measurement at the component level is to gain a comprehensive understanding and provide a potential solution for part distortion caused by the mismatch of the thermal expansion of Al and steel during paint-baking and curing of adhesives during the automotive body assembly process. The experiment will guide, improve, and verify the distortion model developed in this project.

Modeling the joining process provides insights on physical phenomena (e.g., thermal and deformation histories) during joining. This model is a prerequisite for subsequent weld microstructure and performance modeling and understanding the effect of temperature rise due to joining on the thermal expansion coefficient mismatch of two different metals. In addition, component level modeling provides an analytical modeling tool for assisting in design optimization to reduce welding distortion and stresses to a tolerable level. The integrated computational welding engineering approach has been adapted to refine the joining process and to predict joint performance under manufacturing conditions (e.g., paint-baking).

During Phase 2, the “winning” process—FBJ—was selected for further development using prototype-scale BIW assembly level joining. The main objective in Phase 2 is to demonstrate the FBJ process in a controlled production environment. A new FBJ welding head will be designed, manufactured, and integrated with a robot system along with fixtures for coupons and demonstration parts. Coupons and demonstration parts produced by the prototype FBJ welding cell will be further tested and evaluated for mechanical and corrosion performance. Prototype BIW subsystems, selected by the OEM, will be welded and assembled with the robotic joining system to evaluate and validate production readiness of the joining technology for high-volume mass production BIW assembly. Al-steel joints, at both the coupon and prototype scales, will be tested and characterized to determine the performance of the joints in accordance with the requirements in the Funding

Opportunity Announcement and a set of process and performance criteria from the OEM, Tier 1 supplier, and industry partners.

Results

Cyclic Corrosion Testing for Weld-bonded (FBJ + Adhesive) Specimens

Corrosion studies of dissimilar materials at the small coupon level provide insight into corrosion behavior and its effective mitigation method. Cyclic corrosion testing (CCT) was used to evaluate the effect of corrosive media on joint strength. CCT was performed by automotive OEM specifications in three rounds. Acceptance criteria is to maintain 90% of the original joint strength after CCT. In Round 1 CCT, FBJ-only specimens had essentially no remaining strength at the end of CCT, while weld-bonded (FBJ + Adhesive) had 73% and 77% strength reduction for two different adhesives from two different adhesive suppliers. Based on this examination and the analysis of the failure behavior from Round 1 submission, procedures for sample preparation in Round 2 were modified to eliminate factors not associated with the joining processes developed in this project. Post-CCT lap shear tensile test strength was evaluated at 50% and 48% of original pre-CCT strength for the two different adhesives used. The results from Round 2 show much-improved corrosion resistance as compared to Round 1. After examination of post-CCT lap shear specimens, irregular Al flash on the periphery of the joining bit (Gen. 1) can cause non-uniform E-coat on the Al surface, leading to corrosion propagation from the FBJ head. For this reason, a further refined FBJ head shaped to be countersunk into the Al (Gen. 2) was developed to clean the Al surface and minimize surface debris of Al for a better E-coat. Mechanical joint performance of the coupon using the new Gen. 2 met the proprietary evaluation criteria. Weld-bonded samples with two different FBJ head shapes (Gen. 1) and (Gen. 2: new) were prepared and a secondary isolation method was applied prior to the third round of CCT. While weld-bonded Gen. 1 coupons successfully passed OEM's proprietary evaluation criteria and also retained 27% and 23% of their original strength, unexpected issues of the corrosion chamber for Gen. 2 was encountered during CCT. Therefore, evaluation of the corrosion performance of the Gen. 2 coupons will be completed in Phase 2.

In-situ Distortion Measurement by Digital Image Correlation (DIC) Technique

The purpose of the *in-situ* distortion measurement at the component level is to gain a comprehensive understanding and provide a potential solution for part distortion caused by the mismatch of the thermal expansion of Al and steel during paint-baking and curing of adhesives during the automotive body assembly process. The experiments guide, improve, and verify the distortion model developed in this project. The components selected for distortion study in Phase I is illustrated in Figure II.3.A.1. A U-channel of the Al part is bolted to the steel U-channel. Two types of Al alloys—AA6111 (2.46 mm thick) and AA7055 (2.47 mm thick)—were investigated. The steel channel was made of DP1180GA (1.15 mm thick).

In FY 2018, a half-size (475-mm long) and full-size (950-mm long) beam component were studied. The Al channel and the steel channel were fastened together by four bolts at both ends with pitch distance of 425 mm for a half-size and 900 mm for a full-size. For the Al part, different flange heights were used to study the effect on the thermal distortion.

The assembled parts were subjected to a heating and cooling cycle, mimicking the paint-baking and adhesive curing step expected in the auto-body structure assembling process. The initial gap between the Al channel and steel at RT before the heating cycle, the gap at the peak baking temperature (197°C) and final residual gap after cool-down to RT were measured by DIC and summarized in Table II.3.A.1. A caliper was also used to measure the gap after cool-down to RT to compare the accuracy of DIC.

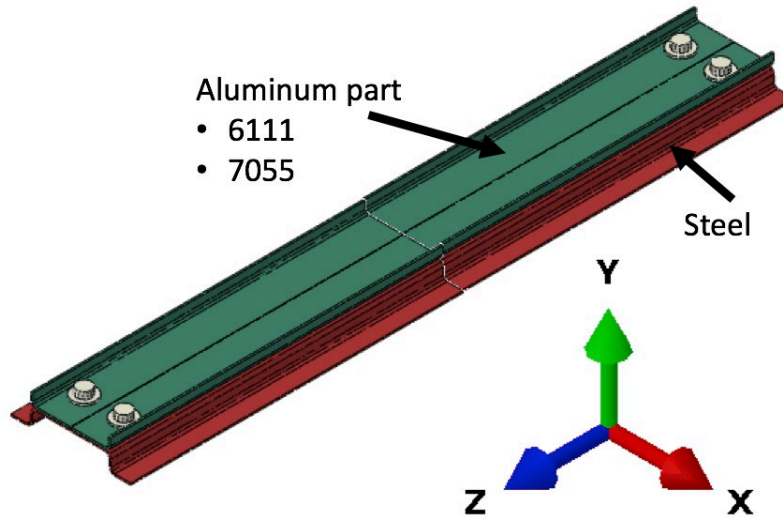


Figure II.3.A.1. A schematic of the component for in-situ DIC measurement. Source: ORNL.

Table II.3.A.1. Distortion Gap Summary for Different Conditions at Peak Paint-Bake Temperature (197 °C).

Panel Length	Flange Height (mm)	Al Alloy	Initial Gap at Center (mm)	Gap at Peak Temperature (mm)	Residual Gap by DIC at RT (mm)	Residual Gap by Caliper at RT (mm)
Half	33.55	7055	N/A	0.32	0.36	N/A
	22.55	7055	N/A	1.29	0.56	0.74
	33.55	6111	N/A	0.24	0	0.19
	22.55	6111	N/A	0.88	0	0.05
	15.55	6111	N/A	2.94	0.29	0.2
Full	33.55	6111	0.5	3.26	0.73	0.67
	22.55	6111	0.6	9.09	2.36	N/A
	33.55	7055	0.4	4.15	1.25	1.13
	33.55	7055	N/A	4.16	1.34	1.36
	33.55 loose*	7055	N/A	4.27	1.41	1.41

Note: *The bolts were tightened up first, then released 90 degree on each.

The following is a quick summary from the *in-situ* distortion measurement:

- When all other conditions were the same, the maximum gap was found from the following order: Quarter Flange (Flange Height = 15.55 mm) > Half-Flange (Flange Height = 22.55 mm) > Full-Flange (Flange Height = 33.55 mm) for both half and full panel lengths.
- Full-size panels had larger gaps than half-size panels.
- In general, AA7055 causes more thermal deformation than AA6111 (e.g., 1.29 mm for half-length 7055 versus 0.88 mm for half-length AA611 and 0.32 mm for full-length AA7055 versus 0.24 mm for full-length AA6111 in Table II.3.A.1).
- Repeated tests on the full-size, full-flange panels show consistent results.
- Panels with loose bolts had a similar gap as the full-size, full-flange panels. The effects of tightness of bolt will need to be further investigated with greater variations.

Development of Component Level Thermal Distortion Model

The primary objective of component level modeling is to understand the part distortion of the bimetallic structure during the paint-bake process. The distortion mode was treated as a thermal buckling problem. ABAQUS was used to simulate the thermal buckling. The simulation model has two channels—one for Al and another for steel—that were bolted together. Figure II.3.A.2 shows a comparison of the gap at the center as measured by DIC and predicted a numerical model for a full-length panel, half-flange height (22.55 mm), and AA6111 case. Deflection of the Al and steel component was plotted along the longitudinal distance to the center for DIC measurement and numerical model prediction. The measured gap at center by DIC was 9.1 mm at peak temperature, while predicted gap at center by numerical model was 10.0 mm. The model prediction shows a good agreement with experimental result. This thermal distortion model can be used to explore options to minimize thermally-induced distortion of Al and steel sub-assembly due to coefficient of thermal expansion mismatch.

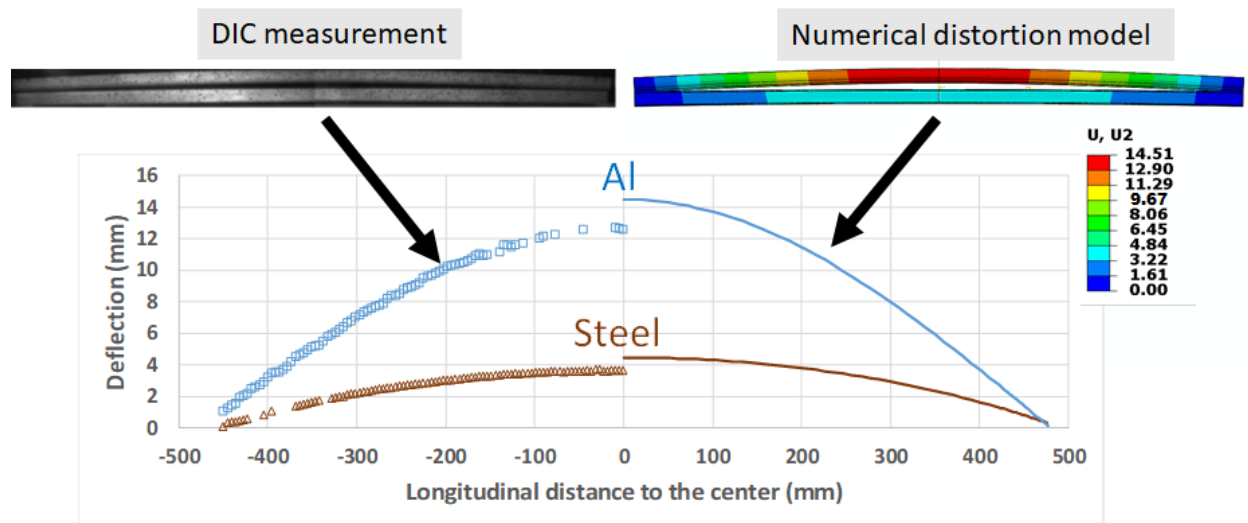


Figure II.3.A.2. Comparison of gap measured by DIC and predicted numerical model at peak paint-bake temperature. Source: ORNL.

Prototype FBJ Work Cell for Demonstration Part-Joining

The FBJ process was selected for further development using prototype-scale BIW assembly level joining in Phase 2. The overall objective in Phase 2 is to demonstrate the FBJ process in a controlled and automated welding cell to join demonstration Al and steel parts selected by OEM, as shown in Figure II.3.A.3. In FY 2018, MegaStir, Brigham Young University, and Honda R&D America collaborated extensively with each other for to develop the research and demonstration plan in Phase 2. The plan included the following tasks. The first task is to design a new FBJ welding head by considering the clearance values for test coupons and final specimens, along with the finalized design of automated bit loading. Baseline design of the new FBJ welding head has completed. In task 2, the finalized FBJ welding head will be manufactured and integrated with the automated bit loading system. Also, the fixture for coupon tests will be constructed. The design of the fixture has completed. In task 3, the new FBJ head unit is integrated with a robot and will be implemented along with the coupon fixture into the welding cell. Honda is going to provide fixtures to the MegaStir facility. In task 4, the newly integrated FBJ system is going to produce test coupons to verify mechanical joint properties as met in Phase 1. Also, corrosion testing specimens will be produced. In task 5, a go/no-go decision will be made for demonstration part-joining based on the evaluation of functionality of the prototype FBJ welding cell. In task 6, the fixture for the demonstration part will be integrated into the FBJ cell. Honda will provide the demonstration parts, while MegaStir will conduct the programming and troubleshooting of the integrated system. In task 7, the demonstration parts will be joined and inventoried for shipment to Honda and ORNL for testing.

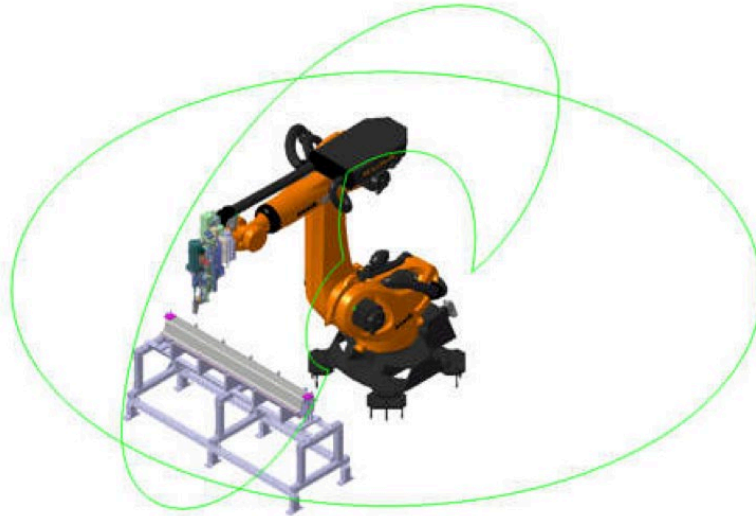


Figure II.3.A.3. Concept of FBJ work cell. Source: ORNL.

Conclusions

Significant improvement on FBJ coupons preparation for CCT has been made. During corrosion testing, FBJ samples successfully met the proprietary target strength criteria set forth by the OEM. The DIC technique was successfully developed to study the distortion of the Al and steel component caused by the mismatch of coefficient thermal expansion during a paint-baking condition. Significant progress on thermal distortion for the component level has been made and showed a good agreement with the experimental DIC results. The team worked on the design and development of the FBJ welding cell for the joining of demonstration parts in Phase 2.

Key Publications

1. Shirley, K., M. P. Miles, S. Grimshaw, Y. C. Lim, Z. Feng, and E. Boettcher, 2018, "Spot Joining of AA 7085 and DP 1180 Steel Using a Friction Riveting Approach," *Sheet Metal Welding Conference XVIII*, October 17–18, 2018, Livonia, MI, USA.
2. Shirley, K., M. P. Miles, S. Grimshaw, Y. C. Lim, Z. Feng, and E. Boettcher, 2018, "Spot Joining of AA 7085 and DP 1180 Steel Using a Friction Riveting Approach," *Materials Science & Technology 2018*, October 14–18, 2018, Columbus, OH, USA.

Acknowledgements

The Principal Investigators would like to thank the following individuals for their contributions to this work:

- ORNL: Yong Chae Lim, Yanli Wang, Lianshan Lin, Ward Manneschildt
- Honda R&D Americas: Eric Boettcher, Alan Seid
- Brigham Young University: Michael Miles, Kevin Shirley, Shane Wood
- MegaStir: Dale Fleck, Bill Johnson, Russel Steel
- OSU: Wei Zhang
- DOW: Mirdamadi Mansour, Gary Hayes
- L&L: David Kosal, Stuart Crump
- Cosma Engineering: Arvind Srilatha, Changji Shi, Erryn Ashmore
- G-NAC: Eric Yousey, Susumu Wakameda, Nick Weisenberger, Robert Clark
- Alcoa: Russel Long, Donald Spinella, Daniel Bergstrom.

II.3.B Solid-State Joining of Mg Sheet to High-Strength Steel (Pacific Northwest National Laboratory)

Piyush Upadhyay, Co-Principal Investigator

Pacific Northwest National Laboratory
902 Battelle Blvd.
Richland, WA 99352
E-mail: piyush.upadhyay@pnnl.gov

Zhilli Feng, Co-Principal Investigator

Oak Ridge National Laboratory
1 Bethel Valley Rd.
Oak Ridge, TN 37831
E-mail: fengz@ornl.gov

Sarah Kleinbaum, DOE Technology Manager

U.S. Department of Energy
E-mail: sarah.kleinbaum@ee.doe.gov

Start Date: October 1, 2017	End Date: September 30, 2020	
Project Funding (FY18): \$525,000	DOE share: \$525,000	Non-DOE share: \$0

Project Introduction

In a modern multi-material vehicle, lightweight materials such as Al and Mg alloys can be a challenge to join and attach to the underlying substructure, usually composed of steel. Even in Al and Mg intensive designs where entire substructures may be constructed of lightweight metals, there remains a need to join the substructure with other parts of the vehicle, such as the predominantly steel passenger safety cage. Joining methodologies available in the cost range relevant to automotive manufacturing include RSW, adhesives, linear fusion welding, hemming, clinching, bolting, and riveting. However, because of the highly dissimilar natures of the materials, Mg to steel joints are extremely problematic. Mg to steel joints simply cannot be fusion-welded due to the extreme differences in their melt temperatures. Additionally, no intermediate phases exist between an Mg and Fe system. Joining methods that require a large amount of plastic strain in the Mg component suffer from Mg's poor ductility at RT.

FSW and USW methods provide joining options that may be able to overcome some of the technical barriers preventing more robust and reliable joining of Mg to steel [1–3]. These methods involve creating a large degree of plastic deformation at the interface while at the same time delivering heat from frictional and plastic work. Both of the methods are solid-state, warm deformation technologies, and take advantage of the enhanced ductility of Mg and Steel at elevated temperatures. There are several identified technical barriers:

1. Lack of understanding of the methods and processing conditions required to achieve robust joints.
2. Lack of comprehensive performance information on joints fabricated by FSW/USW methods (e.g., strength, fatigue, durability, crash performance).
3. Insufficient understanding of the feasible joint geometries.
4. For USW, lack of fundamental understanding of the response of materials and joint geometry to process variables (i.e., frequency, etc.).
5. Lack of understanding of the corrosion protection and mitigation strategies that will be necessary to implement for these joining methods.

In FY 2018, this collaborative project began by performing baseline joint developments in AZ31 and DP590 steel. To understand the joining process and the nature of interfacial chemistry, a range of welding conditions was utilized with and without the joint line disruption.

Objectives

The overall goal of this project is to mature two types of solid-phase joining techniques—FSW and USW—by developing an understanding of the methods and processing conditions required to achieve robust joints between Mg and Steel, thus integrating lightweight materials for multi-material vehicles. The objective for this fiscal year included establishing methods of joint fabrication, joint characterization, and joining process data acquisition.

Approach

The project is divided into three main task areas to ensure risk mitigation and successful completion. These three main tasks are:

- Task 1: The development and assessment of FSW and USW techniques with and without geometric joint line features.
- Task 2: The fundamental study of bond formation and associated mechanical properties.
- Task 3: Interface control and tailoring for improved corrosion and strength.

By utilizing several advanced characterization techniques, we intend to correlate process parameters and variables to resulting interface chemistry and properties to tailor the joint interface that maximizes strength, ductility, and corrosion resistance. This would enable us to develop an applied understanding of:

1. The localized metal forming and potential metallurgical bonding that develops during FSW techniques and USW methods.
2. The intermetallic formation at the interface strategies to tailor the joint interface that maximizes strength, ductility, and corrosion resistance.
3. How the process parameters influence the joint strength and performance of the joints and assemblies produced.
4. How both processes interact with existing corrosion protection methods (coatings) and how they affect the overall corrosion performance of hybrid Mg/steel assemblies.

This project is designed to overcome many of these technical barriers by performing three primary tasks. These tasks and associated deliverables are intended to enable a broader application of solid-phase joining technologies, while further facilitating the joining of Mg to steel.

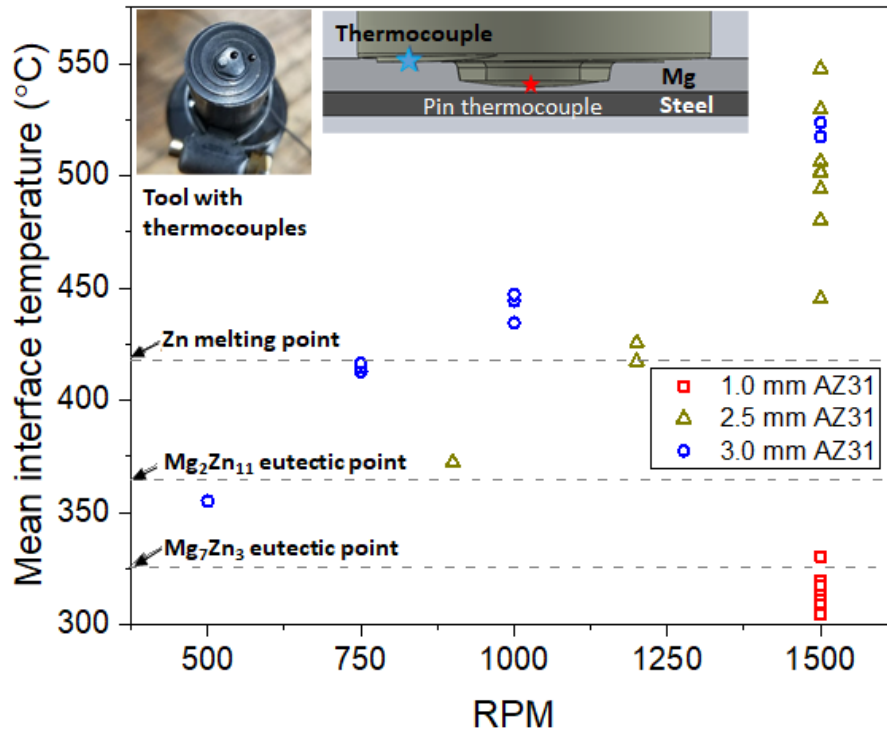
Results

A series of welding trials were conducted to establish baseline joint strength, interfacial chemistry, process variable measurements, and correlations. For the FSW process, two main approaches were studied: (1) conventional FSW such that the pin was not interacting with the bottom steel; and (2) friction stir assisted scribe technique, such that the cutter scribe machined the surface of the steel. For USW, a technique to observe high-frequency interfacial motion and heat generation was developed this fiscal year. Both of these joining processes were evaluated with and without zinc (Zn) coating on the steel.

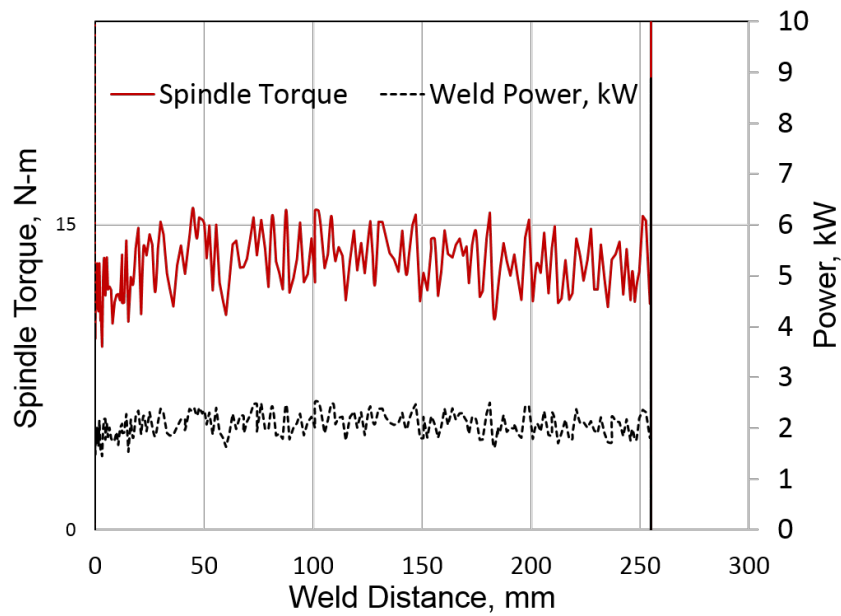
Process Measurements

FSW tools were instrumented with thermocouples at two locations—near the shoulder and at the tip of the pin. This enabled tracking of the weld temperature during the joining process. Figure II.3.B.1.(a) shows the mean interface temperature trends at various FSW trials ranging from 310 – 550°C at various revolutions per minute

(rpm) bit speeds for various thicknesses of AZ31 ranging from 1.0 mm to 3.0 mm. In addition to process temperature, several responses including spindle torque, power, and planar forces were recorded, as depicted in Figure II.3.B.1.(b). These data will function as input parameters into the process/structure-property modeling, non-destructive evaluation and process control applications.



(a)



(b)

Figure II.3.B.1. Data for (a) mean interface temperature trends at various FSW runs and (b) spindle torque and power required for length of welds. Source: PNNL

Instrumentation for *in-situ* process measurements were also performed for USW. The welds were made on the edge of the metal stacks with a dual-sonotrode ultrasonic welder. A speckle pattern was applied to the edge of both sheets prior to welding. A high-speed camera was used to capture the motion across the interfaces. Three material combinations were studied—Mg to Mg, Zn-coated DP590 to Mg, and bare DP590 to Mg. Figure II.3.B.2 shows the reciprocating occurrence of interfacial sliding (e.g., high amplitude) and sticking (e.g., low amplitude) during welding of the Mg-Mg stack. Interruptive welding experiments were conducted to produce Mg-Mg samples that were welded with varying welding times (e.g., 0.1 sec., 0.15 sec., 0.2 sec., 0.3 sec., 0.4 sec., and 0.5 sec.). Post-weld ultrasonic C-scan non-destructive analysis reveals the progressive formation of the weld bond, as shown in Figure II.3.B.3.

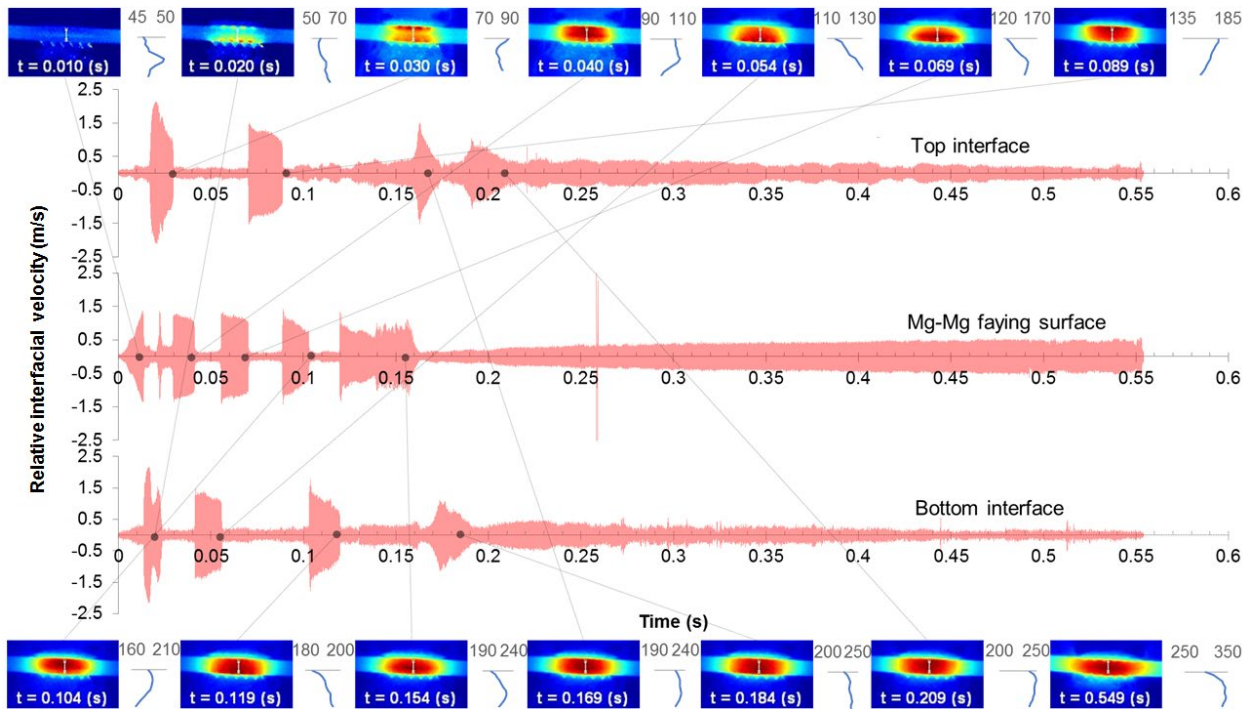


Figure II.3.B.2. Relative interfacial motion during the welding of the Mg-Mg stack showing that interfacial heat generation is associated with the occurrence of sliding (e.g., high amplitudes on the relative velocity curves) during USW. Source: ORNL.

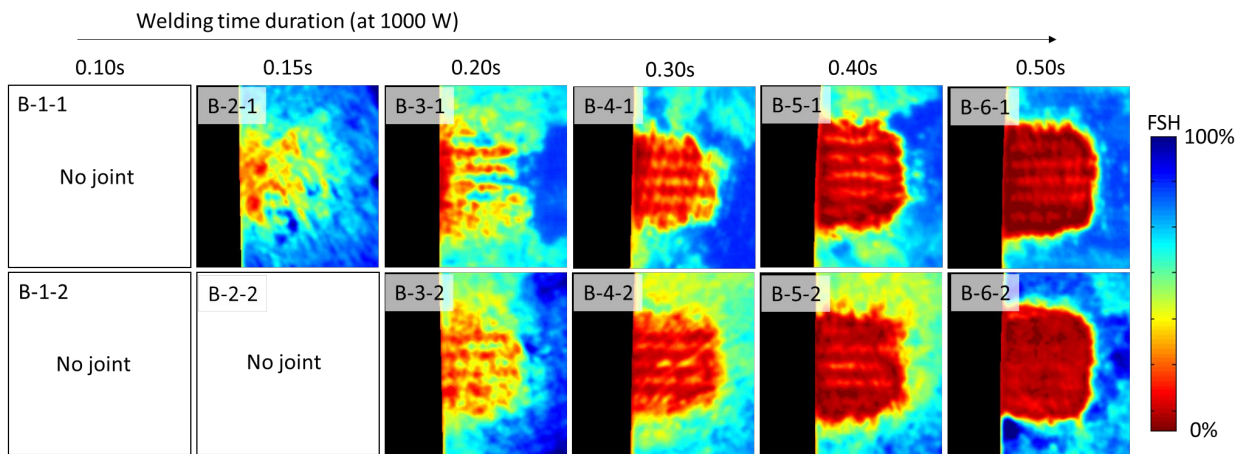


Figure II.3.B.3. Ultrasonic C-Scan non-destructive analysis of the Mg-Mg weld samples (14 mm × 14 mm image area). Source: ORNL.

Joint Structure and Properties

The load versus extension curves obtained from a lap shear test of Mg/steel joints made using FAST and USW are shown in Figure II.3.B.4.(a) and (b), respectively. A load bearing capacity corresponding to 5.3kN for a 25.4 mm (Mg 2.5mm, DP590 0.65mm)-wide sample was obtained for the FAST technique. A high-resolution DIC technique was utilized to capture strain history. Before eventual fracture, strain localized in the loaded side hook region of the top sheet (seen as the red area in the DIC strain map). Similar load bearing capacity was obtained in samples with or without Zn coating. While Zn-coated 270 MPa steel (results not shown) exhibited slightly higher joint strength compared to corresponding bare steel joints, in the case of DP590, the presence of Zn did not seem to affect joint strength (the interface chemistry variation between coated and uncoated are discussed later). This observation points to a fundamental gap in our understanding of the contribution of (1) mechanical feature (hook); and (2) interfacial bonding (i.e., either intermetallic compound [IMC], diffusion bonding, or combination). Efforts are underway to isolate the two facets of joints in association with the interface-by-design modeling task. A recent result obtained using DIC instrumentation suggested that a pronounced hook provided significantly greater ductility compared to the joint made with minimal hooking, while the load bearing capacity was found to be largely independent of the hook size for the studied joint. Simulating this observation in already existing FEA models can provide useful insight that can help decouple the contribution of hook and interface in the mechanical property of the joint.

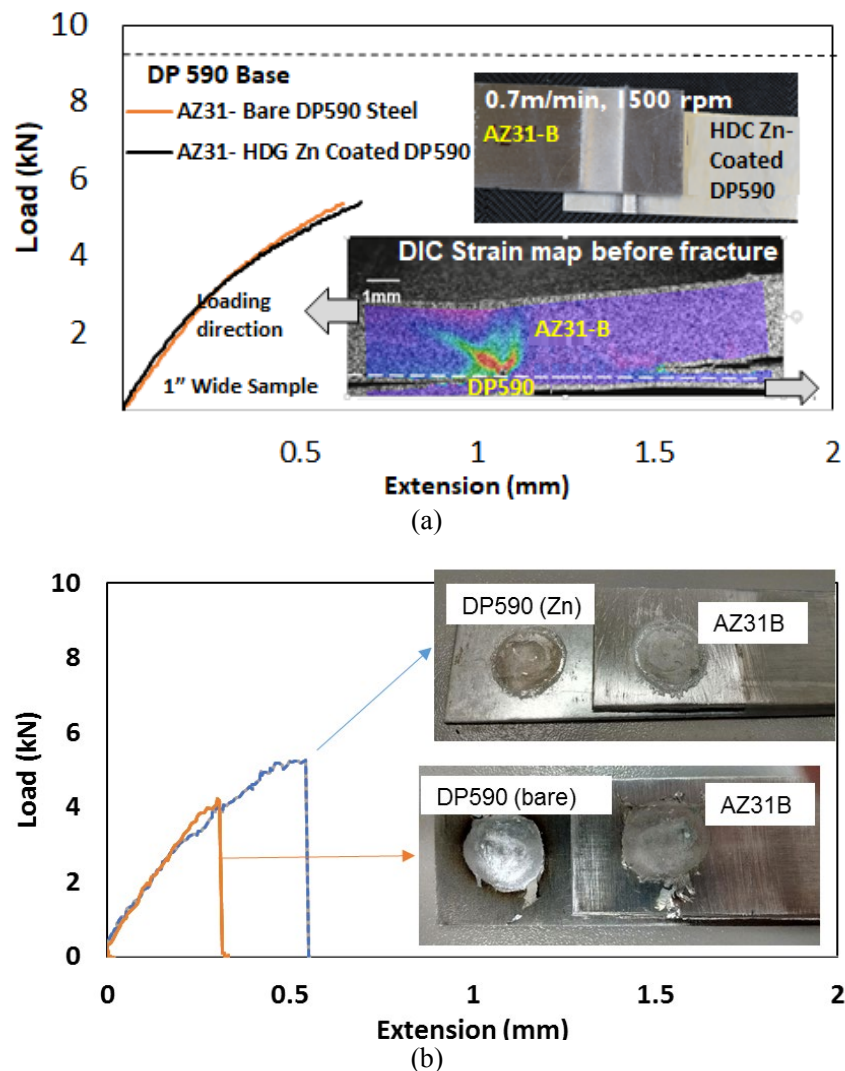


Figure II.3.B.4. Load vs. extension plot of for joints made between AZ31 and DP590 steel made using (a) friction stir scribe technique and (b) ultrasonic welds. Source: (a) PNNL and (b) ORNL.

For the USW case, a single-sonotrode ultrasonic welder was used to join AZ31B Mg to Zn-coated and bare DP590. Lap shear failure load was 4.7 ± 1.2 kN for AZ31B to Zn-coated DP590 and 3.9 ± 0.5 kN for AZ31B to bare DP590. In both joining processes, the fracture modes were interfacial. Figure II.3.B.5 shows the USW joint fracture surface. In the case of joints made with Zn-coated steel (see Figure II.3.B.5.(a)), molten Zn is seen squeezing out of the joint. Similar observations have been made in the case of the FSW joints, with and without a scribe cutter. Interface characterization of FSW joints are discussed later. USW made with a Zn coating shows an intermittent Mg/Zn IMC layer. Interrogation of the IMC layer, using advanced sub-micron level microscopy characterization techniques, has been planned to understand the possible role that the IMC layer may have played to provide greater resistance to fracture compared to the bare steel case. The fracture samples of FAST joints indicate the presence of an IMC layer consisting of a Mg Zn (18 at.%) phase on both sides, as is shown in Figure II.3.B.6. Stray steel fragments are also observed on the Mg side.

Figure II.3.B.7 summarizes the interfacial structures observed between the AZ31 and DP590 FSW joints. As the rotating friction stir scribe tool plunged and traversed into the lap configuration, as shown in Figure II.3.B.7.(a), characteristic [4] hook-like features were obtained on both sides of the joint, as shown in Figure II.3.B.7.(b). A SEM micrograph corresponding to the yellow boxed area (advancing side hook region) for four different cases of Mg/steel interfaces can be seen in Figure II.3.B.7.(c), (d), (e), and (f). Peak temperatures recorded using a thermocouple attached on the FSW tool are indicated on the top left corner of each figure. In the presence of a 20 μm Zn coating, a continuous layer of IMC is observed in the Mg/steel joint, as shown in Figure II.3.B.7.(c). Elemental evaluation using energy dispersive spectroscopy suggests the presence of an intermetallic compound with Mg- (30-40%) at. % Zn. It is speculated that the eutectic reaction between Mg/Zn occurred as the interface temperature of 507°C was measured, which is far beyond the two eutectic points in the Mg/Zn phase diagram. A magnified image of this eutectic IMC layer is shown in Figure II.3.B.7.(g) and an SEM image of the interface outside the weld region showing Mg/Zn eutectic IMC is shown in Figure II.3.B.7.(h).

It is important to note that the IMC layer is well-bonded to both of the Mg and Steel sides beneath the FSW tool. On either side of the hook region where deformation and pressure are reduced, the IMC appears to be detached from the steel side. Because the peak temperature was above the melting point of Zn, as shown previously in Figure II.3.B.1.(a), the interface region most likely had a pool of melting Zn as the FSW tool passed. Upon rapid cooling in the wake of the FSW tool, eutectic phases of Mg/Zn formed at the interface. Eutectic compounds were also observed away from the hook due to elevated temperature and pressure, as shown in Figure II.3.B.1.(h). It can also be surmised that some of the Zn/Mg eutectic may have been jetted/squeezed away from immediately under the FSW. In contrast to the IMC between the hooks, energy dispersive spectroscopy measurement suggests the presence of compounds that are much more Zn rich (e.g., Mg/Zn atomic ratio closer to 50%) outside of the weld region. Additionally, Zn/Mg eutectics are also observed farther away from the joint interface on the Mg underside. This unintended coating of base Mg may provide protection against general corrosion. Preliminary corrosion tests indicate reduced pitting corrosion in this area as shown in Figure II.3.B.8.

With decreased Zn coating, the extent of the IMC layer at the interface decreases, as shown in Figure II.3.B.7.(d) to (e). Nevertheless, a mechanically mixed layer of Mg and Fe was observed in the case of Figure II.3.B.7.(d). This distinct layer was also well-bonded with both the Mg and the steel region. In the case without any Zn coating Figure II.3.B.7.(f), no discernable interfacial compounds were observed by SEM.

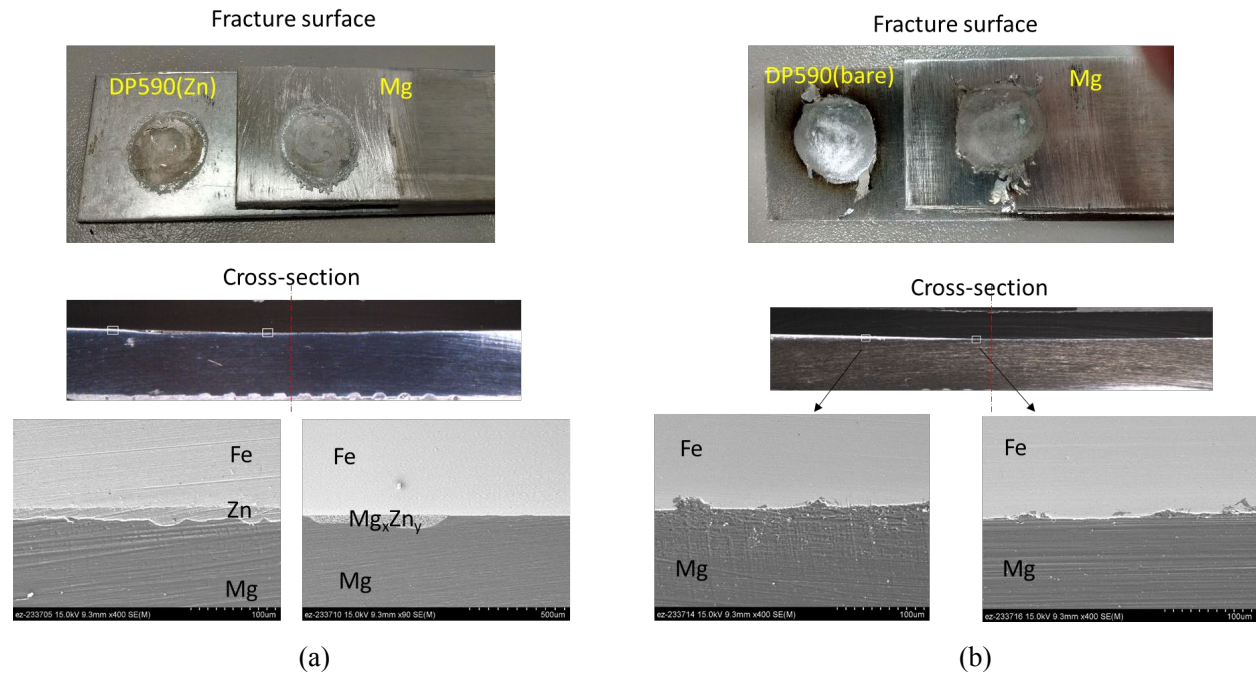


Figure II.3.B.5. Fracture surface and representative joint cross-section of DP 590/Mg joints made with (a) Zn-coating and (b) without Zn-coating with the USW joint cross-sections and micrographs shown below the fracture image. Source: ORNL.

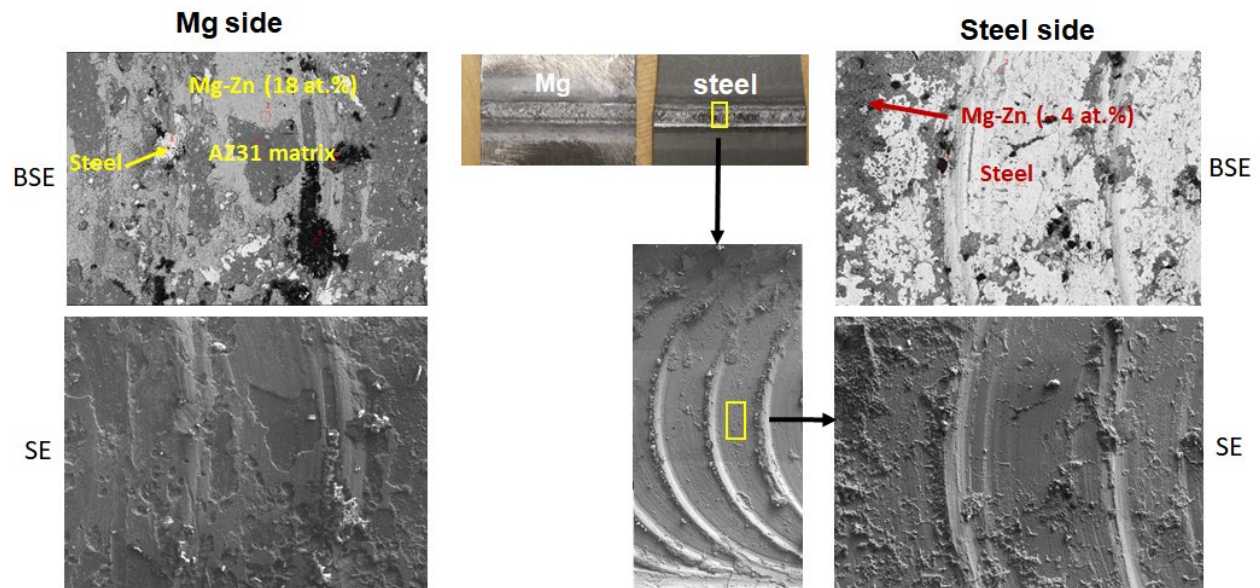


Figure II.3.B.6. Friction stir scribe joint fracture surface. Back-scattered and secondary images of Mg and Steel side show elemental and topography of the fracture. Source: PNNL.

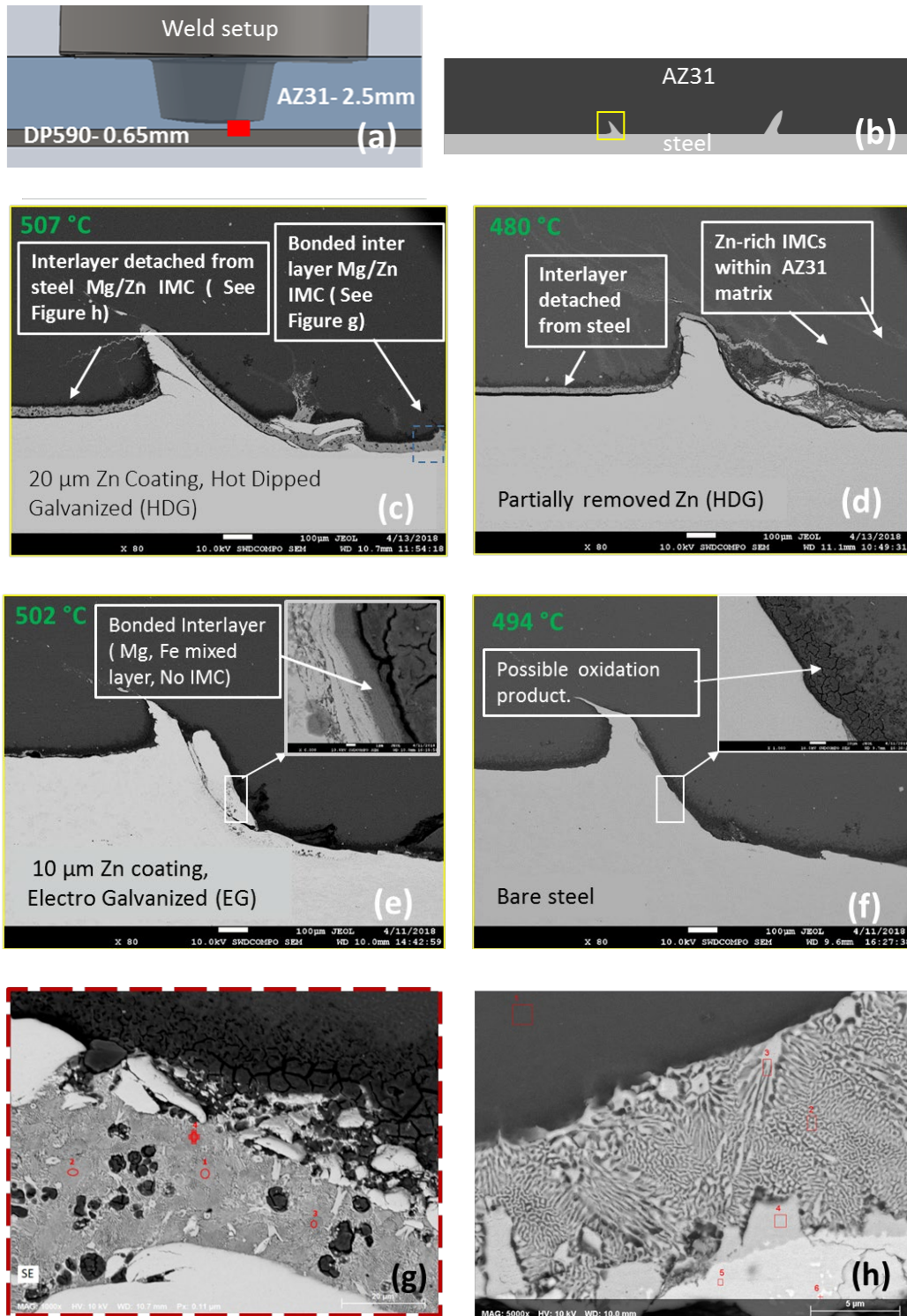


Figure II.3.B.7. Interfacial structures for (a) friction stir scribe setup showing material stackup and (b) schematic representation of welded joints showing hook features. The highlighted yellow square indicates the locations with a higher magnification of SEM images that are shown for joints made with (c) hot dipped galvanized (HDG) coating; (d) partially removed Zn coating; (e) 10 µm electro-galvanized (EG) coating; and (f) no coating. (g) Close-up SEM image of a continuous interlayer observed in the joint made with 20 µm Zn coating. (h) SEM image of interface outside the weld region showing Mg/Zn eutectic IMC. Source: PNNL.

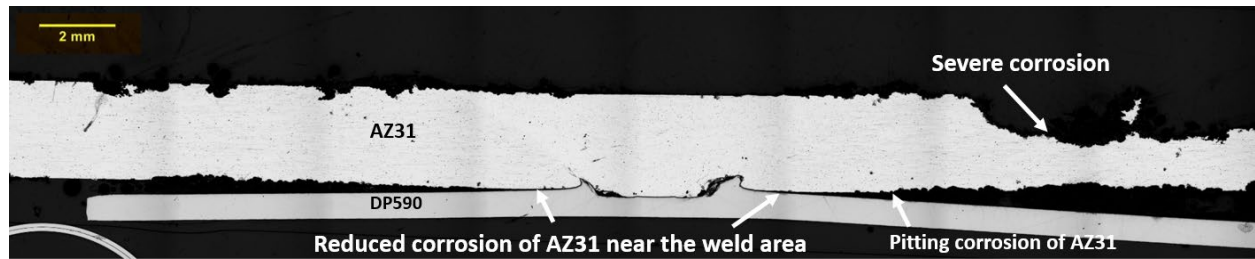


Figure II.3.B.8. Mg/Zn-coated steel joint cross-section that was exposed to 72 hours inside a salt-fog chamber per ASTM B117 showing areas with different extents of corrosion. Source: PNNL

Conclusions

This project aims to develop an applied understanding of two solid-state joining techniques to overcome barriers in joining Mg to steel such that more reliable and robust multi-material joints can be realized. This fiscal year, the project team at PNNL (FSW) and ORNL (USW) established methods for *in-situ* process variable measurements and produced and characterized joints between AZ31 and DP590 steel with and without Zn coating. In both of the joining methods, continuous or intermittent Mg/Zn eutectic compounds were observed at the interface region for welds made with Zn-coated steel. Lap shear testing showed a load bearing capacity of ~5kN per 25.4 mm of weld width with interfacial fracture mode. On the basis of results obtained this year, we will be utilizing advanced microscopy to further determine interface chemistry and properties so that precise mechanism of Mg/steel bonding can be established. This information coupled with interface-by-design modeling activity will enable the project team to create interface microstructure to tailor the joints for optimized joint strength, ductility, and corrosion performance.

References

1. Jana, S., Y. Hovanski, and G. J. Grant, 2010, "Friction stir lap welding of Mg-alloy to steel: A preliminary investigation," *Metall. Mater. Trans. A*, Vol. 41, No. 12, pp. 3173–3182. <https://doi.org/10.1007/s11661-010-0399-8>.
2. Patel, V. K., S. D. Bhole, and D. L. Chen, 2013, "Formation of zinc interlayer texture during dissimilar ultrasonic spot welding of Mg and high-strength low-alloy steel," *Mater. Des.*, Vol. 45, pp. 236–40. <https://doi.org/10.1016/j.matdes.2012.09.018>.
3. Wang, T., H. Sidhar, R. S. Mishra, Y. Hovanski, P. Upadhyay, and B. Carlson, 2017, "Friction stir scribe welding technique for dissimilar joining of Al and galvanized steel," *Sci. Technol. Weld. Joi.*, Vol. 23, No. 3, pp. 249–255. <http://www.tandfonline.com/doi/abs/10.1080/13621718.2017.1381460>.
4. Pan, T.-Y., Z. Feng, M. Santella, and J. Chen, 2013, "Corrosion behavior of mixed-metal joint of Mg to mild steel by ultrasonic spot welding with and without adhesives," *SAE Int. J. Mater. Manuf.*, Vol. 6, No. 2, pp. 271–78.

Acknowledgements

J. Chen and Y.C. Lin performed and characterized the USW at ORNL. At PNNL, welding and data analysis activities were supported by R. E. Rabby and L. Xiao. Testing and characterization of joints were performed by T. Roosendaal, H. Jiang, and A. Guzman. Supervisory roles by D. Herling and G. Grant are also acknowledged.

II.3.C Corrosion Protection of Dissimilar Material and Joining for Next-Generation Lightweight Vehicles (Arconic, Inc.)

Donald J. Spinella, Co-Principal Investigator

Arconic Technology Center
100 Technical Dr.
New Kensington, PA 15069
E-mail: dj.spinella@arconic.com

Daniel B. Bergstrom, Co-Principal Investigator

Arconic Technology Center
100 Technical Dr.
New Kensington, PA 15069
E-mail: daniel.bergstrom@arconic.com

Sarah Kleinbaum, DOE Technology Manager

U.S. Department of Energy
E-mail: sarah.kleinbaum@ee.doe.gov

Start Date: October 1, 2016 End Date: September 30, 2019
Project Funding (FY18): \$1,327,468 DOE share: \$1,049,274 Non-DOE share: \$278,194

Project Introduction

The goal of the project is to demonstrate the use of resistance spot rivets (RSRs) to join steel to Al and Al to CFRP on a prototype-scale. This new technology is being developed by Arconic to leverage the existing automotive RSW infrastructure for high-performance joining of steel to Al and Al to CFRP.

When using this process to join an Al sheet to a steel sheet, a steel rivet is fed to a spot-weld gun. The initial spot-weld cycle heats the steel rivet, which is then forced through the Al sheet. Upon contact with the steel sheet, a resistance spot weld is made between the steel sheet and the rivet. An alternative is to use a pilot hole in the Al sheet and directly weld the rivet to the steel sheet while simultaneously mechanically locking the Al sheet. The process can be reversed by employing an Al RSR, if joining through steel, or CFRP and welding to an Al sheet.

Objectives

In this project, the joint strength and corrosion performance will be documented with and without adhesives between steel and the Al sheet and Al and the CFRP sheet. The weld quality will be evaluated under different process conditions. The production viability will be evaluated with the feed system and integration of the feed system onto a robotic system.

Approach

The second year of this project focused on weld process development for the Al RSR and expanded corrosion testing at both OSU and Honda. All weld process development and electrode life (EL) testing were completed with the Al RSR for joining both Al to steel and Al to CFRP. OSU expanded the corrosion testing to include the American Society for Testing and Materials International (ASTM) G85 corrosion specifications [1–2] and was able to baseline various RSR configurations versus self-pierce rivet (SPR) and flow-drill screw (FDS) technologies. Additionally, OSU was able to complete serial cross-sectioning and characterized the type and depth of the galvanic corrosion attack. Production type condition (e.g., angle, gaps, alignment) testing and the multi-joint demonstrator were developed and planned for the next budget period.

Results

Table II.3.C.1 shows the test plan developed by the team to evaluate the process parameters and performance of RSR versus baseline joining technologies employed in multi-material assembly today. The test plan matrix consists of three broad categories for RSR—joining Al to steel with a steel-based fastener and joining both steel and CFRP to Al with an Al-based fastener. All-steel RSR, SPR, and FDS coupons were produced in budget period 1 (BP1), while the remaining conditions that were joined with the Al RSR were completed during the current budget period.

Table II.3.C.1. Test Plan Matrix for Preliminary EL, Mechanical, and Corrosion Tests.

Joint Stackup Description							Team Member Test Type			Budget Period
Rivet	Pilot	Top	Adh. *	Mid	Adh. *	Bottom	Arconic	Honda	OSU	
Steel Resistance Spot Rivet	Y	AURAL2 3.0mm	Y			JAC980 1.2mm	E	C	C	1
	Y	AURAL2 3.0mm	N			JAC980 1.2mm	M		C	1
	Y	AURAL2 3.0mm	Y	JAC980 1.2mm	N	JAC980 1.2mm	E	C	C	1
	Y	AURAL2 3.0mm	N	JAC980 1.2mm	N	JAC980 1.2mm	M		C	1
	N	MMHF-T4 1.0 mm	Y	Usibor® 1500 1.2mm	Y	JAC980 1.2mm	E	C	C	1
	N	MMHF-T4 1.0 mm	N	Usibor® 1500 1.2mm	Y	JAC980 1.2mm	M		C	1
	Y	AA6013-T4 2.0mm	N			JAC980 1.2mm	M		C	1
	Y	AA5754-O 2.0mm	N			JAC980 1.2mm	M		C	1
	Y	AA7055-T76 2.0mm	N			JAC980 1.2mm	M		C	1
	Y	AA6013-T4 2.0mm	N			JAC590 1.2mm	M		C	1
Aluminum Resistance Spot Rivet	Y	JAC980 1.2mm	Y			AURAL2 3.0mm	E	C	C	2
	Y	JAC980 1.2mm	N			AURAL2 3.0mm	M		C	2
	Y	JAC980 1.2mm	N	JAC980 1.2mm	Y	AURAL2 3.0mm	E	C	C	2
	Y	JAC980 1.2mm	N	JAC980 1.2mm	N	AURAL2 3.0mm	M		C	2
	Y	JAC980 1.2mm	Y	Usibor® 1500 1.2mm	Y	MMHF-T4 1.0 mm	E	C	C	2
	Y	JAC980 1.2mm	N	Usibor® 1500 1.2mm	N	MMHF-T4 1.0 mm	M		C	2
	Y	Semi-iso CFRP 4.0mm	Y			AA6013-T4 2.0mm	E	C	C	2
	Y	Semi-iso CFRP 4.0mm	N			AA6013-T4 2.0mm	M		C	2
	Y	Semi-iso CFRP 4.0mm	Y			AA6013-T4 3.0mm	E	C	C	2
Aluminum Self- Pierce Rivet	N	JAC590 1.2mm	Y			AA6013-T4 2.0mm	M		C	1
	N	JAC590 1.2mm	N			AA6013-T4 2.0mm	M		C	1
Steel Flow Drill Screws Baseline	Y	JAC980 1.2mm	Y			AA7055-T76 2.0mm	M		C	1
	Y	JAC980 1.2mm	N			AA7055-T76 2.0mm	M		C	1
Adh* - Adhesive between sheets						Test Code:	Electrode Life	Mechanical Testing	Corrosion	

In addition to rivet materials, two thickness (2T) and three thickness (3T) stackup combinations were evaluated. The effect of the Honda-supplied adhesive (Dow 5055C) between the Al and steel interfaces on both the joint and corrosion performance was also considered in the test matrix. Al, steel, and CFRP materials and thickness combinations were selected as target conditions and represent a broad class of applications that could be employed by the industry to achieve weight savings over today's baseline steel structure. A complete battery of tests (e.g., EL at Arconic followed by various corrosion tests at Honda and OSU) were either completed or are currently in progress for these target conditions.

Prior to samples being produced for EL and corrosion testing, each combination was tested at several weld settings, establishing the operating parameters to produce joints with sufficient strength. Weld process parameters were optimized through a series of cross-sectioning and peel-testing with the goal of establishing a weld diameter between the RSR and Al sheet that was roughly 3–5 times the square root of the sheet gauge with nugget penetration roughly 50%. Once the parameters were optimized for a combination, a series of joints would be produced at that setting without changing the weld equipment settings and electrodes. Joining through steel and CFRP materials employed the F7 and F5 series of rivets with pilot holes oversized 2 mm from the rivet pin diameter.

EL performance is an important metric in understanding the production robustness of the process. Typical production applications will dress the electrodes after a few hundred welds to maintain tight process control. A special EL procedure was developed in this program such that all members of the team would have access to samples through various stages of electrode wear. The goal was to demonstrate at least 100 consecutive RSR joints whose tensile shear strength (TSS) and cross-tension strength (CTS) values exceeded the targets established in BP1. An EL of 100 was selected since it is representative of electrode dressing values as seen in production RSW of an Al sheet. The TSS and CTS minimum strengths were established by internal Honda models that consider the material properties, gauges, and joint geometry. The mechanical performance of the EL coupons tested at Arconic was in the as-welded condition (i.e., without an additional paint-bake operation).

The EL test results can be seen in Figure II.3.C.1, Figure II.3.C.2, Figure II.3.C.3, and Figure II.3.C.4 for two of the Al RSR conditions evaluated. TSS was monitored at ten different intervals over 200 welds. At each test interval, six consecutive welds were assessed. CTS was monitored at two different intervals with either eight or nine consecutive welds. Figure II.3.C.1 shows the static strengths for two sheets of 1.2 mm 980MPa steel joined to 3.0 mm Aural2. The joint strength was measured between the Al to steel interface. Welds were also sectioned, polished, and etched during the EL, as seen in Figure II.3.C.2, with weld diameter sizes exceeding 8 mm. Weld conditions employed for this joint required roughly two-thirds the current of a spot weld if Aural2 was welded to itself. The TSS and CTS strengths exceeded the minimum targets throughout the 200 welds. Lower values in the TSS were observed during the first 25 welds, but after this break-in period, the strengths exceeded 5kN.

Figure II.3.C.3 and Figure II.3.C.4 show the EL performance of a 2T joint between a piloted CFRP sheet to Al. The strength performance of this joint showed excellent stability in both the TSS and CTS over 200 welds, achieving an average strength of 5.0 and 4.2 kN, respectively. In general, the CTS exceeded the minimum targets established for this joint while the TSS averaged approximately 2 kN lower. In the TSS mode a mismatch in strength levels between the Al rivet and AA6013-T4 along with higher levels of porosity in the weld nugget yielded performance less than the desired target. The average TSS and CTS strengths more closely matched the Al rivet trials on the 3 mm Aural2 indicating the rivet material and not necessarily the base material being welded against drives the joint target strength. The CFRP joints also exhibited higher levels of porosity in the weld nuggets which were associated with the pilot hole quality. All pilot holes were manually drilled into the CFRP since the recommended diameters were developed during the process development. It was observed that the hole-drilling technique caused small delamination which enabled Al to penetrate along ply layers during the welding process as can be seen in Figure II.3.C.4. Excessive wear was observed on the drill bits as well so small changes in the pilot diameter was also a variable during the testing. As the Al in the

rivet pin penetrated any delamination, radial voids could develop in the weld zone, reducing the overall strength. It is expected that improvements in the pilot hole quality should improve the overall consistency of the joint. Figure II.3.C.3 showed a slight break-in period similar to Figure II.3.C.1 where two CTS samples were slightly lower than the minimum target.

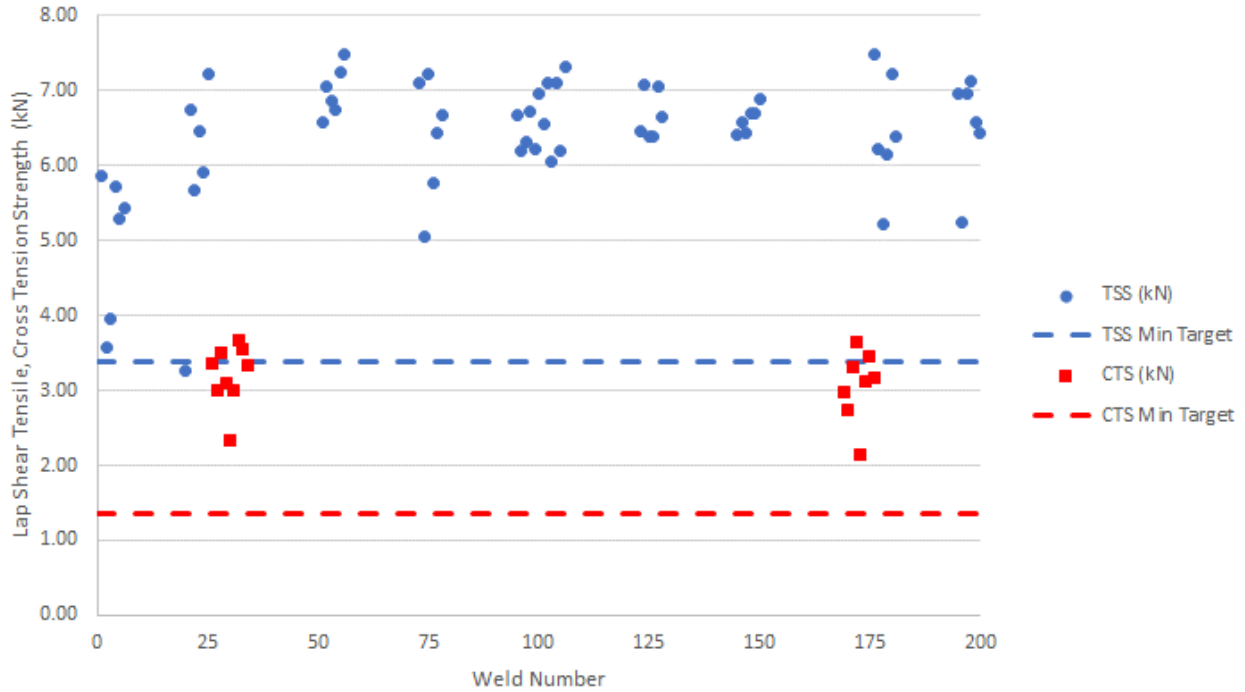


Figure II.3.C.1. EL Trial: 1.2 mm 980MPa to 1.2 mm 980MPa to 3.0 mm Aural 2-T7 (9 mm Pilot in Steel Sheets) through Dow 5055-C with F7-5 Rivet.

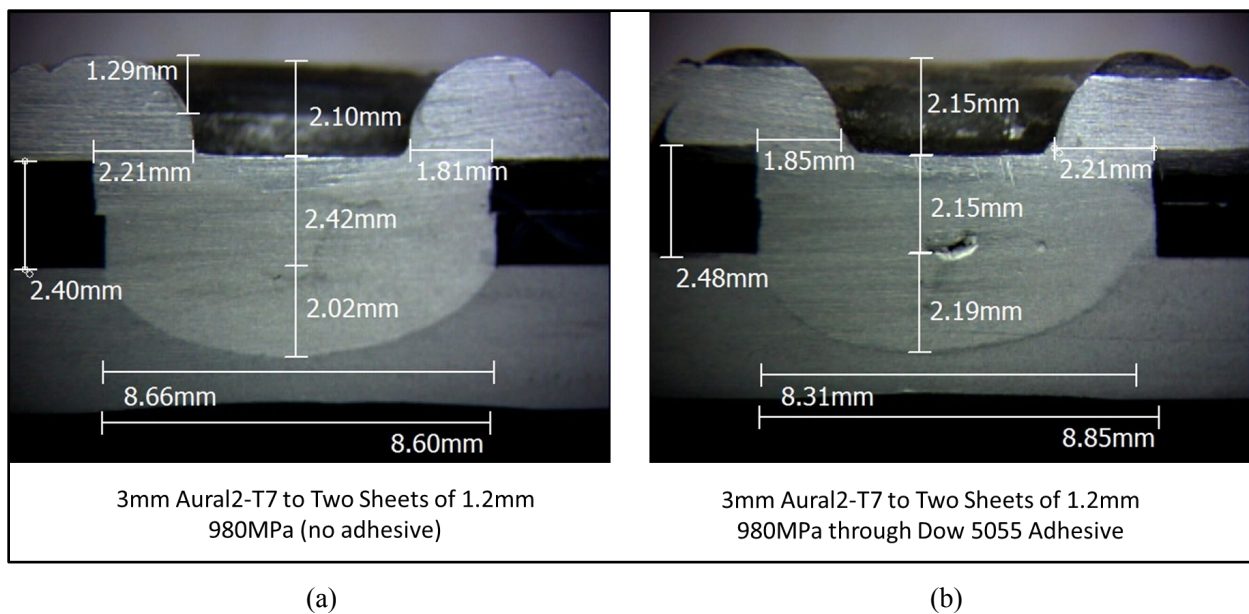


Figure II.3.C.2. Weld Sections of (a) 1.2 mm 980MPa to 1.2 mm 980MPa to 3.0 mm Aural 2-T7 and (b) using the F7-5 and 9 mm Pilot Holes in the Steel Sheets – left no adhesive, right Dow 5055-C adhesive. Source: Arconic.

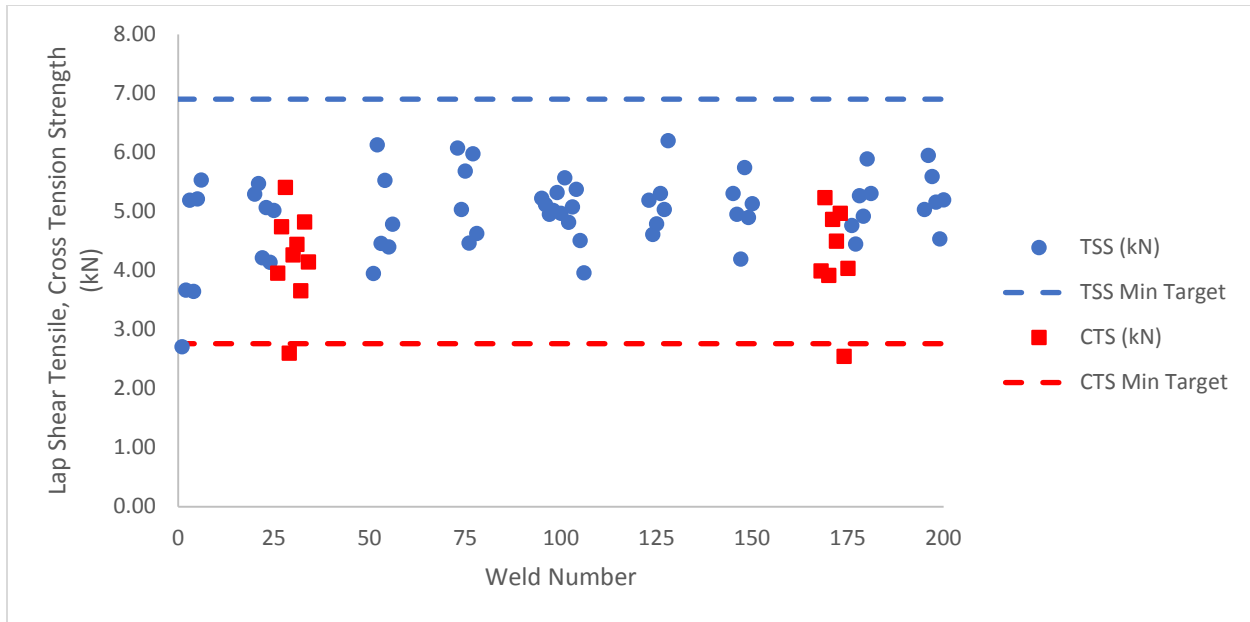


Figure II.3.C.3. EL Trial: 4.0mm CFRP to 3.0mm 6013-T4 with Dow 5055-C Adhesive, F7-7 Rivet, 9mm Pilot.

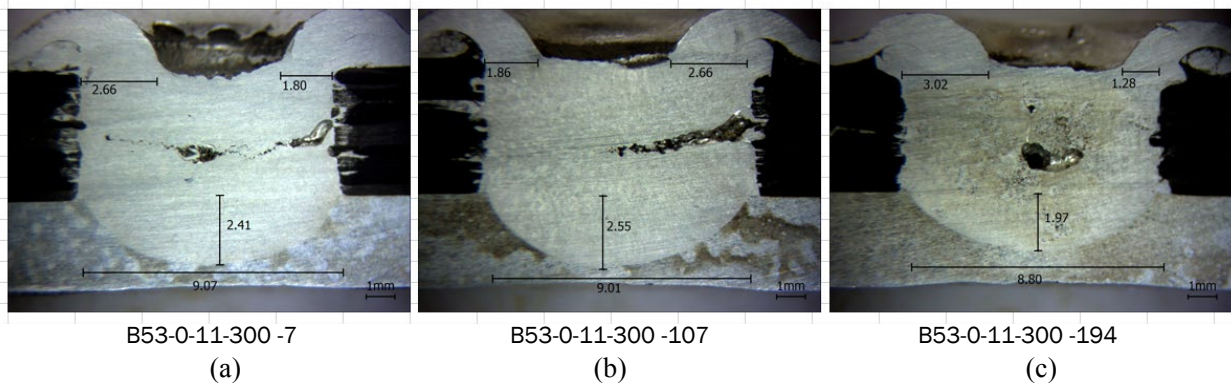


Figure II.3.C.4. EL Trial: 1.2 mm 980MPa to 3.0 mm Aural 2 (6 mm pilot) through Dow 5055-C with R4-6GA-V: (a) Weld #7 Section, (b) Weld #107 Section, and (c) Weld #194 Section. Source: Arconic.

The results of EL testing can be seen measured against the team targets in Table II.3.C.2. The testing exceeded both the strength and EL targets for both joint combinations with 3 mm Aural2. The 3T stackup between 0.85 mm MMHF-T4 and two thicknesses of steel only partially met the target conditions. In this stackup, the CTS mode exceeded the joint targets through 100 welds (dropped below minimum strength target at weld 175) while the TSS dropped below target at weld 97. Though the TSS dropped below the minimum threshold before 100 welds, the TSS and CTS yielded an average strength of 2.75 kN and 1.36 kN across the entire EL trial, exceeding the minimum targets. In general light Al gauges (under 1.0 mm) are more susceptible to electrode wear as compared to heavier gauges so it would be expected that more frequent electrode dressing may be required and/or further improvements in the weld schedules to optimize. Also, the CFRP to Al condition only partially achieved the performance targets. The CTS was able to exceed the minimum target throughout the entire trial but the overall TSS averaged only about 70% of the minimum target. The TSS performance would have exceeded the targets established for 3mm Aural2 but the AA6013-T4 strength drove a higher minimum strength that could not be achieved conventionally. As discussed previously the target strength may be better defined based on the rivet material and properties rather than the base sheet condition for this type of joint combination. Overall, the ability to join Al directly to CFRP with conventional RSW equipment was

demonstrated during this study and it is expected enhancements in the pilot hole quality and welding conditions will further improve the process consistency.

Table II.3.C.2. EL Target Criteria versus Actual Results.

Electrode Life Joint Stack-up Description							TSS Minimum, kN		CTS Minimum, kN		Electrode Life, No. of Welds	
Rivet	Pilot	Top	Adhesive	Middle	Adhesive	Bottom	Target	Measured	Target	Measured	Target	Measured
AL RSR	Y	JAC 980 1.2 mm	Y			AURAL2 3.0 mm	3.38	3.7	1.35	2.1	100	200
	Y	JAC 980 1.2 mm	N	JAC 980 1.2 mm	Y	AURAL2 3.0 mm	3.38	3.3	1.35	2.2	100	200
	Y	JAC 980 1.2 mm	N	USIBOR 1500 1.2 mm	Y	MMHF-T4 0.85mm	1.29	1.1	0.52	0.5	100	97 TSS 175 CTS
	Y	CFRP 4.0mm	Y			6013-T4 3.0mm	5.99	2.7	2.40	2.5	100	0 TSS 200 CTS
Below Target		Met Target		Above Target								

The principle that galvanic corrosion will occur when dissimilar materials are electrically connected by joining and exposed to a common corrosive environment is well-established. During galvanic corrosion, the more electrochemically active metal will corrode faster than in the uncoupled state, while the electrochemically noble metal will be protected and corrode more slowly than in the uncoupled state. OSU is characterizing and quantifying the galvanic corrosion performance of RSR joints of Al to steel and Al to CFRP. Within this, the ability of adhesives, pre-joining surface coatings, and e-coat/paint/sealant packages to protect the RSR joint against galvanic corrosion will be assessed. Additionally, comparisons are being made to the conventional joining technologies of SPR and FDS. Finally, any effect of electrode wear on corrosion performance will be evaluated. While the full body of work will be performed over the three BPs, all material combinations except for the Al to CFRP conditions (supplied in the third quarter of FY 2018) are in various levels of corrosion testing.

Differences in the galvanic corrosion performance of several Al alloys when coupled to 980MPa steel via RSR were analyzed by subjecting samples to up to 32.4 days of ASTM B117 exposure (see Figure II.3.C.5) and up to 21 days of ASTM G85 exposure (see Figure II.3.C.6). ASTM B117 exposure consists of a constant spray of 5% NaCl solution at 35°C. From the macro-observations shown in Figure II.3.C.5, AA7055-T76 and AA5754-O appear to suffer a more severe attack than Aural2 and AA6013-T4, which has been confirmed with measured electrochemical corrosion potentials. ASTM G85 exposure consists of a spray of 5% NaCl with pH adjusted to 3 by the addition of acetic acid for 45 minutes, a dry time for 120 minutes at 7-40% relative humidity, and humid time for 195 minutes at 95% relative humidity, all at 45°C. From the macro-observations shown in Figure II.3.C.6, AA7055-T76 and AA5754-O appear to suffer a more severe attack than the Aural2 and AA6013-T4, which was again confirmed by measured electrochemical corrosion rates. Serial cross-sectioning was also employed to quantify the depth of the attack.

To understand the performance of RSR joints compared to standard joining methodologies, samples joined by FDS and SPR were exposed to ASTM B117 and G85. When compared to RSR samples of the same metallurgy (i.e., AA7055-T76 to 980MPa steel, etc.), there were no observable differences via macro-observation in corrosion performance after ASTM B117 or G85 exposure between RSR and SPR (see Figure II.3.C.7) or between RSR and FDS (see Figure II.3.C.8). Serial cross-sectioning is planned to further understand and quantify any difference in performance due to the joining technology used.

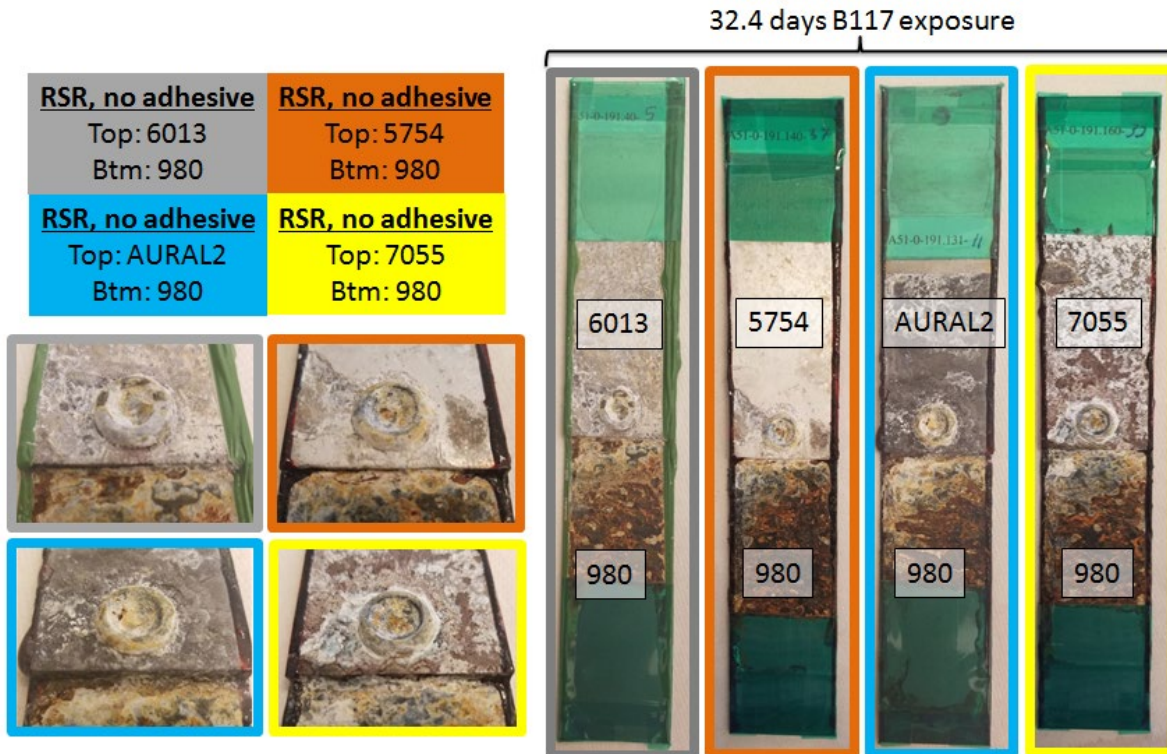


Figure II.3.C.5. Macro-photographs of RSR samples after 32.4 days of ASTM B117 exposure. Source: OSU.

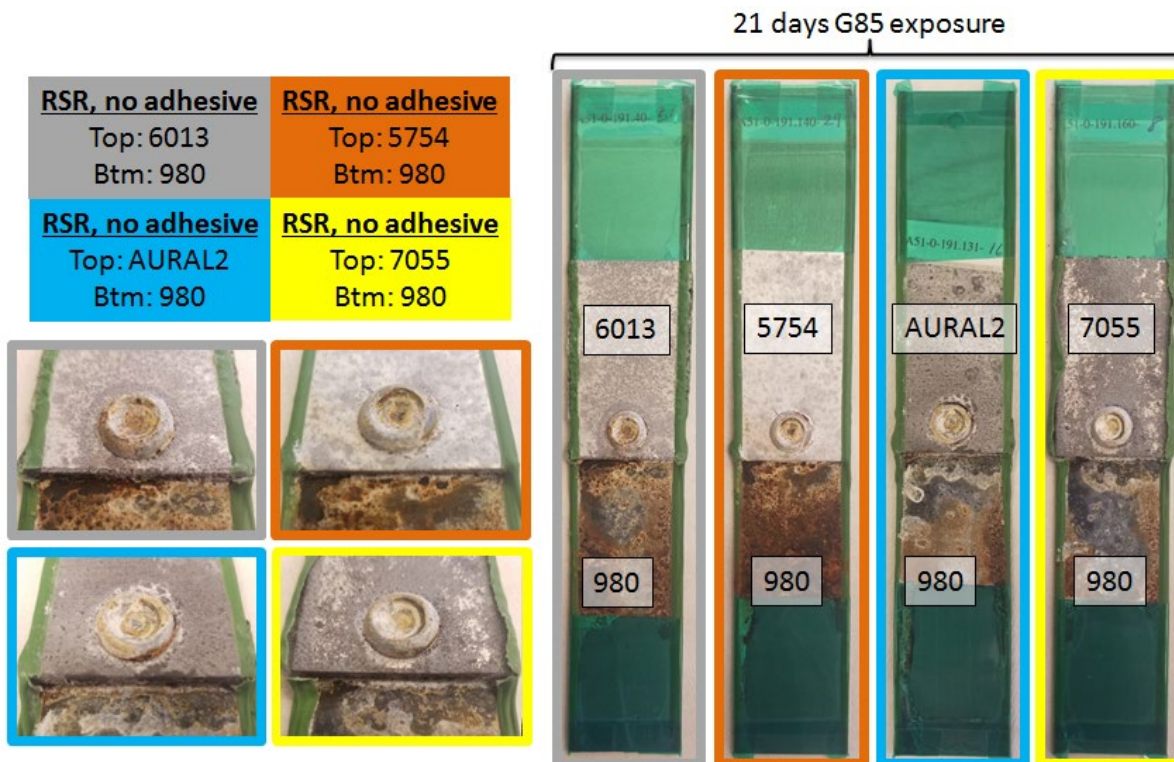


Figure II.3.C.6. Macro-photographs of RSR samples after 21 days of ASTM G85 exposure. Source: OSU.

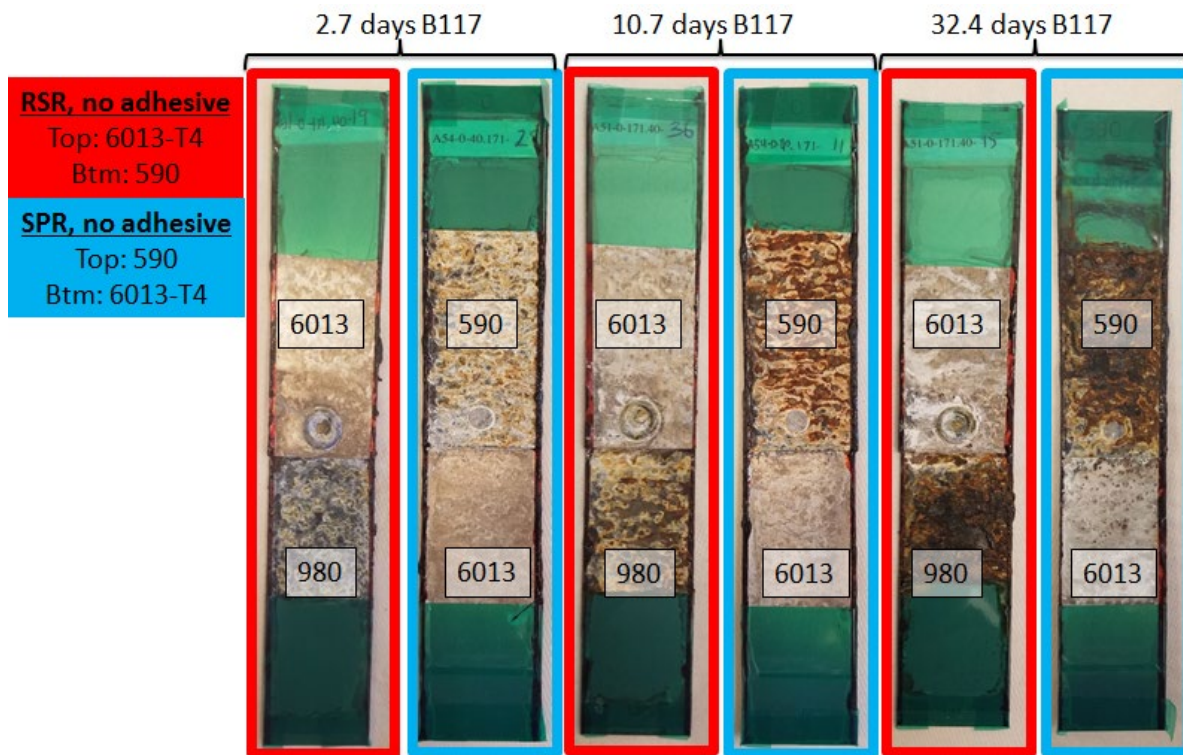


Figure II.3.C.7. Macro-photographs of RSR and SPR joints of the same metallurgy after ASTM B117 exposure. Source: OSU.

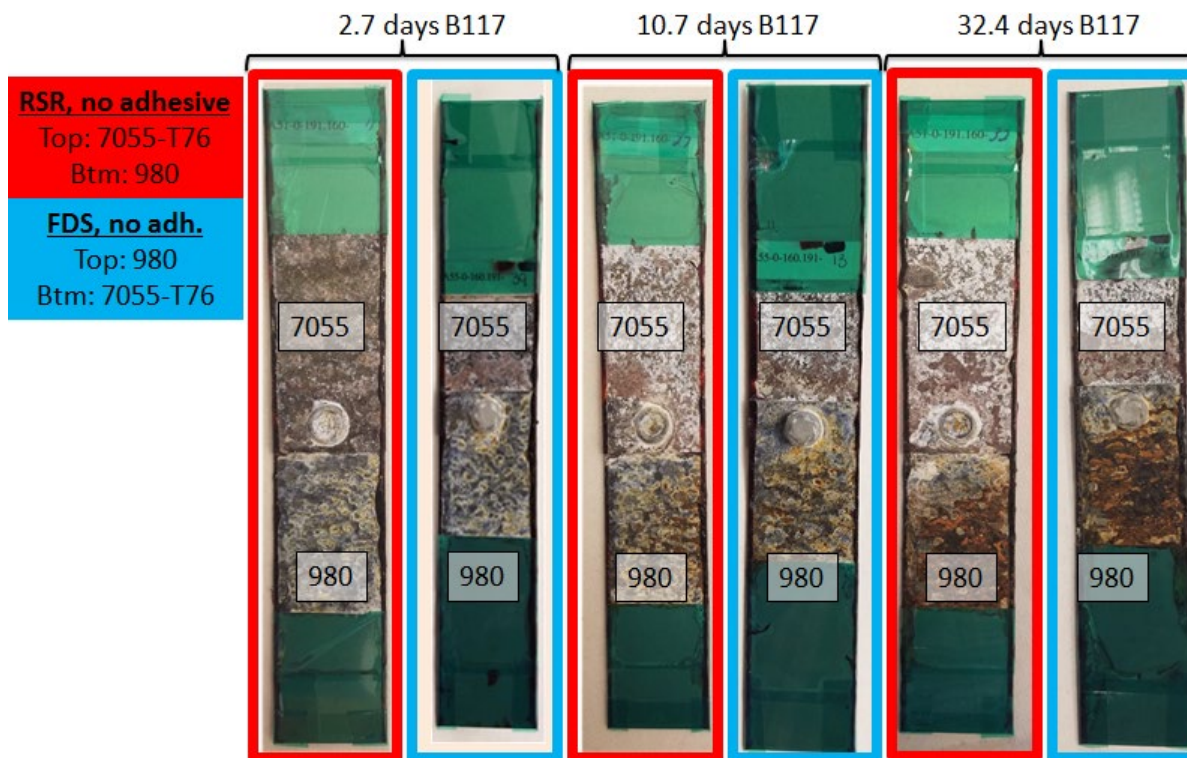


Figure II.3.C.8. Macro-photographs of RSR and FDS joints of the same metallurgy after ASTM B117 exposure. Source: OSU.

ASTM B117 and G85 were used to analyze the effect of adhesive in the joint and the effect of adding a third sheet to the stackup. To understand the effect of adhesive on corrosion performance, RSR joints of the same metallurgy with and without adhesive applied were examined after ASTM B117 and G85 exposure. For all of the stackup types examined, macro-observation did not reveal differences between samples with and without adhesive. Additionally, macro-observations of two and three sheet stack-ups did not reveal differences in corrosion performance.

To understand any effects of electrode wear on corrosion performance, RSR joints of the same metallurgy fabricated at different points in the EL were exposed to ASTM B117 and G85 for various times. Sets of four samples per joint-type were chosen for each exposure time: early (~20 welds), middle-early (~80 welds), middle-late (~140 welds), and near end (~180 welds) of a typical electrode dressing interval. Under macro-level observation, there was no discernible difference in corrosion performance as a function of where in the EL the joint was produced.

Samples exposed to ASTM B117 and G85 were mechanically tested to failure to determine the effect of corrosion on the maximum sustained load of a joint for the exposure durations examined. For both corrosion test types, there was no change in the maximum sustained load across the various Al alloy families. Figure II.3.C.9 shows that when joined to 980MPa steel, RSR stack-ups of AA7055-T76 failed at the highest loads, while the other alloys decreased in order of AA6013-T4, Aural2, and lastly AA5754-O. Mechanical tests of AA7055-T76 joined to 980MPa steel by RSR and FDS show RSR joints consistently fail at higher maximum sustained loads than FDS joints, as shown in Figure II.3.C.10 and Figure II.3.C.11. Mechanical tests of AA6013-T4 joined to 590MPa steel by RSR and SPR show RSR joints consistently fail at higher maximum sustained loads than SPR joints, as shown in Figure II.3.C.11.

Serial cross-sectioning was performed on RSR samples of 980MPa steel joined to AA5754-O, AA6013-T4, and AA7055-T76, as shown in Figure II.3.C.12. These samples were exposed to ASTM G85 for 21 days, mounted in epoxy, cut in half, and polished outward from the rivet towards the outer edge of the sample. Localized corrosion was observed to be more severe near the right crevice than near the left crevice. The separation of the RSR and the bottom steel plate is an artifact of sample cutting and does not indicate separation during exposure. In all cases, no corrosion was observed on the steel rivet or the steel.

Bulk electrochemical properties were measured to baseline galvanic corrosion to rank what alloy is the anode or cathode. Initially, several electrochemical test methods were explored to find the most appropriate for all materials used in this program. The syringe cell method allowed for the characterization of all materials without issue of cell leakage or crevice corrosion and was chosen over Microcell and other flat cell methods.

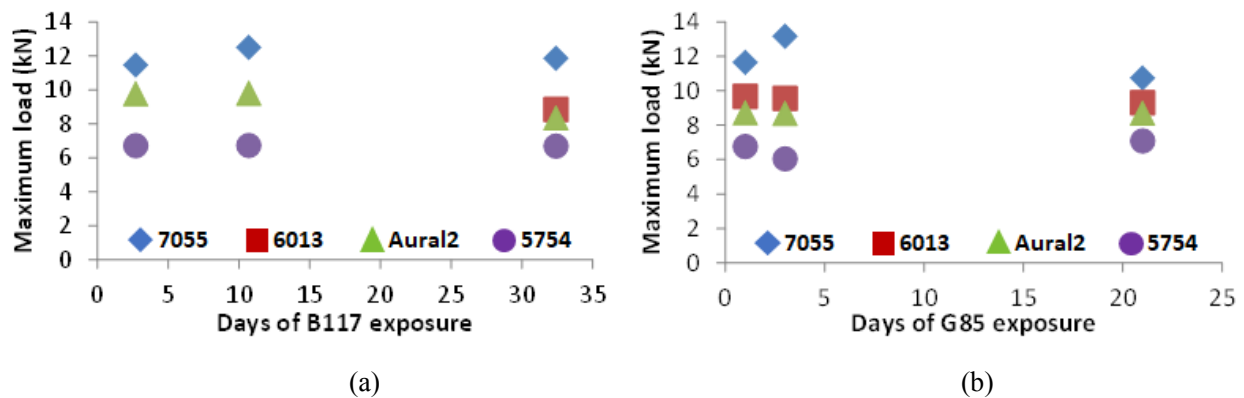


Figure II.3.C.9. Mechanical testing results of steel RSR coupons made with 980MPa steel and various Al alloys after (a) ASTM B117 and (b) G85 exposure.

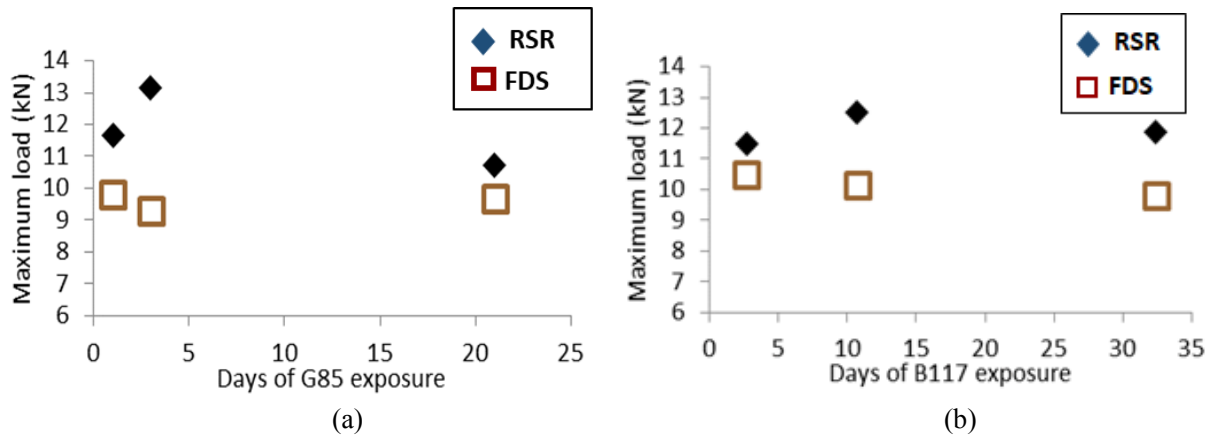


Figure II.3.C.10. Mechanical testing result of steel RSR and FDS coupons made with AA7055-T76 and 980MPa steel after (a) ASTM B117 and (b) G85 exposure.

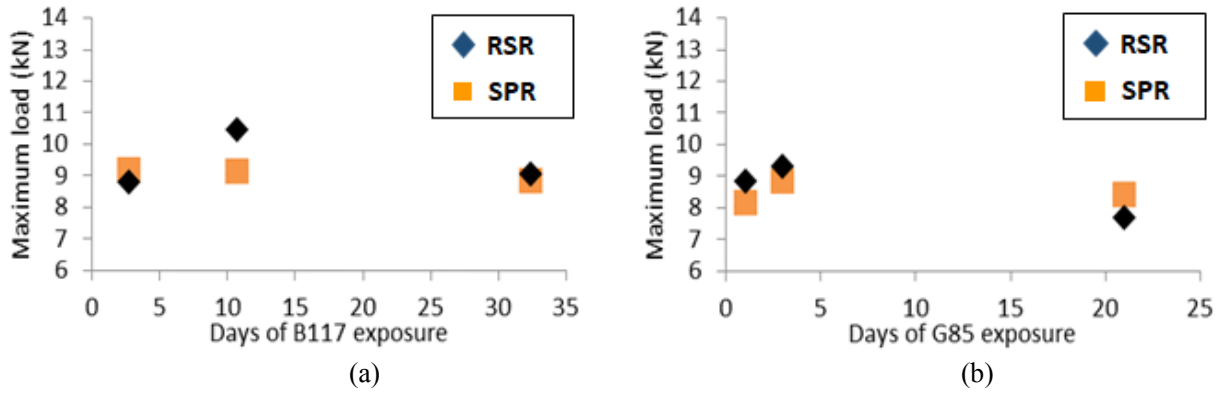


Figure II.3.C.11. Mechanical testing results of steel RSR and SPR coupons made with AA6013-T4 and 590MPa steel after (a) ASTM B117 and (b) G85 (right) exposure.

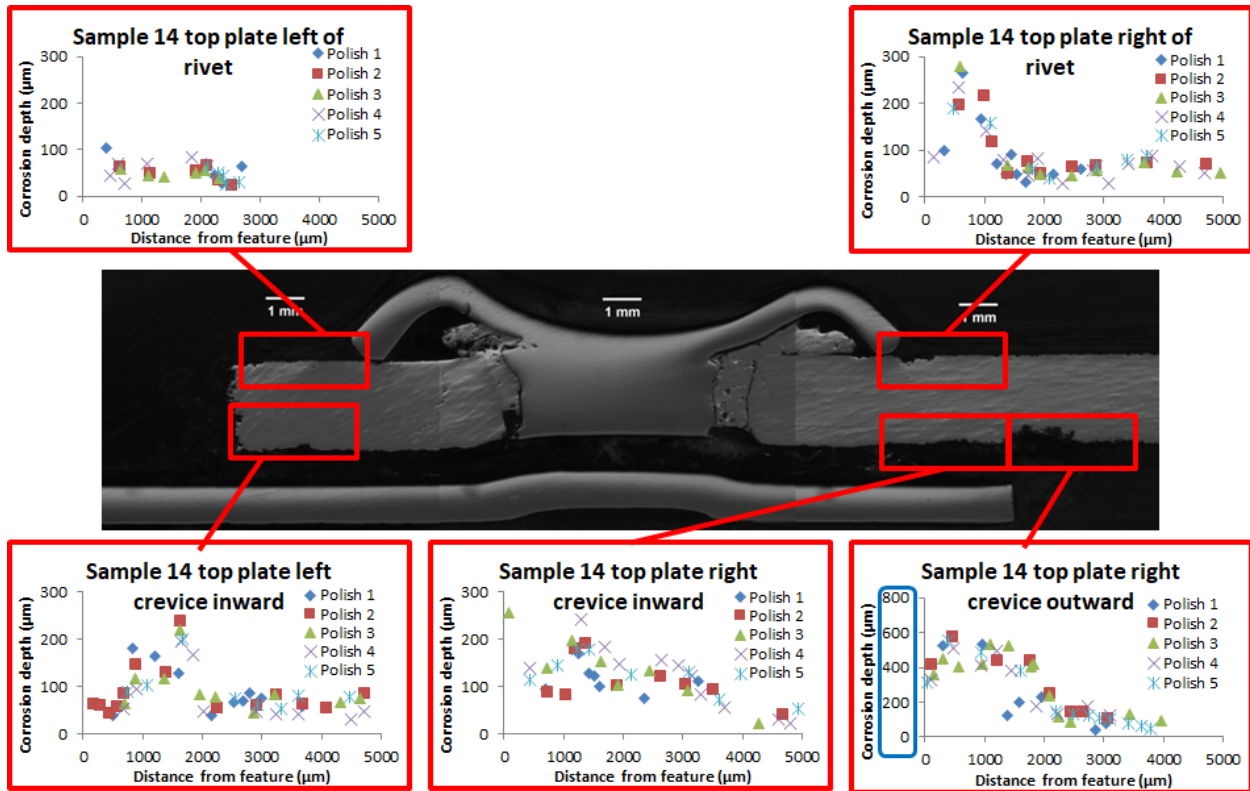


Figure II.3.C.12. Cross-section and corrosion depth attack of a steel RSR joint between AA7055-T76 sheet (top) and 980MPa sheet (bottom) exposed to ASTM G85 for 21 days. Red circles highlight areas of accelerated corrosion. Source: OSU.

The results for the syringe cell testing in both 5 wt% NaCl at neutral pH (to represent ASTM B117 solution) and 5 wt% NaCl with pH adjusted to 3 by the addition of acetic acid (to represent ASTM G85 solution) are shown in Figure II.3.C.13. The 590 and 980MPa steels are cathodic to all Al alloys in this study, which is consistent with that found in 5 wt% at neutral pH. Again, Aural2 and AA6013-T4 have lower average galvanic corrosion rates than AA5754-O and AA7055-T76. When comparing results between the two electrolytes, it can be seen that the ASTM G85 solution is more aggressive than the ASTM B117 solution, as would be expected given the more acidic pH. Al alloys exhibit roughly three times higher galvanic corrosion rates in the ASTM G85 solution than the ASTM B117. This is also illustrated in Figure II.3.C.13 by a black box that shows the ASTM B117 galvanic corrosion rates overlaid onto the ASTM G85 polarization curves. It is important to note that while this information gives us a corrosion current density (i.e., a rate of corrosion for the Al alloy in each couple), it cannot be used definitively as it does not consider the cathode-to-anode area ratio, the rivet material, solution conductivity, or any effects of adhesive.

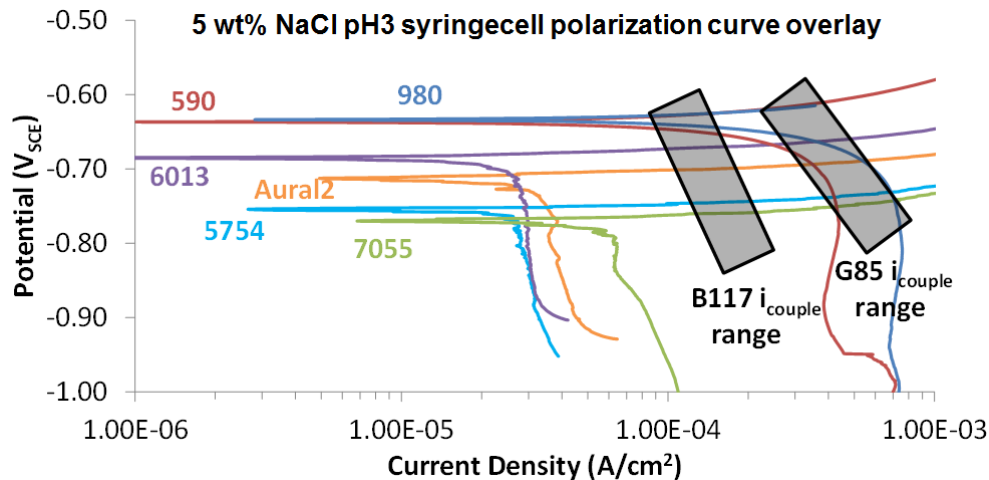


Figure II.3.C.13. Syringe cell polarization curve overlays of in 5 wt% NaCl solution acidified to pH 3. The black box shows the galvanic corrosion rates in a ASTM B117 like solution (5 wt% NaCl at neutral pH).

Conclusions

During the second year of this project, the weld process development for the Al RSR was completed and corrosion work continued at both OSU and Honda. The weld testing included joining to both Al to steel and Al to CFRP. Mechanical performance for the Al RSR coupons met acceptable targets for strength over the EL.

OSU expanded the corrosion testing to include the ASTM G85 corrosion specification and was able to demonstrate that various RSR configurations met or exceeded the performance of baseline SPR and FDS technologies in similar material combinations. OSU performed serial cross-sectioning for G85 exposed joints and characterized the type and depth of the galvanic corrosion attack. Honda is conducting long-term corrosion exposure testing for both TSS and CTS style specimens that were produced during EL testing. Mechanical testing will be completed early in the next budget period.

A bowl-fed rivet delivery system was mounted on a robot gun and RSR joints were performed at multiple angles to demonstrate feasibility. A new rivet delivery system will be installed in the next budget period. This unit has been designed to fit within tight spaces with limited accessibility. Production type conditions (e.g., angle, gaps, alignment) and the multi-joint demonstrator were developed and planned for testing in the upcoming budget period.

References

1. ASTM International, 2018, *Standard Practice for Operating Salt-Spray (Fog) Apparatus*, ASTM B117-18, West Conshohocken, PA, USA. <https://doi.org/10.1520/B0117-18>.
2. ASTM International, 2018, *Standard Practice for Modified Salt-Spray (Fog) Testing*, ASTM G85-11, West Conshohocken, PA, USA. <https://doi.org/10.1520/G0085-11>.

II.3.D HPC Tools to Advance Materials Joining Technology (General Motors)

Blair E. Carlson, Co-Principal Investigator

General Motors Global R&D
30470 Harley Earl Blvd.
Warren, MI 48092
E-mail: blair.carlson@gm.com

Greg Frederick, Co-Principal Investigator

Electric Power Research Institute
1300 West W.T. Harris Blvd.
Charlotte, NC 28262
E-mail: gfrederi@epri.com

Zhilli Feng, Co-Principal Investigator

Oak Ridge National Laboratory
1 Bethel Valley Rd.
Oak Ridge, TN 37831
E-mail: fengz@ornl.gov

Sarah Kleinbaum, DOE Technology Manager

U.S. Department of Energy
E-mail: sarah.kleinbaum@ee.doe.gov

Start Date: February 1, 2017	End Date: June 30, 2018	
Project Funding (FY18): \$354,600	DOE share: \$295,500	Non-DOE share: \$59,100

Project Introduction

The multidisciplinary nature of welding manufacturing and the complicated interactions between the highly localized welding heat source and the material to be welded makes the simulation of welding processes and predictions of the performance of welded structures extremely demanding in computational resources. At the fundamental level, computational welding process simulations essentially solve the transient heat transfer, the transient stress/deformation and the evolution of microstructure distribution that are closely coupled. Even the basic thermomechanical part is computationally demanding, due to: (1) the highly nonlinear thermal-mechanical responses of materials; (2) the fine mesh (on the order of 10^{-3} meter) and short time increment (on the order of 10^{-2} second) necessary to capture the transient and extremely high-temperature, stress, and microstructure and property gradients in the weld region caused by the localized moving welding heat source; (3) the large number of elements to represent complicated geometric shapes and large dimension of the welded components, such as an auto-body structure (with 10^6 to 10^8 degrees of freedom to solve); and (4) the relatively long welding fabrication time (in hours to weeks) of complex structures, such as an auto-body structure, or the construction of a component of a nuclear reactor.

Most welding simulations performed today are done on workstations due to the lack of scalable software and models that can take advantage of HPC clusters. The needs for robust simulation codes that run on HPC hardware can be illustrated with the two real-world component level examples shown in Figure II.3.D.1. The first example, in Figure II.3.D.1.(a), is a roof assembly in a car body structure. It consists of one large roof panel, two large body side panels, one roof bow underneath the roof, and many other connected components. Two laser-seam welds are needed to assemble the roof with the body sides, using many clamping tools and fixtures. The total welding assembling time was in the range of 3–5 minutes. Welding-induced dimensional changes and residual stress were the major concerns. Computational modeling could be used to optimize the welding sequence, clamping force, and fixture design to minimize the dimensional changes and residual stress

to meet the specification. However, modeling welding assembly of this component with consideration of the entire body structure is practically impossible due to the large degrees of freedom being involved. Engineers attempted to greatly simplify the model by only considering the roof, two body sides, and roof bow components, and simplified clamping constraints. Still the much-simplified model resulted in a finite element method (FEM) model running for three days on workstation computers, which was impractical to meet the product development schedule.

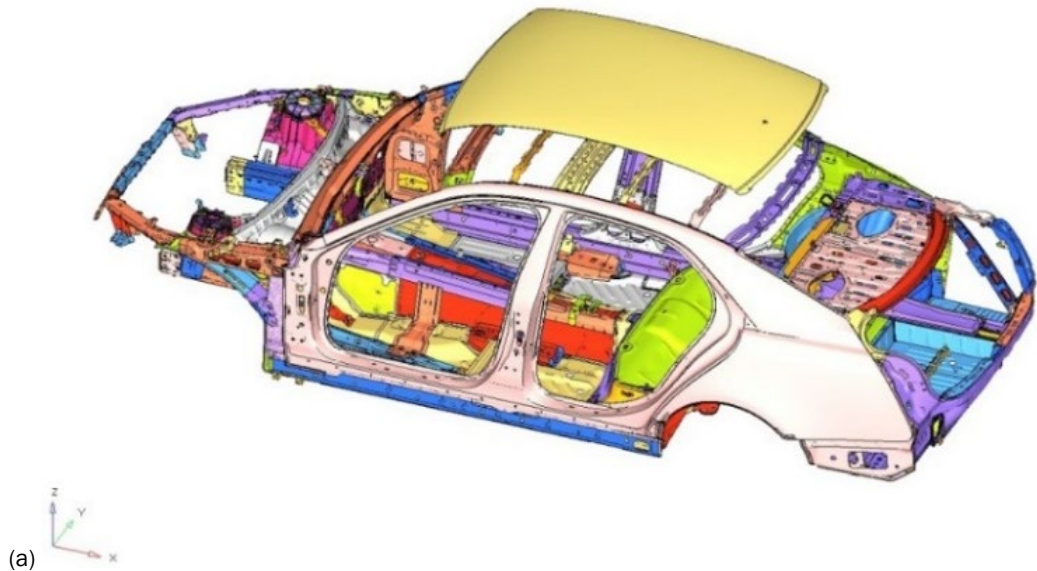


Figure II.3.D.1. Illustrative real-world examples taken from the: (a) automotive; and (b) nuclear power industry, for which HPC welding simulation would make a major impact. Source: (a) GM; (b) Electric Power Research Institute.

The second example is taken from a recent repair welding application to mitigate the stress corrosion cracking (SCC) problem facing the nuclear industry. Figure II.3.D.1.(b) shows a full-size dissimilar metal mockup weld connecting a 36-in diameter stainless steel pipe to the nuclear reactor vessel made of low-alloy steel. This weld connection is a critical component of the nuclear reactor system that provides coolant in the process of converting nuclear energy to electricity. This dissimilar metal weld (DMW) requires the use of multiple weld materials to ensure high-quality welding. It consists of several hundred weld passes and multiple layers, with over 1,500 lbs. weld metal deposited. This repair weld must be designed and engineered to ensure the structural integrity and safe operation of the nuclear reactor for 30–60 additional years. Full three-dimensional (3D) weld simulations would be extremely beneficial to optimize the engineering of this repair weld to control the weld residual stress and prevent SCC from happening again. However, today's industry modeling capability, in terms of both computational resources and modeling approaches, is simply inadequate for the full 3D simulation. Instead, industry primarily relies on expensive (in the range of million(s) of dollars per case) and time-consuming (several months to years) experimental weld mockup and residual stress measurements, augmented with simplified approximate modeling analysis, to generate the necessary technical basis for the weld repair of critical nuclear reactor components.

Today, industry can only use weld process modeling tools for limited, simple cases, which generally require considerable simplification to obtain approximate solutions in a reasonable amount of time. This means that potential reductions in expensive and time-consuming experimental trial and error late in a vehicle or a reactor program, where physical changes are costly, are not realistic by application of conventional weld simulation tools.

Objectives

This HPC4Mfg project was an initial effort aimed at developing and demonstrating the potential of a novel in-house HPC FEM-based code, specifically designed for broad welding and similar manufacturing processes, such as metal additive manufacturing simulation applications. The novelty included the efficient use of computational algorithms and schemes that generally have better scalability on massive parallel HPC systems.

For this initial effort, a measurable technical goal was to demonstrate a substantial increase in computational performance on cluster HPCs with 500 to 2,000 cores, on the order of 100x compared to workstation-based welding simulations today. This means a reduction of wall clock time of computation for a welding simulation from over 12–15 weeks on today's workstation computers to less than 24 hours using an HPC system and computational codes in this project. To the industry members of the project, such computational performance improvements means that the HPC welding process modeling tools could be realistically utilized to effectively analyze various welding fabrication options/scenarios to minimize dimensional distortion, or proactively mitigate the detrimental impact of welding-induced residual stresses within a timeframe, such that expensive and time-consuming iterative physical trial and error can be avoided. A secondary objective is, through this research, to identify critical barriers and gaps in HPC codes, that once solved in the future, would lead to further major breakthroughs in application of HPC for welding simulations.

Approach

In this project, we explored and advanced the ORNL code for large-scale simulation as the basis for a HPC modeling framework for weld simulation and compared this to a commercially available software, ABAQUS. An essential requirement for this code is that it must have robust thermo-electric-plastic stress analysis capability with acceptable scalability on massive parallel computers. The initial HPC weld modeling development and demonstration executed in this project were on cluster-type HPC computers with 500 to 2,000 CPUs or graphics processing units (GPUs). This eases the transfer of the developed HPC weld modeling tool to the industry for near-future applications.

The welding process to be simulated in this project is the laser welding process. It is a high productivity process with increased use in the automotive industry. It is also considered for new construction of advanced

nuclear reactors and life extension of existing nuclear reactors in the U.S. To demonstrate the potential and relevance of HPC weld modeling with broad industrial applications, two real-world welding problems were studied. The first is a laser-welded roof panel from GM for automotive lightweighting. The second is welding and cladding of DMWs from EPRI, which has been identified as a critical component affecting the safety and reliability of long-term operation of nuclear power plants. Through their cost share contributions, both GM and EPRI provided actual experimental results of representative welded structures outlined above to assist the model development and validation.

Our project is based upon close collaboration with ORNL because of their well-known capability in welding process and performance simulations. ORNL has worked with both GM and EPRI in the past and has ongoing collaborations to develop and apply an integrated, computational, welding engineering modeling framework for industrial applications. Specifically, we further developed a novel simulation approach for welding simulation. A sequentially coupled approach was employed in this project. Key R&D activities included: (1) scale-up computational codes of welding heat flow simulations; (2) explicit finite element-based thermal stress analysis to drastically reduce the computational time; and (3) robust data transfer schedule between the heat flow modeling and the FEM weld stress modeling.

Results

GM fabricated A alloy panel coupons by laser welding under different tooling or constraint conditions. In each coupon, two prototypical automotive body panels were laser brazed together by a welding robot with a dual laser beam and filler metal, as shown in Figure II.3.D.2.(a) for the welding direction and Figure II.3.D.2.(b) for the fixture setup. The material of the panels was Al6111-T4 and filler material was Alloy 4047. The four constraint conditions are given as shown in Table II.3.D.1. GM also experimentally measured the distortion of the panel due to welding/brazing for validation of the modeling results. The distortion data of the left panel and the right panel were measured separately by a non-contact tool 3D scanner. After measurement, samples of the weld cross-section were mounted to get the bead shape of the laser weld and used for metallurgical observation. The weld bead will provide the basic geometry information and heat input reference for the model.

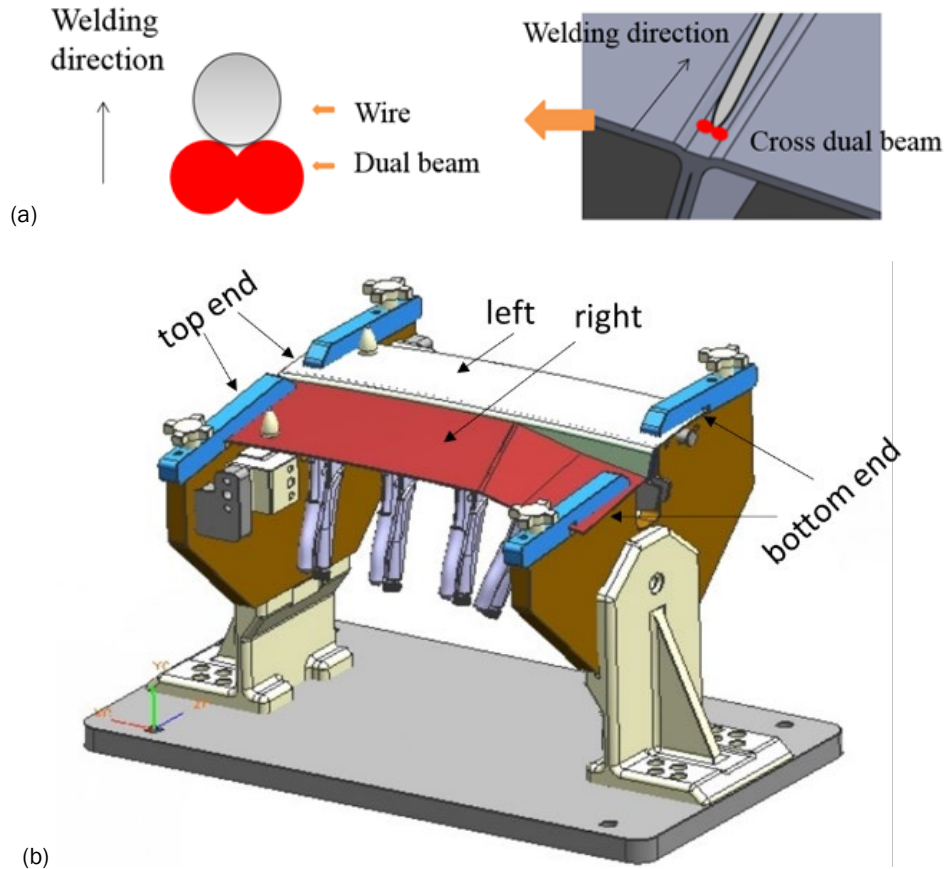


Figure II.3.D.2. Laser beam welding of panel structure: (a) laser beam configuration; and (b) fixture setup. Source: GM.

Table II.3.D.1. Definition of Welding Cases under Different Clamping Methods.

	Clamping Left Side Panel	Clamping Right Side Panel
Case 1	Two Ends	/
Case 2	/	Two Ends
Case 3	Two Ends	Two Ends
Case 4	Top Ends	Top Ends

EPRI provided the detailed information of a round-robin weld model, including the welding condition and the bead cross-sections. This weld is part of an important U.S. Nuclear Regulatory Commission/EPRI collaborative program to address the potential SCC problem of DMW in the primary piping loops of the reactor vessel. Due to the size of the problem, only simplified two-dimensional (2D) weld simulations were carried out in past studies by various modelers. A 3D model is created in this program, and the essential features and complexity of the DMW are shown in Figure II.3.D.3. Fully transient stress analysis for the DMW of the pipe was carried out by the in-house HPC code developed in this project.

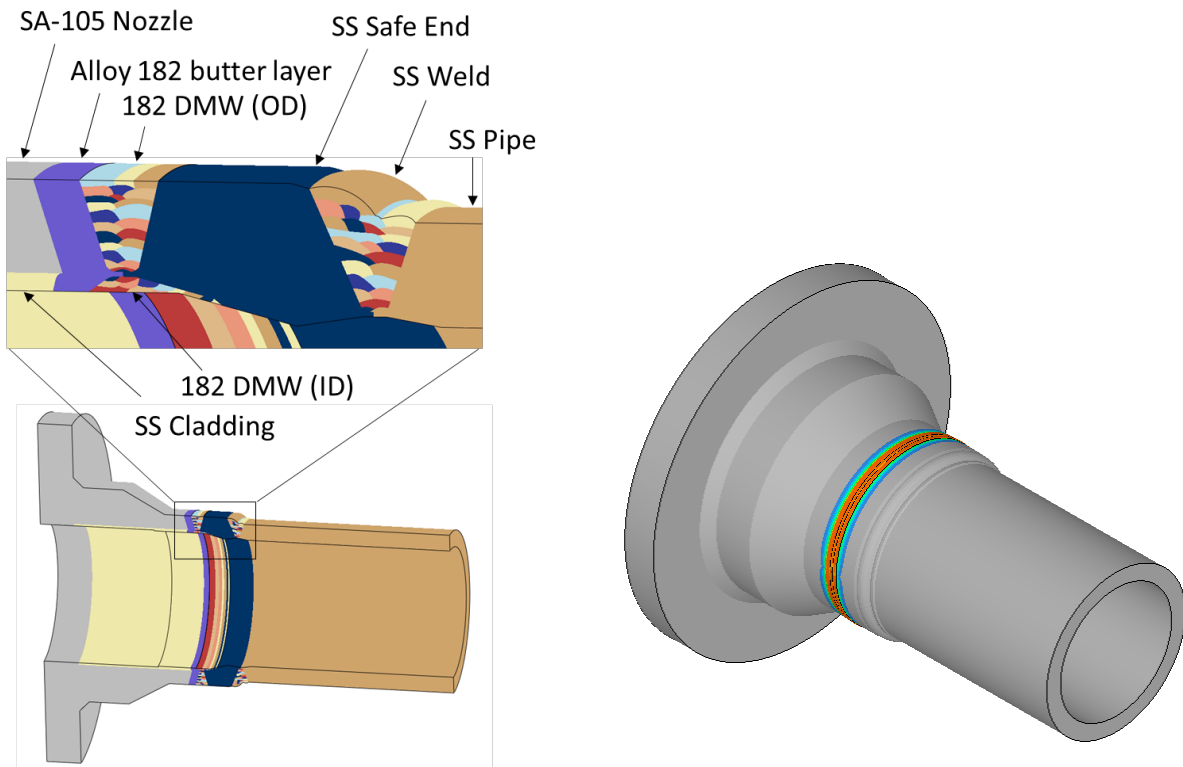


Figure II.3.D.3. Welding pass layout for the EPRI round-robin model. Source: ORNL.

ORNL led the development of the in-house HPC code and performed the calculations of all benchmark examples. The initial development of the in-house code was on a computer equipped with an eight-core Intel Xeon E5v2 CPU (16 threads) and a Tesla K80 GPU (two GPU units with 2496 processing cores on each unit) rated at 2.91TFLOPS for peak double-precision calculation performance. In addition, the accuracy and performance of the in-house code were compared with the ABAQUS commercial software on the same computer.

The ORNL in-house code was initially tested with a single-pass pipe girth welding case. The results are presented in Figure II.3.D.4.(a) for the Mises stress and Figure II.3.D.4.(b) for the equivalent plastic strain. The in-house code and ABAQUS code have shown comparable solution accuracies. With 8 CPU threads and 1 GPU, the latest version of ABAQUS took 24,411 seconds to complete the analysis, whereas our in-house code took only 198 seconds with 1 CPU and 1 GPU, as shown in Table II.3.D.2. This amounts to 123x performance improvement for this relatively simple case.

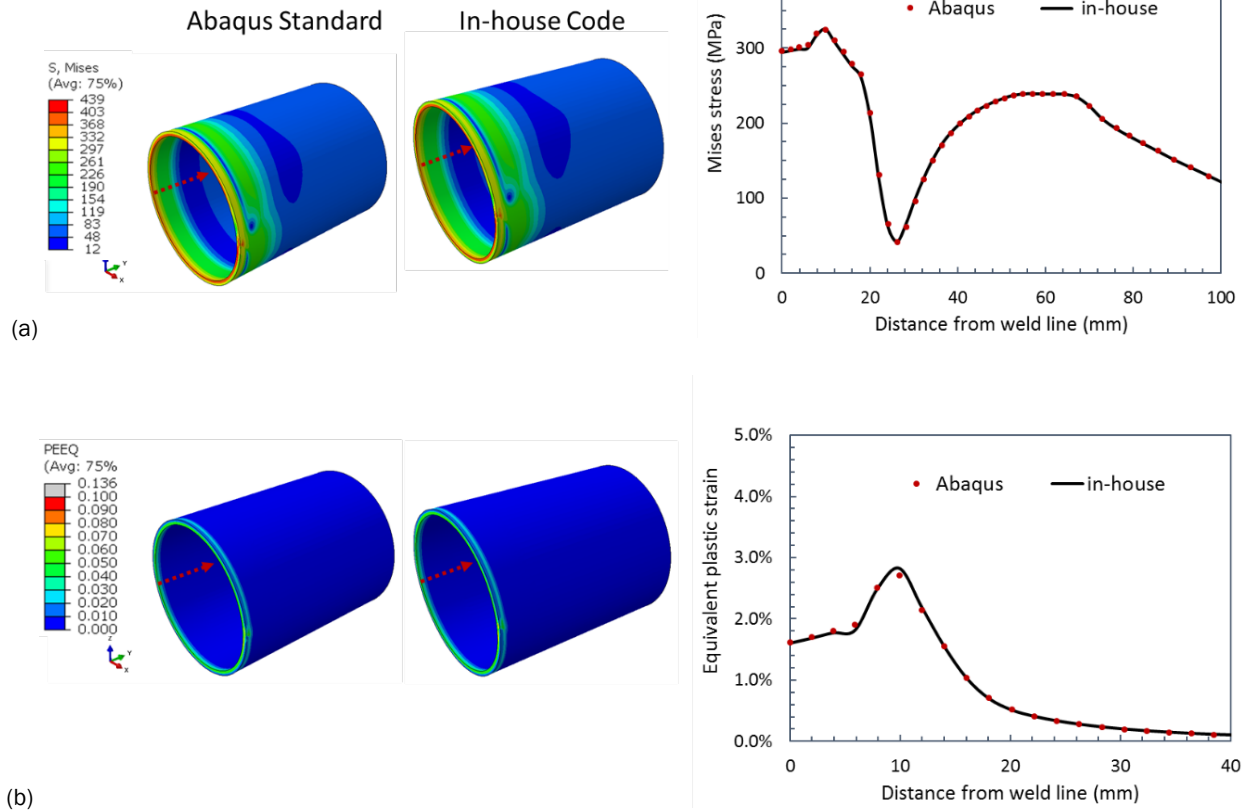


Figure II.3.D.4. Comparison of simulation results between ABAQUS and the in-house codes: (a) Von-Mises stress; and (b) equivalent plastic strain. Source: ORNL.

Table II.3.D.2. Comparison of Time Cost by the Two Codes.

No. CPU Threads	ABAQUS code (CPU mode)					ABAQUS Code	In-House Code
	1	4	8	12	16	8 CPU + 1 GPU	1 CPU + 1 GPU
Time (seconds)	120,099	41,413	28,595	25,552	22,660	24,411	198
Speedup	Ref.	2.9	4.2	4.7	5.3	4.9	606.6
Speedup	0.24	0.69	Ref.	1.12	1.26	1.17	144.4

The second analysis was the EPRI dissimilar metal pipe weld model and the computation cost as summarized in Table II.3.D.3. Due to the extreme complexity of this case, it was impossible to use ABAQUS to complete this analysis in the time allowed for this project. Instead, it was decided to only analyze the first 20 seconds of welding (i.e., total welding time to complete this pipe weld was over 17,500 seconds), to provide a reference benchmark (referred to as “Ref.” in Table II.3.D.3) for comparison with our in-house code. Using the 8 CPU threads and 1 GPU, ABAQUS simulated this 20-seconds of weld in 3.5 days of CPU time, as compared to 8.1 days with 8 CPU threads only. Extrapolating to the 17,500 seconds of welding time required to fabricate this weld, it was estimated that ABAQUS would require 8.5 years to complete the entire analysis with 8 CPU threads and 1 GPU. It would take about 20 years to complete the entire analysis using the 8 CPU threads of the computer only. In comparison, our in-house code completed the first 20 seconds of welding in 288 seconds, and the entire weld in 3.2 days using one CPU and one GPU. This amounts to a 1,000 to 2,000x computational performance improvement. Such a performance improvement was far beyond our own expectations—we

originally aimed for a 100x improvement in this 12-month project. Furthermore, our 3D high-fidelity model revealed several key details about the weld residual stress distribution that are simply impossible to obtain with the 2D modeling analysis in the past. As an example, Figure II.3.D.5 shows the hoop residual stress distribution in both full view and cut view. The residual stress field is clearly non-axisymmetric, which is the fundamental assumption of the 2D axisymmetric model.

Table II.3.D.3. Key Properties of Selected Primers.

Software	ABAQUS Standard		In-House Code
Platform	8 CPU threads	8 CPU threads + 1 GPU	1 CPU + 1 GPU
Trial Analysis 20-Second Welding	8.1 days	3.5 days	388 seconds
Full Pass Analysis	19.6 years	8.5 years	3.2 days
Speedup Factor	Ref.		2,200x
Speedup Factor		Ref.	1,000x

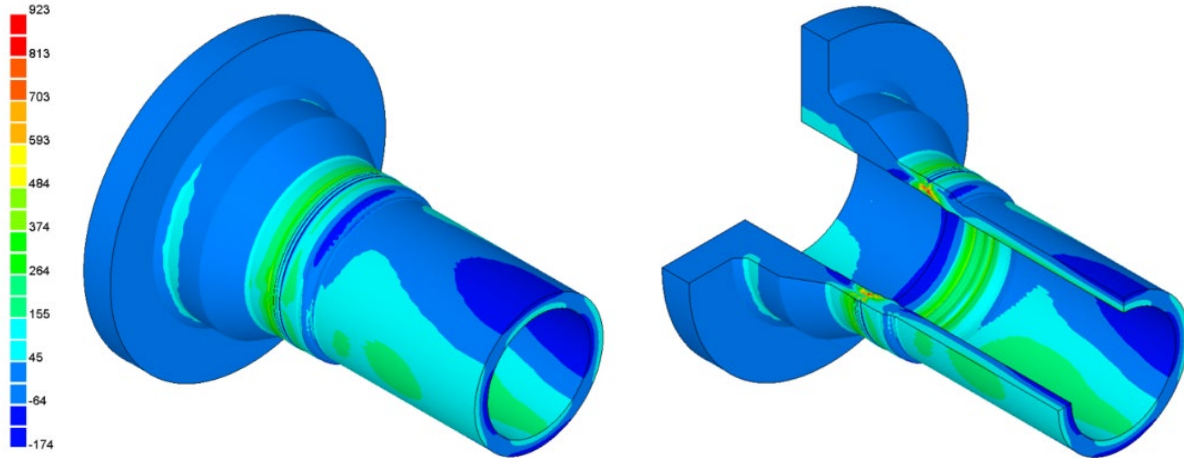


Figure II.3.D.5. Computed hoop stress in full view and cut view. Source: ORNL.

We further extended the in-house HPC code to simulate laser beam weld brazing of relatively large prototypical auto-body panel structure provided by GM. The transient temperature and weld nugget penetration shape predicted by the model are presented in Figure II.3.D.6.(a) and (b), respectively, which shows good agreement with the actual weld nugget shown in the same figure for comparison. Transient thermal stress analyses were carried out by the in-house code on the same Tesla K80 GPU workstation. For each case, the computation time by the in-house code was less than two hours. For benchmarking, ABAQUS was used to run one case (Case 1), which took approximately 152 hours, representing over 70x speed improvement. The out-of-plane distortion of the left and right panels were plotted in Figure II.3.D.7.(a) and (c), and Figure II.3.D.7.(b) and (d), respectively. The predicted welding distortion by the in-house code and ABAQUS code has overall good agreement in distortion magnitude and mode.

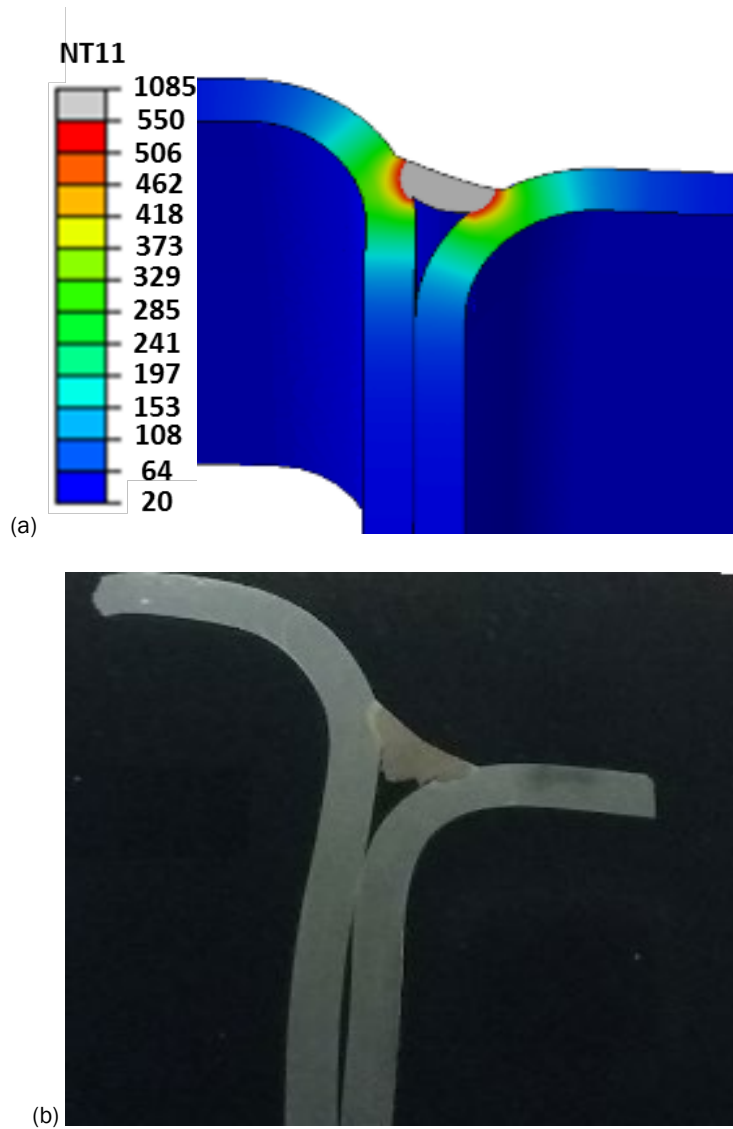
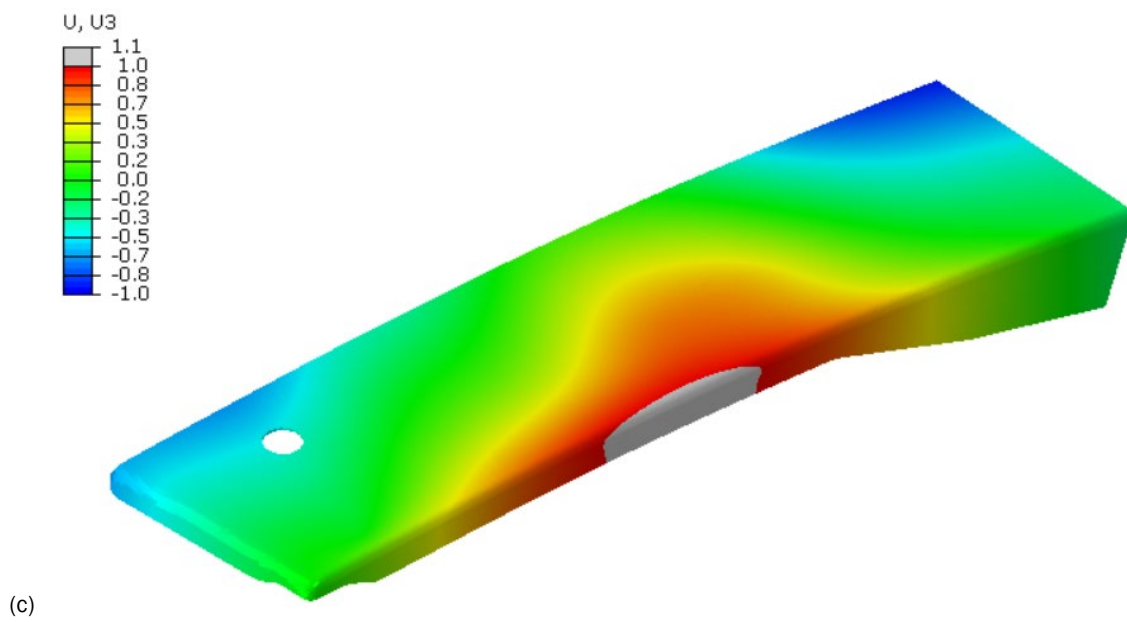
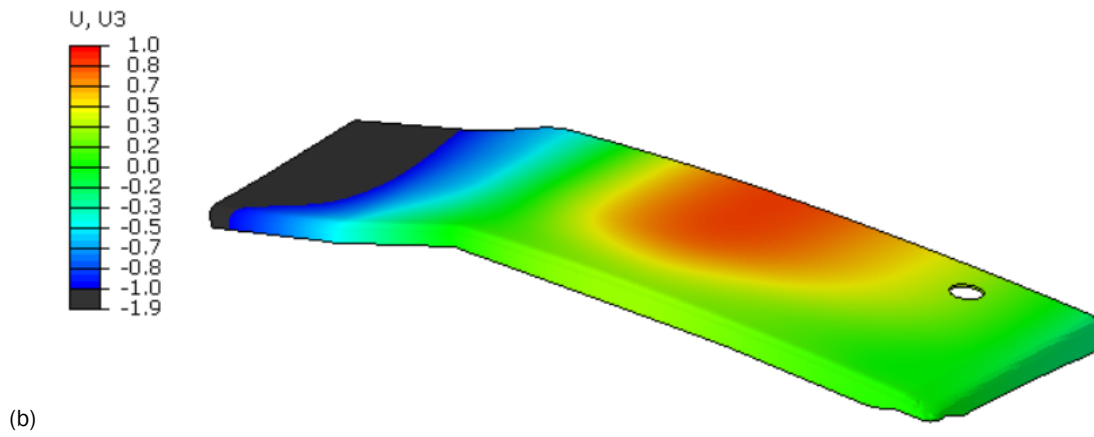
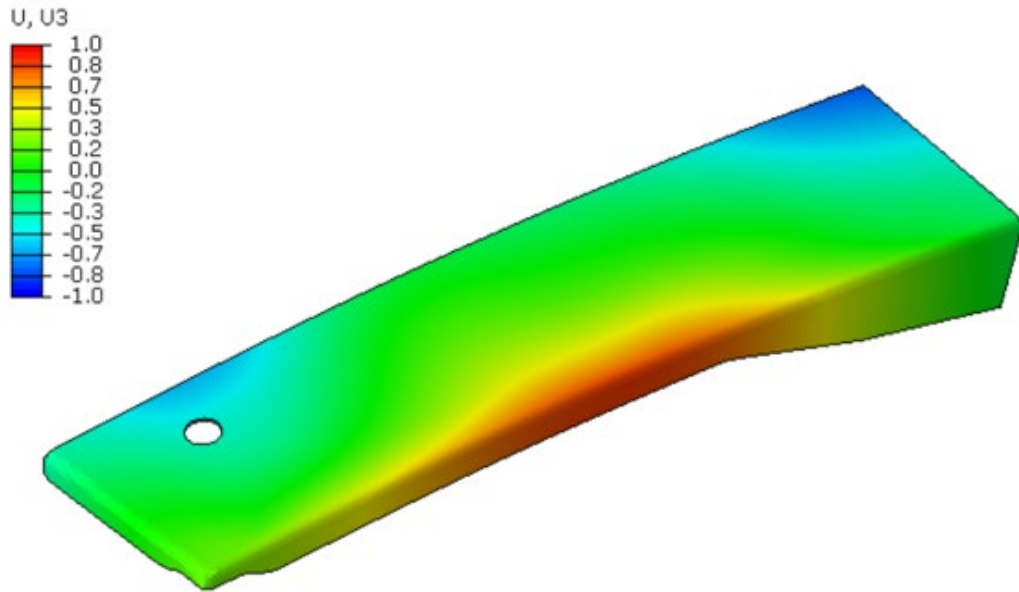
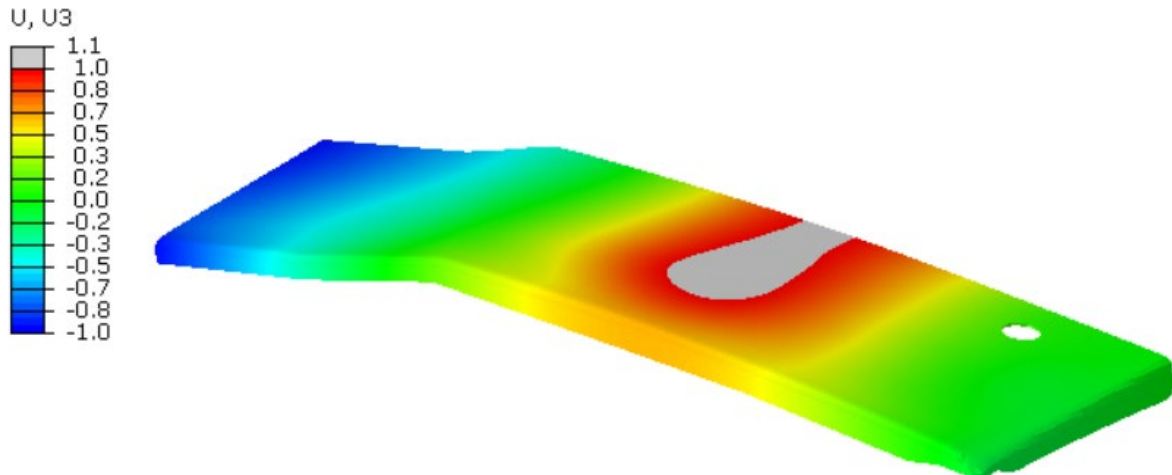


Figure II.3.D.6. Thermal analysis results: (a) transient temperature at three seconds; and (b) weld penetration shape.
 Source: ORNL, GM for photomicrograph.





(d)

Figure II.3.D.7. Simulated distorted shape of the auto-body panel: (a) left panel by in-house code; (b) right panel by in-house code; (c) left panel by ABAQUS code; and (d) right panel by ABAQUS code. Source: ORNL.

Conclusions

This 12-month HPC4Mfg project has produced an initial version of a FEM code from ORNL that resulted in a breakthrough in computational speed for welding and additive manufacturing simulations. Through innovations in computational algorithms and schemes, the ORNL code makes it possible to simulate the highly nonlinear transient thermal-metallurgical-mechanical process in welding based on rigorous physics representations of weld process without unnecessary over-simplifications.

The accuracy of the ORNL HPC code has been confirmed by a benchmark study on a pipe girth weld. The computation time in a large-diameter and multi-pass welding analysis was reduced from years to days by application of the in-house code while keeping confidence in solution accuracy. Computational time for simulations of laser welding of auto-body components was reduced from about a week to approximately two hours. This is a truly remarkable breakthrough in the residual stress analysis of evolving thermal-mechanical processes including welding and additive manufacturing.

Key Publications

1. Huang, H., J. Chen, B. Carlson, H.-P. Wang, P. Crooker, G. Frederick, and Z. Feng, 2018, "Prediction of Residual Stresses in a Multi-Pass Pipe Weld by a Novel 3-D Finite Element Approach," Proceedings of the ASME 2018 Pressure Vessels and Piping Conference, PVP2018-85044, July 15–20, 2018, Prague, Czech Republic.
2. Huang, H., J. Chen, B. Carlson, H.-P. Wang, P. Crooker, G. Frederick, and Z. Feng, 2018, "Stress and Distortion Simulation of AM Process by HPC," Proceedings of the ASME 2018 Pressure Vessels and Piping Conference, PVP2018-85045, July 15–20, 2018, Prague, Czech Republic.

Acknowledgements

The information, data, or work presented herein was funded in part by DOE-EERE under Contract Number DE-AC05-00OR22725.

II.3.E Corrosion Control in CFRP Composite-Al Closure Panel Hem Joints (PPG Industries, Inc.)

Brian Okerberg, Principal Investigator

PPG Industries, Inc.
Coatings Innovation Center
4325 Rosanna Dr.
Alison Park, PA 15101
E-mail: okerberg@ppg.com

Sarah Kleinbaum, DOE Technology Manager

U.S. Department of Energy
E-mail: sarah.kleinbaum@ee.doe.gov

Start Date: October 1, 2016	End Date: March 31, 2020	
Project Funding (FY18): \$955,123	DOE share: \$865,009	Non-DOE share: \$90,114

Project Introduction

This program seeks to develop new coatings and adhesives, new joint geometries, and establish and validate corrosion characterization techniques that enable CFRP/Al hem flange joints. The CFRP/Al closure panels will save over 40 kg per vehicle compared to a vehicle with all Al closure panels. The CFRP/Al hem will meet current specifications for mechanical performance, corrosion resistance, and appearance when cured between 150–180°C. Critical success factors to achieve this goal include the development of novel coatings, adhesives, and/or joining geometries to fully isolate the inner panel from the outer panel in the joint while maintaining the ability to electrostatically paint the inner panel in the paint line. These materials must cure at a lower temperature and be designed to mitigate the coefficient of thermal expansion (CTE) mismatch while enabling processing through a standard paint shop. Extensive electrochemical and SCC testing will be conducted to evaluate the corrosion performance of the new solutions and determine the appropriate accelerated test methods. Outdoor on-vehicle exposure testing will be conducted to verify the proper laboratory accelerated corrosion test method for CFRP/Al hem joints.

Objectives

The objective of this project is to develop new coatings and adhesives, new joint geometries, and establish and validate corrosion characterization techniques that enable Ford Motor Company to implement lightweight closure panels based on a CFRP-inner/Al-outer joined by a hem flange.

Approach

The project has been divided into three project BPs. The focus of the first budget period (BP1) was to understand the nature and extent of the corrosion problem resulting from the CFRP/Al joint. Testing to evaluate the susceptibility to galvanic corrosion and SCC was begun. An investigation began into the level of conductivity needed to promote electrostatic painting, but not galvanic coupling. Development of adhesives and coatings that develop the required cure and corrosion-preventive characteristics in the required temperature range was initiated.

During this report period (comprising the remainder of BP1 and continuing into BP2), prototype conductive primers, adhesives, and E-coats were developed based on our findings from BP1. Hem geometries, which mitigate galvanic coupling and CTE mismatches, were identified. This work, along with the continued investigation of galvanic corrosion, SCC, and the development of an accelerated corrosion test procedure, will continue through the remainder of BP2.

Finally, the solutions developed during BP2 will be optimized and developed during BP3. A surrogate Al-outer/CFRP-inner closure capable of passing Ford's specifications and being processed through a typical paint shop operation will be constructed and tested.

Results

The work performed during this report period is divided into the following task areas:

- Corrosion Performance and Electrochemical Testing (Tasks 1.1, 2.3, and 2.4)
- Screening and Development of Low-cure E-coats, Adhesives, & Conductive Primers (Tasks 1.2 and 2.1)
- Determine impact of CTE Mismatch (Task 1.3)
- Optimize Joint Geometries (Task 2.2).

The details of the work performed in each of these tasks and their respective subtasks, is provided in the sections that follow.

Subtask 1.1.1: Prepare and Test Corrosion Samples (PPG/Ford)

Coupons were prepared that consisted of Al base plates coupled to CFRP, fiberglass, or Al top plates. Both random and twill CFRP top plates were utilized. Bottom plates were composed of either AA6022 or AA6111 alloys. The amount of corrosion was quantified via the measurement of the length of undercutting for coupons exposed on both a test vehicle run through Ford's full vehicle corrosion test (also known as the Michigan Proving Ground (MPG) R-343 Corrosion Test) and through 12 weeks of accelerated corrosion testing using Ford's L-467 test method. Extensive corrosion was observed for both the AA6111 and AA6022 when joined to both random and twill CFRP. Essentially, no corrosion was observed when the Al alloys were joined to Al or fiberglass, which indicated that galvanic corrosion and not crevice corrosion is the dominant mode of degradation.

The amount of corrosion on the base plate was also quantified via a non-contacting profilometry (Keyence MacroScope) measurement of the volume loss of Al after corrosion testing. Extensive metal loss was observed when CFRP, particularly the random CF material, was coupled to the Al.

The depth of the pits on the Al substrate were also quantified via non-contacting profilometry. Some pits were found to perforate through the thickness of the Al base plates. Results mirrored those found from the undercutting measurements—a strong corrosion attack was observed when the CFRP was coupled to either of the two Al alloys, and no corrosion when coupled to the Al or the fiberglass. Perforation was observed on coupons that were e-coated and those that were not, as the galvanic attack occurs under the top plate where the e-coat is not present regardless of the processing history.

These results demonstrated conclusively that galvanic attack of Al coupled to CFRP severely accelerates the corrosion rate of the Al substrate. Based on these results, a new round of testing was devised that involved similar coupons, as well as additional real-world complexity. Specifically, the new round of coupons incorporated adhesives to join the top and bottom plates and incorporated a conductive primer for the CFRP. The primer should aid in painting, but also provide some level of electrical isolation between the CFRP and Al (see other sections on primer development). These coupons have been designed and fabricated and will start corrosion testing (chamber and attached to proving ground vehicles) in the fourth quarter of calendar year 2018.

Subtasks 1.1.2 and 2.3: Galvanic Corrosion Susceptibility Assessment (OSU)

1. Random and twill CFRP samples that were first potentiodynamically polarized from +30 mV to -1.5 V (versus open-circuit potential (OCP)) at a scan rate of 0.3 mV/s in 5 wt.% NaCl solution in aerated conditions were then subjected to attenuated total reflection (ATR) spectroscopy to analyze the effect of cathodic polarization on the surface of CFRP. As-received (unpolarized) and polarized samples of both twill and random CFRP were tested and the results were compared. No significant difference in surface chemistry in the as-received and polarized samples of twill and random was observed. The literature [1-2] suggests that the perhydroxyl ion evolution on the composite surface should degrade the matrix and alter the O-H and C=O stretch bonds. Since no difference in surface chemistry was observed in this experiment, it can be inferred that potentiodynamic polarization to such low potentials did not degrade the surface of the CFRP.
2. Cu was deposited on the random and twill CFRP samples under focused ion beam and SEM to understand the distribution of the conductive regions and the nature of the epoxy cover. Cu deposition was carried out galvanostatically at a current density of 1 mA/cm² for 0.5 seconds. The deposited samples were gold-coated prior to the analysis to facilitate conductivity during SEM imaging. The density of electrochemically active sites per length of exposed CF on the twill sample was 95±4.4/μm. The approximate total length of the fibers that were exposed on the top surface is 0.7 mm/0.5 cm², yielding 3.3E4 sites/cm². Regions of the CF were clearly exposed out of the surface. A few fibers that seem to be exposed showed either very few or no Cu deposits at all. It is possible that the Cu deposits that formed here did not adhere to the surface or that these fibers had no electrical connection with the rest of the fibers. Regions of porosity were also observed.
3. Electrochemical behavior of the conductive primed twill and random CFRP samples was determined by potentiodynamic polarization in 5 wt% NaCl solution. Conductive primers with varying conductivity were named 0, 50, and 100-conductive primers, representing increasing relative conductivity as determined with a Ransburg conductivity meter. The polarization curves in Figure II.3.E.1 show that primed twill and random CFRP samples should have less galvanic corrosion susceptibility when coupled with AA6111 and AA6022 plots than unprimed CFRP. The conductivity of the 100-conductive twill and random samples were sufficient for the measurement of polarization behavior. A clear break between the oxygen reduction reaction and the hydrogen evolution reaction can be observed in the 100-conductive primer. However, the oxygen reduction reaction rate of the 100-conductive primer is 1-2 orders of magnitude lower than that for unprimed CFRP. Insufficient conductivity of the zero conductive primed samples prevented measurement of reasonable curves. The 50-conductive random CFRP samples appear to be more noble than the twill CFRP samples and pass smaller currents.

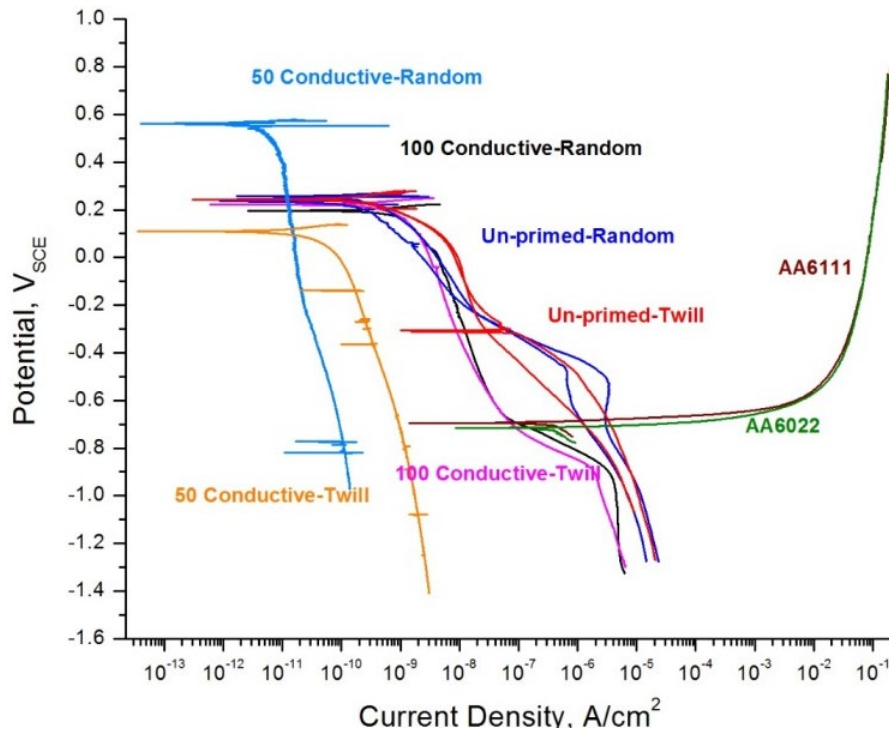


Figure II.3.E.1. Potentiodynamic polarization plot showing overlap of primed and unprimed CFRP and AA6xxx.

Subtasks 1.1.2 and 2.3: Galvanic Corrosion Susceptibility Assessment – OSU

1. The AA6111-T8-like aged sheet material was machined into eccentrically loaded single edge notch tension (ESE(T)) specimens for SCC testing.
2. The servo-electric test frame purchased through this project was fully fabricated and its functionality validated by running comparative tests against another test frame in OSU Locke lab.
3. An AA6111-T8-like ESE(T) coupon was tested in 3.5 wt% NaCl under freely corroding conditions for the OCP at a slow strain rate of $0.25 \text{ MPa}\sqrt{\text{m/hr}}$. The threshold stress intensity (K_{TH}) in this condition was estimated to be $18.4 \text{ MPa}\sqrt{\text{m}}$, but upon post-test inspection, load shielding due to clevis hole yielding was observed, invalidating this preliminary result. Additionally, OSU observed the effect of temperature fluctuation on the measured direct current potential drop voltages (e.g., the signal that measures crack extension per ASTM E647) of the test specimen and implemented a reference specimen in future testing in order to mitigate the temperature effects on the voltage, which influences crack length measurement for the direct current potential drop.
4. SCC testing was conducted on AA6111-T8-like in 3.5 wt% NaCl at OCP at the slow strain rate of $0.25 \text{ MPa}\sqrt{\text{m/hour}}$, utilizing a longer pre-crack to prevent load shielding due to yielding in the sample clevis holes. The K_{TH} for this condition was determined to be $12.7 \text{ MPa}\sqrt{\text{m}}$, as shown in Figure II.3.E.2. The measured corrosion potential during testing, as seen in the Figure II.3.E.2 inset, shows that the potential fluctuates over a range of approximately 70 mV_{SCE} (millivolts of the saturated calomel electrode). At around 22 hours the fatigue pre-cracking segment was halted and switched to a rising displacement loading for the SCC study. There is a drop in the corrosion potential due to a pause in testing during which the solution is not agitated. The drastic drop in potential at around 58 hours corresponds to a temporary pause in the crack growth kinetics, but the reasoning behind it is currently unknown. A fluctuating corrosion potential is common in similar long-term immersion tests, which is why we run an initial freely corroding condition, then test at static potentials. This fluctuation establishes that AA6111-T8 can be susceptible to SCC. Conventional wisdom is that this material is SCC resistant, but no literature reports of any type of SCC studies could be found.

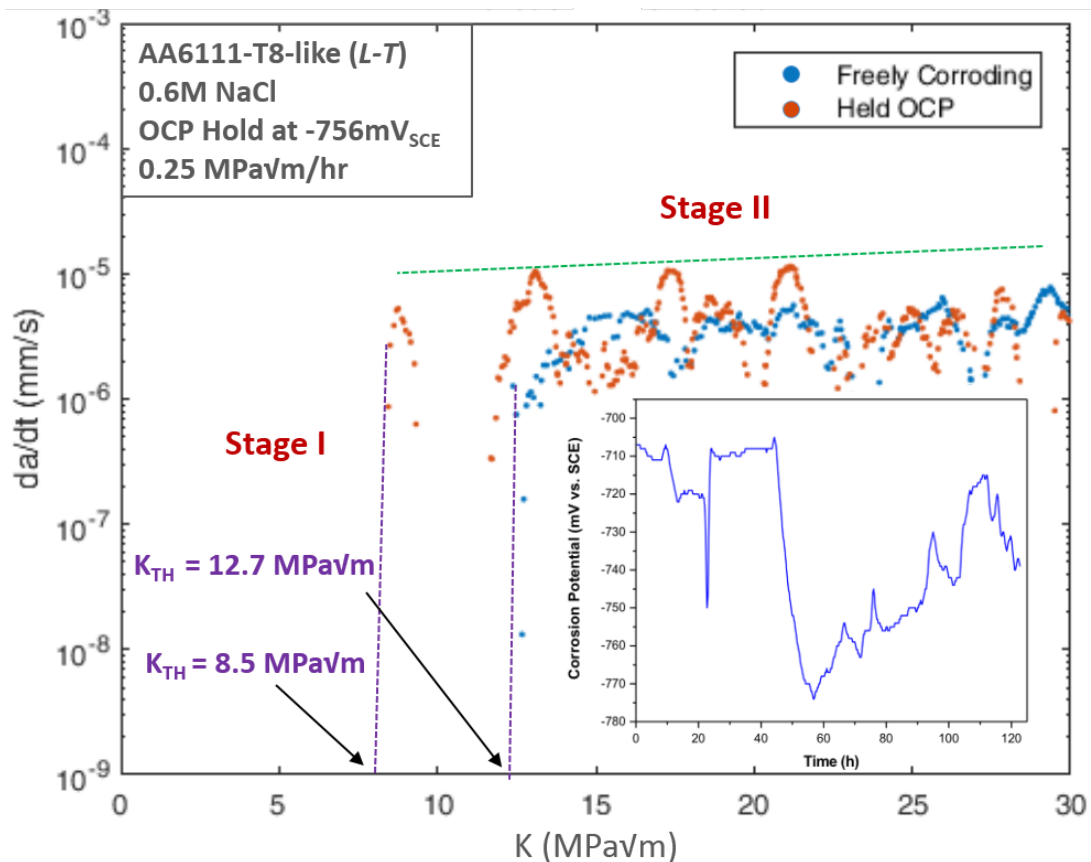


Figure II.3.E.2. Stress intensity curve for freely corroding and Held OCP conditions in 3.5 wt% NaCl under slow strain rate rising displacement testing on AA6111-T8-like showing threshold stress intensity at 12.7 MPa \sqrt{m} and 8.5 MPa \sqrt{m} , respectively. Inset plot shows the fluctuation of corrosion potential over a range of approximately 70 mV_{SCE} during SCC testing under the freely corroding condition.

5. In order to set an iso-potential baseline for the freely corroding condition, an SCC test held at a potential within the OCP range was conducted by holding the potential at -756 mV_{SCE} (referred to hereafter as the “Held OCP” condition). This will serve as the OCP value from which subsequent testing at varied anodic polarization levels will be calculated. The resulting K-curve of this Held OCP shows the K_{TH} for this condition is 8.5 MPa \sqrt{m} , as seen superimposed in Figure II.3.E.2. This lower K_{TH} may be due to natural data dispersion or the fact that the Held OCP test experienced times of anodized polarization during testing. Future tests under full anodic polarization will help illuminate this.
6. An applied anodic polarization level of 50 mV_{SCE} above the Held OCP test was chosen as a first step in assessing the change in SCC behavior in an environment simulating galvanic coupling to CFRP. The SCC test was performed under the same slow strain rate conditions as previous tests in 3.5 wt% NaCl and held at a potential of -706 mV_{SCE}. This test is currently underway. If the results of this test do not show a significant change in SCC behavior, a more severe anodic polarization will be applied on the subsequent SCC test.
7. OSU has created a MATLAB program to process the post-test data using linear-elastic and elastic-plastic fracture mechanics to reduce the time required to analyze the test data.
8. OSU has completed testing of one AA6111-T8-like ESE(T) specimen in air at the slow strain rate of 0.25 MPa $\sqrt{m/hr}$ to determine the fracture toughness of the sheet material. Post-test processing is underway to determine the fracture toughness value to compare all SCC testing against.

Subtasks 1.1.4 and 2.4: Accelerated Corrosion Test Procedure Analysis/Development (OSU)

The chamber to carry out the Corrosion Evaluation Test Procedure L-467 test was installed and the accelerated cyclic corrosion test on the first set of samples was completed. Coupons of uncoated and e-coated AA6022 and AA6111, coupled with twill and random CFRP individually and all their combinations, have been tested. Visual inspection of corroded surfaces indicated that the uncoated and e-coated AA6111-random combination showed maximum corrosion product and blistering of the e-coat, as seen in Figure II.3.E.3. This observation is in correspondence with higher current densities on the random samples than the twill samples during potentiodynamic polarization in 5 wt% NaCl. Although there was very little difference in the electrochemical behavior of AA6111 and AA6022 during potentiodynamic polarization, the AA6022 coupons repeatedly showed less surface damage than the AA6111 ones during chamber testing. The difference in corrosion behavior of AA6111 and AA6022 is because of the Cu content. AA6111 has a higher Cu content (~0.7 wt%) than AA6022 (<0.1 wt%). Other reasons for this behavior are yet to be investigated. Galvanic current measurements were not conclusive because the potentiostat malfunctioned in the uncontrolled lab environment.

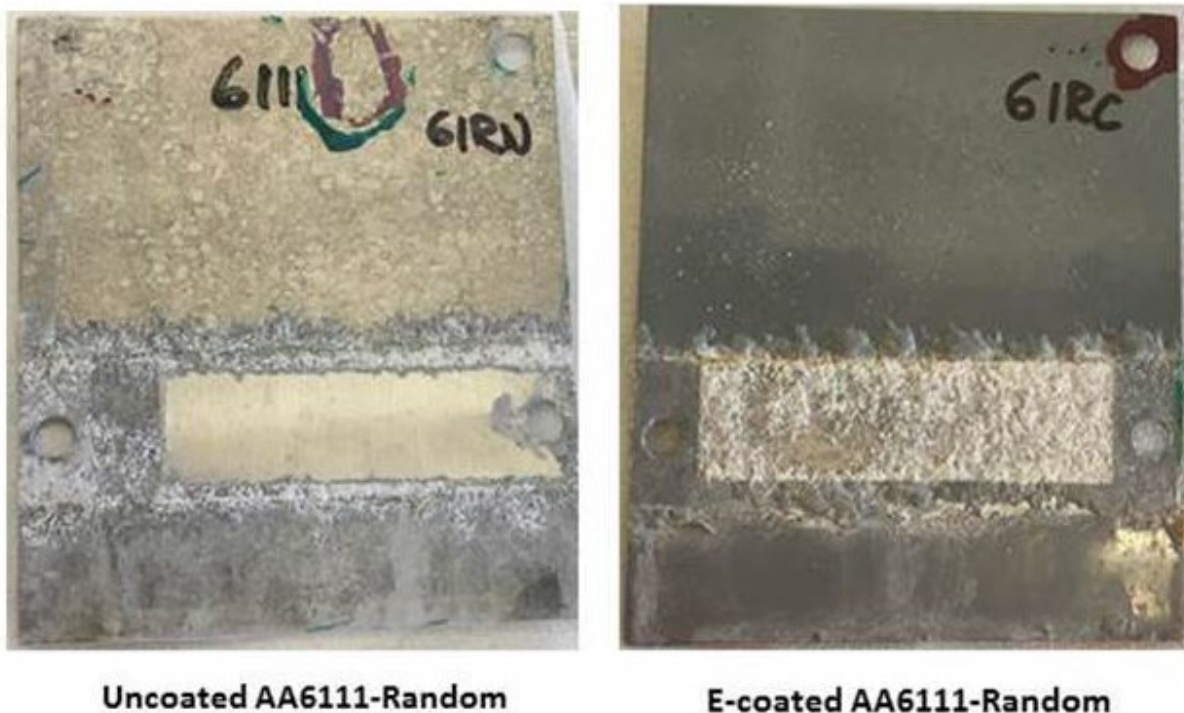


Figure II.3.E.3. Twelve week chamber exposed coupons of uncoated and e-coated AA6111-Random. Source: OSU.

The second trial of chamber testing on uncoated and e-coated AA6111 and AA6022 coupled with random and twill is ongoing. Coupons with multilayer protection over the connections are loaded into the chamber and will be exposed to the test environment for twelve weeks.

Subtasks 1.2.1 and 2.1.1: Screening and Development of Low-temperature Cure E-coat (PPG)

The previous systematic screening of the effect of electrocoat formulation components (i.e., crosslinker type, catalyst type and loading, additive type and loading, backbone type, etc.) on electrocoat key properties (i.e., cure response, appearance, and corrosion) enabled us to arrive at two electrocoat formulations with target key properties. The formulation details and key properties are summarized in Table II.3.E.1.

Table II.3.E.1. Formulation Details and Key Properties of Prototype and Control Electrocoats.

Sample ID	Formulation Variables				Cure 150°C, ten mins	Appearance W_b (μm)	Corrosion G-85 (vs. control)	Throwpower Nagoya Box (G/A)
	Resin	XL	Additive	Catalyst				
P1-B	A	XL1	C	E	pass	0.12	better	69%
P11	B	XL2	G	F	pass	0.13	better	51%
Control	C	XL3	C	E	N/A	0.11	N/A	55%

As shown in Table II.3.E.1, two prototype electrocoat formulations have been optimized to deliver cure response at the target bake condition, appearance values (i.e., W_b , the surface structure value for appearance, determined from a contact Profilometer) and promising throwpower values (i.e., interior panel / exterior panel (G/A) from a Nagoya box). Improved corrosion resistance was also realized for prototype electrocoats as compared with that of control as determined from an American Society for Testing and Materials International (ASTM) cyclic corrosion test (i.e., G-85 A2), as shown in Figure II.3.E.4.

The selected prototype low-cure electrocoat (P11) has been applied for recent overlap coupons of target dissimilar joints of CFRP and AA6022 for various corrosion tests at Ford.

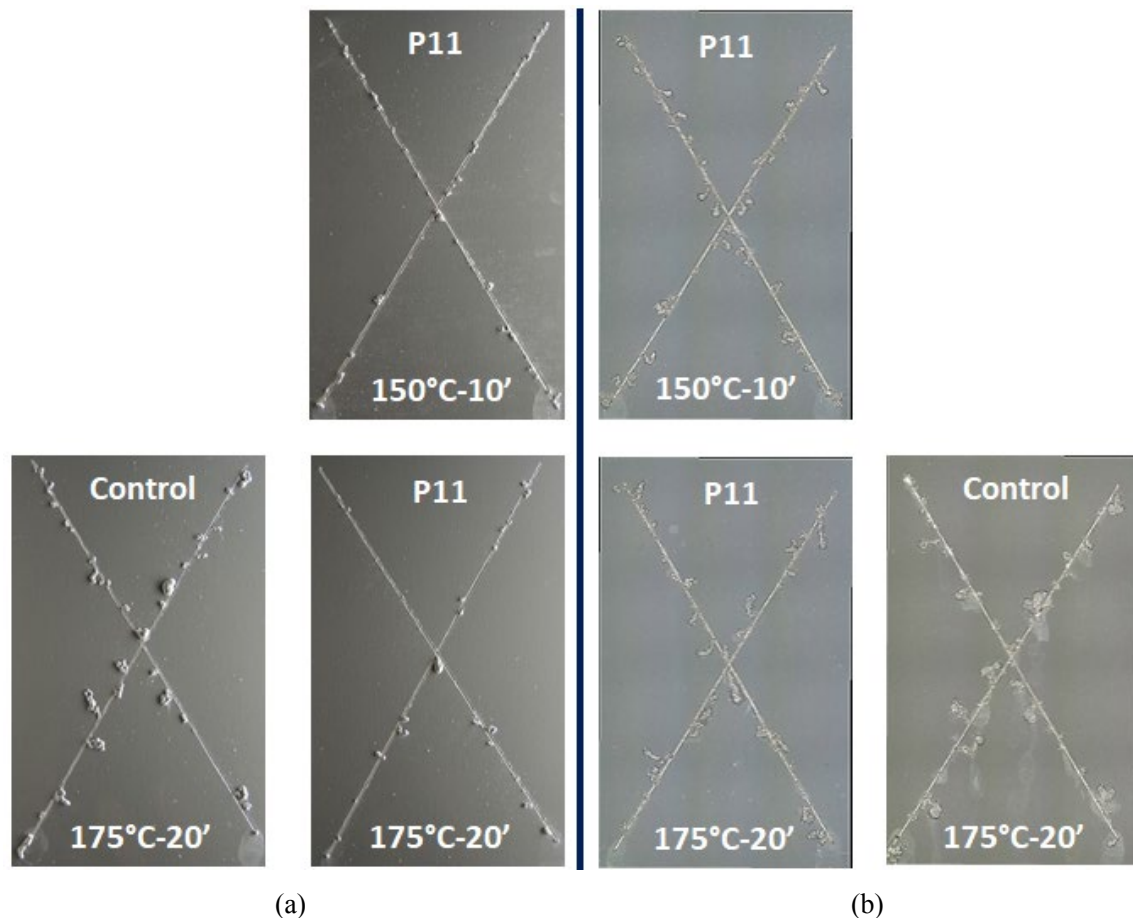


Figure II.3.E.4. Images of prototype and control electrocoats on an AA 6011 substrate upon ASTM A2 G-85 corrosion test for (a) three weeks and (b) six weeks. Source: PPG.

Subtasks 1.2.2 and 2.1.2: Screening and Development of Low-temperature Cure Adhesives (PPG)

Formulation variables including polymer resins, tougheners, curatives, and additives had an important influence on the cure response, lap shear strength, modulus, glass transition temperature (T_g), and rheology of the system. Optimization of the formulation variables to meet the critical requirements enabled us to formulate a prototype adhesive for hem flanges that exhibited desirable cure response, lap shear strength, fracture toughness, and rheological behaviors that meet the project goals and specifications.

The lap shear strengths per Society of Automotive Engineers J1523 for the prototype adhesives baked at 150°C are shown in Table II.3.E.2. The data of the commercial control baked at 175°C is also included for comparison since it was originally formulated to fully crosslink at 175°C. It can be seen that the lap shear strength for the prototype adhesive is significantly greater than that of the control baked at 150°C. Even though the lap shear strength of the adhesive is slightly lower as compared to the control baked at 175°C, the strength value does exceed Ford’s requirement of 13 MPa. The storage modulus as a function of temperature and T_g for the prototype adhesive are depicted in Figure II.3.E.5. The targeted modulus is a magnitude less than 600 MPa. The prototype adhesive shown in Figure II.3.E.5 meets the requirement while exhibiting a desirable T_g of 125°C.

Future adhesive formulation efforts will be devoted to further improve the strength, toughness, and flexibility balance of the adhesive, as well as optimization of viscosity and flow for sag resistance and cold pumpability.

Table II.3.E.2. Lap Shear Strengths of the Control and Prototype Adhesive.

Sample/Bake Temperature	Lap Shear Strength (MPa)	
	150 °C	175 °C
Control	8.5 ± 1.4	17.0 ± 0.6
Prototype Adhesive	15.0 ± 0.6	N/A

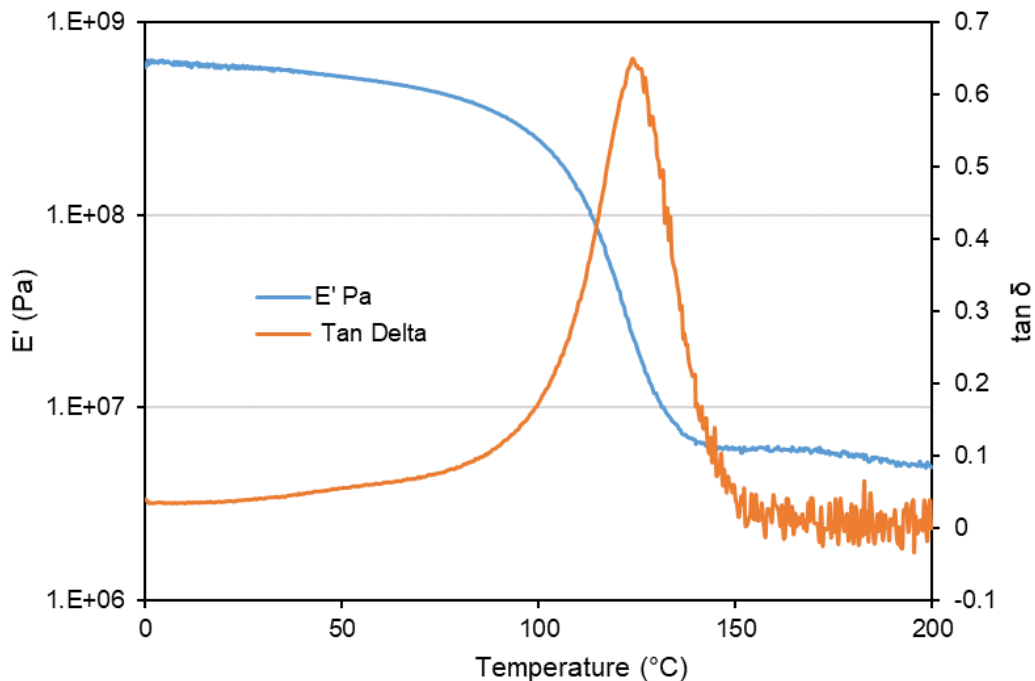


Figure II.3.E.5. Storage modulus and the glass transition temperature (T_g) as a function of temperature for developmental adhesive. Source: PPG.

Subtasks 1.2.3 and 2.1.3: Screening and Reformulation of Conductive Primers (PPG)

Several primer formulations were tested to investigate the effect of conductivity on corrosion in the Al/CFRP joint, with the objective of identifying prototype formulations allowing dynamic variation of conductivity while maintaining appearance. After exploring key properties of robustness of conductivity variation, appearance and adhesion, two primer formulations were selected for further optimization. Key physical properties of the prototype primer formulations are summarized in Table II.3.E.3.

Table II.3.E.3. Key Properties of Selected Primers.

Sample	Wet Resistivity	Solid Resistivity	Adhesion (crosshatch)	Thickness
Primer A	62 k Ω	9.8 G Ω	< 5% removal	~ 28 μ m
Primer C	29 k Ω	0.3 M Ω	< 5% removal	~ 28 μ m

As shown in Table II.3.E.3, two selected primers were optimized in terms of different initial wet resistivity and final solid resistivity that has a direct inverse correlation with conductivity (i.e., conductivity = 1/resistivity). The selected primers exhibited promising adhesion with CFRP and also improved the surface appearance compared with a pristine CFRP surface, as shown in Figure II.3.E.6.

CFRP coupons were coated with the two selected primers and used as the top plate of overlap coupons with AA6022. The effect of CFRP surface conductivity on galvanic corrosion is currently being tested via CCT.

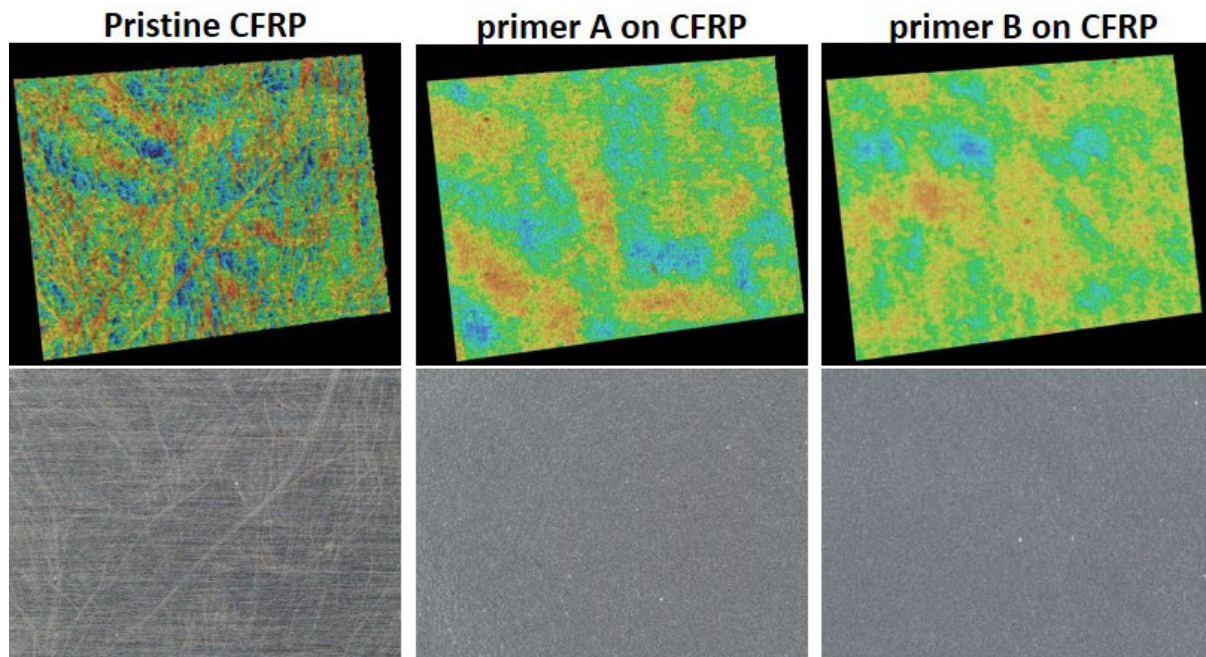


Figure II.3.E.6. Images (first row: 3D false color images from a MacroScope; and second row: 5700 μ m \times 7500 μ m optical images) of the CFRP surface with and without two primers. Source: PPG.

Task 1.3: Coefficient of Thermal Expansion Mismatch Impact (Ford)

FEA modeling of surrogate hem flange joints has been completed. The geometry is shown in Figure II.3.E.7. The FEA simulations account for the thermo-elastic stresses that arise when the hem joint is heated in the e-coat oven. During the initial heating, the CFRP and Al materials expand freely, as the adhesive between them has not yet cured. During the high-temperature hold, the adhesive crosslinks and stiffens. Upon cooling, the CFRP and Al components shrink, but due to their different CTEs, differential stresses will be setup in the component, which can lead to distortion. The cure rate of the adhesive, the adhesive's mechanical properties,

the cure temperature, and the constitutive properties of the Al and CFRP all contribute to the stresses and deformation in the component.

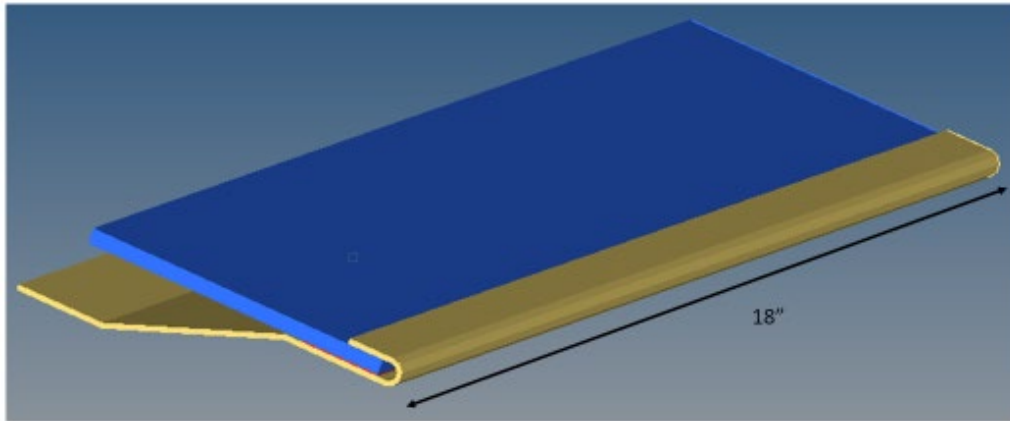


Figure II.3.E.7. Geometry of surrogate hem coupon. Adhesive in the root of the hem joint is not shown for clarity. Inner panel (blue) is CFRP and outer panel (gold) is Al. Source: Ford.

The maximum stresses in the component for the commercial (control) adhesive and several prototype formulations from PPG are shown in Figure II.3.E.8. In one of the low-temperature formulations, the stress has been reduced by ~5 MPa, mainly due to the lower curing temperature (150°C vs. 180°C) and the lower modulus of that adhesive. Further adhesive development is underway at PPG to improve these results.

Comparison of Maximum Stress

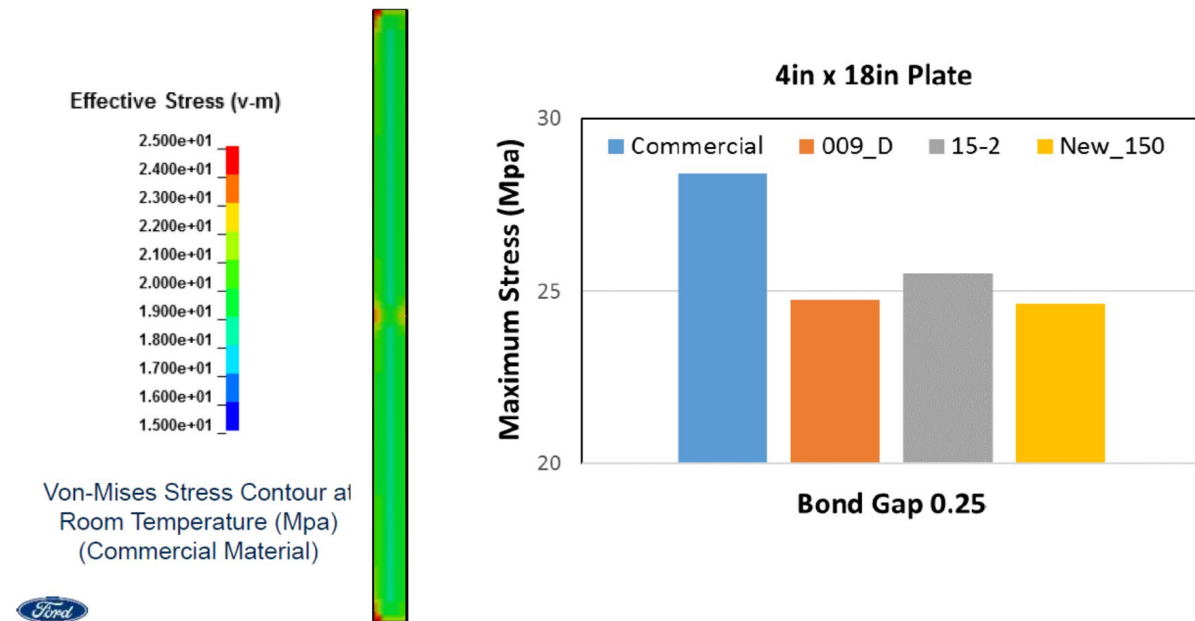
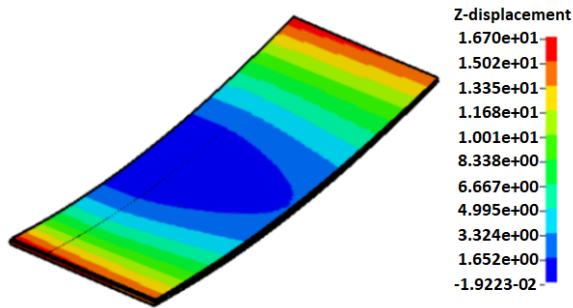
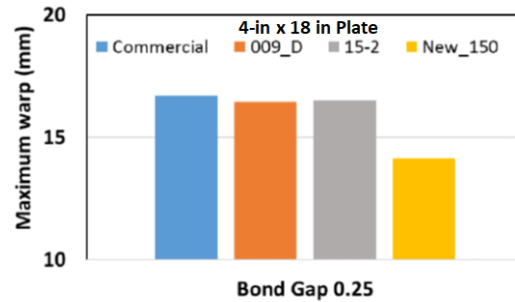


Figure II.3.E.8. Maximum stress in CFRP/Al hem joint with different hem adhesives. Source: Ford.

For vehicle applications, part distortion is the main concern when adhesively bonding dissimilar materials. Part distortion is again minimized by using low modulus, low-temperature curing adhesives. The maximum distortion for the CFRP/Al surrogate hem is shown in Figure II.3.E.9, where again, the benefits of the new 150°C curing adhesive are seen.



Z Displacement Contour under Room Temperature (mm)
(Commercial Material)



Comparison of maximum deflection

Figure II.3.E.9. Maximum deflection of adhesively bonded CFRP/Al surrogate hem joints with different adhesives.
Source: Ford.

Task 2.2: Joint Geometry Optimization (Ford)

Radically different hem geometries have been eliminated from consideration due to the need to use conventional processes to fabricate closure panels. Thus, conventional hem joints will be utilized for prototype components in BP3. The hem radius will be determined by the thickness of the CFRP-inner. The gap between the inner and outer panels will be set by the glass beads (~250 μm diameter) used in the adhesive formulation.

Conclusions

The work performed on this project during FY 2018 further explored the corrosion issues associated with the CFRP/Al couple. Galvanic corrosion is the prime electrochemical degradation mode occurring during both accelerated corrosion cabinet testing and MPG R-343 full vehicle corrosion testing. Further development took place on an electrochemical technique to further understand the conductive features of the CFRP surfaces. E-coats and adhesives prototypes were developed that meet or exceed performance and application requirements while curing at the lower temperatures required by the presence of the CFRP material. A conventional hem joint was selected for the prototype component to be tested in BP3.

References

1. Sloan, F. E., and J. B. Talbot, 1997, "Evolution of perhydroxyl ions on graphite/epoxy cathodes," *J. Electrochem. Soc.*, Vol. 144, No. 12, pp. 4146–4151. doi:10.1149/1.1838157.
2. Srinivasan, R., J. A. Nelson, and L. H. Hihara, 2015, "Development of guidelines to attenuate galvanic corrosion between mechanically coupled Al and CFRE composites using insulation layers," *J. Electrochem. Soc.*, Vol. 162, No. 10, pp. C545–C554.

II.3.F High-Strength Steel-Al Components by Vaporizing Foil Actuator Welding (The Ohio State University)

Glenn Daehn, Principal Investigator

Department of Materials Science and Engineering
The Ohio State University
295 Watts Hall, 2041 College Rd. N
Columbus, OH 43210
E-mail: daehn.1@osu.edu

Anupam Vivek, Co-Principal Investigator

Department of Materials Science and Engineering
The Ohio State University
348 MacQuigg Labs, 105 W. Woodruff Ave.
Columbus, OH 43210
E-mail: vivek.4@osu.edu

Sarah Kleinbaum, DOE Technology Manager

U.S. Department of Energy
E-mail: sarah.kleinbaum@ee.doe.gov

Start Date: October 1, 2016	End Date: September 30, 2020	
Project Funding (FY18): \$758,776	DOE share: \$688,776	Non-DOE share: \$70,000

Project Introduction

This project aims to address the challenge of effectively welding dissimilar materials—steel and Al for creating lightweight, multi-material automotive components. Traditional fusion-based welding between dissimilar combinations of Al and steel is difficult due to starkly disparate melting points and usually leads to the formation of brittle intermetallic compounds at the weld interface. Such joints are weak and cannot be implemented in crash-sensitive components. Structural adhesives and mechanical fasteners of various types including self-piercing rivets, flow drilled screws, friction element welds, and RIVTAC® are currently being utilized for addressing this issue. Solid-state welding techniques, like friction stir and impact welding, offer an elegant alternative solution for joining dissimilar metals without the use of a third body, such as rivets. This project utilizes Vaporizing Foil Actuator Welding (VFAW), an impact welding method developed at OSU [1]. Details on this process can be found in the Materials 2017 Annual Progress Report [2], as well as several journal articles published on this technology.

VFAW has demonstrated much success in welding a wide range of alloys, including Mg-Al, Al-Cu, Ti-Cu, bulk metallic glass-Cu and Ni-Ti. In this project, the focus is on welding specific grades of steel and Al that are relevant to automotive subframes and developing the technology to a level where it can be transitioned to an automotive supplier or an OEM. Besides the research on weldability of different material combinations and determining the ideal parameters through experiment and simulation, the project also includes design, production, and testing of a prototype sub-frame component. Robustness of the process for application in a serial production setting is demonstrated via robotic implementation.

The work in FY 2018 was focused on developing the technique for welding a specific Al-steel combination down-selected from material screening work conducted in Year 1 of the project. Coupon-scale welded samples were created and mechanically tested under static and cyclic loading. The prototype component was also selected and modified into a lighter, multi-material part that can match the baseline performance requirements. Collaborators at PNNL focused on a couple of aspects in FY 2018: (1) the weld process simulations to predict the joint morphology and temperature distributions for several different configurations involving the

interlayer—these simulations were carried out using the validated finite element-based process-structure model developed in FY 2017; and (2) identifying and developing an approach for the structure-property prediction of the welded coupons.

Objectives

This project accelerated and focused the development of VFAW for the production of an automotive component. At project completion, the technology will be ready for adoption within the R&D groups of Tier 1 and OEMs for assembly of any mixed/advanced material bodies.

The overall objectives for the project are:

- 20% weight reduction of a current all-steel automotive component from a 2017 midsize sedan at a cost premium of \$3/lb-saved by developing a mixed-material joining technology capable of high-volume production.
- The produced component should meet or exceed the strength and durability of the incumbent component.
- Develop a predictive modeling capability for relating process, structure, and property of VFAW joints.

The specific objectives for FY 2018 were:

- Obtain reliable process parameters and system for VFAW of a specific material pair within geometric constraints of the prototype component assembly.
- Complete a multi-material-based redesign of the baseline all-steel sub-frame component.
- Based on the process-structure simulations, make recommendations for different angles of the relative angles of the interlayer with respect to flyer and target plates.

Approach

The overall approach for this project is to perform coupon-scale testing at OSU, develop welding systems and part fixtures at OSU and Coldwater, prototype-scale manufacture and testing at Magna, and process simulation at PNNL. Ashland, Arconic, and Hydro are providing material. It was planned that the welding head will be fabricated and tested at OSU and, along with a capacitor bank, installed at Magna. Coupon data will be imported into the design of prototype component and simulated testing and design iterations will lead to the final part. Once the prototype design is released, Magna will produce sub-components and perform assembly at its prototype facility. The assembled prototypes will be tested for strength, durability, and corrosion performance.

Coupon Testing

The Al-steel combination selected from the screening work in Year 1 was AA5754-O (4-mm thick flyer) and high-strength low-alloy (HSLA) 340 (2.2-mm thick target). Some early testing was also performed with 3.3 mm thick AA5754-O. VFAW of this pair requires a 1 mm thick AA3003-H14 intermediate layer (interlayer). Standoff gaps between the flyer, interlayer, and target were provided by dimpling the target and interlayer sheets. In a single shot, the flyer impacts the interlayer, which in turn impacts with the target, and the three layers are welded to each other. This stackup is shown in Figure II.3.F.1. Four different preforming designs were tested to create welds.

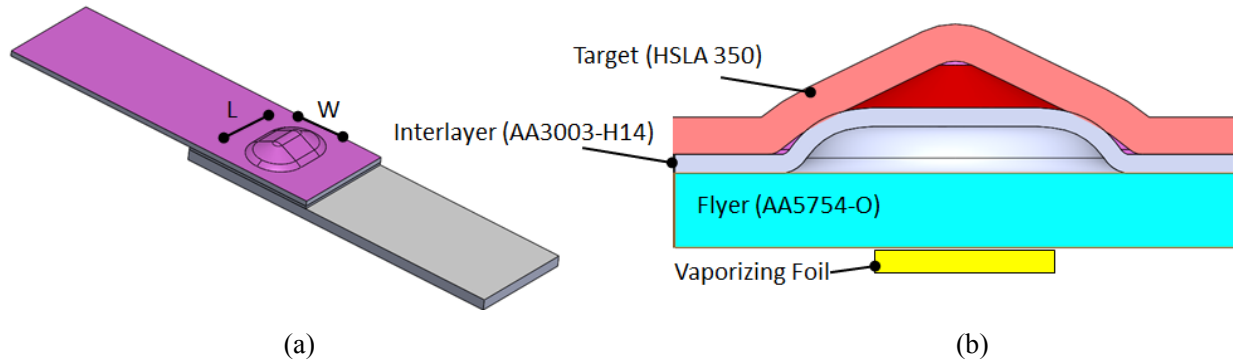


Figure II.3.F.1. Illustrations of (a) the lap joint showing the dimple length (L) and width (W) which varied and (b) the VFAW lay-up with the interlayer. Source: OSU.

Two different pulsed power capacitor banks were used in this work. The first is a 16 kJ Maxwell Magneform system with a short circuit rise time of 12 μ s. This will be referred to hereafter as the Magneform bank. The second system is a 4.2 kJ capacitor bank with a rise time of 6 μ s, which was custom-built by the Center for Design and Manufacturing Excellence (CDME). This will be referred to hereafter as the CDME bank. It should be noted that the CDME bank is significantly faster than the Magneform bank and has a higher-efficiency. As the CDME bank is going to be installed at a Tier 1 supplier facility for prototype assembly, the energy limit for the experiments with that system is 4.2 kJ. The energy input from the Magneform bank was kept under 6 kJ for any experiments performed with it, thereby taking its energy efficiency into account. It was hypothesized that this would replicate the results from the smaller, but faster, CDME bank.

Geometry of the preformed dimples was finalized based on the trials and for generating the strength and durability data to be used in the prototype design simulation. Several samples were prepared with an adhesive between the interlayer and the target. The adhesive was applied around the dimple in order to avoid having to weld through the adhesive. Ashland's two-part, room-temperature-curing adhesive attaches the interlayer to the target, as well as providing a seal around the final weld between the two pieces. There is no adhesive between the flyer and the interlayer as they are both made of Al and are not susceptible to galvanic corrosion. Tension-tension fatigue tests to identify low-(5,000 cycles), medium-(100,000 cycles) and high-(1,000,000 cycles) cycle failure loads began at the end of Year 2.

Design of Prototype

The stamped steel production cradle was purchased and reverse-engineered to create a computer-assisted design model that provided project targets and boundary conditions. Since there is no OEM involvement in the project, performance targets were not provided. Due to this, the reverse-engineered baseline steel cradle was used to create the targets for the multi-material redesign. The goal of the multi-material redesign is to have the same performance or better than the baseline:

- Stiffness targets were developed based on the performance of the steel baseline. For the redesign, the stiffness was set to be 3% or greater in prime locations and 5% or greater in all other areas from the target values.
- Fatigue Block Cycles were developed based on benchmarking efforts:
 - Based on previous experience, we developed a fatigue schedule comprising events (blocks) with a respective number of repeats.
 - Each event has time history loads (road load data) with varying magnitudes of load acting at the cradle hard points in X, Y, and Z global directions.

- Based on each event, we established the magnitude and angle of a resultant vector, which is in one plane to facilitate the test setup and is an exact representation of the load history with a certain finite number of repeats.
- For each event, we obtained the max and min magnitude of loads from road load data acquisition to obtain a force range (Time slice). We then calculated pseudo-damage based on this force range for one repeat.
- We then obtained the total pseudo-damage at selected hard points and directions to determine the percentage of damage contribution of each event at each hard point.
- The current multi-material redesign was evaluated to ensure formability and was updated accordingly to avoid any splits or tears.

Design of the prototype welding head is ongoing in parallel with component design. The size of the component, various approach angles, and space constraints are taken into consideration during weld head design.

Simulation

In the effort towards determining optimal weld process parameters, including weld geometry and impact speed, a high-fidelity and validated process-structure model [3] was utilized to perform several process simulations involving an interlayer. A representative set of simulation models are shown in Figure II.3.F.2.

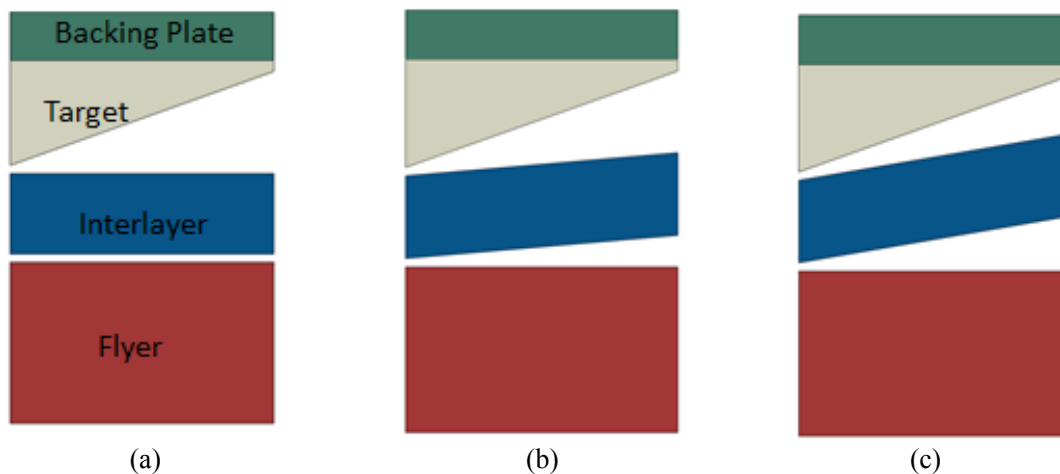


Figure II.3.F.2. Different configurations considered for modeling the impact welding process with the interlayer. The target was kept at the same angle of 20° and the initial velocity of flyer was 770 m/s. Three configurations differ in the angle of the interlayer: (a) 0° (b) 5° and (c) 10° . Source: OSU.

The structure-property predictive model requires appropriate input material and interfacial properties before it can predict joint performance in terms of the load-displacement behavior obtained from the mechanical testing. Typically, calibration approaches are used to back-fit the load-displacement curve by varying the input material parameters, but the calibration approach fails to provide a predictive response even for a different loading configuration or geometry of the joint. In FY 2018, we proposed an approach to determine the interfacial strength and other material input parameters that are necessary for a truly predictive model. However, the testing procedures required for such a purpose are extensive and out of the scope of the current project. Therefore, the team decided to adopt a simpler approach by assuming a *perfect* interfacial bond, implying that the interface between the different components (e.g., flyer-interlayer and interlayer-target) could not fail. Although this assumption is not fully accurate, it still provides a means to study the impact of different weld geometries on the joint performance.

Figure II.3.F.3 shows the model for lap shear test configuration of the Steel-Al welds. The base material properties will be provided by OSU, along with the weld cross-section images to indicate the regions that are bonded within the weld zone. These will be used as the input for the finite element model to predict the load-displacement behavior. The predicted load-displacement behavior will be compared against the experimental measurements. Although it is not expected that the prediction will be very accurate quantitatively, it can provide qualitative guidance on desired bonded regions to achieve required joint performance.

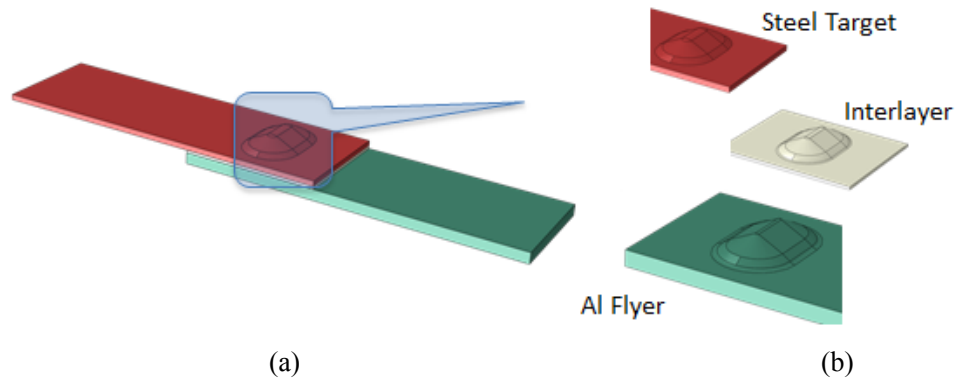


Figure II.3.F.3. Model for the lap shear test configuration of the joint showing (a) the assembled lap shear configuration and (b) the exploded view of the weld assembly showing the Al flyer, the interlayer, and the steel target. Source: OSU.

Results

Coupon Testing

Due to material availability issues, the work in this year began with a 3.3 mm thick AA5754-O flyer. Welds with 15 mm wide dimples were able to be made using the Magneform bank; results of lap shear testing in the direction parallel and perpendicular to the long direction of the dimple are shown in Figure II.3.F.4.

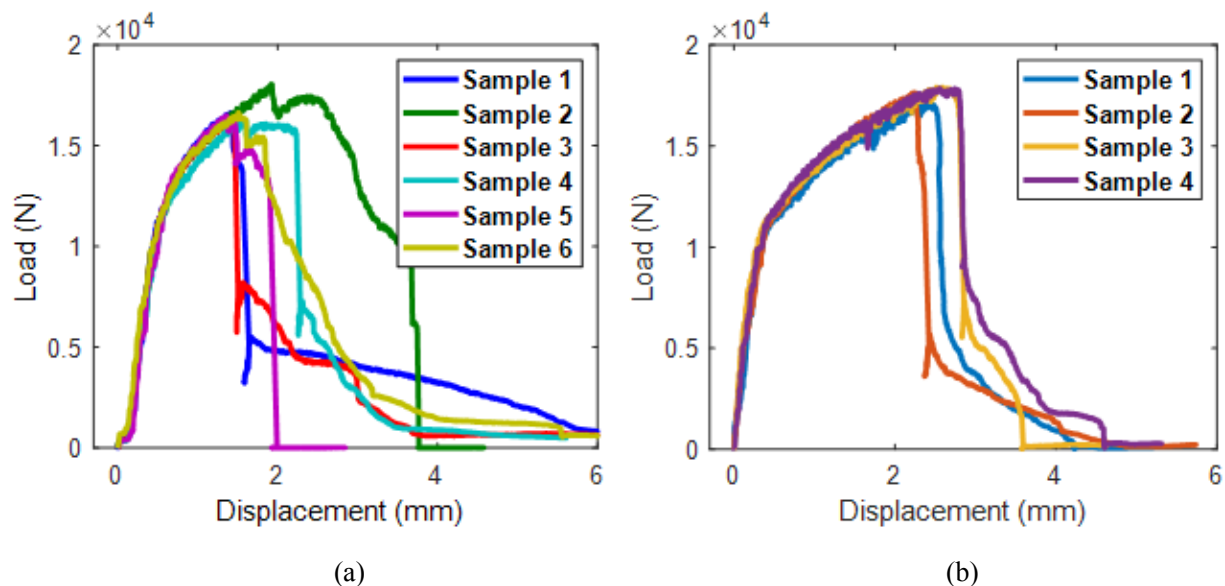


Figure II.3.F.4. Results of lap shear testing of welds made with 3.3 mm thick AA5754-O flyers and 2.2 mm thick HSLA 340 targets where (a) samples have a cross head motion perpendicular to the longer dimension of the weld and (b) samples have welds loaded along their parallel length dimension. Source: OSU.

With the 15 mm wide dimples, welding attempts with the 4 mm thick flyer resulted in weak welds. As a result, the designed dimple was modified to make it 20 mm wide. With the wider dimple, the weld could then be made. However, the welds were below the desired load capacity of 15 kN, which was determined as 70% of the load capacity of an Al/Al weld of the same geometry. Experiments with the same welding geometry were conducted with the CDME bank operating at 4 kJ, where the welds were found to be significantly stronger. The comparison of results from the Magneform and CDME banks is shown in Figure II.3.F.5.

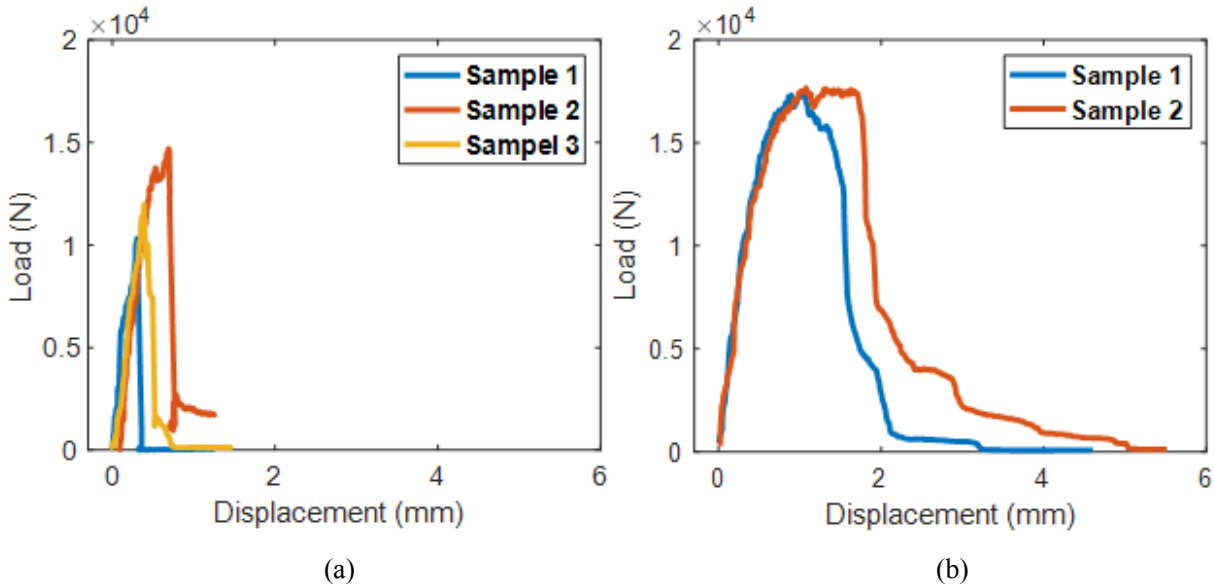
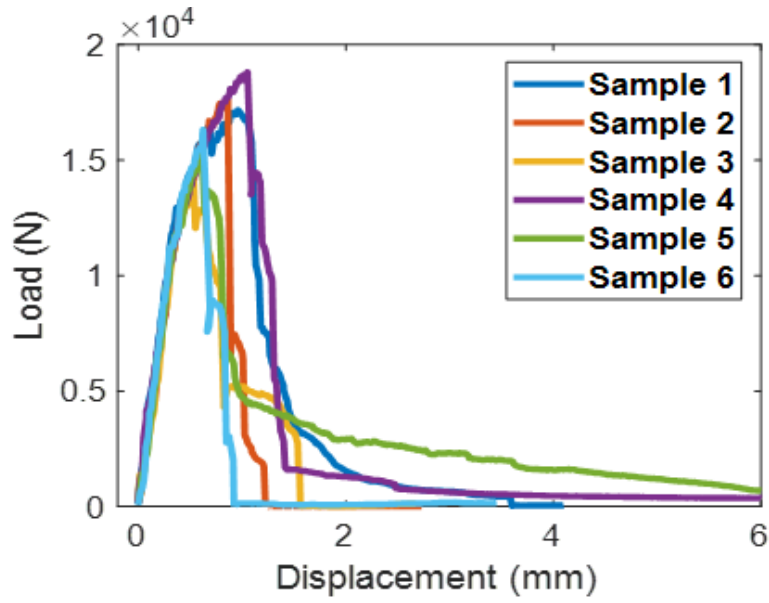
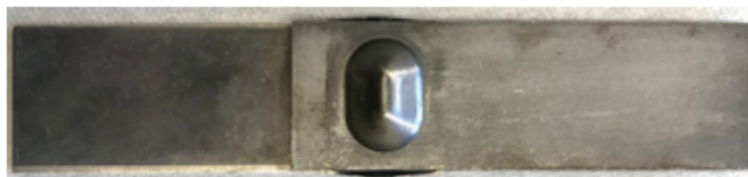
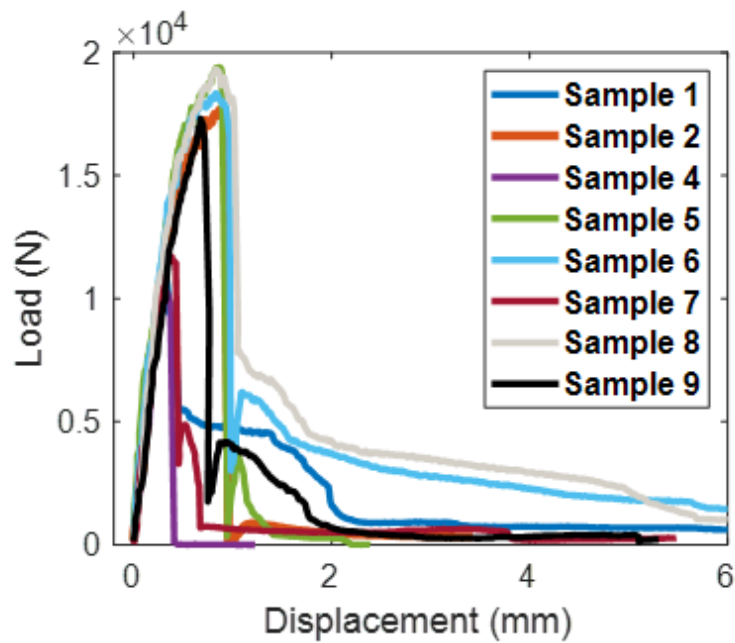


Figure II.3.F.5. Results of lap shear testing of welds made with 4 mm thick AA5754-O flyers and 2.2 mm thick HSLA 340 targets where (a) samples were created with 6 kJ of input energy from the Magneform capacitor bank and (b) samples were created with 4.2 kJ of input energy from the CDME bank.

The final set of coupon testing began in FY 2018, which focused on creating welds in the geometry and sequence planned for the final prototype assembly. These welds were made with an adhesive/sealant between the interlayer and the target. More than 50 samples have been welded with the CDME bank operating at 3.8 kJ input energy. Unlike previous welds, none of the target or flyer sheets had to be surface ground prior to welding. The static lap shear test results in parallel and perpendicular directions are depicted in Figure II.3.F.6. The parallel samples showed repeatable load capacity, whereas the perpendicular ones had three out of eight fail prematurely. This variation can be attributed to misalignment of the foil and dimple features. Going forward, this issue will be abated with the use of hard stops and alignment features in the welding head being fabricated for the prototype assembly. Cyclic testing with a peak load of 40% of static failure load resulted in failure in base Al after 1,100,000 cycles. Several more fatigue tests are to be performed.



(a)



(b)

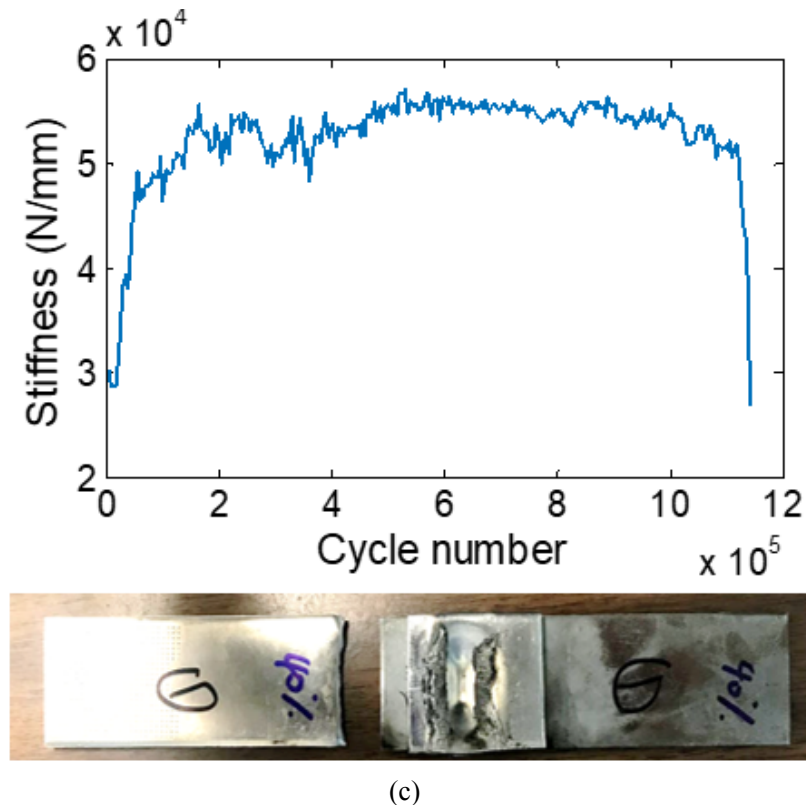


Figure II.3.F.6. Results of lap shear and fatigue testing of welds made with 4 mm thick AA5754-O flyers and 2.2 mm thick HSLA 340 targets with 3.8kJ on the CDME bank where (a) the sample was pulled parallel to the weld, (b) the sample was pulled perpendicular to the weld and (c) the sample was subjected to tension-tension cyclic loading with 40% maximum load and experienced base metal failure after 1.1M cycles. Source: OSU.

Design of Prototype

Cosma has designed a multi-material VFAW front sub-frame that is nearing prototype release. The new sub-frame was designed based on stiffness, parent metal fatigue, and formability. Design considerations may need to be accounted for based on weld fatigue results. The original mass objective was to achieve a 20% weight reduction from the current all-steel production design. This weight savings was achievable with the original concept of an entirely Al rear components that would be vapor foil welded to the steel front rails. However, this design only utilized eight vapor foil welds in an area that does not experience high loads. As a result, a higher percentage steel-optimized design was selected to better evaluate the manufacturing robustness of the welding technology. The current design provides approximately an 8% mass reduction based on adherence to stiffness targets, as shown in Figure II.3.F.7.

		Baseline ARQ631- DRQ2185	ARQ1098 DRQ3965	
Total Mass(kg)				
Rear Steel Mass		24.35		
Rear Portion Mass		15.59	14.32	-8.1%
		3% Prime 5% Other	Stiffness (kN/mm)	% to Target
LCA RR LH	X	49.3	54.9	11.3%
LCA RR LH	Y	177.3	192.6	8.6%
LCA RR LH	Z	13.0	14.5	11.3%
LCA RR RH	X	49.3	55.8	13.0%
LCA RR RH	Y	177.3	195.0	9.9%
LCA RR RH	Z	13.0	14.4	10.8%
LCA FR LH	X	52.8	57.7	9.3%
LCA FR LH	Y	39.3	41.8	6.3%
LCA FR LH	Z	18.9	19.1	0.8%
LCA FR RH	X	52.8	61.0	15.4%
LCA FR RH	Y	39.3	45.5	15.7%
LCA FR RH	Z	18.9	20.4	7.7%
ENG MTG RR	X	93.8	97.8	4.3%
ENG MTG RR	Y	205.8	210.1	2.1%
ENG MTG RR	Z	6.4	6.8	6.0%
STAB BAR LH	X	32.8	40.7	24.3%
STAB BAR LH	Y	18.5	46.1	149.6%
STAB BAR LH	Z	13.5	13.8	2.5%
STAB BAR RH	X	32.8	40.5	23.4%
STAB BAR RH	Y	18.5	47.9	159.5%
STAB BAR RH	Z	13.5	13.5	-0.2%
STRG GEAR LH	X	26.5	33.5	26.1%
STRG GEAR LH	Y	30.0	43.2	43.8%
STRG GEAR LH	Z	8.6	9.3	7.9%
STRG GEAR RH	X	26.5	32.8	23.7%
STRG GEAR RH	Y	30.0	45.3	50.9%
STRG GEAR RH	Z	8.6	9.0	3.7%
TORQUE STRUT	X	6.6	6.9	3.2%
TORQUE STRUT	Y	13.2	14.9	13.1%
TORQUE STRUT	Z	4.9	5.5	13.3%

Figure II.3.F.7. Current sub-frame stiffness performance. Source: OSU.

Figure II.3.F.8 shows the current sub-frame design which includes steel front components connected to a combination Al/Steel rear component and including 48 vapor foil welds. By allowing for more vapor foil welds in various locations, a more extensive evaluation of the technology will take place when prototypes are being built. Having many welds in a variety of areas will challenge the design of the weld head and the manufacturing process to be more robust. Having an increased number of vapor foil welds will also help to properly evaluate the technology’s usefulness for sub-frame applications, and the welds will be subjected to a variety of load paths during physical testing. The design still needs to be evaluated for weld fatigue. Based on fatigue results, Cosma will provide targets that must be achieved with the prototype weld held and process setup. When repeatable welds that meet all performance requirements can be created with the new weld setup, then an official prototype kick-off can occur. Prototypes will not be built unless new setup meets requirements.

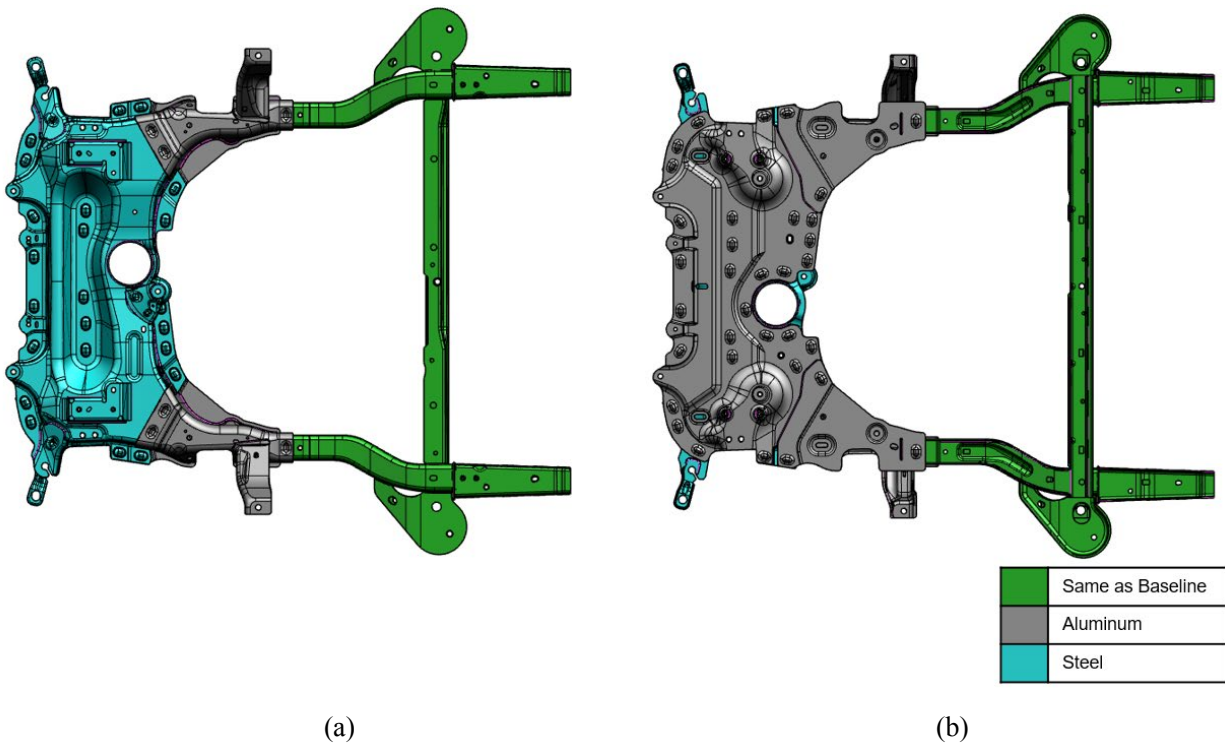


Figure II.3.F.8. Redesigned sub-frame: (a) original design for 20% weight reduction and (b) redesign for a 5-12% weight reduction showing more locations for vapor foil welds. Source: OSU.

Figure II.3.F.9 shows the current design of the prototype weld head in various configurations. The breech, designed to back up the foil during the weld process, and the clamping electrodes are key elements in determining the physical size of the weld head, and subsequently the tool's capability when reaching areas of assemblies to weld. The attempt here was to reduce the breech and anvil to the minimum size necessary to achieve a successful weld with the present weld dimension parameters. This drove the decision to remove the foil dispenser from the tool. The foil clamping feature of the tool is accomplished with a small guided pneumatic cylinder designed to pull the electrodes down to clamp the foil in the same process. Foils can be individually loaded prior to each weld either by hand or by a separate feed type dispenser presenting a single foil ready to clamp.

The anvil, which backs up the parts to be welded opposite the foil side on this tool, has a number of designed-in features. The anvil is easily changeable to a different length, and as-mounted is spring-loaded and includes a locating pin to provide quick angle adjustment to the tool by the operator prior to a weld. The anvil incorporates a concave feature on its part-contact surface to provide a means of aligning the tool over and onto a preformed dimple in the part to be welded, thus locating the tool and weld head to the desired location for the weld. The tool incorporates a larger guided cylinder designed to apply the clamping feature prior to the actual weld process. Just after the tool is located for a weld, it is activated manually by the operator to raise the breech and foil to contact the part under the dimple, thus clamping the part assembly ready to weld. The cylinder is mounted to a main base (anvil arm of the tool) and lifts a second breech arm to a clamping position at full extension of the cylinder.

The tool weight is currently approximately 50 lbs. The operator will be assisted with handling of the tool via a manual/pneumatic assist arm to balance weight and allow for locking of the tool at various angles as required by the parts to be welded. The tool design will incorporate features to allow the operator to adjust position and lock the tool at any angle required prior to approaching the parts to be welded via gauge blocks on the part fixture base(s).

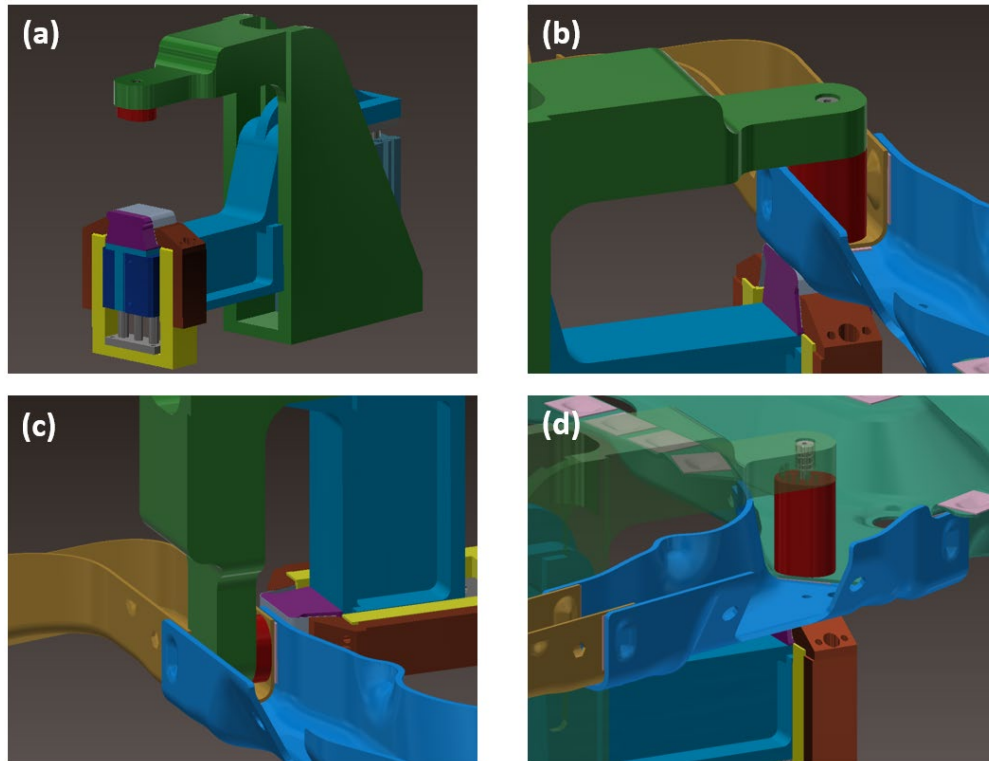


Figure II.3.F.9. Design of the weld head: (a) weld head in open position; (b) part clamped with long anvil; (c) part clamped with short anvil; and (d) part clamped with adjusted-angle anvil. Source: OSU.

Simulation

Figure II.3.F.10 shows the weld interface obtained from the process simulation for the case when the interlayer is placed at an angle of 10° to the flyer and the target is at 20° . The interface shows the desired wave characteristics indicating that this configuration and corresponding relative angles between the flyer, the interlayer, and the target should produce good welds. The design used for actual welds has the target deformed with an angle of 26° to the flyer and the interlayer parallel to the flyer. The results from interlayer angles of 0° and 5° are not presented here because they were uninteresting and did not depict any wavy characteristics at the interface.

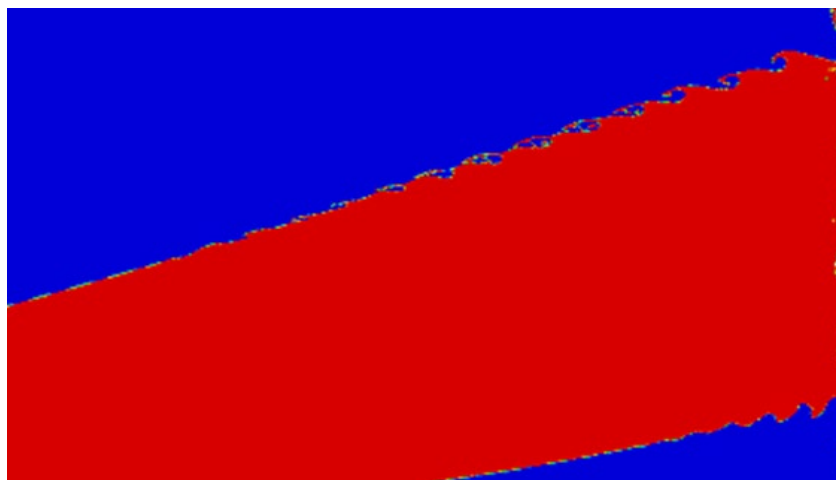


Figure II.3.F.10. Weld interface predicted from the simulation for the case when the interlayer is kept at an angle of 10° .

Conclusions

VFAW has been shown to successfully weld the stamping grade Al and steel pairs selected for prototype production. The welds are strong and have a load bearing capacity greater than 70% of a similar material weld of the same geometry. The baseline sub-frame component has been selected and the redesigned hybrid prototype can be 8% lighter while meeting baseline performance. The reduction in mass savings target is compensated by an opportunity to thoroughly assess manufacturing capability of VFAW. In strength testing there is still some variability that is attributed to alignment issues. The prototype weld head is being designed while addressing this tolerance issue. Durability testing has just begun but will need to be verified with the new weld head and process setup.

Key Publications

1. Gupta, V., T. Lee, A. Vivek, K. S. Choi, Y. Mao, and X. Sun, 2019, "A robust process-structure model for predicting the joint interface structure in impact welding," *J. Mater. Process. Tech.*, Vol. 264, pp. 107–118.
2. Mao, Y., V. Gupta, B. Ufferman, A. Vivek, K. S. Choi, X. Sun, and G. S. Daehn, 2018, "On Process, Structure, Property Relationships in Impact Welding of Al 6061 and Steel 4130," *Eighth International Conference on High-Speed Forming*, May 14–15, 2018, Columbus, OH, USA.
3. Gupta V., X. Sun, K. Choi, A. Vivek, Y. Mao, and G. Daehn. 2017, "A Computational Modeling Approach to Predict the Interfacial Characteristics Obtained in High Velocity Impact Welding of Metals," *Materials Science & Technology 2017*, October 8–12, 2017, Pittsburgh, PA, USA.
4. Gupta V., K. Choi, A. Vivek, Y. Mao, X. Sun, and G. Daehn, 2018, "Prediction of Joint Properties Obtained in the High Velocity Impact Welding of Dissimilar Metals," *TMS 2018 Annual Meeting & Exhibition*, March 11–15, 2018, Phoenix, AZ, USA.

References

1. Vivek, A., S. R. Hansen, B. C. Liu, and G. S. Daehn, 2013, "Vaporizing foil actuator: A tool for collision welding," *J. Mater. Process. Tech.*, Vol. 213, No. 12, pp. 2304–2311.
2. DOE Vehicle Technologies Office, 2018, "Materials 2017 Annual Progress Report," DOE-EERE VTO Report No. DOE/EE-1711, May 2018.
3. Gupta, V., T. Lee, A. Vivek, K. S. Choi, Y. Mao, and X. Sun, 2019, "A robust process-structure model for predicting the joint interface structure in impact welding," *J. Mater. Process. Tech.*, Vol. 264, pp. 107–118.

II.3.G HPC and High-throughput Characterizations towards Interfaces-by-Design for Dissimilar Materials Joining (Oak Ridge National Laboratory)

Xin Sun, Principal Investigator

Oak Ridge National Laboratory
Oak Ridge, TN 37831
E-mail: sunx1@ornl.gov

Erin Barker, Principal Investigator

Pacific Northwest National Laboratory
Richland, WA 99354
E-mail: erin.barker@pnnl.gov

Sarah Kleinbaum, DOE Technology Manager

U.S. Department of Energy
E-mail: sarah.kleinbaum@ee.doe.gov

Start Date: October 1, 2018

End Date: September 30, 2021

Project Funding (FY18): \$850,000

DOE share: \$850,000

Non-DOE share: \$0

Project Introduction

Further weight reduction of automotive body structures depends on the industry's ability to reliably and cost-effectively assemble multiple lightweight materials including CFRP, Mg alloys, Al alloys, and AHSS. Because of their extreme disparities in physical properties such as melting temperature, thermal conductivity, and CTE, dissimilar materials pose a serious challenge for traditional joining process development. There is a lack of fundamental understanding on the interfacial bond formation mechanisms for the different dissimilar materials pairs to enable process development.

Objectives

With the recent advancements in HPC and high-throughput experiments at various materials length scales, this project aims to establish a scientific framework for designing the hierarchical interfacial features and the associated chemical and thermomechanical kinetic pathways to achieve them.

Approach

For each set of materials interfaces, the interfacial characteristics at different length scales are simulated with multiscale materials processing models and the results will be experimentally validated and calibrated with associated experiments at the corresponding scales. The calibrated modeling parameters at the lower length scale will be hierarchically passed to the higher length scale to predict the robust processing parameter windows with quantitative confidence. Once the hierarchical multiscale interfacial modeling framework is established, it can be used to inversely design the dissimilar materials interface and the associated welding process and parameters thereby accelerating the development and deployment of dissimilar materials joining technologies.

In FY 2018, the interface-by-design efforts investigated a Mg/steel interface generated via two different joining methods: ultrasonic welding (USW) and friction assisted scribe technology (FAST). The technical approaches for interface-by-design were carried out in two parallel tasks corresponding to each joining method. Macro-scale modeling of USW was established to quantify the heat generation and temperature profile and history for joining two Mg sheets and joining Mg to uncoated steel. Modeling results were validated by experimental measurements. MD simulation models were established to calculate interfacial strength of Mg/Mg and Mg/Fe under quasi-static and impact welding conditions. For FAST, a finite element (FE) model was utilized to obtain desired temperature distribution and interfacial morphology. FE-based

cohesive zone models were developed to identify the desirable interfacial characteristics needed to achieve desired joint strength.

Results

Task 1. Interface-by-design for USW process

A coupled thermomechanical FEM was developed to predict the temperature profile in USW of a 1.68 mm AZ31 Mg sheet. An USW machine with two sonotrodes was employed as shown in Figure II.3.G.1. An infrared (IR) camera was used to measure temperature at the edge of the sheets. Sonotrode vibration was measured by DIC using a high-speed camera. The welding power was 1,000 W with a vibrating frequency of 20 kHz and nominal clamping pressure of 50 psi. The friction coefficient is generally a function of temperature (T) and pressure (p). To understand the influence of the friction coefficient on the heat generation mechanism, a preliminary study was carried out by assuming constant friction coefficients (μ) with four values: A, $\mu_f = \mu_{hs} = 0.4$; B, $\mu_f = \mu_{hs} = 0.2$; C, $\mu_f = 0.3$, $\mu_{hs} = 0.4$; and D, $\mu_f = 0.5$, $\mu_{hs} = 0.4$, where the subscript “f” denotes the faying (sheet/sheet) interface and “hs” denotes the hone/sheet interface. In addition, case E considers a temperature-dependent friction coefficient, while temperature- and pressure-dependent friction coefficients were considered in case F. The temperature and pressure dependency of friction coefficients were obtained from the open literature.

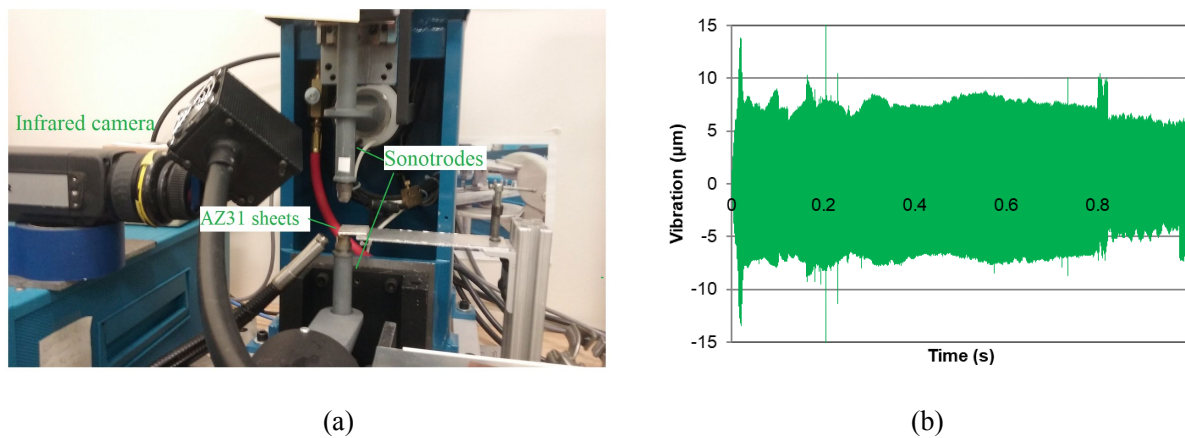


Figure II.3.G.1. Ultrasonic welding system setup (a) and measured sonotrode vibration (b).

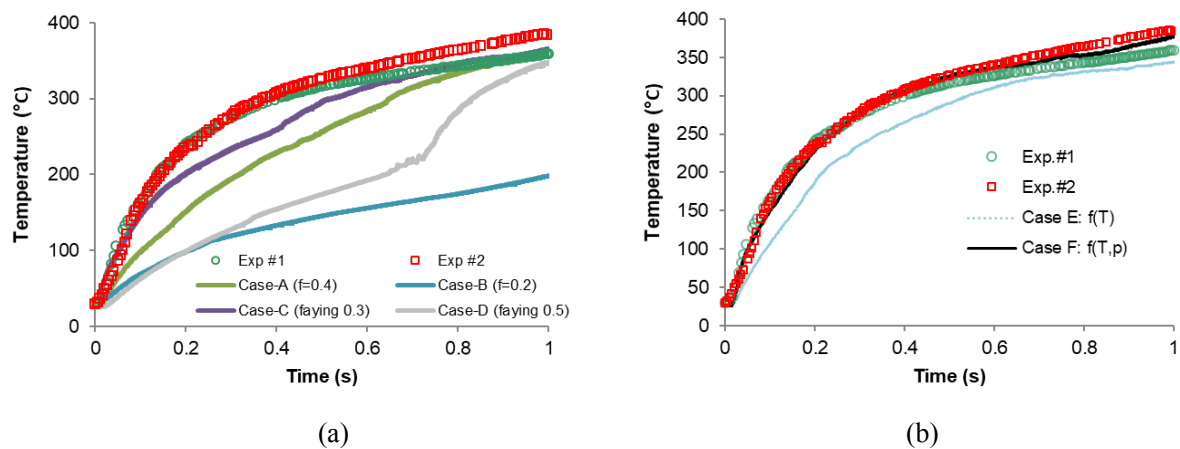


Figure II.3.G.2. Comparison of temperature history at faying interface among (a) cases A~D and (b) cases E-F with experimental measurements (open squares and circles).

Figure II.3.G.2 shows the predicted temperature history at the center of the faying interface compared with the IR measurements (red empty squares) for USW time up to 1 second. The temperature increases monotonically with time and peaks at the end of welding for all cases. The experimental data shows that at the start of the welding process, heating rates at the faying interface are considerably higher than for all of the model predictions from Cases A to D, as shown in Figure II.3.G.2.(a). Case A predicts the peak temperature close to the experiments, but the initial heating rate was much lower than the experimental measurements. Case B, on the other hand, considerably underestimated the temperature, predicting the peak temperature to be just around 200°C. In Case C, the heating rate at the initial welding stage compares well with the experiment. It is interesting to note that Case D with a higher friction coefficient at the faying interface leads to a very low heating rate at the beginning. From about 0.7 s, the temperature started to increase more rapidly. This can be attributed to the indentation of the Mg sheet by the teeth of the horn, which results in higher traction force than the friction force at the faying interface. The peak temperature reached at the end of welding is similar to the experimental measurement. It is also interesting to note that the heating rate in all cases became comparable to experiments at the later welding stage. In Case E, the friction coefficient had sole dependences on the temperature. At the early welding stage, the interfacial temperature was considerably underestimated. Because of the increase of the friction coefficient with temperature, more heat was generated at the interface and conducted throughout the sheet. The teeth of the sonotrode penetrated deeper into the sheet material and accelerated the heat generation on the faying interface. Case F considered the friction coefficient as a function of both temperature and pressure. In this case, the predicted temperature at the faying interface became much more comparable to the experiment. With the IR measurement, a full field temperature on the edge of the weld can be visualized for the whole USW process. Figure II.3.G.3 compares the temperature distribution captured by IR camera (top) and by model predictions (bottom). Both the measurement and the prediction feature an elliptical temperature distribution. Overall, the model prediction shows good agreement with the measured results.

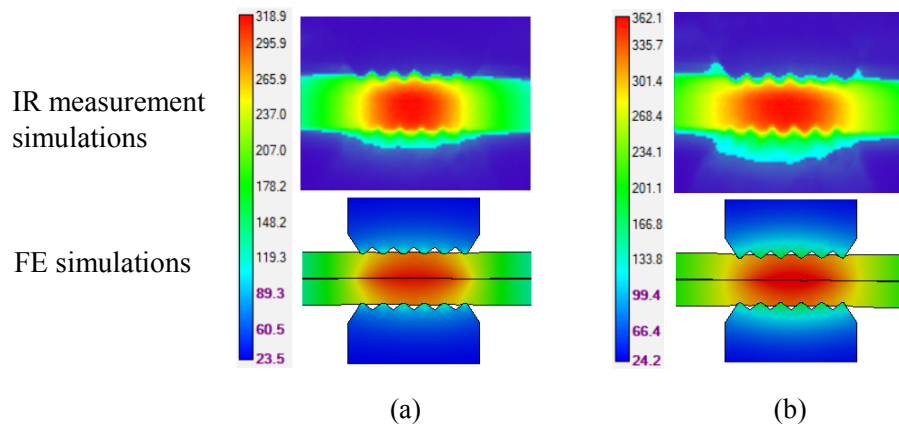


Figure II.3.G.3. Temperature distribution by IR measurement and ABAQUS 2D plane strain FE simulation: (a) $t = 0.5$ s, (b) $t = 1.0$ s.

Next, the validated thermomechanical model is used to predict the heat generation mechanisms and temperature profile during USW of the AZ31/DP590 sheets. The thickness of the DP590 sheet is 1.08 mm, while the AZ31 sheet is 2.34 mm. The zinc-coating was removed from the DP590 surface by acid with energy dispersive spectroscopy confirmation. Figure II.3.G.4 shows the measured temperature profile at the center of the faying interface compared with the predicted results, which validates the accuracy of the numerical model. Under such welding conditions, no bond is formed between the two sheets because the temperature at the faying interface is too low and the solubility of Mg in Fe is limited.

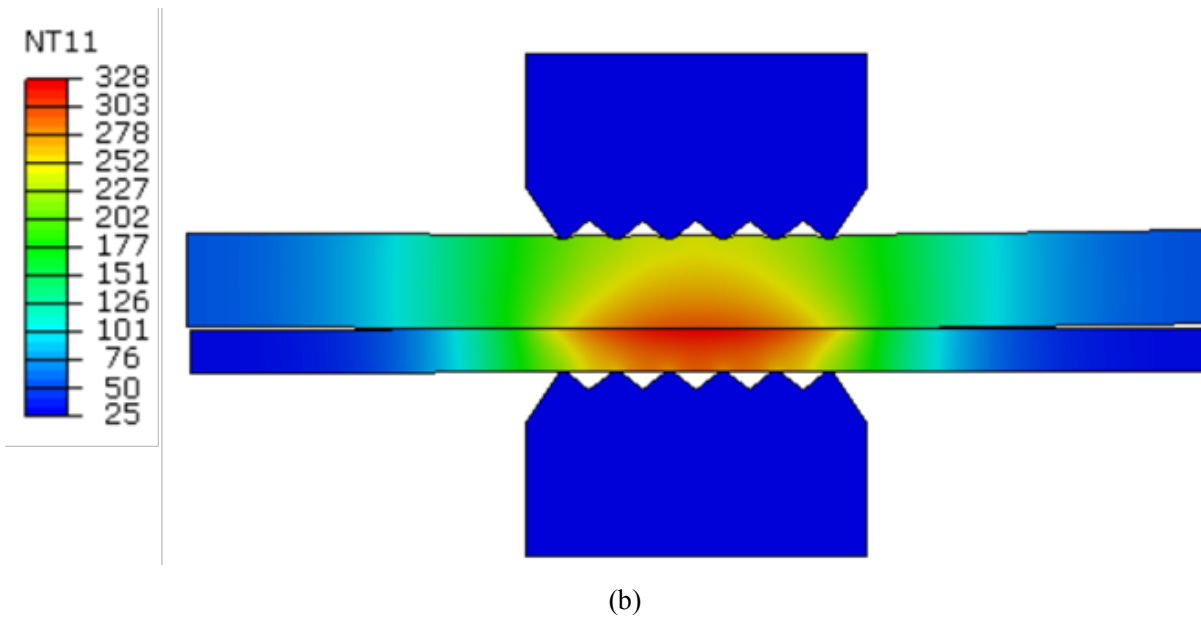
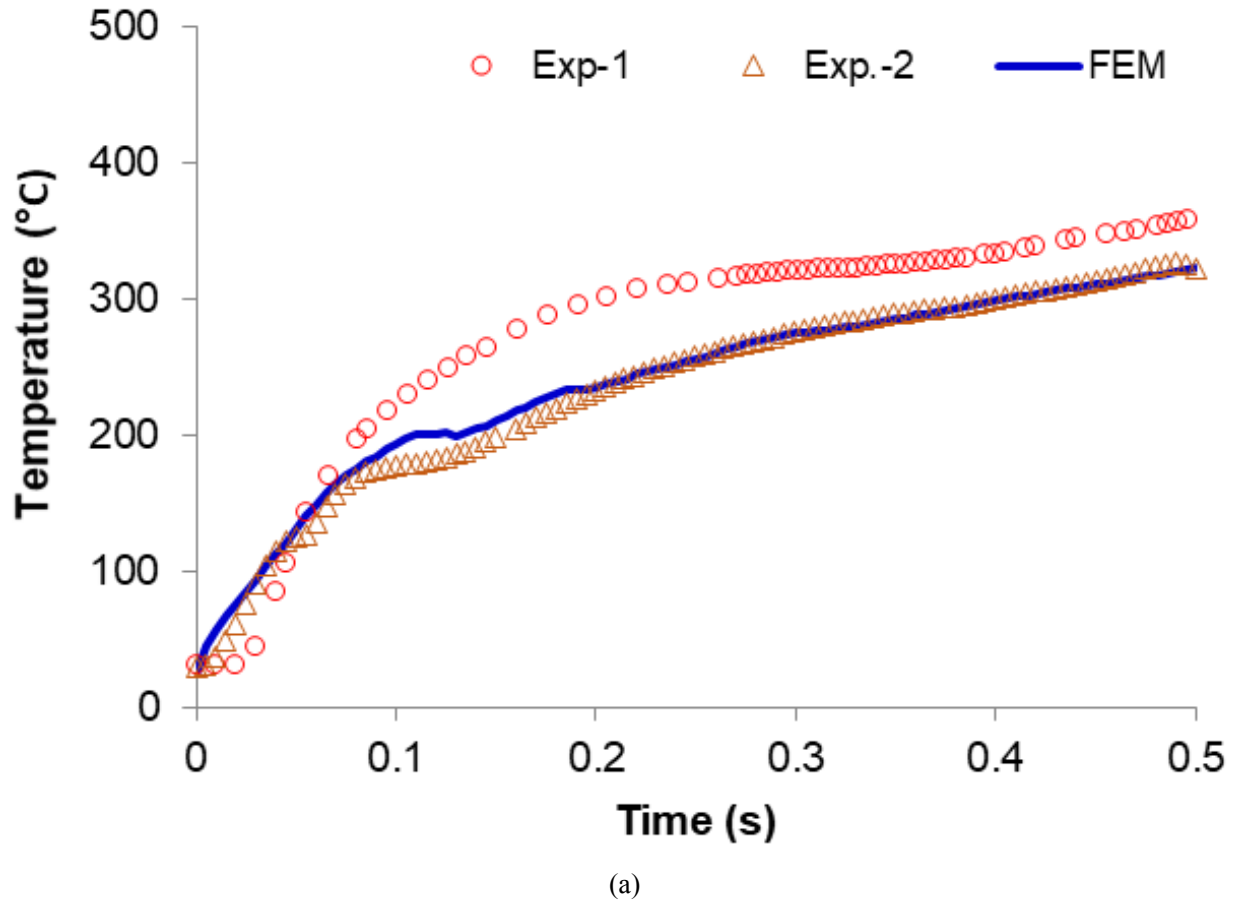


Figure II.3.G.4. Temperature by IR measurement and simulation: (a) Profile at center, and (b) Numerical results from ABAQUS 2D plane strain FE simulations.

We employed the validated model to increase the interfacial temperature by changing the welding conditions, (i.e., increasing the clamping load and welding power [vibration amplitude]) by 20~40%. Although the peak temperature can reach as high as 500°C, the Mg sheet was largely indented by the sonotrode, which is not desirable for weld performance. The experimental setup was later changed to sonotrode/anvil configuration with the Mg sheet facing the anvil side to avoid excessive deformation. A bond is formed under a welding power of 3500 W and a clamping pressure of 60 psi. Further numerical and experimental investigation will be conducted on this welding setup to quantify the necessary temperature and pressure in weld formation.

Next, MD simulations of the Mg/Mg and dissimilar (Mg/Fe) interfaces under static and impact joining conditions were investigated to understand the fundamental bonding mechanisms and to quantify the intrinsic bonding strength between the two materials. The MD simulations are performed with the Large-scale Atomic/Molecular Massively Parallel Simulator (LAMMPS) package and a modified embedded-atom method (MEAM) interatomic potential to describe the atom interactions. The initial size of the simulation cell is $14.3 \text{ nm} \times 9.4 \text{ nm} \times 4.7 \text{ nm}$. Single crystal pure Mg (12852 atoms) in a HCP structure and single crystal pure Fe (24448 atoms) in body centered cubic (BCC) structure are created along the X-axis with a 0.86 nm separation distance. In the Y and Z directions, periodic boundary conditions are applied. To prevent interaction between Mg and Fe atoms across the X-direction periodic boundaries, three layers of atoms at the bottom of Fe and at the top of Mg are fixed along the X-direction. The lattice orientations are $[\bar{1}\bar{1}00]//x$, $[11\bar{2}0]//y$, and $[0001]//z$ for Mg, and $[100]//x$, $[010]//y$, $[001]//z$ for Fe, respectively. The initial velocities of the atoms are assumed to obey a uniform distribution, and the Verlet algorithm is used to integrate Newton's equation of motion to update the position and velocity of atoms. With a Nose-Hoover thermostat adopted, the Mg/Fe is firstly equilibrated at 300K in the condition of an isothermal-isobaric (constant number of particles, pressure and temperature [NPT]) ensemble for ten ps, and then uniaxially compressed along the X-direction under a preset pressure. During the compression, the system is rapidly heated up to a preset temperature and hold under the NPT ensemble for a preset holding period, followed by a cooling with a preset rate and unloading. Finally, the Mg/Fe is subjected to a uniaxial tension along the X-direction to test the strength of the Mg/Fe interface. Temperature (T), pressure (P), holding time (t), and cooling rate (\dot{T}_c) are expected to have a primary influence on the interface and are respectively tested over a large range: T (300K to 2,200K), P (1GPa-4GPa), t (100 ps-3 ns), and \dot{T}_c (7K/ps-140K/ps).

Two more studies were conducted to characterize the intrinsic bond formation mechanisms. First, two Mg single crystals were created instead of Mg/Fe and tested as described above. Different misorientations between the two Mg single crystals were considered in addition to the existing test factors. The second study considers the joining through impact. Mg/Fe are initially separated by 100 nm and a preset velocity (10^4 m/s) of opposite signs along the X-direction are respectively applied to all atoms in Mg and Fe to create impact, followed by a cooling of a different preset rate ($250 \text{ K/ps} - 5,000 \text{ K/ps}$). Upon impact, two reflect wall constraints are applied at the edges on the bottom of Fe and the top of Mg to mimic the effect of bulk.

The simulation results of Mg-Mg joining are presented in Figure II.3.G.5.(a), which shows the stress-strain curves during a post-weld tension test. The two Mg single crystals form a strong bond and do not separate after 20% tensile strain. Plasticity occurs before the break of the interface and leads to stress softening as marked in Figure II.3.G.5.(a). The tensile stress-strain curves for the studies of Mg-Fe static-state joining are shown in Figure II.3.G.5.(b), which shows that the Mg/Fe interfacial strength does not increase significantly with increased temperature (from 300K to 2,200K), due to the low diffusion rates between Mg/Fe even at temperature above the melting point of both.

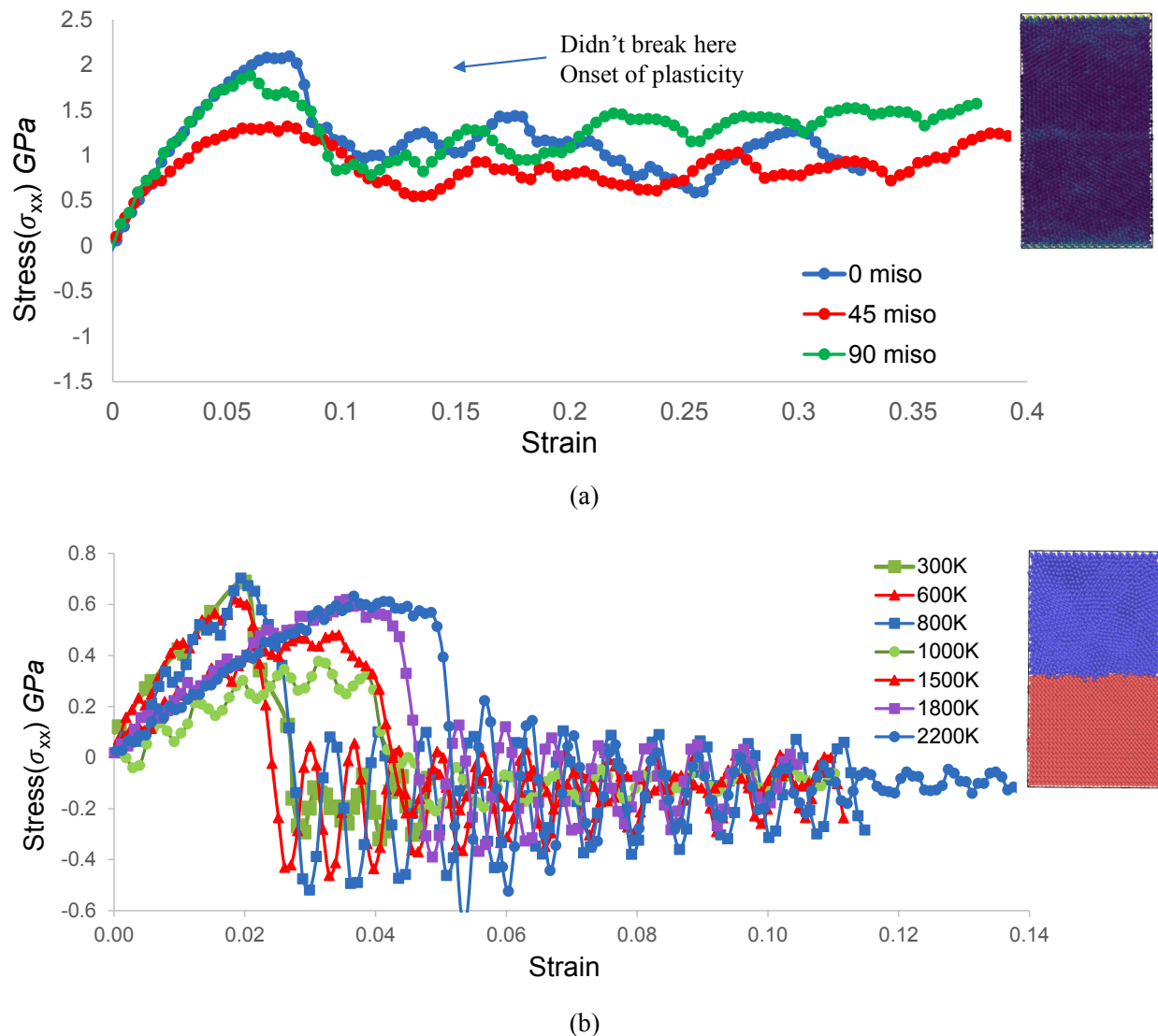


Figure II.3.G.5. Stress-strain for the (a) Mg-Mg and (b) Mg-Fe static bonding tensile test from MD simulation results using LAMMPS.

The impact studies show stronger Mg/Fe interface bonding as shown in Figure II.3.G.6.(a). Upon contact, the impact force drives the Mg and Fe atoms to “mix” at the interface. If the numerical rapid quenching is applied after impact, the very high-cooling rate (5,000K/ps) can preserve the mixed atomic configuration as shown in Figure II.3.G.6.(b). After cooling to RT, this configuration endures 30% tensile strain with a very strong interfacial strength. In contrast, if the cooling rate is not as high and insufficient to keep the interface in a mixed state, the Fe and Mg atoms will segregate and return to clean interfaces as shown in Figure II.3.G.6.(c), which exhibits a lower strength.

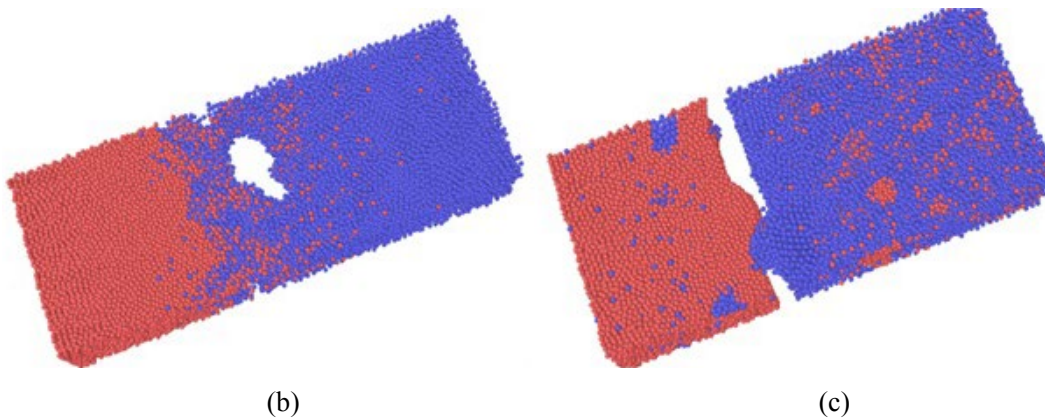
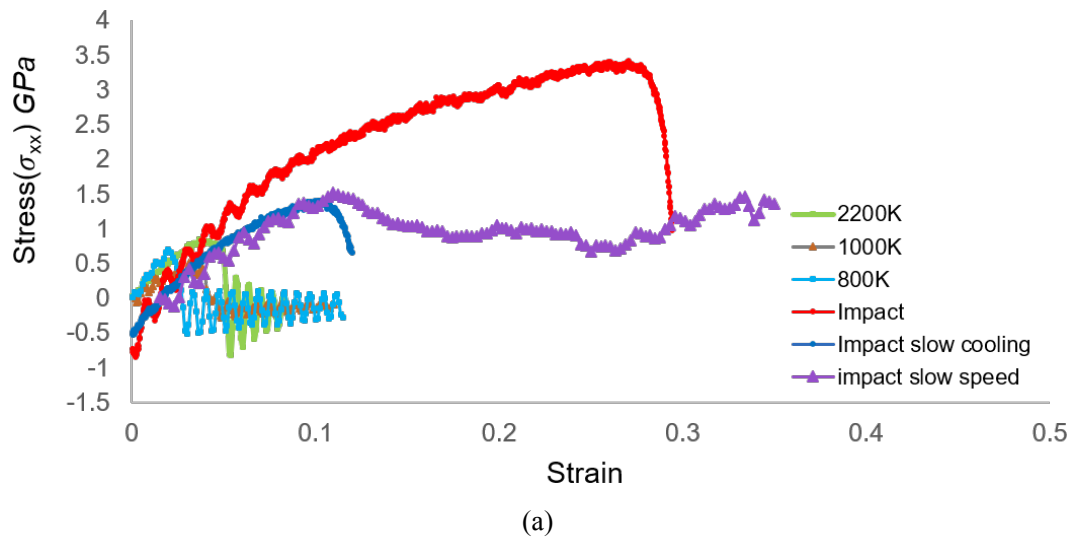


Figure II.3.G.6.(a) The stress-strain curves for different cooling rates after impact loading and Mg-Fe interface failure at (b) 30% strain after rapid cooling and (c) 10% strain after relatively slow cooling from MD simulation results using LAMMPS.

Task 2 Interface-by-design for FAST

A previously developed FEM-based, coupled Eulerian-Lagrangian computational framework for Steel-Al welds was utilized to quantitatively capture the temperature distribution obtained during the FSW process for Mg-Steel welds. The interfacial characteristics resulting from any FSW process are strongly dependent on the temperature distribution near the interface. Therefore, the prediction of temperature distributions obtained during the process can help gain a better understanding of the post-weld microstructure and joint strength. The major outcomes of the model are the prediction of weld interface morphology and the temperature field. Figure II.3.G.7 shows the temperature history predictions obtained from the finite element-based process simulation of the weld between the Mg and Steel plates. As expected, the peak temperature is predicted at the time when the tool passes above those respective points. The predictions were also within acceptable accuracy compared to experimental measurements obtained using the thermocouples installed in the plates and the tool.

With the appropriate input material and interfacial properties, a FEA provides a great tool to predict the joint performance in terms of the load-displacement behavior obtained from the mechanical testing. While the base material properties are readily available from uniaxial testing, acquiring the properties of the disturbed region including the heat-affected zone (HAZ) and thermo-mechanically affected zone (TMAZ) require specialized techniques like micro- and nano-indentation tests. In FY 2018, we developed a robust Python-based software tool that facilitates a high numerical throughput approach for backing out the stress-strain behavior of different phases or regions in a material system.

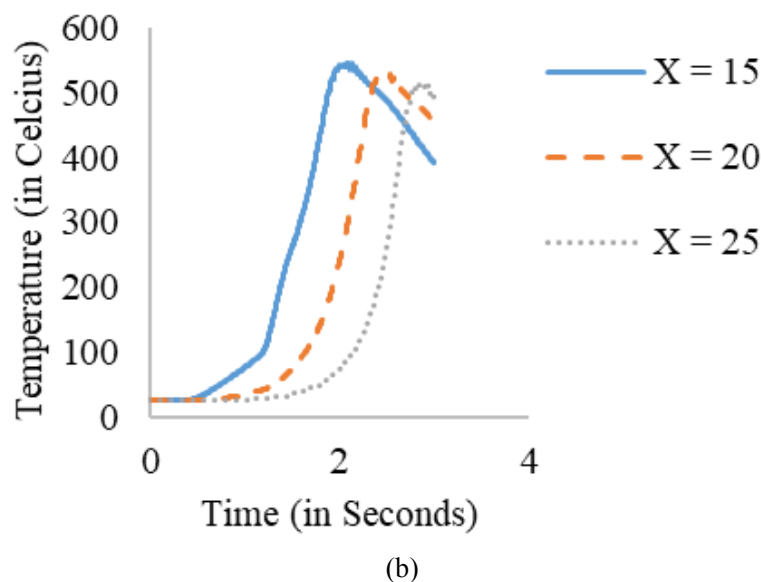
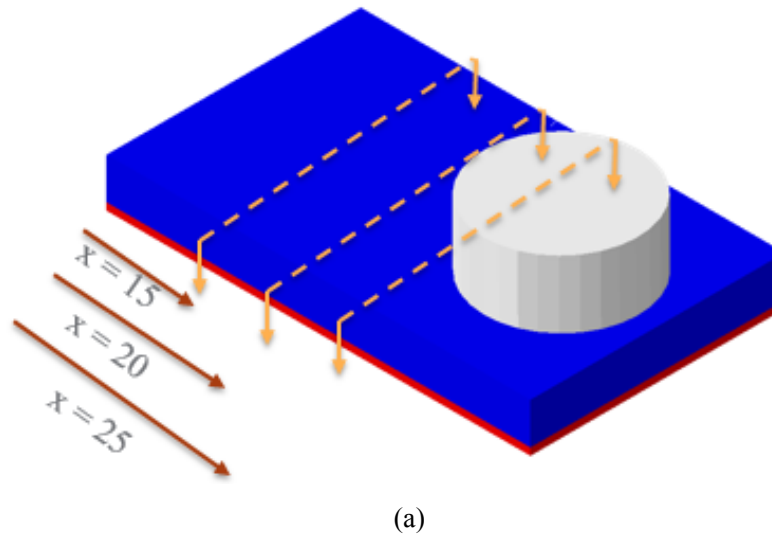
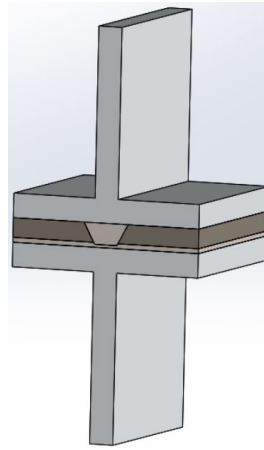
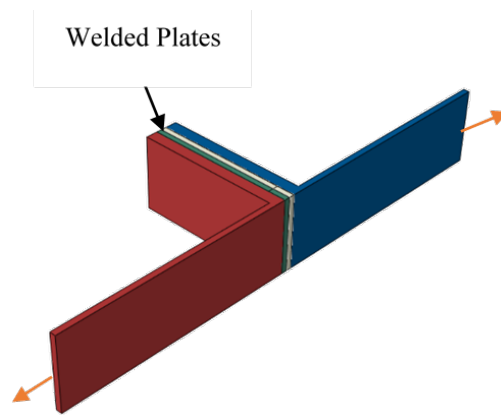


Figure II.3.G.7.(a) Model representation showing the welded Mg (blue) and steel (red) plates and the tool. (b) Temperature history prediction at the interface between Mg and Steel plates at three different locations (in mm) along the length of the weld from ABAQUS coupled Eulerian-LaGrangian FE models.

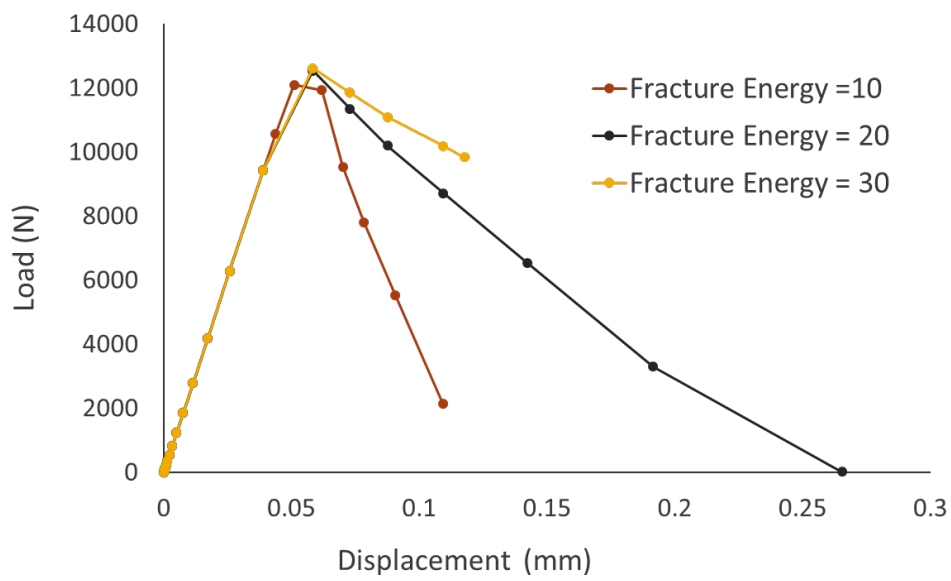
An additional critical input for the predictive structure-property model is interfacial strength. Based on its suitability and feasibility for the FSW joints, a semi-empirical calibration procedure involving both modeling and experiment was proposed to obtain the two important interfacial parameters: strength and fracture energy. The approach includes performing mechanical tests on two different geometric configurations, which have different sensitivities to the two interfacial parameters. It is based on the hypothesis that multiple combinations of the interfacial parameters can yield the same load-displacement behavior for one test configuration; however, appropriately selected multiple test configurations would yield unique interfacial parameters. Here, a FEM for the compact tension test was simulated to verify whether the proposed dimensions would work for a linear weld that spans the width of the test setup. The schematic of the test setup, its model, and the predicted load-displacement behaviors are shown in Figure II.3.G.8. The interfacial strength is kept the same for three different cases while the fracture energy is varied. As can be seen from Figure II.3.G.8, the predicted peak load seems independent of the fracture energy parameter that reinforces the fact that this test can be used for obtaining the interfacial strength. Subsequently, a T-peel test will be utilized to obtain the fracture energy.



(a)



(b)



(c)

Figure II.3.G.8.(a) Schematic compact tension test setup of FSW joints; (b) Quarter FEM for the test; and (c) Load-displacement predictions of the model for three different values of fracture energies.

Conclusions

A thermomechanical model has been established for ultrasonic welding between similar and dissimilar metal sheets. When temperature- and pressure-dependent friction coefficients are applied, the temperature profile and history were accurately predicted for Mg-Mg welding and were validated by experimental measurements when the ultrasonic power is set to 1,000 W. Utilizing the stashed model for Mg-Fe dissimilar metal USW, the temperature was successfully predicted, although the peak temperature at the faying interface is too low to form a metallurgical bond between Mg and Fe. Increasing the power of the ultrasound, hone pressure, and welding time has been found to increase the peak temperature, which led to success in obtaining a bond between Mg and Fe. MD simulations showed bonding between Mg and Mg smooth interfaces is stable, which tend to form single crystal or grain boundaries, depending on relative orientations. Separating the interface will require breaking the cohesive bond between Mg atoms and, before it happens, plasticity and damage will occur. In contrast, the adhesion for the interface between Mg and Fe is weaker. This is because the condensed packing of Fe inhibits the Mg atoms to diffuse into Fe, even when Mg is melted. Fe atoms can diffuse into Mg, but the solubility of Fe in Mg is low even at a temperature above the melting temperature of Fe. Therefore, equilibrium-state temperature increase ($\leq T_{melt}^{Fe}$) does not directly improve the joining of Mg-Fe. Instead, it has an indirect effect by melting Mg and increasing contact areas. High velocity impact converts the kinetic energy into a driving force that “mixes” the Fe/Mg atoms at the interface. If the cooling rate is sufficiently high, a much stronger amorphous Mg-Fe interface can be found. Otherwise, segregation of the Fe-Mg will occur and reduce the interface strength.

The predicted temperature histories from the process simulation of FSW can help understand the interfacial compositions. Also, it can guide experimental design by varying the thermal properties used in the model to virtually test any possible temperature control measure without actually deploying them in experiments. On the structure-property prediction task, the proposed approach of using different geometric configurations to determine the interfacial strength seems promising and a feasible path forward.

Key Publications

1. Huang, H., Chen, J., Lim, Y.C., Feng, Z.L., Hu, X.H., Cheng, J.H., Sun, X. "Quantifying Heat Generation Mechanisms in Ultrasonic Welding of Mg-Alloy Az31 with a validated thermomechanical model." *Journal of Materials Processing Technology* Submitted (2018).
2. Gupta, V. "An Integrated Computational Modeling Approach to Predict Joint Properties Obtained in Solid-State Joining of Dissimilar Materials." In *13th World Congress on Computational Mechanics (WCCM XIII)*. New York, USA, 2018.

II.3.H Adhesive Bonding of Thermoplastic CFRP to AHSS (Oak Ridge National Laboratory)

Zhilli Feng, Co-Principal Investigator

Oak Ridge National Laboratory
1 Bethel Valley Rd.
Oak Ridge, TN 37831
E-mail: fengz@ornl.gov

Kevin Simmons, Co-Principal Investigator

Pacific Northwest National Laboratory
902 Battelle Blvd.
Richland, WA 99354
E-mail: kl.simmons@pnnl.gov

Sarah Kleinbaum, DOE Technology Manager

U.S. Department of Energy
E-mail: sarah.kleinbaum@ee.doe.gov

Start Date: October 1, 2017	End Date: September 30, 2020	
Project Funding (FY18): \$675,000	DOE share: \$650,000	Non-DOE share: \$25,000

Project Introduction

Adhesive bonding is widely used in the automotive industry, primarily for structurally non-critical components. For structurally critical components, weld bonding that combines adhesive bonding and spot welds is more common for joining light-weighting materials such as AHSS to AHSS, or Al alloys to other Al alloys, and fiber reinforced polymers, in order to meet performance requirements in body stiffness, crash and safety performance, and enhanced noise-vibration-harshness characteristics. Innovations in adhesive bonding would allow for the development of new and innovative designs of mixed materials of high-strength steels, non-ferrous metals, plastics, and composites that provide more efficient assembly and weight reductions.

Pure adhesive bonded joints historically suffer from limitations in peel strength, brittle cleavage failure, relatively low toughness, long-term aging degradation, and environmental performance. They also have low crack arrest resistance in dynamic crash events under compressive load. For dissimilar material bonding, a number of unique challenges must be addressed. They include tailoring adhesives to provide strong bonding for two different materials, compatibility with CTE mismatch, and galvanic corrosion effect.

This multi-year early-stage R&D project plans to address several key aspects of adhesive bonding, including the effects of surface conditions of substrates, adhesive chemistry and additives, long-term performance and degradations, inhibition of galvanic corrosion, compatibility with the CTE mismatch, and health monitoring of curing/manufacturing process and structural soundness in-service. Each of these aspects or their combination would potentially lead to significant advancements in multi-material joining.

Objectives

This project focuses on the fundamentals of adhesive bonding of CFRP to AHSS. In concert with the parallel interface-by-design simulation task, innovative adhesive bonding concepts are identified and explored, and predictive tools developed for adhesive bonding performance, joint design, and lifetime prediction. The ultimate goal is to significantly improve the performance and productivity of adhesive bonding in high-volume auto-body production to enable increased use of CFRP in multi-material body structures for weight reduction. ORNL and PNNL are working together on this research to effectively utilize the complementary research capabilities, facilities, and technical knowledge of two national laboratories to achieve the project goals.

Approach

Figure II.3.H.1 outlines the overall research approach and plan. It is organized into four major categories: key governing factors, methods to improve and innovations, interface/adhesive characterization, and joint properties. In recognizing the nature and risks associated with early-stage research, a phased approach will be taken in the proposed R&D. The first phase is a 12 – 18 month effort to explore the feasibility of identified promising concept/ideas. Depending on the outcome from the first phase effort, promising ones will be down-selected for more comprehensive R&D in later phases of the project.

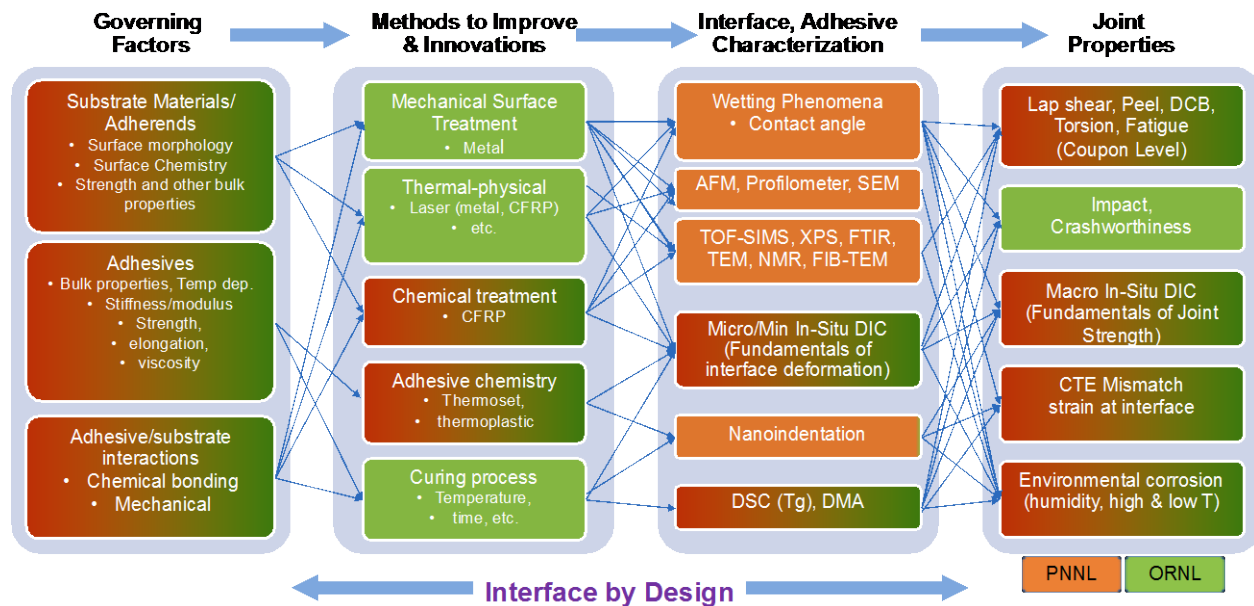


Figure II.3.H.1. Overall research plan. Source: ORNL.

The proposed research will closely interact with the parallel interface-by-design simulation task. Design concepts from the simulation task guide experimental research in this work. At the same time, data from the experimental work in this project assists the simulation effort and provide necessary experimental validation of the simulations.

Chemical bonding of adhesive to the interface of the substrate material requires surface characterization by chemical analysis and of surface roughness. The dissimilar materials of interest have varied chemistry. The steel surface chemistry has a variety of metal oxides based on the alloying elements of Si, Mn, and Cr in the Fe. Galvanized coated metal has a different set of surface chemistries and are more difficult to adhesively bond. Traditional adhesive bonding typically has special surface preparation instructions to achieve the best bond line performance to the metals. The polymer composite systems have a completely different set of chemistries that can be even more complex. These materials are also surface-modified to maximize adhesive performance. The chemistry of these surfaces influences the interphase region, which is a transition zone from the surface into the bulk adhesive. Characterization of the interface and its chemical influence into the transition zone will be important to optimize bonding and understand how it changes over time in extreme environments.

Bondline analysis is critical to understanding what is taking place at the interface, transition zone, and in the bulk of the adhesive. Microscopy analysis will aid in understanding morphological changes in the adhesive, composite, and steel.

Three different approaches will be explored to inspect and monitor the bondline structural soundness and degree of cure. Thermal imaging techniques would provide an overall assessment of the structural soundness

and degree of cure, while acoustic monitoring techniques can track the changes in elastic moduli to infer the degree of curing and formation of voids or other structural defects in the adhesive layer. Modification of the CFRP substrate to embed acoustic sensors will be examined, though the preference will be for sensors that can be placed in contact with the bonded structure for rapid screening. In the third approach, electrical techniques (i.e., resistivity, impedance spectroscopy, electrical impedance tomography, and potential drop methods) may provide additional information on the adhesive layer and will be investigated.

Mechanical testing capabilities will provide full characterization of the substrate and adhesive materials. The testing will also provide joint efficiency performance. With new real-time imaging techniques for analysis, we will focus on understanding how fracture and failure are occurring and how that changes with environmental stresses over time. The data from this task will also be provided as inputs to the lifetime prediction performance models for model correlation and validation.

It is well-known that surface conditions (e.g., chemistry, roughness, morphology) significantly influence adhesive bonding strength. There are techniques to alter surface conditions (such as laser-surfacing) with demonstrated benefits. However, there is a lack of understanding of the most appropriate surface condition and morphology to improve bonding. With interface-by-design modeling tools, it is possible to *proactively* design surface conditions for bonding. This task will take the designs and concepts from the interface-by-design simulations and identify surface modification processes and methodologies to implement such interface design concepts to achieve improved bonding strength.

Results

Interface and Bondline Characterization and Property Testing

Surface adhesion is influenced by chemical and physical surface characteristics. The as-received surfaces of 40% CF/Ultramid A3WC8 (PA66), 40% CF/Ultramid Advanced N UF107AA polyphthalamide (PPA) 40% short CF (PPA), and laminated CF/epoxy (Toray G83C_7-11) (TS) CFRP were characterized using optical microscopy, Fourier transform infrared spectroscopy, laser and contact profilometry, SEM, TOF-SIMS, and water contact angle. Figure II.3.H.2 shows laser profilometry for 40% CF-PA66 (a) smooth surface and (b) rough surface with a non-uniform surface profile, potentially due to molding and demolding processes.

Similarly, physical and chemical surface conditions of as-received DP980 were characterized.

Figure II.3.H.3 (a) shows a cross-section SEM image of as-received DP980, while Figure II.3.H.3 (b) and (c) provide TOF-SIMS images with a zinc coat layer on steel substrate. Surface roughness for both 40% CF/PA66 and DP980 are summarized in Table II.3.H.1.

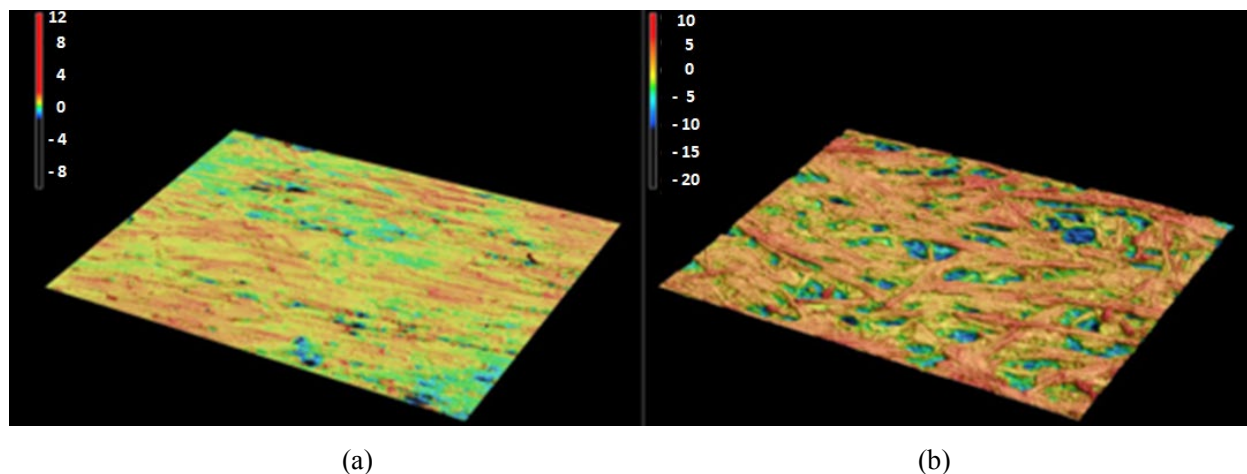


Figure II.3.H.2. Laser profilometry of (a) 40% CF-PA66 plaque 'smooth region' and (b) 'rough region' with 18 μm and 28 μm maximum profile heights, respectively. Source: PNNL.

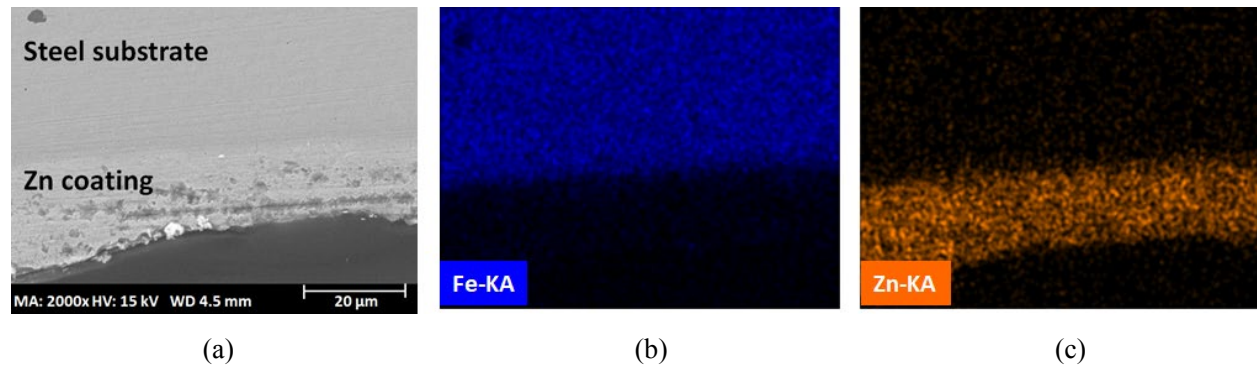


Figure II.3.H.3. (a) Cross-section SEM image of as-received DP980 and (b) and (c) TOF SIMS images showing a Zn coat on DP980. Source: ORNL.

Table II.3.H.1. Summary of Surface Profiles for Thermoplastic CFRP and DP980.

Sample	Average length between the peaks and valleys, Ra (μm)	Average vertical distance from the highest peak to the lowest valley, Rz (μm)
40%CF-PA66 (as-received): smooth region	0.314	18.116
40%CF-PA66 (as-received): rough region	2.213	28.258
Galvanized DP980 (as-received)	0.61 ~ 0.64	8.63 ~ 9.57
Galvanized DP980: zinc removed by mechanical	0.61 ~ 0.88	7.18 ~ 9.37

Adhesive joint strength is a function of bond area, surface chemistry, and varies with adhesive bondline thickness. Adherend test geometries were cut by water jet into 1-in. x 4-in. plaques and shear-machined for DP980. Epoxy-based adhesives from Dow, L&L Products, and 3M were applied and thermally cured according to the manufacturer's instructions. Orientation of adherend pieces during bonding was maintained using engineered jigs. Bondline thickness was initially controlled using glass spheres of a known diameter (i.e., 250 μm) in the bondline. A 1-in. overlap was used for the lap shear coupon. Different material combinations were used to evaluate the adhesive bonding strength with various epoxy-based adhesives. Figure II.3.H.4 summarizes the lap shear tensile testing of steel-steel, steel-CFRP, CFRP(TP)-CFRP(TP). In general, the highest lap shear failure load is found for steel-steel, while the lowest lap shear peak failure load is found for CFRP(TP)-CFRP(TP). The potential explanation for this discrepancy follows. First, these epoxy-based adhesives were initially designed for metal-to-metal bonding, so this appeared to be a good place to begin the bonding research and property characterization. In addition, the surface energy of polyamide is relatively low as compared with metal surfaces. For this reason, adhesion on the polymer side is relatively lower than the adhesion on the metal side. Therefore, adhesive failure mode was typically observed for steel-CFRP(TP) and CFRP(TP)-CFRP(TP) after tensile shear testing, leading to the lower lap shear failure load. Therefore, engineered surface modification on adherend is required to further enhance the adhesive bonding strength.

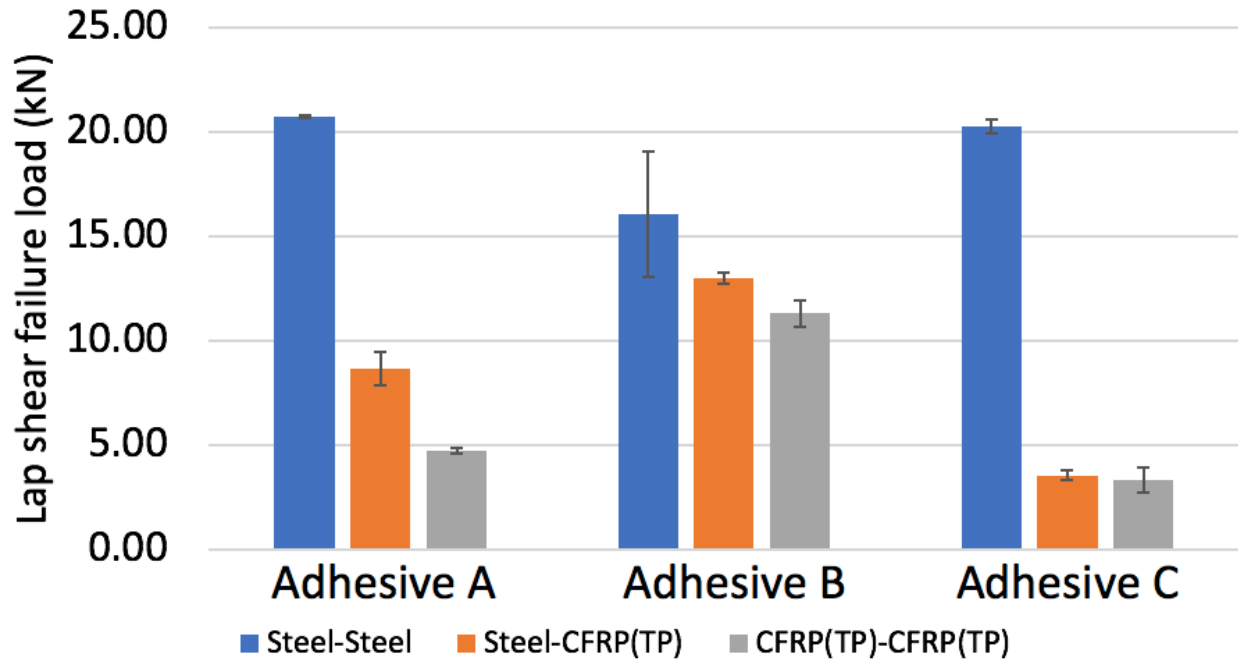


Figure II.3.H.4. Summary of lap shear tensile testing with different material combinations and adhesives. Source: ORNL.

The DIC technique was applied to capture localized deformation of adhesive layers and adjacent adherend, as shown in Figure II.3.H.5. To avoid bending the adherend during lap shear testing, high-strength thermoset CFRP was used to closely match the strength of DP980. In addition, a double lap shear joint configuration was used. Because of non-uniform adhesive bondline thickness between the left and right sides, a much higher strain shows on the right as compared to the left. Fracture was initiated at the thinner adhesive layer first. Final failure occurred at the relatively thick adhesive layer. This result indicates how adhesive bondline thickness has an effect on the overall bonding strength.

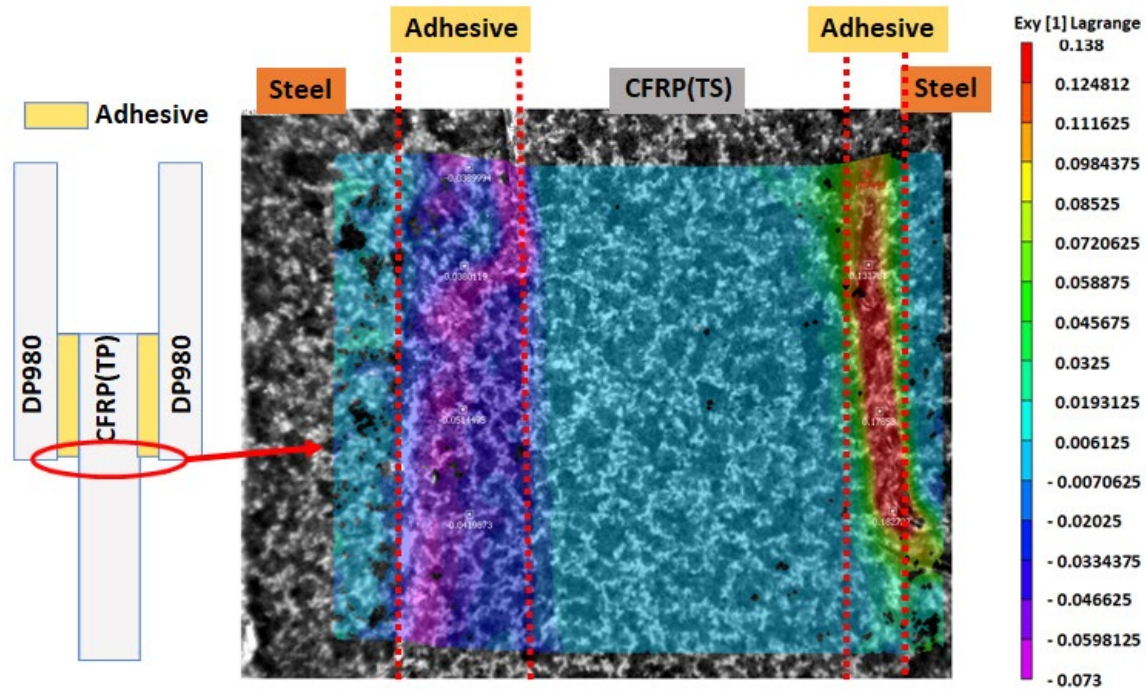


Figure II.3.H.5. Strain map by DIC capturing localized deformation for double lap shear coupon during shear tensile testing. Source: ORNL.

Process for Interface-by-Design to Improve Bonding Strength

Various surface modification methods, such as laser, plasma, chemical, and mechanical abrasion, can be used to enhance adhesive bonding strength. Laser ablation uses a focused high-energy density to modify surface profiles in a non-contact and precise way. During laser ablation, localized plasma can form so additional chemical surface treatment is possible with different shield gas. In this task, pulsed-laser surface texturing was studied using a technique developed at ORNL to increase adherend surface roughness for improved adhesive bonding. PNNL characterized the effects of laser surface treatments on surface wetting by water contact angle measurement. As shown in Figure II.3.H.6, the surface chemistry and surface roughness are modified and ranged from 81.3° contact angle to 37.5° . It is clearly seen that laser surface texturing has great effect on surface modification. The effectiveness of surface modification on adhesive bonding strength will be studied by mechanical testing. Other surface modification methods will also be explored to effectively engineer the surface condition.

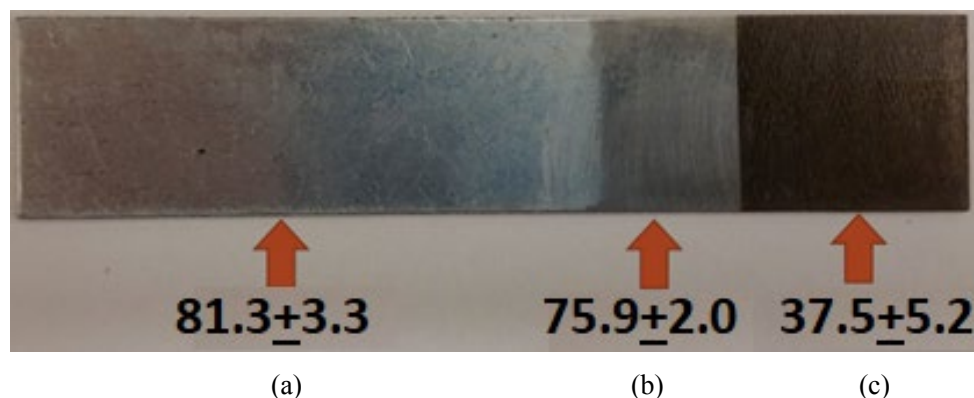


Figure II.3.H.6. Water contact angles of DP980 steel with (a) zinc-coating, (b) zinc removed through abrasion and (c) laser textured on a steel surface. Source: PNNL.

Health monitoring and Non-Destructive Evaluation in Both Manufacturing & Service

Bond quality and bond condition can be quantified through non-destructive evaluation of bonded surfaces during bonding, after production, and during service. Knowledge of acoustic, ultrasound, thermal, dielectric, and other properties of joints in relation to joint target performance, such as mechanical strength, may be used to optimize manufacturing parameters, provide quality control, assess current condition, and predict performance. Figure II.3.H.7.(a) shows the initial feasibility results of applying scanning acoustic microscope images in time-of-flight for back surface response on an adhesive bonded area and Figure II.3.H.7.(b) shows the amplitude of back surface response depicting unbonded regions (in yellow circles) in a thermoset CFRP/thermoset CFRP joint.

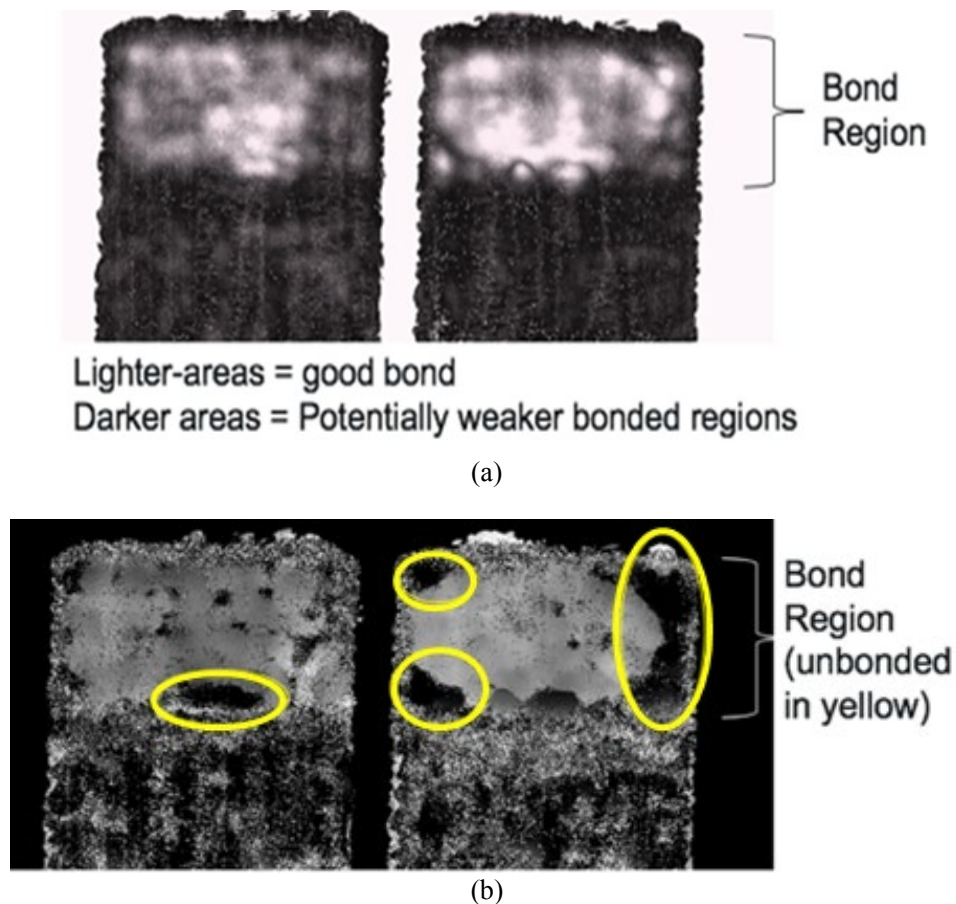


Figure II.3.H.7. Scanning acoustic microscope images in time-of-flight for back surface response (Left) and amplitude of back surface response (Right) reveal unbonded regions in thermoset CFRP/thermoset CFRP joint. Source: PNNL.

Conclusions

Surface chemistry and profiles of thermoplastic CFRP and galvanized and non-galvanized DP980 were characterized by advanced analytical tools. Epoxy-based adhesives from different adhesive companies were used for adhesive bonded coupons, including steel-steel, CFRP(TP)-steel, and CFRP(TP)-CFRP(TP). Lap shear tensile testing was conducted to evaluate the bonding strength for each material combination. The highest bonding strength was found for steel-steel, while the lowest bonding strength was for CFRP(TP)-CFRP(TP) with adhesive failure mode (i.e., interface between adhesive and adherend). Localized deformation of adhesive layer during tensile shear testing was captured with the DIC technique to support and validate interface-by-design modeling task of the program. Laser surface textured on steel adherend showed modification of surface energy by water contact angle measurement. Scanning acoustic microscopy technique was able to distinguish good and poorly bonded adhesive areas.

Key Publications

1. Lim, Y.C., J. Chen, N. Nguyen, D. Warren, A. Naskar, and Z. Feng. (2019). “Adhesive Bonding of CFRPs to AHSS,” Submitted, *The Adhesion Society 42nd Annual Meeting*, Hilton Head, SC, USA, February 17–20, 2019.

Acknowledgements

The Principal Investigators would like to recognize A. Naskar, Y. C. Lim, J. Chen, M. Goswami, N. Nguyen, D. Warren, and X. Sun of ORNL; K. Simmons, L. Fifield, D. Graff, A. Ortiz, and Y. Shin of PNNL, and our industry partners—DOW, L&L, 3M and GM—for their support and assistance with this project.

II.3.I Mechanical Joining of Mg Alloys to CFRPs (Pacific Northwest National Laboratory)

Scott Whalen, Co-Principal Investigator

Pacific Northwest National Laboratory
902 Battelle Blvd.
Richland, WA 99354
E-mail: scott.whelen@pnnl.gov

C. David Warren, Co-Principal Investigator

Oak Ridge National Laboratory
1 Bethel Valley Road
Oak Ridge, TN 37831
E-mail: warrencd@ornl.gov

Sarah Kleinbaum, DOE Technology Manager

U.S. Department of Energy
E-mail: sarah.kleinbaum@ee.doe.gov

Start Date: October 1, 2017	End Date: September 30, 2019	
Project Funding (FY18): \$650,000	DOE share: \$650,000	Non-DOE share: \$0

Project Introduction

Existing methods for joining Mg alloys to CFRC are challenged in varying degrees by corrosion, strength, surface treatment requirements, compatibility with high-volume production, or being too application specific. As part of the Joining Core Program, a task on joining Mg to CFRC has been established to address these challenges. PNNL and ORNL have combined forces in the areas of process development, materials characterization, and materials testing in an effort to identify new and promising technologies for joining Mg to CFRC.

Objectives

The objective of this project in FY 2018 was to explore novel methods for joining Mg to CFRC and determine which approaches should continue development in FY 2019. To this end, projects within this Mg-CFRC task were instructed to explore, to whatever degree possible, joining solutions that held promise for improving strength, corrosion, manufacturability, cost, and other important criteria.

Approach

Five joining methods were investigated in FY 2018: (1) Friction Stir Interlocking; (2) Conventional Bolting; (3) Mg Overcasting; (4) Friction Stir SPR; and (5) Ultrasonic Joining, as shown in Figure II.3.I.1. This report briefly describes the progress made for each of them. The Mg-CFRC project explored multiple techniques in FY 2018 with the understanding that a down-select would occur at the end of the year, and only a subset of the five approaches would continue development in FY 2019.

At the beginning of FY 2018, PNNL and ORNL project members agreed on the Mg sheet, the thermoplastic CFRC, and the thermoset CFRC that would be used as the common materials for all joining techniques and were chosen for their relevance to automotive applications. Table II.3.I.1 provides the specifics on these materials.

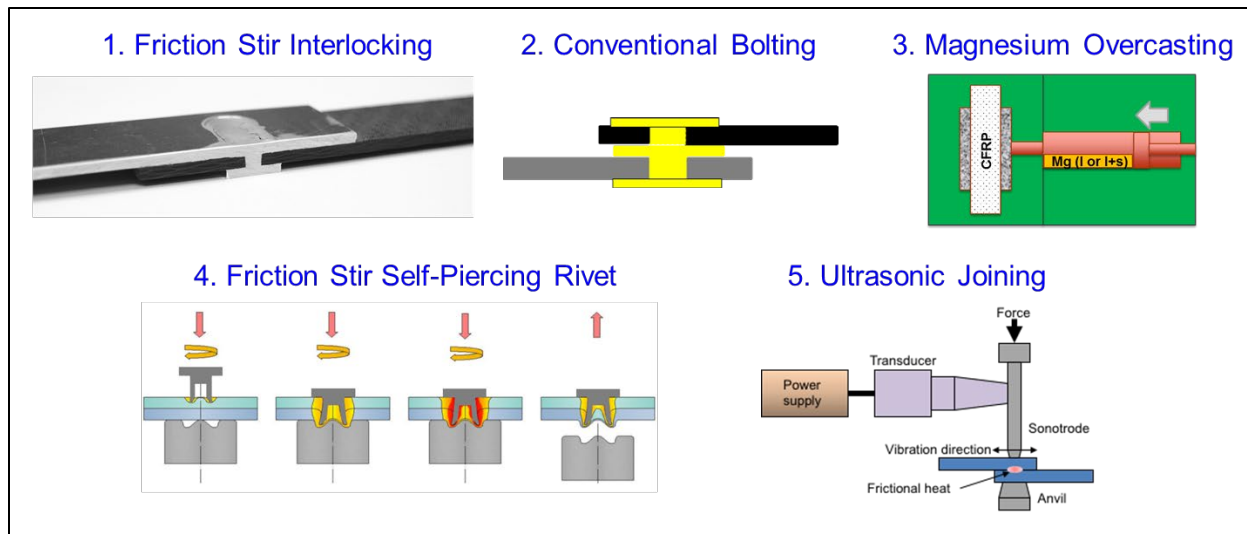


Figure II.3.I.1. The five Mg-CFRC joining methods investigated in FY 2018. Source: PNNL and ORNL.

Table II.3.I.1. Materials used in the Mg-CFRC Task.

Material	Designation	Vendor	Thickness
Mg Sheet	AZ31	Buymetal	2.3 mm
Thermoplastic CFRC	Ultramid® Advanced N XA-3454	BASF	3.0 mm
Thermoset CFRC	T700S/G83 Unidirectional Prepreg 0/90 9 Ply	Clearwater	1.9 mm

Results

Method 1 – Friction Stir Interlocking (PNNL Lead)

This task demonstrated proof-of-concept for joining an AZ31 Mg-alloy sheet to thermoplastic (TP)-CFRC panels by friction stir interlocking (FSI). In this approach, Mg-alloy inserts were inserted through the CFRC panels to which an Mg sheet was joined by FSW in a lap configuration, as shown in Figure II.3.I.2. A thermal bonding film was also incorporated as a barrier to corrosion at the Mg-CFRC interfaces within the joint. An additional advantage of FSI is that multiple mechanical interlocks can be formed quickly in a linear or curvilinear pattern.

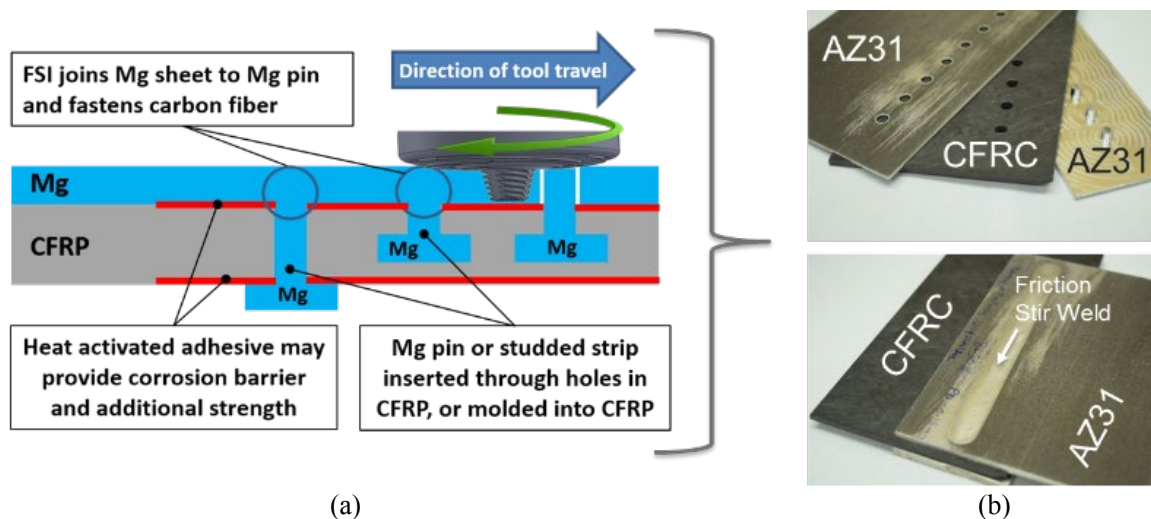


Figure II.3.I.2.(a) FSI and (b) proof-of-concept joints before and after interlocking. Source: PNNL.

A challenge encountered early in the task was that deformation of the TP-CFRP, due to heat and pressure during FSW, led to significant defects in the Mg stir zone. As a result, a large DoE was performed where tool geometry, rotational speed, traverse speed, and tool tilt angle were varied. Figure II.3.I.3.(b) shows the tool geometry and process parameters that eliminated surface defects and worm-holes within the stir zone shown in Figure II.3.I.3.(a).

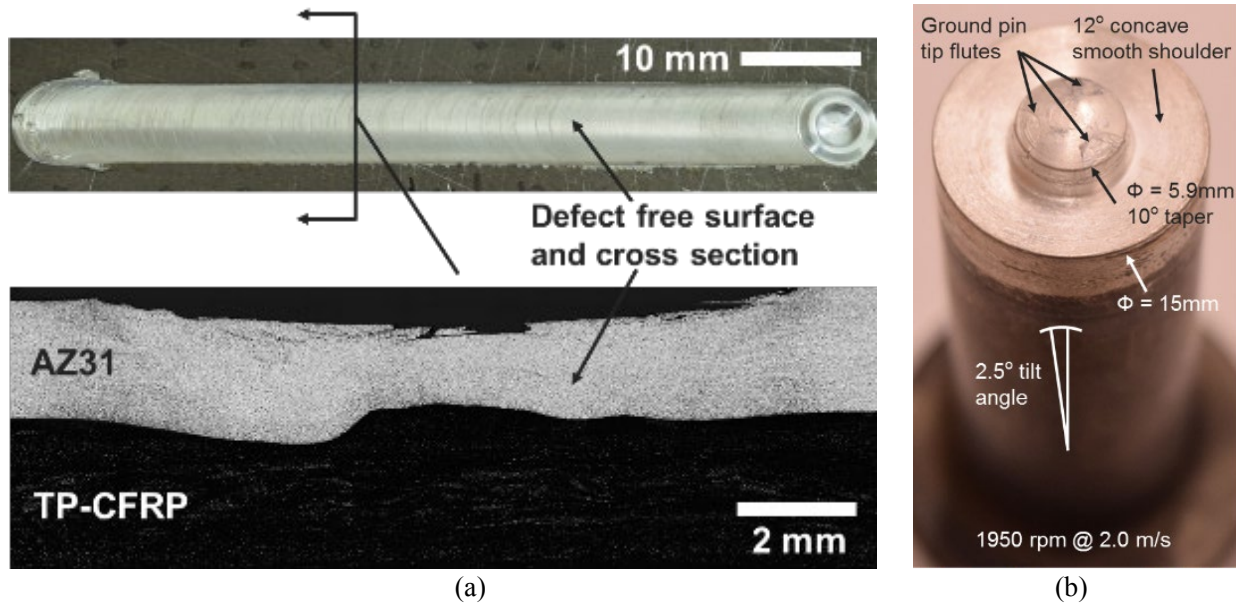


Figure II.3.I.3.(a) Defect free stir zone (b) and tool design with associated process parameters. Source: PNNL.

An additional challenge was the lack of complete mixing between the Mg sheet and the Mg insert. Figure II.3.I.4.(a) shows initial results where mixing was minimal and Figure II.3.I.4.(b) shows that better mixing was achieved after further tool and process development. Nevertheless, more complete mixing is needed to improve joint strength and will be a key research area in FY 2019. Lap shear specimens were tested for Mg to TP-CFRP made by FSI. Specimens, with one Mg pin per test coupon, exhibited a load capacity of 2.0 kN and 152 N/mm normalized to the 13.4 mm width of the samples. Note: wider samples would give a higher normalized strength since failure occurred in the TP-CFRP rather than the Mg pin. However, these values are fairly meaningless at this point because a higher strength can be achieved by simply using a larger diameter pin. The mixing issue needs to be addressed independent of pin diameter.

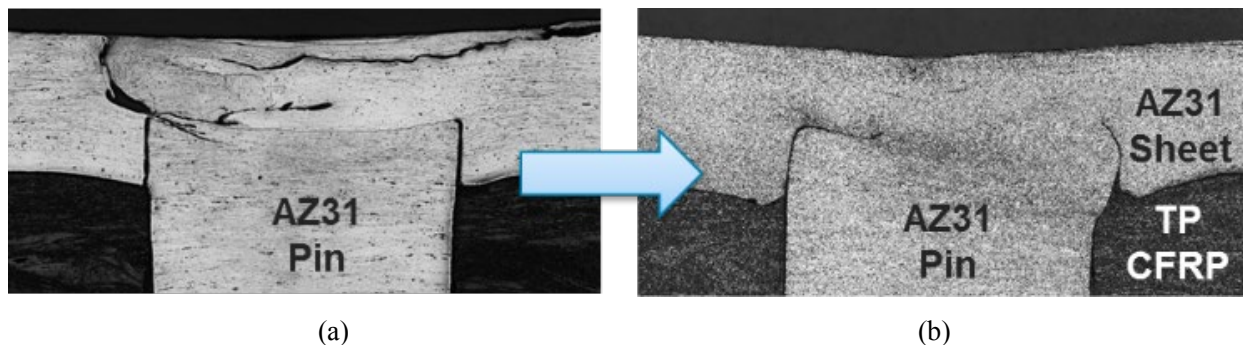


Figure II.3.I.4. FSI joint showing (a) incomplete mixing between the Mg sheet and the Mg pin and (b) with better mixing. Source: PNNL.

As proof-of-concept, FSI joints with a 3M 583 thermal bonding film incorporated at the Mg/CFRC interfaces were subjected to the ASTM B117 corrosion test. Figure II.3.I.5.(a) shows the joint intact after 48 hours of testing and Figure II.3.I.5.(b) shows after breaking open the joint to expose the interface. The thermal bonding film has clearly inhibited penetration of electrolyte into the Mg-CFRC joint.



Figure II.3.I.5. Corrosion test with thermal bonding film incorporated. Source: PNNL.

Method 2 – Conventional Bolting (ORNL Lead)

This task demonstrated proof-of-concept for mitigating damage in the CFRC created during the drilling of holes in the composite, and a proof-of-concept for electrochemically isolating constituents of the joint to inhibit or reduce the severity of galvanic corrosion occurring in the Mg due to contact with steel fasteners and CF. The first step in this task was to determine the impact of different hole-drilling methods on the reduction in strength of both the thermoplastic and thermoset composites. Holes were drilled in 50.8 x 101.6 mm composites using five different methods: (1) laser drilling; (2) water jet cutting; (3) composite drill bits; (4) standard steel drill bits; and (5) hole saws, and five different hole sizes. The specimens were cut from the materials listed above in Table II.3.I.1. The specimens were then tested at quasi-static rates. There was little difference in strength due to the hole-cutting method. There was an expected reduction in strength with increasing hole size, but when the effective cross-sectional area reduction was calculated, there was little impact from the hole size. The same trend held for thermoset.

A method for the mitigation of damage in the composites was then addressed. The method consists of coating the inside of the hole with a resin of very low viscosity that is compatible with the resin and fiber in the composite and has a surface affinity to be drawn into the microcracks of the composite. Working with 3M, a newly designed polymer was identified for this purpose. A method of isolating the components was also developed. A fast cure epoxy is “painted” onto the surface of the Mg at only the places where either the steel washers or the composite will be in contact with the substrate. Within the hole, the crack-filling polymer also provides electrochemical isolation.

Modified and unmodified samples, as shown in Figure II.3.I.6, that had been subjected to corrosion exposure were then cross-sectioned through the bolt and subjected to scanning electron microscopy and energy dispersive spectroscopy for oxygen evaluation to look for corrosion products. Figure II.3.I.7.(a) shows the unmodified samples after corrosion exposure and was found to have oxidized regions within the joint. Modified samples, as shown in Figure II.3.I.7.(b), found no oxidized regions within the joint, but did show oxidation at the Mg to steel washer interface.

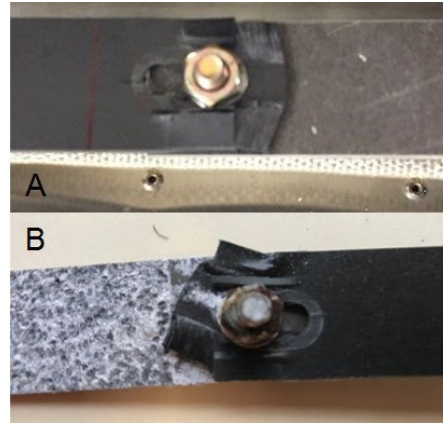


Figure II.3.1.6. Failed bolted Mg to TS-CFRP lapshear samples: (A) unmodified and un-corroded; and (B) modified and after 100 hours of corrosion conditions. Source: ORNL.

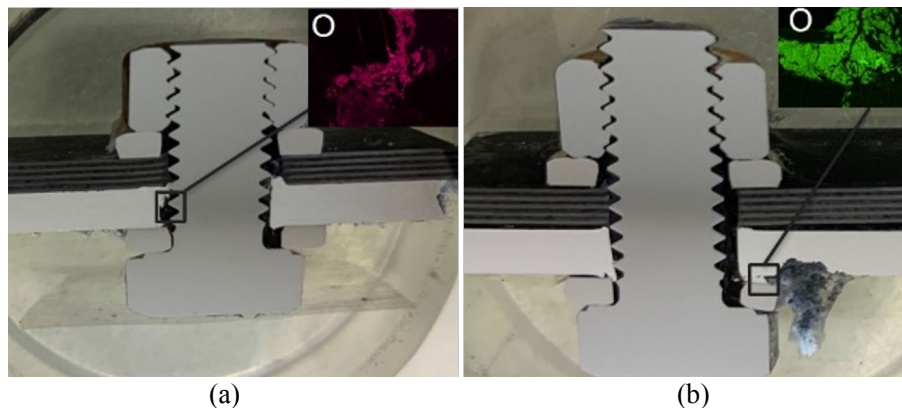


Figure II.3.1.7. Cross-section samples using scanning electron microscopy and energy dispersive spectroscopy evaluation showing (a) unmodified sample after corrosion exposure in the joint and (b) modified sample with no corrosion in the joint but corrosion at the Mg-Steel interface. Source: ORNL.

Method 3 – Mg Overcasting (PNNL Lead)

In the proposed concept, molten Mg-alloy is cast over a CFRP component such that a section of the CFRP is completely embedded within the Mg casting to create a strong mechanical interlocking joint. The key premise of the proposed concept is that even though the polymer melting/degradation temperature is several 100°C below the melting point of the Mg-alloy, the polymer composites may be able to survive an overcasting joining process if the duration of thermal excursion is kept “short” by maintaining a high-cooling rate during the casting solidification (e.g., akin to the conventional HPDC technique). Thus, the main challenge in creating an Mg-CFRP joint by overcasting is to manage the process time to limit the burn-off/thermal decomposition of the CFRP composite when it comes into contact with molten Mg and during subsequent cooling of the solidified casting. If successful, the advantage of this method is that it avoids machining costs and machining-induced fiber breakage (hence, mechanical property degradation) in the CFRP composite while enabling joint geometries that are otherwise cumbersome to machine or not feasible by conventional mechanical fastening methods.

Two types of experiments were performed:

#1 – Dip composite coupons in molten Al (surrogate for molten Mg) to study survivability of the CFRP composite to short-duration excursions above the melting points of Al (Mg).

#2 – Embed bare CFs inside melt-cast Mg to study the survivability of CFs and Mg-Carbon interactions.

The results from experiment #1 showed that a CFRP composite can indeed survive a short-duration (several seconds) of contact with molten Al (and hence, likely with molten Mg as well), thus validating the key premise of this work, as shown in Figure II.3.I.8.(a). Results from experiment #2 showed that CFs survived intact after several minutes in contact with molten Mg, as shown in Figure II.3.I.8.(b), and there seems to be good interfacial adhesion between the two, as shown in Figure II.3.I.8.(c). Thus, project results show that overcasting is a technically feasible joining technique for Mg-CFRP composites.

This technique offers the advantage of a short cycle time, flexibility with regards to component size and thickness, and enabling joining without the use of additional bolts, rivets, etc. From a commercialization perspective, it offers a short cycle time, a short preparation time, commercial availability of the needed equipment, and is suitable for castable metals other than Mg (e.g., Al, Zn, etc.). Future efforts should be directed towards developing the capability to fabricate test coupons and perform analysis of the CF/Mg interface.

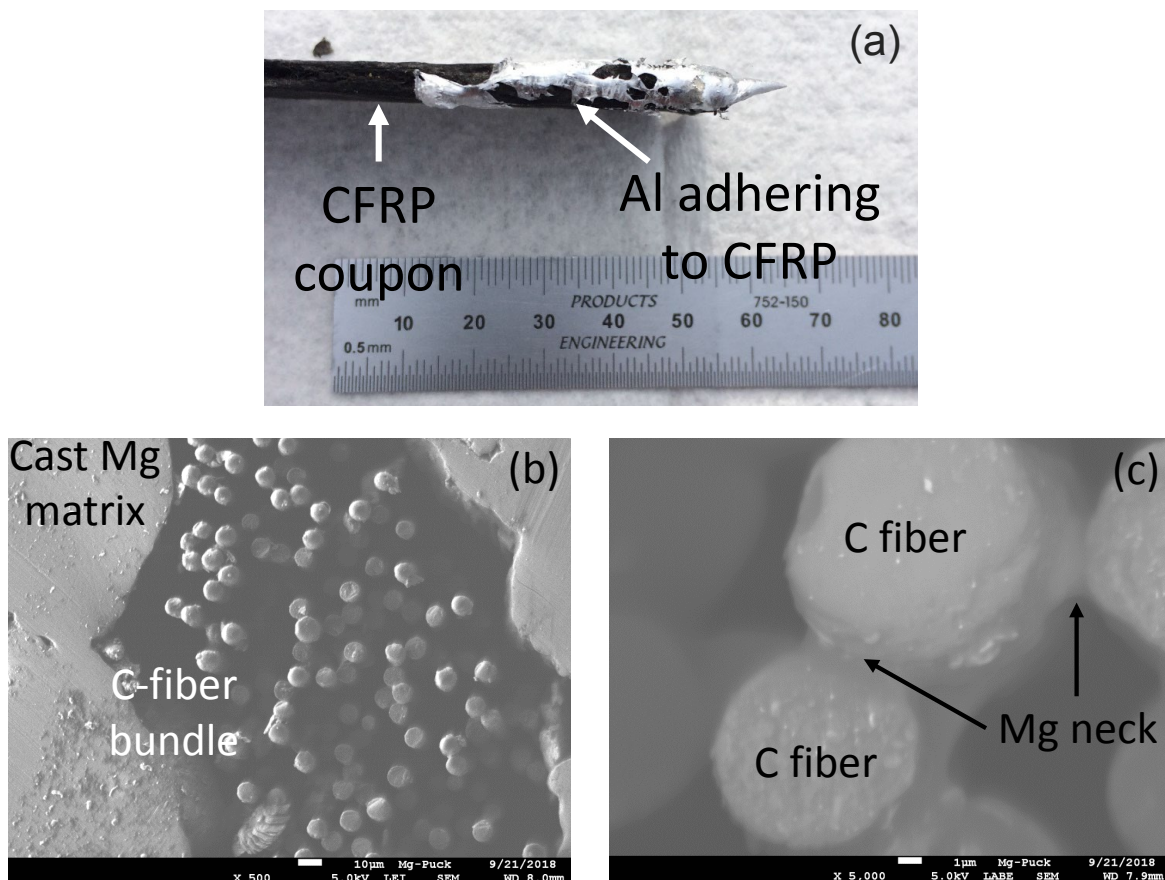


Figure II.3.I.8. (a) Edge-view of a CFRP coupon (black color) after being dipped in molten Al, showing solidified Al (i.e., shiny, silvery color) adhering to the CFRP. (b) CF bundle embedded inside an Mg casting. (c) Close-up of (b) showing good adhesion of Mg to CFs via Mg neck formation between individual CFs [scale bar – 1 µm]. Source: PNNL.

Method 4 – Friction Self-Piercing Riveting (F-SPR) (ORNL Lead)

The F-SPR process uses a rotating piercing rivet to generate localized frictional heating during the process. The friction heating softens the CFRP to facilitate piercing. The friction heating further increases the local ductility of Mg-alloy to avoid cracking issues commonly associated with SPR of Mg-alloy. We successfully demonstrated the feasibility of F-SPR to join both thermoplastic CFRC and thermoset CFRC to Mg-alloy AZ31B. Initial evaluation of the corrosion of the dissimilar material joint was also completed.

Examination of the joint revealed crack-free Mg in the joint region. Static lap shear test results are given in Table II.3.I.2. Average lap shear failure load for thermoplastic CFRC-AZ31B was averaged at 3.07 ± 0.19 kN, while average peak failure load of 5.18 ± 0.12 kN was achieved for the thermoset CFRC-AZ31B. For the thermoplastic CFRC-AZ31B joint, the CFRC failed during the lap shear test, likely due to relatively low strength of the thermoplastic CFRC. For the thermoset CFRC-AZ31B joint, the Mg was pulled out from the joint region (e.g., button pullout failure), revealing a strong interlock between the rivet and the AZ31B. The thermoset CFRC-AZ31 joint was further tested for its CTS. The failure load under cross-tension averaged 2.81 ± 0.11 kN, and the failure location for all samples was button pullout from AZ31B with significant deformation of AZ31B.

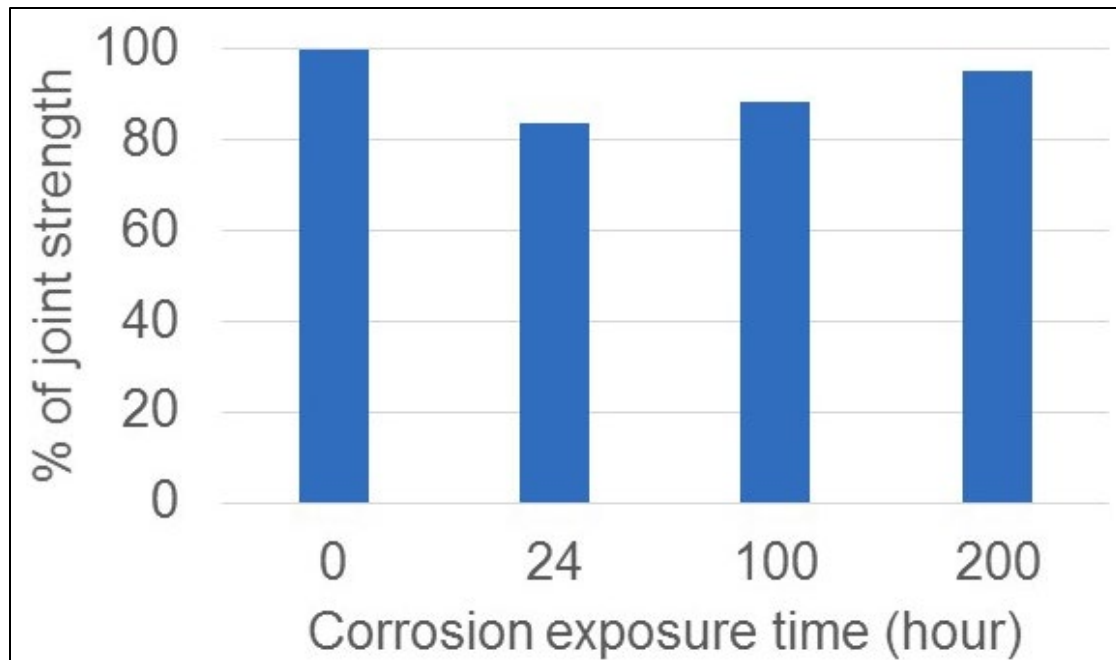
Table II.3.I.2. Summary of F-SPR Lap Shear Test Results.

Sample	Failure Load (kN)	Peak Load/Rivet Diam. (kN/mm)	Absorbed Energy (J)
Thermoplastic CFRC to AZ31B	3.07 ± 0.19	579 ± 35.25	1.58 ± 0.6
Thermoset CFRC to AZ31B	5.18 ± 0.19	977.77 ± 23.48	26.05 ± 1.18

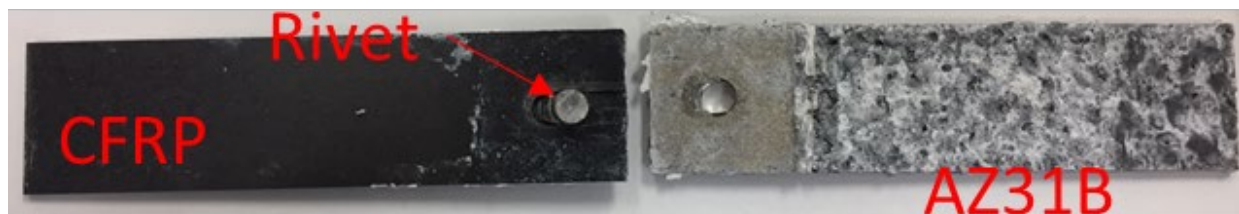
A corrosion test per ASTM B117 was used to investigate the corrosion resistance of thermoset CFRC-AZ31B F-SPR joints. The remaining strength of the joints were determined as a function of exposure times of 24, 100, and 200 hours. Figure II.3.I.9.(a) shows the cross-tension and lap shear configurations for F-SPR of Mg to thermoplastic CFRC that was used in testing. Figure II.3.I.9.(b) summarizes the percentage of joint strength at different corrosion exposure time. Overall, 83 ~ 95% of original joint strength remained when the F-SPR samples were exposed for 200 hours. The failure mode for all corrosion-tested samples was button pullout of AZ31B, which is the same as that of joint before corrosion exposure. No significant corrosion of the steel rivet was observed up to 200 hours, potentially due to the sacrificial anode effect of galvanic corrosion. Significant general corrosion of AZ31B was observed rather than at the joint interface, as shown in Figure II.3.I.9.(c). For this reason, AZ31B surface corrosion protection should be considered to effectively study corrosion at the joint interface.



(a)



(b)



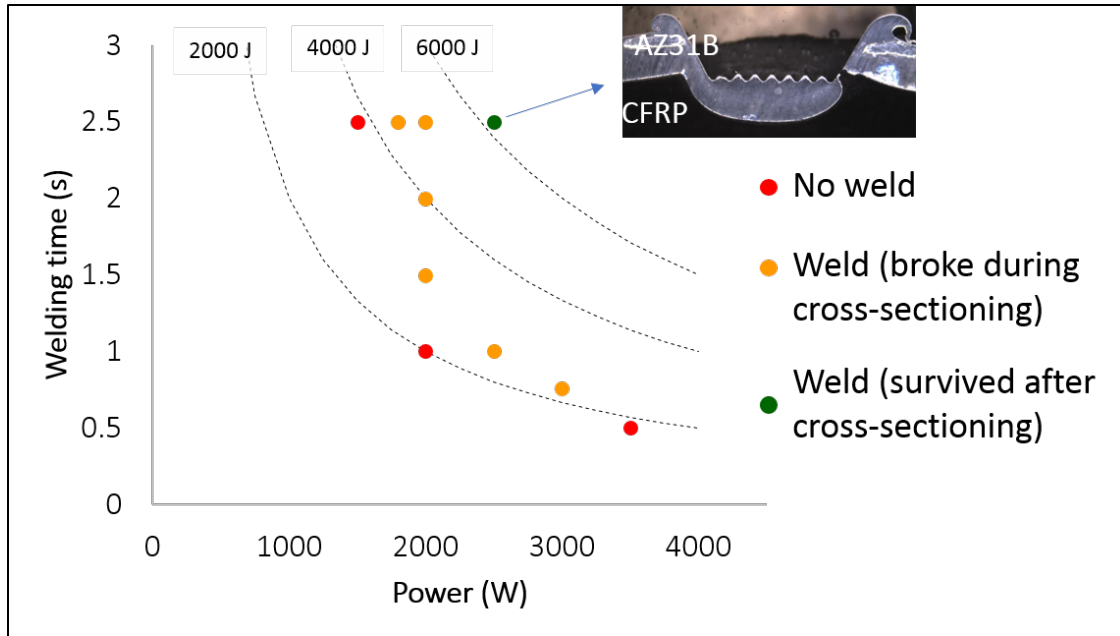
(c)

Figure II.3.I.9. (a) Cross-tension and lap shear configurations for F-SPR of Mg to thermoplastic CFRC. (b) Joint strength after corrosion testing. (c) Tensile testing after 200 hour exposure to ASTM B117. Source: ORNL.

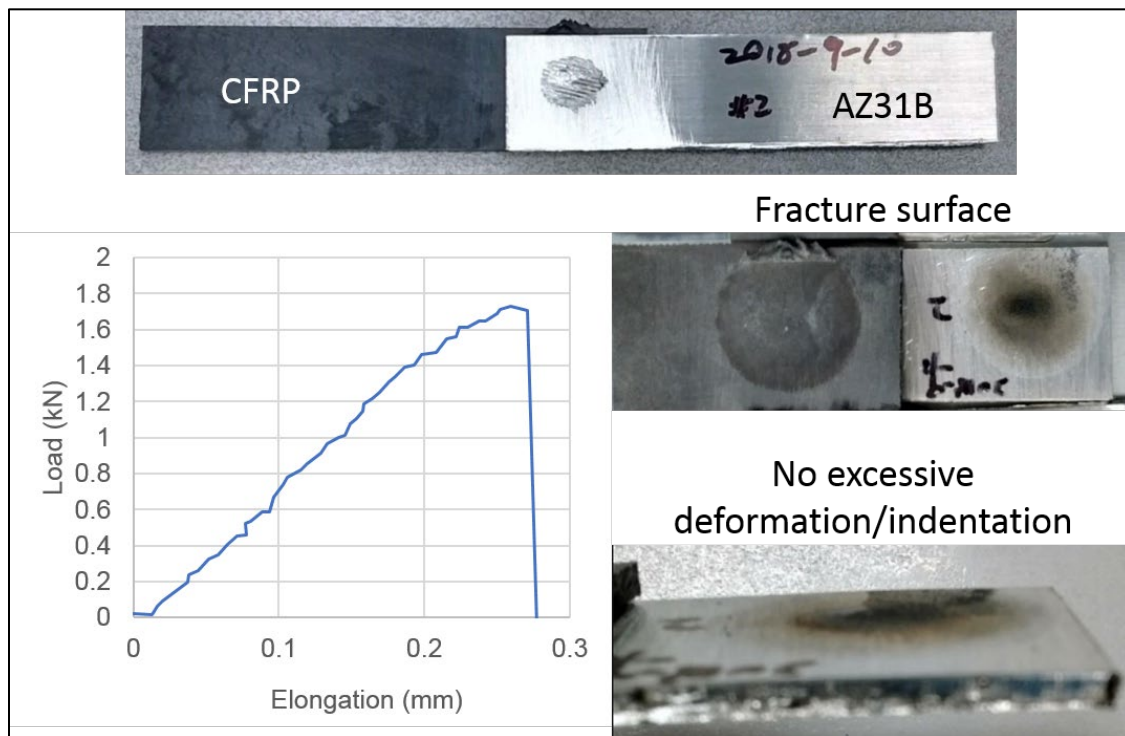
Method 5 – Ultrasonic Welding (ORNL Lead)

Ultrasonic welding (UW) offers the possibility of directly joining CFRC to AZ31B Mg without introducing third-party body elements or pre-drilled holes. The main bonding mechanism would be considered a chemical bond between the polymer and the metal. The research focused on thermoplastic CFRC because it is a reversible crosslinking polymer composite which, unlike thermoset CFRC, will soften and melt during heating. Upon cooling, direct chemical bonding between thermoplastic CFRC and AZ31B could form.

A large set of UW process conditions were investigated. The initial results suggested that an effective bond could only be formed with more than 6,000 J welding energy input, as shown in Figure II.3.I.10.(a). However, the excessive indentation/deformation on the AZ31B side weakened the joint. Modifications of the sonotrode tip design and machine control were used to reduce the excessive indentation. Figure II.3.I.10.(b) shows a weld coupon produced with the improved welding condition. No excessive indentation or deformation was observed. The lap shear failure load was 1.7 kN, while the joint failure was interfacial fracture. Preliminary corrosion testing was conducted in a salt-fog environment (i.e., ASTM B117-16). However, all six coupons fell apart after 24-hour exposure.



(a)



(b)

Figure II.3.I.10.(a) Initial welding process window that produces effective bond but with excessive indentation and (b) the lap shear weld coupon with optimized process parameters. Source: ORNL.

The influence of surface texturing on the joint strength was also investigated. Figure II.3.I.11 shows a weld joint produced with pre-textured AZ31B surface. The lap shear failure load increased to 2.8 kN. The improved strength was the contribution of mechanical interlocking, as well as increased effective contact area produced by the textured features. Research revealed that it is feasible to use UW to directly bond TP-CFRC and AZ31B

Mg-alloy with an appropriate welding setup. The bonding mechanism is chemical bonding. Preliminary corrosion testing shows poor corrosion resistance of the joints. Pre-textured AZ31B surface can improve joint strength by means of interfacial interlocking and increase contact area.

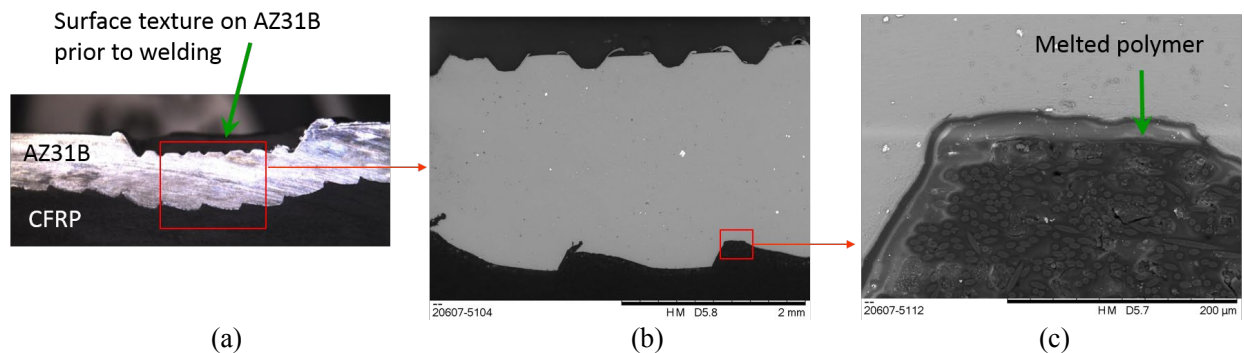


Figure II.3.I.11. Weld joint produced with pre-textured surface on AZ31B. (a) Surface texture on AZ31B before welding. (b) AZ31B and TP-CFRP joint. (c) Expanded view of TP-CFRP melted into AZ31B alloy. Source: ORNL.

Conclusions

At the end of FY 2018, each joining technique was assessed using evaluation criteria established and agreed upon by the DOE Technology Manager and PNNL/ORNL Mg-CFRP project members. Down-select was performed by the DOE Technology Manager, based on the evaluation criteria submitted by the team, at the end of year project review meeting held at ORNL on October 10, 2018. It was determined that approaches relying on the chemical/interfacial bonding would not be pursued in FY 2019. The projects selected for continued development in FY 2019 were FSI, conventional bolting, and friction stir self-piercing riveting. Techniques investigated within this project are now centered on new methods for creating robust mechanical interlocking between Mg and CFRP.

Key Publications

1. Lim, Y., C. Warren, J. Chen, and Z. Feng, 2019, "Joining of Lightweight Dissimilar Materials by Friction Self-Pierce Riveting," Accepted for presentation, *TMS Friction Stir Joining and Welding X*, March 10–14, 2019, San Antonio, TX, USA.
2. Upadhyay, P., Md. Reza-E-Rabby, and S. Whalen, 2019, "Joining of Mg to Reinforced Polymers Using FSI," Accepted for presentation, *TMS Friction Stir Joining and Welding X*, March 10–14, 2019, San Antonio, TX, USA.
3. Lim, Y., D. Warren, J. Chen, and Z. Feng, 2018, "Joining of Composite CFRP to Mg-Alloy by Friction Stir Self-piercing Rivet," *FABTECH and AWS Conference*, November 5–8, 2018, Atlanta, GA, USA.
4. Chen, Y., Y. Lim, and Z. Feng, 2018, "Ultrasonic Welding for Multi-Material Joining," Invited presentation, *Global Automotive Lightweight Materials*, April 21, 2018, Detroit, MI, USA.

II.3.J Mitigating Corrosion in Mg Sheet in Conjunction with a Sheet-Joining Method that Satisfies Structural Requirements within Sub-assemblies (Pacific Northwest National Laboratory)

Aashish Rohatgi, Co-Principal Investigator

Pacific Northwest National Laboratory
902 Battelle Blvd.
Richland, WA 99352
E-mail: aashish.rohatgi@pnnl.gov

Bill Kokosza, Co-Principal Investigator

Magna International – Stronach Centre for Innovation (SCFI)
750 Tower Dr.
Troy, MI 48083
E-mail: bill.kokosza@magna.com

Sarah Kleinbaum, DOE Technology Manager

U.S. Department of Energy
E-mail: sarah.kleinbaum@ee.doe.gov

Start Date: October 1, 2017	End Date: September 30, 2019	
Project Funding (FY18): \$350,000	DOE share: \$150,000	Non-DOE share: \$200,000

Project Introduction

The push for lightweighting solutions for U.S. LD and HD vehicles has identified Mg-alloy sheet materials as a possible candidate. The general consensus in the automotive industry is that the use of multi-material solutions is going to be the trend for future vehicles in order to achieve the desired weight reduction. A recent Multi-Material Lightweight Vehicle report [1] shows 155 kg (47.5%) BIW mass reduction in a Multi-Material Lightweight Vehicle Mach-II design relative to a 2013 Fusion baseline vehicle, where Class A exterior body panels are warm-formed Mg sheets. The use of this Mg sheet up to 51% in closures-in-white applications is proposed in the Mach-II design for a 48% mass reduction over the baseline vehicle. However, the report identified two major challenges related to the use of multi-material solutions: (1) corrosion; and (2) joining. Additionally, for Mg alloys, the need for improved corrosion mitigation is a prime requirement, especially when coupled with a dissimilar metal because of a galvanic corrosion problem. Corrosion behavior of Mg, Mg/Mg, Mg/Al, and Mg/steel joints is being evaluated in this project through environmental corrosion chamber tests and microstructural characterization.

Objectives

The goal of this project is to develop strategies to join Mg with Mg/dissimilar metals to meet structural requirements while simultaneously mitigating corrosion and achieving a Class A surface finish. Following are the objectives to achieve this goal:

- Evaluate corrosion behavior of two types of protective surface coatings on an Mg-alloy sheet.
- Evaluate three different joining techniques for their respective corrosion behavior and structural strength in Mg/Mg similar, Mg/Al, and Mg/Steel dissimilar joints.
- Determine the influence of the joining processes on the corrosion protection efficiency of the surface coatings.

Approach

Magna has initially identified three potential joining techniques for Mg-based similar and dissimilar joints. However, the corrosion behavior of such combinations of material systems and joint designs is unknown, and hence, is the focus of this work.

The three initial joining techniques identified by Magna are (1) Arplas RSW, (2) clinch lock, and (3) breakaway stem rivet. Two types of proprietary coating-based corrosion protection schemes are being provided by Henkel and are labeled as Henkel pretreatment (HP) and Henkel pretreatment + E-coated (HPEC). AZ31 has been selected as the representative Mg material. A comprehensive test matrix was developed by Magna and PNNL and comprises corrosion testing and characterization of a total of 144 coupons with similar joints (AZ31/AZ31), as well as 96 coupons with dissimilar joints (AZ31 to Al/Steel). For base material characterization, 3-in. x 5-in. corrosion test coupons were provided by Magna for testing at PNNL.

Corrosion behavior of the base material was determined according to the American Society for Testing and Materials (ASTM) B117 standard salt (NaCl) spray (fog) test method. As per ASTM B117, corrosion coupons were subjected to a continuous exposure of 5% salt-fog at 35°C for a total duration of up to 1,500 hours (~ 60 days) at a pH of 6.5–7.2. During the course of ASTM B117 testing, corrosion coupons were retrieved at regular intervals, gently washed under tap water, and immediately dried. Subsequently, the coupons were weighed to record the change in weight due to corrosion/corrosion product build-up. The salt-fog setup at PNNL is shown in Figure II.3.J.1.(a), where a row of bare AZ31 coupons can be seen. Figure II.3.J.1.(b) shows a picture of test coupons in bare (i.e., uncoated) and two types of coating conditions (HP and HPEC).

For microstructural characterization, transverse cross-sections of corrosion-tested coupons were prepared using standard metallographic techniques and imaged in a SEM. The samples were imaged using the BSE imaging mode to help distinguish corrosion products, protective coatings, and the base material. Mechanical robustness of the coatings, especially at the coating/base Mg AZ31 interface, was evaluated using nano-indentation technique. Metallographically polished samples of transverse cross-sections of corrosion-tested coupons (e.g., HP and HPEC) were indented along the interface using a Berkovich indenter for a series of loads ranging from 10–200 Mn. The positions of the indents were controlled to be (or, as close as possible) to the coating/base Mg AZ31 interface, or within the coating. Subsequently, the indented locations were imaged in the SEM to examine for propensity and location of cracks (if any) around the indent or along the interface.

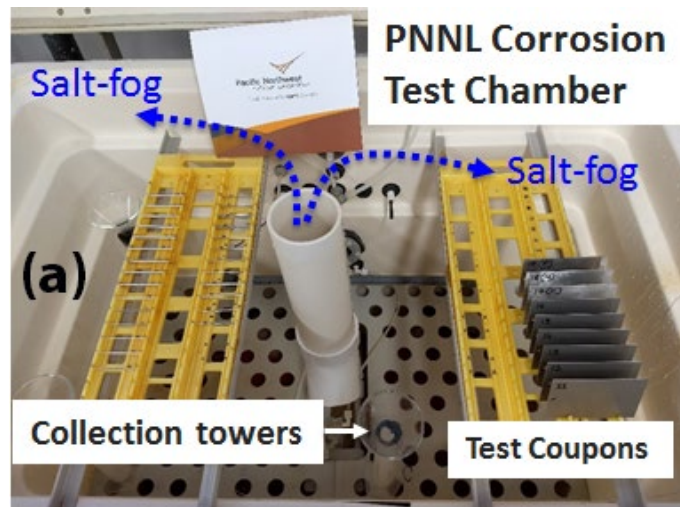


Figure II.3.J.1. (a) Salt-fog test setup at PNNL; (b) Bare and coated (HP and HPEC) AZ31 coupons ready for testing. Source: PNNL.

Results

In FY 2018, the base material (Mg AZ31) coupons were tested in bare (uncoated) and coated (HP and HPEC) conditions using the ASTM B117 test method. These results are described below.

Base Material Corrosion Behavior

Figure II.3.J.2 shows pictures of base AZ31 coupons in bare (uncoated), HP, and HPEC conditions in the as-received untested state and following 1,200 hours of corrosion testing per the ASTM B117 method. Figure II.3.J.2.(b) shows that the bare AZ31 coupons experienced significant uniform and pitting corrosion after 1,200 hours of testing, as evidenced by the mottled black and white surface and material loss at the edges, in contrast to the smooth, uniform, and shiny surface of the untested coupon, shown in Figure II.3.J.2.(a). In the case of the HP coupons, discoloration and loss of shine is noted after 1,200 hours of salt-fog exposure, shown in Figure II.3.J.2.(d) compared to the untested coupon. The best surface appearance after 1,200 hours of corrosion testing is observed in the HPEC coupons shown in Figure II.3.J.2.(f) with no apparent signs of general corrosion very much like the untested coupon in Figure II.3.J.2.(e). In the HPEC sample, small accumulation of corrosion products was also observed around the punch holes and coupon edges, shown in Figure II.3.J.2.(f) as indicated by the arrows, and are likely due to the protective coating being damaged during coupon preparation and leading to localized corrosion of the underlying Mg substrate.

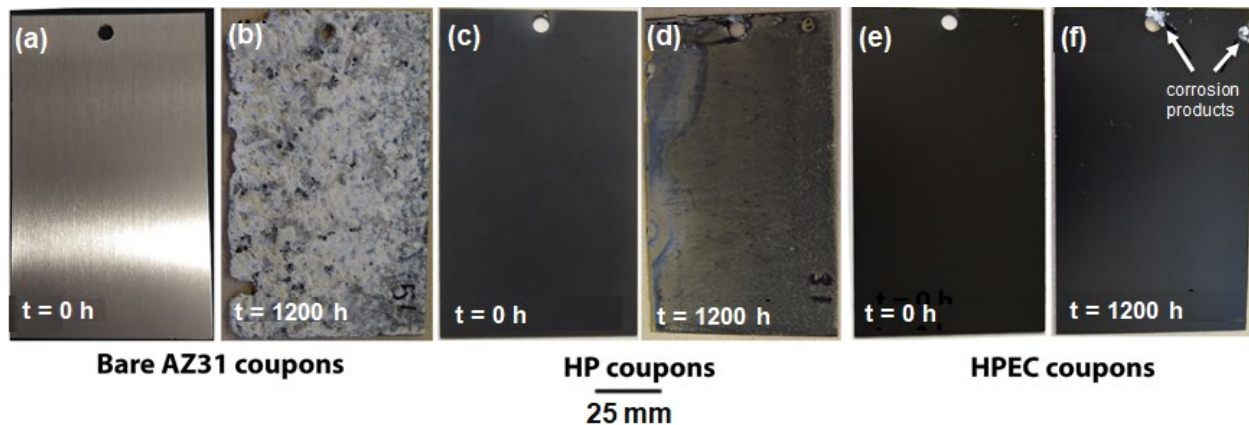
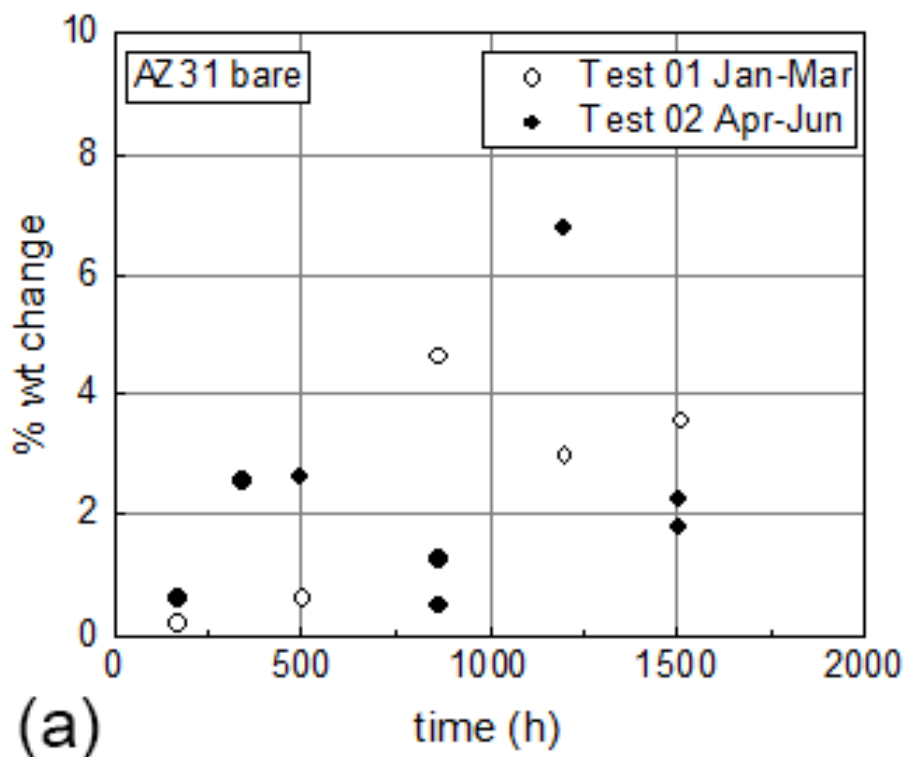


Figure II.3.J.2. External appearance of the corrosion coupons after the ASTM B117 test; bare untested AZ31 - (a) $t = 0$ hours, (b) $t = 1,200$ hours; HP - (c) $t = 0$ hours, (d) $t = 1,200$ hours; HPEC - (e) $t = 0$ hours, and (f) $t = 1,200$ hours. Arrows indicate localized corrosion product build-up. Source: PNNL.

Figure II.3.J.3 shows the plots of change in weight of the three types of coupons (i.e., bare untested AZ31, HP, and HPEC) as a function of corrosion test duration. Bare untested AZ31 coupons, shown in Figure II.3.J.3.(a) were tested in two separate batches; substantial weight gain, as high as 7%, was observed in these coupons. This weight gain is attributed to the formation of $Mg(OH)_2$ due to the reaction between Mg and WV and appears as a white substance sticking on to the coupon surface. As compared to bare Mg, HP coupons, shown in Figure II.3.J.3.(b), show a slight ($<1\%$) weight loss, which may be due to the pretreatment coating being washed off during the course of the test. Some discoloration and loss of shine, relative to untested coupons, was also observed in the corrosion-tested HP coupons, which might be linked to this slight weight loss. Finally, no change in weight was observed in the HPEC coupons, shown in Figure II.3.J.3.(c), indicating the best corrosion protection.



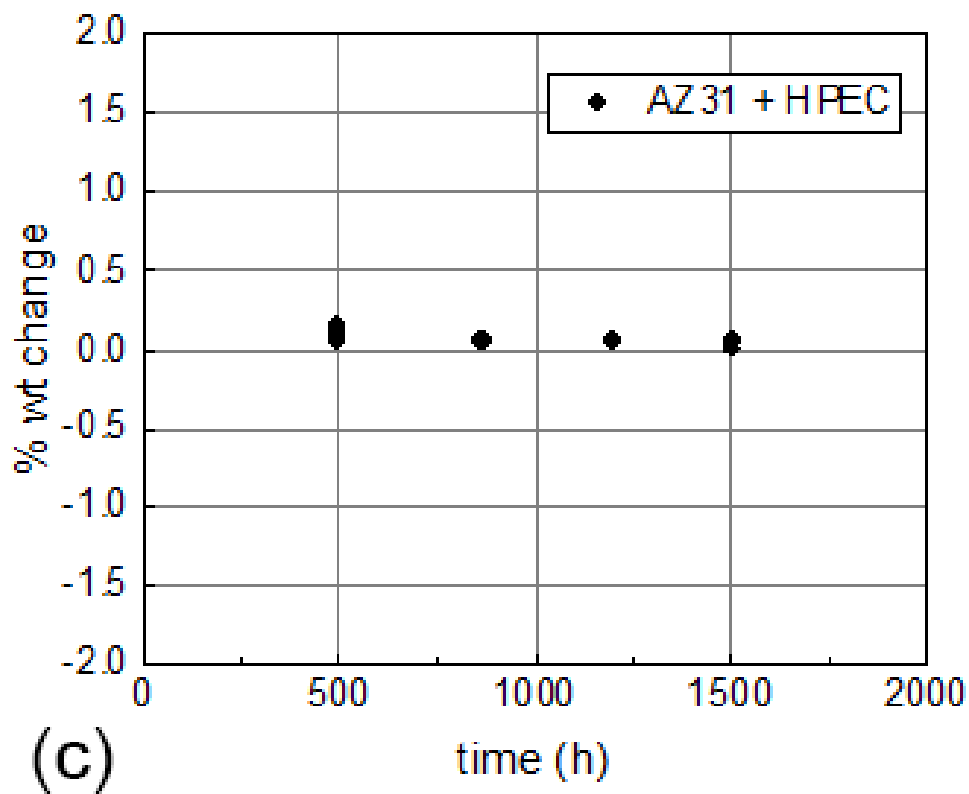
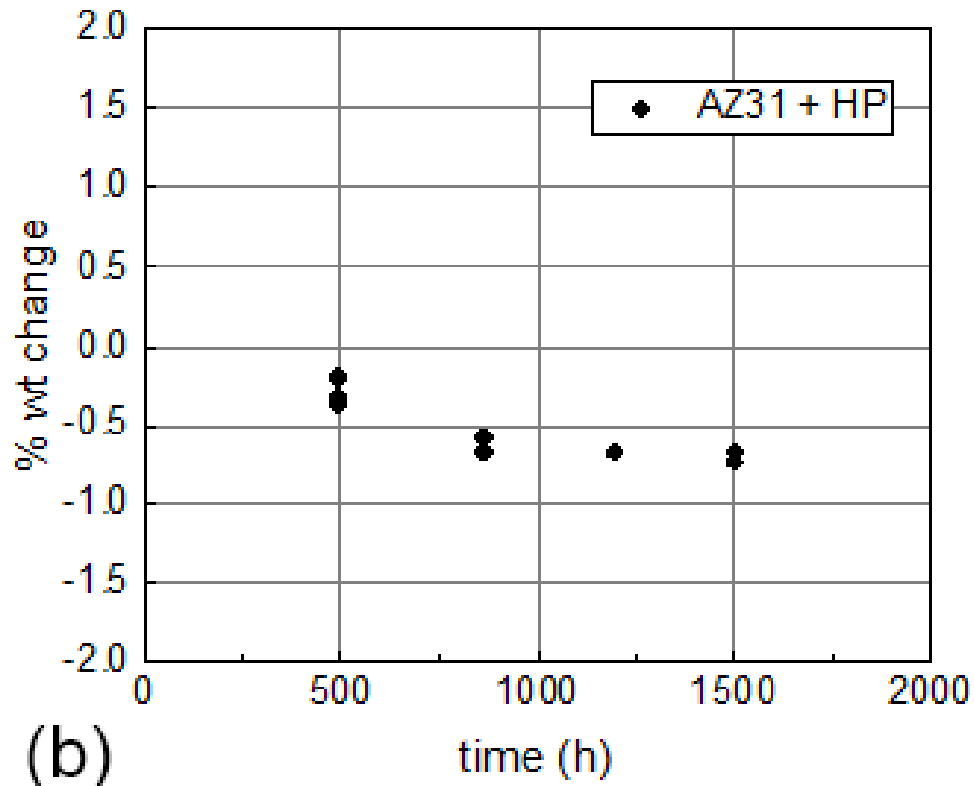


Figure II.3.J.3. Change in coupon weight vs. test duration following ASTM B117 testing: (a) bare AZ31; (b) HP; and (c) HPEC. Source: PNNL.

Microstructural Characterization

Figure II.3.J.4 shows a SEM image of the transverse cross-section of a bare untreated AZ31 coupon after corrosion testing for 500 hours. Build-up of $Mg(OH)_2$ on the coupon surface and inward growth into the AZ31 matrix through pitting is noted in the lower-magnification of Figure II.3.J.4.(b). Further, the corrosion film contains a number of cracks which is evident in the adjoining higher magnification image, shown in Figure II.3.J.4.(a). At a macro-level, presence of numerous such cracks provides easy paths for the corrosive media to contact the underlying base metal, and thus, continue the corrosion process.

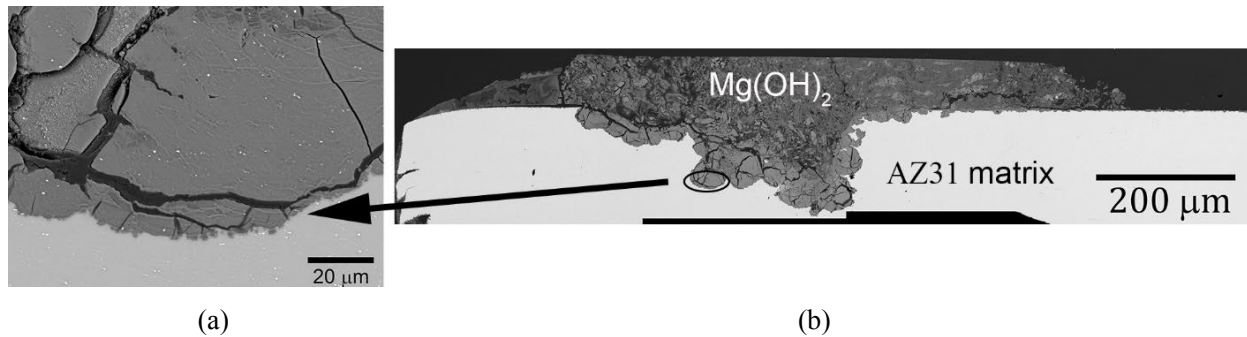


Figure II.3.J.4. Back-scattered SEM image of (a) the transverse cross-section of a bare AZ31 coupon after corrosion testing for $t = 500$ hours. (b) $Mg(OH)_2$, the corrosion product, is noted to form on the surface, and contains multiple cracks that might be responsible for continuation of the corrosion process. Source: PNNL.

Figure II.3.J.5 shows the transverse cross-section images of HP coupons as a function of test duration for 500 hours in Figure II.3.J.5.(a) and 850 hours in Figure II.3.J.5.(b). The thickness of the HP layer is measured to be $\sim 10 \mu m$. In addition, the pretreatment layer is noted to contain pores, which might render it prone to corrosion. Formation of $Mg(OH)_2$, the corrosion product, on the underlying AZ31 matrix could be seen at a location where the pretreatment layer appears to wash off during testing, as shown in Figure II.3.J.5.(c). Although further degradation of the HP layer is observed after 1,500 hours of testing, shown in Figure II.3.J.5.(d), the HP layer seems to be able to protect the underlying metal surface from corrosion.

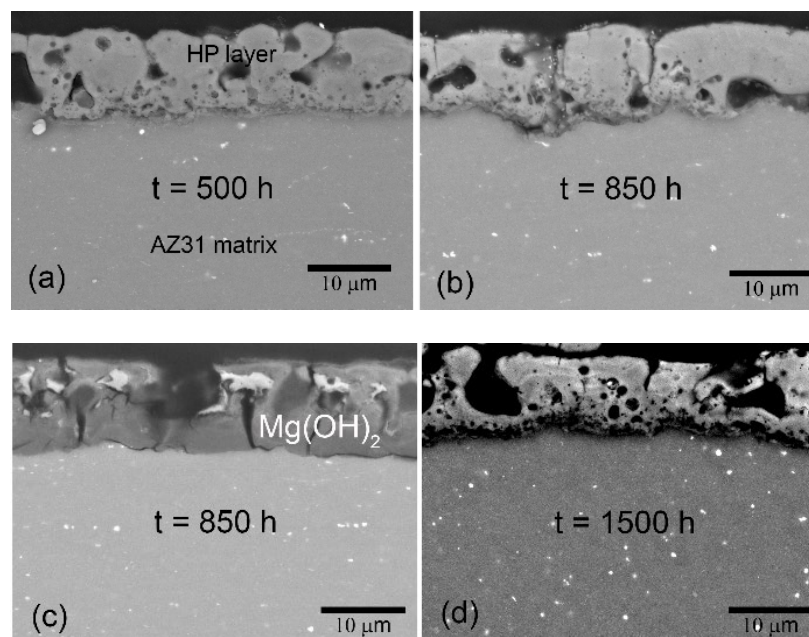


Figure II.3.J.5. SEM images of the transverse cross-section of HP coupons: (a) after 500 hours; (b) after 850 hours; (c) after 850 hours, some areas showed build-up of $Mg(OH)_2$ corrosion product; and (d) after 1,500 hours. Source: PNNL.

Figure II.3.J.6 shows the transverse cross-section images of HPEC coupons as a function of test duration, showing the HP layer in contact with the underlying AZ31 substrate and the E-coat (EC) layer on top of the HP layer. The HP layer is porous and $\sim 10\ \mu\text{m}$ thick, as seen in the HP coupons in Figure II.3.J.5, while the overlying EC layer appears to be pore-free and $\sim 15\text{--}20\ \mu\text{m}$ thick. Additionally, the presence of numerous bright particles could be seen within the EC layer. The EC protective layer appears to be stable, and no apparent damage has been recorded over the course of corrosion testing. However, after 1,500 hours of testing, some cracks, as shown by the arrows in Figure II.3.J.6.(c), could be observed at the HP/AZ31 interface and may act as a potential failure location of the overall corrosion protection scheme. In summary, it appears that the best corrosion protection is obtained in HPEC samples, and the top EC layer remains unaffected when exposed to salt-fog environment of ASTM B117 test for 1,500 hours.

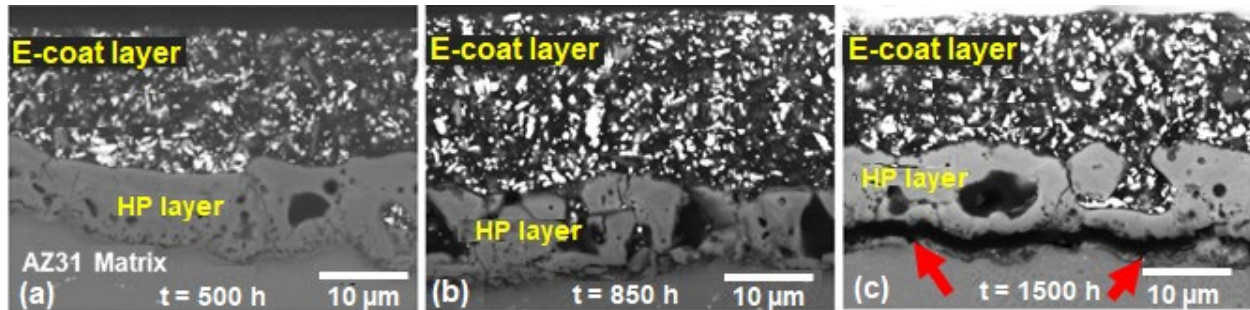


Figure II.3.J.6. SEM images of the transverse cross-section of HPEC coupons: (a) after 500 hours; (b) after 850 hours; and (c) after 1,500 hours. Arrows show cracks at the HP/AZ31 interface. Source: PNNL.

Mechanical Property Characterization

Mechanical robustness of the coatings was evaluated through the nano-indentation technique. If the coatings have poor interfacial adhesion, the use of indentation point load at the coating/base Mg AZ31 interface is expected to lead to interfacial cracking and/or delamination of the corrosion protection layer. Images of the indents on the HP coupons that had been corrosion-tested for 500 hours of ASTM B117 tests prior to indentation, are shown in Figure II.3.J.7. The indents have been marked by a dashed line for the purpose of illustration. No interfacial delamination between the HP layer and the base Mg AZ31 sheet could be noted after the indentation. However, a few cracks could be observed when the indent was located completely within the HP layer, as shown in Figure II.3.J.7.(b) and (c). In the case of indents made on the HPEC coupons, as shown in Figure II.3.J.8.(a) and (b) after 500 hours of ASTM B117 tests, no cracks could be observed inside the EC layer or along the HP/EC interface. The interface between the HP/EC appears to be mechanically strong and no indentation-induced cracks could be observed in the EC layer.

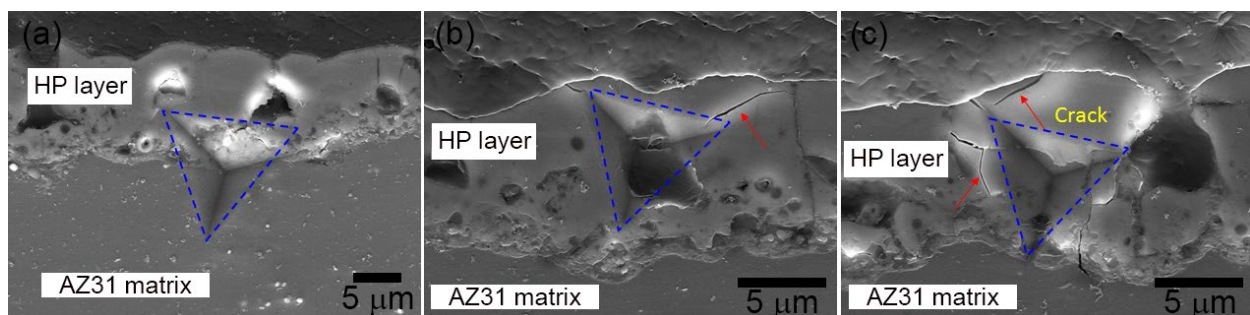


Figure II.3.J.7. SEM image of the indents in HP coupons; (a) indent along HP/AZ31 interface, (b) indent inside the HP layer, (c) some cracking noted around the indent. Source: PNNL.

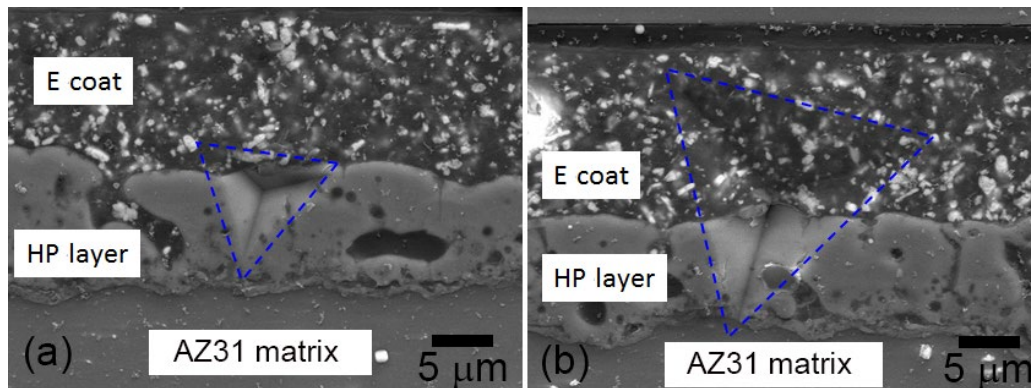


Figure II.3.J.8. SEM image of the indents in HPEC coupon: (a) indent along HP/EC interface; and (b) indent inside EC layer. Source: PNNL

Conclusions

Evaluation of the corrosion behavior of a base AZ31 Mg sheet has been completed. The Mg sheet in three conditions—uncoated, HP, and HPEC—was tested using the ASTM B117 salt-fog test method for up to 1,500 hours. Bare untreated AZ31 undergoes severe corrosion while both HP and HPEC coupons show minimal to no corrosion. In the case of the HP AZ31 coupons, although the coating is porous and some of its original shine is lost, the HP coating is able to protect the underlying AZ31 substrate. In the case of HPEC AZ31 coupons, the topmost layer (E-coat) is pore-free and shows almost no degradation after corrosion testing, although some cracks were observed at the AZ31 base metal/HP layer interface after 1,500 hours of corrosion testing. In summary, both protection schemes used in this work seem to protect the AZ31 Mg sheet from corrosion. Similar corrosion tests as those conducted in FY 2018 will be performed on Mg similar/dissimilar joints and the interactions between the joint-type and coating schemes will be analyzed in FY 2019.

References

1. U.S. Department of Energy, National Energy Technology Laboratory, 2015, “Demonstration Project for a Multi-Material Lightweight Prototype Vehicle as Part of the Clean Energy Dialogue with Canada,” DOE Award # DE-EE0005574. <https://www.osti.gov/servlets/purl/1332277>.

Acknowledgements

Technical contributions of PNNL staff supporting this research is gratefully acknowledged; in particular, Dr. S. Jana for his role in leading the project tasks, Mr. M. Dahl for help with corrosion testing, Mr. N. Canfield for performing microstructural characterization, and Ms. E. Stephens for help with corrosion test procedures.

II.3.K Non-Destructive Inspection of Al-Steel Weld Bond (Oak Ridge National Laboratory)

Zhill Feng, Principal Investigator

Oak Ridge National Laboratory
1 Bethel Valley Rd.
Oak Ridge, TN 37831
E-mail: fengz@ornl.gov

Sarah Kleinbaum, DOE Technology Manager

U.S. Department of Energy
E-mail: sarah.kleinbaum@ee.doe.gov

Start Date: October 1, 2017	End Date: March 31, 2019	
Project Funding (FY18): \$200,000	DOE share: \$200,000	Non-DOE share: \$0

Project Introduction

Material joining or welding is the primary assembly method in the automotive industry. The quality of the welds is critical to the crash resistance and performance of vehicles. The auto industry demands effective and reliable NDE methods to inspect each and every critical joint. It is even more important for dissimilar material joining. The lack of effective and reliable NDE tools suitable to the mass production environment is a barrier to the adoption of lightweight materials and suitable dissimilar material joining technologies by the automotive industry.

As the auto industry increasingly relies on multi-material strategy to balance the performance, fuel efficiency, and cost of auto-body structures, joining of dissimilar materials by means of spot welds and adhesives has become an integral part of dissimilar materials joining solution as exemplified by the introduction of RSW of Al to steel process joints in the seatback of the Cadillac CT6. There is a critical need for reliable and cost-effective NDE technologies that can be used in a high-volume auto structure manufacturing environment to inspect adhesively bonded joints or joints with rough and complex surface patterns. Conventional NDE tools such as ultrasound have been difficult to use for such applications. Ultrasound typically requires physical contact between the transducer and the material surface through use of a gel or fluid couplant at the interface. The patterned surface topography of the resistance spot weld causes difficulty for obtaining good couplant conditions for ultrasonic transmission. It is therefore the goal of this project to introduce and develop an NDE method, which is insensitive to the complex surface topography.

Sponsored by DOE VTO and with close collaboration with automotive industry OEMs and Tier One suppliers, ORNL in the past few years has successfully developed a non-contact online weld NDE technology for inspecting resistance spot welds based on infrared thermography-based NDE technique (IR NDE). This R&D 100 Award-winning technology has received considerable interests for licensing and technology commercialization. However, ORNL's IR NDE development was primarily limited to AHSSs, although limited testing trials suggested feasibility for Al RSW.

Independently, GM has created a novel approach to reduce the glare inherent in IR imaging of highly reflective Al surfaces, which we feel is an enabler for the application of ORNL's IR NDE method to Al-steel RSWs. While our initial scoping tests show promising results, as shown in Figure II.3.K.1 below, the application of IR NDE to inspect Al-steel spot welds needs to be developed further.

In this work, ORNL, in partnership with GM, proposes to develop an IR NDE method that can effectively and reliably inspect dissimilar material joints with complex surface patterns in a highly automated manufacturing environment. This method will be built upon our extensive experience with IR NDE. We plan to evaluate

options to address critical bottlenecks hindering the use of IR NDE for RSW and adhesive bond inspection. Based on such evaluation, the technique will be refined and optimized. A prototype system will be built and tested in a simulative manufacturing environment as a demonstration of this technology.

Objectives

The objective of this research is to extend ORNL's award-winning IR NDE technique to weld bonding of Al to AHSSs to address an immediate and critical NDE need identified by auto OEMs. To achieve this goal, new or improved NDE measurement techniques will be developed to solve unique challenges in dissimilar materials NDE and new thermal signature recognition algorithms specific for Al-steel welds will be investigated. For the latter, artificial intelligence-based ML tools that have become much more powerful in recent years will be explored as a new way to solve the very complicated relationship between joint quality and NDE measurement results. This will lay the ground for adoption and application of artificial intelligence-based ML tools for future R&D of NDE and *in-situ* monitoring of dissimilar material joining.

Approach

Inline Imaging

Thermal images were taken during and immediately after welding. For this setup, a forward-looking infrared A655SC camera was positioned at an angle with a view of the spot weld, which was unobstructed after the weld electrode raised, as shown in Figure II.3.K.1. The camera was automatically triggered to record as the welder started and captured at least three seconds of data at a rate of 200 Hz.

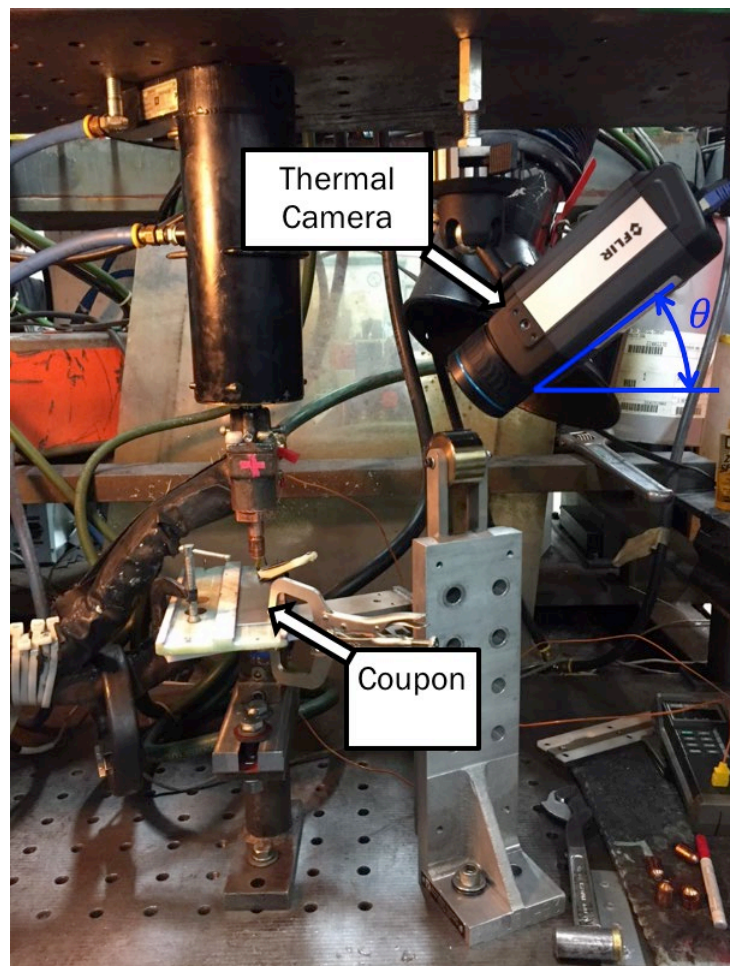


Figure II.3.K.1. Weld setup with thermal camera. Source: ORNL.

Post-Weld Imaging (Flash)

Post-weld through-transmission thermography imaging was conducted after welding using two methods for excitation. The first method used a flash lamp as the excitation method in a through-transmission configuration. Only the hand peel and metallographic specimens were evaluated using this method. Figure II.3.K.2 provides a schematic of this testing setup.

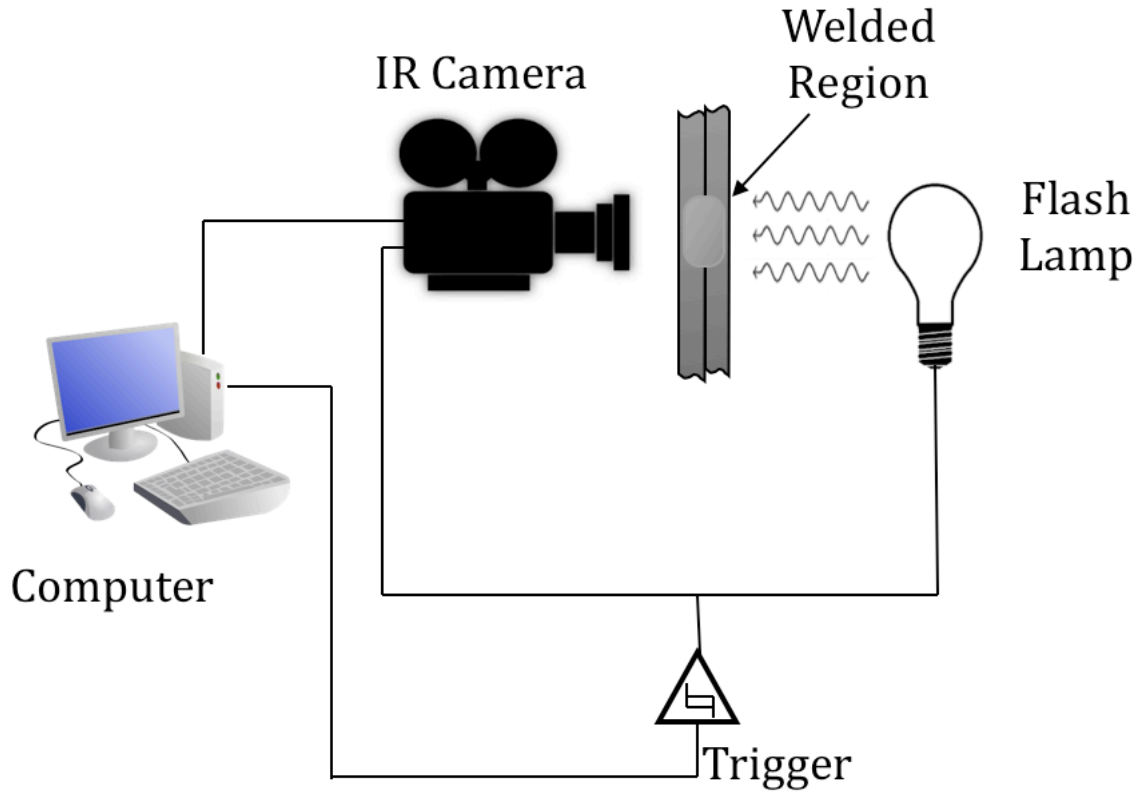


Figure II.3.K.2. Schematic of experimental setup. A pulsed light acted as the heat source, while an IR camera was positioned on the opposite side of the sample for data collection. Source: GM.

Pulsed thermography was employed using a flash lamp (Elinchrom 1200RX) to provide a pulsed heat source at 1,200 watts with a duration of 1/1450 seconds. The samples were mounted to Garolite, a fixture on the end of the lamp, to ensure consistency in placement relative to the camera and light source. Care was taken to isolate the strobe light from the camera, in order to avoid overexposure and contamination of the data. The camera was triggered to record slightly before the pulsed light was triggered. A forward-looking infrared SC8300 thermal camera was used with a frame rate of 187 frames/sec.

Post-Weld Imaging (Induction)

Additionally, post-weld through-transmission thermography imaging was conducted using induction for thermal excitation. An induction heater (Ambrell EasyHeat 0112) of 1,200 watts was used. The induction heater was programmed to provide thermal excitation approximately 3 seconds. During heating, the sample was positioned on a ring stand so that the sample was at a consistent distance from the induction heater. The camera was set to record for 3.5 seconds, beginning at the time of heater excitation. The entire sample set was evaluated using the induction heating method.

RSW Experimental Design

Experimental Test Matrix

Seven weld variations were evaluated in this study that include steel welded to itself, Al welded to itself, and stack-ups with dissimilar metals, thicknesses, and welding electrodes, as presented in Table II.3.K.1. All low carbon steel (LCS) materials were coated with a HDG material, while the Al alloys were uncoated. No cleaning or other surface preparation was used on either material prior to welding the sheet stack-ups.

Welding was performed using a medium frequency direct current welding machine designed for spot welding Al alloys. The system used an inverter weld control from Welding Technology Corporation of Farmington Hills, MI, with medium frequency direct current transformers provided by RoMan Manufacturing of Grand Rapids, MI. Pneumatic actuators were used to apply weld force. Distilled water at ambient temperature was used to cool the welding electrodes at a flow rate of 1.5–2.0 gpm.

Material stack-ups were welded with either 6006 (16 mm diameter) or 6148 (19 mm diameter) CuZr C15000 Cu alloy electrodes. Ballnose electrodes were machined to include a ~5 mm face using GM’s patented multi-ring domed (MRD) electrodes. All weld tests were performed with the Al alloy sheet contacting the positive welding electrode. Electrodes were chosen for each stackup based on the size and type of electrode that would be used in a production body shop.

Weld sizes were chosen based upon GM’s specifications for minimum and acceptable weld sizes in a production teardown situation. Weld currents were adjusted to produce the desired weld size in a hand peel sample. The maximum weld size was chosen when the weld schedule consistently produced internal expulsion (IX). The “High” weld size was the midpoint between the “Target” and “Max” weld sizes.

Table II.3.K.1. Experimental Test Matrix with Weld Sizes

Stackup	Electrodes	Min (mm)	Low (mm)	Target (mm)	High (mm)	Max (mm)
1.0 mm HDG LCS – 1.0 mm HDG LCS	6006 Ballnose	3.0	4.0	5.0	Mid	IX
1.0 mm HDG LCS – 1.0 mm HDG LCS	6006 MRD	3.0	4.0	5.0	Mid	IX
2.0 mm HDG LCS – 2.0 mm HDG LCS	6148 MRD	5.0	6.0	7.0	Mid	IX
0.8 mm x626 Al – 0.8 mm x626 Al	6006 MRD	2.5	3.5	4.5	Mid	IX
1.2 mm 6022 Al – 1.0 mm x610 Al	6148 MRD	3.5	4.5	5.5	Mid	IX
0.8 mm x626 Al – 1.0 mm HDG LCS	6006 Hybrid (MRD/Ballnose)	3.5	4.5	5.5	Mid	IX
1.2 mm 6022 Al – 2.0 mm HDG LCS	6148 MRD	4.5	5.5	6.5	Mid	IX

Sample Configurations

Samples were welded in a non-conductive Garolite fixture, such that the welds were produced in the same location on every test specimen. A total of seven coach peel, cross-tension, and tensile shear specimens plus three hand peel samples and a single metallurgical test specimen were welded for each stackup and weld size, as shown in Table II.3.K.1. To simulate the paint-bake thermal treatment that vehicles undergo in-production, all samples were baked in an oven at 175°C for 35 minutes.

Sample Analysis

Metallographic specimens were sectioned and polished to a surface finish of 0.04 μm using silica polishing media. Samples were examined in the unetched state to evaluate the weld nugget, intermetallic layer, their accompanying defects, and microhardness. Since loading of the weld is greatest at the periphery, the intermetallic layer thickness in this region is of great interest. ImageJ image analysis software, provided by the U.S. National Institutes of Health of Bethesda, MD, was used to measure notch root angle (angle tool), nugget diameter at the faying interface (straight line tool), and nugget cross-sectional area (polygon selections tool). Three welds per weld condition were measured using ImageJ.

Earlier work at GM investigating the mechanical performance of Al-steel welds found that coach peel specimens are a much better discriminator of joint quality than tensile shear specimens. Tensile shear specimens typically exhibit high-strength with little influence of weld defects. For this work, joint mechanical performance was determined using coach peel, cross-tension, and tensile shear tests. Tensile loading tests were completed with all specimen geometries until full fracture at a rate of 5 mm/min using an MTS Systems Corporation load frame. Hand peel specimens were clamped in a static vise and manually pulled with pliers until the complete failure of all four welds. This is a commonly used method for spot weld testing in the industry, so it was adopted for our tests. Weld indentations (i.e., the stackup thickness minus the as-welded thickness in the center of the weld) and weld button sizes (i.e., the average of the maximum and minimum button diameters) were measured using digital handheld calipers.

Results

All experimental work for this project has been completed. Data analysis is ongoing as described in the subsections that follow.

Metallographic Results

The structure of Al-steel RSWs is very distinct compared to similar metal spot welds, as shown in Figure II.3.K.3. In Al-Al and steel-steel spot welds, for instance, the weld structure consists of a single weld nugget comprised of a mixture of material from both metal sheets. In contrast, Al-steel spot weld joints feature a planar interface between the Al and the steel with a weld nugget contained only within the Al alloy sheet. The Al weld nugget is separated from the steel substrate by a layer of intermetallic compounds at the faying interface. These intermetallic compounds are primarily Fe_2Al_5 adjacent to the steel substrate and FeAl_3 adjacent to the Al alloy weld nugget. In some instances, a very small steel nugget can form in the center of the steel sheet surrounded by a large HAZ.

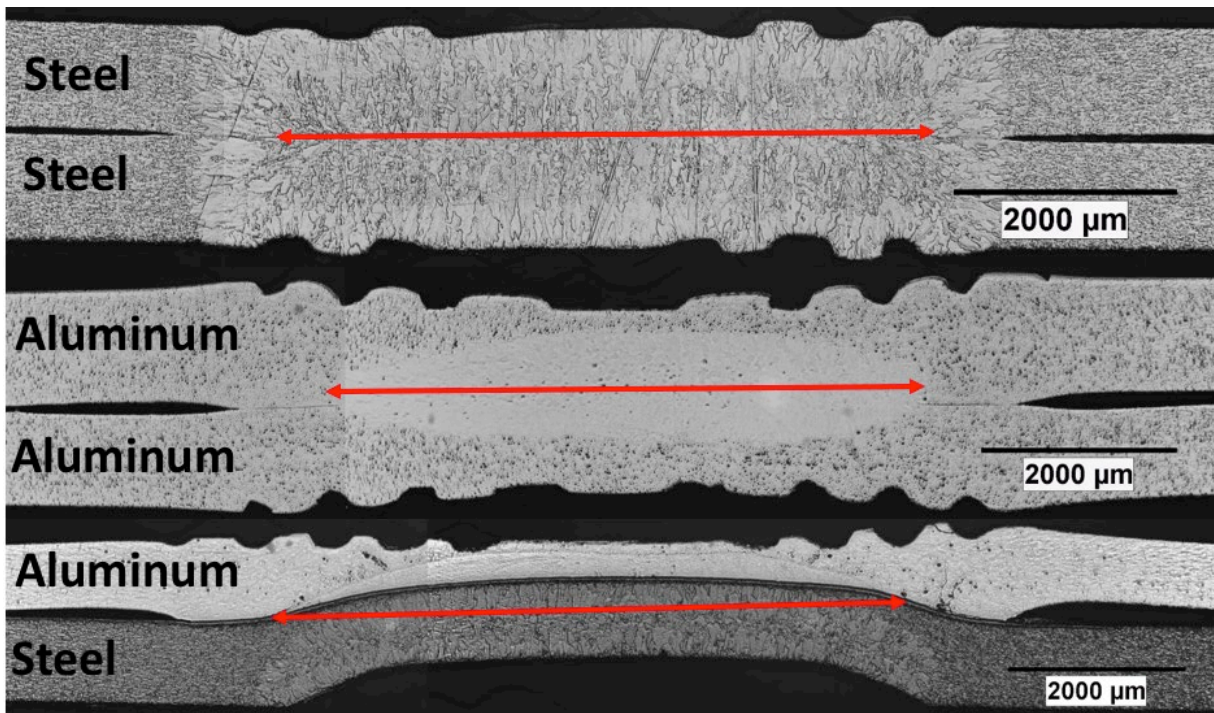


Figure II.3.K.3. Examples of steel, Al, and Al-steel weld cross-sections with nugget diameters highlighted by red arrows. Three nugget diameters for each stackup and weld size have been measured. This data is used as a comparison to the nugget diameters predicted by each of the NDE methods. Source: GM.

Comparison of Weld Nugget Sizes

Once all analyses are complete, statistical analyses will be performed to determine which NDE method or methods accurately predict the actual weld nugget size. Progress is shown in Table II.3.K.2.

Table II.3.K.2. Example Chart Showing Weld Nugget Size Comparisons.

Measured	Inline NDE	Pulsed Thermography	Induction
Completed	Completed	In Process	In Process

Inline NDE Results

A GM internal nugget-prediction algorithm was used to analyze the IR data captured inline (see “Inline Imaging” section above) for the prediction of the nugget diameter. Figure II.3.K.4 contains the GM predicted diameters versus real measured diameters for the entire sample set. The individual measurements are denoted by the color dots for each material and material pairs with the respective electrode used, and the expected 1:1 relation is denoted by the grey dashed line. A proportional trend is observed between the predicted versus real diameters. A relatively large amount of scatter is observed, which can be attributed to the low emissivity and high reflectivity of both Al and steel. The stack-ups containing Al are especially susceptible to noise in the data since Al has a lower emissivity and higher reflectivity than steel.

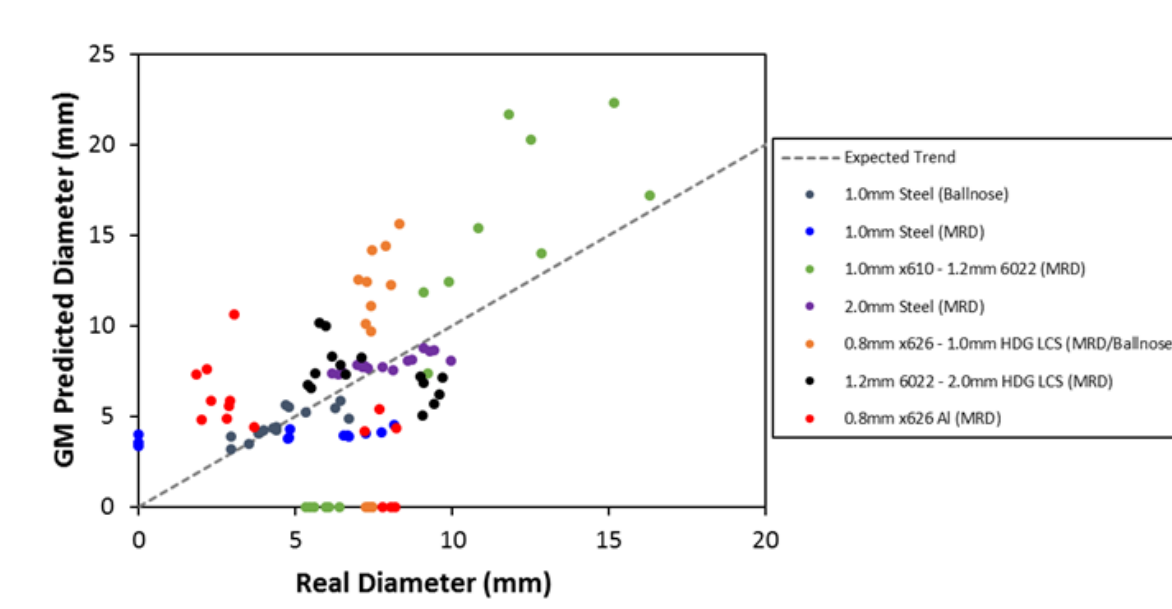


Figure II.3.K.4. GM predicted diameters versus real measured diameters for the entire sample set. The expected trend is represented by the dashed grey line. Source: ORNL and GM.

From Figure II.3.K.4, some zero-value nugget sizes are seen in both the predicted and the real diameters. Zero-value predicted diameters are due to a deficiency in the GM algorithm and is actively being addressed. It is notable that all these zero-value measurements occurred for the stack-ups containing Al, namely: the minimum and low nugget sizes for 1.2 mm 6022 Al-1.0 mm x610 Al and 0.8 mm x626 Al-1.0 mm HDG LCS, and the minimum nugget size for 0.8 mm x626 Al-0.8 mm x626 Al had non-zero nugget sizes incorrectly predicted as zero-value nugget sizes. Generally, the steel-steel stackup measurements exhibited a predicted versus real trend closer to 1:1 than did the Al-Steel or Al-Al stackup measurements.

Post-Weld NDE Results (induction)

The data processing of the post-weld NDE by induction heating is in process. Figure II.3.K.5 is one example of the processed IR images as a function of nominal nugget size that increased from 'min' to 'max' (three images in each nominal nugget size condition). The welds were made from 2T 1.2 mm-6022 Al alloys and 2.0 mm HDG LCS. Thermal signatures related to real nugget size and surface indentation were also extracted as shown in Figure II.3.K.6. Overall, thermal signature 1 (nugget size related) increases with nominal nugget size. Thermal signature two is related to surface indentation, and also increases with nominal nugget size, which is consistent to the relative change between real nugget size and surface indentation. Data is being analyzed with the same manner for welds made with other material combinations and welding conditions. Once the analysis is done, thermal signatures of each individual weld will be compared to the real measurements.

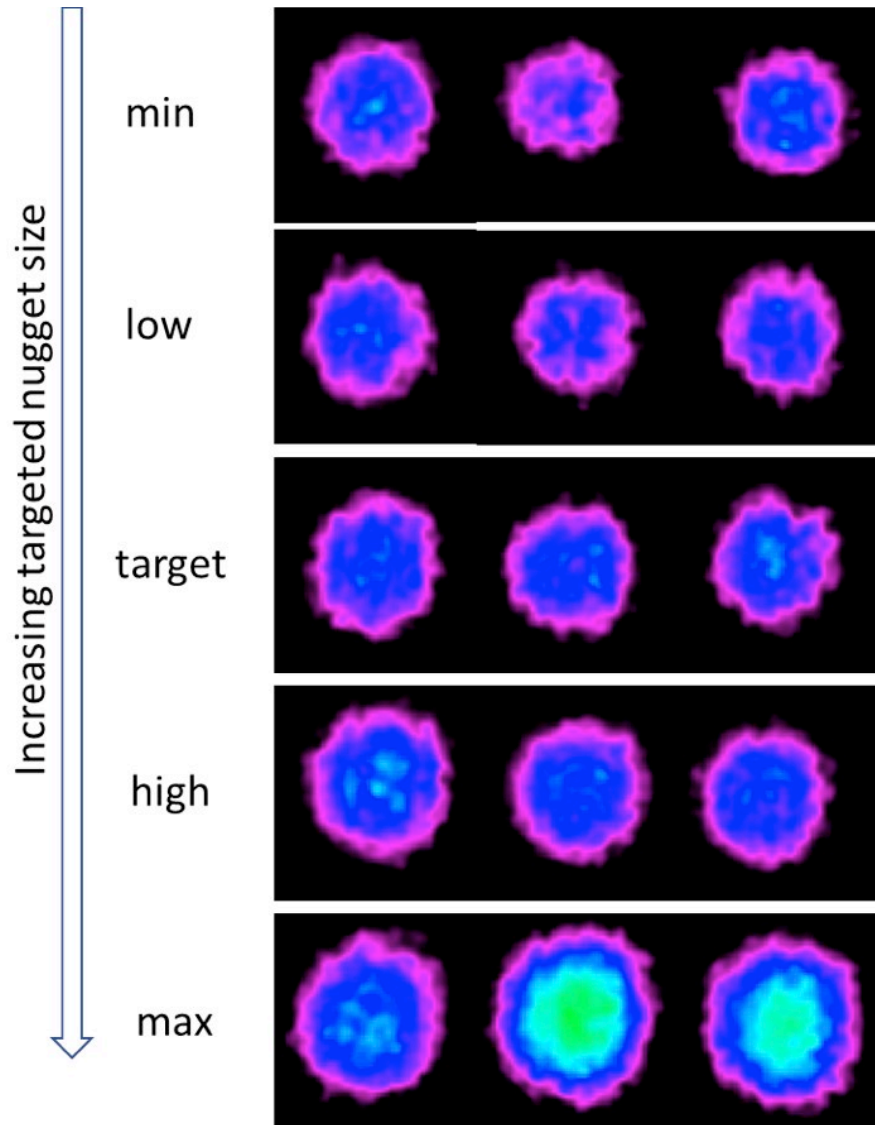


Figure II.3.K.5. Processed post-weld IR images by ORNL's existing induction heating method and algorithms (1.2 mm 6022 - 2.0 mm HDG LCS). Source: ORNL.

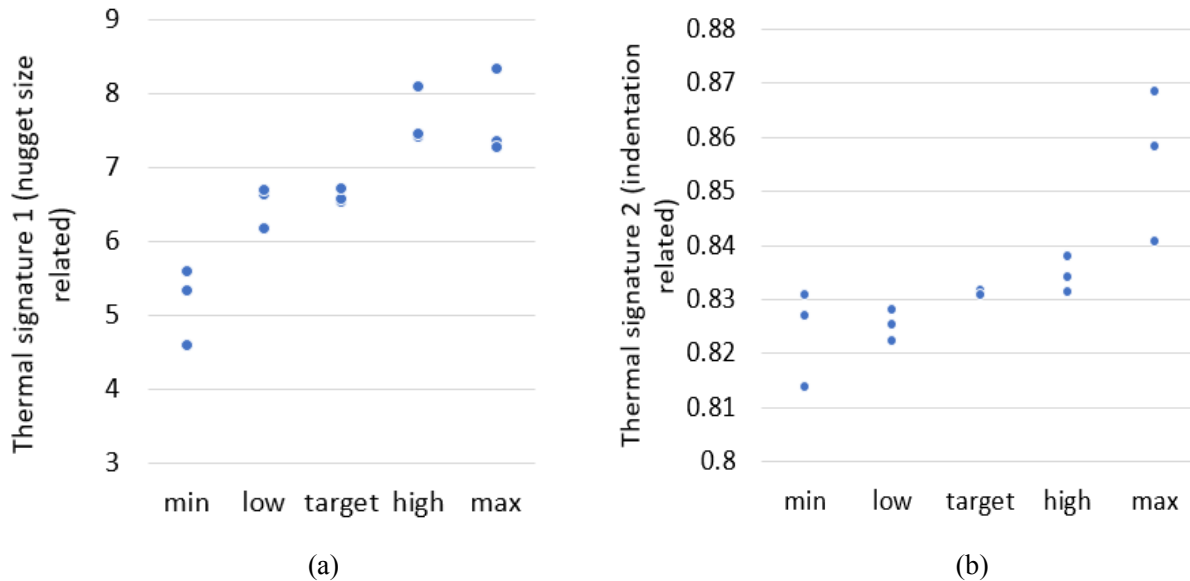


Figure II.3.K.6. Post-weld thermal signatures for (a) nugget size and (b) surface indentation related that were obtained by ORNL's induction heating method and algorithms as a function of nominal nugget size (1.2 mm 6022 - 2.0 mm HDG LCS). Source: ORNL.

Weld Mechanical Properties

All 735 mechanical specimens have been tested; data analysis is currently in process. Mechanical test data includes peak loads at failure, weld size, extension at peak load and at failure, and energy at peak load and at failure.

Conclusions

Data obtained from inline measurements and analyzed using a GM internal nugget-prediction algorithm exhibited a highly scattered proportional relationship. Further work is necessary to improve the algorithm. It was observed that steel-steel stackup nugget predictions exhibited lower error than the Al-steel or Al-Al stackup nugget predictions. This error is caused by the lower emissivity and higher reflectivity of Al compared to steel. An algorithm for the interpretation of post-weld data is currently being developed.

Post-weld NDE thermal signatures obtained by ORNL's induction method and algorithms shows positive correlation with the nominal nugget size. More detailed comparison between the thermal signatures and real measurements of each individual weld will be completed once the data analysis is done for all welds.

Acknowledgements

The principal investigator would like to recognize Jian Chen of ORNL; and Blair Carlson, Megan McGovern, Teresa Rinker, and Amberlee Haselhuhn of GM for their support and assistance in this project.

II.4 Crosscutting

II.4.A Materials Goal Setting Analysis (Argonne National Laboratory)

Michael Wang, Co-Principal Investigator

Argonne National Laboratory
9700 South Cass Ave
Argonne, Illinois, 60439
E-mail: mqwang@anl.gov

Aymeric Rousseau, Co-Principal Investigator

Argonne National Laboratory
9700 South Cass Ave
Argonne, Illinois, 60439
E-mail: arousseau@anl.gov

Jarod Kelly, Co-Principal Investigator

Argonne National Laboratory
9700 South Cass Ave
Argonne, Illinois, 60439
E-mail: jckelly@anl.gov

Ram Vijayagopal, Co-Principal Investigator

Argonne National Laboratory
9700 South Cass Ave
Argonne, Illinois, 60439
E-mail: rvijayagopal@anl.gov

Sarah Kleinbaum, DOE Technology Manager

U.S. Department of Energy
E-mail: sarah.kleinbaum@ee.doe.gov

Start Date: October 1, 2017

End Date: September 30, 2018

Project Funding: \$250,000

DOE share: \$250,000

Non-DOE share: \$0

Project Introduction

Vehicle lightweighting is a critical technology option OEMs and others consider to reduce vehicle energy consumption and to help meet fuel economy regulations. Reductions in vehicle weight can be achieved through the substitution of conventional vehicle materials (such as steel) with lighter materials (such as AHSS, Al, Mg, and CF) for various vehicle components across vehicle and powertrain technologies. Although material substitution for vehicle lightweighting will improve vehicle fuel economy and other performance attributes, the use of lightweight materials usually entails higher costs. Task 1 of this project investigates trends in vehicle component weights over time and vehicle class. It identifies the best-in-class lightweighting options from the available data and compares them against the rest of the vehicle population. It documents these component trends and identifies lightweighting trends in the current market. Task 2 models the cost of vehicle components produced from different materials and compare the costs of lightweight materials versus conventional materials while quantifying the costs for various vehicle lightweighting options. Argonne National Laboratory (Argonne) conducted literature reviews to examine the lightweighting cost per pound saved as reported by previous studies, examined the cost modeling literature and developed a cost model, evaluated cost analyses from the National Highway Traffic Safety Administration (NHTSA), developed a reduced-order cost model from that data, and evaluated cost-reduction strategies.

Objectives

Task 1 will quantify the mass of vehicles and major subsystems and determine the aggregated weight of each material computed at the vehicle level and five sub-levels. It will further identify the lightest vehicle, system, and subsystem, while also quantifying the minimum, average, and maximum weight at every system and subsystem level. It will also present the evolution of weight and material composition of vehicle subsystems over time. Finally, it will examine the impacts of technology on subsystem mass and choice of materials.

Task 2 focuses on modeling the cost associated with vehicle component production, which will allow the evaluation of material options for their cost per pound of weight reduced. This task will first involve a literature review of the cost of lightweighting. Next, it will identify cost modeling approaches and develop a cost model to evaluate the cost of vehicle component production. Then, it will evaluate the cost of different lightweighting solutions to determine their cost per pound saved.

Approach

Access to reliable data is a challenge in analyzing the mass and material composition of vehicle subsystems. In this study, we use data from the A2Mac1: Automotive Benchmarking (A2Mac1) database to overcome this barrier. The A2Mac1 database contains the mass of every part and assembly from a few dozen vehicles. The material classification in this database is not directly usable, but we used automated scripts to reclassify materials to resolve the data. We worked with A2Mac1 to achieve this. The reference material code provided for parts in the raw data uses a mix of naming conventions, including nonstandard names in various languages. We programmatically convert these to standard material codes, and by doing so identify the share of materials in vehicles. Analysis focuses on midsize sedans manufactured since 2010, and includes performance, luxury, and fuel economy vehicles. Material, technology, and component choices vary based on vehicle design objectives. This variation gives a range of vehicle and component weights. The lightest subsystems are identified from this dataset. Such components assembled together form a hypothetical vehicle demonstrating potential weight savings possible with current technology and materials.

Task 2 consisted of two phases. The first was a review of the cost of weight reduction in the literature. This highlights literature results to observe the weight and cost relationship trends related to different vehicle systems. In the second phase, Argonne examined the vehicle cost modeling literature to build its own vehicle part production cost model. In addition, we conducted a meta-analysis of an existing cost modeling tool NHTSA used in evaluating vehicle lightweighting. This meta-analysis served as a check against which to evaluate the cost model developed here, and provided parametric data to inform the model. Further, the numerous parts evaluated in that model allowed the development of a reduced-order model. This reduced-order model allows the estimation of vehicle material component costs in the absence of detailed production data and can quickly estimate the cost of weight reduction.

Results

Task 1 Results

Over the past five years, the U.S. market fuel economy has improved significantly. Vehicle weights have decreased, which may have contributed to this higher fuel economy. A2Mac1 contains a subset of U.S. vehicles; analysis shows that this sample reflects overall U.S. Environmental Protection Agency (EPA) trends seen in vehicle curb weights, as shown in Figure II.4.A.1.

Trends in Vehicle Lightweighting and Vehicle Materials

Examination of the mass of major subsystems provides insight to lightweighting trends. At a high-level, the vehicle is split into two systems: the glider and the powertrain. Most lightweighting efforts focus on the glider. Powertrain weight has not seen a significant change for the past few years, as understood from A2Mac1 data. Figure II.4.A.2 shows the glider and body subsystems. The major glider subsystems are the body and the interior. The major body subsystems are the vehicle frame and closures. Safety systems (i.e., a glider subsystem) are often blamed for the increased weight of modern vehicles, but data show that the combined mass of safety equipment is <25 kg and has seen little growth in recent years. Body design is also influenced

by safety requirements. We see a lightweighting trend in the body subsystem, driven by weight reduction in the frame.

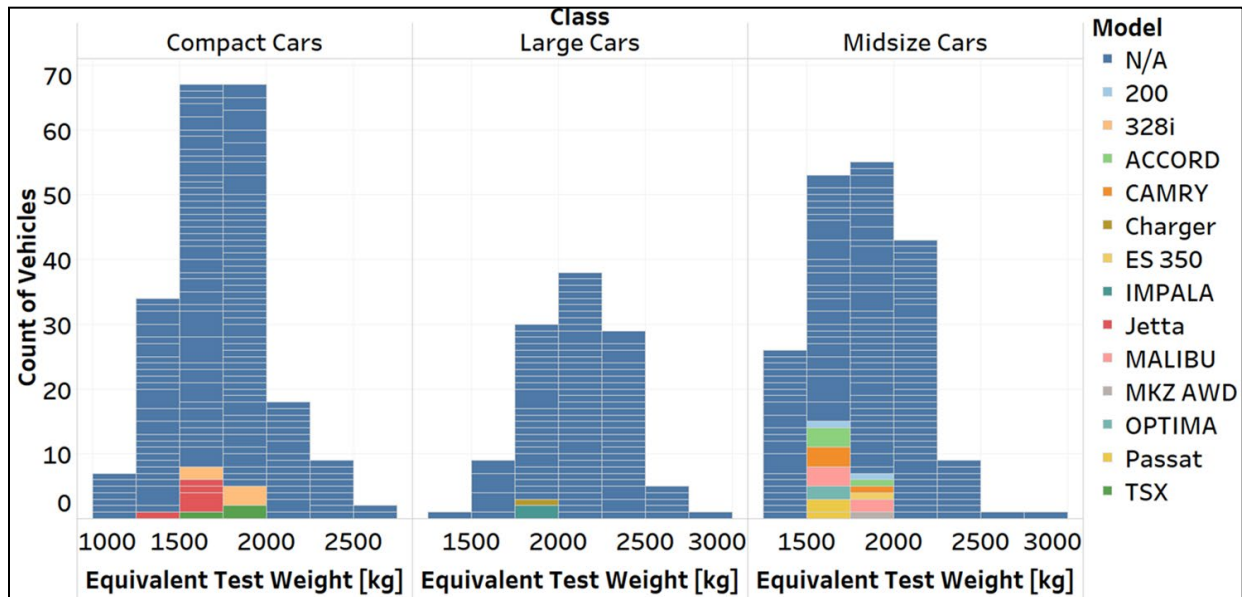


Figure II.4.A.1. EPA (dark blue) and A2Mac1 (colors denote vehicle) reported vehicle weights.

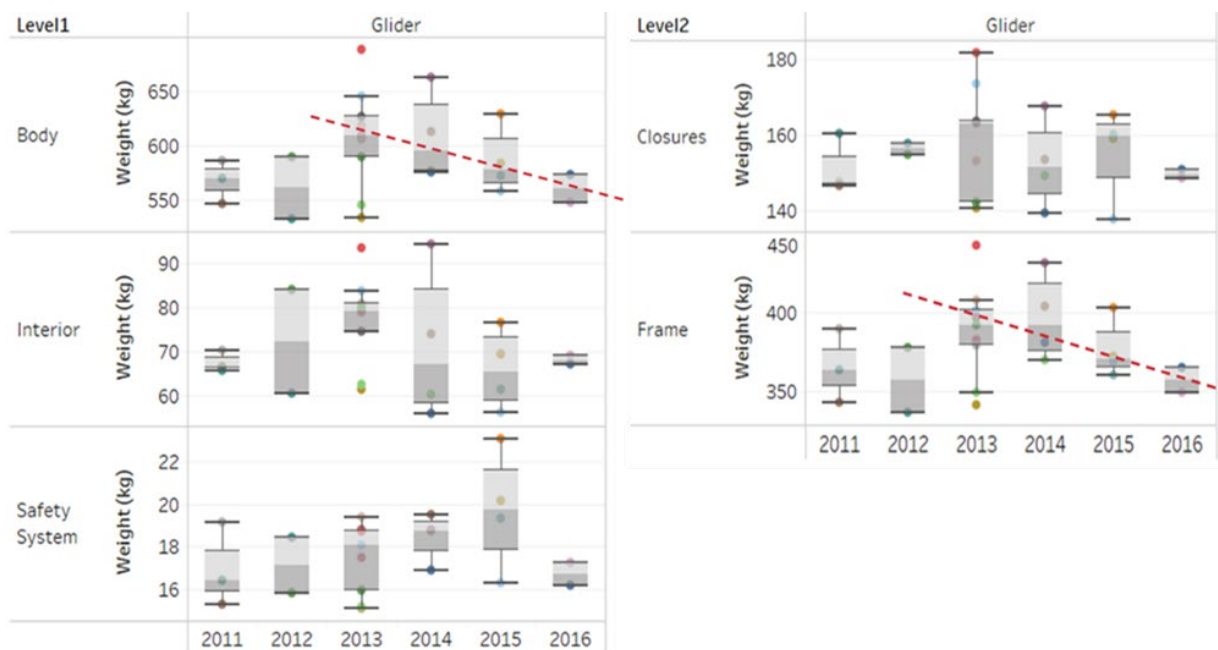


Figure II.4.A.2. Mass of vehicle glider and body subsystems showing trends (2011–2016).

Steel makes up slightly over 50% of the weight of a vehicle. Material classification limits the inferences we can make about the type of steel used in North American vehicles; a follow-up task could improve classification. If we consider European and Asian vehicles, we see increasing use of Al alloys, mostly EN-AW-4xxx.

We identified the lightest glider subsystems in the U.S. midsize sedan market. We find that if a glider is constructed with best-in-class components, it will be 13% lighter than an average glider in the U.S. market, with a mass of 689 kg. It would consist of 62% steel and 35% material classified as “not metal,” with the remainder spread across several different materials.

Trace Weight Savings to Design or Material Choices

In this analysis, we compare the gliders from three vehicles (e.g., Fusion, Sonata, Passat). The Sonata glider is the lightest by ~15 kg. Examining glider subsystems reveals this is mostly due to a difference of 2–3 kg in the mass of the door in each, as shown in Figure II.4.A.3.

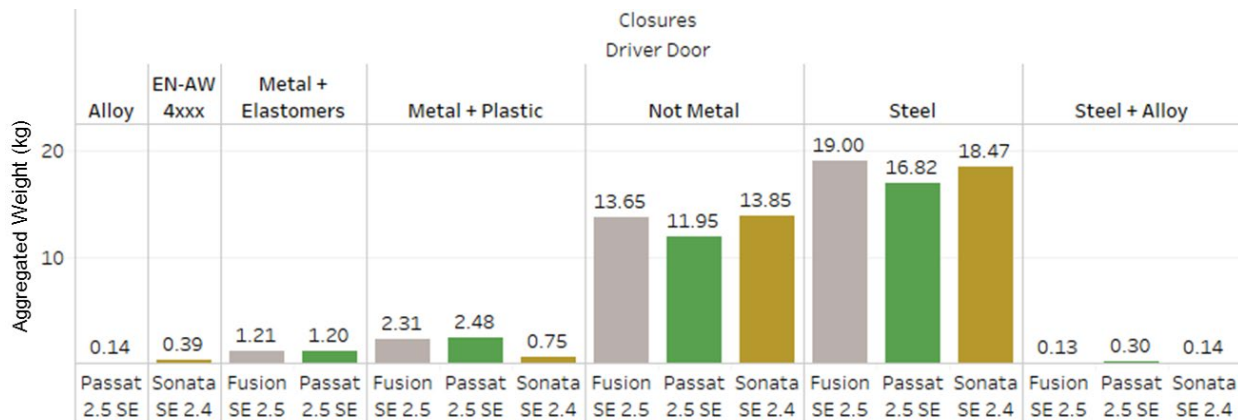


Figure II.4.A.3. Vehicle door mass and composition analysis and comparison for three North American vehicles.

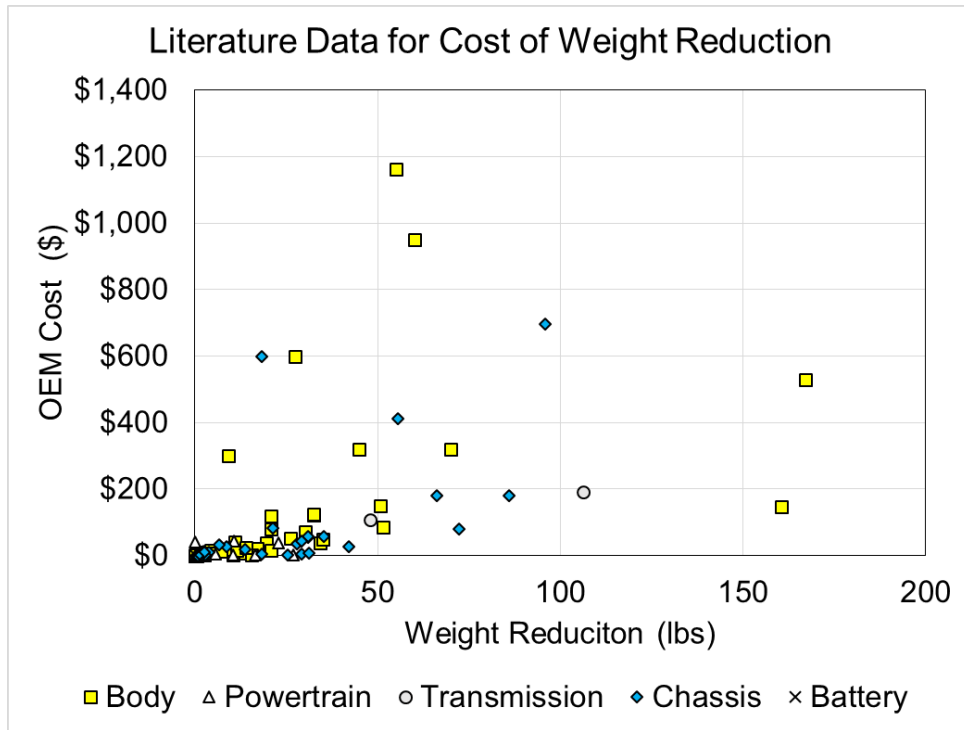
Impact of Technology on Mass and Material Choices

The Ford Fusion has three popular variants that use different engines, each of which is available in the A2Mac1 data: a 2.5-L naturally aspirated engine, a 1.6-L turbocharged engine, and a 2-L Atkinson cycle engine coupled with a hybrid system. We examined these variants to determine the relationship between engine choice and weight savings. We determined that the hybrid system adds motor and battery weight, but saves on crank shaft and engine block weight. We also found that that the engine in a hybrid vehicle uses Al alloys for the engine block, which could be an effort to offset the additional hybrid system weight.

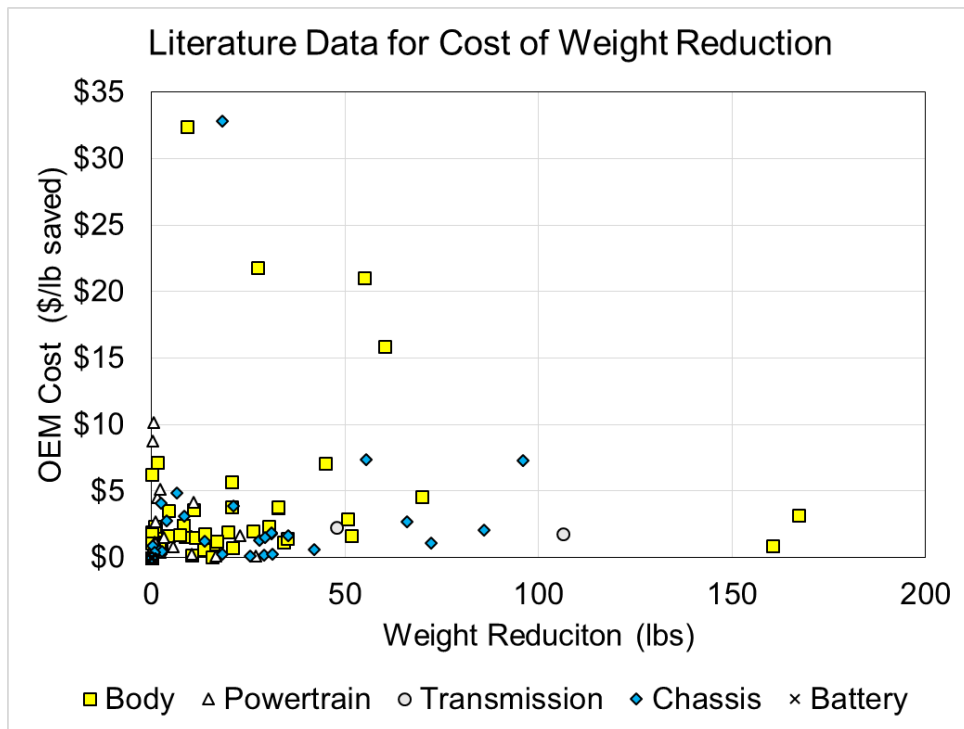
Task 2 Results

Cost per Pound Saved Literature Review

Argonne examined vehicle lightweighting literature to understand the relationship between cost and weight reduction. Costs and weight reductions reported within the literature were collected in a database. Vehicle components were classified into system categories common to Argonne’s Greenhouse Gas Regulated Emissions and Energy in Transportation (GREET®) model (i.e., body, powertrain, transmission, chassis, and battery). Many lightweight options reported are multi-material, so we did not pursue partitioning by material replacement. Figure II.4.A.4.(a) partitioned the data from the literature into the five noted categories, presenting weight reduction versus total OEM cost. Figure II.4.A.4.(b) shows the same data on a cost per pound saved basis. We only present options that increase OEM cost and reduce vehicle weight by no more than 200 lb, because reductions above 200 lb were often aggregations of multiple components. The body and chassis components were the most numerous lightweighting options evaluated within these studies, and greater weight reduction tends to increase cost. That is far from a unique observation, but we also observe numerous instances where a small weight reduction has a large cost. This is easily observed in Figure II.4.A.4.(b) where the y-axis shows the cost per pound reduced. Several weight reduction options that are inexpensive in absolute terms are significantly costlier than other options in a normalized sense.



(a)

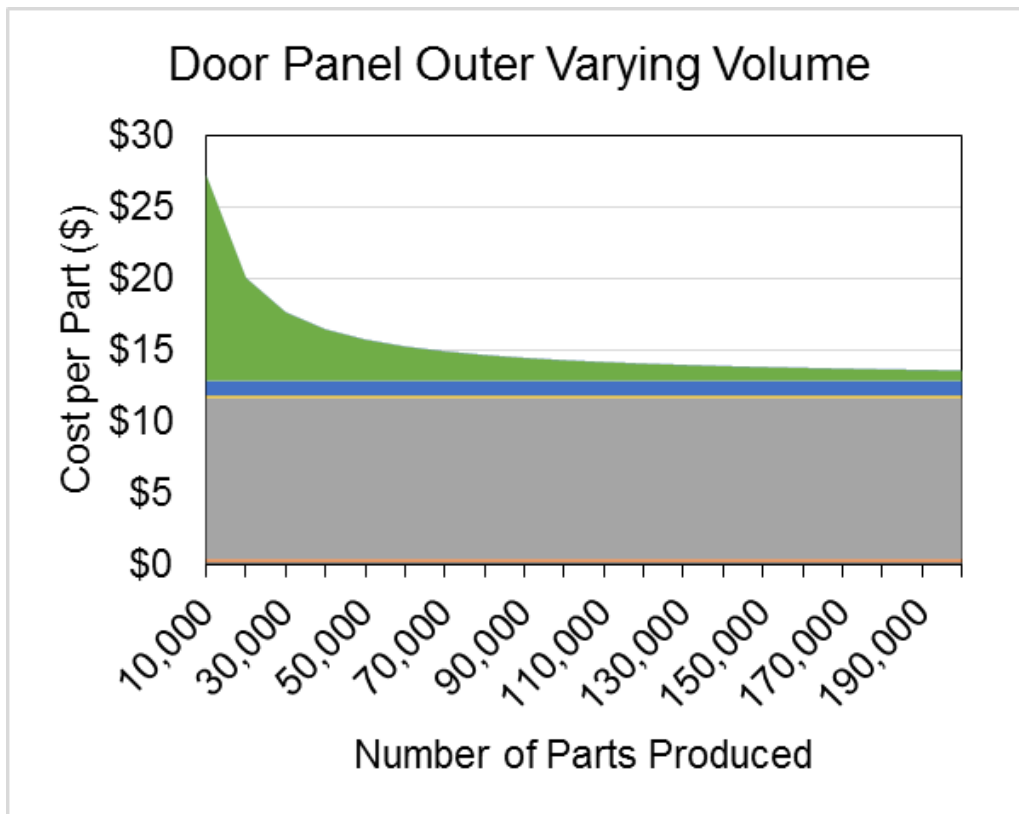


(b)

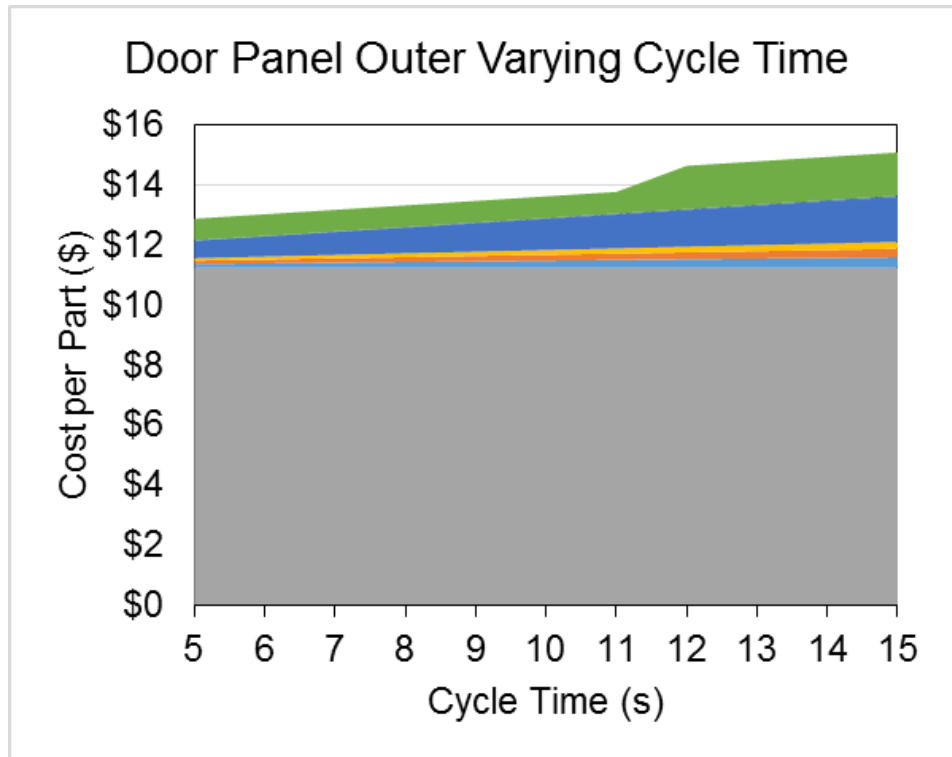
Figure II.4.A.4. (a) OEM cost and (b) OEM cost per pound saved for different weight reduction options cited within the literature. The majority of opportunities investigated were in the body and chassis.

Cost Model Development and Examination

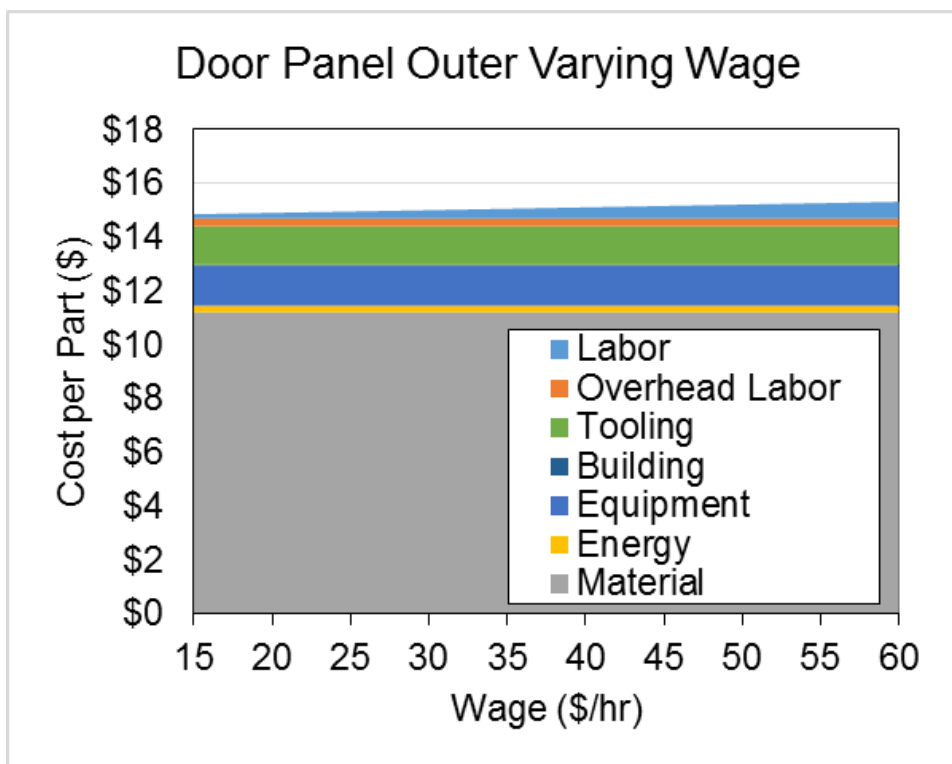
Argonne developed a model based on the technical cost modeling approach described by Kirchain and colleagues at Massachusetts Institute of Technology (MIT) [1,2,3,4]. This approach serves as the basis for other vehicle cost modeling efforts. Each vehicle part is broken into parameters describing its required material mass, and its production operation energy, time, and type on a step-by-step basis. That determines how each production step relates to cost. For instance, an outer body panel will be blanked from a sheet metal coil, then undergo stamping and handling processes. The geometry of the part determines the input material mass. We can determine blanking and stamping energy based on the presses used. The time for each operation contributes to labor, equipment, and building costs. Using this model, we can examine the relationship between parameters such as volume of production, labor rates, interest rates for capital costs, part cycle time, and more. To do this, we need real-world information about each process. We gathered this from NHTSA data on many modeled parts. We used the process data as inputs to our model, and in Figure II.4.A.5 we present three parametric cost relationships (i.e., part volume, direct worker wage, and cycle time) for a steel body panel. Results confirm that part cost is driven by tooling cost when considering volume, direct labor cost when considering wage, and all costs except material when considering cycle time. Increasing production volume from 10,000 to 200,000 units reduced part cost by ~55%, tripling cycle time increased part cost by ~20%, and quadrupling wage increased part cost by ~4%.



(a)



(b)



(c)

Figure II.4.A.5. Parametric analyses of cost per part considering part volume (a), cycle time (b), and direct worker wage (c).

Reduced-Order Cost Model and Cost Comparison of Lightweighting

NHTSA used a cost modeling tool developed by EDAG, Inc. (EDAG), which was based on the same technical cost basis as the model developed here. That model was used to validate the current model. We also used data from that model to develop a reduced-order model based on numerous costed parts in the shared data. The NHTSA/EDAG modeled parts were based on a mass-produced vehicle (200,000 units). We evaluated the data to determine relationships between total cost (material, labor, overhead, energy, equipment, tooling, building, maintenance) and final part mass. The resulting model is linear in material cost (and scrap price), but is invariant for the other costs within the material type. Major changes to wage, energy prices, and tooling may cause changes to total cost. However, this reduced-order model captures the major trends of part cost while not requiring detailed inputs for cycle times, equipment price, or the number of workers. We developed the reduced-order model into an easy-to-use calculator that allows quick comparison of material cost differences for proposed parts. This was used to examine the cost impact of vehicle lightweighting for substitution ratios of conventional steel and lightweight materials. Figure II.4.A.6 shows the relationship for materials available within the modeling study for weight reduction of a 10-kg body part originally made from mild steel with different Al, high-strength steel (HSS), and AHSS variants. At the material limits of practical mass reduction, the cost per pound saved is well under \$2.00 for all materials, but those represent aggressive material substitution that may be more theoretical than practical. Additional materials can be investigated, but the invariant components may need to be adjusted to account for production differences.

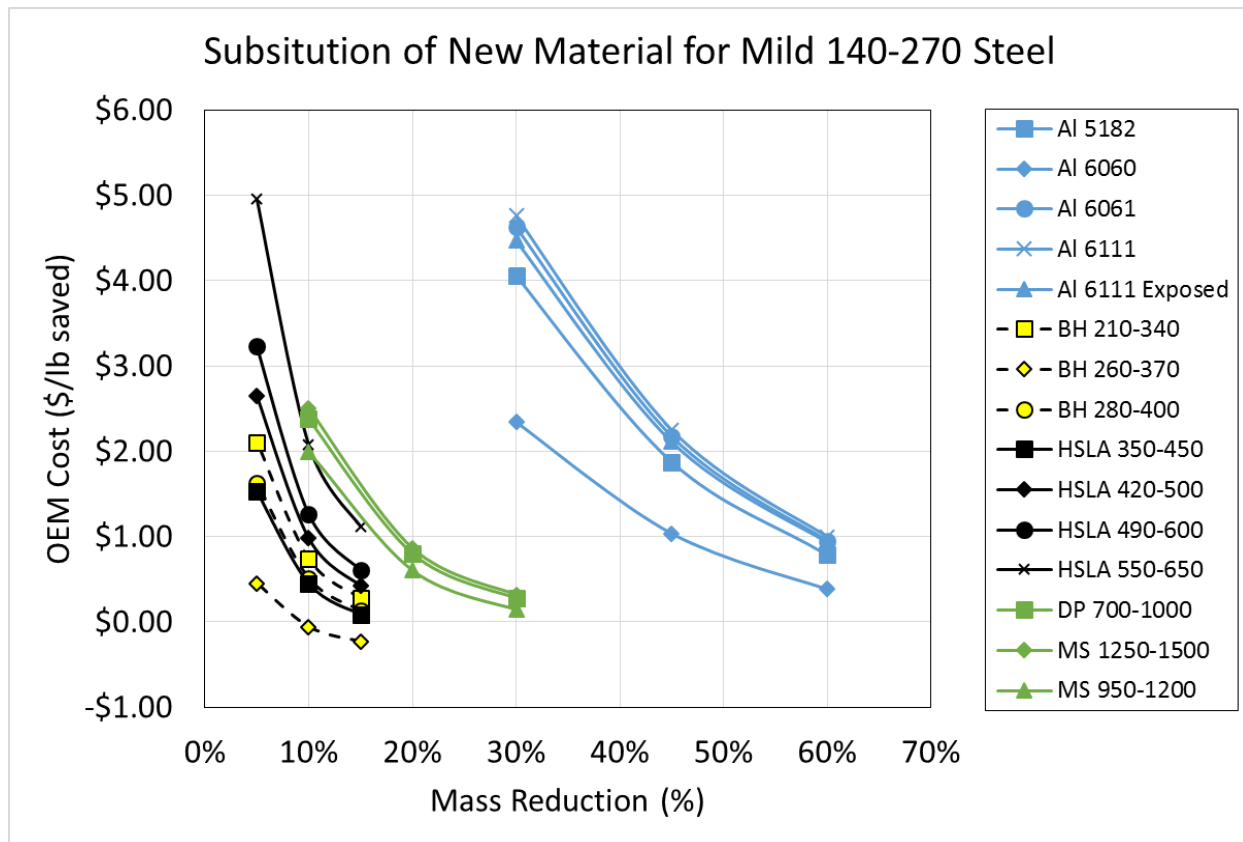


Figure II.4.A.6. OEM cost per pound saved by replacing a 10-kg body part mild 140–270 steel with Al (blue), HSS (black), and AHSS (green) variants using material substitution ratios (complement of mass reduction).

Conclusions

In Task 1, we analyzed midsize sedan data from A2Mac1. Materials are classified into groups, and the aggregate mass of these materials is computed for every vehicle system and subsystem. Best-in-class components are identified at multiple levels (glider > body > closures > doors, etc.). Material composition of each component and temporal evolution is identified. Glider mass can be reduced by ~13% using available technology/materials. Several analysis examples trace the mass differences to material or technology choices. The database with aggregated mass values and material classification is now available in Excel and Tableau to support further analysis. In Task 2, we examined lightweighting literature and collected the information in a dataset. Those data indicate there are opportunities to reduce vehicle weight at a variety of price points. We developed a detailed cost model within Excel and used it to evaluate vehicle components given knowledge of technical production details, and we developed a reduced-order model to provide estimates in the absence of such technical details. The reduced-order model was used with material substitution ratios available in the literature to determine the cost per pound of replacing mild steel with lightweight materials.

References

1. Field, F., R. Kirchain, and R. Roth, 2007, "Process cost modeling: Strategic engineering and economic evaluation of materials technologies," *JOM*, Vol. 59, No. 10, Art. 21.
2. Johnson, M. D., 2004, "A Methodology for Determining Engineering Costs and Their Effects on the Development of Product Families," Ph.D. Thesis, Massachusetts Institute of Technology.
3. Nadeau, M.-C., 2009, "Evaluating Manufacturing Flexibility Driven by Learning," Ph.D. Thesis, Massachusetts Institute of Technology.
4. Nadeau, M.-C., A. Kar, R. Roth, and R. Kirchain, 2010, "A dynamic process-based cost modeling approach to understand learning effects in manufacturing," *Int. J. Prod. Econ.*, Vol. 128, No. 1, pp. 223–234.

II.4.B Ultralight Door Design, Manufacturing and Demonstration Project (Magna)

Tim Skszek, Principal Investigator

Magna International Inc.
750 Tower Drive
Troy, MI 48098
E-mail: tim.skszek@magna.com

Sarah Kleinbaum, DOE Technology Manager

U.S. Department of Energy
E-mail: sarah.kleinbaum@ee.doe.gov

Start Date: December 1, 2015	End Date: December 31, 2018	
Project Funding: \$8,444,583	DOE share: \$4,222,291	Non-DOE share: \$4,222,292

Project Introduction

Mass reduction can be a cost-effective means to reduce fuel consumption and achieve corporate average fuel economy and environmental legislation for vehicles powered by combustion engines. Integration of the structural, mechanical, and electrical subsystems enables a reduction in part count, material usage, and assembly costs, enabling mass reduction beyond that realized by material substitution. The use of commercially available materials, manufacturing processes, and an assembly sequence compatible with the existing manufacturing infrastructure can significantly influence the cost to manufacture a lightweight product.

The engineered mass saving techniques used to lighten the driver's-side door are also applicable to the passenger's side front door and rear doors, thus enabling engine downsizing and a further reduction in fuel usage. A passenger vehicle powered by a turbocharged gasoline combustion engine can realize a 2.38x reduction in fuel usage when the combustion engine is downsized appropriately, while maintaining the acceleration and performance of the baseline vehicle [1–2].

Magna International Inc. (Magna), through a cooperative agreement with DOE and partners Grupo Antolin North America (Grupo Antolin) and Fiat Chrysler Automobiles US LLC (FCA), developed an AI-intensive lightweight door architecture that enables cost-effective lightweighting and engine downsizing resulting in a reduction in fuel consumption and CO₂ emissions.

Objectives

The objective of this project is to demonstrate the feasibility of manufacturing a driver's-side door to meet the DOE program goals of 25% glider weight reduction at less than \$5 per pound saved, while maintaining the functionality, structural performance, and safety characteristics of the baseline vehicle and driver's-side door.

Approach

The project team used the following approach:

- Selection of Door Architecture – The project team selected the “Frame Behind Glass” door architecture and a 2016 production vehicle as the baseline reference. The “Frame Behind Glass” door architecture is applicable to 70% of the lightweight vehicle market.
- Mass Targets and Performance Requirements – The performance characteristics of the baseline door were established, and a target matrix was developed to facilitate the development of a functionally equivalent door, which is lighter than the driver's-side door of the baseline vehicle.
- Concept Design and Selection – Four door design concepts were developed based on the mass and performance targets. The design concepts included CF, AI, and Mg materials and compression-molded,

stamped and cast manufacturing processes. All design concepts appear to be capable of meeting the mass and performance targets; however, cost considerations directed the design selection towards the Al-intensive stamped design.

- **Prototype Design** – A prototype design, shown in Figure II.4.B.1, was developed based on the Al-intensive door structure concept, which evolved to include stamped Al panels and door beam, die-cast A-pillar support, and extruded upper support. The holistic design approach, shown in Figure II.4.B.2, incorporated an electric latch and a bolt-on belt line inner component, which enabled integration of the glass run channels with the door module, outboard lift of the side glass, and reduced complexity of the interior trim components. Application of an advanced projection weld joining technology minimized weld flange width, providing additional mass reduction. The design incorporated the use of a chemically toughened laminate side glass, providing significant mass reduction without degradation in performance. CAE methods were used to establish minimum gauge and section profiles to realize the mass, stiffness, and strength, relative to the performance target matrix.

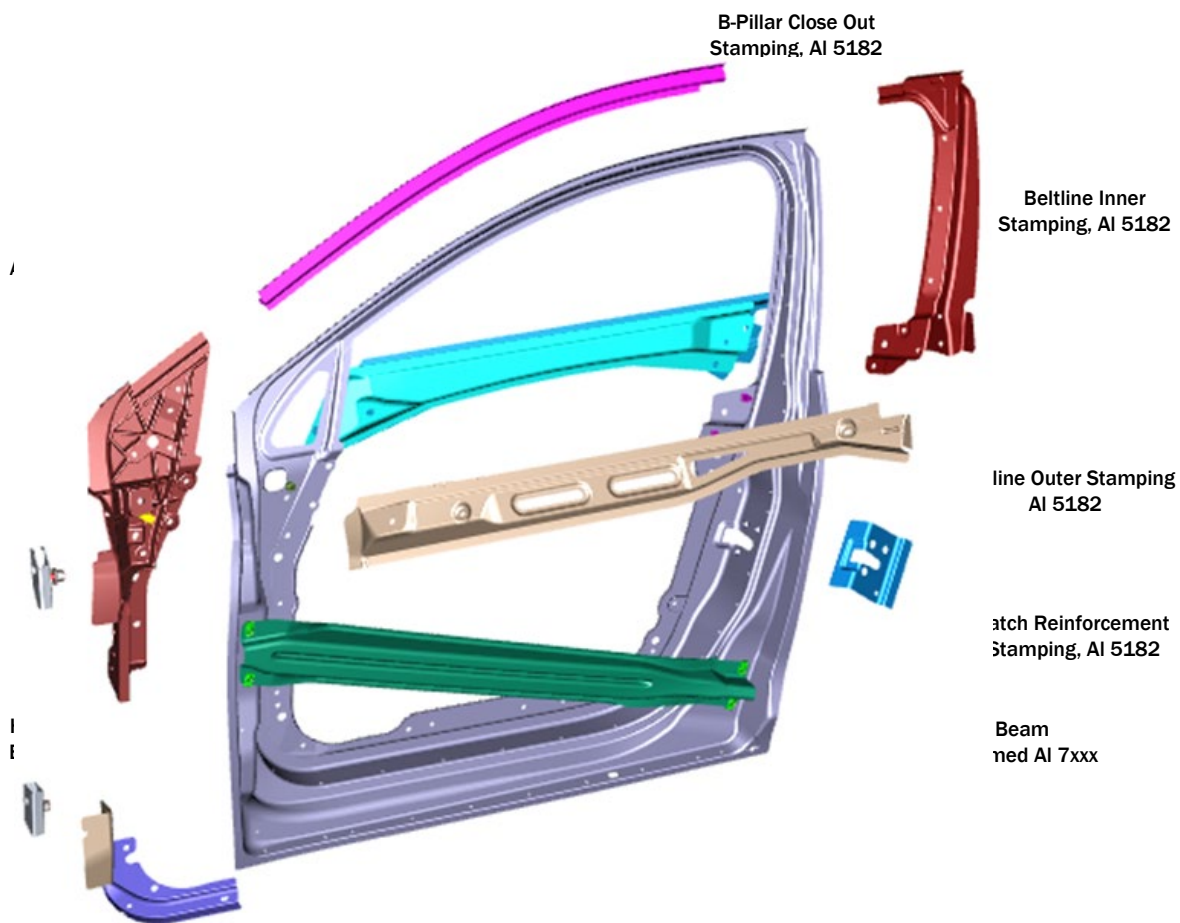


Figure II.4.B.1. Door-in-white subsystem to achieve an 8.11 kg mass reduction. Source: Magna International Inc.

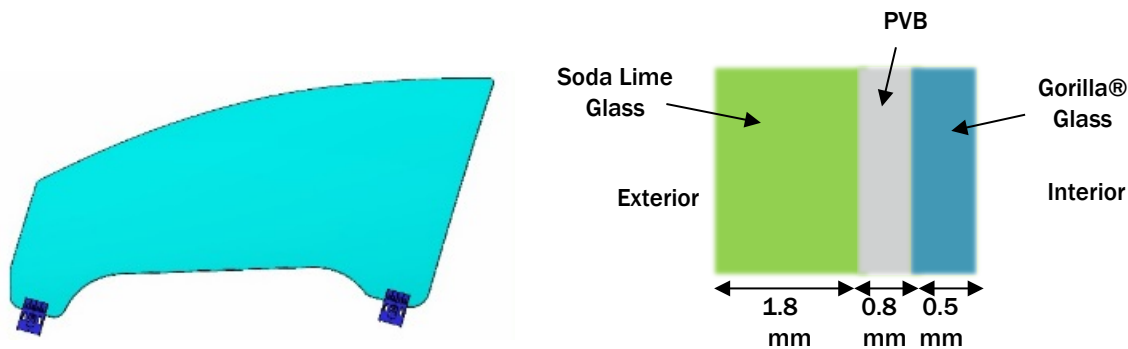


Figure II.4.B.2. Side glass construction to achieve a 1.9 kg mass reduction. Source: Magna International Inc.

- **Prototype Build** – The manufacture of tooling, molds, check fixtures, and assembly fixtures to manufacture door components and manufacture of prototype mechanical, electrical, and glass subsystems.
- **Door Assembly and Vehicle Integration** – The manufacture of lightweight door assemblies, including application of sealant, primer, and paint. The lightweight door assemblies were integrated with baseline production vehicles, required for validation testing.
- **Testing** – The lightweight door assemblies were tested to validate equivalent safety, strength, durability noise, vibration and harshness performance relative to the baseline vehicle.

Results

Corrosion Test

The baseline vehicle, with a lightweight driver’s-side door, was subjected to full vehicle accelerated corrosion testing at the Chrysler Proving Grounds in Chelsea, Michigan, simulating 10 years of service in North America “salt belt” conditions. Each test cycle is comprised of temperature, humidity, salt-spray, and durability track drive cycles. The baseline vehicle with a lightweight door was driven three times per week for four hours per day on durability roads to accumulate various inputs, simulating real-world driving conditions. The salt-spray test takes place in an environmental chamber, exposing the full vehicle to conditions to temperature, humidity, and salt-spray per the SAE J2334 test protocol. After completion of 168 corrosion test cycles, the lightweight door was removed from the baseline vehicle, disassembled and visually inspected. No signs of perforations or loss of functionality were observed. The FCA evaluation team concluded that the lightweight door fully meets functional and appearance requirements for 10 years in-service exposure.

Safety Tests

The safety performance of the lightweight door was evaluated by FCA at the Chrysler Proving Grounds in Chelsea, Michigan, and at the Chrysler Technical Center in Auburn Hills, Michigan, in accordance with the NHTSA New Car Assessment Program (NCAP) side-impact protocol:

- Drop Tower Test (interior trim panel only)
- Moving Deformable Barrier (MDB) Side-Impact Test (38.5 mph)
- Oblique Pole Side-Impact Test (20 mph).

The results of the Drop Tower Test confirmed that the interior trim did not fracture in the pelvic air bag area.

The results for the Side-Impact Test and the Oblique Pole Side-Impact Test for the lightweight door are presented in Table II.4.B.1 along with the NCAP frontal and side ratings. The 5-star NCAP rating demonstrated equivalent performance to the baseline vehicle for the driver’s-side door.

Table II.4.B.1. NCAP Impact Testing Results.

MDB Side-Impact Test (38.5 mph)		VC23650 Values		VC23650 Values	
		50 th Front (ES-2re)		5 th Rear (SID-IIs)	
Injury Assessment Criteria		IAV	Injury Risk	IAV	Injury Risk
HIC (36)		129.3	0.0002	269.9	0.061
Upper rib deflection, mm		20.8	0.0299	Not applicable	
Middle rib deflection, mm		21.6	0.0322		
Lower rib deflection, mm		26.2	0.0483		
Abdominal force, N		921.2	0.0167		
Public force/acetabular and iliac force, N		1051.5	0.0016	2873.4	0.0265
RSR and joint probability of injury		0.44	0.066	0.021	0.032
Star Rating		***** (5.33)		***** (5.68)	
Oblique Pole Impact (20 mph)		VC21355 Values		VC21355 Values	
		50 th Front (SID-IIs)		5 th Front (SID-IIs)	
Injury Assessment Criteria	Unit	IAV	Injury Risk	IAV	Injury Risk
HIC (36)	-	232.1	0.0034	Not applicable	
Combined acetabular and iliac force	N	3342.1	0.0405		
RSR and joint probability of injury		0.029	0.044		
Star Rating		***** (5.56)		Not applicable	
Side Rating Mode		Occupant Rating		Average of Side Mode Ratings	
Front Pole		5.56		***** (5.53)	
Front MBD		5.33			
Rear MBD		5.68			

VC23650: Vehicle Code (specific to vehicle VIN used during test)

VC21355: Vehicle Code (specific to vehicle VIN used during test)

MDB: Moving Deformable Barrier

ES-2re: 50th Male Side-Impact Dummy

SID-IIs: 5th Female Side-Impact Dummy

IAV: Injury Assessment Value

HIC (36): Head Injury Criteria (limited to 36 milliseconds)

RRS: Relative Risk Score

Noise Vibration and Harshness (NVH) Testing

The NVH performance of the lightweight door was evaluated by FCA US LLC at the Chrysler Technical Center in Auburn Hills, MI. The subjective impression of the door slam noise indicated the prototype driver's-side door was better by about a 1.5 subjective rating (1 – 10 scaling) than the passenger's-side production door. The door slam objective noise testing indicated that the driver's-side door loudness level was reduced (versus the front passenger's-side door) by about 24% on the exterior of the vehicle and by 22% in the interior of the vehicle.

A full vehicle aero-acoustic **Wind Tunnel Test** was conducted with **87 mph wind force and zero degrees relative to yaw axis**. The noise level was reduced at the driver's left ear level over the frequency range of 600 Hz to 6 kHz when the baseline 5-mm laminated soda lime glass was replaced with 3.1 mm laminated glass

with 0.5 mm chemically toughened glass inner layer. No significant difference was observed in the sound quality articulation index relative to the baseline window. Table I.1.1.2 provides the results for the sound quality performance for the lightweight glass window design and for the baseline window glass.

Table II.4.B.2. NVH Test Results.

Sound Quality Performance at Driver’s Left Ear Level for 87 mph Wind				
Window Description	Total (Mn)	Loudness (sones)	Articulation Index (%)	Sharpness (acum)
Chemically Toughened Glass	3.1	1.8	0.76	1.21
Soda Lime Glass (baseline)	5	2.1	0.76	1.14

Door Structural Integrity and Durability Tests

The performance of the lightweight door was evaluated by the FCA contractor, MGA Research Corporation in Troy, MI, in accordance with Federal Motor Vehicle Safety Standards (FMVSS) protocol.

Two FMVSS Static 214 tests were conducted. The initial test achieved 98% of the FMVSS minimum requirement; however, the door underperformed relative to the baseline door and FCA specifications. It was determined that the projection weld parameters and placement of structural adhesive were not optimized. The nonconforming issues were addressed, and the test was repeated. The test result, reported by FCA associated with the second FMVSS Static 214 side-impact test, indicates equivalent or improved performance relative to the driver’s-side door of the baseline vehicle.

The results associated with the structural performance and durability tests reported by FCA for the Oil Can, Sag/Set, Anti-theft and Water Test indicate equivalent or improved performance relative to the driver’s-side door of the baseline vehicle.

Evaluation of the lightweight door after the Hardware Slam Test revealed a small stress crack in the inner door panel on a contour near the latch mounting surface as shown in Figure II.4.B.3. Subsequent failure analysis revealed the primary cause to be the loss of torque associated with the hinge bolts, which was attributed to the paint on the hinge mounting surface. Paint was removed from the hinge mounting surface, reflecting the production “bill of process” sequence, and the Hardware Slam Test was repeated. The results associated with the second Hardware Slam Test revealed no loss of hinge bolt torque and validated equivalent performance relative to the driver’s-side door of the baseline vehicle.

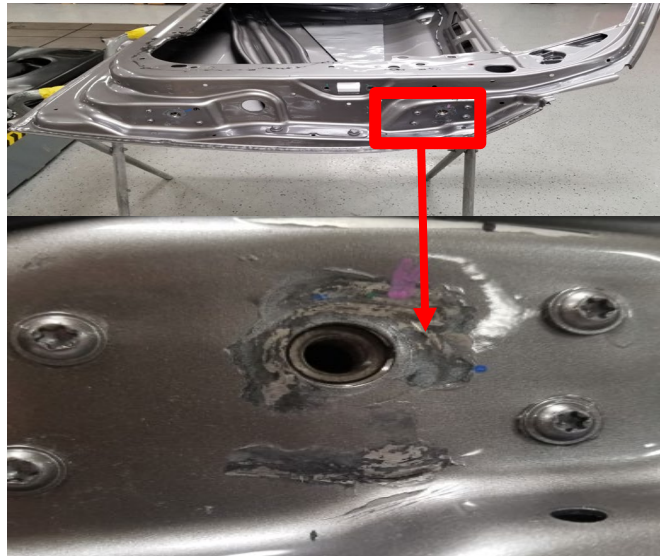


Figure II.4.B.3. Stress crack near the hinge mounting surface induced by the loss of bolt torque.
Source: Magna International, Inc.

Conclusions

The ultralight door design demonstrated the feasibility of manufacturing a driver's-side door that is 40% lighter than the baseline equivalent door which exceeds the DOE program goal of 25% weight reduction while maintaining the functionality, structural performance and safety characteristics. The ultralight door design will provide an incremental cost of \$2.81 per pound saved which is significantly less than the DOE program goal of \$5 per pound saved.

Key Publications

1. Bushi, L., T. Skszek, and T. Reaburn, 2018, "New ultralight automotive door life cycle assessment," *Int. J. Life Cycle Assess.*, Open Access. <https://doi.org/10.1007/s11367-018-1515-z>.
2. Bushi, L., T. Skszek, and T. Reaburn, 2018, "Magna's New Ultralight Door - A Comparative LCA Study of the Lightweight Design as per ISO 14040/44 LCA Standards and CSA Group LCA Guidance Document for Auto Parts," SAE Technical Paper 2018-01-0661. doi:10.4271/2018-01-0661.
3. Reaburn, T., and T. Skszek, 2018, "Ultralight Weight Automotive Door: Design and Validation," SAE Technical Paper 2018-01-0111. doi:10.4271/2018-01-0111.

References

1. CSA Group, 2014, "Life cycle assessment of auto parts — Guidelines for conducting LCA of auto parts incorporating weight changes due to material composition, manufacturing technology, or part geometry," CSA-SPE-14040-14, May 2014.
2. Bushi, L., T. Skszek, and T. Reaburn, 2018, "New ultralight automotive door life cycle assessment," *Int. J. Life Cycle Assess.*, Open Access. <https://doi.org/10.1007/s11367-018-1515-z>.

II.4.C Ultralight Hybrid Composite Door Design and Rapid Manufacture (TPI Composites, Inc.)

Nathan Gravelle, Principal Investigator

TPI Composites Inc.
373 Market St.
Warren, RI 02885
E-mail: ngravelle@tpicomposites.com

H. Felix Wu, Ph. D, DOE Technology Manager

U.S. Department of Energy
E-mail: felix.wu@ee.doe.gov

Start Date: December 1, 2015

End Date: December 31, 2018

Project Funding: \$8,444,583

DOE share: \$4,222,291

Non-DOE share: \$4,222,292

Project Introduction

New corporate average fuel economy regulations require improved fuel efficiency of the future vehicle fleet. Weight reduction is key to achieving these targets. Replacing metallic body and chassis components with CFRCs offers the most weight reduction potential at up to 70%. The introduction of the BMW i3 and i8 in 2014 required mass production processes to meet 20,000+ units per year. Preforming with HP-RTM) has been implemented and meets rate, cost, and performance requirements. Our team members, Krauss Maffei, Hexion, and Saertex[®] were extensively involved in technology development (i.e., manufacturing, materials, and preforming) with BMW and brought this experience to our team, led by TPI, the vehicle OEM, and the University of Delaware Center for Composite Materials (UD-CCM). We will advance these technologies to develop an ultralight driver's side door for the vehicle with production rates of 80,000 units annually per plant in Detroit, MI.

TPI has over 40 years of experience in the design, testing, prototyping, and production of lightweight composite structures and is leading the team of industry and academic partners with knowledge in all aspects of vehicle design and composite materials. The OEM will provide system requirements, integrate the ultralight door into the vehicle, and validate the design during vehicle testing. Krauss Maffei, Hexion, Saertex[®], and Creative Foam will demonstrate their next-generation material and process solutions, while UD-CCM is world-renowned for their composite expertise in all aspects of composites R&D. The team will implement the new composite door design and evaluate integration and manufacturing challenges to meet automotive rate and cost targets.

Objectives

The objectives for this project are to address the following targets and technology gaps:

Target: Reduce part count and full-system weight by a minimum of 42.5%.

Gap: Current materials and methods utilize steel as the main structural component, adding mass to the overall structure, thereby reducing the vehicle fuel efficiency.

Target: Cost increase will not exceed \$5 per pound of weight saved.

Gap: One of the major lightweighting materials at our disposal—CF—is upwards of \$10-15/lb. This material must be used judiciously to meet cost targets.

Target: Materials and processes will be demonstrated to meet the production rate and performance requirements (an approximate four- to five-minute cycle time is required to meet annual production rate).

Gap: Standard composite manufacturing processes can process these parts at a cycle time of about one hour per part. New injection technologies and resin formulations have opened the possibility of faster cycle times.

Approach

Development of a vehicle BIW is a very complex and time-consuming process because various, often-conflicting, functional requirements must be considered. Introducing new designs to reduce vehicle weight requires a systems approach where new designs can be quickly iterated and refined to evaluate their performance. This is particularly true when metals are replaced with composite materials because composite materials have significant potential to reduce weight when designs are fully optimized for parts consolidation and engineered properties using a variety of available material, fiber layups, and processing choices.

A typical automotive door is made from a combination of materials, including steel, plastic, and glazing. The structural materials are heavy, while the non-structural components do not contribute significantly to structural performance. Elements are joined together, increasing manufacturing and assembly cost and weight. We propose to replace all structural parts of the front-side driver's door with continuous reinforced composites (with a weight savings of up to 60%), reduce part count and system weight through part consolidation, and evaluate alternative glazing materials. This approach has the potential to meet and exceed the goals of 42.5% system weight reduction as compared to the steel door baseline and to meet cost targets of \$5 per pound weight saved. The team will take a systems approach to meet the targets, as seen in the flow diagram in Figure II.4.C.1.

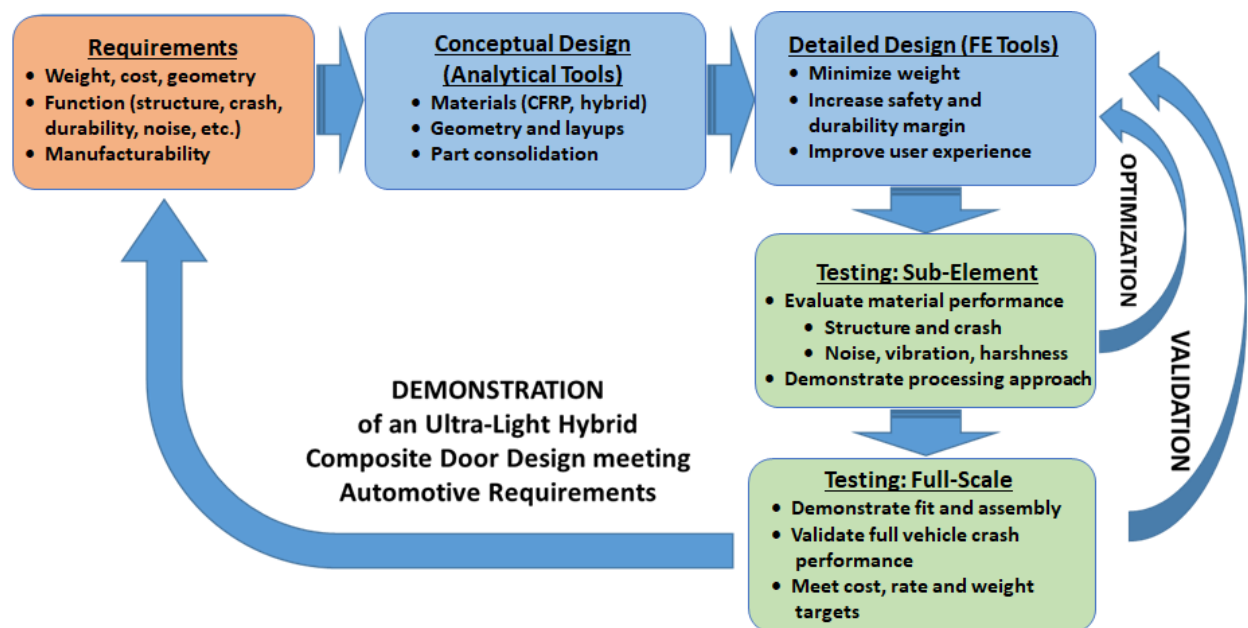


Figure II.4.C.1. Systems approach for reducing weight in complex automotive structures including the use of FE tools for detailed design. Source: University of Delaware.

This approach relies on the use of computational engineering analysis and simulation tools combined with sub-element testing to rapidly develop and evaluate design changes while full-scale testing is used to proof out the final design. The program will define the design requirements (such as weight and cost targets), functional and topology constraints, and consider the ability to manufacture the door at the required rate and performance. Cost; structural; crash; noise, vibration, and harshness; and manufacturing simulations exist and will be utilized. These individual simulation tools are state-of-the-art, commercially available, and have been validated on numerous occasions. Conceptual designs will be evaluated at the sub-element level to evaluate material performance (i.e., structure; crash; and noise, vibration, and harshness) and to demonstrate that the processing approach meets rate and quality targets. Full-scale test articles will be manufactured to validate form, fit, function, and cost of all integrated structural and non-structural components. A small number of design iterations may be required to optimize the various configurations. The approach will allow: (1) a shortened

design cycle, resulting in reduced development time and costs; (2) elimination of trial and error process and part trials reducing tooling and manufacturing costs; and (3) an optimum door configuration at minimum weight leading to a more cost-competitive product. The overall approach will be demonstrated on a composite door solution for the vehicle, but it is also applicable to a wide variety of automotive components. The comprehensive systems approach for designing, manufacturing, and validating a complex ultra-lightweight composite automotive component using a validated, multidisciplinary design tool with a small number of manufactured components for validation will reduce risk to convert metal structures to composites.

Predictive engineering tools guide material and design down-selection and are critical for eliminating trial and error and reducing cost and time. Figure II.4.C.2 shows the design environment the team will employ to evaluate the composite door structure.

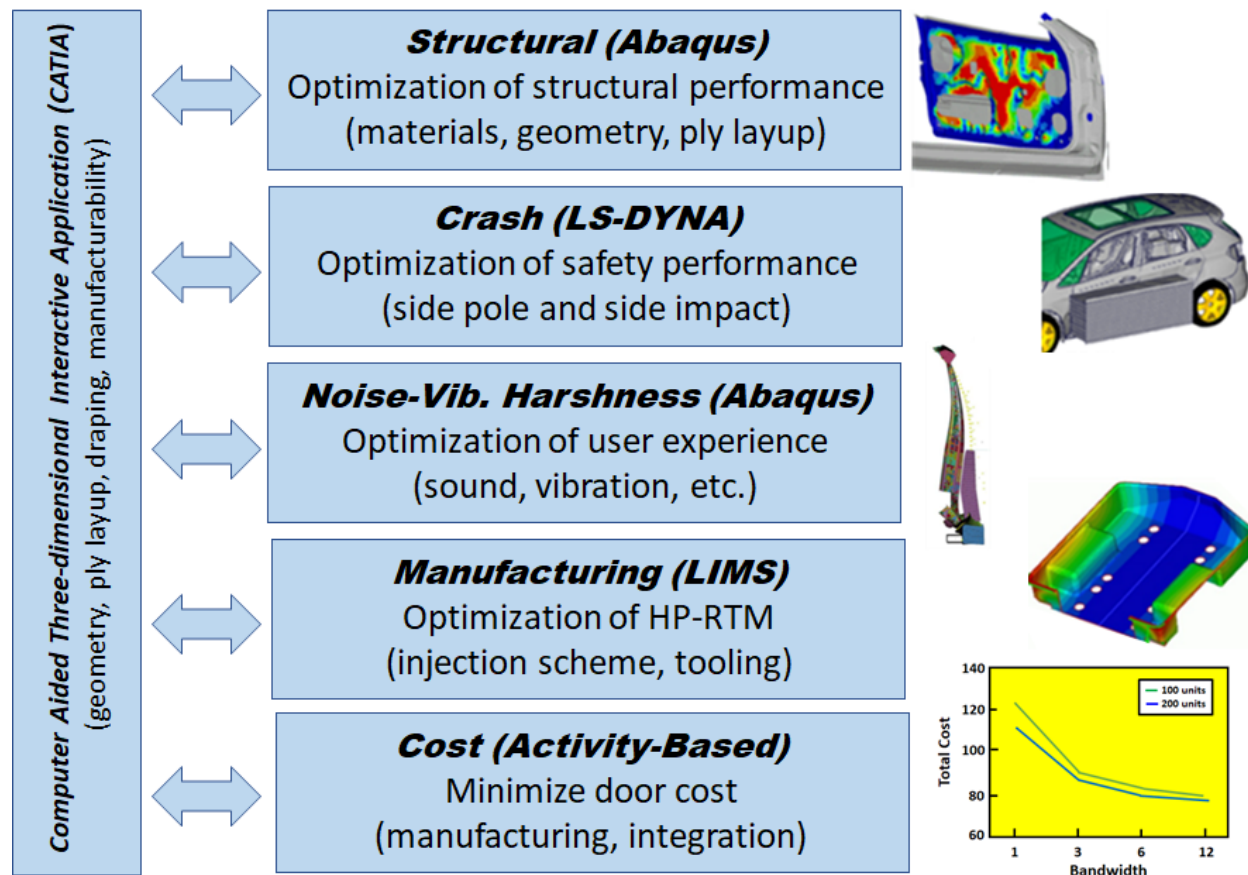


Figure II.4.C.2. Integrated predictive engineering environment. Source: University of Delaware.

Dassault System’s computer-aided three-dimensional interactive application (CATIA) product design solution is our product development platform that easily communicates with other simulation tools. This enables multiple disciplines to share geometry, ply lay-up, and manufacturing-induced fiber orientations. Thus, designs are developed in one environment and then evaluated in the specialist applications across all phases of the product development process. For example, an important aspect of composite manufacturing is the effect of draping the fiber layer onto the mold surface, resulting in changes of the local fiber orientation. This can affect the infusion behavior during resin injection and the structural and crash performance of the final part. Our approach captures manufacturing-induced variations in the design and feeds these properties into all sub-models. Another example is potential sandwich constructions where the design not only improves structural stiffness, but also noise attenuation (improving ride experience) with novel foam solutions. Integration of other

non-structural functional door items (e.g., speakers, glazing, and electronics) are captured in the design and are fed into the appropriate models and concepts.

The existing vehicle steel door is used as a baseline and the ability to reduce part count with a composite structure will be investigated. Part consolidation reduces weight and cost because a smaller number of parts must be manufactured. Assembly time and associated labor costs can be significantly reduced as well. The HP-RTM process allows complex geometry part fabrication, which enables integration of features into one component. Figure II.4.C.3 illustrates the potential part count reduction of a steel door with an equivalent composite structure. Part count reduction alone will not be able to meet our weight reduction goals of 42.5%, but in combination with hybrid and/or CFRCs material replacement and lower weight window solutions, it will reduce the weight of the door structure to the required levels.

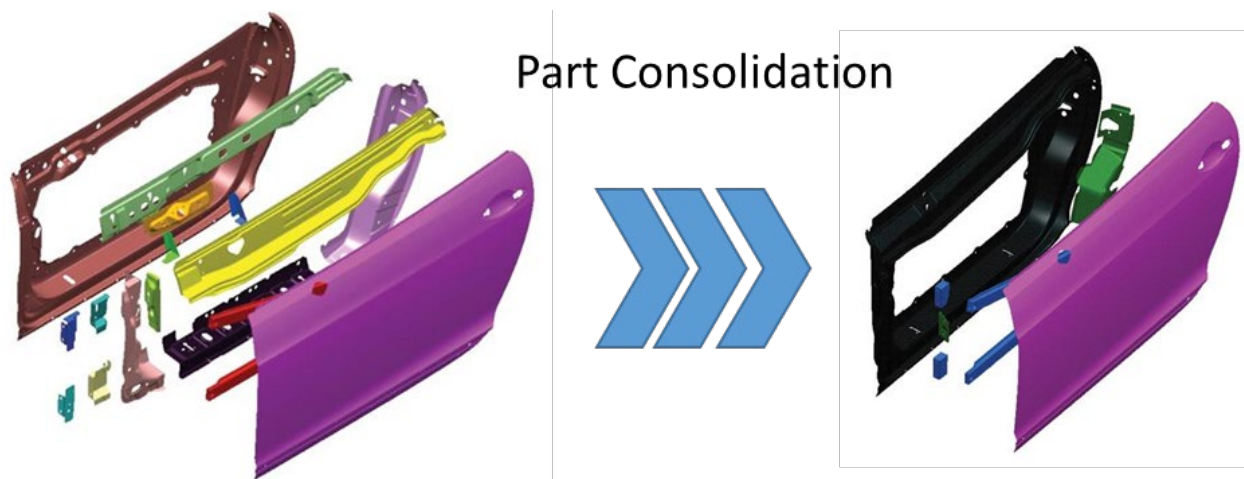


Figure II.4.C.3. Composites allow part consolidation, which further reduces cost and weight. Source: Composites World (<http://www.compositesworld.com/articles/auto-composites-quest-one-minute-cycle-time>).

Our hybrid solution will evaluate a variety of material solutions, including glass and CFs. Fiber modulus and strength depend on the fiber selection with specific properties being the highest for CFs. Design solutions without cost consideration will use 100% CFs and provide the best structural performance at the lowest weight. A hybrid design will incorporate alternative fiber solutions at a lower cost and meet structural performance. Our optimal design will consider all options and will meet structural requirements and cost and weight targets.

Lower-density glazing (such as polycarbonate glazing) has been recently developed for automotive applications. Transparent polymers can be easily molded into complex shapes, and it offers a 50% weight savings compared to standard glass solutions. The new materials have been demonstrated in both concept and production cars, including the Chevrolet Volt, Hyundai European Design concept cars, the Mercedes SMART, and Toyota V (station wagon version of the Prius) vehicles [2]. New window solutions also address the requirement for improved cabin comfort. Because glazing thicknesses have been reduced to save weight, the noise level within the car has increased. Integrating transparent acoustic layers within the glazing can be used to increase damping performance and thinner and lighter weight glazing can be employed without compromising cabin comfort or safety. Polycarbonate glazing enables new design concepts because complex geometry windows can be fabricated. Polycarbonate glazing with integral ribs lock the parts onto the vehicle or support other features. This program will evaluate a polycarbonate solution, which should not only impact the weight of the glazing, but the overall design of the composite door solution. This will simplify assembly and have the potential to lower the cost and weight of the total door solution.

All considered concepts will be evaluated at the component and full-door level using structural FEA tools. The composite laminate structure can be varied and will change the anisotropic stiffness and strength behavior of the part. The selection of fiber materials will impact performance and cost. Optimization of the layups, materials, and geometries needs to result in a manufacturable design at minimum weight while meeting all design requirements. The team has significant experience in design and analysis using commercially available structural static and dynamic FEA tools for vehicle structures that will be key for evaluating and optimizing the designs.

Crashworthiness will be evaluated using LS-DYNA, allowing simulation of the door and full vehicle under dynamic conditions. In particular, we will consider the crash performance under side-impact meeting Federal Motor Vehicle Safety Standard 214's protection requirements (other Funding Opportunity Announcement crash scenarios will be considered). The simulation will evaluate inward deflection as a function of time during impact for the baseline steel door and our composite solution. A conservative design goal would require the composite solution provide a deflection profile that stays below the transient intrusion levels of the steel baseline door. This would ensure the safety mechanisms (such as the side airbag) are able to be deployed in time and space and the passenger is protected in case of a side collision. UD-CCM has significant experience with crash predictions and under a current NHTSA program evaluates composites for a steel B-pillar replacement. Strain-rate-dependent material properties for composites are available; however, additional properties for the HP-RTM resins and fibers may have to be determined using coupon and subscale element testing. The test data will provide the programs with a database of material properties for crash designs.

The program will implement the HP-RTM process to fabricate sub-elements and full-size components. The process has been proven to produce Class A finished structural components at automotive rates. Cycle times of less than ten minutes have been demonstrated in-production on the BMW i3 and i8; this program will further reduce cycle time and performance using the most recent advances in resins and reinforcements developed by our team members (i.e., a four to five-minute cycle time would meet current vehicle production rates). Our partner, Krauss Maffei, has implemented a production cell to automate the process. Structural components, sidewall panels, floor pans, front-end carriers, crash boxes, and CF design components are applications that have been implemented via HP-RTM. Fiber mats or fabrics are preformed and then positioned in the mold. A variety of low viscosity polymers (such as polyurethane, epoxy, and polyamide) can be used as matrix material. The material components are mixed and heated in a metering system and injected into the heated mold. The resin quickly cures in the closed tool and the part can be demolded. Trimming occurs onsite. The HP-RTM process can produce parts with fiber content up to 70%. The process allows reuse of scrap material, improving material yield. Components manufactured using high-pressure RTM exhibit Class A surface quality and can produce high-quality (low-defect) parts with an aesthetically pleasing C appearance. The procedure has been fully automated and is suited for series production from the manufacturing of preforms up to post-mold processing. The program will use the existing HP-RTM as the baseline process, evaluate opportunities to reduce cycle time through innovative new materials (Saertex[®] and Hexion), and evaluate new process improvements (Krauss Maffei, UD-CCM, and TPI).

New resin materials are currently being developed at Hexion and will be optimized for this program. These resins (e.g., EPIKOTE[™] 05475) and appropriate curing agents have low initial viscosity (below 100 centipoise) and allow rapid infusion of reinforcement during the injection phase of the HP-RTM process [3]. The rheology of the EPIKOTE[™] resin with three different curing agents is discussed in Hillermeier et al. [3] and shows the ability to control the viscosity profile, while ensuring rapid cure without significant exothermic reaction of the polymer. Recent advances show full property translation and rapid (i.e., snap) cure in less than two minutes at elevated temperature. The low viscosity profile allows reduced injection pressure throughout the infusion cycle, relaxing the requirements of the preform, tool, mixer, and press. This, in turn, reduces preform distortion, cycle time, and capital cost.

NCFs provide the best fiber property translation and, using multi-axial systems, can be combined in a preform used in the production of large series vehicle components. These preforms are manufactured to the correct geometry and fiber lay-up, allowing rapid placement of the reinforcement into the HP-RTM tool. This enables minimum cycle time during the process, paired with the high-quality of the final product. It is important to optimize the preform to reduce scrap material and lower material cost. Our partner, Saertex[®], is the worldwide leader in tailor-made NCF materials and they will support development of low-cost preforms for this program.

A key challenge of the HP-RTM is design of the mold and preform to ensure full infusion of the polymer into the reinforcement. Tooling cost is a significant capital expense because applied pressures are high, and the tool is expected to last over the entire production run. UD-CCM is an expert in modeling the infusion behavior in liquid molding of hybrid preforms with complex geometry. The permeability and drapability of the reinforcement, as well as the rheology of the resin, are key material properties and are needed to allow optimization of the injection port locations and resin pressure cycle during infusion processing. We will evaluate the feasibility of the proposed designs to be manufactured and optimize the mold features for successful infusion, eliminating any required tool changes due to resin infusion issues. The program will ensure manufacturability of the proposed concept with HP-RTM and use virtual process tools to optimize tooling and infusion approaches. Tooling cost for HP-RTM is a significant investment and can only be amortized over a large production run. Conventional RTM processing of prototypes with equivalent part properties will be conducted as part of our risk reduction strategy.

The performance of our designs will be evaluated at the coupon, sub-element, and full-door component level. This will include structural performance testing (i.e., static and crash) and other functionalities such as durability to environmental exposures and noise, vibration, and harshness. Our team has existing testing capabilities in these areas and a comprehensive test plan will be developed as part of the program. Coupon testing is needed to characterize the mechanical and microstructural (i.e., void content and fiber volume fraction) properties of the hybrid composite design made with the Hexion resin and HP-RTM process. Other data (such as durability, acoustical damping, and environmental performance) may need to be generated and may require larger component testing.

Results

Ply Shape Validation

The major door tooling was comprised of three tools: the door outer panel, the door inner panel, and the intrusion beam. All ply shapes were validated before the preforms for molding could be cut.

Door Outer

The outer door was fabricated via the liquid compression molding technique. This process was conducted via robotically pouring resin onto a ply stack and then placing it into a mold and compressing it with heat to cure the part. During this process, the ply stack with resin was placed onto the lower tool and a clamp comes down with the upper tool to fix the preform in place while the tool closes. The ply pattern needs to have enough excess around the perimeter to ensure good clamping, as shown in Figure II.4.C.4.(a) and (b).

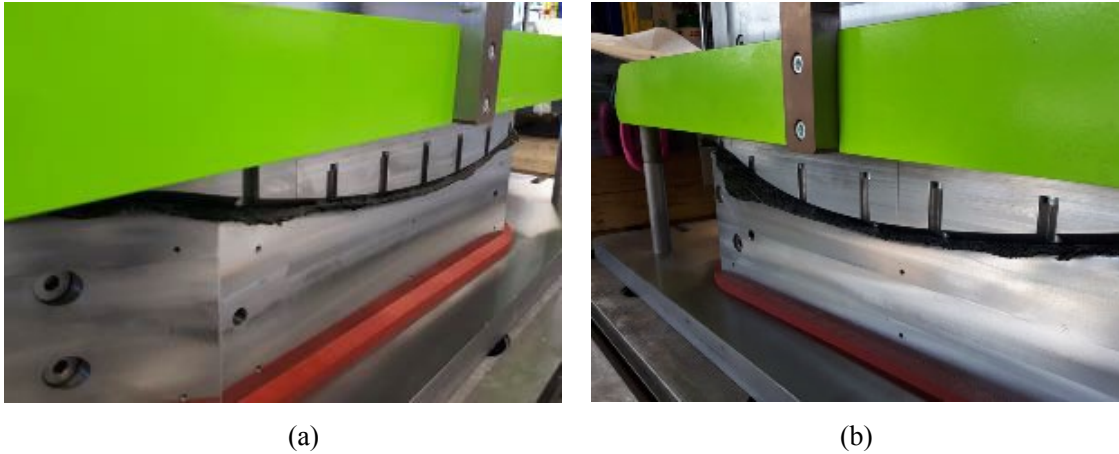


Figure II.4.C.4. Ply clamping showing (a) right side of mold; and (b) left side of mold. Source: Alpex.

Once clamped, the press closes and ensures that no wrinkles occur in the part, as is shown in Figure II.4.C.5.(a) and (b).



Figure II.4.C.5. Ply pressing trial showing (a) ply stack pre-pressing; and (b) ply stack post-pressing. Source: Alpex.

Inner Door

The inner door was fabricated using the HP-RTM technique. This process was performed by placing pre-consolidated ply stacks in a mold, closing the mold, and injecting resin at high rates and pressures to fill and cure the part in minutes. This process is typically used where parts have more detail and a deeper draw into the tool. As previously discussed, the inner door was comprised of five preforms, which were fabricated off-line on the preform tool, as is shown in Figure II.4.C.6.(a) and (b).



Figure II.4.C.6. Inner door preform tool with (a) placing pre-consolidated ply stacks in a mold; and (b) cured finished part. Source: TPI Composites.

These plies need to be nested in a cutting software configuration as shown in Figure II.4.C.7 to ensure the most efficient usage is obtained.

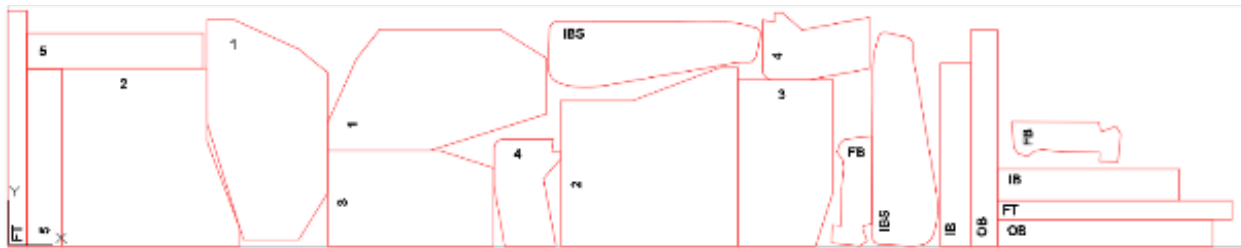


Figure II.4.C.7. Nesting ply shapes for optimum material usage. Source: TPI Composites.

Manufacture of Outer Door

The outer door part was manufactured in Munich, Germany, at the Krauss Maffei laboratory. This laboratory was chosen for its expertise with the liquid compression molding process, which is well-suited for this part, having little geometric detail.

Preparation

TPI cut all of the material for the door in advance at their Rhode Island facility, and shipped it to the Munich location. Each laminate stack consisted of four non-crimped fabric layers with full coverage to create a 1.3 mm thick quasi-isotropic laminate. This laminate is obtained using 4 layers of non-crimped fabric at orientations of $[\pm 45, 0/90, 90/0, \mp 45]$. A full-sized ply stack gripper/handler was also created by TPI and shipped to Munich to be retrofitted to their robot to maneuver the plies to the resin application station and then to the press for molding.

Programming

The shipped TPI materials were delayed at International Customs and arrived at Krauss Maffei on the same day the TPI engineers arrived. Due to this delay, it was decided to use the newly installed Krauss fiber stack gripper shown in Figure II.4.C.8 that was already installed on the robot to decrease delays in startup.



Figure II.4.C.8. Krauss Maffei fabric gripper. Source: TPI Composites.

The gripper was manually adjusted to securely lift the preform at the edges of the fabric to keep the resin out of the area. The robot was then programmed to pick up the ply from the presentation table and place it on the resin application table. The resin application robot, shown in Figure II.4.C.9, was then programmed to apply resin in four passes (shown as blue arrows) on the top surface of the ply stack.

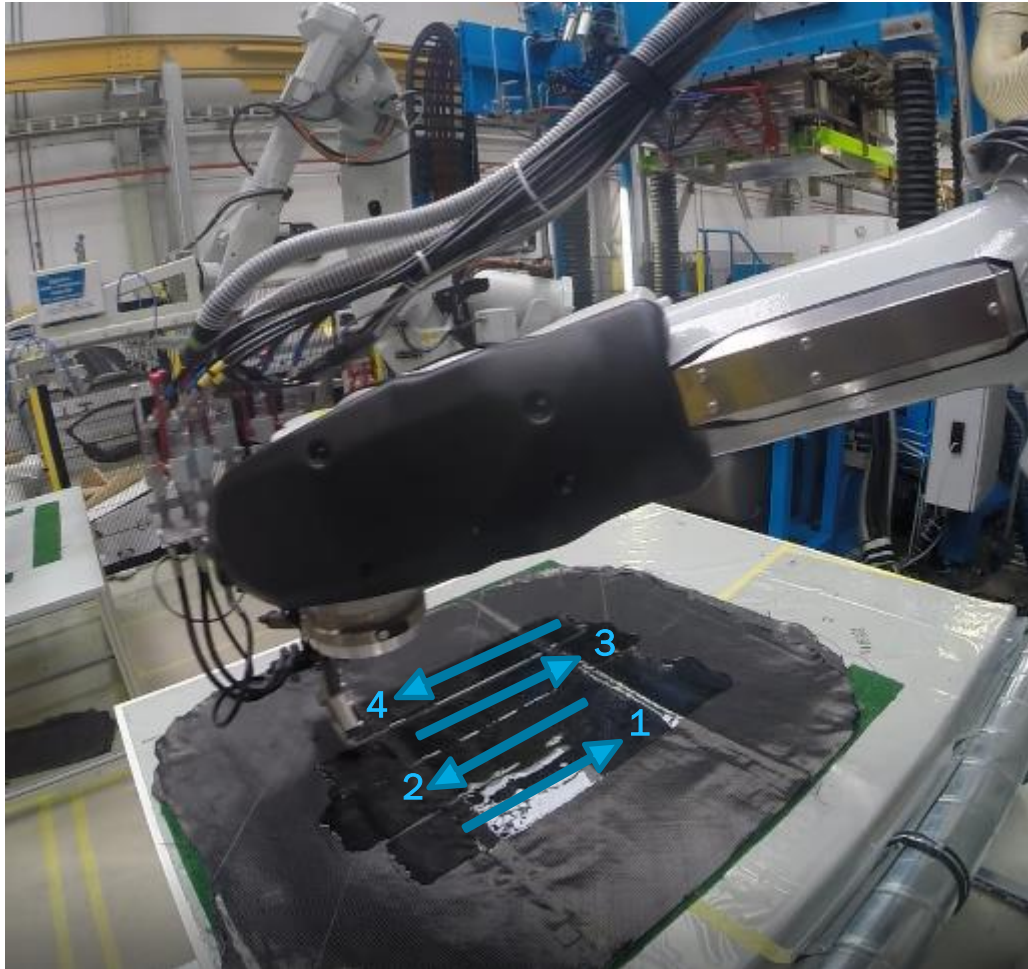
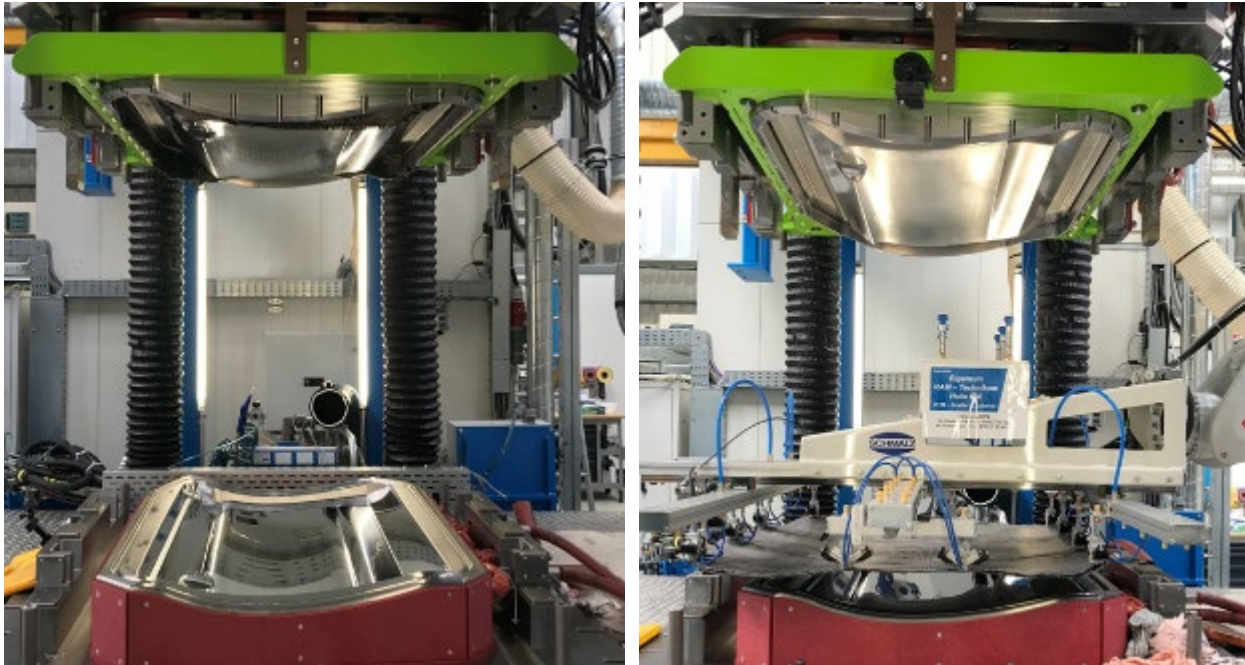


Figure II.4.C.9. Resin application to the ply stack. Source: TPI Composites.

The robot's motion was tested on a dry run and then on sacrificial material, which was placed on top of the resin application for an actual application trial, in order to preserve the preforms. Unfortunately, there was no communication between the application robot and the Krauss Maffei Meter Mix machine to start the flow of resin. This took approximately 1.5 days to resolve.

Following the resin application, the first robot then picks up the stack a second time and places it onto the lower half of the outer door tool in the press, as shown in Figure II.4.C.10.(a) and (b).

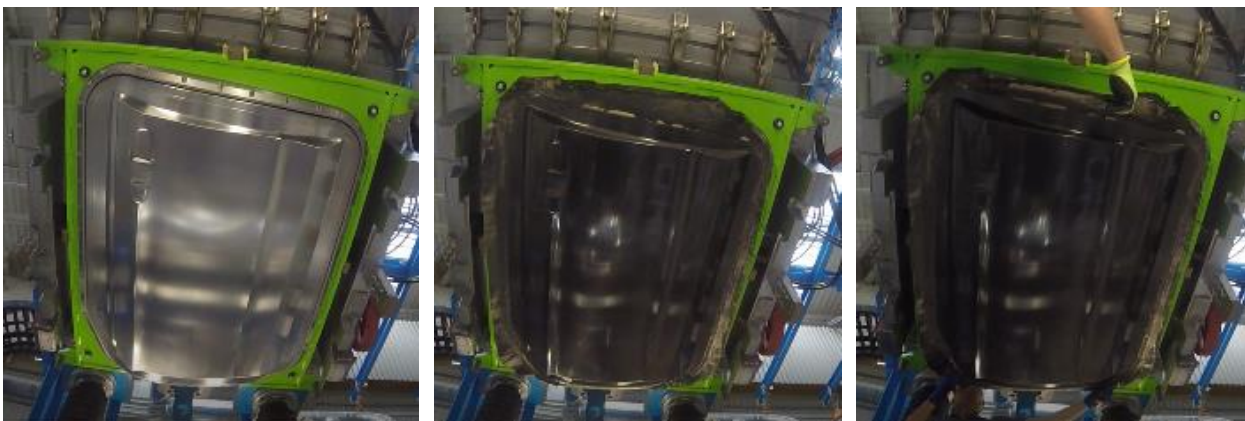


(a)

(b)

Figure II.4.C.10. Loading the preform into (a) the empty tool; and (b) with the loading tool and form in place.
Source: TPI Composites.

The loaded tool receives a signal to close once the loading robot is out of the way. The tool closes rapidly to minimize cycle time and then within a few millimeters of completely closed switches to a slow-close mode to allow the resin to flow to the edges of the part and then get pushed through the thickness. The part then dwells in the closed mold to cure. After the curing process is complete, the tool opens, and the ejector pins and shop air assist push out of the part from the upper mold. In a production setting, the robot would pick out this part, but in our laboratory trials, we just removed the part from the upper mold manually, as shown in Figure II.4.C.11.(a), (b), and (c).



(a)

(b)

(c)

Figure II.4.C.11. Part removal from tool starting with (a) the top of the empty tool with (b) the cured molded part; and (c) the part being manually removed. Source: TPI Composites.

Production Trials

The final day at the Krauss Maffei laboratory in Munich was dedicated to making parts as quickly as possible using the process that was developed. We were able to achieve a nine-minute cycle time, “button to button” (i.e., from the start of the cycle to the start of the next cycle), using the process that was programmed into the robots over the previous days.

It was clear that the robots’ movements could be optimized to further reduce times. The robots were moving very serially, one robot coming to a complete stop before the next one started. Through film review, the team has determined that further optimization could be achieved to get the cycle time down to a seven-minute cycle time. Additionally, the cycle time could be further reduced by switching to a two-minute cure resin from the five-minute cure that we had been used. Making these adjustments would get the cycle time down to the four to five-minute timeframe. A sub-five-minute cycle time would be needed to support 50,000 units per year, assuming 250 working days, three shifts, and at 80% efficiency. Doing this would allow us to meet the 40,000 units/year goal of the program.

In all, 36 usable parts were manufactured and are currently being shipped back to the U.S. to be machined. Figure II.4.C.12 provides an image of the finished product.



Figure II.4.C.12. Finished molded outer door. Source: TPI Composites.

Manufacture of Door Inner Panel

The door outer panel was manufactured at Fraunhofer Institute of Chemical Technology (ICT) in Pfintzal, Germany. This facility was chosen for its expertise with the HP-RTM process. This location was chosen due to its closeness to Alpex in Mils, Austria, which is where the tool was manufactured. Should the tool need any rework to facilitate a revision on resin gating or similar, this closeness will reduce the amount of downtime for a replacement tool to be re-manufactured.

TPI cut all of the materials for the door inner panel in advance at the Rhode Island facility, which they then shipped to Fraunhofer ICT. The individual plies of various weights and angles were cut via an Eastman automated ply cutter. At this point, each laminate stack was created by hand to get the correct orientation of the stack. These plies were then laid on top of a heated Al tool with a Si vacuum bag, as shown in

Figure II.4.C.13.(a) and (b), for the purpose of consolidating the fabric. The as-received non-crimped fabric from Chomarat was manufactured with a light thermoplastic veil stitched on to facilitate consolidation of the preform. The Al preform tool was designed to create all five preforms required for the inner door. Figure II.4.C.14.(a) shows the preform on the mold, while Figure II.4.C.14.(b) shows the preform after consolidation and trimming.



Figure II.4.C.13. Images of (a) the Al preform tool with (b) the silicone vacuum bag. Source: TPI Composites.



Figure II.4.C.14. Preform fabrication showing (a) preform on the mold; and (b) preform after consolidation and trimming. Source: TPI Composites.

The materials were placed onto the tool and smoothed by hand and danted where necessary to allow the material to lay flat. Then the silicone bag was closed, and a vacuum was applied. The tool was then heated above 265°F to allow the thermoplastic to flow and bind the material layers together. The tool was then cooled to stabilize the material before its removal. This binding process is performed to prevent the fabrics from moving around in the tool during the injection process. The injection process takes place at such a high velocity that the plies tended to shift, thereby causing a bad part. Figure II.4.C.15.(a) and (b) provide details of the preform breakup on the inner door. Enough parts were preformed to fabricate a total of 50 parts and an image of a final parts is shown in Figure II.4.C.16.

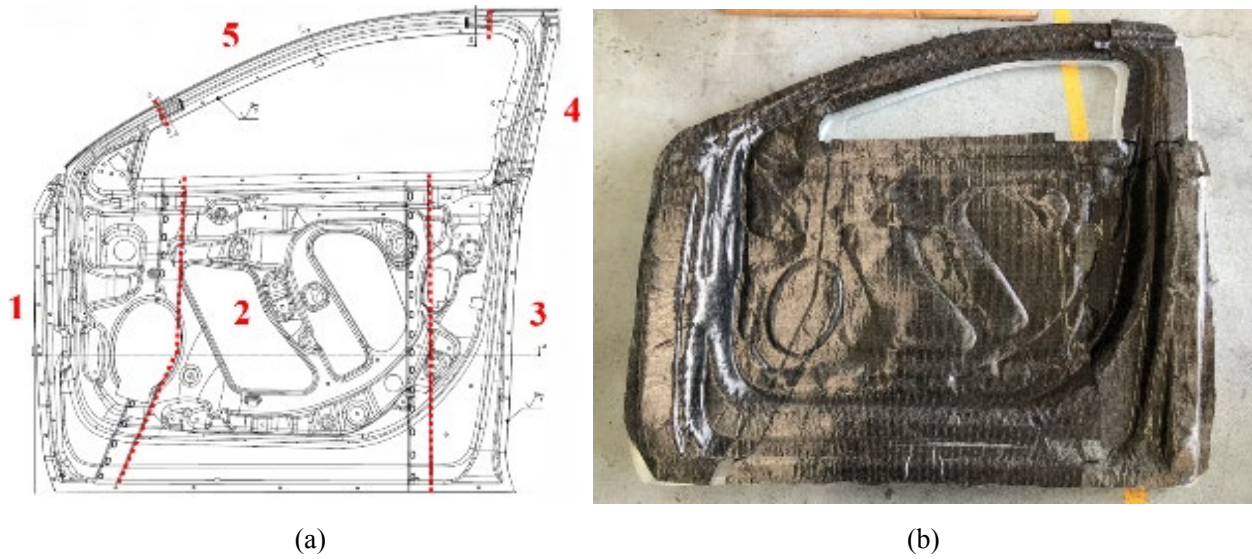


Figure II.4.C.15. Preform breakup on the inner door at (a) five locations for (b) preformed door. Source: TPI Composites.



Figure II.4.C.16. Finished preforms ready to ship to Germany. Source: TPI Composites.

The Door Inner Panel Mold shown in Figure II.4.C.17.(a), (b), and (c) was fabricated at Alpex in Austria, and then shipped to Fraunhofer ICT in Pfinzthal, Germany. This location was chosen for two reasons: (1) their knowledge of the HP-RTM process; and (2) as a risk mitigation should the tool need to be shipped back to Austria for re-machining.

The Fraunhofer facility has a Dieffenbacher Compress Plus press combined with a Krauss Maffei resin dosing system for the manufacture of HP-RTM composite parts. Our team arrived in mid-August, and the tool was subsequently preheated and connected to the press, thereby ready for the trials.

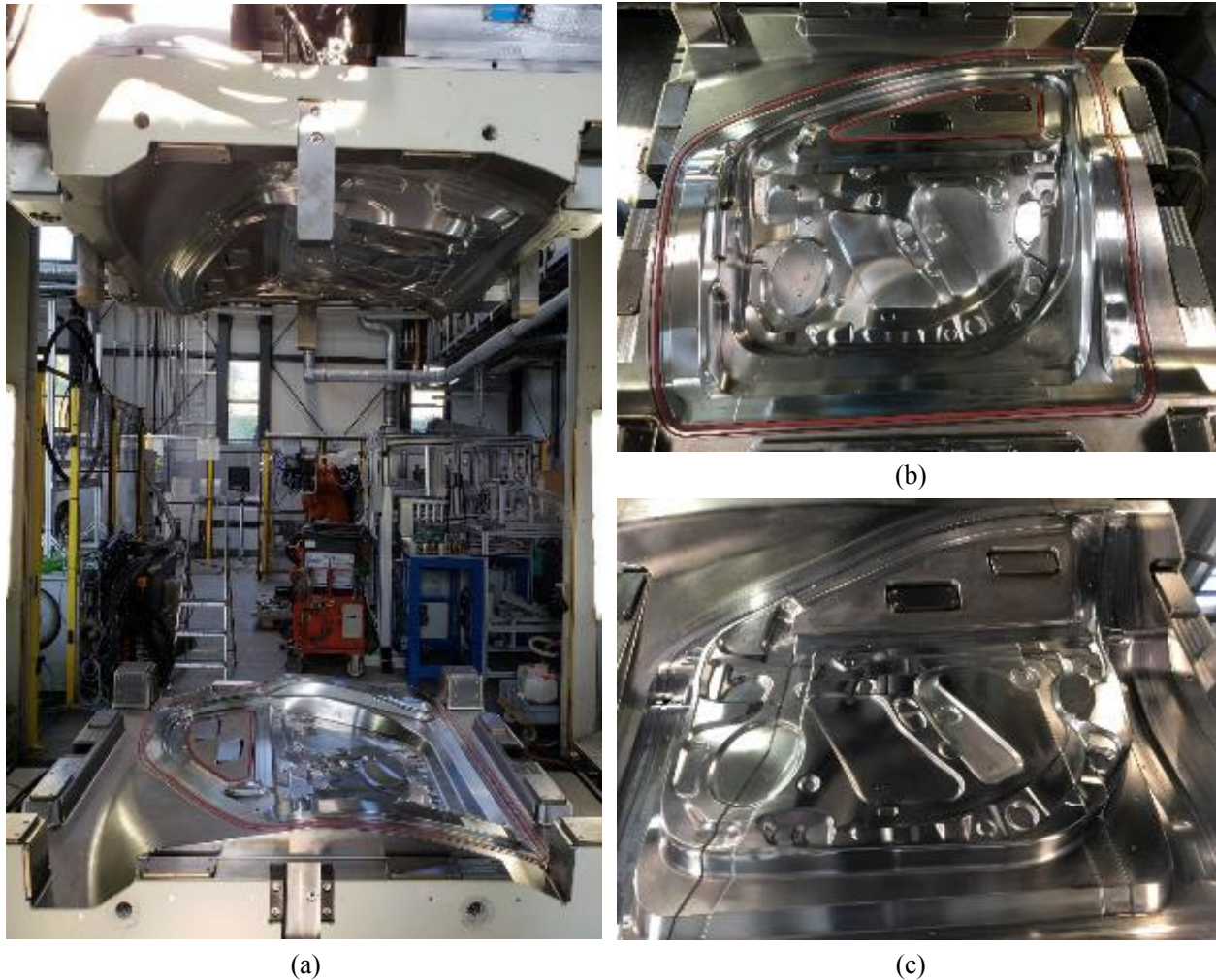


Figure II.4.C.17. Completed inner door tool (a) mounted in the press with (b) lower surface and (c) upper surface.
Source: TPI Composites.

The first injection performed was made up of just pure resin to validate the mold volume and the tool filling. This was performed with good results. Next, a 50% resin shot, shown in Figure II.4.C.18.(a), and a 90% resin shot, shown in Figure II.4.C.18.(b), were used with the preforms to investigate how the tool would fill the tool. The resin will fill, or “race-track” around the perimeter of the tool, and then fills the overlap sections in the center. This filling scenario is adequate as the tool cavity is evacuated via vacuum prior to introducing the resin; hence, there is little chance of trapped air due to filling.



(a)



(b)

Figure II.4.C.18. Partial tool filling for (a) 50% fill; and (b) 90% fill. Source: TPI Composites.

The subsequent injected parts were focused around the complete filling of the tool and trying to characterize preform movement during filling. There were some efforts to try to keep the preforms from moving in the tool, such as adding a gasket in the tool. These trials had little effect, as shown in Figure II.4.C.19.(a) for the dry preforms and Figure II.4.C.19.(b) for the molded part.



Figure II.4.C.19. Inner door in tool with (a) dry preforms; and (b) molded part. Source: TPI Composites.

These new preforms were fabricated at a separate facility from where the tool was located. The luxury of “dry fitting” the preforms was not afforded us while making the preforms, which led to some issues while trying to mold the first parts.

The overlap tab at the mirror mount portion of the door would not stay in place while the tool closed. This tab would slide down the vertical face of the tool when closing and get pinched, causing a local high fiber volume. Figure II.4.C.20.(a) and (b) illustrate how the preform slides out of place during tool closing. The dotted red line is where the preform should be and the solid yellow line is where the preform ended up after injection.



Figure II.4.C.20. Sliding preform at the mirror mount for (a) the area of interest; and (b) at the displaced location. Source: TPI Composites.

Another issue that was seen during the molding process was the separation of preform edges where they were designed to be butt joints. These joints as trimmed for these trials could not be affected as they were trimmed with no excess and the joint always “opened up” during the process, as seen for three locations in Figure II.4.C.21.(a), (b), (c), and (d).

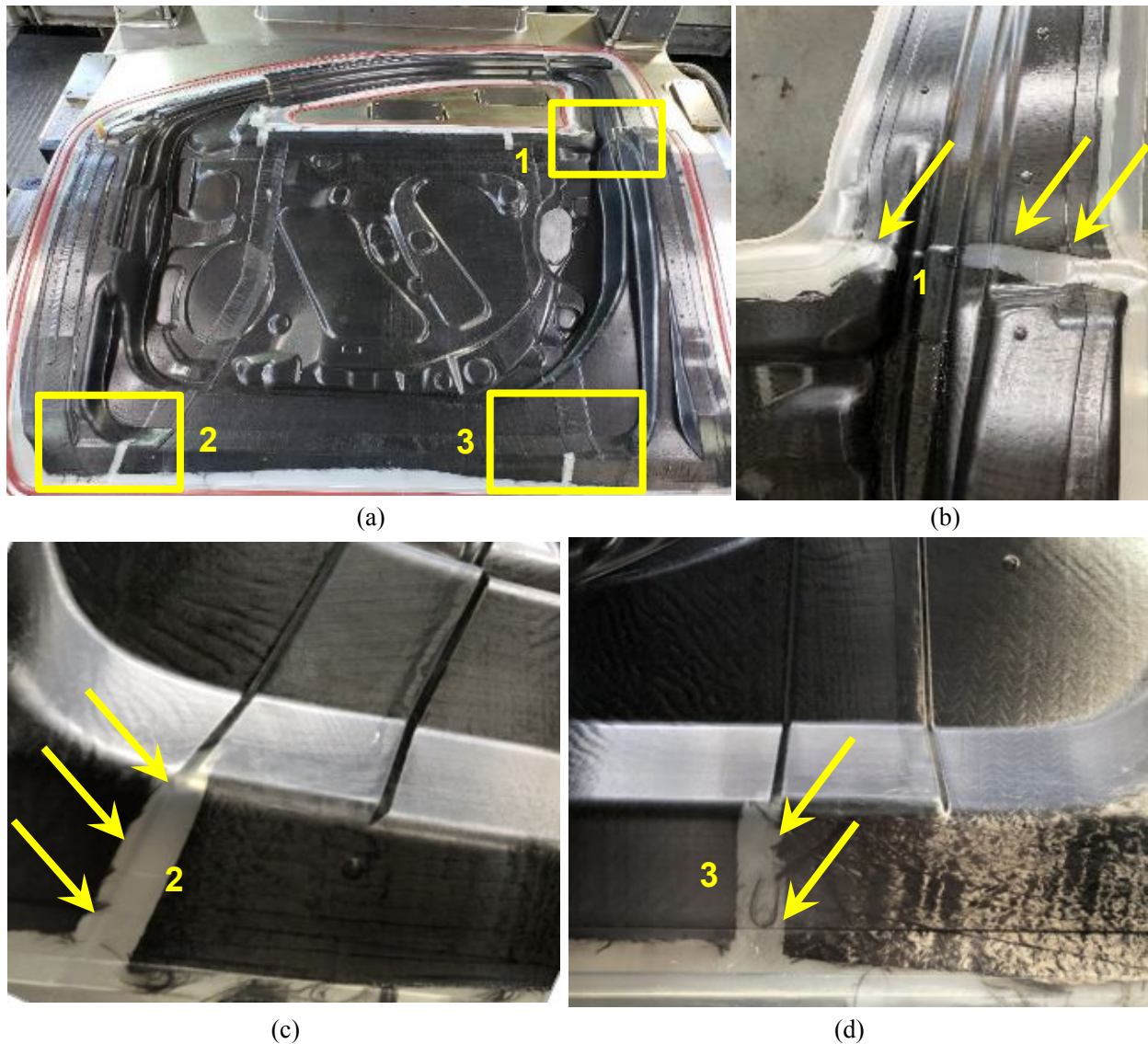


Figure II.4.C.21. Preforms separating during injection at (a) three separate locations and enhanced images at (b) first location, (c) second location, and (d) third location. Source: TPI Composites.

Wrinkling of the preform occurred across the part, even in relatively flat sections, as is shown for three areas in Figure II.4.C.22. Initially, it was thought that the resin injection rate was causing the fabric to move, but tests that were run from a 30 g/sec up to a 150 g/sec injection rate and saw no difference in the wrinkles. This is thought to have been caused by preform bulk captured in the forming process.

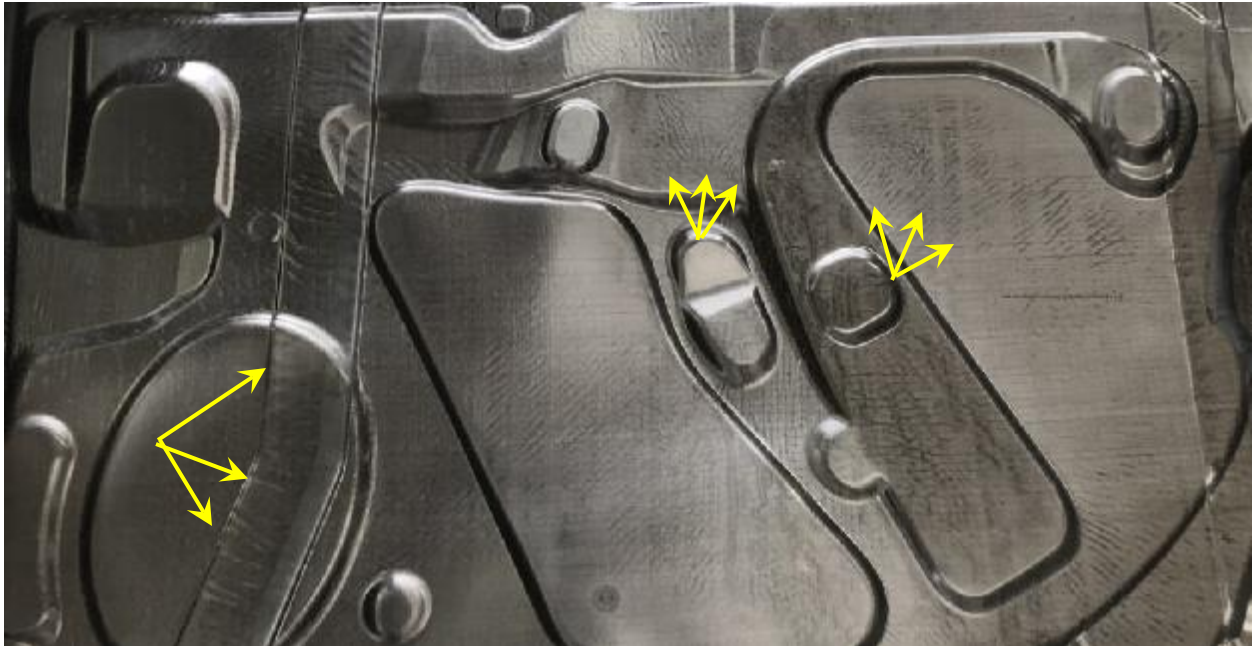


Figure II.4.C.22. Part wrinkling. Source: TPI Composites.

Status to Target

The design solutions presented in this report represented a cost of \$715 per door at a mass of 22.8 kg (or 50.2 pounds), as depicted in the charts shown in Figure II.4.C.23 and Figure II.4.C.24. This is a savings of 30 pounds over the existing baseline door design. The cost increase of \$138 per part and 30 pounds of mass saved yields a \$4.58 cost increase per pound of weight saved, exceeding the program targets. The total mass saved is 38% going from 36.5 kg to 22.8 kg. This target proves to be more difficult as the total mass of the door is included in this calculation. The window track/motor, latch, hinges, and other sub-assemblies represent 56% of the total mass of the door and they are harder to lightweight than the structure.

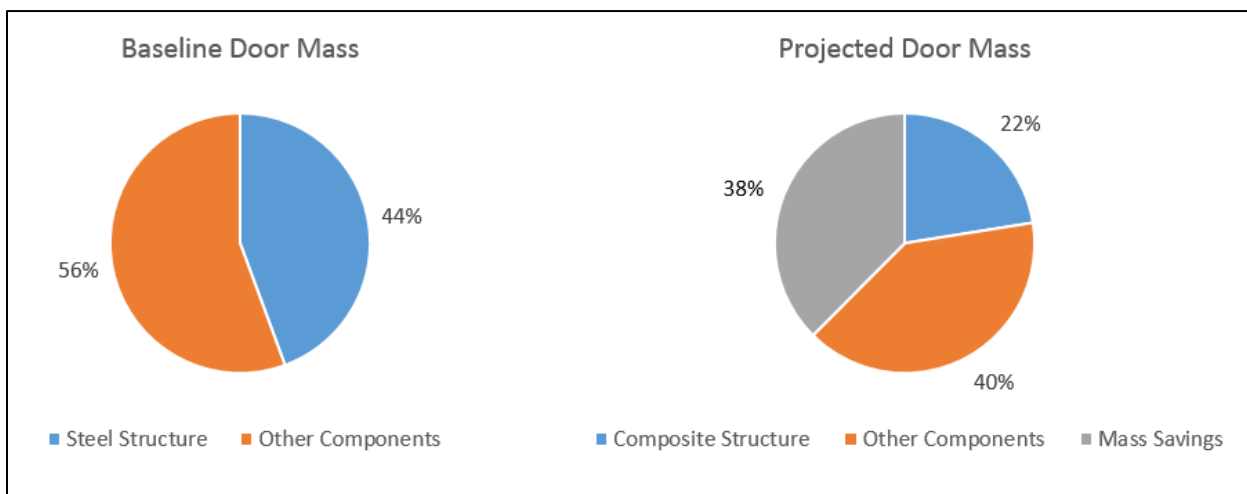
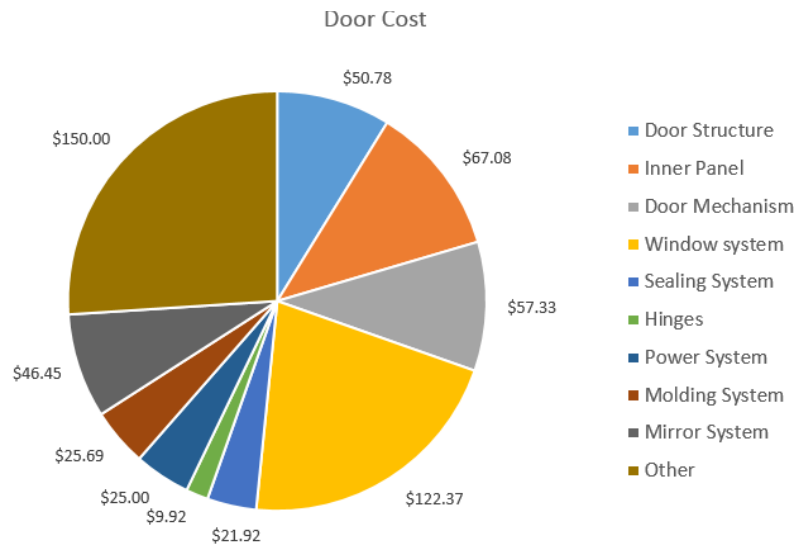


Figure II.4.C.23. Door mass breakdown.

Component	Cost
Door Structure	\$ 50.78
Inner Panel	\$ 67.08
Door Mechanism	\$ 57.33
Window system	\$ 122.37
Sealing System	\$ 21.92
Hinges	\$ 9.92
Power System	\$ 25.00
Molding System	\$ 25.69
Mirror System	\$ 46.45
Other	\$ 150.00
TOTAL	\$ 576.54



Component	Current Mass [kg]
Door Structure	16.2
Inner Panel	4.1
Door Mechanism	1.7
Window system	5.7
Sealing System	2.6
Hinges	1
Power System	1.1
Molding System	0.9
Mirror System	1.6
Other	1.6
TOTAL	36.5

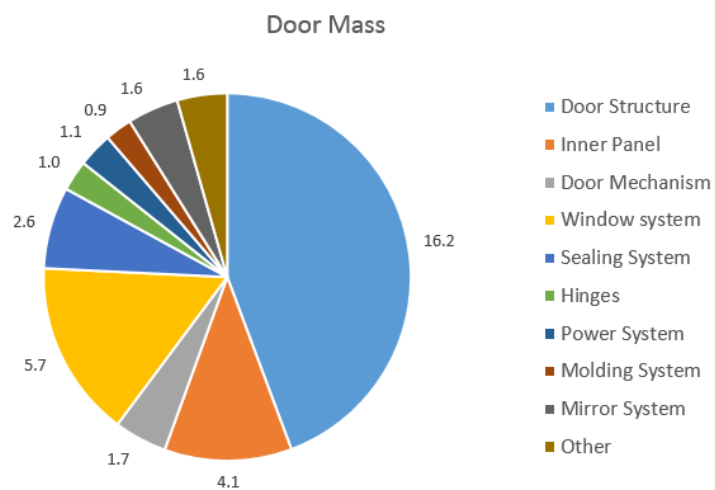


Figure II.4.C.24. Baseline door cost and mass.

The optimized design as defined during the previous years' work yields a 38% mass save and a \$5.47 cost increase per every pound saved. This is based on the input fiber, Zoltek Panex 35, at a cost of \$7.75 per pound. Should the low-cost CF from ORNL be commercialized and realize an input fiber cost of \$4.75, we could then exceed the cost target even further, getting down to as low as \$4.33 per pound saved as shown in Table II.4.C.1.

Table II.4.C.1. Status to Target.

Input CF Cost: \$7.75/lb		Input CF Cost: \$4.75/lb	
Optimized Design		ORNL LCCF Design	
Weight Reduction (lb)	30.3	Weight Reduction (lb)	30.3
% Reduction	38%	% Reduction	38%
Cost Increase	\$165.72	Cost Increase	\$131.13
Dollars/Pound Saved	\$5.47	Dollars/Pound Saved	\$4.33

Conclusions

We are close to the major goals of reducing part count and full-system weight by a minimum of 42.5% (38% achieved), the cost increase not exceeding \$5 per pound of weight saved (\$4.33 achieved with LCCF), and materials and processes meeting the production rate and performance requirements.

References

1. Sloan, J., 2012, "Auto composites quest: One-minute cycle time?," *Composites World* (August), <http://www.compositesworld.com/articles/auto-composites-quest-one-minute-cycle-time>.
2. Motavalli, J., 2011, "Shattering glass: Low-weight plastic car windows are coming," *CBS Money Watch* (July), <http://www.cbsnews.com/news/shattering-glass-low-weight-plastic-car-windows-are-coming/>.
3. Hillermeier, R., T. Hasson, L. Friedrich, and C. Ball, 2013, "Advanced Thermosetting Resin Matrix Technology for Next-Generation High-Volume Manufacture of Automotive Composite Structures," SAE Technical Paper 2013-01-1176, <https://doi.org/10.4271/2013-01-1176>.

II.4.D Functionally Designed Ultra-Lightweight CF Reinforced Thermoplastic Composites Door Assembly (Clemson University)

Srikanth Pilla, Principal Investigator

Department of Automotive Engineering
 Department of Materials Science and Engineering
 Clemson University
 4 Research Dr., Suite 340
 Greenville, SC, 29607
 E-mail: spilla@clemson.edu

H. Felix Wu, Ph. D, DOE Technology Manager

U.S. Department of Energy
 E-mail: felix.wu@ee.doe.gov

Start Date: December 1, 2015 End Date: January 31, 2020
 Project Funding (FY18): \$1,384,519 DOE share: \$624,023 Non-DOE share: \$760,496

Project Introduction

One of the most promising routes for achieving the 2025 Corporate Average Fuel Economy standards involves decreasing vehicular weight by incorporating lightweight materials, coupled with component redesign, in order to improve overall fuel efficiency. Indeed, one recent study indicates that the simple replacement of current metallic doorframes with CF reinforced plastic composites can reduce the overall weight of the component by nearly 58% [1]. The objectives of this project are to achieve a weight reduction of at least 42.5%, compared to the baseline door structure, at the cost of less than \$5/lb. while saving on energy metrics without compromising the fit, function, crash, and noise, vibration, and harshness requirements. The strategy for achieving these targets involves a holistic systems approach through the integration of unique designs, novel materials, manufacturing technologies, and joining/assembly of subsystems to ensure the developed technologies are ready for commercialization.

Objectives

The objective of this project is to reduce the weight of a door assembly by at least 42.5% compared to a baseline driver's side front door with an expected cost increase of less than \$5/lb. in weight saved. A 2013 mid-sized sport utility vehicle's door from our OEM partner with an assumed production volume of 20,000 vehicles annually is the basis for design. These criteria will either meet or exceed the fit, function, crash, NVH requirements of the baseline door.

The intent is to: (1) enable the radical redesign of the baseline door via a holistic systems approach through the integration of unique designs; (2) use novel materials that render the door 100% recyclable; and (3) investigate manufacturing technologies and joining/assembly of subsystems to ensure the developed technologies are ready for commercialization. The partner organizations listed in Table II.4.D.1 are providing highly leveraged knowledge expertise to ensure the success of this effort.

Table II.4.D.1. Project participants.

Universities	Industry Partners	Computation Partners
Clemson University	OEM	Altair Engineering
	BASF, Polyone	Core-Tech Systems (Moldex 3D)
University of Delaware	Krauss Maffei, Trexel Inc.	MSC Software (Digimat)
	Corning	LS-DYNA

Approach

The project entails the use of a systems-level approach that begins with systematic evaluation and benchmarking of the door and its sub-assemblies. In collaboration with our partnering companies and commercial suppliers, researchers are evaluating a variety of CF thermoplastic material forms for structural components (i.e., novel unidirectional and fabric prepregs, co-mingled fabrics, high aspect ratio discontinuous fibers, performance thermoplastic resins, novel fiber architectures, and localized reinforcements) and alternative solutions for glazing, trim, and other sub-components. The initial focus involves creating the structural component and a materials database for all parts of the door structural assembly (i.e., outer shell, inner panel, carrier, and anti-intrusion beam(s)).

A two-phase integrated design and manufacturing optimization approach was adopted to obtain the optimal manufacturing process parameters of the thermoplastic materials and the optimal structural design parameters of the door. The Principal Investigators also conducted a top-level trade study to determine at least two candidate designs for optimization. The design parameters will incorporate: (a) thermoforming and injection molding parameters (e.g., pressure and temperature); (b) fiber parameters (e.g., material, length, diameter, and volume fraction); (c) matrix parameters (e.g., material and volume fraction); (d) structural wall thickness; and (e) material density distribution. The research team will use four analysis tools—Moldex3D, Digimat, and LS-DYNA Implicit, and Explicit—to construct the manufacturing-to-response analysis pathway [2-4]. The team will fabricate a door based on this optimal design for testing in accordance with OEM performance requirements.

Results

Concept Development

The team's focus in fiscal year 3 was on design for integration and manufacturing. Given that the addition of sub-component integration increases weight, cost, and complexity, significant decisions were required regarding the material systems and manufacturing processes. While the initial target entails the predominant use of fiber reinforced thermoplastics in the structural frame, the acquisition of specific mechanical requirements, such as energy absorption and ductility are a difficult endeavor. Specifically, in full car crash modes (i.e., FMVSS 214: RP and DB), the very stiff inner panel failed prematurely in the lower section of the door. Therefore, to improve performance and decrease cost, we made three significant changes to the previous year's design as detailed below.

- a. Anti-intrusion beam (Composite hat section to circular steel beam):

In the FMVSS 214 quasi-static and RP test, the anti-intrusion beam is the primary load-dissipating member of the doorframe with the desirable mechanical characteristics of high-energy absorption capacity and progressive failure (i.e., ductile behavior). A 45°/-45° laminate was used to engineer this behavior and a 16-ply laminated used to engineer the desired axial strength. Although significantly heavier and costlier than initially planned, our resulting steel anti-intrusion beam, as seen in Figure II.4.D.1, exhibited a much-improved performance with no penalty on weight while also significantly cheaper.

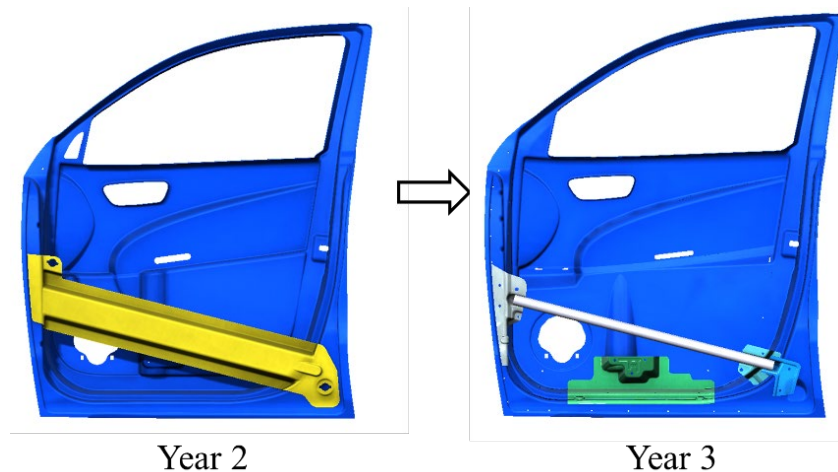


Figure II.4.D.1. Anti-intrusion beam design update. Source: Clemson University.

b. Removal of lower hinge stiffener:

The lower section of the inner panel prematurely failed in FMVSS 214 quasi-static and RPs test. Initially, a corner profile section was used to reinforce this region for minimizing door sag, the undesired consequence of this profile is a stress concentration in the lower frame section. By removing the lower hinge stiffener, the team was able to delay the failure in this region during crash tests. There was a noticeable decrease in the door sag stiffness but was quickly rectified by increasing the thickness of the laminate at the hinge region to rectify the sag.

c. Simplification of the lower door frame:

Perimeter beads were initially designed in the lower frame to improve panel stiffness and NVH performance, but these complex geometries posed an undeniable risk for manufacturing. The team decided to smoothen this region by increasing the draft angles and eliminating the beads as seen in the Figure II.4.D.2. The results were a further reduction in the performance in door sag and speaker mount stiffness, this was deemed a fair trade-off to minimize the risk during manufacturing. The stiffness performance was rectified by slightly increasing the thickness of the laminate in this region.

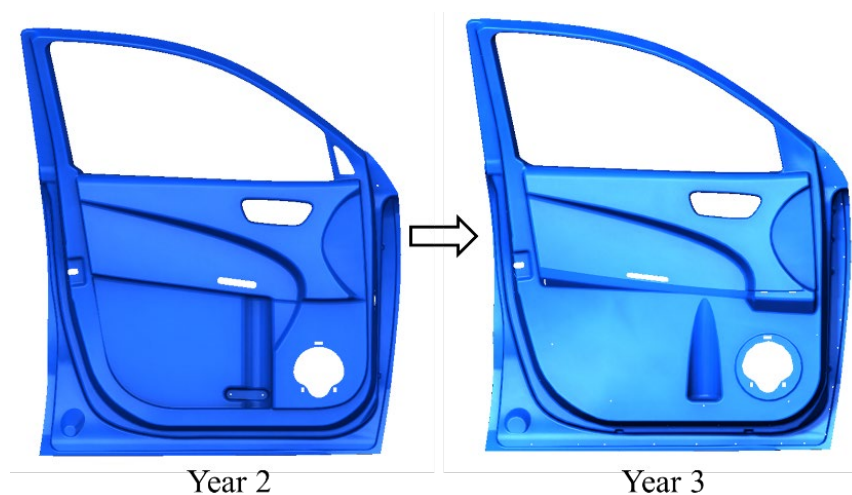


Figure II.4.D.2. Inner panel design update. Source: Clemson University.

Manufacturing-to-Response Pathway

Manufacturing-to-response pathway is a loop that utilizes mechanical performance as a feedback to the manufacturing process in an effort to optimize the manufacturing process parameters while satisfying the set of constraints of mechanical analysis. The pathway consists of a forming simulation, followed by a mechanical (static/dynamic) analysis of the formed part. In the present study, the first step of the pathway (i.e., forming analysis) was carried out on the outer panel stiffener of the door, as shown in Figure II.4.D.3. This outer panel stiffener is one of the few door components manufactured by the thermoforming process at a later stage in the project. Considering the current capability of modeling features available with the Altair Hyperworks software, forming analysis is simulated at a steady temperature in the present study.

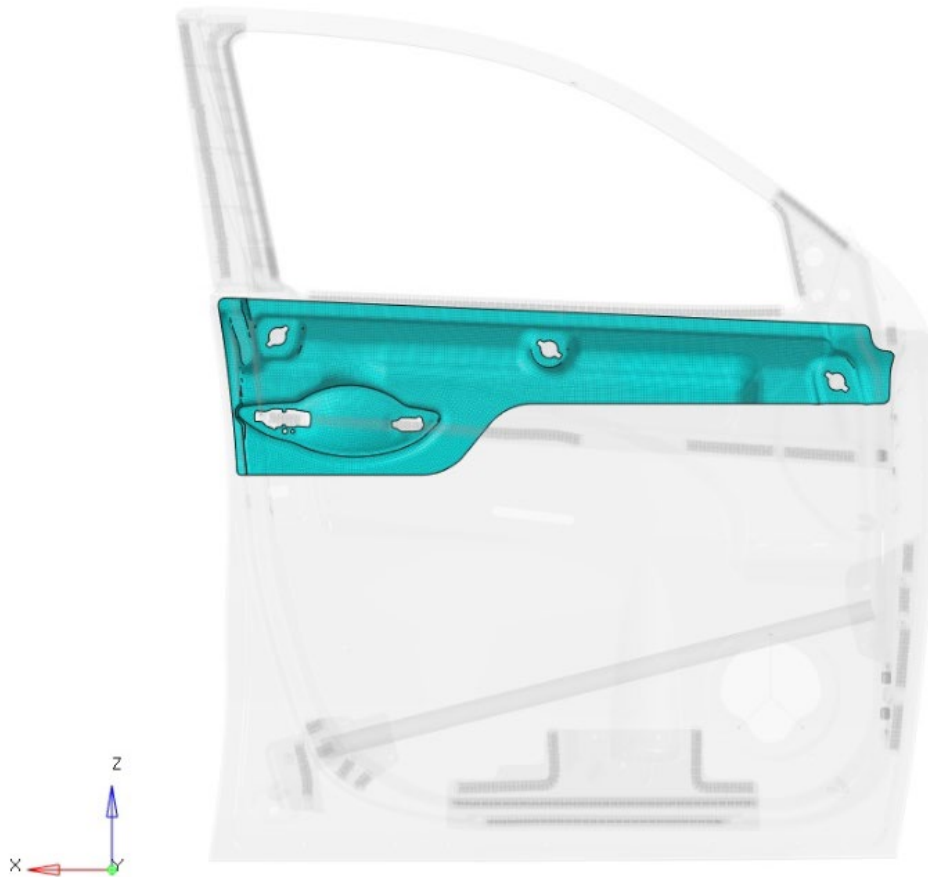


Figure II.4.D.3. Outer panel stiffener of the door. Source: Clemson University.

The forming components (e.g., punch, binder, composite blank, die) is shown in Figure II.4.D.4. The binder is loaded with a “binder force” that holds it firmly over the blank and facilitates proper punching. A punch is defined as a velocity of 2,000 mm/sec to form the composite blank while traveling towards the die. AS4/PA-66 material is assigned to the composite blank. We use a connection material to separately model and bond the components of the composite blank (i.e., the fabric and resin) as separate layers. Two fabric layers of 45° and -45° orientation are used with a resin layer in between in the current study. The fabric is modeled using shell elements and assumes hyperelastic anisotropic behavior, whereas solid elements are used to model elastoplastic resin behavior. Using this model, forming results, such as stresses and strains, can be captured in the two (warp and weft) directions of the fabric, independently. Also, shear stress and strain as a function of shear angle can be obtained.

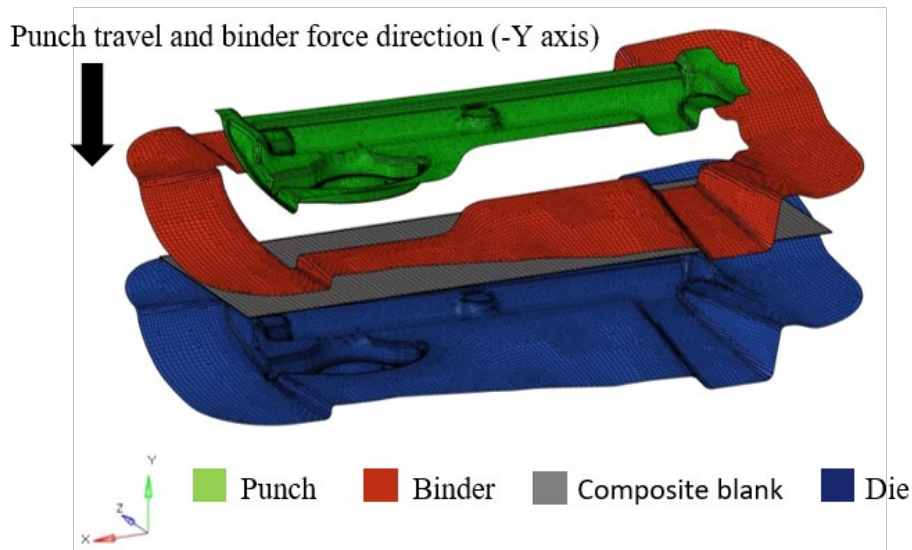


Figure II.4.D.4. Forming setup and components. Source: Clemson University.

In the forming simulation setup, parameters such as binder force, tool mating friction, and punch velocity exhibited a considerable effect upon the forming process results. In the present study, the effect of binder force as a forming parameter on the forming results is investigated. Two simulations with binder values of 10 kN and 20 kN are carried out and the results are compared in the plots in Figure II.4.D.5.

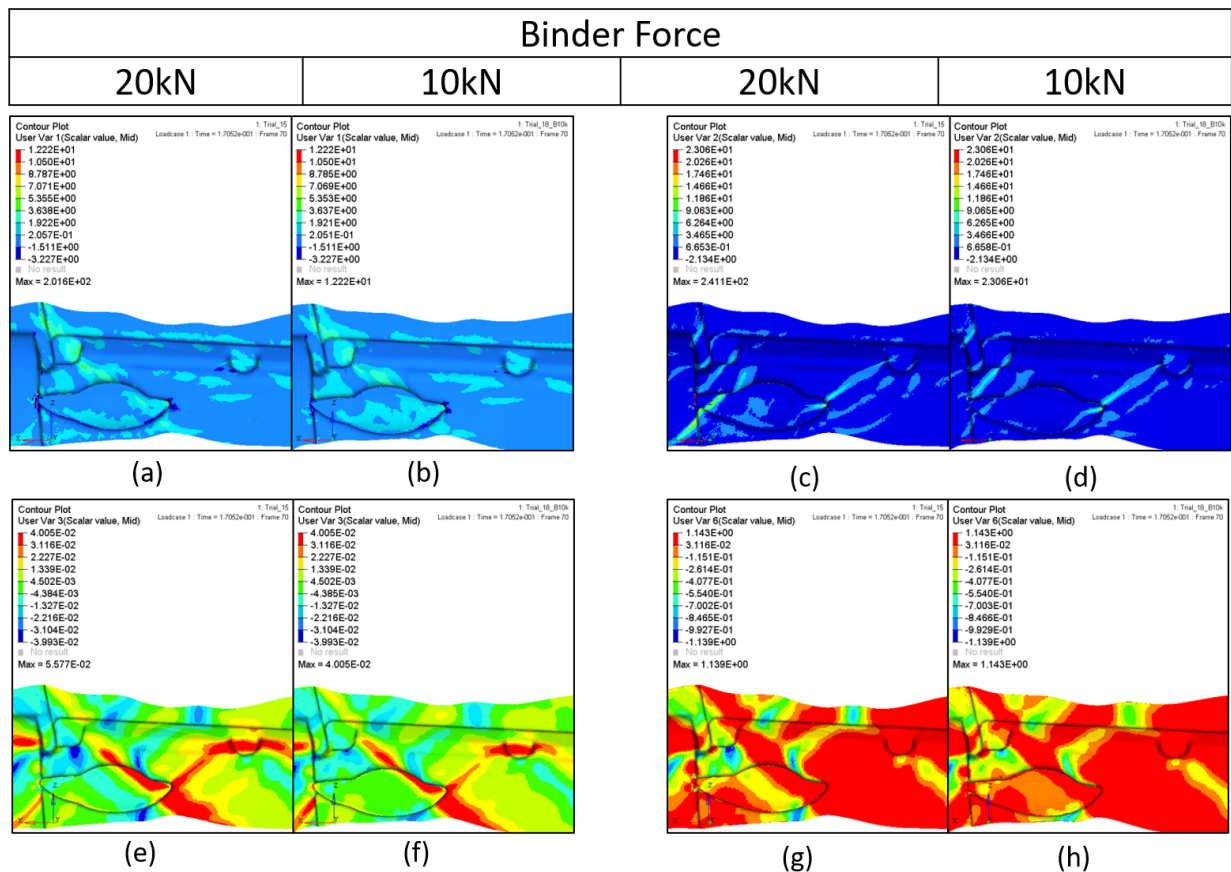


Figure II.4.D.5. Forming setup and components. Source: Clemson University.

Figure II.4.D.5 shows the comparison plots of forming results obtained from the two simulations using binder force values as 20 kN in the first and 10 kN in the second setup. The stress plots (b) and (d) in the two fiber directions show significantly lower maximum stress value as compared to plots (a) and (c). However, a comparison of shear stress in plots (e) and (f) and shear strain in plots (g) and (h) does not show appreciable change due to the application of different values of binder force. Thus, these results indicate a greater influence of the binder force as a forming parameter upon the stress plots in the two fiber directions than in the shear direction. Consequently, it is important to find an optimum value of a forming parameter that is specific to a given forming setup and dependent on the part complexity, part material, and other forming parameters.

Future tasks will try to automate the pathway from forming to mechanical analysis to obtain optimized forming parameters, which would satisfy the mechanical performance target values. Also, the forming simulation model will be improved to include strain rate and temperature dependence.

Summary of FEA Results

The team began the third year by evaluating the static performance of the door with the composite hat section using the FEM. Upon receiving feedback from the FMVSS 214 quasi-static and RP simulations, the team decided to update the door design with the circular steel beam. Therefore, the team re-evaluated the updated design in order to optimize the initial setup of ply lay-up and laminate thickness.

The team first determined the initial thickness for the components that satisfies prescribed static load cases, followed by a three-step composite optimization to reduce the door mass. The static load cases were obtained from both literature as well as from specific requirements provided by the OEM partner. Eleven static load cases and design constraints are prescribed on structural parts: (i) door sag (two subcases); (ii) sash rigidity (two subcases); (iii) door over opening; (iv); beltline stiffness; (v) outer panel stiffness; (vi) mirror mount rigidity (two subcases); (vii) speaker mount rigidity; and (viii) window regulator stiffness. Given the absence of the OEM design constraint requirements of beltline stiffness, door over opening, and mirror mount stiffness, we obtained these requirements by applying the same load cases on the baseline steel door.

This was succeeded by the optimization process—(i) free-size, (ii) size, and (iii) shuffle—performed using the Altair software suit. In free-size optimization, the total thickness of each of the FEs in a component is reduced from its initial value to a feasible value satisfying the load cases and manufacturing constraints. In size optimization, discrete thickness values are assigned to each ply in the component. Finally, in shuffle optimization, the stacking sequence of the plies in laminates is determined for improved stiffness. It is to be noted that the BIW component is eliminated in the optimization runs to ensure a higher computational efficiency. Although, the effect of BIW deformation is incorporated by adjusting the door sag requirement and considering BIW deformation at the hinges.

Figure II.4.D.6 presents the thickness distribution plot of the inner panel (IP) and the beltline stiffener (BS) for the two designs where (a) and (b) represent the design with the composite beam and the design with the steel beam, respectively. The minimum thickness is predefined as 1.2 mm to meet the minimum manufacturing thickness criteria for laminate. Our earlier studies have shown us that reducing minimum thickness value gives much lighter door design. Specifically, in design (a), the maximum thickness for BS is 3.6 mm around the hinge and latch regions, whereas in design (b), the maximum thickness of 3.3 mm of the steel beam is predominant almost throughout the BS region. A comparison of the thickness distribution of IP for both designs shows that maximum thickness obtained for case (a) is 5.7 mm and for case (b) is 6 mm. In case (a), this region is very small and located around the hinges, while in case (b), a major area of thick quasi-isotropic zone reaches maximum thickness. Also, the average thickness of the IP for case (a) is almost 1.5 times that of case (b). The mass of BS and IP is higher by 0.32 kg and 1.45 kg, respectively, for the steel beam case. The static performance for both designs along with baseline door is presented in Table II.4.D.2.

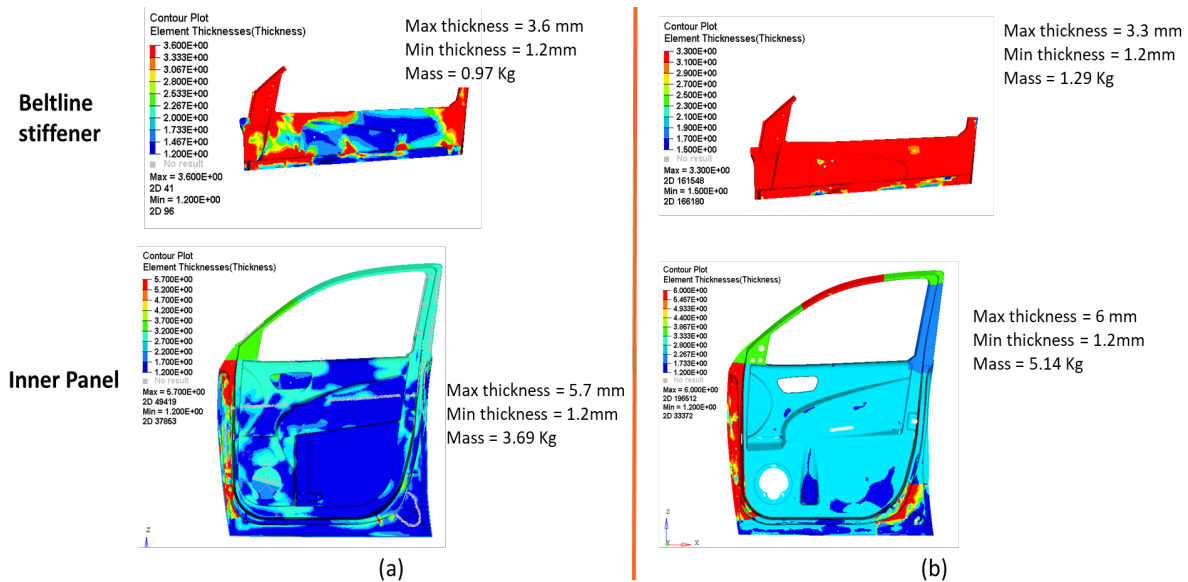


Figure II.4.D.6. Thickness distribution for BS and IP for two designs of composite door (a) with composite anti-intrusion beam and (b) with steel anti-intrusion beam. Source: Clemson University.

The overall mass of the door with the composite beam was obtained as 8.71 kg, while the door with the circular steel beam was obtained as 11.15 kg. It is important to note that both designs satisfied design constraints, a few of which are listed in Table II.4.D.2; however, the door design with the steel beam is heavier by 1.73 kg from the target value.

Table II.4.D.2. Optimization results for composite door designs.

Sample No.	Target Category Subcase (Units)	Target	Case (a) – Door with composite beam	Case (b) – Door with steel beam
1	Mass Target			
1.1	Structural frame mass (kg)	9.42	8.71	11.15
1.2	Total Mass (kg)	18.28		
2	Frame Related			
2.1	Door Sag (mm)	Req.	4.97 < Req.	4.55 < Req.
2.2	Sash Rigidity at B (mm)		3.73 < Req.	3.26 < Req.
2.3	Beltline stiffness – IP (mm)		0.64 < Req.	0.49 < Req.
2.4	Window Regulator (mm)		0.47 < Req.	0.18 < Req.
2.5	Mirror mount rigidity in X (mm)		0.73 < Req.	0.78 < Req.
2.6	Door Over Opening (mm)		11.55 < Req.	10.71 < Req.
2.7	Speaker mount stiffness (mm)		0.35 < Req.	0.35 < Req.

Three dynamic load cases were simulated, namely the FMVSS 214, the FMVSS DB, and the RP. The first load case is a quasi-static cylindrical barrier intrusion test, involving the use of a barrier to deform the door (e.g., quasi-static loading rate) to a depth of 18 inches, which follows the FMVSS 214s standard. The other two load cases are dynamic impact scenarios: The DB test per FMVSS 214 and the RP test per FMVSS 214. The following sections document the simulation model setup in LS-DYNA for all dynamic load cases and procedures to map geometry and materials selection into the meshed models for dynamic impact simulations.

A complete baseline metal door model was provided by our OEM partner, including the geometry, materials, and assembly features. The baseline door was modified by deleting appropriate metal parts that are being replaced by lightweight composite components. This approach keeps all carryover metal components (those that are not being replaced) intact in the appropriate geometric locations and assembly configurations. Constraints, boundary conditions, and loading conditions remain unchanged. Each composite component that is added to the door assembly is saved as a separate file, so that modular assembly and updating of component design is simplified. The bolted connections within the door, as well as from the hinges to the door, are modeled as ridged bodies. The latch was carried over and a minimal transformation had been performed to fit the draft angles for composite geometries. The window-rail system is also carried over from the OEM metal door. Adhesive connections had been modeled with solid cohesive elements and the contact formulation CONTACT_TIED_EDGE_TO_SURFACE. The quasi-static pole test entails measuring a cylinder pushed into the door with a constant velocity and the force-displacement response. Figure II.4.D.7.(a), (b), and (c) show the baseline metal door response and shows the targets by the FMVSS as well as the OEM standards. Note that the OEM requirements are generally higher than the FMVSS requirements.

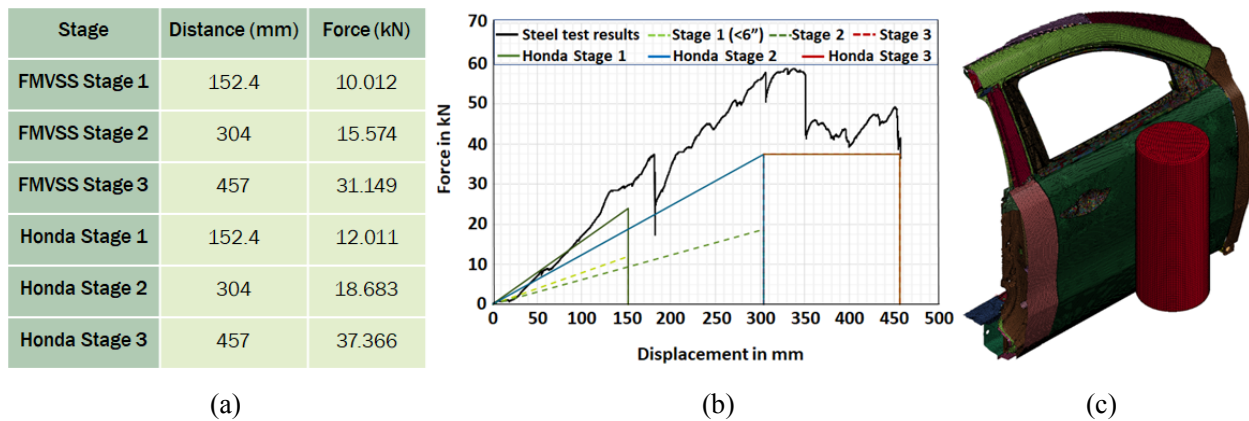


Figure II.4.D.7. (a) Quasi-static pole performance targets; (b) metal door response; and (c) metal door model. Source: Clemson University.

A number of initial material and ply lay-up analysis have been performed in order to understand deformation and failure modes of the door and door sub-components during the applied load case and have been documented in quarterly reports. Previous simulations showed that one crucial location in the composite door is the area where the window regulator is mounted at the bottom of the door IP. This area is critical as it lies directly below the impactor at the lower half of the door panel and represents the most severe local deformation during the test. To improve deformation response in this zone, a metal plate is integrated (either bonded or insert molded from a process perspective) that also provides the mounting provisions for the window regulator. In addition, studies have also been done for two impact beam scenarios: using the baseline metal impact beam in the door assembly, and the composite impact beam in the door assembly show in Figure II.4.D.8.

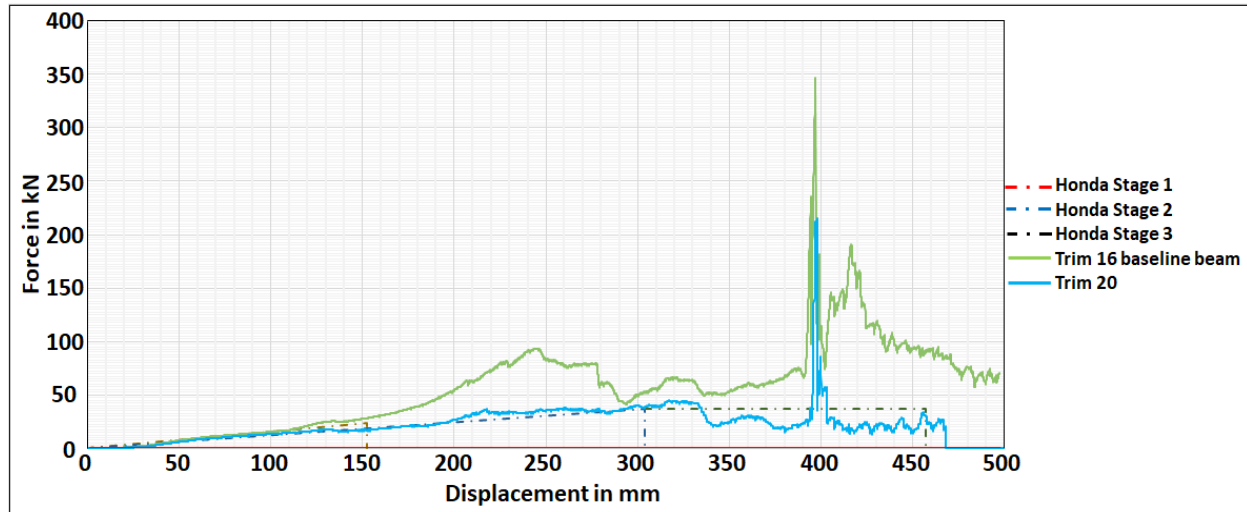


Figure II.4.D.8. Force-displacement response with baseline metal and composite impact beam for Trim 16. Trim 16 design uses a composite IP with a metal insert near the window regulator location. Trim 20 is another design, which provided lower force in the OEM Stage 3 zone. Source: Clemson University.

In addition to the quasi-static pole case, two full car simulations from the OEM partner are available for the DB and RP tests, followed by the incorporation of the composite door in these models to analyze the global response of the door. The success criteria for both of our DB and RP simulations were discussed with the OEM in terms of ensuring the absence of either cracks or breaks visible to the driver, as well as to ensure there is no failure of the intrusion beam, particularly in terms of trim slippage or breakage of the entire beam. In addition to these requirements, neither the windowsill nor the rocker should exhibit a catastrophic failure. We will use a LS-DYNA post-processing template provided by the OEM partner to capture the intrusion requirements and tracking points implemented on the outer panel for deformation modes. In Figure II.4.D.9.(a), (b), and (c), we illustrate the failures from the RP full car simulation. The two pictures on the left show the composite beam, while the picture on the right shows the failure with the baseline beam. The failure modes are similar for both the baseline beam and the composite intrusion beam.

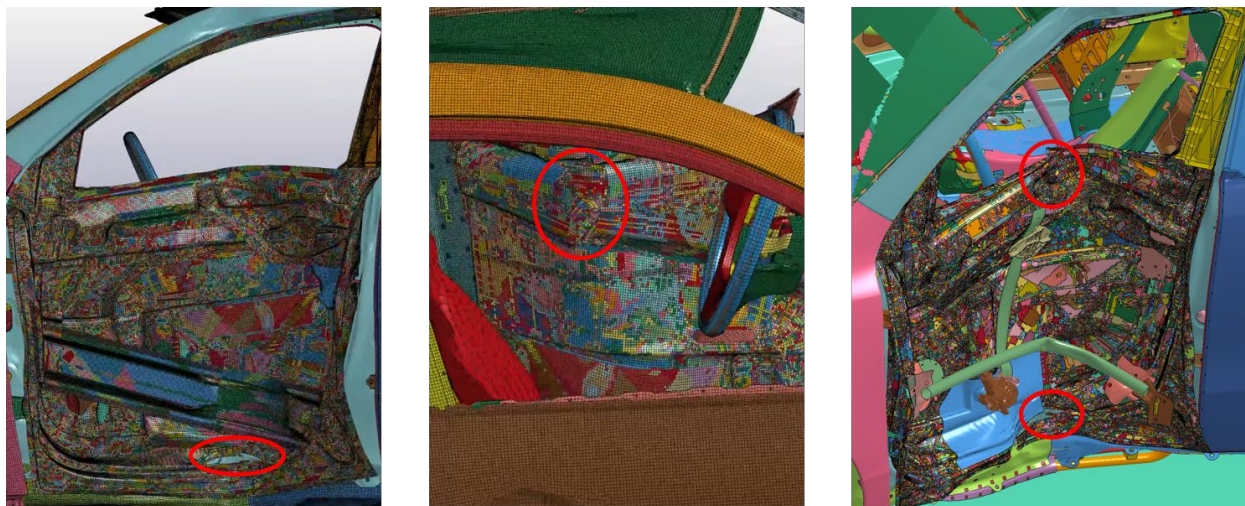


Figure II.4.D.9. RP full car simulation results for two locations (a) and (b) of the composite door with composite intrusion beam and (c) the metal intrusion beam. Source: Clemson University.

The performance in the DB test is roughly the same in both models, where no major failures were noted. We are now analyzing the DB test results with OEM-supplied templates to assess all of the performance metrics, particularly the intrusion and failure modes, as shown in Figure II.4.D.10.



Figure II.4.D.10. Deformation and damage under DB impact conditions. Source: Clemson University.

Summary of NVH Simulations

Two methods were used to analyze the NVH performance of the composite door. The first approach involved modeling and evaluation of the Eigen-frequencies and mode shapes of full vehicle (simplified model) using FE model at low frequencies (< 200 Hz). The second approach involved the use of Statistical Energy Analysis (SEA) to evaluate Sound Transmission Loss (STL) through the composite door panel at high frequencies (>1,000 Hz).

To perform the low frequency analysis, an acoustic noise problem is setup to simulate both external and ambient noises, such as traffic noise or road construction noise. A unit acoustic source is placed at 1 m distance from driver side window and response is observed at driver ear location. A FE acoustic mass is modeled representing oversimplified geometry of full vehicle compartment (i.e., BIW along with doors, windshield, and windows), which is placed in a fluid domain. This analysis is limited to low frequency range (<200 Hz) due to several FEA limitations, one of which is the size of the elements that should be smaller than 1/6 of the acoustic wavelength. It is computationally impractical to use the FE approach at higher frequencies. The primary focus here is to understand the effect of different material systems on low frequency vibro-acoustic response, namely steel vs composite and conventional laminated soda lime glass (SLG) vs Gorilla hybrid glass (GHG). To this end, four different acoustic models are developed and investigated by a baseline door with SLG, a composite door with SLG, a baseline door with GHG, and a composite door with GHG, as shown in Figure II.4.D.11.

The response at the driver's ear location is observed by evaluating sound pressure level (SPL), which is presented in Figure II.4.D.12. The SPL at the driver's ear is higher for the composite door when compared to the baseline door at a low frequency range, as seen from Figure II.4.D.12.(a). The maximum difference of about 20 dB is obtained at 110 Hz. This is because for low frequencies, acoustic behavior is mostly controlled by component mass. A comparison of the conventional window (SLG) with 30% thinner hybrid (GHG) window indicates no significant change in the SPL at the driver's ear.

At high frequencies, particularly those between 2,000 to 5,000 Hz, even a slight change in SPL can cause an adverse effect upon human hearing. At these high frequencies, the dynamic system becomes very complex due to the high number of degrees of freedom and the high sensitivity of the Eigen-frequency to even a slight perturbation in the system properties; thus, a less detailed system using SEA to describe the average response of the dynamic system. Commercial SEA software SEAM[®] by Cambridge Collaborative Inc. is being used to setup the model and run the analysis. The investigation is carried out by setting up a two-room sound test for the door panel wherein one room acts as an acoustic source and the other as a receiver. A total of four structural components—IP, BS, outer panel, and anti-intrusion beam—along with the window and the weather seals is modeled for investigation. The response is compared for baseline steel and composite door by determining the STL through the door panel, which is presented in Figure II.4.D.13.(a). At lower frequencies vibro-acoustic behavior is generally mass controlled which justifies high STL for baseline door which is 50% heavier. However, for the peak sensitive range to human hearing which is 2-6 kHz, the difference is 1.5 – 4.5 dB. Further the effect of adding a leakage and effect of replacing a conventional SLG with GHG is studied and presented in Figure II.4.D.13.(b) and (c), respectively.

Note that the addition of a small leakage area of 20 mm² reduces STL for the baseline door by 2-10 dB results in noise levels that can significantly damage human hearing. Note also, however, in Figure II.4.D.13.(c), a significant improvement of STL by 1-4 dB when embedded into the composite door. Sensitivity analysis determined that that minimizing leakage and incorporating Gorilla hybrid window design will significantly improve NVH performance of composite door. Further investigation will be carried out with a more refined model that captures various structural connections appropriately.

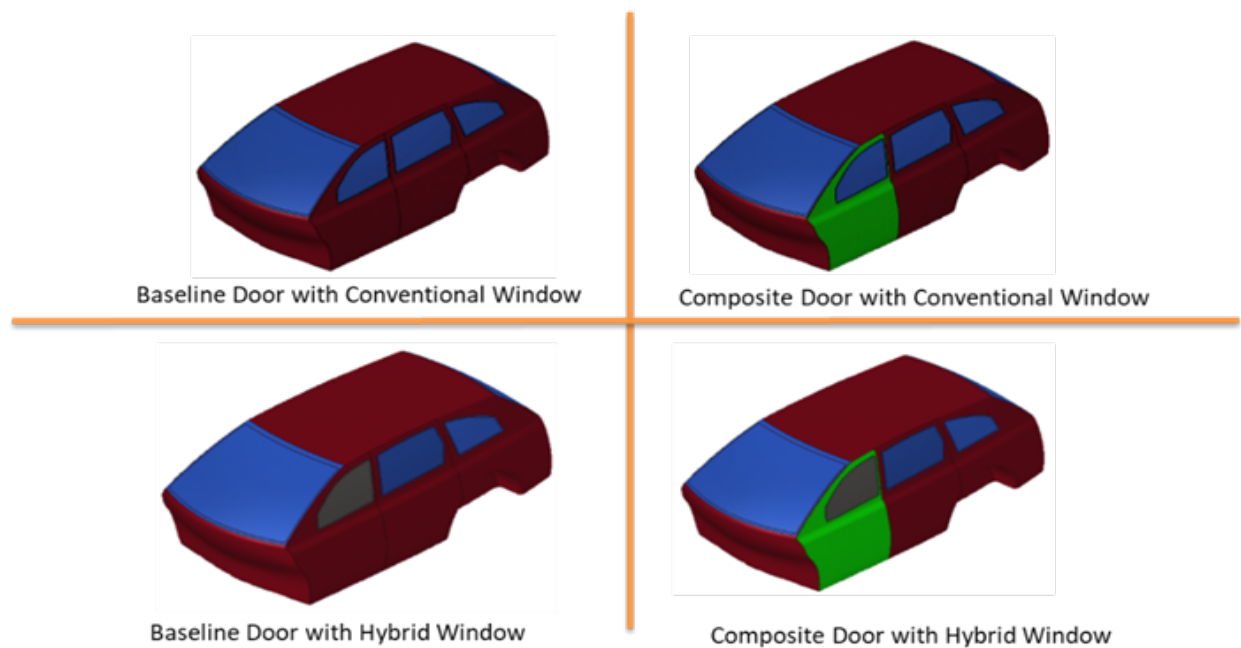


Figure II.4.D.11. Deformation and damage under DB impact conditions. Source: Clemson University.

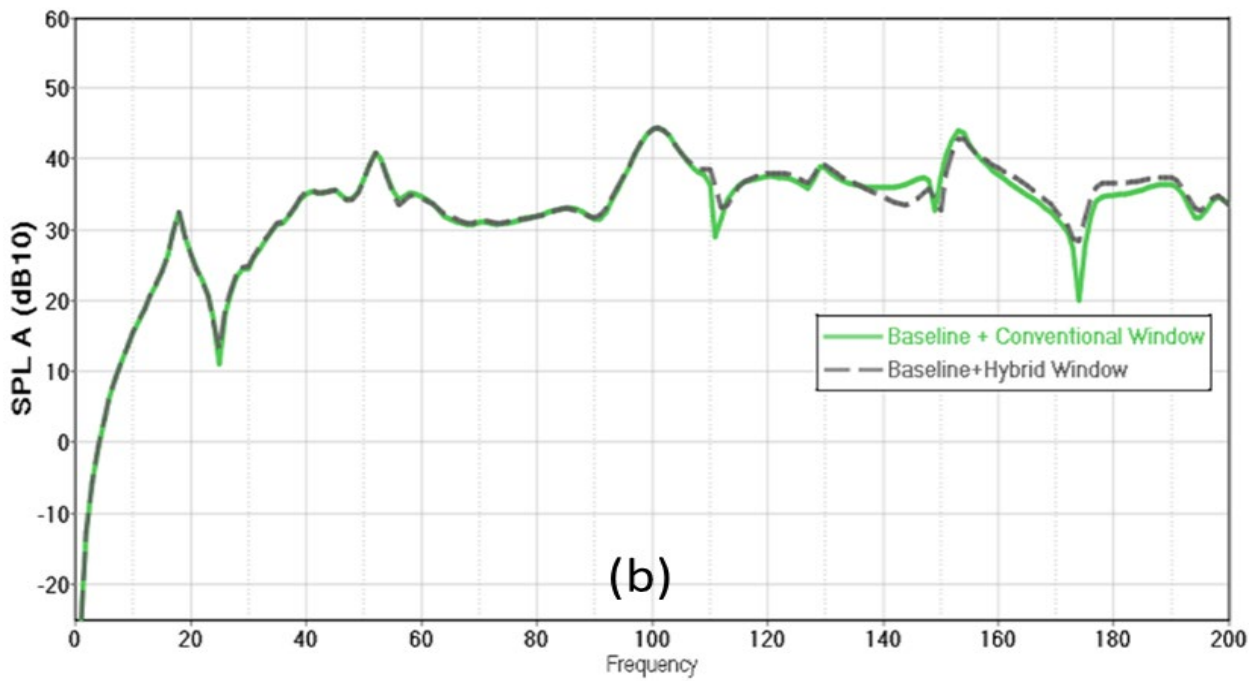
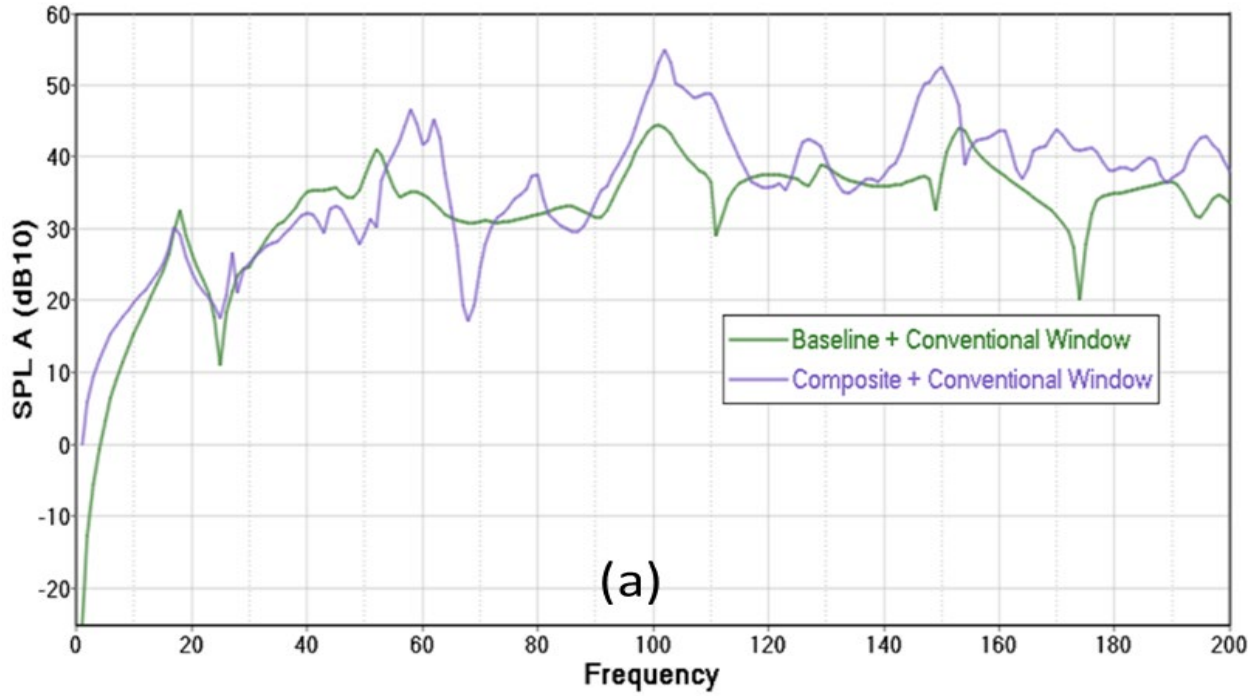


Figure II.4.D.12. SPL at driver ear at low frequencies for (a) Baseline vs Composite door; and (b) Conventional window vs Gorilla hybrid window. Source: Clemson University.

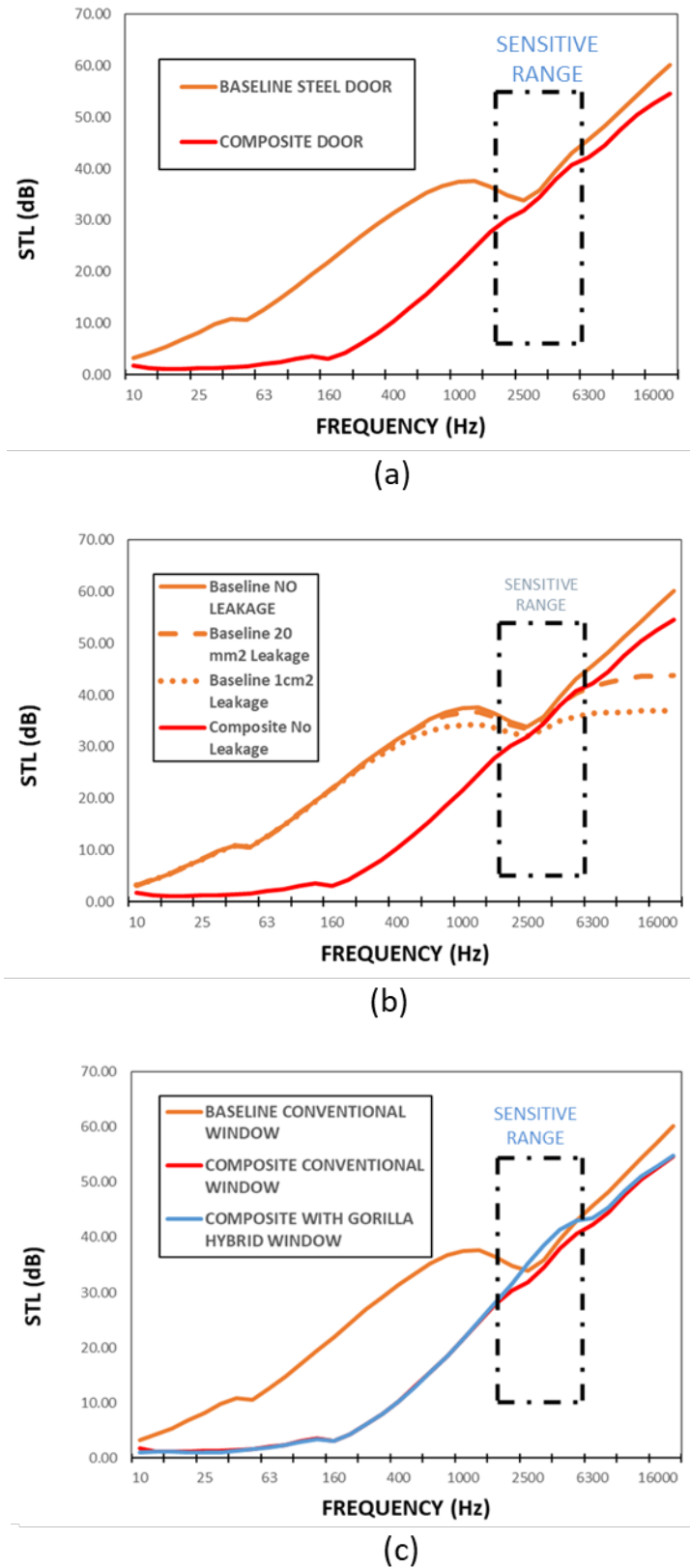


Figure II.4.D.13. Plot of STL vs frequency (a) Baseline vs Composite door; (b) effect of leakage area on baseline door; and (c) effect of Gorilla hybrid window on composite door. Source: Clemson University.

Cost Modeling Summary

Currently, the team is working on developing a detailed factory layout using Tecnomatix Plant simulation. A detailed layout for thermoforming, as shown in Figure II.4.D.14, (e.g., IP, upper beltline outer section, upper beltline inner section, anti-intrusion beam, lower hinge reinforcement) and injection molding (e.g., sash reinforcement, weather seal holder, lower class A panel, Sash garnish, map pocket, door handle structure) processes and the assembling of the parts have been developed. The detailed setup time, recovery time, processing time, and cycle time are entered for each of the individual processes. Currently, we are deriving on-the-line balancing aspects for increasing the throughput and optimizing the factory layout.

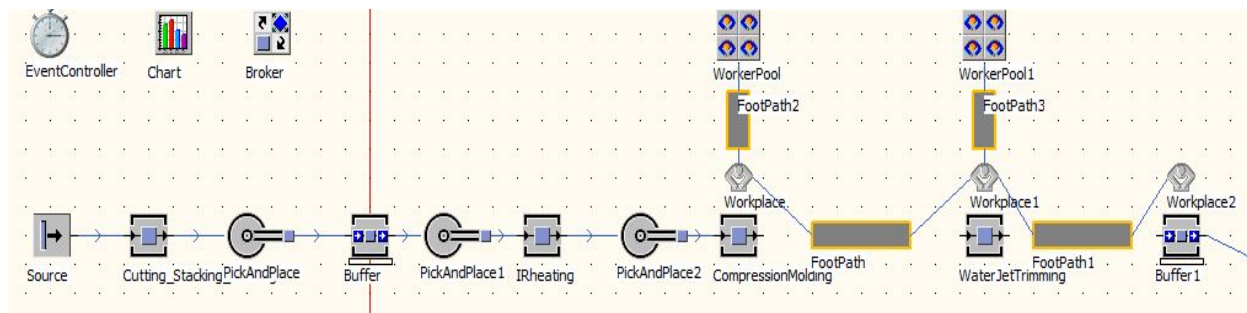


Figure II.4.D.14. Thermoforming process layout. Source: Clemson University.

Conclusions

The research focus during FY 2018 involved the refinement of the door design using an iterative process involving design development, cost analysis, static, and crash simulations. The refined door frame was further re-engineered for manufacturability and sub-component integration. This design for manufacturing inadvertently increased the overall door weight. The team is currently evaluating different component designs and materials in order to achieve the mass target.

Key Publications

1. Yerra, V., S. A. Pradeep, I. B. Ozsoy, A. Kothari, G. Li, S. Pilla, L. Fuessel, B. Haque, S. Yarlagadda, S. Malcolm, and D. Detwiler, 2018, "A systems approach to develop ultra-lightweight composite door using fiber reinforced thermoplastics," Proceedings of the Society of Plastics Engineers Automotive Composites Conference and Exhibition (SPE-ACCE), September 5–7, 2018, Novi, MI, USA.
2. Limaye, M., A. Kothari, S. Pilla, and G. Li, 2018, "Manufacturing-to-response pathway of lightweight thermoplastic composite parts for automotive applications," Proceedings of the SPE-ACCE, September 5–7, 2018, Novi, MI, USA.
3. Kothari, A., M. Limaye, A. Yerra, G. Li, and S. Pilla, 2018, "NVH performance analysis of a thermoplastic composite door for lightweight vehicle design," Proceedings of the SPE-ACCE, September 5–7, 2018, Novi, MI, USA.

References

1. Kelly, J. C., J. L. Sullivan, A. Burnham, and A. Elgowainy, 2015, "Impacts of vehicle weight reduction via material substitution on life cycle greenhouse gas emissions," *Environ. Sci. Technol.*, Vol. 49, pp. 12535–12542.
2. Mi, H.-Y., X. Jing, J. Peng, L.-S. Turng, and X.-F. Peng, 2013, "Influence and prediction of processing parameters on the properties of microcellular injection molded thermoplastic polyurethane based on an orthogonal array test," *J. Cell. Plast.*, Vol. 49, pp. 439–458.

3. Chang, S. H., and S. S. Cheon, 2006, “In-plane directional mechanical properties of C fabric skins in sandwich structures after thermoforming,” *Compos. Struct.*, Vol. 75, pp. 577–581.
4. Yu, Y., J. Ye, Y. Wang, B. Zhang, and G. Qi, 2013, “A meso-scale ultrasonic attenuation FE model of composites with random-distributed voids,” *Compos. Sci. Technol.*, Vol. 89, pp. 44–51.

Acknowledgements

The team acknowledges the financial support provided by the Department of Energy (Project # DE-EE0007293). The team would also like to thank our OEM partner for their inputs, insights and knowledge transfer over the duration of all our research tasks. The team would also thank Corning Inc. for supporting this effort by prototyping a lightweight glazing. Lastly the team would like to thank our material suppliers Tencate, BASF and Polyone for supplying us with various material forms used for characterization.

(This page intentionally left blank)

U.S. DEPARTMENT OF
ENERGY

Office of
**ENERGY EFFICIENCY &
RENEWABLE ENERGY**

For more information, visit:
energy.gov/eere/vehicles

DOE/EE-1827 April 2019